Proceedings of 15:th Scandinavian International Conference on Fluid Power

Editors: Petter Krus, Liselott Ericson & Magnus Sethson

Published by Linköping University Electronic Press, 2017

Series: Linköping Electronic Conference Proceedings, No. 144
ISSN: 650-3686, eISSN: 650-3740
ISBN: 978-91-7685-369-6
URL:http://www.ep.liu.se/ecp/contents.asp?issue=144

© The Authors

SICFP2017

This is the proceedings of the 15th Scandinavian International Conference on Fluid Power held at Linköping University in Sweden on 7-9 June 2017. The theme of the conference was "Fluid Power in the Digital Age". The contributions are well aligned with this theme, and are indeed reflecting the great developments. We are very grateful to the effort put in by the authors to produce such high quality papers, and also to those taking time to review papers to further enhance the quality. The contributions clearly shows that the fluid power industry, and academia, have both challenges as well as opportunities in keeping up with the evolving capabilities provided by the digitalization. It was with great joy to see old and new colleagues and friends attending our conference and the division of Fluid and mechatronic systems, at Linköping University. The conference is a bi-annual event, with alternating localization between Linköping in Sweden and Tampere in Finland. The process of hosting such an event is a great effort for our organization and I would like to thank all those involved in organizing this conference, and wish good luck with the next one to our Finnish colleagues.
Thank you!
Prof. Petter Krus
Head of Division Fluid and Mechatronic Systems.

Review Process

Each author attending the conference days had the opportunity to select from three different ways of presenting their contribution. Firstly, a reviewed process with at least two international reviewers of each contribution. The process resulted in most cases with feedback from the reviewers with comments spanning everything between diagram legends to scientific methods. Some proposed papers where rejected upon recommendations from reviewers. Secondly contributions where also presented in industry sessions where the review process where internal only by the staff of the division. A third extended abstract presentation format where also presented during the conference.

This proceedings contain all presented contributions from the reviewed papers in the first section and thereafter the non-reviewed papers in second section. All reviewed papers are marked in the footer by the acceptance date.

Content

The conference contributions are divided into two sections, peer-reviewed and non-reviewed.

Peer-reviewed Papers

Hydraulic Infinite Linear Actuator – The Ballistic Gait Digital Hydro-Mechanical Motion
Martin Hochwallner and Petter Krus
Page 10.

Experimental Investigation of a Displacement-controlled Hydrostatic Pump/Motor by Means of Rotating Valve Plate
Liselott Ericson, Samuel Kärnell and Martin Hochwallner
Page 19.

Use of LMS Amesim® Model to Predict Behavior Impacts of Typical Failures in an Aircraft Hydraulic Brake System
Mário Maia Neto and Luiz Carlos Sandoval Góes
Page 29.

Modeling and Simulation of a Single Engine Aircraft Fuel System
Nathan Raphael do Nascimento Pinheiro and Luiz Carlos Sandoval Góes
Page 45.

Modeling and Parametric Identification of a Variable-Displacement Pressure- Compensated Pump
Filipe Spuri and Luiz Goes
Page 52.

Emission reduction of mobile machines by hydraulic hybrid
Seppo Tikkanen, Elias Koskela, Ville Ahola and Kalevi Huhtala
Page 62.

Model Based System Identification for Hydraulic Deep Drawing Presses
Tobias Schulze and Jürgen Weber
Page 69.

Cloud-Based System Architecture for Driver Assistance in Mobile Machinery
O. Koch, B. Beck, G. Heß, C. Richter, V. Waurich, J. Weber, C. Werner and U. Aßmann
Page 81.

Enhancing safety of independent metering systems for mobile machines by means of fault detection
B. Beck and J. Weber
Page 92.

Real-Time Parameter Setpoint Optimization for Electro-Hydraulic Traction Control Systems
Addison Alexander and Andrea Vacca
Page 104.

Model-based Analysis of Decentralized Fluidic Systems in Machine Tools
Linart Shabi, Juliane Weber and Jürgen Weber
Page 116.

Optimal Control for Hydraulic System with Separate Meter-In and Separate Meter-Out
Gerhard Rath and Emil Zaev
Page 125.

Simulation study of a digital hydraulic independent metering valve system on an excavator
Miikka Ketonen and Matti Linjama
Page 136.

Sensorless position estimation of simulated direct driven hydraulic actuators
T. Sourander, M. Pietola, T. Minav and H. Hänninen
Page 148.

An Approach to Combine an Independent Metering System with an Electro-Hydraulic Flow-on-Demand Hybrid-System
M. Wydra, M. Geimerg and B. Weiss
Page 161.

An Zero-Flowrate-Switching (ZFS) Control Method Applied in a Digital Hydraulic System
Shuang Peng
Page 172.

A Hardware-In-The-Loop (HIL) Testbed for Hydraulic Transformers Research
Sangyoon Lee and Perry Y. Li
Page 179.

Decentralized Hydraulics for Micro Excavator
Shuzhong Zhang and Tatiana Minav and Matti Pietola
Page 187.

Modelling Dynamic Response of Hydraulic Fluid Within Tapered Transmission Lines
Jeremy ven der Buhs and Travis Wiens
Page 197.

Predictive Dynamic Engine Speed Reduction in Mobile Hydraulic Equipment
Travis Wiens
Page 206.

Study of Energy Losses in Digital Hydraulic Multi-Pressure Actuator
Mikko Huova, Arttu Aalto, Matti Linjama and Kalevi Huhtala
Page 214.

System level co-simulation of a control valve and hydraulic cylinder circuit in a hydraulic percussion unit
Håkan Andersson, Kjell Simonsson, Daniel Hilding, Mikael Schill and Daniel Leidermark
Page 225.

A study on a mathematical model of gas in accumulator using van der Waals equation
Shuto Miyashita, Shuce Zhang and Kazushi Sanada
Page 237.

Displacement Control Strategies of an In-Line Axial-Piston Unit
L. Viktor Larsson and Petter Krus
Page 244.

Non-reviewed Papers

Water Hammer Induced Cavitation - A Numerical and Experimental Study
Marcus Jansson, Magnus Andersson, Maria Pettersson and Matts Karlsson
Page 256.

Early Insights on FMI-based Co-Simulation of Aircraft Vehicle Systems
Robert Hallqvist, Robert Braun and Petter Krus
Page 262.

Energy Efficiency Comparison of Electric-Hydraulic Hybrid Work Implements Systems
Björn Eriksson, Vivek Bhaskar and Ralf Gomm
Page 272.

The Hydraulic Infinite Linear Actuator with Multiple Rods
Magnus Landberg, Magnus Sethson and Petter Krus
Page 279.

The Lattice Boltzmann Method used for fluid flow modeling in hydraulic components
Bernhard Manhartsgruber
Page 295.

A Global Optimisation of a Switched Inertance Hydraulic System based on Genetic Algorithm
Min Pan
Page 302.

Non-linear Control of a Piezoelectric Two Stage Servovalve
Johan Persson, Andrew Plummer, Chris Bowen and Phil Elliott
Page 310.

Assessment of Electric Drive for Fuel Pump using Hardware in the Loop Simulation
Batoul Attar and Jean-Charles Mare
Page 320.

A study on thermal behavior of pump-controlled actuator
T.A. Minav and M. Pietola
Page 333.

Modeling and Verification of Accumulators using CFD
Victor Irizar, Peter Windfeld Rasmussen, Olivier Doujoux Olsen and Casper Schousboe Andreasen
Page 340.

Torque Control of a Hydrostatic Transmission Using Extended Linearisation Techniques
Robert Prabel and Harald Aschemann
Page 352.

Design and Optimization of a Fast Switching Hydraulic Step-Down Converter for Position and Speed Control
Marcos P. Nostrani, Alessio Galloni, Henrique Raduenz and Victor J. De Negri
Page 361.

Analysis of Flow Angles and Flow Velocities in Spool Valves for the Calculation of Steady-State Flow Forces
Patrik Bordovsky and Hubertus Murrenhoff
Page 371.

Barrel tipping in axial piston pumps and motors
Peter Achten and Sjoerd Eggenkamp
Page 381.

An Open-Source Framework for Efficient Co-simulation of Fluid Power Systems
Robert Braun, Adeel Asghar, Adrian Pop and Dag Fritzson
Page 393.

Towards Finding the Optimal Bucket Filling Strategy through Simulation
R. Filla and B. Frank
Page 402.

Peer Reviewed Papers

The following papers are peer-reviewed by at least two independent reviewers within the international fluid power community. Each contribution is marked at the bottom of each page with its final date for acceptance during the review process.

Hydraulic Infinite Linear Actuator – The Ballistic Gait Digital Hydro-Mechanical Motion

Martin Hochwallner and Petter Krus

Division of Fluid and Mechatronic Systems, Linköping University, Linköping, Sweden
E-mail: martin.hochwallner@liu.se

Abstract

The Hydraulic Infinite Linear Actuator, HILA, has been presented in [1], [2], and [3]. The novel actuator consists of one, two or more double acting cylinders with a common piston rod and hydraulically detachable pistons. In the basic gait [1], alternatingly, one cylinder engages and drives the load while the other retracts, the HILA thus works in a kind of rope climbing motion. But the concept allows also other gaits, pattern of motion.
This contribution focuses on the ballistic gait, a pattern of motion where one cylinder engages to give the load a push. Then the load carries on with its motion by inertia, cylinders disengaged. The actuator realizes thus hydro-mechanical pulse-frequency modulation (PFM).
This gait is energy efficient and able to recuperate energy.

Keywords: novel actuator, infinite linear motion, digital fluid power, digital hydro-mechanical motion, energy recuperation

1 Introduction

The gait of the Hydraulic Infinite Linear Actuator, HILA, Figure 1, where alternatingly one cylinder disengages to retract has been studied and presented in for example [1]. This gait is characterized by, that all time at least one cylinder is engaged to drive the load, Figure 3a. A smooth, high performance motion can be realized by this actuator in this gait. Gaits define pattern of motion. HILA can be operated in various gaits, whereby gaits are suitable for various situations and shall be used in together in an application to achieve optimal performance. This contribution presents another gait, the ballistic gait, Figure 3b, where temporarily all cylinders are disengaged to allow some kind of freewheeling exploiting the inertia of the load.

Conventional hydraulic linear actuators, i.e. cylinders, are common and mature components of hydraulic systems. Ongoing research focuses on secondary control with multi-chamber cylinders [5], various concepts of digital hydraulics [6], individual metering [7], advanced control concepts [8, 9], and sensor-less positioning with stepper drives [10].

In [11] presented Gall and Senn a linear hydraulic drive exploiting the inertia of the load in combination with so called freewheeling valves for saving energy [6]. In the ballistic gait, this basic idea is applied on HILA. The freewheeling valves allow motion without discharging flow from the supply line. The ballistic gait goes one step further and decouples the full hydraulics, even the cylinder, from the load and thus eliminates losses in the hydraulics and friction losses in the cylinder. The drawback is the necessity of retracting the cylinder. In this contribution, the simple but inefficient way of using the supply flow is applied. Research on effective alternatives is necessary.

The actuator can be operated solely in the ballistic gait, but the highest benefit is expected in systems combining gaits.

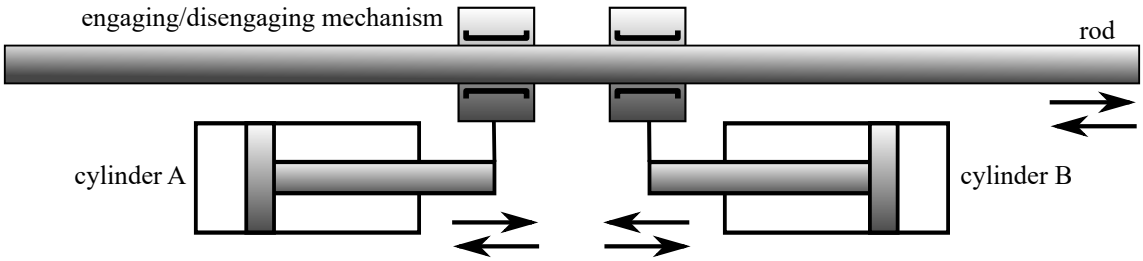

Figure 1: HILA: Two double-acting cylinders temporarily engage/disengage to the common rod to driving the load. The load may be attached to the rod or to the actuator.

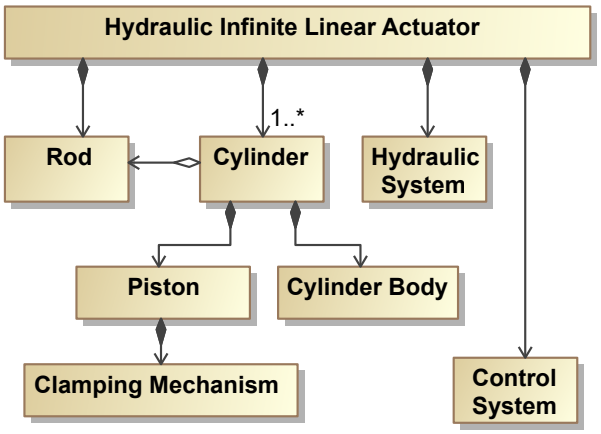

Figure 2: Structural breakdown as SysML Block Definition Diagram [4].

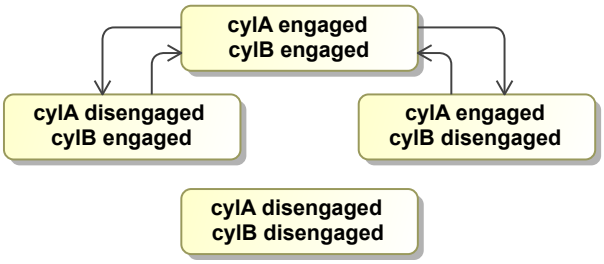

(a) The basic gait.

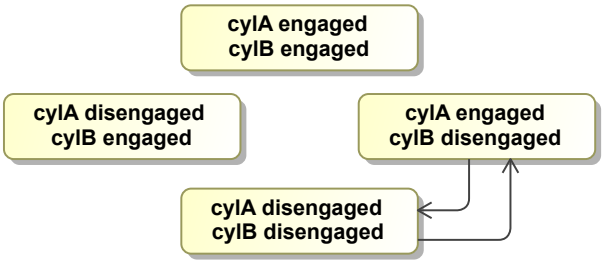

(b) The ballistic gait.

Figure 3: Gaits as Activity Diagram.

For example, machines may require the following working modes and thus gaits. A high performance, high accuracy working stroke with medium to infinite stroke length applying the basic gait. A short high force work stroke, where the force and stiffness of two cylinders are added up. A holding period utilizing the infinite hydraulic stiffness presented in [2] where no power is required. And a fast and efficient not-work stock for retraction realized by the ballistic gait. One application field could be mounting plates of machines for advanced injection molding.

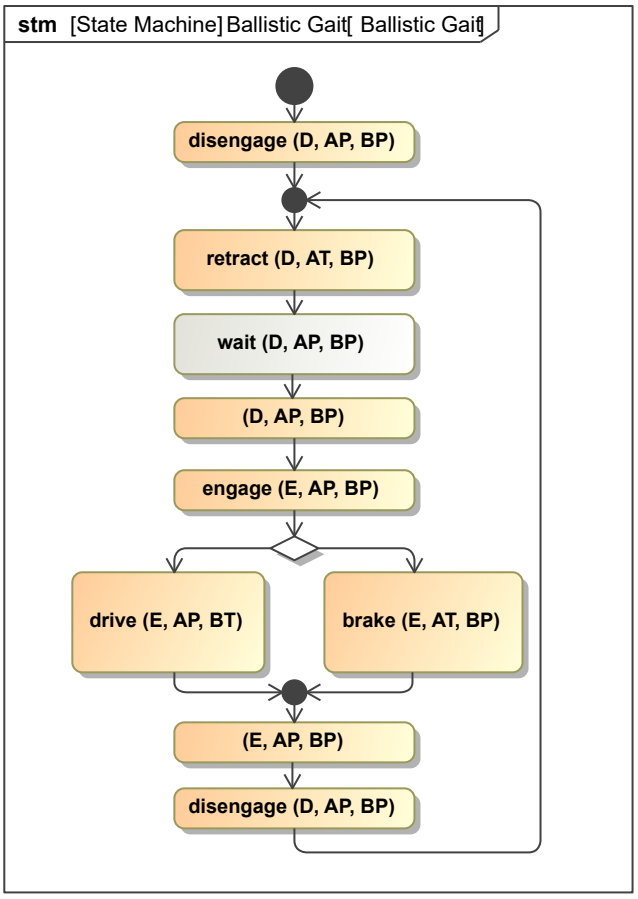

Figure 4: Control sequence depicted as SysML State Machine [4].
The controller outputs are stated in braces: E: engaged, D: disengaged, AP, AT, BP, AT: chambers: A, B; pressure levels: P: supply, T: tank.

2 Basic Concept

The control concept is shown in Figure 4 and the corresponding schematics of the hydraulic circuit in Figure 6. To move the load, first the cylinder retracts to the retracted position. An end-position cushion is used to stop the cylinder. The cylinder does not drive any load beside the piston assembly and so the kinematic energy is low. After waiting for the engaging condition both valves are switched fully to the high pressure side so that the motion of the cylinder is not locked. Now the cylinder engages and the increasing friction in the clamping mechanism accelerates the piston to the velocity of the rod. By switching the valve of chamber B to the low pressure side, force is applied to accelerate the load. If instead, the valve of chamber A is switching to the low pressure side a force to deaccelerate the load is applied. When the cylinder reaches the end of driving stroke, both valve are switched to the high pressure side and so the rod drives the cylinder. Then, the cylinder disengages, before the piston hits the end-position cushion. To repeat the cycle the cylinder retracts to the retracted position.

effective load force	F_L	0 kN
effective mass / inertia	m_L	50 t
effective damping	b_L	2000 N s/m
supply pressure		250 bar
tank pressure		10 bar

Table 1: Parameters for the load and system in simulation

type		symmetric
piston area	A_{Pij}	1180 mm^2
free stroke		±100 mm
chamber volume at $x_{cyl} = 0$m	V_{0ij}	300 cm^3
piston mass	m_{Pi}	18 kg
viscous friction coefficient	b_{cyli}	1000 N s/m
coulomb friction		300 N

Table 2: Parameters for the cylinders in simulation

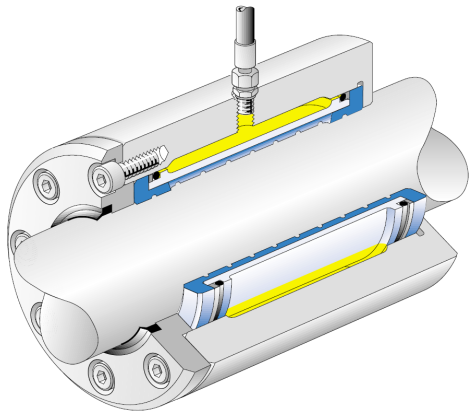

Figure 5: Hydraulic hub-shaft connection Octopus from ETP Transmission AB [12]

3 System

Figure 1 shows the schematic of the actuator. The actuator may drive a load attached to the rod or to the actuator itself (the rod is stationary). The assumed load consists of inertia, i.e. a mass m_L, and additional force F_L, and viscous friction. The parameters for the simulation are presented in Table 1 and 2.

The engaging / disengaging subsystem is the enabler for HILA. One component which can realize the engaging / disengaging subsystem is the COTS hydraulic hub-shaft connection [12], see Figure 5. The hub-shaft connection engages due to the hydraulically actuated membrane being pressed against the rod so that the friction between membrane and rod transfers the cylinder force. To actuate the hub-shaft connection the fast switching valve FSVi 4.1 [13] from Linz Center of Mechatronics GmbH is used. This system can fully engage and disengage within 10 ms.

Two exemplary hydraulic schematics to drive the cylinders are shown in Figure 6 and 7. The schematic in Figure 6 shows a system using one fast proportional valve per cylinder chamber and resemble thus an independent-metering valve.

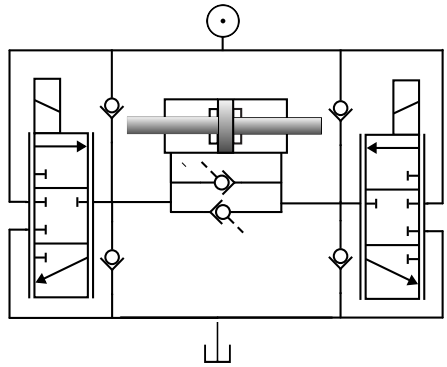

Figure 6: Schematic, system P, with independent-metering valve, one cylinder.
Independent-metering valve, modeled as one individual proportional valve per chamber. Four check valves protect against over pressure and cavitation. Two lockable check valves allow cross flow when required. Table 2 and 3 show the parameter.

nominal flow at 35 bar per edge	q_{nom}	25 L/min
corner frequency for small amplitudes	f_V	200 Hz
damping	δ	0.7
actuating time for signal step 0 to 1	$T_{V\,step}$	5 ms

Table 3: Parameters for the Proportional Valve in Simulation

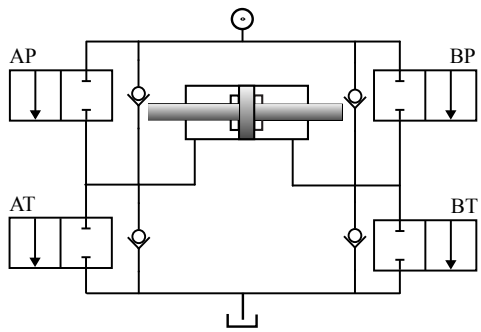

Figure 7: Schematic, system D, with four fast on/off valves, one cylinder.
A candidate for the on/off valves is the fast switching multi poppet valve from the Linz Center for Mechatronics (LCM) GmbH, [14]. Four check valves protect against over pressure and cavitation. Table 2 and 4 show the parameter.

nominal flow at 5 bar	q_{nom}	85 L/min
opening / closing time	T_V	2 ms

Table 4: Parameters for the On/Off Valve in Simulation. The parameters are based on th fast switching multi poppet valve from the Linz Center for Mechatronics (LCM) GmbH, [14].

Therefor, this system can be used to implement other gaits, for example for smooth motion as presented in [1]. Applications may require combining various gaits to fulfill their requirements. The system is dimensioned as an ordinary hydraulic

servo system to facilitate position control and not for high velocity. Additional to their protective function against overpressure and cavitation, the check-valve provide additional flow paths and thus increase the efficiency and reduce the requirements on the proportional valves. A capable check-valve design is presented in [10]. For this concept the proportional valves are used as three position on/off valves. The three positions are: P, when the cylinder chamber is connected to the supply pressure; T, when connected to the tank pressure; and off, when the valve is closed.

A second concept, fully digital, is shown in Figure 7. In cases where other gaits are required this concept can be combined with for example hydraulic switching technology as the Hydraulic Buck Converter [6], or it cam be equipped with parallel proportional valves resembling the system in Figure 6. In the level of detail as this contribution goes, the mayor difference between this two systems is the valve size. The on/off valves have 9 times the nominal flow rate of one edge of the proportional valves and produces thus only 1 % of the pressure drop. This system is dimensioned for high flow rates and thus high velocity. The additional flow path through the check valves is thus not relevant.

4 Simulation Results

Figures 8 and 9 show simulation results of the two presented systems. In both cases, the actuator accelerates the load, then keeps the velocity beyond the desired velocity, and after a few strokes the actuator deaccelerates the load to stop, whereby it recuperates energy. The systems go for different desired velocities. Although both systems and thus both simulation results are similar, the different working conditions emphasize different aspects of the concept. Some aspects appear when comparing the two results. Both systems use only one cylinder.

Plot 1 and 2 show the position of the load and the cylinder. The cylinder retracts, then thrusts the load, and then repeats.

While retracting, the velocity is limited to $-0.65\,\mathrm{m/s}$, and $-5.2\,\mathrm{m/s}$ respectively by the pressure drop through the fully opened valve. Plot 6, chamber pressure, for the system P, shows that in the load pressure, the difference between the chamber pressures, is small while retracting as it only covers the cylinder friction. For system D the force is a bit higher as the velocity is higher. As the retraction is much faster details can not be seen in the plot. Plot 5, F_{cyl}, does not include cylinder friction as it shows the force of the cylinder applied on the load, i.e. the force passing the engaging/disengaging mechanism.

During the acceleration phase the thrusts take less and less time as the velocity increases. Especially in the case of system P, decreases the force with increasing velocity as the pressure drop in the valves increase. With system D, this effect is small for the shown velocity. As shown in plot 4, supply flow, the needed flow is identical to a conventional cylinder, blue area, orange dashed line, but there is additional flow used for retraction, green area.

When a velocity beyond the desired velocity is reached, the actuator waits with the next thrust for the velocity to fall below the desired. For that time in contrast to a conventional cylinder no flow is needed, area below the orange dashed line. Therefor energy is saved.

In the deacceleration phase, chamber A instead of B is switched to the low pressure side and thus the force direction inverted. Now the cylinder drives the flow through the valve and thus the pressure drop through the valve increases the load pressure. Therefor the force and thus the acceleration is higher in the deacceleration than in the acceleration phase. The pressure drop and thus the force decreases with falling velocity. During this phase the check-valves provide an additional flow path and therefore, the pressure drop through the valve is much smaller as in the acceleration phase. The flow direction is reversed and thus the oil drawn from the tank and delivered into the supply line. Hence, energy is recuperated. As the flow from the tank has to pass trough the valves, boosted tank pressure is necessary, see Table 1. The check-valves improve the efficiency, especially in system P. The valves in system D are sufficient big so that check-valves influence in minor.

5 Analysis

The thrust stroke length L_{T} of a full thrust is constant, ignoring second order effect. Therefor, the energy added to the load is:

$$E_{\mathrm{T}} = F_{\mathrm{cyl}} L_{\mathrm{T}} \tag{1}$$

whereby the cylinder force F_{cyl} can be calculated as:

$$F_{\mathrm{cyl}} = (p_{\mathrm{A}} - p_{\mathrm{B}}) A - F_{\mathrm{losses}} \tag{2}$$

This is also the energy removed from the load while braking one full thrust.

Ignoring the friction losses and the pressure drop through the valves the nominal cylinder force $F_{\mathrm{cyl}N}$ is calculated as:

$$F_{\mathrm{cyl}N} = (p_{\mathrm{S}} - p_{\mathrm{T}}) A \tag{3}$$

and the nominal energy added per full thrust is

$$E_{\mathrm{T}N} = (p_{\mathrm{S}} - p_{\mathrm{T}}) A L_{\mathrm{T}} \tag{4}$$

For system D the nominal values represent the system well. The further analysis assumes a system which can sufficiently approximated by this nominal system, i.e. a system like system D.

The velocity of the load increases from the velocity before the thrust v_0 to the velocity after the thrust v_1 according to:

$$v_1 = \sqrt{v_0^2 + \frac{2}{m}(E_{\mathrm{T}} - E_{\mathrm{L}}^*)} \tag{5}$$

whereby E_{L}^* stands for the reduction of kinetic energy of the load due to load forces and friction in the duration corresponding to E_{T}.

The trend of the velocity during acceleration phase can thus be approximated by the following equation, where k is the

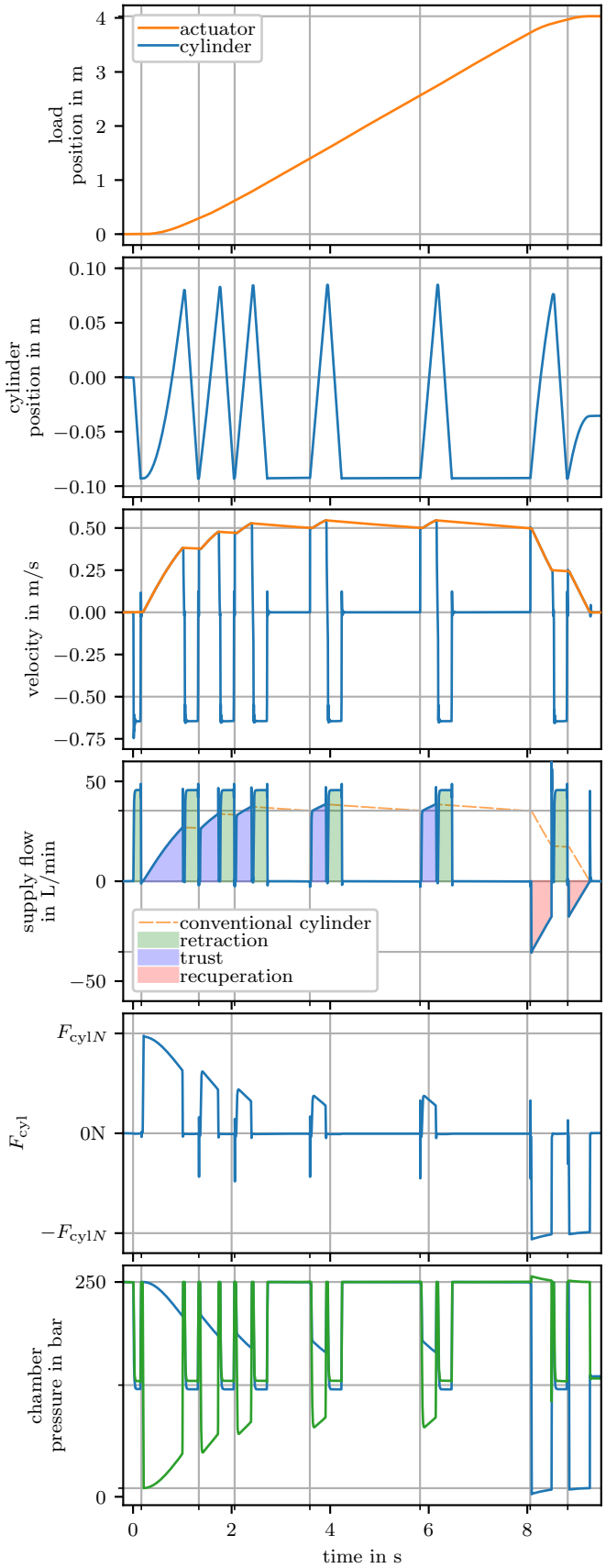

Figure 8: Simulation results system P: two proportional valves / independent metering,
Schematic Figure 6. The desired velocity is 0.5 m/s.

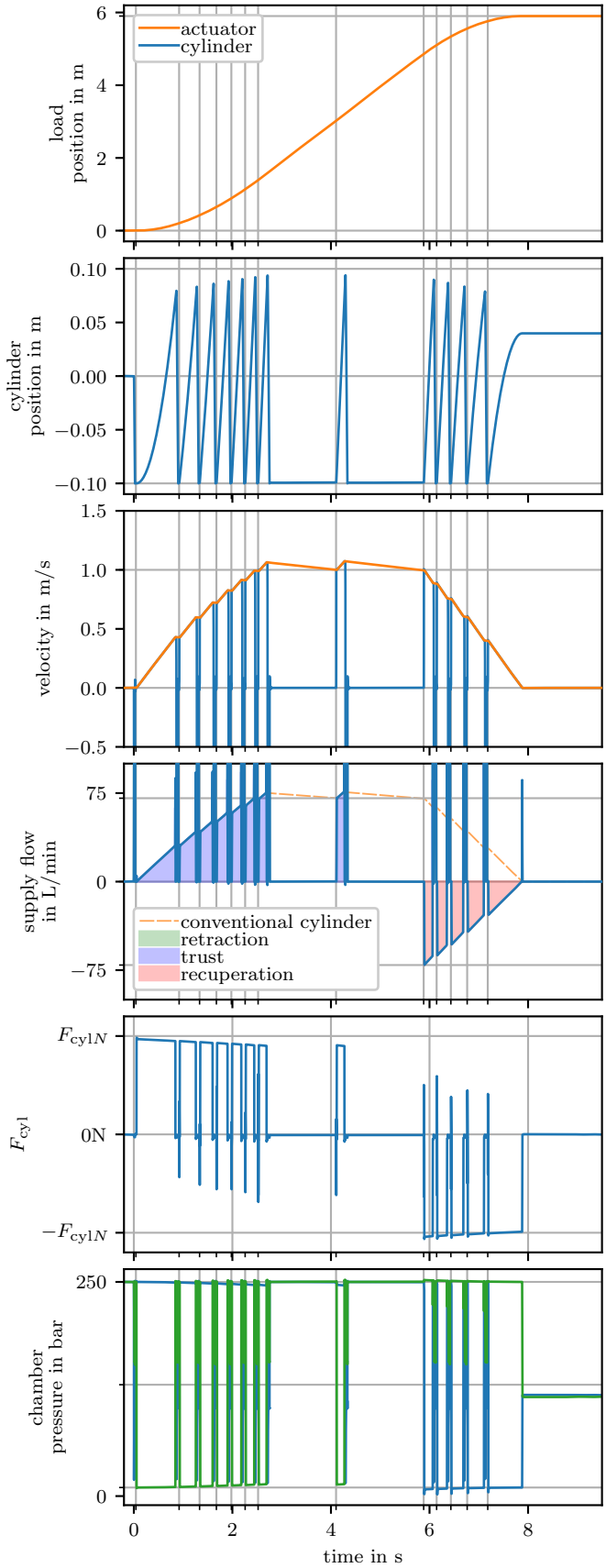

Figure 9: Simulation Results system D: on/off valves,
Schematic Figure 7. The desired velocity is 1 m/s.

number of thrusts. Losses, friction and external forces are ignored.

$$v_k = \sqrt{\frac{2}{m} E_{\mathrm{T}N}\, k} \tag{6}$$

This trend can be seen in Figure 9, where the velocity after four thrusts is twice as high as after one.

During the keeping velocity phase the actuator has to counteract the reduction of kinetic energy of the load by external forces and friction by recurring thrusts. Assuming a quasi-constant load force F_{LX}, considering external forces and friction, leads to the relation:

$$F_{\mathrm{cyl}}\, L_{\mathrm{T}} = E_{\mathrm{T}} \quad = \quad E_{\mathrm{L}}^{\#} = F_{\mathrm{LX}}\, L_{\mathrm{C}} \tag{7}$$

whereby $L_{\mathrm{C}} = L_{\mathrm{T}} + L_{\mathrm{B}}$ and thus:

$$\frac{F_{\mathrm{cyl}}}{F_{\mathrm{LX}}} = \frac{L_{\mathrm{C}}}{L_{\mathrm{T}}} = 1 + \frac{L_{\mathrm{B}}}{L_{\mathrm{T}}} = \frac{T_{\mathrm{C}}}{T_{\mathrm{T}}} \tag{8}$$

The undesired variation of the velocity during the keeping velocity phase can be characterized with the absolute variation Δv and the relative variation r of the velocity, which can be expressed as:

$$\Delta v = v_1 - v_0 = \sqrt{v_0^2 + \frac{2}{m}\left(E_{\mathrm{T}} - E_{\mathrm{L}}^{*}\right)} - v_0 \tag{9a}$$

$$\leq \widehat{\Delta v} = \sqrt{v_0^2 + \frac{2}{m} F_{\mathrm{cyl}}\, L_{\mathrm{T}}} - v_0 \tag{9b}$$

$$r = \frac{v_1 - v_0}{v_0} = \sqrt{1 + \frac{2\left(E_{\mathrm{T}} - E_{\mathrm{L}}^{*}\right)}{m\, v_0^2}} - 1 \tag{10a}$$

$$\leq \widehat{r} = \sqrt{1 + \frac{2\, F_{\mathrm{cyl}}\, L_{\mathrm{T}}}{m\, v_0^2}} - 1 \tag{10b}$$

For the limits it is assumed that $E_{\mathrm{L}}^{*} > 0$ and always reduces the kinematic energy of the load, i.e. friction.

Both, the absolute variation and the relative variation of the velocity gets smaller with increasing velocity.

5.1 Scaling, Limitations and Design Estimations

In walking mechanics [16], the Froude number, $\mathbf{F} = \frac{v^2}{lg}$, where v is the velocity, l the leg length, and g gravity, is used to characterize the transition from walking to running. Remarkable, the inner fraction in Equation 10b has the same structure and the following can be derived.

$$\mathbf{F} = \frac{v_0^2\, m}{L_{\mathrm{T}}\, F_{\mathrm{cyl}}} = \frac{v_0^2}{L_{\mathrm{T}}\, a_{\mathrm{cyl}}} \tag{11}$$

Also this dimensionless value $\mathbf{F}$ can be used to characterize the locomotion. A similar value will result in a similar relative variation of the velocity.

Equation 10 together with Equation 8 provide a stronger statement for scaling and characterizing a system than Equation 11. These equations can be used for dimensioning the system.

In the keeping velocity phase, $L_{\mathrm{C}}/L_{\mathrm{T}}$, Equation 8, defines how efficient the ballistic mode is. Assuming that the dimensioning of the cylinder and thus F_{cylN} is defined by other load cases, like acceleration or applying a force at slow motion, then the used energy of a conventional cylinder is $E_{\mathrm{CC}} = F_{\mathrm{cylN}}\, L$. The energy not used for the motion is dissipated in the valve. In the ballistic mode during the keeping velocity phase the used energy is:

$$E = F_{\mathrm{cylN}}\, L\, \frac{L_{\mathrm{T}} + L_{\mathrm{R}}}{L_{\mathrm{C}}} \tag{12}$$

whereby L_{R} is the stroke of the retraction including disengaging and engaging. L_{R} may be suppressed in this equation if the retraction is powered by a low pressure flow source, e.g. an accumulator loaded with the tank flow during the thrusts. In the simulated example is $L_{\mathrm{R}} = L_{\mathrm{T}} + L_{\mathrm{overhead\,ED}} \approx L_{\mathrm{T}}$, whereby $L_{\mathrm{overhead\,ED}}$ is the additional distance the cylinder moves while engaging and disengaging. By comparing the energy used by a conventional cylinder and HILA in ballistic mode, the energy consumption factor e_{B} can be defined:

$$e_{\mathrm{B}} = \frac{L_{\mathrm{T}} + L_{\mathrm{R}}}{L_{\mathrm{C}}} = \frac{1 + \frac{L_{\mathrm{R}}}{L_{\mathrm{T}}}}{\frac{F_{\mathrm{cyl}}}{F_{\mathrm{LX}}}} \tag{13}$$

$$\approx 2\, \frac{F_{\mathrm{LX}}}{F_{\mathrm{cyl}}} \tag{14}$$

For the limit case $F_{\mathrm{LX}} \approx F_{\mathrm{cyl}}$, which can not be realized, is $e_{\mathrm{B}} = 2$ and HILA in the ballistic mode would use approximately twice the energy of a conventional cylinder. The break-even point is at $F_{\mathrm{LX}} \approx \frac{1}{2} F_{\mathrm{cyl}}$, where the distance of the ballistic distance L_{B} is approximately the equal to the thrust stroke length L_{T}. For the case $F_{\mathrm{LX}} \ll F_{\mathrm{cyl}}$ the energy consumption factor e_{B} approachs zero as there is nearly no energy used in the ballistic mode.

The system's implementation, Figures 6 and 7, defines a quasi-constant duration for retracting, disengaging and engaging which in sum defines a lower limit for T_{B}, $T_{\mathrm{B}} \geq T_{\mathrm{B\,limit}} = T_{\mathrm{R}}$. T_{B} is the duration the load moves autonomously between two thrusts. L_{B}, the distance the load moves between two thrusts, can be estimated by:

$$L_{\mathrm{B}} = v_0\, T_{\mathrm{B}} + \frac{F_{\mathrm{LX}}}{m} \frac{T_{\mathrm{B}}^2}{2} \tag{15}$$

This results in following condition for the load force.

$$F_{\mathrm{LX}} < \frac{F_{\mathrm{cyl}}}{1 + \frac{v_0\, T_{\mathrm{B\,limit}} + \frac{F_{\mathrm{LX}}}{m} \frac{T_{\mathrm{B\,limit}}^2}{2}}{L_{\mathrm{T}}}} \tag{16}$$

$$\approx \frac{F_{\mathrm{cyl}}}{1 + \frac{v_0\, T_{\mathrm{B\,limit}}}{L_{\mathrm{T}}}} \tag{17}$$

The simplifications made lead to that also a load force near this limit may not be valid, but of the relevant case of small r, Equation 10, and high velocities v_0, this is a valuable condition.

In an application, the relative variation r, Equation 10, and absolute variation Δv, Equation 9, of the velocity has to be

reasonable small. Equations 5 and 9 lead to following condition limiting the absolute variation in velocity:

$$m_L > \frac{2\,F_{\mathrm{cyl}}\,L_{\mathrm{T}}}{v_1^2 - v_0^2} \approx \frac{2\,F_{\mathrm{cyl}}\,L_{\mathrm{T}}}{\widehat{\Delta v}^2} \tag{18}$$

The approximation is applicable for small r and thus high velocities. A condition to limit the relative variation in velocity is derived from Equation 10b:

$$m_L > \frac{2\,F_{\mathrm{cyl}}\,L_{\mathrm{T}}}{(\widehat{r}+1)^2 - 1}\,\frac{1}{v_0^2} \tag{19}$$

5.2 Control Inputs

In the presented gait the system has the following control inputs which can be used to control the motion and to adjust to changing load conditions. The inputs can be used in combination to achieve optimal performance and efficiency.

5.2.1 When to trigger the next driving stroke

This control input is used for velocity control in the simulation, where the results are shown in Figures 8 and 9. The velocity control is simply realized by the state *wait*, Figure 4, by waiting for the velocity of the actuator to drop below a specified limit, before triggering the next thrust. Alternatively the duration between two thrusts can be used as control input which is commonly known as Pulse-Frequency Modulation (PFM).

5.2.2 Force direction

By choosing the cylinder chamber to connect to tank pressure while driving the load, the direction of the force is selected. In the simulated example that is used for accelerating, chamber B, and braking, chamber A.

Extending this concept, more than two different supply pressure levels can be utilized.

5.2.3 Stroke length, when to disengage

The energy delivered during a thrust depends on the stroke length, Equation 1. The stroke can be varied from zero to the stroke length of the cylinder considering margins for engaging and disengaging. In the case of a constant thrust frequency this control method is commonly known as Pulse-Width Modulation.

Stroke length variation is effective and efficient control input. The system's efficiency is only minimally reduced, see Equation 13. An advantage is that it also reduces the relative variation r, Equation 10, and absolute variation Δv, Equation 9, of the velocity, i.e. it makes the trajectory smoother.

5.2.4 Valve opening

In case of system P, Figure 6, the valves can be used to throttle the flow and thus reduce the cylinder force. This adds losses to the system but allows intervention during a thrust.

5.2.5 Switching

As in system D the necessary valves are already in place, the ballistic mode can be combined with hydraulic switching technology, see for example the hydraulic buck converter [6].

5.2.6 Supply pressure

The energy delivered during a thrust depends on the cylinder force and thus the supply pressure, Equation 4. This method has similarities to load sensing systems.

This method reduces the efficiency of the actuator but may improve the system's efficiency. It reduces also the relative variation r, Equation 10, and absolute variation Δv, Equation 9, of the velocity, i.e. it makes the trajectory smoother.

5.2.7 Number of cylinders

The presented concept uses only one cylinder. A second cylinder, or any number of cylinders, can be used in parallel to increase force and thus acceleration. Also cylinders with different piston areas can be combined. By selecting the pistons, the actuator adjusts to a varying load or varying acceleration requirements. This method is commonly known as Pulse-Code Modulation.

Alternatively, a second cylinder can be used also to increase the maximum frequency.

6 Conclusion

The presented ballistic gait for HILA is intended to be used exclusively or in combination with other gaits. One other gait is presented in [1], where alternatingly, one cylinder engages and drives the load while the other retracts, to provide a smooth motion. The ballistic gait is energy efficient and supports high velocities but the motion is bumpy.

The ballistic gait brings switching technology, see for example the hydraulic buck converter [6], into the hydromechanical world. It has the ability to effectively recuperate energy.

This gait is feasible for loads with sufficient high mass and sufficient low load force, as external forces and friction. It is well suited for horizontal motion of huge masses but less suited for lifting.

Fast engaging and disengaging is necessary as it limits the achievable velocity and reduces the efficiency

This contribution presents the results of simulations of two systems realizing the ballistic gait. The system is analyzed, presenting equations for estimates of the undesired variation in velocity, energy efficiency, scaling, system limitations and design estimations.

Various control inputs are presented and analyzed concerning undesired variation in velocity and energy efficiency.

Nomenclature

Designation	Denotation	Unit
F_{cyl}	cylinder force	N
F_{L}	external load force	N
F_{LX}	load force including friction	N
L_{B}	distance, the load moves autonomously between two thrusts	m
L_{C}	distance, the load moves during one cycle, $L_{\mathrm{C}} = L_{\mathrm{T}} + L_{\mathrm{B}}$	m
L_{T}	thrust stroke length	m
p_{A}	pressure in cylinder chamber A	Pa
p_{B}	pressure in cylinder chamber B	Pa
T_{B}	duration, the load moves autonomously between two thrusts	s
T_{T}	duration of a thrust	s

References

[1] Martin Hochwallner and Petter Krus. Motion Control Concepts for the Hydraulic Infinite Linear Actuator. In *Proceedings of the 9th FPNI PHD Symposium on Fluid Power*, 2016. ISBN: 978-0-7918-5047-3.

[2] Martin Hochwallner, Magnus Landberg, and Petter Krus. The Hydraulic Infinite Linear Actuator – properties relevant for control. In *Proceedings of the 10th International Fluid Power Conference (10. IFK)*, volume 3, pages 411–424, 2016. http://nbn-resolving.de/urn:nbn:de:bsz:14-qucosa-200646.

[3] Magnus Landberg, Martin Hochwallner, and Petter Krus. Novel Linear Hydraulic Actuator. *ASME/BATH 2015 Symposium on Fluid Power & Motion, Chicago, United States*, 2015.

[4] Website of NoMagic – Cameo Systems Modeler. http://www.nomagic.com/products/cameo-systems-modeler.html, visited 2017-03-15.

[5] Matti Linjama, H-P Vihtanen, Ari Sipola, and Matti Vilenius. Secondary Controlled Multi-Chamber Hydraulic Cylinder. In *The 11th Scandinavian International Conference on Fluid Power, SICFP09, Linköping, Sweden*, 2009.

[6] Helmut Kogler. *The Hydraulic Buck Converter - Conceptual Study and Experiments*. PhD thesis, 2012. ISBN: 978-3990330593.

[7] Björn Eriksson and Jan-Ove Palmberg. Individual Metering Fluid Power Systems: Challenges and Opportunities. *Proceedings of the Institution of Mechanical Engineers. Part I, Journal of Systems and Control Engineering*, 225(12):196–211, 2011.

[8] Andreas Kugi. *Non-linear Control Based on Physical Models: Electrical, Mechanical and Hydraulic Systems*. Number 260 in Lecture Notes in Control and Information Sciences. Springer, 2000. ISBN: 99-0147115-X.

[9] Mohieddine Jelali and Andreas Kroll. *Hydraulic Servo-systems: Modelling, Identification and Control*. Advances in Industrial Control. Springer, 2004. ISBN: 978-1-4471-1123-8.

[10] Christoph Gradl and Rudolf Scheidl. Performance of an Energy Efficient Low Power Stepper Converter. *Energies*, 10(4):445, 2017.

[11] Heinz Gall and Kurt Senn. Freilaufventile-Ansteuerungskonzept zur Energieeinsparung bei hydraulischen Linearantrieben. *Olhydraulik und Pneumatik*, 38(1):38–44, 1994.

[12] ETP Transmission AB. ETP-OCTOPUS – Datasheet for Octopus.

[13] Linz Center of Mechatronics GmbH – Hydraulic Drives. FSVi 4.1 Datasheet – Fast Switching Valve Technolog, 2016. http://www.lcm.at/.

[14] Bernd Winkler, Andreas Ploeckinger, and Rudolf Scheidl. A Novel Piloted Fast Switching Multi Poppet Valve. *International Journal of Fluid Power*, 11(3):7–14, 2010.

[15] John Watton. *Fundamentals of Fluid Power Control*. Cambridge University Press, Cambridge, UK New York, 2009. ISBN: 9780521762502.

[16] Wikipedia: Transition from walking to running. https://-en.wikipedia.org/wiki/Transition_from_walking_to_-running, visited 2017-05-18.

Experimental Investigation of a Displacement-controlled Hydrostatic Pump/Motor by Means of Rotating Valve Plate

Liselott Ericson, Samuel Kärnell, and Martin Hochwallner

Department of Management and Engineering, Fluid and Mechatronic Systems, Linköping University, Linköping, Sweden

E-mail: liselott.ericson@liu.se, samka878@student.liu.se, martin.hochwallner@liu.se

Abstract

Interest in the control of variable fluid power pumps/motors has increased in recent years. The actuators used are inefficient and expensive and this reduces the variable units' usability. This paper introduces displacement control of pumps/motors by means of a rotating valve plate. By changing the angle of the valve plate, the effective use of the stroke is changed. The rotating valve plate is experimentally verified by a modified in-line pump. In the prototype, the valve plate is controlled with a worm gear connected to an electric motor. The results show potential for this kind of displacement control. However, the rotating valve plate creates pressure pulsations at part-displacement due to the commutation being performed at high piston speeds. If the piston speed and hence the flow from each piston is low, the pressure pulsation is acceptable.

Keywords: Fluid power pump/motor, displacement actuator

1 Introduction

Interest in the control of variable fluid power pump/motor units has raised in recent years. To increase the efficiency of fluid power systems, variable machines are important. However, the displacement control actuators are considered to be unnecessarily inefficient. Also, variable machines are in general more expensive than fixed machines due to the additional control mechanism.

A summary of different displacement variations can be found in [1]. The paper concludes that variations in displacement control should require minimum actuation effort and have no negative effect on the machine's steady-state performance (efficiency, oscillation, reliability, etc.). [2] shows that the pulsating piston force acting on the swash plate causes swash plate oscillations. These oscillations cause both losses and noise issues according to Achten. In [3], three different in-line axial piston pumps were tested and their losses due to the swash-plate controller determined. The paper concludes that the main losses occur due to the constant leakage through the damping orifice.

The most common method to control the displacement of an in-line machine is to adjust the angle of the swash plate. This means that the stroke length of the pistons is varied. Control is usually purely hydraulic or electro-hydraulic. Another way to control displacement is by changing the angle of the valve plate, this means that the effective use of the stroke is varied. This displacement control is investigated in this paper.

Other research using similar concepts is described in [4], [5] and [6]. In [4], a new fluid power machine concept was presented, the Innas Hydraulic Transformer (IHT), where the valve plate has three ports. The pressure and flow are controlled by rotating the valve plate. The main issue with the concept is the difficulty with the computation zones between the ports. A large pressure build-up and cavitation occur when the land between the ports appears at other positions than piston dead centre. This problem was addressed in [7], where a shuttle valve was implemented between the ports to reduce the pressure build up and also minimise the risk of cavitation. The concept was further investigated in [8]. The papers clearly show the problem, especially at high speed where the piston speed increases the pressure build-up problem.

In [5], an original swash-plate controller is assumed to be combined with an indexing valve plate, i.e. a rotating valve plate, to reduce the self-adjusting forces and in this way reduce the force for the controllers.

In [6], valve plate rotation is used to reduce the flow pulsation produced in the pump by actively changing the position of the compression angle.

This paper presents displacement-controll of a machine by means of a rotating valve plate. By rotating the valve plate, the effective stroke is adjusted and hence the amount of flow the machine delivers per rotation. The function is verified by measurement on a modified variable in-line pump. The valve plate rotation is realised by an electric motor with a worm gear. The article amplifies problems and benefits with the rotating valve plate control. Only pump application is tested by measurements.

2 Concept Analysis for Rotating Valve Plate

By rotating the valve plate the effective stroke of the machine is reduced. Due to this, the displacement can be controlled by rotating the valve plate. Figure 1 shows three different valve plate rotation angles. $\varepsilon = 1$ shows the position for full pump displacement. At bottom dead centre (BDC) (0°), the piston connects to the high-pressure port and flow is pressed out from the cylinder until top dead centre (TDC) at 180°. At $\varepsilon = 0$, the valve plate is turned 90° and the piston strokes 90° in the low-pressure kidney and 90° in the high pressure kidney and hence no flow is moved through the machine. All angles between 0° and 90° produce a part flow from the pump. At angles between 90° and 180°, the flow direction is changed and the machine works as a motor.

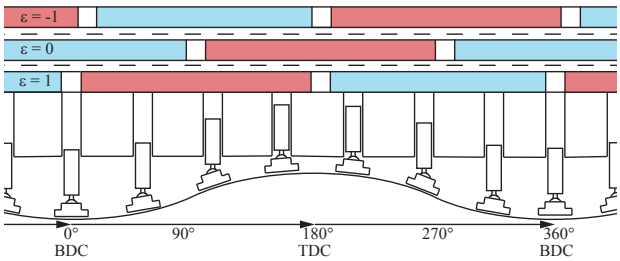

Figure 1: The valve plate location at three different locations; full pump-mode, no-flow and full motor-mode. Darker grey or red rectangles signify high-pressure port and lighter grey or blue low-pressure port.

The principle of displacement control by rotation of a valve plate in figure 1 is equivalent to swash plate control with over-centre control. The rotating valve plate can be combined with changed rotation direction and changed high- and low-pressure ports. Figure 2 shows the optimal principle design of the valve plate for a normal swash-plate controlled machine. The pre- and de-compression angles are used to equalise the pressures in the cylinders to minimise compressible flow pulsations, [9]. The feature uses the piston movement to compress the oil before connecting to the high- and low-pressure ports. In the top left figure the pre-compression angle is used to compress the oil before entering the high-pressure kidney while the de-compression angle is used to lower the cylinder pressure before connecting to the low-pressure port. The angle at bottom dead centre (BDC) is bigger because the cylinder volume is bigger at this position.

The location of the pre- and de-compression angles is important to decide the rotation direction for the different driving modes. When the valve plate is rotated, a fictive pre- and decompression angle is produced and hence for best circumstances, the valve plate should rotate towards the high-pressure kidney. Figure 3 shows all available driving modes. In this paper only left direction of the valve plate rotation is investigated. The functionality is no different between left and right driving modes for the pump itself.

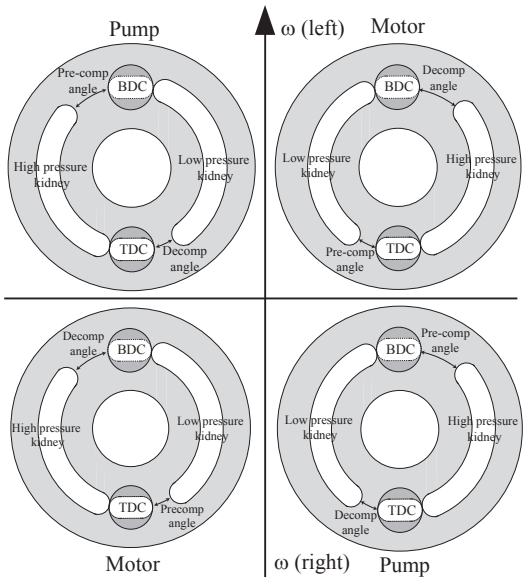

Figure 2: Principle design of optimised valve plate design for different operation quadrants for a fluid power pump/motor. The modes can be supported by a rotation valve plate to create four additional quadrants. BDC stand for Bottom Dead Centre and TDC Top Dead Centre.

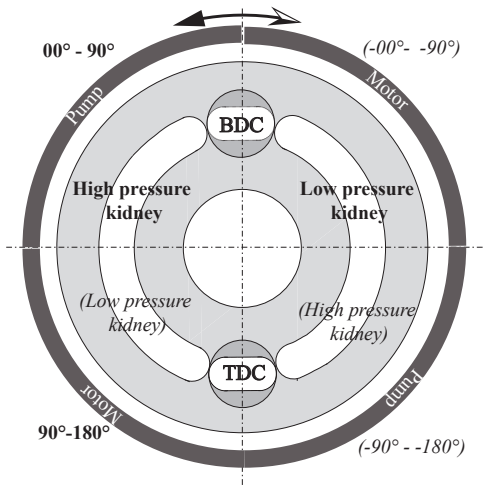

Figure 3: Rotation direction for high-pressure kidney to the right and left respectively. The valve plate should rotate towards the high pressure kidney which means negative angles is connected to the high- respective low pressure kidney in italic font.

3 Simulation Model

A one-dimensional simulation is used to validate the proposed controller. The model describes the flow and force pulsations in a comprehensive study of the rotational valve plate. The components are implemented with transmission line theory, TLM, see e.g. [10]. The model techniques use a distributed model structure which makes the calculations very effective due to allowableness of distributed solvers and the numerical stiffness due to the finite signal propagation speed.

The flow in one cylinder is calculated with the continuity

equation as

$$\sum q = \frac{\mathrm{d}V}{\mathrm{d}t} + \frac{V_{cyl}}{\beta_e}\frac{\mathrm{d}p}{\mathrm{d}t} \tag{1}$$

where the last part is the cylinder capacity and represents the compressible flow. β_e is the effective bulk modulus of the oil, air and container. $\frac{\mathrm{d}p}{\mathrm{d}t}$ is the pressure change inside the cylinder while V_{cyl} is the cylinder volume, which changes during barrel rotation as

$$V_{cyl} = V_{dead} + (\tan\alpha_{max} + \tan\alpha\sin\Phi)\tan\alpha_{max}R_bA_p \tag{2}$$

The kinematic flow is modelled as the derivative of the cylinder volume as

$$\frac{\mathrm{d}V_{cyl}}{\mathrm{d}t} = R_b\tan\alpha\omega\cos\Phi A_p \tag{3}$$

Figure 4 shows the normalised kinematic flow from one cylinder, where positive flow coming out from the cylinder and negative flow are sucked in. In figure 4a, the valve plate has no rotation and hence the pump delivers full displacement, i.e. all flow goes into the high-pressure kidney. Figure 4b shows the valve plate rotation angle at 45°. Only part of the flow is connected to the high-pressure kidney and hence flow is reduced.

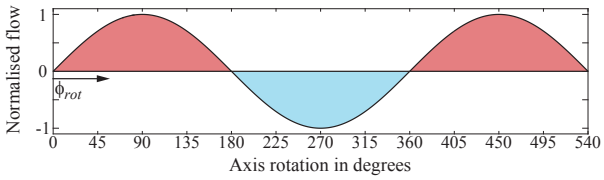

(a) Flow at zero valve plate rotation, hence full displacement.

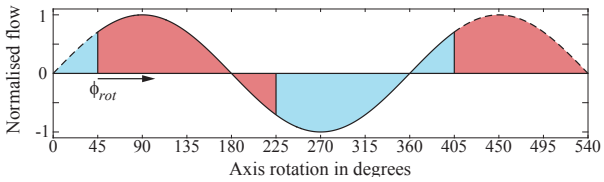

(b) Flow with 45° valve plate rotation, hence ε_ϕ = 0.7.

Figure 4: Normalised flow from one cylinder. Light grey or blue areas are the volumes entering the cylinder from the low-pressure kidney and dark grey or red is the volume leaving the cylinder to the high-pressure kidney.

The flow from the pump depends on the rotation angle and from figure 4b it can be seen that the setting ratio can be expressed as 4. Figure 4 shows the setting ratio as a function of valve plate rotation angle.

$$\varepsilon_\phi = \cos\phi_{rot} \tag{4}$$

where ϕ_{rot} is the rotation angle of the valve plate.

This can be compared to the setting ratio for an original variable swash-plate pump/motor and is stated in equation (5). The angle is almost linear in the full range -16° $\leq \alpha \leq$ 16° as shown in figure 5b.

$$\varepsilon_\alpha = \frac{\tan\alpha}{\tan\alpha_{max}} \tag{5}$$

α_{max} is maximum displacement angle and α is the current displacement angle. The slow displacement change at dead

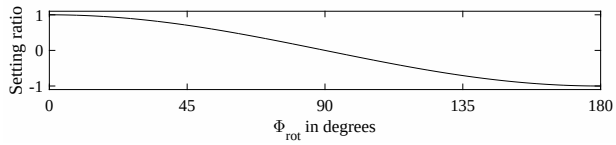

(a) Setting ratio for valve plate rotation, ε_ϕ.

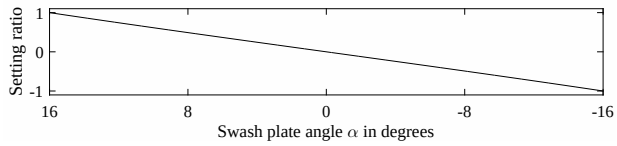

(b) Setting ratio for swash plate angle, ε_α.

Figure 5: Setting ratio for valve plate rotation and swash-plate tilting.

centres can be used to minimise flow pulsations at full displacements, [6].

The sum of the flow in equation (1) consists only of the flow entering or leaving the cylinder and is in this application the flow through the kidney openings. No leakage or cross-porting is considered. This restrictor is modelled with the steady state equation for a turbulence restrictor as

$$q_r = C_qA\sqrt{\frac{2}{\rho}\Delta p_r} \tag{6}$$

Δp_r is the pressure drop over the valve, C_q is the flow coefficient and is known to be a function of the Reynolds number and the area difference between the orifice and pipe. The value is difficult to estimate for a pump environment and the standard value for turbulent orifice 0.60 according to [11] is therefore chosen.

The restrictor opening area A can be considered in different ways. Traditionally, the ports are circular and hence the opening area is modelled as the intersection between two circles, named "A" in figure 6. The opening area will be gradually opened. Another useful opening geometry is a square opening, named "B" in figure 6. This opening is faster and also linear over the full transaction area. The simulation is val-

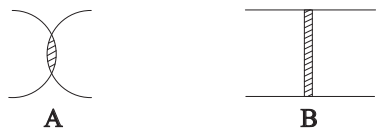

Figure 6: Two different restrictor opening geometries.

idated in earlier contributions by for example Johansson et al. [12].

3.1 Simulation results

Some interesting phenomena appear when the displacement is controlled by rotating of the valve plate. When using a variable in-line machine, the displacement angle can be changed.

This allows the piston flow to be reduced, which has the benefit of reducing the pressure peak in the cylinder. In the results below, both displacement control of the swash plate angle α and displacement control by using the rotation valve plate ϕ_{rot} are used. The kidney restrictor does not open instantly and hence the cylinder volume will be compressed by the piston motion before the flow through the restrictor is bigger than the kinematic flow of the piston. Changing piston speed and hence the piston flow can be done in two ways: setting ratio by α or rotational speed. The two ways will have different impacts on the flow pulsation and pressure build-up in the cylinders.

Figure 7 shows the cylinder pressure at the same amount of flow but different setting ratios and rotational speeds. The graph shows how the pressure changes during a full stroke by means of valve plate rotation. The maximum cylinder pressure is reached at $\approx 90°$, i.e. when the commutation between the cylinders is performed at maximum piston speed. The piston's linear speed in the cylinder port is the same for both curves but higher rotational speed will show smaller pressure build-up compared to higher displacement angles (α). By changing the flow with rotational speed the restrictor opening rate will also change, which means that the pressure build-up will be smaller if the flow is increased by rotational speed compared to displacement angle.

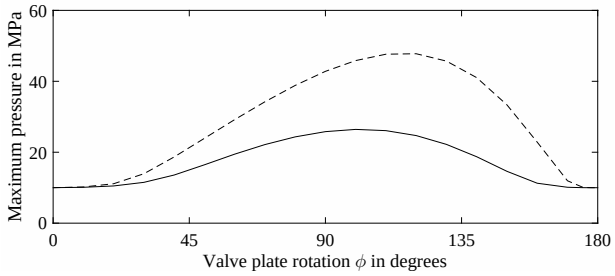

Figure 7: Maximum cylinder pressure at same flow and same piston speed but different rotational speed and displacement angles. Solid line shows 2000 rpm with setting ratio 0.4 and dashed line shows 1000 rpm with setting ratio 0.8.

In figure 8, the speed dependency is amplified. In the figure, the opening area and cylinder pressure build-up are shown. The opening rate is increased by the rotational speed but the flow is also increased and hence the flow rate is increased more than the opening rate and the increased pressure rate is a fact. The pressure build-up is reduced by the compressible part of equation (1).

The pressure build-up depends on the continuity equation. If the flow is decreased, the pressure build-up will be reduced. The compressible part of the equation will damp the pressure build-up. Figure 9 shows the cylinder pressure and the corresponding flow pulsation amplitude as

$$\Delta q_H = \max(q_H) - \min(q_H) \tag{7}$$

where q_H is the flow in the high pressure kidney.

The flow pulsation amplitude is first reduced due to changed pre-compression of the cylinder volume and when the flow

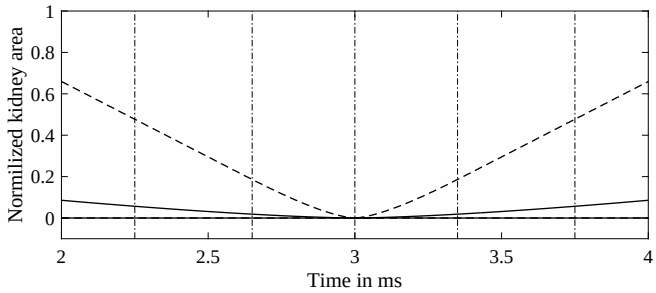

(a) Kidney opening area as a function of time.

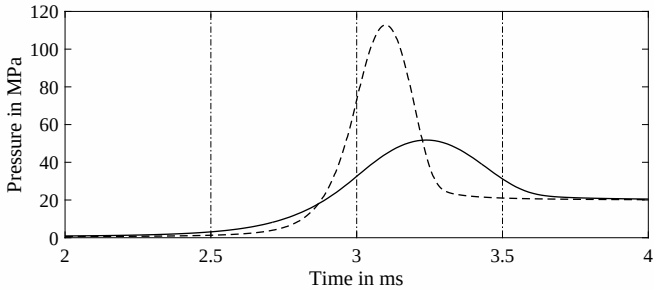

(b) The cylinder pressure in the commutation zone between low- and high-pressure kidney.

Figure 8: Differences between different rotational speeds when the valve plate rotation angle $\neq 0$. Dashed line shows 5000 rpm and solid line shows 1000 rpm.

is decreased by valve plate rotation the flow amplitude increases. The maximum cylinder pressure decreases with setting ratio and a reasonable amplitude is reach at $\varepsilon_\alpha \approx 0.4$. The flow pulsation is also fair here.

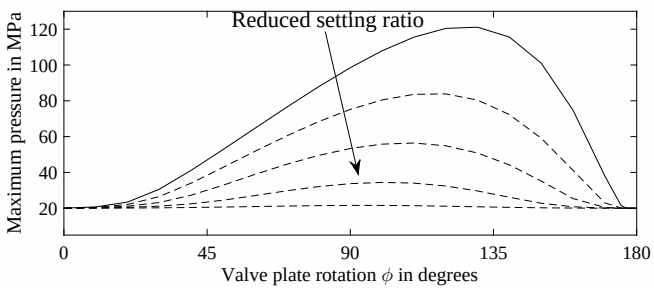

(a) Maximum cylinder pressure as function of valve plate rotation.

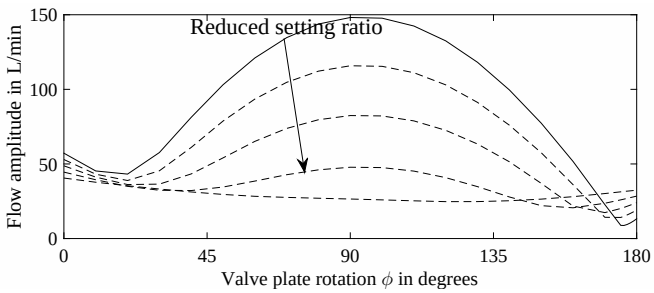

(b) Flow pulsation amplitude as function of valve plate rotation.

Figure 9: Results at 200 bar and 3000 rpm at different setting ratios, i.e. different piston velocities. The restrictor is modelled as circles. Solid line shows full displacement and the other curves show decreased setting ratio with steps of 0.2.

Figure 10 shows different speeds in combination with different pressure levels at $\varepsilon_\alpha = 0.4$. The cylinder pressure build-up is larger than the port pressure decreases with increased pressure level due to the compressible part of equation (1). Increased speed will cause a larger pressure build-up as explained earlier.

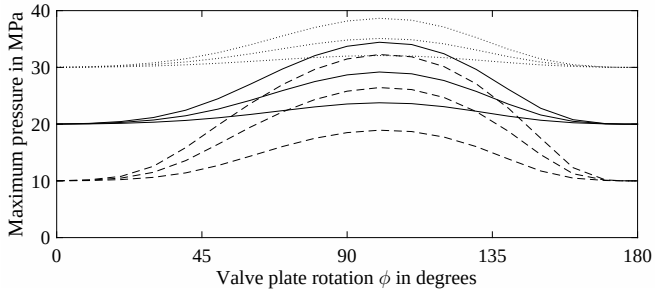

(a) Maximum cylinder pressure as a function of valve plate rotation.

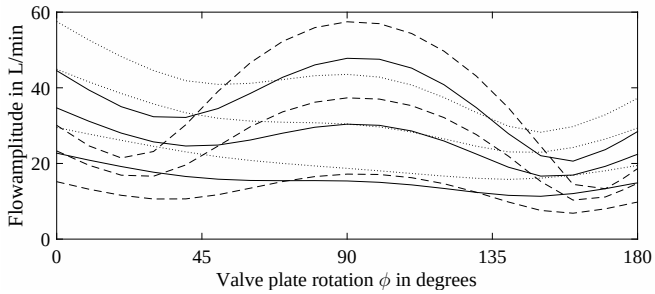

(b) Flow pulsation amplitude as a function of valve plate rotation.

Figure 10: Results at different rotational speeds and pressure levels at setting ratio 0.4. Dashed lines show 100 bar, solid lines show 200 bar and dotted lines show 300 bar. The different lines at the pressure level are 1000 rpm, 2000 rpm and 3000 rpm from below.

To additionally reduce the cylinder pressure build-up a square opening can be used, named "B" in figure 6. This is shown in figure 11 and should be compared to figure 9. The cylinder pressure is then reduced by ≈ 50 %.

4 Hardware Design

The application used is a variable in-line pump with important parameters as shown in table 1. One quadrant operation is tested. To reduce the pressure build-up the setting ratio is set to $\varepsilon_\alpha = 0.5$ in all tests and the rotation speed is limited to 1500 rpm. The restrictor has a circular design with a zero lapped valve plate, i.e. when one kidney is just completely closed, the next kidney will start to open up. The pump is variable

Variable	Description	Value	Unit
D_p	Displacement	60	cm^3/rev
α_{max}	Displacement angle	16	deg
ε_α	Setting ratio	0.5	-

Table 1: Parameters for the variable in-line pump used.

with a constant pressure controller. The pressure is set to a

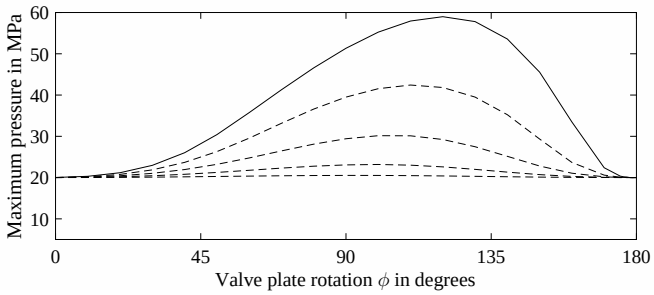

(a) Maximum cylinder pressure as a function of valve plate rotation.

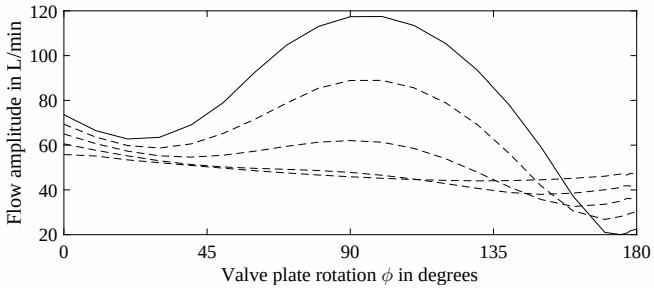

(b) Flow pulsation amplitude as a function of valve plate rotation.

Figure 11: Results at 200 bar and 3000 rpm at different setting ratios, i.e. different piston velocities. The restrictor is modelled as square. Solid line shows full displacement and the other curves show decreased setting ratio with steps of 0.2.

larger pressure than used in the system however, and hence the pump is displaced to the maximum setting angle at all times. The benefit of using a variable pump is that the maximum displacement angle can be set to an appropriate value. Figure 12 shows the tested machine.

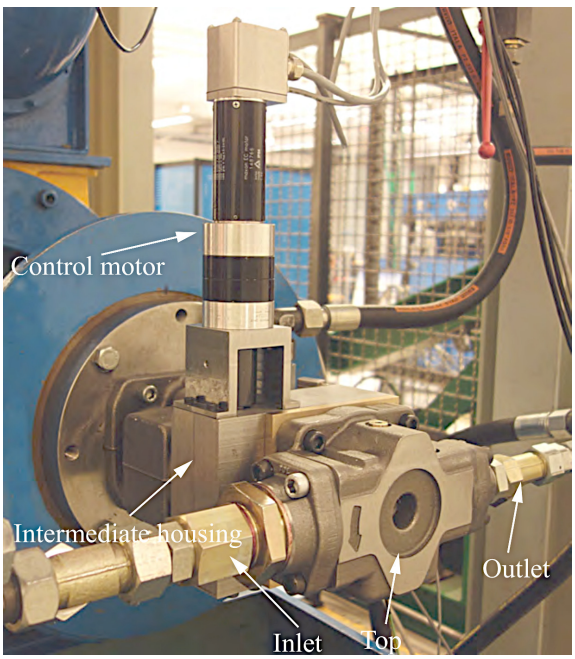

Figure 12: The final pump design mounted on the test rig.

4.1 Mechanical construction

There are two obvious methods to control the flow to the correct port in the radial sliding ring method, where the kidneys connect to the port radially, the channels become rather narrow and expected to be long. The other method is axial connection, where the channels of the valve plate are extended and the connection between the valve plate and the ports is made axially. The rotating valve plate is balanced with hydrostatic bearings. The tested pump is designed with an axial connection system. The first prototype was designed as a student project at Linköping University in autumn 2016, [13]. This prototype has since been updated.

Figure 13 shows all the parts of the rotating valve plate. It is designed to not have any impact on the original pump and hence the pump can be tested both as original and with the rotating valve plate control. The design consists of a worm gear (*Worm wheel* and *Worm screw*) connected to a brush-less DC-motor (*Control motor*). On the either side of the worm wheel, adapters (*Adapter 1* and *Adapter 2*) are made to direct the flow. These parts can be seen as an extension of the valve plate and are made out of several parts for manufacturing reasons. The original valve plate is mounted on adapter 1. The *top extension* is made to increase the size of the possible rotation angle and is also made in a bronze kind material for better sliding behaviour of the rotating valve plate. Figure 14 shows

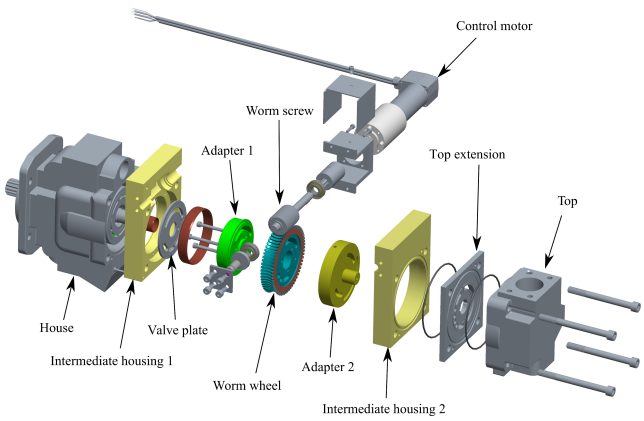

Figure 13: The mechanical design of the prototype. The top and housing are unchanged from original pump.

the working principle applied on the mechanical design. Adapter 1, the worm wheel and adapter 2 are called a rotating drum. The valve plate is fixed connected to this drum. The valve plate and drum are the parts which rotate. The kidneys are reduced in length at the connection to the top extension. The possible rotation angle is mechanically restricted to the range between -5° and 99°, and a full pump stroke can be tested.

4.2 Drive of valve plate

The worm screw is driven by a brush-less DC-motor with planetary gear head, encoder and hall-sensors, which is connected to a motor controller. A MyRIO is used as the main controller hardware. MyRIO features a real-time processor

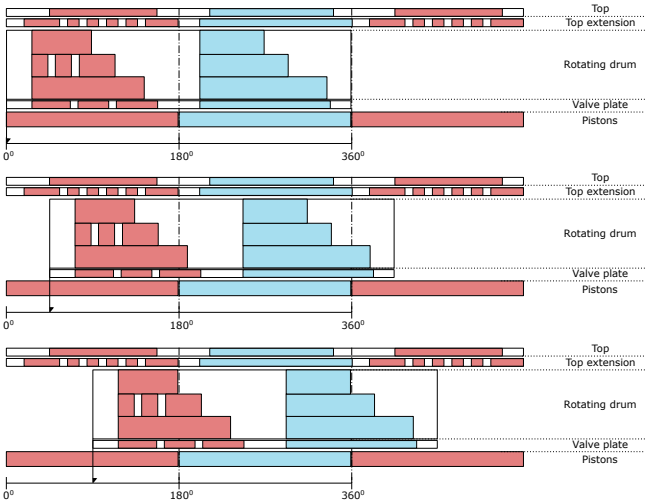

Figure 14: The construction in a linear view of the different layers in the design. In the bottom layer, the barrel and pistons are shown. The valve plate and drum are the rotating part. The top picture shows full displacement, the full stroke and hence all flow goes to the high-pressure kidney. The middle figure shows when the setting ratio is $\varepsilon_\phi = 0.7$ and the bottom when no flow is delivered.

and an FPGA, whereby both are programmed in LabVIEW. Both the motor controller and MyRIO, use the encoder signals from the motor, whereby the motor controller realises speed control and the position controller is implemented in MyRIO. The motor controller provides a signal corresponding to the motor current which is used to estimate the motor torque.

The accuracy of the valve plate angle measurement is dominated by the stiffness of the gear head and most of all the play in the home-made worm gear. The play in the worm gear is small.

The parameters of the drive are shown in table 2. With the stated maximum speed and gear ratio, the setting time from $\varepsilon_\phi = 0$ to 1 is approximately 1.8 s.

Variable	Discription	Value	Unit
i	Total gear ratio	1191	-
n_{cm}	Speed continuous	10000	rpm
T_{con}	Torque continuous	316	Nm

Table 2: Parameters of the valve plate drive.

5 Test Set-up

Figure 15 shows the test set-up. The pump is driven by a 90 kW DC-motor. The pump is connected directly to an electrically controlled pressure relief valve. Outlet and inlet flow and pressures are measured as well as the rotational speed of the drive motor. The pump's inlet is pressurised to prevent cavitation. The current and position are measured at the control motor. The position is judged as the position of the valve plate

rotation. The current is used to calculate the torque needed to control the valve plate. All measurement is made at $\varepsilon_\alpha = 0.5$.

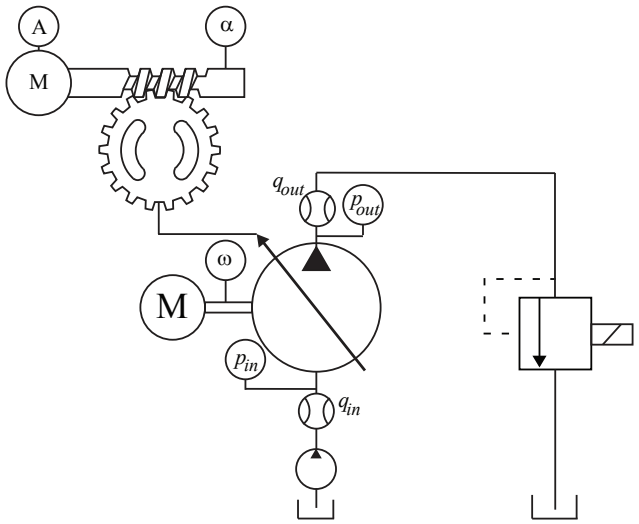

Figure 15: Set-up for testing the displacement-controlled pump with a rotating valve plate. The figure shows the transducers used.

This is done to reduce the maximum cylinder pressure.

6 Results

Equation (4) is verified with figure 16. Theoretical value of ε_ϕ is shown with the measured normalised flow. The losses have been taken out from the flow calculations.

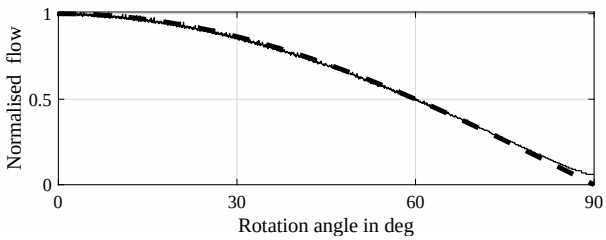

Figure 16: The flow characteristics of the displacement-controlled pump. Thick dashed line is the theoretical value of ε_ϕ while the solid line is the measured flow. The deviation at rotation angles > 80 degrees may be caused by inaccuracy of the flow meter.

Figure 17 shows the flow at step response measurements. The theoretical flow at rotational speed of 750 rpm and maximum displacement 30 cm^3/rev is 22.5 L/min, which means the volumetric efficiency is ≈ 0.8. The pressure difference over the pump is here just 2.5 MPa.

Figure 18 shows the response for different pressure levels and step sizes. The full setting time is 1.8 sec. The main limitation of the step time is the maximum rotational speed of the control motor.

The torque of the control motor is shown in figure 19. When the motor accelerates full continuous torque is used. The torque peaks which are seen at bigger rotational angles than

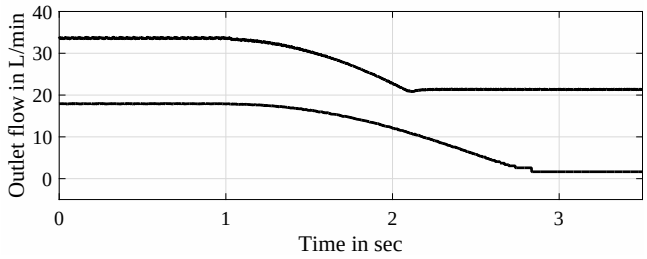

Figure 17: Flow at 750 rpm and 1500 rpm with a step of 90° and 50° respectively. The pressure increase over the pump for the 750 rpm curve is 1 MPa and for 1500 rpm 2.5 MPa.

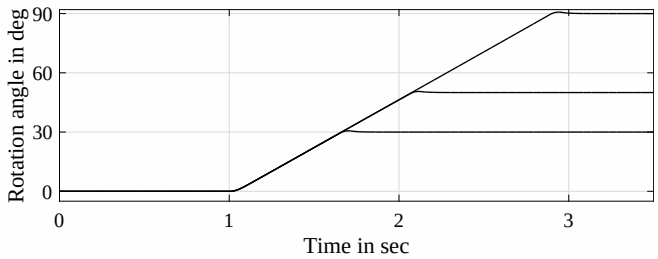

(a) The setting ratio is decreased.

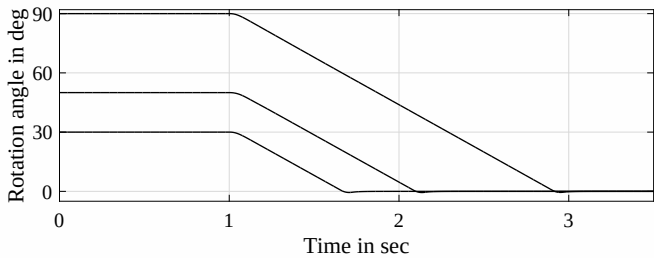

(b) The setting ratio is increased.

Figure 18: Step responses at displacement stroke of 30°, 50° and 90°. The pressure and rotational speed are different between the steps.

45° have the frequency of the teeth of the worm gear. This is most probably caused by the design and its tolerances.

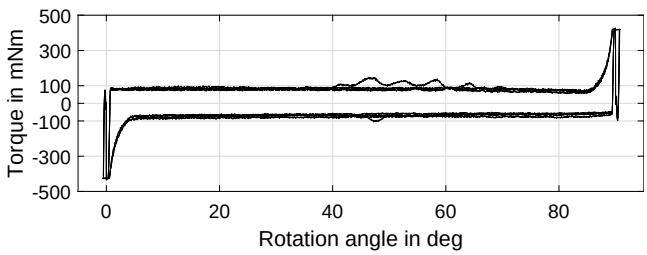

Figure 19: The torque at the full stroke step responses at different rotational speeds (750 rpm and 1500 rpm) and pressures 0.2-8 MPa. The positive values are when the setting ratio is increased while the negative values are at a decreasing setting ratio.

7 Discussion

A simulation model used to investigate the flow pulsation created when the valve plate rotates. The pressure pulsation is worst at smallest displacement setting ratio, i.e. when the commutation is made when the piston has maximum speed. This will be an issue when controlling the displacement by rotating valve plate. This was also found by [7] who tried to reduce the issue by means of shuttle valves. It can be reduced by implementing square ports.

Displacement control by rotating valve plate is verified with the pump prototype. The flow follows the theoretical value. Volumetric efficiency is poor due to insufficient manufacturing quality. The hydrostatic bearing between the rotating valve plate and housing is over-balanced. The leakage can be reduced by decreasing the sealing areas between drum and top extension. For larger rotations, i.e. for over-centre control, radial port location is probably a necessity.

The setting time is long due to the high gear ratio implemented. The setting torque is about 0.1 Nm while the maximum continuous torque is 0.3 Nm. The torque is almost independent of the rotation direction and pressure level.

The main setting time is caused by the limited rotational speed. The setting time can be reduced approximately three times by decreasing of the gear ratio between the control motor and the valve plate. The new setting time will be 0.6 sec, which is a more realistic time for many applications. The setting time can be reduced further by increasing the power of the electric motor or an electro-hydraulic solution. The power needed is still small compared to swash-plate actuator forces.

8 Conclusions

The article shows an experimental verification of displacement control by means of rotating valve plate. An in-line axial piston pump is modified so that the valve plate can be rotated by an external electric motor. The displacement setting time for the prototype is rather slow and the volumetric efficiency is low. However, this is not limited by the principle of the rotating valve plate as such. The pressure pulsation and hence the noise level may be an issue but with correct design and low piston speeds, the noise problem can be handled.

9 Acknowledgement

This research was partially funded by the Swedish Energy Agency (Energimyndigheten).

Nomenclature

Designation	Denotation	Unit
q	Flow	m^3/s
α	Displacement angle	deg
α_{max}	Maximum displacement angle	deg
V_{cyl}	Cylinder volume	m^3
β_e	Effective bulk modulus	Pa
p	Pressure	Pa
V_{dead}	Cylinder dead volume	m^3
Φ	Barrel rotation	deg
A_p	Piston area	m^2
R_b	Barrel radius	m
ϕ_{rot}	Valve plate rotation	deg
q_H	Flow in high pressure port	m^3/s
ε_ϕ	Setting ratio valve plate rotation	deg
ε_α	Setting ratio swash plate	deg

References

[1] Karl Hartmann and Ludger Frerichs. Development of innovative solutions for displacement variation in hydrostatic machines. In *10th International Fluid Power Conference*, volume 1, pages 427–440, 2016.

[2] P Achten. Dynamic high-frequency behaviour of the swash plate in a variable displacement axial piston pump. *Institution of Mechanical Engineers, Part I: Journal of Systems and Control Engineering published*, 227(6):1–12, June 2013.

[3] Jan Lux and Hubertus Murrenhoff. Experimental loss analysis of displacement controlled pumps. In *10th International Fluid Power Conference (10. IFK)*, Dresden, Germany, March 8 - 10 2016.

[4] P Achten, Z Fu, and G Vael. Transformer future hydraulics: a new design of a hydraulic transformer. In *Proc. of The 5th Scandinavian International Conference on Fluid Power, SICFP'97*, Tampere, Finland, May 21-23 1997. CD.

[5] Junhee Cho, Xiaoping Zhang, Noah D. Manring, and Satish S. Nair. Dynamic modelling and parametric studies of an indexing valve plate pump. *International Journal of Fluid Power*, 3(3):37–48, 2002.

[6] T Grahl. Geräuschminderung an axialkolbenpumpen durch variable umsteuersysteme. *O+P, Ölhydraulik und Pneumatik*, 5:437–443, November 1989.

[7] Peter A.J. Achten and Georges E.M. Vael. 'shuttle' technology for noise reduction and efficiency improvement of hydrostatic machines. In *Proc. of The 7th Scandinavian International Conference on Fluid Power, SICFP'01*, Linköping, Sweden, May 28-30 2001.

[8] A Johansson, R Werndin, and J-O Palmberg. Dynamic analysis of shuttle technique performance applied on hydraulic transformer. In *Proc. of 3rd International Fluid Power Conference, IFK'3*, volume 2, pages 249–261. Aachen, Germany, March 2002.

[9] K A Edge and J Darling. A theoretical model of axial piston pump flow ripple. *Journal of Institution of Mechanical Engineers*, 200(B1):45–54, September 1986.

[10] P Krus, A Jansson, J-O Palmberg, and K Weddfelt. Distributed simulation of hydromechanical systems. In *Proc. of 3rd Bath International Fluid Power Workshop*, Bath, UK, September 13-14 1990.

[11] H E Merritt. *Hydraulic Control Systems*. John Wileys and Sons, Cincinnati, Ohio, 1967. ISBN 0-471-59617-5.

[12] A Johansson, J Ölvander, and J-O Palmberg. Experimental verification of cross-angle for noise reduction in hydraulic piston pumps. *Journal of Institution of Mechanical Engineers, Part I: J. Systems and Control Engineering*, 221(I3):pp. 321–330, 2007.

[13] Emil Lindborg, Emma Sandström, Karin Gustafsson, Samuel Kärnell, Simon Ward, and Vincent Liljeholm. *Displacement and pulsation control by implementation of a rotatable valve plate on a hydraulic piston pump*. Technical report, Fluid and Mechatronic Systems, Department of Management and Engineering, Linköping Universiity, 2016. LIU-IEI-RR-16/00260-SE, Supervisors: Liselott Ericson and Martin Hochwallner.

Use of LMS Amesim® Model to Predict Behavior Impacts of Typical Failures in an Aircraft Hydraulic Brake System

Mário Maia Neto and Luiz Carlos Sandoval Góes

Department of Mechanical Engineering, Aeronautical Institute of Technology, São José dos Campos, SP, Brazil
E-mail: mario.maia.neto@gmail.com, goes@ita.br

Abstract

The brake system performs an important, safety-related function in aircraft operation throughout the world nowadays. However, the requirement of an acceptable performance and satisfactory reliability has become stricter as the aircraft landing weights and speeds increased substantially along the last decades and the regulatory authorities improved their certification basis requirements aiming a safer operation. Therefore, the brake system design, architecture and functionalities have evolved through the years and the development of the antiskid system, part of the brake system of several aircraft since 1940s, comprised an important milestone in aircraft brake system history. Besides the main function of preventing the locking of braked wheels, the antiskid system is normally also responsible for avoiding wheel braking at the instant of the first contact of the tires with ground during landing. The system also provides indication to the crew in case of system failure and helps minimize the inadvertent yaw suffered by the aircraft in case of passage of the tires on surfaces with different friction coefficients. As a result, the appropriateness of the brake system performance, which is mostly supplied by hydraulic power in recent commercial and military aircraft, shall be completely verified in normal and faulty conditions, as well as in all expected operational envelope. For that purpose, model simulations, rig tests and flight test campaigns are usually applied. Therefore, the present work aims to demonstrate the use of a computational model of a hydraulic brake system, parameterized in LMS Amesim® software, to assess the behavior of system relevant variables in normal operational conditions and the potential effects of typical failures in system performance. In addition to help support the verification process of system compliance with performance and safety requirements, such approach could also be applied for early identification of failures and operational problems still during the product development phase, highlighting the gains of applying the aforementioned tool in the context of aeronautical systems engineering.

Keywords: Brake System, Modeling, Amesim, Hydraulic, Failure.

1 Introduction

The aircraft brake system is responsible not only for decelerating the vehicle during a landing or a rejected takeoff, but it can also be applied to assist the speed control when taxiing and to park the aircraft. The use of brakes to improve ground handling due to differential braking and even to halt wheel rotation at landing gear retraction are other examples of aircraft brake system functionalities [1].

Due to their inherent advantages and installation characteristics, most of brake systems in recent commercial and military aircraft are powered by hydraulic sources. According to [2], the hydraulic system presents a high power-to-weight ratio, relatively low initial costs, acceptable maintenance levels, installation flexibility, good reliability and also the self-lubricating aspect of their components.

However, the requirement of an acceptable performance and satisfactory reliability for the brake system has become increasingly stricter as the aircraft landing weights, speeds and complexity improved substantially along the last decades. Federal Aviation Regulations CFR 14 Part 25 and MIL-HDBK-516 are examples of civil and military certification bases frequently applied during the development and certification phases of these types of airplanes throughout the world. In order to guarantee an acceptable degree of safety level on operation, certification requirements impose functional and safety-related aspects that shall be taken into consideration when developing the brake system and aircraft systems in general.

Therefore, the brake system design, architecture and functionalities have evolved through the years and the development of the antiskid system, part of the brake system of several aircraft since 1940s, comprised an important milestone in aircraft brake system history. Besides the main function of preventing the locking of braked wheels, the antiskid system is also normally responsible for avoiding

wheel braking at the instant of the first contact of the tires with ground during landing. The system also provides indication to the crew in case of system failure and helps minimize the inadvertent yaw suffered by the aircraft in case of passage of the tires on surfaces with different friction coefficients.

Basically, the antiskid control system operates by measuring the rotational speed of the aircraft wheels and actuating on the applied brake pressure. Depending on its control logic, the antiskid system is classified by [3][4] in three different categories: on-off, quasi-modulating and fully-modulating types. The on-off systems are the simplest ones and operate by releasing the brake pressure every time an incipient locked-wheel condition is detected, allowing the brake pressure reapplication only after the wheel has spun up to its synchronous speed. On the other hand, the first generation of the modulating systems, called quasi-modulating, has a control logic based on a pre-programmed sequence, in which brake pressure is held off according to skid depth, being later reapplied to a lower level and subsequently ramped up until a new skid starts. Finally, the fully-modulating systems are the most recent ones and make use of adaptive control logics. Based on the wheel-speed time history, those systems allow a better control over the optimum braking performance.

The current development of computational resources has facilitated the practice of an approach referred by [5] as "concurrent engineering", characterized by the design of products and their related processes in an integrated, concurrent manner, including their support and manufacturing. In the context of the "concurrent engineering" and motivated by the existing competitiveness in aeronautical market and the constant search for safety levels improvement, the increasing use of simulation models became practically indispensable for reducing aircraft system development cycles as well as in predicting field operational problems. Figure 1 illustrates the several applications of simulation model in product development process.

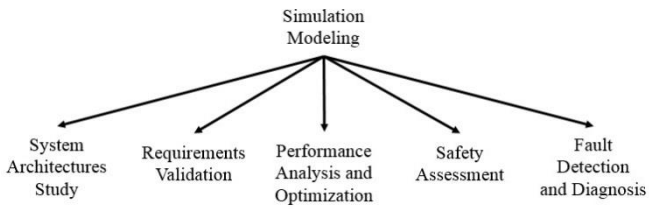

Figure 1: Simulation modeling applications

The early detection of failures in aeronautical systems has become a real necessity in order to keep its high level of safety. For that purpose, the execution of operational and functional tests of systems during maintenance tasks and the incorporation of real-time failure detection functions comprise solutions normally applied. Besides the check of system properly functioning after implementing a modification or replacing a system component, functional tests are commonly performed in aircraft systems in a periodic manner, mainly for latent failures identification. The execution of those tests is also part of predictive maintenance aiming to notice symptoms that can reveal a potential degradation of the system under investigation. On the other hand, supervisory functions, like the *built-in test* (BIT), can be incorporated in critical electronic systems to detect failure occurrences in real time. They allow corrective actions to be taken in time automatically or by the crew after the appearance of a particular alarm.

However, the nature of the failure plays a significant role in the way it is dealt. Abrupt failures are those that occur in a sudden manner and should be immediately detected in safety-related systems. Incipient failures are normally linked to component wear and take place slowly. These failures are associated with a gradual variation of a system parameter in a lower magnitude, making its detection difficult during maintenance tasks [6].

The model-based fault detection and diagnosis comprises an alternative to the aforementioned methods whose use has been growing for decades. With the advantage of eliminating the installation of physical redundancies like additional sensors coupled to the system, the model-based approach makes use of mathematical models to raise analytical redundancies for it. Its development requires, nevertheless, the compliance with some relevant requirements as the desired capability of uncoupling failures and a low sensitivity to modeling errors, which are usually considered as system unknown inputs and could lead to false alarms [6]. According to [7], wrong diagnoses resultant from imprecise or incomplete models, or even from erroneous reasoning, may also originate unnecessary maintenance actions.

Several techniques of model-based fault detection and diagnosis have been studied since 1990s. As described in [6] and [8], the quantitative methods are based on the manipulation of analytical redundancies, called "residuals", and may apply different methods like parameter estimation, parity equations and state/output observers for the determination of the real system model. An example of the construction of the "fault signature matrix", a binary matrix determined from the residuals and applied to isolate the system failures, can be found in [9]. The model-based fault detection and diagnosis techniques can also be qualitative, as illustrated in [10] by the use of knowledge-based methods and the fault signature matrix just as a starting point for the method. The temporal causal graph representation covered in [11] consists in another tool that can help in detecting and diagnosing failures in a qualitative manner. Finally, the methodology presented in [7] comprises the use of a binary matrix referred to as "D-matrix" to support the fault detection and diagnosis, which states the relationship between system failure modes and particular types of system tests, being the latter any kind of information about the system functioning state.

On the other hand, the detection and segregation of failures might not be an easy task even with the modeling support. The method's robustness to modeling errors is reduced when multiple or simultaneous failures are considered. Moreover, in order to raise mode detailed information about the failure such as its type, magnitude and cause, the contribution of a system specialist is normally required to correlate with them additional factors like equipment operational conditions, aging level, maintenance history, and so on [6][8].

Based on this background, the present work aims to demonstrate the use of a computational model of a hydraulic brake system, parameterized in LMS Amesim®, to assess the behavior of system relevant variables in normal operational conditions and the potential effects of typical failures in system performance. Due to the current availability of physical modeling software with fast simulation time, this approach could represent a good solution for a quick, preliminary assessment of system behavior on particular conditions.

The hydraulic brake system illustrated in Figure 2 comprises a system of a variable-wing fighter aircraft and will be applied for the present analysis. The technical information and test results published in [12][13] for the respective brake system will be used as reference in order to validate the nominal model developed herein.

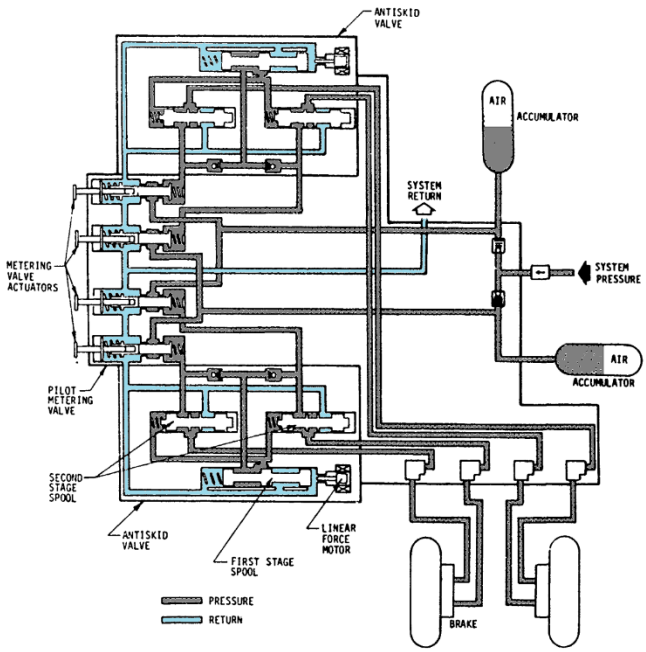

Figure 2: Hydraulic brake system schematics. Source: [13]

2 Modeling and Formulation

The brake system is supplied by the aircraft hydraulic power generation system with a 3.000-psig pressure, which is later duplicated to independently provide hydraulic power for each brake assembly. In each subsystem line, a hydraulic accumulator is installed to allow brakes application in emergency conditions or with the main hydraulic system turned off. Two antiskid valves, one for each brake assembly, and four metering valves, required by the system architecture and responsible for modulating the braking demand applied by the pilots, are located inside a unique valve assembly. The metering valve consists in a control pressure valve, whose output pressure is directly proportional to the force applied by the pilots on the brake pedals. The antiskid valve is composed of two stages and actuated in the first stage by means of a linear motor. Once the input signal is received from the antiskid system control unit, a new force balance is established in both stages of the antiskid valve, leading to the control of the hydraulic pressure resultant in the brake assemblies. Finally, each brake assembly is supplied by both hydraulic subsystems, existing a total segregation between the piston chambers operated by each subsystem in the interior of the brake assembly [13].

An equivalent hydraulic diagram of the hydraulic brake system is provided in Figure 3. For simplification purposes, the metering valves are represented by proportional directional control valves and the brake assemblies are illustrated only by a pair of hydraulic pistons. The supply and the return pressures are described as lumped sources.

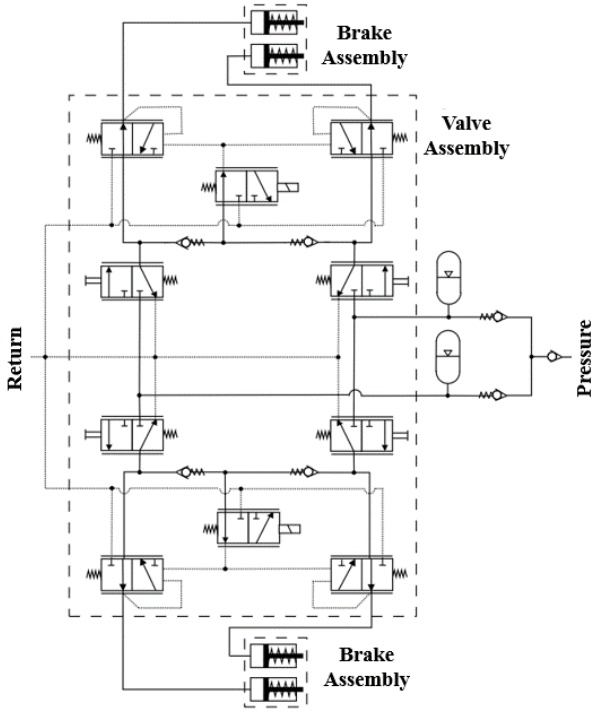

Figure 3: Brake hydraulic system diagram

The LMS Amesim® model of the diagram of Figure 3 is presented in Figure 4. The hydraulic brake system architecture shown is composed of three elements with well-defined boundaries, which are the valve assembly, the brake assemblies and the inputs blocks. Components associated with the hydraulic generation and distribution system, represented by the power source, reservoir, accumulators, tubing, hoses and a check valve, are also part of the diagram.

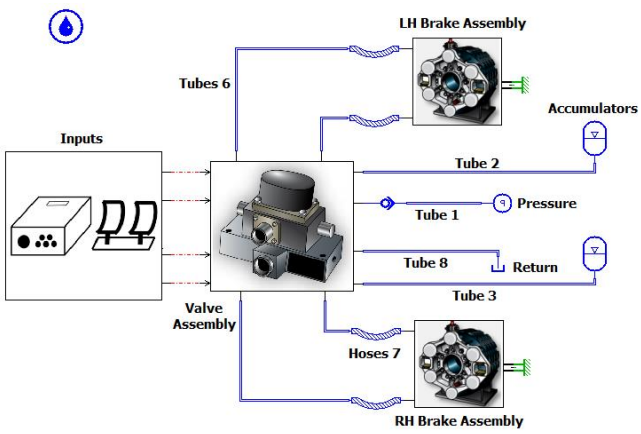

Figure 4: Brake hydraulic system model in LMS Amesim®

The basic modeling and formulation that compose the brake system model will be divided into two separated topics: the hydraulic system model and the brake assembly dynamic model. More details about the inputs block will be provided later in chapter 3, during the model validation discussion.

2.1 Hydraulic System Modeling

The components of the hydraulic generation and distribution system are described by common blocks that exist in the LMS Amesim® hydraulic library. Meanwhile a hydraulic pressure source element is applied to simulate the ideal pressure provided to the brake system by the aircraft hydraulic pump, the aircraft reservoir is modeled by means of a constant pressure source tank element. At the same time, the main hydraulic fluid properties used for flow calculations, like its viscosity, density, bulk modulus and air/gas content, are given by the indexed hydraulic fluid properties element located in Figure 4 at the top of left-hand side.

Among the main functions of the hydraulic accumulators, it is possible to highlight the supply of flow by short periods of time and the attenuation of system pressure pulsations [14]. The hydraulic accumulators of Figure 4 are modeled applying the respective element without inlet orifice, which comprises a hydropneumatics accumulator that supplies hydraulic pressure as a result of its equilibrium with the pressure of the gas located in an isolated volume within. The hydraulic accumulator element of LMS Amesim® hydraulic library considers the polytropic law of gases to calculate the gas properties inside the accumulator [15].

A hydraulic check valve with linear characteristic element is used to simulate the behavior of the check valve that exists in real system supply line. After achieving the cracking pressure, the element model makes use of a linear relationship between pressure drop and flow, without incorporating any dynamics. However, the model allows a mild hysteresis to be taken into consideration for the valve opening and closing actions [15].

The LMS Amesim® software makes available several types of models to represent the hydraulic tubes, which are basically divided into a group of models based on lumped elements and a unique option of continuous parameters modeling that solves 1D Navier-Stokes equations [15]. For the present work, a model with lumped elements is chosen to represent the hydraulic tubing, which is characterized by the segregation of flow important behavior effects like compliance, inertance and pressure drop as discrete elements, connected by means of the continuity law or specific pressure conditions.

The following equations illustrate the relationship between pressure and flow for each main effect that exist in a hydraulic line. The first effect is called *system compliance* and is related to the pressure-dependence variation that the fluid density exhibits. The ideal compliance is related to fluid flow and line pressure through eq. (1) [14].

$$C_f \triangleq \frac{\int Q dt}{P} \tag{1}$$

Due to its kinetic energy, the fluid flow exhibits another effect known as *fluid inertance*. The relation between pressure variation and fluid flow in the fluid inertance element is given by eq. (2) [14].

$$\Delta P \triangleq I_f \frac{dQ}{dt} \tag{2}$$

The last effect observed in the flow dynamics through hydraulic lines consists in the fluid resistance, also referred to as *pressure drop*. The fluid pressure drop in a horizontal straight tube and completely developed flow can be given by the semi-empirical equation of eq. (3). The first term in the right-hand side of the equation is called the "friction factor" and is dependent on tubing relative roughness and also on Reynolds number [16].

$$\Delta P = f \frac{L}{D} \frac{\rho {V_L}^2}{2} \tag{3}$$

Components like valves result in locally situated pressure drops. The relation between the fluid flow and the pressure drop through their orifices can be expressed by a non-linear equation for turbulent flows, as shown in eq. (4), or by a linear equation for laminar flows, given by eq. (5) [16].

$$Q = C_d A_o \sqrt{\frac{2}{\rho}(\Delta P)} \tag{4}$$

$$Q = \frac{2\delta^2 D_0 A_o}{\mu} \Delta P \tag{5}$$

Figure 5 describes how the hydraulic line is divided into lumped elements in LMS Amesim®, being each node characterized by the sum of each main behavior effect. For the node, the compliance, inertance and pressure drop are illustrated by their equivalent effects in a mechanical system, given by the damping, inertia and friction losses, respectively. A total of 3 (three) nodes are applied in the present model for each tube. However, the same methodology is not used for the hoses in LMS Amesim® hydraulic library. For the hose model, those effects are taken into consideration in an equivalent manner for its whole length, without segregating it into discrete nodes.

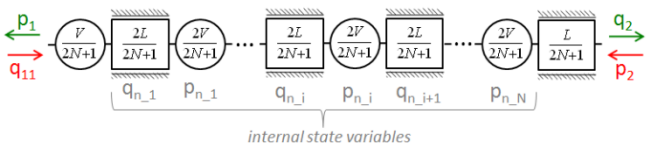

Figure 5: Internal state variables of line lumped model. Source: [15]

The LMS Amesim® software applies similar or adapted formulation from those presented herein in order to calculate the pressure and flow derivatives in the model nodes. Moreover, the software has the capability of considering the effect of flow frequency in the pressure drop calculation along the tube in a phenomenon called *frequency-dependent friction* (*FDF*). Basically, the FDF addresses the changes in laminar flow profile due to viscosity effects in high frequency flows or during quick transients, which are taken into consideration with higher or lower intensity according to the dissipation number given by eq. (6) [15].

$$D_n = \frac{\vartheta L}{cR^2} \tag{6}$$

The valve assembly internal model is shown in Figure 6. Since the metering valve actuating mechanism is not modeled in the present study, the same 2-position, 3-port hydraulic valve element of LMS Amesim® hydraulic library is applied to model the metering valves and both stages of the antiskid valves. This element comprises a 2nd order internal dynamics. With electrical operation and return by spring, the actuation signals of the metering valves and the 1st stage of the antiskid valves are supplied by the block representative of the system inputs through dimensionless connections of signal type. For simplification purposes, no feedback is assumed in the 1st stage of the antiskid valve because a 2nd order dynamics already takes place between the input signal and its spool internal position.

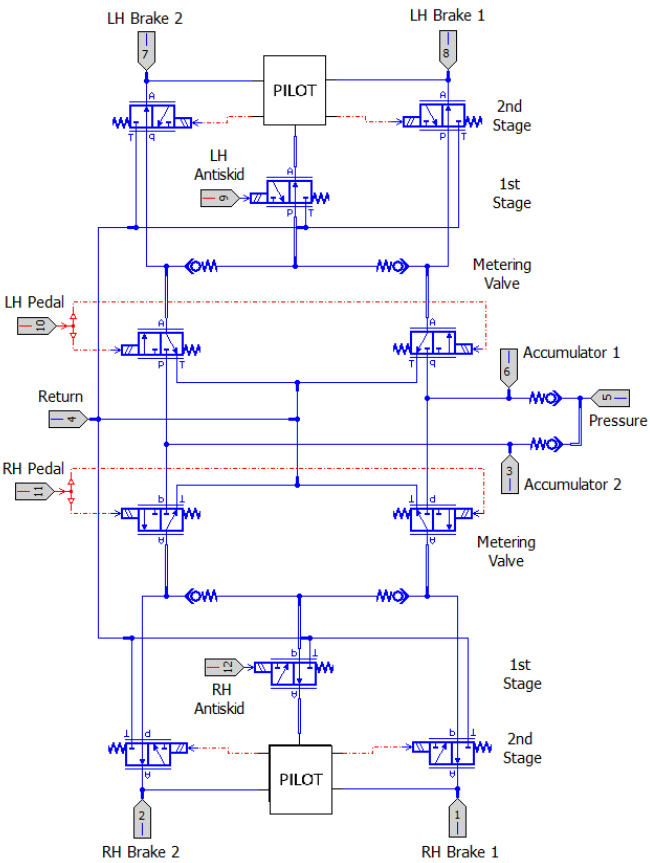

Figure 6: Valve assembly internal model

Since the hydromechanical interface between its stages is no deeply detailed in the schematics of Figure 2, a simplified model for the antiskid valve 2nd stage is adopted as illustrated in Figure 7. The modeling of an electrohydraulic servovalve with force feedback could include high order dynamics according to [16]. However, the present model considers, besides the own 2nd order dynamics of the hydraulic valve element of LMS Amesim® hydraulic library, an internal loop between the output pressures of the 1st and 2nd stages in order to define the pilot pressure of the valve 2nd stage. In Figure 7 the fixed hydraulic orifice and simple hydraulic chamber elements are used to help system stability. In practice, they might represent detailed internal characteristics of the real physical component like passage restrictions or dead volumes. Moreover, the actuation area of each pressure is weighted by means of the gain associated with each hydraulic pressure sensor element, being the resultant force simplified by a dimensionless signal responsible for operating the 2nd stage. The normalization and unit adequacy of the dimensionless control signals are done by adjusting the internal properties of the hydraulic valves blocks.

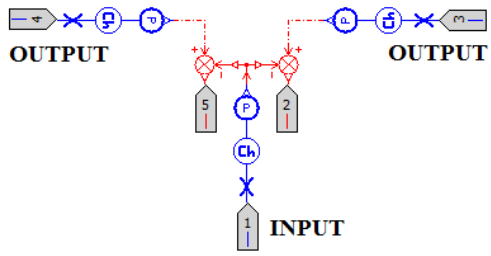

Figure 7: Pilot scheme for antiskid valve 2nd stage model

Finally, the check valves located inside the valve assembly are modeled making use of the spring-loaded check valve element of LMS Amesim® hydraulic library. The relationship between pressure drop and flow in that element obeys the pressure drop through orifices formulation but considering the change in the orifice passage area as a function of its internal spool position. The present check valve model does not incorporate any internal dynamics and, nevertheless, allows a mild hysteresis to be taken into consideration for the valve opening and closing actions [15].

2.2 Brake Assembly Modeling

In an aircraft hydraulic brake system with antiskid function, characterized by fast and cyclic braking pressure actuations, the brake assembly dynamics assumes an important role in the overall system performance. Therefore, in the current brake assembly designs, whose constructions normally apply steel or carbon disks in a multiple disk configuration, the behavior of the disk friction coefficient is extremely relevant.

The materials used in the brake assembly disk design should present particular relevant characteristics, responsible for allowing to them a satisfactory useful life, efficient heat absorption and dissipation, and an appropriate behavior in the brake torque. According to [17], properties like a consistent, high friction coefficient, low wear rate, good resistance to high temperatures, minimized volumetric expansion and high values of thermal conductivity and specific heat denote desirable characteristics for those materials.

Figure 8 describes the equilibrium of forces in a multiple-disk hydraulically operated brake assembly. With the disks totally compacted, the piston tangential brake force can be given by eq. (7). It is a function of the disk friction coefficient, the acting force resultant from hydraulic pressure application and the opposing force of the piston return mechanism. The overall brake torque can be obtained from eq. (8).

$$F_{braking_j} = 2\mu_{disk}\left(F_{action_j} - F_{return_j}\right) \tag{7}$$

$$T_{braking} = R_{piston} N_{rotors} \sum_{j=0}^{N_{pistons}} F_{braking_j} \tag{8}$$

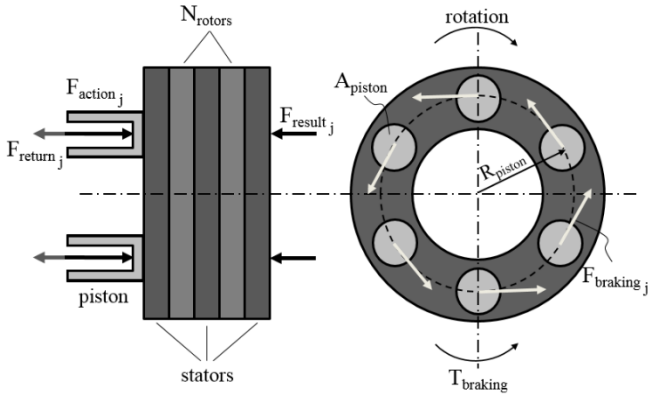

Figure 8: Forces acting on a multiple-disk hydraulically operated brake assembly

The LMS Amesim® model of brake assembly is shown in Figure 9, where a total of 6 (six) pistons is assumed for the equipment. The physical and constructive properties of each piston are represented by the mass and piston elements of mechanical and hydraulic component design libraries, respectively. The piston dynamics is also modeled by two elements of the mechanical library: an elastic contact element, responsible for simulating the piston free displacement until its contact with the disks, and by an ideal linear spring element, representing the piston return mechanism. The compacting behavior of the brake heat sink, given by the rotors and stators, is modeled in the right portion of the figure. For that purpose, mechanical elements like masses, dampers and ideal springs with variable stiffnesses are applied.

The overall internal volume of the brake assembly is split into two identical hydraulic volumes with pressure dynamics elements, being each one supplied by an independent line of the brake system and connected to a group of three pistons. Those elements are also capable of representing the volumetric variation due to pistons displacements.

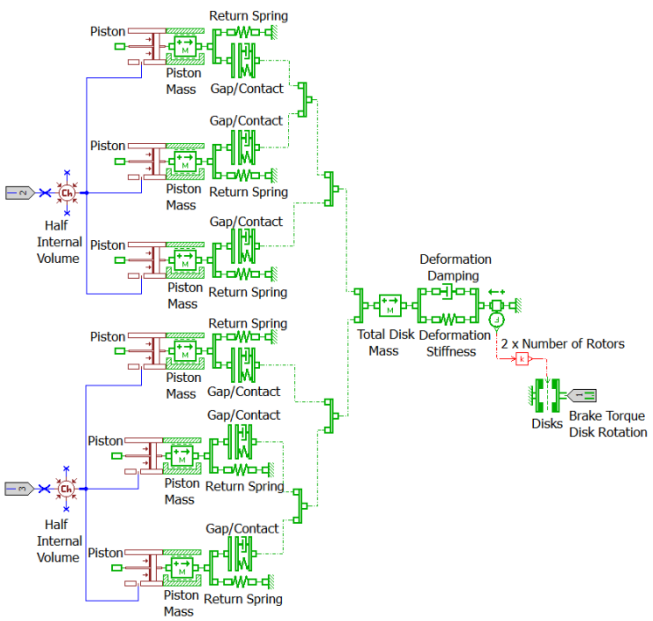

Figure 9: Brake assembly model in LMS Amesim®

Lastly, different models are available in practice to reproduce the friction behavior of the brake assembly disks. Depending on the relevant characteristics like static friction, lubricant effects and dynamic behavior, the most appropriate model can be selected and its fidelity in reproducing the brake torque real behavior shall be later validated through dedicated tests.

For the present work, the brake torque is obtained by means of the rotary Coulomb and stiction friction element from the LMS Amesim® mechanical library, which considers the wheel speed and the compacting force as inputs. Applying the reset-integrator model, it allows the stiction effect modeling through the use of a dynamic model whose integrator is introduced by means of an internal variable associated with the pre-slip displacement. The resultant brake torque given by the reset-integrator model can be represented as a function of the relative angular displacement and velocity between the contact surfaces as shown in the graphs of Figure 10. Different values for the static torque and Coulomb friction torque may be adopted in this model, as well as a continuous transition between them as known as the *Stribeck effect*. The existence of viscous friction in the static friction region may also be considered to avoid the occurrence of non-physical oscillations [15].

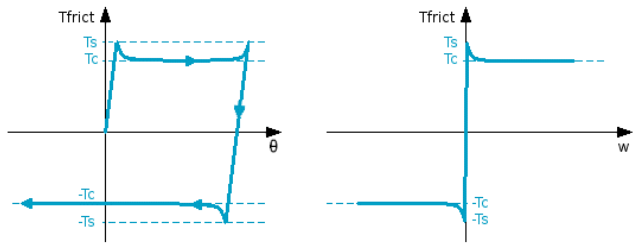

Figure 10: Friction torque as a function of relative angle and velocity. Source: [15]

3 Model Simulation and Validation

In order to guarantee the representativeness of a mathematical model, it becomes necessary to compare the simulation results with reference data, which could be taken from the literature, dedicated tests, component qualification data or even from full-scale aircraft tests.

Therefore, the information provided in [12][13] for the fighter aircraft brake system under analysis will be applied herein to validate the developed model. The studies addressed in [12][13] afford technical information and results of tests accomplished in brake systems of aircraft from 1950s and 1960s, which have become public and can be used for analysis and validation of computational models.

The simulation and validation of the hydraulic brake system model will be presented in two steps: the brake assembly and the hydraulic system behavior analyses.

3.1 Brake Assembly Analysis

The results of brake assembly nominal model validation are shown as follows. The graph of Figure 11 presents the relationship between the hydraulic volume filled inside the brake assembly and the applied brake pressure. As it can be

noticed, the simulated curve approximates satisfactorily the reference curve from [13]. Singular points like the beginning of the pressure increase when the piston return mechanism preload is surpassed by the brake pressure (at about 15 cm^3) and the stiffness increase at the effective contact between the disks (from 30 cm^3 to 40 cm^3) become the simulated curve similar to ones typically applied in brake system specifications. On the other hand, the difference noticed between them at the beginning of brake assembly pressurization could be explained by some factors like: the hydraulic dynamics resultant from the way the pressure was applied in the reference test, the definition method used for raising the tested curve, or even by some functional property change of the brake assembly used in the aforementioned test.

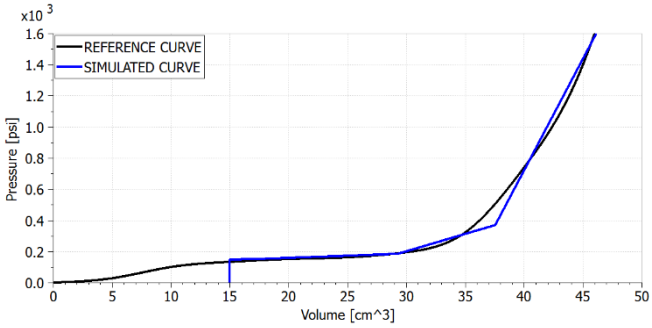

Figure 11: Brake volume x brake pressure curve

The brake torque responses for a hydraulic pressure application of 1600 psig (11.0 MPa) are shown in Figure 12 and Figure 13 for a constant rotational velocity of 1000 rpm and 1 rpm, respectively. Hydraulic pressure is applied at 0.5 second from simulation start to disregard any undesirable oscillation due to algorithm initialization.

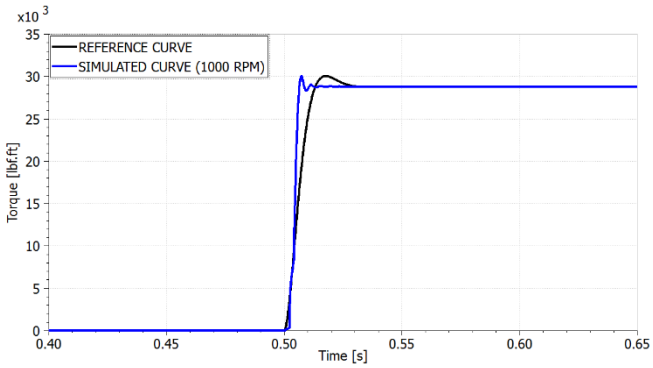

Figure 12: Brake assembly torque curve (1000 rpm)

Since the model constructed to reproduce the brake assembly performance is made out of a combination of damper and stiffness elements, the simulated output in Figure 12 does not fit exactly the 2nd order curve suggested by [12]. However, the obtained curve is considered satisfactory to reproduce the dynamic response of the brake torque because it presents the same overshoot, a few oscillations and basically the same settling time after the peak as the reference curve.

In Figure 13 a small rotational velocity is applied to the disks to allow the assessment of the static friction behavior of the brake assembly model. The validation is done by adjusting the torque peak value in that condition to be in agreement with the peak torque gain informed in [12]. On the other hand, the meaning of the peak torque gain as provided in the reference seems to be more comprehensive since [12] associates its start with a particular wheel velocity. Therefore, it could be related to a more complex behavior of the friction coefficient at low velocities during the rotors deceleration, or even to the impacts of heat sink temperature. Nonetheless, those effects are not simulated in the current model.

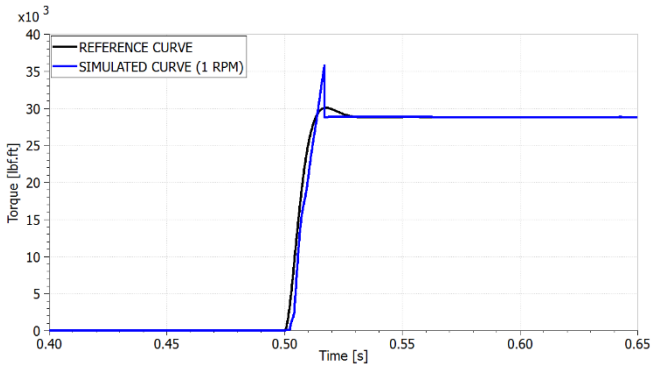

Figure 13: Brake assembly torque curve (1 rpm)

3.2 Hydraulic System Analysis

The dynamic response of the brake hydraulic system described in Figure 6 and Figure 7 is validated in three steps. Firstly, the step response of brake pressure is compared to the reference curves provided in [13], allowing the determination of most of the valve parameters in the valve assembly, mainly those related to pressure drops and dynamic responses. Afterwards, a frequency response analysis is accomplished and checked against main properties provided in [13], in order to confirm the valve assembly response is appropriate. Finally, some last adjustments are made in the antiskid valve parameters by assessing the adequacy of the provided brake pressure as a function of the valve input signal if compared to reference boundaries of [13].

The graphs shown in Figure 15 and Figure 16 describe the simulated step response in brake pressure, with a supply pressure of 1650 psig (11.4 MPa), in two different conditions: pressure increase and pressure removal. However, since it is not detailed in the reference if the pressure step was simulated by the supply pressure or by a brake pedal deflection, the latter was adopted in the present work because it better represents the system functioning principle. Figure 14 illustrates the use of piecewise linear signal source elements and constant signal elements, both from LMS Amesim® signal and control library, to simulate the metering valve and antiskid valve inputs, respectively. For the current simulation, the step input is applied in both metering valves, meanwhile the other inputs are kept null.

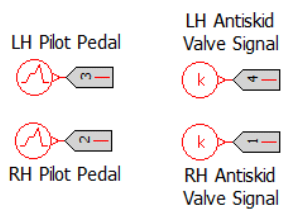

Figure 14: Input block elements for step response analysis

In both figures the pedal application or removal takes place at 0.5 second of simulation time. As it can be noticed, the simulated curve in Figure 15 approximates satisfactorily the reference curve of [13]. Dynamic characteristics like delay response time for pressure increase, rise time, overshooting and damping behavior are adequate if compared to the reference curve, which was measured in [13] during a test rig experiment. The difference between the steady state values is of only 48 psig (0.33 MPa).

An acceptable result is also obtained in Figure 16, which plots brake pressure response when the brake pedal actuation is removed. The reference curve of [13] is reproduced superimposed on the simulated graph for comparison. The only significant difference between the curves is noticed at about 0.9 second of simulation, when the model curve presents some pressure fluctuations that are not found in the reference one. Those oscillations start at the exact moment the brake assembly pistons return to their mechanical stop, which creates a phenomenon similar to suction and that could, in the real system, lead to the occurrence of a localized cavitation. The absence of that behavior in the real system curve of [13] could be explained by one or a combination of the following factors: use of a lower data acquisition rate during the test, pressure measurement in a system different point since the effect is less pronounced along the tubes that connect the assembly valve to the brakes hoses, or indeed due to a higher damping existing in the piston stop of the real brake assembly. Nevertheless, those pressure fluctuations are not relevant to the brake torque and, subsequently, to brake assembly performance because they result in a piston force that is smaller than the return mechanism preload.

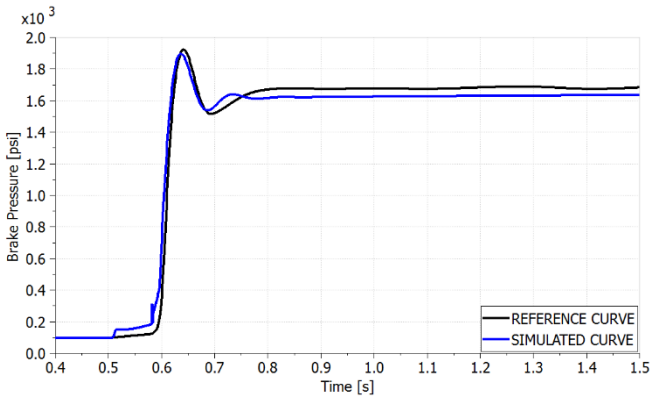

Figure 15: Step response (increase) for 1650 psig

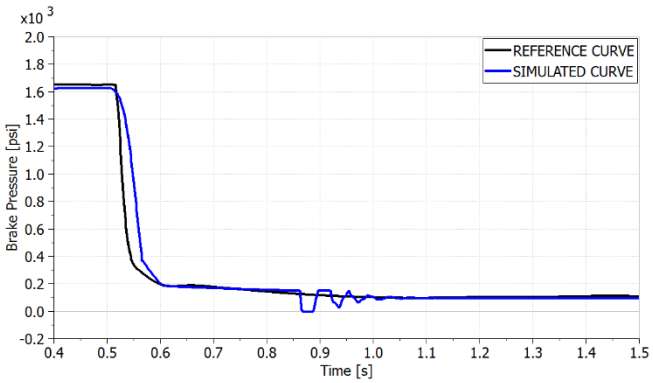

Figure 16: Step response (removal) for 1650 psig

The same brake response simulation is accomplished in other two different conditions of supply pressure, 1490 psig (10.3 MPa) and 825 psig (5.7 MPa), and compared to the main properties informed in [13] for tested curves. The obtained values and respective errors of the simulated curves are summarized in Table 1 and Table 2 for pressure increase step and removal step, respectively, for the three supply pressure conditions. The results are assessed as satisfactory.

Table 1: Step response (pressure increase)

Test Pressure (psig)	Delay Response Time (s)		Response Time to 80% of Pressure Change (s)		Percentage Overshoot of Step Change	
	Measured (1)	Error (s)	Measured	Error (s)	Measured	Error (%)
1650	0.081	0.003	0.109	-0.005	16.2	-1.1
1490	0.084	0.037	0.111	-0.009	18.8	-0.1
825	0.107	0.019	0.137	-0.006	30.4	28.8

(1) Value corresponds to the instant of pressure increase after initial step in graph

Table 2: Step response (pressure removal)

Test Pressure (psig)	Delay Response Time (s)		Response Time to 80% of Pressure Change (s)		Percentage Overshoot of Step Change	
	Measured (1)	Error (s)	Measured	Error (s)	Measured	Error (%)
1650	0.006	-0.010	0.078	0.021	0	0
1490	0.006	-0.007	0.083	0.018	0	0
825	0.006	-0.006	0.362	0.102	0	0

The next step of the validation process comprises the system frequency response, which evaluates the system steady state output when a sinusoidal input is applied. Since reference [13] does not describe in details how the oscillating pressure was supplied during the system tests, some assumptions needed to be made in the present modeling.

The oscillating input pressure is applied in the LMS Amesim® model by considering a constant value for the hydraulic pressure source element of Figure 4, equal to the maximum value within the tolerance informed by the reference, and a sinusoidal input only in the LH pilot pedal as illustrated in Figure 17. The average and amplitude values of the sinusoidal signal are adjusted in such way that, when statically simulated to its minimum and maximum values, a pressure range close to the tested one of [13] is obtained. Null values are adopted for the other inputs. The brake pressure is measured in the LH brake assembly.

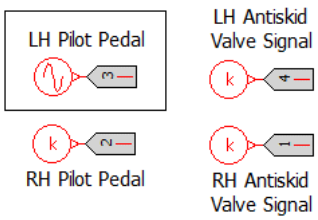

Figure 17: Frequency response analysis input elements

For the frequency response analysis, LMS Amesim® software requires the system model linearization at an operational point. Therefore, for each simulated condition, a 1-Hz input signal is applied for 5 seconds and the linearization point is defined after reaching the steady state behavior. Figure 18

shows the linearization point for the first simulated condition, which considers a 750 psig (5.2 MPa) supply pressure. For the pilot pedal input, a dimensionless signal with average of 0.73 and amplitude of 0.27 is adopted. It leads to a hydraulic pressure range of 344 psig (2.4 MPa) to 744 psig (5.1 MPa) in the brake assembly when the input is applied statically (with null frequency) at its limits. As a result, a simulation condition with an average brake pressure of about 550 psig (3.8 MPa) is obtained.

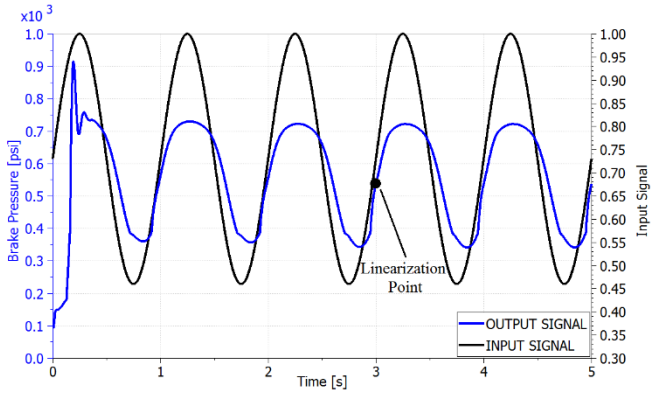

Figure 18: Linearization point for 550 psig condition

The Bode plot of the hydraulic brake system model is shown in Figure 19 for the 550 psig pressure condition. The reference frequency response, raised by test and provided in [13], is also reproduced in Figure 20.

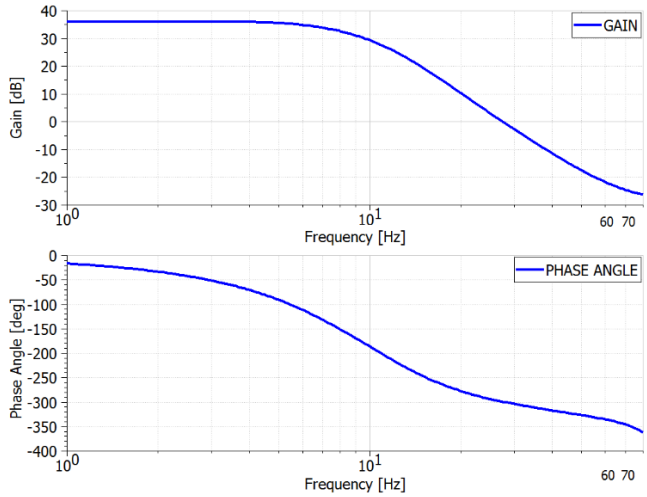

Figure 19: Frequency response for 550 psig condition

Although the gain reference curve presents a different scale, probably due to the use of another approach for applying the oscillating input pressure, it is possible to notice in Figure 19 the same very smooth resonant peak before the frequency of 8 Hz, followed by a about -40dB decay in the frequency range of 10 Hz to 40 Hz. However, the frequency response beyond 50 Hz is not modeled herein and understood as not relevant for the system dynamics. Concerning the phase angle behavior, the simulated curve in Figure 19 is considered acceptable if compared to the one illustrated in Figure 20. In general terms, both curves comprise a phase angle change from a small absolute angle, between 0º e -30º, in the frequency of 1 Hz, up to approximately -270º to -320º at 40 Hz. As a result, the gain and phase angle curves approximates reasonably the curves raised by test for practically the same test condition.

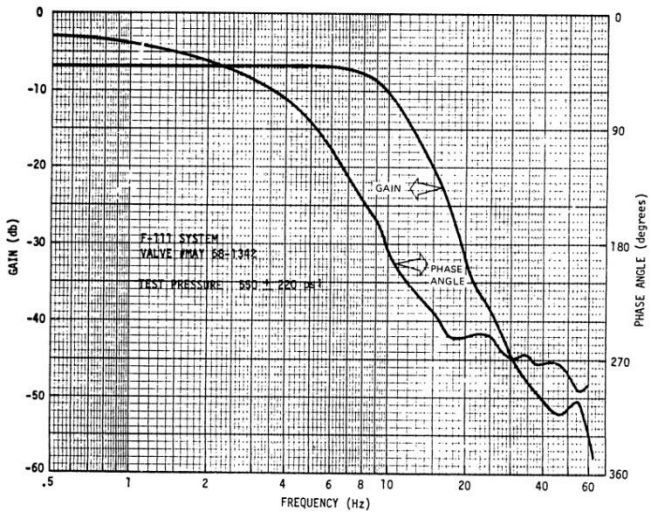

Figure 20: Reference frequency response for 550 psig condition. Source: [13]

Another test condition is also simulated considering a constant supply pressure of 1300 psig (9.0 MPa) and a dimensionless input signal for pilot brake pedal with an average value of 0.81 and an amplitude magnitude of 0.19. The resultant brake pressure ranges from 883 psig (6.1 MPa) to 1291 psig (8.9 MPa) when the input is applied statically at its minimum and maximum values. Therefore, it represents a simulation condition with an average brake pressure of about 1110 psig (7.7 MPa).

Table 3 summarizes the main properties of the frequency response determined by means of the simulational model for both operational conditions. The results comparison with the data provided in [13] is not so straightforward, because the reference presents the results of tests accomplished at four different conditions with average pressures close to the ones simulated herein but with two different amplitudes for each case. In general terms, close values for the properties are found for both simulated conditions. On the other hand, the result values shown in Table 3 have averages smaller than the ones found in the test results of [13]. Finally, it is important to highlight that, despite [13] refers to the phase angles as positive values, they are understood as negative magnitudes based on the axle orientation shown in Figure 20 and also on the own dynamics expected for the system under evaluation.

Table 3: Frequency response main properties

Reference Test Pressure (psig)	Resonant Point Frequency or -3 dB Frequency (Hz)	Gain at Resonance or -3 dB point (dB)	Phase Angle at Resonance or -3 dB (degrees)	Frequency at -90º Phase Angle (Hz)
544 ± 200	3.0	0.12	-51	5.0
1087 ± 204	3.0	0.09	-50	5.1

The last phase in the hydraulic system validation process consists in the static evaluation of the brake pressure under the antiskid valve actuation. For this purpose, the relationship between the antiskid valve input and the resultant brake

pressure is verified by applying a step input in the antiskid valve 1st stage and measuring the hydraulic pressure in the brake assembly after the necessary stabilization time has elapsed. Figure 21 illustrates the antiskid valve step input.

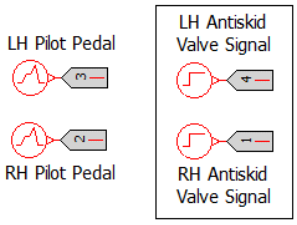

Figure 21: Input elements for antiskid valve actuation analysis

For a supply pressure condition of 1660 psig (11.4 MPa) and pilot brake pedals full application, Figure 22 depicts the brake pressure response when a step input of 46% of its total scale is introduced at 0.5 second of simulation. As it can be seen, the brake pressure presents an oscillatory transient associated with the opening kinematics of the antiskid valve, illustrated in the figure by the relative position of its 1st stage internal spool. Afterwards, due to the dynamics of the system hydraulic accumulators, the brake pressure magnitude is slowly reduced before reaching a more constant value after some seconds of simulation.

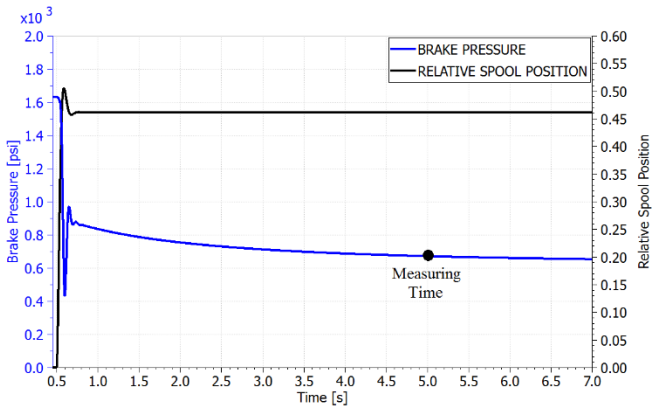

Figure 22: Brake pressure with a 46% step input in the antiskid valve

Several simulations are run with incremental improvements of 0.5 in the antiskid valve input signal and the brake pressure is measured after elapsing 5.0 seconds of simulation. Figure 22 highlights the measuring point. The same process is repeated for three distinct supply pressure conditions, that is, 1660 psig (11.4 MPa), 1020 psig (7.0 MPa) and 490 psig (3.4 MPa), and the results are plotted in Figure 23, Figure 24 and Figure 25, respectively. The expected range of system response, probably due to valve hysteresis, is provided in [13] for each simulated condition and reproduced in the figures for a better comparison. The x-axis comprises the valve input signal, which is dimensionless in the present model and has a limit value of 13.

The results obtained through LMS Amesim® computational model demonstrate a good relationship with the reference boundaries for lower and higher magnitudes of antiskid valve input signal. The main divergence is observed for intermediate input signals, when the simulated brake pressures assume values inferior to the limits informed in the reference.

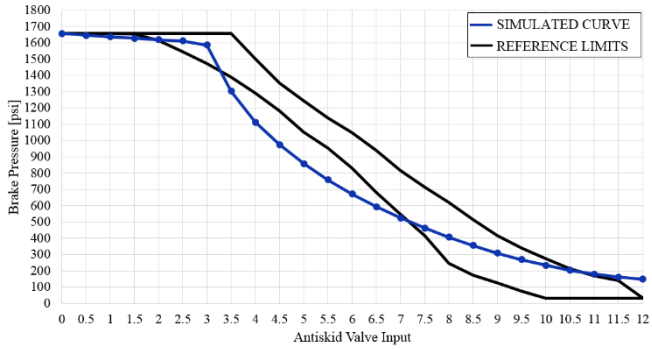

Figure 23: Brake pressure as a function of antiskid valve actuation for 1660 psig

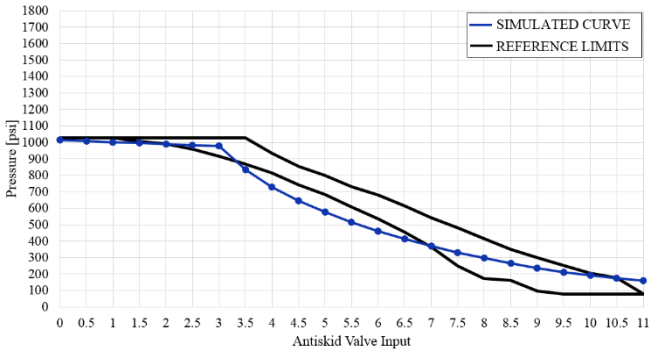

Figure 24: Brake pressure as a function of antiskid valve actuation for 1020 psig

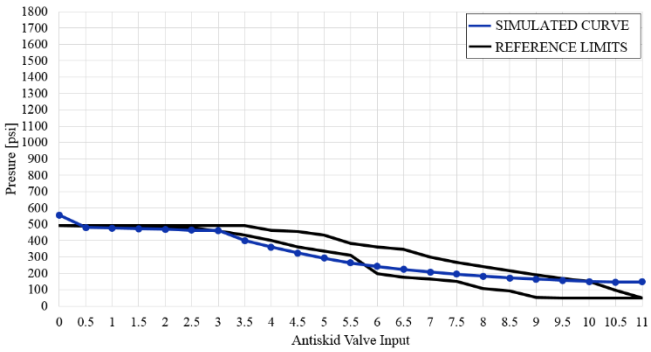

Figure 25: Brake pressure as a function of antiskid valve actuation for 490 psig

Regarding the intermediate antiskid valve input values, difference in the time adopted for pressure measurement or the own simplification adopted in the current modeling for the pilot dynamics between the antiskid valve stages are factors that might help explain the lower brake pressure values found in the simulation for those conditions. In order to illustrate the first point, simulations are repeated in Figure 26 for a supply pressure condition of 1660 psig (11.4 MPa), but reducing the measurement time to 1.0 second of simulation. As illustrated, results better adjusted to the boundaries are obtained if compared to the previous results of Figure 23.

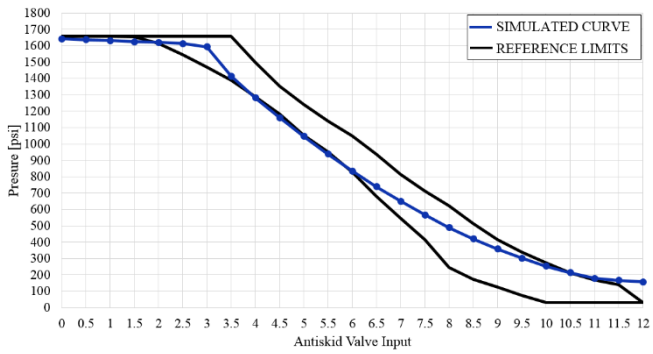

Figure 26: Brake pressure as a function of antiskid valve actuation for 1660 psig (measuring at 1.0 second)

Finally, a brake pressure higher than the supply pressure is noticed in Figure 25 for the null input condition. The justification for this behavior lies on the fact that an accumulator precharge pressure (700 psig) (4.83 MPa) higher than the supply pressure (550 psig) is adopted in the simulation. This condition, together with the presence of check valves in the system, allows the occurrence of a phenomenon similar to hydraulic lock. However, this effect does not impact the system operation since the hydraulic pressure supplied for the brake system in normal conditions (3000 psig) (20.68 MPa) is significantly higher than the one applied in that simulation case.

4 System Fault Simulation

As described in chapter 1, there are currently several structured methodologies and others ongoing studies to support the use of models in fault detection and diagnosis of aeronautical systems. Complete and well-organized processes like the ones described in [18] are also commonly applied when developing the safety assessment of aircraft airborne systems and equipment. Moreover, robust methods like the MSG-3 are nowadays used as reference for the elaboration of maintenance programs in aviation industry.

Considering this background, the present activity does not aim to replace the aforementioned methods, but just to illustrate a simplified, alternative or complementary approach to making a faster assessment of failure impacts on system behavior. The present methodology could be applied during detailed or even conceptual design phases of a system development process. It takes advantage of the current availability of physical modeling software with fast simulation times, which is exemplified herein by the LMS Amesim® model, simulated and validated in chapter 3.

This methodology is described in the flowchart of Figure 27 as divided into six steps. Each phase will be discussed as follows during the execution of an example for the brake system under analysis.

Phase 1:

Three particular failure modes are selected for the present study: a piston jam at extended position in one brake assembly, relevant internal leakage between the stages of antiskid valve, and noise in antiskid valve input signal.

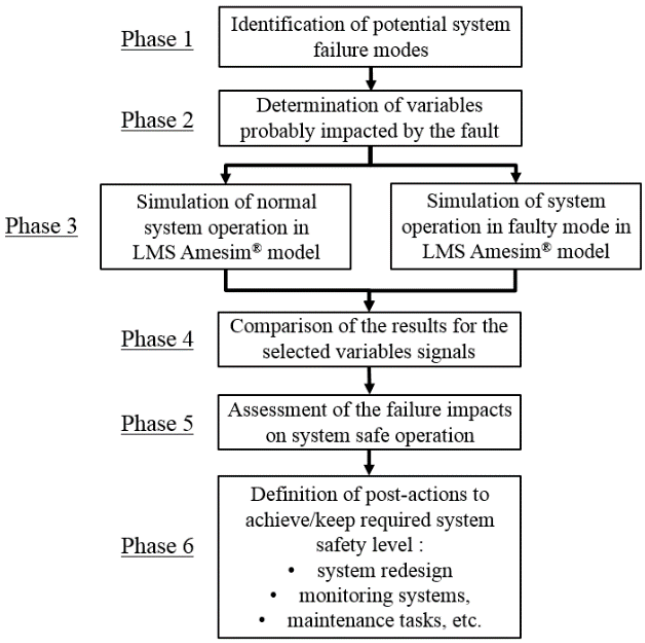

Figure 27: Simplified approach of model-based fault assessment in system operation

Phase 2:

Although more than a single variable might be impacted by each of the failure modes previously selected, only one signal per simulated failure will be chosen herein for demonstration purposes. Therefore, the brake torque will be applied to assess the impacts of the piston jam failure condition, meanwhile the brake pressure will be used to evaluate the effects of the other two failure modes.

Phase 3:

The impacts of a system failure mode shall be evaluated throughout the operational envelope. However, the current assessments will be limited to plotting only a single condition of operation for each failure mode to not be so extensive. A supply pressure of 1650 psig (11.4 MPa) is considered for the analyses.

The first simulated failure mode comprises the piston jam condition in one brake assembly. Since the gap before the beginning of disks compacting is 2.0 mm and the overall piston stroke is about 3.5 mm, it is adopted a hypothetical piston jam condition at 2.5 mm for the simulation. The implementation of this failure mode in LMS Amesim® model is straightforward, done by changing the initial displacement of one mass element of Figure 9 to 2.5 mm. In order to avoid computational errors, its lower and higher displacement limits are also updated to a small tolerance upon that value, that is, 2.4 mm and 2.6 mm, respectively. Therefore, a comparison between the brake assembly torque responses at 1000 rpm for both nominal and failed conditions is reproduced in Figure 28. The simulation consists of applying full pilot brake pedals in 0.5 second and releasing them at 1.5 seconds of simulation.

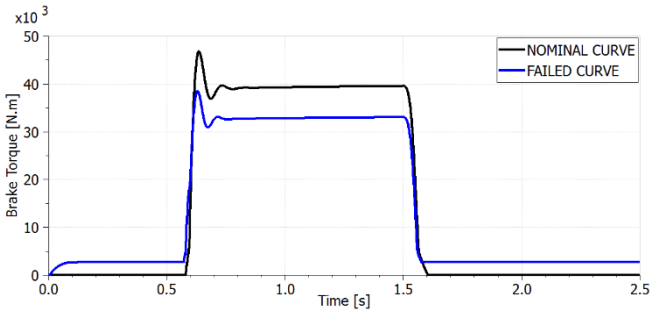

Figure 28: Brake torque response (nominal x failed)

The second failure mode to be analyzed is a significant internal leakage between the stages of one of the antiskid valves. Aiming to implement that failure, the pilot scheme shown in Figure 7 is updated for only one of the two antiskid valves by introducing a fixed laminar hydraulic orifice element between the outputs of the 1st and 2nd stages of the valve. The internal leakage implementation is depicted in Figure 29. Assuming the leakage is resultant of an increased gap in the spool bearing, the following dimensions are adopted for the orifice: 10 mm of width, 0.3 mm of clearance and 10 mm of length.

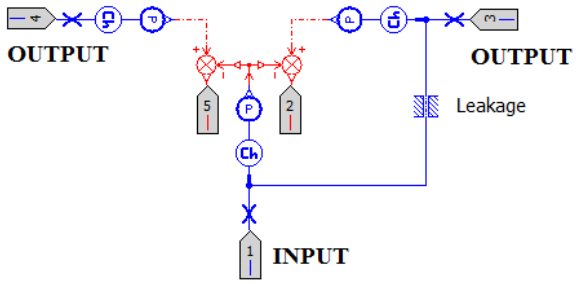

Figure 29: Antiskid valve internal leakage implementation

At first, no relevant difference is noticed in the brake pressure curves of both nominal and failed conditions when the same simulation input of the previous analysis, that is, full pilot brake pedals application in 0.5 second and release at 1.5 seconds of simulation, without any antiskid valve actuation, is applied. Therefore, a new condition is simulated considering now the actuation of the antiskid valve. For that purpose, the antiskid valve input signal illustrated in Figure 30 is used to exemplify the brake system behavior under antiskid system actuation. Full brake pedals application is assumed throughout the simulation time interval.

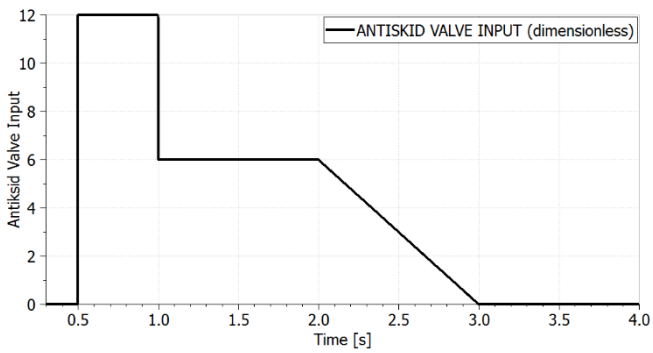

Figure 30: Antiskid valve input signal adopted for analysis

As a result, the brake pressures measured in both group of pistons of the brake assembly subjected to the actuation of the faulty antiskid valve are plotted in Figure 31. The pressure response in the other brake assembly, used herein as reference, is also provided in the same figure.

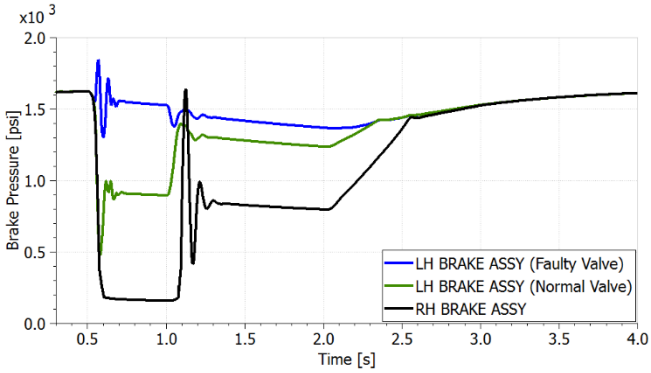

Figure 31: Brake pressure response (normal x faulty valve)

Finally, the third failure mode analysis consists in evaluating the impacts of a noisy antiskid valve input signal. That condition is simulated by adopting the same input signal profile of Figure 30, but adding a pseudo-random element in one of the antiskid valve signals as described in Figure 32. Again, full brake pedals application is considered along the whole simulation time interval.

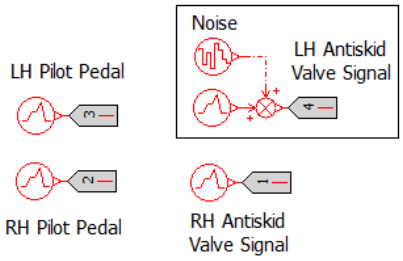

Figure 32: Noise added in LH antiskid valve signal

The resultant noisy signal of LH antiskid valve input is shown in Figure 33. A pseudo-random function of 50 Hz and amplitude equal to 1.2, which represents 10% of the maximum value of Figure 30, is adopted for the simulation.

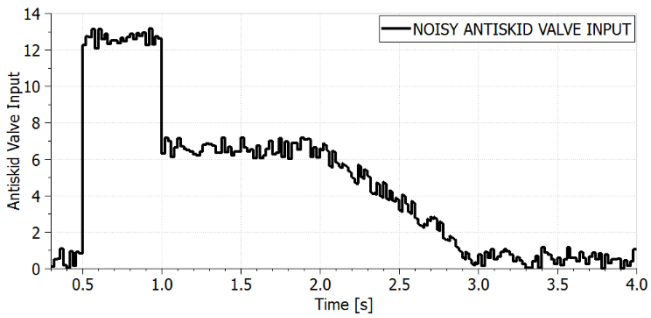

Figure 33: Noisy signal of LH antiskid valve input

The measurements of the resultant brake pressures in both brake assemblies are reproduced in Figure 34. The noisy input signal of Figure 33 is applied to the antiskid valve that operates the LH brake assembly, while the pure signal of Figure 30 is used for the RH brake assembly antiskid valve.

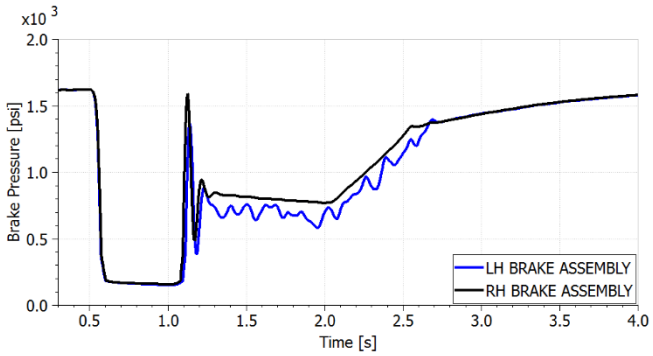

Figure 34: Brake pressure in brake assemblies (LH x RH)

Phase 4:

The two main effects of a piston jam condition in brake assembly can be noticed in Figure 28 for the brake torque behavior. For the simulated conditions, the unavailability of one piston represents a loss of 16.5% in the maximum torque value and the existence of a residual torque of 2662 N.m after brake pressure removal.

Several effects of a significant internal leakage between the stages of antiskid valve are identified through Figure 31. First of all, the leakage impacts not only the group of pistons actuated by the 2nd stage with the failure, but also the other group in the brake assembly since it is under the control of the same antiskid valve. The second effect regards the brake pressure level achieved at each stage of the antiskid system actuation. As represented by the black curve, the normal valve allows a brake pressure dump of about 90% in the first stage (from 0.6 to 1.0 second of simulation) and 50% in the second stage (from 1.5 to 2.0 seconds) if compared to the initial brake pressure at 0.3 second. On the other hand, reductions of no more than 6% in the first stage and 15% in the second stage of the initial brake pressure are achieved for the most critical group of pistons (blue curve) when the failure is present. Finally, the pressure curves of the brake assembly actuated by the faulty antiskid valve reach the final asymptotic curve in the end of cycle approximately 0.65 second earlier than the nominal curve.

The last simulated failure mode demonstrates in Figure 34 to have no relevant impact on the first stage of pressure dump (from 0.6 to 1.0 second of simulation), but the second stage is characterized by an oscillatory behavior with an average value about 14% smaller than the original curve, which lasts until simulation time reaches 2.7 seconds.

Phase 5:

The objective of the present phase is not to determine herein the severities or probabilities of the failure modes, but only to make a qualitative assessment about the potential impacts of those failures in the system safe operation.

As evaluated in the previous phase, the piston jam condition might be responsible for a reduction in the available brake torque of a brake assembly, as well as for the existence of a residual torque on it. As a result, the overall aircraft stopping distance in landing might be jeopardized by the first effect and an adverse condition referred to as dragging brake might occur due to the second effect. A dragging brake condition may eventually lead to inadvertent yaws on the ground or even to a tire burst event because of the generated heat on the tire.

Due to the abnormal behavior identified in the brake pressure curve during the operation of antiskid valve with internal leakage, the antiskid system performance is the most affected by that condition. The inability of dumping the brake pressure when required significantly impacts the antiskid system principle of operation, increasing the possibility of a wheel skid and, consequently, a tire blowout.

Lastly, the impacts of the noisy antiskid valve signal condition might not be so relevant as those of the previous failure modes. However, the present failure condition might contribute to the reduction of the antiskid system efficiency and potentially lead to some landing gear vibration issues due to the unexpected oscillations developed in the brake pressure response.

Phase 6:

A piston jam event is not a failure condition easy to be detected at real-time, except perhaps by its potential effects. The brake temperature monitoring system (BTMS) can normally identify a brake overheating due to a dragging brake during takeoff and alert the crew to not retract the landing gear on that condition, avoiding a more critical scenario for aircraft safety to take place. On the other hand, during ground maneuvers the crew will need to pay attention to any perception of inadvertent yaw in order to counteract it by means of landing gear steering and rudder pedals. Moreover, the accomplishment of regular brake assembly overhauls and the execution of system periodic functional tests may help the detection of abnormalities with the brakes pistons.

A valve internal leakage comprises a failure mode difficult to be diagnosed during maintenance tasks. Since it might have significant impacts on the antiskid system functionalities, the development of a monitoring control loop to detect the resultant effects of that failure could be a solution that needs to be evaluated and have its feasibility checked. The antiskid valve redesign aiming to minimize the impacts of an internal leakage between its stages could also be another option for further analysis.

Finally, the detection of undesirable noise in control unit signals represents one of the most challenging tasks during failure investigations. Besides the possibility of happening only at some particular operational conditions, which makes it difficult to reproduce the failure during maintenance activities, the effects of a noisy signal might not be so pronounced as those of other failure conditions. Consequently, architecture solutions to avoid noise and vibration sources, a good component qualification test campaign and the execution of several system integration tests on the aircraft might represent solutions to minimize the noise occurrence. The implementation of a health monitoring system to predict system degradation based on the measurement of the quality of relevant variables signals could also be an alternative to be studied during the system development phase.

5 Conclusions

The objective of the present work was to demonstrate the use of a computational model of an aircraft hydraulic brake system to assess the behavior of system relevant variables in normal operational conditions and the potential effects of typical failures in system performance.

The example of modeling and simulation accomplished in LMS Amesim® software seemed to be satisfactorily representative of an aircraft hydraulic brake system based on the results of the model validation process. Data from the literature for a real aircraft brake system was applied to support validation.

The current work also covered a review of aircraft brake systems, their functionalities and some methodologies currently applied for model-based fault detection and diagnoses. Moreover, a simplified approach to making a quicker assessment of failure impacts on system behavior was introduced and its main steps better described by means of some practical examples. The present methodology takes advantage of the current availability of physical modeling software with fast simulation times, which is exemplified herein by the use of a LMS Amesim® model.

Simulation of more failure mode cases and the integration of the current model with the antiskid system controller, aircraft body dynamics and wheel/tire model are instances of potential future works. In a fully-integrated model, the brake assembly and hydraulic brake system models could be deeply evaluated considering their interfaces. Besides the check of performance requirements like aircraft stopping distance, it would also allow a quantitative assessment about the failure impacts by comparing the results of efficiency parameters of the antiskid system in normal and faulty operational modes.

Finally, the topics addressed in the current work could be applied to help support the verification process of system compliance with performance and safety requirements, as well as for early identification of failures and operational problems still during the product development phase, highlighting the gains of applying them in the context of aeronautical systems engineering.

Nomenclature

A list of the variables and parameters referred to in this article is present below.

Designation	Denotation	Unit
A_o	Orifice area	[m^2]
c	Sound speed	[m/s]
C_d	Discharge coefficient	
C_f	Ideal compliance	[m^3/Pa]
D	Tube inside diameter	[m]
D_o	Restrictor orifice diameter	[m]
D_n	Dissipation number	
f	Tube friction factor	
F_{action}	Piston acting force from pressure application	[N]
F_{result}	Piston resultant force	[N]
F_{return}	Piston opposing force from return mechanism	[N]
i	Node index	
j	Index of number of pistons	
I_f	Inertance parameter	[kg.m^4]
L	Tube length	[m]
N	Number of nodes	
$N_{pistons}$	Number of pistons	
N_{rotors}	Number of rotors	
P	Line pressure	[Pa]
p_i	Pressure in node with index i	[Pa]
Q	Fluid flow	[m^3/s]
q_i	Flow in node with index i	[m^3/s]
R	Tube internal section radius	[m]
R_{piston}	Application radius of brake force	[m]
t	Time	[s]
$T_{braking}$	Brake torque	[N.m]
T_c	Coulomb friction torque	[N.m]
T_{frict}	Friction torque	[N.m]
T_s	Static torque	[N.m]
V	Tube internal volume	[m^2]
V_L	Flow velocity	[m/s]
δ	Laminar flow coefficient	
ΔP	Pressure variation	[Pa]
θ	Relative angular displacement between surfaces	[rad]
μ	Fluid dynamic viscosity	[Pa.s]
μ_{disk}	Disk friction coefficient	
ϑ	Kinematic viscosity	[m^2/s]
ρ	Fluid density	[kg/m^3]
ω	Relative angular velocity between surfaces	[rad/s]

References

[1] N S Currey. *Aircraft Landing Gear Design: Principles and Practices*, AIAA Education Series, Washington, 1998. ISBN 0930403-41-X.

[2] I Moir, and A Seabridge. *Aircraft Systems: Mechanical, electrical, and avionics subsystems integration*. 2. ed. Bury St Edmunds: Professional Engineering Publishing, 2001. pp. 91-124. ISBN 1-86058-289-3.

[3] Federal Aviation Administration. *Flight Test Guide for Certification of Transport Category Airplanes*. AC 25-7C. Washington: U.S Department of Transportation, 2012.

[4] Society of Automotive Engineers. SAE Aerospace. *AIR1739B: Information on Antiskid Systems*. Warrendale, 2012.

[5] P Khapane. *Simulation of Landing Gear Dynamics and Brake-Gear Interaction*. Thesis (Doctor of Engineering), Technischen Universität Carolo-Wilhelmina zu Braunschweig, Braunschweig. 2008.

[6] P M Frank. Fault Diagnosis in Dynamic Systems Using Analytical and Knowledge-based Redundancy – A Survey and Some New Results. *Automatica*, v. 26, n. 3, pp. 459–474, 1990.

[7] J W Sheppard, and S G W Butcher. A Formal Analysis of Fault Diagnosis with D-Matrices. *Journal of Electronic Testing: Theory and Applications*, United States, v. 23, n. 4, pp. 309-322, August. 2007.

[8] R Isermann. Model-based fault-detection and diagnosis – status and applications. *Annual Reviews in Control*, v.29, n.1, pp.71-85, 2005.

[9] K Medjaher. A bond graph model-based fault detection and isolation. In: J Andrews, C H Bérenguer, and L Jackson. *Maintenance Modelling and Applications*. Det Norske Veritas, pp. 503-512, 2011. <https://hal.archives-ouvertes.fr/hal-00635549>.

[10] J C da Silva, A Saxena, E Balaban, and K Goebel. A Knowledge-based system approach for sensor fault modeling, detection and mitigation. *Expert System with Applications: An International Journal*, v.39, n.12, pp.10977-10989, September 2012.

[11] P J Feenstra, P J Mosterman, G Biswas, P C Breedveld. Bond Graph Modeling Procedures for Fault Detection and Isolation of Complex Flow Processes. Proc. of *International Conference on Bond Graph Modelling (ICBM'01)*, SCS Publishing, v.33, pp.77-82, 2001.

[12] M K Wahi, S M Warren, and H H Straub. *An Extended Prediction Model for Airplane Braking Distance and a Specification for a Total Braking Prediction System*: Volume I. Ohio: 1977. (ASD-TR-77-6 Vol.I).

[13] M K Wahi, S M Warren, and H H Straub. *An Extended Prediction Model for Airplane Braking Distance and a Specification for a Total Braking Prediction System*: Volume II. Ohio: 1977. (ASD-TR-77-6 Vol.II).

[14] E O Doebelin, *System Dynamics: Modeling, Analysis, Simulation, Design*. Marcel Dekker, New York, 1998, pp. 54-75, 206-255. ISBN 0-8247-0126-7

[15] LMS. *AMESim Help*. AMEHelp, 2013.

[16] H E Merritt. *Hydraulic Control Systems*. John Wileys and Sons, Cincinnati, Ohio, 1967. ISBN 0-471-59617-5.

[17] D A Bailey. *Investigation of Improvements in Aircraft Braking Design*. Thesis (Doctor of Philosophy) - Cranfield University, Cranfield. 2004.

[18] Society of Automotive Engineers. SAE Aerospace. *ARP4761: Guidelines and Methods for Conducting the Safety Assessment Process on Civil Airborne Systems and Equipment*. Warrendale, 1996.

Modeling and Simulation of a Single Engine Aircraft Fuel System

Nathan Raphael do Nascimento Pinheiro, and Luiz Carlos Sandoval Góes

Engineering Mechanic Department, Instituto Tecnológico de Aeronáutica, São José dos Campos, São Paulo/Brazil
E-mail: nathan.raphael@gmail.com, and goes@ita.br

Abstract

The primary function of an aircraft fuel system is to provide a reliable fuel flow at a rate and pressure established for proper engine functioning for each operational condition and aircraft certification requirement. However, to provide fuel flow at a given pressure all sub-functions of the fuel system must work properly simultaneously and integrated as the pressure refueling, quantity gauging, control, and ventilation systems. The present work describes the model creation and simulation for aircraft fuel system during pressure refueling and single engine operation. Since the fuel system is composed of several subsystems highly integrated to each other, the proper functioning of the fuel system depends on this integration and a literature review was accomplished in order to raise the required information regarding sub-functions integration to create the model in LMS Amesim®. The LMS Amesim® model created to represent the existing correlations between each sub-system was simulated for pressure refueling and engine operations. Finally, the result of model simulation shows the functioning of the fuel system for normal operational conditions in conjunction with its sub-systems.

Keywords: Modeling, simulation, aircraft, fuel, system

1 Introduction

The primary function of an aircraft fuel system is to provide a reliable fuel flow at a rate and pressure established for proper engine functioning for each operational condition and aircraft certification requirement. Without the constant fuel supply (within the proper limits) the motive thrust provided by the engine could be compromised as well as aircraft ability to sustain flight. Thus, the fuel system shows itself as essential for a safe flight and mission accomplishment [1].

Other functions of the fuel system in modern aircraft are given by the close relation between overall systems performance as shown in fig.1. The fuel system can interfere in the aircraft performance by moving the CG positioning thus changing flight control stability margins. The fuel can be used as heat sink for systems with high rates of heat generation, or even as hydraulic fluid [2] for example in case of the Lockheed SR-71 Blackbird fuel valves located close to the afterburner [3].

The fuel system is composed of several subsystems to comply with the functions required by the propulsion system. In this way, the system is divided in the following subsystems: engine feed, fuel storage, refuel and defuel, fuel transfer, engine feed line fuel pressurization, vent systems, fuel jettison, in-flight refueling, and others. The proper functioning of the fuel system depends on the performance and integration of the aforementioned subsystems, for this reason some of them, depending on the aircraft missions, must be tested to guarantee its integration [4].

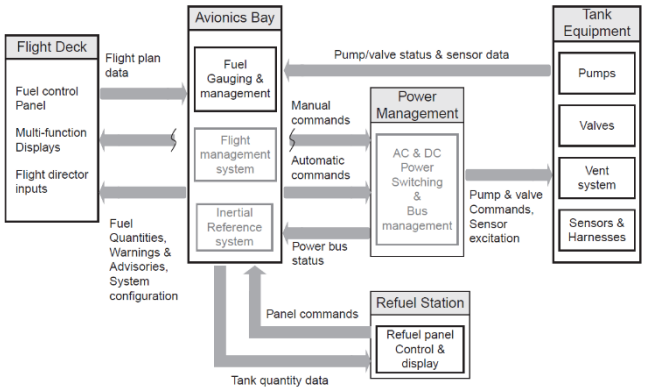

Figure 1: Fuel system typical schematic [1]

The work presented herein aims to model and simulate the fuel system of a single engine aircraft to determine the behavior of the entirely system by the simultaneous and integrated simulation of it sub functions. The fuel system architecture chosen for the simulation is based on military aircraft applications in order to represent specific operational conditions and restrictions, as the use of a main tank which needs to be completely full during operation. The focus of this work is to model and simulate an aircraft fuel system for refueling and defueling operations, and also pressurization of engine feed line. All system models are implemented in LMS Amesim®. The main components

behavior is presented in graphs to validate the hypotheses made and requirements to modeled system.

The LMS Amesim® is a multi-physics model and simulation software where different domains can be integrated and analyzed simultaneously. In addition it has specific aerospace libraries such as the fuel system library which presents already implemented application as gaging system and fuel tank models. The LMS Amesim® was chosen for this analysis because of the already modeled components and the capability of integrating different domains in the same model.

2 Modeling and Simulation

The modeling process adopted for this work consists of identifying the fuel system functions to be tested, the components used to perform system functions, and fuel properties. Therefore a specific fuel system was chosen based on the real application and also to represent the aspects related to a generic aircraft fuel system model presented in fig.2. The fuel system model was developed with LMS Amesim®. The hypotheses and simplifications applied to fuel system model adopted for analysis, as well as generic parameters used to represent real components will be described in next sections.

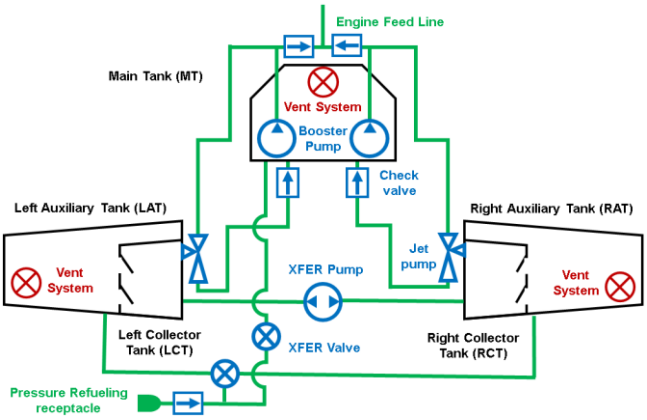

Figure 2: Fuel system adopted for analysis

In the modeling process adopted for this work, Jet A-1is considered as the fuel reference for all analysis. As Jet A-1 is widely used for jet turbine and its properties are well known for the range analysis, all simulations shown in this section were developed using Jet A-1 properties.

There are a series of limitations imposed by the assumptions made on LMS Amesim® libraries that work for fuel system simulation as fundamental hypotheses. These simplification hypotheses are listed below:

- The liquid temperature is homogeneous within the tank;
- The gas temperature is homogeneous within the tank;
- The fuel inertia is not considered while analyzing fuel accelerations effect, thus slosh is not accounted for in the presented analysis;
- The reference frame definition is fixed, that is why the tank has a one meter cubic form;
- The composition of the gas in the tank is not affected by the fuel pressure and temperature state;
- Wall orifices are circular.

As the right and left tanks have the same characteristics, components and functions, in this work it was used only the left and collector tank to represent the entirely system. Therefore the lack of information regarding right wing tank functioning, the left wing tank in addition with the collector tank present enough information about the functions to be tested regarding the completely system, thus saving computational effort.

As the collector tank has the purpose of providing fuel flow at pressure and flow rate established by engine fuel consumption during aircraft operation, it is very important to have this tank full whenever it is possible [5]. To guarantee that the collector tank will be full whenever the system has enough fuel to accomplish it, this tank will be the first to be refueled and the last tank to sold out during engine operation.

The block diagram presented in fig.3 represents the fuel system architecture chosen for analysis and presented in fig.2. To represent all existing components in the metaphysics simulation, the following libraries were chosen from LMS Amesim® category path list: Aircraft Fuel System, Signal, Control, Mechanical, Hydraulic, Pneumatic, Thermal, Thermal Hydraulic, and Aeronautics & Space. In this way all the components needed to represent the system architecture in fig.2 were modeled in fig.3 for the fuel system simulation.

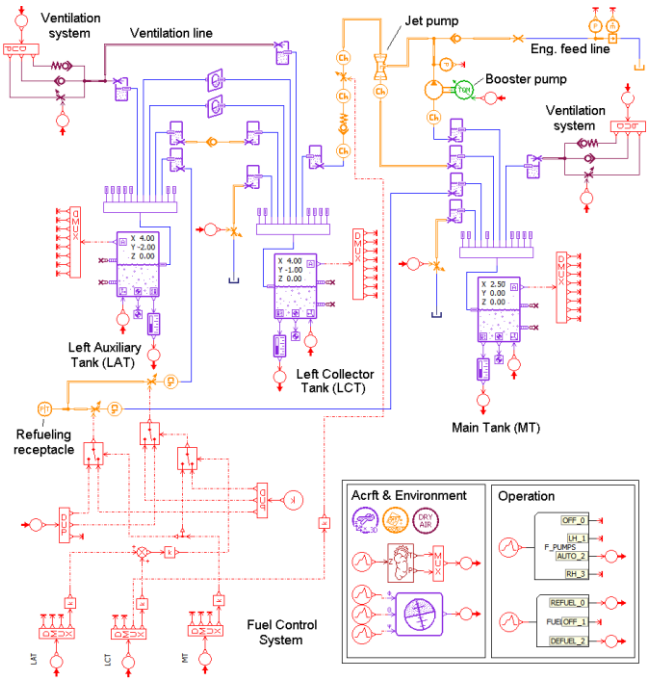

Figure 3: Fuel system model in LMS Amesim®

To run the presented fuel system model on LMS Amesim® the program configuration chosen is a standard integrator with a tolerance of 10-6.

3 Results

The fuel system functions are highly integrated. The ventilation, gauging, and management systems work in parallel with the refueling, defueling, engine feed line, and transfer fuel system. For this reason the simulation results presented in this section corresponds to the fuel system simulation as a whole. In the fig.4 and fig.5 it is presented the parameters chosen to validate that the subsystems are working properly to guarantee that all fuel system functions are performed correctly. Time slices are shown to analyze specific functions or operational procedures.

The operation of the refueling system requires an interaction between the aircraft and ground service team or flight crew. In the figures presented herein these interfaces are represented as signal controls. During the simulation time, the main signal controls are shown to exemplify the actuation of two operational procedures: refueling and fuel pumps activation. In fig.4 it is shown the signal controls for the simulation model.

Firstly, the refueling signal, generally given by the ground service team, shows that the refueling operation is performed from 0 seconds until instant 800 seconds. During this time defueling signal and fuel pump electrical signal are not activated. After the completion of fuel tanks the fuel pump is activated at instant 900 seconds and the fuel is pressurized through the engine feed line until the end of simulation at instant 46,886 seconds.

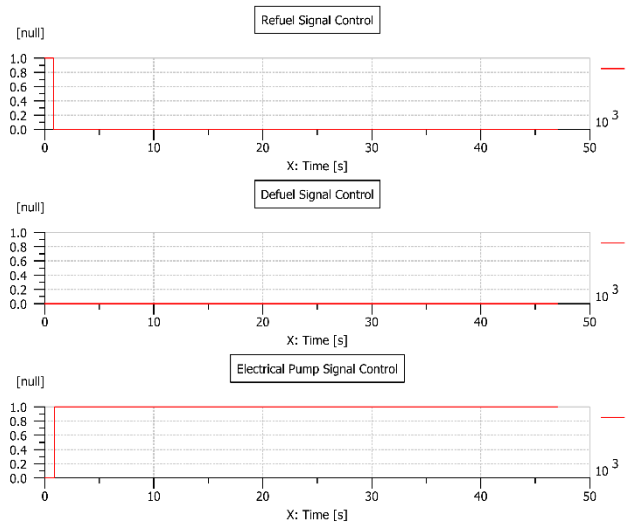

Figure 4: Signal control

The fuel tanks dimensions adopted for the simulation are cubes of one meter edge size only to simplify the gauging system. The gauging system is composed of fuel probes which inform the fuel level stored in each tank. The indication of zero meters means that there is no fuel stored, and one meter means that there is one cubic meter of fuel stored, i.e. the fuel tank is completely full. Therefore, the value presented by the fuel gauging system can be interpreted as tank percentage completion.

In fig.5 it is shown fuel tank levels in meters during the entire operation. The first graph shows the main tank (MT) level responsible to provide fuel to the engine feed line, the second shows the left collector tank (LCT) level designed to collect all fuel from the left auxiliary tank and transfer it to the main tank, and the third graph presents the left auxiliary tank (LAT) designed to store fuel. These three tanks (MT, LCT and LAT) are presented in fig.3.

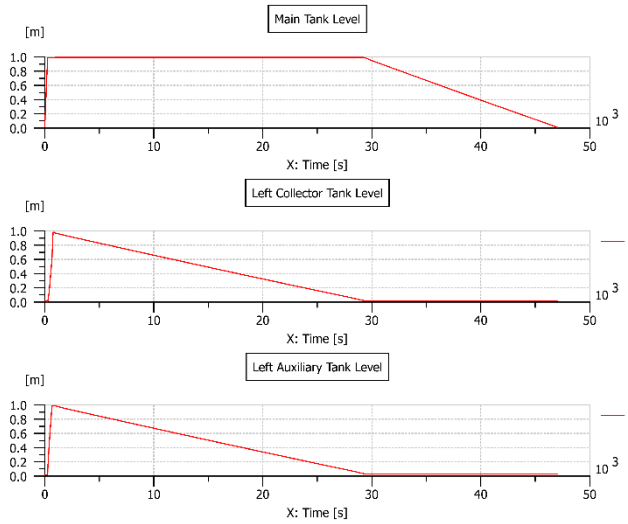

Figure 5: Tanks level during system fuel system operation

As shown in the system architecture in fig.2 and model in fig.3, there is one main liquid communication between the left auxiliary tank and the left collector tank which is the flapper valve. There are also two holes that connect one tank to another, one hole is located in the bottom of the tanks and the other in the top. Once the left auxiliary tank is refueled and the liquid level reaches a minimum height to pressurize the check valve, the check valve opens to allow fuel flow from the outer to the inner wing tank. In fig.6 it is shown that once the left auxiliary tank level increases, the fuel flow in the check valve also increases until the end of the fuel transference between tanks. Once the left collector tank is fully refueled there is no pressure differential, so there is no more fuel flow through the check valve.

At the instant 650 sec shown in fig.6, the upper hole that connects both tanks (as shown in fig.3) is closed. As the pressure inside the left auxiliary tank increases because of the fuel level, the fuel flow rate through the check valve also increases. Then, at instant 675 sec the left auxiliary tank is completely refueled, as shown in fig.6 in the first chart. As the duel flow is constant during tanks refueling, and the left auxiliary tank is already fulfilled, the fuel flow rate for the remaining tank increases, as shown in fig.6 in the second chart, instant 675 sec.

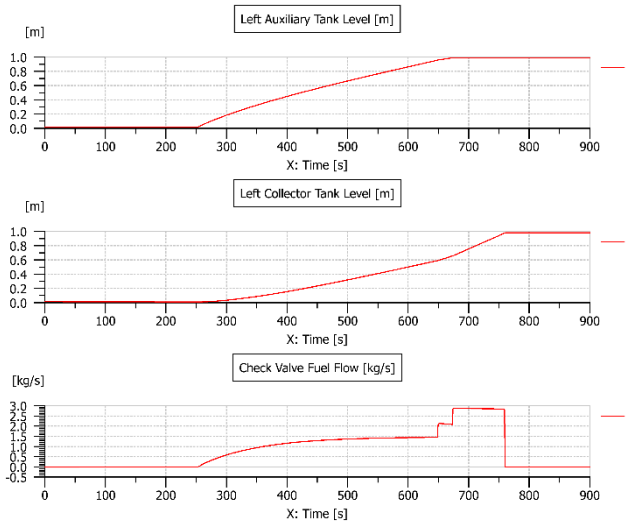

Figure 6: Tanks level and check valve fuel flow

To guarantee that the fuel tank is completely refueled at the time needed using the pressure refueling system and without causing any structural damage to the aircraft, it is necessary to permit that the volume of air stocked in the tanks gets to the atmosphere [6]. For this reason vent valves with relatively high admissible flow rates are opened by the same refueling signal. Thus the air stored in the tanks is removed while tanks are refueled.

Because of the fuel system architecture adopted for the analysis and also because of the tank refueling sequence, while the main tank is refueled, the volume of air remaining in the tank is expelled through the venting system at the same rate the tank is refueled as suggested by graphs in fig.7. The negatives values shown in the second row indicates that the fuel is getting in to the fuel tanks. Since the left auxiliary and collector tank ventilation system are the same, the collector tank ventilates through the auxiliary tank.

From instant 0 to 250 sec in the third chart of fig.7, as the main tank is refueled, the maximum air flow through the ventilation port is observed. From instant 250 sec to 650 sec, the left auxiliary and collector tanks are refueled. As the refueling point is located in the left auxiliary tank, the auxiliary tank is refueled faster than the collector tank. For this reason the air flow through its ventilation port is higher than in the auxiliary tank. However, the sum of air flow measured in both wing tanks has the same magnitude as the flow measured between instants 0 to 250 sec in the main tank.

At instant 650 sec in fig.7, the fuel level reaches the ventilation hole located in the upper part of the wing tanks. As the auxiliary tank is already full, and the ventilation hole internal outlet is below the fuel level, the air flow stops in the auxiliary tank ventilation port. As mentioned before, once the auxiliary tank is refueled, all the fuel flow once divided by the two tanks is directly transferred to the left collector tank. For this reason, after instant 650 sec, the fuel level in the left collector tank increases in a higher rate compared to instant 250 sec to 650 sec. As the refueling ratio increases, the air flow through the ventilation system also increases from 650 sec to 760 sec, shown in the third chart of fig.7.

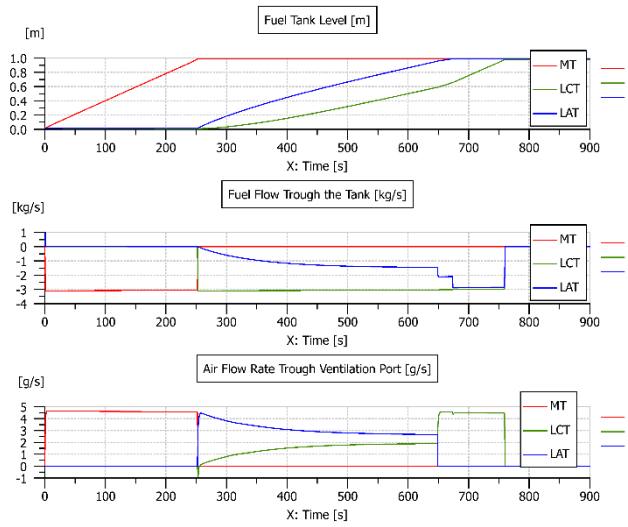

Figure 7: Ventilation system operating during refueling

The most important function of the fuel system is to feed the engine in any point of the aircraft flight envelope [5]. So in order to avoid fuel starvation, the situation where the aircraft has fuel but cannot provide it at require flow rate and pressure to the engine, the fuel feed line is in many applications pressurized by booster pumps. In this simulation, a flow rate of 150 kg/h and line pressurization of at least 6 psi adopted to guarantee that the engine will receive the quantity of fuel needed for operation without cavitation in the feed line. The engine's manufacturer recommends an overpressure of 2 psi above fuel vapor pressure in the worst envelope condition, and the maximum fuel flow must be determined according to the maximum engine consumption.

The fig.8 shows the main parameters related to engine feed line pressurization during engine operation. The first chart shows the fuel pump control signal used to actuate the electrical pumps, in this case booster pumps. The fuel pump is actuated just before tank refueling from instant 900 seconds until the end of simulation. The second chart presents the fuel pressure provided by the booster pumps to the engine feed line. In this case the pressure is measured upstream to the check valve for engine feed line pressure monitoring. The fuel pump parameters for analyses were chosen to guarantee that the pressure in the fuel line remains at least at 6 psi, however, according to simulation results, the minimum pressure during aircraft operation is 8.7 psi. The third chart shows the fuel flow through the check valve during simulation. From instant 900 seconds to the end of the simulation, the lowest registered flow rate is 152 kg/h. Finally, the fourth chart shows the fuel tank level decreasing while the engine is operating. Because of the fuel system architecture adopted for the analyses, the booster pump pressurizes the engine feed line and the jet pump. Therefore fuel is transferred from the left auxiliary to collector tank by the jet pump. Once there is no more fuel in the wing tanks (left auxiliary and collector tanks), the fuel volume in the

main tank decreases and then pressure inside the tank drops until the vent valve reacts opening the check valve to allow air to come into the main tank. For this reason a step is observed in the pressure and fuel flow rates curves (second and third charts) when the wing tanks are just empty.

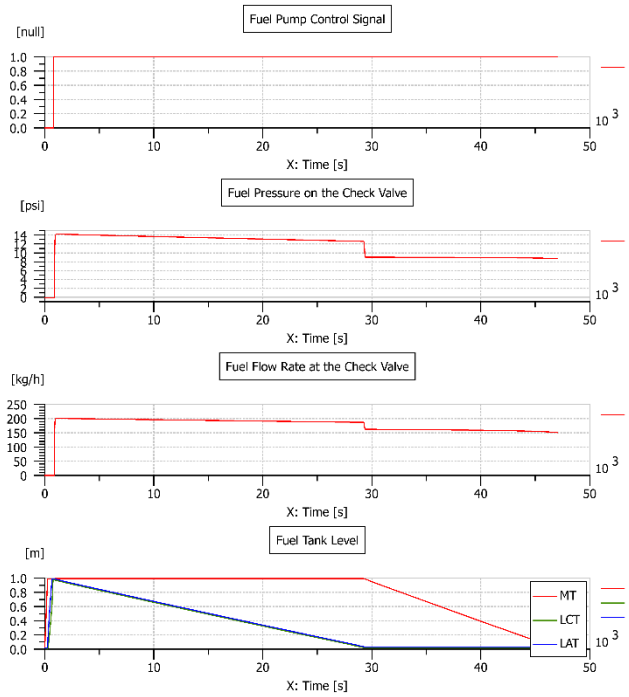

Figure 8: Engine feed line pressurization

4 Conclusions

In the work presented herein aspects of correlation between the fuel system sub-functions, and their integration were studied using simulation. For the two operations simulated, refueling and engine feed line pressurization, the interactive behavior of gaging, ventilation, management, transfer, and refueling subsystems was observed.

For the refueling operations simulation results shown that while the main tank is refueled, an induced air flow proportional to the refueling rate is observed in the ventilation system. As the flow rate remains the same during wing tanks refueling, the sum of the air flow from both wing tanks exhausted by the ventilation system is the same observed in the main tank. This behavior is similar to the one observed in real aircraft.

Also for the refueling operations, the gaging system actuates the shut-off valves to guarantee that the aircraft tanks will be refueled in the correct sequence. As the operation starts, the shut-off valve is opened while the valve located in the left auxiliary tank remains closed. Once the main tank is refueled, through the management system actuation, the shut-off valve located in the left auxiliary tank opens through the management system actuation, based on the information provided by the gaging system. Finally, the refueling operation is interrupted when the gaging system identifies that all tanks have been fully refueled. A signal control is sent to the management system that actuates the shut-off valves and finalizes the operation as shown in fig.4, as in a real aircraft normal operation.

For the engine feed line pressurization operation the fuel pump actuates pressurizing the engine feed line for a given pressure. The pump is commanded through an electrical motor which provides torque to the fuel pump. The engine feed pressurization provide the required pressure and fuel flow rate to the ejector pump, thus transferring fuel from the left collector tank to the main tank. During engine feed line pressurization, while there is usable fuel in the wing tanks, the fuel level is not affected. Only after all the fuel is exhausted from the wing tanks the main tank fuel level is affected. During the fuel transference from left collector tank to the main tank, the fuel level from the collector tank decreases causing a pressure differential between it and the left auxiliary tank. Because of this pressure differential the fuel level is gravitationally transferred from the auxiliary to the collector tank, as shown in fig.6. For both cases the transfer fuel system operates properly as in a real setup, the flapper valve opens due to a fuel level difference and the fuel is transferred through the ejector pump to the main tank.

During wing tank refueling, as shown in fig.7, three steps in the air flow curve were observed in the ventilation system. The steps are related to the refueling rate of each tank. At the first instants of operation both tanks have the same fuel level, when the fuel level in the left auxiliary tank reaches the ventilation hole between the two wing tanks, as the left auxiliary tank is almost full and ventilation area is reduced, the fuel flow to the left collector tank increases. For this reason the air flow instantly steps up. When the auxiliary tank is completely full and all the fuel transferred to the aircraft is directly refueled in the left collector tank, the fuel flow increases again, leading the ventilation flow to a higher step. In this case, the ventilation system works to relief the excess of pressure in the fuel tanks. The air flow through the ventilation system is proportional to the refueling ratio, as observed in real aircraft operation.

Therefore, in this study, modeling and simulation of a single engine aircraft fuel system, regarding refueling operations and pressurizing of the engine feed line, was accomplished through the model presented in fig.3. The fuel system architecture chosen for the simulation was based on military aircraft applications in order to represent specific operational conditions and restrictions, for example the capability to perform aerobatic maneuvers due to the existence of a full collector tank. The fuel system sub functions as ventilation, fuel quantity gauging, and fuel management control were implemented in the model and the results show the integrated functioning of all sub-functions to accomplishment of fuel system main functions.

The main conclusion is that the modelling and simulation approach can be applied to determine fuel system behavior during early development project phases. For example, the model can be adapted and used to determine the number of fuel pumps in the fuel tanks to provide adequate fuel flow to the engine, and also to actively control aircraft center of gravity via transferring of fuel between tanks. Another example is the study of best location of fuel probe gages

best for optimal accuracy. The work can also be used in model-based system design processes to foresee system solutions and issues during product development phases. The simulation can provide reliable information to decision making process. The process adopted herein is also applicable to existing aircraft aiding in troubleshooting investigations, gaging systems studies, ventilation system dimensioning, and fuel management system tests.

References

[1] MOIR, I.; SEABRIDGE, A. *Aircraft System*. Third. [S.l.]: John Wiley, 2008.

[2] LANGTON, R.; CLARK, C.; HEWITT, M.; RICHARDS, L. *Aircraft Fuel System*. First. [S.l.]: John Wiley, 2009.

[3] SR-71A Flight Manual. [S.l.]. Section I, page 4. 2016. <http://www.sr-71.org/> Acessed on 2016-12-13 at 20 p.m.

[4] MIHALYI, L. *Multi Objective Optimization and Probabilistic Design on Aircraft Fuel System*. Master's Thesis. Luleå University of Technology, 2007.

[5] GAVEL, H. On *Aircraft Fuel System Conceptual Design and Modeling*. Dissertation. Linköpings Universitet, 2007.

[6] MOIR, I.; SEABRIDGE, *A. Design and Development of Aircraft System*. [S.l.]: John Wiley, 2013.

Modeling and Parametric Identification of a Variable-Displacement Pressure-Compensated Pump

Filipe Spuri and Luiz Goes*

Mechanical Engineering Division, Instituto Tecnológico de Aeronáutica, ITA, São José dos Campos, São Paulo/Brazil
E-mail: filipespuri@gmail.com, goes@ita.br

Abstract

This work deals with bond-graph modeling and identification of variable-displacement pressure-compensated pump using a gray-box modeling approach. The model structure is defined using the bond graph technique, a graphical representation based on flow of energy in the system, which is implemented in the 20-sim software. The bond graph model is converted to state-space representation and the unknown parameters of equations of state are estimated applying parametric identification technique, the Prediction Error Method (PEM) on the SITB (System Identification Toolbox) MATLAB® software. The obtained model is validated collecting an experimental data set on test rig and comparing to simulation results.

Keywords: bond graph, system identification, variable displacement pump

1 Introduction

A variable displacement pressure compensated pump provides nearly constant pressure through the entire flow range (from zero to full flow). In aircraft systems, this type of hydraulic pump is typically used for hydraulic power generation, since for different flight phases the hydraulic demand varies and the hydraulic consumers such as control surface actuators require a minimum pressure for deflection of surfaces. The system is capable to adapt to a given aerodynamic load, and to maintain the desired performance.

The design definitions of a hydraulic pump plays a very important role to meet the requirements of a hydraulic supply system in order to satisfy the needs of the hydraulic consumers, such as to guarantee a minimum pressure and minimum time interval to reach the steady state pressure for variation of the load in the system. The use of a mathematical model for the design of a hydraulic pump or the analysis in the integrated hydraulic system is very useful to performance analysis, definition and sensitivity analysis of design parameters.

This work aims to develop a variable-displacement pressure-compensated pump model using the graphical modeling approach, based on bond-graph, which in conjunction with the Prediction Error Method (PEM), can be used to estimate the unknown hydraulic physical parameters. Delgado and Garcia [1] have implemented a software package DESIS that consists of a parametric identification module using the bond graph technique to represent the model structure.

In [2], Casoli and Anthony have developed a model of load sensing variable displacement pump using the bond graph methodology realized through the AMESim® simulation software. The white box modeling approach was used to model the flow compensator and pressure compensator, while the pump (control piston and swash plate) was modeled through the black box modeling by means of the correlation between control piston pressure and the system pressure.

Li and Thurner [3] have proposed the combination of black and grey box model identification to multi-axial testing systems with servo-hydraulic test cylinders. In this method, a white box model of the whole system is built and the unknown parameters are roughly estimated according to previous experience. To improve the white box model, the black box model identification is applied in order to adjust some model parameter estimates. Lastly, the grey box model identification is realized using the improved model as a new initial model. This approach is useful when the initial value of unknown system parameters cannot be accurately estimated.

In addition, two modeling techniques for variable piston pump are proposed in [4]: a black box model of the swash plate dynamic identified by performing a frequency response test and analysis, using a linear transfer function; and a non-linear grey box model, where all the unknown model parameters have been identified through non-linear optimization in MATLAB. Both approaches results in models with a good accuracy. However the grey box model has presented the best non-linear model of the swash plate angle control circuit.

In [5], the results of a systematic research for basic hydrostatic system containing a servo pump with different types of controls are presented. Theoretical models are developed by AMESim® and the experimental tests are performed using LabVIEW software.

In this work, the grey box system identification is applied to the state space model of a variable displacement pump integrated with the pressure compensator valve, which is obtained by the bond-graph method.

The alternative white box system identification technique is based on the physics of the process studied, and the perfect knowledge of the physical parameters, but the detailed knowledge of the system required to obtain accurate models are not usually known. In order to overcome these problems, the parameter estimation of the systems is used to obtain an accurate mathematical model of the processes under study.

The black box modeling is a system identification approach based on input/output model ("curve fitting"), with no prior knowledge of the physics of the process. However the model and its parameters have little physical significance. The gray box modeling approach combines prior physical knowledge (white box) with input/output data information (black box). In this case, the model may be not completely described by the physical equations, but equations and parameters are physically interpretable. One of advantages of grey box modeling is that missing data and noise are easily dealt; in addition it is possible to estimate environmental variables that are not directly measured.

The motivation to use the bond-graph approach as physical representation is that the graphical representation is very close to the physical system, making clear the relationship between the components of the system. Additionally, it allows working with different energy domains (mechanical / hydraulic) in a direct way, as in the development of the hydraulic pump model. The mathematical formalism intrinsic to it allows evaluating the quality of the model, such as the existence of an algebraic loop and differential causality that causes undesirable behaviors to the model, and also allows obtaining of state equations by means of algorithm, model structure used to apply the parametric identification method.

2 Variable-displacement pressure-compensated pump

The variable displacement pressure compensated pump is essentially comprised of a three-way pilot valve (pressure compensator valve) and a piston with spring return (control piston), that controls the tilt angle of swash plate [6] as presented in fig. 1 and fig. 2.

Initially, considering that there is no load (resistance to flow) in the system, the pump pressure is zero and the displacement is maximized due to the maximum swash plate angle. As the load increases the pressure consequently increases. The pump flow is at maximum until the pressure reaches the pressure adjusted by the compensator valve spring. A pressure above the setting causes the spool valve displacement allowing the flow to the control piston and decreasing the swash plate angle. Consequently, the pump flow decreases until the system reaches the pressure setting again. In case of decreasing load, the pressure decreases causing displacement of the control piston, so that it allows the flow from this to the return line, increasing the swash plate angle, thus the flow delivered by pump increases until the pressure setting is reached [8, 9].

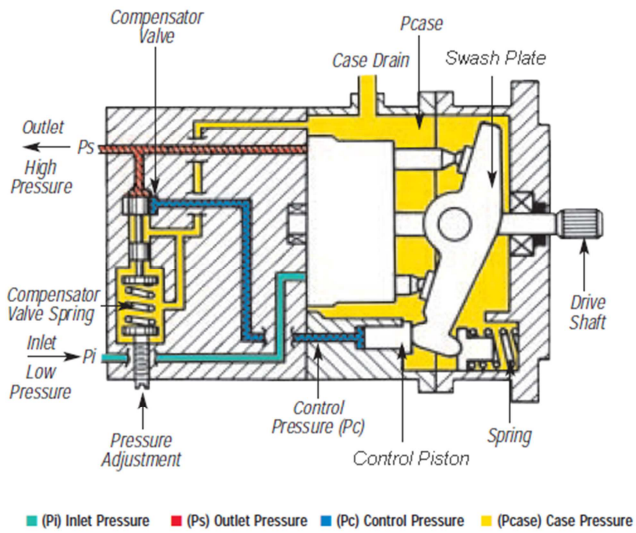

Figure 1:Cross-sectional view of variable-displacement pressure-compensated pump [7].

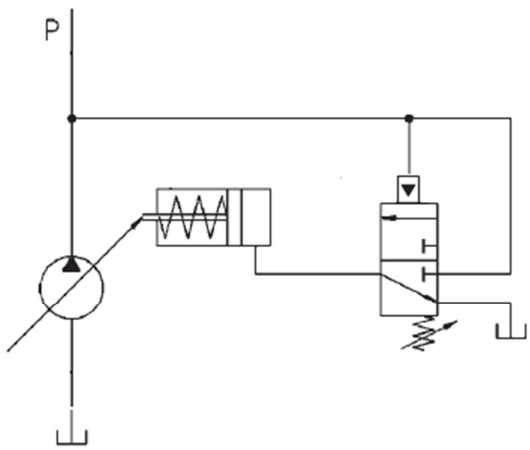

Figure 2: ISO schematic diagram of variable displacement pump with pressure compensator valve.

2.1 Bond-Graph model

Using the 20-sim software [10], a graphical representation of the energy bonds is represented [11, 12, 13], as shown in fig.3.

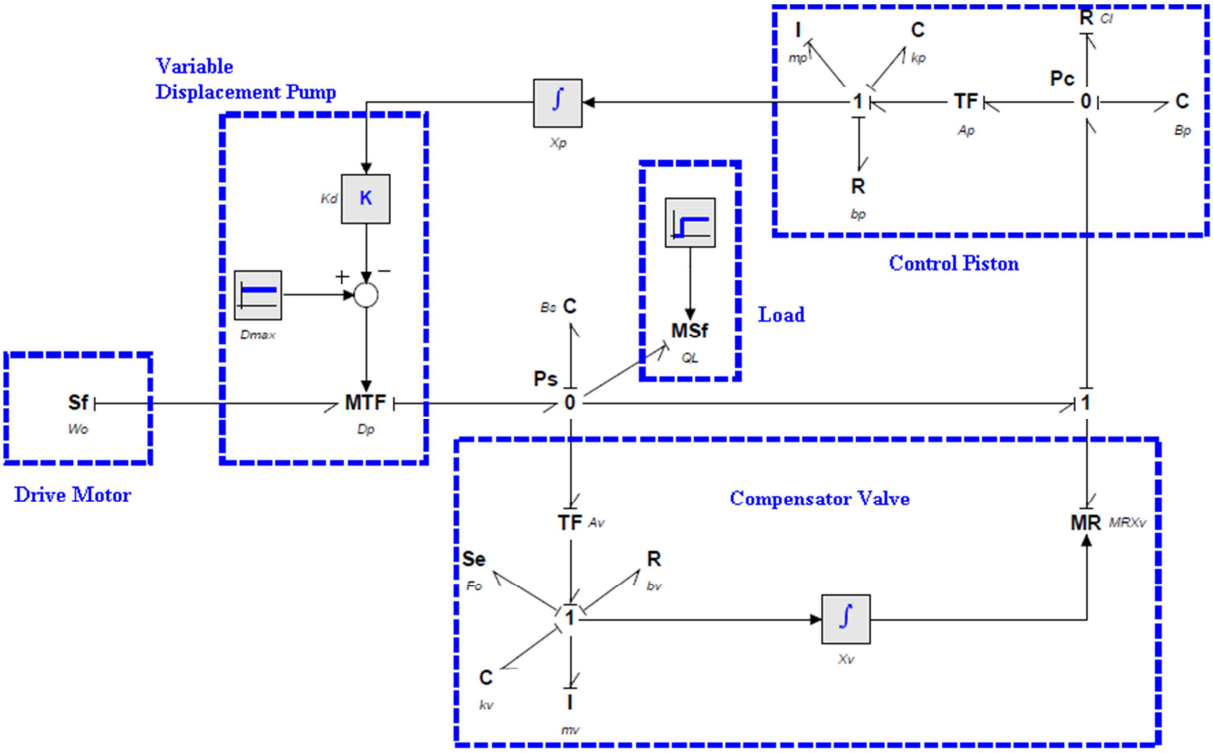

Figure 3: Bond Graph representation of variable-displacement pressure-compensated pump.

The compensator valve is modeled by the transformer element $TF{:}A_v$ that represents the area effect of the valve, which transforms the pump outlet pressure into a force acting upon the mass of the valve. To generate a displacement of the valve it is needed to overcome the force of the spring preload adjusted on compensator valve, represented by the effort source $Se{:}\ F_0$, where the F_0 is calculated according to eq. (1) considering the pump setting pressure, P_{sa}. The orifice of the compensator valve is modeled as a resistor modulated by the valve position, $MR{:}x_v$, defined as orifice equation eq. (2). Using Taylor series expansion and considering pressure gain $K_c << 0$, the linearized form of equation is presented in eq.(3).

$$F_0 = P_{sa}.A_v \tag{1}$$

$$Q_v = C_d.A_w.X_v.\sqrt{\frac{2}{\rho}\Delta P}\ sign(\Delta P) \tag{2}$$

$$\Delta Q_v = K_q.\Delta X_v \tag{3}$$

The control piston chamber is represented by storage node C-type, $C{:}B_p$, where the fluid compressibility B_p is defined in eq. (4). The capacitance of the fluid generates a pressure on the area of the piston defined by the transformer element $TF{:}A_p$.

$$B_p = \frac{V_p}{\beta} \tag{4}$$

The flow generated by the pump rotation is represented by $MTF{:}D_p$, a transformer element modulated by the volumetric displacement of the pump, which is calculated according to eq. (5), based on the displacement of the control piston x_p and the displacement gradient of the pump K_d.

$$D_p = D_{max} - K_d.X_p \tag{5}$$

Lastly, the flow demanded by hydraulic load is modeled using the representation of a modulated flow source, $Msf{:}Q_L$, which represents the flow demand variation. In addition, the capacitive effect at the pump outlet due to fluid compressibility is represented in eq. (6).

$$B_s = \frac{V_t}{\beta} \tag{6}$$

2.2 State space model

From the bond graph model, the state equations system is obtained by a systematic approach. Using the 20-sim software, the dynamic equations are defined and put in the state space form. Six state variables are required for the system representation, since the system has six energy storage elements. The state variables are defined in eq. (7) as state vector.

$$x(t) = \begin{bmatrix} x_1(t) \\ x_2(t) \\ x_3(t) \\ x_4(t) \\ x_5(t) \\ x_6(t) \end{bmatrix} = \begin{bmatrix} P_c(t) \\ P_s(t) \\ x_p(t) \\ x_v(t) \\ \dot{x}_p(t) \\ \dot{x}_v(t) \end{bmatrix} \tag{7}$$

The input vector u (t), according to eq. (8), is composed of the pressure compensator spring preload, F_0; the rotational speed of the drive motor, W_0; and the flow Q_L demanded by the hydraulic load.

$$u(t) = \begin{bmatrix} u_1(t) \\ u_2(t) \\ u_3(t) \end{bmatrix} = \begin{bmatrix} F_0(t) \\ W_0(t) \\ Q_L(t) \end{bmatrix} \tag{8}$$

Through the flow balance at the common effort junctions (0-junction) and the effort balance at the common flow junctions (junction 1) the state equations eq. (9), eq. (10), eq. (11), eq. (12), eq. (13) and eq. (14) are obtained.

$$\dot{x}_1 = \frac{1}{B_p}.\left[-\frac{1}{C_l}.x_1 + K_q x_4 - A_p.x_5\right] \tag{9}$$

$$\dot{x}_2 = \frac{1}{B_s}.[u_2.(D_{max} - K_d.x_3) - K_q x_4 - A_v.x_6 - u_3] \tag{10}$$

$$\dot{x}_3 = x_5 \tag{11}$$

$$\dot{x}_4 = x_6 \tag{12}$$

$$\dot{x}_5 = \frac{1}{m_p}.[A_p.x_1 - K_p.x_3 - b_p.x_5] \tag{13}$$

$$\dot{x}_6 = \frac{1}{m_v}.[A_v.x_2 - K_v.x_4 - b_v.x_6 - u_1] \tag{14}$$

Linearizing the equations at the operating point W_{0e} and x_{p0}, the equations in the state space form is defined according to eq. (15), eq. (16), eq. (17), eq. (18) and eq. (19).

$$\begin{cases} \dot{x}(t) = A.x(t) + B.u(t) \\ y(t) = C.x(t) + D.u(t) \end{cases} \tag{15}$$

$$A = \begin{bmatrix} -\frac{1}{B_p.C_l} & 0 & 0 & \frac{K_q}{B_p} & -\frac{A_p}{B_p} & 0 \\ 0 & 0 & -\frac{K_d.W_{0e}}{B_s} & -\frac{K_q}{B_s} & 0 & -\frac{A_v}{B_s} \\ 0 & 0 & 0 & 0 & 1 & 0 \\ 0 & 0 & 0 & 0 & 0 & 1 \\ \frac{A_p}{m_p} & 0 & -\frac{K_p}{m_p} & 0 & -\frac{b_p}{m_p} & 0 \\ 0 & \frac{A_v}{m_v} & 0 & -\frac{K_v}{m_v} & 0 & -\frac{b_v}{m_v} \end{bmatrix} \tag{16}$$

$$B = \begin{bmatrix} 0 & 0 & 0 \\ 0 & \frac{(D_{max} - X_{p0}.K_d)}{B_s} & -\frac{1}{B_s} \\ 0 & 0 & 0 \\ 0 & 0 & 0 \\ 0 & 0 & 0 \\ -\frac{1}{m_v} & 0 & 0 \end{bmatrix} \tag{17}$$

$$C = [0 \quad 1 \quad 0 \quad 0 \quad 0 \quad 0] \tag{18}$$

$$D = [0 \quad 0 \quad 0] \tag{19}$$

The model inputs F_0 and W_0 are defined as constant, therefore the input of model is given by the pump outlet flow Q_L and the outlet pressure P_s is considered as model output.

This choice of model input/output was defined in order to capture the characteristic dynamic behavior of pump for variable flow demand, specifically for aircraft hydraulic system, where the flow demand varies according to flight phase and a minimum effective pressure must be guaranteed for the correct operation of hydraulic actuators.

3 Parametric identification

After the state equations system is defined, using an experimental data set obtained on the test rig, the parametric identification technique is applied to estimate the values of the unknown parameters.

3.1 Experimental setup

The system data acquisition experiment consists of obtaining outlet pressure data for a variation of the flow demand while keeping constant the pump rotational speed. With the hydraulic pump operating at its setting pressure (2.034×10^7 Pa / 2950 psi), and providing the maximum flow

rate (1.61×10^{-3} m^3/s / 25.5 GPM) for the operating speed (390 rad/s / 3724 rpm), the hydraulic flow demand is a step input. The fig. 4 shows the schematic diagram of the experimental setup used to obtain input and output data from the system. This is comprised of a pressure transducer to measure the outlet pressure of the pump P_s and a flow sensor to measure the hydraulic flow demand Q_L of the simulated load through the variable orifice valve. The rotational speed sensor of the hydraulic pump is only used to monitor the speed of rotation at the set operating point W_{0e}.

The data plot of the flow demanded by the load and the pump outlet pressure, are presented in the fig. 5 and fig. 6, respectively.

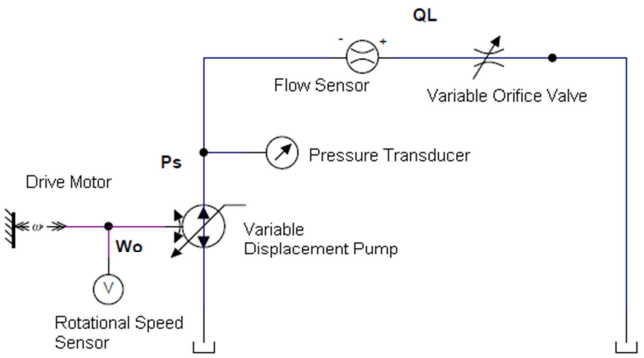

Figure 4: Schematic diagram of the rig test.

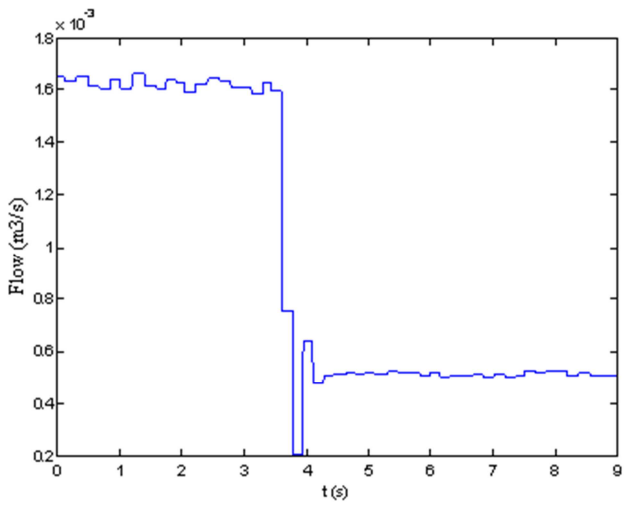

Figure 5: Hydraulic flow demanded by the load (step input).

As shown in the fig. 6, there is a ripple in the pump outlet pressure signal due to the movement of the pistons inside the pump cylinder; however the model under study does not include the piston to modeling of the ripple effect. Therefore it is necessary the pre-processing of data in order to use it in parametric identification method.

To smooth out the pressure signal ripple, a general moving average filter, Savitzky-Golay filter [14], was used. It attempts to fit a polynomial of a specified order over a specified number of samples. Using a uniformly weighted moving average filter it is possible to remove any component that is periodic with respect to the duration of the filter.

Considering the ripple frequency f_r and the signal sampling frequency f_s, the frame length N_f of the filter, in number of samples is defined according to eq. (20); and the ripple frequency is estimated using the eq. (21) as presented in [15].

$$N_f = \frac{f_s}{f_r} \tag{20}$$

$$f_r = \frac{N_o}{2\pi} W_0 \tag{21}$$

Figure 7 shows the outlet pressure curve of the hydraulic pump after the filtering.

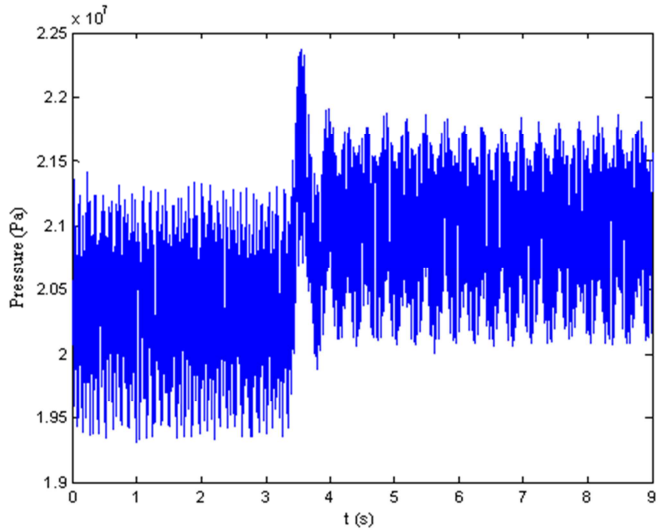

Figure 6: Pump outlet pressure.

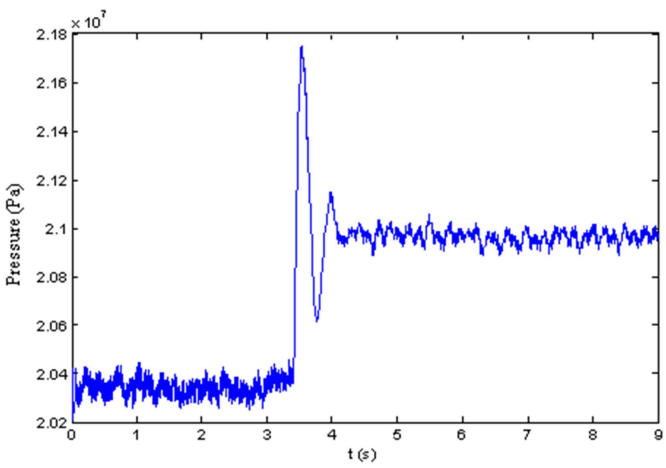

Figure 7: Filtered pump outlet pressure.

3.2 Parameter estimation

It is considered a set of candidate models to represent a system and a set of data obtained experimentally on the system under study, defined in eq. (22) and eq. (23) respectively.

$$\mu^* = \{\mu(\theta) | \theta \in D_\mu\} \tag{22}$$

$$Z^N = [y(1), u(1), y(2), u(2), \dots, y(N), u(N)] \tag{23}$$

According to Ljung [16], the estimation of the vector of parameters θ, consequently of the model $\mu(\hat{\theta})$ defined in μ^* consists in performing the mapping of Z^N in D_μ as defined in eq. (24). Such mapping consists of the parameter estimation method.

$$Z^N \rightarrow \hat{\theta}_N \in D_\mu \tag{24}$$

The model can be seen as a way to predict the output y (t) of a Z^N data set, where $\hat{y}\ (t|\theta)$ is a prediction of the output y (t) determined by a candidate model μ (θ). In this way, the prediction error can be defined according to eq. (25):

$$e(t, \theta) = y(t) - \hat{y}\,(t|\theta) \tag{25}$$

A model is considered good when produces small prediction errors, however, it is necessary to define criterion for the predictor function. Defining a scalar value function R (θ), called the criterion function and applying a norm is defined the eq. (26).

$$V_N(\theta, Z^N) = \frac{1}{N}\sum_{t=1}^{N} R(e_f(t, \theta)) \tag{26}$$

Thus, the problem of estimating the parameters of the model becomes an optimization problem that consists of the minimization of the criterion function, as defined in eq. (27).

$$\hat{\theta}_N = \arg min\, V_N(\theta, Z^N) \tag{27}$$

This method is known as prediction error method (PEM). In summary, this process consists of three steps: choosing the structure of the model, choosing the criterion (defining the scalar value function R (θ)) and minimization of the criterion function.

The criterion function chosen for PEM application is the covariance matrix of the prediction error, given by eq. (28). Assuming that the prediction error follows a Gaussian distribution, the optimal parameter vector θ should minimize the covariance matrix of e (t, θ).

$$R_N(\theta) = \frac{1}{N}\sum_{t=1}^{N} e(t, \theta).\, e^T(t, \theta) \tag{28}$$

Since the criterion function must be a scalar value, $R_N(\theta)$can only be applied directly when *e (t, θ)* is a scalar sequence. For the case where the system has more than one output it is necessary to map $R_N(\theta)$ to a scalar, we can then define this mapping function as in eq. (29) for applying the criterion in the general case.

$$h(R_N(\theta)) = \det(R_N(\theta)) \tag{29}$$

The choice of this criterion function from the statistical point of view is considered optimal, since it leads to maximum likelihood for prediction errors with Gaussian distribution as presented in Ljung [16].

Using the criterion function (eq. 29), the estimation of the parameter vector is given by the minimization of it, as defined in eq. (30).

$$\hat{\theta}_N = \arg min\, det(\frac{1}{N}\sum_{t=1}^{N} e(t, \theta).\, e^T(t, \theta)) \tag{30}$$

To minimize the criterion function, the Gauss-Newton method was considered. As presented by Soderstrom and Stoica [17], this method uses a numerical search routine called the Newton-Raphson algorithm.

The Gauss-Newton method generally presents a linear convergence, however if the model is defined with more parameters than necessary, the approximate Hessian becomes very close to a singular matrix, with inversion problems occurring. In general, when the model structure is correctly selected and a good initial estimate of the parameters is available, the algorithm converges rapidly, called superlinear convergence.

The script used to estimate the parameters is presented in fig. 8. This is developed in the System Identification Toolbox [18] of MATLAB® software, making use of the *pem (data, mi)* function. The argument *data* contains the input (*F0*, *W0* and *QL)* and the output (*Ps*) from the experimental data set. The parameter *mi* defines the structure of the model represented by the *idgrey class*, composed by an instance of the function that represents the model in the state space form and the vector of free parameters, which are estimated from an initial value. The

pem function uses the prediction error minimization method to estimate the unknown parameters.

Applying the prediction error method, the parameters are estimated. The result of the new model when compared to the experimental data shows a fit of 85.36%, as shown in fig. 9.

```
%Load data
load 'RigDataFilt.mat';
%Free-parameters vector
parameters = [Kv Kq Cl Kp Vt];
%Experimental data set
data = iddata(Ps,[FO WO QL],Ts);
%Model structure
sys = idgrey('varDispPump', parameters, 'c');
%Model with estimated parameters
syse = pem(data,sys,'trace','full','SearchMethod','gn');
%Estimated parameters
paramEst = th2par(syse);
```

Figure 8: Script MATLAB® to estimate the model parameters.

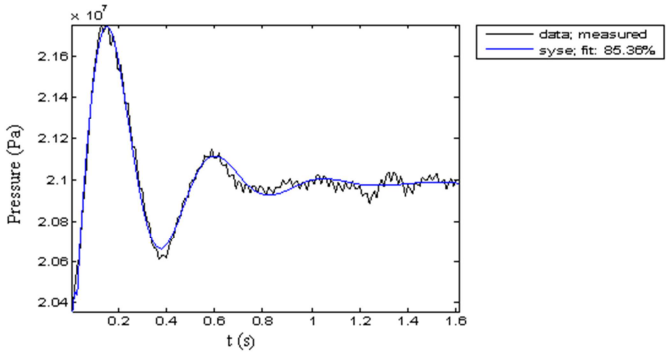

Figure 9: Comparison between the simulation and the experimental data.

4 Validation of Simulation Model

To validate the simulation model a different data set from that used in parametric identification is considered, in this way it is possible to verify if the model is able to represent the system for different conditions and if there is some dynamics not represented by the model. Therefore, another set of data was obtained to verify the representativeness of the model. These data were acquired considering the scenario which a flow pulse demanded by the load occurs as shown in fig. 10.

In this scenario it is expected that initially during the rising step of flow demanded should occur a reduction in the output pressure of the hydraulic pump, consequently the control piston must move in order to increase the flow delivered by the hydraulic pump. During the descent step the pressure increase and the return of the piston to the previous position should occur. Figure 11 describes the behavior of the outlet pressure of the simulated and actual pump. Even for a different scenario from which the parameters of the model were estimated, it can represent properly the dynamics of the system for which it was proposed.

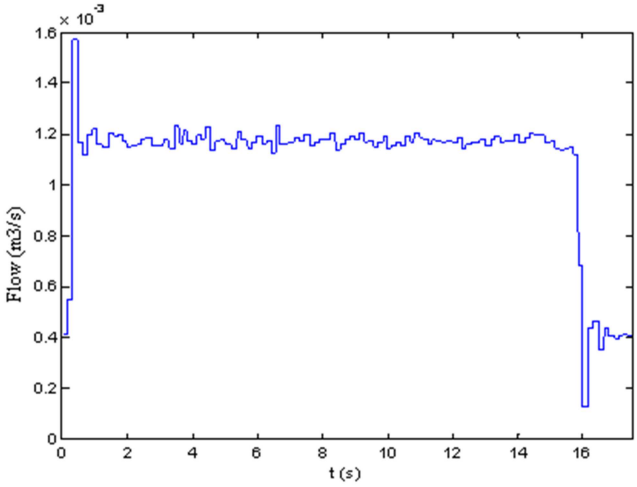

Figure 10: Flow pulse requested by the load.

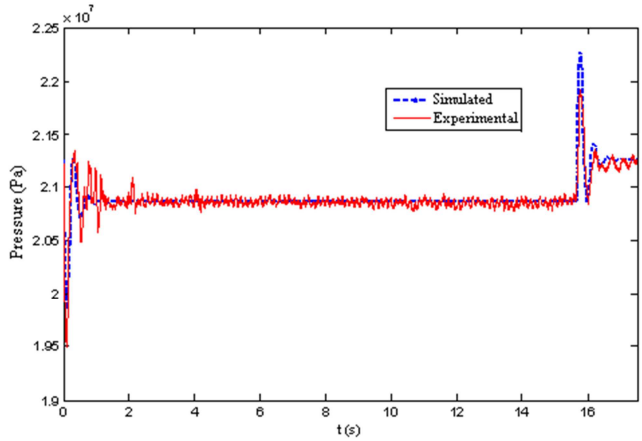

Figure 11: Comparison between the simulation and the experimental data (flow pulse).

5 Conclusion

The proposed goal of developing a model for a variable displacement pressure compensated hydraulic pump using the combination of physical modeling techniques and system identification was achieved. It can be observed that the combination of both, gray-box modeling, allows to obtain models more representative of the system under study. This method combines the advantages of white-box and black-box modeling, and it is possible to obtain a model without diverging from its physical meaning and also to insert in this information obtained by means of system identification. However, the application of this approach depends on the availability of data about the system that are not always available, either because of the difficulty of acquiring data with the required quality or even when it is not possible, such as during the project which the system does not yet exist.

Regarding the parametric identification, the prediction error method proved to be quite effective, however attention is needed in the choice of the search criteria and method, which must be adequate to the data and the structure of the

analyzed model. In addition, the data used to identify the system should be chosen correctly, taking care that they represent properly the dynamics to be modeled.

Nomenclature

Designation	Denotation	Unit
A_v	Effective area of compensator valve spool	m^2
A_p	Effective area of control piston	m^2
A_w	Gradient area	m^2/m
b_p	Viscous friction coefficient of control piston	N/m/s
b_v	Viscous friction coefficient of compensator valve	N/m/s
B_p	Fluid compressibility in control piston chamber	m^3/Pa
B_S	Fluid compressibility in hydraulic pump outlet	m^3/Pa
C_d	Discharge coefficient orifice	
C_l	Internal leakage coefficient	
D_{max}	Maximum volumetric displacement of hydraulic pump	m^3/rad
D_p	Volumetric displacement of hydraulic pump	m^3/rad
f_r	Ripple frequency	Hz
f_s	Sampling frequency	Hz
F_0	Pre-load of compensator valve spring	N
K_d	Displacement gradient of pump	m^2/rad
K_p	Spring constant of control piston	N/m
K_q	Flow gain of compensator valve orifice	m/s
K_v	Spring constant of compensator valve	N/m
m_p	Mass of control piston	kg
m_v	Mass of compensator valve spool	kg
N_f	Number of samples	
N_o	Number of pistons	
P_S	Hydraulic pump outlet pressure	Pa
P_{Sa}	Pump setting pressure	Pa
P_C	Control pressure	Pa
Q_L	Volumetric flow rate consumed by load	m^3/s
V_p	Volume of control piston chamber	m^3
V_t	Volume between pump outlet and compensator valve	m^3
Q_v	Volumetric flow rate of compensator valve orifice	m^3/s
x_p	Position of control piston	m
$\dot{x}_p$	Speed of control piston	m/s
x_v	Position of compensator valve	m
$\dot{x}_v$	Speed of compensator valve	m/s
W_0	Rotational speed	rad/s
β	Bulk modulus of fluid	N/m^2
ρ	Fluid density	kg/m^3

References

[1] M Delgado, and J Garcia. *Parametric identification on bond graph models*. In: Systems, Man and Cybernetics. 'Systems Engineering in the Service of Humans', Conference Proceedings. Vol.1 pp 583 – 588, 1993.

[2] P Casoli, and A Anthony. *Gray box modeling of an excavator's variable displacement hydraulic pump for fast simulation of excavation cycles*. Control Engineering Practice.v.21, 483-494, 2013.

[3] L Li, and T Thurner. *Accurate modeling and identification of servo-hydraulic cylinder systems in multi-axial test applications.* Institute of Lightweight Design, Graz University, Austria, 2013.

[4] S S Tørdal, A Klausen. *System Identification of a Variable Piston Pump and Design of a Hydraulic Load Circuit*. Master's theses in Mechatronics, University of Agder, 2015.

[5] C G Negoita, D Vasiliu, N Vasiliu, and C Calinoiu. *Modeling, simulation, and identification of the servo pumps.* IOP Conference Series: Earth and Environmental Science, Vol.12(1), p.012054, 2010.

[6] H E Merrit. *Hydraulic Control Systems*. New York: Jhon Willey & Son, 1967.

[7] EATON. *A Descriptive Summary of Vickers Inline Pumps and their Applications*, 2000.

[8] E E Lewis, and H Stern. *Design of Hydraulic Control Systems*. New York: McGraw-Hill,1962.

[9] J S Cundiff. *Fluid Power Circuits and Control: Fundamentals and Applications*, CRC Press, 2001.

[10] C Kleijn, M A Groothuis, H G Differ. *20-sim 4.3 Reference Manual*. Controllab Products B.V., 2013.

[11] P J Gawthrop, and D J Balance. *Bond graphs in the design of engineering systems*. Glasgow: University of Glasgow, 1998.

[12] D C Karnopp, D L Margolis, and R C Rosenberg. *System Dynamics: A Unified Approach*. John Wiley, 1990.

[13] W Borutzky, B Banard, and J U Thoma. *Describing bond graph models of hydraulic components in Modelica.* Mathematics and Computers in Simulation, v. 53,381-387, 2000.

[14] S J Orfandis. *Introduction to Signal Processing*. Englewood Cliffs, NJ: Prentice-Hall,1996.

[15] N D Manring. *The Discharge Flow Ripple of an Axial-Piston Swash-Plate Type Hydrostatic Pump.* Journal of Dynamic Systems, Measurement, & Control, v.122 (2), p.263-269,2000.

[16] L Ljung. *System Identification: Theory for the Users*, Prentice-Hall, 1987.

[17] T Soderstrom, and P Stoica. *System Identification*. Prentice-Hall, 1989.

[18] L Ljung. *System Identification Toolbox™ User's Guide*. The MathWorks, Inc, 2014.

Emission reduction of mobile machines by hydraulic hybrid

Seppo Tikkanen, Elias Koskela, Ville Ahola, Kalevi Huhtala

Tampere University of Technology
Laboratory of Automation and Hydraulic Engineering
Korkeakoulunkatu 6
Tampere, Finland
E-mail: seppo.tikkanen@tut.fi

Abstract

Emission regulations of the mobile machines have created lot of work for the machine manufacturers in recent years because of the Stage 4 /Tier 4 final regulations. The work will continue because the new EU stage 5 emission regulations for non-road-mobile-machines was published at the year 2016. Emission reduction is realized by different emission reduction systems that are located in the exhaust system in combination with sophisticated combustion control. The after treatment systems increase complexity and size of the exhaust system. Increased creation of NOx and particle emissions are related to sudden load and speed changes of the engine. This paper introduces effect of driving style on the real emissions of the municipal tractor and solutions to decrease emissions with hydraulic hybrid. Measurements show that the sudden load changes increase raw NOx and particle emissions (non after-treated emissions) and operators driving style has effect on the emissions. Stabilizing the load of the engine by the hybrid system reduces NOx and particle generation. When the engine load variation is minimized the size of the exhaust after treatment systems can be reduced.

Keywords: non-road mobile machine, exhaust emissions, hydraulic hybrid

1 Introduction

The efficiency of the mobile machines has been studied widely during last decade. Lot of effort have been put to reduce fuel consumption and CO2-emissions. At the same time the exhaust emission regulations of the engines in Europe, the USA and Japan have become more and more strict and reduced emissions of new mobile machines. The emission regulations limit emission of hydrocarbons (HC), carbon monoxide (CO), nitrogen monoxide (NOx) and particle matter (PM) per produced kWh. However, the regulations limit the emissions of the engines, not the emissions of the machines directly. The validation tests are made for the engine in laboratory conditions with predefined load cycles. The loading cycle of the emission tests are composed of various measured real cycles but still they are laboratory test without variation of real conditions and load cycles [1].

"Volkswagen Gate" and also previously known but partly ignored studies have shown that the real world emissions of cars differ drastically from emissions tested in the laboratory conditions [2]. We can assume that this is also valid for the mobile machines although the test cycle for non-road mobile machine include load and speed changes.

The most critical emissions of diesel engine are nitrogen oxiden, NOx, and particle matter emissions, PM, because they have harmful effect on human health. Both nitrogen oxide and particle emission are limited by regulations and the limiting values have been decreased gradually being now over 20-times lower than in mid 1990s.

Each diesel engine produces nitrogen oxide and particle emissions and their amount varies on engine operation point. Because of this fact, the engine emissions are reduced by additional systems. Nitrogen oxides are reduced by exhaust gas recirculation (EGR) and separate systems like Diesel oxidation catalyst (DOC), selective catalyst reduction (SCR) or NOx storage catalyst (NSC) which are part of exhaust system. Particle emissions are reduced by particulate filters. The size of these systems increase remarkably the size of the

exhaust system. The size of the after treatment systems are depending on the emission reduction performance and if the raw emission can be reduced, the size of the after treatment systems can be smaller respectively.

NOx and particle emissions are increased when engine load and/or speed are changed rapidly compared to constant load situation [3]. Rapid and continuous changes of engine loading are typical for mobile machines like excavator, forest harvesters, and wheel loaders for example. Secondly, the load and speed changes are depending also on the operator's behavior.

In previous studies by Heidari and Marr [4], Ericson, Westerberg and Egnell [5] and Lindgren[6] have shown that NOx and particulate matter emissions factors are depending on the engine transients.

The first research question is: What are the real emissions of the machine during the operation and how they are depending on the operator's driving style? The second research question is: How much raw emissions (emission before after treatment systems) can be reduced by minimizing changes in engine load and speed? The third research question is: Can the load changes compensated by control means and by hydraulic hybrid?

2 Emission measurements

The basic problem of the real emission measurements is the question of representativeness of measurement. The aim of the laboratory measurements is to guarantee reproducibility of test event and results, which is base for the quality assurance. Although the laboratory measurement arrangement ensure reliable measurements, the question is; How well the laboratory measurements represent real working conditions? The second issue is that the standard tests are made for the engine, not for the machine. The engines are used in various machines and applications and the consequence is that the same engine produce different amount of emissions in different applications. However, the measurements of individual machines gives valuable information on real emissions although the generalization of the results is restricted.

The difference between real emissions of cars and emissions during certification tests has widely reported in past years because some car manufacturers have tuned the engine control units to recognize the test situation and changing the parameters in order to reduce emissions. In latest emission regulations, this has been tried to solve by implementing randomly chosen combination of test cycles and real driving measurements for new and used cars.

In the latest European emission regulations for the non-road mobile machines in-use-measurements are introduced. This means that engine manufacturer has to show that their engines fulfill the regulations also in application use as new and used. This regulation concerns only gaseous emissions. [1]

The second problem is the realization of measurements, because the emission measurement system is relatively big in volume and weight. This yields situation that the real emissions of small machines are almost impossible to measure without disturbing the operation of the machine.

2.1 Measurement system

The measurement platform consisted of machine and measurement system. The used machine was a municipal tractor *Wille 655* that is equipped with 100 kW diesel engine, hydrostatic driveline and load sensing hydraulics with variable pump for the boom and auxiliary devices. The weight of the machine is 5400 kg without measurement systems and over 6000kg with the PEMS-system. The maximum speed of the municipal tractor is 40 km/h.

The measurement system was Portable Emission Measurement System (PEMS) by AVL and the PEMS enables measurement of real emission of the machine during the work. Figure 1 shows the Wille-municipal tractor with the PEMS-system assembled on the rear frame above the engine.

Figure 1: Wille-municipal tractor with the portable emission measurement system.

The emission level of the diesel engine is Tier 3A meaning that limit for combined NOx and HC emission limit is 4.0 g/kWh and 0,3 g/kWh for the particulate matter. This engine does not have any particular systems for emission reduction. Currently the new machines have to fulfill Tier 4 final limits that are 10-times lower, respectively 0,4 g/kWh for NOx and 0,025 g/kWh for Particulate matter at 100 kW power class. To reach this emission level additional emission reduction systems like, DOC, SCR and DPF are required.

The used portable emission measurement system consists of gas analyzer and particle analyzer and it is able to measure concentrations of total hydrocarbons, THC, nitrogen oxides NO and NO_2, carbon monoxide, CO and carbon dioxide CO_2 and oxygen O_2. The particle analyzer consist of soot and particle mass measurement devices. The measurement system included also fuel consumption measurement device and the used fuel was typical "winter type" diesel fuel, which is usable to -34°C.

The gas analyzer consisted several analyzers: Flame Ionization Detector (FID) unit for hydrocarbon measurement, Non-dispersive ultra violet resonant absorption spectroscopy (NDUV-RAS) for NOx measurements, Non-dispersive

infrared spectroscopy for CO and CO_2-measurement and finally O_2-sensor to detect oxygen in exhaust.

The measurement system consisted heated sample lines and separate power source (batteries and generator) for the emission measurement system so that the PEMS would not create additional load to the engine.

The engine does not have any exhaust after treatment system and all the measured emissions are raw emissions and not affected by any after treatment system.

2.2 Test Cycle

To evaluate the real emissions of the machine different tests were done. Tests included load and carry cycle with two operators having different driving styles.

The tractor was equipped with forks and the load was pallet with metal plates and its weight was 1,5 ton. The load and carry cycle included driving with and without the load. First, the pallet was picked from top of the container and then operator drove about 140m and left the pallet on the ground level. This was followed by driving phase, about 280 m and the pallet was picked again and returned to the initial point, top of the container. The cycle contained 280 m driving with the pallet and 280m driving without the pallet. The route included up- and downhills. The maximum speed was 25 km/h. The cycle was driven 6 times without stops.

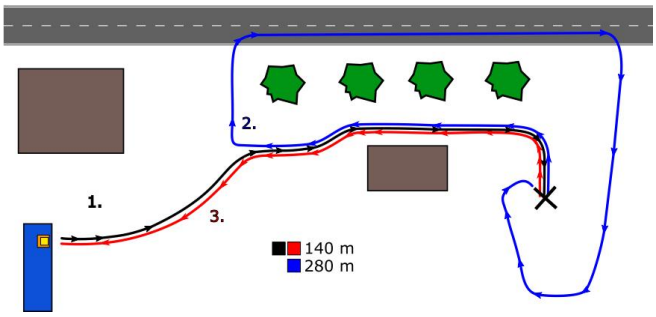

Figure 2: Load and carry cycle route [7].

2.3 Operators

To study what is the effect of driving styles of the operator, two operators were used. Both operators drove load-and-carry-cycle. The first operator, operator A had smooth driving style while the second operator, operator B had more aggressive driving style.

3 Results

Measurements showed clearly that there is variation in the emissions and the fuel consumption between the operators. Operator A had 22% higher average power than operator B but fuel consumption was only 10% higher. Because the used power was higher, the operator A finished the job much quicker: 1715 vs. 1478 seconds. The productivity of operator A was 15 % higher.

Figure 3 shows one load and carry cycle and the time scale is relative time i.e. percentage of total used time for one cycle. There is no major difference on the engine loading or emissions between operators and curves show very similar behavior. The differences are in some operation points. Operator B use maximum loading more often than operator A. The use of maximal power by the operator B is clearly seen at the time of 45% when the particulate matter and CO-emissions have peak indicating full fuel amount and lack of fresh air for the combustion.

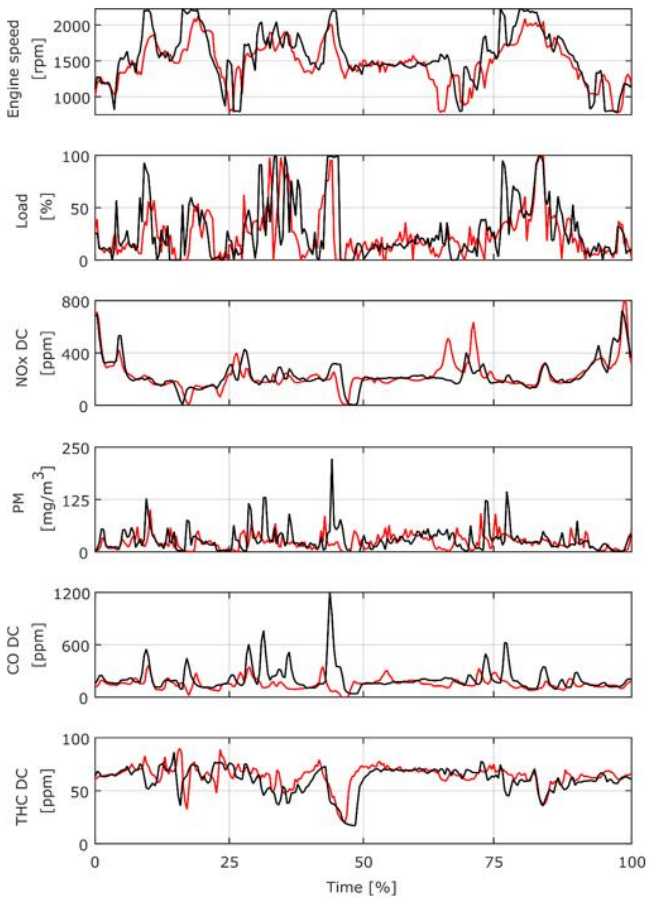

Figure 3: Engine data and emissions for one load and carry-cycle. Red line: Operator A, black line: Operator B.[7]

Table 1: Average engine values for the work cycle

Operator	Engine speed [rpm]	Engine Torque [Nm]	Fuel consumption [l]	Time [s]
A	1479	99	2,90	1715
B	1575	114	3,18	1478

Operator B was more productive because he was remarkably quicker in work but at the same time, he consumed more fuel.

Table 2: Exhaust emissions for the work cycle

Operator	NOx [g/kWh]	PM [g/kWh]	CO [g/kWh]	THC [g/kWh]
A	4,86	0,30	2,34	0,41
B	4,53	0,42	3,33	0,36

The measurements show that emission level vary according to operator, however results are not such that was expected because the aggressive drive style did not result higher emissions in all cases. The operator B resulted lower NOx emissions although the difference was only 7 per cent. Opposite to the NOx emissions operator B emitted remarkably higher, 40 per cent, particulate matter emissions than operator A. In the CO-emissions, we see same phenomenon and it seems that the PM and the CO emissions correlate with each other.

The engine of the municipal tractor has rather high NOx-emissions at certain low load points during test cycles. The same phenomenon was observed during constant load measurements: At low engine speed range the engine has relatively high specific NOx-emissions that are caused by inadequate mixing of the fuel and air resulting high local temperatures creating NOx. This phenomenon is clearly seen during acceleration phase below 1000 rpm.

When the mean emission levels are compared to the Tier 3 limits, we can see that the engine produces in this test more both combined NOx+HC emissions and particulate matter emission than the limit value is. Combined NOx+HC emissions are 22 / 32 per cent above the limit value and the particulate matter emissions are almost 40% above the limit value in the case of the operator B.

The mean used power for operator A were 15,5 kW and respectively for operator B 18,8 kW. Compared to the maximum power of the engine that is 100 kW, the mean power level is low. Figures 4 and 5 show loading points of the engine in load and carry –cycle for both operators.

Load points show that engine hardly never operates at the best efficiency area (1200 -1600 rpm/300-480 Nm). This is due to the automotive-type transmission control algorithm that is not utilizing the best efficiency area effectively. Driving style difference is seen in the load points, operator B uses more maximum engine speed and maximum engine power [7].

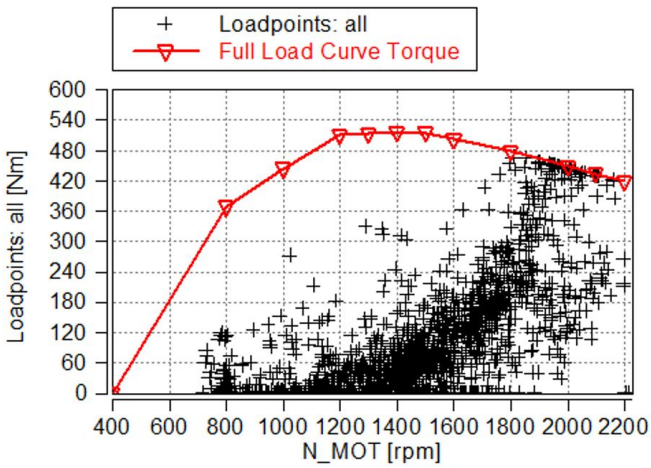

Figure 4: Load points for operator A in load and carry cycle

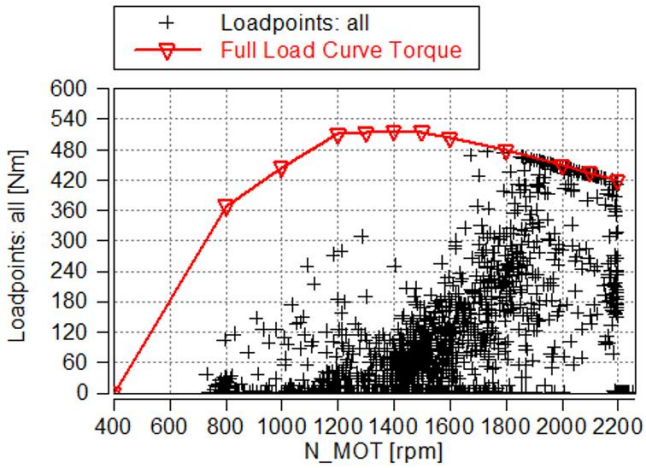

Figure 5: Load points for operator B in load and carry cycle

4 Emission reduction through hybridization

Hybrids are usually understood as solution to reduce fuel consumption and the hybrid system is designed accordingly. Hybrid system design can have several other objectives and functions such as boost function; hybrid system provides extra power when needed and enables engine downsizing [8]. Another function is engine load stabilization that is used with engine downsizing but it also can help to reduce the emissions at the same time.

The hypothesis of this study was that by reducing the engine load variation harmful emissions can be reduced. The parallel hybrid system allows engine operate at the mean power level and the hybrid system filters load variation and delivers extra power when needed and stores energy when the load power is below the mean power.

To estimate the effect of the steady state load to the emissions some steady state measurements were made for the machine by loading the implemented hydraulic system by throttling the fluid flow.

If we assume that hybrid system could keep the engine running at the mean operation point, this would mean that load of this engine would be only around 20 % of its maximum. This operation point is far from the ideal for the used engine, because the operation point is not minimizing neither efficiency nor emissions. The emission would be around 4,5 g/kWh for NOx and about 0,65 g/kWh for PM emissions. Lower specific consumption and lower specific emissions would require higher engine loading. At the loading point 50% of maximum at 1500 rpm, the emissions would be around 3,2g/kWh for NOx and 0,25g/kWh for particulate matter. This is remarkably lower than during the test cycles. To move the average operation point towards higher loading requires smaller engine and this is the reason why the smaller engine should be chosen for the hybrid systems. However, both operators used in tests the maximum load at high speed range (Figures 4 and 5) and the hybrid system should provide the power in these operation point if the engine was smaller.

Simple simulation study using measured load power was performed in order to define accumulator size for parallel

hydraulic hybrid with different load stabilizing goals. The parallel hydraulic hybrid is consisting of an accumulator and over-centre capable variable open circuit pump/motor that is attached to the engine power take-off. The basic control principle of the hydraulic hybrid is the hybrid unit provides the power that equals the load power reduced by the engine power.

$$P_{hybrid}(t) = P_{load_estimation}(t) - P_{engine_average} \qquad (1)$$

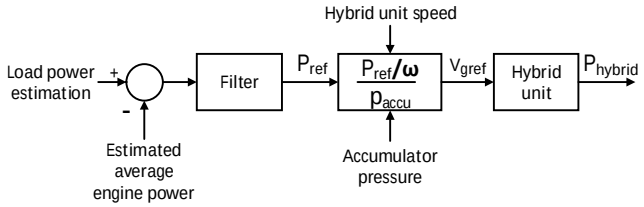

Figure 6: Determination of delivered hybrid power

The determination of the delivered hybrid power is straightforward calculation and the system is open loop control system, and it is accepted that the delivered hybrid power is not exactly accurate. The engine has speed controller and it adapts to the varying load conditions as it does without hybrid assistance. The set value for the engine power is the assumed average power. The load power estimation is calculated from the pressure and the volume flow of the hydraulic pumps and other engine loads. The filter-function eliminates the low frequency load changes of the load estimation, because the goal is to remove rapid load changes by the hydrid unit.

The hybrid unit was modelled using first order transfer function and rate limiter so that the stroke time of from 0 to 100 per cent was 100ms.

The dimensioning the energy storage for the parallel hybrid system depends on the desired functionality. The hybrid system can be designed to stabilize fully the engine load and then the engine speed and load are nearly constant during the work cycle. For the analysis the recorded load information from the hydraulic systems (including circuits of hydrostatic drivetrain, implemented hydraulics and cooling/steering system) was used and the hybrid system was assumed to handle the load variation. The integration of the calculated hybrid power over time resulted required storage capacity.

Calculation resulted energy storage capacity of 800 kJ for the studied working cycles and the driving style did not had effect on the storage capacity. To have 800 kJ as available energy from the accumulator, the required energy should be multiplied by at least 1,25 resulting 100 L accumulator with 100 bar precharge pressure and 350 bar as maximum pressure level.

The size of accumulator of the hybrid can be reduced if the engine load and the speed are allowed to change moderately. This means that hybrid system is only filtering the rapid load changes and for the studied cycle this results 200 kJ energy storage capacity and this requires an 30 L accumulator.

The blue line in Figure 7 shows the case when the hybrid system was designed to compensate fully the load changes of the studied work cycle (storage capacity 800 kJ). In this case the engine load was almost constant at 18.5 kW and hybrid system stabilized the load variation completely. The red line in Figure 7 shows the measured unfiltered load power during one cycle for operator A.

In the case of the moderate load stabilizing and using 200 kJ storage capacity and the filter was set to pass frequencies higher than 1 Hz. This means that the hybrid system compensates only load transient which frequency is higher than 1Hz. The black line in Figure 7 shows this case and the curve shows clearly that the high frequency transient are compensated and the peak values of rapid load changes are reduced. This design allows engine load vary quite much, but engine load is more stable than without hybrid unit.

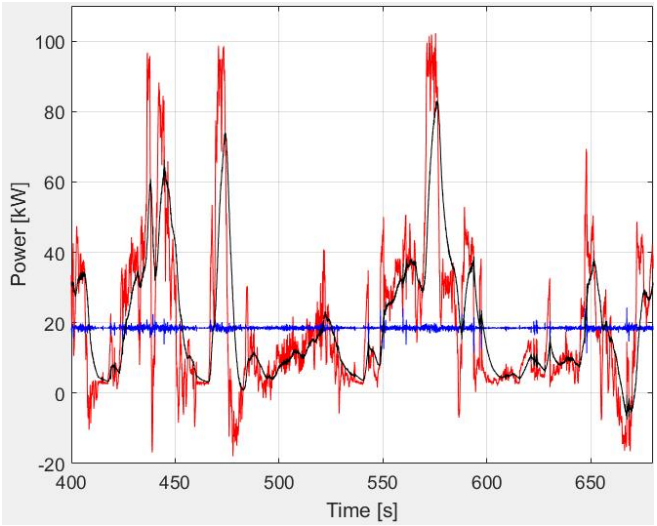

Figure 7: Power curves for different hybrid designs. Load power: Red line, Full stabilized engine load: Blue line, Moderately stabilized engine power: Black line.

The moderate hybrid design can filter rapid load changes. Hagena et al [3] showed that the change of the rise time of the load transient from 1 sec to 5 sec diminish totally the NOx and PM emission peaks caused by the transients. Therefore, we can say that the moderate design of hybrid storage should reduce both NOx and PM emissions, although it does stabilize the engine load completely.

Remaining question is, how representative the results are and in which cases they are valid. Comparing the earlier results and the results of this study, we can say that emissions are depending on the operators driving style and the real emissions differ from the emissions in the laboratory tests. The dependence of the operator is influenced by many factors, such engine type, after treatment system, machine type, working environment, processed material and operator. Further work is needed to determinate the influence of the mentioned factors and their correlations.

The next step is to realize the moderate hybrid system in machine and perform same tests in order to validate hypothesis in real life.

5 Conclusion

The exhaust emissions of the mobile machines are strongly dependent on the work cycle and the operator. The real emissions during the work are higher than is set in emission regulations because standard tests do not correspond the real conditions.

Amount of the generated harmful emissions NOx and PM are depending on the driving style of operator and especially PM emissions are increasing together with aggressiveness of driving style.

The emissions can be reduced by stabilizing the load fully or partly by hybrid system. The moderate storage design has remarkably smaller accumulator but still has potential to reduce harmful emissions remarkably.

6 References

1. EU. 2016. Regulation (EU) 2016/1628, 14.9.2016. On requirements relating to gaseous and particulate pollutant emission limits and type-approval for internal combustion engines for non-road mobile machinery, amending Regulations (EU) No 1024/2012 and (EU) No 167/2013, and amending and repealing Directive 97/68/EC

2. Weiss, M., Bonnel, P. Hummel, R., Manfredi, U., Colombo, R., Lanappe, G., Le Lijour, P., Sculati, M. (2011a): Analyzing on-road emissions of light-duty vehicles with Portable Emissions Measurement Systems (PEMS). JRC Technical and Scientific Report 62639, EUR 24697 EN. Ispra, Italy

3. Hagena J.R, Filipi, Z.S., Assanis D.N. 2006. Transient Diesel Emissions: Analysis of Engine Operation during a Tip-In. SAE Paper 2006-01-1151. 2006 SAE World Congress, Detroit April 3-6, 2006

4. Heidari B., Marr L., C., 2015. Real-time emissions from construction equipment compared with model predictions. Journal of the Air&Waste management Association. 62:2, 115-125, DOI: 10.1080 /10962247.2014.978485

5. Ericson C., Westerberg B., Egnell R., 2005. Transient Emission Predictions with Quasi-Stationary Models. SAE Paper 2005-01-3852. Powertrain Fluid Systems Conference and Exhibition San Antonio, Texas USA October 24-27, 2005.

6. Lindgren M, 2004. Engine Exhaust Gas Emissions from Non-road Mobile Machinery. Dissertation Uppsala University, Acta Universitatis Agriculturae Suecia, Agraria 481. ISBN 91-576-6753-5.

7. Koskela E. 2017. Effects of driving style on the emissions of non-road mobile machinery. Master thesis, Tampere University of Technology. In Finnish.

8. Thiebes, P., 2011. Hybridantriebe für mobile Arbeitsmaschinen – Grundlegende Erkenntnisse und Zusammenhänge, Vorstellung einer Methodik zur Unterstützung des Entwicklungsprozesses und deren Validierung am Beispiel einer Forstmaschine. Karlsruher Institut für Technologie. Dissertation. 2011. ISBN 978-3-86644-808-7

Model Based System Identification for Hydraulic Deep Drawing Presses

Dipl.-Ing. Tobias Schulze, Prof. Dr.-Ing. Jürgen Weber

Chair of Fluid Mechatronic Systems (Fluidtronic)
Institute of Fluid Power, TU Dresden, Germany
E-mail: tobias.schulze2@tu-dresden.de

Abstract

The paper describes the development of an automated system identification algorithm for the die cushion drive in hydraulic deep drawing presses. The algorithm could successfully be implemented on the drive controller to automatically identify the system parameters of the drive. Main aspect of the paper is the application driven development of an appropriate system model and identification algorithm with its implementation on the drive controller. It could be verified with experiments on a 2500 kN hydraulic deep drawing press. This thorough knowledge of the system model with its parameters shows a high potential to be further evaluated for system diagnosis and could also be used for system simulation and controller design.

Key points are the limited processing power of the drive controller and the occurring signal noise. A grey-box system model was chosen and its parameters were identified by means of a recursive least square algorithm. The implementation on the drive controller required adaptions due to restricted cycle time and additional signal processing to reduce noise that will also be discussed in the paper.

Keywords: industrial hydraulics, hydraulic deep drawing press, system identification, system simulation, grey box model, valve control, parameter estimation, orthogonal correlation, moving average filter, symmetrical derivative

1 Introduction

The requirements on modern industrial hydraulics are rising. The operator sets highest demands on energy efficiency, best dynamic and static behavior, highest reliability and even requests new functionality. The die cushion in deep drawing presses is a typical application for modern servo hydraulics as it offers a precise adjustability of the counter-holding force on the blank. With velocities of up to 300 mm/s and cylinder forces of more than 1000 kN the dynamic behavior needs to be most accurate. Modern blank materials, the raising cushion speeds and more complex tool geometries set an even higher demand on the die cushion. In addition the operator requests low set-up time and minimal service requirements.

An extensive and thorough set-up process and a time consuming maintenance scheme with qualified and experienced technical staff is currently necessary to fulfil these demands (/1/, /2/, /3/). The intensive set-up process is required for every newly installed deep drawing press and also after every modernization of the hydraulic system.

Model based system optimization methods offer the possibility to support with the set up process and even to increase the quality of the hydraulic drive. But on the other hand those simulation models and optimization methods require a thorough knowledge of the system and its parameters. This is where the method of automated parameter estimation steps in providing a possible solution to identify the system parameters within a few seconds.

The literature offers a high variety of system identification methods (/4/, /5/, /6/) out of which the most suitable for the hydraulic die cushion drive is to be chosen. Jelali and Kroll /7/ proved the feasibility of system identification for hydraulic drives in an experimental environment. However, the implementation within the drive controller for an industrial machine has not been realized yet.

The use of the current parameters and system model from the identification algorithm are versatile. They can be evaluated for condition monitoring, for fault diagnosis, to increase reliability and to reduce the required time for manual servicing. They can also be used for system simulation and controller design to reduce the set-up time and ensure a high control quality of the hydraulic drive. Several published works show that a model based controller design can be based on an identified system model and deliver an improved control accuracy. The identification algorithm is therefore an important step towards an improved system performance.

The aim of the presented paper is to develop and implement a parameter estimation algorithm within the machine controller of the hydraulic die cushion system. This allows to easily access the current set of parameters by an identification process or even during regular application of the machine.

2 Test setup

The research was conducted on an hydraulic deep drawing press that is available at the Institute of Fluid Power at the TU Dresden (see fig. 1). It features a hydraulic slide with a maximum force of 2500 kN and a modern hydraulic four-point die cushion with a total force of 1000 kN. The press can be equipped with different tools, such as a rectangular pan tool and a round cup tool for deep drawing, a cutting tool and a test block that allows the press to work at any possible operating point up to maximum force and speed. All experiments presented in this paper were conducted with this test block representing a deep drawing tool. The deep drawing press is equipped with several additional sensors for hydraulic, mechanic, and electric signals as well as a tailor made measuring system.

Year of manufacture	2012
Slide force	2500 kN
Slide stroke	600 mm
Slide speed	300 mm/s
Forming speed	41 mm/s
Die cushion force	4 x 250 kN

Figure 1: Hydraulic deep drawing press at the IFD

For the hydraulic die cushion, a model based system identification algorithm will be implemented on its drive controller. The controller, a MOOG Servo Drive MSD, features a 32-bit processor with 400 MHz and 256 MB of RAM. Available machine signals from the die cushion drive are the cylinder position z_{dc}, the cylinder pressure in both cylinder chambers p_A and p_B and the applied valve voltage U_v at the servo valve as well as the return signal for the actual valve spool position y_v for each of the four cylinders. All machine signals are read with Ether CAT connected IO-modules.

The behavior of the hydraulic die cushion will be further investigated within this paper and its model parameters will be identified. The hydraulic structure of the die cushion is shown in fig. 2 for one of the four die cushion cylinders. They are used for position- as well as force-control of the die cushion as there is no dedicated lifting cylinder. An axial-piston pump with internal and external pressure control provides the necessary volume flow for all four cylinders. The hydraulic layout was adapted to allow for a permanent rapid traverse motion on the cylinder-out movement. The cylinder-in movement is simplified in the way that only the pressure chamber on the piston side is controlled by the servo-valve and the pressure chamber on the rod side is directly connected to the axial piston pump. A changing valve position of the servo valve does therefore only affect the pressure in the piston side.

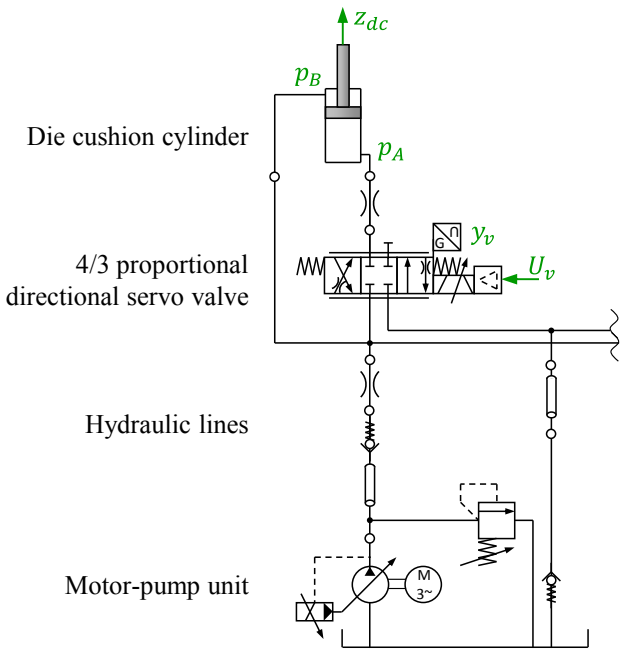

Figure 2: Hydraulic structure of the die cushion and measured system variables

3 Development of the system model

The system model forms the basis for the identification algorithm and defines the possibilities for evaluating the model parameters and system characteristics. The system model should behave as close to the real system as possible and allow to describe the real system as accurate as possible. At the same time, the structure and complexity of the system model must meet all requirements for an automated system identification, so the model complexity is limited.

The model derivation was based on the physical principles in order to retain the model parameters with a physical value and equivalent. A so-called white box model with its physically based mathematical equations is a common and widely verified tool to describe the behavior of hydraulic servo systems to a high level of detail. There parameters have a physical meaning and can therefore be checked on fundamental correctness as well as compared with other systems. It also offers a high variety of possibilities for future applications, such as controller design, condition monitoring or fault diagnosis based on the physical system model. However, a pure white-box model with a sufficient accuracy would require a high level of complexity with numerous parameters. Therefore, the physical behavior is described with basic mathematical equations for the fluidic system and is extended with black-box model assumptions in order to achieve a sufficient accuracy with reduced model complexity and fewer model parameters. The system was divided in a model for the fluidic system that is described as a white-box model and the valve dynamic as a black-box model. Within this paper, only the state of force control for the die cushion during the process of deep drawing is considered. This is the most relevant state for the die cushion as it controls the drawing process with the applied force and therefore directly influences the quality of the produced part.

Figure 3 shows the chosen model structure with its (measureable) system variables for hydraulic pressure (p_t, p_A, p_B and p_0), servovalve voltage U_v and –position y_V and the cylinder position z_{dc}. The system boundaries are the supply pressure p_0, the oil tank pressure p_t, the cylinder position z_{dc} and servovalve voltage U_v. The system and oil tank pressure were experimentally verified to be constant at approximately $p_{t/0} \approx 0\ bar$. The cylinder position is determined by the ram of the deep drawing press, which is why the cylinder speed $\dot{z}_{dc}$ is assumed as a constant value.

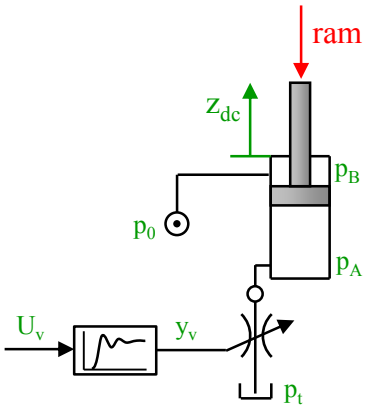

Figure 3: Reduced system model for one die cushion drive cylinder

The differential equations of the hydraulic model are:

$$\dot{p}_A = \frac{K'}{V_0 + A_A \cdot z_{dc}} (-A_A \cdot \dot{z}_{dc} - q_A) \quad (1)$$

$$Q_A = sign(p_A - p_t) \cdot \frac{Q_{v,nom}}{\sqrt{\Delta p_{nom}}} \cdot \sqrt{|p_A - p_t|} \cdot (y_v - y_{0v}) \quad (2)$$

And respectively for the valve dynamics that is modelled as a 2nd-order PT2-element with an additional dead-time:

$$U_v^* = U_v(t - T_{dead}) \quad (3)$$

$$\frac{1}{\omega_{0v}^2} \ddot{y}_v + \frac{2D_v}{\omega_{0v}} \dot{y}_v + y_v = K_v \cdot U_v^* \quad (4)$$

This leads to a model with eight system variables ($p_0, p_A, \dot{p}_A, p_B, Q_A, y_v, z_{dc}, \dot{z}_{dc}$) and ten parameters ($A_A, K', V_0, Q_{v,nom}, \Delta p_{nom}, y_{0v}, T_{dead}, \omega_{0v}, D_V, K_v$).

Figure 4 shows the system model as a block diagram:

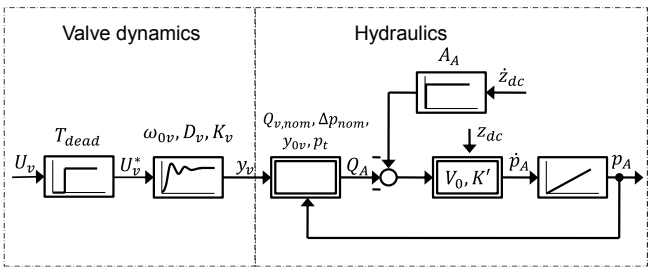

Figure 4: Reduced system model as block diagram

4 Identification algorithm

The reduced system model contains 10 parameters that need to be identified. The parameter for the cylinder-area A_A can be taken from the data sheet of the hydraulic cylinder easily and with a high accuracy. The nominal pressure drop Δp_{nom} is directly connected to the nominal volume flow $Q_{v,nom}$ on the servo valve and can therefore be set to a chosen value. The remaining eight parameters need to be identified from the system behavior. An automated identification algorithm should be developed, as a manual process would be highly time consuming.

Isermann describes different methods for system identification with its pros and cons (see /4/, pages 16f). The identification highly depends on the chosen model structure and in this particular case must meet all requirements for an online-computation on an industrial PC, respectively machine controller. Therefore a *parameter estimation with recursive least square* will be implemented for both subsystems, the hydraulics as well as the valve dynamics. The model estimation is capable to identify the parameters of a parametric model, as it was developed in the previous chapter. Furthermore it can be implemented on the machine controller as a recursive algorithm. The requirement on the model structure is to be linear within the parameters with the $(m \times 1)$-sized parameter-vector $\boldsymbol{\theta}$, the $(1 \times n)$-sized systeminput-vector $\boldsymbol{u}$ and the system output γ according to equation (5). The number of parameters is represented by m and the number of input values represented by n.

$$\gamma = \boldsymbol{\theta} \cdot \boldsymbol{u} \quad (5)$$

The task of the parameter estimation algorithm is to determine the model parameters θ_i such that the output error ε is minimized. The system model is impinged with the same (measured) input $\boldsymbol{u}$ as the real system. The model output can then be calculated with the identified system parameters for each timestep from eq. (5). The output error ε, calculated from the measured output of the real system minus the output of the system model delivers a value for the accuracy of the system model and its parameters. A low value ε means that the system model and its parameters resemble the behavior of the real system very good. Figure 5 shows the identification process as a schematic figure.

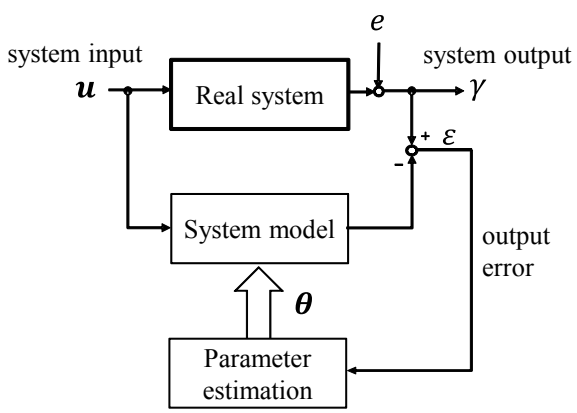

Figure 5: Identification process, schematic

4.1 The hydraulic subsystem

The subsystem for the hydraulic model can be transformed to fit equation (5). Eliminating the volume flow q_A in equation (1) with equation (2) leads to the complete system equation that has to be transformed to fit the format in eq.(5). It leads to the following equations:

$$\gamma = A_A \cdot \dot{z}_{dc} \tag{6}$$

$$\boldsymbol{\theta} = \begin{pmatrix} \theta_1 \\ \theta_2 \\ \theta_3 \\ \theta_4 \end{pmatrix} \tag{7}$$

$$\theta_1 = -\frac{Q_{v,nom}}{\sqrt{\Delta p_{nom}}}$$

$$\theta_2 = -\frac{V_0}{K'}$$

$$\theta_3 = -\frac{A_A}{K'}$$

$$\theta_4 = \frac{Q_{v,nom}}{\sqrt{\Delta p_{nom}}} \cdot y_{0v}$$

$$\boldsymbol{u} = (u_1 \;\; u_2 \;\; u_3 \;\; u_4) \tag{8}$$

$$u_1 = sign(p_A - p_t) \cdot \sqrt{|p_A - p_t|} \cdot y$$

$$u_2 = \dot{p}_A$$

$$u_3 = z_{dc} \cdot \dot{p}_A$$

$$u_4 = sign(p_A - p_t) \cdot \sqrt{|p_A - p_t|}$$

The systeminput-vector $\boldsymbol{u}$ is calculated from four measured values: p_A, $\dot{p}_A$, z_{dc} and y (with the tank pressure being set to $p_t \approx 0$). Furthermore, the system output needs to be calculated from the derivative of the measured cylinder position, respectively the cylinder speed $\dot{z}_{dc}$. All these values are available at the die cushion drive of an hydraulic press and can be evaluated within the machine controller. An additional requirement for the applicability of the chosen algorithm is for the elements of the input vector $\boldsymbol{u}$ to be independent. This can be proven with a singular value decomposition /5/. Despite the elements 2 and 3 correlating by the factor z_{dc} and elements 1 and 4 correlating by the factor y, the singular value decomposition shows sufficient independency.

The parameter estimation is calculated as a recursive algorithm for each time step k. This means that with each time step of the machine controller, the system values (input $\boldsymbol{u}$ and output γ) are measured, the model output ($\boldsymbol{\theta} \cdot \boldsymbol{u}$) is calculated and a new set of parameters $\boldsymbol{\theta}$ is determined from the error ε. The parameter estimation algorithm calculates a correcting vector $\boldsymbol{L}$ with each time step to determine the influence of the output error on the new set of parameters:

$$\boldsymbol{\theta}(k) = \boldsymbol{\theta}(k-1) + \boldsymbol{L}(k) \cdot [\gamma(k) - \boldsymbol{\theta}(k-1) \cdot \boldsymbol{u}(k-1)] \tag{9}$$

$$\begin{matrix} New \\ Parameter \end{matrix} = \begin{matrix} Old \\ Parameter \end{matrix} + \begin{matrix} Correcting \\ Vector \end{matrix} \cdot \begin{pmatrix} Output \\ Error \end{pmatrix}$$

The correcting vector $\boldsymbol{L}$ itself is calculated from the covariance matrix $\boldsymbol{P}$, the system input $\boldsymbol{u}$ and a forgetting factor λ, see equation (10).

$$\boldsymbol{L}(k) = \frac{\boldsymbol{P}(k-1) \cdot \boldsymbol{u}(k)}{\lambda + \boldsymbol{u}^T(k) \cdot \boldsymbol{P}(k-1) \cdot \boldsymbol{u}(k)} \tag{10}$$

The covariance matrix is also recalculated for each time step according to equation (11):

$$\boldsymbol{P}(k) = \frac{1}{\lambda}[\boldsymbol{P}(k-1) - \boldsymbol{L}(k-1) \cdot \boldsymbol{u}^T(k) \cdot \boldsymbol{P}(k-1)] \tag{11}$$

In order to start the algorithm, initial values for $\boldsymbol{P}(0)$ and $\boldsymbol{\theta}(0)$ need to be predefined as well as an appropriate value for the forgetting factor. The covariance matrix $\boldsymbol{P}$ is of the size $(n \times m)$. Its initial value should be calculated from the identity matrix multiplied with a constant factor α:

$$\boldsymbol{P}(0) = \alpha \cdot \boldsymbol{I} \tag{12}$$

The factor α can be chosen from a value $\alpha = 100 \ldots 10000$ /4/. For the investigated application of the die cushion drive, a value $\alpha = 500$ was chosen. It can be interpreted that the choice of a large value α allows the algorithm to make large changes to the next set of parameters within one single time step at the beginning of the identification /4/. Yet the choice of this parameter only has marginal influence on the result of the identification. The forgetting factor however can significantly influence the result of the identification. For the presented identification algorithm, a factor $\lambda = 0{,}998$ was chosen. The initial value for the parameter vector $\boldsymbol{\theta}(0)$ was set to $\theta_i = 1$ for each element.

The actual system parameters of the hydraulic system $K', V_0, q_{v,nom}$ and y_{0v} can then be calculated from the parameter vector as follows:

$$Q_{v,nom} = -\sqrt{\Delta p_{nom}} \cdot \theta_1 \tag{13}$$

$$K' = -\frac{A_A}{\theta_3} \tag{14}$$

$$V_0 = -\theta_2 \cdot K' \tag{15}$$

$$y_{0v} = \frac{\sqrt{\Delta p_{nom}}}{Q_{v,nom}} \cdot \theta_4 \tag{16}$$

4.2 The valve dynamics subsystem

The system equation for the valve dynamics subsystem from equations (3) and (4) is:

$$\frac{1}{\omega_{0v}^2}\ddot{y}_v + \frac{2D_v}{\omega_{0v}}\dot{y}_v + y_v = K_v \cdot U_v(t - T_{dead}) \qquad (13)$$

The unknown system parameters are the natural frequency ω_{0v}, the damping coefficient D_v, the valve gain K_v and the dead time T_{dead}. This equation though, cannot be transformed to meet the requirements of the above described parameter estimation that was applied to the hydraulic subsystem (see eq. 8). In Addition, an identification in the time domain would require the valve position y_v as well as two more derivatives ($\dot{y}_v$ and $\ddot{y}_v$). With the technically inevitable signal noise, those signals cannot be calculated for the high dynamic of the servo valve.

Therefore an identification within the frequency domain was implemented. This requires a multi-step identification with the determination of the frequency response from measured data that is followed by the parameter estimation. This identification cannot be implemented as an online process. It contains the following steps:

1) Employ a sinusiodial test signal with a frequency f_p to the servo valve
2) Calculate real and imaginary part of the frequency response with an orthogonal correlation
3) Calculate Magnitude and Phase shift for the current frequency
4) Repeat steps 1-3 for different frequencies in order to obtain the complete frequency response with magnitude and phase shift
5) Apply a parameter estimation on the magnitude and identify the parameters ω_{0v}, D_v, and K_v
6) Apply a parameter estimation on the phase shift and identify the last parameter T_{dead}.

The frequency response with magnitude and phase shift can be determined with the help of an orthogonal correlation, which is the "most important frequency response measurement technique for linear systems" (/4/, p. 134). Therefore a sinusoidal signal at a fixed frequency is applied to the servo valve. As the valve is equipped with an onboard position control for the spool, the current position can be measured. From the applied voltage as test signal and the returned spool position, the magnitude and phase shift for the current frequency can be obtained. Figure 6 shows the measured signals. The phase shift and magnitude can clearly be seen and could also be measured and calculated manually.

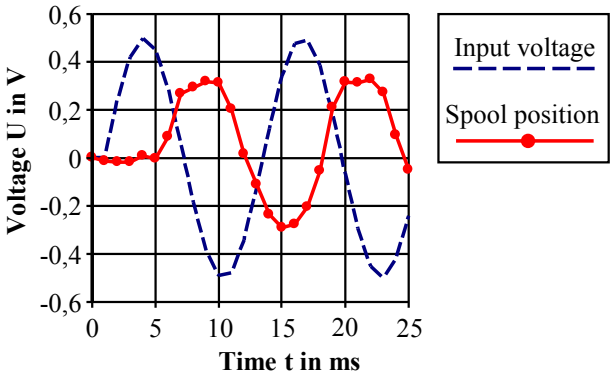

Figure 6: Input voltage and spool position for the servo valve ($U_{max} = \pm 10V$), measurements

The algorithm is based on the orthogonality relations of trigonometric functions. Its main arithmetic operations are the multiplication of the input and output signal followed by an integration. This leads to the imaginary and real part $Im[G(j\omega)]$ and $Re[G(j\omega)]$ of the frequency response for the current test signal frequency f_p and amplitude U_0. The orthogonal correlation is an ongoing algorithm over n full periods where the accuracy of the calculated frequency response increases with the number of periods integrated. Detailed description on this method can be found in /4/. The equations to determine the frequency response are as follows:

$$Re[G(j\omega)] = \frac{2}{U_0^2} \cdot \frac{f_p}{n} \cdot \int_0^{n \cdot \frac{1}{f_p}} U_0 \sin(\omega t) \cdot y_v \, dt \qquad (14)$$

$$Im[G(j\omega)] = \frac{2}{U_0^2} \cdot \frac{f_p}{n} \cdot \int_0^{n \cdot \frac{1}{f_p}} U_0 \cos(\omega t) \cdot y_v \, dt \qquad (15)$$

The correlation should not start before the system reached its steady state. Furthermore, the accuracy increases the longer the integration is calculated. Figure 7 shows the values of the real and imaginary part for a measurement at a test signal frequency of $f_p = 20\ Hz$. Both values tend towards a static value after less than 0.5 seconds. This time is even lower for higher frequencies.

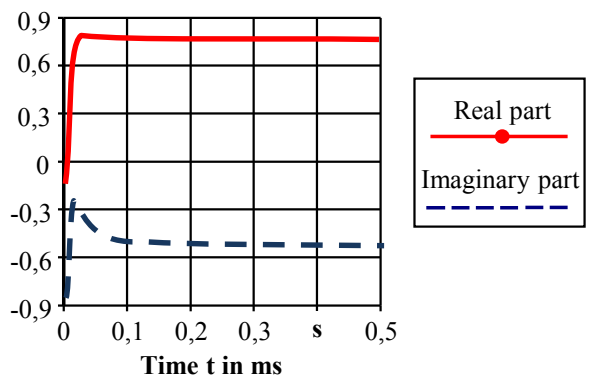

Figure 7: Real- and imaginary part for a test signal frequency $f_p = 20\ Hz$

Magnitude $|G(j\omega)|$ and phase shift φ can then be calculated from the orthogonal correlation, see equations 16 and 17:

$$|G(j\omega)| = \frac{K_v}{\sqrt{\left(1-\frac{\omega^2}{\omega_{0v}^2}\right)^2 + \left(2D_v \cdot \frac{\omega}{\omega_{0v}}\right)^2}} \tag{16}$$

$$\varphi = -T_{dead} \cdot \omega - \arctan\left(\frac{2D_v \frac{\omega}{\omega_{0v}}}{1-\frac{\omega^2}{\omega_{0v}^2}}\right) \tag{17}$$

The system behavior of this second order transfer function in the frequency domain can now be transformed to a parameterlinear equation, as demanded in eq. (5). This leads to the following equations for the magnitude at each frequency ω:

$$\gamma_{gain} = \boldsymbol{\theta}_{gain} \cdot \boldsymbol{u}_{gain} \tag{18}$$

$$\gamma_{gain} = |G(j\omega)|^2 \tag{19}$$

$$\boldsymbol{\theta}_{gain} = \begin{pmatrix} \theta_{1,gain} \\ \theta_{2,gain} \\ \theta_{3,gain} \end{pmatrix} \tag{20}$$

$$\theta_{1,gain} = \frac{2-(2\cdot D_v)^2}{\omega_{0v}^2}$$

$$\theta_{2,gain} = \frac{1}{\omega_{0v}^4}$$

$$\theta_{3,gain} = K_v^2$$

$$\boldsymbol{u}_{gain} = (u_{1,gain}\ u_{2,gain}\ u_{3,gain}) \tag{21}$$

$$u_{1,gain} = \omega^2 \cdot |G(j\omega)|^2$$

$$u_{2,gain} = -\omega^4 \cdot |G(j\omega)|^2$$

$$u_{3,gain} = 1$$

Applying the above described algorithm of the parameter estimation on equations 18 to 21, the valve parameters ω_{0v}, D_v, and K_v can be identified. Only the parameter T_{dead} remains unknown. It can be identified from the phase shift φ:

$$\gamma_{phase} = \theta_{phase} \cdot u_{phase} \tag{22}$$

$$\gamma_{phase} = \varphi + \arctan\left(\frac{2D_v \cdot \frac{\omega}{\omega_{0v}}}{1-\frac{\omega^2}{\omega_{0v}^2}}\right) \tag{23}$$

$$\theta_{phase} = -T_{dead} \tag{24}$$

$$u_{phase} = \omega \tag{25}$$

5 Practical implementation on the drive controller

The processing power of the controller and the available signal quality are the key points for the practical implementation. The identified system sets its characteristic requirements towards high signal quality and sampling time.

5.1 Signal quality

The noise on the measured signals is a major problem during the practical implementation of the identification algorithm. Due to electromagnetic interferences, the existing signal quality is rather low. Mainly the frequency converters and electric motors induce a significant noise level on the machine signals. The identification of the valve dynamics does only require the movement of the valve spool. Therefore the frequency converters and electrical motors are completely switched off and only marginal noise occurs such that no additional filters are necessary.

However, for the identification of the hydraulic system, the deep drawing press needs to be in full operation where high electromagnetic interferences and signal noise occur. The machine signals are filtered and the derivatives are calculated as symmetrical derivative over several measure points. The aim was to retrieve an acceptable signal quality while at the same time retaining the dynamic of the signal with a reasonable effort and complexity towards the applied filter. The chosen signal filter is a moving-average filter (see /8/ for further information). More complex filter algorithms may offer a better filter behavior, especially in the frequency domain, but the moving average filter offers best usability for the chosen application. It can easily be implemented within the machine controller as well as connected to the identification algorithm while at the same time delivering sufficient results for the time domain encoded and processed signal. For every time step k, the filter calculates the average over a set number of measure points. Equation 26 shows the moving average filter for a width of $M = 5$. The equation for the symmetrical derivative is given in eq. 27 for a width of 5. The effect of a rising filter width is shown in figure 8. The equations are formulated for an offline-processing in order to reduce the time delay. For the practical implementation on the controller this requires to save $(M + 1)$ data points where the filtered data is calculated with a time delay of $[0{,}5 \cdot (M+1) \cdot T_a]$. This needs to be applied to all measured signals in order to retain synchronism.

$$y_{filt,k} = \frac{y_{k+2} + y_{k+1} + y_k + y_{k-1} + y_{k-2}}{5} \tag{26}$$

$$\dot{y}_{filt,k} = \frac{y_{k+2} + y_{k+1} - y_{k-1} - y_{k-2}}{6} \tag{27}$$

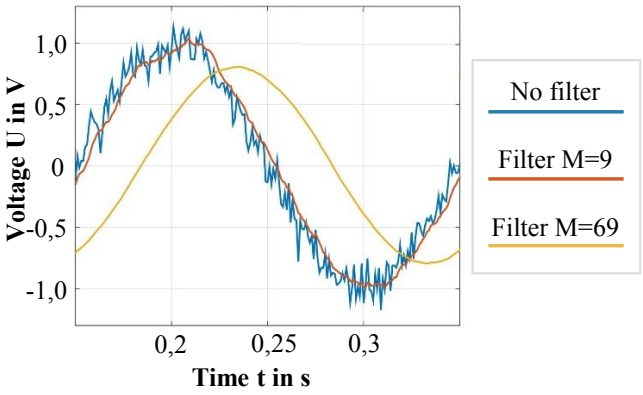

Figure 8: Effect of different filter parameters on the signal processing

In order to determine the optimal filter parameters, a simulation model of the hydraulic system was used together with a model of the occurring noise. With the help of the simulation model, a noise-free reference could be found for the identification. The filter parameters could be optimized in a way that the identification result with noise and the result without noise were compared for best results. The method is shown in Figure 9:

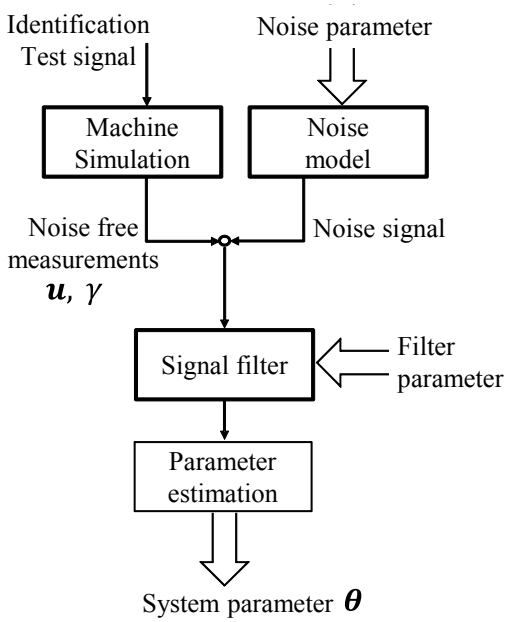

Figure 9: Method for finding optimal filter parameters

The machine simulation is a verified system model of the deep drawing press from previous research activities (see /9/ and /10/). The noise model was generated from analyzing the actual occurring noise as seen in figure 10. Signal noise can be considered as white noise for most applications /11/. Therefore the measured signal noise was evaluated. Its deviation is similar to a normal distribution, though it does not pass the Chi-Squared-Test. This can be explained as there are specific frequencies that occur more frequent, such as at 50 Hz and 100 Hz. Nevertheless, most frequencies are evenly distributed and the parameters for a normal distributed white noise signal can be obtained with reasonable effort. The corresponding parameters of an ideal white noise signal for the current test setup are given in table 1. The median μ is zero for all measured signals and the standard deviation σ differs due to the different gain factors for the analog signal processors.

Table 1: noise parameters for the modelled white noise signal with normal distribution

	Pressure	Position	Valveposition
μ	$0\ Pa$	$0\ m$	$0\ \%$
σ	$2{,}2\ \times 10^{5}\ Pa$	$1{,}2\ \times 10^{-4}\ m$	$6{,}8\ \times 10^{-3}\ \%$

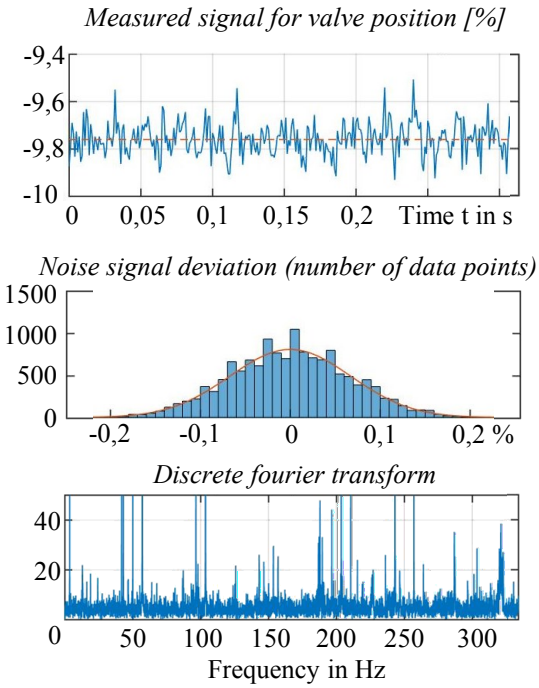

Figure 10: noise on the valve position signal and the occurring deviation

The quality of the filter will be evaluated by computing 150 parameter estimations with the added noise model with one set of filter parameters. Due to the chosen random noise generator, the estimated parameters θ_i will result in a different result for every single simulation. The bias and standard deviation of all 150 estimation results will be used to evaluate the quality of the chosen filter parameters. Figure 11 shows the deviation of the system parameter θ_3 for 150 simulation with the noise parameter as shown in table 1 and no filter applied. All values are normalized. The mean value of the identification result is at 6% of the value without noise (Bias) and the standard deviation within the 150 simulations is at 48% (interval from -42% to 54%). This means that the parameter estimation does not deliver reliable results.

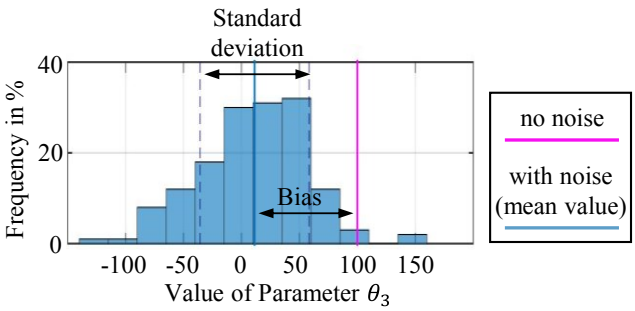

Figure 11: Bias and Standard deviation for θ_3 without filter

This process is repeated for a different set of filter parameters from $M = 0 \dots 50$ for the moving average filter as well as for the symmetrical derivative with 150 simulations for each filter. The bias of the identified system parameters for $\theta_{1\dots3}$ is shown in figures 12 to 14 in dependence from the filter parameters for a time step of the machine controller of $T_a = 2ms$. It can be seen that the parameter θ_1 delivers best results with a maximum relative deviation of 0,702 %. This is because there is no signal derivative necessary to calculate its value:

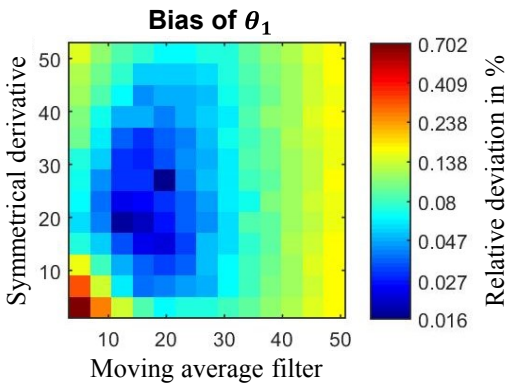

Figure 12: Bias of θ_1 for different numbers of data points for the moving average filter and the symmetrical derivative

Both other parameters $\theta_{2,3}$ show a clear dependence. For θ_2 the number of data points on the symmetrical derivative and the moving average filter should be similar and even a high filter parameter still delivers good results.

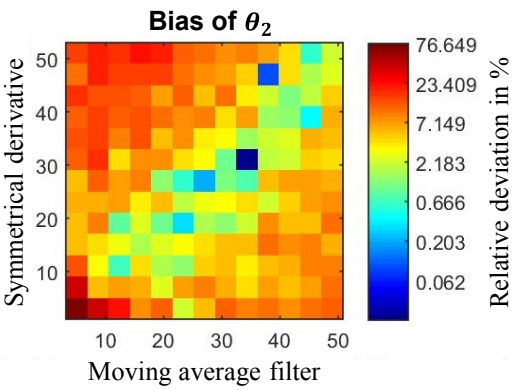

Figure 13: Bias of θ_2 for different numbers of data points for the moving average filter and the symmetrical derivative

However, the accuracy of parameter θ_3 decreases with rising filter parameters. The optimum for the filter parameters can be found at about $M = 20 \dots 30$ for the moving average filter as well as for the symmetrical derivative.

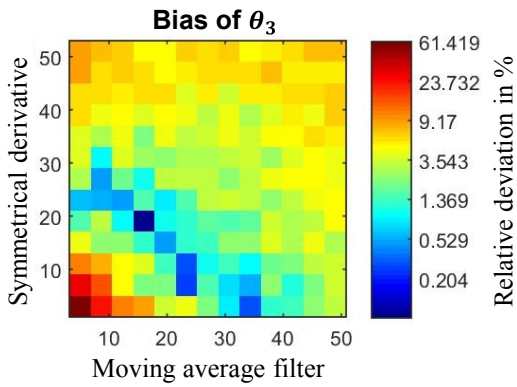

Figure 14: Bias of θ_3 for different numbers of data points for the moving average filter and the symmetrical derivative

The standard deviation shows a similar behavior for all identification parameters. The value decreases monotonous with rising filter width, as shown in figure 15.

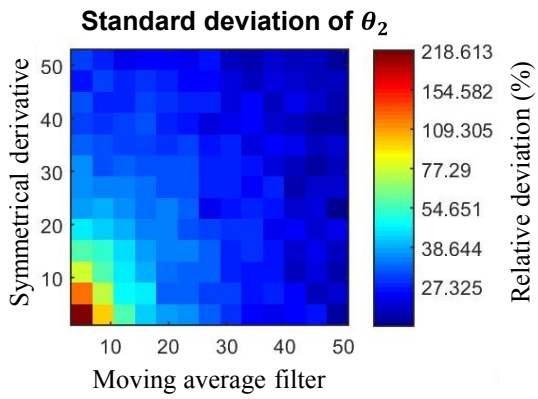

Figure 15: Standard deviation for θ_2 for different numbers of data points for the moving average filter and the symmetrical derivative

5.2 Sampling time

A constant sampling time of the machine controller is essential for the algorithm as all signal derivations are calculated within the algorithm. The Nyquist-Shannon sampling theorem states that the measuring frequency theoretically should be double the highest frequency content of the signal. Otherwise, aliasing would occur. The identification algorithms requires a signal that includes no less than the highest system frequency, otherwise the system cannot be identified correctly. Each of the subsystems has its own dynamic and for each identification, the sampling time must be low enough to measure this dynamic and additionally to allow for sufficient filtering in order to suppress noise. For the valve dynamics subsystem the limiting frequency is the eigenfrequency of the valve, respectively the highest applied test signal frequency. The hydraulics subsystem can be

characterized by means of a step response test and the t_{63} time constant for an assumed PT1 first-order lag element. The t_{63} time constant was derived from a sample step response test at the machine. With a step function on the valve, the pressure response was measured. The t_{63} time constant is when the pressure signal passes 63% of its final static value. For the assumed first-order lag element, the t_{63} is equivalent to the time constant T, respectively the inverse breakpoint frequency $1/\omega_B$. The sampling time should be as low as 0.1 t_{63}.

The investigated servo-valve has a high eigenfrequency and the test signal frequency goes up to $f = 160Hz$, so the sampling time should be at about $T_a \approx 1\,ms$. The time constant of the hydraulic system is at $t_{63} \approx 90ms$ (breakpoint frequency of merely $\omega_B = 69\,Hz$), sampling time should be no higher than $T_a = 9\,ms$. It has to be noted, that the investigated hydraulic deep drawing press has a comparable low ram speed of $v_{ram} = 40\,mm/s$. Industrial servo presses feature speeds of up to $300\,mm/s$. Experimental data shows that the characteristic time constant for these machines is at $t_{63} = 3\,ms$. The sampling time should be equally lower. With regards to the applied digital signal filters, an even lower sampling time is preferred. Therefore an individual task for signal processing was implemented within the machine controller that runs at $2\,ms$. The identification algorithm is executed every $10\,ms$. This leads to sufficient results for the hydraulic subsystem with minimal required processing power. However, the identification for the valve subsystem is calculated in a specific task at $1\,ms$ to take the high system dynamic into account.

6 Identification results

The above described parameter estimation algorithm was successfully implemented on the machine controller of the die cushion in a hydraulic deep drawing press.

The identification of the valve dynamics subsystem is shown in figure 16. A frequency of $(10, 20 \ldots 160)Hz$ at $0.5\,V$ (5 % of the nominal valve voltage) was applied at the servo valve and the magnitude and phase shift calculated by means of the orthogonal correlation. Due to the low voltage level, no spool velocity saturation should occur. This also means that the different behavior for different amplitudes is not modelled and the model is only valid for low voltage magnitudes. During identification, no signal filter was applied as all machine drives were switched off and there was no significant signal noise. The parameter estimation algorithm identified the system parameters for the assumed second order system with an additional dead-time (see eq. 13). The system parameters are as follows:

Damping ratio: $D = 0.6735$
Natural frequency: $\omega_{0v} = 183.9\,Hz$
Gain: $K_v = 1.005$ and
Dead Time: $T_{dead} = 0.00\,s$

The Bode plot of the identified system model shows a good accuracy in comparison to the measured data (see fig. 16).

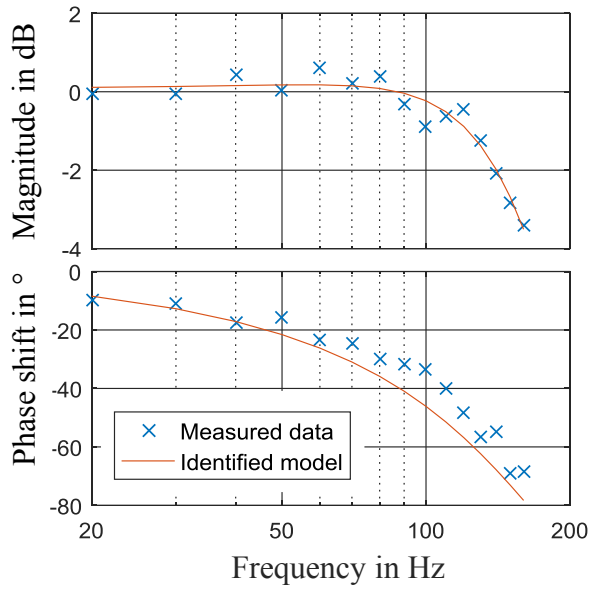

Figure 16: Magnitude and Phase shift for the identified servo valve in in the deep drawing press

The identification of the hydraulic subsystem is more difficult, as it sets higher standards towards signal quality and correct implementation of a signal filter. With the applied filter, the identification algorithm delivers good results. Figure 17 shows the identification of the bulk modulus over time from the machine controller with the implemented recursive least square identification algorithm. It can be seen that it approaches towards a constant end value. The parameters were as follows:

Sampling time (signal processing): $t_S = 2\,ms$
Sampling time (identification): $t_i = 10\,ms$
Moving average filter (width): $b = 31$
Symmetrical derivative (width): $d = 25$
Forgetting factor: $\lambda = 0{,}998$
Parameter initial values: $\theta_{1\ldots4} = 1$

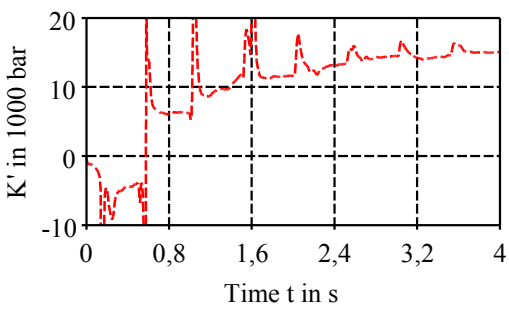

Figure 17: Identification of the bulk modulus

The identification result and the speed at which it approaches towards the static value can be improved by setting initial values as a "good guess". However, the algorithm still shows good results at a reasonable speed even with the defined initial values being set at '1'.

The identification algorithm was executed numerous times in order to determine its stability and robustness. The identification results for 30 consecutive measures are shown in figure 18 for the nominal volume flow, the dead volume and the bulk modulus. The figure also shows the mean value though all identifications with a solid line. It has to be noted that the oil temperature is not constant throughout all 30 measures, but rises from 26°C for the first identification to 32°C for the last identification. This explains the characteristic of the nominal volume flow $Q_{v,nom}$ due to changing properties of the hydraulic fluid.

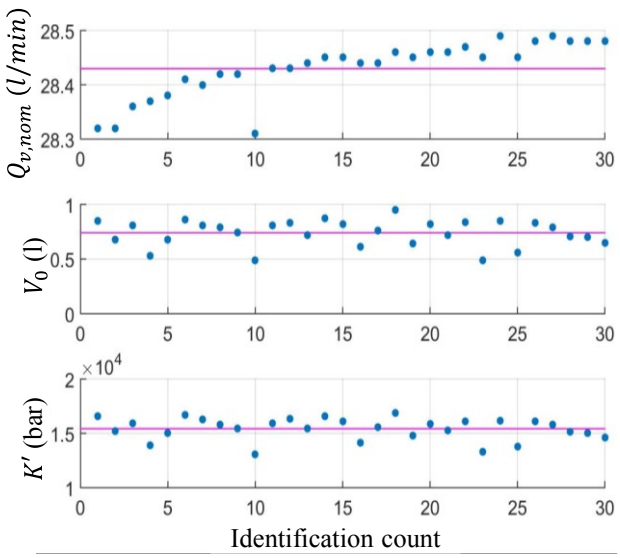

Figure 18: Identification results for 30 consecutive experiments

7 Outlook

The paper shows the successful implementation of an identification algorithm within the machine controller of an industrial type hydraulic deep drawing press. This offers a high potential for further applications to reduce manual maintenance and increase the performance of the hydraulic drive. The online-identification algorithm is able to detect changing system parameters that can be used for condition monitoring, predictive maintenance or fault diagnosis. The described method can further be applied for other hydraulic systems and is not limited to the deep drawing press. In addition, the now fully identified system model can be used for controller design. The implementation of a feed-forward element based on the volume flow characteristics of the servo valve is a common method to improve the control quality of hydraulic die cushion drives [12] and the system parameters $Q_{v,nom}, \Delta p_{nom}$ and y_0 could significantly improve the system behavior. Experimental results for the control behavior of the die cushion that was described in this paper are shown in Figure 19.

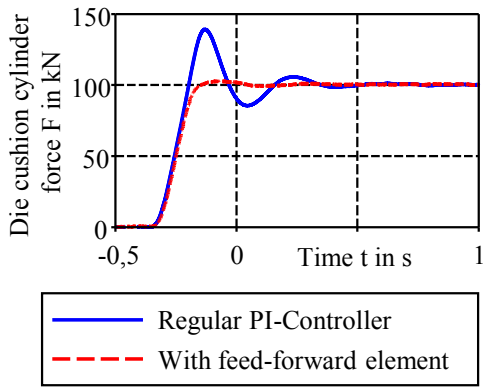

Figure 19: Control accuracy of the die cushion

8 Acknowledgements

The presented research is part of the project KF2453605LP3 – "Entwicklung eines neuartigen adaptiven Regelsystems zur automatisierten und selbstoptimierten Inbetriebnahme hochdynamischer elektrohydraulischer Pressen mit integrierter Parameternachführung im laufenden Betrieb", which is funded by the Federal Ministry for Economic Affairs and Energy, Germany within the ZIM program.

Supported by:

Federal Ministry for Economic Affairs and Energy

on the basis of a decision by the German Bundestag

9 References

[1] Lohse, Harald; Helduser, Siegfried; Marthiens, Olaf; Matthias, Thorsten; Behrens, Bernd-Arno (2010): *Reglerauslegung für hydraulische Tiefziehpressen Unterstützt durch ganzheitliche Simulation*. In: O+P Ölhydraulik und Pneumatik 2010 (3), S. 68.

[2] Helduser, Siegfried (2006): *Elektrisch-hydraulische Systemtechnik. Entwicklungsschwerpunkte in der Stationärhydraulik.* In: O+P Ölhydraulik und Pneumatik 2006 (1), S. 16–23.

[3] Schoppel, Georg (2003): *Beiträge zur automatischen Inbetriebsetzung und Regelung hydraulischer Zylinderantriebe*. Aachen: Shaker.

[4] Isermann, Rolf (2011): *Identification of Dynamic Systems*, Springer.

[5] Keesmann, K. J. (2011): *System identification an introduction, Advanced textbooks in control and signal processing*, Springer.

[6] Ljung, L. (2009): *System Identification. Theory for the user*, Prentice Hall.

[7] Jelali, M.; Kroll, A. (2004): *Hydraulic servo-systems. Modelling, identification and control*. Springer London Ltd.

[8] Orfanidis, S. J. (1996): *Introduction to signal processing, Prentice Hall signal processing series*. Prentice Hall

[9] Schulze, T.; Weber, J.; Penter, L.; Großmann, K. (2014): *Modelling and Simulation of the die cushion in a hydraulic deep drawing press*. 16th ITI Symposium, Dresden

[10] Schulze, T.; Weber, J.; Großmann, K.; Penter, L.; Schenke, C. (2015): *Hydraulic die cushions in deep drawing presses – analysis and optimization using coupled simulation.* ASME/BATH 2015 Symposium on Fluid Power and Motion Control, Chicago

[11] Smith, S. W. (1999): *The scientist and engineer`s guide to digital signal processing*. California Technical Publication

[12] Helmke, M.; Majer, H.; Thanassakis, A. (2016): *Improvement of hydraulic control quality for deep drawing presses through retrofit*. 10th IFK 2016, Dresden,

Cloud-Based System Architecture for Driver Assistance in Mobile Machinery

O. Koch , B. Beck , G. Heß*, C. Richter*, V. Waurich*, J. Weber , C. Werner**, and U. Aßmann**

Chair of fluid-mechatronic systems, Technische Universität Dresden, Dresden, Germany
E-mail: benjamin.beck@tu-dresden.de, oliver.koch@tu-dresden.de, mailbox@ifd.mw.tu-dresden.de
*Chair of construction machinery, Technische Universität Dresden, Dresden, Germany
E-mail: georg.hess@tu-dresden.de, christian.richter1@tu-dresden.de, volker.waurich@tu-dresden.de
**Chair of software technology, Technische Universität Dresden, Dresden, Germany
E-mail: uwe.assmann@tu-dresden.de, christopher.werner@tu-dresden.de

Abstract

Using the example of a wheel loader, this paper presents a cloud-based system architecture enabling intelligent machine behavior. In order to achieve the final goal of a fully automated bucket filling routine, while controlling the loaders engine, travel drive and attachment, different levels of automation are processed gradually. As a first step towards automation, driver assistance can be considered. The paper explains the design choices for a cyber-physical-system architecture in the context of construction machinery. This comprises the communication framework and the cloud-application for self-adapting systems (i.e. the MAPE-K loop). As a validation of the architecture and as a demonstrator, a driver assistance functionality has been implemented. Calculations from the cloud-application give the operator feedback about efficiency, loads and task status. A developed visualization app on a tablet serves as user-interface. Concurrent simulation allow an optimization of control algorithms for the machine control and the trajectory planning. Besides changing the parametrization of the underlying models, a solution to change ECU-code at run-time without interrupting the operation is presented. The developed system architecture is the basis for further implementations of adaptive algorithms that improve future machine operation.

Keywords: cloud computing, smart metering, IIoT, construction machinery, systems architecture

1 Introduction

Applications in the field of automation and cyber-physical systems (*CPS*) are still a recent topic of research. For mobile machinery, the development tendencies in this direction are obvious, both in industry and academia.

Besides the typical challenges of control engineering in hydraulic systems and the abstraction of operating processes for automation purposes, new challenges arise, i.e. to design a suitable system architecture for CPS applications in the domain of construction machinery.

Within this paper, a proposal for a cloud-based architecture to operate an automated wheel loader is described. The goal is to implement an assistance function to automatically fill the wheel loader's bucket and design an appropriate driver interface. As the working conditions for a wheel loader are rarely constant and predictable, a self-adaptable and experience-based automation strategy is feasible. This means, that the algorithms for detecting the pile, computing a target trajectory as well as controlling the loaders engine and hydraulic system are parametric and can vary throughout various operation cycles. Increasing flexibility and guaranteeing self-adaption in combination of optimization requires to change the machines control algorithms. An interruption of the machine usage for changing a control strategy will not be accepted by the operator. Therefore, a run-time exchange of machine software is necessary. To collect, store and process the required data, a cloud-based network architecture has been implemented.

The availability of a comprehensive network that is able to monitor the machinery and to manipulate its operating logic, reveals new fields of applications. As a typical practice, additional information of the machine and its working conditions can be provided for the driver. The processing of raw data to meaningful information (i.e. called smart metering) integrates well with the proposed architecture and creates additional value for the driver as well as for the monitoring site operator. These assistance features are the first steps to approach the goal of an automated machine and it serves as a proof-of-concept for the implemented network architecture.

The following chapters will describe the implemented system architecture in detail. Chapter 2 describes the initial situation and the state-of-the-art in the field of CPS in construction machinery. Chapter 3 gives an overview of the applied architec-

ture and chapter 5 deals with the software adaption strategy on run-time. In chapter 4, the driver assistance functionality is described and finally, chapter 7 summarizes the paper and gives an outlook.

2 State of the Art

2.1 Levels of Automation

Designing a completely autonomous construction machine from scratch demands enormous efforts. In order to approach this goal gradually, a development starting from a non-automated system seems much more realizable. The levels of automation of decision and action selection by [1] can serve as a guidance on the way to an automated construction machine. A coarse classification, based on the SAE-standard J3016 [2] transferred to mobile machinery depicts as follows:

- **No Automation**
  The driver monitors and controls the system at all times and is fully responsible to move into a safe state.
- **Driver Assistance**
  The system partly sets the controls whereas the driver has to monitor the system at all times and is able to control it manually.
- **Partial Automation**
  The system sets the controls partly over a certain period of time whereas the driver has to perform the remaining tasks at all time.
- **Conditional Automation**
  The system sets the controls completely over a certain period of time whereas the driver has to monitor the system and needs to be ready for control at all times.
- **Highly automated**
  The system sets the controls completely over a certain period of time whereas the driver has to take the control after automated operation.
- **Fully automated**
  The system sets the controls completely whereas the driver does not need to monitor the system. The driver can take control but the system is able to go into a safe state at any time.

In industrial hydraulic applications, the boundary conditions like temperatures, process forces and duty cycles are mostly good known. Furthermore, there is a less cost pressure because investments into plants recoup early due to large quantities of produced products. This results in a higher level of automation like shown on an example of a hydraulic power unit in [3]. But the task of monitoring and analyzing data is application independent. Concerning mobile hydraulic applications, just a few assistance functions like a return-to-dig routine in a wheel loader are integrated in mobile machines (Driver Assistance), nowadays. Most of the tasks are operator controlled (No Automation). This is mainly due to the diverse working tasks, the harsh environmental conditions like vibrations, dust and a wide temperature range in combination with a required high availability of the machine. However, the continously increasing demands on productivity and efficiency require the steps of automation, because the operator cannot have an overall comprehension of the process and additionally has a decreasing productivity due to an increasing tiredness. An example is the filling and dumping cycle, which can be repeated sufficiently often in order to apply automation in a productive way. As stated in [4], the efficiency of wheel loader bucket filling strongly depends on the trajectory of the bucket. Inexperienced drivers are likely to move too much soil through the pile and hence, the filling is expensive in terms of energy. An energy-efficient trajectory would be to slice a thin chip of soil until the bucket is filled [5]. Therefore, the bucket filling is a worthwhile task for automation.The key challenges in automation and tele-remote operation of earth-moving machines concerning these levels of automation are summarized in [6]. Especially, the short-loading cycle of a wheel loader with an in-depth review of different automatic bucket loading strategies is analyzed. The authors also address the problem of material description as well as communication aspects. As a result, they suggests semi-automation as short to mid-term solution for earth moving machines. For integrating the levels of automation into mobile machinery, the following tasks have to be solved:

- Path planning for driving
- Collision detection, avoidance and navigation
- Path planning for the work equipment

Thereby the following requirements have to be taken into account [6]

- Performance of the work task (fill factor and cycle time)
- Fuel efficiency
- Safety

According to [6] there are many publications on modeling for control, automatic loading, pile characterization, localization and navigation as well as path planning. Volvo has researched on autonomous machines for more than one decade. In [7] they demonstrated how an autonomous wheel loader together with an autonomous articulated hauler reached 70% of a skilled operator's performance during a predefined cycle in an asphalt mine. The autonomous control algorithm and the autonomous bucket control are described by [8, 9]. However, the paths are predefined, there is no communication between the machines and no process optimization. Furthermore, an industrial PC along with a Simulink-based control algorithm is used [8], which are suitable for prototyping but not for commercial applications. This example shows possibilities in the development of mobile machines. Additional, autonomous functionalities or services offer novel innovations. The variety of the applications is almost unlimited. Today, it is easily possible to adapt a parameter in a control algorithm without interrupting the machine. It guarantees a little flexibility. Unfortunately, it is nearly impossible to foresee all eventualities within the design of the control algorithms. There are research approaches dealing with machine learning to consider the uncertainties. It needs a lot of computer resources that are not available on a mobile machine. The communic-

ation technologies offer a solution. Implementing a wireless network structure and bundling powerful computer resources in a cloud architecture that is able to change algorithms on a mobile machine enables a flexible and adaptable machine control structure. Learning algorithms, optimizations or condition monitoring can be executed within that cloud. The machine itself performs the specific working tasks. If a new task requires a completely new functionality that the machine is currently not able to perform, the cloud-based supervisor will learn and modify the machine's algorithms. This concept leads to the question of changing software algorithms on runtime that are currently not available on the embedded device. At the time of publication, there are no contributions to cloud-based hardware and software architectures for realizing adaptive control algorithms for mobile machines.

2.2 Cloud Solutions

Cloud platforms play a big role in the IoT world. They offer many advantages to create large IoT applications e.g. predefined analyzing functions, on demand extendable data storage, and a variable amount of computational power. Important cloud providers in this area are Amazon's AWS IoT-Platform, the Google Cloud Platform, Microsoft's Azure IoT Suite, Bosch IoT, ThingWorx IoT Platform, and IBM's Watson IoT, which are presented in [10]. All of them present different implemented modules, which internally fit perfect together to a larger IoT solution for a variety of applications. The modules offer data storage, analyzing features, and visualization interfaces. In the year 2005, IBM published a paper called "An architectural blueprint for autonomic computing" [11]. There, they present the control loop called MAPE-k. Figure 1 shows the loop in the proposed system architecture consisting of the four MAPE phases and the k representing the data storage as knowledge base. In the monitoring step all incoming data is collected and saved. The analyze phase offers functionality to correlate the data and to create high level information. Then, in the planning step, the information from the analyze step is used to compare the incoming data with the predefined objectives that should be reached and to adapt the system if necessary. The last part comprises the execution phase, which distributes new information to connected applications. This loop is integrated in most processes to create adaptable software.

IBM named its cloud architecture "open cloud architecture" [12] to create interfaces for open source standards, projects, and applications. This generates an mechanism to easily extend applications and connect them to related open source frameworks. They also implemented e.g. OASIS, W3C, IETF, and OMG standards and thereby have integrated the MQTT-Protocol. The MQTT-Protocol [13] offers existing open implementations for a lot of programming languages like C++, JAVA, or Python. It provides a publish/subscribe service with different quality metrics. On the lower level the MQTT-Protocol implements sockets that enables a fast connection and the possibility to use different data formats.

3 Overall System Architecture

Figure 1 illustrates the basic concept of the chosen system architecture consisting of the main modules wheel loader, communication interface, cloud application and user interface (i.e. a tablet).

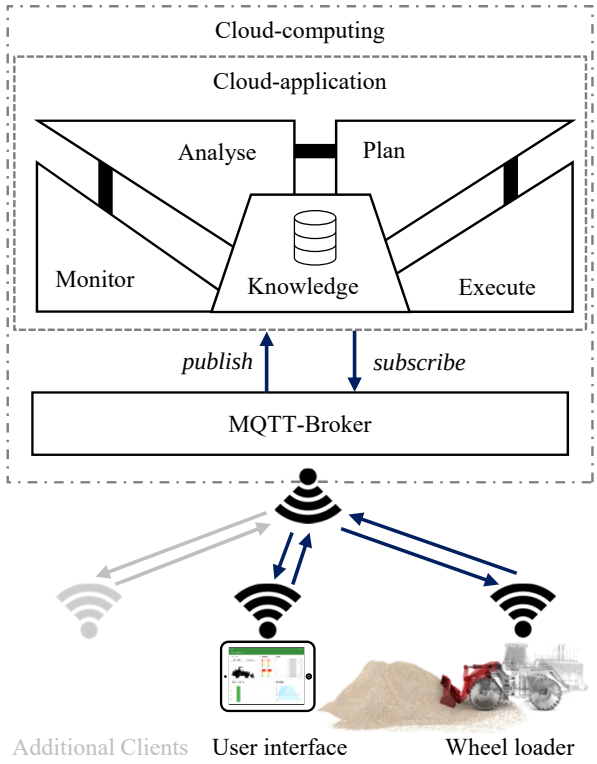

Figure 1: Overall System Architecture

3.1 Cloud Structure and Applications

The cloud is the central node which collects data from connected clients and performs the overall optimization and analysis. A client represents a specific device, a machine or a software component within the cloud which sends and/or receives data to/from another client. The MQTT-Broker plays a central role and manages all inter-communication processes between different clients. The broker itself takes only an intermediary role and routes all data messages.

All cloud-applications implementing the concept of the MAPE-k loop [14] in different abstraction levels covering the four phases: monitoring, analyzing, planning, and execution, which is depicted in fig. 1 and introduced in sec. 2.2. The data-flow between these phases is visualized by a bold line. In the *monitoring phase*, the cloud application collects all incoming sensor and machine data from the wheel loader over the communication interface, converts it into a object oriented data format and sends it to depending analyze algorithms. Furthermore, this phase saves all information into the connected database. This first implementation uses SQLite. All processes own read and write access to the knowledge database. With arrival of a certain devices first message the application creates a new database table. All following

messages will be written into this table. Subsequently, the *analyzing phase* creates high-level information by connecting recent data with historical data. In this first implementation step, the analyzing phase only computes the Smart Metering data for the wheel loader application. Additionally, the execution of Modelica-based simulation models are integrated to test this opportunity as well. They will be used for later optimization and the basis for generating changed algorithms for the wheel loader's control unit. The *planning phase* compares actual data with the target data and decides whether an algorithm has to be modified. Basically, two different options are possible. While modifying a control model's parameterization does not necessarily afford an software exchange, a replacement of a complete strategy requires downloading another software version. The last step in the cloud covers the *execution phase*. Modifications will be propagated to clients. Therefore, an FTP connection transfers the generated code to the machine and for parameterization the MQTT infrastructure is used directly.

Currently, the cloud executes every service for the implemented smart meetering application in a separate thread. It enables an independent development and test of all routines. Furthermore, all services inherit an application prototype. This already realizes basic functions to gather data from and commit data to the knowledge base. Python 3.5 serves as programming language. To reduce the amount of communication overhead and redundant software parts, merging all services in just one major cloud application is recommended and will be realized in further developments. A suitable plugin concept then allows an easy addition of new programmed services.

3.2 Network Communication

The connection between the cloud and the machine is managed by a communication interface based on the MQTT-Protocol [15]. It guarantees the creation of an adaptable, secure and scalable communication structure. Clients have to authenticate themselves to the server. The messages are encrypted by SSL/TLS. In order to add a new functionalities without changing the clouds overall implementation, the connections to services can be accomplished on the fly (Figure 1). An MQTT-Broker with a publish/subscribe interface is responsible for the clients communication. Different clients can connect themselves to the broker an subscribe and publish messages for related topics. It only requires implementing the MQTT-Client interface. For the prototypical implementation, the open source MQTT-Broker Mosquitto [16] is used.

According to individual machines, an initialization message is required to register a specific machine client. Within this initial handshake, the message protocols are exchanged. It considers varying communication processes and guarantees a certain flexibility. Reconfiguring the protocol only requires an update through a new configuration message. JSON serves as exchange format and contains application-depended key-value pairs.

3.3 Wheel Loader as a Network Client

Figure 2 illustrates the machine's control architecture consisting of two levels. The Machine Level represents the basic wheel loader functionality as it could be developed for ordinary operating tasks. The Adaptive Control Level implements additional control functionality that is used for automation and optimization during an operation.

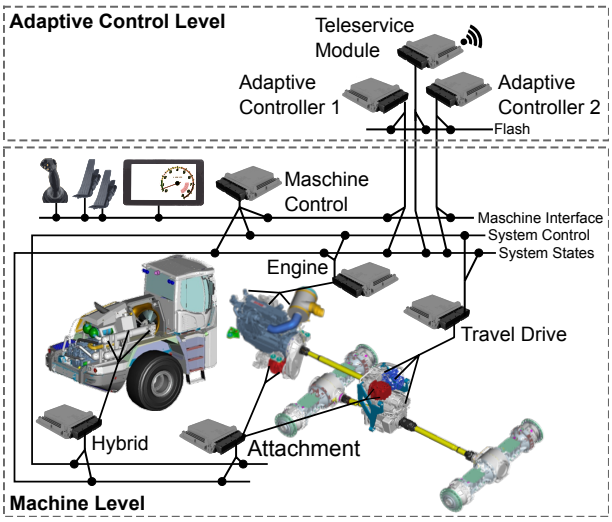

Figure 2: Wheel loader's system architecture

Therefore, the Machine Level represents a master-slave control system with three different CAN-networks. Operator devices communicate over the Machine-Interface bus with the Machine Control. This central unit interprets the operator inputs and generates the subsystems' set values according to the implemented operating strategy. Additionally, it handles functions such as control of peripheral systems, monitoring and calibration routines. Each subsystem comprises a separate controller for realizing the machine controller's demands from the System-Control bus by controlling the subsystem's integrated actors. Furthermore, subsystem-specific data acquisition and monitoring functions are implemented. They are transfered via the System-States bus.

Today, a typical mobile control unit does not usually allow changing software parts of a control algorithm on run-time. It almost always needs a reboot to start the internal flash-loader. This loader program expects getting a new complete control software from an interface and stores it in its designated memory. From there, the program will be loaded into the RAM and executed after starting the device. Operating systems usually offer a mechanism for an easy program exchange without the need for rebooting the device. Unfortunately, they cannot be installed on a today's mobile controlling unit. But novel developments usually designed for multimedia applications generate powerful embedded devices which allow running an operating system that provides this needed functionality.

This leads to two major opportunities depending on the selected embedded control unit. Using a typical mobile control device requires a control architecture consisting of at least two

redundant devices. While one controller executes the current algorithm the other unit is ready for rebooting and flashing a new program. A handshaking protocol handles switching the control units' responsibilities that the devices will change their operating state. After a software update, the recent updated control unit executes its algorithm while the other goes of and waits for a flash demand. If an embedded device with operating system shall be installed, only one device is necessary. Then, the handshake process happens between two programs on the unit itself.

The implemented Adaptive-Control-Level architecture consists of a teleservice device and two additional adaptable modules. The teleservice module acts as interface to the cloud. It handles flashing and monitoring the adaptive control units as well as gathering cloud-relevant machine data. The adaptive controllers are responsible for automated tasks that shall be modified during machine operation. They are connected to the machine interface to send control values to the master. These modules are typical mobile control units with an additional Linux board installed. It enables using both software change strategies and therefore a high flexibility. A separate installed CAN-bus (flash) handles the communication between teleservice module and adaptive control units. It shall guarantee a certain independence that an error within the adaptive control level does not directly affect the main machine behavior. All three modules listen to the System-State bus to get necessary machine information.

4 Analysis Modules in the Cloud Application

Besides several other cloud applications like on-board diagnostic (OBD), smart-metering, slip and fatigue computation will be described in the following chapters.

4.1 Smart Metering

In the context of industrial applications like mobile machinery, smart metering describes the intelligent evaluation of machine data provided by the installed sensors in combination with an appropriate visualization for the operator so that he can improve his control. Thereby the following questions have to be answered:

1. Which information or which value would improve the operator's control?
2. How can an appropriate visualization look like?
3. Which algorithms are needed to provide this data from the installed sensors?

Ideally, the algorithms should come along with the already installed sensors which are needed from the functional view. The wheel loader demonstrator already contains a variety of sensors to measure, e.g.:

- The angles in the joints of the work equipment,
- The swash plate angle of the pumps,
- The cylinder pressures and
- The shaft torque and rotational speeds at the gear output.

This application can be seen as an outlook for future development opportunities. Although this demonstrator is just a prototype and does not represent a today's commercial vehicle, the trend of installing electronic and software into mobile machines also expects an increase of sensors to detect various system states. According to the provided data for the operator, the vehicle's tire slip and a wear computation will be exemplary described in this paper.

4.2 Slip Computation

The illustration of the tire slip value λ can be divided into an optimal slip section and a section with an expected increase of tire wear. The operator shall recognize an unnecessary high tire wear and be able to reduce the wheel loader's output torque via its drive pedal. The optimum varies between 5 - 20 % depending on the environmental conditions like weather or ground conditions. This is expressed by the tire slip - friction coefficient curve displayed in fig. 3.

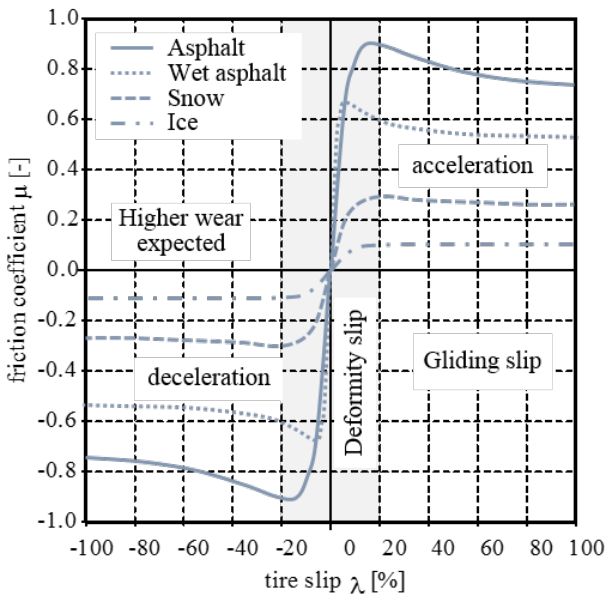

Figure 3: λ-μ-curves for different surfaces according to [17]

Because the machine only provides the output torque and rotational speed of the travel drive, there are two tasks for estimating the actual tire slip. First, an calculation algorithm is required and secondly, the machine's slip-free velocity $v_{machine}$ has to be measured. The calculation of the longitudinal tire slip λ_x is given by eq. (1), whereas n_{wheel} and D_{wheel} are the rotational speed and diameter of the wheel.

$$\lambda_x = \frac{\pi \cdot n_{wheel} \cdot D_{wheel} - v_{machine}}{\max(\pi \cdot n_{wheel} \cdot D_{wheel}, v_{machine})} \tag{1}$$

In the case of deceleration the numerator causes a negative velocity difference and the maximum function in the denominator becomes $v_{machine}$ resulting in a negative slip. On the other hand, an accelerating wheel has a positive numerator. The denominator becomes $\pi \cdot n_{wheel} \cdot D_{wheel}$ and a positive slip is returned. Furthermore, the ratios of the differential gear and the wheel hubs as well as the dynamic wheel diameter must be

taken into account. Because these values are specific machine parameters, they have to be transferred from a machine client to the cloud application during the subscription process. The tire slip calculation is implemented in the programming language Python. It gathers the gear ratios, the dynamic wheel diameter, the output torque and rotational speed of the travel drive, the actual time as well as the machine velocity from the knowledge data base. In return, the routine publishes its actual tire slip estimation as a result to the data base. Due to the wheel loader's permanently coupled wheels, the algorithm only generates one common slip value.

4.3 Fatigue and Wear Computation

With information about the current tire slip, it is possible to estimate the tire wear. A simplified first implementation in Python calculates the cumulative frequency W_{tire} if the tire slip exceeds the deformity slip range. There, due to the gliding slip, a higher wear is expected and can be estimated according to eq. (2).

$$W_{tire} = \frac{1}{T_{life}} \sum_{i=1}^{j} t_i, \text{ if } \lambda_x \geq \lambda_{limit} \tag{2}$$

Another exemplary feature is the monitoring of mechanical damage based on the calculated stress and providing it to the operator. To estimate the load acting on the structure, it is necessary to solve the equations of motion as well as the kinematics of the equipment. To reduce calculation time, the nonlinear equation system of the kinematics has to be avoided. Therefore, the angles are calculated with causal equations instead of nonlinear systems of equations. With those calculated values and the sensor data, the equation of motion of all bodies becomes a linear problem with the unknown joint forces. This system can be solved with a QR decomposition algorithm. The execution of this calculations is done in real time and thus the results can be saved in addition to the raw data on the cloud storage. To predict a failure of a component, the joint forces have to be transformed to a load spectrum. Afterwards, the fatigue can be derived. The total fatigue accumulation serves as an indicator for failure or wear.

4.4 Implementation

The algorithms have been virtually tested in a simulation environment. The next step includes the validation of the services by means of the real machine. Therefore, a sensor to measure the slip-free machine velocity must be installed. The most important use case for optimizing the tire slip of a wheel loader is presumable filling the bucket while driving into a pile. This requires a good accuracy at lower velocities. Because GPS-sensors do not fulfill this requirement [18], alternative techniques have to be discussed. Optical sensors address this problem but are cost-intensive at the same time [19, 20]. Inertia measurement units are one promising technology for mobile machines as shown in [21]. Additionally, they will be needed to compensate dynamic effects in the calculation of digging forces or loaded mass from the cylinder pressure signals. On the basis of the slip calculation, traction control algorithms can be developed in future work to reduce the tire wear and to increase the driving behavior during an autonomous loading cycle.

5 Planing Modules in the Cloud Application

5.1 Software Adaption on Run-Time

Figure 4 illustrates a basic software architecture that is applicable for both hardware variants (board with Linux operation system and mobile controlling unit). It represents a state machine and an algorithm component. This approach allows a separation of static code from variable software algorithms. While the state machine implements algorithm-independent software parts that usually do not vary between software updates, the algorithm component realizes a specific changeable strategy. The two interfaces StmInterface and Algorithm allow an interaction between them. A concrete algorithm has to provide the interface Algorithm for updating and reseting its output values. The architecture considers automated functions that prohibit an interruption during the process as well as interruptible semi-automated functions. Therefore, a concrete algorithm uses the StmInterface to lock and unlock a deactivation or a shutdown process. The teleservice module is able to send different commands to the adaptive control devices. They will be redirected to the state machine. If an activate command is received the state machine will execute the algorithm logic by calling its update function. The deactivation command disables updating the algorithm. A reboot command shuts down the controller. Restarting the device allows flashing a new control software. A change request turns the devices' activation. The currently operating algorithm will be disabled while the inactive algorithm will be enabled. Additionally, a kill command forces a reboot of the device.

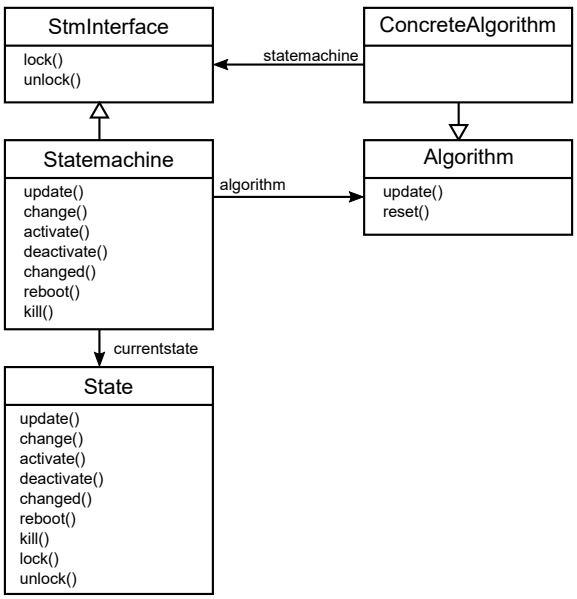

Figure 4: Components

Figure 5 defines the state machine's states and transitions. Depending on the current state, a received command causes

a different change in state. There are eight states available. After booting, the device stays inactive and the algorithm is reseted. An activation command instantly activates the installed algorithm by switching the controllers state to process whereas a change request leads to the intermediate state change requested. This synchronizing state guarantees that the currently operating algorithm turns inactive before another strategy can be performed. The new algorithm stays inactive until the device receives the notification changed from its counterpart. The process state cyclically calls the algorithms update operation. If an automated service is activated that shall not be interrupted, the algorithm can lock the state machine and the current state switches to operate. From there, various intermediate states are available. All also trigger the current algorithm to update its values until they will be unlocked. Depending on the previous command, the state machine then changes over to its desired state.

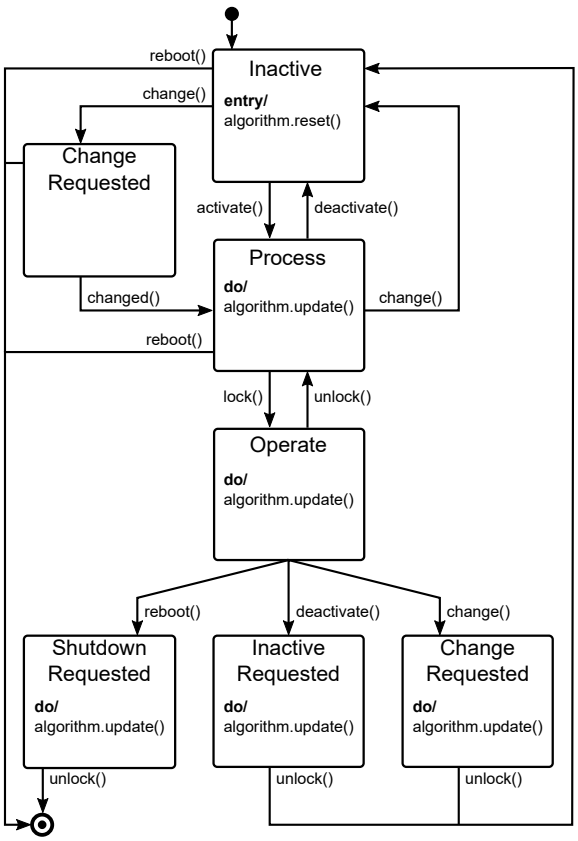

Figure 5: State machine

5.2 Flash Function

The flash function is the key point to change the run-time code on control units. It is implemented on the Teleservice device as an event based algorithm. It gets a new binary code file from the cloud via ftp connection. A separate start command initiates the flash sequence to download a new software version to a machine's control unit. It is shown in Algorithm 1. At the beginning, the routine searches for the current inactive slave module. If an inactive node is detected, the algorithm will reboot and flash it. Otherwise, a failure will be reported to the cloud. After the node successfully changed its software, restarted, and reported back its status, both control nodes receive a command to change their current operating state. From this point, the flash sequence waits for the active control device to deactivate itself. Receiving a new binary file from the cloud, again restarts the process.

Data: file = new binary flash file
Result: algorithm successful
inactive node = get inactive node;
if *inactive node is null* **then**
  start error correction;
  return *false*;
end
reboot (inactive node);
flash (inactive node with file);
while *inactive node is not restarted* **do**
  wait;
end
send change activity command;
while *active node is changed to inactive* **do**
  wait;
end
reboot (second node);
flash (second node with file);
while *second node is not restarted* **do**
  wait;
end
return *true*;

Algorithm 1: Flash Algorithm

The flash memory's write cycles are usually limited. It is useful to reduce the need for flashing a controller. Two additional opportunities are implemented. If a modification only consists of a changed parameter set, the Teleservice device is able to pass a new set from the cloud to a control node without changing the whole software code by the flash loader. Therefore, the JSON-based messages are transformed into CAN-based messages and sent to the specific node. Another possibility exists if more than one algorithm is implemented into the current control software. The abstraction to a general algorithm interface allows an easy exchange of the current logic by redirecting the state machine's algorithm reference to a new designated strategy.

6 Virtual Validation

6.1 Simulator

During the development process, it is necessary to test new functions and services quickly and with little effort. Attempts on a real machine are not always the easiest way to accomplish that. This has various reasons, e.g. a real machine is not always available, ready for use or an experiment would be to expensive. An alternative to experimental validation is virtual validation, in which the real environment is replaced by a virtual mock-up. For this purpose, a simulation tool has

been developed, which allows coupled simulations between machine and process models. The structure of the software tool is shown in fig. 6

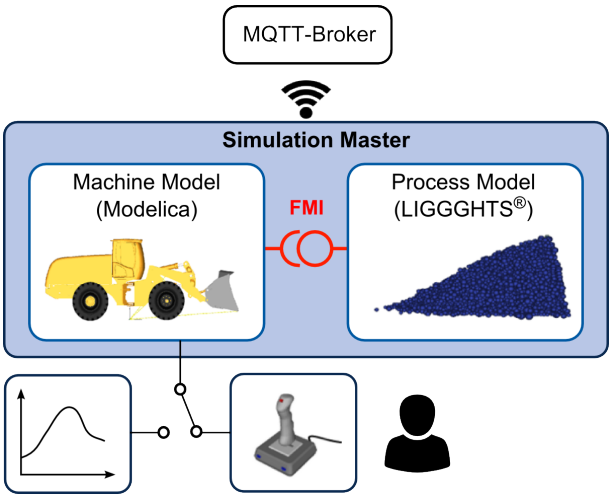

Figure 6: Interactive Machine and Process Simulator

The machine (wheel loader) was created as a comprehensive system model in the description language Modelica [22]. The model exists in different levels of detail, starting with a simple mechanical multibody system up to complex variants representing also hydraulic parts and control systems. The simulation model is exported as an *Functional Mock-up unit (FMU)* [23]. *FMU* is a tool-independent standard for the exchange of system models among both proprietary and non-proprietary software tools.

The process model, which is designed to simulate the behavior of the granular material, is based on the *Discrete Element Method (DEM)* first mentioned by P. A. Cundall [24]. For computation, the open source software *LIGGGHTS®* [25] has been applied. Due to the efficient use of multi-processor architectures, as well as the large number of available contact models, *LIGGGHTS®* is considered to be particularly powerful. In recent years, various methods to link and communicate among *LIGGGHTS®* and Modelica Models [26] or *FMUs* [27] have been developed. In order to correctly link the machine and process model, the *FMU* require defined inputs and outputs. Outputs are position, orientation and speed of the wheel loader's bucket. These values and necessary geometric information are transmitted to *LIGGGHTS®*, whereupon the resulting normal and tangential forces on the bucket are calculated. The outcome is returned to the *FMU* via corresponding input signals.

An extra simulation MQTT-client is responsible for the simulation control. It guarantees the proper data exchange after each calculation step and saves relevant results for post-processing. Additionally, the simulation master interacts with the cloud's MQTT-broker and regularly transmits current state values.

There are two possibilities for controlling the wheel loader during simulation run-time. The first option is the application of predefined trajectories. They can be calculated by algorithms or originate from real measurements and stimulate the machine model. The second option is an interactive user control. Therefore, the *Modelica_DeviceDrivers* library [28] is used. It contains models and functions for reading signals from external control devices such as joysticks or keyboards.

6.2 Smart Metering Application

An Android application running on a separate tablet gives the operator feedback about machine status, current working tasks and performance values. The device is not directly connected to the machine and needs an internet connection to show the cloud services' evaluations. Therefore, the tablet application also inherits the MQTT-Client interface and subscribes to its needed topics. The visual design consists of different modularized views. Incoming messages triggers updating all of them. Figure 7 represents an exemplary view. This consists of five modules. The illustration (1) above left shows the actual bucket's position and reports its height and the loaded mass as a numerical value. In the middle of the upper line, the bar graphs (2) informs about the estimated tire slip. Depending on the current values, the graphs change their color. While operating in a green range means an optimal traction, a yellow to red colored bar expresses a to high tire wear. The list (3) above right tells the operator about its remaining tasks. They are prioritized, named and supplemented with deadlines and objectives. The current progress status is presented as well. On the left side of the lower line, the performance graph (4) compares the efficiency of the last loading cycles. Each value represent the amount of moved material related to a cycle's energy consumption according to eq. (3). Thereby, the working efficiency P_{work} is defined as the weight of loaded material $m_{material}$ devided by the total amount of consumed energy within one working cycle E_{total} (loading a bucket starting at i.e. floating position ending in with a defined bucket height for transportation) respective to the cycle time span t_{cycle}.

$$P_{work} = \frac{m_{material}}{E_{total} \cdot t_{cycle}} \tag{3}$$

The last figure on the lower right illustrates the pile's virtual cross section (5) and its planed optimal bucket trajectory.

7 Summary and Outlook

The presented paper proposes an overall system architecture for cyber-physical systems in the context of construction machinery. The IIoT messaging protocol MQTT is well suited for these kinds of applications. Multiple clients can connect to the cloud and are integrated in the cloud application services. The cloud implementation follows the design of a MAPE-K loop. The central knowledge base stores the data history of the system. The analyse modules perform computations on raw data and the plan modules modify the logic for client. This structure has been implemented in a prototype and has been tested using a driver assistance user-interface. Physical-based simulations emulates the machine's behavior and feed the current cloud application. A monitoring visualization app on a tablet represents a service application inside

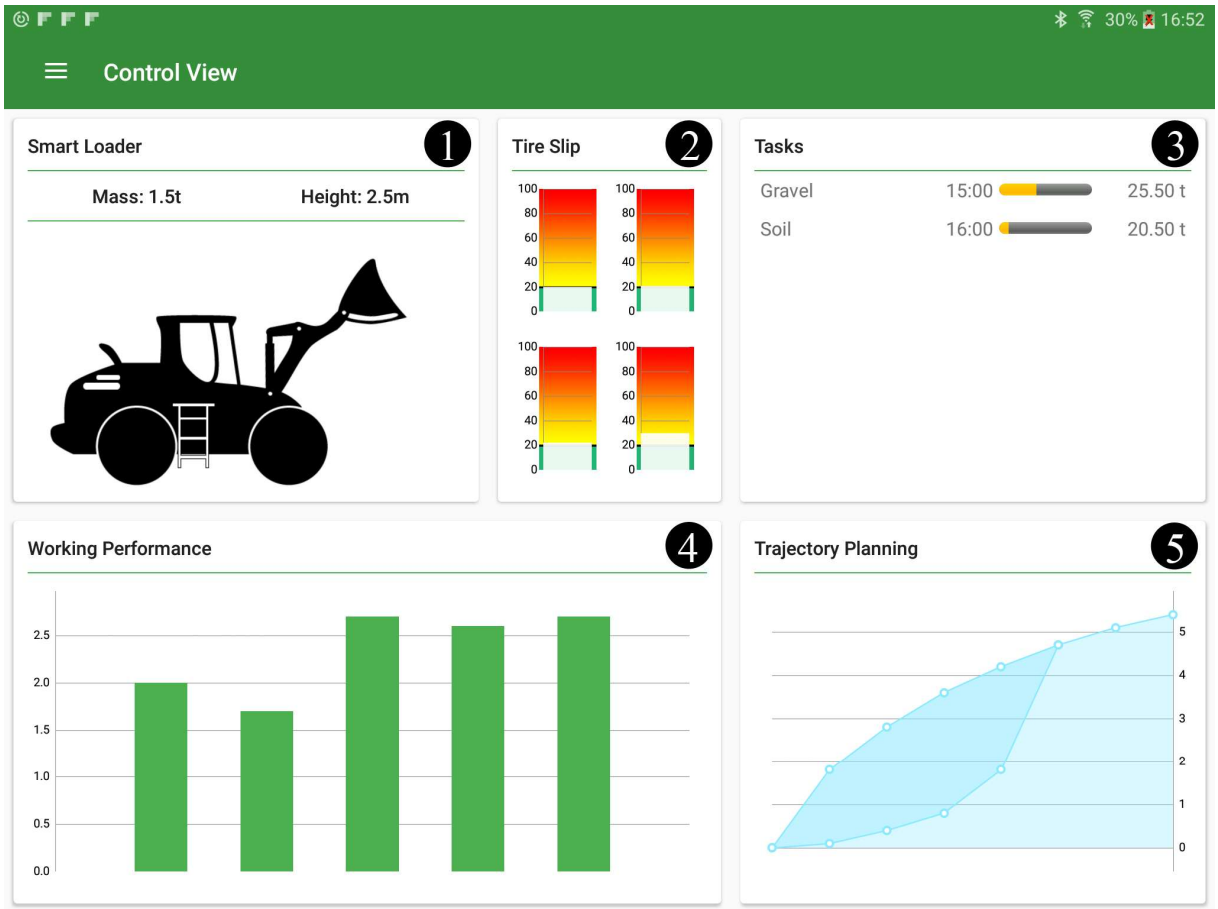

Figure 7: Application Screenshot

the CPS. The implemented cloud architecture enabled an adaptable driver assistance and defines the basis for further developments achieving high level automation functionality in mobile applications. Therefore, additional sensor technologies for environment detection are needed. With the help of the simulation models, bucket filling strategies can be easily tested but they have to be calibrated with real measurements. For further developments, an assisted, partially automated bucket filling process is obvious. In the long term, a highly automated bucket filling procedure is desirable whereas the operation of a fully autonomous wheel loader for a construction purpose seems less conceivable. The currently developed cloud implementation will be extended to an adaptable fog architecture. This means the use off more locally available computational infrastructure to split time-critical algorithms from the machine to near computational elements and not all to the cloud. This decreases latency.

Nomenclature

Designation	Denotation	Unit
λ	tire slip	%
n_{wheel}	wheel's rotational speed	min^{-1}
μ	friction coefficient	-
D_{wheel}	wheel diameter	m
$v_{machine}$	slip-free machine velocity	m/s
W_{tire}	tire wear	%
T_{Life}	life time	h
t_i	time variable	h
P_{work}	working efficiency	kg/(l·s)
$m_{material}$	weight of loaded material	kg
E_{total}	energy consumption	J
t_{cycle}	loading cycle time	s

References

[1] R. Parasuraman, T. B. Sheridan, and C. D. Wickens. A model for types and levels of human interaction with automation. *Trans. Sys. Man Cyber. Part A*, 30(3):286–297, May 2000.

[2] Sae j3016 - taxonomy and definitions for terms related to on-road motor vehicle automated driving systems.

[3] Martin Laube and Steffen Haack. Condition monitoring for hydraulic power units–user-oriented entry in industry 4.0. In *10th International Fluid Power Conference (10. IFK) March 8 - 10, 2016 in Dresden*, volume 2, pages 393–402. Dresdner Verein zur Förderung der Fluidtechnik e.V.

[4] Reno Filla. Evaluating the efficiency of wheel loader bucket designs and bucket filling strategies with non-coupled dem simulations and simple performance indicators. pages 274–292, Dresden.

[5] Reno Filla. A study to compare trajectory generation algorithms for automatic bucket filling in wheel loaders.

[6] S. Dadhich, U. Bodin, and U. Andersson. Key challenges in automation of earth-moving machines. 68:212–222, 2016.

[7] Elisabet Altin and Brian O'Sullivan. Volvo construction equipment reveals prototype autonomous machines, 2016.

[8] Jonatan Björkman. Control of an autonomous wheel loader.

[9] Anders Bergdahl. Autonomous bucket emptying on hauler, 2011.

[10] H. Derhamy, J. Eliasson, J. Delsing, and P. Priller. A survey of commercial frameworks for the internet of things. In *2015 IEEE 20th Conference on Emerging Technologies Factory Automation (ETFA)*, pages 1–8, Sept 2015.

[11] Autonomic Computing et al. An architectural blueprint for autonomic computing. *IBM White Paper*, 31, 2006.

[12] Angel Diaz and Chris Ferris. Ibm's open cloud architecture. *IBM Corp., Armonk, New York*, 2013.

[13] OASIS Standard. Mqtt version 3.1.1, 2014.

[14] Yuriy Brun, Giovanna Di Marzo Serugendo, Cristina Gacek, Holger Giese, Holger Kienle, Marin Litoiu, Hausi Müller, Mauro Pezzè, and Mary Shaw. *Engineering Self-Adaptive Systems through Feedback Loops*, pages 48–70. Springer Berlin Heidelberg, Berlin, Heidelberg, 2009.

[15] Vasileios Karagiannis, Periklis Chatzimisios, Francisco Vazquez-Gallego, and Jesus Alonso-Zarate. A survey on application layer protocols for the internet of things. *Transaction on IoT and Cloud Computing*, 3(1):11–17, 2015.

[16] Roger Light. Eclipse mosquitto, 2010. An Open Source MQTT v3.1/v3.1.1 Broker.

[17] Fredrik Gustafsson. Slip-based tire-road friction estimation. 33(6):1087–1099, 1997.

[18] Heinrich Schneider and Peter Reitz. GPS zur geschwindigkeitsmessung. 51(5):264–265, 1996.

[19] LUXACT - optical sensor for non-contact displacement and speed measurement, 2013.

[20] Correvit s-motion - berührungslose optische sensoren, 2016.

[21] Chris C. Ward and Karl Iagnemma. A dynamic-model-based wheel slip detector for mobile robots on outdoor terrain. 24(4):821–831, 2008.

[22] Modelica® - a unified object-oriented language for systems modeling language specification version 3.3, 2012.

[23] Torsten Blochwitz, Martin Otter, Johan Akesson, Martin Arnold, Christoph Clauss, Hilding Elmqvist, Markus Friedrich, Andreas Junghanns, Jakob Mauss, Dietmar Neumerkel, et al. Functional mockup interface 2.0: The standard for tool independent exchange of simulation models. In *Proceedings of the 9th International MODELICA Conference; September 3-5; 2012; Munich; Germany*, number 076, pages 173–184. Linköping University Electronic Press, 2012.

[24] Peter A Cundall. A computer model for simulating progressive large scale movements in blocky rock systems. In *Proceedings Symposium Int. Soc. Rock Mech (ISRM)*, volume 1, pages 8–11, Nancy Metz, 1971.

[25] Christoph Kloss and Christoph Goniva. Liggghts–open source discrete element simulations of granular materials based on lammps. *Supplemental Proceedings: Materials Fabrication, Properties, Characterization, and Modeling, Volume 2*, pages 781–788, 2011.

[26] Christian Richter. A new approach for integrating discrete element method into component-oriented system simulations. In *ASIM 2016 - 23. Symposium Simulationstechnik 07.-09.09.2016. Zusammenfassung der Beiträge*, pages 91–97, HTW Dresden, 2016.

[27] Günther Kunze, Andre Katterfeld, Christian Richter, Hendrik Otto, and Christian Schubert. Plattform- und softwareunabhängige simulation der erdstoff-maschine interaktion. In *5. Fachtagung Baumaschinentechnik*, Dresden, 2012.

[28] Tobias Bellmann. Interactive simulations and advanced visualization with modelica. In *Proceedings of the 7th International Modelica Conference; Como; Italy; 20-22 September 2009*, number 043, pages 541–550. Linköping University Electronic Press, 2009.

Enhancing safety of independent metering systems for mobile machines by means of fault detection

B. Beck, J. Weber

Chair of fluid-mechatronic systems, Technische Universität Dresden, Dresden, Germany
E-mail: benjamin.beck@tu-dresden.de, fluidtronik@mailbox.tu-dresden.de

Abstract

Systems with independent metering offer a high potential for increasing the functionality and efficiency of valve-controlled hydraulic drives. But nowadays there are only a few prototypical applications. One reason for that are the so far insufficient safety investigations. Besides the structural investigations carried out at the research institute, this contribution deals with a fault detection by means of limit checking of the applied pressure sensors. A detection algorithm is derived from several software-in-the-loop simulations of the independent metering system applied at an excavator arm. The functionality and limits of the fault detection will be shown by means of measurements. As a result, all safety-critical faults can be detected which leads to a Diagnostic Coverage of $DC = 99\%$ and thus allows the use of independent metering up to a Performance Level $PL = e$.

Keywords: hydraulic systems, independent metering, machine safety, ISO 13849, fault detection

1 Introduction

A significant contribution to the improvement of machine and process efficiency of mobile working machines is the use of (semi-)automated functions. Hydraulic drive systems with independent metering offer outstanding prerequisites to fulfill the requirements of (semi-)automated functions. Besides good structural properties and the further degree of freedom to control the system, there are additional potentials by transferring the functionality into the electronic control device and for the software. Thereby, the function's flexibility increases. Furthermore, the use of standardized valves becomes possible leading to reduced component costs. Despite these potentials there are only a few industrial applications with independent metering systems. One main reason is the so far insufficient analysis of safety and reliability aspects.

Previous contributions have shown which kind of system architectures meet the different safety requirements of mobile machines [1]. One suitable valve structure in combination with pressure sensors and a single-variable control approach was applied to the boom function of an excavator test rig at the research institute [2]. This system can reach a maximum Performance Level PL = e if the Diagnostic Coverage is DC = 99%, which depends on the fault detection. Fault detection methods were categorized and evaluated by Isermann [3]. An overview over these fault detection methods with corresponding publications on hydraulic drive systems is displayed in Figure 1. Additional publications for example on electrical drives can be found in [4]. There is a variety of publications on model-based fault detection methods as it can be seen in Figure 1.

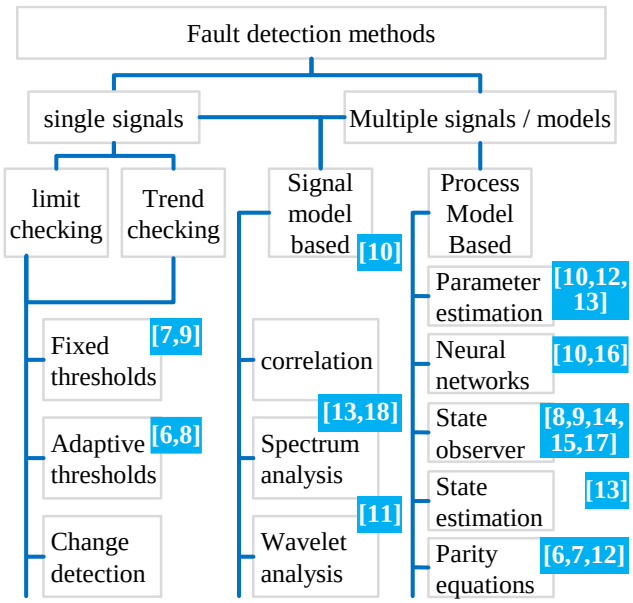

Figure 1: Fault detection methods [3] and related publications

On the one hand this is due to the fast detection and the diagnosis possibility of faults. On the other hand model-based methods require sufficient system models which result in a high implementation and computing effort [5]. These are reasons for simple approaches like limit checking being

widely spread in mobile hydraulic applications. Nevertheless, Nurmi and Mattila used a model-based approach to detect faults in typical mobile hydraulic valves in a crane application. With a reduced-order model, the measurement of the cylinder positions, the chamber pressures, the tank pressure, the pilot pressure and the intermediate pressure between the pressure compensator and the main spool as well as an adaptive threshold generating algorithm sensor biases of 3 bar can be detected [6]. But this contribution on the one hand only makes investigations on component level (focus on the valves). On the other hand a constant pressure system is assumed which is not typical for a mobile hydraulic system.

Concerning safety aspects of independent metering systems, there are only a few publications. Schmitz presents a steer-by-wire system consisting of eight 2/2 valves, two electronic control units (ECU), a redundant supply unit and two sensors to measure the steering wheel and wheel angle respectively. The main focus of this work is the development of a robust closed loop angle control of the wheels in order to compensate certain faults. In case of high control deviations, an off-duty self-test as well as an on-duty model-based fault detection on the basis of parity equations is introduced. Tests show that the fault detection only works sufficient with pressure compensated valves with a very low hysteresis [7]. To avoid the high component effort Fischer presents a superimposed steering system with independent metering. As well as Schmitz, Fischer focuses on fault compensation through an appropriate control concept. This makes the use of limit and trend checking methods for fault detection possible, because the safety shutdown of the electrohydraulic steering part is not time-critical any more [19]. The requirements on the working hydraulics' drive system vary greatly from the steering system's requirements. Besides the well-known load situation, there are mostly no cross-influences between several actuators due to the priority valve in steering systems. Furthermore, energy efficient operation modes have an impact on the system states. Similar to Schmitz and Fischer, Siivonen developed a fault tolerant controller for a digital hydraulic valve system consisting of 20 seat-type screw-in on/off valves. He uses an online fault diagnosis on the basis of measuring electrical quantities for re-configuration [20]. But the problem is the detection of sensor faults. Additionally, Siivonen developed an off-line fault detection algorithm based on pressure sensors [21]. He proved the functionality of both detection methods on a mobile crane test rig using a constant pressure net and a dSpace microcontroller system [22]. But during the off-line test the system cannot be used. To the author`s best knowledge, there are no publications on online fault detection for the working hydraulic of mobile machines using independent metering systems. Rannow introduces a fault tolerant algorithm for the reconfiguration of an existing independent metering valve product. But in his paper he assumes that faults are already detected and diagnosed [23].

In this paper the development of an online fault detection based on limit checking of pressure signals, using software-in-the-loop, is described. Therefore, the system model and validation will be shown firstly. After that, the fault detection algorithm will be derived from system simulation. The parameters of the limit checking are tuned by measurements on an excavator test rig. Finally, these tests as well as a discussion about the accuracy and the limits of the fault detection will be described.

2 Design of fault detection

Basis of the design of the fault detection is a model of the excavator test rig at the research institute. The system layout is displayed in Figure 2. It consists of the subsystems supply unit, input, logic, output, actuator and the work equipment. The supply unit comprises an electric motor, which is operated at a constant speed of $n_1 = 1450\ \mathrm{min}^{-1}$, an electronically controlled variable displacement axial piston pump, a pressure relief valve and oil treatment elements like a filter. The operator generates a command signal through the joystick as part of the subsystem input, which are connected via CAN with the ECU (subsystem logic). The ECU calculates the valve`s control current depending on the operator command. Therefore, the ECU contains the control algorithm for each axis, the operation mode management, the failure insertion for the test of system faults and the fault detection algorithm. The subsystem output represents the valve block with independent metering. The displayed valve system is just one possible solution but provides a high flexibility, so that different control concepts can be investigated. It consists of two 2/2 bidirectional proportional spool valves (no. 5-6) for velocity and pressure control and four 2/2 bidirectional switching poppet valves (no. 1-4) for connecting each cylinder chamber with pump or tank line. A load independent movement is achieved through the individual pressure compensator (IPC – no. 8). To ensure that the inlet flow is always regulated from the IPC, an additional switching valve (no. 7) is installed. The system is described in detail in [2].

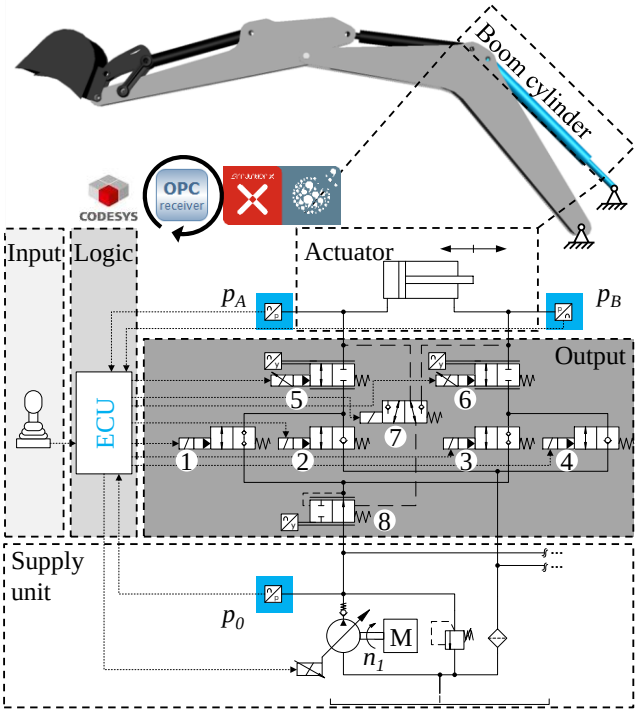

Figure 2: System structure / Test rig setup

At the test rig, pressure sensors in the pump line and each cylinder chamber, displacements sensors on the proportional valves and the pressure compensator as well as angle sensors for the boom, stick and bucket from which the position of the concerning cylinders are derived are installed. But for the proposed fault detection only the pressure sensors are used. Due to the fact that load on each cylinder depends on the equipment's mass distribution, a multi body-system with CAD-data has been built up. The valves have been measured separately on a valve test rig. The static characteristic diagram of the proportional valves and their dynamics are implemented in the model. The pump is modeled as a volume flow rate with its efficiency and dynamic. The model parameters especially the volumes are gained from the excavator test rig. The supply unit, the valves, the actuator, the work equipment and the input are modelled by using the system simulation software *SimulationX*. The control algorithm and fault treatment is directly programmed in the development environment *CODESYS*. This has two main advantages: Firstly, the restrictions from the hardware (discrete cycle time of 10 ms) should have taken into account by developing the algorithms. Secondly, a premature software implementation reduces commissioning costs. An *OPC* Server is used for the communication between the tools *CODESYS* and *SimulationX*. Since a fully extended equipment without loaded mass delivers high frequent pressure signals, the fault detection will be developed using the boom cylinder as a worst case scenario in this paper. Because of the kinematics of the work equipment the rod side of the boom cylinder is always on the high pressure side. This results in a retraction with a resistive load and an extension with an overrunning load during the lifting and lowering cycle.

2.1 Model Validation

The main goal of a fault detection is the feature generation. Therefore, it is necessary to know about the system's usual behavior. For that the built-up system model must be validated. Figure 3 displays the comparison of the software-in-the-loop simulation and measurements on the test rig of the lifting / lowering cycle using the boom cylinder.

The lift movement proceeds from 0 – 10 s and the lowering movement from 10 – 20 s. In the upper diagram the target and actual nominal velocity of the boom cylinder and in the diagrams at the bottom the corresponding pressure values are displayed. The simulation results, displayed in dashed lines, fit well to the measurements, displayed in solid lines. Deviations in the velocity signal are due to neglected leakage in the valve model. The higher velocity in the simulation leads to a movement of the boom cylinder into the end stop by using the same target velocity (operator command). This is why the pressure p_0 rises up to 250 bar at approx. 9 s. Due to the internal leakage of the cylinder, the pressure difference between the cylinder chambers equals slowly from 9 -16 s. During this time the set velocity is zero. At approx. 16 s the lowering movement starts. To that, the valve 6 has to control the volume flow, so that the overrunning load can be controlled and therefore the cylinder pressure p_A does not drop to zero (anti cavitation). During the movement phase from 16 – 20 s the simulation results fit well to the measurement. Overall, the system model represents the normal behavior very well and is therefore suitable for the development of fault detection.

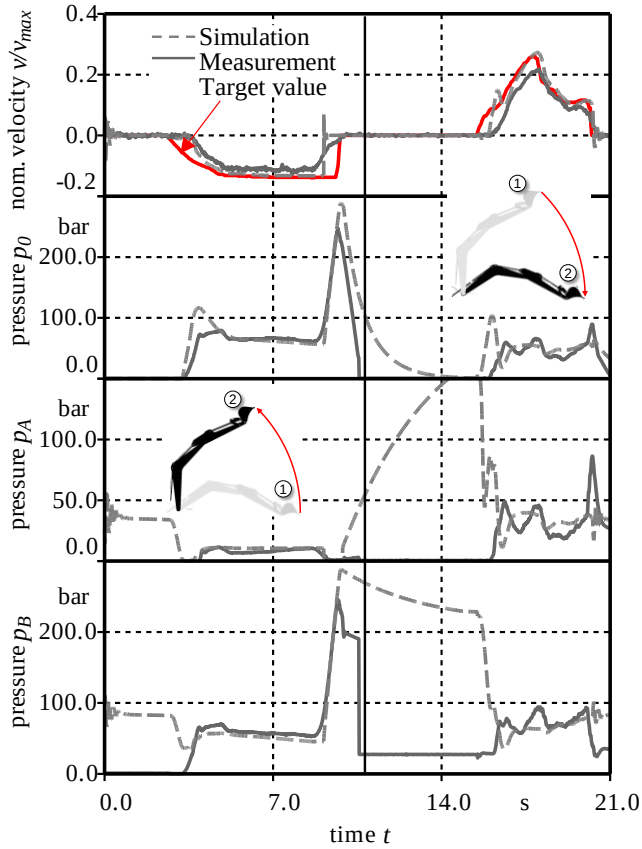

Figure 3: Model validation on lifting / lowering cycle

2.2 Analysis of fault behavior

To analyze the fault behavior, faults must be impressed upon the model. The fault insertion can be divided into four different levels:

1. Machine condition
2. Fault location
3. Type of fault
4. Moment of the fault occurrence

The machine condition is given through the considered cycle. Regarding the fault location, faults will be impressed upon the three pressure sensors and the valves 1 – 7. Faults of the IPC are not investigated because the compensator is (hydraulically-) mechanically controlled and thus basic and proven safety principles can be applied. The standard ISO 13849-2 defines fault types for mechanical, electrical, electronical, pneumatic and hydraulic elements [24]. The relevant faults for the insertion upon the model are summarized in Table 1.

Table 1: fault types regarding to ISO 13849-2

Valves	1	Change in switching times
	2	Failing to switch (stay fully closed or fully open or in every single position between)
	3	Change of neutral position without command
	4	Leakage
	5	Change of leakage volume flow during operation time
	6	Burst of housing and fasteners
	7	Hydraulic faults which cause uncontrollable behavior
sensors	1	Changes in the data acquisition and the output

Concerning a deep fault diagnosis a good description of the fault is necessary to identify the cause of the failure. But for the detection it is sufficient to know that there is a fault. Therefore, a fault needs to have an impact on the system behavior. The bigger the impact, the more critical the system behavior will be. Another question is how to insert these fault types into the model and the test rig. Because of the use of electronic controlled components it is obvious to use synthesized signals to manipulate the set values. To cover the fault types from ISO 13849 except valve fault six the signals in Figure 4 are used. The burst of the valve housing can be covered through the basic and proven safety principles like oversizing.

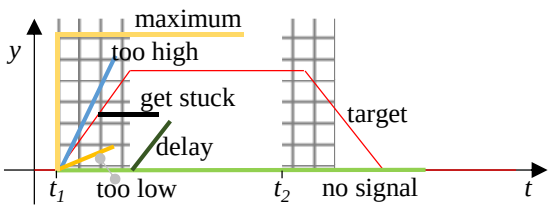

Figure 4: Synthesized signals to insert fault types

From the system's view a maximum signal equals a signal which is too high but with a bigger impact. In the same way no signal equals a signal which is too low and a signal delay with regard to a certain time. In the context of detecting safety critical states and to limit the variant only the signals "maximum", "delay" and "no signal" will be investigated in this paper. Finally, the time of the fault insertion can be varied as it is displayed in Figure 4. Therefore, it has to be mentioned that there are fault combinations which are not appropriate, e.g. the fault type "get stuck" when the set signal is constant or the fault "no signal" on a valve which already gets no signal due to the control algorithm. On the basis of this investigations a failure insertion unit with a related visualization as user interface has been programmed in *CODESYS*. The SIL simulation has been used to analyze the fault variations displayed in Table 2. Here only valve faults are shown. The simulation results with inserted sensor faults has shown that the impact on the cylinder movement is the same as inserting valve faults. This is due to the control algorithm, which reacts on the pressure signals to set the valve currents.

The simulation results show that there are six safety critical faults, which are highlighted in Table 2. A fault is safety critical within the context of the excavator application if:

- The boom will move faster than commanded from the operator or,
- The boom will move in the opposite direction than commanded from the operator or,
- The cylinder pressure will rise higher than the set value of the pressure relief valve.

The last case occurs when the boom cylinder extends and the downstream valves are closed. Due to the differential cylinder the chamber pressure p_B will be precisely higher by the amount of the area ratio of the differential cylinder (see section 3.1). The other fault variations lead to no movement or cavitation while the target movement is reached. Due to the defined safety function "safe stop", these faults do not need to be detected. But in the context of availability the identification of these faults enables countermeasures like a quick repair or reconfiguration. But in the following the safety critical faults will be described and a fault detection algorithm derived.

Table 2: fault variations for SIL simulation

	no.	location	type	time
Lifting movement	1	Valve 1	Maximum	t_2
	2	Valve 2	No signal	t_1
	3	Valve 2	Maximum	t_2
	4	Valve 3	No signal	t_1
	5	Valve 3	Maximum	t_2
	6	Valve 4	Maximum	t_2
	7	Valve 5	No signal	t_1
	8	Valve 5	Maximum	t_2
	9	Valve 5	Get stuck	t_2
	10	Valve 6	No signal	t_1
	11	Valve 6	Maximum	t_2
	12	Valve 6	Get stuck	t_2
	13	Valve 7	No signal	t_1
Lowering movement	14	Valve 1	Maximum	t_2
	15	Valve 1	No signal	t_1
	16	Valve 2	Maximum	t_2
	17	Valve 3	Maximum	t_2
	18	Valve 4	No signal	t_1
	19	Valve 4	Maximum	t_2
	20	Valve 5	No signal	t_1
	21	Valve 5	Maximum	t_2
	22	Valve 5	Get stuck	t_2
	23	Valve 6	No signal	t_1
	24	Valve 6	Maximum	t_2
	25	Valve 6	Get stuck	t_2
	26	Valve 7	No signal	t_1

In the following fault no. 1 and 24 will be investigated exemplary. Therefore, both simulation and measurements were taken out. The measurements complement the

simulation and serve to analyze the behavior of the operator. The simulation and measurement results of fault no. 1 are displayed in Figure 5. During the cycle, the work equipment lifts due to a retracting boom cylinder which drives against the load. In the fault-free state from 0 – 4.8 s the pump volume flow is directed into the rod side (chamber B) of the boom cylinder through the open switching valve 3 and the correspondingly open proportional valve 6. This leads to a pressure built-up in cylinder chamber B at approx. 2.5 s. At the same time, the valves 5 and 2 are open which allow a volume flow from cylinder chamber A to the tank. As a result, the cylinder begins to move as it can be seen in the solid grey line in the velocity diagram of Figure 5. During the movement, the simulation results (dashed lines) fit again well to the measurements. Since there is no ground contact in the model, the initial values of the pressure p_A and p_B are higher than in the measurement.

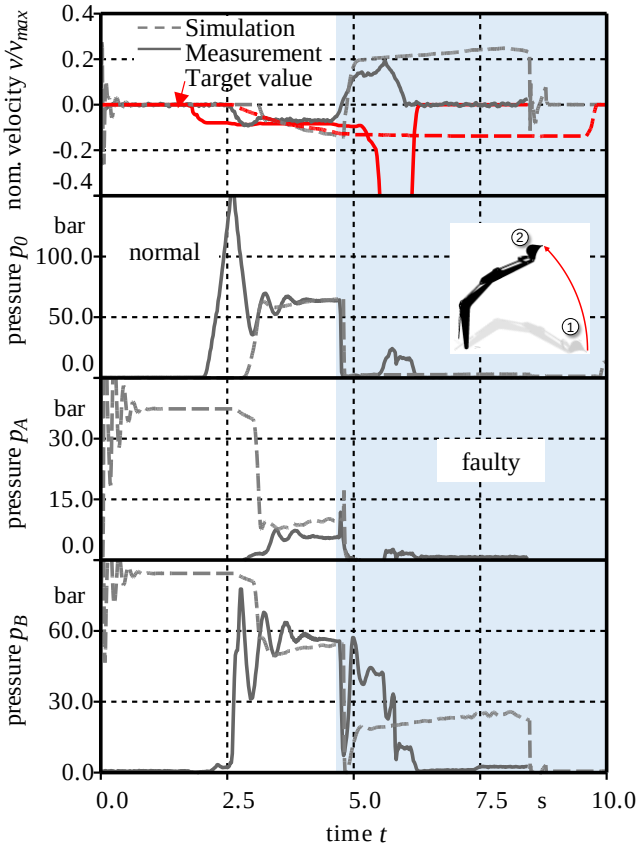

Figure 5: Results of fault no. 1

If the switching valve 1 unintentionally opens in the event of a fault at approx. 4.8 s, the pump is connected to the tank via the normally open switching valve 2. The pump pressure falls to a pressure level of approx. 10 bar at 5 s, determined by the pressure losses across the IPC and the switching valves. Likewise, the rod side of the boom cylinder, which is under pressure, is connected to the tank via the valves 1, 2 and 3. Thus p_B falls and the load force can no longer be overcome by the cylinder force. The boom sinks downwards due to its weight, which can be seen in the solid grey line of the nominal velocity v/v_{max}. Since the velocity of the piston and thus also the direction of the volume flow through valve 6 is reversed, p_B initially drops to 0 bar, and then rises again to the value of the pressure loss over valve 6. Since the piston speed slows down before the movement direction reverses, the volume flow conveyed via valve 5 also drops. By the same opening cross section of valve 5, the pressure drop decreases and thus also p_A. Since only p_T prevails before valve 5, not enough oil flows into the piston chamber as would be required by the cylinder velocity v. As a result, p_A falls further and remains at 0 bar. While the target velocity in the simulation (displayed in dashed red lines) remains constant due to a not modelled operator the reaction of a real operator can be seen in the solid red line. The measurements were performed in pairs. One controlled the fault insertion and the other one moved the joysticks. The operator reinforces the faulty lowering movement intuitively which can be seen in the velocity diagram of Figure 5 between 5 – 6 s.

Looking on the fault-free case of the lowering movement between 0 – 5.5 s in Figure 6, the rod side is connected to the tank by the correspondingly open valve 6 and the open valve 4. The piston side is connected to the pump by the correspondingly open valve 5 and the open valve 1. When sinking, a pulling load is applied to the piston (load force and velocity vector point to the same direction). The control edge on the load side *B* has the task of braking the piston. The ECU calculates the opening cross-section, so that a feed pressure p_A of approx. 10 bar is maintained on the piston side.

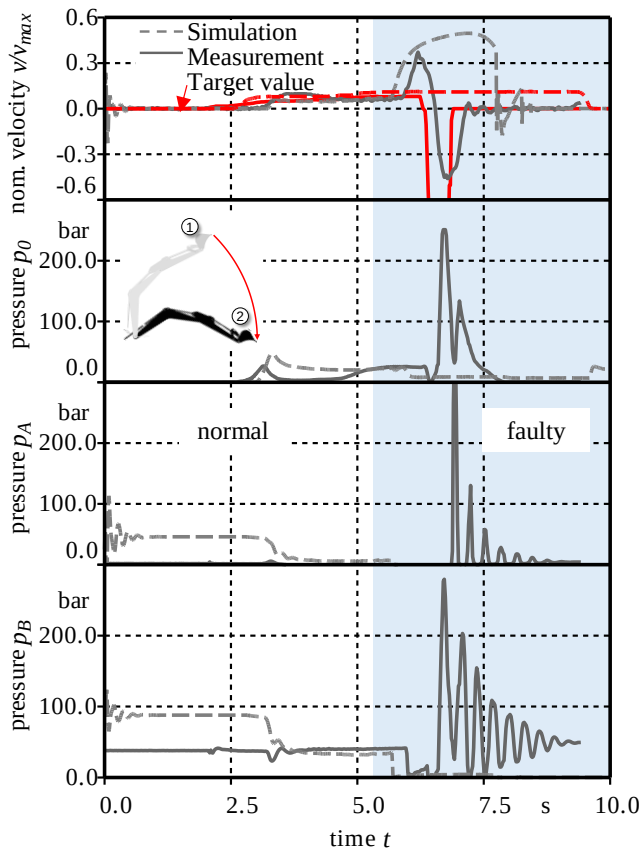

Figure 6: Results of fault no. 24

Fault no. 24 is displayed in Figure 6 from 5.5 s to the end of the movement. In this case, the proportional valve 6 on the load side opens to the maximum. This valve error has an immediate effect on the boom axis since there is a deviation between the required and actual opening cross-section immediately. The piston speed v rises significantly. This results in a pressure drop p_B and due to the equilibrium of forces at the cylinder also in p_A. Since the boom falls much faster, it moves into the end position of the cylinder with a given joystick presetting before the switching valves close in the simulation. Therefore, there is no pressure peak in p_B. The measurements show a slightly different situation. As it can be seen in the target velocity (solid red line) the operator is overwhelmed with the situation. A quick and strong displacement of the joystick in the opposite direction indicates that the operator firstly wants to compensate the fault. Due to that command p_0 increases to the maximum bounded by the pressure relief valve at approx. 6.6 s. Shortly after that he releases the joystick. The target velocity is at zero and all the valves are closed at approx. 7 s. The high velocity of the boom cylinder is braked by the closed valves. This leads to the stop of the cylinder and to high frequency oscillations in the pressure signals p_A and p_B. As mentioned above, this leads also to the risk of bursting hoses. A countermeasure is a secondary pressure limitation function (see section 3.1).

2.3 Description of fault detection algorithm

As described above, all fault variants displayed in Table 2 were simulated. Concerning the lifting movement, the comparison of the pressure signals in every simulation run leads to the following equation for the fault detection:

$$p_B > p_0 \text{ when } v_{set} < 0 \quad (1)$$

$$p_A < p_T \text{ when } v_{set} < 0 \quad (2)$$

Relation 2 has the disadvantage that it is likely also true in the error-free case. A fault detection based on this equation would then provide false alarms. Valve 5 acts as an outlet throttle during lifting and generates power loss due to the pressure drop. To save energy, valve 5 can be fully opened due to the independent metering system. This minimizes the pressure drop across valve 5 and thus also the pressure losses. The pressure p_A is consequently also minimal and calculated as the sum of tank pressure p_T, the pressure losses of the fully open proportional valve 5 Δp_{v5} and the open switching valve 2 Δp_{v2}.

$$p_A = p_T + \Delta p_{v2} + \Delta p_{v5} \quad (3)$$

Then, p_A will be only slightly above p_T especially at slow movements, and fall below p_T when the boom oscillates. Due to the application of more energy efficient operation modes, relation 1 should be preferred. Either way, relation 2 also occurs in the error-free case at the beginning of the movement between 2 s and 2.5 s (see measurements in Figure 5). Due to the applied flow matching control algorithm the pump pressure p_0 is zero at the beginning of the movement, and thus lower than p_B. As a result, the boom would lower and p_A falls to 0 bar.

Concerning the lowering movement, the comparison of the pressure signals in every simulation run lead to relation 4 for the fault detection:

$$p_A < p_T \text{ when } v_{set} > 0 \quad (4)$$

Equation 4 can also be true in the error-free case. This occurs in particular when the valves are being opened at the start of the movement and the necessary pump pressure has not been established yet, similar to the lifting movement. One countermeasure for this problem is a delay between the control of the pump and the valves (virtual load holding valve). By opening the proportional valves at a later time, the pump has an appropriate amount of time to increase the swash plate angle and thus build up a pressure p_0 upstream of the valves. A time constant is however not effective, because the pressure build – up is dependent on the required volume flow, and also the valve dynamics depend on the target value. An alternative solution is discussed in the next chapter. At the very least, error detection should be designed in such a way that short – term minima of p_A are tolerated. For that a fault must remain for a certain amount of time until the fault reaction (close every valve) is initiated. Because from the dynamical pressure signal view, lifting and lowering are different, the following relations are used to check the faulty time:

$$t_{fault} \geq \Delta t_{max,lift} \quad (5)$$

$$t_{fault} \geq \Delta t_{max,lowering} \quad (6)$$

Regardless of the type of fault detection, a well – tuned system with a robust control concept allows a simpler and safer parameter finding. As it is displayed exemplarily in the p_A-signal in Figure 6 between 3.5 s and 5.5 s a good pressure control wouldn't cause false alarms. Aspects of the control algorithm are discussed in detail in [2]. Another aspect is the pressure built – up problem which will be discussed below.

2.4 Special event handling

Particularly in the case of low volumetric flow requirements, the disadvantages of the use of a time constant for the query of the pressure build – up become clear. If sufficient pressure has not yet been built up in the pump line and the valves are actuated, the boom first drops. During lowering, the proposed error detection in equation 4 would report false alarms for the period shortly after the pressure build-up phase. In order to solve these problems, the pressure build – up phase has to be determined by pressure signals. The pressure build – up phase (*p_up*) is terminated for lifting when $p_0 = p_B$. Thus, the pumping pressure can support the load force in any case and sagging is prevented. In the case of lowering, the pressure build – up phase (*p_up*) is not to be terminated until the pump has built up a pressure of p_A = 10 bar in the piston chamber. As a result, the pump has already been increased its swash plate angle and can deliver the full required volume flow from the time in the valve 6. As a result, a sufficient volume flow can be fed into the piston chamber from the beginning, and p_A does not drop. During the pressure build – up phase, the currents of the load – side valves are zero, whereby single valve errors are also intercepted during this phase due to the

series circuit. The effect of the pressure build-up phase can be seen exemplarily in Figure 5. There is a time – delay between the target (red line) and the actual (grey line) velocity at between 2 s and 2.5 s.

To summarize the aforementioned arguments, the proposed fault detection with limit checking is based on the equations and parameters, which are derived from several SIL simulations.

Table 3: Fault detection equations and parameters

Lifting movement: $v_{set} < 0$	
Equation	$p_B - p_1 > p_{tol,1} \cap p_up = False$
$p_{tol,1}$ [bar]	3
$\Delta t_{max,lift}$ [ms]	200
Lowering movement: $v_{set} > 0$	
Equation	$p_A < p_{tol,2} \cap p_up = False$
$p_{tol,2}$ [bar]	3
$\Delta t_{max,lowering}$ [ms]	200

3 Implementation and test of fault detection

The presented fault detection algorithm has been integrated into the control software and has first been tested by means of SIL simulations on the model. Here again the advantage of the SIL simulation has been demonstrated. By means of early detection of programming errors, a quick commissioning on the test stand was possible. The tests for the secondary pressure limiting function and the safety function "safe stop" at the excavator arm test stand are presented below.

3.1 Test of the electronic secondary pressure relief function

As described in section 2.2 there are high cylinder chamber pressure in some cases, which can lead to bursting hoses. Usually, separate valves are used in mobile machines for this function. Since systems with independent metering require a higher number of components on the one hand and lead to flexible flow paths and thus a high degree of functional diversity on the other hand, it is presented here how an electronic secondary pressure limitation can be implemented. To avoid influences of this function on the movement of the cylinder, the valves on the load side must not be changed in their control. This means that a pressure reduction is only possible via the opposite side of the load. This control has two stages. If the pressure of a cylinder chamber exceeds the first threshold value, the switching valve which controls the incoming volume flow (valve 1 or 3) is first closed. Thus, the pressure which in the unfavorable case is reinforced by the cylinder, cannot increase further. If the pressure of a cylinder chamber exceeds the second threshold value, the tank valve (valve 2 or 4) on the opposite chamber side of the load is being opened. The hydraulic clamping of the cylinder is thereby canceled and both of the cylinder chamber pressures can be reduced down to the static pressure resulting from the applied load force. The functionality of this algorithm is displayed in Figure 7 exemplarily for the case of fault no. 23 (closed downstream valve, here valve 6). The normalized target and actual cylinder speed is shown in the upper part of the diagram. Below, the pressure signals and the normalized control currents of the switching valves of the opposite side of the load are shown. For an improved representation of the results, the time interval in which the pressure stages are exceeded is selected. The values of the pressure stages, which are selected exemplarily, are p_{Stage_I} = 180 bar and p_{Stage_II} = 240 bar.

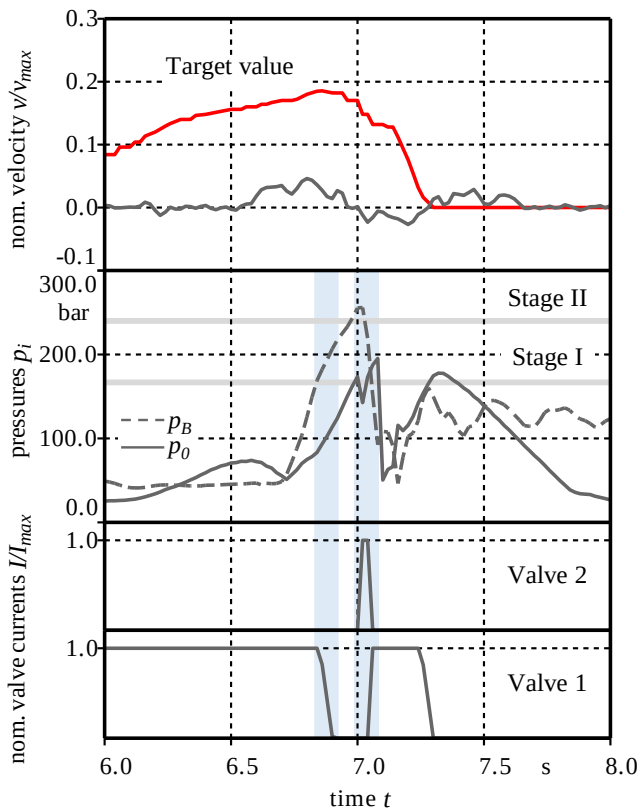

Figure 7: Experimental test of secondary pressure limitation at occurrence of fault no. 23

It can be seen how valve 1 closes when the first pressure stage is exceeded and valve 2 opens when the second pressure stage is exceeded. The functionality of the secondary pressure limitation function has thus been demonstrated. This complies with the requirements of ISO 4413. However, it should be checked which additional requirements apply by the use of electronic pressure relief valves. But overall this shows which functions can be integrated into independent metering systems.

3.2 Test of the safe stop function

Finally, the functionality of the developed fault detection is demonstrated, both in the normal operation and in the event of a fault. In Figure 8, the lifting and lowering cycle is depicted as in the case of the model validation. The equipment is lifted by the retracting boom cylinder between 0 s and 10 s. The pressure built – up phase can be seen in the time delay between the target and actual velocity again. In that time (between 4 s and 5 s) the fault variable t_{fault} rises up to a value of 90 ms. This is because the switching valve 2 of the load opposite side is already controlled. Thereby the pressure p_A drops under 3 bar. However, to detect valve faults during this phase, for example a faulty open tank valve 2 or 4 which would prevent the pressure built – up, a smaller increase of the fault variable t_{fault} is used. On the one hand this ensures the required pressure built – up and allows the fault detection on the other hand. Subsequently, the lowering movement takes place by the extension of the boom cylinder. At approx. 13.8 s the fault no. 24 (fully open valve 6) is inserted. The error begins to affect the movement at approx. 14 s. A detailed view of this phase is displayed in Figure 9.

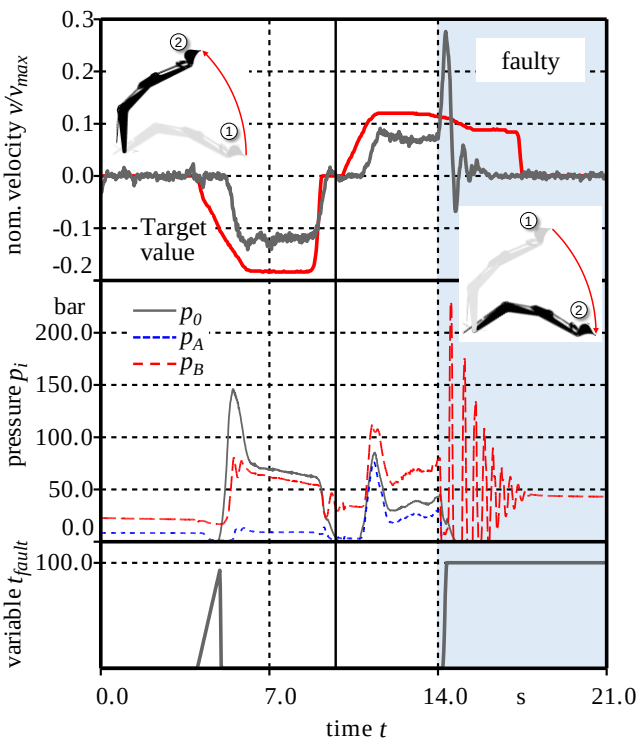

Figure 8: Experimental test of safe stop function by occurrence of fault no. 24

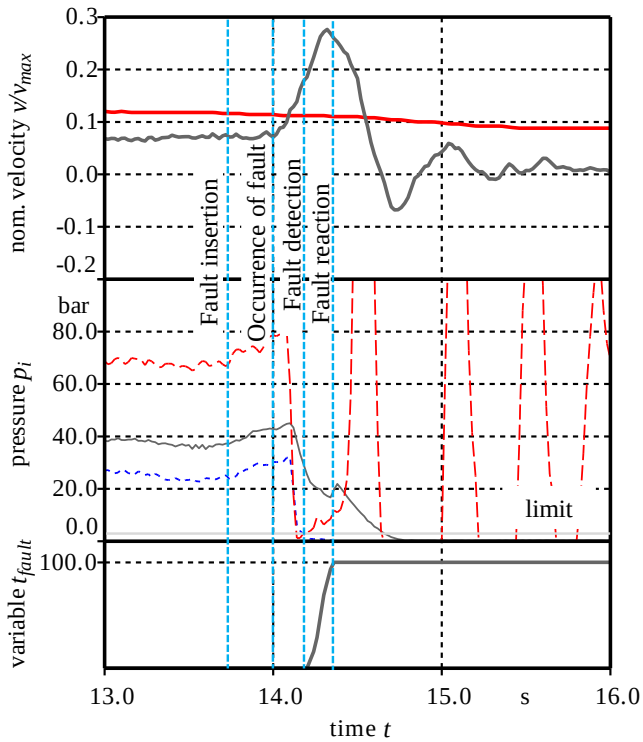

Figure 9: Enlarged section of Figure 8

The effect of the fault can be seen in the increasing cylinder velocity v. As a result of that p_A drops under the specified limit of 3 bar at approx. 14.2 s. This leads to the rise of the fault variable t_{fault} up to the specified limit of 100 ms. Therefore, all valve currents are set to zero at 14.3 s. The falling boom is hydraulically stopped by the closing switching valve 4 at 14.36 s. Because of the high velocity difference, the pressure peaks in p_B and thus also in p_A are significantly high (need for secondary pressure limitation; see section 3.1). An enlarged section of the error phase is shown in Figure 10.

3.3 Discussion of limits and accuracy

Fault no. 24 is the most safety critical fault due to the high boom cylinder velocity. Thus, the accuracy and limits of the proposed fault detection will be discussed using fault no.24. Figure 10 shows the trajectory of the excavator arm. The red dots highlight the movement during the occurrence of the fault. In the time between fault formation and fault reaction, the excavator arm lowers by approx. 593 mm. This drop height can be quantified with the difference of the Tool-Center-Point height Δy_{TCP} and is made up of the following parts.

$$\Delta y_{TCP} = \Delta y_{detect} + \Delta y_{remain} + \Delta y_{react} \qquad (7)$$

The first part is the fall height Δy_{detect} of the equipment, which arises in the time of the fault occurrence to fault detection and, therefore, the limit p_{tol} is exceeded.

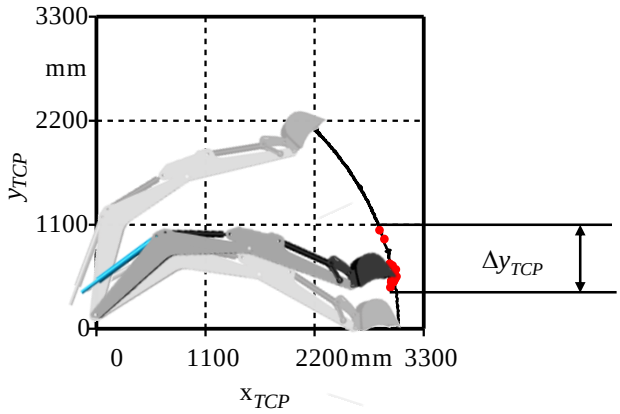

Figure 10: Trajectory of the excavator arm in case of fault no. 24

The required detection time depends on the following influencing factors:

- The current load situation,
- The current cylinder velocity,
- The pressure reduction time which depends on the dead volumes in the tubing and
- The specified limit p_{tol}.

Because the first two aspects are given through the operator command only the last two can be influenced in construction. The second part is the fall height Δy_{remain} of the equipment, which is given during the time of the selected limit Δt_{max} of the fault variable t_{fault}. If the system immediately reported an error according to the detection algorithm, this component of the fall height could be reduced to zero. To ensure that this fraction of the drop height is kept small and the fault detection is still robust against false alarms, Δt_{max} should be as small as possible. The value was successively reduced from 200 ms over 150 ms to 100 ms on the test bench. As a result, the overall fall height could be reduced by 244 mm. Here, there is little optimization potential for reasons of machine availability.

The last part of equation 7 represents the fall height Δy_{react} which is returned in the time of the fault reaction. The fault reaction measures related to the safety function "safe stop" are the simultaneous closing of all valves and the reduction of the swash plate angle of the pump. Influence factors of Δy_{react} are:

- The dynamic behavior of the applied components in combination with
- The control concept and thereby the cycle time of the ECU and again
- The operation point of the drive (load and velocity).

Again, the last aspect cannot be influenced because the operation point is given through the work task and the operator, respectively. But with fast components and an adequate control algorithm this time and the fall height respectively can be reduced. The measurements with the aforementioned variations of Δt_{max} showed that the overall fall height Δy_{TCP} is significantly influenced by the reaction time of the system (Δy_{react} / Δy_{TCP} = 66 %). 32 % of that value are attributable to the valve dynamics. The rest of Δy_{react} (68 %) arises from the boom cylinder oscillations before the static value of Δy_{TCP} is reached. Only 25 % of Δy_{TCP} are related to the selected maximum time limit Δt_{max} when the fault is detected and another 9 % arise from the detection itself ($p_A < p_{tol,2}$). As a result, a large part of the fault detection's optimization potential lies in the system parameters (volumes between valve and cylinder) and the dynamic of the components.

Finally, Table 4 gives an overview of the determined fall heights of the safety critical tests carried out.

Table 4: sensitivity of detection parameters

Fault no.	Description	Δt_{max} [ms]	Δy_{TCP} [mm]
1	Valve 1 maximum signal	200	144
6	Valve 2 maximum signal	200	132
24	Valve 6 maximum signal	200	837
24	Valve 6 maximum signal	150	751
24	Valve 6 maximum signal	100	593
25	Valve 6 get stuck	100	465

4 Conclusion and outlook

With the help of the validated simulation model, calculations with a targeted imprinting of previously defined errors could be carried out. The result of these simulations is on the one hand the knowledge about the safety-critical conditions in the system. On the other hand, information on deviations from error cases to normal behavior is provided. By analyzing the simulation results, it was possible to derive clear error patterns. These form the basis for the developed fault detection by means of pressure sensors. The use of the same pressure sensors for function and error detection does not incur any additional costs, which makes this solution particularly attractive.

Final tests at the test stand excavator arm show the functionality of the fault detection and the safety function. Unintentional false alarms are not reported during the movement in the normal mode of the independent metering system and all safety critical faults can be detected. Thus a Diagnostic Coverage of DC = 99 % can be assumed. This allows the use of this drive structure up to a performance level of PL = e. But unfortunately, the fall height during the detection and reaction is very high. Future work should address this problem. Nevertheless, the results provide a good basis for the further development of fault detection by means of pressure sensors and show the limits of simple detection methods like limit checking for mobile hydraulic systems. However, the dynamics of fault detection and the consideration of extended operating modes of the

independent metering system, dynamic load changes as well as parallel driven consumers still offer considerable development potential. An expansion of fault detection for fault locating would also significantly improve the availability of systems with independent metering.

5 Acknowledgements

The presented research activities are part of the project "Safety concepts for mobile hydraulic systems using independent metering "(Sicherheitskonzepte für mobilhydraulische Antriebsstrukturen mit getrennten Steuerkanten - Ref. No. 702910). The authors would like to thank the Fluid Power Research Fund of the VDMA for the funding and support.

Nomenclature

Designation	Denotation	Unit
DC	Diagnostic Coverage	-
n_1	Rotational speed of motor	min^{-1}
p_A	Cylinder chamber pressure A	bar
p_B	Cylinder chamber pressure B	bar
p_0	Pump pressure	bar
p_T	Tank pressure	bar
$p_{tol,i}$	Tolerated pressure limit	bar
$p_{Stage,i}$	Secondary Pressure limitation stage i	bar
p_up	Internal pressure built-up var.	-
Δp_{vi}	Pressure drop over valve i	bar
PL	Performance Level	-
t_{fault}	Fault variable	ms
$\Delta t_{max,i}$	Time limit i	ms
v	Cylinder velocity	mm/s
v_{max}	Maximum cylinder velocity	mm/s
v_{set}	Target cylinder velocity	mm/s
y_{TCP}	Height of tool center point	mm
Δy_{TCP}	Height difference of TCP	mm
Δy_{detect}	Height difference of TCP during fault detection	mm
Δy_{remain}	Height difference of TCP during $\Delta t_{max,i}$	mm
Δy_{react}	Height difference of TCP during fault reaction	mm

References

[1] B. Beck and J. Weber. Safety and Reliability of Independent Metering Systems in Mobile Machinery. Risk, Reliability and Safety: Innovating Theory and Practice: Proceedings of ESREL 2016, Tylor & Francis Group, London, 2017.

[2] J. Lübbert, A. Sitte, and J. Weber. Pressure compensator control – a novel independent metering architecture. 10th International Fluid Power Conference (10. IFK) March 8 - 10, 2016 in Dresden, Dresden, 2016, vol. 1, pp. 231–246.

[3] R. Isermann. Fault-Diagnosis Applications. Berlin, Heidelberg: Springer Berlin Heidelberg, 2011.

[4] M. Münchhof, M. Beck, and R. Isermann, "Fault-tolerant actuators and drives—Structures, fault detection principles and applications. Annual Reviews in Control, vol. 33, no. 2, pp. 136–148, 2009.

[5] J. Richalet. Industrial applications of model based predictive control. Automatica, vol. 29, no. 5, pp. 1251–1274, 1993.

[6] J. Nurmi and J. Mattila. Detection and Isolation of Faults in Mobile Hydraulic Valves Based on a Reduced-Order Model and Adaptive Thresholds. Proceedings of ASME/BATH 2013 Symposium on Fluid Power and Motion Control, Sarasota, 2013.

[7] D. Schmitz. Entwurf eines fehlertoleranten Lenkventils für Steer-by-Wire Anwendungen bei Traktoren. Karlsruher Institut für Technologie (KIT), Karlsruhe, 2014.

[8] Z. Shi, F. Gu, B. Lennox, and A. D. Ball. The development of an adaptive threshold for model-based fault detection of a nonlinear electro-hydraulic system. Control Engineering Practice, vol. 13, no. 11, pp. 1357–1367, 2005.

[9] H. Khan, S. C. Abou, and N. Sepehri. Nonlinear observer-based fault detection technique for electro-hydraulic servo-positioning systems. Mechatronics, vol. 15, no. 9, pp. 1037–1059, 2005.

[10] T. Ramdén. Condition monitoring and fault diagnosis of fluid power systems: approaches with neural networks and parameter identification. Linköping: Dep. of Mechanical Engineering, Linköping Univ, 1998.

[11] Y. Gao, Q. Zhang, and X. Kong. Wavelet-based pressure analysis for hydraulic pump health diagnosis. Transactions of the ASAE, vol. 46, no. 4, pp. 969–976, 2003.

[12] M. Münchhof. Fehlerdiagnose für hydraulische Servo-Achsen (Fault Diagnosis for Hydraulic Servo Axes). at – Automatisierungstechnik, vol. 55, no. 2, 2007.

[13] A. Kazemi-Moghaddam. Fehlerfrühidentifikation und-diagnose eines elektrohydraulischen Linearantriebssystems. TU Darmstadt, 2000.

[14] C. Stammen. Condition Monitoring für intelligente hydraulische Linearantriebe. RWTH Aachen, Aachen, 2005.

[15] S. Richter and J. Weber. Sicherheit geregelter Antriebe der Fluidtechnik - Weiterentwicklung von Sicherheitskonzepten. Institut für Fluidtechnik, Dresden, Abschlussbericht FKM-Nr.: 702390, 2011.

[16] J. Schaab, M. Muenchhof, M. Vogt, and R. Isermann. IDENTIFICATION OF A HYDRAULIC SERVO-AXIS USING SUPPORT VECTOR MACHINES. IFAC Proceedings Volumes, vol. 38, no. 1, pp. 722–727, 2005.

[17] P. Garimella and B. Yao. Fault detection of an electro-hydraulic cylinder using adaptive robust observers. ASME 2004 International Mechanical Engineering Congress and Exposition, pp. 119–128, 2004.

[18] K. Mollazade, H. Ahmadi, M. Omid, and R. Alimardani. Vibration-based fault diagnosis of hydraulic pump of tractor steering system by using energy technique. Modern Applied Science, vol. 3, no. 6, p. 59, 2009.

[19] E. Fischer, A. Sitte, J. Weber, E. Bergmann, and M. de la Motte. Performance of an electro-hydraulic active steering system. 10th International Fluid Power Conference (10. IFK) March 8 - 10, 2016 in Dresden, Dresden, 2016, vol. 1, pp. 375–386.

[20] L. Siivonen, M. Huova, and M. Vilenius. FAULT DETECTION AND DIAGNOSIS OF DIGITAL HYDRAULIC VALVE SYSTEM. The Tenth Scandinavian International Conference on Fluid Power, May 21-23, 2007 Tampere, Finland, Tampere, 2007.

[21] L. Siivonen, M. Linjama, M. Huova, and M. Vilenius. Pressure Based Fault Detection and Diagnosis of a Digital Valve System. Power Transmission and Motion Control (PTMC 2007), Bath, 2007, pp. 67–82.

[22] L. Siivonen, M. Linjama, M. Huova, and M. Vilenius. Jammed on/off Valve Fault Compensation with Distributed Digital Valve System. International Journal of Fluid Power, vol. 10, no. 2, pp. 73–82, 2009.

[23] M. Rannow. Fail Operational Controls for an Independent Metering Valve. 10th International Fluid Power Conference. Dresden: Dresdner Verein zur Förderung der Fluidtechnik e.V., 2016.

[24] DIN Deutsches Institut für Normung e.V. Sicherheit von Maschinen – Sicherheitsbezogene Teile von Steuerungen – Teil 2: Validierung (ISO 13849-2:2012), 2013.

Real-Time Parameter Setpoint Optimization for Electro-Hydraulic Traction Control Systems

Addison Alexander and Andrea Vacca

Mechanical Engineering, Purdue University, West Lafayette, IN USA
E-mail: addisonalexander@purdue.edu, avacca@purdue.edu

Abstract

Many modern off-road construction machines incorporate traction control systems to provide better performance and stability in harsh driving conditions. These systems are capable of controlling wheel slip in such a way that the tractive force is increased, tire consumption is reduced, and the overall safety of the machine is improved. However, the driving surface conditions can have a strong impact on the optimal control parameters for the traction control system. This paper sets forth a method of automatically tuning the controller parameters in real time, so that the system can maximize the tractive force on its own.

Toward this end, a simple longitudinal wheel dynamics model is developed using a construction machine as a reference. This model incorporates considerations for the generation of tire force, wheel slip dynamics and machine transmission. Then, a simple traction control structure using proportional-integral-derivative (PID) control is presented which attempts to keep the machine wheels from slipping excessively. Finally, a real-time optimization scheme using the extremum-seeking algorithm was included in the system in order to automatically improve the setpoint of the controller by maximizing the pushing force of the machine. Using the vehicle model of the system, the auto-tuning controller is tested to determine the capability of the system to improve the performance. The optimization scheme allows the controller to find the optimal point, meaning that the output force can be increased when starting at a poor setpoint. Given the availability of a proper feedback signal, this system should be widely applicable to a wide range of different vehicle systems for incorporating traction control.

Keywords: Traction control, electro-hydraulic braking, optimization, automatic parameter tuning

1 Introduction

Traction control systems have become standard components in on-road vehicle systems over the past decades. Other industries such as heavy construction machinery have not seen such a strong proliferation of these systems, though there are some examples of traction control in commercially available construction machines [1]–[3]. The benefits gained by achieving a proper control of a vehicle's tires are well documented, and they include reduced tire consumption, increased traction force and increased vehicle drivability and safety. Therefore, it is desired to design an appropriate traction control system for use with construction equipment.

While the previous efforts listed above toward traction control for construction machines have been successful in reducing slip in certain operating conditions, little effort has been documented in literature in the direction of systems which can adjust to actually improve the traction control as conditions change. This paper describes the structure of an automatically-tuned controller for an electro-hydraulic braking system that reduces wheel slippages by acting on the wheel brakes. In the case of excessive torque from the transmission system causing slip at one wheel, the controller applies a proper braking torque to set the wheel at an optimum slip condition. The vehicle considered as a reference is a wheel loader (fig. 1).

One of the most difficult aspects of designing a traction controller is determining the setpoint for the control signal. Construction machines present a very particular set of problems, due to the unpredictable rapid changes in the operating conditions and diving surfaces used. Because of this, the controller parameters have to be able to quickly adapt to different conditions to avoid poor performance.

Therefore, this work focuses on devising a strategy for updating the controller parameters of the traction control system in real time so that the controller can function in the best possible condition on all surfaces. To do that, a simple traction control system has been designed and simulated to determine the effectiveness of the auto-tuning control approach.

In order to determine the effectiveness of a potential traction control strategy on the reference machine, a simulation model was created using standard vehicle dynamics formulations.

This model was then run using a simple feedback control structure to actuate the brakes in order to reduce the occurrence of excessive wheel slip. The simulation model incorporates both the dynamics of the machine itself and its wheels, as well as a model of the tire-road surface interaction and generated forces at each wheel.

This paper sets forth the outline of such a self-tuning controller. First, the dynamic system model is described, taking into account both vehicle dynamics and tire force generation. Next, a simple but effective control structure is developed which can keep the machine wheels from slipping beyond a desired value. Then, the ES optimization algorithm is incorporated into the model alongside the traction controller. Finally, a simulation is run using the simulation model which shows the performance capability of the system and the usefulness of incorporating the optimization structure into the control structure.

Figure 1: Reference vehicle and setup for testing traction control.

2 State of the Art

Many different methods have been developed for modeling the dynamic behavior of vehicles. The overall vehicle dynamics model incorporated into this work is based on models like those in Gillespie [4], Jazar [5], and Rajamani [6]. For considering the traction at the tire-road interface, a more specific model is needed. For this study, the slip-friction relationship of the tire-surface interface is modeled using Pacejka's Magic Formula tire model [7]. This is a semi-empirical tire friction model which fits a curve of values with particular characteristics to a data set.

Next, a simple traction control structure for maintaining wheel traction was developed. This control structure attempts to increase tractive force and decrease tire slip by actuating the system brakes. There are numerous different traction control strategies which have previously been developed for various different vehicle systems. Often these strategies are constructed in order to overcome specific limitations within the system. It is very common to incorporate structures such as sliding-mode control, adaptive controllers, and fuzzy logic into the designed controls for these systems [8], [9]. Due to the uncertain nature of the various system parameters, tools like state estimators are also frequently utilized in these systems [10], [11]. For this work, instead, a self-tuning proportional-integral-derivative (PID) control was formulated. This controller can be incorporated well into many different systems. The optimization aspect of this controller allows it to account for model complexities such as the transmission system effects without requiring a complicated model-based control structure.

After selecting the PID controller structure, the actual parameters to be used must be determined. In particular, the wheel slip setpoint for the controller can have a strong impact on the system performance. Depending on the ground condition, the optimal setpoint can change quite a bit, and a poor setpoint will not allow the system to reach its maximum possible tractive force. Furthermore, because of the complex interactions of the different system components, if the wheels are on different ground conditions, the restrictions given by the transmission system can make determining the optimal setpoint for all four wheels rather difficult. Therefore, an optimization technique was employed to tune the controller setpoint automatically.

Due to the well-conditioned behavior of the slip-friction relationship, several different optimization techniques could be used for this system. For the purposes of this work, the optimization method selected is the extremum-seeking (ES) algorithm. The ES algorithm has been shown to be useful for real-time optimization of dynamic systems [12]. This method has previously been used by the authors' research team for other real-time optimization applications, specifically with regard to vibration reduction in a mobile crane [13], [14]. Having constructed the full system including an optimization strategy, it can be simulated in order to determine its capability to find the maximum tractive force.

3 Vehicle Dynamics

In order to determine the capability of the traction control system, it must be simulated using a sufficiently accurate model of the machine dynamics. The vehicle model needs to account for the motion of both the chassis and the wheels, as well as the transmission system which connects the wheels together.

It is important to note that the system model developed here considers only straight-line motion of the wheel loader. This simplification is due to the fact that the primary operational mode for implementing traction control on this system is when the machine is pushing into a work pile. In the most common loading and unloading cycles (e.g. the Y-cycle), the wheel loader approaches the work pile in a straight line and does not turn significantly until it reverses out of the pile. As this is the primary operation which will likely need significant traction control, the system model has only been developed for longitudinal motion. Should the need arise for incorporating lateral motion into the model, that can be done at a later time.

3.1 Quarter-Car Vehicle Model

Before taking into account the complete vehicle system with weight transfer and multiple interconnected wheels, the general motion of the machine and its coupling to a single wheel is developed. Essentially, this creates a system modeled as a single point mass on top of a single wheel. As the full system contains four wheels, this simplified model is known as a *quarter-car* vehicle model.

Essentially, this model takes into account the force balance on the vehicle mass and the torque balance on the wheel to describe the motion of those bodies.

$$m\dot{v}_x = F_x - F_{roll}\,\mathrm{sgn}(v_x) - F_{resist}\,\mathrm{sgn}(v_x) \qquad (1)$$

$$I_w\dot{\omega} = T_E - T_B\,\mathrm{sgn}(\omega) - r_d F_x \qquad (2)$$

In eq. (1), m represents the quarter-car vehicle mass, v_x is the longitudinal vehicle velocity, F_x is the longitudinal force produced by the tires, F_{roll} is the rolling resistance, and F_{resist} is all other resistive forces acting on the vehicle (including air resistance, etc.). Equation (2) also contains the wheel moment of inertia I_w, the wheel rotational velocity ω, the input engine torque to the wheel T_E, braking torque T_B, and the dynamic radius of the wheel r_d.

For the simulation, the inputs to the system are engine torque and braking torque. Resistive forces are typically modeled either as constants or as functions of system velocity, though there are other more complex models which can be applied [5], [6], [15]. The wheel force F_x is typically calculated as a function of wheel slip, which is discussed at length in Section 4 of this paper.

Of course, this model is overly simplistic for modeling a complete vehicle system. Therefore, it must be expanded toward a full model by including wheel dynamics equations, equivalent to eq. (2) for each wheel. This means that the full machine model will actually have five equations in total: four for the dynamics of the wheels and another for the linear motion of the vehicle chassis. However, the input to the system remains a single engine torque, so the model needs to be expanded further to account for the distribution of this torque to each wheel.

3.2 Two-Axle Vehicle Model

The next step toward developing a complete vehicle model is examining how the normal forces at each tire shift as the machine moves. As this model is only considering a wheel loader which is moving forward and backward in plane, it is assumed that the weight is balanced equally from right to left and does not shift. This is a reasonable assumption in general, since the only action being modeled for the machine is straight-line digging.

On the other hand, the forces at the front and rear axles can vary quite a lot depending on the motion of the wheel loader and outside forces acting on it. The normal forces at the front and rear axles are calculated using a force and moment balance in the plane of the wheel loader motion. This results in the following equations.

$$F_{z1} = \frac{1}{2}mg\frac{l_2}{l} - \frac{1}{2}ma_x\frac{h_{CG}}{l} - F_p\frac{h_p}{l} \qquad (3)$$

$$F_{z2} = \frac{1}{2}mg\frac{l_1}{l} + \frac{1}{2}ma_x\frac{h_{CG}}{l} + F_p\frac{h_p}{l}, \qquad (4)$$

In eq. (3) and (4), F_{z1} and F_{z2} are the normal forces at the front and rear axles, respectively. Again, these are assumed to be split equally between the right and left wheels on each axle. Calculating these forces utilizes the coefficient of gravity g, the horizontal distances from the machine center of mass to the front (l_1) and rear (l_2) wheels, the horizontal distance between the axles $l = l_1 + l_2$, the longitudinal acceleration of the vehicle a_x, the height of the center of gravity h_{CG}, the external force on the wheel loader (pile force F_p, assumed horizontal), and the height of that external force h_p.

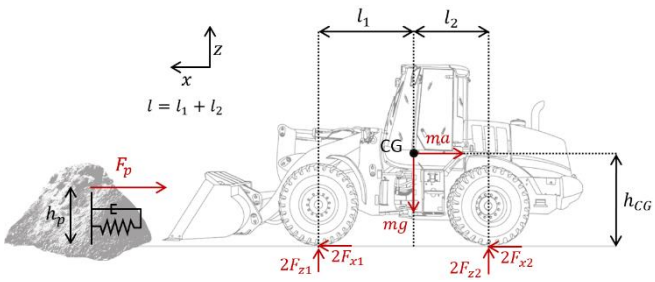

Figure 2: Wheel loader force diagram.

As the traction control system for this machine is being developed primarily for standard working conditions, the simulated operation is pushing into a work pile, which is modeled simply as a horizontal resistive force. As this work is only focused on generating excessive wheel slip and not on developing an extremely accurate digging material model, the work pile itself has been represented simply as a horizontal resistive force pushing back against the motion of the machine. The horizontal force F_p is modeled as a spring-damper system, which only acts against the motion of the machine once it has made contact.

$$F_p = \begin{cases} k_p x_p + c_p\dot{x}_p, & x_p \geq 0 \text{ and } \dot{x}_p \geq 0 \\ 0, & \text{else} \end{cases} \qquad (5)$$

In this equation, k_p and c_p are the spring and damper constants of the simulation pile, respectively, and x_p is the distance the machine has driven into the simulated pile. This allows a large resistive force to be built up quickly, but not so quickly that it causes simulation problems.

From these equations, it can be seen that, as the wheel loader accelerates forward, its weight is transferred from the front to the rear axles. Furthermore, when the machine encounters the resistive force from the pile, this also causes weight to be shifted from the front axle to the rear axle. This assumes a strictly horizontal resistive force from the pile. When digging

into a material pile, the material compaction and added weight in the machine bucket can have other effects on weight transfer which are not considered here, as they can be exceedingly complex to model properly. The changing normal force at each wheel will affect the longitudinal force that wheel is capable of producing, as the wheel force is equal to the product of the normal force and the wheel coefficient of friction (see Section 4.2).

3.3 Transmission Model

Having developed the model for transferring normal force from one axle to the other, the torque distribution to the wheels can be determined. For the wheel loader in question, this involves modeling both the front and rear differentials, which connect the driveshaft to the axles, and the transfer case, which connects the transmission to the driveshaft. It is assumed for this model that the engine torque to the driveshaft is known, so effects like the torque converter and gearbox are ignored here.

The first component of the transmission to be modeled is the differential. There are two of these in the machine linking the front and rear axles to the driveshaft. The primary purpose of the differential is to allow the wheels on each side of the axle to rotate at different velocities while still being driven by the engine. Through use of a planetary gear, the torque from the driveshaft is split in half to each wheel on the axle.

$$T_{i,L} = T_{i,R} = \frac{1}{2} R_{diff} T_{DS,i} \,, \tag{6}$$

where $T_{i,L}$ and $T_{i,R}$ are the driving torques into the left and right wheels of axle i, R_{diff} is the gear ratio of the differential, and $T_{DS,i}$ is the torque input to axle i from the driveshaft.

In order to split the torque evenly, the differential allows the wheels at each side of the axle to turn at different speeds. Of course, there is still a relationship between the driveshaft speed $\dot{\theta}_{DS,i}$ and the wheel speeds $\dot{\theta}_{L,i}$ and $\dot{\theta}_{R,i}$.

$$\dot{\theta}_{DS,i} = \frac{R_{diff}}{2}\left(\dot{\theta}_{i,L} + \dot{\theta}_{i,R}\right) \tag{7}$$

That is to say, the driveshaft speed is equal to the average of the wheel speeds on a given axle, scaled by the gear ratio.

What remains is to determine the driveshaft torque to each axle. In some vehicle systems, the driveshaft itself is driven by a central differential, splitting the torque evenly to the front and rear axles. The wheel loader in this study, however, has what is known as a *locked transfer case*, which means the front and rear section of the driveshaft are connected directly. This means that, instead of each section being able to rotate independently, they are constrained to turn at the same rate. Therefore, the torque to each axle can vary based on the load at that axle. By treating the driveshaft as a rotational mass-spring-damper system with some simplifications (as in [16]), the following equations result for describing the torque distribution to each axle.

$$T_{DS,F} = \frac{1}{2}T_E - \frac{k_{DS}}{2}\left(\theta_{DS,F} - \theta_{DS,R}\right) - \frac{c_{DS}}{2}\left(\dot{\theta}_{DS,F} - \dot{\theta}_{DS,R}\right) \tag{8}$$

$$T_{DS,R} = \frac{1}{2}T_E + \frac{k_{DS}}{2}\left(\theta_{DS,F} - \theta_{DS,R}\right) + \frac{c_{DS}}{2}\left(\dot{\theta}_{DS,F} - \dot{\theta}_{DS,R}\right) \tag{9}$$

In eq. (8(8) and (9), $T_{DS,F}$ and $T_{DS,R}$ are the torques distributed to the front and rear axles via the driveshaft, respectively, T_E is the torque into the transfer case from the engine, $\theta_{DS,F}$ and $\theta_{DS,R}$ are the angular positions of the front and rear sections of the driveshaft, respectively, and k_{DS} and c_{DS} are the rotational spring and damper constants of the driveshaft sections.

Using equations (1) through (9), the full vehicle dynamics for straight line motion have been described. Assuming a good estimate of the input torque to the transfer case and the braking torque at each wheel, this model should be appropriate for simulating the system to get an idea of controller performance.

3.4 Braking System Dynamics

A simplified schematic of the braking system designed for implementing an electronic traction control in the reference machine is shown in fig. 3 below. The traction control system uses a pressure reducing valve (1) to command a desired pressure based on the controller output. A check valve (2) is used to ensure that the higher pressure is always selected and sent to the brake caliper (3). This allows the system to operate as normal when no pressure is commanded from the traction control system, meaning that the pressure from the standard braking foot valve is seen directly by the brakes. The system is also unable to decrease the braking pressure below that of the foot valve. This is done for safety reasons, but it also means that the current system cannot implement an anti-lock brake system (ABS) or any other functionality which would require decreasing the braking pressure from the foot valve.

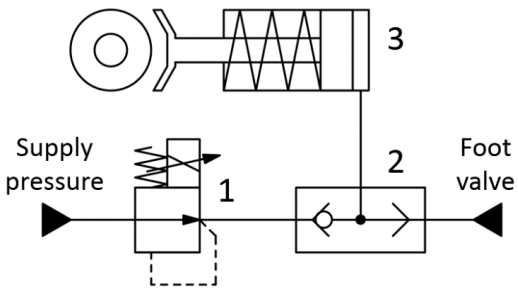

Figure 3: Simplified schematic of braking system for implementing traction control.

The modeling of this system, including valves and other braking system components like lines and shuttle valves, was accomplished using the Simscape library in Matlab Simulink. Using this library allows the simulation to account for valve dynamics, fluid compressibility, and other important hydraulic system effects. The resulting system model was then verified by comparing it with real-world system test data.

4 Tire Slip Dynamics

Where traction control is concerned, the most important component of the entire vehicle system is the interface between the tire and the road surface. This interface represents the only connection between a typical vehicle and the road, and it is also the location where the forces for propelling the vehicle are generated. Correct modeling of the interaction between a vehicle's tires and the road surface is crucial to properly modeling the vehicle system and generating an acceptable traction control structure.

4.1 Wheel Slip

Under normal operation, wheels which are being driven or braked do not rotate at a velocity which matches exactly the velocity of the road surface. In general, any time a torque is applied to the wheel deformation in the tire and other phenomena cause a small amount of slip (or micro-slip) to occur at the tire-road interface [15].

This micro-slip is different from visible slip (or macro-slip) one tends to think of when discussing wheel slip, such as spinning or sliding against the ground. In fact, micro-slip is a necessary component for force generation at the tire-road interface, as the primary force production mechanism there is friction between the tire and road surface.

Of course, it is possible to have too much slip at the tire-road interface, and in cases of excessive slip, the amount of friction force generated can decrease significantly, while also causing problems such as increased tire wear and controllability. In order to determine the effect of tire slip on tractive force, a proper model is required.

4.2 The Magic Formula Tire Model

Perhaps the most widely used model for representing the relationship between slip and force is Pacejka's Magic Formula model [7]. The Magic Formula tire model was developed as a relatively compact and simple way of representing the relationship between tire slip and the friction coefficient (i.e. tractive force) between the wheel and the road surface. It is a semi-empirical model, meaning that it is a relationship based on the general shape of slip-friction curves, which is adapted to best fit a data set for a given driving condition.

The Magic Formula is not based directly on physics equations, but it is adequate to describe the behavior of most systems. It has the form:

$$\mu_{x,i}(\kappa_i) = D_{x,i}\sin\left(C_{x,i}\tan^{-1}\left[B_{x,i}\kappa_i - E_{x,i}\left(B_{x,i}\kappa_i - \tan^{-1}\left[B_{x,i}\kappa_i\right]\right)\right]\right), \tag{10}$$

where $\mu_{x,i}$ and κ_i are the longitudinal friction coefficient and the slip ratio at wheel i, respectively. Coefficients $B_{x,i}$, $C_{x,i}$, $D_{x,i}$, and $E_{x,i}$ are parameters affecting the shape of the Magic Formula curve, and they are adjusted in order to approximate a given data set as closely as possible. The data itself can be generated through several different methods, such as the one developed by Rajamani [17].

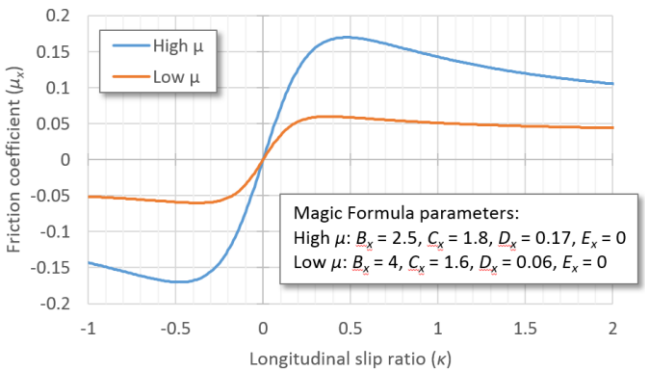

Figure 4: Example Magic Formula plots.

What results from the proper setting of the Magic Formula parameters is a plot similar to the examples shown in fig. 4. These example curves were taken from real-world test data and were used for the simulations shown in Section 7 of this work. Using the form in eq. (10), the result is an odd function. Typically, though not always, this plot has a well-defined maximum at some optimal value of κ. The objective of the traction control system is usually to keep the wheel slip at or below this value.

To convert the friction coefficient from eq. (10) to a longitudinal tractive force, it simply has to be multiplied by the normal force at that wheel.

$$F_{x,i} = \mu_{x,i}F_{N,i}\,, \tag{11}$$

where $F_{x,i}$ is the tractive force and $F_{N,i}$ is the normal force at the wheel in question. Depending on the desired accuracy of the model, the normal force can either be considered constant or it can be modeled as a time-varying force. The longitudinal force generated from eq. (11) can then be fed back into the equations of motion for the vehicle to update the linear dynamics.

4.3 Tire Slip Modeling

Since tire tire-road friction (and hence tractive force) is a function of tire slip, it is necessary to have an acceptable model for slip ratio which approximates well the behavior of the system.

In general, the tire slip model simply needs to quantify the relationship between the longitudinal motion of the vehicle and the rotational motion of each wheel. The simplest form definition of the tire slip ratio is an algebraic relationship, such as the one shown below [4].

$$\kappa_i = \frac{r_d\omega_i - v_x}{v_x} \tag{12}$$

In eq. (12), v_x represents the longitudinal velocity of the vehicle, r_d is the dynamic radius of the wheel, and ω_i is the rotational velocity of wheel i. This relationship is adequate for many modeling applications, but in some cases a more complex definition is needed. Traction control systems in

particular represent such a case, as the low velocities where they are most commonly used cause eq. (12) to vary rapidly with small variations in v_x. Furthermore, it cannot be used in the case where the vehicle stops completely ($v_x = 0$).

Therefore, a different tire slip formulation is needed which does not have such issues at low velocities. For the purposes of this research, the following definition has been defined, based on the work of Bernard [18].

$$\dot{\kappa}_i + \frac{|v_x|}{B}\kappa_i = \frac{r_d\omega_i - v_x}{B}, \qquad (13)$$

where B is the longitudinal relaxation length of the tire, and all other coefficients are the same as above. This new tire slip definition is a differential relationship, as opposed to the previous algebraic relationship. Thus, the velocities are allowed to approach and reach zero without creating the same problems.

Using eq. (13) to model the wheel slip and eq. (10) with the proper parameter values, the force generation dynamics at each tire of the vehicle can be adequately modeled.

5 Traction Control Design

A traction control system seeks to achieve relatively simple goals. First, there should be a reduction in tire macro-slip (i.e. significant visible slip against the ground surface) to reduce the amount of tire wear and increase system stability. Furthermore, this reduction in slip should also see payoffs in terms of tractive force. By maintaining better traction against the ground surface, the system is able to attain higher pushing force at each wheel. Both tire slip and pushing force are measurable quantities which can provide a numerical value to the performance increase when using the traction control.

The control structure chosen for this work is a very simple proportional-integral-derivative (PID) controller. The PID is a very common control structure with well understood design principles [19]. It is also typically well-behaved for many different kinds of systems, so it is suited quite well to the machine system considered here.

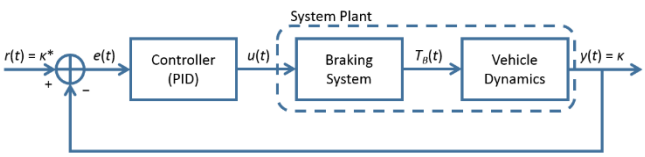

Figure 5: Overall control system block diagram.

Once the controller itself has been determined, it is important to determine how the controller should be incorporated into the overall system design. It is necessary to define an error signal from which the controller can generate the signal for the braking system. For this investigation, the control system was defined as seen in fig. 5.

From this figure, it can be seen that the feedback variable being used in this construction is the tire slips κ. Here, κ is usually a vector of slip values at all four wheels. By comparing the wheel slips to some vector of desired values κ^*, an appropriate error signal $e(t)$ is created.

One consideration which should be noted about the slip setpoint for traction control systems is that while the general controller design attempts to keep the slip *at* a certain value κ^*, in actuality the goal of the system is to keep the wheel slip *at or below* that value. As brakes are single-acting actuators, only capable of acting against the motion of the wheel, the signal itself is physically saturated in the real-world system. However, for some simulations it may be necessary to saturate the output to zero to ensure the brakes are not attempting to increase the wheel speed. The concept of brakes as single-acting inputs also plays an important role in developing the optimization algorithm in Section 6 of this work.

6 Real-Time Controller Setpoint Optimization

Having defined a proper control strategy for the traction control system, it is important to correctly set the parameters of the system for the best possible control performance. The simplest way to do this would be to pick a wheel slip setpoint which is reasonable for all wheels and allow it to remain constant. While such a setup would most likely show an improvement over no traction control system, it is also probable that a better setup can be achieved. Ideally, the controller would be able to identify the slip setpoint which maximizes traction force (see fig. 4) on its own.

6.1 The Extremum-Seeking Algorithm

For this particular work, the optimization strategy chosen is the extremum-seeking (ES) algorithm. This is a non-model-based approach which uses sinusoidal perturbations to ascertain the gradient of an objective function. The parameter or parameters to be optimized are then adjusted according to the cost function gradient to either minimize or maximize the objective function. The general continuous-time implementation of this algorithm is shown below (as formulated by Ariyur [12].

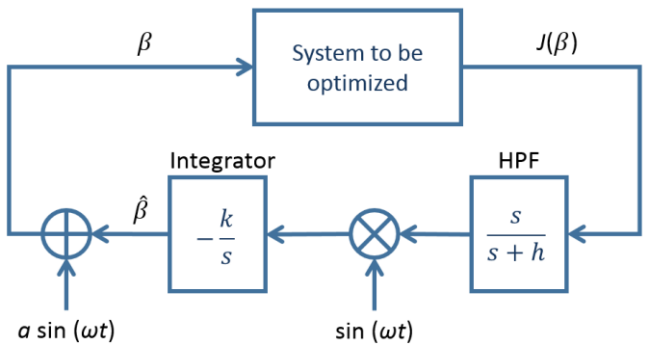

Figure 6: Basic extremum-seeking optimization scheme.

Essentially, the ES algorithm begins with an estimate of the optimal parameter value $\hat{\beta}$. By applying an additive sinusoidal perturbation to this signal, the actual parameter value β which is used in the system in question causes a response in the objective function $J(\beta)$. By passing the

resulting signal through a high-pass filter (labeled "HPF" in fig.6), "demodulating" it with using a multiplicative perturbation of the same frequency, and using an integrator to remove high-frequency components, the estimate of the optimal parameter value $\hat{\beta}$ is driven toward the actual optimal value for the system β^*.

If the objective function of the system $J(\beta)$ has a well-defined optimum J^* at β^*, the ES algorithm has been shown to converge to that value, given proper setting of the ES parameters [12]. Perhaps the most difficult aspect of implementing the ES algorithm: it introduces four new terms which must themselves be set before using the optimization strategy: ω, the frequency of the perturbation frequency, a, the additive perturbation gain, h, the high-pass filter pole, and k, the integrator gain. These parameters do add a degree of difficulty to implementing the optimization, but once they are tuned sufficiently, the algorithm can work quite well.

It should also be noted that this particular system is quite well-suited to the ES optimization technique. In general, the slip-friction characteristic of tire-road surface interfaces looks something like the plot in fig. 4. These plots are continuous, and each has a single, easily definable maximum at some slip $\kappa^* > 0$. Therefore, given proper settings for the ES algorithm, the system should be able to find the best setpoint for the controller relatively efficiently.

6.2 Integration into Controller Structure

There are multiple important parameters within the controller, including the gains K_P, K_I, and K_D for the proportional, integral, and derivative components of the control law, respectively. These can have a strong impact on the system if set incorrectly, even causing an otherwise stable system to become unstable in certain circumstances [20]. However, once set correctly within reason, small changes in other parameters, specifically the tire slip setpoint, should not cause the system to become unstable. Therefore, the controller gains were not chosen as the optimization parameters for the ES algorithm.

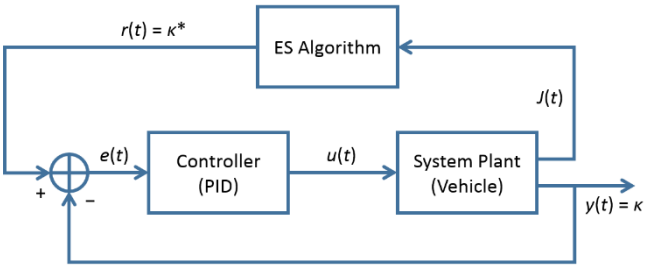

Figure 7:Control system block diagram including setpoint optimization.

Instead, the parameter to be optimized for each wheel is the tire slip setpoint. By selecting the slip setpoint instead of the controller gains, at most one value per wheel needs to be optimized, instead of potentially three or more for each wheel. This greatly simplifies the optimization process. Furthermore, the tire slip setpoint is controlled directly by the operating condition for the vehicle, so it should be a fitting parameter to use for optimizing the controller.

In order to do this, the ES algorithm must be inserted into the block diagram of fig. 5. What results is a system in which the tracking setpoint $r(t)$ is modified in real time. This reference trajectory is the equivalent of β, the output of the ES algorithm in fig. 6.

6.3 Feedback Signal Considerations

As optimization methods require a quantifiable objective function, the ES algorithm in fig. 7 receives some feedback information $J(t)$ from the system plant. The signal chosen for this feedback can have a drastic effect on the capability of the ES algorithm to optimize the controller performance.

In general, $J(t)$ needs to be chosen as a signal which quantifies the system performance in some meaningful way. For traction control systems, the primary desired output of the system is tractive force at the wheels. In standard on-road vehicle applications, the force can be approximated using the linear acceleration and wheel velocities, etc., as the vehicle is only propelling itself and is not attempting to interact with an external body [21], [22]. For construction machines like the one in question, however, the range of operating conditions and uses is significantly higher. In fact, the typical driving operation for this machine takes place at relatively low speeds, and its weight is enough that loss of traction when driving is usually not an issue.

For implementation in a real-world machine, a representative objective function needs to be constructed from available sensor data. This may not always be simple, but when specifically considering wheel loaders, a good estimate of the wheel force could potentially be generated using implement boom and bucket cylinder pressures and angles. Similar systems have already been developed for estimating the payload in the machine bucket [23], [24].

On the other hand, simulations allow for much more direct access to the system states. Therefore, the objective function for simulations can simply be the total pushing force $F_{x,tot}$ of the machine. That is,

$$J(t) = F_{x,tot} = \sum_i F_{x,i} \,. \tag{14}$$

This objective function may be overly simplistic for some applications. For instance, Osinenko [25] includes a term for "traction efficiency," which can be included as an optimization tradeoff. Other systems may want to take into account the amount of wheel slip when creating the feedback objective function. Nevertheless, for the sake of this study, the purpose of the optimizer is simply to maximize the total pushing force of the machine.

The ES algorithm updates parameters based on the assumption that all changes in the parameters are reflected in the objective function. However, if the current braking control signal is negative, the wheel speeds are not being

affected at all. Therefore, during instances where the control signal is negative, the optimization code receives incorrect information about its effect on the system. This can cause the algorithm to converge to an incorrect point. Therefore, some logic has been added to the ES algorithm so that it does not modify the guess of κ^* unless the wheels are being braked (fig. 8). The scheme incorporating this update logic is referred to in this work as the *augmented* extremum-seeking algorithm.

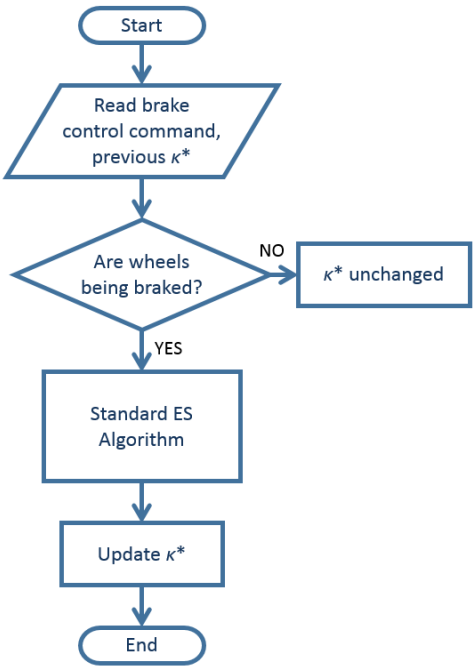

Figure 8: Augmented extremum-seeking algorithm.

7 Simulation Results

Now that the system has been properly constructed and the optimization algorithm set in place, it is necessary to determine how well the system can perform. For this work, the performance metric will be assessed using a simulation conducted in Matlab Simulink and based on the model developed in Sections 3 and 4 of this paper.

Before the traction control simulation was conducted, it was first desired to assess the accuracy of the vehicle model. This was done by running a test with a series of accelerations and braking actions and recording an estimate of the input torque to the system. This torque was then used as an input to the simulation model. The resulting simulation was compared to the results of the machine test (fig. 9).

The next simulation used for this system was a simplified digging cycle, similar to the setup shown in fig.1. In the simulation, the machine approaches the simulated pile and pushes against it for a few seconds. During that time, the controller and optimizer work together to maximize the pushing force of the machine. In theory, this increased pushing force translates, in real-world operation, to increased digging force along with decreased tire slip.

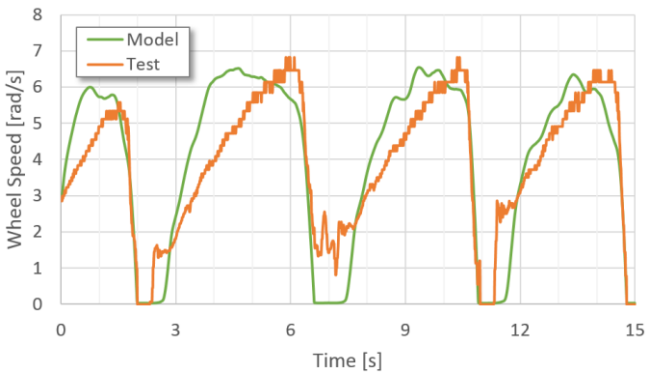

Figure 9: Simulation model validation.

For the first test, the vehicle is on a ground condition with relatively high friction for all four wheels (the high-μ example from fig. 4). The wheel loader begins the simulation by advancing toward the work pile without the wheels slipping against the ground. Once the machine reaches the pile and begins pushing against it, however, the tires begin to slip (with the vehicle velocity actually slowing down) and the tractive force is reduced. As the wheel slip increases, the traction control system activates and slows down the wheels until they are kept at the proper slip ratio. The vehicle and wheel velocities for this simulation are shown in fig. 10

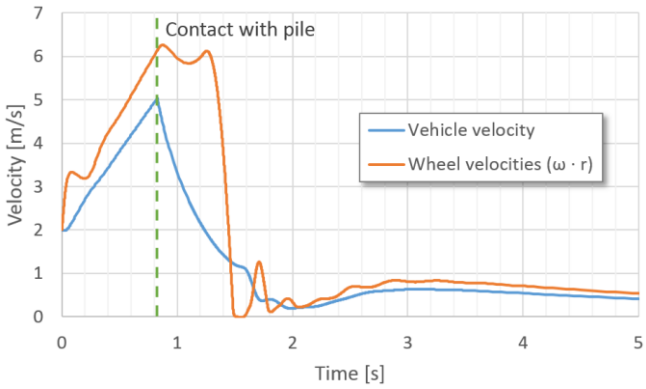

Figure 10: Traction control simulation velocities (high-friction simulation).

The overall effect of this is that the tractive force is increased and the machine can dig farther into the pile. Figure 11 shows the pushing force of the machine over time for the machine. It makes contact with the work pile after just before 1 second and quickly begins losing tractive force. As the traction control activates, at first the brakes are actuated too strongly. This causes an overshoot where the vehicle is actually slowed down for a brief moment. Very quickly, however (within two seconds), the optimization algorithm finds the correct setpoint value, and within three seconds the system has converged to a very good tractive force value. In fact, the system achieves a final force which is 54.7% higher than the final force without the traction control system (21.9 vs. 14.1 kN in this simulation). Furthermore, the wheel slip is greatly reduced in this case. This indicates that the controller is in fact meeting the requirements set for it in Section 5 of this paper. The speed at which the algorithm is able to converge

suggests that this system could be well-suited for implementation on a real-world machine.

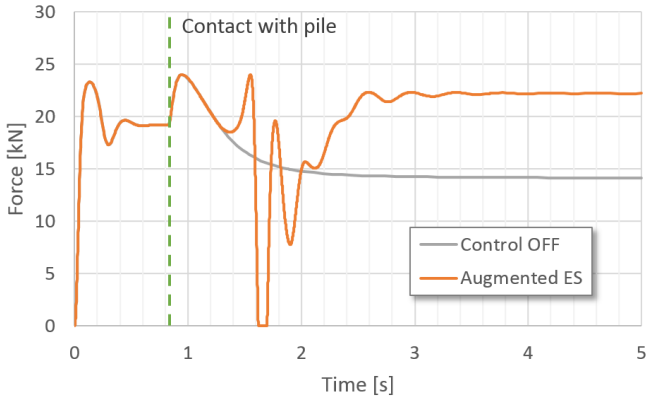

Figure 11: Longitudinal force for vehicle simulation in high-friction condition.

Figure 12 shows the result of the setpoint optimization for this simulation using the augmented extremum-seeking algorithm, as well as a comparison to the same simulation using an unmodified ES algorithm (i.e. exactly as shown in fig. 6). The tire-road interface has a known maximum friction coefficient at a slip ratio of around $\kappa^* = 0.5$. This is found by determining the location of the maximum friction coefficient for the slip friction curve, shown in fig. 4. To determine the location of the slip that maximizes the friction, the curve is differentiated with respect to κ, and then the location where the derivative curve crosses zero is taken as κ^*.

It can be seen that, even when the system is not being braked, the unmodified ES algorithm still attempts to use the force information to update the setpoint. As a result, it ends up overshooting the actual optimum value and, as the force continues to change, it could potentially wander farther from the correct point. If, on the other hand, the optimization is updated only when the brakes are being actuated (as in the augmented ES algorithm), the optimization avoids the effect of bad objective function information. Therefore, instead of the haphazard development of the standard ES algorithm, the updated ES algorithm pauses when no wheels are being braked and consistently approaches the correct setpoint as time progresses.

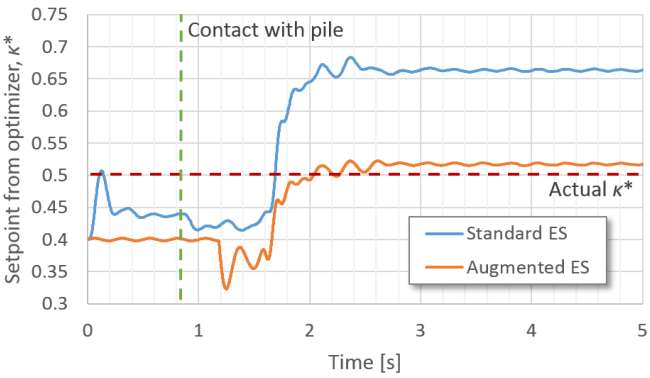

Figure 12: Performance comparison of standard ES algorithm with updated version (high-friction).

A second simulation was then run using the same system in a different ground condition. This time, all four wheels were simulated as being on slick ground (the low-μ example from fig. 4). In this condition, the traction control system must work much more to keep the wheels from spinning. Furthermore, the maximum pushing force is found at a different value of slip ratio ($\kappa^* \approx 0.36$). This means that, whereas the ES algorithm needed to increase the setpoint in the previous simulation, with this condition it must decrease the setpoint somewhat. The results of this simulation are shown in fig. 13.

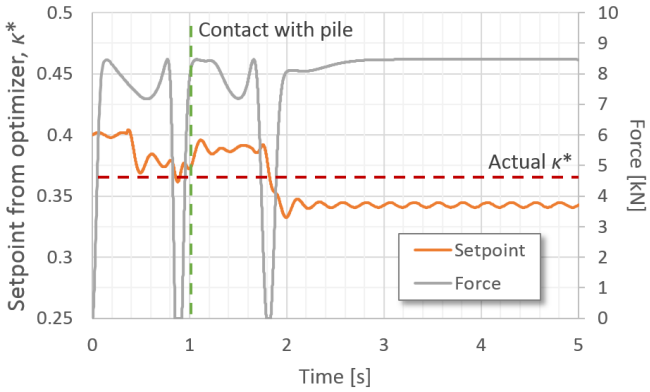

Figure 13: Simulated system performance (low-friction).

In this simulation, the controller setpoint was again initialized at a non-optimal value. In fact, it started at the same point as the high-friction simulation ($\kappa_0 = 0.4$). In this case, the ES algorithm decreased the setpoint during the simulation, so that it achieved a better setpoint. Furthermore, the traction control system was able to contain the wheel slip to an appropriate value such that the tractive force was maximized (again, after some initial overshoot where the tractive force was briefly decreased). Even in a worse ground condition, this system far outperforms a simulation with no traction control.

These simulations indicate that the system developed in this work is capable of determining and reaching an optimal slip value given the proper feedback signal for the optimization objective function.

8 System Potential

Generating the feedback signal is relatively simple in simulation, as most states can be computed fairly easily. In practice, however, it is more difficult to obtain, for instance, a proper estimate of the wheel force. Nevertheless, if an acceptable objective function can be computed, this system should be equally applicable to real-world vehicle systems. In terms of generating a longitudinal force estimate, the wheel loader presents some potential for accomplishing this. For instance, if it is being used to dig or push, the pressure in the implement boom and bucket hydraulic cylinders can be processed in such a way that a reasonable estimate of pushing force can be determined. This could potentially incorporate a system similar to the payload sensing apparatus described in [23], [24].

Nevertheless, if a suitable feedback signal can be generated, this system has quite a lot of potential toward being applicable to other systems. Using a basic PID structure for the controller means that there are very few parameters which need to be adjusted in order to apply it to a new vehicle. Other more complex model-based controllers may have somewhat better performance, but they are also very specific to the machine for which they are designed, and transferring them to other systems could require some rigorous work.

Furthermore, using the extremum-seeking algorithm also makes the controller design relatively simple to transfer to new machines. As long as the objective function is well-behaved and has a relatively well-defined maximum (or minimum), the ES algorithm is a fairly robust method for optimizing the system. Therefore, this system should be applicable toward the development of other traction control systems without very much needed modification.

9 Conclusions

This paper presents a self-tuning controller for eletro-hydraulic traction control systems in vehicles. By focusing on the case of a construction machine, a simple vehicle model is developed for simulating the performance of the traction control system. This model includes considerations for wheel force generation, including wheel slip dynamics. A relatively simple controller consisting of a PID structure was then included in order to control the wheel slip to some value.

Much work was conducted toward finding the optimal wheel slip value, which can change from one ground condition to the next. Therefore, a feedback structure was created which utilized a real-time optimization method (the extremum-seeking algorithm) in order to determine this value online. In order to do this, an objective function for the system was designated and the extremum-seeking parameters were tuned to appropriate values.

By using the automatic tuning controller, simulations were run which showed that it has the ability to determine the optimal slip value for the wheels on its own and to control the wheels to that value. This resulted in a simulation in which the wheel force was optimized in real time while pushing against a work pile (modeled as a resistive force). In all, this control structure shows promise for tuning traction control systems in vehicles which work on varied surfaces.

Nomenclature

Designation	Denotation	Unit
a_x	Longitudinal acceleration	m/s^2
B	Tire longitudinal relaxation length	m
B_x	Magic Formula parameter	none
C_x	Magic Formula parameter	none
c_{DS}	Damping rate of driveshaft section	$\frac{\text{N·m·s}}{\text{rad}}$
c_p	Damping rate of pile resistive force model	N·s/m
D_x	Magic Formula parameter	none
E_x	Magic Formula parameter	none
F	Force	N
g	Acceleration of gravity	m/s^2
h	High-pass filter pole for extremum-seeking algorithm	none
h_{CG}	Height of center of gravity	m
h_p	Height of pile force application	m
I_w	Wheel moment of inertia	kg·m^2
J	Objective function value for optimization	none
k	Integral gain for extremum-seeking algorithm	none
k_{DS}	Spring rate of driveshaft section	N·m/rad
k_p	Spring rate of pile resistive force model	N/m
l	Horizontal distance	m
m	Vehicle mass	kg
R_{diff}	Gear ratio of differential	none
r	Reference trajectory for control system	none
r_d	Dynamic radius of wheel	m
T	Torque	N·m
v_x	Longitudinal vehicle velocity	m/s
x_p	Distance of travel into pile	m
β	Optimization variable(s) for extremum-seeking algorithm	none
$\hat{\beta}$	Estimate of variable optimum value for ES algorithm	none
θ	Rotational position	rad
κ_i	Slip ratio at wheel i	none
μ_x	Longitudinal friction coefficient	none
ω_i	Rotational velocity of wheel i	rad/s

References

[1] J Sjögren. “Anti spinning device, a vehicle comprising the device and a method for reducing slip during advancing of a vehicle,” US 8226177 B2, 24-Jul-2012.

[2] K Uematsu, K Hatake, and A Nomura. “Vehicle speed estimator and traction control device,” US 8538635 B2, 17-Sep-2013.

[3] B J Holt, J E Jensen, S Marathe, and S A Marks. “Electronic traction control system,” US 6631320 B1, 07-Oct-2003.
[4] T D Gillespie. *Fundamentals of Vehicle Dynamics*. Warrendale, PA: Society of Automotive Engineers, 1992.
[5] R N Jazar. *Vehicle Dynamics: Theory and Application*, 2nd ed. New York: Springer, 2014.
[6] R Rajamani. *Vehicle Dynamics and Control*, 2nd ed. New York, NY: Springer, 2012.
[7] H B Pacejka and E Bakker. “The Magic Formula Tyre Model.” *Vehicle System Dynamics*, 21(S1):1–18, Jan. 1992.
[8] J Li, Z Song, Z Shuai, L Xu, and M Ouyang. “Wheel Slip Control Using Sliding-Mode Technique and Maximum Transmissible Torque Estimation.” *Journal of Dynamic Systems, Measurement, and Control*, 137(11):111010, Aug. 2015.
[9] H Lee and M Tomizuka. “Adaptive Vehicle Traction Force Control for Intelligent Vehicle Highway Systems (IVHSs).” *IEEE Transactions on Industrial Electronics*, 50(1):37–47, Feb. 2003.
[10] T Nakakuki, T Shen, and K Tamura. “Adaptive control approach to uncertain longitudinal tire slip in traction control of vehicles.” *Asian Journal of Control*, 10(1):67–73, Jan. 2008.
[11] S Kuntanapreeda. “Traction Control of Electric Vehicles Using Sliding-Mode Controller with Tractive Force Observer.” *International Journal of Vehicular Technology*, 20141–9, 2014.
[12] K B Ariyur and M Krstić. *Real-Time Optimization by Extremum-Seeking Control*. Hoboken, NJ: John Wiley & Sons, Inc., 2003.
[13] D Cristofori, A Vacca, and K Ariyur. “A Novel Pressure-Feedback Based Adaptive Control Method to Damp Instabilities in Hydraulic Machines.” *SAE International Journal of Commercial Vehicles*, 5(2):586–596, Sep. 2012.
[14] G F Ritelli and A Vacca. “Energy Saving Potentials of a Novel Electro-Hydraulic Method to Reduce Oscillations in Fluid Power Machines: The Case of a Hydraulic Crane.” *SAE International Journal of Commercial Vehicles*, 6(2):269–280, Sep. 2013.
[15] H B Pacejka and I Besselink. *Tire and Vehicle Dynamics*, 3rd ed. Amsterdam: Elsevier/Butterworth-Heinemann, 2012.
[16] M M Tinker. “Wheel Loader Powertrain Modeling for Real-Time Vehicle Dynamic Simulation,” Master’s thesis, The University of Iowa, Iowa City, 2006.
[17] R Rajamani, G Phanomchoeng, D Piyabongkarn, and J Y Lew. “Algorithms for Real-Time Estimation of Individual Wheel Tire-Road Friction Coefficients.” *IEEE/ASME Transactions on Mechatronics*, 17(6):1183–1195, Dec. 2012.
[18] J E Bernard and C L Clover. “Tire Modeling for Low-Speed and High-Speed Calculations,” 1995.
[19] N S Nise. *Control Systems Engineering*, 6th ed. Hoboken, NJ: Wiley, 2011.
[20] W S Levine, Ed. *The Control Handbook*, 2nd ed. Boca Raton, Fla.: CRC Press, 2011.
[21] H Hamann, J K Hedrick, S Rhode, and F Gauterin. “Tire force estimation for a passenger vehicle with the Unscented Kalman Filter,” in *Intelligent Vehicles Symposium Proceedings*, Dearborn, MI, USA, 2014, 814–819.
[22] J Matuško, I Petrović, and N Perić. “Neural network based tire/road friction force estimation.” *Engineering Applications of Artificial Intelligence*, 21(3):442–456, Apr. 2008.
[23] H Kang, W Jung, and C Lee. “Modeling and Measurement of Payload Mass of the Wheel Loader in the Dynamic State based on Experimental Parameter Identification,” in *SAE Technical Paper 2016-01-0469*, 2016.
[24] A Shatters. “Method and system for estimating payload weight with tilt position compensation,” US 9464403 B2, 11-Oct-2016.
[25] P V Osinenko, M Geissler, and T Herlitzius. “A method of optimal traction control for farm tractors with feedback of drive torque.” *Biosystems Engineering*, 12920–33, Jan. 2015.

Model-based Analysis of Decentralized Fluidic Systems in Machine Tools

Linart Shabi*, Juliane Weber, and Jürgen Weber

Institute of Fluid Power, TU Dresden, Helmholtzstraße 7a, 01069 Dresden, Germany
E-mail: linart.shabi@tu-dresden.de, juliane.weber@tu-dresden.de, mailbox@ifd.mw.tu-dresden.de
* Institute of Fluid Power, TU Dresden, Helmholtzstraße 7a, 01069 Dresden, Germany

Abstract

Power losses in machine tools, e.g. during production process, are converted into thermal energy. This leads to a warming of the machine frame and further machine parts and accordingly to the displacement of the tool center point (TCP) of the machine. Consequently, the accuracy of the machine during the production process is reduced. The warmed-up parts or components need to be cooled; therefore, fluidic systems are installed to prevent this effect. Previous research projects mainly focused on the energy demand of the machine tool and its main drives, reducing the energy consumption by developing more efficient components and control strategies. However, the thermal behavior of the fluidic systems, especially of the cooling system, has not yet been described in detail. Therefore, a detailed analysis of the existing cooling system and its effectivity is necessary.

The main target of this paper is to analyze the thermal behavior and improve the system structure of the cooling system in a demonstration machine tool. This investigation will help to examine the efficiency of the cooling system for an idle and a manufacturing process. This makes it possible to study new concepts for the system structure of the cooling system in order to ensure a uniform temperature distribution of the machine tool at minimal energy consumption.

Firstly, the paper will describe the main fluidic systems of the demonstration machine DBF630 with a special focus on the cooling system. Secondly, with the aid of experimental investigation the thermal behavior of the cooling system will be investigated. Furthermore, a network-based model of the cooling system for two processes is developed and validated against the measured data. Lastly, the new concept of a decentralized supply unit will be studied with the network-based simulation model.

It can be shown that the decentralization of the cooling system has a high potential towards a better thermal behavior and a lower energy consumption of the machine tool. The simulation results show a more stable temperature profile of the components as well as a lower energy consumption of the cooling system.

Keywords: Fluidic system, Machine tools, Simulation, Cooling system, Thermo-elastic deformation, Energy consumption

1 Introduction

Besides increasing the productivity, the demand for a high accuracy of the workpieces and improved energy efficiency of the production processes also increases. The thermo-elastic characteristics of machine tools are strongly controlled by the fluidic systems such as cooling system. Typical fluidic systems in machine tools are the cooling system, the cooling lubricant system, the lubrication system, and the hydraulic system. On the one hand, fluidic systems (cooling, cooling lubricant and lubrication system) allow heat dissipation from the overall machine tool structure as well as the main components in order to achieve lower temperature changes and to homogenize the temperature distribution. On the other hand, fluidic systems themselves are essential energy consumers and, therefore, a significant heat source within the machine tool. Previous studies were carried out in [1, 2, 3] to analyze and determine the energy consumption and the energy distribution at the machine tools. However, these focus on decreasing the energy consumption of the components of the machine tools through constructive measures as well as developing a shutdown control of components during waiting times. The thermal behavior and the effectivity of the fluidic systems, especially the cooling system has not yet been described in detail. Therefore, a detailed analysis of the existing cooling system structures and their thermal behavior is necessary to increase the efficiency of the machine tools and provide a uniform temperature distribution. A well-designed fluidic system should therefore

improve the accuracy while at the same time being more energy-efficient.

The main goal of this work is to analyze the thermal behavior of the cooling system and its subsystems for two different processes, idle and manufacturing process. This investigation will help to obtain information concerning the efficiency of the cooling system. This makes it possible to derive new optimization approaches, such as a decentralization of the system structure. This allows to improve the thermal behavior of the cooling system by providing a stable temperature profile of the components and reducing the energy consumption of the cooling system.

Chapter 2 gives an overview of the fluidic system with the special focus on the cooling system. Here, the status quo analysis of the cooling system for an idle and a manufacturing process as well as the modeling approach for the simulation are shown. In chapter 3 the decentralization concept of the system structure and its potential against the current system structure is presented.

2 Status quo analysis of the fluidic system

The selected and experimentally analyzed demonstrator machine in Figure 1, type Scharmann DBF630, has three linear feed axes with ball screw drive (X, Y, Z) and one rotary feed axis (B). The additional U axis is used only for the turning process and is inactive during the drilling or milling processes. The spindle of DBF630 is a gear spindle with two gear steps. In gear step 1, the spindle rotation speed ranges to 1200 min-1, and the transmission ration is i1=8.2080. In this step, a high cutting performance due to high torque of 1700 Nm could be applied. In gear step 2, the spindle rotation speed ranges to 3500 min-1, the transmission ration is i2=1.5. So the spindle speed range can be varied by the transmission ratio and by motor through the frequency converter. The overall driving power of the machine is 35 kW [4].

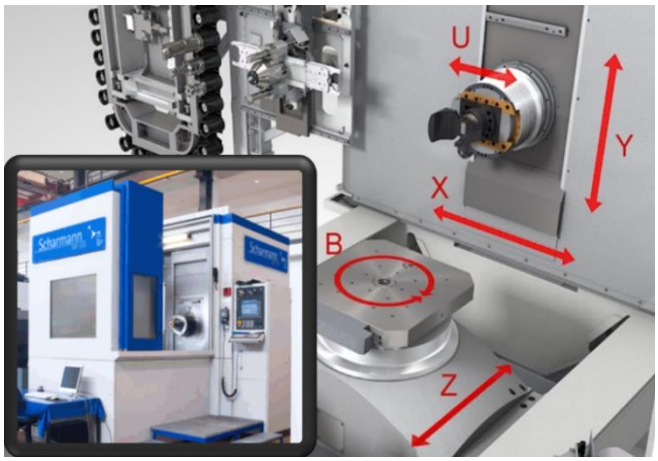

Figure 1: Schematic representation of axes configuration of DBF630 [6]

Detailed information about the demonstration machine and the function of their fluidic systems can be found in [5, 6]. As mentioned previously, the fluidic system in machine tools are divided into cooling, hydraulic, lubrication and cooling lubricant system. Figure 2 shows the main fluidic systems of the demonstration machine DBF630.

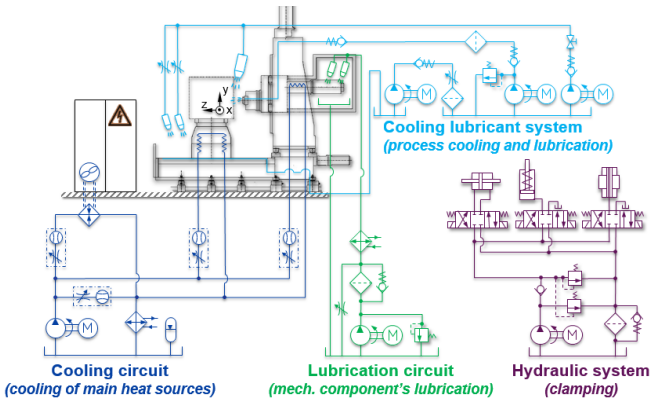

Figure 2: Main fluidic system of DBF630 [5]

2.1 Status quo analysis of the cooling system

As shown in Figure 3, the cooling system consists of three subsystems: electrical cabinet 6, rotary table 4, and main drive 7. A fixed displacement pump 14 supplies the cooling medium with a flow rate of 40 l/min at a pressure level of 5.2 bar according to the machine documentation. As cooling medium, a mixture of water and at least 20 % Antifrogen® is used. The rotary table 4 and the main drive 7 are cooled directly by the cooling medium that flows through integrated cooling channels. The cooling of the electrical cabinet takes place via an air heat exchanger 12. The cooling unit 13 in DBF630 is integrated directly into the return flow side and cools down the heated fluid to a set temperature. Its functional principle is a two-point temperature control similar to that of refrigerators. The cooling unit is switched on as soon as the temperature exceeds the upper limit of the set temperature, and is switched off when the cooling medium is cooled to the lower set temperature.

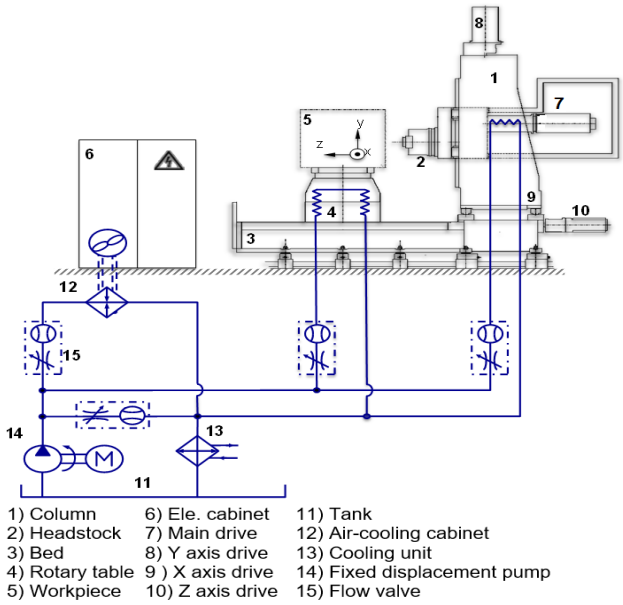

Figure 3: Cooling system of DBF630

In order to determine the thermal behavior as well as the energy consumption of the machine and of the individual subsystems, experimental machine measurements were carried out. Additional temperature sensors (thermocouples type T class 1) and flow sensors were installed. For the investigation of DBF630, four phases were chosen: warm up process, idle process, setup process, and manufacturing process. The results of the idle and the manufacturing process are shown in this paper. The idle process of the DBF630, see Figure 4, is based on the ISO 230-3 [7], where typical load cycles are considered. Referring to the idle process of DBF630 in Figure 4, at the beginning, the main drive accelerates several times to its maximum speed of 3500 min^{-1} and decelerates again. Afterwards, the rotary table rotates with its maximum rotational speed for approx. 10 s. Following this, the linear axes X, Y and Z are moved.

In the production process, several steel blocks (S235 JR) were face-milled with two different tools. The tool-specific characteristics and the resulting cutting conditions are shown in Figure 5.

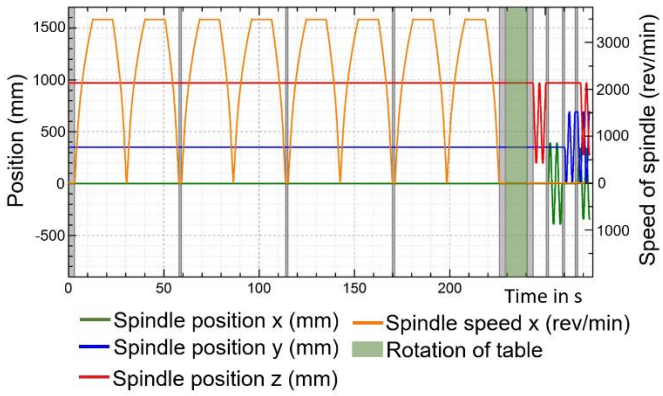

Figure 4: Idle process of DBF [4]

	Tool 1 R390-32T16-11M	Tool 2 R390-080Q27-17M
Cutter diameter	32 mm	63 mm
Cutting depth	2 mm	4 mm
Speed	2100 min^{-1}	1100 min^{-1}
Feed rate	630 mm/min	660 mm/min
Teeth number	3	6
Coolant supply	Internal, external	External

Figure 5: Cutting tools used for manufacturing process [4]

Due to the two-point temperature control of the cooling unit, all temperature profiles of the idle process can be divided into three phases: in phase 1 and 3, the cooling unit is off whereas it is being activated in phase 2. Figure 6 shows the temperature of the cooling medium at the inlet side and the outlet side of the electrical cabinet, the rotary table, the main drive and tank. At the electrical cabinet and the rotary table, the temperature difference between the outlet and the inlet is about -1 K, so the cooling medium is cooled while the components are warmed up. Only the main drive is cooled actively during all phases. Here, the outlet temperature of the cooling medium is higher (ΔT=1.5 K) than the inlet temperature.

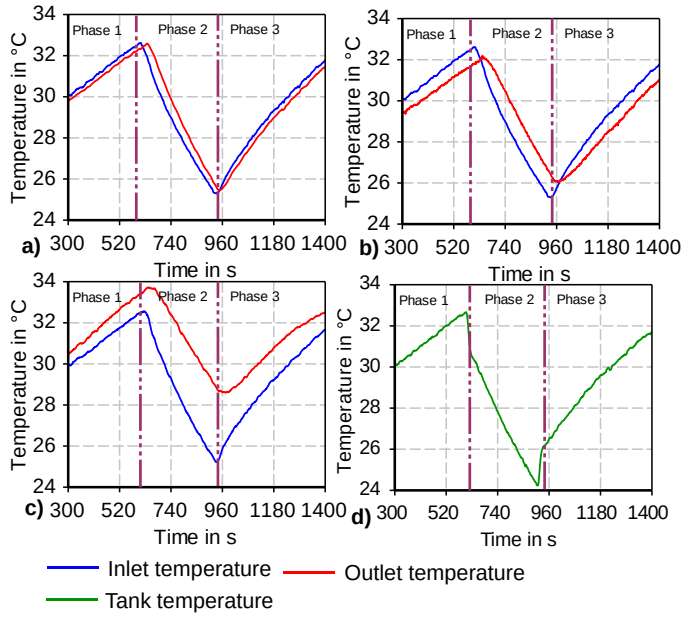

Figure 6: Temperature characteristics in the idle process a) Electrical cabinet b) Rotary table c) Main drive d) Tank

With the aid of the measured temperatures T and volume flow $\dot{m}$, the heat flow $\dot{Q}$ and the thermal energy E of the electrical cabinet, the rotary table and the main drive (spindle) are calculated as follows:

$$\dot{Q} = P_{th} = \dot{m} \cdot C_{fluid} \cdot \Delta T + \frac{1}{\rho} \cdot \Delta P \qquad (1)$$

$$E = \int_{t1}^{t2} P_{th} dt \qquad (2)$$

Figure 7 and Table 1 depict the heat flow and the thermal energy in the idle process. In phases 1 and 3, the generated heat of the spindle is dissipated by the cooling medium. However, the electrical cabinet and the rotary table are heated by the cooling medium. A clear difference is recognized when the cooling unit is switched on in phase 2 between t_{on}= 600 s and t_{off} = 900 s.

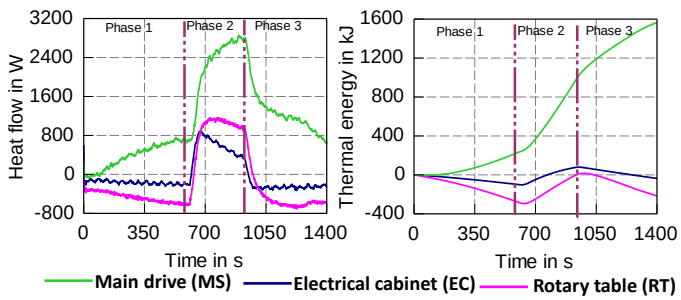

Figure 7: Heat flow and thermal energy in the idle process

When the cooling liquid is actively cooled, the heat flow increases and all three components transfer thermal energy to the cooling system and are thus cooled.

Table 1: Thermal energy of electrical cabinet (EC), rotary table (RT) and main drive (MS) during idle process

	ΔQ_{EC} *in kJ*	ΔQ_{RT} *in kJ*	ΔQ_{MS} *in kJ*
Phase 1	-99	-280	230
Phase 2	165	248	656
Phase 3	-101	-183	651

These three different cooling phases can also be found in the temperature profile of the manufacturing process, see Figure 8. In phases 1 and 3, the cooling unit is activated while in phase 2 it is turned off. The temperature development in the electrical cabinet and rotary table is similar to that in the idle process. The temperature difference between the outlet and the inlet at the electrical cabinet and the rotary table for phase 2 is about -0.3 K to -1 K, so the cooling medium is cooled while the components are warmed up. Only the main drive is cooled actively during all phases, the maximum temperature difference between outlet and inlet is about 3.3 K.

With the aid of equation (1) and (2), the thermal energy of electrical cabinet, rotary table and main drive for the manufacturing process are calculated. The cooling unit is switched on in phase 1 (from 0 s to 95 s) and in phase 3 (from 820 s to 1100 s). Figure 9 and Table 2 give an overview concerning the heat input during the manufacturing process.

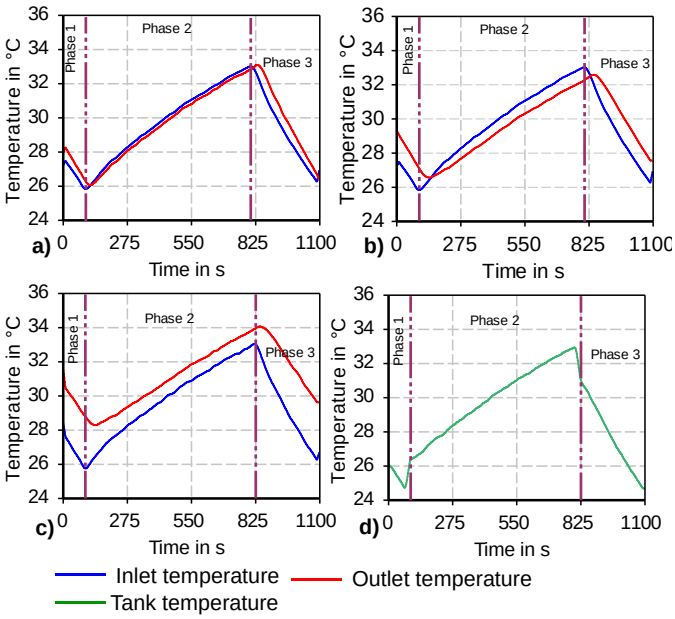

Figure 8: Temperature characteristics in the manufacturing process a) Electrical cabinet b) Rotary table c) Main drive d) Tank

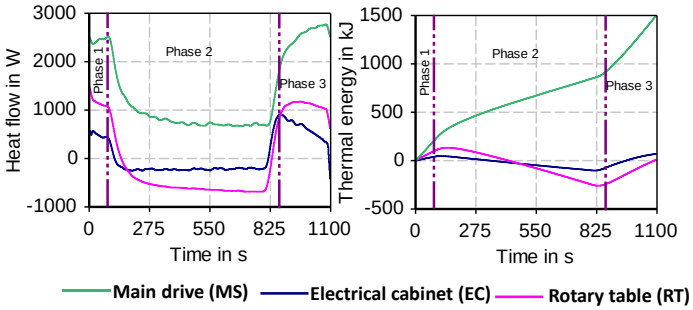

Figure 9: Heat flow and thermal energy in the manufacturing process

Table 2: Thermal energy of electrical cabinet (EC), rotary table (RT) and main drive (MS) during manufacturing process

	ΔQ_{EC} *in kJ*	ΔQ_{RT} *in kJ*	ΔQ_{MS} *in kJ*
Phase 1	44	110	233
Phase 2	-58	-147	627
Phase 3	-32	-248	642

2.2 Model development and simulation

Simulation models offer a good and flexible way to investigate the behavior of a system. In order to be able to derive reliable statements from simulation models, it is necessary to analyze the behavior of the real system. The aim of the modelling is to describe the real system with appropriate mathematical and physical approaches [8]. The rules of Kirchhoff's circuit laws, Kirchhoff's node rule, and Kirchhoff's loop rule in electrical engineering and the laws for series and parallel connection of resistance can be applied to the hydraulic and thermodynamic domain. The calculation of the thermal and hydraulic resistances R_{th} and R_{hy} between two nodes is based on the following relationships [9, tab. 1]:

$$R_{th} = \frac{\Delta T}{\dot{Q}} \tag{3}$$

$$R_{hy} = \frac{\Delta p}{\dot{V}} \tag{4}$$

Regarding to node rule of Kirchhoff:

$$T = \frac{1}{C_{th}} \int \sum_{i=1}^{n} \dot{Q}_i \cdot dt \tag{5}$$

$$p = \frac{1}{C_{hy}} \int \sum_{i=1}^{n} \dot{V}_i \cdot dt \tag{6}$$

Figure 10 illustrates a basic thermo-hydraulic network model. The fluid volume or the mass properties are concentrated in the junction points. These nodes display the hydraulic and thermal capacities. Thermal and hydraulic resistors connect the nodes to each other.

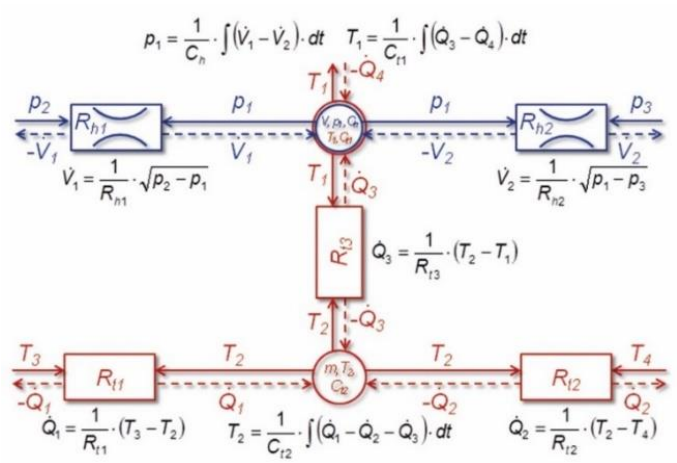

Figure 10: Basic description of the thermo-hydraulic network model [10]

Additionally, the convective heat transport through the cooling medium in the pipes is taken into account. The heat transfer coefficients are determined by the following equations [11]:

$$Re = \frac{D_H \cdot \dot{V}}{\nu \cdot A} \tag{7}$$

$$Pr = \frac{C_{fluid} \cdot \rho \cdot \nu}{\lambda_{fluid}} \tag{8}$$

$$Nu = 0.0235 \cdot (Re^{0.8} - 230) \cdot (1.8 \cdot Pr^{0.3} - 0.8) \cdot [1 + \left(\frac{d_i}{l}\right)^{\frac{2}{3}}] \tag{9}$$

$$\alpha_{con.} = \frac{\lambda_{fluid} \cdot \mathrm{Nu}}{d_i} \tag{10}$$

A Simulation model of the cooling system was developed based on the model description as well as the machine documents. The cooling system consists mainly of a pump, flow control valves, hydraulic pipes, a cooling unit and the component (electrical cabinet, rotary table, and main drive) as heat source. In the simulation, each hydraulic pipe is modelled by a hydraulic volume and a hydraulic resistance. The geometrical parameters (length, inner and outer diameter) of the pipes are taken directly from the machine documentation. Moreover, the heat transfer between the pipes and the environment is taken into account. Figure 11 shows the model structure of the cooling system implemented in the simulation.

For the model-based study of the system, a domain-crossing system simulation with SimulationX (ESI ITI GmbH) was carried out. Figure 12 and Figure 13 show a direct comparison of the simulation and the measurement of the idle and the manufacturing process. The simulation model of the cooling system shows a high accuracy of the thermal and hydraulic quantities of the considered components. The simulation model could therefore be validated and will be used for further studies such as a sensitivity analyses [12].

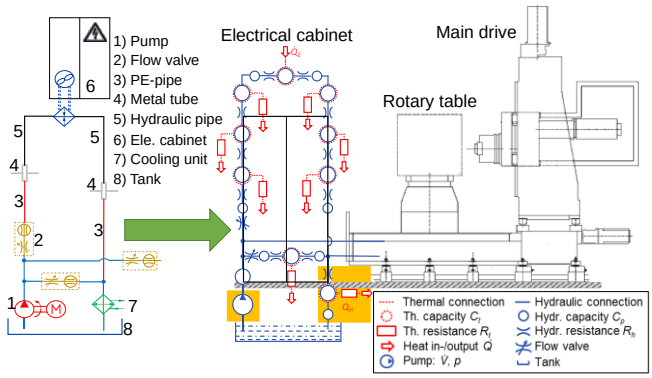

Figure 11: Model structure of cooling system for the idle and manufacturing process

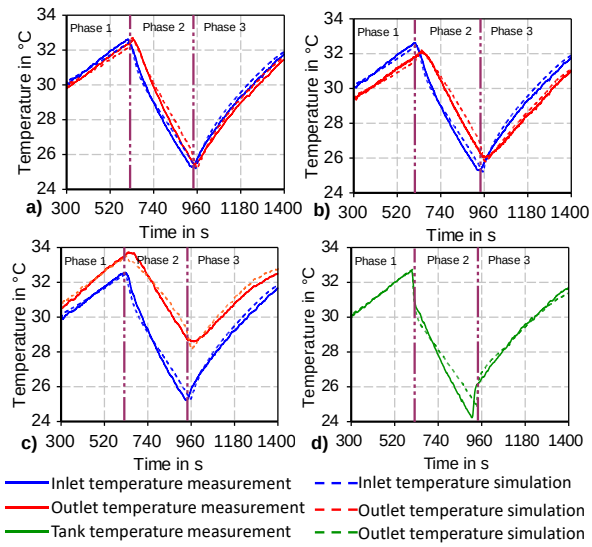

Figure 12: Comparison of temperature development simulation and measurement in the idle process a) Electrical cabinet b) Rotary table c) Main drive d) Tank

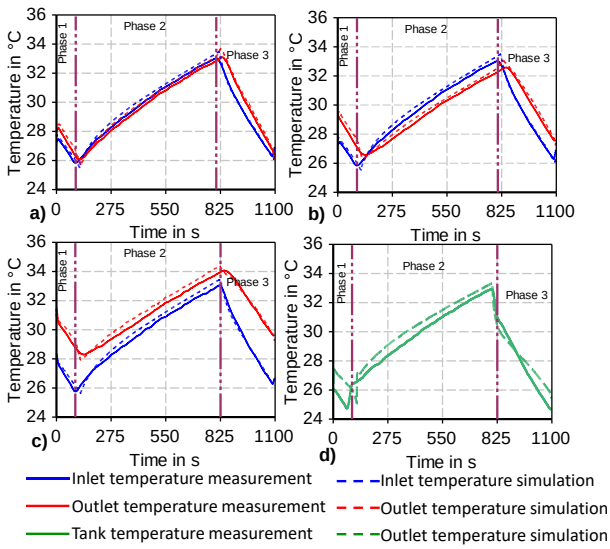

Figure 13: Comparison of temperature development simulation and measurement in the manufacturing process a) Electrical cabinet b) Rotary table c) Main drive d) Tank

3 Potential analysis of decentralized system structure

The investigation of two demonstration machines shows that the fluidic systems together require in the idle process 44 % (DBF630) and 51 % (DMU80) of the total energy consumption of the machine tool [5, 6]. Therefore, there is a major potential for reducing the energy demand and increasing the efficiency of machine tools by improving the function of the fluidic systems. Furthermore, the investigation of the DBF630 in the idle and in the manufacturing process depicts that sufficient cooling capacity exists but that the cooling is insufficiently adjusted to the process and to the individual demand of the machine components. In order to address this deficit, it is necessary to think about new concepts and new structures of fluidic systems. Such an approach is the decentralization of the system structure. Figure 14 displays the decentralization of the cooling system at different individualization stages [13].

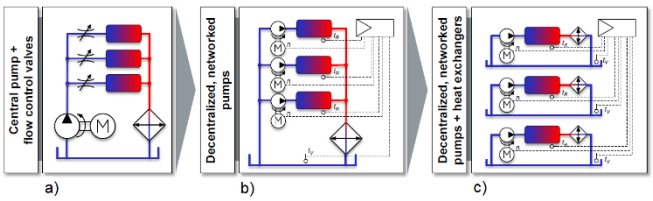

Figure 14: Decentralization steps of system structure a) Current structure b) Distributed pump, stage I c) Distributed pump and cooling unit, stage II

Decentralized, independent systems allow an adequate and component-specific supply and thus a targeted temperature control. The studied variants for optimizing the cooling system are evaluated according to the following criteria: stable temperature profile in the components, low pump pressure (short hydraulic pipes), and low energy requirements. As previously shown, in a centralized cooling system, a fixed displacement pump delivers a constant volume flow to the system. The volume flow does not correspond to the individual requirement and to the temperature development of the respective component. Therefore, the cooling medium is cooled while the components are warmed up (negative heat flow). Another deficit is the two-point temperature control of the cooling unit. This controls the mixing temperature in the tank and not the component temperature.

Optimization according to stage I

Figure 15 shows the first optimization step, stage I, applied to the DBF630. The components are cooled with individual pumps that are connected to a common tank and cooling unit. This system design does not require a flow control valve to control the volume flow to the components. The control of the cooling system compares the actual and set temperature of the individual components and on this basis, adjusts the speed-controlled pumps. Therefore, each pump delivers a different, demand-oriented cooling volume flow. If the temperature development in the component does not exceed predefined limits, the pump remains inactive. The cooling unit remains in the two-point temperature control and refers to the mixing temperature of all components. The temperature signal ϑ_{actual} corresponds to the average component temperature. The temperature detection is carried out via sensors in the components. For this purpose, a suitable concept for sensor integration is necessary.

In the decentralized simulation model, three set temperatures were defined for the components, for the electrical cabinet ϑ_{set} = 26 °C, for the rotary table ϑ_{set}=27 °C and for the motor spindle ϑ_{set}=28 °C. This individual temperature control is not possible with the current system structure. In addition, an average equivalent heat flow was determined from the calculated heat flows in the idle process for each individual component. It was 1500 W for the main drive and 150 W for the electrical cabinet and rotary table. Moreover, only static operating points of the cooling system were considered in the simulation, so that the thermal capacity of the components was not required.

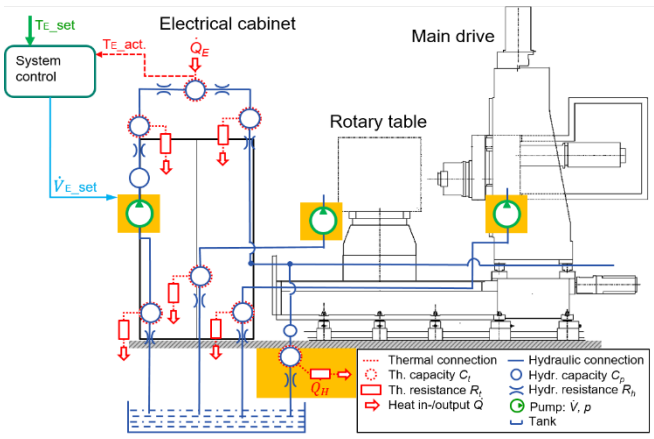

Figure 15: Decentralization of the cooling system structure according to stage I

Figure 16 shows the simulation results of the fluid outlet temperature development in the electrical cabinet, rotary table and main drive as well as the required cooling volume flow in the decentralized system in comparison of the central system. Figure 16 a - c represent the direct comparison of the fluid outlet temperature between central and decentralized system. The fluid outlet temperature of the component remains constant at the set temperature (26 °C, 27 °C, 28 °C) in the decentralized system despite an increased power loss. In the central system, the fluid outlet temperature increases with rising power losses, therefore the actual temperature of the fluid is dependent on the heat input to the component. With a closer look into the volume flow characteristics of the pumps, it should be noted that the cooling medium flow in the decentralized system increases with rising power losses, in contrast to the current system, were the volume flow is constant. In example of the machine tools main drive (motor spindle), the pump in the decentralized system delivers the cooling medium flow based on the components temperature, depending on the current power loss. The delivered flow rate varies between 8 l/min to 16 l/min.

As shown in Figure 16 d, the volume flow control is a way to design the system in a more energy-efficient way based on each individual components demand. For the simulation, it is

assumed that the pumps are located next to the components, i.e. shorter pipe lengths were taken into account. For this reason, the pump pressure is also very low.

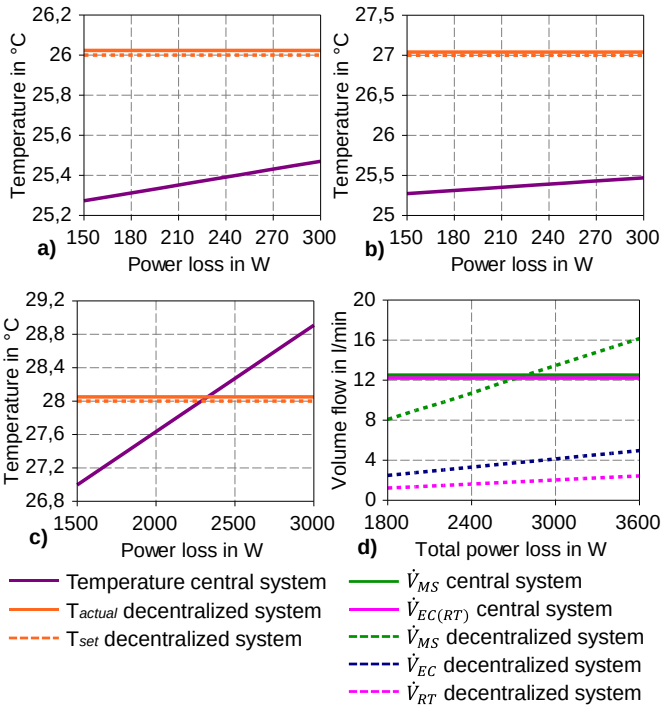

Figure 16: Simulation results fluid outlet temperature of component in the decentralized system in comparison of central system a) Electrical cabinet b) Rotary table c) Main drive d) volume flow profile

Figure 17 illustrates the total hydraulic power of the pumps in the central and decentralized system for different power losses. The total hydraulic power at maximal power loss of the pumps in the decentralized system is 80 W. The hydraulic power of the fixed pump in the central system is approx. 370 W (40 l/min at 5.5 bar), hence, a significant energy saving is possible. The new functional principle of the pump is significantly more energy-efficient compared to the current state of the DBF630 with a continuous flow volume.

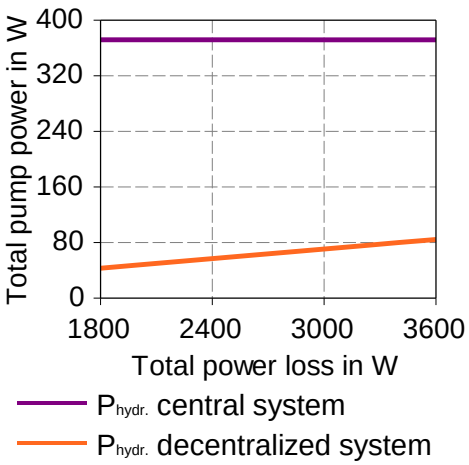

Figure 17: Pump performance, decentralization stage I

4 Summary

In order to increase the productivity and manufacturing accuracy of the workpieces with a simultaneous decrease of the energy consumption, the minimization of thermo-elastic deformation and, consequently, a minimization of the TCP displacement is necessary. The warmed-up parts or components need to be cooled, therefore, fluidic systems such as cooling system are an essential element for controlling the thermo-elastic characteristics of machine tools.

The main goal of the paper was to analyze the thermal behavior and improve the current system structure of the cooling system in a demonstrator machine tool.

Firstly, the authors showed the existing fluidic system of the demonstrator machine DBF630 and described in detail its cooling system. With aid of experimental investigation and machine documents a network-based model of the cooling system for two processes, the idle and manufacturing process, was developed and validated against the measured data. The validated model was used for further studies such as decentralization of supply unit.

As a result, the investigation of the cooling system of the DBF630 in the idle and in the manufacturing process shows that sufficient cooling capacity is available but that the cooling is insufficiently adjusted to the process and to the individual demand of the machine components (negative heat flow in Figure 7 and Figure 9). Furthermore, independent systems and demand-oriented component cooling was studied with the help of a simulation model. The delivered coolant flow is controlled individually according to the temperature development in the component. The simulation results have shown that a stable fluid outlet temperature of the components compared to the initial state can be achieved. Moreover, the demand-oriented fluid supply of the pumps leads to a successful improvement of the machine tools energy efficiency. This results in a reduction of the required total pump power for the DBF630 from 370 W to 80 W.

Acknowledgements

The presented research activities are part of the project “Thermo-energetic description of fluid systems” (Ref. No. CRC/TR 96, A04). The authors would like to thank the German Research Foundation (DFG) for the financial support.

Funded by DFG Deutsche Forschungsgemeinschaft

Nomenclature

Designation	Denotation	Unit
A	Area of pipe	m²
C_{fluid}	Specific heat capacity at constant pressure	J/kg·K
C_{th}	Thermal capacity	J/K
C_{hy}	Hydraulic capacity	m³/Pa.
D_H	Hydraulic diameter	m
di	Inner diameter	m
E	Energy	J
l	Length of pipe	m
$\dot{m}$	Mass flow	Kg/s
Nu	Nusselt number	-
Re	Reynolds number	-
p	Pressure	Pa.
Δp	Outlet/ Inlet pressure difference	Pa.
Pr	Prandtl number	-
$\dot{Q}, P_{th}$	Heat flow	W
t	Time	s
Q_{EC}, Q_{RT}, Q_{MS}	Thermal energy of the electrical cabinet, rotary table, main drive	J
$\dot{V}$	Volume flow	m³/s
ϑ	Temperature	°C
α	Heat transfer coefficient	W/m².K
T	Temperature	K
ΔT	Outlet/ Inlet temp. difference	K
λ_{fluid}	Thermal conductivity	W/m.K
ν	Kinematic viscosity	m²/s
ρ	Density	Kg/m³

References

[1] B. Denkena and T. Graber. NCplus Prozess- und wertschöpfungsorientiert gesteuerte Werkzeugmaschine. PZH Verlag, 2013

[2] C. Brecher. Effizienzsteigerung von Werkzeugmaschinen durch Optimierung der Technologien zum Komponentenbetrieb-EWOTeK. Apprimus Verlag, Aachen, 2012.

[3] U. Götze, HJ. Koriath, A. Kolesnikov, R. Lindner, J. Paetzold and C. Scheffler. Energetische Bilanzierung und Bewertung von Werkzeugmaschinen. *Tagungsband Energieeffiziente Produkt- und Prozessinnovationen in der Produktionstechnik eniPROD*. Chemnitz, 2010.

[4] J. Weber and J. Weber. Thermo-Energetic Analysis of the Fluidic Cooling Systems in Tooling Machines. *9th International Fluid Power Conference, Aachen*, March 24-26, 2014.

[5] J. Weber and J. Weber. Thermo-energetic Modelling of Fluid Power Systems. In: Großmann K, editor. *Thermo-energetic Design of Machine Tools*. Heidelberg Springer-Verlag; 2015. p. 49-60.

[6] L. Shabi, J. Weber and J. Weber. Analysis of the Energy Consumption of Fluidic Systems in Machine Tools. *The 50th CIRP Conference on Manufacturing Systems, Taiwan*, May 3th - 5th, 2017

[7] International standard ISO 230-3. Test code for machine tools, part 3: Determination of thermal effects. Second edition 2007-08-15.

[8] D. Abel and A. Bollig. Rapid Control Prototyping-Methoden und Anwendungen. Springer Verlag Berlin Heidelberg 2006. s. 77-80

[9] J. Weber and J. Weber. Thermo-energetic analysis and simulation of the fluidic cooling system of motorized high-speed spindles. *SICFP2013, Linköping, Sweden* June 3th-5th ,2013

[10] J. Weber and J. Weber. Analyse und Simulation der fluidischen Kühlung einer einfach gewendelten Motorspindelkühlhülse. O+P Journal 3/2013

[11] E.Doering, H.Schedwill and M. Delhi. Grundlagen der Thermodynamik.7 Auflage, Springer Verlag Vieweg 2012

[12] L. Shabi, J. Weber and J. Weber. Investigation of Fluidic Systems in Machine Tools. *22nd International Conference on Hydraulics, Pneumatics, Tools, Sealing Elements, Fine Mechanics, Specific Electronic Equipment & Mechatronics (HERVEX 2016)*, November 9-11, Romania, 2016

[13]. Weber and J. Weber. Thermo-Energetic Analysis of the Fluidic Systems in Cutting Ma-chines. *10th International Fluid Power Conference, Dresden*, March 08-10, 2016.

OPTIMAL CONTROL FOR HYDRAULIC SYSTEM WITH SEPARATE METER-IN AND SEPARATE METER-OUT

Gerhard Rath and Emil Zaev*

University of Leoben, Chair of Automation, Leoben, Austria
*SS. Cyril and Methodius University of Skopje, Faculty of Mechanical Engineering, Automation Department, Skopje, Macedonia
E-mail: gerhard.rath@unileoben.ac.at, emil.zaev@mf.edu.mk

Abstract

Individual meter-in and meter-out proportional control of hydraulic cylinders allow more flexible strategies how to handle a payload while optimising certain aspects of the motion. An optimal control approach based on the Hamiltonian is used to plan a motion path for a separate meter-in and separate meter-out system. One goal is to avoid oscillations at the end of the motion in the sense of active vibration damping. With the mathematical model presented, it is possible to include the cylinder pressures into the optimisation goals. Not only the the final values for position and speed of the load can be acquired, but also desired values for the pressures at the end of the motion. Maintaining a minimum pressure level is important in order to avoid cavitation and to keep the stiffness of the system. The course of the pressures follows from the design of the motion and will reach the desired values in an open loop control. In order to estimate the computing effort, the algorithm was tested on three platforms. One of those is an ARM-based hardware that represents the computing power of modern embedded systems, to demonstrate that an implementation on such system is possible. Several motion experiments were carried out in simulation to study the behaviour and to discuss application issues.
Keywords: Hydraulic actuator, optimal control, separate meter-in/separate meter-out

1 Introduction

In standard hydraulic systems with proportional valves speed is controlled by opening or closing two orifices on a single spool. Careful design of load-sensing and pressure compensation is necessary for a good performance [1]. Introduction of a second valve in separate meter-in/separate meter-out controlled systems (SMISMO) gives possibility to control one additional variable, usually back actuator pressure independent from speed of the actuator [2] [3] [4]. This possibility to control the back pressure is especially useful when moving high inertia loads fast, since in this case, stopping the load using only one valve without having oscillation is extremely difficult [5] [6]. In those cases SMISMO has the potential to make the hydraulic system stiffer, to increase the back pressure, and with this to obtain less vibrations [7] [8].

Motion of payloads needs energy, causes oscillations and wears mechanical systems. For this reasons, optimisation methods are of increasing importance to minimise or maximise some physical property. In vibration damping, optimisation is applied in order to have a high energy dissipation [9]. Or, the motion path of a manipulator is planned so, that stress is equally distributed over the links [10]. Effort is done to integrate optimal control in the function of a hydraulic valve [11]. Since hydraulic systems are highly nonlinear, it is also evident to consider such behaviour for design of optimal controllers [12].

Several approaches are used for optimisation. A common technique is input shaping, that forms the signal sent to the servo-valve in order to suppress oscillations. Such shaping filters can be applied to the input of a drive system [13], to the input of a control circuit [14], or within a loop between controller and system [15]. The latter presents an application in a hydraulic system. Another approach is the design of linear-quadratic regulators (LQR) based on the solution of the Matrix Ricatti differential equation [11] [12]. Optimisation based on the Hamiltonian (e.g. in [9]) is used for the actual work.

Recent development of electronic hardware and software allows an increasing integration of complex algorithms in industrial control. Modern hydraulic valves offer simple integration of separate meter-in and separate meter-out control with various operation modes [16]. This makes optimal control techniques more appealing for practical application in servo-hydraulic systems.

In this work a Hamiltonian-based approach is presented, which offers movement of the high inertia loads without oscillations and open-loop control of speed and position of the

cylinder. Additionally, the pressures in the actuator are included in the design. Firstly, a mathematical model of a servo-hydraulic drive is derived in state-space representation as a linear time-invariant (LTI) system. Then the optimisation goal is described in the form of a functional. Using the Hamiltonian, the differential equation system, which delivers the optimal control, is found. The numerical solution requires finding the initial conditions first, before the system can be solved. This is demonstrated with an example. Then implementation and numerical effort are considered in order to estimate calculation times. Finally, in section six, some case studies are shown to demonstrate the correctness of the approach and to allow discussion.

2 Model of the System

2.1 Mechanical System

The mechanical system consists of a big mass moved with a lever rotating around the point O (fig. 1). For modelling purposes the mass of the system is concentrated in a single point with a mass of M, the lever of the length L is regarded to be massless. A hydraulic cylinder applies the force F to the small lever of the length l. For small motions around the actual point the effective mass is

$$m = \left(\frac{L}{l}\right)^2 M. \tag{1}$$

The motion is carried out horizontally, hence no force of gravity is regarded.

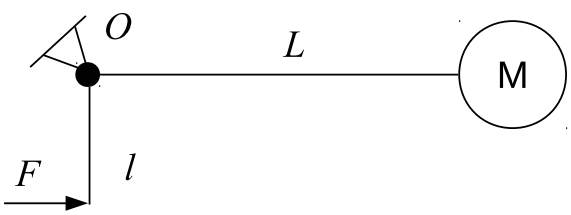

Figure 1: Sketch of the mechanical system

2.2 Hydraulic System

The main parts of the hydraulic system in fig. 2 are a double acting, single rod cylinder and two proportional valves that allow individual control of the oil flows q_A and q_B. Auxiliary components, like load-sensing and pressure compensation are not displayed in the figure.

2.3 Mathematical Model

If the position of the mass m in fig. 2 is designated as x_1, the motion equation follows with

$$m\ddot{x}_1(t) = p_A(t)\cdot A_A - p_B(t)\cdot A_B - b\cdot\dot{x}_1(t). \tag{2}$$

In a system with hydraulic actuators, friction consists of several components. The motion of the payload contributes, also the motion of the steel structure. Oil flow over an orifice depends on the pressure and hence causes additional damping.

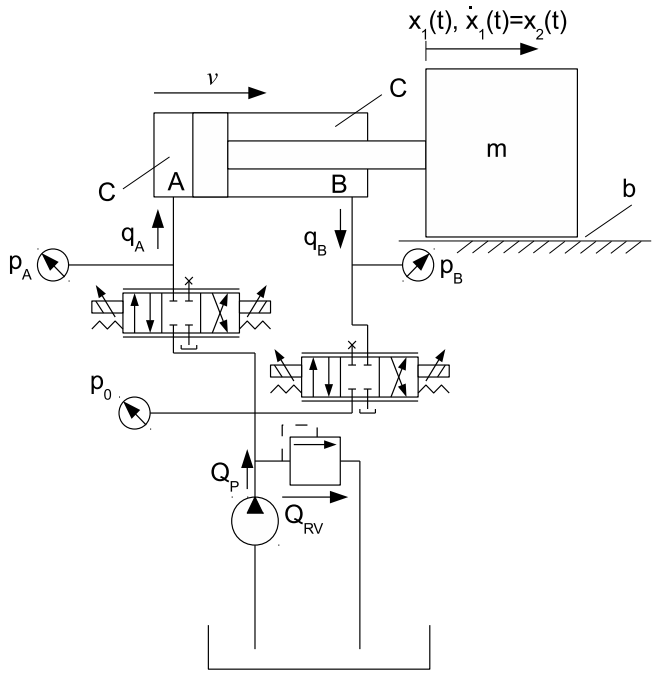

Figure 2: Hydraulic system

Finally, the sealing in the cylinder offers a highly nonlinear friction behaviour. A comprehensive mathematical model of friction includes Coulomb and viscous friction, stiction and the Stribeck effect [17]. In the actual machine, the main contribution is coming from a rotating load that performs a cutting process. It is assumed to be viscous with a coefficient of b in the dynamic model eq. (2).

The motion is controlled with two independent valves. The electronic control provides several operation modes [16], e.g. to establish constant oil flows automatically corrected with the help of integrated pressure sensors. This allows direct control of the oil flows, hence we use the oil flows q_A and q_B as inputs, which change the pressures in the cylinder

$$\begin{aligned} \dot{p}_A(t) &= \tfrac{1}{C_A}\left(q_A(t) - A_A\cdot\dot{x}_1(t)\right) \\ \dot{p}_B(t) &= \tfrac{1}{C_B}\left(q_B(t) + A_B\cdot\dot{x}_1(t)\right). \end{aligned} \tag{3}$$

The hydraulic capacity can be calculated for a volume V with

$$C = \frac{V}{E}, \tag{4}$$

where E is the bulk modulus of the fluid. The hydraulic capacities C_A and C_B depend on the volumes of the chambers and hence on the position of the piston, which results in a nonlinear system. The assumption of a constant capacity means, that the considerations are valid only for small position changes. The compliance of the tubes between valves and cylinder also contribute to the capacity. For simplification, we assume both chambers to have the same values, hence $C_A = C_B = C$.

If a new variable x_2 is introduced for the speed of the system

$$\dot{x}_1 = x_2, \tag{5}$$

the system can be written in its state-space formulation

$$\begin{pmatrix} \dot{x}_1 \\ \dot{x}_2 \\ \dot{p}_A \\ \dot{p}_B \end{pmatrix} = \begin{pmatrix} 0 & 1 & 0 & 0 \\ 0 & -\frac{b}{m} & \frac{A_A}{m} & -\frac{A_B}{m} \\ 0 & -\frac{A_A}{C} & 0 & 0 \\ 0 & \frac{A_B}{C} & 0 & 0 \end{pmatrix} \cdot \begin{pmatrix} x_1 \\ x_2 \\ p_A \\ p_B \end{pmatrix} + \\ + \begin{pmatrix} 0 & 0 \\ 0 & 0 \\ \frac{1}{C} & 0 \\ 0 & \frac{1}{C} \end{pmatrix} \cdot \begin{pmatrix} q_A \\ q_B \end{pmatrix}. \tag{6}$$

3 Optimal Control

The state-space representation can be used to design a digital controller according to methods found in [18]. Here an optimal control approach is chosen based on variational calculus using the Hamiltonian [19].

If the quality criterion is selected to be

$$J(x,q) = \frac{1}{2}\int \left(\mathrm{x}^{\mathrm{T}}\mathrm{Q}\mathrm{x} + \mathrm{q}^{\mathrm{T}}\mathrm{R}\mathrm{q}\right) \cdot \mathrm{d}t, \tag{7}$$

the matrix Q rates the state variables during the motion, and the matrix R regards the input variables, which are the oil flows in and out from the cylinder chambers. The matrix R rates the sum of the squares of the flows q_a and q_b during the motion.

Usually the functional is used to minimise energy consumption, but in the case of hydraulic systems, the power delivered by the supply is not to be described with linear functions. Anyway, it is a good idea to minimise the square of the oil flows, since it is related to the opening of the valve orifices. In the similar way, the square of the motion variables (rated with the matrix Q) minimises elongations and oscillations in the system.

Now the Hamiltonian [19] can be formulated as

$$\mathrm{H} = -\frac{1}{2}\left(\mathrm{x}^{\mathrm{T}}\mathrm{Q}\mathrm{x} + \mathrm{q}^{\mathrm{T}}\mathrm{R}\mathrm{q}\right) + \psi^T\left(\mathrm{A}\mathrm{x} + \mathrm{B}\mathrm{q}\right). \tag{8}$$

Moving on the optimal path,

$$\frac{\partial \mathrm{H}}{\partial \mathrm{q}} = 0 \tag{9}$$

yields the control law

$$-2\mathrm{R}\mathrm{q} + \mathrm{B}^T\psi = 0 \tag{10}$$

and finally

$$\mathrm{q} = \frac{1}{2}\mathrm{R}^{-1}\mathrm{B}^T\psi. \tag{11}$$

The adjunct system ψ follows from the canonical equations with

$$\dot{\psi} = -\frac{\partial \mathrm{H}}{\partial \mathrm{x}} = 2\mathrm{Q}\mathrm{x} - \mathrm{A}^T\psi \tag{12}$$

and then

$$\dot{\mathrm{x}} = -\frac{\partial \mathrm{H}}{\partial \psi} = \mathrm{A}\mathrm{x} + \mathrm{B}\mathrm{q} = \mathrm{A}\mathrm{x} + \frac{1}{2}\mathrm{B}\mathrm{R}^{-1}\mathrm{B}^T\psi. \tag{13}$$

Putting Equations 12 and 13 together delivers the *canonical system*

$$\begin{pmatrix} \dot{\mathrm{x}} \\ \dot{\psi} \end{pmatrix} = \begin{pmatrix} \mathrm{A} & \frac{1}{2}\mathrm{B}\mathrm{R}^{-1}\mathrm{B}^T \\ \mathrm{Q} & -\mathrm{A}^T \end{pmatrix} \cdot \begin{pmatrix} \mathrm{x} \\ \psi \end{pmatrix} \tag{14}$$

The numerical solution of this system yields the controlled variable q, which is a vector of the input flows q_A and q_B, from the adjunct system ψ in eq. (11).

4 Numerical Solution

4.1 Initial Conditions

For solving the canonical system in eq. (14) the initial conditions of

$$\mathrm{x}(0) = \begin{pmatrix} x_1(0) & x_2(0) & p_A(0) & p_B(0) \end{pmatrix}^T \tag{15}$$

with a number of $n = 4$ are known. The system is eight by eight, the initial conditions

$$\psi(0) = \begin{pmatrix} \psi_1(0) & \psi_2(0) & \psi_3(0) & \psi_4(0) \end{pmatrix}^T \tag{16}$$

are still missing. With the final conditions

$$\mathrm{x}(t_f) = \begin{pmatrix} x_1(t_f) & x_2(t_f) & p_A(t_f) & p_B(t_f) \end{pmatrix}^T \tag{17}$$

the initial condition for ψ can be found. With the abbreviation

$$\mathrm{M} = \begin{pmatrix} \mathrm{A} & \frac{1}{2}\mathrm{B}\mathrm{R}^{-1}\mathrm{B}^T \\ \mathrm{Q} & -\mathrm{A}^T \end{pmatrix} \tag{18}$$

the canonical system eq.(14) turns to

$$\begin{pmatrix} \dot{\mathrm{x}} \\ \dot{\psi} \end{pmatrix} = \mathrm{M} \cdot \begin{pmatrix} \mathrm{x} \\ \psi \end{pmatrix}. \tag{19}$$

This system can be solved for the final target time t_f with the help of the exponential matrix and gives

$$\begin{pmatrix} \mathrm{x}(t_f) \\ \psi(t_f) \end{pmatrix} = e^{\mathrm{M}\cdot t_f} \cdot \begin{pmatrix} \mathrm{x}(0) \\ \psi(0) \end{pmatrix} \tag{20}$$

After partitioning the exponential matrix

$$e^{\mathrm{M}\cdot t_f} = \begin{pmatrix} \mathrm{S}_{11} & \mathrm{S}_{12} \\ \mathrm{S}_{21} & \mathrm{S}_{22} \end{pmatrix} \tag{21}$$

the initial conditions can be found with

$$\psi(0) = \mathrm{S}_{12}^{-1} \cdot \left(\mathrm{x}(t_f) - \mathrm{S}_{11} \cdot \mathrm{x}(0)\right). \tag{22}$$

4.2 Solution and Control

Now the canonical system eq. (14) can be solved as an standard initial value problem (IVP). Then, with the help of the control law eq. (11), the oil flows q_A and q_B follow, which should be used as controlled variables for the hydraulic system. The numerical solution of eq. (14) additionally yields a model of the physical system. It also contains the pressures as state variables. This information can be compared with sensor values of the real system and help to add some feedback correction for the nonlinear characteristics of the valves.

4.3 Application Example

The system parameters are cylinder areas of $A_A = 0.06\,\mathrm{m}^2$ and $A_B = 0.04\,\mathrm{m}^2$, a reduced mass of $m = 300\,000\,\mathrm{kg}$, the hydraulic capacity of one oil chamber $C = 10^{-11}\,\mathrm{m}^3\mathrm{Pa}^{-1}$. The viscous friction b was assumed to be zero to ensure, that all oscillation damping is done by the control algorithm.

Now the quality functional eq. (7) is established with the matrix

$$\mathrm{R} = \begin{pmatrix} 1 & 0 \\ 0 & 1 \end{pmatrix}, \tag{23}$$

which rates the squared size of the oils flows. Here q_A and q_B have the same weight.

The matrix Q describes the contribution of state variables to the functional eq. (7), which should be minimised. With

$$\mathrm{Q} = \begin{pmatrix} 0 & 0 & 0 & 0 \\ 0 & 0.002 & 0 & 0 \\ 0 & 0 & 0 & 0 \\ 0 & 0 & 0 & 0 \end{pmatrix} \tag{24}$$

the speed variable x_2 is rated. All state variables (the position x_1, the speed x_2, and the pressures p_A and p_B) have defined initial and end values. Taking the speed into the matrix Q leads to the damping of oscillations.

The initial parameters are a position $x_1(0) = 0\,\mathrm{m}$, an initial speed $x_2(0) = 0\,\mathrm{ms}^{-1}$ and the pressure $p_A(0) = 10\,\mathrm{bar}$. The dynamic and static force is initially zero, from this follows the initial value for p_B.

The target time for the motion is $t_f = 0.8\,\mathrm{s}$, the position should be $x_f = 0.01\,\mathrm{m}$. The pressure in chamber A at the end of the motion should be $p_A(t_f) = 50\,\mathrm{bar}$. The pressure in B follows from p_A, when no external load is present at the end position.

The simulation result in fig. 3 shows that the motion targets are accomplished. The load stands still, no force is applied, hence no oscillation remains, and the cylinder chambers have the desired pressure levels.

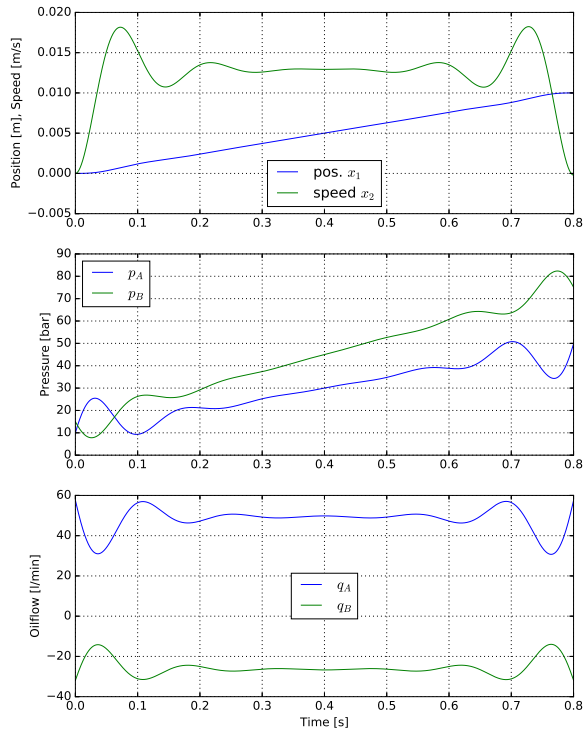

Figure 3: Variables during the motion

5 Implementation

5.1 Computing Procedure

The procedure to plan and to control a motion follows three steps.

5.1.1 Model Initialisation

At first eq. (18), which is the dynamic matrix of the canonical system, must be established. The matrix depends on the physical parameters of the system and will not change during the motion. When the load changes, for example, the matrix will be affected and the step has to be repeated.

5.1.2 Processing Boundary Conditions

The next task in planning the motion is to process the desired target values (maybe from operator input), the initial conditions (usually from sensors) and the final time. The planned final time of the motion t_f is required to find the exponential matrix for eq. (20), to partition it and to invert the partition S_{12} in eq. (22). With the boundary conditions of the state variables x, eq. (22) yields the initial values for the adjunct system ψ.

5.1.3 IVP solution

Now the initial value problem (IVP) eq. (14) can be solved. It delivers the state variables x, which is a simulation model of the system. Furthermore, the IVP solution outputs ψ. The oils flows q_A and q_B follow with the help of eq. (11) and can be output as controlled variables.

There are two possibilities to solve the IVP.

1. Solution before the start of the motion: The calculation is done after processing the boundary conditions, but the output of the controlled variables starts afterwards together with the motion cycle. For this case, a fixed-step-size ODE solver from a library can be used.

2. The solution is done during the motion. On each sample time instant values for the outputs are computed, which are forwarded to the valve control. This computing mode needs fixed-step-size ODE solvers that can return a new single value after each call. In the examples in this work, a simple forward Euler method was implemented.

5.2 Hardware and Software

Electronic controllers for industrial control must be robust and dependable. In order to achieve this also for the program-

ming software, standard languages were developed early [20] and are still used today. They are not suitable to program complex systems, like they are demanded today [21], consequently modern industrial controls allow to implement software modules written in different languages. The optimisation algorithms described in this work could be written directly in C++, using e.g. the ODEINT library to solve the IVP. To avoid a general purpose language, cross-development can be used to generate code that can run on a real-time system. For example, Matlab®/Simulink® provides a suite for this purpose. The C code generated with such tools can be compiled in the environment of the programmable controller und be integrated in the automation system.

A second approach to integrate a program for complex algorithms with a machine control is to utilise modern communication, preferably UDP from the TCP/IP suite. The optimal control can run on an industrial PC that communicates with the PLC.

5.3 Computing Times

For the task to implement the actual algorithm on a computer or an embedded system, it is important to know about the numerical effort. In order to give a feeling for the required calculation, three time measurements were done. The first was a PC with Windows, i3-2120 CPU @ 3.3 GHz (PC/W in tab 1), the second a PC with Linux, i5-4210U CPU @ 1.70 GHz (PC/L in tab 1), and the third, closer to an embedded system, a Raspberry Pi 3B with Raspbian Linux, ARM Cortex-A53 @ 1.2 GHz (ARM in tab 1).

The language for the test was Python with the advantage, that the same code runs on all three platforms without any modification. The results are shown in tab 1.

Table 1: Computing times.

Step	PC/W	PC/L	ARM	Unit
Initialisation	24	0.33	6	[ms]
Boundary conditions	30	13	210	[ms]
IVP solution	0.6	0.3	6.4	[s]
IVP solution per step	36	19	410	[μs]

The initialisation is just the assembling of the matrices, processing boundary conditions requires mainly calculating the exponential of an 8 by 8 matrix and the inversion of a 4 by 4 matrix. The solution of the IVP is done with Forward Euler method in 16 000 steps.

5.4 Practical Aspects

The numerical solution of the canonical system eq. (14) delivers the adjunct system ψ, from which the vector q (containing the controlled variables q_A and q_B) follows with eq. (11). If the voltage signals fed to the servo valve represents the opening of the orifices, the resulting oil flows are not proportional to the control output. Hydraulic or electronic pressure compensation improves the situation.

With additional pressure sensors, a control loop can be established to maintain the desired oil flows, e.g. like in [16].

In [22] the following approach was presented and verified. Valve opening is predicted for one flow direction with

$$\begin{aligned} y_A &= y_{\max} \cdot \frac{Q}{Q_N} \cdot \frac{\sqrt{\Delta p_N}}{\sqrt{p_P - p_A}} \\ y_B &= y_{\max} \cdot \frac{Q}{Q_N} \cdot \frac{\sqrt{\Delta p_N}}{\sqrt{p_B - p_T}}, \end{aligned} \tag{25}$$

where y_A and y_B are the signals from the controller (here the desired value for flow, q_A or q_B), y_{max} is the limit for the input, Q represents the desired flow value. Q_N and Δp_N are the nominal parameters of the orifice, p_P is the pressure on the pump side, and p_T on the tank side. When a pressure sensor fails, the pressure terms in eq. (25) can be omitted. Further fail-safe features in different operating situations can be found in [22].

The solution of the canonical system eq. (14) also outputs the state variables of the mechanical system. This is a simulation model, which delivers also predictions for the pressures in the cylinder. The information about the desired pressures p_A and p_B can be used to establish a multi-variate control for flow and pressure.

6 Simulation Results

6.1 Some Case Studies

Figure 3 shows that the motion ends with the desired load position and a speed of zero after the proposed time. Additionally, the cylinder pressures meet the demanded values.

High pressure levels increase the power loss, lower levels may cause cavitation and reduce the stiffness of the oil volume. In the motion example in fig. 3 pressures do not fall under a value of 10 bar. If the motion is turned into the other direction (fig. 4), cavitation occurs after the start. In this case, the system gets nonlinear, and the simulation model is not valid anymore. With the initial lowest pressure of 50 bar, the problem does not occur (fig. 5).

Consequently it is better to keep the desired pressure at 50 bar for this example. The forward motions will look like in fig. 6, where the lowest pressure occurs in the breaking phase.

The motion in fig. 7 is too fast to damp the oscillation properly without causing cavitation.

Figure 8 displays the results of a longer or slower motion. The solution gives a constant value for the speed after the oscillation is vanished. It shows that the problem could be split into a start phase and a stop phase. This approach can be used for a travel with constant speed, and the design of the path will be independent from the distance.

When the travelling time is increased while the number of steps is held constant, the step width has to grow. Figure 9 shows that the solution of the IVP, eq. (14), does not meet the end conditions exactly. This is a problem with stiff numerical systems. It turns out, that many solvers have the problem with the actual example. One critical point is the computation of the exponential matrix in eq. (20) [23]. Current work is

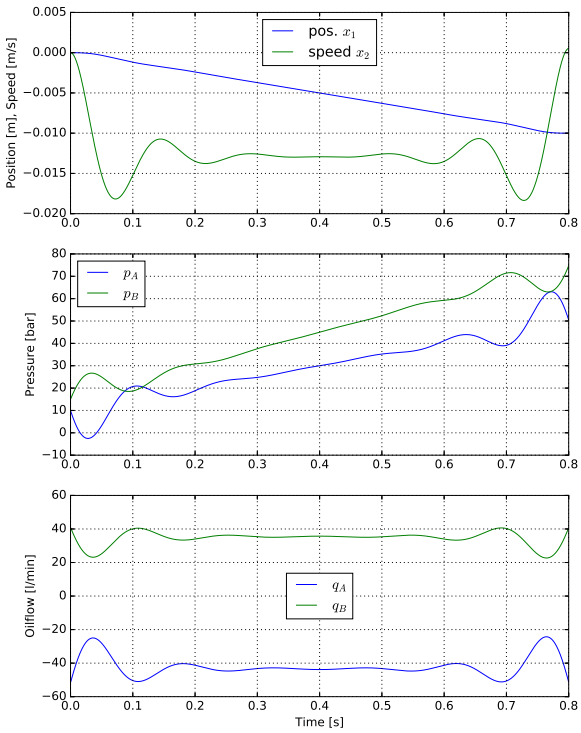

Figure 4: Reverse motion with too low initial pressures

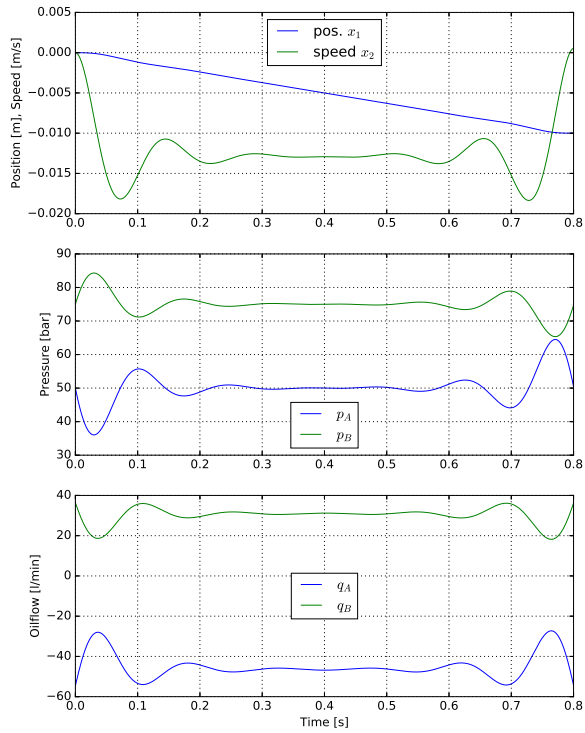

Figure 5: Reverse motion

done to work on a solving method that always meets the final conditions exactly [24].

6.2 Comparison With Start/Stop Motion Control

A system is taken for a simulation with Simulink®, which has the same properties as the system before, but with a damping of $b = 5 \cdot 10^6$. For a motion a constant input signal was generated with a ramp-up and ramp-down of 0.1 s. The input level was adjusted experimentally so, that the same travelling distance is reached. The oil flow q_A is directly proportional to the signal input, q_B is determined by an orifice, that opens synchronously with the input signal. The size of the orifice was chosen experimentally such that the desired pressure levels at the final position are obtained. In the real system, this is a standard operating mode provided by the electronic valve control [16]. Additionally meter-in and meter-out valves have a first-order time delay of 30 ms. A positioning experiment is done and compared with the results of the proposed method. In both cases the valves are closed after the target time of 0.8 s.

Figure 10 shows the positions over time, fig. 11 the speeds, fig. 12 the pressures in the cylinders, and fig. 13 the oil flows. It can be seen from these diagrams that the proposed procedure brings the load to the end position without leaving oscillations after the end time. The time delays of the spools with a value of 30 ms were not included in the design of the optimal control, since the numerical solvers used could not find a solution for this problem. A new approach [24] will make this possible. The additional delay is the reason, why the valves do not close immediately at the end time. The consequence is a short delay of the stopping time instance, but still the target conditions are met without oscillation, which is an advantage against the start/stop control.

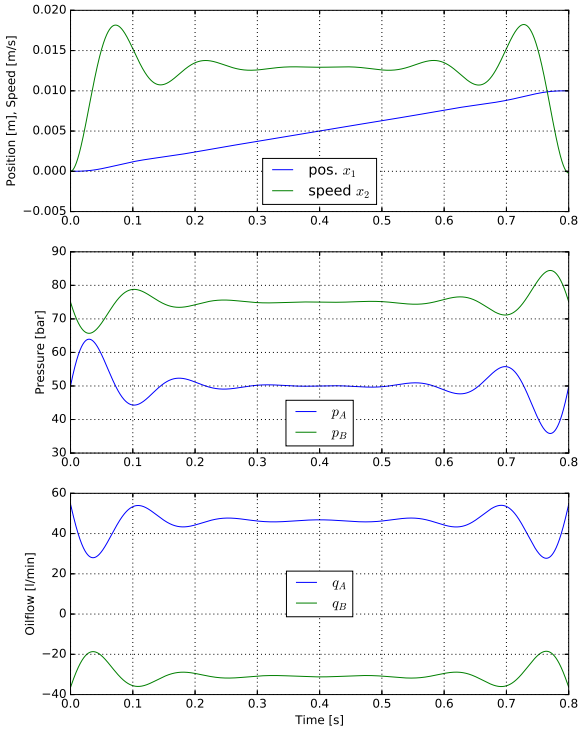

Figure 6: Forward motion starting at $p_A = 50$ bar

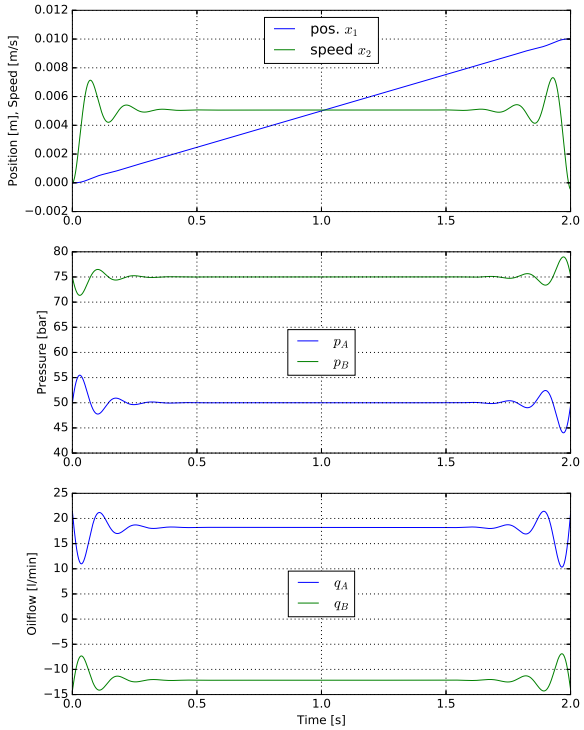

Figure 8: Long-time motion with quasi-stationary travel

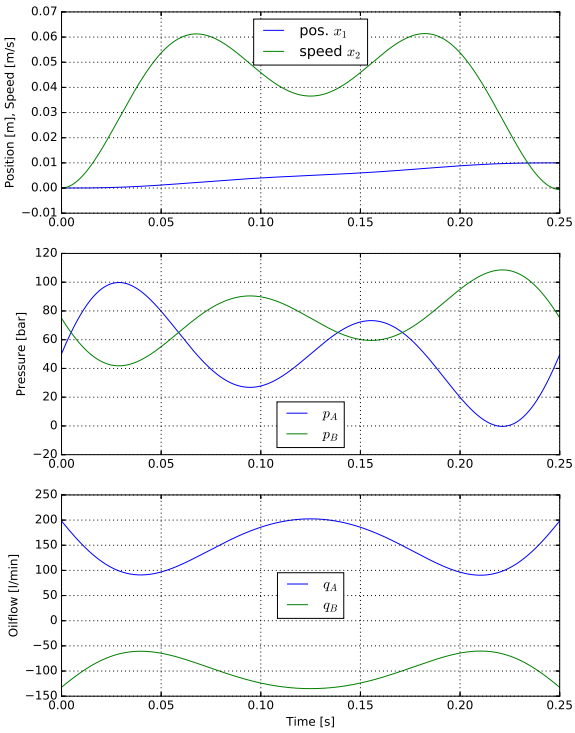

Figure 7: Motion in shorter time, appearently too fast

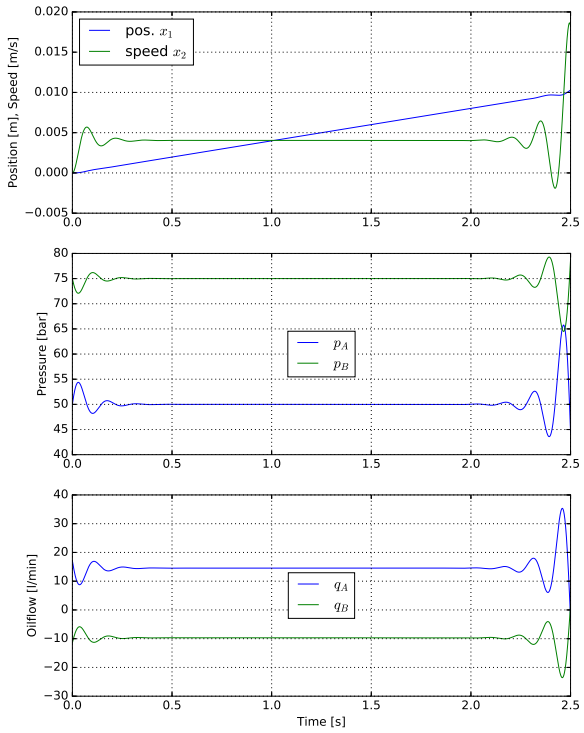

Figure 9: Demonstration of numerical problems

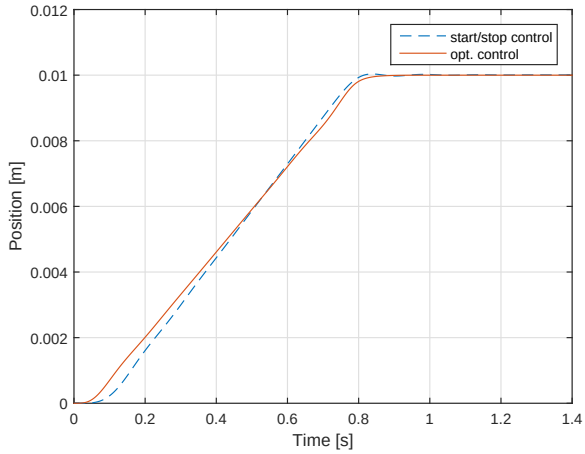

Figure 10: Positions start/stop vs. optimal control

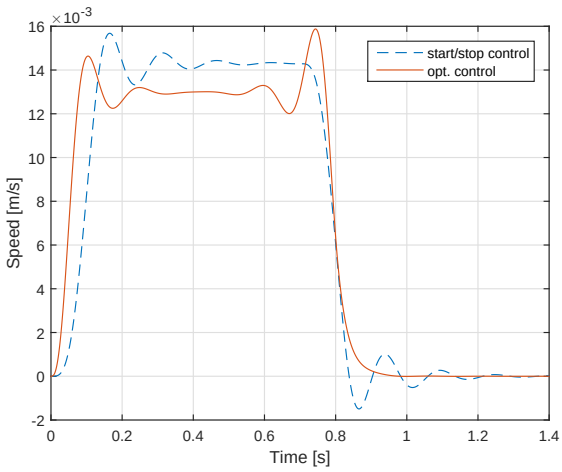

Figure 11: Speeds start/stop vs. optimal control

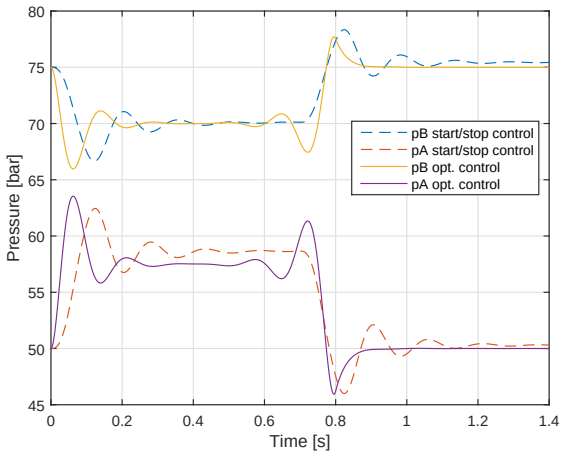

Figure 12: Pressures start/stop vs. optimal control

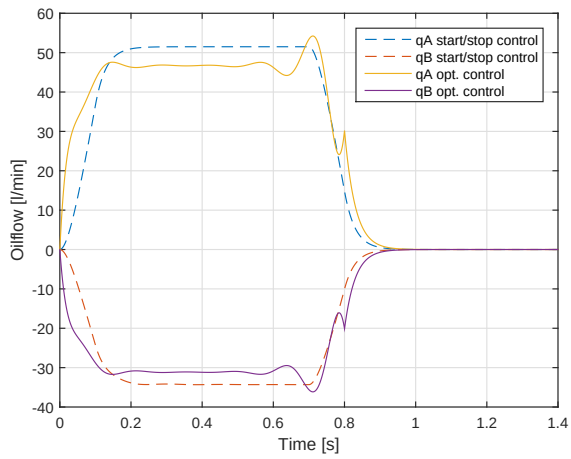

Figure 13: Oils flows start/stop vs. optimal control

7 Conclusions

The proposed method of designing a motion for a SMISMO-controlled hydraulic system allows suppressing oscillations at the end of the motion. In a separate-meter-in/separate-meter-out system it is possible to include the pressure levels in the cylinder into the motion design procedure, which means, desired values are met after the motion is finished. This is important to keep the pressures low for energy efficiency and also to avoid cavitation. The computing times are short enough to be applied for motion planning in industrial automation or even in embedded systems.

Some case studies with a simulation model with different speeds in both directions show that the results are practically reasonable. The outputs of the calculation are desired flow values. To establish constant flow in the physical system, hydraulic or electronic pressure compensation is required. This can be provided by modern valves with integrated electronics. As an alternative, a proposal to control a proportional valve with an external linarisation model was given.

It turns out that ODE solvers have problems, when the planned time exceeds a certain length. Even dedicated stiff solvers can fail. A simple Euler method with small step size turned out to work well. This kind of numerical problems is a topic of ongoing research.

Nomenclature

Designation	Denotation	Unit
x_1	Position of the load	m
x_2	Speed of the load	m/s
t_f	Final target time of the motion	s
p_A	Pressure piston side (chamber A)	Pa
p_B	Pressure rod side (chamber B)	Pa
p_P	Pressure valve input on pump side	Pa
p_T	Pressure valve output on tank side	Pa
q_A	Flow into chamber A	m^3/s
q_B	Flow into chamber B	m^3/s
Q	Oil flow through a valve	m^3/s
Q_N	Nominal oil flow of a valve m^3/s	
p_N	Nominal pressure for Q_N	Pa
y	Control input of valve	V
y_{max}	Max. control input of valve	V
m	Reduced mass	kg
A_A, A_B	Areas	m^2
b	Viscous friction coefficient	Ns/m
C	Hydraulic capacity	m^3/Pa
E	Bulk modulus	N/m^2
V	Volume	m^3

References

[1] D Wu. *Modeling and Experimental Evaluation of a Load-Sensing and Pressure Compensated Hydraulic System*. PhD thesis, University of Saskatchewan, Canada, 2003.

[2] J A Aardema et al. Systems and method for controlling an independent metering valve. United States Patent 5960695, 1999.

[3] B Eriksson. Control strategy for energy efficient fluid power actuators utilizing individual metering. Master's thesis, Univ. of Linkoping, Linkoping, Sweden, 2007.

[4] K Heybroek. Saving energy in construction machinery using displacement control hydraulics-concept realization and validation. Master's thesis, Univ. of Linkoping, Linkoping, Sweden, 2009.

[5] P Krus. *On Load Sensing Fluid Power Systems with Special reference to Dynamic Properties and control Aspects*. PhD thesis, Univ. of Linkoping, Linkoping, Sweden, 1988.

[6] P Krus and J-O Palmberg. Dampening of fluid power systems in machines with high inertia loads. In *Proc. SICFP*, Sweden, 1998.

[7] B Eriksson and J-O Palmberg. Individual metering fluid power systems: challenges and opportunities. *Proceedings of the Institution of Mechanical Engineers, Part I: Journal of Systems and Control Engineering*, 225(2):196–211, 2011.

[8] E Zaev, G Rath, and H Kargl. Energy efficient active vibration damping. In *Proceedings of the SICFP2013*, Linkoping Sweden, 2013.

[9] P Kasturi and P Dupont. Constrained optimal control of vibration dampers. *Journal of Sound and Vibration*, 215(3):499 – 509, 1998.

[10] P Hołobut. Time-optimal control of hydraulic manipulators with path constraints. *Journal of Theoretical and Applied Mechanics*, 43(3):523–538, 2005.

[11] Liu S-J, M-S Zhu, and J-F Zhou. Optimal control of hydraulic position system employing high speed on/off solenoid valve. *Journal of Central South University of Technology*, 7(1):46–48, 2000.

[12] F Liccardo, S Strano, and M Terzo. Real-time nonlinear optimal control of a hydraulic actuator. *Engineering Letters*, 21(4):241–246, 2013.

[13] M Goubej, R Škarda, and M Schlegel. Input shaping filters for the control of electrical drive with flexible load. In *Proceedings of the 17th International Conference on Process Control '09*, pages 595–601, Štrbské Pleso, Slovakia, 2009.

[14] N C Singer and W P Seering. Preshaping command inputs to reduce system vibration. *ASME Journal of Dynamic Systems, Measurement, and Control*, 112:76–82, 1990.

[15] J Bhatti, A Plummer, P Iravani, and M Sahinkaya. Implementation of closed loop signal shaping in a hydraulic system. In *Mechatronics 2012: The 13th Mechatronics Forum International Conference*, 2012.

[16] Eaton Hydraulics Group, Eden Prairie, USA. *CMA200 Advanced Independent-Metering Mobile Valve*, 2016. Technical guide.

[17] K J Aström and C Canudas de Wit. Revisiting the lugre friction model. *IEEE Control Systems Magazine*, 28(6):101–114, 2008.

[18] G F Franklin, J D Powell, and M L Workman. *Digital Control of Dynamic Systems*. Addison-Wesley Longman, Inc., Menlo Park, CA, USA, third edition, 1997.

[19] D E Kirk. *Optimal Control Theory*. Dover Publications, Inc., NY, USA, 2004.

[20] R W Lewis. *Programming Industrial Control Systems Using IEC 1131-3*. The Institution of Electrical Engineers, 1996.

[21] E A Lee and S A Seshia. *Introduction to Embedded Systems - A Cyber-Physical Systems Approach*. LeeSeshia.org, 2011.

[22] E Zaev. *Hardware-In-The-Loop for real-time simulation of complex mechanical systems and their control*. PhD thesis, Ss. Cyril and Methodius University in Skopje, Macedonia, 2013.

[23] C Moler and C Van Loan. Nineteen dubious ways to compute the exponential of a matrix, twenty-five years later. *SIAM Review*, 45(1):3–49, 2003.

[24] G Rath and M Harker. Direct numerical solution of optimal control problems. In *2016 5th Mediterranean Conference on Embedded Computing (MECO)*, pages 304–308, June 2016.

Simulation study of a digital hydraulic independent metering valve system on an excavator

M. Sc. Miikka Ketonen, Adj. Prof. Matti Linjama

Laboratory of Automation and Hydraulics, Tampere University of Technology, Tampere, Finland
E-mail: miikka.ketonen@tut.fi, matti.linjama@tut.fi

Abstract

Independent metering valve (IMV) control of working hydraulic systems in mobile machines has been studied for more than two decades and during the past few years it has also been adopted to commercial excavators. The main advantages of the IMV systems, compared to load sensing and open centre systems are the possibility of optimizing the pressure losses of the metering edges and the possibility of re-routing the hydraulic energy between actuators. Energy re-routing can be realized without storing the energy to accumulators and thus avoiding the losses of additional routing valves and energy conversions. IMV combined with a hybrid system allows even more improved energy efficiency. Digital hydraulic IMV (D-IMV) allows additional benefits to the IMV systems with more fault-tolerant operation with robust components, faster and more precise control and leak-free valves.

The purpose of this study is to apply a D-IMV system to a midsize (20t) excavator and to study the differences in energy consumption of the working hydraulic system with four actuators. This paper presents the controller designed for the D-IMV and a simulation model for analysing the system. The energy consumption of the D-IMV is compared to the measured energy consumption of a state-of-the-art excavator with a load-sensing hydraulic system.

The Controller of the D-IMV system is realized with a sub-optimal mode control, so that instead of calculating and optimizing the total energy consumption of all possible mode combinations, simpler control logic is defined to remove the complex structure of the controller and ease the computational burden. Simulation study shows that the hydraulic input energy can be reduced 28-42% compared to a standard LS-controlled excavator. Detailed analysis of where the reduction emerges is presented.

Keywords: Digital hydraulics, Independent metering valve, mobile hydraulics, excavator

1 Introduction

Demands for the off-road machine builders by markets and legislations are driving new technologies to the traditionally conservative field of hydraulic engineering. Many of the construction equipment vendors have brought the hybrid systems to the markets and a few manufacturers are also utilizing independent metering valves (IMVs) in off-road machines. Excavators are the biggest machine type along with the wheeled loaders, which makes them perhaps the most important research subject in the field of mobile machines.

Most common state-of-the-art excavator valve systems are based on open centre flow control (OFC) or a load-sensing (LS) principle. There seems to be a trend that LS systems can be found in excavators below the 25 ton-class and above that the excavators have an open centre valve system. LS systems, and especially electronically controlled eLS systems, have proven to be more energy efficient, but have only become popular among European excavator manufacturers, while Asian and American manufactures seem to favour open centre type valve systems. Main energy consuming features of current excavator valve systems are the throttling losses occurring when multiple actuators are used simultaneously and throttling losses occurring when an actuator operates far from the designed operation point due to the mechanically coupled inlet and outlet metering edges of the spool. Often it is considered a typical LS system lacks the operator feeling and response that operators tend to like.

Studies recently have also proposed many alternatives for the open centre and LS systems. These includes, for example flow demand-based eLS control systems [1], multiple constant pressure rail systems [2, 3], displacement control systems [4, 5] and different kinds of hydraulic hybrid systems [6, 7].

The advantage of an IMV-system compared to other technologies is the relatively simple system components. The system can be improved with only a single pump, keeping the manufacturing costs of the machine low. An IMV allows the

hydraulic system to transfer hydraulic fluid between actuators and actuator chambers through the supply line or through the return line without additional routing valves. An IMV also can operate without additional pressure compensator valves. [8]

It is possible to implement the IMV technology to existing excavators with relatively small changes, and it can further improve energy consumption of LS systems by using differential and regenerative modes when the load force is suitable. An IMV also allows more flexibility in programming the boom control as requested by the user. [8,9]

For full performance, IMV systems require relatively high demands from the valves. Valves need to have high enough bandwidth, low pressure losses at high flows, bi-directionality, good repeatability and robust operation in changing environmental conditions. [10]

IMV systems are still used in only a few commercial applications; for example, the Caterpillar 336E H excavator, in which the IMV technology, or as they call it, the Adaptive Control System (ACS), is used together with a hydraulic hybrid system. [11]

1.1 Digital hydraulic independent metering valves

D-IMV systems consist of 4 independently controlled metering edges per actuator. Each of the metering edges consists of a series of parallel connected on/off-valves. The benefits of parallel connected digital valves, compared to traditional proportional valves, are the fault tolerance, the robustness and the fully repeatable and fast flow control. In some of the previous studies, a fifth flow metering unit between the A and B chambers also has been proposed, to give an extra degree of freedom for the system. [9]

In most cases, both IMV and D-IMV systems require pressure sensors in actuator ports, in the supply line and in the return line, and sophisticated control algorithms that estimate the load force and act upon it. Algorithms of IMV and D-IMV systems generally consist of the mode selection, and to calculate a target flow rate for each metering edge. [8]

2 Digital hydraulic IMV in an excavator

2.1 Digital hydraulic valves for an excavator

The D-IMV studied in this paper consists of four actuators: The boom, the arm, the bucket and the swing. Independent metering is realized with four flow metering units per actuator. The system layout is shown in Figure 1.

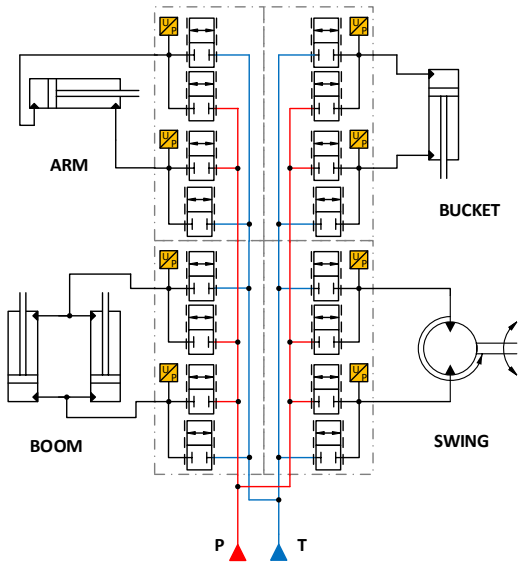

Figure 1. D-IMV valve system in excavator consisting of two pressure lines, 16 flow metering units and four actuators and chamber pressure sensors.

Pressure line P in Figure 1 is an electronically controlled LS-pump pressure supply line and the pressure line T is a return line with a low pressure realized with a spring loaded check valve or a pressure relief valve. Each of the flow metering units, also known as digital flow control units (DFCUs), consists of seven on/off-valves with mixed PCM (Pulse Code Modulation) & PNM (Pulse Number Modulation) coding of the valve sizes. In PCM coding, each valve has a different flowrate capacity, and the number of different available flowrate combinations is 2^n-1, where n is the number of valves. In PNM coding, each valve is equally sized. In practise, the flowrate capacity is adjusted by adding an orifice in line with part of the valves. Table 1 presents selected valve sizes for this study. [12]

Table 1. Selected flow rate series of each metering edge of the excavator. [l/min @ 0.5MPa]

Valve:	1	2	3	4	5	6	7
Boom: PA-edge, PB-edge & BT-edge. Arm & Bucket: all metering edges	35	35	35	17,1	8,7	4,3	2,2
Boom: AT-edge, Swing: all metering edges	35	35	17,1	8,7	4,3	2,2	1,2

Figure 2 shows the control–flow characteristics of both of the control edge varieties presented in Table 1. The number of different possible opening combinations varies from 68 to 96. Control resolution, i.e., the relation between the maximum flowrate and the maximum flowrate step between two consecutive steps varies from 52.3 to 71.5. Resolution was selected based on simulation responses to handle cylinder motions without additional oscillation compared to the measured system and also based on available on/off valves.

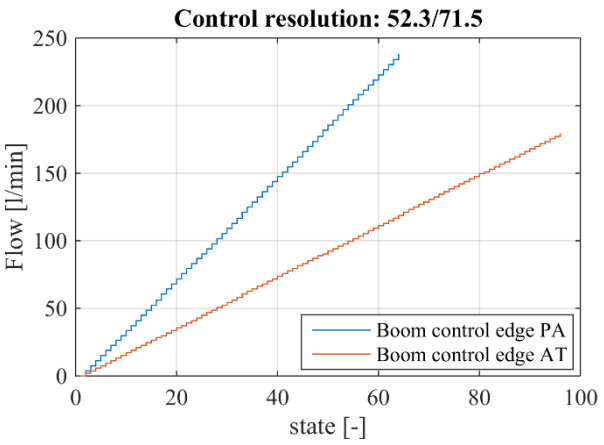

Figure 2. Possible flow rates of metering edges PA and AT of the boom at 1.5MPa.

2.2 Operation modes of IMV

The different modes are referred to as: PTe, PTr, TPe, TPr, PPe, PPr, TTe and TTr, in which the first letter describes whether the pump line (P) or tank line (T) is connected to the A-chamber, while the second letter describes which line is connected to the B-chamber. The third letter describes the direction of the movement, e for extending and r for retracting. Figure 3 presents the active metering edges with each mode.

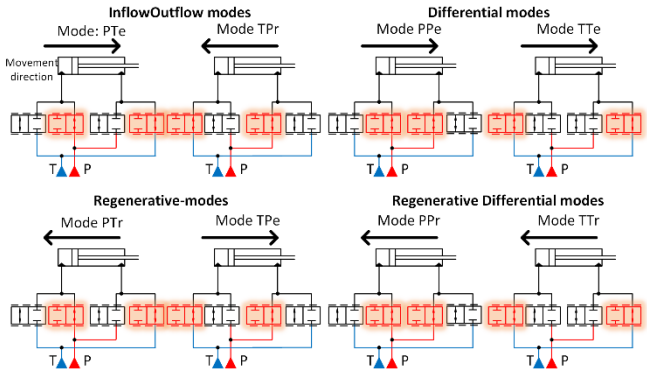

Figure 3. Different operation modes of the D-IMV system.

3 Controller

Many of the digital hydraulic valve controllers presented in earlier studies have been designed for powerful computers, such as the dSPACE Microautobox or PCs. More accurate and smoother control can be achieved if a more computationally demanding, model based valve control is used, but it has been shown in [13] that sufficient control for mobile application can be achieved also using simpler controllers that can be realized with commercially available controller units.

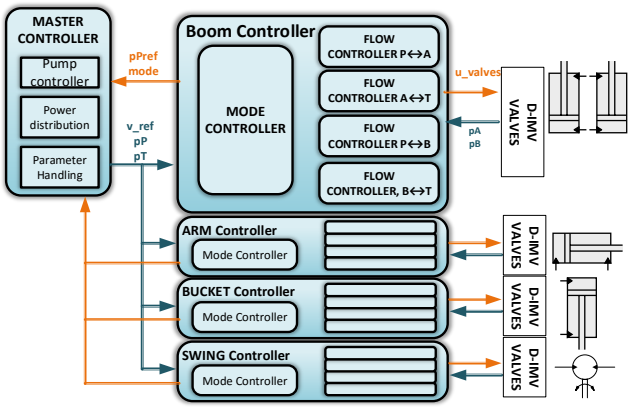

Figure 4. D-IMV controller structure.

The upper-level controller structure presented in Figure 4 includes four actuator controller subsystems and a master controller subsystem that includes the pump controller and the power distribution. Actuator controllers are identical to each other with a different set of parameters. Parameters are tuned in this study so that velocities and velocity oscillations are close to the measured responses of the reference excavator with LS-valve system.

3.1 Master Controller

The master controller structure is presented in Figure 5. Inputs to the controller are the measured supply line pressure *pP* and the return line pressure *pT*, joystick signals and pump pressure requests from the actuator controllers. Outputs are the velocity references for the actuators, pump control signal and the filtered supply line and return line pressures for the actuator controllers. The Master controller realizes the eLS pump control by selecting the maximum of actuator supply pressure requests as a pump pressure reference and turns it into a control signal for the pump control valve. The Power and torque distribution block ensures that the engine will not stall and that the desired operation of actuators is ensured when the power demand exceeds the available hydraulic power.

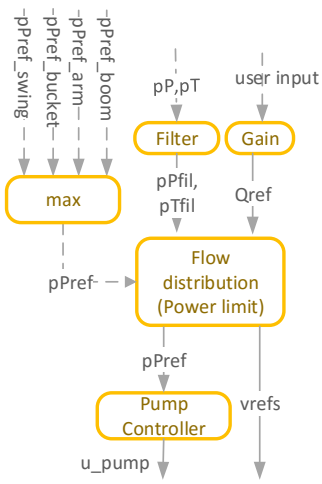

Figure 5. Master controller structure.

3.1.1 Power distribution and limitation

In case the controller power demand or flow rate demand exceeds the machine limits, velocity references are lowered so that the total hydraulic power requirement is within the power limits of the system and maximum flow rate is not exceeded. In case the power demand exceeds the power limit, new velocity references for the actuators are calculated with an equation

$$v_{ref_{new}} = v_{ref} \frac{P_{limit}(n_{engine})}{QP_{ref} \cdot \max(pP_{Refs})} W_{dist} \quad (1)$$

where v_{ref} is the user velocity reference, $P_{limit}(n_{engine})$ is the available power with the current engine speed, pP_{Refs} is the vector of supply pressure references from the actuator controllers, W_{dist} is a weighting factor for the actuator to determine the priority of the actuator velocity reference and QP_{ref} is the total flow requirement. W_{dist} is calculated with equation

$$W_{dist} = \frac{\overline{\boldsymbol{W}}_{dists,k} \, {}^{v_{ref}}/_{\overline{\boldsymbol{v}}_{maxs,k}}}{\sum(\overline{\boldsymbol{W}}_{dists} \, {}^{\overline{\boldsymbol{v}}_{refs}}/_{\overline{\boldsymbol{v}}_{maxs}})} . \quad (2)$$

where $\overline{\boldsymbol{v}}_{refs}$ is the vector of velocity references, $\overline{\boldsymbol{v}}_{maxs}$ is the vector of maximum actuator velocities and $\overline{\boldsymbol{W}}_{dists}$ is the vector including all four weighting gains of four actuators. By adjusting the relations between the gains, a desired relation of the actuator's velocities can be achieved. QP_{ref} is calculated as a sum of actuator flow rate demands, which is calculated using the equation

$$QP_{ref_i} = \begin{cases} v_{ref_i} A_{A_i}, & v_{ref_i} > 0 \\ |v_{ref_i}| A_{B_i}, & v_{ref_i} < 0 \end{cases} \quad (3)$$

where A_A and A_B are the cylinder chamber areas or the radian chamber volumes of the swing motor.

If flowrate demand is exceeded, new velocity references are calculated with equation

$$v_{ref_{new}} = v_{ref} \frac{Q_{limit}(n_{engine})}{QP_{ref}} W_{dist} \quad (1)$$

where $Q_{limit}(n_{engine})$ is the available power with the current engine speed.

In the case of the swing actuator, desired operation is achieved also by limiting the swing torque. New pressure reference for the swing actuator is calculated with the equation

$$pP_{ref_sw_new} = pP_{ref_sw} \frac{P_{limit}(n_{engine})}{QP_{ref} \cdot \max(pP_{Refs})} W_{dist} \quad (4)$$

To achieve equal operation in simulations and in the reference measurements, power distribution is limited by only limiting the swing torque. In case the boom, arm or bucket actuators have bigger pump pressure requests than the swing actuator, the swing torque cannot be limited and only the velocity reference of the swing actuator is reduced.

3.1.2 Motion Controller

In the simulation study, cylinder velocity references are derived from the position and velocity measurements of the reference machine. Reference velocities for the control system are calculated with a motion controller realizing the equation

$$v_{ref} = K_{FF} v_{meas} + K_P (x_{meas} - x_{sim}) \quad (5)$$

where K_{FF} is feedforward gain and K_P is feedback gain, x_{meas} is the reference cylinder position from the reference measurements and x_{sim} is the actuator position in simulations. The motion controller is only required for simulation purposes.

For the swing actuator, measured pilot pressures of the control valve in the reference measurement are used to define the start moment of the joystick actuation and a smooth trajectory going from 0 to 1 is applied to mimic the joystick control signal. Control duration is applied so that the steady-state swing positions are equal to the measured reference positions.

3.2 Mode controller

The mode controller structure is presented in Figure 6. The mode controller is built with a sub-optimal principle. It is known that typical pumps used in mobile machines have poor efficiency at high pressures and low flowrates, and that high pressures also tend to wear system components and thus to increase maintenance costs. The differential modes are not used to calculate the pump pressure reference, but are still used when possible to lower the pump flowrate demand.

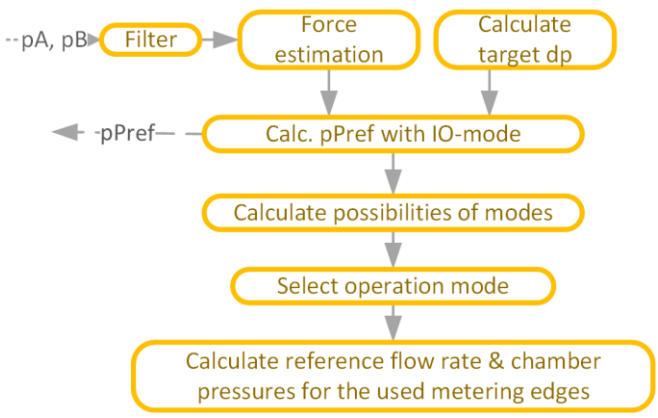

Figure 6. Mode controller flow chart.

Actuator force or torque is estimated from the measured chamber pressures and using a filter developed in [6]. This

non-linear filter improves the dynamics of the force estimation, although a linear first-order filter works well in a simulation environment.

Most of the mode selection code is realized with a Matlab/Stateflow chart. The mode controller changes state from idle to running mode when $|v_{ref}|$ is above the tolerance velocity v_{tol}. If the actuator is moving, it goes to the idle mode when $|v_{ref}| < v_{tol}/2$.

3.2.1 Target pressure difference

Target pressure difference over the valves is calculated as a function of the velocity reference v_{ref} to allow minimum pressure difference during low and mid-high velocities, and increased cylinder velocity by increasing the pressure difference over the valves. There are two parameters for setting the target pressure difference: minimum pressure difference target (dp_{nom1}) and the maximum pressure difference target (dp_{nom2}). dp_{ref} is calculated with equation

$$dp_{ref} = max\left(dp_{nom1}, \min\left(dp_{nom2}, \left(\frac{|v_{ref}|A_A}{Q_{dp1nom_max}}\sqrt{dp_{nom1}}\right)^2\right)\right) \quad (6)$$

where Q_{dp1nom_max} is the flowrate when the valve metering edge P↔A is fully open and the pressure difference is equal to dp_{nom1}.

For the swing actuator sufficient acceleration is done by using dynamic target pressure difference calculation that increases the dp_{ref} value when joysticks move rapidly. This will increase the pump supply pressure more rapidly when swing motion is started, and thus will improve the acceleration of the swing motion. For the swing motion, dp_{ref} is calculated with the pseudo code:

if (v_{ref} - $v_{ref_previous}$) > $v_{ref_diff_limit}$
→ dp_{ref}=*min*(dp_{nom2},$dp_{ref_previous}$+*inc_rate*)
else if $dp_{previous}$> dp_{nom2}
→ dp_{ref} = *max*(dp_{nom1}, $dp_{ref_previous}$ –*inc_rate/3*)
else
→ dp_{ref} = dp_{nom2}

where $v_{ref_diff_limit}$ is the parameter describing how fast the joystick motion must be for starting to increase dp_{ref}, and *inc_rate* is a parameter to adjust the length of the increased dp_{ref} duration.

3.2.2 Supply pressure reference

The pump pressure reference pP_{ref} is calculated for the standard inflow-outflow modes (IO-modes), first by calculating the required chamber pressures from the force/torque (F) and given limitations. First, the outflow-side pressure is calculated with the equation:

$$p_{out} = \min\left(\max\left(p_{min}, p_T + dp_{out_{ratio}} \cdot dp_{ref}\right), p_{\max}\right) \quad (8)$$

where p_{min} and p_{max} are given lower and higher chamber pressure limits and dp_{out_ratio} is a parameter to lower the outflow side target pressure difference to improve the energy efficiency.

Inflow-side chamber pressure is then calculated with the equation

$$p_{in} = \begin{cases} (F + p_{out}A_B)/A_A, & v > 0 \\ (F - p_{out}A_A)/A_B, & v < 0 \end{cases} \quad (9)$$

where A_A and A_B are the piston areas or radian volumes of the motor. From these *pPref* is calculated with equation

$$pP_{ref} = \min(\max(pP_{min}, p_{min} + dp_{ref}), pP_{\max,}\, p_{in} + dp_{ref}) \quad (10)$$

where pP_{min} and pP_{max} are limits for the supply pressure.

3.2.3 Calculation of possible modes

After pP_{ref} is calculated, the current possibility of each mode is checked. For the positive direction, the possibilities of modes are calculated with equations:

$$\begin{aligned} &PT_pos = (pP_{ref} - pP) < 0.5dp_{ref} \\ &PT_notpos = pP < (pP_{ref} - dp_{ref}) \\ &TP_pos = F < force(pT - dp_{ref}, pP + 0.5dp_{ref}) \\ &TP_notpos = F > force(pT - dp_{ref}, pP + dp_{ref}) \\ &PP_pos = F < force(pP - 2dp_{ref}, pP + dp_{ref}) \\ &PP_notpos = F > force(pP - dp_{ref}, pP + dp_{ref}) \\ &TT_pos = F < force(pT - 2dp_{ref}, pT + dp_{ref}) \\ &TT_notpos = F > force(pT - dp_{ref}, pT + dp_{ref}) \end{aligned} \quad (11)$$

where the *force(p1,p2)* calculates the equation

$$force(p1, p2) = p1A_A - p2A_B \quad (12)$$

For the negative directions the possibilities are calculated with equations:

$$\begin{aligned} &TP_pos = (pP_{ref} - pP) < 0.5dp_{ref} \\ &TP_notpos = pP < (pP_{ref} - dp_{ref}) \\ &PT_pos = F > force(pP - 2dp_{ref}, pT - dp_{ref}) \\ &PT_notpos = F < force(pP - dp_{ref}, pT - dp_{ref}) \\ &PP_pos = F > force(pP + 2dp_{ref}, pP - dp_{ref}) \\ &PP_notpos = F < force(pP + dp_{ref}, pP - dp_{ref}) \\ &TT_pos = F > force(pT + dp_{ref}, pT - 2dp_{ref}) \\ &TT_notpos = F < force(pT + dp_{ref}, pT - dp_{ref}) \end{aligned} \quad (13)$$

3.2.4 Mode selection

The mode for extending motion is selected in the state machine presented in Figure 7. For the rectracting motion the principle is identical. For certain work cycles the controller cannot utilize all the modes, and thus the tables

enable_ext_modes and *enable_ret_modes* are declared to allow only certain modes to be used. The logic of the state machine decides the best possible mode, or if none of the modes is possible, the logic selects the hold mode to wait for the proper supply line pressure.

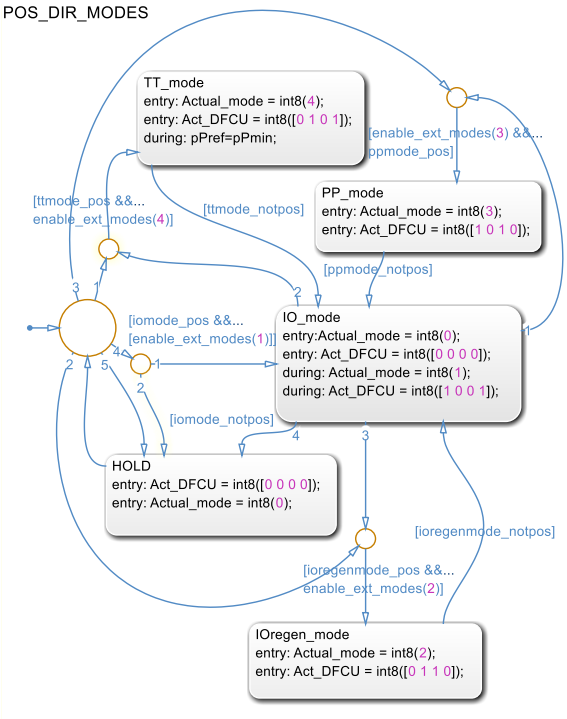

Figure 7. Mode selection in the state machine for positive direction.

3.2.5 Calculation of reference values for the flow controller

After the mode is selected, the controller selects which of the metering edges are to be used. For these metering edges, reference flowrates and chamber pressures are calculated for each valve.

Target flowrates are calculated for PA and AT-metering edges with equation

$$Q_{ref,PA/AT} = v_{ref} * A_A \tag{13}$$

and for metering edges PB and BT with equation

$$Q_{ref,PB/BT} = -v_{ref} * A_B \tag{13}$$

Pressure references for the flow controller are set so that outflow-side is minimized, and maximum and minimum pressure limits are not exceeded. The inflow-side chamber pressure is set according to the current force level.

3.3 Flow Controller

The actuator controller includes a flow controller (Figure 8) for each metering edge, to calculate the optimal opening of the digital hydraulic valves. When the mode selection algorithm sends the flow requirement and target pressures for the active metering edges, the flow controller calculates the flowrates for each valve with the equation

$$Q_{valve_i}(p_1, p_2) = \begin{cases} K_{1i}(p_1 - p_2)^{x_{1i}}, & b_{1i}p_1 < p_2 \le p_1 \\ K_{1i}[(1 - b_{1i})p_1]^{x_{1i}}, & p_2 \le b_{1i}p_1 \\ -K_{2i}(p_1 - p_2)^{x_{2i}}, & b_{2i}p_{21} < p_1 \le p_2 \\ -K_{2i}[(1 - b_{2i})p_1]^{x_{2i}}, & p_1 \le b_{2i}p_2 \end{cases} \tag{12}$$

where K_{1i} is the flow coefficient, x_{1i} is the exponent and b_{1i} is the critical pressure ratio of a single valve in the flow direction 1→2, and K_{2i}, x_{2i}, and b_{2i} are the parameters for the opposite direction. For the simulation study, exponent values of 0.5 and critical pressure ratios of 0.25 were used. Flow rates of the individual valves are presented in Table 1 in Chapter 4.

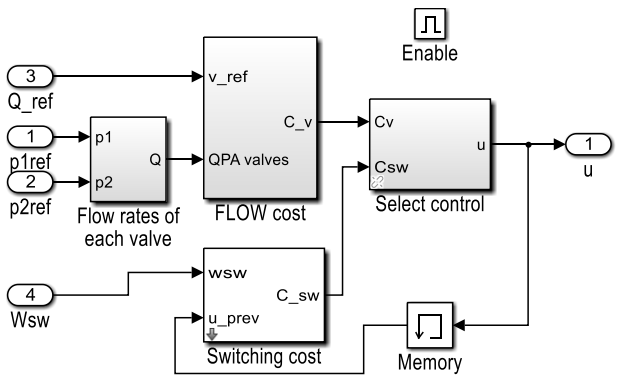

Figure 8. Flow Controller structure of Boom PA metering edge.

To avoid excessive valve switching, the final valve opening combinations are selected by minimizing the cost function, taking into account velocity error and the amount of valve state switching required. The valve opening combination is calculated with the equation

$$u_{state} = \min(\bar{v}_{error} + w_{sw}(\bar{Q}_{NOM} \times |(\bar{u}_{prev} \times \bar{u}_{ones} - \bar{u}_{ctrl_mtrx})|) \tag{13}$$

where $\bar{v}_{errors}$ is the array of the velocity errors for each valve opening combination, w_{sw} is the weighting gain for the switching term, $\bar{Q}_{NOM}$ is a vector of nominal flow rates of the valves, $\bar{u}_{prev}$ is an array of the current state of valves, $\bar{u}_{ones}$ is an all-ones array with a length equal to the number of combinations and $\bar{u}_{\mathrm{ctrl_mtrx}}$ is a matrix of valve states with each combination.

4 Simulation Model & Reference Data

The machine selected for comparison is a 21-ton LS-controlled excavator (Volvo EW210C, Figure 9). This excavator has a single pump for controlling all the actuators and the travel motors, and additional small auxiliary pumps for fan motor, pilot pressure supply and for other necessities. The excavator was instrumented with a pump flowrate sensor, actuator position sensors and actuator-chamber pressure sensors.

Figure 9. Volvo EW210C wheeled excavator used in reference measurements.

4.1 Simulation model

The simulation model (Figure 10) includes the D-IMV controller and the mechanical model of the excavator realized with Matlab Simulink. The mechanical model includes the inertias and kinematics modelled with SimMechanics, including the cross connection between the actuators. Supply pressure dynamics, control valves, hoses and actuators are modelled with Simulink. Model was verified to the measurement data from the excavator.

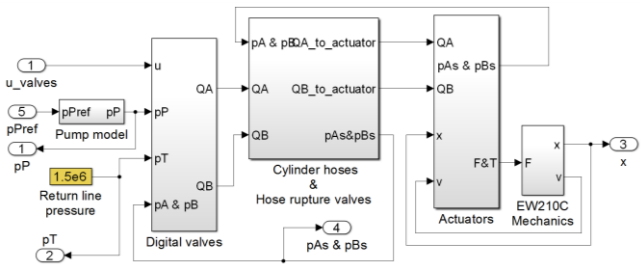

Figure 10. Hydraulic and mechanical model of the EW210C in Simulink.

The model of the digital valves includes four valve blocks, including 4x7 leak free on/off-valves per actuator. Flow rates of the on/off-valves are adjusted with orifices to accommodate the maximum velocity of the actuators and a control resolution that also allows low velocities.

The diesel engine is not modelled because the focus of the paper concentrates on the hydraulic efficiency comparison. The pump is modelled to have typical dynamics for an open circuit mobile pump, but the efficiency of the pump is neglected because it is out of the scope of this study. The return line is modelled as a constant pressure line.

4.2 Reference Data

Reference data include measurements of a simulative 90-degree truck loading cycle and earth grading cycle that are based on a JCMAS H 020 standard (Figure 11). The standard defines trajectories for comparing fuel consumptions of different sized machines in real life-like movements without touching the earth. This standard is selected to avoid the complex modelling of the earth and to realize as uniform conditions as possible for repeatable measurements, although it is does not match exactly the real world test cycles.

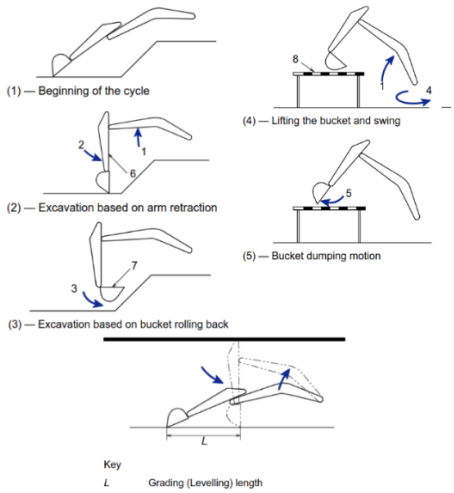

Figure 11. Truck loading cycle phases 1-5 and the grading cycle according to JCMAS H020. [15]

5 Simulation results

5.1 Truck loading cycle

Figure 12 presents the actuator positions and velocities in a single work cycle. There are some differences in velocity curves, but the final positions of simulations and measurements match. The simulation tends to oscillate a little more when hitting the end of the actuators because of the lack of a cylinder end damping model.

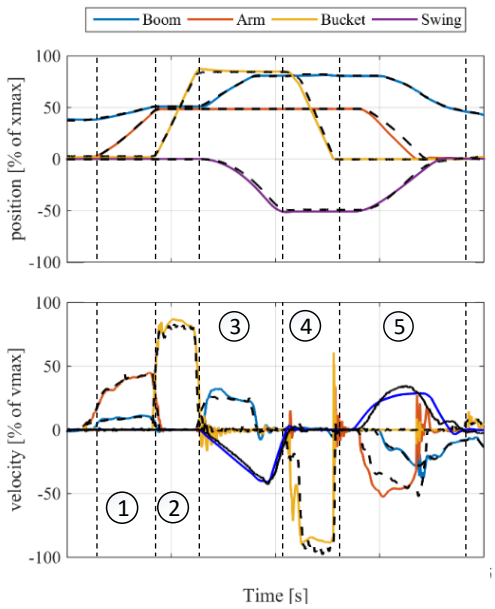

Figure 11. Positions and velocities from the reference measurements (dashed line) and from the simulated D-IMV system (solid lines) with different phases of the JCMAS digging cycle.

The upper graph of the Figure 13 presents the input and output powers of the simulated D-IMV system and the measured LS system, as well as the supply line pressure and flow rates. It can be seen that 19 kJ more work was done in the simulations than what was measured. This can be explained with a slight difference in velocity curves and in force/torque curves, but the relation to the input energy is so small that it can be considered negligible. Most of the difference comes from the behaviour difference of the swing drives. The peaks in the measured input power at phase 4 are due to the arm and bucket actuators hitting the end of the cylinder. The simulated system does not increase the cylinder force after hitting the end. In a truck loading cycle, a rapid force increase is not required when opening the bucket. The difference in the input energy comes from the lowered flow rate requirement because of the utilization of different modes.

Figure 14 presents the different modes used during the cycle. Phase 1 consists mostly of lifting the boom and extending the arm cylinder. As the boom lifting requires high pressure, the arm operates at differential modes and thus required input energy is reduced the around 40 percent. During the closing of the bucket in phase 2, the bucket cylinder is the only actuator and it operates in inflow-outflow mode. During the phase 3, inflow-outflow modes are used by the boom and the swing actuator, and in phase 4 the bucket is opened in inflow-outflow mode. When returning to the starting position, the boom is lowered with the TTr –mode, in which zero pump flow is used simultaneously with the arm retraction and swing motion, which are done in inflow-outflow mode.

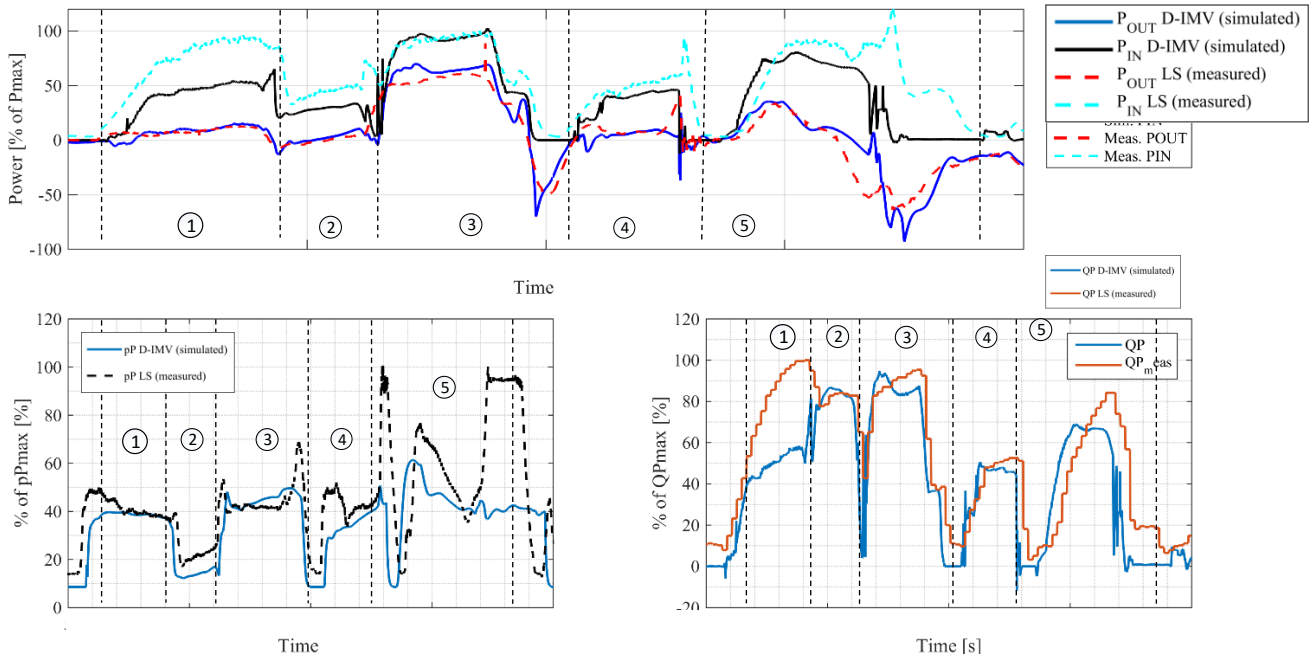

Figure 13. Hydraulic input powers (P_{IN}) and mechanical output powers (P_{OUT}), pump pressures and pump flow rates of the measured LS reference system (meas.) and the simulated D-IMV syste (sim.) in a JCMAS truck loading cycle (phases 1-5 divided in figure).

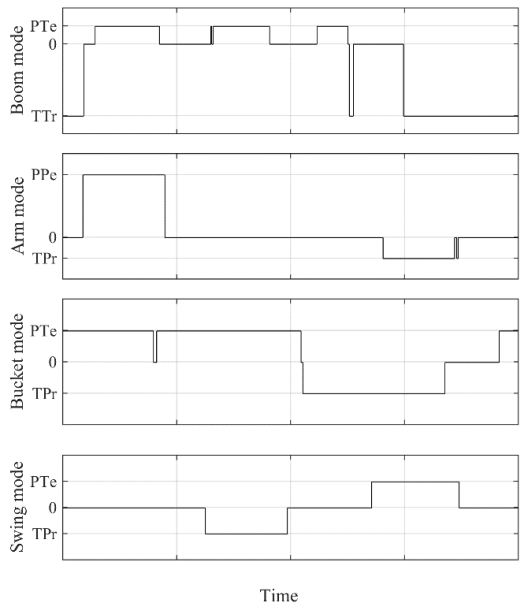

Figure 14. D-IMV Actuator modes in digging cycle simulations.

Figure 15 presents the cumulative input and output energies of four truck loading cycles. The total input energy was reduced 28 percent with D-IMV compared to the measured LS system.

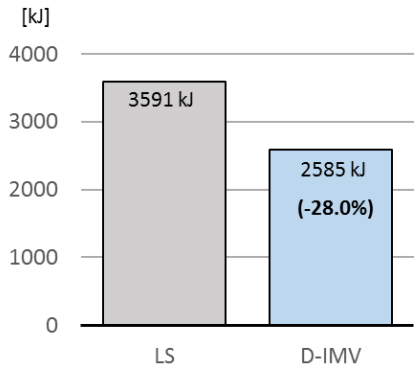

Figure 15. Measured and simulated cumulative energy consumptions in four consecutive truck loading cycles.

Total energy consumption of the working hydraulic circuit was reduced 28% in the digging cycle.

5.2 Grading cycle

Figure 16 presents the simulated and measured actuator positions, velocities and modes in a single grading work cycle. The bucket tip remains at a steady height from even ground surface, and the bucket is drawn from the out position to the in-position, and back.

Figure 17 presents the measured and simulated input and output powers, supply pressures and pump flowrates in the grading cycle. In the grading cycle, the main difference comes from the arm differential mode PPe used in the out-to-in motion and the boom TTr-mode used in the in-to-out motion. Also, the metering losses are reduced during the in-to-out motion.

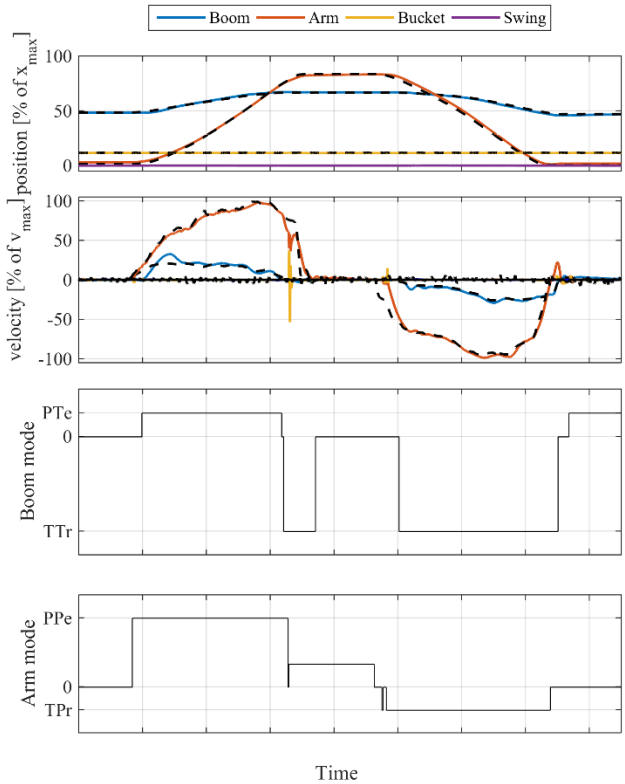

Figure 16. Simulated (D-IMV system) and measured (LS system) grading cycle position and velocities and modes used in simulation.

Figure 18 presents the cumulative input energies in four consecutive cycles. The total required energy was reduced 41.5% compared to the measured LS system.

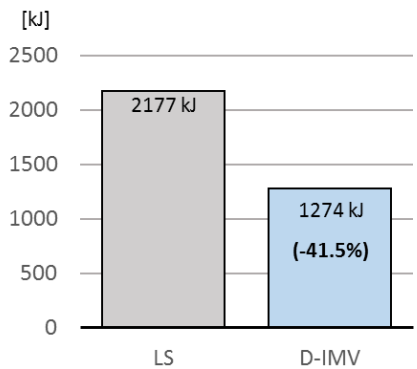

Figure 18. Measured and simulated cumulative input and output energies of four grading cycles.

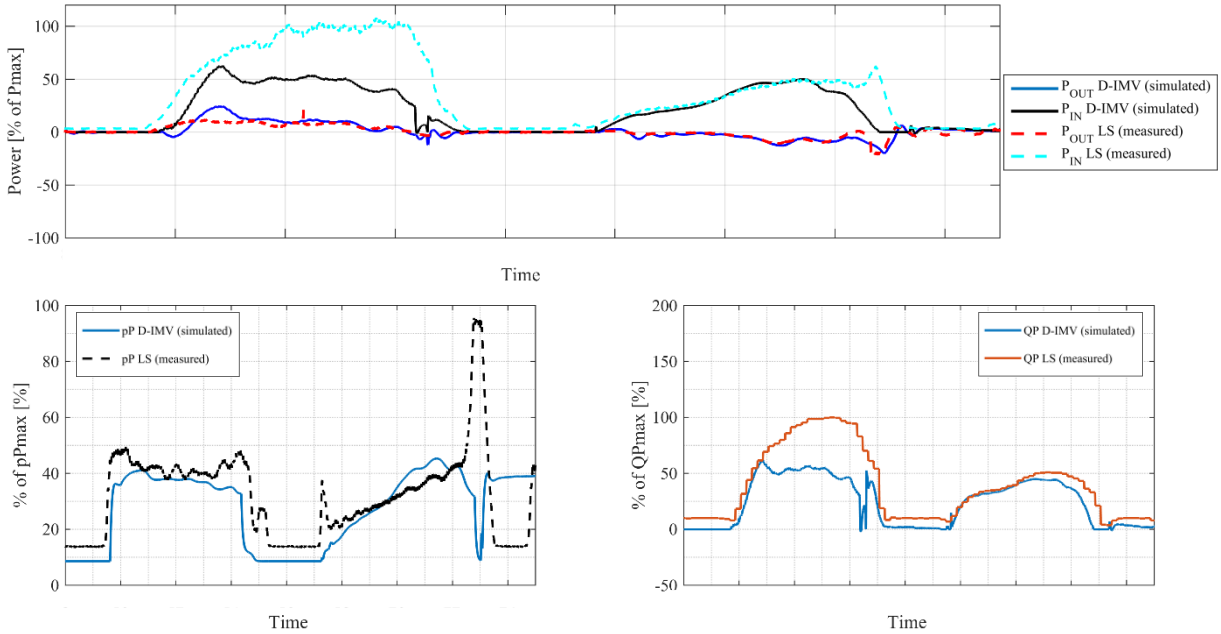

Figure 17. Hydraulic input powers (PIN) and mechanical output powers (POUT), pump pressures and pump flow rates of the measured LS reference system (meas.) and the simulated D-IMV system (sim.) in a JCMAS grading cycle.

6 Conclusion

D-IMV systems, and IMV systems in general, have great potential to improve the efficiency of mobile machines that often use working hydraulics with several actuators. This paper presented study comparing the measurement from a state-of-the art LS excavator and a simulated digital hydraulic IMV excavator. Comparison was done with a controller that utilizes different modes of the actuator, and thus lowers the flow rate required from the pump. The controller also keeps the supply pressure lower or at a similar level than that of current LS-systems.

In this study, system modifications other than those involving the valve system were kept to a minimum so as to compare the IMV system to a state-of-the-art LS-valve system in a 21-ton excavator. The comparison included only hydraulic input energies, and it was shown that even without regenerative modes, hydraulic energy required for the two standard working cycles can potentially be decreased 28-42 percent.

Research continues in applying D-IMV technology to an actual test case to validate the results and study the system in actual work cycles.

Acknowledgment

This work was supported by the Doctoral School of Industry Innovations (DSII).

References

[1] Lettini, A., Havermann, M., Guidetti, M., & Fornaciari, A. (2010). Electro-Hydraulic Load Sensing: a Contribution to Increased Efficiency Through Fluid Power on Mobile Machines. *Fuidotecnica*, *345*.

[2] Vukovic, M., Leifeld, R., and Murrenhoff, H., 2016. STEAM a hydraulic hybrid architecture for excavators. 10th International Fluid Power Conference (10. IFK), 8–10 March, Dresden, Germany.

[3] Linjama, M., Vihtanen, H-P., Vilenius, M. Secondary controlled multi-chamber hydraulic cylinder, The 11th Scandinavian International Conference on Fluid Power, SICFP'09, June 2-4, 2009, Linköping, Sweden

[4] K. Heybroek, G. Vael, and J.-O. Palmberg, "Towards resistance - free hydraulics in construction machinery," in The 8th International Fluid Power Conference, 8. IFK, Dresden, Germany, 2012.

[5] C. Williamson and M. Ivantysynova, "Power optimization for multi-actuator pump- controlled systems," in The 7th International Fluid Power Conference, 7. IFK, Aachen, Germany, 2010.

[6] K. Einola and M. Erkkilä, "Dimensioning and control of a hydraulic hybrid system of a cut-to-length forest harvester," in The 9th International Fluid Power Conference, 9. IFK, Aachen, Germany, 2014

[7] Lin, T., Wang, Q., Hu, B., & Gong, W. (2010). Development of hybrid powered hydraulic construction machinery. *Automation in Construction*, *19*(1), 11–19. https://doi.org/10.1016/j.autcon.2009.09.005

[8] Eriksson, B., Palmberg, J.-O., Individual metering fluid power systems: Challenges and opportunities. Proceedings of the Institution of Mechanical Engineers, Part I: Journal of Systems and Control Engineering, 225:196–211, 2011.

[9] Nielsen, B. (2005). Controller Development for a Separate Meter-In Separate Meter-Out Fluid Power Valve for Mobile Applications, 237. Available http://vbn.aau.dk/files/74051350/brian_nielsen.pdf

[10] Heybroek, K., Larsson, J., Palmberg, J.-O., Mode Switching and energy recuperation in open-circuit pump control. In The Tenth Scandinavian International Conference on Fluid Power, Tampere, Finland, May 21-23 2007. Available http://liu.diva-portal.org/smash/get/diva2:133010/FULLTEXT01.pdf

[11] Caterpillar website, http://www.cat.com/en_ID/news/machine-press-releases/cat-sup-174-sup-336ehhydraulichybridexcavatordeliversnocompromis.html , visited 10.1.2017

[12] Linjama, M., Digital fluid power - state of the art. In The Twelfth Scandinavian International Conference on Fluid Power, Tampere, Finland, May 18-20 2011, available: https://pdfs.semanticscholar.org/a1a3/afd27352191866b5614af9abea93ff5a9cf7.pdf

[13] Huova, M., Ahopelto, M., Ketonen, M., Ahola, V., Linjama, M., Huhtala, K., Characteristics of digital hydraulics with commercial controllers, The Seventh Workshop on Digital Fluid Power, February 26-27, 2015, Linz, Austria.

[14] Karvonen, M. (2016). Energy Efficient Digital Hydraulic Power Management of a Multi Actuator System. (Tampere University of Technology. Publication; Vol. 1384). Tampere University of Technology.

[15] JCMAS H020. Japan Construction Mechanization Association. Standard for of excavator fuel efficiency measurement procedure. 2010.

Sensorless position estimation of simulated direct driven hydraulic actuators

T. Sourander, M. Pietola, T. Minav, and H. Hänninen

Department of Mechanical Engineering, Aalto University School of Engineering, Espoo, Finland
E-mail: tom.sourander@aalto.fi,matti.pietola@aalto.fi, tatiana.minav@aalto.fi, henri.hanninen@aalto.fi

Abstract

In this study, sensorless position control of hydraulic cylinders is investigated. Direct driven hydraulics units are utilized as a prime mover. Direct driven hydraulics is a valveless pump controlled hydraulic system that uses an electric motor to drive pumps for a single actuator. This brings energy saving and controllability advantages to traditional valve controlled hydraulics. Advantages and disadvantages of various types of position sensors, which are available on the market were investigated for hydraulic cylinder application. These sensors, while accurate, have been noted to be rather expensive and not suitable for harsh environment applications. Virtual sensors can provide an alternative to physical position sensors. Using only torque and speed data received from electric motor controller it is possible to simulate the position of a cylinder, provided that all relevant parameters are known. Simulation model of direct driven hydraulic system of a mining loader test platform was realized using Matlab/Simulink Simscape blocks. Results within the simulation show that the model can reach an accuracy within a few millimeters for a single cycle. A cumulative error for repeated cycles was observed, which recommends simple cylinder end or middle point proximity sensors to be used as reference points.

Keywords: Sensorless position control, Virtual sensors, Direct driven hydraulics, Electrohydraulic actuator

1 Introduction

Improving the energy efficiency of hydraulic powered machinery has led to increasing efforts to find solutions for replacing conventional systems. In industrial and automotive fields, the common solution has been electric powertrains due to the high efficiency of electric power transfer and motors. In hydraulics, electric motors have generally been utilized in stationary applications however, the hydraulic systems themselves traditionally have been valve-controlled that have issues with flow losses. In addition, hydraulic machines are experiencing more automatization, which requires the implementation of more advanced control technologies.

To remedy this, increasing interest has been devoted to electric-driven pump-controlled actuators, which work as a hydrostatic transmission for cylinders. Unlike traditional hydrostatic transmissions, in which a combustion engine powered variable displacement pump is driven at constant speed, electric motors provide fast response time, which allows the utilization of more affordable fixed displacement pumps. This offers not only increased energy efficiency due to reduced idling losses but also a chance for implementing a sensorless position control system for the cylinders utilizing sensor virtualization. The advantages are increased redundancy and reduced the dependency on expensive absolute position sensors normally utilized in cylinders.

With increased use of automated processes in hydraulic applications such as mobile machines, the role of position sensors has become a vital part of these systems. Several types of position sensors, both internal and external types exist for measuring the linear movement of hydraulic cylinders. However, even position sensors that seem simple and robust can be surprisingly costly or challenging to implement in applications requiring reliability and robustness in harsh environments. It has also been noted that wires and connectors can be prone to damage and devices relying on position sensors can be incapacitated if an error or malfunction appears in sensors. Thus, it would be useful if the position of hydraulic actuated joints could be measured by indirect means for redundancy and cost saving. [1]

Cylinder internal sensors apart from draw-wire types require drilling a hole in the piston to mount a transducer rod, which significantly increases cost. Longer pistons require longer bore holes, which increases the difficulty and the cost of manufacturing internal sensors for large cylinders. Furthermore, if an internal sensor malfunctions, the entire cylinder needs to be disassembled. External types are cheaper and easier to install due to the transducer being mounted on the surface of the cylinder. However, external mounting causes the sensor and its cabling to be more vulnerable in harsh environments. Proper protection of these is required, which complicates servicing and replacing parts. [1]

Therefore, to reduce the amount of sensors needed in machines and to provide a level of redundancy, sensor virtualization has been increasingly researched. This method utilizes information from other sensors to indirectly calculate a desired value based on a physical model of the process. Examples of application utilizing sensor virtualization include a car electric window position sensing from measuring current fluctuations of a DC drive motor [2], calculating fluid level in process tank and calculating the thickness of a steel sheet on rolling mill [3]. It is often necessary to perform test measurements from real processes to validate and calibrate simulations and thus try to minimize any accumulative errors. While virtual sensors can lead to saving in component and mechanical design costs, other design costs and time will increase. However, with simulation becoming more routine in all design processes, planning virtual sensors could become more commonplace. As mentioned, sensor virtualization provides a method for implementing position control of pump-controlled hydraulic cylinders.

Traditional valve controlled open-loop hydraulics tend to waste power due to idling losses either through a pressure relief valve or open centered valves. To improve the efficiency of hydraulic power transfer, it is necessary to reduce wasted power during idling and partial flow to actuators. One solution is to move from valve-controlled systems to pump-controlled, in which a motor drives a pump to control the flow to a single actuator. Pump-controlled hydraulic cylinders are often known as electro-hydrostatic actuators (EHA). In this study, a variation of EHA, Direct driven hydraulics (DDH) will be utilized. DDH uses an electric motor to drive a pump only when needed, which eliminates idling losses and reduces cooling requirements. Other benefits include reduced valve and pipe pressure losses due to requiring no directional valves and shorter pipelines. Pump-controlled hydraulic cylinders have been rare due to difference in the volume between the cylinder sides of single-rod cylinders and thus the required flow rate. This ratio problem has usually been solved by using double-rod cylinders where both sides of the cylinder piston have the same area and thus equal required flow [4, 5]. However, more space is needed for the double-rod cylinder. This can be acceptable in some applications and for short movements however, for instance in an excavator or a loader boom not often enough space is available for the opposite rod. While most EHA systems have used double-rod cylinders due to the ratio problem, systems with the more compact and common single-rod cylinders have been increasingly researched [6, 7]. Most common solutions to the ratio problem involve check valves in a single pump system or two pumps that ideally have the same output flow ratio as the cylinder.

Typically, the driving engine and pumps are often dimensioned to produce enough power to drive the actuators and overcome the losses. In DDH however, every flow resistance and pressure loss is undesired if it can be avoided since one advantage of DDH is shorter flow lines and less valves. Hoses and other pipelines tend to be ignored, either due to irrelevance and small effect on overall efficiency or simply having to dimension them according to how they can be fit inside a machine. In this research, the hose sizing was found to be a somewhat significant pressure loss source. This can sometimes be an unavoidable problem since the size can often be limited by the physical dimensions and movement of the machine.

Commonly the position control of these EHA systems have been realized by using cylinder position sensors. When accounting most benefits in a DDH system, it should in theory, be possible to estimate the position of a hydraulic actuator utilizing only information from the motor in a sensor virtualization algorithm. The idea is to use torque and speed data from a motor controller to calculate the pressure and flow produced by the pump and estimate the movement of the cylinder. However, in contrast to mechanical linkages, hydraulic power transfer lines always contains errors and losses compared to an ideal case due to properties of hydraulic fluids. Considering position control of a linear actuator, these errors are mainly caused by leakages through pumps but also somewhat by compressibility under high pressure and small leakage through cylinder piston seals. Leakages are dependent on various fluid properties, most importantly kinematic viscosity, and pressure according to [8].

Examples of previous research on sensorless position estimation of electro-hydraulic cylinders include position estimation of a DDH actuated cylinder with measuring the pump leakage in the locked position and calculating a slip coefficient that accounted for all leakages [8] and sensorless position control in an electro-hydraulic forklift [9]. These studies were based on measurements and did not account for temperature changes and [9] assumed constant pump efficiencies. Results obtained in both showed error in the range of 1-3 % during lifting and lowering. Also in [8], accumulation of error was observed in repeated lift-lower cycles due to inaccuracy in pressure estimation.

This study expanded on the research of sensorless position calculation of DDH cylinders by investigating the feasibility of sensorless position control of a DDH actuated hydraulic bucket arm mechanism of a test platform mining loader. The approach was to calculate the position of a two hydraulic cylinder actuating a bucket arm mechanism using only data from the servomotor controllers driving the pumps. The position calculation was realized by simulating the interaction between the DDH unit pumps and cylinder movement with various cylinder loads and oil temperatures. The remainder of this paper is organized as follows. Section 2 introduces test platform, its simplified simulation model and components and explains the operational principles of the system. Simulation results and analysis of error are described in Sections 3. Sections 4 and 5 contain discussion and conclusions, respectively.

2 Simulation model of the test platform

The simulation model is based on a mining loader of conventional diesel hydraulic type that had its original

hydraulic system replaced with DDH units and power system with a diesel-electric hybrid drivetrain. The front section consists of a boom and bucket. The boom is actuated by two parallel cylinders and the bucket by one cylinder. The base of the bucket cylinder is attached to a linkage mechanism that keeps the bucket angle stationary during the lifting of the boom. Figure 1 shows a 3D visualized model of this. Table 1 presents relevant information for the cylinders. Cylinder frictions were based on previous measurements with smaller cylinders and linearly scaled up to the loader cylinder dimensions [10].

The DDH units are designed to produce flow rates to both cylinder sides in a ratio that is as close as possible to the ratio of the cylinder areas. The units consist of an electric motor, motor controller, belt reduction transmission for fine-tuning the displacement ratios, intermeshing gear pumps [11], pressure relief valves, anti-cavitation valves, cylinder safety valves and oil reservoir.

Table 1. Relevant parameters for the mining loader hydraulic cylinders.

Parameter	Boom cylinder	Bucket cylinder
Stroke (mm)	311.15	850
A-side area (mm^2)	10261	18050
B-side area (mm^2)	7096.9	11847
Area ratio	1.4458	1.5236
Static friction (N) [10]	570	760
Coulomb friction (N) [10]	170	220
Viscous friction (N/(m/s)) [10]	41000	41000

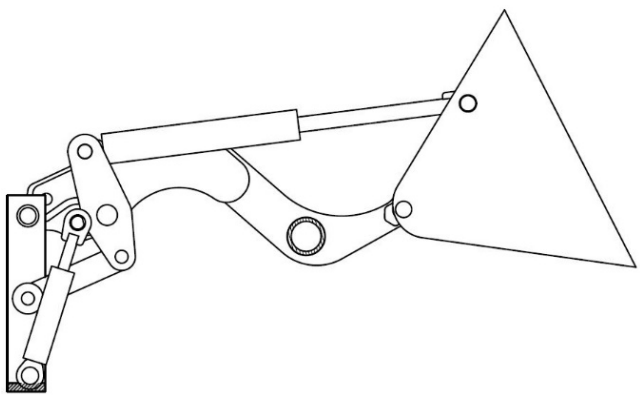

Figure 1. Visualization model of the mining loader bucket arm.

Hydraulic circuit diagram of the boom DDH unit is shown in fig. 2. The bucket DDH unit is identical with only different sized pumps and one cylinder. The instrumentation of the DDH units consist of pressure [12], temperature [13] and cylinder rod position wire-distance sensors [14]. Power is received from a lithium-titanate battery pack [15] that is recharged by the main hybrid power system [16]. Table 2 presents relevant parameters of the chosen pumps. Note that x2 in pump name means that the pumps are double chambered and the displacement in the name is for one chamber. X2 at the end means two parallel pump units, which will work as a single pump unit.

In a DDH system, the pump speed corresponds to fluid flow and torque to pressure, which in an electric motor can be measured as voltage and current. Correspondingly, the fluid flow rate affects the speed of a cylinder and pressure on the force. There are multiple sources for non-linearities and errors caused by the nature of hydraulics and its components, which makes calculating positions of the cylinders challenging. In addition, parameters of some components are based on estimations and simple calculations as measuring them would be impractical.

The estimation of cylinder rod positions is based on a simulation model of the bucket arm hydraulic systems. The model consists of kinematics and hydraulics parts. The model is created in Matlab/Simulink using ready-made Simscape multibody for kinematics and Fluid power blocks for hydraulics. Due to the kinematics of the loader arm, the cylinder loads are not constant during a lifting and lowering cycle. Thus to simplify the calculation of required motor torque a simple cylinder model was used with a load force applied to each cylinder to simulate cylinder movement dependence on pressure and pump operation. Since pressure, pump speed and oil viscosity affect pump leakages, the tests are performed with increasing cylinder force and varying oil temperature at each subsequent cycle.

Hydraulic cylinder force is caused by pressure difference acting on the piston surfaces in both piston sides as in equation 1:

$$F_p = \left(p_A A_{cyl_A} - p_B A_{cyl_B}\right)\eta_{hm_{cyl}} \quad , \qquad (1)$$

where F_p is the piston force, p_A and p_B pressures on each piston side, A_{cyl_A} and A_{cyl_B} the areas of the piston sides and η_{hm_cyl} is the hydro-mechanical efficiency of the cylinder. Area on side B is smaller due to the piston rod taking part of the space.

Piston movement is caused by the pumps forcing fluid into the cylinder. The piston moves at speed of:

$$v_{cyl} = \frac{Q_p}{A_{cyl}} \eta_{v_{cyl}} \quad , \qquad (2)$$

where v_{cyl} is the movement speed if the piston, Q_p the flow produced by the pump and η_{v_cyl} the volumetric efficiency of the cylinder. The pump is able to produce flow dictated by its rotational speed:

$$Q_p = \eta_{v_p} V_p \omega \quad , \qquad (3)$$

where Q_p is flow rate of the pump, η_{v_p} the volumetric efficiency of the pump or relative leakage back through the pump caused by pressure, V_p is rotational displacement and ω is rotational speed.

The pump volumetric efficiency is particularly important here as majority of the leakage losses are through the pump. The volumetric efficiency factor depends primarily on pressure difference between the pumping elements, gears in this case and viscosity of the oil. Various factors affect the pump specific efficiency curves, mostly clearance gaps between the gears and the chamber surface. It is known that volumetric efficiency has a more significant effect on total efficiency. Hydromechanical efficiency is affected by the internal friction of the pump, which is in turn affected by the lubricating effect of the leakage flow. Thus, the mechanical efficiency is also dependent on pressure and oil viscosity as well as the rotational speed of the pump [17]. Therefore, this simulation model uses nominal efficiencies from the manufacturer's datasheet. Efficiency variation is calculated within the pump model with the volumetric efficiency based on Hagen-Poiseuille laminar pipe flow model.

Table 2. Relevant parameters for the boom and bucket DDH unit pumps [11].

Parameter	Boom pumps A-side	Boom pumps B-side	Bucket pumps A-side	Bucket pumps B-side
	PGI100-008x2X2	PGI100-013+011	PGI100-016x2X2	PGI100-022x2
Total displacement (cm^3/rev)	15.8 * 2 = 31.6	24.2	31.6 * 2 = 63.2	44.4
Maximum circuit work pressure (bar)	270	70	70	172
Nominal volumetric efficiency at 250 bar and 1450 rpm	0.93	0.94	0.95	0.95
Nominal hydromechanical efficiency at 250 bar and 1450 rpm	0.91	0.91	0.92	0.93
Maximum rotational speed (rpm)	4200	4000	4000	3600
Gear ratio, motor to pump	28/41	41/47	28/44	44/47
A- and B-side geared flow ratio	1.416		1.542	

The torque required to run a pump depends on the pressure it needs to produce:

$$T_p = \frac{V_p \Delta p}{\eta_{hm}} \quad , \tag{4}$$

where T_p is pump torque, Δp pressure difference between pump outlet and inlet and η_{hm} hydro-mechanical efficiency that consists of friction of mechanical parts and fluid flow.

Hydromechanical efficiency is calculated with equation 4 and volumetric efficiency from equation 3:

$$\eta_{hm} = \frac{V_p \Delta p}{T_p} \quad , \tag{5}$$

$$\eta_v = \frac{Q_p}{V_p \omega} \quad , \tag{6}$$

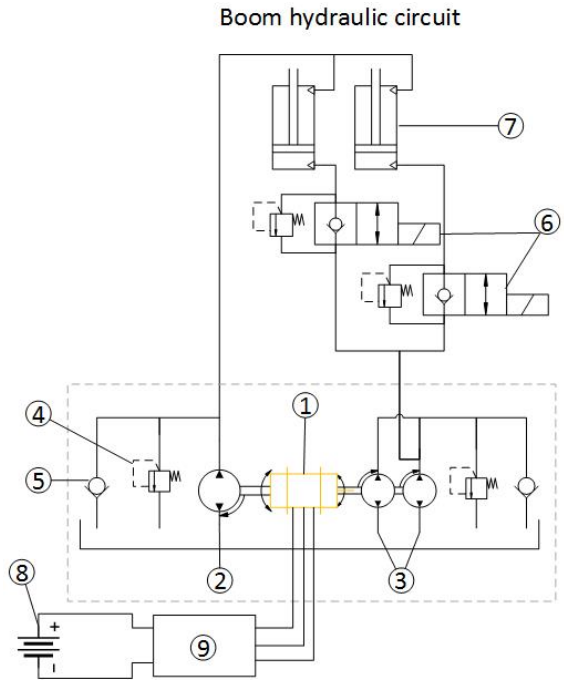

	Component	Model
1	Electric motor	Motenergy ME1304
2	B-side pump	HYDAC PGI100
3	A-side pumps	HYDAC PGI100
4	Pump pressure relief valve	HYDAC DB10P-01
5	Anti-cavitation valve	HYDAC RV12A-01
6	Safety valves	HYDAC WS16ZR-01
7	Hydraulic cylinder	EJC90 original
8	Battery	Altairnano 96 V
9	Motor controller	Sevcon Gen 4 Size 6

Figure 2. Components of the boom DDH unit. [Courtesy of T. Lehmuspelto. Aalto University. 2016]

As an example, fig. 3 shows volumetric and hydro-mechanical efficiencies of several gear pump sizes in relation to pressure at nominal pump speed of 1450 rpm.

Of these, sizes 8, 13, 16 and 22 are used. Size 8 efficiencies are available in a similar figure. In the figure, it can be seen that the volumetric efficiency decreases linearly with increasing pressure. In contrast, the hydro-mechanical efficiency increases rapidly at lower pressures and settles to almost constant but slightly increasing value at higher pressures. However, these efficiencies apply only for the oil viscosity and pump rotational speed used for measuring these graphs. Efficiencies at other oil viscosities and pump speeds are calculated as described. Direct measurements of volumetric and hydromechanical efficiencies is not feasible with the available test equipment, meaning that efficiencies will only be calculated in the simulation model and not measured.

Based on fig. 3 and the basic hydraulic equations of pump flow, pressure and efficiencies as well as piston force, a hypothesis can be formed for the cylinder movement under load. When cylinder payload increases, more pressure is needed to move it, which requires more pump torque. Higher pressure reduces the volumetric efficiency and thus causes more flow losses. Thus, the cylinder lifting movement against the load by flow produced by a pump revolution should decrease and reversely the lowering movement should increase. Figure 4 summarizes a diagram of the interaction between different parts and factors related in the sensorless position calculation process.

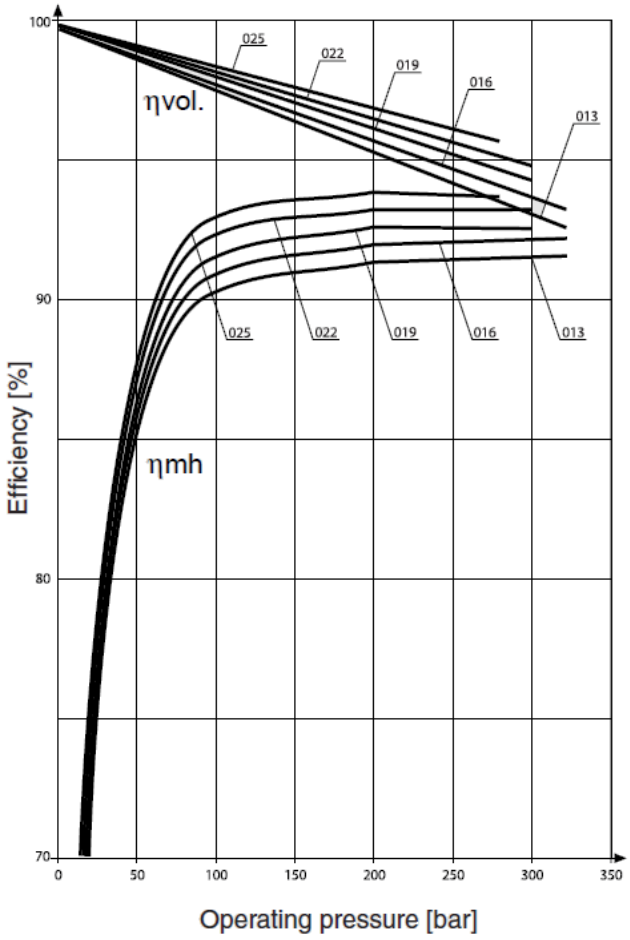

Figure 3. Efficiencies of several HYDAC gear pump sizes with VG46 equivalent oil at speed of 1450 rpm. [11]

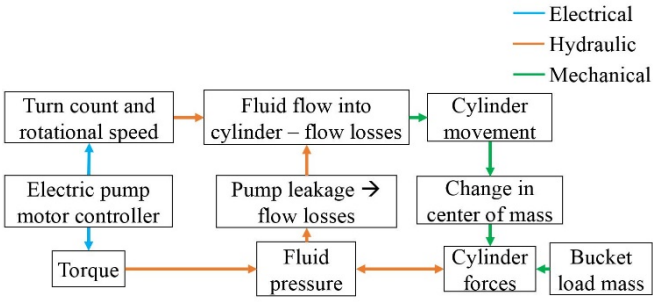

Figure 4. Relation between DDH simulation parts in sensorless position control.

In this study, models of the boom side DDH units is used as an example. In fig. 5 simplified version of the boom hydraulics blocks are presented. The hydraulics model is built based on the original schematics. Input for the pumps is produced by an ideal rotational velocity source that is supposed to act as a speed controlled motor. Pipelines add a significant amount of flow resistance and thus pressure loss. They also provide additional hydrostatic pressure dampening by allowing the pipelines to expand, which is important for the stability of the model as otherwise the model would be too stiff to allow proper interaction between the hydraulic and the kinematic parts. The safety valves are closed during lifting and opened during lowering according to motor speed. Some parameters of valves such as maximum opening areas are not given in manufacturer datasheets so the values are calculated from other information. Oil used is based on Shell Tellus T 32, which is VG32 equivalent hydraulic oil meaning it has a kinematic viscosity of 32 mm^2/s at temperature of 40 °C. Viscosity dependancy on temperature data is taken from Shell Tellus T oils datasheet [18].

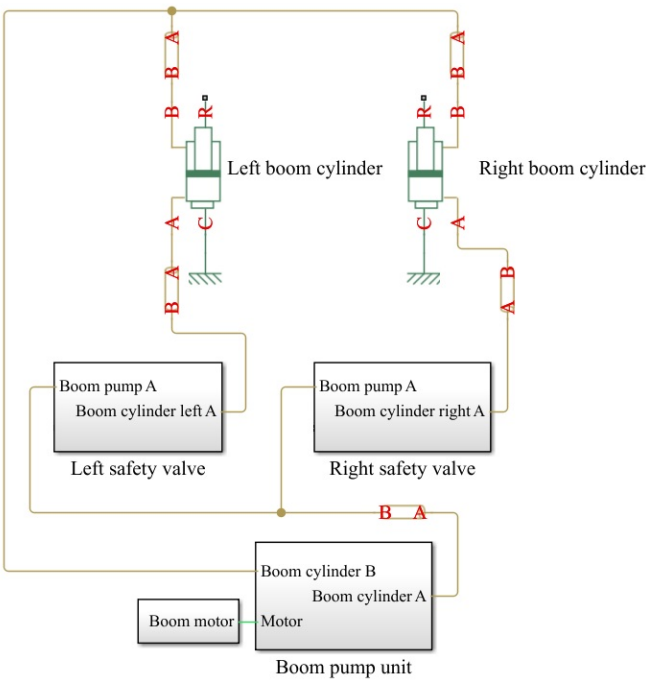

Figure 5. Simplified presentation of the Simscape model blocks used for modelling the boom DDH and cylinders.

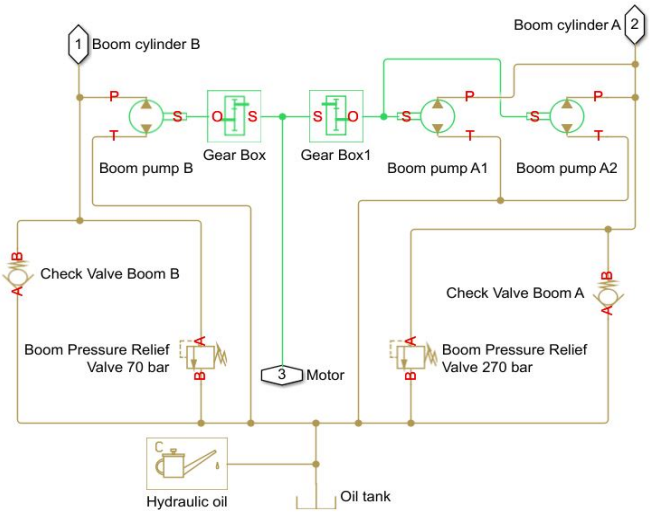

Figure 6. Simplified model of the boom pump system.

Figure 6 illustrates a simplified model of the boom pump system. The pumps are presented by fixed displacement hydraulic machines, which can work in both pump and motoring modes. This allows the pumps to run freely in motoring mode during lowering movements and as such do not cause disruptions in flow as regular pump model blocks would. The pump model has included loss calculation for leakage and friction. The losses can be computed either analytically or from table data efficiencies. Since it is often only necessary to verify whether the pump has specified parameters that are close enough to required, the manufacturer datasheets of the pumps only provide volumetric and mechanical efficiencies at one specific oil viscosity and pump speed [11]. As it was not feasible to perform leakage measurements with the real pumps, it was not possible to form lookup tables for the pump efficiencies at various oil temperatures and pump speeds, which is why the analytical method was utilized. For the sake of simplifying the problem, it is assumed that the physical properties of the pumps and other hydraulic components such as sealant wear, do not change. [19]

The analytical efficiency calculation uses nominal parameters of the pump to calculate Hagen-Poiseuille coefficient for laminar pipe flows. The nominal parameters of rotational speed, oil kinematic viscosity and density, pressure gain, volumetric and mechanical efficiencies are taken from the pump datasheet. The nominal rotational speed is 1450 rpm, oil kinematic viscosity is 46 mm^2/s at temperature of 40 °C, density is 872 kg/m^3 at temperature of 15 °C and pressure gain is the pump rated pressure of 250 bar. The efficiencies are taken from graphs of fig. 4 at the points of nominal pressure. Additional parameters required are No-load torque, which is left as default of 0.5 Nm and friction torque vs pressure gain coefficient, which is calculated from the volumetric and total efficiencies and pump displacement. [11, 17, 18]

Other parameters that were not possible to obtain from datasheets include cylinder frictions and hose flexibility. The cylinder frictions were estimated based on previous measurements of smaller cylinders and scaled to the size of the mining loader cylinders [10]. While this method does not provide the most accurate estimates due to differences in cylinder construction and seals, it grants a perspective to what scale the actual cylinder frictions are.

Friction torque τ_{Fric} is calculated according to equation 7:

$$\tau_0 + K_{TP} |\Delta p| \tanh\left(\frac{4\omega}{\omega_{Thresh}}\right) \quad , \tag{7}$$

$$\tau_{Fric} = ¿$$

where τ_0 is no-load torque, K_{TP} is friction torque vs pressure gain coefficient, Δp is the current pressure gain, ω is current pump angular velocity and ω_{Thresh} is threshold angular velocity between pump and motor mode transition.

The is friction torque vs pressure gain coefficient is calculated as:

$$K_{TP} = 1.5915 * 10^{-7} * V_p * \left(\frac{\eta_{v,Nom}}{\eta_{Tot}} - 1\right) \tag{8}$$

,

where V_p is pump displacement, $\eta_{v,Nom}$ is the volumetric efficiency at nominal state and η_{Tot} is total efficiency. The

Leakage flow q_{Leak} is calculated as the current pump pressure gain times the Hagen-Poiseuille coeffcient K_{HP}:

$$q_{Leak} = K_{HP} \Delta p \quad , \tag{9}$$

The Hagen-Poiseuille coefficient in this model is calculated as in:

$$K_{HP} = \frac{\nu_{Nom}}{\rho \nu} \frac{\rho_{Nom} \omega_{Nom} V_p}{\Delta p_{Nom}} \left(1 - \eta_{v,Nom}\right) \tag{10}$$

,

where ν_{Nom} is the oil kinematic viscosity at nominal state, ν is the current kinematic viscosity, ρ_{Nom} is the nominal oil density, ρ is the current oil density, ω_{Nom} is the nominal pump angular velocity and Δp_{Nom} is the nominal pressure gain.

Due to lack of data on the oil density dependance on temperature and the assumption that change in density with changing temperature is small with liquids, in this model the oil density stays constant. This assumption should not have a significant effect because as seen in eq. 5, the Hagen-Poiseuille coefficient depends on the ratio of nominal and current density. As the density change is small, it can be assumed that this the value of this ratio will stay close to one.

As mentioned, problems in modelling the loader arm are caused by changing cylinder load during the movement as well as stiffness of the combined hydraulics and kinematic model. Thus, the model was reduced to only the cylinders with load forces applied to the piston rods. The test load

force affecting a cylinder was set between a small force of 1 kN to a force that causes the cylinder pressure to be at relief valve pressure. Maximum lift force for both boom cylinders is about 554.1 kN and for the bucket cylinder it is about 203.8 kN. When the relief valves start to open, part of the flow is diverted through them, which causes the cylinder position calculation process be no longer valid since it assumes that all flow leakage is through the pumps.

Results from running the simulation of cylinder movement under increasing loads and oil temperature, and measuring the required torque was saved as table data of motor torque vs cylinder movement per motor revolution. Positive and negative movement of the cylinders have their own tables with the motor direction determining which to use. Since the simulation was run at variable time step, the amount of motor revolutions per step varies. Thus, the current cylinder speed was calculated from the current motor speed and the cylinder movement per motor revolution. Integrating this calculated speed gives the cylinder movement during the time step. Cumulatively summing the movement steps gives the current position of the cylinder relative to the starting position. This requires the maximum time step to set short enough so that there can be no significant variations of these values during a step. Figure 7 shows the process flow and the parameters of the cylinder position calculation in the simulation.

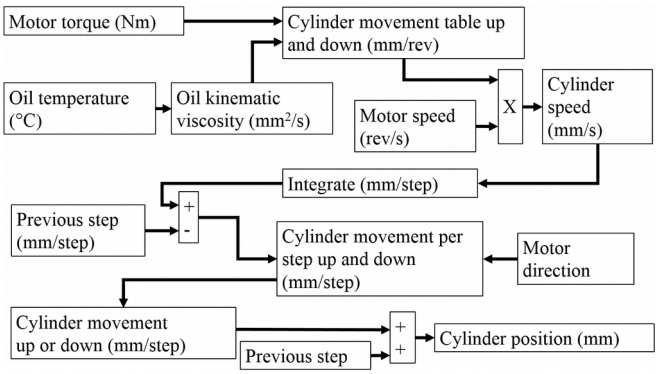

Figure 7. Process flow and parameters of the cylinder position calculation in the simulation model.

Figure 8 provides the explanation for the sensorless control of a DDH actuated cylinder. The user in this case is the high-level input source and can be either human or an automated process that provides control inputs to the DDH motor controller. The motor controller in turn feeds back torque and speed data from the motor sensors, which are used to calculate the cylinder position. This position data is then given to the user. This way the cylinder position calculation functions as a normal position sensor for the user.

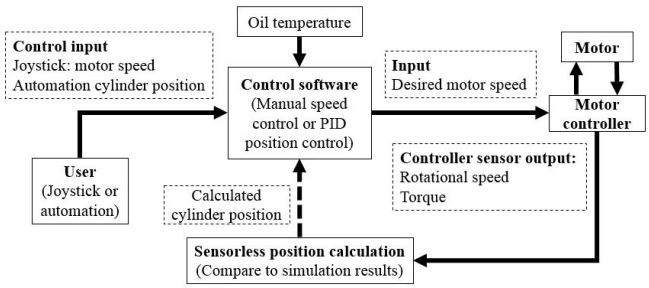

Figure 8. Diagram flowchart for the sensorless control of DDH.

The following section introduces results of simulated lift-lower cycles, which test the accuracy of the sensorless position calculation.

3 Results

Presented in figs. 9 and 10 illustrate examples of a simulation-based result of the boom and bucket cylinder movement per pump motor revolution in function of torque. The bucket motor torque is reverse to the boom due to the bucket cylinder rod-side being the lifting side and thus the motor is driven in negative direction. The figures illustrate that increasing cylinder load and pressure, and thus torque causes less cylinder movement per pump revolution during lifting due to increasing pump leakage and vice versa for lowering. Rapid drop at high torque in the lifting graph is caused by pressure reaching pressure relief valve limit. At higher temperatures, oil viscosity is lower thus causing more pump leakage and lower cylinder movement ratio. The sensorless position calculation is based on lookup tables consisting of these graphs at various temperatures.

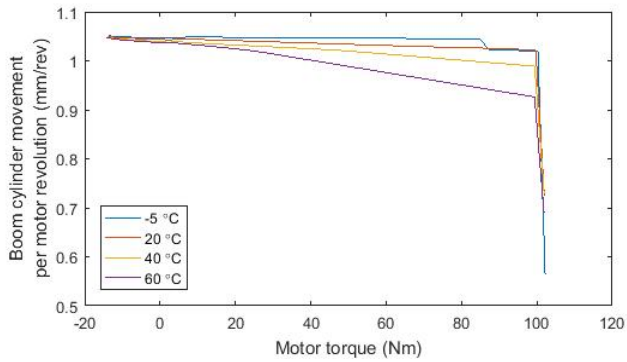

Figure 9. Boom cylinder movement per motor revolution in function of torque at various temperatures.

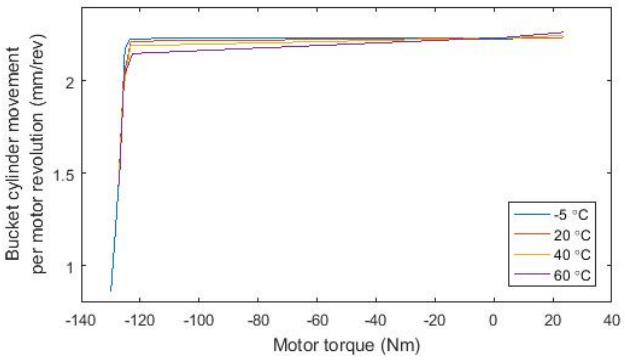

Figure 10. Bucket cylinder movement per motor revolution in function of torque at various temperatures.

Figure 11 shows the boom cylinder position at low cylinder load and fig. 12 with high load based on the simulated actual cylinder position and the position calculated with the look up tables. The cycle consist of running the motor for a fixed amount of time at constant speed. In these figures, results of a lift-lower cycle of the boom and bucket cylinders with a low and a high load with oil temperature of 40 °C are shown as the examples. These loads are ¼ and about ¾ of the maximum load limited by the pressure relief valves. The oil temperature of 40 °C for these examples was chosen as it is in the range of the most commonly expected running temperature of hydraulic oil, from about 40 – 60 °C and nominal oil viscosities are most commonly given at temperature of 40 °C.

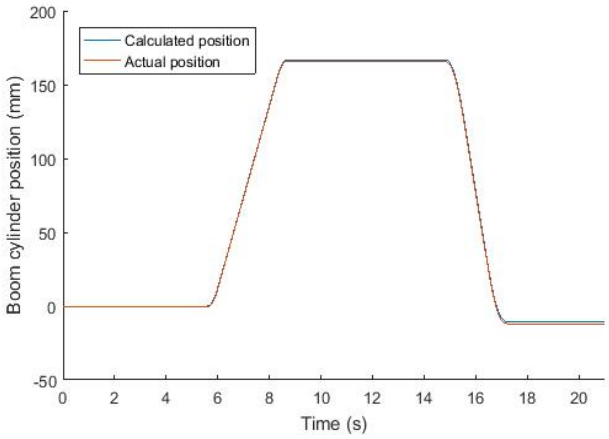

Figure 11. Calculated and actual simulation boom cylinder position with cylinder ¼ load of 129 kN and oil temperature of 40 °C.

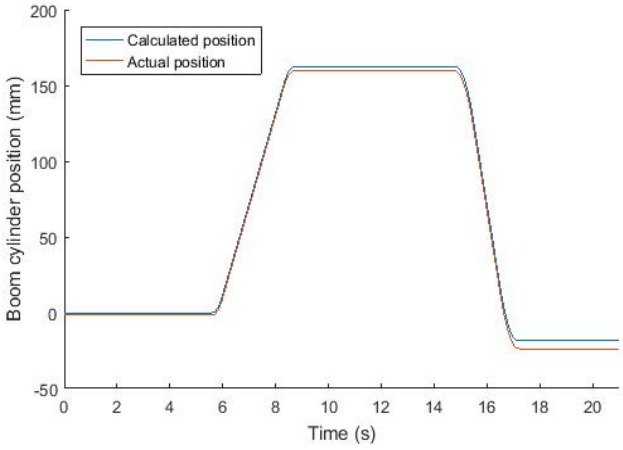

Figure 12. Calculated and actual simulation boom cylinder position with ¾ cylinder load of 441 kN and oil temperature of 40 °C

Figures 13 and 14 show the graphs for the bucket cylinder with the same conditions. As mentioned, the lift direction of the cylinder is retraction.

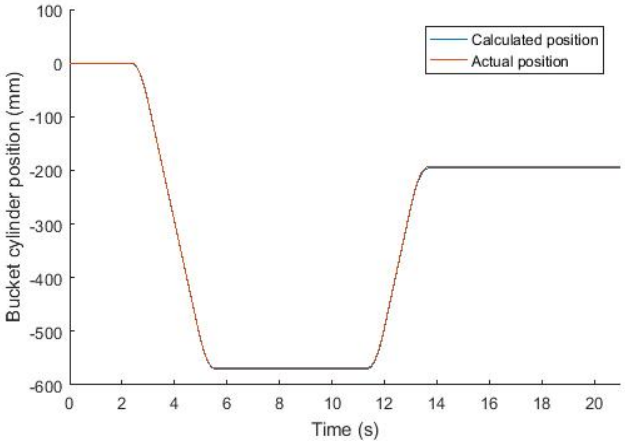

Figure 13. Calculated and actual simulation bucket cylinder position with cylinder ¼ load of 48 kN and oil temperature of 40 °C.

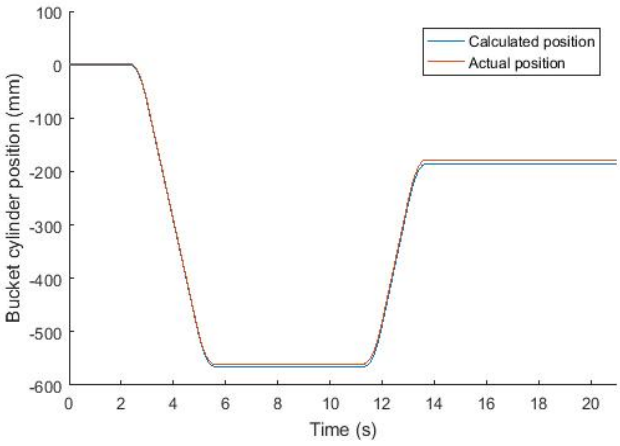

Figure 14. Calculated and actual simulation bucket cylinder position with cylinder ¾ load of 162 kN and oil temperature of 40 °C.

Figures 15 and 16 present the errors of the boom and bucket cylinder positions at various load levels. The light load is again ¼, medium is ½ and high is about ¾ of the maximum theoretical cylinder load.

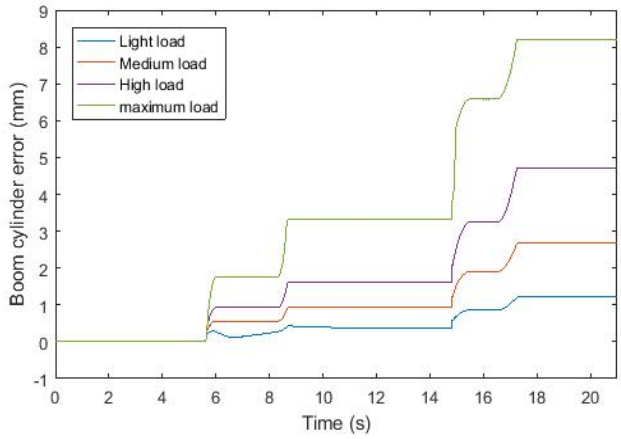

Figure 15. Error between the actual simulation and calculated boom cylinder position at various load levels at oil temperature of 40 °C.

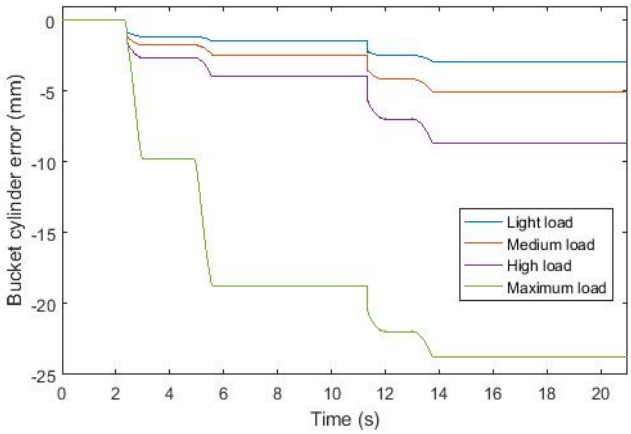

Figure 16. Error between the simulation true and calculated bucket cylinder position at various load levels at oil temperature of 40 °C.

4 Discussion

Presented sensorless position study based on DDH was illustrated for a mining loader case, however, it can also be extended for stationary application.

Based on the simulation results, the sensorless positioning of this DDH system provides sufficient accuracy within tested conditions for a single lifting lowering work cycle and chosen medium load. Best achieved accuracy was within a few millimeters for a single cylinder. During the movement, the position calculation accumulates no error as the calculation process is based on simulation of the cylinder movement with constant motor speed. However, there is a notable accumulation of error, which is mainly caused by errors induced during the motor acceleration and deceleration phases. A typical work cycle of a mining loader consist of lifting a load and dumping it during which the cylinder pistons will certainly reach the end-points or pass through the middle. Therefore, this error for repeated cycles can be resolved by adding simple proximity sensors in the cylinder end or middle points to be used as reference points for the sensorless position calculation.

It is also useful to discuss the degree of accuracy needed. In conventional systems, direct measurement of cylinder position provides the greatest accuracy at the cost of more expensive sensor equipment. However, if millimeter scale accuracy is not needed and centimeters are enough, sensorless positioning is likely viable and cheaper. However, direct driven servo hydraulics are needed to implement sensorless positioning of cylinders. Also depending on the layout of the DDH system, more pump units are needed if multi-pump system is chosen. In this study, the efficiency of the energy storage and power electronics were not considered in this stage of research. Consequently, DDH brings advantages such as sensorless position control but also disadvantages with requirements of more components and extra expenses. However, further investigation of these components will be included in close future.

As such, if direct driven hydraulics are utilized to drive a cylinder, sensorless positioning almost comes with it. If parameters of a single DDH unit and the actuator it drives are known, it is easier to simulate and predict the behavior of the system since at known pressure level and flow rate the cylinder moves at constant speed and a constant pump motor torque and rotational speed is required for this. However, in some cases it could be difficult to obtain all the necessary information to build accurate simulation models of a given system.

In this study, pump leakages were assumed to match the manufacturer datasheets. Pump leakages are mainly dependent on fluid viscosity and pressure, which makes behavior more predictable. Only inaccuracies that remain are how accurately the pump volumetric and mechanical efficiencies as well as frictions are defined by the manufacturer. This becomes a significant source of error in a more unknown system. The cylinder friction was also based on assumptions of previous friction measurements with a smaller cylinder, which is likely to provide in some amount inaccurate values. Measurements with the mining loader will be executed for more accurate friction values. In a real life system, factors such as seal wear cause additional non-linearity sources, which can be difficult to predict unless accurate wear models are taken into account. In addition, properties of the oil change with time as the oil ages and impurities from various sources mix in. Thus, it will be easier to implement a sensorless positioning logic into an EHA unit designed from scratch where all relevant parameters are known. If the cylinder is separate, additional measurements will be needed to define friction.

5 Conclusion

This study researched the viability and methods of sensorless position control of direct driven hydraulic

cylinder via simulation model. Simulation results of comparing the actual and calculated cylinder position during a single lift-lower cycle showed an accumulated error at high load within about 5 mm for the boom cylinder and about 10 mm for the bucket cylinder. The error was smaller at lower loads. The notable error accumulation and problems near and over the maximum pressure limits would require means of providing a reference point, for example with proximity sensors. Further research is needed to validate the simulation results by performing test measurements with the real DDH units.

Acknowledgements

This research was enabled by the financial support of Tekes, the Finnish Funding Agency for Technology and Innovation, (project EL-Zon) and internal funding at the Department of Mechanical Engineering at Aalto University. The cooperation with Lehmuspelto Teemu and Tammisto Otto is highly appreciated.

Nomenclature

Designation	Denotation	Unit
F_p	Piston force	[N]
p_A	A-side pressure	[Pa]
p_B	B-side pressure	[Pa]
A_{cyl_A}	Piston A-side area	[m^2]
A_{cyl_B}	Piston B-side area	[m^2]
η_{hm_cyl}	Cylinder hydro-mechanical efficiency	
η_{v_cyl}	Cylinder volumetric efficiency	
v_{cyl}	Cylinder piston velocity	[m/s]
Q_p	Pump flow	[m^3/s]
η_{v_p}	Pump volumetric efficiency	
η_{hm_p}	Pump hydro-mechanical efficiency	
V_p	Pump displacement	[m^3/rev]
T_p	Pump torque	[Nm]
τ_{Fric}	Friction torque	[Nm]
τ_0	No-load torque	[Nm]
K_{TP}	Friction torque vs pressure gain coefficient	[Nm/pa]
Δp	Pump pressure gain	[Pa]
Δp_{Nom}	Nominal pump pressure gain	[Pa]
ω	Pump angular velocity	[rad/s]
ω_{Nom}	Nominal pump angular velocity	[rad/s]
ω_{Thresh}	Threshold angular velocity between pump and motor mode transition	[rad/s]
$\eta_{v,Nom}$	Nominal volumetric efficiency	
η_{Tot}	Total efficiency	
q_{Leak}	Leakage flow	[m^3]
K_{HP}	Hagen-Poiseuille coefficient	
ν_{Nom}	Nominal oil kinematic viscosity	[m^2/s]
ρ_{Nom}	Nominal oil density	[kg/m^3]
ρ	Current oil density	[kg/m^3]

References

[1] E. E. Herceg. Taking a Position on Hydraulic Cylinder Sensors. Alliance Sensors Group. *Hydraulics & Pneumatics*. 2015. Available: http://hydraulicspneumatics.com/cylinders-actuators/taking-position-hydraulic-cylinder-sensors

[2] A. Consoli, G. Bottiglieri, R. Letor, R. Ruggeri, A. Testa, S. De Caro. Sensorless Position Control of DC Actuators for Automotive Applications. *IAS 2004. MIUR-PRIN 2003: Innovative conversion topologies for electric drives.*

[3] Pedro, A, Goodwin G. Virtual Sensors for Control Applications. *Annual Reviews in Control 26* (2002) 101-112.

[4] Manring, N. *Hydraulic Control Systems*. Hoboken, N.J: John Wiley & Sons, 2005. 446 p. ISBN 0-471-69311-1

[5] S. Habibi. A. Goldenberg. Design of a New High-Performance ElectroHydraulic Actuator. *IEEE/ASME TRANSACTIONS ON MECHATRONICS, VOL. 5, NO. 2*, JUNE 2000. P. 158-164

[6] K. Heybroek. Saving Energy in Construction Machinery using Displacement Control Hydraulics, Concept Realization and Validation. PHD Thesis. *Linköping University, Division of Fluid and Mechanical Engineering Systems, Department of Management and Engineering*. Lingköping. 2008. 127 p.

[7] T. Minav, C. Bonato, P. Sainio & M. Pietola. Direct Driven Hydraulic Drive. In: *The 9th International Fluid Power Conference*. 2014

[8] C. Bonato, T. Minav, P. Sainio, M. Pietola. Position control of direct driven hydraulic drive. *Proceedings of the 8th FPNI Ph.D Symposium on Fluid Power, FPNI2014*. 2014, June 11-13, 2014, Lappeenranta, Finland

[9] T. Minav, L. Laurila, J. Pyrhönen. Relative position control in an electro-hydraulic forklift. *International Review of Automatic Control (I.RE.A.CO.), Vol. X, n. X*. 2012

[10] A. Järf. Flow compensation using hydraulic accumulator in direct driven hydraulic differential cylinder application and effects on energy efficiency. Master's thesis. *Aalto University, School of Engineering*. Espoo 2016. 102 p.

[11] Hydac. Medium heavy duty series size 2 PGI100. http://www.hydac.com/fileadmin/pdb/pdf/PRO00000000000000000000002905010012.pdf. Visited on: 5.2.2017

[12] Parker. SCPT-CAN Pressure/Temperature sensor. https://promo.parker.com/parkerimages/promosite/SensoControl/UNITED%20STATES/About%20SensoControl/PDF/SCPT-CAN-Manual.pdf. Visited on: 5.2.2017

[13] JUMO. CANtrans TRTD temperature probe with CANopen output. https://www.jumo.net/attachments/JUMO/attachmentdownload?id=4533. Visited on: 5.2.2017

[14] Posital Fraba. LINARIX Linear Sensor. https://www.posital.com/en/products/linear-sensors/linarix-product-finder/LM0-CA00B-1212-2C00-PAM/125004001/detail.php. Visited on: 5.2.2017

[15] Altairnano. 24V 60Ah Battery module. http://www.altairnano.com/products/battery-module/. Visited on: 5.2.2017

[16] T. Minav, T. Lehmuspelto, P. Sainio, M. Pietola. Series hybrid Mining loader with zonal hydraulics. *10th International Fluid Power Conference*. 2016

[17] T. Schimmel. Efficiency of Hydraulic Fluids – Theory and Field Testing. Evonik Oil Additives. Evonik Industries. Helsinki 2013.

[18] Shell Lubricants. Shell Tellus oils T Technical datasheet. http://www.epc.shell.com/Docs/GPCDOC_X_cbe_24855_key_140002044283_6623.pdf. Visited on: 12.11.2016

[19] The MathWorks Inc. Fixed-Displacement Pump. 2016. https://se.mathworks.com/help/physmod/hydro/ref/fixeddisplacementpump.html. Visited on: 5.2.2017

An Approach to Combine an Independent Metering System with an Electro-Hydraulic Flow-on-Demand Hybrid-System

M. WYDRA , M. GEIMER , and B. WEISS*

Karlsruhe Institute of Technology, Chair of Mobile Machines, Karlsruhe, Germany
E-mail: marco.wydra@kit.edu, marcus.geimer@kit.edu, bweiss@weiss-can-sps.de
*Weiss Mobiltechnik GmbH, Rohrdorf, Germany

Abstract

By combining an electro-hydraulic flow-on-demand system with an independent metering of the actuators in- and outlet, a higher efficiency and a better controllability compared to conventional hydraulic-mechanic load sensing systems can be reached. It also enables the integration of a hydraulic accumulator to recuperate energy due to active loads. This paper presents an alternative control strategy for this kind of hydraulic propulsion systems. Connected with the pump and during passive loads the meter-in flow controls the velocity of the actuator. Otherwise the velocity control is achieved by the meter-out flow while the oil flows into the accumulator or tank. Exemplary this system is simulated for a mobile forestry crane. Further steps are building up a test bench for optimization and validation as well as an implementation into a real machine for testing the suitability in use.

Keywords: flow-on-demand, independent metering, control, recuperation, hybrid system

1 Introduction

With the investigation of electronic components the automation of processes gets more important. This means that in times of *Industry 4.0*, machines are fully integrated with sensors to observe the current status. In mobile machines this leads to change the current manual hydraulic-mechanic actuation to automated electro-hydraulic actuation. A first step is to change the hydraulic-mechanic components of the hydraulic system with obtainable electric-hydraulic components. Hereby the possibility to improve the efficiency of mobile machines is increased. [1]

For this, *Scherer* presents in [2] an electro-hydraulic flow-on-demand system (eBSS) which needs an electric actuated pump and valves. eBSS may reduces the used energy of the pump up to 10-12 % depending on the application and the load cycle of the machine. This is caused by the reduction of pressure losses between system pressure and load sensing (LS) pressure from usually 10-30 bar in LS-systems [3] to 8-10 bar in eBSS-systems, cf. fig. 1 diagram (I) & (II). In LS-systems the LS-pressure losses can also be reduced by pump pressure settings, but this influences the dynamic behaviour of the system [2].

Actuating the pump and the valves simultaneously by the same control signal, such control is more immediately and comfortable [2].

Due to the electro-hydraulic actuation of the valves, the consecutive step is to separate the meter-in and meter-out control edge, which is well researched by [4], [5], [6].

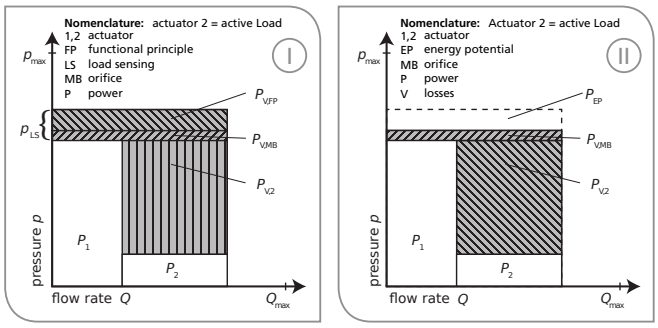

Figure 1: Pump performance for several systems: (I) LS-system, (II) eBSS-system [2]

Especially *Axin* declares in [4] different kinds of operating modes called normal operation mode, regenerative operation mode, energy neutral operation mode and recuperative operation mode. These new modes can reduce the needed pump performance as shown in the diagrams (III) & (IV) in fig. 2.

Based on the proposed systems, this paper will show a control strategy using the electro-hydraulic flow-on-demand by separating the actuators meter-in and meter-out control edges and implementing a hydraulic accumulator due to the possible operating modes.

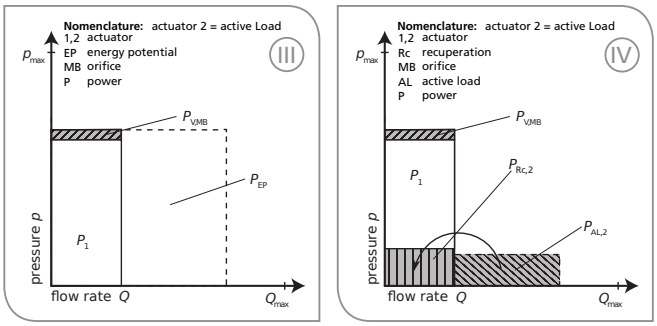

Figure 2: Pump performance for several systems: (III) eBSS+IM-system, (IV) eBSS+IM-system with hybridization [2]

1.1 Operation Modes

By using independent metering, it is possible to choose between several operation modes. To classify these operation modes, it is necessary to monitor the actuators status and match it with the possibilities to connect the actuators in- and outlet with the pump, tank or accumulator.

The actuators status is defined by its movement and the resulting forces due to the loads, friction and pressure, see fig 3. The resulting force F_{Load} to an actuator is defined in equation (1). For the following explanations, a differential-cylinder is used as an exemplary actuator.

$$F_{Load} = p_B \cdot A_B - p_A \cdot A_A + F_{Fric} \tag{1}$$

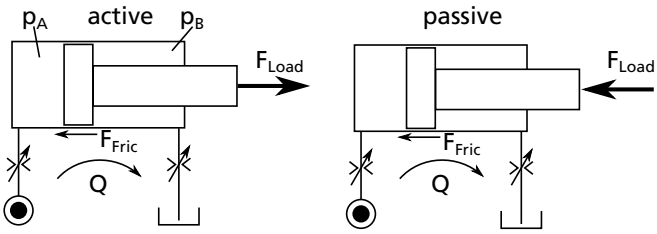

Figure 3: Active and passive loads

When both, the motion and load force vector have the same direction, the status is called active load, otherwise it is a passive load. In passive load situations, an actuator is always moved by the flow rate of the pump. In this paper, the actuators movement is referred to as the movement demanded by an operator. The decisions in the controller design will be independent of the measured actuator velocity.

Separating the meter-in and meter-out control edge gives the possibility to connect the actuator as shown in fig. 4. In normal operation mode (NOM), the inlet is connected to the pump, the outlet to the tank. With an independent metering it is possible to optimize the meter-out control edge throttle losses [4]. Furthermore, the regulation of the meter-out control edge influences the pressure in the inlet chamber. With a pressure control of the inlet chamber, the system can be forced to be in passive load status. Therefore, cavitation in the inlet chamber can be minimized. The velocity of the actuator is adjusted by the meter-in control edge. The same functionality is offered by a lowering brake valve.

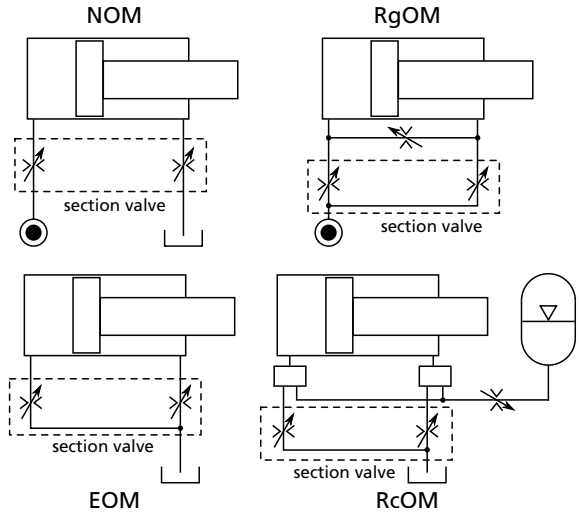

Figure 4: Possibilities to connect an actuator with separate control edges; NOM - normal operation mode, EOM - energy neutral operation mode, RgOM - regenerative operation mode, RcOM - recuperative operation mode

Connecting the pump with the in- and outlet of the actuator, the operation mode is called regenerative operation mode (RgOM). RgOM can reduce throttle losses in hydraulic systems with great pressure differences between the various actuators [4]. This is caused by increasing pressure due to a smaller operation area. The oil supply by the pump is reduced in amount of the out-flowing oil, see equation (3). In this paper the RgOM is neglected, because it will increase the complexity and the number of necessary components.

$$Q_{Pump,NOM} = Q_{In} \tag{2}$$

$$Q_{Pump,RgOM} = Q_{In} - Q_{Out} \tag{3}$$

The energy neutral operation mode (EOM) is a special part of regeneration. Here the actuators chambers are connected to the tank, so the flow rate to the inlet is the sum of the out-flowing oil and, if necessary, oil from the tank, see equation 5. No oil from the pump is needed here. This reduces the throttle losses as well as the demanded power by the primary energy supply and in addition influences the oil temperature. Here, the meter-out orifice adjusts the actuator's velocity. [4]

$$Q_{Pump,EOM/RcOM} = 0 \tag{4}$$

because of

$$Q_{In} = Q_{Out} (+Q_{Tank}) \tag{5}$$

The last operation mode is the recuperative operation mode (RcOM). This mode is very close to the EOM. Instead of

connecting the outlet with the tank, it is connected to the accumulator [4]. Therefore, a reduction of pressure losses will be achieved by a smaller pressure difference between the actuator's outlet pressure p_{Out} and the rising accumulator pressure p_{Acc}, see figure 5. Like in EOM, the meter-out orifice is used to control the actuator's velocity. This operation mode will be preferred by active loads and swaps with the EOM during operation.

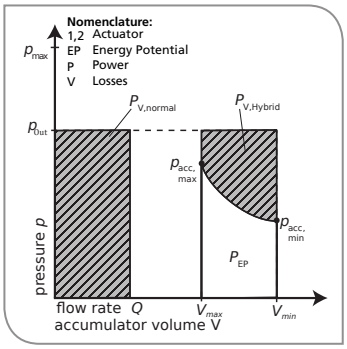

Figure 5: Throttle losses for active loads: relaxing to tank(left) and to accumulator(right); throttle losses to accumulator depends on p_{acc}

The way of using the RcOM strongly depends on the given load situations and the operations strategy. In this paper, the authors primarily focuses on buffering energy into the accumulator. The buffered energy will not be used in a specific way. More information and possibilities to use the recuperative potential can be found in [7] or [8].

The accumulator can also be used to reduce the throttling losses at the section valves during the NOM. *Siebert* wrote about this possibility in [9]. The current paper focuses on the filling of the accumulator without evoking a unsuitable operation behaviour for the operator.

2 Application to a Mobile Forestry Crane

Within a public funded research project at the Karlsruhe Institute of Technology (KIT), the following controller design will be tested on a mobile forestry crane like in [2] with the eBSS system before. First of all it is tested in a simulation, then on a test bench and finally the system will be integrated in a demonstrator. For that, the following lines show the system structure and the provided controller design.

2.1 System Structure

The electro-hydraulic flow-on-demand system integrates a load independence due to individual secondary pressure compensator [2]. The system is a flow-sharing system, which means during a higher demand of flow rate than the maximum flow rate of the pump, all actuators will operate with a reduced velocity. The displacement of the pump is adjusted by an electro-hydraulic controller which controls the delay angle of the swash plate [2]. The pump controller is overlain by a pressure control valve which regulates the maximum pressure of the hydraulic system, cf. fig. 6.

The position of the section valve spool is forced by the control-signal u. For this, the section valves are equipped with an internal position control of the spool. Thus, it is possible to match the actuators flow rate via the section valves to the current displacement of the pump.

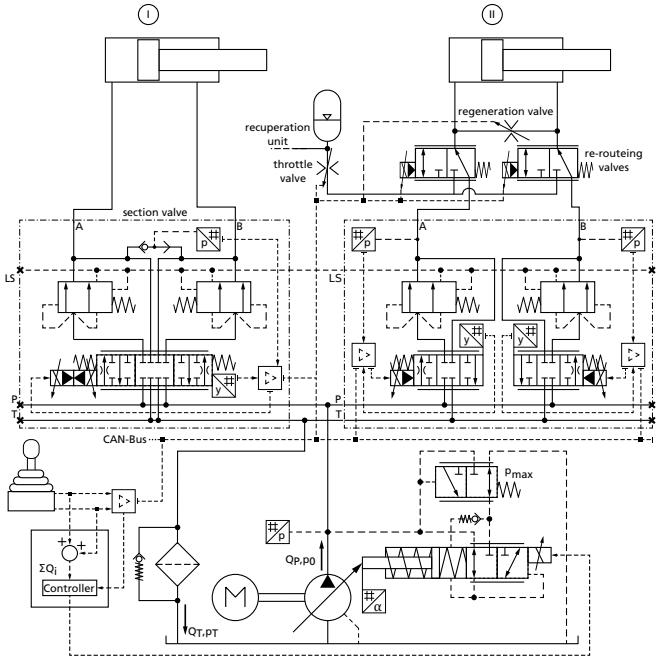

Figure 6: eBSS-system with conventional valve (I) and with separated control edges (II)

For each section, the current 8/4-valve will be replaced by two 4/3-valves, so the in- and outlet of an actuator can be controlled independently. Figure 6 shows a hydraulic circuit with two actuators including all needed components for all possible modes. While actuator one (left-handed) is equipped with the conventional section valve, the second actuator is equipped with the new section valve. Each valve possess a secondary pressure compensator.

As mentioned in 1.1, the regenerative operation mode (RgOM) could only be realized in this system by adding a valve from the outlet to the inlet between the actuator and the section valves, cf. fig. 6. This is necessary to omit the secondary pressure compensator and allow a flow rate from the inlet to the outlet. For now, this mode is not considered.

To include the hybrid system in the hydraulic circuit and thus the recuperative operation mode (RcOM), it is necessary to reroute the out flowing oil. This will be done by a 3/2-valve in each line of the actuator, cf. re-routeing valve in fig. 6. In several modes, those valves can redirect the oil to the accumulator. Depending on the operation strategy, it is possible to use only one or more accumulators in the system. For this choice, e.g. the actuators pressure level will be one criterion.

To control the actuators velocity, it is also necessary to implement a flow rate controlling component to the accumulator. In this paper, it is represented by an orifice (throttle valve), cf. fig. 6. To reduce the needed pressure difference compared to regular flow-control valves, this element will be realized by a

proportional throttle valve, where the flow rate is controlled by eq. (7).

This bases on the formula for orifices after Bernoulli, eq. (6) [10]. α_D is the flow coefficient and ρ is the density of the oil. Both are assumed to be constant for this controller design. Therefore, K is a composition of all constant values in eq. (6). The actuator's out-coming flow rate $Q_{Out,ref}$ is equal to the flow rate to the accumulator Q_{Acc}. So the spools position y will be controlled in dependency of Q_{Acc} and the difference between the actuator's outlet pressure p_{Out} and the accumulator pressure p_{Acc}. Several researches have been done on this topic by [11] and [12].

$$Q = \alpha_D \cdot \sqrt{\frac{2}{\rho}} \cdot A(y) \cdot \sqrt{\Delta p} \tag{6}$$

$$Q_{Acc} = Q_{Out,ref} = K \cdot y \cdot \sqrt{p_{Out} - p_{Acc}} \tag{7}$$

A similar control strategy will also be used to control the flow rate to the tank. This will be discussed in detail in the next section.

2.2 Controller Design

The primary task of this controller design is to decide which operation mode (OM) is temporarily the best for energy saving and safety. The RcOM is the most energy efficient but also, because of its conditions, the most unstable OM. The next efficient mode in this ranking is the EOM, because no primary energy is used, but the throttle losses are higher than in RcOM. The NOM has no efficiency advantages compared to a conventional LS-system. However, NOM is the most stable OM compared to EOM and RcOM. Therefore, it is used as the fall-back OM in critical situations.

To choose the right OM, the controller combines the operator's requested movement, detected by the joystick-signal u_{Joy}, and the actuator's outlet pressure p_{Out} as well as the accumulator pressure p_{Acc}, cf. fig. 7. In parallel, the controller calculates (calculator block) different control-signals for each OM, depending on the current system status. A simple boolean algebra (mode switch) then decides which control-signals (u_{In}, u_{Out}) are released to the adjusted section valves, cf. fig. 7. The valve to control the inlet flow depends on the actuators movement. Figure 7 shows exemplary the signal routing for the extension of the cylinder.

The mode switch consists of several decisions. The sequence for these is shown for a predefined situation in fig. 8. A grey cylinder chamber implies high pressure. At first the controller design has to check the moving direction due to u_{Joy}. This leads to the information which chamber is the outlet of the actuator and so it is possible to allocate the calculated control-signals to the specific valve.

The next important information is to know the value of p_{Out}. The controller design assumes for a closed section valve, that an active load situation is represented by an high pressure at the actuator's outlet. If the value of p_{Out} is higher than the upper limit $p_{EOM,on}$, the controller design will activate the EOM.

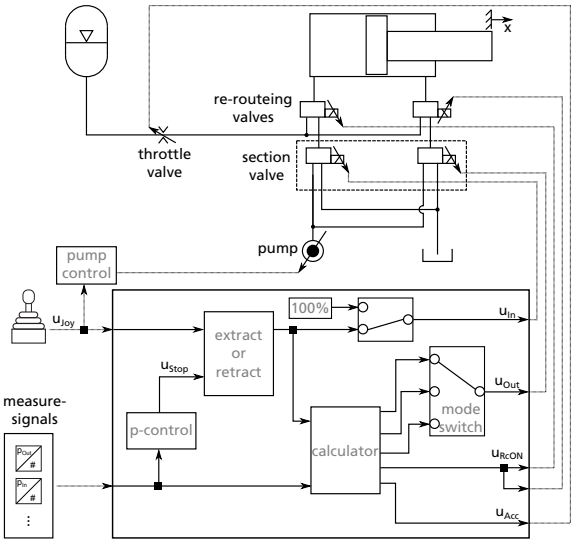

Figure 7: Scheme of the controller design

Using only the independent metering without the hybrid system, the mode switch of the controller design is complete and does not need any other conditions.

To include the RcOM, there are more selections needed, cf. fig. 8. To swap between EOM and RcOM the controller design has to check if p_{Out} is able to transport oil into the accumulator. For this, the condition in eq. (8) has to be fulfilled [13].

$$p_{Out} - p_{Acc} > \Delta p_{Losses} + \Delta p_{RcOM,on} \tag{8}$$

The left part of the equation is the maximum pressure difference possible to force oil to the accumulator. The right part consists of the current pressure losses Δp_{Losses} in the piping from the outlet to the accumulator plus the upper switching condition $\Delta p_{RcOM,on}$. Δp_{Losses} variates with the flow rate and the operation of the throttle valve to the accumulator. The throttle valve losses can be calculated by eq. (6).

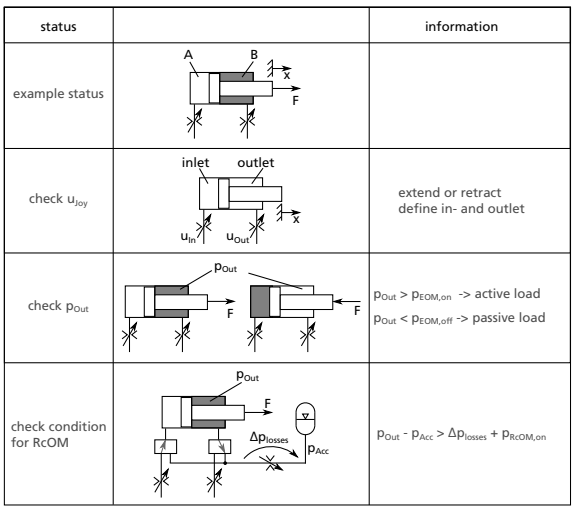

Figure 8: Selection sequence of the mode switch block

Working with discrete OMs has the disadvantage of periodical switching between different OMs. This can influence the system's stability and its suitability in use badly. Like in a two-point switch, there is a higher and a lower switching condition to minimize the frequency of such situations. The function of the two-point switch is shown in fig. 9. If the new OM is selected at time t_1, a PI-controller will align the control-signal of the current OM into line with the control-signal $u_{In/Out}$ of the new OM. In fig. 9 the control-signal changes from NOM to EOM. On account on that, the control-signal is a steady function. All these features have influences on the dynamic behaviour of the system and have to be adapted for a performance accepted by the operator.

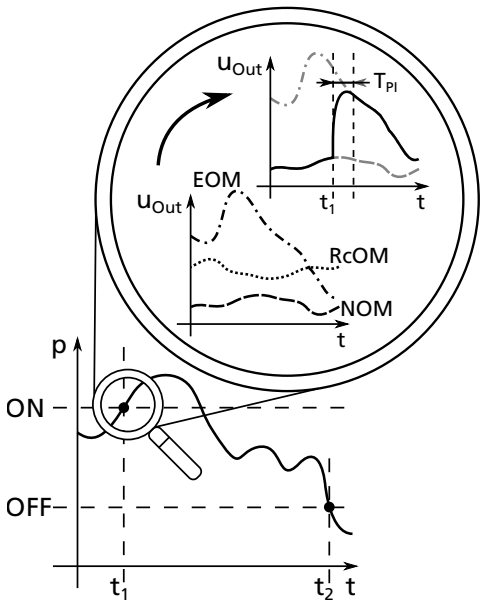

Figure 9: Representation of the two-point switch behaviour of the mode switch and the matching of the control-signals

Another problem shown in [2] is the behaviour of the controller, when an actuator drives against obstacles or reaches its end stop. At that moment, no oil flows to this actuator, but the operation signal would still adjust the pump. An increasing velocity of the active actuators is the result of this effect, while simultaneously the system pressure raises to its maximum. A maximum system pressure closes all individual secondary pressure compensator, so all other active actuators will stop afterwards. [2]

To avoid this, *Scherer* overlays the operation signal with an individual section pressure-control, which reduces the demand of oil for the regarded actuator [2]. The same safety mechanism will be used in this controller design.

2.2.1 Calculating the Control-Signals

According to [4], the current implemented controller design considers the *normal operation mode (NOM)*, *energy neutral operation mode (EOM)* and *recuperative operation mode (RcOM)*. The operator controls the inlet flow rate $Q_{In,ref}$ with an operation signal u_{Joy} via an operator specified look-up table. This leads to the option making the controller design more aggressive or soft. By using the look-up table, the theoretical outlet flow $Q_{Out,ref}$ is predicted in eq. (9). α is the surface ratio of a differential cylinder. For actuators without a transforming property, the surface ratio α is equal to 1.

$$\begin{aligned} Q_{In,ref} &= f(u_{Joy}) \\ Q_{Out,ref} &= \alpha \cdot Q_{In,ref} \text{ , with } \alpha = \frac{A_{Out}}{A_{In}} \end{aligned} \tag{9}$$

During the NOM, the control-signal u_{In} for the inlet chamber is directly controlled by u_{Joy}. The actuator is connected to the pump and the secondary pressure compensator. This ensures a load independent flow rate. The position of the outlet valve spool y_{Out} is calculated with eq. (11). Δp is the difference between the actuators pressure in the outlet chamber p_{Out} and the pressure of the tank p_T. No other influences are considered. The control edges flow surface $A_{CE,Out}$ is estimated according to equation (10). $A_{CE,Out}$ can also be represented by a look-up table to consider the proper geometry.

To avoid failure calculations because of complex solutions, caused by the square root in eq. (11), the outlet control-signal u_{Out} will change to a value proportional to the inlet control-signal u_{In}. The proportional factor depends on the behaviour of the meter-in and meter-out control edge. To prevent cavitation in the inlet chamber, an additional pressure control will reduce the outlet control edge percentile to the calculated, see fig. 10. This control forces the system to be always in a passive load status. It is comparable to a load control valve.

$$A_{CE,Out} = \pi \cdot d_{Spool} \cdot y_{Out} \tag{10}$$

$$y_{Out} = K \cdot \frac{\alpha \cdot Q_{In,ref}}{\alpha_D \cdot \sqrt{\frac{2}{\rho}} \cdot \pi \cdot d_{Spool} \cdot \sqrt{\Delta p}} \tag{11}$$

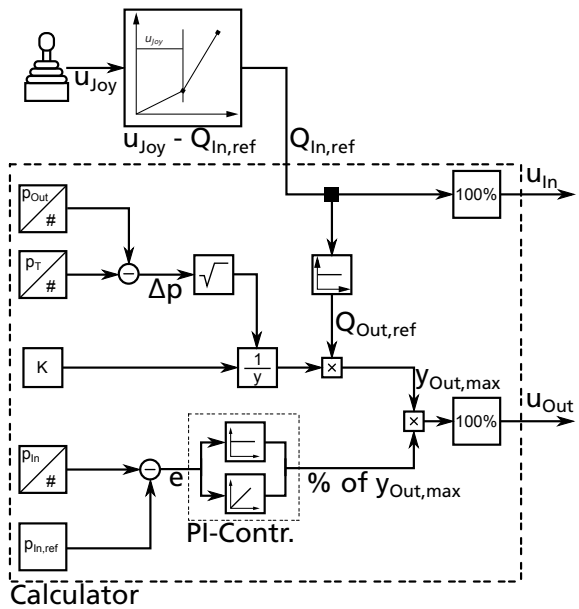

Figure 10: Pressure control of the inlet chamber

Only in active load situations the EOM and the RcOM are used. In both OMs, the inlet chamber is completely connected to the tank, so the actuator has the ability to pull oil from the tank line with less losses as possible. In EOM, the actuator can also use the outlet flow rate, which reduces the required flow rate from the tank. During the retraction of a differential cylinder, the outlet flow rate is higher than the inlet flow rate, thus no oil from the tank is needed. The position of the outlet control edge is also calculated with eq. (11). While in EOM Δp is the pressure difference between the outlet chamber and the tank line, in RcOM Δp is the pressure difference between the outlet chamber and the accumulator, including all other pressure losses, cf. eq. (8).

3 Simulation

The controller design is tested in a co-simulation model first for only one actuator, later for the hydraulic circuit of a mobile forestry crane. Both hydraulic circuits are built up in the simulation software *DSHplus*. The controller design and the virtual operator are built up in *Matlab/Simulink*. The section valve is represented by several orifices, which directly acts by the spool position. The spool position is calculated by the controller design without considering any valve dynamics. The influences of pipes, current losses and others are partially considered. The pump is driven by a constant speed. The load cycle for the mobile forestry crane is given by [2], cf fig. 18. In the following subsection, the results of the single-actuator systems will be discussed explicitly.

3.1 Load Cycles for the Single-Actuator System

Several tests are needed to investigate the usability of the controller design. Here a differential cylinder is used as a single-actuator, cf. fig. 6 actuator two. The cylinder will extend and retract under several load conditions. A virtual operator (VO), which is represented by a closed-loop control of the pistons' position, is used to operate the cylinder. Therefore, it is possible to examine the operation commands, which will show the suitability in use. The VO is implemented according to [14]. The errors of the piston's position will be calculated with eq. (12). x_{ref} is the reference position and x_{tc} represents the actual position related to the different test cycles $(x_{VO/F_{-200/-100/100/200}/OLC})$.

$$\Delta x_{max,ref} = \frac{max(|x_{ref} - x_{tc}|)}{max(x_{ref})} \tag{12}$$

To create a reference cycle, the movement of the cylinder was simulated by an open-loop control of the system. Therefore, a constant operation signal $u_{Joy,ref}$ is used and no load is applied to the cylinder. $u_{Joy,ref}$ and the resulting movement x_{ref} are shown in fig. 11. This movement is used as a reference path for the VO, which tries to follow the path under different loading conditions. As shown in fig. 11, the VO induces a delayed operation signal $u_{Joy,VO}$ causing a displaced movement of the cylinder.

The maximum absolute error appears for the maximum of $u_{Joy} = 100\,\%$ in amount of $\Delta x_{max,100} = 6,2\,\%$. For $u_{Joy} = 60\,\%$ the absolute error between the nominal path and the controlled path is $\Delta x_{max,60} = 4,6\,\%$. The smallest error is caused by an operation signal of $u_{Joy} = 30\,\%$ in amount of $\Delta x_{max,30} = 3,2\,\%$.

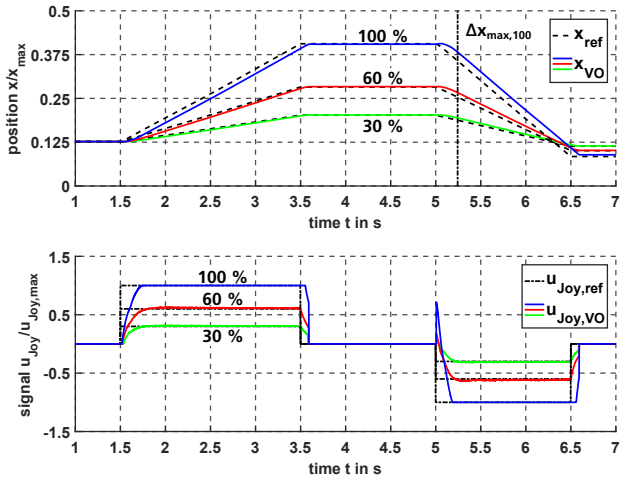

Figure 11: Piston's position x_{ref} as the result of an open-loop control of $u_{Joy,ref}$ and the position x_{VO} as the result of the closed-loop control represented by the virtual operator signal $u_{Joy,VO}$

An overview of the different load conditions is given in fig. 12. Test cycle 2 shows the behaviour of the cylinder for different constant loads $(\pm 100\,kN, \pm 200\,kN)$ during the whole test cycle. This represents for example the boom cylinder of a crane.

Test cycle 3 represents a load, which changes its direction abruptly during extension and retraction. During extension, the load changes from pulling to pushing $(-200\,kN$ to $200\,kN)$, for retraction vice versa. The duration of the load change amounts to $\Delta t_{Change} = 0,2\,s$. This load situation can be found in similar manner e.g. at the gripper or the stick cylinder of a crane.

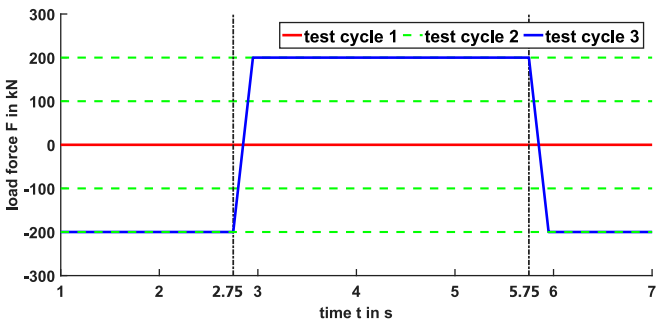

Figure 12: Load cycles for the single-actuator system

3.2 Discussion of the Single-Actuator System

To discuss the different load cycles, the author describes the cylinders movement, the control-signals, the behaviour of pressure and flow rate and the opening positions of the section valve's control edges.

3.2.1 Test Cycle 2

The results of test cycle 2 indicate that the cylinders movement is influenced by an absolute error in amount of $\Delta x_{max,ref} = 7,5\,\%$ compared to the reference position x_{ref}, cf. fig. 13. Considering the maximum error of the VO $\Delta x_{max,60}$, the total absolute error is ca. $\Delta x_{max,VO} = 2,9\,\%$, cf. eq. (13).

$$\Delta x_{max,VO} = \Delta x_{max,ref} - \Delta x_{max,60} \tag{13}$$

The operation signals for a constant load of $F = 100\,kN$ and $F = 200\,kN$ show a distinctive amplitude at the beginning of the extension at $t \approx 1,5\,s$, cf. fig. 13. This is caused by the structure of the VO, which tries to minimize the gap between the current pistons' position $x_{F200/F100}$ and the nominal position x_{ref}. This gap results from the initial conditions of the simulation and has been neglected for this research. This leads to an acceptable suitability in use for actuators charged by constant loads.

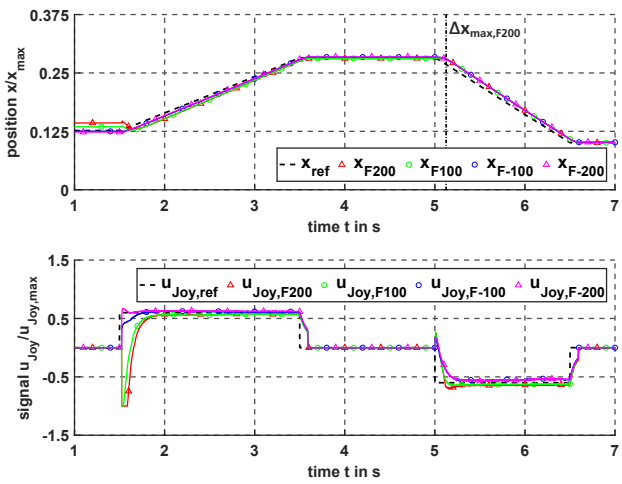

Figure 13: Piston's position of test cycle 2 and the operation signals of the VO for the different load cases; $u_{Joy,ref} = 60\,\%$

The system pressure p_{Sys} only rises, when the pump is connected to the actuator, cf. $t = 1,5\,s$ to $3,5\,s$ in fig. 14. The reason for the rising pressure at $t = 5\,s$ can be found in the mode switch of the controller design. In nominal position the OM of the system is the NOM, cf. status II in fig. 14. By adjusting u_{Joy}, at first the pump is connected to the actuator for a short duration until the control-signals for the EOM are released and the pressure drops. This time is long enough to transfer the pressure from the section valve to the pump.

One critical problem of the system is cavitation during the EOM, here during retraction. One possible way to solve this problem is adjusting the PI-controller of the pressure control, cf. section 2.2.1. Further criteria to activate EOM can help to reduce cavitation too. For example, the flow rate demanded by an actuator can be compared with the sum of the back-flowing oil of other simultaneously operated actuators. If no oil is available, the EOM will not be activated. Furthermore, a by-pass from the tank to the necessary actuator, can avoid high pressure losses on the line.

Fig. 14 also shows the flow rate of the pump and of the control edges of the section valve. Q_{PA} and Q_{PB} are the flow rate from the pump to the cylinder chambers A and B. Q_{AT} and Q_{BT} are the flow rate from the actuator to the tank line. During extension, status (I), the pump supports the actuator and the pressure in the outlet chamber manners $p_{Out} = 2\,\%$ of p_{max}. During retraction, the pump is not used any more and the required flow rate of the actuator will be supplied by the tank-line.

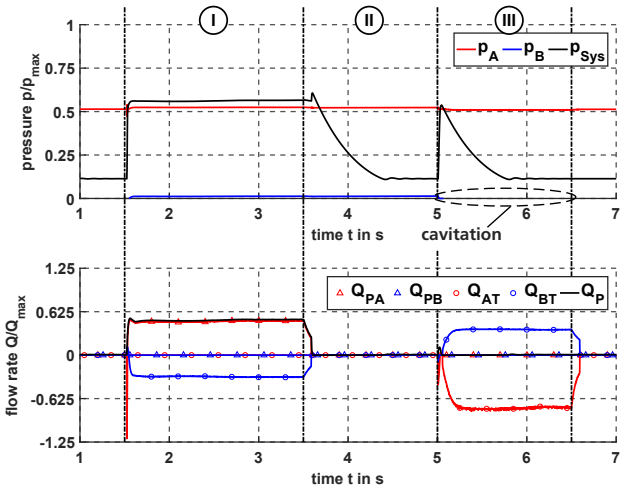

Figure 14: Pressure of the system and the cylinders' chambers A and B in test cycle 2 ($F = 200\,kN$), cf. 3; flow rate of the pump and the control edge of the section valve; PA/B - pump to chamber A/B, A/BT - chamber A/B to tank line

3.2.2 Test Cycle 3

Test cycle 3 is operated in a closed-loop control (CLC) by the VO as well as in an open-loop control (OLC) for a given operation signal $u_{Joy} = 60\,\%$. This test shows the behaviour of the system, when the operator does not adapt to changing loads. It also shows the ability of the operator to stabilize the system. While in OLC, the piston drifts away, x_{OLC}, and causes an error of $\Delta x_{max,OLC} = 12\,\%$ to the reference path x_{ref}, the VO can stop this drifting by its fast, but short reaction, $u_{Joy,VO}$ and control the system into the new OM, cf. fig. 15. So the maximum error can be reduced to $\Delta x_{max,VO} = 5\,\%$. Compared to test cycle 2, the operator only has to stop for a short time or, in this test cycle, the operator has to expect a step of the piston from about $\Delta x_{step} = 3\,\%$ with respect to the maximum extension of the cylinder x_{max}. The amount of the step generally depends on the current operation signal u_{Joy} and the magnitude of the load change.

Figure 16 shows the pressure and the flow rate during test cycle 3, controlled by the VO. The pressure in the actuators' chambers changes with the magnitude of the load. When the load swaps from pulling to pushing the pressures in chamber A and B are equal. Then the piston accelerates because of the active load situation and the VO reacts by an operation signal into the opposite direction, cf. fig. 15 at $t \approx 2,8\,s$. This entails that the actuators status for the controller design changes to passive load and the pump is connected to cham-

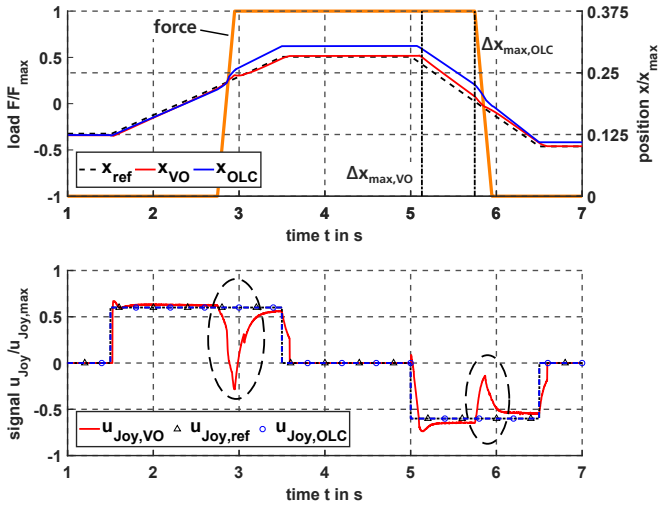

Figure 15: Piston's position of test cycle 3 and the operation signals of the VO and accordingly of the OLC for the different load cases

ber B, what causes an increasing pressure in that chamber, cf. fig. 16 at $t \approx 2,8\,s$. So the force is held by the section valve and can now be controlled by the meter-out orifice to the accumulator, which is not shown in the diagrams. In fig. 16 it is recognizable, that orifice AT has a positive flow rate and thus in-flowing oil. Out-flowing oil is not mentioned, because in this moment, the oil flows into the accumulator.

The problem of cavitation still remains during the EOM, which is one point to be focused on in the further research.

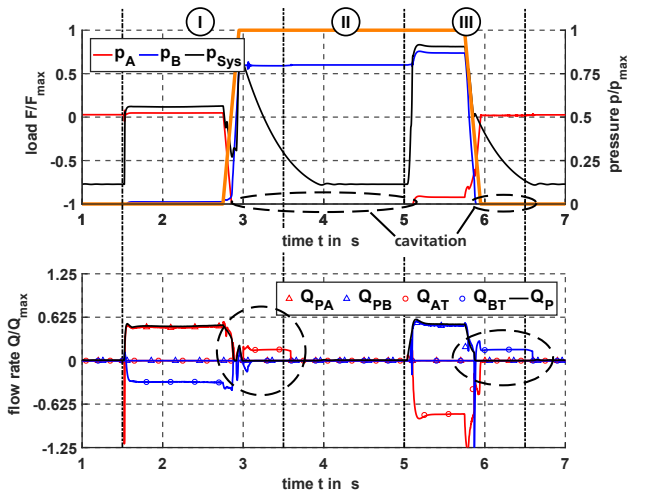

Figure 16: Pressure of the system and the cylinders' chambers A and B in test cycle 3, cf. fig. 3; flow rate of the pump and the actuator; system is controlled by the VO; PA/B - pump to chamber A/B, A/BT - chamber A/B to tank line

A look to the upper diagram of fig. 17 shows the opening position $y_{PA/PB/AT/BT}$ of the control edges for test cycle 3 operated by the OLC. When the load changes its direction, the mode switch of the controller design swaps the operation signals from NOM to EOM. The valve controlling chamber A changes from the pump to a fully opened connection to the tank. The valve for chamber B also opens to the tank, but with the position calculated according to sec. 2.2.1. The lower diagram of fig. 17 shows the opening position of the control edges operated by the VO.

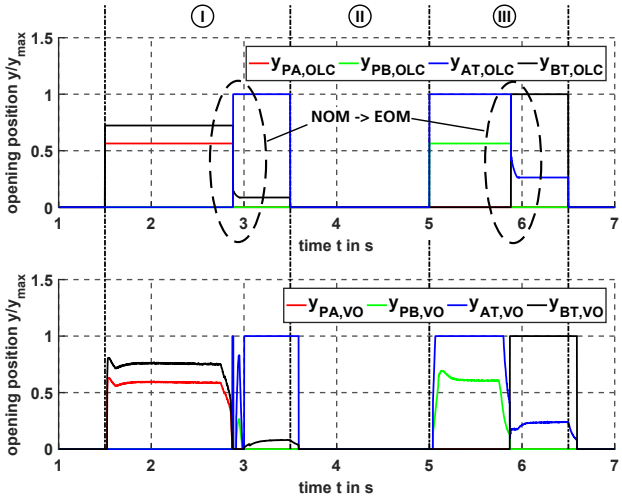

Figure 17: Opening of the section valves control edges due to the signals of the controller design during the load change. OC - open-loop control, VO - virtual operator; PA/B - pump to chamber A/B, A/BT - chamber A/B to tank line

3.3 Potential for the Mobile Forestry Crane

The controller design is implemented in a simulation model of an hydraulic circuit consisting of three actuators. The first actuator is a boom cylinder, the second represents a group of slewing cylinders and the last one is a rotation unit of the gripper. Each actuator is actuated by the same adjustment of the virtual operator (VO), who tries to follow the given positions, cf. fig. 18. Simultaneously, a given load is applied on the actuators. Thus, this simulation represents a typical load cycle of a mobile forestry crane. The actuators positions and the given loads are shown in fig. 18. The data were measured and defined by *Scherer* [2].

The red deposited surfaces show the potential periods for the boom cylinder to be controlled by EOM or RcOM during the load duty cycle.

Four different kinds of systems are shown in fig. 19. The first system is the normal electro-hydraulic flow-on-demand system with conventional valves. This system acts as the reference one. For the second system, the conventional valves are replaced by separated control edges. In the controller design only the normal operation mode (NOM) with a pressure controlled inlet chamber is implemented. The third system uses the energy neutral mode (EOM) to disconnect the pump during active loads. This mode is only implemented for the boom cylinder, because this actuator is most suitable for the EOM. The last system includes an hydraulic accumulator, so the system becomes a hybrid system with the possibility to recuperate energy.

For every system, the used hydraulic energy E_{Hydr} of the pump is calculated by eq. 15. The energy stored in the ac-

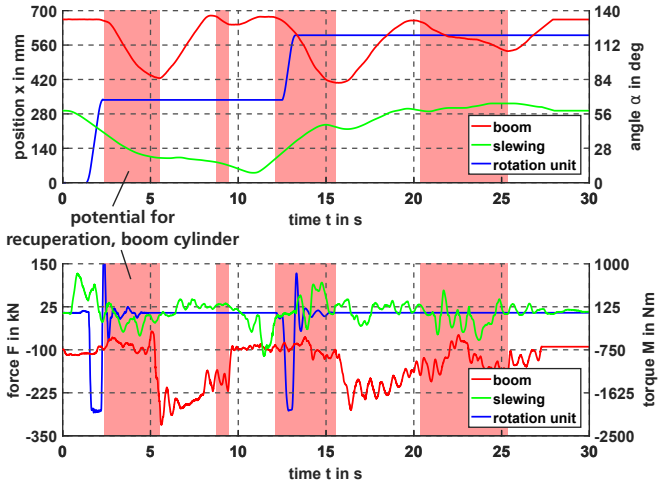

Figure 18: Load duty cycle of a mobile forestry crane; actuator movements and loads [2]

cumulator is calculated equally by using the pressure of the accumulator and the flow rate into it.

$$P_{Hydr} = \Delta p_{Sys} \cdot Q_P \tag{14}$$

$$E_{Hydr} = \int P_{Hydr}\, dt \tag{15}$$

The energy demand of the pump during one duty cycle sums up to $E_{Hydr} = 353\,kJ$ for the first system. Compared to the second system, the energy saving potential is 0.85 %. With the introduction of the EOM in this application, it is possible to reduce the energy demand up to 18.7 %. Introducing the hydraulic accumulator and the RcOM, the energy demand of the pump is nearly the same as of the third system. However, now it is possible to use recuperated energy of app. 8.8 % of the energy demand of the pump.

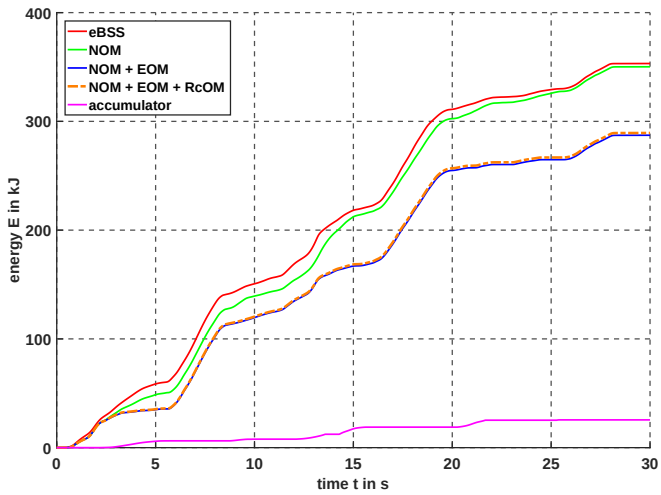

Figure 19: Energy demand of the pump for different systems

4 Outlook

During preparation of this paper, the installation of the test bench is still in progress, so the first results are expected for autumn 2017. On the test bench, the calculated values in section 2.2 will be used as an orientation to generate the actuation signals via look-up tables. This will allow a safe controlling of the actuators without measuring the flow rate. Building up the test bench will give more information about problems and operating feedback.

In a last step the tested and evaluated system will be implemented in a prototype to achieve information about the effort and influences on the forestry crane.

5 Acknowledgements

These perceptions are based on a research project funded by the Deutsche Bundesstiftung Umwelt (DBU) and our partner Weiss Mobiltechnik GmbH. Furthermore special thanks goes to FLUIDON GmbH providing the simulation software DSHplus free of charge.

Nomenclature

Designation	Denotation	Unit
EOM	energy neutral operation mode	-
eBSS	electro-hydraulic flow-on-demand system	-
IM	independent metering	-
LS	load sensing	-
NOM	normal operation mode	-
OM	operation mode	-
OLC	open-loop control	-
RgOM	regeneration op. mode	-
RcOM	recuperation op. mode	-
VO	virtual operator	-
α	surface ratio	-
α_D	flow coefficient	-
ρ	density of oil	[kg/m^3]
$A_{A/B}$	surface chamber A or B	[m^3]
$A_{CE,Out}$	flow surface control edge	[m^3]
A_{In}	surface inlet chamber	[m^3]
A_{Out}	surface outlet chamber	[m^3]
E_{Hydr}	hydraulic energy	[J]
F_{Load}	resulting load force	[N]
K	constant	-
Q	flow rate	[l/min]
Q_{Acc}	flow rate to accumulator	[l/min]
Q_{In}	inlet flow rate	[l/min]
$Q_{In,ref}$	ideal inlet flow rate	[l/min]
Q_{Out}	outlet flow rate	[l/min]
$Q_{Out,ref}$	ideal outlet flow rate	[l/min]
$Q_{Pump,NOM}$	flow rate in NOM	[l/min]
$Q_{Pump,RgOM}$	flow rate in RgOM	[l/min]
$Q_{Pump,EOM/RcOM}$	flow rate in EOM or RcOM	[l/min]
Q_{Tank}	flow rate to the tank	[l/min]
P_{Hydr}	hydraulic power	[W]

Designation	Denotation	Unit
d_{Spool}	diameter of valve spool	[m]
Δp	pressure difference	[bar]
Δp_{Losses}	pressure losses	[bar]
$\Delta p_{Q,Acc}$	pressure for full opened valve	[bar]
$\Delta p_{RcOM,on}$	upper limit for RcOM	[bar]
$p_{A/B}$	pressure chamber A or B	[bar]
p_{Acc}	pressure of accumulator	[bar]
$p_{EOM,on}$	upper limit for EOM	[bar]
p_{Out}	pressure outlet chamber	[bar]
p_T	pressure tank	[bar]
p_{Sys}	system pressure	[bar]
Δt_{Change}	duration of load change	[s]
t_1	moment of mode switch	[s]
u	several control-signals	[-]
$u_{In/Out}$	control-signals to section valve	[-]
$u_{Joy,...}$	operation signal	[-]
u_{Pump}	operation signal of the pump	[-]
y	valve spool position	[m]
y_{Out}	outlet valve spool position	[m]
$y_{PA/PB/AT/BT}$	opening position of control edge	[-]
Δx_{max}	several maximum errors	[-]
Δx_{step}	error by load change	[-]
x_{ref}	reference position	[m]
x_{tc}	position in test cycle	[m]

References

[1] Shelley Nation and Aaron Jagoda. Smart Machines. *ivt International Off-Highway 2017*, pages 72–74, 2017.

[2] Martin Scherer. *Beitrag zur Effizienzsteigerung mobiler Arbeitsmaschinen: Entwicklung einer elektrohydraulischen Bedarfsstromsteuerung mit aufgeprägtem Volumenstrom*. PhD thesis, Karlsruhe, 2015. Zugl.: Karlsruhe, KIT, Diss., 2015.

[3] Dieter Will. *Hydraulik : Grundlagen, Komponenten, Schaltungen*. SpringerLink : Bücher. Springer Berlin Heidelberg, 2011.

[4] M. Axin. *Fluid Power Systems for Mobile Applications with a Focus on Energy Efficiency and Dynamic Characteristics*. PhD thesis, Linköping University, Linköping, Sweden, 2013.

[5] A. Sitte and J. Weber. Structural design of independent metering control systems. pages 261–270. Proceedings of the 13 th Scandinavian International Conference on Fluid Power, Linköping, Sweden 2013.

[6] Ruqi Ding, Bing Xu, Junhui Zhang, and Min Cheng. Bumpless mode switch of independent metering fluid power system for mobile machinery. In *Automation in Construction 68*, pages 52–64. 2016.

[7] P. Nagel. *Entwicklung einer Betriebsstrategie zur Energierückgewinnung in hybriden Mehrverbrauchersystemen*. PhD thesis, Karlsruhe, 2016.

[8] P. Thiebes. *Hybridantriebe für mobile Arbeitsmaschinen: grundlegende Erkenntnisse und Zusammenhänge, Vorstellung einer Methodik zur Unterstützung des Entwicklungsprozesses und deren Validierung am Beispiel einer Forstmaschine*. PhD thesis, Karlsruhe, 2012. Zugl.: Karlsruhe, KIT, Diss., 2011.

[9] Jan Siebert and Marcus Geimer. Entwicklung eines effizienzgesteigerten Load-Sensing-Systems für mobile Arbeitsmaschinen durch Reduzierung systembedingter Druckverluste. In *9. Kolloquium Mobilhydraulik : Karlsruhe, 22./23. September 2016*, pages 11–27. KIT Scientific Publishing, Karlsruhe, sep 2016.

[10] Dietmar Findeisen. *Ölhydraulik : Handbuch für die hydrostatische Leistungsübertragung in der Fluidtechnik*. VDI-[Buch]. Springer, Berlin, 5., neu bearb. aufl. edition, 2006.

[11] Wolfgang Backé, Gerd-Dieter Wobben, and Elmar Wassenberg. *Untersuchungen des stationären und dynamischen Verhaltens mechanisch und elektrisch vorgesteuerter Druckbegrenzungsventile*. Forschungsberichte des Landes Nordrhein-Westfalen ; 2811 : Fachgruppe Maschinenbau, Verfahrenstechnik. Westdt. Verl., Opladen, 1979.

[12] Wolfgang Backé, Nicolae Hamburger, and Hans-Peter Riedel. *Untersuchungen über das dynamische Verhalten von Stromregelventilen*. Forschungsberichte des Landes Nordrhein-Westfalen ; 2435. Westdt. Verl., Opladen, 1974.

[13] Zhiming Wu. Einbindung einer hydraulischen Rekuperationseinheit in ein elektr.-hydr. Bedarfsstromsystems mit getrennten Steuerkanten. Master's thesis, Karlsruhe Instiute of Technology - KIT, January 2017.

[14] P. Thiebes and T. Vollmer. Modellierung des Fahrers zur Untersuchung von Antriebssträngen in der 1D-Simulation am Beispiel eines Radladers mit Hybridantrieb. In *Tagungsband zur 3. Fachtagung Hybridantriebe für mobile Arbeitsmaschinen*, pages 47–59, Karlsruhe, 2011.

An Zero-Flowrate-Switching (ZFS) Control Method Applied in a Digital Hydraulic System

Shuang Peng

School of Mechanical&Mechatronic Engineering, Wuhan University of Technology, Wuhan, China
E-mail: shuang.peng@whut.edu.cn

Abstract

During past decades digital hydraulic technology has become the new trend in hydraulic area due to less consumed power, better controllability and larger tolerance of contaminations. In some digital hydraulic systems, PWM controller is applied to regulate the system flowrate. Thus pressure pulses and switching power loss resulted in by high frequent switching becomes the challenge of digital hydraulics. In this work, it aims to develop a control system where the digital valve always switches off at the moment when the value of the flowrate through the valve is around zero. In this paper a Zero-Flowrate-Swiching (ZFS) control system is presented in a application of a typical 2-valve digital hydraulic system. Operating principles and mathematical models are presented in the paper. According to the simulation results, the system with ZFS controller consumes 14.7% switching power loss compared to that of a Hard-Switching (HS) control system. This gives a bright sight view that ZFS control method can be a potential solution for pressure pulses and switching power loss resulted by high frequent switching in digital hydraulic systems.

Keywords: Zero-flowrate-switching (ZFS), digital hydraulics, energy efficient.

1 Introduction

In 1988 Muto proposed a 2-way-solenoid-valves-system with PWM control for a hydraulic actuator [1]. In last decades digital hydraulic systems with different configurations have been more and more researched due to their potentials in higher efficiency performance and better characteristics of control methods. In 2000 Mattila published a two-valve actuator instead of a servo hydraulic system to actuate a manipulator arm with a load of 620kg [2]. The proposed actuator have saved 15% of the total input energy. Peng compared the performance of four digital hydraulic systemsw with different configurations [3]. The results indicate that two-valve digital hydraulic systems show better energysaving performance than other systems.

However pressure pulses are the main challenge for the application of such digital hydraulic systems. When a digital valve switches off suddenly with high pressure and large flowrate, large pressure pulses would occur. During this process, energy would be wasted as switching loss and pressure pulses would make system response less accurate.

ZFS control method is to make valve switch off when the flowrate through the valve is reduced to zero[4-5]. In earlier work, ZFS control method is only modeled without cylinder load. Thus, dynamic capacitance from the cylinder is not included in old models. In this paper an improved Zero-Flowrate-Switching (ZFS) control method is applied in a two-valve digital hydraulic system. Capacitance from the load cylinder is included for better controllability.

This paper is organized as following sections. Section 2 introduces the operating principles and mathematic model of a ZFS control system applied in a typical 2-valve digital hydraulic system. Section 3 presents simulation results for the tested systems.

2 A ZFS digital hydraulic system

A typical 2-valve digital hydraulic system is concerned in this paper (shown in fig. 1). In this system valve 1 and valve 3 are used to control the directions of the flow. Two flow paths are presented by white/black arrows, respectively. In a ZFS control system, an accessory line (a resonant line) is mounted paralleled with valve 1 (shown in fig. 2). Small-amplitude waves in pressure output of regular pumps are used as the excitation of the resonant line. When the cylinder is retracting, the fluid goes as white arrows guide, valve 3 works at low pressure, switching loss is minor and pressure pulses can be ignored; when the cylinder is extending, the fluid flows following black arrows. During this process, valve 1 and valve 2 work at supply pressure. Large pressure pulses and considerable switching power loss happened here. Thus a ZFS control unit is designed here. A ZFS unit contains two parallel lines: one consists of valve 1; the other is accessory line which includes valve 2, a hydraulic capacitance and a hydraulic inductance. Valve 1 is the main control valve which is responsible for regulating

flowrate for the cylinder when extending. When valve 1 is about to switch off, the accessory line starts to work until both valve 1 and valve 2 switch off at zero-flowrate moment.

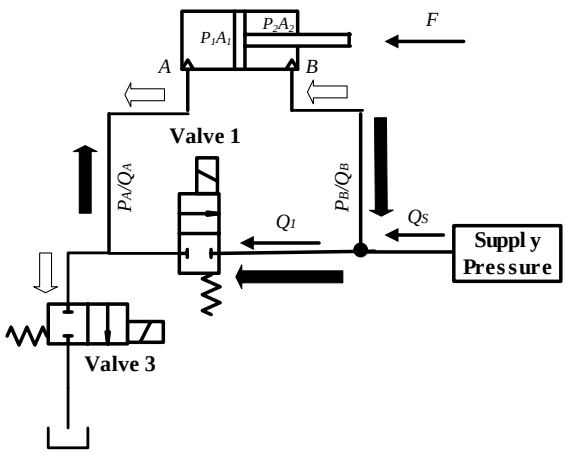

Figure 1 Schematic of a digital hydraulic system with two digital valves

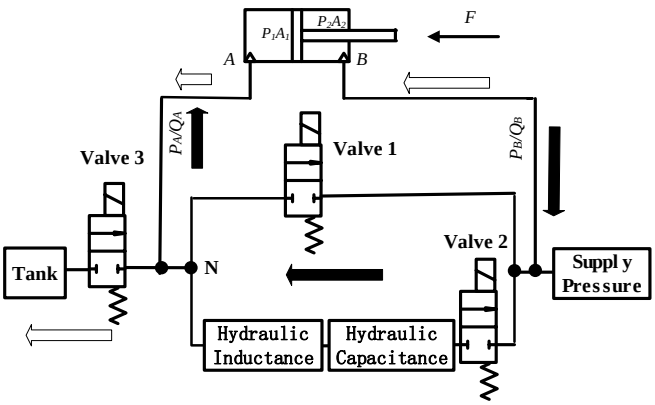

Figure 2: Schematic of a ZFS digital hydraulic system.

2.1 Operating principles during extending process

When the cylinder is extending, valve 1 works at high pressure, thus an accessory line is designed to make the valves switch off at zero-flowrate moments. The schematic of the system for extending motion is presented in fig. 3.

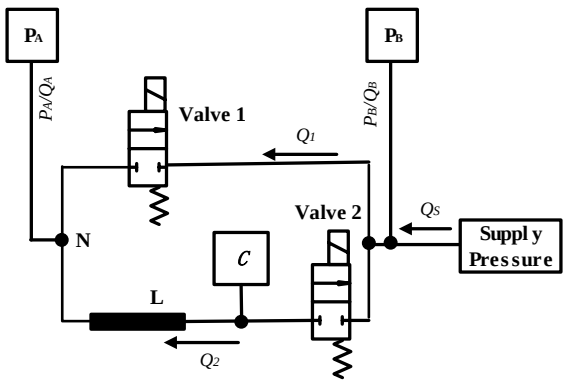

Figure 3: Schematic of a ZFS Unit.

The switching-off process is provided into four modes.

Mode 1

In mode 1, valve 1 is on and valve 2 is off. Valve 1 functions the main control valve which regulates the load.

Mode 2

In mode 2, valve 2 switches on while valve 1 still keeps on. Both the supplier and the RLC oscillator (shown in fig. 4) supply flow to the load.

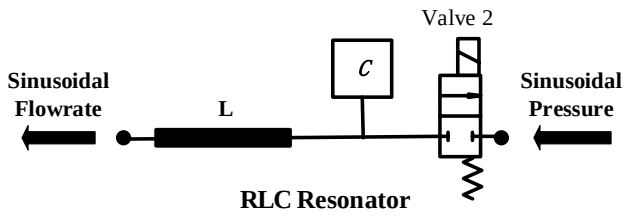

Figure 4: A Hydraulic RLC Resonator.

Mode 3

When the transient value of the sinusoidal flowrate out from the *RLC* oscillator is equal to the value of required Q_A, the flow from both the supplier and rod-side of the cylinder is relived, the system switches to mode 3: valve 1 switches off at zero-flowrate moment, the accessory line supplies the load independently.

During this mode, the resonant flowrate is reduced gradually; After it oscillates back to zero, it flows to the opposite direction.

Mode 4

When its value is equal to Q_B+Q_{Smax}, the flowrate along accessory line is zero. Then valve 2 switches off, the system works in mode 4.

The state matrix of the valves are shown in Table 1.

Table 1 State matrix of the valves

Operating Modes	Valve 1	Valve 2
Mode 1	ON	OFF
Mode 2	ON	ON
Mode 3	OFF	ON
Mode 4	OFF	OFF

2.2 Mathematic models for extending process

The supply pressure of the system is

$$P_S = P_{S0} + P_{Sa}\, sin(\omega t) \tag{1}$$

The system works as a regular differential system in Mode 1

$$Q_S = Q_A - Q_B \tag{2}$$

In mode 2 and mode 3, a resonator participates to actuate the system. Mathematics for mode 2 and mode 3 are presented

to analyze the system performance. Following assumption are made for these models:

The orifice openings of valve 1 and valve 2 share the same shape and dimensions;

The *pressure-vs-flowrate* characteristic of valve 1 and valve 2 is linear within certain range of flowrate: $R=p/q$;

The *flowrate-vs-opening-area* characteristic of valve 1 and valve 2 is linear.

Mode 2

In this mode, both the main line and the accessory line are working (shown in fig. 5). The backflow of the cylinder and the flow from the supplier meet together, and then are split evenly into the main line and the accessory line. In the same time, the *RLC* resonator starts to generate resonant flowrate Q_{res}.

$$Q_1 = \frac{1}{2}(Q_S + Q_B) \tag{3}$$

$$Q_2 = \frac{1}{2}(Q_S + Q_B) + Q_{res} \tag{4}$$

$$Q_{res} = \frac{P_{Sa}}{R}\sin(\omega t) \tag{5}$$

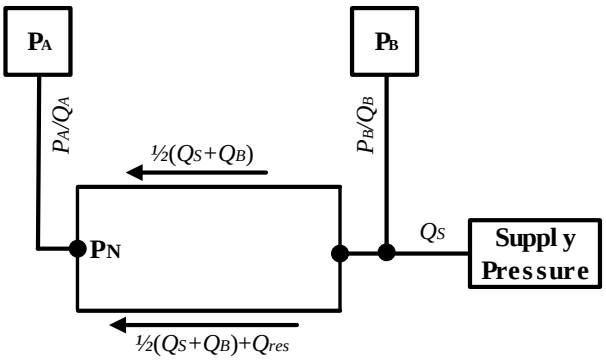

Figure 5: System schematic for mode 2

Right after valve 2 switches on, Q_S is

$$Q_S = Q_A - Q_B - Q_{res} \tag{6}$$

Then Q_S decxreases as Q_{res} increases from zero(presented by red line in fig. 6).

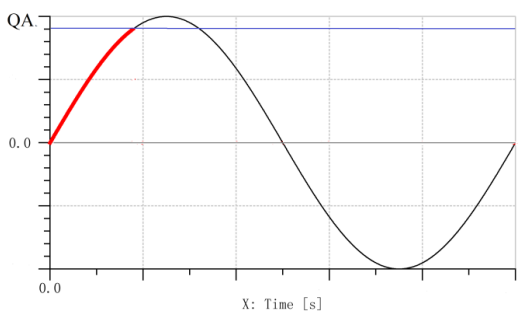

Figure 6: Resonant flowrate in mode 2

When the resonant flowrate Q_{res} is up to Q_A, Q_S is reduced to zero, QB is also relived by the relieve valve of the pump.

It is assumed that $Q_{res}(t^*)=Q_A$. At the moment $t=t^*$, the system behavior is complex. Here system behavior at the moments before and after $t=t^*$ is discussed.

The system at the moment $t=t^*-1/\infty$

When time is about to achieve t^*, Q_{res} is about to achieve Q_A

$$Q_{res} + \frac{1}{\infty} = Q_A \tag{7}$$

Thus

$$P_N < P_S \tag{8}$$

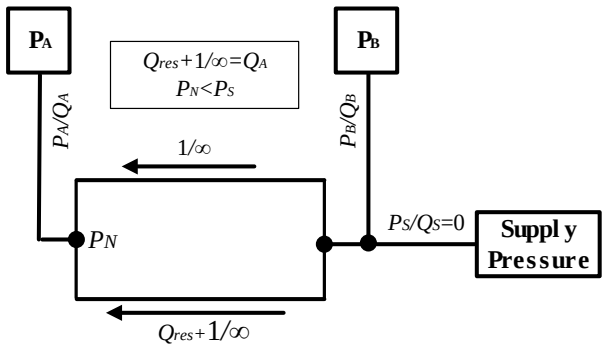

Figure 7: System schematic when $t=t^*-1/\infty$

At this moment both lines are still working as presented in fig. 7.

The system at the moment $t=t^*+1/\infty$

When time is right after t^*, Q_{res} is a little bit larger than Q_A, which is

$$Q_{res} + \frac{1}{\infty} = Q_B + Q_{Smax} \tag{9}$$

Then the actual flowrate to the rodless-side chamber is more then required (Q_A), which results

$$P_N > P_S \tag{10}$$

The fluid cannot flow to the rodless-side chamber by the main line, thus

$$Q_1 = 0 \tag{11}$$

$$Q_2 = Q_B + Q_{res} \tag{12}$$

The direction of Q_1 is from node N to the power supplier. The schematic is presented in fig. 8.

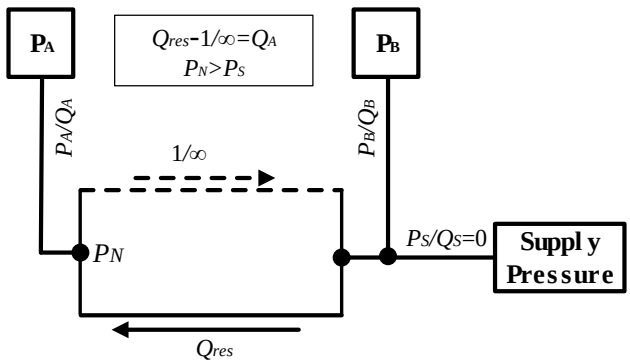

Figure 8: System schematic when $t=t^*+1/\infty$

Mode 3

In mode 3, the resonant flowrate Q_{res} (shown by red line in fig. 9) keeps going up until it achieves the peak value; during this process, the pressure of P_A is slightly boomed since valve 1 is switching off. After that Q_{res} starts to fall down.

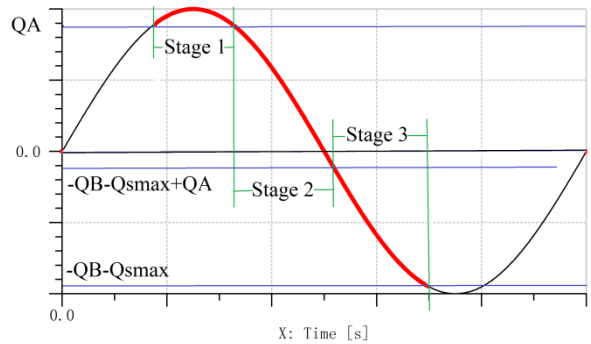

Figure 9: Resonant flowrate in mode 3

The schematic for mode 3 is presented in fig. 10.

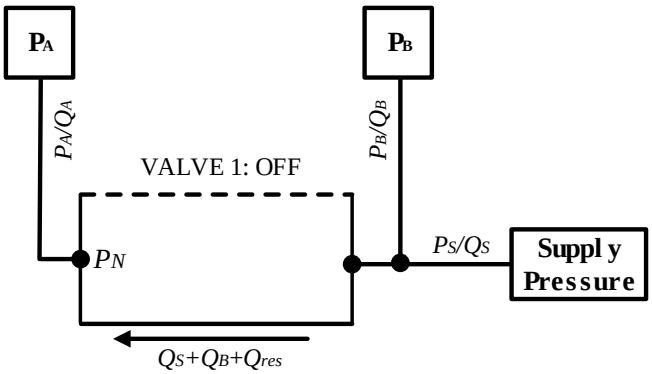

Figure 10: Resonant flowrate in mode 3

The system goes through three stages in mode 3.

Stage 1

Valve 1 is switching off, Q_B and Q_S stops supplying the system.

$$Q_1 = C_{orif}(Q_{res} - Q_A) \tag{13}$$

$$Q_2 = Q_{res} \tag{14}$$

where

$$C_{orif} = 1 - \frac{\Delta t}{T_s} \tag{15}$$

Stage 2

Valve 1 is off, Q_{res} is less than Q_A, thus part of Q_B+Q_S helps supplying the system to make Q_2 equal to Q_A.

$$Q_1 = 0 \tag{16}$$

$$Q_2 = Q_A \tag{17}$$

At the end of stage 2

$$Q_{res} = Q_A - Q_B - Q_{Smax} \tag{18}$$

Stage 3

Valve 1 is off. The direction of Qres is from node N to the power source. As the value of Qres increases, all the flow of QB and QSmax is supplying the system, however, Q2 is still less than QA.

$$Q_1 = 0 \tag{19}$$

$$Q_2 = Q_{Smax} + Q_B + Q_{res} \tag{20}$$

At the end of stage 3

$$Q_{res} = -(Q_B + Q_{Smax}) \tag{21}$$

Q_2 turns to zero, valve 2 is ready to switch off.

Mode 4

Valve 1 is off. At the very beginning, valve 2 is switching off, thus Q2 is derived

$$Q_2 = C_{orif}(Q_{Smax} + Q_B - Q_{res}) \tag{22}$$

2.3 Switching power loss

Theoretically, the fast switching valve works only in ON and OFF states, the switchging power loss is supposed to be zero. However, Physical valves are not idea ones. During the switching process, both flowrate and pressure difference exists, switching power loss is small but not zero.

During the switching process, switching power loss happens twice, for valve and valve 2, respectively.

At the beginning of mode 3, the switching power loss for valve 1 is derived as

$$E_{loss_1} = \int_t^{t+T_S} (P_S(t) - P_A) C_{orif}(Q_{Smax} + Q_B - Q_{res})\, dt \tag{23}$$

At the beginning opf mode 4, the switching power loss for valve 2 is derived as

$$E_{loss_2} = \int_t^{t+T_S} (P_S(t) - P_A) C_{orif}(Q_{Smax} + Q_B - Q_{res}) dt \tag{24}$$

3 Simulation model and result analysis

3.1 Simulation model

To analyze a ZFS control system, a supply pressure averaged at 20.5MPa with wave frequencies of 113Hz is used as power source; the amplitudes for both waves are 2bar; the capacitance volume of the resonator is 0.8L. The closing time of the valve is assumed to be 0.002s.

The differential cylinder is actuated as shown in fig. 1. The piston of the cylinder moves at constant speed. Since the switching-off process is very short, P_A is assumed to be constant to simplify the model.

As contrast a system without accessory line is used to compare power assumption with the tested system. This system is also called Hard-Switching (HS) control system.

More details about the system parameter is presented in Table1.

Table 2 System parameters

Operating Modes	Values
ρ	860kg/m^3
E	14000bar
V	0.8L
D	0.008m
l	0.2m
f_1	113Hz
P_{Sa}	2bar
P_{S0}	205bar
P_A	190bar
Q_{norm}	20L/min@5bar
Q_A	7L/min
Q_B	2.195L/min
Q_{Smax}	4.805L/min

3.2 result analysis

Fig. 11 and fig. 12 presents an entire switching process for the two control systems. In a HS control system (Fig. 10), the valve linearly switch off, thus the flowrate decreases linearly. The transient power consumed over the valve goes up firstly and then goes down until the switching is finished. The peak power consumption is about 175W. The total switching power loss is 1570J.

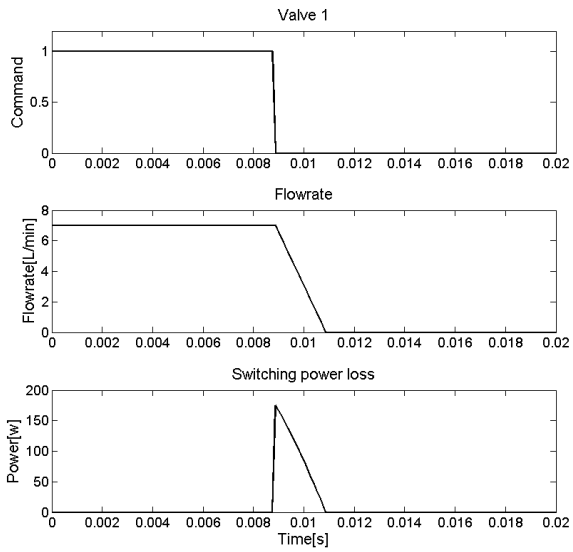

Figure 11: Simulation result for HS system

Fig. 12 presents the results for ZFS control system. at the beginning of the test, valve 1 (the control valve) is on and valve 2 (the resonant valve) is off; then valve 2 switches on and Q_2 goes up along the sinusoidal trajectory; correspondingly Q_1 decreases accordingly; soon Q_1 reaches zero. When Q_1 achieves zero-flowrate moment valve 1 is switched off. At the same time, Q_2 keeps going down until it achieves zero. Then valve 2 switches off. During the switching of valve 1 and valve 2 the power consumption happens since orifice flowrate exists. This is an entire zero-flowrate-switching control process. The peak power consumption is about 60W. The switching power loss consumed by ZFS system is about 230J compared to 1570J consumed by the counterpart. The result indicates that by introducing ZFS control method, the switching power loss is reduced to 14.7%.

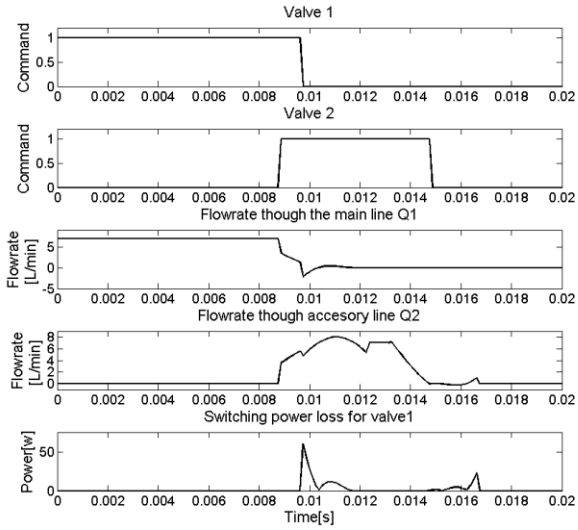

Figure 12: Simulation result for ZFS system

4 Conclusions and future work

This paper proposes a ZFS control method for a typical 2-valve digital hydraulic system. The work focuses on switching power loss of digital valves. The result indicates that switching energy consumed by the valve in ZFS control system is about 14.7% compared to that in a HS control system. Since this method is to greatly reduce switching power loss, and theoretically remove switching pulse, it is a potential solution to improve the performance of digital hydraulic systems and other systems which need frequent switching.

In this paper, constant P_A is applied to discuss the studied case. When the load is varied, the system response would change accordingly. Dynamic load with varied load force and changing movements will be discussed in future work.

Acknowledgement

This work is funded by State Key Laboratory of Fluid Power and Mechatronic System, the funding number is GZKF-201520, as well as Wuhan University of Technology, the funding number is 2017IVA013.

Nomenclature

Designation	Denotation	Unit
Q_1	Flowarte through valve 1	L/min

Q_2	Flowarte through valve 2	L/min
Q_A	Flowrate at rodless side	L/min
Q_B	Flowrate at rod side	L/min
Q_S	Flowrate from the supplier	L/min
Q_{Smax}	Maximam flowrate from the supplier	L/min
Q_{res}	Resonant flowrate	L/min
q	Flowrate	L/min
P_A	Pressure in rodless-side chamber	Bar
P_B	Pressure in rod-side chamber	Bar
P_N	Pressure at node N	Bar
P_S	Supply pressure	Bar
P_{S0}	Average value of supply pressure	Bar
P_{Sa}	Amplitude of the pressure waves	Bar
P^*	Pressure generated by the various volume of the rodless-side chamber of the cylinder	Bar
P_{loss_1}	Switching power loss for valve 1	W
P_{loss_2}	Switching power loss for valve 2	W
p	Pressure	Bar
L	Coefficient of inductance	
C	Coefficient of capacitance	m^3/Pa
C_{orif}	Orifice coeffecient	Null
E	Bulk modules of the fluid	Bar
F	Load force	N
R	p/q	Bar•min/L
V_{pipe}	volume of the pipe between the node N and the port of the rodless-side chamber of the cylinder	m^3
x	Position of the cylinder piston	m
A_{pis}	Area of the cylinder piston	m^2
ω	Angular frequency of the supply pressure waves	Rad/s
t	Time	s
t^*	The end of mode 2	s
Δt	Time difference	s
T_S	Switching time	s

References

[1] T. Muto, H. Yamada, Y. Suematsu. PWM-Digital control of hydraulic actuator utilizing 2-way solenoid valves. *Jour. Jpn. Hydraulic & Pheumatica Soc.*, (in Japanese), Vol. 14, No. 7, pp. 61~68.

[2] J. Mattila, and T. Virvalo. Energy-efficient motion control of a hydraulic manipulator. Proc. of *the International Conference on Robotics & Automation*, Sanfrancisco, CA, USA, 2000.

[3] S. Peng, D. Branson, E. Guglielmino, and D. G. Caldwell. Simulated performance assement of different digital hydraulic configurations for use on the HyQ leg. Proc. of *International Conference on Robotics and Biomimetics*, Guangzhou, China, 2012.

[4] S. Peng. The concept of a zero-flowrate-switching controller. Proc. of *Eighth Workshop on Digital Fluid Power*. Tampere, Finland, 2016.

[5] S. Peng. A zero-flowrate-switching (ZFS) control system applied in a simple hydraulic line. Proc. of *9th International Conference on Fluid Power Transmission and Control*, Hangzhou, China, 2017.

A Hardware-In-The-Loop (HIL) Testbed for Hydraulic Transformers Research

Sangyoon Lee and Perry Y. Li

Department of Mechanical Engineering, University of Minnesota, Minneapolis, MN USA
E-mail: sylee@umn.edu, lixxx099@umn.edu

Abstract

A hardware-in-the-loop (HIL) testbed for testing and evaluating experimental hydraulic transformers has been developed. The testbed is capable of emulating a variety of loading conditions specified by the desired work cycle operation of various hydraulic machines, such as humanoid robots or excavators. The HIL testbed is a useful research tool as it allows studying the dynamics of many desired loading conditions without having to obtain and reconfigure the said physical hardware for each case. This paper discusses the background, construction, and control of the HIL testbed with the experimental results. Preliminary results demonstrating the functionality of an experimental switch mode hydraulic transformers are also presented.

Keywords: Hydraulic Transformer, Switch mode Transformer, Hardware-In-The-Loop testing, Load Emulation

1 Introduction

A hydraulic transformer transforms an input pressure and flow combination into an output pressure and flow combination in an energy conservative manner. It is a key component in realizing a common pressure rail (CPR) system where a common input pressure source feeds multiple services. Compared to valve based control, hydraulic transformers do not rely on throttling to transform pressures and allows energy regeneration. Thus they have the potential to improve hydraulic system efficiencies. Moreover, since pressure can be boosted as well as bucked, system pressure can be kept low to reduce losses.

Although much research has been done on hydraulic transformer configured using a rotatable 3-ported port plate such as the INNAS Hydraulic Transformer (IHT) in [1], a hydraulic transformer can also be configured simply as a combination of a hydraulic pump and motor connected mechanically on a common shaft. We refer to the latter as a Pump-motor or PM transformer. In a PM transformer, hydraulic power is converted by varying the relative displacements of the pump and of the motor. If the hydraulic transformer is configured with axial piston pump/motors, swash plate angles of the units will determine the pressure (or flow) transformation ratio.

In our previous work, we identified that 3 distinct configurations (PM-1, PM-2, PM-3) can be obtained by connecting the ports of a PM transformer variously to the supply pressure line, the load, and the return line (Fig. 1). By switching between these modes, a *switch mode transformer* has benefits in compactness, efficiency and operating region [2, 3].

While methodologies to design a hydraulic transformer as a component in a hydraulic system are well studied [4, 5], control algorithms for hydraulic transformer had received less attention. Werndin and Palmberg [6, 7], Ahn and Ho [8] are among the few who investigated control algorithms for a hydraulic transformer to control actuators. In order to fill this gap, our group designed a passivity based backstepping controller and experimentally demonstrated the control performance for a trajectory tracking control [9] and a human power amplifier control [10, 11]. These results were obtained for each PM transformer configuration, and suggest using the more efficient transformers need not sacrifice control performance as compared to control valves.

A major challenge in experimentally validating the control performance and efficiency of transformers in various applications and duty cycles is the difficulty of obtaining the needed hardware. It is often cost prohibitive to develop a machine and the loads. Consequently, a controller could only be tested for limited cases. Additionally, prototype transformers need to be duplicated to test a multi degree-of-freedom system.

A Hardware-In-the-Loop (HIL) testbed can provide a convenient solution for the aforementioned challenges. In a HIL system, the actual machine is replaced with a dynamic simulation executed in software, while the hydraulic component to be tested are presented physically with the pressure and flow conditions as in the actual machine. This allows a hydraulic component to be tested for a variety of operating scenarios without having to physically obtain the hardware.

Several HIL testbeds had been constructed by various research groups to overcome similar challenges in investigating hydraulic system. For example, Zhang et al [12] developed a HIL testbed to develop a controller for a hydraulic earthmoving vehicle, addressing the challenge in reproducing the digging cycles. Du et al [13] developed a hydrostatic dy-

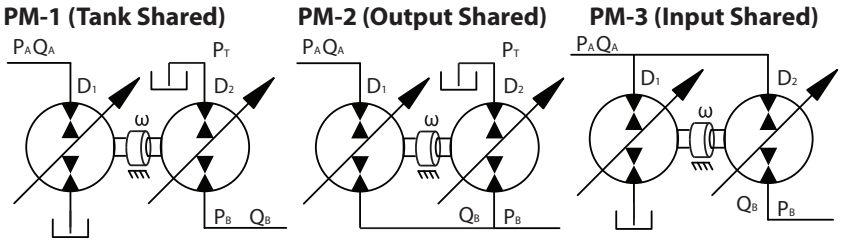

Figure 1: Three distinct transformer configurations

namometer for testing hydraulic hybrid vehicles, capable of emulating a variety of driving conditions and vehicle characteristics.

In this paper, a HIL testbed for hydraulic transformer is developed to test the performances of hydraulic transformer controlled systems. Each degree of freedom can be tested individually without needing the physical actuator or inertial load. The same testbed can also be used to test the transformer in different machine configurations and duty cycles by simply reprogramming the dynamic simulation. This testbed has a simple construction and can emulate both resistive and overrunning loads.

The rest of the paper is organized as follows. Section 2 describes the hydraulic transformer being studied in our group. Section 3 describes the HIL testbed construction and its control strategies. Implementation results and concluding remarks are given in Section 4 and 5.

2 Hydraulic Transformer in Research

The hydraulic transformer being studied in this paper is a traditional pump/motor type (PM transformer) configured with 3.15 cc/rev variable displacement micro-axial piston pump/motors from Takako. Three distinct configurations (PM-1, PM-2, PM-3) can be obtained by connecting the ports of a PM transformer differently (Fig. 1).

For each of the configuration, the transformer shaft speed ω acting with a rotational inertia J to produce port flows out of transformer at input port Q_A and output port Q_B are given by following sets of equations:

PM-1:

$$\begin{aligned} J\dot{\omega} &= (P_A - P_T)\frac{D_1}{2\pi}u_1 + (P_T - P_B)\frac{D_2}{2\pi}u_2 - b_t\omega - T_{loss} \\ Q_A &= -\omega \cdot \frac{D_1}{2\pi}u_1 - Q_{leak'} \\ Q_B &= \omega \cdot \frac{D_2}{2\pi}u_2 - Q_{leak} \end{aligned} \tag{1}$$

PM-2:

$$\begin{aligned} J\dot{\omega} &= (P_A - P_B)\frac{D_1}{2\pi}u_1 + (P_T - P_B)\frac{D_2}{2\pi}u_2 - b_t\omega - T_{loss} \\ Q_A &= -\omega \cdot \frac{D_1}{2\pi}u_1 - Q_{leak'} \\ Q_B &= \omega \cdot \left(\frac{D_1}{2\pi}u_1 + \frac{D_2}{2\pi}u_2\right) - Q_{leak} \end{aligned} \tag{2}$$

PM-3:

$$\begin{aligned} J\dot{\omega} &= (P_A - P_T)\frac{D_1}{2\pi}u_1 + (P_A - P_B)\frac{D_2}{2\pi}u_2 - b_t\omega - T_{loss} \\ Q_A &= -\omega \cdot \left(\frac{D_1}{2\pi}u_1 + \frac{D_2}{2\pi}u_2\right) + Q_{leak'} \\ Q_B &= \omega \cdot \frac{D_2}{2\pi}u_2 - Q_{leak} \end{aligned} \tag{3}$$

where D_1 and D_2 are the maximum volumetric displacements of the pump/motor units in m^3/rev, u_1 and $u_2 \in [-1, 1]$ are the control inputs which are the normalized displacements, b_t is the damping coefficient, $Q_{leak'}$, Q_{leak} and T_{loss} are the lumped volumetric losses at the A and B ports and the mechanical loss inside the transformer due to friction. These losses are configuration, pressure and shaft speed dependent.

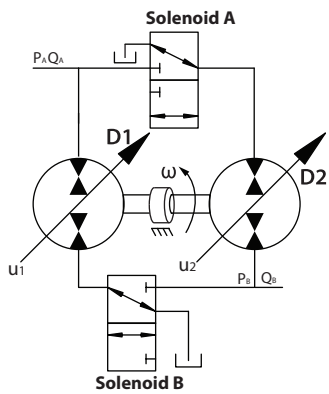

Figure 2: Switch Mode Transformer

Adding two 3-way solenoid valves as in Fig. 2 allows all three configurations to be realized. By switching between the configurations, the total volumetric displacement of the pump/motors (hence overall size) can be reduced for a given flow capability and shaft speed [2,3]. For example, a switched mode PM transformer needs only be 13% larger than IHT with equivalent flow capability as compare to 33% larger when compared to using just one configuration. In addition, by picking the configuration with the highest efficiency, the overall transformer efficiency and operating region can be improved.

Fig. 3 shows the efficiency map of an early stage prototype transformer with a constant 6.895 MPa (1000 psi) pressure rail for each configuration. The relatively low efficiency of this prototype is due primarily to the unusually high mechan-

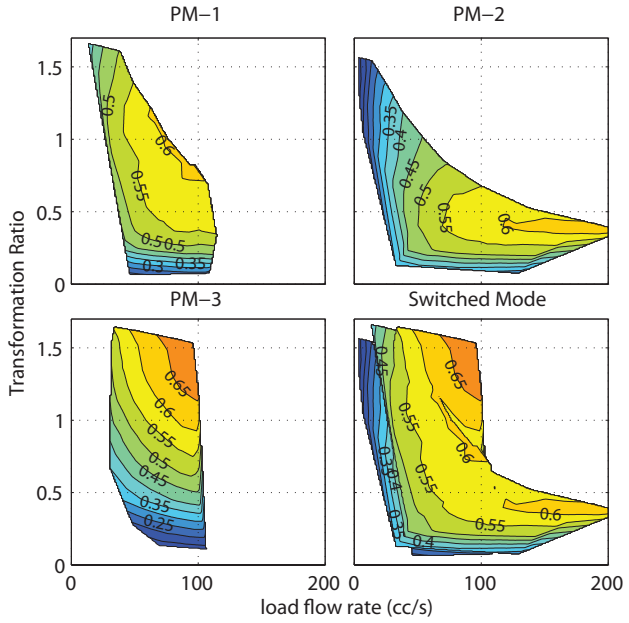

Figure 3: Efficiency contours of individual PM-1, PM-2, PM-3 transformer configurations and switched configurations

ical loss of the common shaft. Incorporating a bearing is expected to significantly improve the efficiency. Nevertheless, this prototype can still demonstrate the implications of using a hydraulic transformer for system control. One can also discern that the switch mode transformer widens the operating region with high efficiency by picking the best configuration for each operating point (Fig. 3, bottom right).

In our prototype switch mode transformer, two Sun Hydraulics DMDA-MBN 3-way solenoid-operated directional spool valves are placed at both sides of the transformer as shown in Fig. 2. At the default position, the transformer is configured in 'PM-1' configuration, which has the shared line connected to the return line. If solenoid valve B is triggered, then the transformer is configured in 'PM-2' configuration, with the shared output port. Lastly, if solenoid A is triggered, the transformer is in 'PM-3' configuration with the input port shared between two units.

3 HIL Testbed for Hydraulic Transformer

3.1 Components of HIL System Architecture

The hydraulic schematic of the HIL Testbed for hydraulic transformer is shown in Fig. 4. The system is powered by a main pressure compensated pump, which provides, via a pressure reducing valve, the constant pressure P_S to the system.

Switch mode transformer discussed in Section 2 is being studied with this HIL Testbed. As mentioned, actuating the solenoid valves switches the hydraulic transformer to be in one of the three configurations shown in Fig. 1. This setup can also be used to study other transformer designs, such as an IHT.

Pressure (P) and flow (Q) sensors are placed at various places as shown in Fig. 4. The transformer shaft speed ω is measured with an optical encoder. The transformer controller determines the displacement control inputs u_1 and u_2 that will deliver the desired flow Q_B^d to the actuator while maintaining the desired shaft speed ω_d [9, 10].

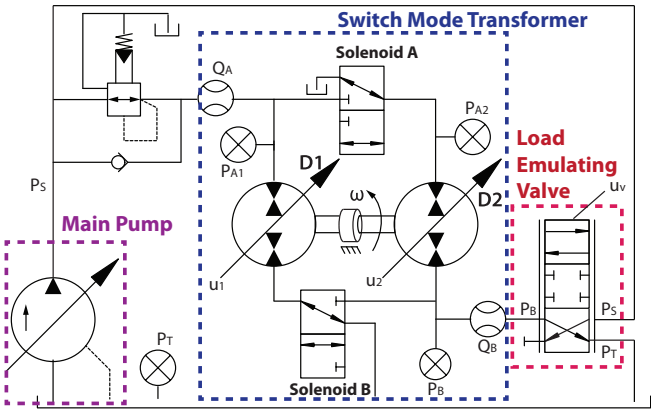

Figure 4: HIL Circuit for testing Switch Mode Transformer

In the HIL testbed, a load emulating valve (LEV) is utilized in place of the hydraulic actuator. A Moog 760 series servo valve (rated at 9.5 LPM), connected to the main pump prior to the pressure reducing valve and to tank, is used for this purpose. One outlet port is connected to the transformer output while the other port is blocked. As will be described in Section 3.4, the servo valve command u_v is used to create an appropriate pressure condition for the transformer that mimics the actual load condition.

The fact that the LEV is connected to a supply pressure P_S is higher than the input port pressure of the transformer P_A allows this HIL system to emulate both resistive and overrunning loads just using one main pump. This configuration is advantageous as only one main pump is needed to power the whole testbed as opposed to having separate pumps for emulating load and running a hydraulic transformer.

3.2 Data and Signal Flow in the HIL Testbed

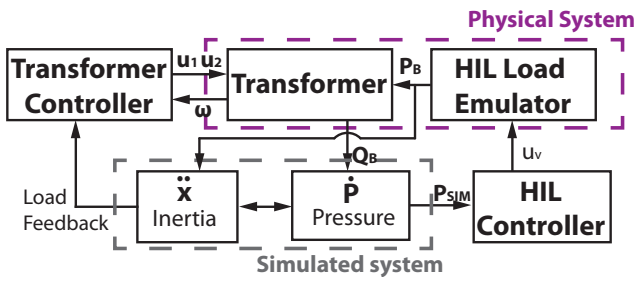

Figure 5: HIL Control Scheme

Fig. 5 shows the block diagram illustrating the data flow within the testbed. The output flow Q_B from the transformer is measured and is provided to simulate the pressure dynamics $\dot{P}$, creating a simulated pressure P_{SIM} in return. In case of a hydraulic actuator shown in Fig. 6, the pressure dynamics of the capside chamber which is to be (virtually) connected to

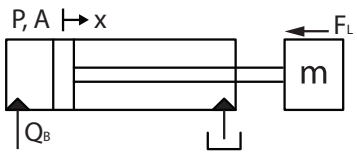

Figure 6: Example cylinder being simulated

the transformer is given by:

$$\dot{P}_{SIM} = \frac{\beta}{V_0 + Ax}(Q_B - A\dot{x}) \tag{4}$$

where V_0 is the volume in the capside chamber and hose when the actuator is at the position $x = 0$, and β is the bulk modulus of the fluid. Integrating $\dot{P}_{SIM}$ yields a P_{SIM} which is fed into a HIL controller to determine the LEV control u_v to match the actual pressure P_B with P_{SIM}.

The measured pressure P_B in turn drives the simulated inertia dynamics, $\ddot{x}$:

$$m\ddot{x} = -b\dot{x} + \underbrace{P_B(t)}_{measured} A + F_L \tag{5}$$

where m is the mass of the cylinder and rod to be simulated, A is the cap side area of the hydraulic actuator, b is the viscous friction coefficient, and F_L is the load force that would encapsulate any external load including gravity and environment forces. Integrating $\ddot{x}$ yields the velocity $\dot{x}$ and the position x which are used in (4). Note that this simulated inertia dynamics take the measured pressure to account for any movement change due to pressure dynamics associated with transformer mode switch.

Finally, the transformer controller takes the feedback of the above information to determine the transformer control inputs u_1 and u_2 to achieve the desired flow for the (emulated) load and the desired torque for the (actual) transformer speed regulation.

The pressure dynamics $\dot{P}$ and the inertia dynamics $\ddot{x}$ in (4)-(5) can be set to simulate any desired actuator type with specified loading conditions, generating appropriate motion and mechanical load. If desired, the simulated system dynamics could simply be replaced by a duty cycle information providing the desired pressure and flow traces.

3.3 Hydraulic Transformer Controller

The objective of the hydraulic transformer controller is to provide the desired flow Q_B^d for the given task and the desired torque T^d to regulate the shaft speed [9, 10].

PM-1:

$$\begin{bmatrix} u_1 \\ u_2 \end{bmatrix} = \begin{bmatrix} 0 & \omega \cdot \frac{D_2}{2\pi} \\ (P_A - P_T)\frac{D_1}{2\pi} & (P_T - P_B)\frac{D_2}{2\pi} \end{bmatrix}^{-1} \begin{bmatrix} Q_B^d \\ T^d \end{bmatrix} \tag{6}$$

PM-2:

$$\begin{bmatrix} u_1 \\ u_2 \end{bmatrix} = \begin{bmatrix} \omega \cdot \frac{D_1}{2\pi} & \omega \cdot \frac{D_2}{2\pi} \\ (P_A - P_B)\frac{D_1}{2\pi} & (P_T - P_B)\frac{D_2}{2\pi} \end{bmatrix}^{-1} \begin{bmatrix} Q_B^d \\ T^d \end{bmatrix} \tag{7}$$

PM-3:

$$\begin{bmatrix} u_1 \\ u_2 \end{bmatrix} = \begin{bmatrix} 0 & \omega \cdot \frac{D_2}{2\pi} \\ (P_A - P_T)\frac{D_1}{2\pi} & (P_A - P_B)\frac{D_2}{2\pi} \end{bmatrix}^{-1} \begin{bmatrix} Q_B^d \\ T^d \end{bmatrix} \tag{8}$$

3.4 Load Emulating Valve (LEV) Controller

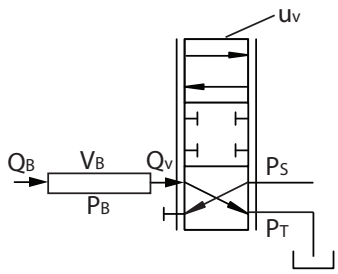

Figure 7: Load Emulating Valve

The most important aspect of the HIL testbed is the load emulating valve (LEV) reproduced in Fig. 7, which will provide the desired loading condition through pressure. For $u_v > 0$, the flow is released to the tank (as shown on the figure) and for $u_v < 0$, the flow is taken from the main pump to increase pressure. The flow Q_v traveling across the valve from the transformer output to be exposed to P_T or P_S is given by the supply pressure or the tank pressure:

$$Q_v = \begin{cases} k_v u_v \sqrt{|P_B - P_T|}, & \text{for } u_v > 0 \\ k_v u_v \sqrt{|P_B - P_S|}, & \text{for } u_v < 0 \end{cases} \tag{9}$$

(assuming $P_S > P_B > P_T$) where k_v is the valve coefficient, and u_v is the valve command to be designed. For the controller design, consider the pressure dynamics within the hose that lies between the hydraulic transformer and the LEV:

$$\dot{P}_B = \frac{\beta}{V_B}(Q_B - Q_v) \tag{10}$$

where V_B is the volume of the hose between the transformer and the LEV, Q_B is the flow out of the transformer that is measured, and Q_v is the flow command to be designed. Define pressure error as $e = P_B - P_{SIM}$. For a constant (or slowly changing) desired simulated pressure, $\dot{e} = \dot{P}_B$. Defining the desired valve port flow Q_v^d as:

$$Q_v^d = Q_B + K_p e + K_I e_I \tag{11}$$

where $\dot{e}_I = e$ and K_p and K_I are the proportional and integral gains. To show that the desired pressure P_{SIM} can be achieved for the HIL testbed, consider the Lyapunov function:

$$\begin{aligned} W &= \frac{1}{2}\frac{V_B}{\beta}e^2 + \frac{1}{2}K_I e_I^2 \\ \dot{W} &= e(Q_B - Q_v) + eK_I e_I \end{aligned} \tag{12}$$

With Q_v given by (11),

$$\dot{W} = -K_p e^2 \tag{13}$$

which shows that for $K_p > 0$, $K_I > 0$, $e \to 0$ and P_B will track P_{SIM}, providing the simulated pressure.

In summary, the LEV controller is a PI controller with a feedforward information coming from the measured flow out the transformer.

4 Experimental Results

4.1 Pressure Tracking Results

To validate that (11) is appropriate, the transformer displacements were held steady while only the desired pressure loading condition was varied. This type of experiment can be used to analyze the steady-state operation for the hydraulic transformer under various loading conditions.

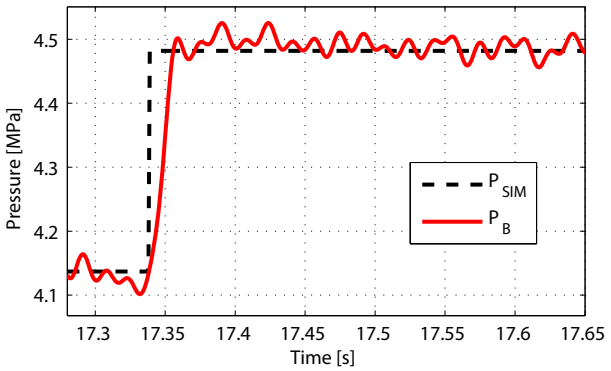

Figure 8: Step response

Fig. 8 shows the step pressure response for a 0.345 MPa (50 psi) step pressure command. Negligible overshoot with 10 ms rise time is observed. Fig. 9 shows various responses of the same step size.

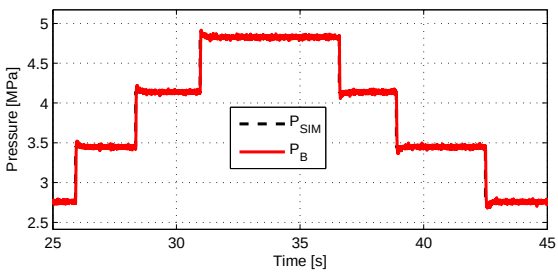

Figure 9: Various step responses

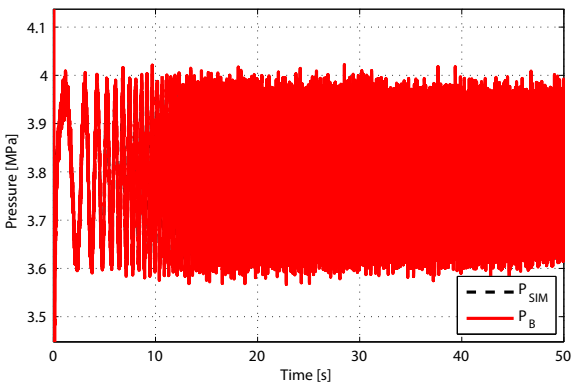

Figure 10: Chirp signal response

Figure 10 shows a response for the chirp signal and Fig. 10 shows the same response zoomed around at select frequencies. The reference chirp signal, an amplitude of 0.345 MPa (50 psi), started as 0.01Hz at $t = 0$ and approached 10 Hz at $t = 50$. Phase lag of 36 degree was observed at the peak frequency, while phase lag is negligible around 3 Hz. Thus, it will be safe to claim this testbed can be operated satisfactorily under 3 Hz load profile. Careful tuning of the parameters along with better valve identification will lead to even better performance. As transformer itself has a limited bandwidth due to the swashplate actuation, HIL testbed is more than capable of simulating the loads for the transformer.

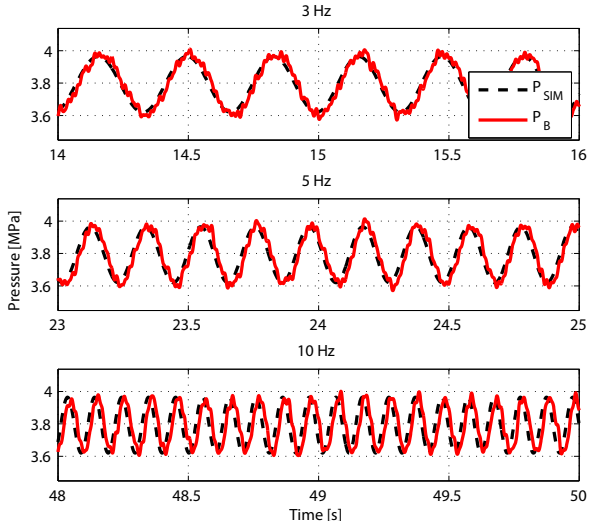

Figure 11: Chirp signal zoomed in at select frequencies

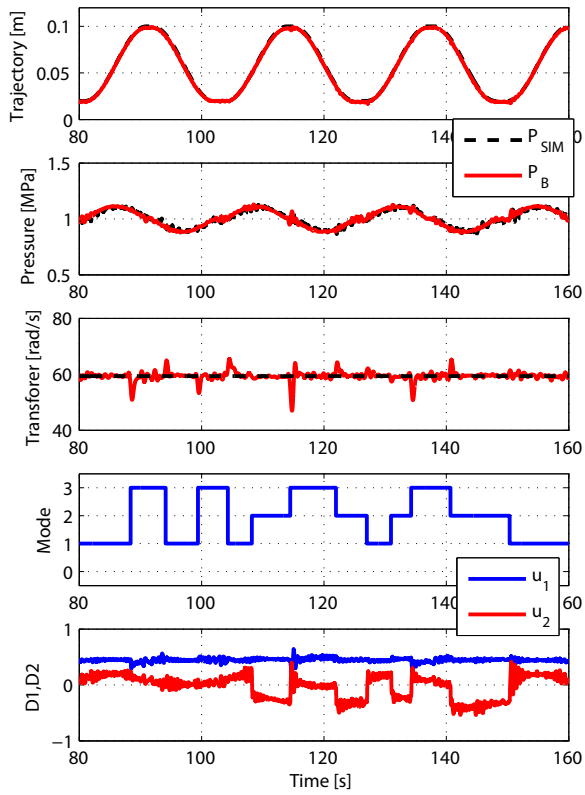

Figure 12: Simulated cylinder tracking result

4.2 Flow and Pressure Tracking Results

An operating condition where a LEV and transformer are simultaneously controlled is shown in Fig. 12. For this implementation, a cylinder with vertical gravity load following a filtered trapezoidal trajectory was studied with a transformer operating in 3 different modes. Controller determining flow demand and the transformer displacement commands is taken from [9]. While the transformer mode switch is manually triggered for this experiment, further development of the transformer control will have the mode automatically determined to maximize the operating efficiency.

In this operating mode, HIL provides a loading condition to which trajectory tracking controller decides the transformer control inputs to be implemented. As described, the trajectory is generated in simulation using the measured flow and pressure. It is observed that trajectory tracking is still satisfactory even as the operating mode switch causes some sharp change of dynamics. In the meantime, HIL control is tracking the simulated pressure P_{SIM}.

5 Conclusion

This paper presents a development of a HIL testbed for hydraulic transformer, with a focus on the control architecture. Using a single hydraulic power supply and a servo-valve, a HIL testbed is configured, providing a platform for further transformer control development.

A closed loop controller designed for the actual system for a trajectory tracking is easily implemented for the HIL testbed. Initial performance experiments indicates the ability of this testbed to emulate various loading conditions.

Acknowledgment

This work is performed within the Center for Compact and Efficient Fluid Power (CCEFP) supported by the National Science Foundation under grant EEC-05040834. Component donation from Takako Industries is gratefully acknowledged. Sangyoon Lee is supported by a 2016-2017 Doctoral Dissertation Fellowship at the University of Minnesota.

Nomenclature

Designation	Denotation	Unit
A	Piston Area	m^2
b	Cylinder viscous friction coefficient	N/(m/s)
b_t	Transformer viscous friction coefficient	N·m·s
D_1, D_2	Volumetric displacements	m^3/rev
e	Pressure error	Pa
e_I	Integral of pressure error	Pa
F_L	Load force	N
J	Transformer shaft inertia	kg·m^2
K_I	Integral control Gain	
K_p	Proportional control gain	
k_v	LEV valve coefficient	
m	Mass of cylinder	kg
P_A, P_B, P_T	Transformer port pressures	Pa
P_S	Main pump supply pressure	Pa
P_{SIM}	Simulated pressure	Pa
Q_A, Q_B	Transformer flows	m^3/s
Q_B^d	Desired flow of transformer	m^3/s
Q_{leak}, $Q_{leak'}$	Flow loss of transformer	m^3/s
Q_v	Flow across the valve	m^3/s
Q_v^d	Desired flow across the valve	m^3/s
T^d	Desired torque for transformer	N·m
T_{loss}	Mechanical loss of transformer	N·m
u_1, u_2	Displacement ratio inputs	
u_v	Valve command	
V_0	Initial volume in cylinder cap-side	m^3
V_B	Fluid volume in hose	m^3
W	Lyapunov energy	J
x	Piston displacement	m
β	Bulk modulus	Pa
ΔP_v	Pressure drop across the valve	Pa
ω	Transformer shaft speed	rad/s

References

[1] P.A.J. Achten, Z. Fu, and G.E.M. Vael. Transforming future hydraulics: a new design of a hydraulic transformer. In *The Fifth Scandinavian International Conference on Fluid Power SICFP '97*, page 287ev, 1997.

[2] Sangyoon Lee, Pieter Gagnon, and Perry Y Li. System configuration and control using hydraulic transformers. In *Fluid Power Innovation and Research Conference*, Chicago, IL, October. 14-16 2015.

[3] Pieter J Gagnon. Configuration and performance of hydraulic transformer power distribution systems. Master's thesis, University of Minnesota, 2016.

[4] Peter AJ Achten, Titus van den Brink, Johan van den Oever, Jeroen Potma, Marc Schellekens, Georges Vael, Martijn van Walwijk, and BV Innas. Dedicated design of the hydraulic transformer. volume 3, pages 233–248, 2002.

[5] PAJ Achten, TL Van den Brink, T Paardenkooper, T Platzer, HW Potma, MPA Schellekens, and GEM Vael. Design and testing of an axial piston pump based on the floating cup principle. In *The Eighth Scandinavian International Conference on Fluid Power SICFP '03*, pages 805–820, May 2003.

[6] R. Werndin and J-O Palmberg. Controller design for a hydarulic transformer. In *The Fifth International Conference on Fluid Power Transmission and Control ICFP '01*, volume 5, pages 56–61, 2001.

[7] R. Werndin and J-O Palmberg. Hydraulic transformer in low-speed operation - a study of control strategies. In *The 5th International Symposium of Fluid Power, JFPS '02, Nara, Japan*, 2002.

[8] Triet Hung Ho and Kyoung Kwan Ahn. A study on the position control of hydraulic cylinder driven by hydraulic transformer using disturbance observer. In *International Conference on Control, Automation and Systems 2008*, pages 2634–2639. IEEE, 2008.

[9] Sangyoon Lee and Perry Y Li. Passivity based backstepping control for trajectory tracking using a hydraulic transformer. In *ASME/BATH 2015 Symposium on Fluid Power and Motion Control*, pages V001T01A064–V001T01A064. American Society of Mechanical Engineers, 2015.

[10] Sangyoon Lee and Perry Y Li. Passive control of a hydraulic human power amplifier using a hydraulic transformer. In *ASME 2015 Dynamic Systems and Control Conference*, pages V002T27A004–V002T27A004. American Society of Mechanical Engineers, 2015.

[11] Sangyoon Lee, Fredrik Eskilsson, and Perry Y Li. Multi degree-of-freedom hydraulic human power amplifier with rendering of assistive dynamics. In *ASME 2016 Dynamic Systems and Control Conference*, page V001T07A002. American Society of Mechanical Engineers, 2016.

[12] Rong Zhang, Don E Carter, and Andrew G Alleyne. Multivariable control of an earthmoving vehicle powertrain experimentally validated in an emulated working cycle. In *ASME 2003 International Mechanical Engineering Congress and Exposition*, pages 515–524. American Society of Mechanical Engineers, 2003.

[13] Zhekang Du, Tan Cheng, Perry Y Li, Kai Loon Cheong, and Thomas R Chase. Virtual vehicle control concept for hydrostatic dynamometer control. *Journal of Dynamic Systems, Measurement, and Control*, 139(2):021009, 2017.

Decentralized Hydraulics for Micro Excavator

Shuzhong Zhang[1,2], Tatiana Minav[1], and Matti Pietola[1]

1. Department of Mechanical Engineering, Aalto University, Espoo, Finland
2. School of Mechanical Engineering and Automotive, Fujian University of Technology, Fuzhou, China
E-mail: Shuzhong.Zhang@aalto.fi, Tatiana.Minav@aalto.fi, and Matti.Pietola@aalto.fi

Abstract

Environmental restrictions and economic opportunities create demand to investigate the potential of further hybridization of non-road mobile machinery (NRMM). Many proposals for energy saving in hydraulic systems have been researched. In addition to well-established methods, there are zonal or decentralized hydraulics – an approach first introduced in the aircraft industry. In a fully decentralized system, the hydraulic pumps are disconnected from the engine and replaced with hydraulic power packs distributed throughout the system. In this study, decentralized hydraulics are realized with a direct driven hydraulics drive (DDH). By applying DDH, further hybridization can be achieved which will lead to increased productivity, minimized energy consumption, and robust performance in mobile machines operating in various environments. Therefore, the aim of this paper is to investigate the energy efficiency of the excavator hydraulic system equipped with DDH under typical digging cycles. For this purpose, a model which coupled multi-body dynamics, hydraulic system, and an electric motor is developed in the Matlab Simulink environment. Simulation results are validated by a simplified representation of micro excavator (one example of DDH) as a proof of concept.

Keywords: Decentralized hydraulics, Construction machinery, Direct driven hydraulics (DDH), Excavator, Energy Efficiency, Energy consumption distribution

1 Introduction

The rapid rise of oil prices and government-enforced CO_2 regulations lead to increasing demand for energy efficient construction machinery [1], such as excavators and wheel loaders. Electric and hybrid drives are seen as a solution to meet these requirements. In particular, non-road mobile machinery (NRMM) is a challenging field of electrification and hybridization applications due to duty cycles which may include high and short power peaks and extreme working conditions.

In a conventional excavator, the hydraulic power corresponding to the maximum workload is always supplied from a pump, and excessive power is dissipated as heat. It is often difficult to reduce input power, even during low-workload operation, because combined controls of actuators require distribution of flows and interflows [2]. In addition, potential and kinetic energies at the time of lowering and slewing stoppage of attachments are also dissipated as heat. Multi-actuator construction machinery is often equipped with load sensing (LS) systems. In LS systems of hydraulic excavators, the supply pressure of a pump is adjusted to match the highest load pressure plus a constant pressure offset. When multiple actuators operate simultaneously, the power losses of lower-load actuators are particularly significant. Up to 35% of the energy losses during the working cycle could be avoided by removing the control valves in a typical digging cycle, and up to an additional 8% of the total energy could be recovered [3]. State-of-the-art, diverse hybrid systems are developed for construction machinery, like series or parallel hybrid hydraulic excavators [4]. The hybrid system allows eliminating the power peaks normally required from the engine. Low-varying engine operation saves significant amounts of fuel, prolongs the engine lifetime, and lowers maintenance costs.

Market demand has led to examples such as the Logset hybrid [5], Komatsu 20-ton parallel hybrid excavator [6], and Hitachi ZH200 hydraulic hybrid excavator [7]. Many proposals for energy saving in hydraulic systems have been discussed in the literature [8].

Rising trends in the industry include valveless or displacement control. An example of displacement control of actuators was realized in [9], where authors demonstrated potential engine downsizing up to 50% in a mini-excavator. Another recently introduced energy saving method is the so-called common pressure rail. In [10], it was shown that fuel consumption can be reduced 21% compared with the original LS excavator.

In addition to well-established methods, there is zonal or decentralized hydraulics – an approach first introduced in the aircraft industry. Simplifying its design as well as broadening its orientation and performance options will support similar development in construction equipment. In a fully decentralized system, the hydraulic pumps are disconnected from the engine and replaced within hydraulic power packs distributed throughout the system [11].

Figure 1 shows the theoretical efficiencies of the different configurations for construction machinery, based on various assumptions. Direct driven hydraulics (DDH) as a variation of pump control demonstrates the best result concerning parasitic losses.

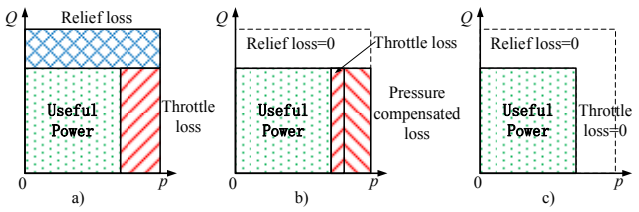

Figure 1: Comparison of differing hydraulic systems. a) convectional control, b) LS, c) direct driven hydraulics or pump control.

The goal of this research is to apply the concept of decentralized hydraulics in micro excavators. The concept will be realized by DDH. Figure 2 illustrates converting a conventional micro excavator into an excavator equipped with actuators driven by DDH independently. The swing motions are driven by an electric motor and the kinetic energy of the upper body is regenerated into electric energy when the swing stops.

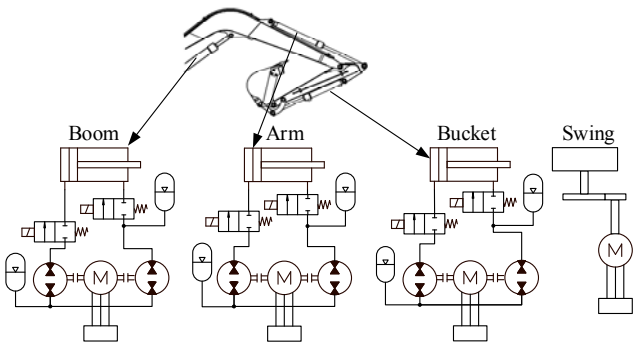

Figure 2: Simplified schematics of DDH excavator.

DDH combines the best properties of traditional hydraulics and electric intelligence allowing the following benefits to be achieved in construction machinery:

- easy electrification of construction machinery
- higher efficiency compared to conventional machines
- reduction of potential leakage points
- smoothness and precision of movements
- power-on-demand control
- potential energy regeneration

In this research, a 1-ton class JCB micro excavator was chosen as the test case. In [12], this excavator was electrified by replacing the 14kW diesel engine with a 10 kW electric motor plus four Altairnano lithium-titanate battery modules. Extension of the operation time of the micro excavator was investigated by introducing a start-stop logic system of electric motor operation to improve energy efficiency with conventional valve control. The benefits of this system were measured using an artificial working cycle test. Results show operation time can be extended by at least 50% compared to the original system [12].

By applying decentralized hydraulics to the existing platform of a fully electric excavator and realizing a power-on-demand strategy, further improvement in the excavator operation time can be achieved. Consequently, the aim of this paper is to investigate the energy efficiency of an excavator hydraulic system with DDH for typical digging cycles [13]. For this purpose, a coupled multi-body dynamics, hydraulic system, and electric model is developed in the Matlab Simulink environment. Simulation results are validated by a simplified representation of micro excavator.

The remainder of this paper is organized as follows. The case study is presented in Section 2, where Sections 2.1 and 2.2 present principles and a detailed description of the developed Matlab/Simulink model. The results of simulation and experimental investigation are described in Sections 3 and 4, respectively. Finally, Section 5 and 6 contain discussion and concluding remarks.

2 Study case: excavator with DDH

In this study, a micro excavator is used as an example application of DDH to achieve a more efficient construction machinery. In the future, this results of this study could be implemented to other NRMM.

Internal gear motors are adopted for DDH units, with operating mode can be switching between pumping and motoring. To avoid confusion, from here on these will be referred to as pump/motors.

2.1 Principle

As shown in fig. 2, the original valve control system for boom, arm and bucket is replaced with three DDH units respectively. In the DDH unit, a fixed displacement pump/motor with a speed-controlled electric servo motor directly controls the amount of hydraulic oil pumped into and out from the system. The hydraulic pump/motor creates a flow depending on the rotating speed of the servo motor. Additionally, a hydraulic accumulator is used as a conventional tank replacement [14].

In DDH, dimensions of a utilized double-acting single-rod cylinder bring requirements for pump/motors. Therefore, an ideal cylinder ratio R_{ideal} was established for choosing pump displacement, where R_{ideal} is the surface area ratio between the annulus area and the piston of each cylinder. Due to available pump units, the realized pump displacement ratio R_{real} differs from R_{ideal}, where R_{real} is the displacement ratio between pumps connecting to the rod side and the piston side. This leads to sizing error in some cases if pump unit is slightly under-dimensioned. Thus, fluid from the cylinder B-chamber is not pumped out at a corresponding rate to that of the fluid

pumped into the A-chamber. This leads to a rise of pressure in the B-chamber, which should be mitigated. In this study, the sizing error is mitigated by adding hydraulic accumulator D as shown in fig. 2.

2.2 Modeling

In order to acquire the dynamic response and energy consumption distribution of the actuators, this study constructed a particular model in Matlab/Simulink, which integrated with mechanics, hydraulics, electrics and control systems of the micro excavator.

2.2.1 Mechanical model

The prototype is a 1-ton class JCB micro excavator with a conventional valve control system, as shown in fig. 3a. The 3D solid mechanical model was constructed and the material was assigned to each part in PTC Creo. As shown in the fig. 3b, the multibody dynamic model was created by exporting from PTC Creo and importing into Matlab Simscape using Simscape Multibody Link Plug-In.

a) b)

Figure 3: a) The prototype, b) multibody dynamic model.

2.2.2 Hydraulic model

The mathematical models of cylinder, pump/motors, accumulators and pipes of DDH are built in Matlab/Simulink. Most of their detailed explanations refer to work in [15].

In order to make accurate energy efficiency calculations, Vivoil gear motors with displacements of $22.8 \cdot 10^{-6}$ and $14.4 \cdot 10^{-6}$ m^3/rev, with leakage submodels obtained by measurements in [16], were chosen respectively and adopted for all three DDH units.

The parameters of cylinders were obtained from the micro excavator and the ideal pump/motor ratios R_{ideal} and real pump/motor ratios R_{real} are shown in Table 1. The sizing errors for bucket cylinder and arm cylinder are both 1.57%, namely less than 2%, which would not cause excess pressure [15]. However, the pump/motor ratio for boom demands compensation for the sizing error.

Table 1: Parameters of each DDH.

	Cylinder [mm]	Ratio		Accumulator	Accumulator
		R_{ideal}	R_{real}	C	D
Boom	60/30×325	0.75	0.63	0.7L@1bar	0.7L@10bar
Arm	50/30×400	0.64	0.63	0.7L@1bar	—
Bucket	50/30×290	0.64	0.63	0.7L@1bar	—

Considering the load of boom cylinder is mainly negative force, the compensating hydraulic accumulator D is located at the opposite side of the rod and another one C operating as tank is mounted between two pump/motors as shown in fig. 4. As a result, each DDH model consists of pump/motors, a hydraulic cylinder, two on/off valve and one or two hydraulic accumulators.

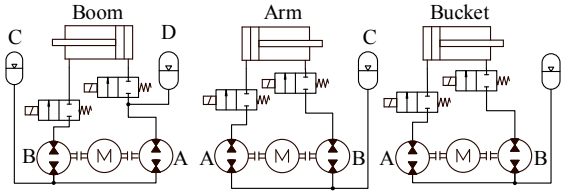

Figure 4: Modified DDH for micro excavator.

Figure 5 illustrates the micro excavator model with multibody and a triple DDH built in Matlab/Simulink.

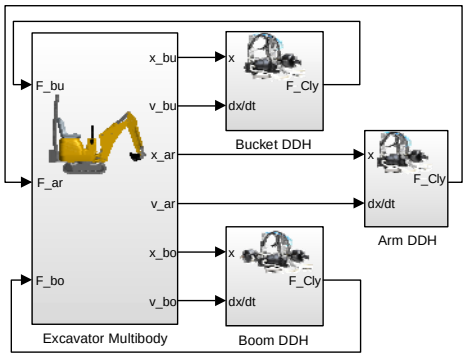

Figure 5: Simulink model of excavator with DDH.

Pump/motor leakage consists of all internal and external leakage flows as a function of the pressure difference over the pump and the pump flow equation is given by eq. (1):

$$q_P = V_P n - q_L \,. \tag{1}$$

The pump produces a flow q_P which is dependent on the rotational speed n, its displacement V_P and leakage flow q_L. q_L is a function of the pressure difference of over the pump at 20°C, obtained by a cross sectional linear regression after measurements [16], as shown by eq. (2).

$$q_L = \alpha + \beta \Delta p + \gamma \sqrt{\Delta p} + \varepsilon \,, \tag{2}$$

where α, β and γ are regression coefficients as shown in Table 2, Δp is pressure difference of over the pump, and ε is an error term.

Table 2: Leakage model coefficients [16].

Pump	α	β	γ	ε
22.8mL/rev	$-3.61 \cdot 10^{-4}$	$-2.66 \cdot 10^{-13}$	$4.44 \cdot 10^{-9}$	$1.89 \cdot 10^{-4}$
14.4 mL/rev	$-2.60 \cdot 10^{-4}$	$6.09 \cdot 10^{-13}$	$1.96 \cdot 10^{-9}$	$1.23 \cdot 10^{-4}$

The model describing the pressure in an asymmetrical cylinder is divided into two parts as shown in eq. (3) and (4):

$$\dot{p}_A = \frac{B(p)}{V_{0A} + A_A x} [q_A - K_L(p_A - p_B) - A_A \dot{x}] \,, \tag{3}$$

$$\dot{p}_B = \frac{B(p)}{V_{0B} + A_B(x_{max} - x)} [q_B + K_L(p_A - p_B) + A_B \dot{x}], \tag{4}$$

where $B(p)$ is the bulk modulus for oil varying with pressure; V_{0A} and V_{0B} are the dead volume of the cylinder's piston side chambers; K_L is the leakage constant between the cylinder

chambers, A and B; q_A and q_B are the flows into the cylinder's piston side respective chambers.

$$F = (p_A A_A - p_B A_B) - F_r - F_{end}, \quad (5)$$

where the friction force F_r of the cylinder is calculated by utilizing the LuGre model [17], and the simulation parameters are from reference [16], which have been verified by measurements; F_{end} is the end force.

2.2.3 Electric drive

The model of 3 phase permanent magnet synchronous motor (PMSM) was built in Matlab/Simulink [18]. In this study, it is assumed that the utilized synchronous machine has surface-mounted permanent magnets, rotor is magnetically round (non-salient) and has the same reluctance along any axis through the center of the electric machine. The vector control i_d=0 is utilized for controlling of PMSM.

Space vectors transformation from a-b-c phase into equivalent *dq* quantities is implemented. The *dq* transformation is used for a simplified application of control method for electric motor.

Applying these simplifications, electromagnetic torque can be calculated as shown in eq. (6).

$$T_{em} = \frac{N_p}{2} \lambda_{fd} i_{dq}, \quad (6)$$

where N_p is pole pairs, λ_{fd} is the flux linkage of the stator *d* winding that produced by the rotor magnets, i_{sq} is stator current in *q* axis.

Stator voltages in *dq* transformation are shown in eq. (7) and (8):

$$v_{sd} = R_s i_{sd} - \omega_m L_s i_{sq}, \quad (7)$$

$$v_{sq} = R_s i_{sq} + \omega_m L_s i_{sd} + \omega_m \lambda_{fd}, \quad (8)$$

where L_s is stator inductance, R_s is stator resistance, i_{sd} is stator current in *d* axis and ω_m is related to actual rotor speed ω_{mech} as shown in eq. (9).

$$\omega_m = \frac{N_p}{2} \omega_{mech}. \quad (9)$$

The electromechanical torque acts to the load connected to the motor, resulting in actual (mechanical) speed of the rotor ω_{mech}:

$$\frac{d\omega_{mech}}{dt} = \frac{T_{em} - T_L}{J_{eq}}, \quad (10)$$

where J_{eq} is combined motor load inertia, T_l is load torque.

PI controllers are utilized for realization of i_d=0 control for adjusting i_d and i_q currents. In this research, it is assumed that the inverter has fixed switching losses. In realized design, the current feedback controller (PI control) is tuned for the desired phase margin at the chosen open-loop crossover frequency. The speed feedback controller (self-adjusting parameter fuzzy PID control), is used to adjust the shaft speed to be independent of the load-torque disturbance coming from hydraulics, according to a reference signal. The parameter of the motor was set according to its datasheet as shown in Table 3.

Table 3: PMSM characteristics [19].

Parameter	Value
Rated Speed	3000 rpm
Rated torque	8.1 N·m
Stall current	5.9 A
Rated power	2.54 kW
R_s - Resistance(phase)	2.02 Ω
L_s - Inductance(phase)	$13.27 \cdot 10^{-3}$ H
Inertia	$9.0 \cdot 10^{-4}$ kg·m^2
Stall Torque	9.4 N·m
Peak torque	28.2 N·m

2.2.4 System control

In this model, closed-loop PID controls between the frequency converter and the electric motor, and position control with P regulator are utilized, as illustrated in fig. 6.

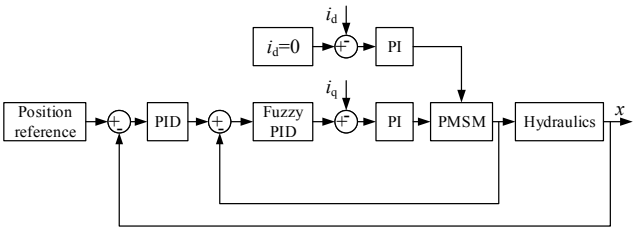

Figure 6: System control schematic.

3 Simulation and results

In this simulation, a typical excavator digging cycle was selected for simulation. This cycle represents an excavator digging a load of earth, rotating, releasing the load onto a pile, and then returning to its initial position [3]. The cycle inputs shown in fig. 7 are the relative cylinder displacements.

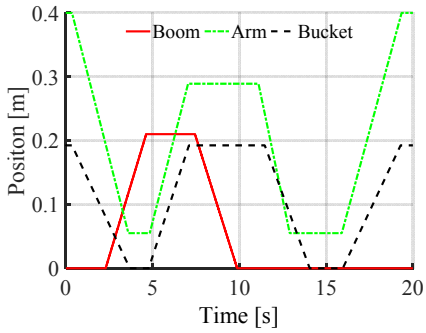

Figure 7: Input reference of a typical digging cycle [3].

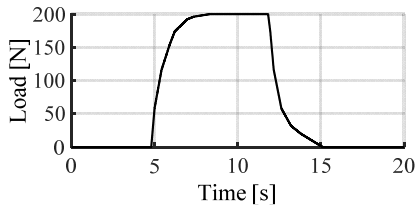

Figure 8: Digging load of loose dry dirt [3].

The rated capability of the bucket is 17 L, and the density of loose dry dirt is 1220 kg/m^3. Consequently, a time-dependent

bucket load is 20 kg, which was implemented into the working cycle [3]. The load increases to a 20 kg of dirt as the bucket rotates in loading mode and then decreases to zero as the bucket rotates in the dumping motion, as provided in fig. 8. The outputs of position and velocity adopting position control in this cycle are presented in fig. 9.

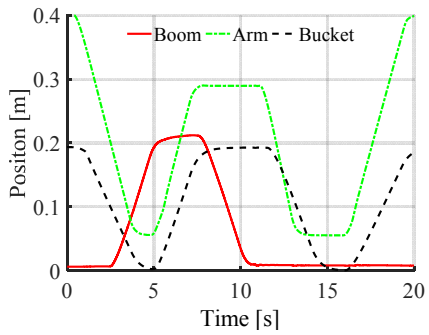

a)

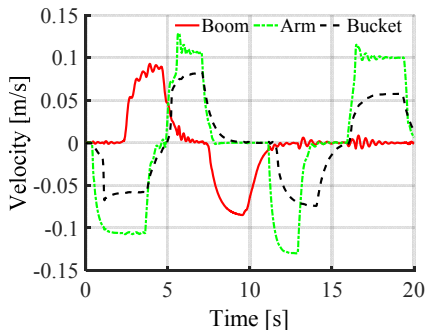

b)

Figure 9: a) Position output, b) velocity output.

Table 4: Definitions of power and energy.

Equation	Symbol
$P_{cylinder}=(p_A A_A - p_B A_B)\cdot\dot{x}$	$P_{cylinder}$ – input power of cylinder, W p_A, p_B – pressure of piston side and rod side of cylinder, Pa A_A, A_B – effective cross area of cylinder piston side and rod side, m^2 $\dot{x}$ – velocity of cylinder piston, m/s
$P_{pump}=T_P n_P$	P_{pump} – input power of pump, W T_P – torque of pump shaft, N·m n_P – speed of pump shaft, rad/s
$P_{motor}=T_M n_M$	P_{motor} – output power of motor, W T_M – torque of motor shaft, N·m n_M – speed of motor shaft, rad/s
$P_{PMSM}=v_a i_a + v_b i_b + v_c i_c$	P_{PMSM} – input power of PMSM, W v_a, v_b, v_c – phase voltage, V i_a, i_b, i_c – phase current, A
$E_{cylinder}=\int P_{cylinder}dt$	$E_{cylinder}$ – input power to cylinder ($P_{cylinder}>0$), in lifting/pumping mode, J
$E_{PMSM}=\int P_{PMSM}dt$	E_{PMSM} – energy consumed by PMSM ($P_{PMSM}>0$), J
$E_{Regeneration}=\int P_{PMSM}dt$	E_{PMSM} – energy regenerated by PMSM ($P_{PMSM}<0$), J
$\eta=\frac{E_{cylinder}}{E_{PMSM}}$	η, Energy efficiency of DDH, %

The main objective of this part is to compute the energy efficiency of DDH units and overall efficiency of them in the typical digging cycle, and to discover the energy recovery potential. The power of components was calculated as shown in Table 4, and the energy was obtained by integrating the power.

The cylinder power is calculated as the product of the hydraulic pressure force in the respective actuator and its velocity, including frictional effects. Calculation of η efficiency includes following losses: all internal and external leakage of pump, hydromechanical friction of pump, pressure loss of cylinder outlet caused by extra pressure rise due to dynamic flowrate error between ideal ratio R_{ideal} of cylinder and real ratio R_{real} of pumps.

When boom goes down, the pump/motor B runs in motoring mode. Therefore, PMSM generates electricity, absorbing the potential energy as shown in fig. 10. While boom lifting, pump/motor B runs in pumping mode.

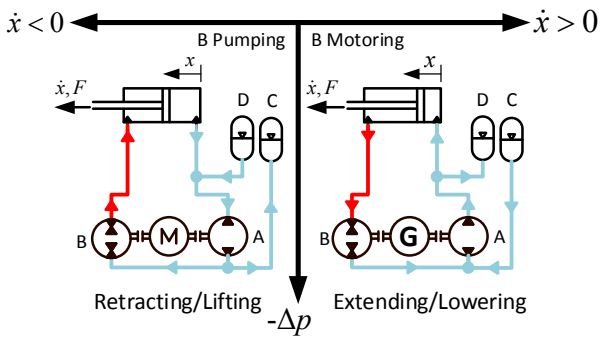

Figure 10: Operating mode of boom pump/motor B and PMSM.

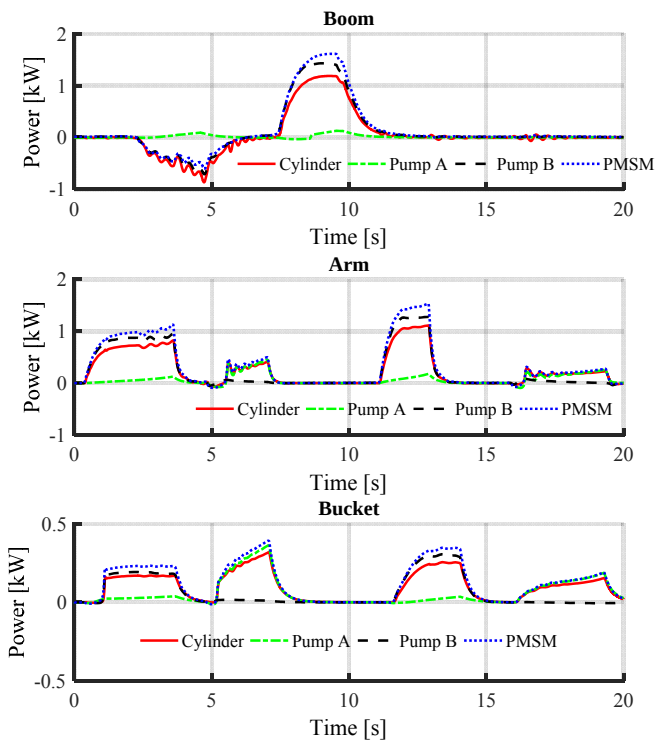

Figure 11: Simulated power consumed by each DDH component for boom, arm, and bucket.

In boom DDH (fig. 11), the pump/motor B was in motoring mode from 2.5 to 5.5 s while lowering, and in pumping mode from 7.5 to 10.5s while lifting. The maximum power consumed by pump A is 0.12 kW in a short period during lifting, to charge the hydraulic accumulator C.

After calculation, the energy consumption amount of the cylinder and input energy for the PMSM are presented in Table 5. Furthermore, the energy efficiency of each unit is figured out. The results show the energy efficiency of the boom DDH, arm DDH, and bucket DDH was 67.5%, 75.4%, 77.5% respectively for performed cycle (fig. 9a). The overall efficiency of front attachment with three DDH units was found to approximate to 73.3%, much higher than 31.4% (efficiency of a 5-ton excavator with LS system in [3]). Furthermore, the potential energy recovery for boom DDH estimated as 1.54 kJ.

Table 5: Energy consumption and efficiency.

DDH		Energy [kJ]	Efficiency [%]
Boom	Cylinder	2.90	67.5
	PMSM	4.29	
	Regeneration	1.54	—
Arm	Cylinder	5.16	75.4
	PMSM	6.84	
	Regeneration	0.04	—
Bucket	Cylinder	1.96	77.5
	PMSM	2.54	
	Regeneration	0	—

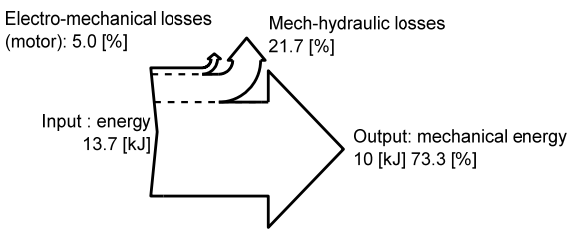

Figure 12: Energy flow of DDH system.

Additionally, the Sankey diagram of the decentralized excavator with a triple DDH units is shown in fig. 12. The electro-mechanical losses are 5%, due to 95% fixed efficiency in the PMSM model. The mech-hydraulic losses account for 21.7%, including hydro-mechanical friction (hydro-mechanical efficiency 0.85, estimated from datasheet), internal and external leakage, and pressure losses caused by sizing error. 73.3% of overall energy is consumed by cylinders and loads.

4 Validation

For simplicity, a standalone DDH will be utilized as a proof of concept to validate simulation results for the micro excavator. In this validation study, it is assumed a standalone DDH power pack represents bucket or arm cylinder of the excavator, due to one degree of freedom (DOF) and the same required pump/motor displacement ratio R_{real}. Figure 12 illustrates the proposed validation setup with schematic and the data acquisition system.

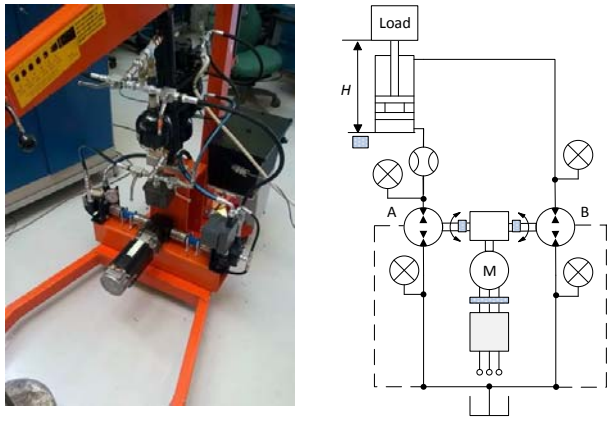

a) b)

Figure 12: a) Standalone DDH (crane), b) schematic.

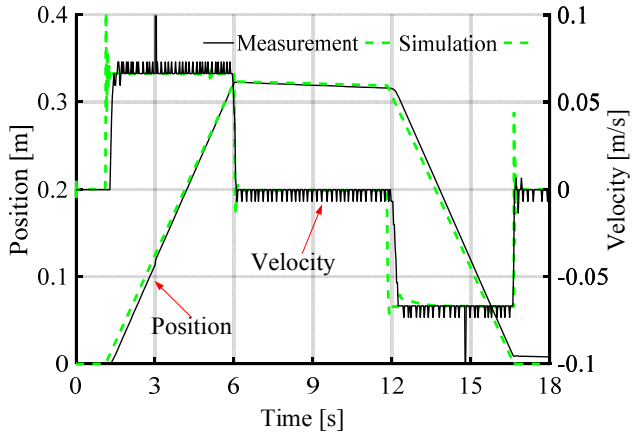

a)

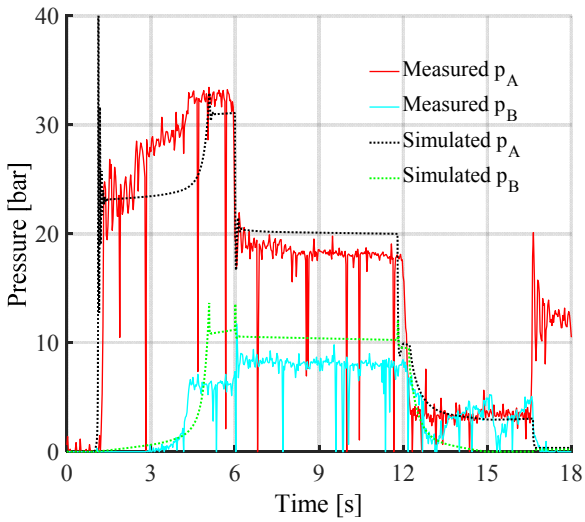

b)

Figure 13: Validation of simulation: a) velocity and positon, b) pressure of chamber A and B.

In the proposed validation setup, the speed and position control of a double-acting cylinder is implemented directly with an electric motor drive in a closed-loop system without conventional control valves [14].

An example of measurement data of standalone DDH with payload of 120 kg and rotating motor speed 750 rpm is displayed in fig. 13. The simulation results of position, velocity, and pressures of chamber A and chamber B show acceptable accuracy, compared with the measurement results. Therefore, the developed model can be used to evaluate the system performance of decentralized excavator.

5 Discussion

In this research, a typical working cycle for a micro excavator was studied. Initial investigation of the excavator with decentralized hydraulics is based on a Matlab/Simulink model coupled with multibody dynamics. The purpose of the model is to investigate the efficiency of decentralized hydraulics for micro excavator applications.

The model was developed on the basis of following simplifications. The LuGre model was chosen for cylinder friction, in which temperature and pressure difference are not taken into account. The pump leakage model considers only pressure difference and does not take into account speed and temperature variation. The on/off valves are not included in this model, and piping is regarded as static fluid volumes. For this initial stage of research, these simplifications are considered acceptable. However, for future development, some of these simplifications should be taken into account. Cavitation problems were not investigated yet in this study, but should be included in the future.

The load model was simplified, as the actual digging cycle does not have penetration into the pile. This was excluded due to the complexity of the terra-mechanical forces. At the moment, data acquisition is not available for quantifying these forces.

System control for DDH and decentralized hydraulics was not the focus of this research and was not investigated in detail. A self-adjusting fuzzy PID control was implemented as a speed control for the electric motor, using a fixed PID control as current control (electric motor vector control id=0) and position control (cylinder) as a response to load–torque disturbance coming from the hydraulics.

Since decentralized hydraulics were implemented without a proportional control valve, the damping of the system is low compared to conventional systems, which leads to some oscillations. Therefore, the control strategy of the DDH can be improved in the future. Further evaluation of the dynamic performance of the hydraulic system should be made. In addition, the properties of the electric motor should be considered by the model and evaluated.

For simplicity, it is assumed that a standalone DDH power pack represents a bucket or arm cylinder of the excavator, due to one degree of freedom (DOF) motion. Experimental data is utilized to validate the developed model and used as proof–of-concept of decentralized hydraulics applied to the micro excavator.

Validation of the model showed acceptable results. The detail level of the model could be improved based on validation results.

Efficiency behaviors of DDH components and the overall efficiency of the triple DDH system were determined. The efficiency estimation was based on simulation combining data from manufacturers and experiment. Productivity and efficiency analysis should be performed for the proposed decentralized approach to investigate the benefits of this system in more detail.

Table 5 shows system efficiency is in the range of 67.5 to 77.5%. Among three DDH units, boom DDH has the lowest efficiency due to pressure losses caused by the sizing mismatch and higher leakage produced by the higher load. In fig. 12, Sankey diagram shows details about the energy loss distribution and the overall efficiency is 73.3%. The dominate losses are hydro-mechanical and simulation results show higher efficiency compared to LS systems (literature state-of-the-art [3]). However, future detailed modelling will affect these values, and increased energy consumption due to temperature, pressure, viscosity, and friction. As part of this project, decentralized hydraulics should be compared with conventional valve-controlled systems in modelling and experiment, in order to demonstrate the full benefits of this approach.

Regeneration of energy with DDH was shown, which gives additional benefits for this kind of system. The potential energy recovery for the boom DDH was estimated as 1.54 kJ, which can be transformed into electrical power. In this study, the inverter for the DDH was directly powered from the electrical grid, and the energy storage, inverter, power electronics were not considered in this stage of research. Consequently, the regenerated potential energy was not stored. However, energy storage could be accomplished using a battery or super capacitor. Disadvantages are additional components expenses needed. Energy storage and its management system, power electronics, and three inverters will affect price, efficiency, and maintenance of the decentralized hydraulics. However, further investigation of these components will be included in the near future.

6 Conclusion

This research has shown that typical cycle control and potential energy recovery by DDH for work-set are feasible in a micro excavator. Efficiency behaviors of DDH components and the overall efficiencies of the triple DDH system were determined. The efficiency estimation was based on simulation combining data from manufacturers and experiment.

According to simulation, the energy efficiency of the boom DDH, arm DDH, and bucket DDH was 67.5%, 75.4%, 77.5%, respectively. Furthermore, the potential energy recovery for boom DDH was estimated as 1.54 kJ.

For simplicity, a standalone DDH was utilized as a proof of concept to validate simulation results for the micro excavator.

The simulation showed that combining the efficiency of three DDH units and energy recovery for each actuator, the overall efficiency could reach 73.3% for performed cycle. It is higher than efficiency of LS system (a 5-ton LS excavator).

Therefore, the decentralized approach could be suggested for construction equipment.

Acknowledgments

This research was enabled by the financial support of the Tekes (project EL-Zon), internal funding from the Department of Mechanical Engineering at Aalto University, Finland. This work was partly supported by the Natural Science Foundation of Fujian Province, China (No. 2016J01203) and by the Scientific Research Fund of Fujian University of Technology (No. GY-Z15096).

Nomenclature

Designation	Denotation	Unit
F_i	Force	[N]
$p_{A,B}$	Pressure	[Pa]
B	Bulk modulus	[Pa]
q	Flowrate	[m^3/s]
A	Area	[m^2]
x	Displacement	[m]
V	Displacement	[m^3/rev]
n	Rational speed	[rpm]
P	Power	[W]
E	Energy	[J]
R	Displacement ratio	—
$v_{a,b,c}$	Phase voltage	[V]
$i_{a,b,c}$	Phase current	[A]
Np	Pole pairs	—
i_{sq}	Stator current in q axis	[A]
i_{sd}	Stator current in d axis	[A]
R_s	Stator resistance	[Ohm]
L_s	Stator inductance	[mH]
ω_{mech}	Actual rotor speed	[rad/s]
ω_m	Angular speed	[rad/s]
λ_{fd}	Flux linkage of the stator d winding	[$kg \cdot m^2 \cdot s^{-2} \cdot A^{-1}$]

References

[1] Tier 4 emission standards for nonroad diesel engines, online, https://www.dieselnet.com/standards/us/nonroad.php#tier4.

[2] M Kagoshima, M Komiyama, T Nanjo, and A Tsutsui. Development of new hybrid excavator. *Kobelco Technology Review*, (27): 39-42, 2007.

[3] J D Zimmerman, M Pelosi, C A Williamson, and M Ivantysynova. Energy consumption of an LS excavator hydraulic system. *ASME 2007 International Mechanical Engineering Congress and Exposition*, 117-126,2007.

[4] T Lin, Q Wang, B Hu, and W Gong. Development of hybrid powered hydraulic construction machinery. *Automation in Construction*, 19(1): 11-19, 2010.

[5] 12H GTE hybrid harvester , http://www.logset.com/12H_GTE_Hybrid

[6] Anon. Komatsu introduces the world's first hydraulic excavator: hybrid evolution plan for construction equipment. *Komatsu press release*, 05: 2008, http://www.komatsu.com/CompanyInfo/press/2008051315113604588.html

[7] New Generation Hybrid Excavator ZH200-5B, online, http://www.hitachi.com/environment/showcase/solution/industrial/hybrid_excavator.html

[8] M. Edamura, E. S. Ishida, S. Imura, and S. Izumi. Adoption of electrification and hybrid drive for more energy-efficient construction machinery. *Hitachi Review*, 62(2): 118, 2013.

[9] R Hippalgaonkar, and M Ivantysynova. A series-parallel hydraulic hybrid mini-excavator with displacement controlled actuators. *The 13th Scandinavian International Conference on Fluid Power*, *SICFP2013*, June 3-5, 2013, Linköping, Sweden

[10] W Shen, J Jiang, X Su, and H Karimi. Energy saving analysis of hydraulic hybrid excavator based on common pressure rail, Hindawi, https://www.hindawi.com/journals/tswj/2013/560694/

[11] T Minav, T Lehmuspelto, P Sainio, and M Pietola. Series hybrid mining loader with zonal hydraulics. 8-10 March 2016, IFK-2016, Dresden, Germany

[12] T Hassi, A Korva, S Markkula, etc. Improving energy efficiency of an electric mini excavator. *11th International DAAAM Baltic Conference "Industrial engineering"*, 20-22 April 2016, Tallinn, Estonia

[13] J D Zimmerman. Towards optimal multi-actuator displacement controller mobile hydraulic systems, 2012, Purdue University: Indiana, USA.

[14] T Minav, and M Pietola. Position control of direct-driven hydraulic drive without conventional oil tank for more electric aircraft, *MEA2015 More Electric Aicraft*, 2015, Toulouse, France.

[15] A Järf. Flow compensation using hydraulic accumulator in direct driven hydraulic differential cylinder application and effects on energy effciency. 2016, Aalto University: Espoo, Finland.

[16] A Järf, T Minav, and M Pietola. Nonsymmetrical flow compensation using hydraulic accumulator in direct driven differential cylinder, Proceedings of the *ASME 2016 9th FPNI Ph.D. Symposium on Fluid Power, FPNI2016,* October 26-28, 2016, Florianópolis, SC, Brazil

[17] C Canudas de Wit, H Olsson, K J Astrom, and P Lischinsky. A new model for control of systems with friction. *IEEE Transactions on automatic control* 40(3): 419-425, 1995.

[18] Ned Mohan. Advanced electric drives: analysis, control, and modeling using MATLAB/Simulink. John wiley & sons, 2014.

[19] Emerson Industrial Automation. Technical Data Unimotor FM and HD High performance AC brushless servo motors, 2013. http://www.emersonindustrial.com/en-en/documentcenter/ControlTechniques/Brochures/unimotor_technical_data.pdf .

Modelling Dynamic Response of Hydraulic Fluid Within Tapered Transmission Lines

Jeremy ven der Buhs and Travis Wiens

Department of Mechanical Engineering, University of Saskatchewan, Saskatoon, Saskatchewan, Canada
E-mail: jeremy.venderbuhs@usask.ca, travis.wiens@usask.ca

Abstract

This paper examines modelling the laminar dynamic fluid responses within hydraulic transmission lines that have a tapered shape from the inlet to outlet. There are excellent models available for fast simulation of pressure and flow dynamics within uniform lines, however the established models for tapered lines have some notable inaccuracies and simulation complexities. The transmission line method (TLM) structure is applied in this paper since it can be computed quickly and has shown to accurately model the effects of frequency-dependent friction. This paper presents a method of optimizing the TLM weighting functions, minimizing the error between the TLM transmission matrix terms and a numerical exact solution. Optimizations have shown that using the TLM to model tapered lines has improved accuracy over the existing models when compared in the frequency domain. Two-dimensional interpolation of a look-up table is possible allowing for quick selection of the optimized parameters. This model can be used in numerous applications where line dynamic effects must be accounted for, especially with digital hydraulic switched inertance converters.

Keywords: Transmission line method, TLM, tapered fluid lines, optimization, modelling, simulation.

1 Introduction

Computer modelling of fluid transmission lines of constant cross-sectional area is an area of hydraulics where extensive research has been performed previously as well as very recently [1–7]. However, the established research into the modelling of tapered transmission lines has some shortcomings which requires further study and refinement. Time domain models describing line dynamics are greatly desired as it allows for simple implementations with time domain numerical solvers, and interfaces well with nonlinear component models such as valves and accumulators. The ability to model pressure and flow transients within fluid lines is important for predicting the performance of hydraulic systems, especially those where line effects should be considered.

As shown in fig. 1, the transmission line method (TLM) is a method of modelling which uses a network of linear transfer functions and time delays to model wave propagation [1], and has had recent enhancements accurately modelling the effects of frequency-dependent friction, all while solving within the time domain [2, 3]. While the TLM currently works for uniform lines of constant cross-section, it has not yet been applied to tubes of varying cross-section. The first mention of modelling tapered lines employs a method of characteristics (MOC) solution to the differential equations, however, the proposed MOC solution was only used and analyzed for a uniform line [4]. An approximated analytical solution for

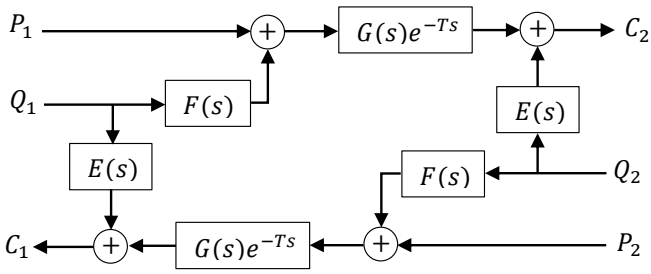

Figure 1: Block diagram of the TLM [1].

frequency dependent flow through tapered lines was derived in [5]. The approximate transmission matrix they derived was taken further in [6] by applying modal analysis (MA) and rational polynomial transfer function approximations (RPTFA) of the transcendental functions in the solution, allowing for simulations to be performed in the time domain. No further research into modelling tapered lines has appeared in the literature until this point, and the need for a robust, fast, and accurate model for tapered transmission lines has heightened with the growth in switched inertance converter research [8].

This paper will look at modelling tapered fluid lines using the TLM model and optimization procedure similar to that in [3] where weighted transfer functions make up the E, F, and G transfer functions. The equations and optimization procedure

are described in detail. Frequency domain results will be analyzed, and comparisons will be made between previous models, the exact solution, and the proposed model. Also, time domain simulations of the model will be discussed.

2 Previous Models

The differential equations that describe one-dimensional flow, Q, and pressure, P, through the tapered tube shown in fig. 2 are the equations of motion and continuity, expressed in the Laplace domain, respectively [7]:

$$\frac{dP(x,s)}{dx} + \frac{\rho s}{A(x)} Q(x,s) N(x,s) = 0 \tag{1}$$

$$P(x,s) = -\frac{\partial Q(x,s)}{\partial x} \frac{K}{A(x)s} \tag{2}$$

where ρ is the fluid density, and s is the Laplace operator. N is the frequency-dependent friction term, commonly used in previous research defined as [1–7]

$$N(x,s) = -\frac{J_0\left(jr(x)\sqrt{\frac{s}{\nu}}\right)}{J_2\left(jr(x)\sqrt{\frac{s}{\nu}}\right)}. \tag{3}$$

Frequency-dependent friction has shown to be a realistic phenomenon, and models that implement it have shown to be significantly more accurate than models that use steady friction. Since the proposed model natively uses a summation of weighting functions, it can be expected that there would be negligible computational time savings if steady friction were considered. As such, frequency-dependent friction will be exclusively considered in this paper.

Within a tapered transmission line, the radius varies linearly from inlet to outlet given by eq. (4), and is visualized in fig. 2.

$$r(x) = r_1 + \frac{(r_2 - r_1)x}{l} \tag{4}$$

The existing model for modelling tapered fluid lines was developed in [5, 6]. The transmission matrix, eq. (5) and (6), is not an exact solution, but rather an approximated analytical solution to the set of ordinary differential equations previously defined. Within its derivation, higher order terms of a Taylor series expansion were rejected in order to allow the possibility of a closed form solution in the frequency domain. This simplification creates notable inaccuracy at higher frequencies.

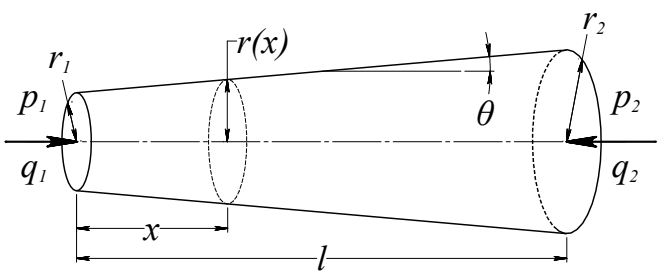

Figure 2: Schematic of a tapered transmission line.

$$\begin{pmatrix} P_1 \\ Q_1 \end{pmatrix} = \begin{pmatrix} \cosh\Gamma - \frac{\xi\lambda_o}{DS\sqrt{N}}\sinh\Gamma & Z_c\sqrt{N}\sinh\Gamma \\ \frac{1}{Z_c\sqrt{N}}\sinh\Gamma & \cosh\Gamma + \frac{\xi\lambda_o}{DS\sqrt{N}}\sinh\Gamma \end{pmatrix} \begin{pmatrix} \frac{P_2}{1-\xi\lambda_o} \\ \frac{Q_2}{1+\xi\lambda_o} \end{pmatrix} \tag{5}$$

where,

$$\begin{aligned} \Gamma =& DS\gamma_o[1+\xi(1-\lambda_o)],\ D = \frac{\nu l}{cr_1^2},\ Z_c = \frac{\rho c\gamma_o}{\pi r_1^2}, \\ \lambda_o =& \frac{1}{2}\left[1 - \left\{\frac{\chi_o(\gamma_o^2-1)}{2\gamma_o}\right\}^2\right],\ t_o = \frac{r_1^2}{\nu},\ S = st_o, \\ \gamma_o =& \left[-\frac{J_o\left(j\sqrt{S}\right)}{J_2\left(j\sqrt{S}\right)}\right],\ \chi_o = \sqrt{S},\ \xi = \frac{\theta l}{r_1}. \end{aligned} \tag{6}$$

This model is presented in nondimensional form, with parameters nondimensionalized with respect to the inlet radius, r_1. In its current form, this transmission matrix cannot be solved in the time domain, a similar problem that previous researchers have encountered with simulating transmission lines. Further approximation is necessary in order to solve this system of equations in the time domain. In [6], modal analysis (MA) and rational polynomial transfer function approximations (RPTFA) were performed in order for the transmission matrix to be solved in the time domain. While these approximations, tabulated in their paper, show good agreement with the approximate transmission matrix proposed by [5], it is important to note that the transmission matrix is an approximated closed form solution, and has some notable discrepancies to the exact analytical solution, and has a very limited range of accuracy.

In order for a true two-port (inlet and outlet), 4-terminal (pressure and flow at each end) transmission line model to work accurately it needs to provide symmetrical solutions, meaning that given the same boundary conditions and dimensions, the transfer function must be the same if the ends are exchanged. Consider 2 cases, Case 1 has a diverging tube with a blocked outlet, and Case 2 has a converging tube with a blocked inlet. In both cases, the blocked port has the larger radius, and the smaller radius is open. By maintaining the same dimensions, the pipe in Case 2 is simply a flipped version of Case 1. The transfer functions in eq. (5) and eq. (6) were calculated and are compared in fig. 3. The logical result of this study should have shown the transfer functions be exactly the same, however there is a noticeable shift in the frequency peaks. The same study was performed using the exact solution calculated numerically from the set of ordinary differential equations previously defined, and showed that, in this case, the results are the same. This asymmetry in the approximate transmission matrix leads to significant inaccuracy when implemented in the time domain.

Another issue with the existing transmission matrix is inaccuracies at higher harmonics. Figure 3 shows how the

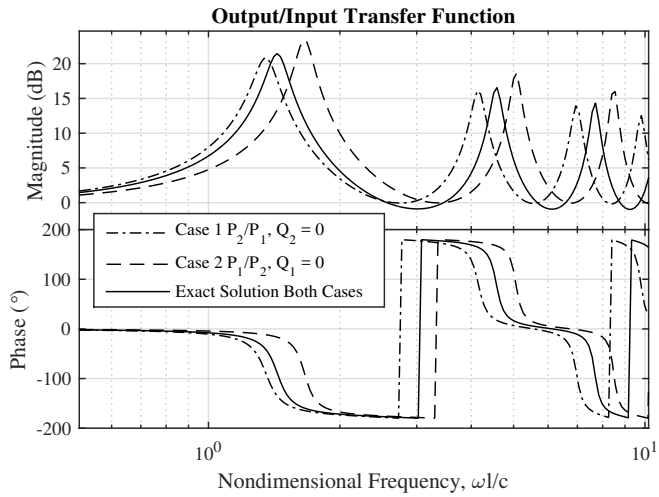

Figure 3: Transfer function asymmetry and comparison to the exact numerical solution.

P_2/P_1 transfer function for a blocked outlet compares from the transmission matrix solution to the exact numerical solution. While the first resonance is modelled closely, higher resonances of significant power are not closely matched. This difference becomes greater with increased transmission line taper.

3 Proposed Model

The proposed model is similar to the one developed for uniform transmission lines in [3]. The 2-port model relating pressure and flow at the inlet, to the pressure and flow at the outlet is given by the transmission matrix in eq. (7) [3]. The characteristics C_1 and C_2 are related to pressure and flow by eq. (8) and (9) [1]. The characteristic impedance of the tapered line is Z_c.

$$\begin{pmatrix} P_1 \\ Q_1 Z_c \end{pmatrix} = \begin{pmatrix} t_{11} & t_{12} \\ t_{21} & t_{22} \end{pmatrix} \begin{pmatrix} P_2 \\ Q_2 Z_c \end{pmatrix} \tag{7}$$

$$P_1 = C_1 + Z_c Q_1 \tag{8}$$

$$P_2 = C_2 + Z_c Q_2 \tag{9}$$

For a tapered line, the characteristic impedance can be derived using the definition in [9] where wave propagation time is divided by the hydraulic capacitance of the pipeline. The volume of a tapered pipeline is that of a right circular cone frustum, and is included in the calculation of hydraulic capacitance. Therefore:

$$Z_c = \frac{3\rho c}{\pi r_{max}^2}\left(1+\lambda+\lambda^2\right)^{-1} \tag{10}$$

where λ is the taper ratio, which is simply defined as the minimum pipe radius divided by the maximum pipe radius:

$$\lambda = \frac{r_{min}}{r_{max}}. \tag{11}$$

This parameter is the same regardless if the pipe is converging or diverging in shape. The steady state resistance of a tapered transmission line, R, is defined by integrating uniform Hagen-Poiseuille pressure drops over the entire length of the pipeline. Lubrication theory is employed since the change in radius over a small element length dx is considerably smaller than the size of the pipe itself. The hydraulic resistance is then found to be:

$$R = \frac{8\rho\nu l}{\pi r_{max}^4}\left[\frac{1+\lambda+\lambda^2}{3\lambda^3}\right]. \tag{12}$$

Having obtained expressions of characteristic impedance and resistance, the dissipation number, β, for a tapered transmission line can be found using the following relationship:

$$\beta = \frac{R}{8Z_c} = \frac{\nu l}{c r_{max}^2}\left[\frac{\left(1+\lambda+\lambda^2\right)^2}{9\lambda^3}\right]. \tag{13}$$

It is important to note that for a pipeline of uniform cross section, the taper ratio would be 1, and the resulting characteristic impedance, laminar resistance, and dissipation number would reduce to the same as used in the previous models for uniform tubes [2, 3].

The TLM structure contains linear transfer functions E, F, and G which are arranged in the configuration shown in fig. 1 and are defined by the weighting functions as follows [3].

$$E(s) = Z_c \sum_{i=1}^{k} \frac{m_{Ei}}{n_i + Ts} \tag{14}$$

$$F(s) = Z_c + bE(s) \tag{15}$$

$$b = 1 - \frac{8\beta}{\sum_{i=1}^{k} \frac{m_{Ei}}{n_i}} \tag{16}$$

$$G(s) = 1 - \sum_{i=1}^{k} \frac{m_{Gi} Ts}{n_i + Ts} \tag{17}$$

$$T' = \tau T = \tau \frac{l}{c} \tag{18}$$

The weighting factors m_{Ei}, m_{Gi}, and τ are found using a constrained optimization which is explained in the following section. Here, the F transfer function is scaled off of the E transfer function. This gives the model the ability to accurately compute the pressure drop during steady state conditions. The weighting factors n_i, are the same as in the series proposed in [3], which are given as follows:

$$n_1 = \frac{0.3}{1+3\beta}, \quad n_{i+1} = 3n_i. \tag{19}$$

Using separate weighting factors for F was also investigated, but it provided no significant increase in accuracy, and added considerable time to the optimization procedure. Similar to [3], better results were obtained by slightly modifying the wave propagation time T by a factor, τ. From the TLM structure and applying some algebra, the transmission matrix terms can be found as follows:

$$t_{11}^* = \frac{(E+Z_c)G^{-1}e^{j\omega T'} + FGe^{-j\omega T'}}{E+Z_c+F} \tag{20}$$

$$t_{12}^* = \frac{(E+Z_c)^2 G^{-1} e^{j\omega T'} - F^2 G e^{-j\omega T'}}{E+Z_c+F} \tag{21}$$

$$t_{21}^* = \frac{G e^{-j\omega T'} - G^{-1} e^{j\omega T'}}{E+Z_c+F} \tag{22}$$

$$t_{22}^* = -t_{11}^*. \tag{23}$$

Unlike uniform hydraulic transmission lines, tapered lines are asymmetrical in their geometry. This lead to the investigation of using different transfer functions for the inlet and outlet in order to see if there was an increase in accuracy of the TLM approximation. The following scenarios were examined:

- Separate G transfer functions with separate weighting factors. Resulted in no increase in accuracy, and increased optimization effort.
- Separate wave propagation times T' for either direction. Resulted in increased error.
- Separate E transfer functions, with the corresponding F transfer function scaled from it. Resulted in no increase in accuracy, and increased optimization effort.
- Separate E and F transfer functions where F is not scaled off of E. Resulted in significant error in magnitude and phase, as well as substantial increase in optimization effort.

These investigations showed no increase in accuracy over the standard TLM configuration, and all resulted in longer computation time, which was not desirable.

4 Optimization Algoritm

As with all optimization problems, an objective function to be minimized must be defined. In [3], Johnston et al. define an objective function for a uniform tube that minimizes the error in t_{12} and t_{21} in eq. (21) and (22), but ignores t_{11} and t_{22}. Here, the objective function, f, similar to the function used in [3], is used but with the addition of the t_{11} and t_{22} terms. This objective function attempts to minimize the error between the exact transmission matrix and the TLM approximated transmission matrix.

$$f = \sum_{0.01 \le \omega T \le n_k} \frac{\left| \frac{t_{12} - t_{12}^*}{Z_c} \right|^2}{\omega T} + \sum_{0.01 \le \omega T \le n_k} \frac{|(t_{21} - t_{21}^*) Z_c|^2}{\omega T} + \sum_{0.01 \le \omega T \le n_k} \frac{|(t_{11} - t_{11}^*)|^2}{\omega T} + \sum_{0.01 \le \omega T \le n_k} \frac{|(t_{22} - t_{22}^*)|^2}{\omega T} + \varepsilon_E + \varepsilon_G \tag{24}$$

$$\varepsilon_E = \sum_{i=3}^{k} [\max(0, m_{Ei} - 3m_{Ei-1})]^2 \tag{25}$$

$$\varepsilon_G = 10 \left[\max\left(0, \sum_{i=1}^{k} (m_{Gi}) - 1\right) \right]^2 \tag{26}$$

In this case, the transmission matrix terms denoted with an asterisk represent the approximation from the TLM, while the terms without the asterisk represent the numerical solution yielded from solving the boundary value problem of eq. (1) and (2). The terms ε_E and ε_G are the same soft constraints presented in [3]. The optimization was calculated with 50 points per decade over the frequency range of $0.01 \le \omega T \le n_k$.

The optimization procedure first required the exact solution of eq. (1) and (2). The exact solution is calculated numerically using MATLAB® and its `bvp4c` boundary value problem solver. The exact solution is the transmission matrix in eq. (7) for a given tapered tube. By setting Q_2 to 0, t_{11} and t_{21} can be found. Then by setting P_2 to 0, t_{12} and t_{22} can be calculated. It is important to note that solving this boundary value problem does add significant computation time to the optimization procedure. However, computation time can be reduced when the problem is solved in parallel, and with more available cores, the problem becomes faster to solve. Also, the boundary value problem only needs to be solved once for each parameter set. After computing the numerical solution, the optimization of eq. (24) is performed using the `fmincon` function in MATLAB®, where the only set constraint was a lower bound of 0 on the parameters. This ensures the parameters are all positive, similar to the constraint in [3]. The results for a uniform tube given in [3, 10] were used as an initial guess for the iterative solver. Using this algorithm and initial guess does not necessarily find the global minimum, but for this application, the local minimum appears to provide adequate accuracy.

It was found that the same weighting factors would result as long as the taper ratio and dissipation number were held constant. This allows for a look-up table to be used, and only β and λ are required to find all the parameters. The optimization was performed over a range of dissipation numbers of $10^{-4} \le \beta \le 10^0$ with 8 points per decade. Providing the boundary value solver any smaller values of β resulted in a singular Jacobian within the solver. Adjusting solver tolerances and improving initial guesses provided no solution to this error. The range of taper ratio considered for the optimization was $1 \ge \lambda \ge 0.5$, linearly spaced with 10 points. For this paper, only 6 parameters for m_E and m_G were considered ($k = 6$); it has been shown that varying the number of parameters has a noticeable effect on accuracy for uniform tubes [3], and the same result is expected here.

A smooth transition between the weighting factors was desired as it allows for interpolation for in-between values of dissipation number and taper ratio. The optimization first selected a value of β and performed the optimization for a λ value of 1 using the initial guess from [3, 10]. Once complete, the taper ratio was reduced to the next value ($\lambda = 0.95$), while maintaining the same dissipation number. In order for the series to be smooth, the initial guess parameters for successive iterations were the optimized parameters from the previous λ. The result of the optimization are 2 three-dimensional matrices of m_E and m_G, and 1 two-dimensional matrix of τ. Two-dimensional interpolation is required to find the weighing factors and propagation time modifier for a given transmission line.

5 Frequency Domain Results

Figure 4 shows the results of the optimization for a dissipation number of 10^{-3} and a taper ratio of 0.75. The t_{12} and t_{21} (anti-diagonal) transfer functions resulting from the TLM are closely matched to the exact solution. The other two functions t_{11} and t_{22} (principal diagonal) are still accurately approximated, however not to the extent of the other anti-diagonal terms. As can be seen in t_{11} and t_{22}, the first resonant peaks are not perfectly aligned, but all subsequent peaks are matched well. Also to note, the magnitude of the principal diagonal transfer functions are shifted slightly within the exact solution, however, the TLM approximation does not follow this shift. This magnitude shift becomes greater as more taper is added to the model. In all cases, this new model is a better approximation than the previous models given in [5, 6].

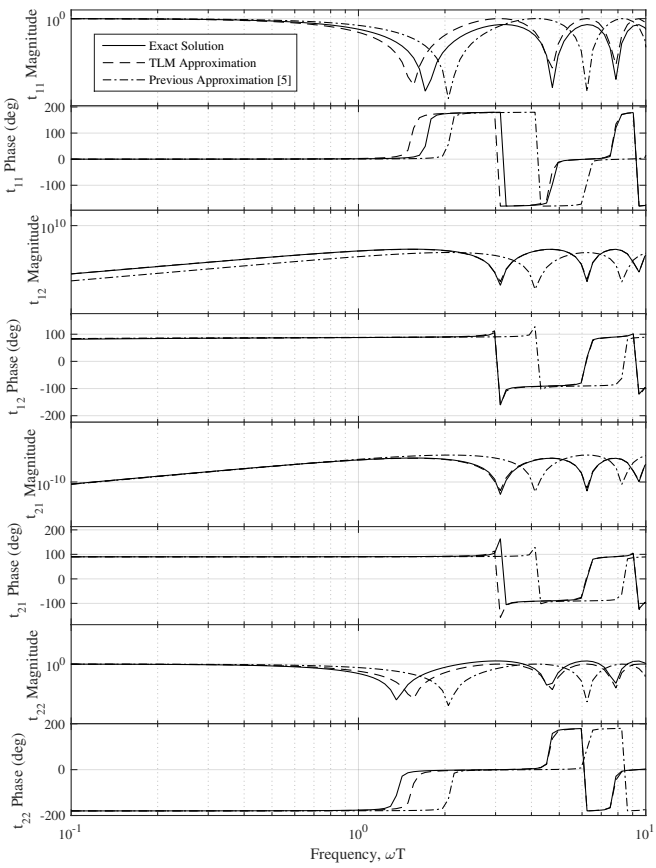

Figure 4: Transmission matrix for $\beta = 0.001$ and $\lambda = 0.75$.

In order to show some contrast, fig. 5 shows the transmission matrix results for the less extreme case of a larger dissipation number of 10^{-1} and a taper ratio of 0.9. In this case it can be seen that there is a closer approximation of the first resonant peak. Also, it can be seen that the anti-diagonal terms of the transmission matrix are approximated accurately.

Unlike uniform lines of constant cross sectional area, the weighting factors that make up the transmission line model not only vary with dissipation number, β, but vary also with the taper ratio, λ. In order to evaluate the accuracy of the model over a range of β and λ, an overall value of error must be defined in order to make relative comparisons. The error

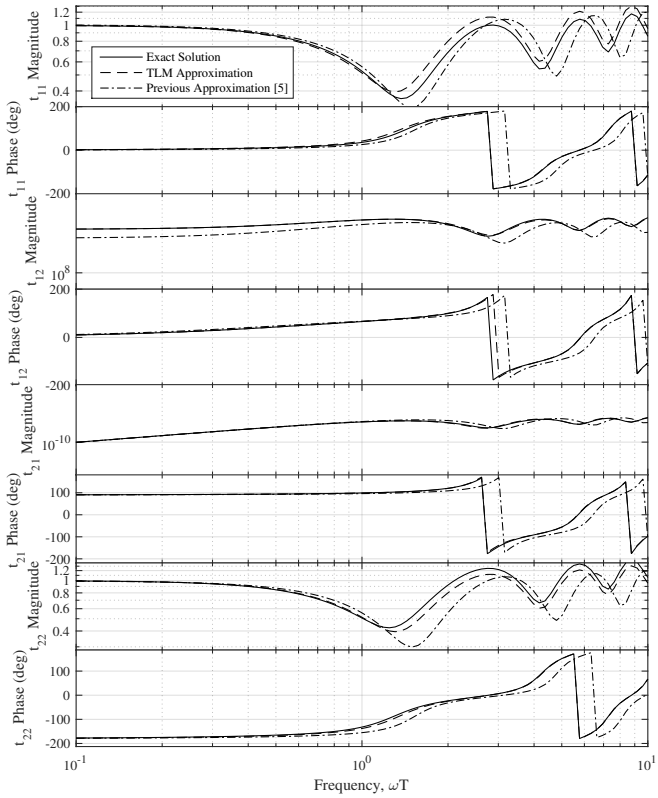

Figure 5: Transmission matrix for $\beta = 0.1$ and $\lambda = 0.9$.

function indicating the accuracy of fit is given below. This error value was chosen over the optimized minimum calculated from eq. (24) since it is not scaled by frequency. This error value quantifies the exact difference between the magnitude of the transmission matrix terms:

$$\varepsilon = \frac{1}{\Omega}\sum_{i=1}^{\Omega}\left[\left|\frac{t_{12}-t_{12}^{*}}{Z_c}\right| + |(t_{21}-t_{21}^{*})Z_c| + |(t_{11}-t_{11}^{*})| + |(t_{22}-t_{22}^{*})|\right]. \tag{27}$$

where Ω is the number of frequency points on which the optimization was performed. The error value in this case is an average of the overall error function. Figure 6 is a visualization of how the error varies with dissipation number and taper ratio. A general observable trend is that the error between the approximated TLM and the exact solution increases with the amount of taper (i.e. decreasing taper ratio) and increases with dissipation number. The optimizations performed in [3] were considered acceptable as long as $\beta \leq 0.5$. So by maintaining the same error from $\lambda = 1$ to lower dissipation numbers and taper ratios, an approximately triangular region of acceptance can be found. In order to keep error low, it is recommended to stay within the bounded region as shown in the figure ($\varepsilon < 0.5$).

In order to better demonstrate the improvement this model has over previous tapered transmission line models, consider fig. 7. The same error plot was calculated as previously, except in this case the error was calculated using the approximated

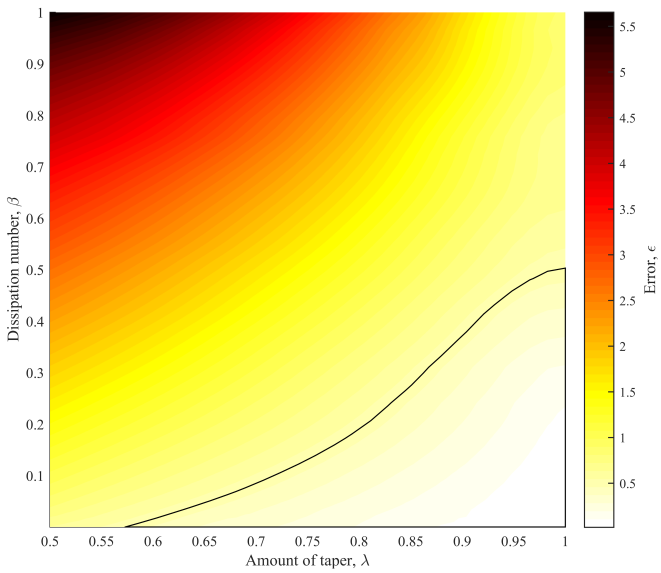

Figure 6: Error analysis for tapered TLM. The black lines show the region of acceptable error, as defined by $\varepsilon < 0.5$.

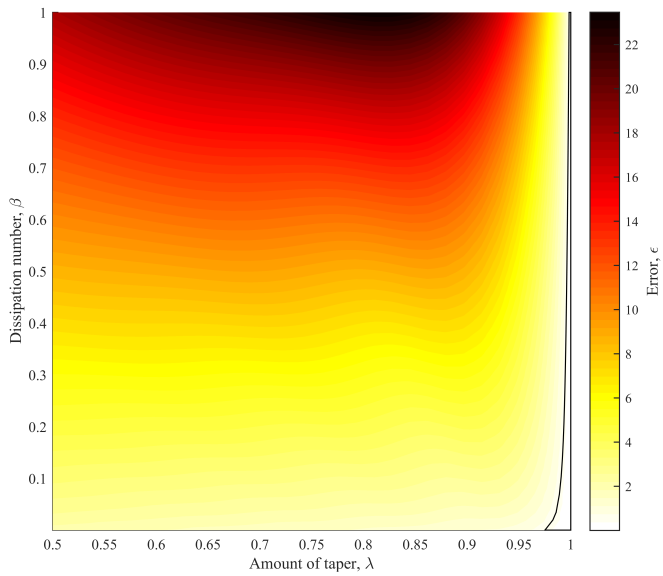

Figure 7: Error analysis for approximate solution from [5]. The black lines show the region of acceptable error, as defined by $\varepsilon < 0.5$. *Note that the error scale is different than the scale in fig. 6*

transmission matrix from eq. (5) for comparison to the exact solution. In general, the error is significantly higher, with its scale around 4 times larger than that in fig. 6. When $\lambda = 1$, the approximated transmission matrix analytically becomes the exact solution. This is the reason for the low error region around this value. However, the amount of error increases rapidly with any increase in the amount of taper in the transmission line for the full range of dissipation numbers. Using the same error level as previouly, the enclosed region of acceptability indicated in fig. 7 is considerably smaller. It is also important to note that in its current form eq. (5) cannot be implemented in the time domain. The work performed in [6] approximates eq. (5) for simulations in the time domain. However, being based off this approximated transmission matrix, it can be expected that the error would only be greater than the error shown in fig. 7.

6 Time Domain Results

In order to simulate the proposed model in the time domain, a MATLAB® Simulink® model was created, available for download at [11]. The overall model can be seen in fig. 8. The E, F, and G transfer functions were implemented using the equations described previously. The $e^{-j\omega T}$ block contains a transport delay of time T' which applies the modified wave propagation time to the model. The E transfer function block is shown in fig. 9 to demonstrate how the summation of weighted transfer functions was implemented.

The TLM can be arranged with any combination of inputs and outputs depending on how it needs to fit into a simulation model, and what other models it needs to connect to. For simplicity, only one combination of inputs and outputs is examined here. The inputs to the TLM are inlet flow and outlet pressure, while the outputs are inlet pressure and outlet flow. The outlet pressure was held constant at 0, and the flow inlet was given a step in flow rate. The simulation arrangement is

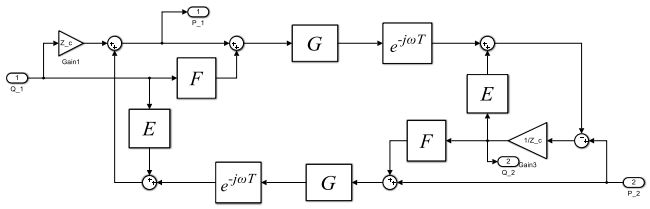

Figure 8: MATLAB® Simulink® model of the tapered TLM.

shown in fig. 10.

Using the same parameters from the transmission matrices computed in fig. 4 and fig. 5, time domain simulations were performed and are shown in fig. 11 and fig. 12 respectively. The solver that was used is MATLAB®'s `ode23t` with a relative tolerance of 10^{-6}. This solver was chosen as it works well for stiff problems such as this, and has shown to solve TLM models relatively quickly when compared to non-stiff solvers such as `ode45`. The outlet flow and inlet pressure response are shown for the 2 parameter sets. The flow response is normalized through dividing by the step change in flow. In both simulation cases, the flow response oscillations always settled to 1, thus indicating that the model has proper flow continuity. The inlet pressure response is normalized through dividing by the step change in flow multiplied by the characteristic impedance of the line. The model does appear to respond in a stable manner when a step input is applied. This is an important characteristic as these models are typically used in simulations where high frequencies are present. These simulated responses look as expected, as they are similar to that seen in [2,3]. Previously, the TLM has been used to model inertance tubes within switched inertance converters [3], a type of hydraulic circuit that efficiently converts pressure and flow by switching a digital hydraulic valve at very high frequency.

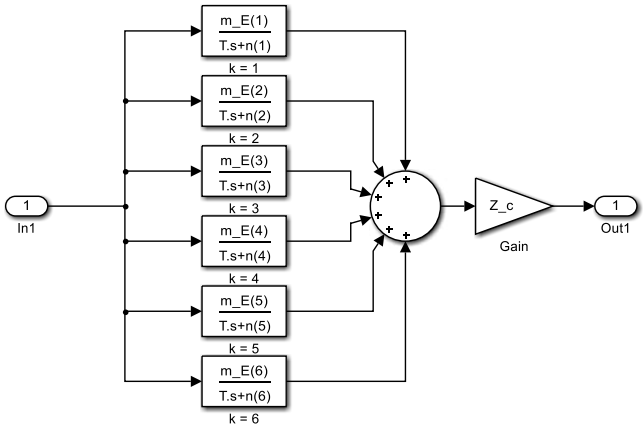

Figure 9: MATLAB® Simulink® implementation of the E transfer function.

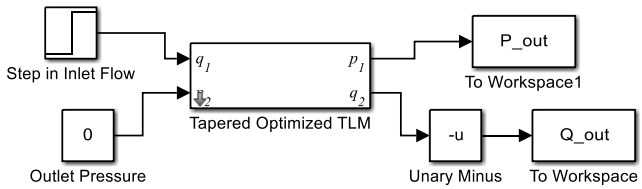

Figure 10: Simulation set-up.

The model presented here is believed to suit well for this area of fluid power research.

7 Conclusions

While excellent models exist for modelling fluid dynamics within transmission lines of uniform cross-section, further development in modelling tapered transmission lines was required. This research looks at modelling the fluid dynamics within tapered lines by using the TLM structure and weighted transfer functions. The results of this TLM approximation show significantly improved accuracy over previous tapered transmission line models. This model can be used for a variety of applications where line dynamics must be considered, such as switched inertance converters. A complete Simulink® library with the parameter set and the parameter generation code in MATLAB® are now available for download [11]. Future work on this topic plans to look at performing experiments to validate the proposed model, as well as look at applying the TLM to flexible walled transmission lines. Also, research is planned to investigate the effects of shaped inertance tubes on the performance of switched inertance converters. Transmission lines of arbitrarily changing cross section can be modelled using this approach by successively connecting multiple tapered transmission line segments together. Using shaped inertance tubes has theoretically shown an increase in efficiency over using uniform tubes [8], and by applying this model, higher accuracy and speed in these simulations are expected.

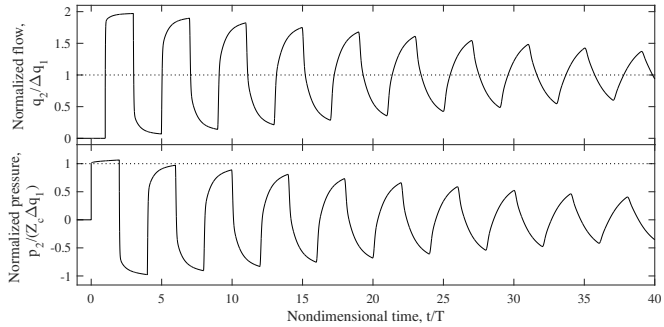

Figure 11: Simulated results for $\beta = 0.001$ and $\lambda = 0.75$.

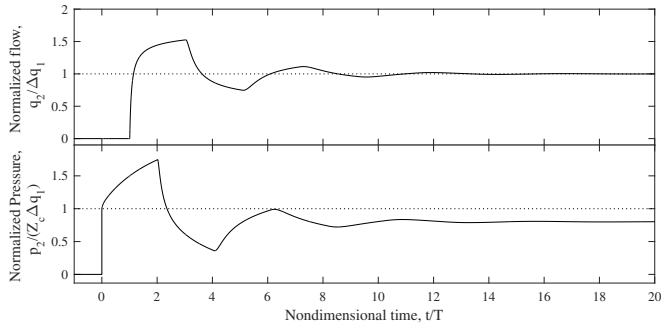

Figure 12: Simulated results for $\beta = 0.1$ and $\lambda = 0.9$.

References

[1] P Krus, K Weddfelt, and J O Palmberg. Fast pipeline models for simulation of hydraulic systems. *Journal of Dynamic Systems Measurement and Control*, 1994.

[2] N Johnston. The transmission line method for modelling laminar flow of liquid in pipelines. *Journal of Systems and Control Engineering*, 226(5):586–597, 2012.

[3] N Johnston, M Pan, and S Kudzma. An enhanced transmission line method for modelling laminar flow of liquid in pipelines. *Journal of Systems and Control Engineering*, 228(4):193–206, 2014.

[4] W Zielke. Frequency-dependent friction in transient pipe flow. *Journal of Basic Engineering*, 90(1):109–115, 1968.

[5] T Muto, Y Kinoshita, and R Yoneda. Dynamic response of tapered fluid lines (1st report, transfer matrix and frequency response). *Bulletin of the JSME*, 24(191):809–815, 1981.

[6] M Tahmeen, T Muto, and H Yamada. Simulation of dynamic responses of tapered fluid lines. *JSME International Journal, Series B*, 44(2):247–254, 2001.

[7] T J Viersma. Analysis, synthesis and design of hydraulic servosystems and pipelines. *Studies in Mechanical Engineering - Volume 1*, 1980.

[8] T Wiens. Analysis and mitigation of valve switching losses in switched inertance converters. In *Proceedings*

of the ASME/BATH 2015 Symposium on Fluid Power & Motion Control, 2015.

[9] P Krus, A Jansson, J Palmberg, and K Weddfelt. Distributed simulation of hydromechanical systems. In *Third Bath International Fluid Power Workshop*, 1990.

[10] N Johnston. Simulink models, http://people.bath.ac.uk/ensdnj/models/newtlm.html, 2014.

[11] J ven der Buhs and T Wiens. Transmission line models, https://github.com/tkw954/, 2017.

Nomenclature

Designation	Denotation	Unit
$A(x)$	Cross-sectional area of transmission line at point x	m^2
b	E transfer function scaling factor	
C_1, C_2	Characteristic pressures of the TLM	Pa
c	Local speed of sound	m/s
D	Dissipation Number [6]	
E, F, G	TLM weighted transfer functions	
f	Optimization objective function	
J_0, J_2	Bessel functions of the first kind	
j	Imaginary designation	
k	Number of weighting factors	
l	Length of transmission line	m
m_{Ei}, m_{Gi}	Weighting factors	
N	Frequency-dependent friction term	
n_i	Weighting factors	
P	Fourier transform of pressure	
p	Pressure	Pa
Q	Fourier transform of flow	
q	Flow	m^3/s
R	Steady state resistance	$Pa{\cdot}s/m^3$
r	Pipe radius	m
S	Normalized Laplace operator [6]	
s	Laplace operator	
T	Wave propagation time	s
T'	Modified wave propagation time	s
t	Time	s
t_{11} ,t_{12}, t_{21}, t_{22}	Transmission matrix exact terms	
t^*_{11} ,t^*_{12}, t^*_{21}, t^*_{22}	Transmission matrix approximated terms	
x	Axial direction	
Z_c	Characteristic impedance	$Pa{\cdot}s/m^3$
β	Dissipation number	
Γ	Propagation operator [6]	
ε	Error	
θ	Taper angle	rad
λ	Taper ratio	
ν	Kinematic viscosity	m^2/s
ξ	Convergence/Divergence parameter [6]	
ρ	Fluid density	kg/m^3
τ	Wave propagation time modifier	
Ω	Number of frequency points on which the optimization is performed	
ω	Frequency	rad/s

Predictive Dynamic Engine Speed Reduction in Mobile Hydraulic Equipment

Travis Wiens

Department of Mechanical Engineering, University of Saskatchewan, Saskatoon, Canada
E-mail: t.wiens@usask.ca

Abstract

This paper presents an analysis of the potential for engine speed reduction in hydraulic equipment, taking into account not only the minimum engine speed required to meet the current flow demand, but also the minimum speed capable of accelerating the engine to meet increased flow demand in the near future. This is a predictive task, as it requires an estimate of the operator's intention to increase flow demand. We present an analysis of the potential for engine speed reduction using a work cycle from a 40 ton excavator loading a truck, which results in a 33% reduction in the mean engine speed with no reduction in useful work rate. We also present an engine speed control algorithm to perform this predictive task. This controller is easy to tune and requires only a small amount of information about the plant and work cycle. A simulation study is performed that demonstrates the controller's performance and studies the effect of tuning parameters.

Keywords: Fuel efficiency, Diesel engine, Speed Reduction

1 Introduction

The hydraulic system of an excavator is typically powered by a diesel engine turning one or more variable-displacement pumps. While there are other loads on the engine (air conditioning, generator, cooling, etc.), the vast majority of engine power is consumed by the pump and other loads are generally tolerant of varying engine speed. In most cases, the engine speed of conventional excavators is fixed at a near-constant speed and the hydraulic system flow is controlled by varying the pump displacement.

Typical excavator systems exhibit lower specific fuel consumption at lower engine speeds (and higher torque), due to a combination of lower auxiliary function loading, and lower internal frictional losses [1]. Some commercially models of excavator feature an "efficiency mode" where the constant engine speed is lowered [2].

Lowering the engine speed also limits the useful work rate, as the pump flow is limited to the pump displacement multiplied by the engine speed. Thus, the pump flow may be controlled by either adjusting the displacement or engine speed. If the pump is not running at full displacement, the engine speed can be lowered and displacement increased without affecting flow. However, while the pump displacement has a response time in tens of milliseconds, a diesel engine's response time can be on the order of hundreds of milliseconds, too slow to meet dynamic requirements of operator flow demands. Due to the slow response of the engine, the chosen engine speed must not only be sufficient to meet the current flow demand, but also the flow demand expected in the near future, during the time required to accelerate the engine. Some researchers have developed systems to dynamically adjust engine speed to meet the current load and recent history (typically for hybrid architectures [3-6 and others]), but it is believed that this paper is the first to consider this dynamic effect in a predictive manner.

2 Speed Reduction Potential

In order to study the potential for engine speed reduction in a practical work cycle, we examined the pump flow of a previously recorded excavator data set [7]. This was recorded for a 40 ton excavator loading a truck on the same level with a 90° swing, which is believed to be representative of a typical excavator work cycle. One pump (of two on the machine) was considered, but the same analysis could be applied to the combined effect. This data cycle was scaled to match the power available in the target engine.

At each time step in the dataset, we used a dynamic simulation to find the minimum speed that is capable of fulfilling all future flow demands if the engine is accelerated at full available torque. This was calculated using a simplified system, modelled as an ideal variable-displacement pump with instantaneous response, driven by a turbo-charged diesel engine. This model is intended to be a generic representation of a typical system, with simple parameters that are easy to understand, rather than an attempt to accurately model a specific system.

The engine load is modelled as an ideal pump with inertia:

$$\dot{\omega} = \frac{1}{J}(T_e - T_p) \tag{1}$$

where ω is the engine shaft speed, J is combined inertia of engine and pump, T_e is the engine torque and T_p is the pump torque, given by

$$T_p = P_s \frac{D}{2\pi} \tag{2}$$

where P_s is the pump pressure (from the recorded data set), and D is the pump displacement (in terms of volume per revolution).

The pump displacement controller is assumed to have a fast reaction time (relative to the slow engine dynamics) and sets the displacement to

$$D = \hat{Q}\frac{2\pi}{\omega} \tag{3}$$

where $\hat{Q}$ is the pump flow demand (from the dataset). This displacement is limited to the range of 0 to D_{max}, the maximum pump displacement.

As this analysis is interested in the engine acceleration time, the engine torque is the maximum available, limited by both the engine's torque curve, as well as a rate-limited torque rise to model the turbocharger response. The engine's torque curve was modelled as an eight-point lookup table with respect to shaft speed. This was based on published data for a four cylinder 4.4L turbocharged diesel engine with air to air charge cooling, shown in Figure 1 [8]. The data was extrapolated to zero torque at zero speed.

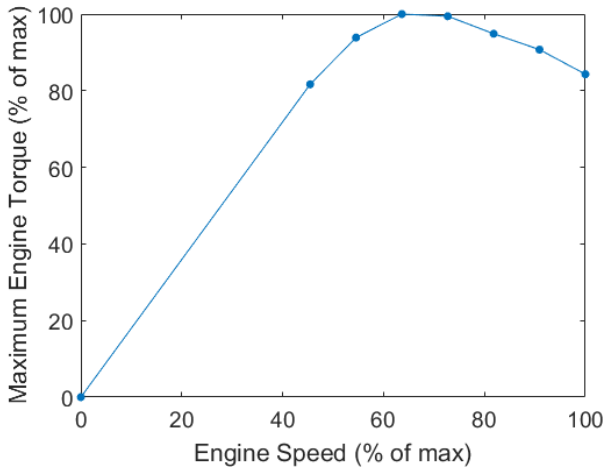

Figure 1: Diesel engine torque curve [8].

The turbocharger and smoke map response was modeled as a constant rate-limit on the engine torque, with the time taken for the torque to rise from zero to the engine maximum denoted as Δt_{turbo}. This is a relatively simple model, but is believed to capture the gross engine dynamics without losing generality by targeting a specific engine.

Parameters used for the simulation study may be found in Table 1.

Starting at each time step in the data set, the system of nonlinear ordinary differential equations above is solved for a given initial engine speed, with the torque rise limiter initially set at the torque required to meet the current torque demand. The initial engine speed is then varied to solve for the minimum engine speed, ω_{min} such that the system can accelerate to meet all future flow demands without the required engine displacement exceeding D_{max}. This was achieved using the nonlinear root finding algorithm fzero in Matlab, based on Forsyth's algorithm [9].

2.1 Results

The resultant minimum engine speed for one cycle of the data set is shown in Figure 3 along with the flow demand, based on the pressure demand shown in Figure 2. This cycle is believed to representative of the dataset. Notice that the minimum engine speed tracks the small changes in flow demand, but needs to lead the demand for the rapid increases around time 227 and 234 s.

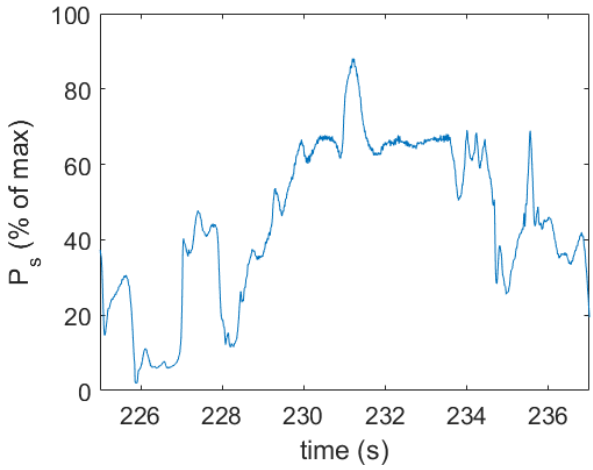

Figure 2: Pressure demand for a single cycle of the excavation dataset. Confidentiality concerns prevent presentation of the entire dataset or non-normalized data.

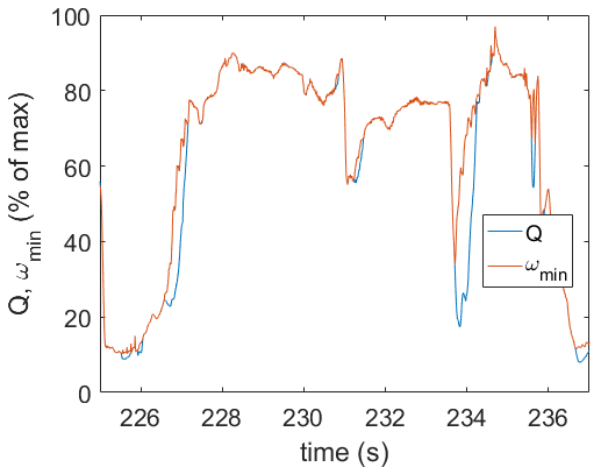

Figure 3: Flow demand and engine speed required to meet future flow demands. This shows one cycle of the dataset.

Figure 4 shows a map of minimum required engine speed capable of accelerating to meet future flow demand vs current flow demand. An application with a slowly varying flow demand would result in all points lying on the diagonal, while an application with a more high frequency content in the flow demand would have more points toward the upper part of the plot. In this case, 95% of all points fall below the red line. The black line shows a histogram of all points. The average engine speed for this dataset can be reduced by 34.3% below a constant speed capable of doing the same work, with corresponding fuel savings dependent on the engine's BSFC curve.

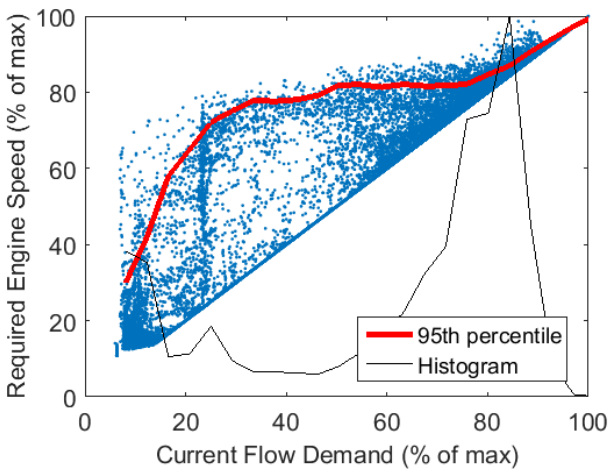

Figure 4: Engine speed required to meet future flow demands for a simulated 40-ton excavator, using an experimentally recorded work cycle. Each dot represents one data point in time. The black line shows a histogram of the time spent at a given flow demand.

2.2 Effect of Turbo Lag

In order to quantify the effect of turbocharger dynamics, the above analysis was repeated, varying the torque rise rate limit. Figure 5 shows the 95th percentile of required engine speed for torque rise values of 500 ms and 1000 ms. The mean engine speed reduction for the 500 ms case is 35.1% (compared to 34.3% for the 1000 ms case). Although the difference in curves is significant, the overall engine speed reduction difference is more modest for this work cycle (as shown in Fig 6), as much of the time is spent in the right-hand part of the curve where the difference is smaller. This effect would be more noticeable for a work cycle with more time spent at lower flow demand.

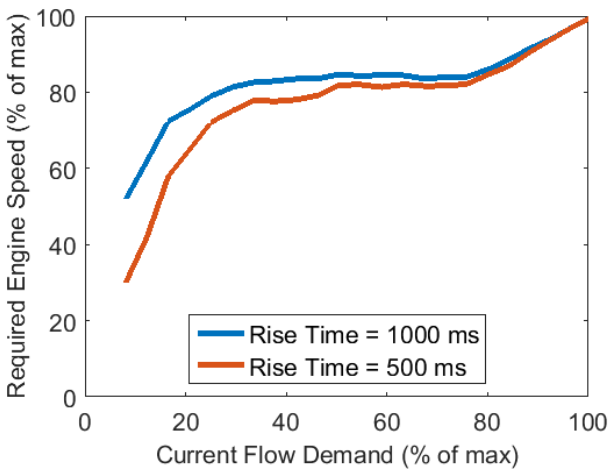

Figure 5: Engine speed required to meet future flow demands 95% of the time for varying torque rise times.

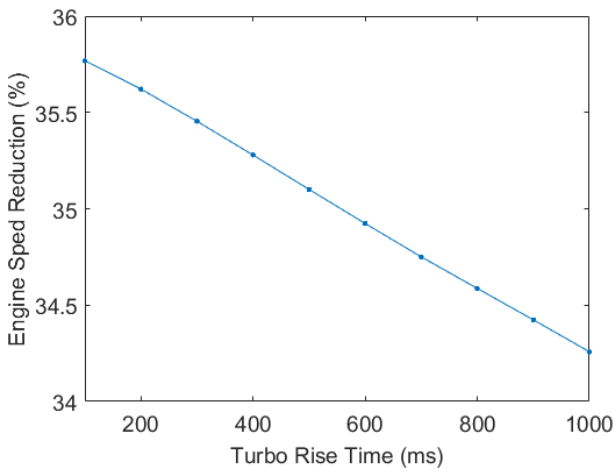

Figure 6: Potential for average engine speed reduction with respect to turbocharger rise time.

3 Control Scheme

The above analysis presents a best-case scenario for reducing the engine speed with no reduction in output pump flow. This section presents a preliminary controller which attempts to achieve this by predictively setting the engine speed based on the current flow demand. The predictive model is continually updated, in retroactive response to over- or under-prediction of the flow demand, so that it can track changes in operator style or task at hand.

The proposed controller is based on a speed adjustment factor, $K(\hat{Q})$, defined so that

$$\hat{\omega} = \frac{\hat{Q} + (Q_{max} - \hat{Q})K}{\frac{D_{max}}{2\pi}} \tag{4}$$

where $\hat{\omega}$ is the controller's requested engine speed, Q_{max} is the flow at maximum engine speed and displacement. This means that if $K = 0$ then the desired engine speed is set just sufficient to meet the current demand flow with no margin for future increases, and if $K = 1$ then the engine speed is set to the maximum.

This adjustment factor is implemented as an N-element lookup table with linear interpolation between values. The elements are updated based on the excess displacement, defined as

$$D_e(k) = D(k - d) - D_{max} \tag{5}$$

where k is the time step and d is the estimated engine response time (in time steps). The controller attempts to minimize this excess displacement while avoiding it being negative (not meeting flow demand). At each time-step the adjustment factor is modified by

$$\Delta K(\hat{Q}(k)) = \begin{cases} -\Delta K^{+} \; if \; D_e > 0 \\ 0 \; if \; D_e = 0 \\ \Delta K^{-} \; if \; D_e < 0 \end{cases} . \quad (6)$$

This could be practically implemented in a real load-sensing system by monitoring the load-sense margin pressure: if the pump is able to maintain margin $D_e \geq 0$, otherwise $D_e < 0$.

This adjustment is used to modify the two lookup table points bracketing the current flow. If a subscript 1 denotes the lookup table point just below the current flow and a 2 denotes the point equal to or just above it, then the table is updated according to

$$K_1(k+1) = K_1(k) + \Delta K(\hat{Q})\Delta t \phi_1 \quad (7)$$

$$K_2(k+1) = K_2(k) + \Delta K(\hat{Q})\Delta t \phi_2 \quad (8)$$

$$\phi_1 = \frac{Q_2 - \hat{Q}}{Q_2 - Q_1} \quad (9)$$

$$\phi_2 = \frac{\hat{Q} - Q_1}{Q_2 - Q_1} \quad (10)$$

where Δt is the sample time. The lookup table is saturated to ensure no points fall outside the range of $0 \leq K \leq 1$.

3.1 Parameter Tuning

The proposed controller has two tuning parameters, ΔK^{+} and ΔK^{-} which control how the adjustment factor adapts to past history. A large ΔK^{+} will tend to reduce the engine speed more aggressively, while a large ΔK^{-} will aggressively react to not meeting flow demand, by increasing the engine speed. Large values of both will tend to cause the system to adapt quickly, while small values will tend to smooth out variations.

For a stationary operator model, the expectation of the probability of meeting the flow demand ($D_e > 0$) is

$$\hat{p} = \frac{\Delta K^{-}}{\Delta K^{-} + \Delta K^{+}}. \quad (11)$$

For the case where $\hat{p}$>>0.5 then the minimum time to adapt K from 1 to 0 is

$$\Delta t_{adapt} = \frac{1}{\Delta K^{+}}. \quad (12)$$

Therefore given a desired success probability and speed of adaptation, the above two equations can be used to set the required parameters.

The third tuneable parameter is the estimated engine response time, d. This parameter controls how far ahead in time the controller tries to predict the engine's response. It should be selected to be close to the actual engine's response time (which varies with operating point), but need not be exact.

3.2 Simulation Results

The proposed controller was simulated using the same excavator truck-loading work cycle described above. The $K(Q)$ lookup table was initialized with zeros, the most aggressive engine speed reduction.

The goal of this controller is to meet the desired probability of meeting the flow demand (in this case $\hat{p} = 0.95$). This is shown in Figure 7, with the simulated p calculated from the Boolean success in meeting flow demand, with a first order filter with time constant 50 s. As desired, the simulated probability quickly increases, before settling around the target value of 95%. Note that this simulation was carried out with an aggressive initial condition; if the $K(Q)$ lookup table was initialized with ones, the probability would start at 100% and fall to the desired value, resulting in a higher initial performance, but lower fuel savings.

Figure 8 shows the flow demand and the simulated actual flow, with the flow demand generally being met, except for some flow peaks and rapid increases (which is expected with the $\hat{p} = 0.95$ target).

The evolution of the engine speed adjustment factor is shown in Fig 9. By the end of the run (red), the curve has settled to a position where the engine speed is aggressively reduced for low and high flow demands, with smaller engine speed reductions in the middle. This curve is strongly dependent on the operator's aggressiveness and the work cycle performed.

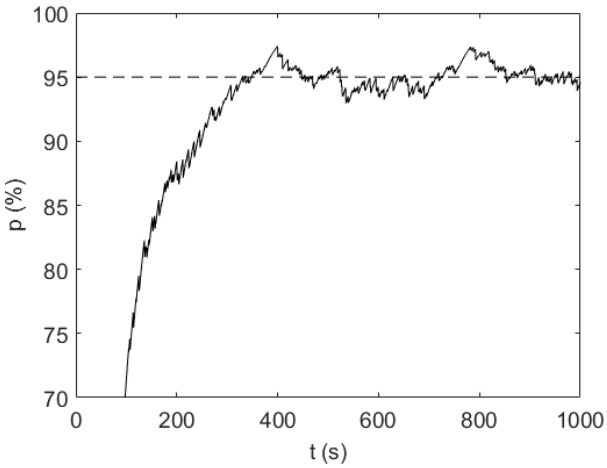

Fig 7: Probability of meeting flow demand (filtered with a 50 s time constant). The target value is 95%.

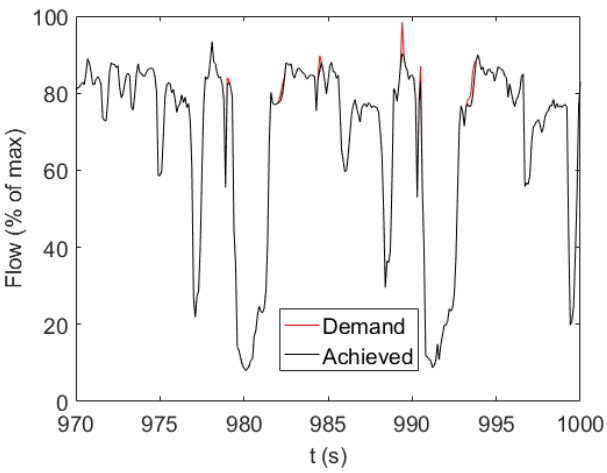

Fig 8: Flow demand and the achieved performance.

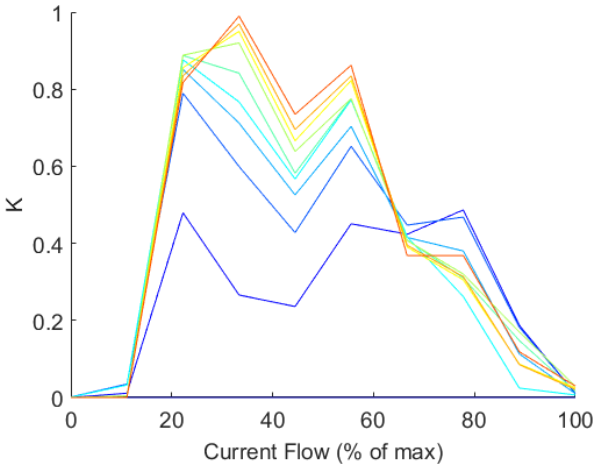

Fig 9: Evolution of $K(Q)$ lookup table, plotted at ten evenly spaced points in time between t=0 (blue) and t=1000 s (red).

The effect of the $\hat{p}$ tuning parameter is shown in Fig 10 and 11. Fig 10 shows the final adapted engine speed vs current flow demand lookup table after running for 1000 s on the same excavator loading cycle. The blue line ($\hat{p} = 80\%$) shows a more aggressive reduction in engine speed (at the cost of not meeting flow demand approximately 20% of the time), while the red line ($\hat{p} = 99\%$) shows the effect of more priority applied to meeting the flow demand. Figure 11 shows the resultant mean engine speed over the cycle, demonstrating the tradeoff of flow performance with engine speed reduction.

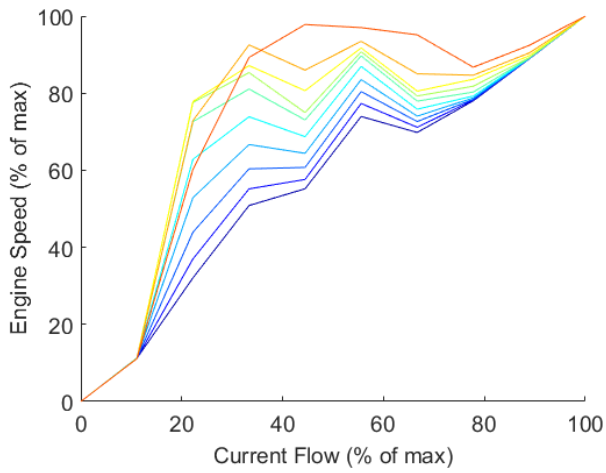

Fig 10: Engine speed based on the adapted K(Q) lookup table after 1000 s of running the excavator work cycle, showing ten evenly spaced values of $\hat{p}$ between 80% (blue) and 99% (red).

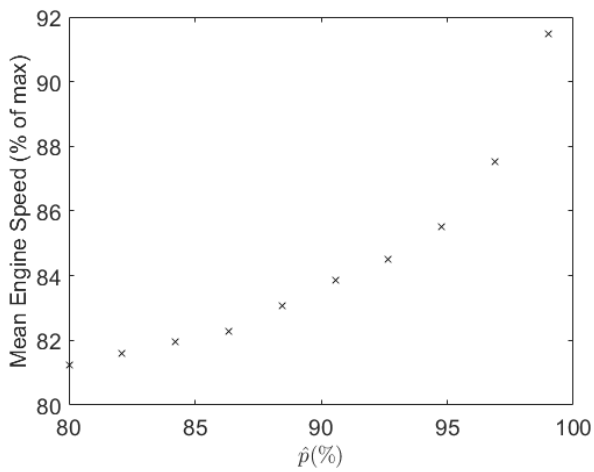

Fig 11: Effect of the $\hat{p}$ tuning parameter on the mean engine speed.

The adaptation dynamics also have an effect on the controller. Figures 12 and 13 show the effect of the controller adaptation time scale, Δt_{adapt}, which scales the adaptation gains. This parameter controls how quickly the controller adapts to change in operating style and also how long it "remembers" a prior operating style. These plots show Δt_{adapt} varying from 10 s (blue) to 500 s (red), after the controller is initialized at $t = 0$. Clearly the fastest settings are tracking the short-term operator inputs rather than learning and predicting the behavior. It is also possible that the controller exhibits some nonlinear instability for very fast settings, although this has not been studied (it appears that the lowest Δt_{adapt} would be set by predictive ability rather than stability in any case). At higher settings, the response is not particularly sensitive to the value of Δt_{adapt}, and a general value can likely be used, with little need for fine tuning.

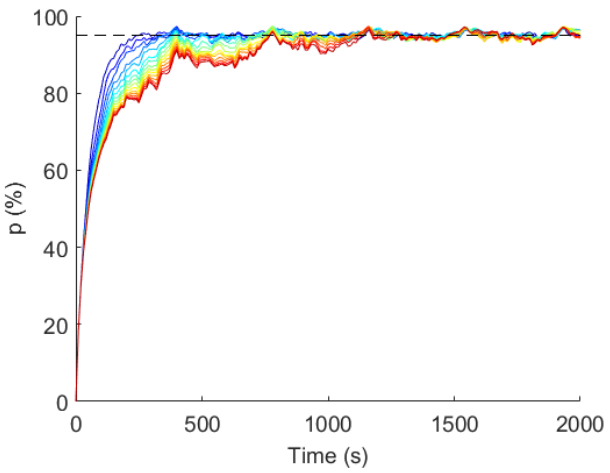

Fig 12: Likelihood of meeting flow demand, for Δt_{adapt} varying from 10 s (blue) to 500 s (red). The desired value of 95% is shown by the dashed line.

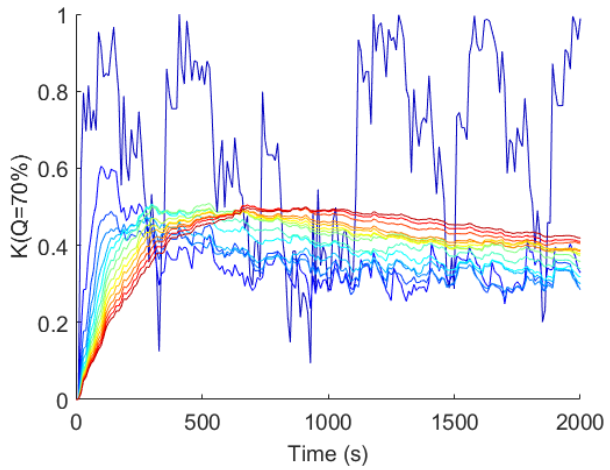

Fig 13: Adaptation dynamics for the same varying adaptation times as Fig 12, in this case showing the K value for 70% flow.

4 Conclusions

The presented results show the potential for reducing engine speed while not significantly reducing the useful work output of an excavator. In this case, the engine speed may be reduced by a maximum of 34% relative to a constant engine speed capable of doing the same work, which would be expected to provide significant fuel savings.

We also present a controller that predicts the future flow demand based on the current flow, and can automatically adapt to changes in operator style. This controller attempts to meet a preset desired probably of meeting flow demand by adjusting a lookup table relating the required engine speed to the current flow demand. Simulation studies suggest that this controller behaves as expected on a simple engine model. Future work will apply this controller to a real engine including pump dynamics, and will consider its specific BSFC curve.

Nomenclature and Base Parameters

Table 1: Nomenclature and Selected Simulation Parameters

Symbol	Denotation	Unit	Base Value
F_i	Force	N	variable
d	Estimated engine lag	samples	500
D	Pump displacement	m^3/rev	variable
D_e	Excess displacement	m^3/rev	variable
D_{max}	Maximum pump displacement	m^3/rev	100×10^{-6}
J	Inertia of pump and engine	kg m^2	1.723
K	Speed adjustment factor		variable
N	Number of points in $K(Q)$ table		10
$\hat{p}$	Desired probability of meeting flow demand		0.95
P_s	Pump pressure	Pa	variable
T_e	Engine torque	Nm	variable
T_e	Engine torque	Nm	variable
T_{max}	Max engine torque	Nm	Fig 1
T_p	Pump torque	Nm	variable
Q	Pump flow	m^3/s	variable
$\hat{Q}$	Pump flow demand	m^3/s	variable
ΔK^+	Control adaptation gain	1/s	0.010
ΔK^-	Control adaptation gain	1/s	0.190
Δt_{adapt}	Control adaptation time	s	100
Δt_{turbo}	Turbocharger rise time	s	1.0
Δt	Sample time	s	1×10^{-3}
ω	Shaft speed	rad/s	variable
ω_{max}	Maximum shaft speed	rad/s	230.4
ω_{min}	Minimum shaft speed to meet flow demand	rad/s	variable

References

[1] Goering, C., Stone, M., Smith, D., and Turnquist, P., 2003. *Off-road Vehicle Engineering Principles.* American Society of Agricultural Engineers, St. Joseph, MI.

[2] Bennick, C. 2012. "Excavators: Get to Know the Working Modes" Equipment Today, Sept 2012.

[3] Kim, H., Choi, J. and Yi, K., 2012. Development of supervisory control strategy for optimized fuel consumption of the compound hybrid excavator. *Proceedings of the Institution of Mechanical Engineers, Part D: Journal of Automobile Engineering*, *226*(12), pp.1652-1666.

[4] Lin, X., Pan, S.X. and Wang, D.Y., 2008. Dynamic simulation and optimal control strategy for a parallel hybrid hydraulic excavator. *Journal of Zhejiang University-SCIENCE A*, *9*(5), pp.624-632.

[5] Hippalgaonkar, R. and Ivantysynova, M. 2015. Optimal Power Management for DC Hydraulic Hybrid Multi-Actuator Machines - Part 1: Theoretical Studies, Modeling and Simulation. ASME Journal of Dynamic Systems, Measurement, and Control, Vol. 138, Issue 5

[6] .Hippalgaonkar, R. and Ivantysynova, M. 2015. Optimal Power Management for DC Hydraulic Hybrid Multi-Actuator Machines - Part 2: Machine Implementation and Measurement. ASME Journal of Dynamic Systems, Measurement, and Control, Vol. 138, Issue 5

[7] Wiens, T. and Bitner, D., 2016. "An Efficient, High Performance and Low-Cost Energy Recovering Hydrostatic Linear Actuator Concept. Proceedings of the 2016 Bath/ASME Symposium on Fluid Power and Motion Control, Bath, UK.

[8] Perkins Engines Company Limited, 2005, "Technical Data 1100 Series", Publication No TDP 1502E, Peterborough, UK.

[9] Forsythe, G. E., M. A. Malcolm, and C. B. Moler, 1976, *Computer Methods for Mathematical Computations*, Prentice-Hall.

Study of Energy Losses in Digital Hydraulic Multi-Pressure Actuator

Mikko Huova, Arttu Aalto, Matti Linjama and Kalevi Huhtala

Laboratory of Automation and Hydraulic engineering, Tampere University of Technology, Tampere, Finland
E-mail: mikko.huova@tut.fi, aalto.arttu90@gmail.com, matti.linjama@tut.fi, kalevi.huhtala@tut.fi

Abstract

A digital hydraulic multi-pressure actuator is a new actuator concept, which aims at lowering energy losses and decreasing dynamic requirements of a prime mover in mobile hydraulic applications. The actuator consists of an integrated hydraulic accumulator, which serves as an energy storage and a number of asymmetric cylinders acting as discrete pressure transformers. Leak-free on/off-valves are used to direct flow from the discrete pressure transformers to the actuator. Input power is supplied by charging the local accumulator with a small fixed displacement pump. Thus, the actuator requires only mean input power, while the output power peaks can be multifold. This paper concentrates on studying the controllability of the actuator concept and analyses the power losses and their sources through experimental study. The energy losses of the concept are measured in a mobile hydraulic boom mock-up and compared to earlier measured losses of a load sensing proportional valve based system. The measurements show that up to 77 % of the losses can be avoided by using the new concept. Three controller types are studied numerically and experimentally and their effect on control resolution and energy efficiency is evaluated.

Keywords: Digital hydraulics, Integrated actuator, Multi-pressure system

1 Introduction

Hydraulic systems are used in mobile machines because they enable good power to weight ratio and generation of big forces. There are, however, few well-known downsides in the use of traditional valve-controlled hydraulic systems such as low efficiency in many operation points. Furthermore, the input power of the hydraulic supply unit is directly coupled to the output power of the actuators. In many mobile machines, the supply pump is driven by a diesel engine, which results in a system, where the diesel engine is frequently driven in a bad operating point. Furthermore, the operating point of the engine is often rapidly changing due to the changing actuator demands. This results in excessive fuel consumption and emissions [1].

The reduction of power losses in hydraulic actuators and their control valves is often important when improvement to the overall efficiency of a mobile machine is sought after. Although only a part of the total power loss occurs in the control valves, it is worth to note that also this lost hydraulic power needs to be generated by a diesel engine driven pump. They both generate considerable amount of power loss while producing the excess hydraulic power to be lost in the control valves.

To avoid above-mentioned problems, different types of hybrid mobile machines are studied. One such system is STEAM, which consists of two accumulators maintaining two separate pressure levels utilized by the control valves of an excavator [2]. Another example of a hydraulic hybrid system used in a mobile machine is the Liebherr Pactronic® system, where an accumulator is used to store energy during load lowering to be utilized during peak loading [3]. There are steps taken towards utilization of hydraulic hybrids also in forest machinery, where an example system consists of a hydraulic accumulator which energy can be fed to a working hydraulics of a cut-to-length forest harvester via a diesel driven pump/motor [4]. Other methods improving the energy efficiency of cylinder drives include both analogue and digital hydraulic transformers [5, 6, 7] and pump controlled systems [8].

This paper studies a hydraulic hybrid actuator, which includes a hydraulic cylinder, control valves, a local energy storage and a discrete pressure converter. Figure 1 presents a simplified hydraulic diagram of the system studied. The digital hydraulic multi-pressure actuator consists of high-pressure supply line HP, pressurized tank line LP and, in this example, two medium pressure lines generated by the converter cylinders. The idea of the concept was presented in [9] and the first measurement result in [10] and this paper studies the concept further through experimental measurements.

The system shares some of the operational principles with the digital hydraulic transformer [11, 12]. In this case, there is a

number of different pressure levels available at all times. The controller structure is based on secondary control scheme of a multi-chamber cylinder [13] and in the core of the controller structure is a discrete force controller, which tracks the force reference given to the actuator. The actuator is controlled by directing optimal pressure level to piston side chamber A and to rod side chamber B via the on/off-valves to generate desired actuator force. In this example, there are sixteen different pressure combinations to select from. The inflow-side pressure source is discharged, while the outflow-side pressure source is charged simultaneously. It is worth to note that the small converter cylinders have limited fluid volumes and therefore it is crucial that the control system tracks the capacity (piston position) of the converter cylinders and prefers control combinations, which tend to return the converter pistons to the middle positions.

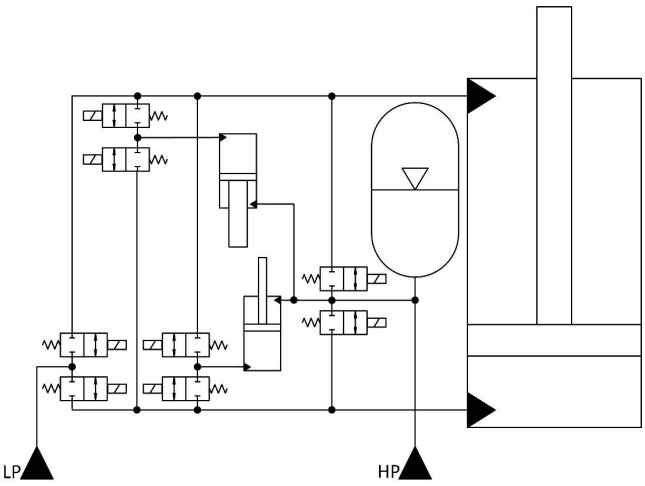

Figure 1: Simplified hydraulic diagram of a digital hydraulic multi-pressure actuator with four pressure levels

This paper studies the controllability and energy efficiency of the concept. There are three different control algorithms developed and their effect on controllability is studied numerically and experimentally. Energy efficiency is studied experimentally in a trajectory tracking application. Furthermore, the sources of the power losses are investigated in separate measurements where the pressure losses of the converter circuit are investigated in more detail.

2 Controller design

Figure 2 presents the upper-level block diagram of the control system.

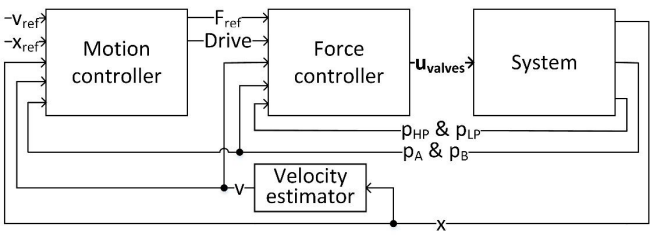

Figure 2: Block diagram of the control system

The digital hydraulic multi-pressure actuator is essentially a force generating device as all hydraulic cylinder actuators. In this case the on/off-valves are controlled such that the output force of the cylinder tracks the force reference. However, position tracking is desired in the test system and thus the motion controller forms the outer control loop as presented in fig. 2.

2.1 Motion control

The motion controller is designed based on the PI-type controller presented in [13]. The motion controller calculates an internal velocity reference signal v_{ref_c} using the sum of PI-type position controller output and the velocity of the target trajectory v_{ref}. PD-type velocity controller takes v_{ref_c} and the estimated velocity v as inputs and outputs the force reference F_{ref}. The velocity is estimated from the position measurement using a first order low pass filter and filtered discrete time derivative:

$$\dot{y}(t) = \frac{1}{35\Delta}[5y(t) + 3y(t-\Delta) + y(t-2\Delta) - y(t-3\Delta) - 3y(t-4\Delta) - 5y(t-5\Delta)] \quad (1)$$

[14]

where Δ is the sample time. Stopping and starting of the motion is handled by the motion controller. The controller uses position and velocity thresholds to calculate the Boolean signal *Drive*. While the *Drive* is true, the force controller outputs its on/off-valve command signals to the valves; otherwise the valves remain closed. The chamber pressure measurements p_A & p_B are input to the motion controller and they are used to reset the I-term of the PI-type position controller at the beginning of the motion. The I-term is set to match the current load force estimated from the chamber pressures.

2.2 Basic force controller

The force controller tracks the force reference and takes care of utilizing the medium pressure supplies such that the converter cylinders are not driven to cylinder ends. The basic version of the controller selects an optimal pressure supply for piston and piston rod side of the actuator and opens the flow path of the corresponding pressure supply. There are two parallel connected on/off-valves in each flow path in the experimental test system (in contrast to the simplified circuit in fig. 1), and they are both opened simultaneously to decrease the pressure drop. Therefore, there are N_p^2 possible control combinations to select from, where N_p is the number of supply pressure levels. The pressure drop across the on/off-valves has a significant effect on the force of the actuator. The controller models the pressure drop by assuming that the piston velocity corresponds the velocity reference. Dynamic effects are neglected and thus the actuator flow rates are:

$$Q_A = v_{ref}A_A; \quad Q_B = -v_{ref}A_B \quad (2)$$

Where A_A is the piston side chamber area and A_B is the piston rod side chamber area. The absolute values of the pressure

drops across the control valves follow the square root model of a turbulent orifice:

$$|\Delta p_A| = \left(\frac{Q_A}{K_V}\right)^2 ; \quad |\Delta p_B| = \left(\frac{Q_B}{K_V}\right)^2 \tag{3}$$

where K_V is the sum of flow coefficients of the two parallel connected on/off-valves. The force of the actuator is therefore:

$$F = \begin{cases} (\boldsymbol{p_S}(i_A) - |\Delta p_A|)A_A - (\boldsymbol{p_S}(i_B) + |\Delta p_B|)A_B, v_{ref} \geq 0 \\ (\boldsymbol{p_S}(i_A) + |\Delta p_A|)A_A - (\boldsymbol{p_S}(i_B) - |\Delta p_B|)A_B, v_{ref} < 0 \end{cases} \tag{4}$$

where $\boldsymbol{p}_S(i_A)$ is the pressure level of the i_A^{th} pressure source.

Figure 3 presents the possible forces produced by Ø 80/40 actuator as a function of the piston velocity. The supply pressure p_{HP} is set to 15 MPa and the return line pressure p_{LP} to 1 MPa. The area ratios of the four converter cylinders are $\boldsymbol{R} = [2.78\ 2.08\ 1.56\ 1.24]$ and the cylinder sizes Ø 50/40, Ø 50/36, Ø 50/30 and Ø 50/22 as in the experimental test system presented in section 3.1. The six supply pressure alternatives are thus

$$\boldsymbol{p_S} = \left[p_{LP}\ \frac{p_{HP}}{\boldsymbol{R}(1)}\ \frac{p_{HP}}{\boldsymbol{R}(2)}\ \frac{p_{HP}}{\boldsymbol{R}(3)}\ \frac{p_{HP}}{\boldsymbol{R}(4)}\ p_{HP}\right] \tag{5}$$

The nominal flow of the two parallel connected on/off-valves are according to the manufacturer data sheet approximately Q_N = 25 l/min at Δp_N = 0.5 MPa [15]. The flow coefficient is

$$K_V = \frac{Q_N}{\sqrt{\Delta p_N}} \tag{6}$$

Figure 3 shows the N_p^2 = 36 force levels generated by the different valve control combinations.

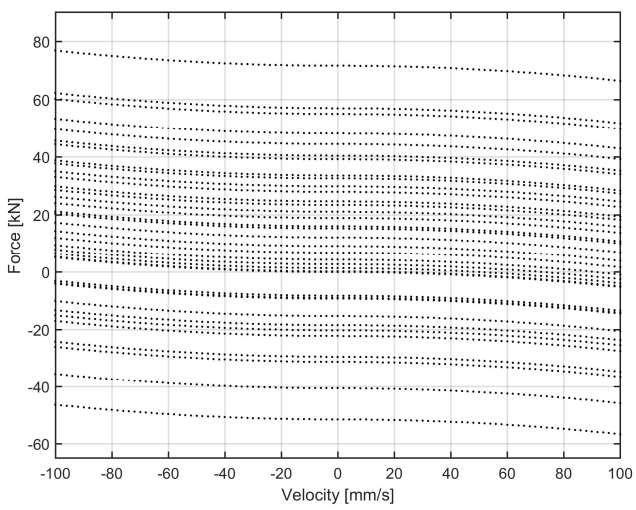

Figure 3: Possible actuator forces

The force levels generated are not evenly spaced between the minimum and maximum force. The force resolution is very coarse outside the range -31 to 57 kN, when zero velocity region is studied. Also inside this force range there are relatively big step sizes found especially just below 0 kN at zero velocity. When velocity differs from zero, the pressure drops of the on/off-valves shift the force series depending on the movement direction and absolute value of the velocity. However, it is worth to note that the force control step sizes remain independent of the velocity.

2.3 PNM-controller

In order to increase the resolution, the two parallel connected on/off-valves can be controlled separately. The valves are similar sized and therefore pulse number modulation (PNM) control is the selected control mode. Flow path from the pressure supply to the cylinder chamber may be controlled by opening zero, one or two parallel on/off-valves. Thus the control matrix defining the possible valve control candidates for a single cylinder chamber is:

$$\boldsymbol{u_{PNM}} = \begin{bmatrix} 1 & 2 & 0 & 0 & 0 & 0 & 0 & 0 & 0 & 0 & 0 & 0 \\ 0 & 0 & 1 & 2 & 0 & 0 & 0 & 0 & 0 & 0 & 0 & 0 \\ 0 & 0 & 0 & 0 & 1 & 2 & 0 & 0 & 0 & 0 & 0 & 0 \\ 0 & 0 & 0 & 0 & 0 & 0 & 1 & 2 & 0 & 0 & 0 & 0 \\ 0 & 0 & 0 & 0 & 0 & 0 & 0 & 0 & 1 & 2 & 0 & 0 \\ 0 & 0 & 0 & 0 & 0 & 0 & 0 & 0 & 0 & 0 & 1 & 2 \end{bmatrix} \tag{7}$$

where the six rows represent the six pressure sources, the columns the different control candidates and the numbers correspond to the number of opened valves.

By opening a single valve, the pressure drop Δp_A or Δp_B can be increased to generate additional unique force levels at the cost of the energy efficiency. The number of control alternatives is now $(N_{valves} \cdot N_p)^2$ = 144, where N_{valves} is the number of valves in each flow path. The possible forces are presented in fig. 4. The possible flow coefficients of the flow paths are now $2.95 \cdot 10^{-7}$ m^3 / (s Pa$^{1/2}$) and $5.89 \cdot 10^{-7}$ m^3 / (s Pa$^{1/2}$) depending on the number of opened valves. The opening of a single valve only generates excessive pressure drop at higher velocities leading to very high or low chamber pressures. Therefore, those control candidates, which produce chamber pressures exceeding the limits p_{max} = 25 MPa or p_{min} = 0 MPa or generate more than 2 kW power loss, are disregarded.

The force resolution is greatly improved, when velocity is outside the range -30...30 mm/s. At smaller velocities, the flow rates do not generate significant pressure drop across the control edge even if only a single valve is opened. Therefore, the use of two-valve PNM-control does not solve all problems related to the controllability. Furthermore, the most accurate control is typically desired at slow velocity movements. However, the velocity range, where the PNM-control is effective, can be altered by increasing the number of the parallel valves and by modifying the flow capacity of the valves. In order to extend the fine resolution range closer to zero velocity, the valve flow coefficients can be selected e.g. ¼ & ¾ instead of the ½ & ½ ratio presented. However, in that case the pressure drop of the smaller valve becomes excessive at relatively low velocities limiting the usable fine force resolution to narrow velocity range.

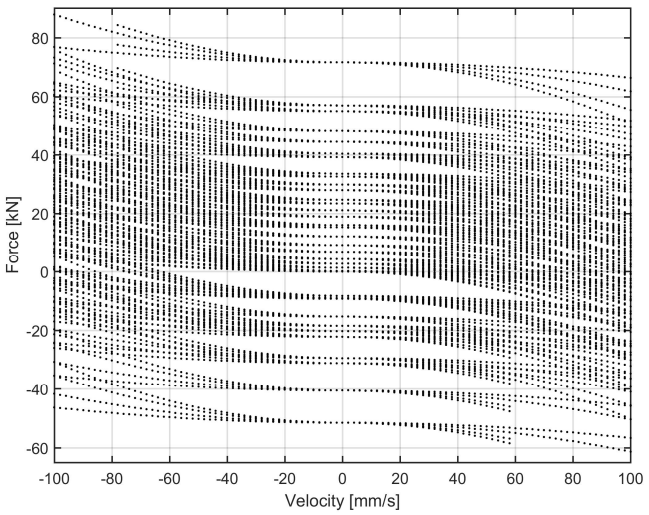

Figure 4: Possible actuator forces when 2-bit PNM-control is enabled

2.4 Controller enabling crossflow-connection

Improving the velocity range close to zero velocity is difficult by using PNM-control. Crossflow from a pressure supply to another pressure supply through a cylinder chamber is a viable method to increase the force resolution even if the net flow rate to the cylinder chamber is zero or small. The idea is to open e.g. a single control valve of the flow path P4 à A and another valve of the flow path P3 à A. In the equilibrium, the flow rates satisfy:

$$\boldsymbol{Q_S}(4) = v_{ref}A_A - \boldsymbol{Q_S}(3) \tag{8}$$

where the positive flow rate Q_S is from the pressure supply to the cylinder chamber. The chamber pressure p_A depends on the supply pressures, piston velocity and the flow coefficients of the two flow paths. In the equilibrium, following equation holds:

$$K_{V4}\sqrt[*]{\boldsymbol{p_S}(4) - p_A} = v_{ref}A_A - K_{V3}\sqrt[*]{\boldsymbol{p_S}(3) - p_A} \tag{9}$$

where $\sqrt[*]{x} = sign(x)\sqrt{|x|}$. Bisection method is utilized to find the equilibrium chamber pressure p_A satisfying the condition.

In order to limit the flow rate between the converter cylinders and thus the power loss, only two adjacent supply pressure levels are used in crossflow connection. Furthermore, control candidates where both flow paths are activated by opening two valves are disregarded. Therefore, only following valve control combinations are allowed to generate the crossflow connection:

$$\boldsymbol{u_{crssflw}} = \begin{bmatrix} 1 & 2 & 1 & 0 & 0 & 0 & 0 & 0 & 0 & 0 & 0 & 0 & 0 & 0 & 0 \\ 1 & 1 & 2 & 1 & 2 & 1 & 0 & 0 & 0 & 0 & 0 & 0 & 0 & 0 & 0 \\ 0 & 0 & 0 & 1 & 1 & 2 & 1 & 2 & 1 & 0 & 0 & 0 & 0 & 0 & 0 \\ 0 & 0 & 0 & 0 & 0 & 0 & 1 & 1 & 2 & 1 & 2 & 1 & 0 & 0 & 0 \\ 0 & 0 & 0 & 0 & 0 & 0 & 0 & 0 & 0 & 1 & 1 & 2 & 1 & 2 & 1 \\ 0 & 0 & 0 & 0 & 0 & 0 & 0 & 0 & 0 & 0 & 0 & 0 & 1 & 1 & 2 \end{bmatrix} \tag{10}$$

If both control candidates of the PNM-control matrix $\boldsymbol{u}_{\mathrm{PNM}}$ and the crossflow-control matrix $\boldsymbol{u}_{\mathrm{crssflw}}$ are considered, all the force levels presented in fig. 5 are possible. Again, all control candidates producing chamber pressures exceeding the allowed range or producing more than 2 kW of power loss are disregarded. The number of control candidates is now $(2\cdot N_p+3\cdot(N_p-1))^2 = 729$ for the system with two parallel valves in each flow path and the limitations concerning the crossflow mentioned.

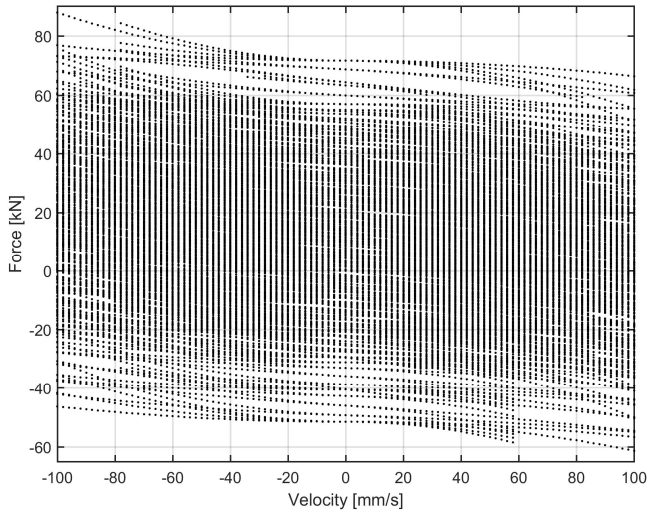

Figure 5: Possible actuator forces when PNM-control and crossflow connection are enabled

2.5 Summary

Figure 6 presents a summary of the control resolution. The three different types of controller are compared in the figure. The sum of squared force step sizes is given as a function of the actuator velocity. The figure clearly shows, that although the 2-bit PNM-control method improves the controllability significantly at higher velocities, the improvement is negligible at smallest velocities, where typically the fine control resolution is desired.

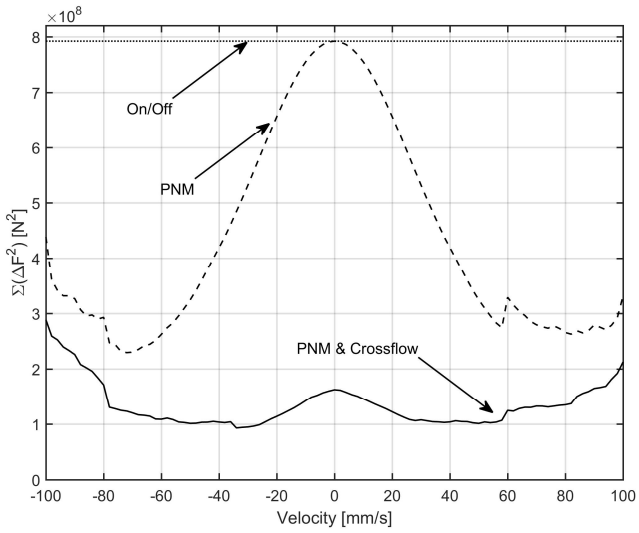

Figure 6: Sum of squared force step sizes (power loss of 2 kW is allowed)

The controller enabling crossflow-connection can significantly improve the controllability at slow velocities.

Figure 7 presents similar summary of the force resolution, when the allowed power loss is limited to 1 kW. The use of crossflow connection is drastically decreased. However, still the force resolution near zero velocity is significantly improved when compared to the On/Off-type control.

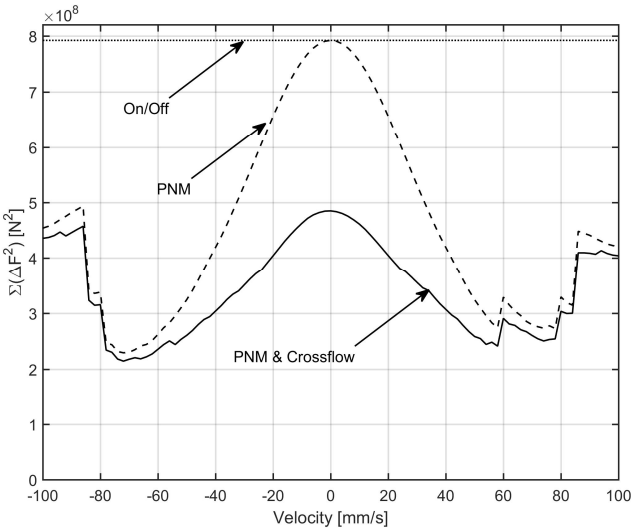

Figure 7: Sum of squared force step sizes (power loss of 1 kW is allowed)

3 Experimental study

The controllability of the actuator concept is studied experimentally in a mobile boom mock-up. Furthermore, the energy efficiency is compared to previously measured energy efficiency of load sensing mobile proportional valve based system [16] and four-chamber cylinder based system [13]. The sources of the partial power losses are studied using separate measurements.

3.1 Measurement system

The measurement system is based on a four-meter-long boom mock-up (detailed dimensions of the boom can be found in [10]). The hybrid actuator concept is equipped with a number of pressure and position sensors as presented in fig. 8. There are also flow sensors connected to the supply line and the return line in order to measure the input power. Small fixed displacement pump with a start/stop logic delivers the hydraulic input power and the supply pressure reference is set to 15 MPa. In addition to the diagram presented, there are pressure relief valves in supply line and the actuator lines for safety reasons.

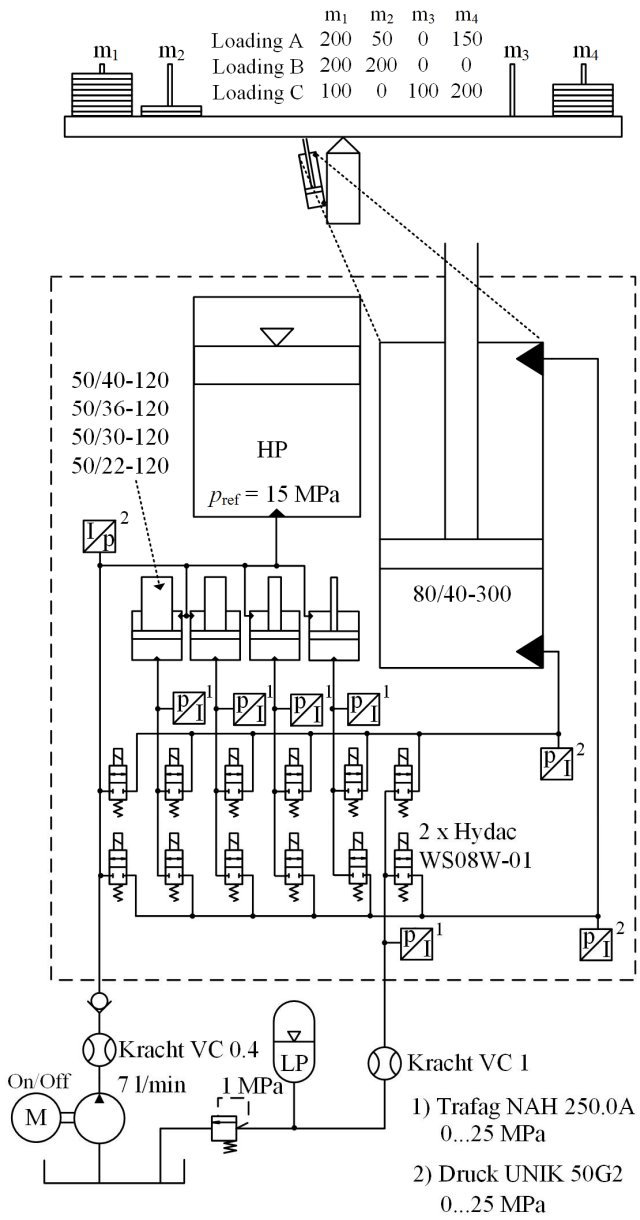

Figure 8: Experimental test setup and the three different loadings measured (kg).

3.2 Measurement results

The measurements are performed to study the energy efficiency and controllability of the system. The energy efficiency of the system is investigated using a special smooth position trajectory, which has been previously utilized while studying different types of digital hydraulic systems and load sensing proportional valve based system [16]. The control resolution of the three different controller types is studied using a modified position trajectory, where the velocities are halved and the movement times doubled such that identical piston strokes are driven.

3.2.1 Controllability

The controllability of large inertia load during high velocity movements is relatively good even with the basic controller and the actuator concept enables fast response due to small capacitances and fast on/off-valves. However, the control resolution at slow velocities requires improvement to enable smooth velocity tracking, accurate positioning and to avoid oscillations during stopping of the movement as seen in fig. 9. All measured trajectories presented are measured with the loading B.

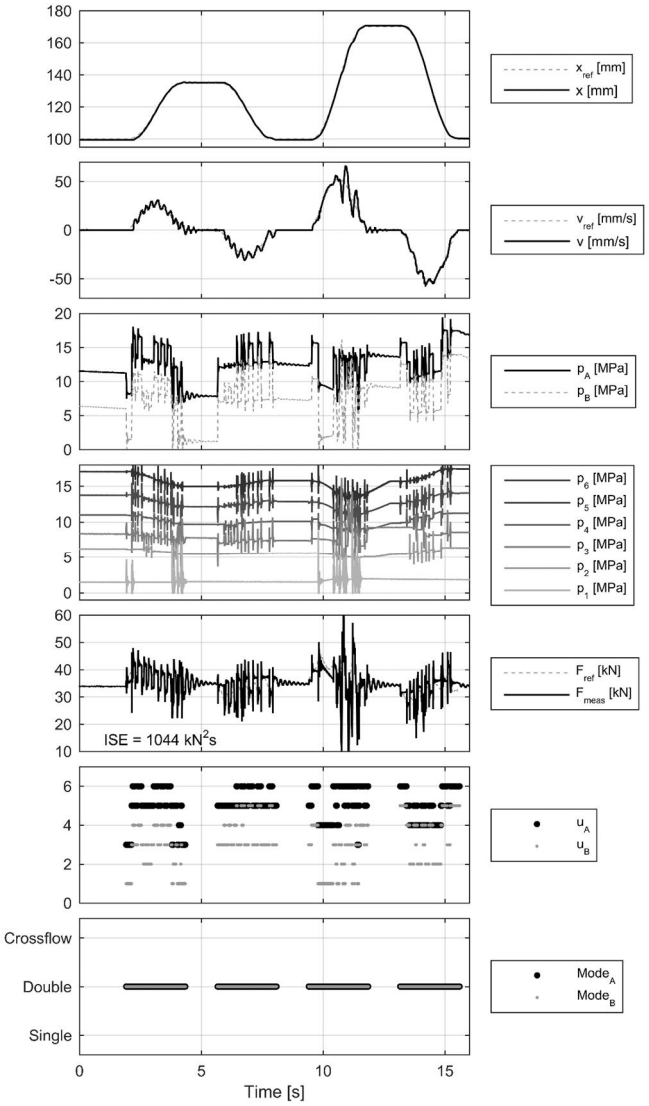

Figure 9: Measured slow velocity trajectory with basic controller

Figure 9 includes measured position and velocity together with their reference values in the two topmost diagrams. The piston side chamber pressure p_A, the rod side chamber pressure p_B and the supply pressures $p_1 ... p_6$ are given in the middle. The third lowest diagram presents the force reference generated by the motion controller as well as the actual force calculated from the measured chamber pressures. Furthermore, the integral square error (ISE) of the force control is given. The ISE value is calculated based on the complete measurement including five repetitions of the trajectory shown. The two lowest diagrams relate to the valve command signal for piston side and rod side on/off-valves. The lowest diagram shows whether a single valve is opened (Single) or both parallel-connected valves (Double) are opened between cylinder chamber and the pressure source. The third option is that the cylinder chamber is connected to two pressure sources (Crossflow). The second lowest diagram shows which pressure sources are connected to the cylinder chambers (1 = LP ... 6 = HP).

The force control resolution is coarse resulting in considerable velocity error and relatively high accelerations despite the smooth velocity reference. Due to coarse resolution, the amplitude of the measured oscillations in supply pressures and chamber pressures is high. The controllability can be improved by introducing PNM-control as presented in fig. 10.

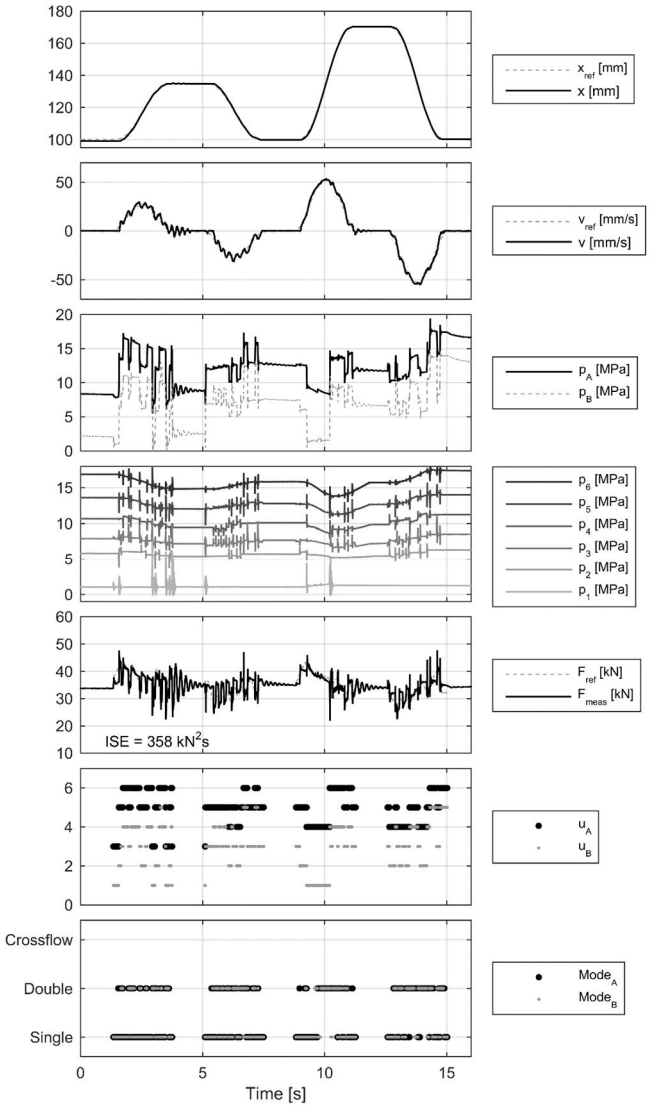

Figure 10: Measured slow velocity trajectory with PNM-control enabled

As the numerical study in section 2 shows, the two-valve PNM-control is capable of improving the control resolution

at certain velocity range. In this case, the resolution is not improved when the movement velocity is close to zero. Thus, the smoothness of the smaller movement having a peak velocity of 26 mm/s is not significantly improved. However, the pressure oscillations are suppressed compared to the measurement carried out with the basic controller. In addition, the smoothness of the velocity tracking is improved during the larger movement having a peak velocity of 53 mm/s. Force tracking result is improved as the significant change in the ISE value demonstrates. The third controller type enables also the crossflow connection and thus the best resolution of the controller types tested. The measurement results of the controller type are presented in fig. 11.

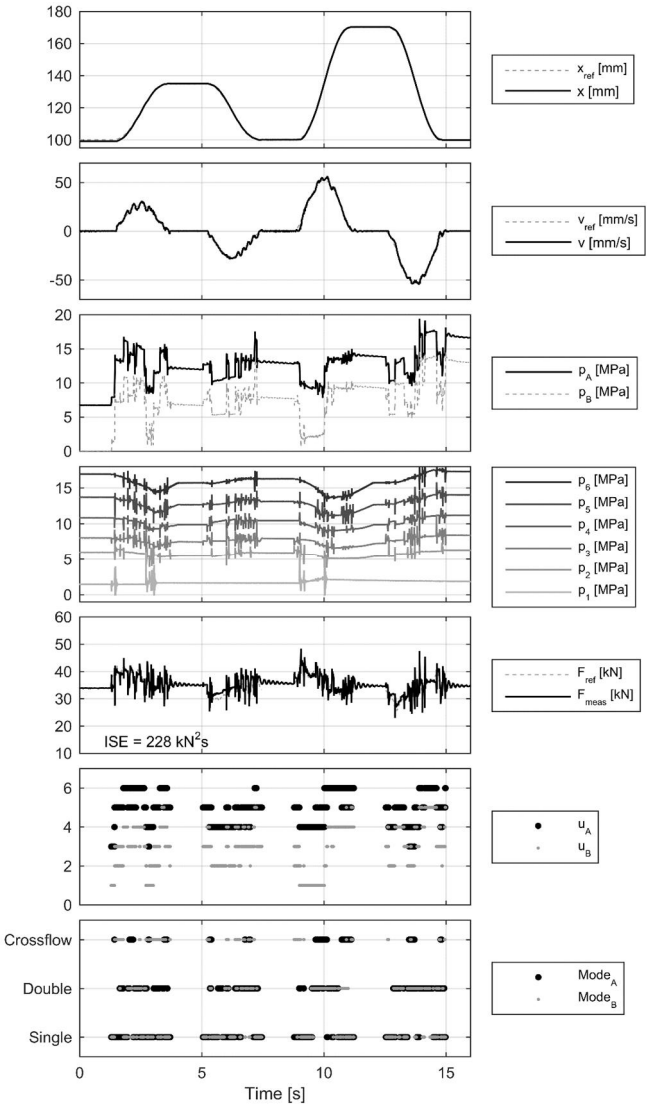

Figure 11: Measured slow velocity trajectory with PNM-control & crossflow enabled

The crossflow connection enables improvement on force control resolution also during slow velocity movements. However, the measured response shows that even with the PNM-control and the crossflow connection enabled, there are small velocity oscillations still present. Nevertheless, by enabling the PNM-control and the crossflow connection, the velocity error and oscillations are decreased when compared to the simpler controllers and the ISE value of the force tracking is considerably improved.

3.2.2 Energy efficiency

Figure 12 presents part of the measured faster trajectory tracking result using PNM-control and crossflow connection. The total output energy of the movement includes only piston friction and small flow losses. The input energy is measured from the hydraulic supply line and pressurized tank line using the pressure and flow sensors. The trajectory shown is repeated five times during a single measurement. The measurement is then repeated five times thus leading to 25 repetitions of the trajectory. The average energy loss of a single trajectory (PNM & Crossflow; loading B) is 2.9 kJ if the energy returned to the pressurized tank line is not lost but can be utilized.

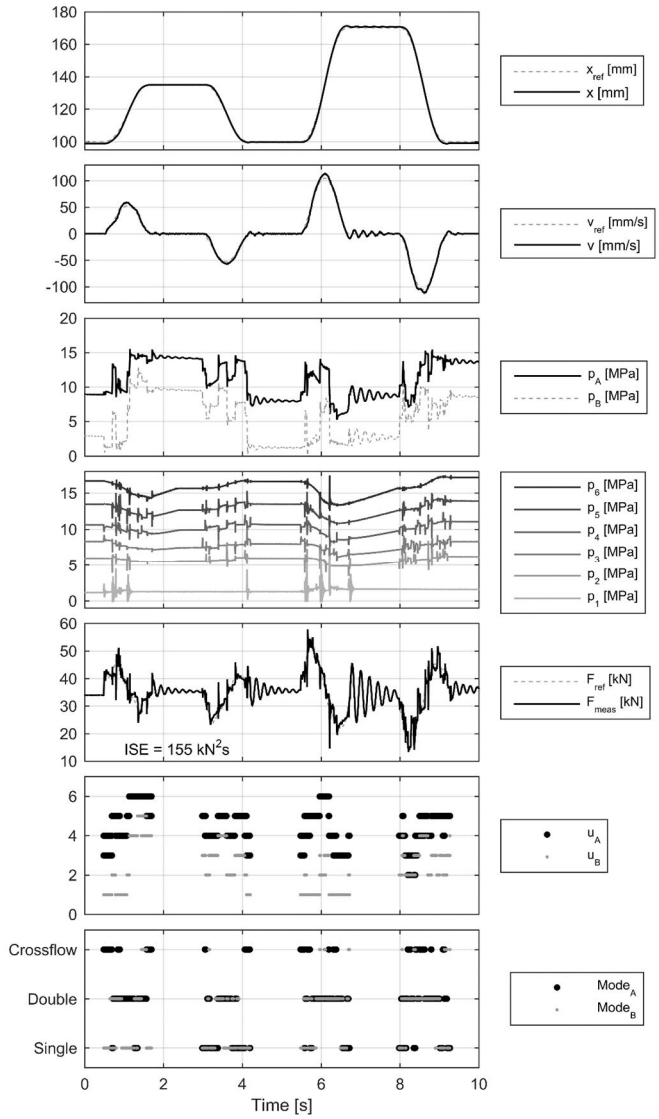

Figure 12: Measured fast velocity trajectory with PNM-control and crossflow enabled

The average energy losses of the three loadings driven with the different control methods are given in tab. 1. The energy losses are scaled according to the total movement distance of

the piston (210 mm) to enable a comparison with different kind of trajectories.

Table 1: Average energy loss / movement distance [J/mm] in fast velocity trajectory

	Load A	Load B	Load C
Basic	10.2	10.9	10.9
PNM	9.9	11.3	9.9
PNM & Crossflow	12.7	13.6	14.1

Figure 13 compares the average energy losses of a single trajectory to previously measured results with load sensing proportional valve based system [16] and secondary controlled four-chamber system [13]. The proportional valve used in the reference measurements was a Bosch Rexroth M4-12 and the load sensing pressure margin was set to 1.0 MPa. The results concerning energy efficiency of the concept are remarkable: the new concept can avoid up to 77 % of the losses generated by the proportional valve based system depending on the controller type used.

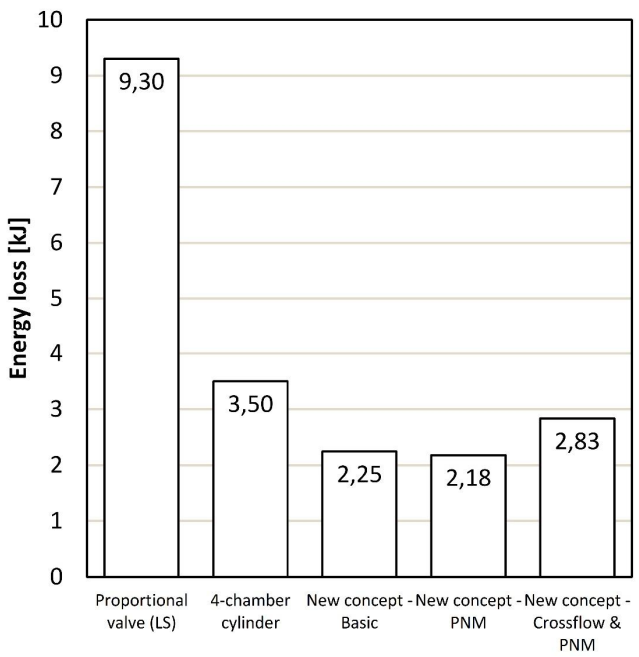

Figure 13: Comparison of measured energy losses in fast velocity trajectory

Even though the new concept increases the energy efficiency considerably, there are still significant energy losses present. To find the reasons for these losses, partial power losses of the system are studied next.

3.2.3 Sources of energy losses

Figure 14 presents an example of the partial power losses in the actuator concept. The total power loss of the system is formed by the pressure drop in the on/off-valves, flow losses in the piping, cylinder friction, thermodynamic energy losses in the accumulator and losses related to the pressurization and de-pressurization of the actuator chambers.

The figure presents following partial power losses:

- Pressure loss of the on/off-valve
- Pressure loss of the pipe between converter cylinder and the valve block
- Friction loss of the converter cylinder & pressure loss in the cylinder fittings
- Pressure loss of the pipe between high pressure accumulator and converter cylinder

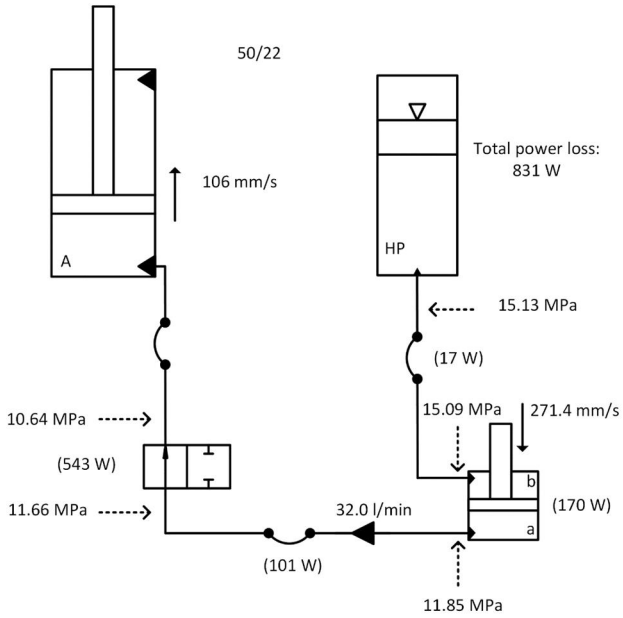

Figure 14: Power loss of the converter circuit at maximum velocity

The flow rate on both sides of the converter cylinder is estimated from the position measurement of the actuator. The flow rates are approximated from the derived velocity and cylinder areas. The velocity and pressure readings are examined, when the velocity is constant and the pressure fluctuations induced by the valve activity are settled. 32 l/min flow rate is the maximum designed flow rate of the system enabling roughly 0.1 m/s maximum velocity of the actuator. The pressure drop of the logic valve induces majority of the power loss in the circuit. The flow through the valve is turbulent and thus the power losses decrease rapidly as the flow rate is decreased: halving the flow rate decreases the valve power loss to 1/8.

Figure 15 presents the summary of the power losses in each converter cylinder circuit when maximum velocity is driven and the converter cylinder is connected to actuator piston-side chamber. All converter cylinders are measured with flow rate 32.0 l/min, except for cylinder 50/30 where the flow rate is approximately 2 % higher: 32.6 l/min.

When average values of the four converter cylinders are considered, the on/off-valve generates 66 %, the medium pressure line generates 12 %, the cylinder friction generates 21 % and the accumulator line generates 1 % of the total power loss. The power loss of the accumulator line clearly depends on the converter area ratio, but its effect on the total power loss is negligible. The friction loss of the converter

cylinder together with pressure drop occurring in the cylinder ports and fittings is relatively small.

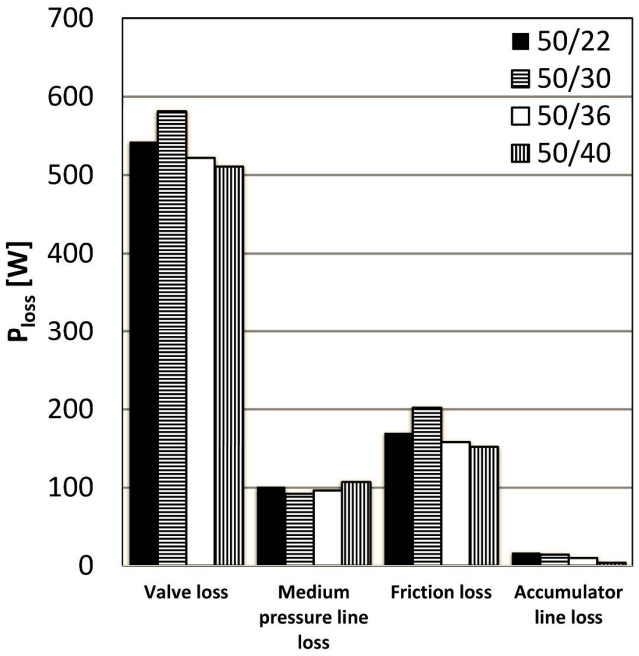

Figure 15: Measured partial power losses of the converter cylinder circuits

4 Discussion and conclusions

The paper presents an experimental study of a new digital hydraulic multi-pressure actuator. The energy efficiency of the concept is high compared to traditional four-way load sensing proportional valve based system. The measurements show up to 77 % reduction in energy losses. Furthermore, the measurement results show that the single biggest remaining source of power loss in the concept is the on/off-valve at least at high velocities.

Three different controller types are studied in the paper. The first type is a simple on/off-type controller, where each flow path is either fully open or closed. The second type called pulse number modulation takes advantage of the fact that there are two parallel-connected on/off-valves in each flow path. The pulse number modulation enables independent control of the two valves thus allowing adjustment of the pressure drop across the flow path. The third controller type enables crossflow from a pressure supply to another thus allowing the generation of chamber pressures between the discrete supply pressure levels. The use of pulse number modulation and crossflow connection improves the control resolution significantly as the numerical and experimental results show. However, the use of crossflow connection adds power losses considerably and thus the excessive use of the connection should be avoided.

The controllability of the new concept compared to load sensing proportional valve is twofold: the dynamics of the control system are fast due to the control type and fast on/off-valves leading to e.g. small position tracking error; on the other hand, there are small amplitude oscillations present during slow velocity movements indicating slightly limited resolution. If needed, the controllability can be further improved by e.g. increasing the number of parallel valves. The new concept enables considerably higher efficiency when compared to proportional valve based load sensing systems, which are common in commercial mobile machine applications. Furthermore, the concept enables the decoupling of input and output power. As the generation and utilization of the power are decoupled, the prime mover of the mobile machine can be driven against constant or slowly varying loading. Furthermore, the prime mover, which is usually a Diesel engine at the moment of writing, can be driven in efficient operating range.

The results presented were obtained with a proof-of-concept prototype, where the system was built based on separate standard components. As such, the cost of the new actuator concept is considerably higher than e.g. traditional actuator driven by a load sensing valve. On the other hand, the new concept enables certain amount of cost reduction on system level, where a smaller constant displacement pump can be utilized in place of the variable displacement unit. Whether the increased manufacturing costs are justified by the decreased fuel costs, depends heavily on the application type and its load cycle.

Acknowledgement

The research was funded by Academy of Finland (Grant No. 278464).

References

[1] M Lindgren, and P-A Hansson. Effect of Transient Conditions on Exhaust Emission from two Non-road Diesel Engines. *Biosystems Engineering, Vol 87, Issue 1, 2004*.

[2] M Vukovic, R Leifeld and H Murrenhoff. STEAM – a hydraulic hybrid architecture for excavators. Proc. of *10th International Fluid Power Conference*. 8-10 March, 2016, Dresden, Germany.

[3] K Schneider. Liebherr Pactronic® – Hybrid Power Booster, Energy Recovery and Increased Performance with Hybrid Power. Proc. of *8th International Fluid Power Conference*. 26-28 March, 2012, Dresden, Germany.

[4] K Einola and A Kivi. First Experimental Results of a Hydraulic Hybrid Concept System for a Cut-to-Length Forest Harvester. Proc. of *14th Scandinavian International Conference on Fluid Power*. 20-22 May, 2015, Tampere, Finland.

[5] P Achten and T van den Brink. A hydraulic transformer with a swash block control around three axis of rotation. Proc. of *8th International Fluid Power Conference*, 26-28 March 2012, Dresden, Germany.

[6] H Kogler and R Scheidl. Energy Efficient Linear Drive Axis Using a Hydraulic Switching Converter. *Journal of*

Dynamic Systems, Measurement and Control. 2016, Vol 138(9). doi: 10.1115/1.4033412.

[7] M Pan, J Robertson, N Johnston, A Plummer and A Hillis. Experimental investigation of a switched inertance hydraulic system. Proc. of *ASME/Bath Symposium on Fluid Power and Motion Control 2014 (FPMC14).* Bath, UK.

[8] C Williamson, J Zimmerman, and M Ivantysynova. Efficiency Study of an Excavator Hydraulic System Based on Displacement-Controlled Actuators. Proc of *ASME/Bath Workshop on Fluid Power and Motion Control 2008 (FPMC08).* Bath, UK.

[9] M Linjama, M Huova, M Pietola, J Juhala, and K Huhtala. Hydraulic Hybrid Actuator. Theoretical Aspects and Solution Alternatives. Proc. of *The 14th Scandinavian International Conference on Fluid Power*, May 20-22, 2015, Tampere, Finland.

[10] M Huova, A Aalto, M Linjama, K Huhtala, T Lantela, and M Pietola. Digital Hydraulic Multi-Pressure Actuator - the Concept, Simulation Study and First Experimental Results. *International Journal of Fluid Power*. http://dx.doi.org/10.1080/14399776.2017.1302775.

[11] E Bishop. Digital Hydraulic Transformer – Approaching Theoretical Perfection in Hydraulic Drive Efficiency. Proc. of *The 11th Scandinavian International Conference on Fluid Power*, June 2-4, 2009, Linköping, Sweden.

[12] E Bishop. Linearization of Quantized Digital Hydraulic Transformer Output. Proc. of *The Third Workshop on Digital Fluid Power*, October, 13-14, Tampere, Finland.

[13] M Linjama, H-P Vihtanen, A Sipola, and M Vilenius. Secondary Controlled Multi-Chamber Hydraulic Cylinder. Proc. of *The 11th Scandinavian International Conference on Fluid Power*, June 2-4, 2009, Linköping, Sweden.

[14] A Harrison and D Stoten. Generalized Finite Difference Methods for Optimal Estimation of Derivatives in Real-Time Control Problems. *Proceedings of the Institution of Mechanical Engineers, Part I: Journal of Systems and Control Engineering* 1995, Vol 209: 67–78.

[15] Hydac WS08W-01 datasheet. Available: www.hydac.com.br/wp-content/uploads/e5924_ws08w01.pdf. January 27th 2017.

[16] M Linjama, M Huova, P Boström, A Laamanen, L Siivonen, L Morel, M Walden and M Vilenius. Design and Implementation of Energy Saving Digital Hydraulic Control System. Proc. of *The Tenth Scandinavian International Conference on Fluid Power*, 2007, Tampere, Finland.

System level co-simulation of a control valve and hydraulic cylinder circuit in a hydraulic percussion unit

Håkan Andersson[1,2], Kjell Simonsson[2], Daniel Hilding[3], Mikael Schill[3], and Daniel Leidermark[2]

[1]Construction Tools PC AB, Dragonvägen 2, 391 27 Kalmar, Sweden
[1]E-mail: hakan.andersson@se.atlascopco.com
[2]Division of Solid Mechanics, Linköping University, 581 83 Linköping, Sweden
[3]DYNAmore Nordic AB, Brigadgatan 5, 587 58 Linköping, Sweden

Abstract

In this study a previously developed co-simulation method that is based on a 1D system model representing the fluid components of a hydraulic machinery, within which structural 3D Finite Element (FE) models can be incorporated for detailed simulation of specific sub-models or complete structural assemblies, is further developed. The fluid system model consists of ordinary differential equation sub-models that are computationally very inexpensive, but still represents the fluid dynamics very well. The co-simulation method has been shown to work very well for a simple model representing a hydraulic driven machinery. A more complex model was set up in this work, in which two cylinders in the hydraulic circuit were evaluated. Such type of models, including both the main piston and control valves, are necessary as they represent the real application to a further extent than the simple model, of only one cylinder. Two models have been developed and evaluated, from the simple rigid body representation of the structural mechanics model, to the more complex model using linear elastic representation. The 3D FE-model facilitates evaluation of displacements, stresses, and strains on a local level of the model. The results can be utilised for fatigue assessment, wear analysis and for predictions of noise radiation.

Keywords: Co-simulation, Fluid-structure coupling, System simulation, Functional mock-up interface, Fluid power machinery, Transmission line modelling

1 Introduction

The need of a computationally inexpensive co-simulation method for fluid power equipment and specifically oil hydraulic percussion units to achieve accurate predictions is of high importance to the industry. The end-product performance and fundamental mechanisms in these types of machines are highly affected by the fluid-structure interaction. The demands on such a simulation method are on one hand to facilitate the evaluation of global parameters but also to represent the detailed mechanisms at the fluid-structure interfaces. Global parameters must be evaluated from a system simulation model that often is built up by a network of sub-models represented by 1D components.

Detailed simulations of hydraulic machinery could be performed using existing Fluid-Structure Interaction (FSI) methods that today are available in many software suits, e.g. LS-DYNA [1] and ANSYS [2], where the fluid-, and the structural-mechanic systems are co-simulated. A few examples of these types of simulations from the machine building industry have been found, but are in general very rare. In the paper by Wang et al. [3] the valve system of a reciprocating air compressor was analysed through FSI-methods and in the paper by Campbell et al. [4] an FSI-analysis of a highly flexible impeller was conducted. A major drawback for the FSI-method is the need for extensive computational resources when solving these problems, especially when the models are used for system level simulations. Such computational resources are generally not available within the machine building industry, which requires less computationally demanding simulation methods to solve fluid-structure coupling problems.

It has been found that the functional behaviour of a product can be studied through system simulation models that are described by Ordinary Differential Equations (ODE), or 1D Partial Differential Equations (PDE) [5]. Simulation models based on Computational Fluid Dynamics (CFD) or the Finite Element Method (FEM) are used when phenomena's are studied at a much more detailed level. When combining these types of models proper boundary conditions can be provided at a low computational cost. In the work by Andersson et al. [6] such a co-simulation method is proposed that incorporates the fluid-structure coupling for a fluid power system. Here the fluid system is represented by a 1D system model, using the system simulation tool Hopsan [7], and the struc-

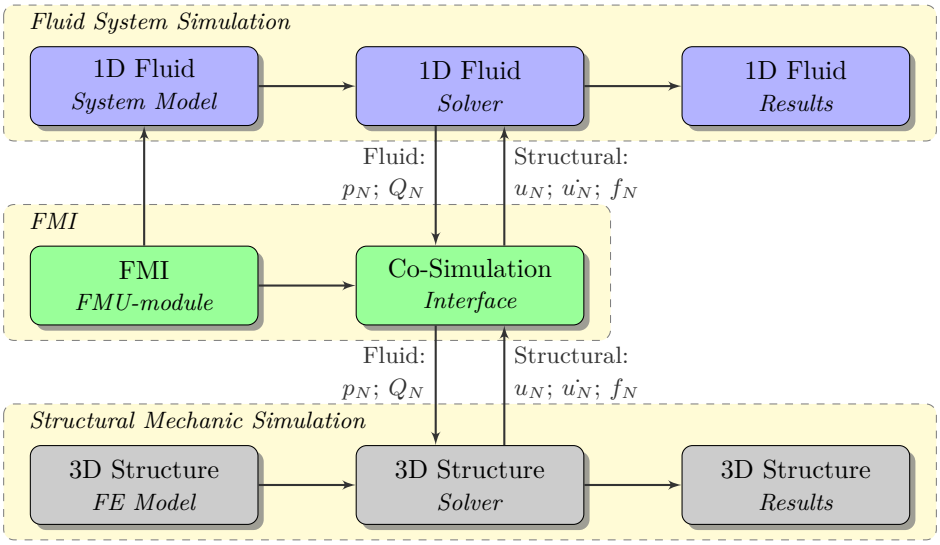

Figure 1: Overall simulation method sequence. The N subscript indicates that multiple co-simulation sub-models are enabled

tural part is modelled in the Finite Element (FE) software LS-DYNA. The models are then co-simulated using a communication module that is based on the Functional Mock-up Interface (FMI) standard [8], where a Functional Mock-up Unit (FMU) is defined on the system side to represent and connect to the FE-model. Using this technique the fluid system simulation will be computationally inexpensive but still reflect a correct dynamic behaviour, and it will also provide relevant input for the FE-simulation. This is particularly important for simulations over long time periods. Since the models are coupled it is also possible to evaluate the response from all fluid and structural loads.

In the literature, applications have been found where a 1D system model is co-simulated with a 3D model in the fluid or structural domain, to include global system behaviour into the 3D-model. These applications were often found to be of single domain simulations, i.e. fluid domain or structural domain, and consisting of two models communicating over a co-simulation interface. Two examples are found in [9], a 1D system model of ODE and a CFD-model in the fluid domain, and an example for the structural domain is found in [10], where a multi body simulation model and a 3D FE-model are co-simulated. These examples only consist of one sub-model for co-simulation and no example with multiple sub-models for co-simulation have been found. Furthermore, there are many other applications where a co-simulation setting is applicable, for instance, in fluid and multi-body mechanic interactions [11] and simulations based on meta-models [12].

Today's design tools for fluid and structural systems that are used for product development of hydraulic percussion units, are based on uncoupled analyses. This circumstance makes it very hard to capture coupled phenomenon at the design stage, and these are then first discovered during the prototype testing. At this stage it is time consuming and expensive to initiate redesign work that often can be quite extensive. In the previous paper by Andersson et al. [6] the proposed method was evaluated for one sub-model for co-simulation, representing the structural part of a hydraulic cylinder. In order to achieve a more complete simulation model, see above, it was considered necessary to evaluate this method for multiple sub-models for co-simulation, as more accurate simulation models are continuously required. In the here presented work an FMU, which has been configured to contain multiple ports, is communicating with two hydraulic cylinders in the FE-model. The main hydraulic cylinder and the control valve, representing a hydraulically controlled piston with a hydraulic position feedback control signal. For these units the wave propagation and transmission in both fluid and structure are crucial and are often of short duration/high amplitude characteristic, and these data are transferred over the co-simulation interface that will be stressed to a high limit.

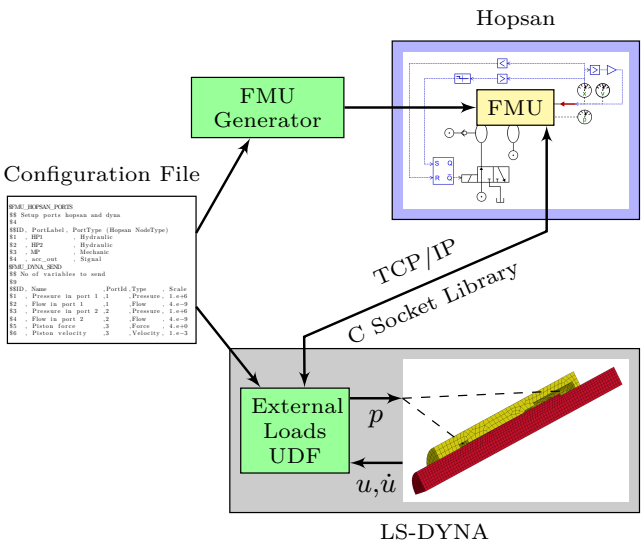

Figure 2: Overview of the co-simulation work flow

The outline of the paper is as follows. First, a brief presentation of the used simulation method and the previously im-

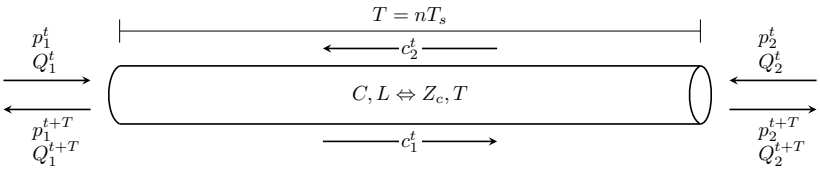

Figure 3: A TLM element, illustrated by a pipe, introduces a time delay (T) of the effort (p) and flow (Q) variables entering on either side. Eq. 1, 2 and 3 gives the TLM boundary equations

plemented co-simulation interface is given. The application example and two different co-simulation cases are then explained and the accuracy of the method is evaluated and compared to an equivalent system-level simulation model.

2 Simulation Method

The simulation method that is used in this work is illustrated in Figure 1. As described by Andersson et al. [6] the implementation is based on the FMI-standard and a stand-alone software was developed to create and to configure the FMU that is used for the co-simulation interface. This software allows that several connection points for the FMU are defined. Thus, several ports for communication can be defined, which is here used to configure a co-simulation interface for two sub-models. The 1D system model consists of a number of sub-models describing different components in the hydraulic fluid system, e.g. valves, cavities, orifices etc.

In the FE-model, the fluid system is represented as actions on pressurised surfaces. From the fluid system model the pressure p is delivered to the FE-model, while the displacement u, velocity $\dot{u}$ and mechanical force f are received, see Figure 1. Since these values must be scalars in the 1D system, the average displacements and velocities over the pressurised surfaces are used.

At the end of the simulation the fluid domain variables are available and system properties such as performance and efficiency can be evaluated. From the FE-results it is possible to evaluate displacements and velocities of the 3D geometry, which can be used for instance as input data for acoustic analyses. The stresses and strains are also available e.g. for stress analysis and structural fatigue evaluation.

3 The Co-simulation Implementation

The same implementation as in the previous work by Andersson et al. [6] has also been used here, with the open-source 1D system-simulation program Hopsan [7, 13], for simulation of the hydraulic fluid components, and the commercial FE-software LS-DYNA [1], for the structural part. Hopsan is based on the Transmission Line Modelling (TLM) method for modelling of physical components, which has been shown to be suitable for simulation of hydro-mechanical systems [14]. In LS-DYNA the explicit solver is used as it is fast and appropriate for analysing stress waves in solid structures. The co-simulation interface is realised as an FMU on the Hopsan side and for LS-DYNA the User Defined Function (UDF) is used. Previous work by Larsson et al. [15], where they compared different integration methods for co-

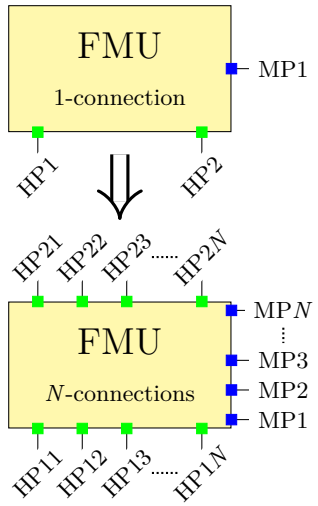

Figure 4: This figure shows the development of the simulation method to increase the number of sub-models for co-simulation. At the top is an FMU configured for one sub-model. The FMU at the bottom is more general, containing N-number of sub-models. HPxx are the hydraulic ports and MPx are the mechanical ports

simulation, shows that co-simulation based on TLM offers very good numerical stability. The investigation showed that co-simulation based on TLM had superior stability properties. The numerical stability has not been further investigated in this work.

In order to achieve high performance and flexibility in communication the co-simulation interface uses the TCP/IP for transfer of data during the simulation.

A custom made configuration file based on the native *Keyword* format in LS-DYNA is utilised both to set-up the FMU and to configure the UDF in LS-DYNA. The FMU is built using an in-house developed automatic software generator. In the UDF the connection between the FE-model, nodes and element segments, and the hydraulic- or mechanial ports is specified. The co-simulation connectivity and work flow is illustrated in Figure 2.

A brief overview of the Hopsan simulation tool and the UDF is given below, for further details regarding this co-simulation implementation and other issues related to the used softwares, please see [6].

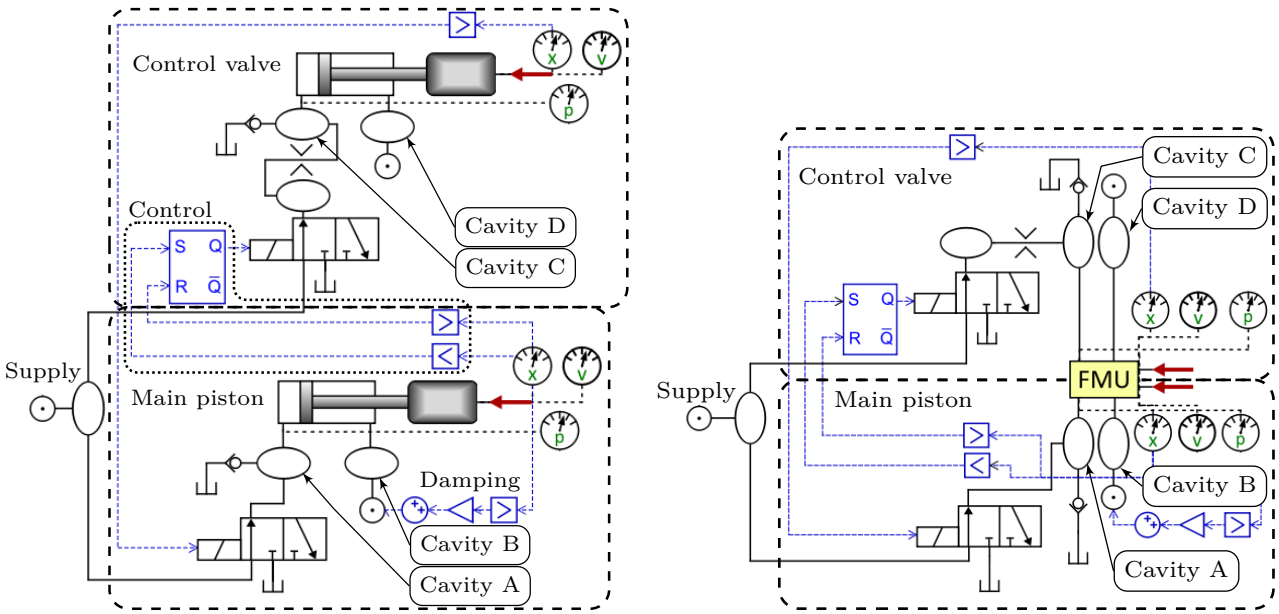

(a) Hopsan reference sytem model

(b) Hopsan system model for co-simulation

Figure 5: System models for Hopsan simulations. The components for each hydraulic cylinder, the main piston and the control valve are encircled by dashed lines. The valve control is encircled by dotted line, i.e. Control, and the components for the piston damping mechanisms are indicated, i.e. Damping. The meters are sensors for different quantities; X=Displacement u, V=Velocity $\dot{u}$ and p=Pressure. X and V are Hopsan standard nomenclature, but the latter ones will be used throughout this work. The displacement and the velocity sensors are connected to the control valve and to the main piston. The pressure sensors are connected to Cavity A in the main piston cylinder and to Cavity C in the control valve cylinder

3.1 The Hopsan Simulation Tool

Hopsan is a free multi-domain 1D system simulation tool that uses the TLM method for modelling and simulation of physical systems. The TLM method, or bi-lateral delay line modelling, firstly presented by Auslander [16] in 1968, is an approach to model dynamic systems by a network of distributed sub-models, i.e. TLM elements. The core in this technique is that a time delay is introduced by using the one-dimensional wave equation in the element, which decouples the connection points and make it possible to solve each part separately. Since the connection points by the time delay are weakly coupled, explicit methods rather than iterative methods, can be used for solving the simulation model very effectively.

This co-simulation implementation is based on loss-less, single-time-step TLM elements, see Figure 3. The governing equations for the time-domain are given in Eq. 1, 2 and 3, where p_1 and p_2 are the 'effort' variables and Q_1 and Q_2 are the 'flow' variables at the boundaries [17]. During the delay, waves represented by c_1 and c_2 travel in the respective directions through the element. The loss-less element's characteristic impedance Z_c is a scalar property that relates the physical properties, capacitance C and inductance L, to the introduced time delay T.

$$p_2^{t+T} = \overbrace{p_1^t + Z_c Q_1^t}^{c_1^t} + Z_c Q_2^{t+T} \tag{1a}$$

$$p_1^{t+T} = \underbrace{p_2^t + Z_c Q_2^t}_{c_2^t} + Z_c Q_1^{t+T} \tag{1b}$$

$$Z_c = \sqrt{\frac{L}{C}} \tag{2}$$

$$T = \sqrt{LC} \tag{3}$$

The pressure acting on the piston in the FE-model is calculated according to Eq. 4. As can be noticed from this equation the flow variable, Q_2^t, is taken from the previous time step, which is an approximation and a possible source of error. However, the difference for small time steps should not be of importance.

$$p_{2,approx}^{t+T} = c_1^t + Z_c Q_2^t \tag{4}$$

3.2 LS-DYNA User Defined Function

On the structural side, the general non-linear ODE, i.e. the equation of motion, that is solved by LS-DYNA is given by Eq. 5.

$$\mathbf{M}\ddot{\mathbf{u}} + \mathbf{C}\dot{\mathbf{u}} + \mathbf{f}_{Int} = \mathbf{f}_{Ext} \tag{5}$$

where $\mathbf{M}$ is the mass matrix, $\mathbf{C}$ is the damping matrix and $\mathbf{f}_{Int}$ is the internal force vector. The external force vector, $\mathbf{f}_{Ext}$,

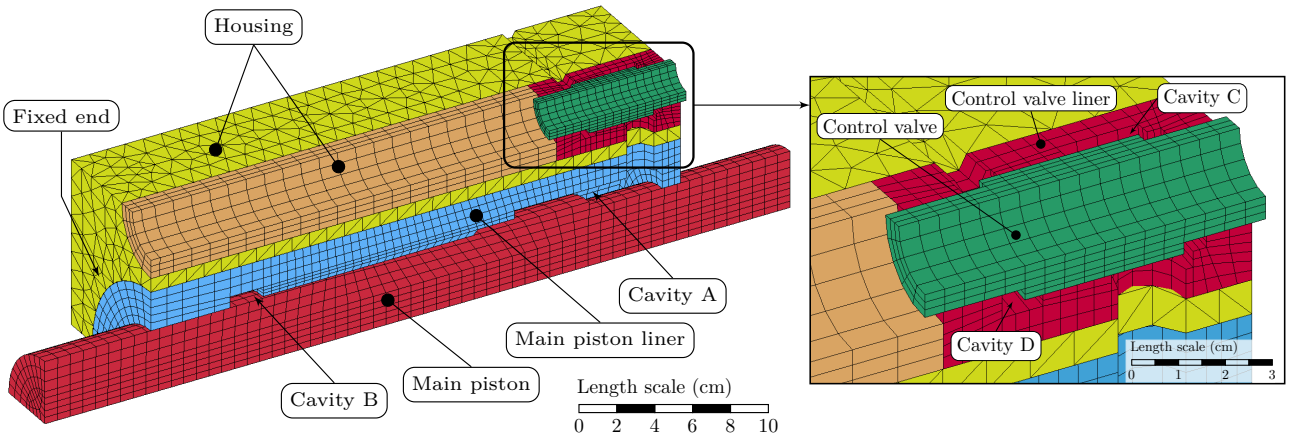

(a) Complete FE-model

(b) Control valve details

Figure 6: The quarter FE-model that is used in Case 1.

represents all external loads acting on the FE-model. The input variables (c and Z_c), representing the pressure, from the system model are used to calculate the external loads $\mathbf{f}_{Ext}$ and the user defined configuration file specifies on which locations they are to be applied through the UDF. The displacement $\mathbf{u}$ is solved explicitly by the central difference time integration scheme described by Eq. 6 and 7. For further description regarding the explicit integration scheme see e.g. [18].

$$\dot{\mathbf{u}}^{n+\frac{1}{2}} = \dot{\mathbf{u}}^{n-\frac{1}{2}} + \ddot{\mathbf{u}}^{n}\Delta t^{n} \tag{6}$$

$$\mathbf{u}^{n+1} = \mathbf{u}^{n} + \dot{\mathbf{u}}^{n+\frac{1}{2}}\Delta t^{n+\frac{1}{2}} \tag{7}$$

The resulting displacements and velocities are sent back from the FE-model to the system model, and this procedure is repeated for each time step until the analysis is completed.

3.3 Multiple Components for Co-simulation

As mentioned above, the main idea in this work was to implement co-simulation couplings for multiple sub-models, and has here been implemented and evaluated for two sub-models representing two hydraulic cylinders, and the FMU was configured to contain the necessary ports for these sub-models. This feature facilitates co-simulation of more than one component, or region, and it can be used for several important areas of fluid-structure interaction mechanisms in the simulation model.

Figure 4 shows a general picture where the FMU from the presented work of Andersson et al. [6] is shown at the top, which is configured for one sub-model. At the bottom is an FMU shown configured for an arbitrary number of interface ports. This implementation only supports one FMU on the Hopsan side and one FE-model, but the interface can handle more than one sub-model as long as it is connected to the same FMU and to the same FE-model.

The interface was evaluated for two sub-models and the upper limit of the number of connections is not examined. The FMU was reconfigured using the FMU-generator and the new ports were added in the configuration file. The system simulation model in Hopsan was extended to also include the necessary components for the control valve, which were connected to the added hydraulic- and mechanical ports on the redefined FMU. On the LS-DYNA side, the FE-model was redesigned to also include the structural parts of the control valve, and the element segments for each cavity were specified in the UDF.

4 Simulations and Results

As discussed above, a simple fluid power model of a hydraulic percussion unit was set-up in order to validate the co-simulation method for an extended number of hydraulic cylinders. This model contains two hydraulic cylinders, the first represents the main piston and the second is representing the control valve, which concludes the main structural parts that affects the fluid-structure coupling in a hydraulic percussion unit. The model reflects important features, such as short duration dynamics in the fluid and the structural systems.

A reference model was set-up in Hopsan, where the fluid system consists of two hydraulic cylinders, the necessary fluid volumes, a valve and the pressure supply component, see Figure 5a. The valves, controls the oil flow to each cylinder, while Cavity A - D represent the fluid properties of the oil volumes inside each cylinder, also shown in Figure 6. The fluid properties used for the hydraulic oil can be found in Table 1. A point mass, representing a rigid body, is connected to the piston part of each hydraulic cylinder. Each

Table 1: The fluid and solid material properties used in the simulations

Quantity	Material	Symbol	Unit	Value
Bulk modulus	Oil	K	GPa	1.6
Density	Oil	ρ_{oil}	kg/m^3	890
Elastic stiffness	Steel	E	GPa	210
Poissons ratio	Steel	ν	–	0.3
Density	Steel	ρ_{steel}	kg/m^3	7850

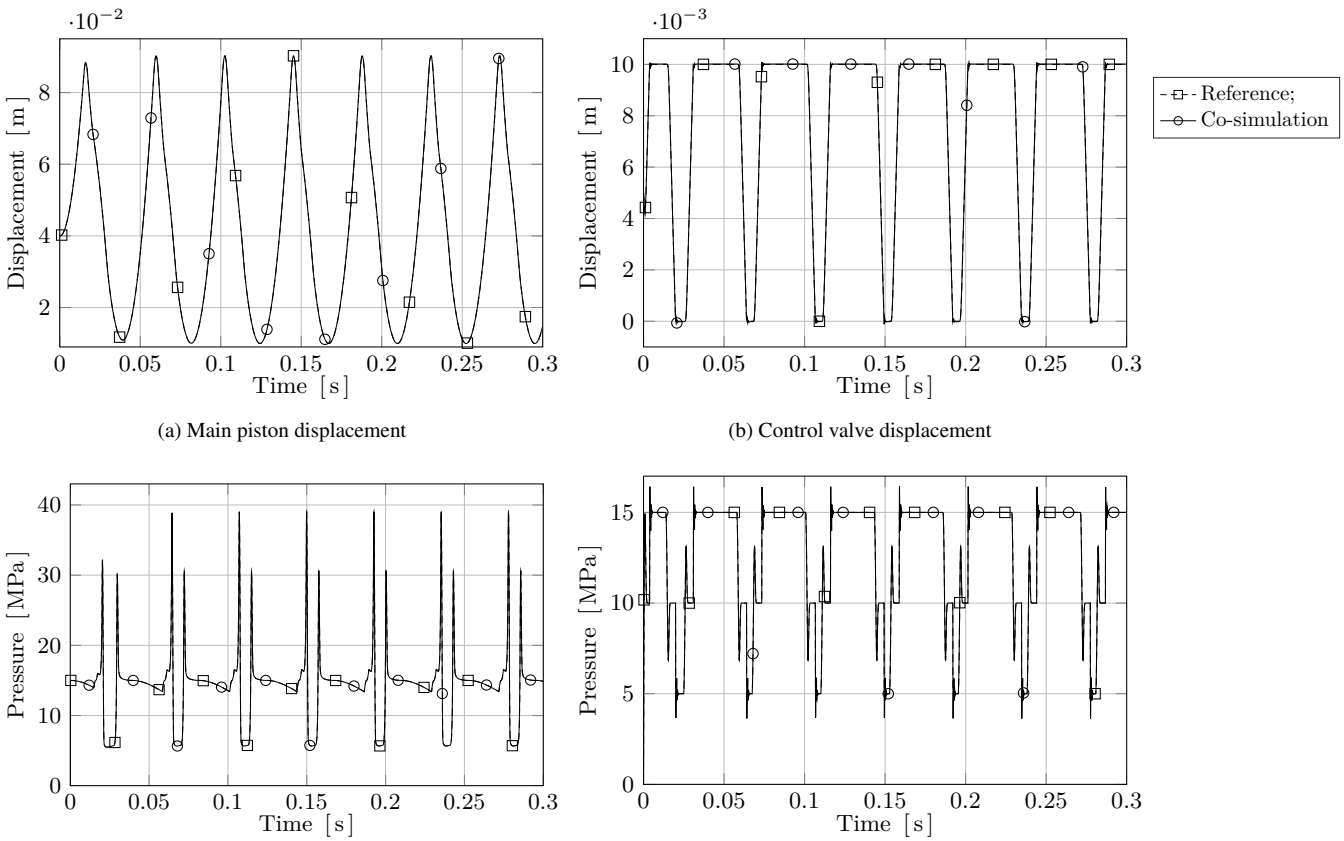

(a) Main piston displacement

(b) Control valve displacement

(c) Pressure in piston Cavity A

(d) Pressure in control valve Cavity C

Figure 7: Simulation results from Case 1, showing the difference between the reference and the co-simulation models

valve is controlled by a network of logical components, the control circuit, see Figure 5a. The position of the control valve controls the main piston valve and vice versa. Signals are generated at pre-determined positions for each cylinder to achieve the reciprocal movement for the main piston. A hydraulic damping mechanism for the main piston is used to prevent mechanical impact at the outer end position, see Damping in Figure 5a. This mechanism significantly increases the pressure above the normal level in Cavity B when the piston reaches a pre-set position that is located a small distance inside the mechanical end point. The increased pressure will cause the piston to stop and reverse inwards. When the piston is inside the pre-set position again the pressure will decrease to the normal level. Several sensors, see the meters in Figure 5, were used to collect data during the simulation. The displacement and the velocity sensors are connected to each of the pistons and the pressure sensors are connected to Cavity A and C. The reference system model is completely simulated in Hopsan and its results are used as a reference during the evaluation of the co-simulation results. A second system model was defined for the co-simulation approach, see Figure 5b. This is identical to the reference model, except for the hydraulic cylinders. The cylinders have been replaced by the imported FMU. The FMU is for this example configured to contain interface ports for two cylinders. This system model uses the FE-model shown in Figure 6 for co-simulation with LS-DYNA.

The FE-model of the hydraulic cylinder assembly consists of the main piston, the control valve, the liners and the housing parts. The mesh consists of 7211 8-node hexahedral- and 9855 4-node tetrahedral solid elements, which gives a total number of 17066 elements. All tetrahedral elements belong to the main housing. A full integration scheme was used for all solid elements. The liners and the housing parts are rigidly connected to each other by tied contacts in LS-DYNA. Typical elastic material properties for steel were used in the FE-model, see Table 1. Due to symmetry, a quarter model is used, and the associated boundary conditions are applied to the nodes on the symmetry planes. The main piston and the control valve are free to move in the axial direction, but due to symmetry constrained in all the other directions. The axial mechanical end points for these components are defined by surface to surface contact definitions. Oil is present at the contact surfaces that will dampen the contact forces. This behaviour is accounted for by introducing a viscous dampening for the contact definition. A factor of 60% of the critical viscous damping was applied. The axial movement of the cylinder housing is constrained due to the fixed boundary condition on the end surface and the other directions are constrained due to symmetry. The total mass for each part is defined by the FE-mesh and the material density. Since a quarter FE-model is used, a scaling routine implemented in the co-simulation in-

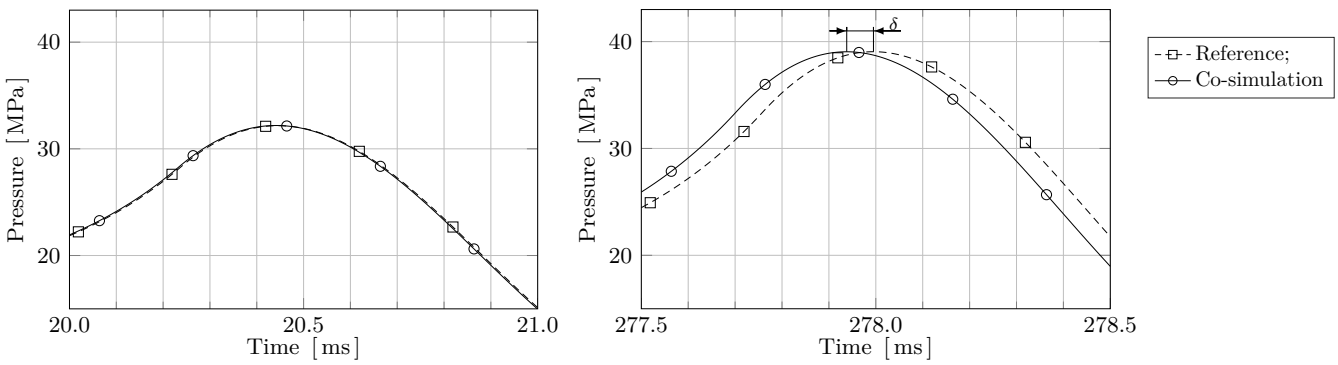

(a) First pressure peak

(b) Second last pressure peak

Figure 8: These curves are the same as in Figure 7c but shown at a much smaller time scale. A time period of 1.0 ms is displayed around a) the first and b) the second last pressure peak. The parameter δ denotes the time shift between the two simulation systems

terface was utilised to get the equivalent full model response on the Hopsan side. Each cylinder has two hydraulic control surfaces that are associated with its respective cavity. The pressure, based on c and Z_c, from the Hopsan simulation is applied to all element segments that belong to each cavity. A control routine keeps track of when the element segment on the moving part is inside or outside the cavity. When the segment is outside the cavity the pressure is removed, and when it has moved inside again the pressure is restored.

The start values for the simulation, at $t = 0$ s, were as follows: main piston position $u = 0.04$ m, control valve position $u = 0.005$ m, velocity and acceleration for the main piston and the control valve, $\dot{u} = \ddot{u} = 0$, pressure in all cavities, $p = 10^5$ Pa. At the start of the simulation a pressure of $p = 15$ MPa at the Supply sub-model will be transferred to each component in the hydraulic circuit. When the pressure increase reaches the main piston and the control valve, they will start to move and this event determines the starting point for the first working stroke, and the main piston will reach a steady state behaviour after a few working cycles.

The co-simulation method for two hydraulic cylinders has been evaluated through two different simulation cases. These are:

Case 1	Hydraulically controlled main piston and control valve, with rigid body representations
Case 2	Hydraulically controlled main piston and control valve with linear elastic material properties for the structural parts. Repeated impacts against an elastic cylinder is analysed

Case 1 represents, for the main piston, a moving mass that is purely driven by hydraulic pressure and no external loads are applied, and for the control valve the mass is moving between its mechanical end points. The contact mechanism is not modelled in Hopsan, but in LS-DYNA and will therefore give rise to a difference between the two simulation models. These forces will affect the motion of the valve at the end points. Case 2 gives a demonstration of the method when somewhat more realistic conditions, such as elastic materials and real contact definitions, are used. This makes it possible to simulate deformations, stresses and strains. For Case 1 the co-simulation results are investigated and compared with the results from the reference model in Hopsan. This is not possible for Case 2 since the impact mechanism between the piston and the tool can not be modelled using the standard components libraries in Hopsan.

The simulations were run on an Intel Xeon E5-1660 (3.0 GHz, 8 core) workstation with 32 GB RAM under Windows 7 (64-bit). Eight processor cores with shared memory were used for the LS-DYNA analyses and one core for the Hopsan analyses. Both Hopsan and LS-DYNA were run on the same computer.

4.1 Case 1

This case simulates the effects when hydraulic pressure is applied to both the main piston and the control valve. The time step $T = 10^{-6}$ s was used here based on a convergence study of the Hopsan reference model, cf. Fig. 5a. The method for this convergence study was as follows: The simulations were made using the following time step values, $T_i = 10^{-i}$ s. From each simulation, using the time step T_i, the piston displacement u_{T_i}, cf. Fig. 7a, was extracted and the Root Mean Square (rms) value for this signal was calculated, $u_{T_i rms}$. The reference value, $u_{T_{i+1} rms}$, was calculated from a simulation performed with a time step one decade shorter, i.e. T_{i+1}. The error ε_i was defined according to Eq. 8. The procedure was repeated until the error level was below 0.1%, which was considered acceptable for this application. An error level of $\approx 0.07\%$ was reached for $i = 6$, which gives a time step of $T = 10^{-6}$ s.

$$\varepsilon_i = \frac{u_{T_i rms}}{u_{T_{i+1} rms}} \tag{8}$$

The parasitic masses for each hydraulic cavity were estimated and is found in Table 2. The parasitic masses were found to be very small and can be neglected in comparison to the mass of the main piston and the control valve.

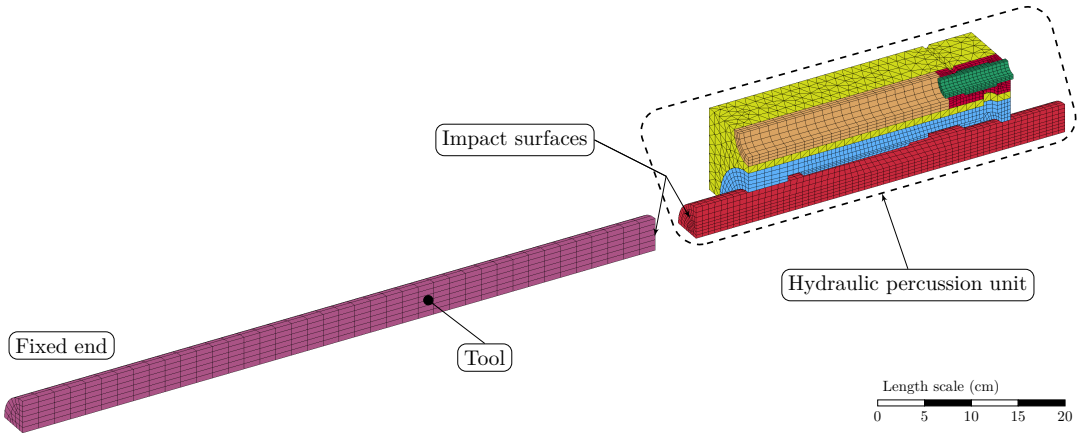

Figure 9: The FE-model used in Case 2. The hydraulic percussion unit is the same as in Case 1, see Figure 6, except for the elastic material properties. The left cylindrical part represents the tool. The left end of the tool is rigidly fixed and on the other surfaces symmetry conditions are applied

The computational time for the co-simulation was approximately 7 minutes and for the pure Hopsan reference model 0.3 s. Simulation results are shown in Figure 7.

Figure 7a shows that the main piston moves in and out of the housing with a stroke length of ∼0.08 m at an impact frequency of ∼23 Hz, and Figure 7b shows that the control valve is moving 0.01 m between its mechanical end positions. It can be seen that the results for the reference and the co-simulation model coincide. This was to be expected since the two system models are the same except for the piston movement simulation. In Figure 7c it can be seen that the curves are right on top of each other, but when the curves are examined at a greater magnification, a maximum time shift of ∼57 μs can be noticed at the second last pressure peak, see Figure 8. It was also found that the time shift is increasing throughout the simulation.

The pressure curve, Figure 7c, shows that the simulation method is able to handle short duration dynamics in the fluid system, causing pressure peaks of high amplitude and a duration of approximately 1.5 ms. The results also show that the piston reaches a steady state behaviour after two working cycles, which implies that this method is stable for this simulation model. The FE-results in this case consist of the piston movement and the forces that are acting on the piston.

4.2 Case 2

In the second simulation case elastic material properties were used to evaluate deformations, stresses and strains in the structural parts. A tool was also added to simulate the impact from the main piston on the tool and to analyse the responses in the structure and in the fluid. The system simulation model used is found in Figure 5b. A straight cylindrical part that represents a typical tool for a hydraulic hammer was added to the previous FE-model, see Figure 9. This set-up is used to give a more realistic picture of the structural responses that occurs in the hydraulic percussion unit when the fluid-, and structural-couplings are accounted for. The far end from the impact surface of the tool was rigidly fixed and the other surfaces are constrained due to symmetry conditions. The elastic material properties stated in Table 1 were used in the FE-model to simulate the elastic behaviour. The mesh for the tool consists of 1040 fully integrated 8-node hexahedral solid elements that gives a total number of elements of 18106. In order to reduce the noise in the stress results an appropriate amount of structural damping that correspond to a loss factor of ∼1.5%, was applied in the FE-model. The time step used here was $1.76 \cdot 10^{-7}$ s to fulfil the Courant-Friedrichs-Lewy condition, i.e. the smallest element size in the FE-model determines the maximum time step [1], resulting in a computational time of 1 hour and 50 minutes. The other parameters in the Hopsan model were the same as in Case 1.

Table 2: Estimation of the parasitic inductances for this case

	Cavity				
Parameter	A	B	C	D	
Volume	$151.1 \cdot 10^{-6}$	$21.3 \cdot 10^{-6}$	$7.50 \cdot 10^{-6}$	$2.61 \cdot 10^{-6}$	m^3
$Z_{c,fluid}$	$1.76 \cdot 10^7$	$8.35 \cdot 10^7$	$35.6 \cdot 10^7$	$68.2 \cdot 10^7$	Pa·s/m^3
Parasitic mass	$7.9 \cdot 10^{-6}$	$3.2 \cdot 10^{-6}$	$14 \cdot 10^{-6}$	$39 \cdot 10^{-6}$	kg
Component mass	11.2	11.2	0.3	0.3	kg

The results, shown in Figure 10, indicate that the percussion unit reaches a steady state condition after only a few working strokes. The values for the piston movement are calculated by averaging over the nodes on the piston impact surface. The piston displacement curve, Figure 10a, shows that the piston follows the same sequence as described in Case 1. The difference is that an elastic impact is simulated in this case, instead of driving the piston against the hydraulic damping mechanism. The impact on the tool occurs at a position of 0.085 m. A stress wave is generated at the piston impact surface at the time of impact, and the noise in the pressure curve, see Figure 10c, after the first impact, represents the stress wave travelling back and forth in the piston. The pressure curve, Figure 10c, is very similar to the curve in Case 1 and it follows the same pattern. The hydraulic pressure in Cavity A shows a rapid variation at the time of impact, see region N in Figure 10c. At this time the piston 'bounces' on the tool and the piston moves away from the tool. This movement will cause

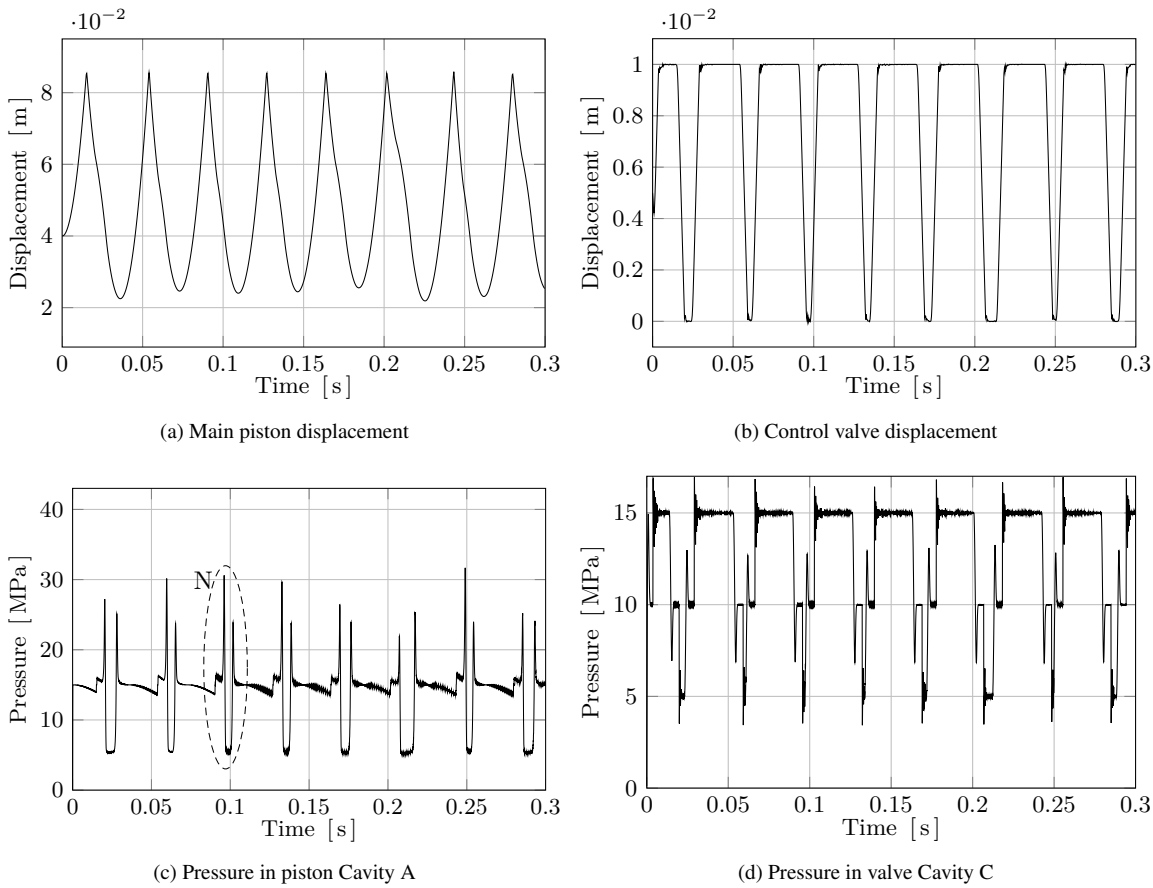

(a) Main piston displacement

(b) Control valve displacement

(c) Pressure in piston Cavity A

(d) Pressure in valve Cavity C

Figure 10: Simulation results from Case 2. Region N indicates the pressure behaviour at the time of impact

an increased pressure in the fluid contained in Cavity A, since the piston is moving back into the cavity. As the pressure increases in the cavity the fluid force on the piston will also increase, and this will affect the piston movement.

Figure 11 and 12 show some examples of FE-results that are available from the simulation. In this case the equivalent von Mises stress is shown, but also displacements are available. The transient stress curve in Figure 12 exhibits the same behaviour as the pressure curve from Cavity A, cf. Figure 10c.

5 Discussion

In this work a previously presented co-simulation method [6] has been extended to include an increased number of submodels for co-simulation, which has been used to increase the number of hydraulic cylinders in the simulation model (FE-model). This has been analysed through two different simulation cases and deviations from a reference model are in this case negligible. No similar work within this area have been found in the literature.

The FMU was configured for two hydraulic cylinders using the co-simulation interface configuration software. This resulted in twice as many ports on the FMU as before and twice as much data were also needed to be communicated over the interface, which will experience twice as high load as evaluated in the previous work. Note that the limiting number of ports was not analysed in this paper. This is of course an important aspect that needs further evaluation.

In Case 1 a co-simulation of a 1D hydraulic system model and a 3D structural FE-model was studied. Here two hydraulic cylinder components were co-simulated, representing the main piston and the control valve of a hydraulic percussion unit, respectively. The comparison between the results from the reference and the co-simulation model shows an identical behaviour, except for a small time shift. The time shift is probably caused by:

- The implementation approximation according to Eq. 4
- Since different solving techniques are used by Hopsan and LS-DYNA, numeric differences are unavoidable, which also will be accumulated throughout the simulation and result in an increasing absolute error

Here a simulation time period of 0.3 ms was used and during this period 7–8 working cycles were completed, and a time shift error of $\sim$57 μs for the last working cycle was noticed. From an industrial point of view and for this application, this error can be considered negligible.

Another difference between the models is the modelling of the contact mechanics for the control valve at the mechanical end points. In Hopsan these contacts are perfectly inelastic, which

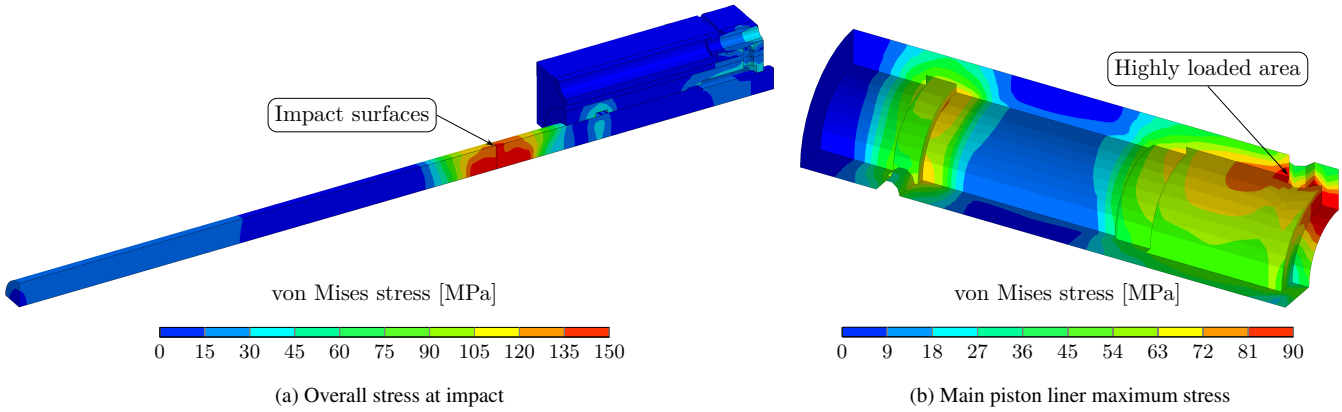

(a) Overall stress at impact

(b) Main piston liner maximum stress

Figure 11: FE results from Case 2, showing a) the von Mises stress in the piston and tool at the time of impact, b) the maximum von Mises stress in the Main piston liner during the analysis, $t = 286.3$ ms. Notice that different fringe-levels are used

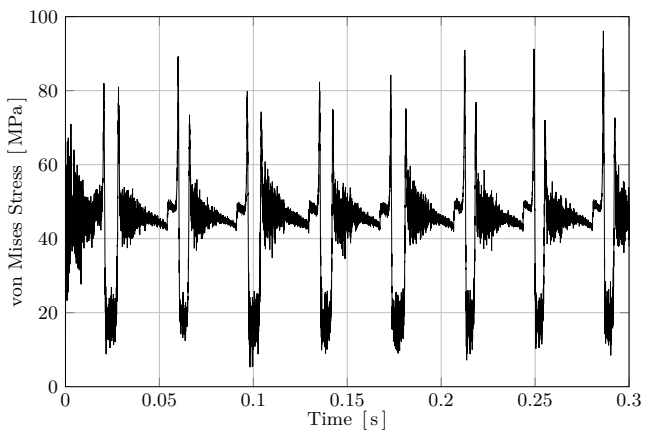

Figure 12: Time history FE-results from Case 2. Stress results from an element at the highly loaded area, shown in Figure 11. The load cycle in the material becomes very clear

means that the control valve will attach to the end point once it is reached. In the co-simulation model the contact mechanics are defined in the LS-DYNA model, and here is the contact of an elastic nature. This means that the momentum of the control valve during the collision will be preserved, and this will cause the control valve to bounce when it hits the end point. In order to reduce the bounces a reasonable amount of contact damping was applied. However, this is not expected to be too unphysical since the collision will occur when oil is present at the contact surfaces, which will reduce the contact forces.

In Case 1 a short duration/high amplitude pressure peak arises in Cavity A, see $t \approx 0.28$ s in Figure 7c. This is an effect of an important mechanism for a hydraulic percussion unit that is captured by the used simulation technique. The identified behaviour indicates that correct and stable results are obtained, and that short duration dynamics are resolved.

Case 2 is meant as a demonstration of the proposed method for an industrial application, closer to reality. No reference model was used for comparison here because no deformable bodies are implemented in Hopsan. The fluid system is the same as before, but the FE-simulation is somewhat more complex due to the deformable bodies and the contact calculations for the impact. The co-simulation coupling method will also be more stressed than in the first case, since the effects of stress waves must be handled. The results from the fluid simulation is similar to the first case. The noise in the pressure curves of Cavity A and C, Figure 10c and 10d, is caused by the stress waves that are travelling back and forth in the components.

The FE-results here chosen consist of deformation and stresses for the whole 3D-geometry and for the simulated time period. The second case shows that the proposed method is capable of simulating the coupled fluid-structure problem where complex dynamic properties, such as mechanical contacts and changing direction of flow, are present. The coupling between the structural- and fluid dynamics that is captured in the proposed co-simulation method is difficult, or impossible, to achieve with decoupled simulation models.

6 Acknowledgements

The authors would like to thank the project initiator Erik Sigfridsson and Atlas Copco Construction Tools for funding the project. Furthermore, Mr Peter Nordin and Dr Thomas Borrvall are greatly acknowledged for all their help with developing the co-simulation interface.

7 Concluding Remarks

This paper presents a method to co-simulate multiple components of 1D-fluid and 3D-structural models. In order to represent the real mechanisms in a hydraulic percussion unit to a larger extent, this was considered to be a fundamental functionality for a new simulation method. As presented in the previous work [6], the fluid system is modelled in a 1D-system simulation tool and a conventional FE-system is used for the 3D structural simulation. Full 3D results will be available to be used in stress analysis, fatigue assessments or acoustical radiation analysis. The method for simulating the fluid system will capture important system dynamic behaviour without the need for 3D CFD methods, which will give

a computationally very efficient fluid simulation.

The most important contributions from this work are:

- A co-simulation method for multiple fluid-structure couplings has been developed
- The implemented co-simulation interface, which is based on the FMI-standard and TLM, is shown to also support multiple sub-models for co-simulation
- Full 3D results and time history data from the structural FE-simulation are available for a more complete model of a hydraulic percussion unit

References

[1] LSTC. *LS-DYNA Theory Manual*. Livermore Software Technology Corporation, Livermore, USA, 2015.

[2] ANSYS. Inc. *ANSYS Multiphysics User's Guide*. Canonsburg, Pennsylvania, USA, 2015.

[3] Y Wang, J Feng, B Zhang, and X Peng. Modeling the valve dynamics in a reciprocating compressor based on two-dimensional computational fluid dynamic numerical simulation. *Proceedings of the Institution of Mechanical Engineers, Part E: Journal of Process Mechanical Engineering*, 227(4):295–308, 2013.

[4] R Campbell and E Paterson. Fluid–structure interaction analysis of flexible turbomachinery. *Journal of Fluids and Structures*, 27(8):1376–1391, 2011.

[5] R Sinha, C. J. J Paredis, V.-C Liang, and P. K Khosla. Modeling and simulation methods for design of engineering systems. *Journal of Computing and Information Science in Engineering*, 1(1):84, 2001.

[6] H Andersson, P Nordin, T Borrvall, K Simonsson, D Hilding, M Schill, P Krus, and D Leidermark. A co-simulation method for system-level simulation of fluid–structure couplings in hydraulic percussion units. *Engineering with Computers*, pages 1–17, 2016.

[7] M Axin, R Braun, A Dell'Amico, B Eriksson, P Nordin, K Pettersson, I Staack, and P Krus. Next generation simulation software using transmission line elements. In *Fluid Power and Motion Control*, Bath, England, October 2010.

[8] T Blochwitz, M Otter, J Åkesson, M Arnold, C Clauss, H Elmqvist, M Friedrich, A Junghanns, J Mauss, D Neumerkel, H Olsson, and A Viel. Functional mockup interface 2.0: The standard for tool independent exchange of simulation models. In *Proceedings of the 9th International Modelica Conference*, pages 173–184, Munich, Germany, September 2012.

[9] G Rauch, J Lutz, M Werner, S Gurwara, and P Steinberg. Synergetic 1D-3D-coupling in engine development part i: Verification of concept. Technical report, SAE Technical Paper, 2015.

[10] P Bayrasy, M Burger, C Dehning, I Kalmykov, and M Speckert. Applications for MBS-FEM-coupling with MpCCI using automotive simulation as example. In *Proceedings of the 2nd Commercial Vehicle Technology Symposium (CVT 2012)*, pages 385–394, Kaiserslautern, Germany, March 2012.

[11] R Braun, L Ericsson, and P Krus. Full vehicle simulation of forwarder with semi active suspension using co-simulation. In *ASME/BATH 2015 Symposium on Fluid Power and Motion Control*, Chicago, USA, October 2015.

[12] A Siemers, D Fritzson, and I Nakhimovski. General meta-model based co-simulations applied to mechanical systems. *Simulation Modelling Practice and Theory*, 17(4):612–624, 2009.

[13] B Eriksson, P Nordin, and P Krus. Hopsan NG, a C++ implementation using the TLM simulation technique. In *The 51st Conference On Simulation And Modelling*, Oulu, Finland, 2010.

[14] P Krus, A Jansson, J.-O Palmberg, and K Weddfelt. Distributed simulation of hydromechanical systems. In *The Third Bath International Fluid Power Workshop*, Bath, England, 1990.

[15] J Larsson and P Krus. Stability analysis of coupled simulation. In *ASME 2003 International Mechanical Engineering Congress and Exposition*, volume 1, pages 861–868, 2003.

[16] D. M Auslander. Distributed system simulation with bilateral delay-line models. *Journal of Basic Engineering*, 90(2):195–200, 1968.

[17] T. J Viersma. *Analysis, Synthesis and Design of Hydraulic Servosystems and Pipelines*. Elsevier Scientific Publishing Company, Amsterdam, The Netherlands, 1980.

[18] T Belytschko, W. K Liu, B Moran, and K Elkhodary. *Nonlinear finite elements for continua and structures*. John Wiley & Sons, 2013.

A study on a mathematical model of gas in accumulator using van der Waals equation

Shuto Miyashita*, Shuce Zhang**, and Kazushi Sanada***

* Department of Mechanical and Control Engineering, Graduate School of Science and Engineering
Tokyo Institute of Technology, Ookayama, Tokyo, Japan
** Department of Systems Integration, Graduate School of Engineering
Yokohama National University, Yokohama City, Japan
*** Faculty of Engineering, Yokohama National University, Yokohama City, Japan
E-mail: sanada-kazushi-sn@ynu.ac.jp

Abstract

As mathematical models of hydraulic accumulator, thermodynamics, heat transfer, and gas models are briefly described, including the isothermal and the adiabatic equations of the van der Waals equation. Measurement of gas behavior using a bladder type accumulator and a piston type accumulator was carried out. Measured data of a discharge test of the bladder accumulator and a charge test of the piston type accumulator were used to validate the models.

Keywords: Accumulator, Gas model, Van der Waals equation, Oil-hydraulics

1 Introduction

An accumulator is an important component for oil-hydraulic circuits. Because of complexity of gas behavior in the accumulator, it is not easy to do accurate prediction of the accumulator performance. There have been many research papers on modeling the gas behavior of the accumulator. Otis introduced a concept of the thermal time constant representing heat transfer effect [1][2][3].

In addition to the heat transfer effect and thermodynamics, a real gas model is needed to predict the accumulator performance. Beattie-Bridgeman equation [3] and Soave-Redlich-Kwong equation [4] are typical mathematical models. The van der Waals equation is a basis of these real gas models. It is easy to treat the van der Waals equation mathematically. For examples, the adiabatic equation and the isothermal equation are established as simple mathematical equations.

In this study, an experiment of a bladder type accumulator and a piston type accumulator was performed. These accumulators were connected to each other. Discharge process and charge process of the accumulators were measured simultaneously. The measured data were used to validate the adiabatic and the isothermal equation of the van der Waals equation.

In the section 2, a mathematical model of accumulator using thermodynamics and heat transfer are briefly introduced. Ideal gas model and real gas models are described in the section 3. Measurement of a bladder type accumulator and a piston type accumulator is explained in the section 4. In the section 5, the adiabatic equation and the isothermal equation of the van der Waals equation are validated with the measured data. Finally, results are summarized in the section 6.

2 Accumulator model

In a mathematical model of gas-charged accumulator, thermodynamics, heat transfer and a gas model are considered. In this section, the thermodynamics and the heat transfer are briefly introduced[3].

Energy balance of accumulator is shown in Figure 1. Nitrogen gas of mass, m_{gas}, has internal energy of u. The nitrogen gas receives thermal energy Q from the surroundings and performs work W to the surroundings. Mathematical modelling begins by the conservation of energy equation:

$$m_{gas}\frac{du}{dt} = \frac{dQ}{dt} - \frac{dW}{dt}. \tag{1}$$

Heat transfer between gas and the surroundings is represented by:

$$\frac{dQ}{dt} = hA(T_w - T). \tag{2}$$

Rate of work output is:

$$\frac{dW}{dt} = P\frac{dV}{dt}. \tag{3}$$

Change of internal energy of gas is represented by:

$$du = c_v dT + \left[T\left(\frac{\partial P}{\partial T}\right)_v - P\right] dv \tag{4}$$

Substituting Eq.(2), Eq. (3), and Eq.(4) to Eq.(1) yields:

$$\tau\frac{dT}{dt} + T = T_w - \frac{T\tau}{c_v}\left(\frac{\partial P}{\partial T}\right)_v \frac{dv}{dt}. \tag{5}$$

The parameter τ is called the thermal time constant:

$$\tau = \frac{m_{gas}c_v}{hA}. \tag{6}$$

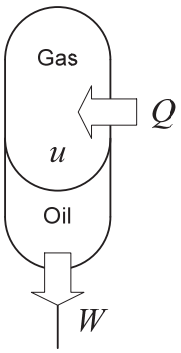

Figure 1: Energy balance of accumulator

The concept of thermal time constant, Eq.(6), represents heat transfer between gas and the surroundings through rubber bag and vessel wall. Figure 2 is a plot of charged-gas pressure. A quick compression process from A to B increases the gas pressure. Due to the quick compression, gas temperature is increased. Then thermal energy of gas will be transferred to the surroundings through the rubber bag and the wall of the accumulator. Due to the heat transfer, gas pressure decreases gradually as shown in Figure 2. The thermal time constant τ is the time it takes for the gas pressure to drop by 63.2 percent.

3 Mathematical models of gas in accumulator

As shown in Figure 3, during the charge process from A to B and the discharge process from C to D, gas volume changes between V_1 and V_2. The PV diagram is shown in Figure 4. The process from A to B is the charge process. Gas volume decreases from V_1 to V_2. The process from C to D is the discharge process. Gas volume increases from V_2 to V_1. Gas pressure changes depending on the volume and the state change of gas. Models of state change of gas are ideal gas model and real gas model.

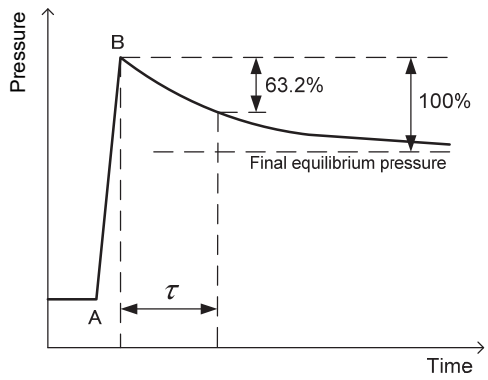

Figure 2 Thermal time constant [3]

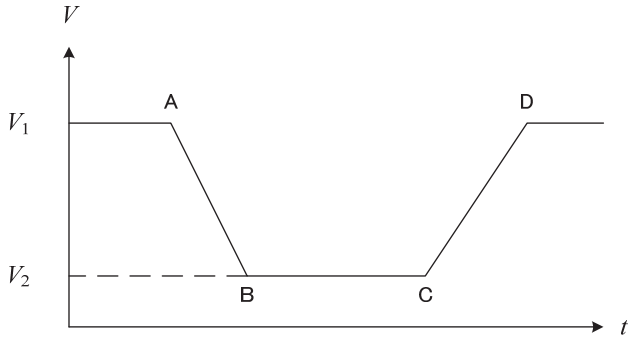

Figure 3 Volume change of gas in the accumulator

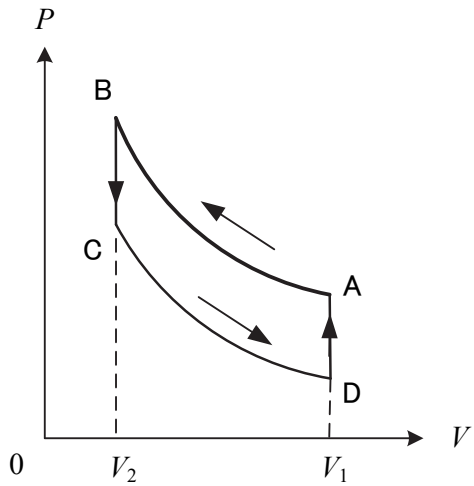

Figure 4 P-V diagram of accumulator gas

3.1 Ideal gas model

The ideal gas model is a virtual model in which volume of gas molecule and intermolecular force are ignored. Ideal gas state equation is

$$PV = mRT. \tag{7}$$

This equation represents the relationship of state variables, such as pressure, volume, and temperature.

For isothermal change of ideal gas, the relationship between absolute pressure P and volume V is represented by:

$$PV = \text{Const.}, \tag{8}$$

which is known as the Boyle's law.

For adiabatic change of ideal gas,

$$PV^{\kappa} = \text{Const.}, \tag{9}$$

where κ is a specific-heat ratio.

For the case in which the state of ideal gas changes in between isothermal and adiabatic conditions, the polytropic change of state is used:

$$PV^{n} = \text{Const.}, \tag{10}$$

where n is the polytropic exponent.

3.2 Real gas models

It is well known that every material has three phases, such as solid, liquid, and gaseous phases as shown in Figure 5. The state of material is determined by temperature and pressure. By the change of temperature and pressure, the state of material may change. A boiling point is the temperature at which liquid state changes to gaseous state. The higher the pressure, the higher the boiling point. However, the increase of the boiling point is limited. The maximum limit of the boiling point is the critical point. When material exits under temperature and pressure beyond the critical point, the state is called "super critical fluid". The super critical fluid has both gaseous and liquid characteristics. In Table 1, critical properties of nitrogen gas are listed. These critical properties are used for real gas models.

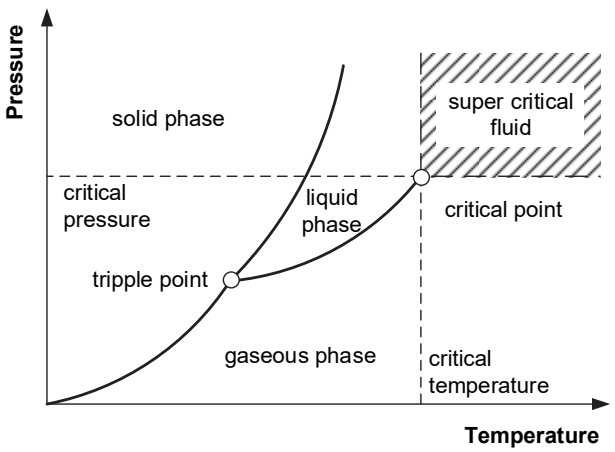

Figure 5 Phase diagram and super critical fluid

Table 1 Critical properties of N_2 gas

Critical pressure	P_c	3.394388 MPa, abs.
Critical specific volume	v_c	9.003×10^{-5} m^3/mol
Critical temperature	T_c	126.1 K
Gas constant	R	8.314501 J/(Kmol)

The van der Waals equation is a basic equation of real gas model:

$$\left(P + \frac{am^2}{V^2}\right)(V - mb) = mRT. \tag{11}$$

The parameters a and b are calculated from the critical properties:

$$a = \frac{9}{8} R v_c T_c\,, \tag{12}$$

$$b = \frac{1}{3} v_c. \tag{13}$$

Assuming constant temperature, the isothermal equation is obtained:

$$\left(P + \frac{am^2}{V^2}\right)(V - mb) = \text{const.} \tag{14}$$

The equation of state for adiabatic process of the van der Waals equation of state is

$$\left(P + \frac{am^2}{V^2}\right)(V - mb)^H = \text{const.} \tag{15}$$

where the adiabatic exponent H is

$$H = \frac{R}{c_v} + 1. \tag{16}$$

The isothermal equation of the van der Waals equation, Eq.(14), and the adiabatic equation of the van der Waals equation, Eq.(15), correspond to those of ideal gas, Eq.(8) and Eq.(9), respectively. The adiabatic exponent H of Eq.(16) of the van der Waals equation corresponds to the specific-heat ratio κ of Eq.(9) of ideal gas. For real gas, the adiabatic exponent H is not identical to the specific-heat ratio κ. In ideal gas case, because of the Mayer law, $c_p - c_v = R$, the adiabatic exponent H is equal to the specific-heat ratio $\kappa = c_p/c_v$.

A more accurate real gas model is the Beattie-Bridgeman model [1][2]. The Beattie-Bridgeman equation is more complex:

$$P = \frac{RT}{v} + \frac{\beta}{v^2} + \frac{\gamma}{v^3} + \frac{\delta}{v^4}. \tag{17}$$

Pourmovahed [3] used the Benedict-Webb-Rubin equation which is much more complex:

$$P = \frac{RT}{v} + \frac{\left(B_0RT - A_0 - \frac{C_0}{T^2}\right)}{v^2} + \frac{(bRT - a)}{v^3} + \frac{a\alpha}{v^6} + \frac{c\left(1 + \frac{\gamma}{v^2}\right)e^{-\gamma/v^2}}{v^3T^2}. \quad (18)$$

A commercial software AMESim [5] uses the Soave-Redlich-Kwong model [4]:

$$\left(P + \frac{a\alpha(T)}{v(v+b)}\right)(v - b) = RT. \quad (19)$$

$$a = \frac{0.4278R^2T_c^2}{P_c} \quad (20)$$

$$b = \frac{0.0867RT_c}{P_c} \quad (21)$$

$$\alpha(T) = \left[1 + m\left(1 - \sqrt{1 - \frac{T}{T_c}}\right)\right]^2 \quad (22)$$

Hansen and Rasmussen [6] carried out experiments using a piston accumulator for wind turbines under a wide range of temperature. They compared the Benedict-Webb-Rubin Equation and the Soave-Redlich-Kwong equation with the experiments and concluded that the Soave-Redlich-Kwong equation is more efficient and accurate enough for wind turbine applications.

It is known that the van der Waals equation has limited accuracy. Improved real gas models have been used, such as the Soave-Redlich-Kwong equation. However, the van der Waals equation is easy to treat mathematically. For examples, the adiabatic equation and the isothermal equation can be derived from the van der Waals equation, as introduced by Eq.(14) and Eq.(15).

4 Measurement of gas behavior

In this study, experiments were carried out to measure gas behavior during charge and discharge processes using a bladder type accumulator and a piston type accumulator. An experimental circuit is shown in Figure 6. The bladder type accumulator (a) and the piston type accumulator (b) were connected by a valve (e). The oil-hydraulic pump (f) with the relief valve (k) supplied pressurized oil to one of the accumulators. By opening the stop valve (g) and closing the valves (e), (h), (i) and (j), the pump prefilled the bladder type accumulator (a). The condition was kept for seven hours to reach steady state condition of temperature of the accumulators. All windows in the laboratory were covered by black cardboards to keep the room temperature. Temperature of the room was regulated by air condition. By opening the valve (j), the piston type accumulator (b) was fully extracted. Closing the valve (g) and (j), and opening the valve (e), the bladder type accumulator was discharged and the piston type accumulator was charged. The piston displacement was measured by a potentiometer (d) and gas volume in the piston type accumulator was calculated. Gas volume in the bladder type accumulator was calculated based on the volume of oil charged in the piston type accumulator. The piston displacement, the surrounding temperature, and pressure of gas in both accumulators were recorded.

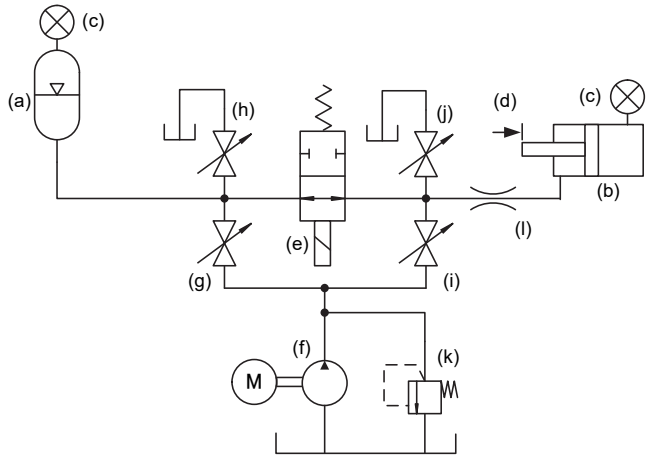

Figure 6 An experimental circuit using a bladder type and a piston type accumulators

5 Considerations

As an example of the measurements, a PV-diagram of a discharged test of the bladder type accumulator is shown in Figure 7. The discharge process was carried out by 10 seconds and the surrounding temperature was 301K. The black solid line is the measured results. The point A is the initial condition of 34.5 MPa, abs. and 2.65×10^{-3}m^3 (2.65L). By discharging, the gas volume increased to the point B and the gas pressure decreased. A broken line is calculated results of Eq.(15), the adiabatic equation of the van der Waals equation (indicated by "vdW(adiabatic)"). A dotted line is calculated results of Eq.(14), the isothermal equation of the van der Waals equation (indicated by "vdW(isothermal)"). In this particular measurement, the discharge process of 10 seconds showed similar behavior as the adiabatic equation of the van der Waals equation.

Measured results of a charge test of the piston type accumulator are plotted in Figure 8. The measurement was performed simultaneously as the data shown in Figure 7. The point A is the initial condition of 4.4 MPa, abs. and 7.4×10^{-3} m^3 (7.4L). The discharge process was carried out by 10 seconds and the surrounding temperature was 301K. The solid line is the measured results. By charging, the gas volume decreased and the gas pressure increased. The point B is the end of charge process. After the charge process, beyond the point B, the gas pressure decreased by about 0.6 MPa. It can be estimated that it was due to the heat transfer effect between the gas and the surroundings. The broken line and the dotted line are calculated results of the adiabatic equation of Eq.(15) and the isothermal equation of Eq.(14) of the van der Waals

equation. The measured results almost follow the adiabatic line, but there can be seen a certain degree of discrepancy from the adiabatic equation. As described in the reference [6], in the piston accumulator, thermal energy of gas can transfer directly through the accumulator wall to the surroundings. The adiabatic condition is not easy to establish. Heat conductive phenomenon inside the rubber membrane and the steel wall of accumulator is needed to investigate.

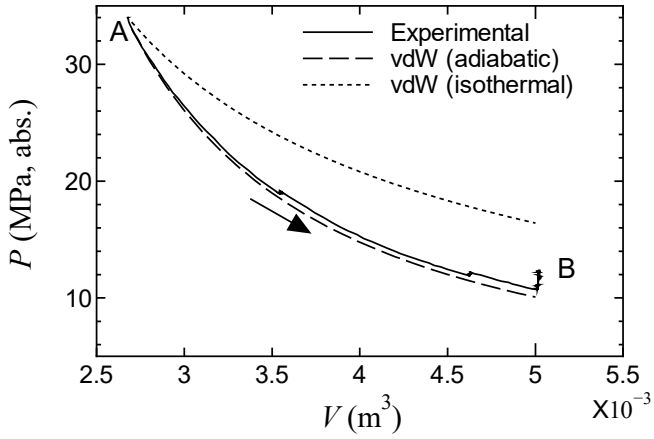

Figure 7 Measured results of discharge test of the bladder type accumulator and calculated results of the van der Waals equations (10s, 301K)

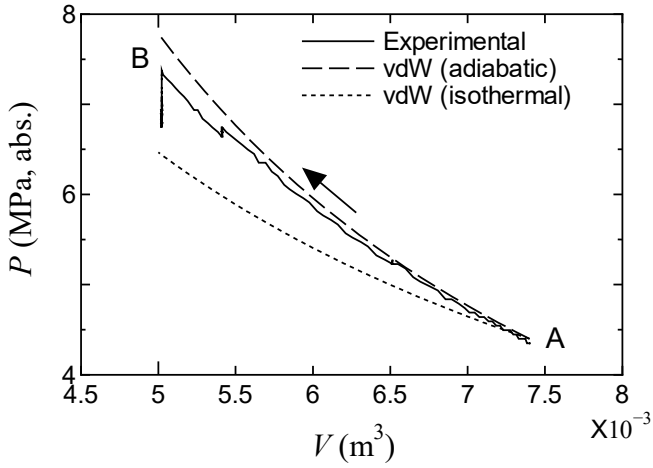

Figure 8 Measured results of charge test of the piston type accumulator and calculated results of the van der Waals equations (10s, 301K)

6 Conclusions

The van der Waals equation is a basis of real gas model. The isothermal and the adiabatic equation are established as a simple mathematical equation. In this study, measurements were performed using a bladder type accumulator and a piston type accumulator. These accumulators were connected to each other. Discharge and charge processes were measured simultaneously. The measured data were compared with the adiabatic equation and the isothermal equation of the van der Waals equation. The test processes of 10 seconds were almost approximated by the adiabatic equation of van der Waals equation. Other experiments of process time of longer than 10 seconds have been conducted. It is a future work to investigate these measured data by comparison of real gas models, such as the van der Waals equation and the Soave-Redlich-Kwong equation.

Nomenclatures

Designation	Denotation	Unit
A	surface area of wall	m^2
c_p	constant pressure specific heat	J/(kgK)
c_v	constant volume specific heat	J/(kgK)
h	heat transfer coefficient	$W/(m^2K)$
m	number of moles	-
m_{gas}	mass of gas	kg
n	polytropic exponent	-
P	absolute pressure of gas	Pa, abs.
Q	heat energy	J
R	gas constant	J/(kgK)
T	gas temperature	K
T_w	wall temperature	K
t	time	s
u	internal energy	J
v	specific volume	m^3/kg
V	gas volume	m^3
κ	specific-heat ratio	-
τ	thermal time constant	s

Acknowledgements

Professor Kitagawa and Professor Kagawa (Tokyo Institute of Technology) gave constructive comments and warm encouragement. Nippon Accumulator Co., Ltd. supported the experiments.

References

[1] D. R. Otis, New developments in predicting and modifying performance of hydraulic accumulators, *National Conference on Fluid Power*: 473-483, 1974.

[2] F. T. Elder, D. R. Otis, Accumulators: The role of heat transfer in fluid power losses, *4th International Fluid Power Symposium*: D2-27-D2-37, 1975.

[3] A. Pourmovahed, D. R. Otis, An experimental thermal time-constant correlation for hydraulic accumulator, *Transactions of the ASME, Journal of Dynamic Systems, Measurement, and Control*, Vol.112: 117-121, March 1990.

[4] G. Soave, Equilibrium constants from a modified Redlich-Kwong equation of state, *Chemical Engineering Science*, Vol.27, pp.1197-1203, 1972.

[5] LMS Amehelp, HA0021 – hydraulic accumulator with heat exchange (semi-perfect or real gas behavior), 2010.

[6] H. B. Hansen, P. W. Rasmussen, Modeling Hydraulic Accumulators for use in Wind Turbines, *The 13th Scandinavian International Conference on Fluid Power, SICFP2013*, p.327-324, 2013.

Displacement Control Strategies of an In-Line Axial-Piston Unit

L. Viktor Larsson and Petter Krus

Division of Fluid and Mechatronic Systems, Department of Management and Engineering
Linköping University, Linköping, Sweden
E-mail: viktor.larsson@liu.se, petter.krus@liu.se

Abstract

The need for efficient propulsion in heavy vehicles has led to an increased interest in hybrid solutions. Hydraulic hybrids rely on variable hydraulic pumps/motors to continuously convert between hydraulic and mechanical power. This process is carried out via the implementation of secondary control which, in turn, is dependent on a fast displacement controller response. This paper reports on a study of a prototype axial piston pump of the in-line type, in which the displacement is measured with a sensor and controlled using a software-based controller. A pole placement control approach is used, in which a simple model of the pump is used to parametrise the controller using desired resonance and damping of the closed loop controller as input. The controller's performance is tested in simulations and hardware tests on the prototype unit. The results show that the pole placement approach combined with a lead-compensator controller architecture is flexible, easy to implement and is able to deliver a fast response with high damping. The results will in the future be used in further research on full-vehicle control of heavy hydraulic hybrids.

Keywords: Hydraulic hybrids, displacement control, pole placement

1 Introduction

Increased oil prices and environmental concerns are driving research on energy efficient solutions for propulsion of heavy construction machines. One solution that has recently attracted great interest is hybridisation. This concept involves a combination of an internal combustion engine and a rechargeable energy storage device, and may yield energy savings for example by down-sizing the engine and incorporating energy recuperation [1]. In hydraulic hybrids, the energy storage device is a hydraulic accumulator which stores energy in compressed gas [2]. In turn, this energy-storing process relies on efficient variable pumps/motors that may transfer power between the hydraulic and the mechanical domains [3].

The inclusion of an accumulator in a hydraulic circuit causes the system pressure to be constant, or *impressed* [4] by the accumulator's state-of-charge. As a consequence, the controlled variable of a pump/motor connected to an accumulator is the shaft torque via the variable pump/motor displacement. This concept is central to hydraulic hybrid vehicles and is commonly referred to as *secondary control*. Secondary control in turn implies specific demands on variable displacement control, such as rapid response and the ability to realise negative displacement [5].

For safety reasons, it is usually desired to implement a cascaded control strategy, in which the displacement controller constitutes the innermost loop [6]. The response of the displacement controller should therefore be as fast as possible compared to the outer loop. In addition, in multiple-mode power-split hydraulic hybrids, too slow displacement actuators cause drops in vehicle output torque during the mode shift [7]. The response requirements depend on properties such as maximum displacement, system pressure and experienced inertia, as well as the control strategy applied in the outer loop [4]. Numerical values of the requirements are therefore difficult to give without a specific application, but to manage the mode shifts the authors found that a swivel time (time from 0 to maximum displacement) below approximately 0.2-0.3 seconds was necessary for a medium-sized (9000 kg) construction machine [7].

Different pump/motor types fulfil the demands on displacement controllers to different degrees. This paper concerns swash-plate axial-piston units as they are considered a suitable compromise between efficiency and displacement controllability. In swash-plate pumps/motors, changing the swash-plate angle varies the displacement. This action may be realised by different actuating systems which may be mechanical, electro-mechanic, hydraulic or electro-hydraulic. Of the four types, actuators that use hydraulics are preferable for fast response [8].

Some research has been done on displacement control in swash-plate pumps/motors with hydraulic actuation, e.g. [6, 9–11]. However, [6] and [10] focus on 4-way servo-valve solutions. Moreover, Manring [11] considers a system with mechanical feedback which means that the valve dynamics

may be ignored [12]. In an early publication, Green et al. [9] compare 4-way valve and 3-way valve solutions, but do not consider units connected to accumulators.

This paper studies control strategies for a hydraulic, 3-way proportional valve actuator solution for displacement control in an axial-piston pump of swash-plate design connected to a circuit with an accumulator. Control concepts considered are proportional control and proportional-lead control. These concepts are parametrised with a pole placement approach, in which the desired resonance and damping of the closed-loop system are used as input.

The control strategies were tested and compared qualitatively and quantitatively in computer simulations and hardware tests on a prototype pump.

1.1 Delimitations

The effect of an accumulator in the circuit is studied to the extent that the system pressure is seen as impressed. Quantitative comparisons with a system without accumulator, or the effect of accumulator properties (size, pre-charge pressure etc.) on the system behaviour are not carried out. Furthermore, the pump/motor shaft dynamics' influence on the displacement controller is not considered in this paper.

2 Bosch A11VO Prototype Pump

The axial-piston, swash-plate unit studied in this paper is shown in fig. 1. It is a Bosh Rexroth A11VO prototype pump with a maximum displacement of 110 cm^3/revolution. It has a maximum allowed operating pressure of 350 bar and a maximum allowed shaft rotational speed of 2800 rpm. The A11VO unit is intended to be used for secondary control in hybrid applications, and therefore one modification compared to its previous version is the ability to realise negative displacement. The particular unit studied in this paper, however, is equipped with a valve plate optimised for pump operation. All the tests have therefore been carried out with positive direction of the shaft.

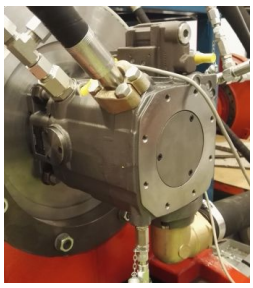

Figure 1: Bosch A11VO pump studied in the paper.

2.1 Displacement Actuator

The displacement actuator circuit of the A11VO pump is shown in fig. 2. A proportional spool valve (**1**) controls the flow to the control piston (**2**) that acts on the swash plate (**3**), thereby changing the displacement angle, α. The proportional valve (**1**) is actuated with a solenoid that is fed with a

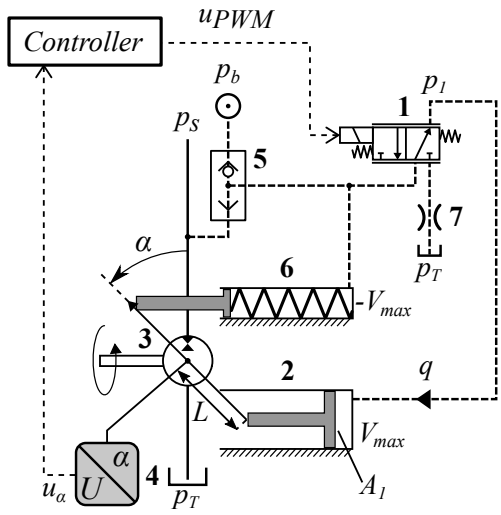

Figure 2: Controller mechanism in the A11VO pump.

pulse-width-modulated (PWM) voltage signal, u_{PWM}. An orifice (**7**) is mounted at the valve tank port for extra damping of the control mechanism. The displacement angle is measured with a Hall-effect sensor (**4**) and sent to an external controller for closed-loop control of the displacement.

The supply pressure to the valve (**1**) is either an external boost pressure, p_b, or the system pressure, p_s, managed by the shuttle valve (**5**). Here, p_b is assumed to be used only during start-up and that $p_s > p_b$ during normal operation of the pump. Furthermore, a spring-loaded piston (**6**), supplied with the same pressure as the valve (**1**), acts on the swash-plate (**3**) in the opposite direction compared to the control piston (**2**). The spring forces the pump into maximum displacement in the case of insufficient supply pressure to the valve (**1**). This feature is useful in a pump, as it allows for pressure to build up from start-up by the pump itself.

In a secondary controlled transmission, the spring forcing the unit into maximum displacement could be dangerous as it would result in maximum unit output torque, thus accelerating the vehicle. In future versions of the A11VO, it might therefore be necessary to change the start-up displacement configuration. This could for example be done by adding a spring acting on the control piston, thereby centering the displacement to zero [8]. The unstable nature of secondary controlled systems could imply further issues related to the displacement controller, such as in the event of a control valve power-outage. These issues are outside the scope of this paper, but should be considered in a final design.

3 Model

A model of the displacement actuator has previously been developed by the authors. In this paper, the same model is used for controller design and evaluation. For the controller design, a linearised representation is used, while the full model used for evaluation contains several non-linearities. The model's features of main importance are presented in this section. See [13] for further details concerning the model.

3.1 Linearised Representation

The linearised open-loop system is modelled as:

$$\Delta\varepsilon = G_O(s) \cdot \Delta u_{PWM} = \frac{K_s}{s\left(\frac{s}{\omega_v}+1\right)} \cdot \Delta u_{PWM} \tag{1}$$

where the input is the PWM voltage, Δu_{PWM}, and the output is the relative displacement, $\Delta\varepsilon$. ω_v is the valve break frequency that lumps the valve spool and solenoid dynamics. K_s is the lumped system gain:

$$K_s = \frac{k_{PWM} K_q}{A_1 L \alpha_{max}} \tag{2}$$

where α_{max} is the maximum swash plate angle, A_1 is the pressurised area of the control piston ((**2**) in fig. 2), and L is the distance from the swash plate's centre of rotation to the contact point of the control piston. k_{PWM} is the static gain from PWM duty cycle to valve spool position. K_q is the valve flow gain, calculated at a linearisation point $(p_{s,0},\ p_{1,0},\ p_{T,0})$:

$$K_q = -\frac{\partial q}{\partial x_v} = \begin{cases} C_q d\pi\sqrt{\frac{2}{\rho}\left(p_{1,0}-p_{T,0}\right)}, & x_v \geq 0 \\ C_q d\pi\sqrt{\frac{2}{\rho}\left(p_{s,0}-p_{1,0}\right)}, & x_v < 0 \end{cases} \tag{3}$$

where p_1 is the pressure in the control piston chamber, C_q is the valve flow coefficient, x_v is the valve displacement, ρ is the oil density and d is the valve spool diameter. Since the pump is assumed to be connected to an accumulator, the system pressure, p_s, is viewed as constant from a control perspective. The tank pressure, p_T, is assumed negligible compared to the other pressures. The damping orifice (**7** in fig. 2) is lumped in the valve model.

3.2 Non-linearities

The full model is implemented in Hopsan, a system simulation tool developed at Linköping University [14]. An overview of the model structure is shown in fig. 3. As can be seen, the rotational motion is translated to a translational one, and the mechanism is viewed as a 3-way valve controlled piston.

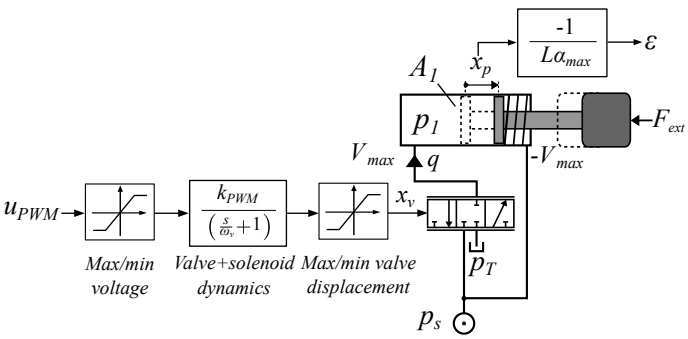

Figure 3: Schematic overview of Hopsan model.

Apart from the non-linearity of pressure-dependent flow gain shown in eq. (3), other relevant non-linearities included in the Hopsan model are:

- Saturation in valve stroke.
- Saturation in PWM voltage due to current limitations.
- Mean value of a speed- and pressure-dependant self-adjusting torque acting on the swash plate (F_{ext} in fig. 3).

The two first items act on the input signal of the system, as illustrated in fig. 3, while the self adjusting force is implemented as an external force, F_{ext}, that acts on the piston.

4 Control

The pure integrator in G_O requires a feedback loop for stabilisation. The controller is implemented as shown in fig. 4.

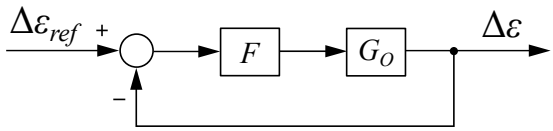

Figure 4: System (G_O, from eq. (1)) with controller (F) and feedback loop.

Two candidates for F are studied. The first candidate is a standard proportional controller (P):

$$F = K \tag{4}$$

The second candidate is a proportional controller with lead compensator (P-lead):

$$F = K\frac{\frac{s}{\omega_1}+1}{\frac{s}{\omega_2}+1} \tag{5}$$

None of the candidates contain purely integrating elements. This is motivated partly by the existence of a pure integrator in G_O, and partly by a desire to avoid problems caused by integrator wind-up when the controller is used as an inner loop in a full system. In other words, some static error is considered tolerable since it will be handled by an outer loop.

Compared to the P-lead controller, the P-controller has the advantages of simpler implementation and lower complexity. On the other hand, the P-lead controller offers higher flexibility and potentially higher performance than the P-controller. The achieved performance, however, depends on how K, ω_1 and ω_2 are chosen. That is, how the controller is parametrised.

4.1 Parametrisation: Pole Placement

With pole placement, the controller is parametrised by placing the poles of the closed-loop system according to given requirements [15]. The location of these poles depends on the system, which means that a system model is needed in the controller design for accurate results. Here, it is assumed that the input from the controller designer is desired resonance, ω_a, and relative damping, δ_a, of the closed loop system:

$$G_C = \frac{F \cdot G_O}{1 + F \cdot G_O} = \frac{1}{\frac{s^2}{\omega_a^2} + \frac{2\delta_a}{\omega_a} s + 1} \tag{6}$$

4.1.1 P-controller

Equations (1) and (4) with identification of ω_a and δ_a in eq. (6) yields that the controller gain, K, in the P-controller may be chosen as:

$$K = \frac{1}{\omega_v K_s} \omega_a^2 \tag{7}$$

or

$$K = \frac{\omega_v}{4K_s} \frac{1}{\delta_a^2} \tag{8}$$

Equations (7) and (8) show the limited flexibility of a proportional controller, as the controller gain is determined either by desired resonance or desired damping. It can be shown that for the P-controller:

$$\omega_a \delta_a = \frac{\omega_v}{2} \tag{9}$$

With a P-controller there is thus a compromise between damping and resonance (i.e. response), and to increase both of them simultaneously, a faster valve is required.

4.1.2 P-lead-controller

Equations (1) and (5) with identification of ω_a and δ_a in eq. (6) yields that ω_1 in the P-lead-controller may be chosen as:

$$\omega_1 = \omega_v \tag{10}$$

ω_2 may be chosen as:

$$\omega_2 = 2\omega_a \delta_a \tag{11}$$

The controller gain, K, may be chosen as:

$$K = \frac{\omega_a}{2K_s \delta_a} \tag{12}$$

With the P-lead-controller, the damping and resonance are decoupled, and may therefore be chosen independently of each other. Equation (10) means that there is a pole cancellation of the valve dynamics. With an ω_2 significantly higher than ω_v, a significantly faster response with maintained damping is therefore possible with the P-lead-controller compared to the P-controller. By transforming K and ω_2 into ω_a and δ_a, this response may in turn be trimmed in an intuitive and simple way.

4.2 Choosing ω_a and δ_a

As seen in section 4.1, ω_a and δ_a are achieved if the open loop system gain, K_s, and the valve break frequency, ω_v, are known. If this is the case, the P-controller could be designed either by choosing ω_a and accepting the resulting δ_a or vice versa. With the P-lead-controller on the other hand, ω_a and δ_a may be chosen arbitrarily. This situation, however, is not entirely realistic, primarily for two reasons:

1. K_s and ω_v are subjects to system operating point- and day-to-day-variations.

2. Hardware limitations do not allow for infinitely fast response.

4.2.1 Parameter Variations

Figures 5 - 7 show how the system behaviour changes if K_s and ω_v deviate from the values with which the controller was designed. The plots have been generated with the linear model in eq. (1). The P-controller is parametrised with eq. (8) with $\delta_a = 0.9$. The P-lead-controller is parametrised with eqs. (10)-(12) with $\omega_a = 90$ rad/s and $\delta_a = 0.9$, which have been found to be suitable values in experiments. Both controllers are parametrised for $K_{s0} = 0.72$ and $\omega_{v0} = 26.6$ rad/s, which are estimates for a shaft speed of 1000 rpm and a system pressure of 200 bar.

As can be seen in figs. 5a and 5b, an increase in K_s with a P-controller decreases the phase margin, with a less damped response and higher resonance frequency as a result. The same principal behaviour is present with the P-lead-controller, which is why those corresponding graphs are not included in this section.

In contrast to K_s, an increase in ω_v increases the phase margin with a P-controller, as shown in fig. 6b. As seen in fig. 6a, this leads to a better damped response. With the P-lead-controller, fig. 7, a faster valve also increases the phase margin. However, if $\omega_1 \neq \omega_v$, the resulting closed loop is no longer of purely second order, as seen in fig. 7a.

From the discussion above, it may be concluded that from a stability point of view, the most critical point is when the system gain is at its highest and the valve break frequency its lowest. In a conservative approach, ω_a and δ_a should therefore be chosen at this point, with acceptance of slow performance in the other operating points. However, the dominance of low-order dynamics in the system makes it robust in the sense that it can tolerate quite large deviations in parameter values without reaching instability (the phase shift is always less than 180 degrees). The controller may therefore be trimmed at a point of interest and still be stable when deviating from this point, as long as changes in behaviour are tolerated. If too much oscillation occurs, the controller is then easily trimmed by increasing δ_a. Here, it is important to note that the linear model is simplified and does not, for example, include the hydraulic resonance or time delays in the software. These are factors that add phase shift and could become relevant if the system gain increases too much.

In this system, K_s has been observed to be the parameter that changes the most. The major reason for this is the change in the valve flow gain, K_q. As seen in eq. (3), this parameter changes with the pressure drop over the valve, which in turn depends on the system pressure, p_{s0} and the static pressure in

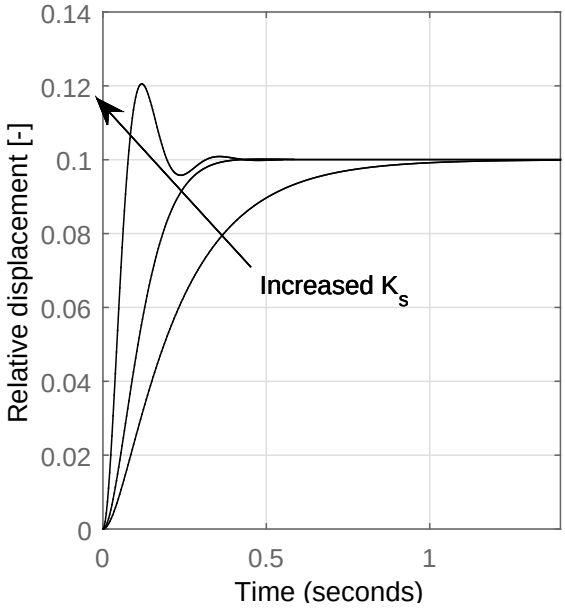

(a) Step response with varying K_s.

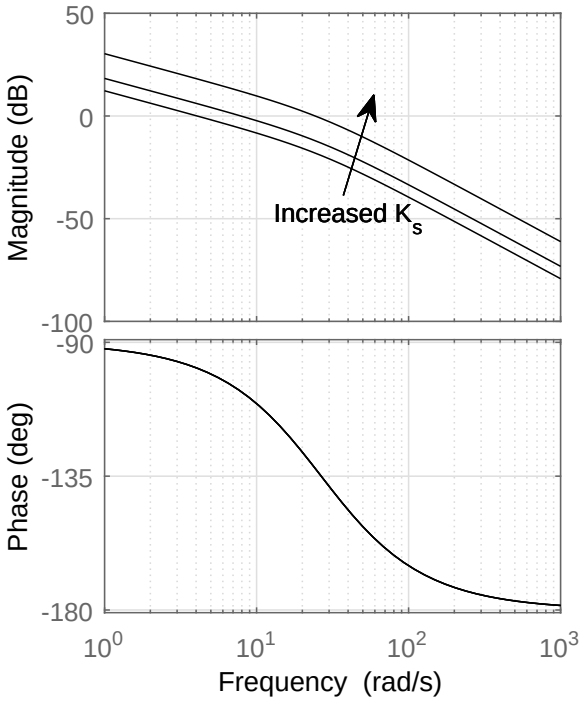

(b) Bode plot of $G_O \cdot F$ with varying K_s.

Figure 5: Changes in system behaviour due to changes in system gain if a P-controller is used. K_s is scaled with a factor of 0.5, 1.0 and 4.0 with respect to K_{s0}.

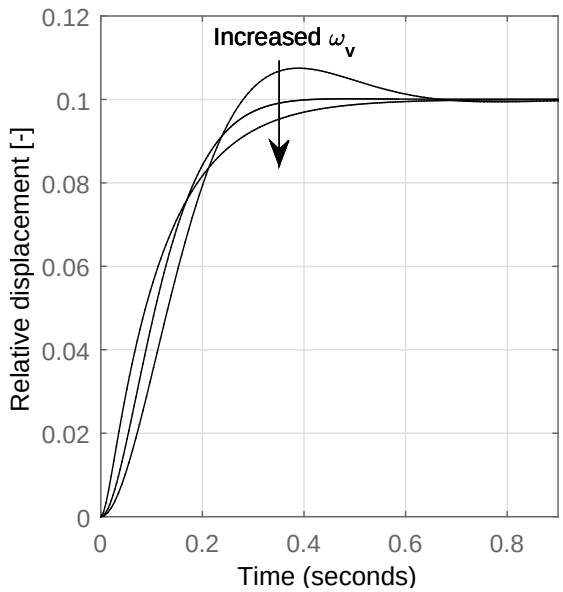

(a) Step response with varying ω_v.

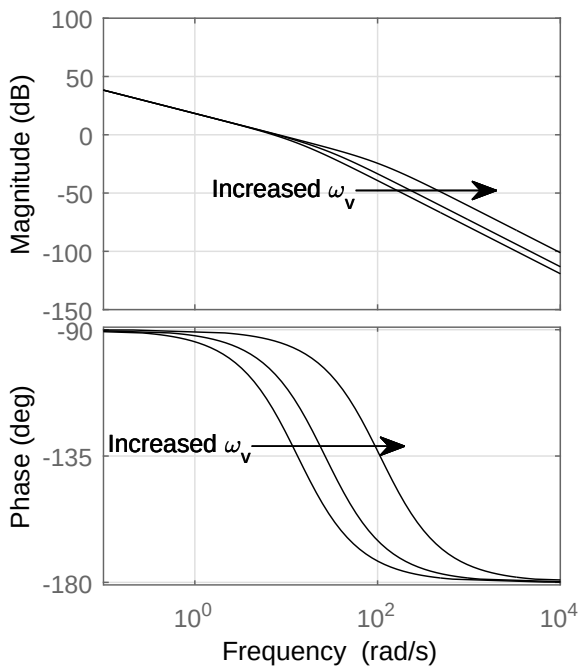

(b) Bode plot of $G_O \cdot F$ with varying ω_v.

Figure 6: Changes in system behaviour due to changes in valve break frequency if a P-controller is used. ω_v has been scaled with a factor of 0.5, 1.0 and 4.0 with respect to ω_{v0}.

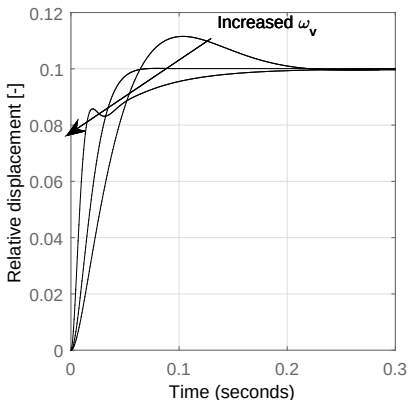

(a) Step response with varying ω_v.

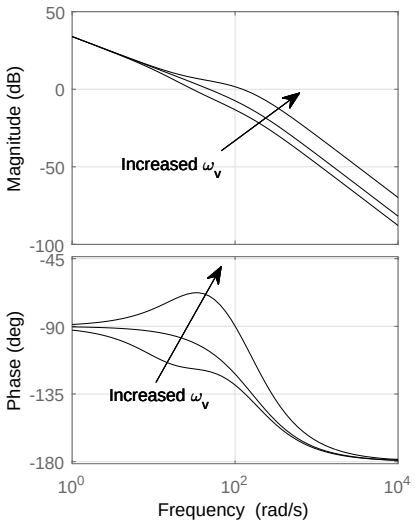

(b) Bode plot of $G_O \cdot F$ with varying ω_v.

Figure 7: Changes in system behaviour due to changes in valve break frequency if a P-lead-controller is used. ω_v has been scaled with a factor of 0.5, 1.0 and 4.0 with respect to ω_{v0}.

the control piston chamber, $p_{1,0}$. $p_{1,0}$ is a consequence of the force equilibrium of the swash plate mechanism.

The variation in K_q is shown in fig. 8. As can be seen, there is a difference in flow gain depending on the direction of the valve displacement. This difference is mainly a consequence of the area ratio of the control piston and the counter-acting piston (see fig. 2). The flow gain also changes with shaft speed because of the speed-dependent self-adjusting torque. The parameter with greatest impact on K_q, however, is the system pressure. From fig. 8 it may be concluded that the highest value of K_q is approximately 3 times its smallest value. If other uncertainties are taken into account, a change in system gain of maximum a factor 4 is considered reasonable.

ω_v has been observed to be relatively constant, where approximately 50 % is considered a conservative number for changes.

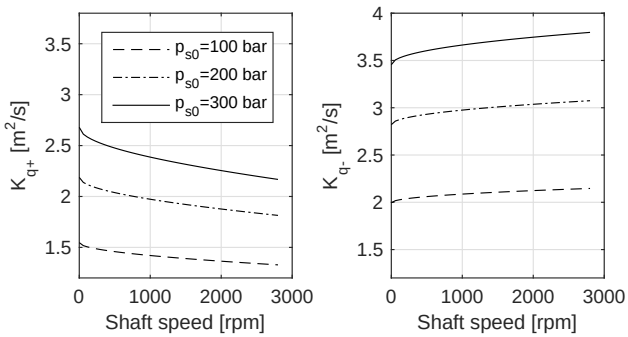

Figure 8: Variation in flow gain, K_q, for different system pressures. K_{q+} (left) is the flow gain for positive displacement of the valve, and K_{q-} (right) is the flow gain for negative displacement of the valve. The graphs were generated with eq. (3).

Since both system pressure and shaft speed are measured, gain-scheduling could be used if predictable behaviour is desired at more operating points. This approach is outside the scope of this paper, but may be considered in future work.

4.2.2 Hardware Limitations

In a linear system, it appears that ω_a and/or δ_a may be chosen arbitrarily. In a real system, however, some limitations in the hardware does not allow for this. One limitation of high significance is saturation in input signal. Here, the maximum stroke of the valve limits the maximum flow to the control piston. Also, the limitation in voltage to the solenoid tends to give over-damped responses. For the control design, this means that the choice of ω_a is limited, as too high a value would demand too high input signals.

Another issue that comes with a sampled system is noise. In particular, this concerns the P-lead-controller, due to its derivative element. For the controller design, this limits both the choice of ω_a and δ_a, as may be seen in (11). If very high δ_a and ω_a are desired, ω_2 will be very high, and the lead-compensator turns into a high-pass filter which is very sensitive to noise.

4.2.3 Summary

To summarise, changes in the values of the system gain and valve break frequency do not allow the chosen ω_a and δ_a to be achieved at all operating points with the simple model used. Rather, the introduction of the two parameters allows the controller to be trimmed in a simple and intuitive way. In particular, the parametrisation of the P-lead-controller is simplified, as the resonance and damping are directly tuned instead of gain and filter frequencies. However, the achievable values of ω_a and δ_a are ultimately limited by the maximum stroke of the valve and the hardware's sensitivity to noise.

5 Hardware Tests

To study the performance of the controllers, tests were carried out on an A11VO pump in a test rig. The test rig is briefly presented in the following subsection, while the specific test set-up and configuration which was used for the results are described in section 5.2. See [13] for more details concerning the test rig.

5.1 Test Rig

The principle of operation of the Hardware-in-the-loop (HWIL)-simulation test rig is illustrated in fig. 9. Two A11VO units are connected in an open circuit with two 20-litre Hydac accumulators. The shaft of each A11VO unit is connected to a servo-valve-controlled pump/motor which is used to simulate the surroundings of the hydraulic circuit, by either torque or speed control. The rig is thereby a typical set-up for testing of a secondary controlled transmission. In a typical use case, HWIL-simulation of a vehicle with transmission and engine is carried out. Flywheels are mounted on the shafts to lower the impact of disturbances on the speed control and to simulate engine and vehicle inertia.

The input and output signals to the hardware are handled by a data acquisition system with hardware from National Instruments (NI). During the tests, the calculations are carried out by an NI PXI-8110-RT computer that runs LabView^{TM} in real-time with a sampling frequency of 1 kHz. Controllers and models are compiled Simulink models that are uploaded onto the PXI computer. The during-test communication with the PXI computer is handled via an Ethernet interface and a graphical user interface (GUI) on a PC.

In this paper, the displacement controller is the subject of interest. Therefore, although suitable for HWIL-simulations of secondary controlled transmissions, the rig controllers are used to maintain constant speeds of the shafts as described in the following section.

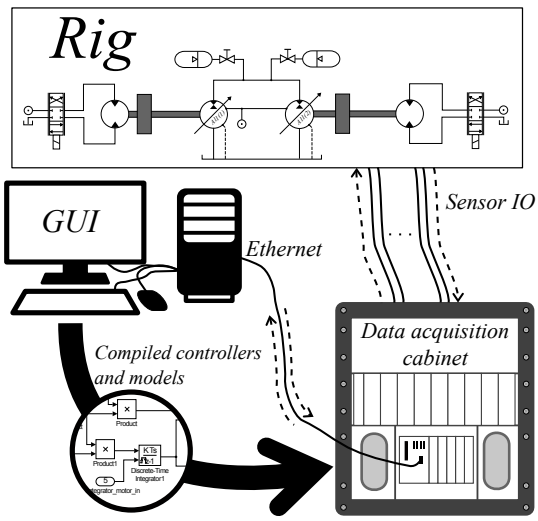

Figure 9: Principle of operation of the hardware-in-the-loop simulation rig used in the tests.

5.2 Test Set-up

Figure 10 shows the set-up that was used in the tests. The shaft of each A11VO unit was controlled at constant speed. Unit 1 was controlled at 1800 rpm and unit 2 at 1000 rpm. A pressure controller was implemented on unit 1 to control the pressure in the circuit. Unit 2 was then the subject of testing, in terms of different controllers (F) implemented in the software. The signal sent to the A11VO units was the duty cycle of the PWM signals with a PWM frequency of 200 Hz and PWM voltage of 24V. All tests were carried out at the operating temperature of the oil (approximately 40°C) and warm solenoids of the displacement actuators. Due to slow drift of the solenoid, because of temperature changes, a very small integrating element was used with the controllers. This element had very slow dynamics, and had a negligible contribution (less than 1%) to the signal in the dynamic tests that were conducted.

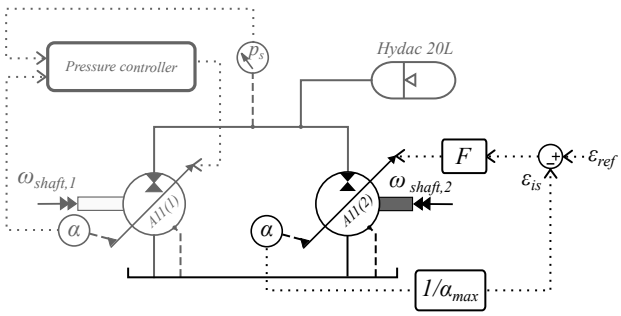

Figure 10: Set-up used in the tests.

Since neither the pressure controller nor the speed controllers were completely stiff, changes in displacement on unit 2 introduced dynamic disturbances in both the system pressure and the shaft speed of unit 2. Due to the high inertia of the flywheel and the high capacitance of the accumulator, these disturbances were, however, very slow and had negligible effect on the results.

5.3 Test Cases

The P- and P-lead-controllers were tested at 100 bar and 1000 rpm with different values of ω_a and δ_a to study the difference in performance of the two controllers and the functionality of the pole-placement approach. The tests consisted of step responses in ε from 0 to 0.1.

The P-lead-controller was also tested with larger steps at system pressures of 100 bar, 200 bar and 300 bar. The purpose of these tests was to study the influence of the limitations in valve input signals on system behaviour. The time constant, i.e. the elapsed time from 0 to 63% of the step size, was measured for these steps as a comparable measure of performance.

The P-controller was designed with a desired ω_a as input, i.e. with eq. (7). For both controllers, $\omega_v = 26.6$ rad/s and $K_s = 0.76$ were used. These values correspond to a shaft speed of 1000 rpm and a system pressure of 100 bar, if $K_q = K_{q-} > K_{q+}$ (see fig. 8) is used for conservative reasons.

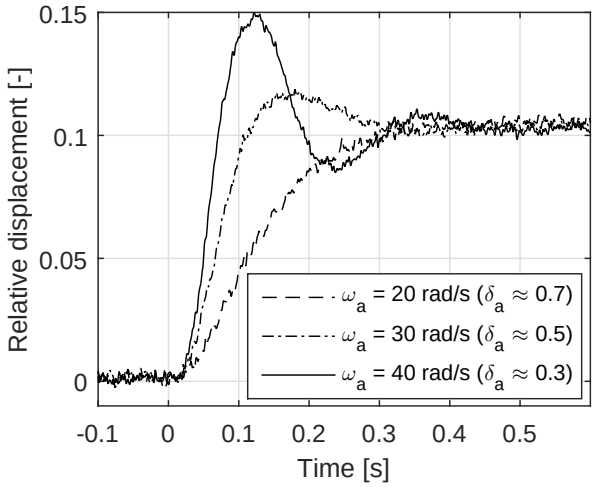

(a) P-controller.

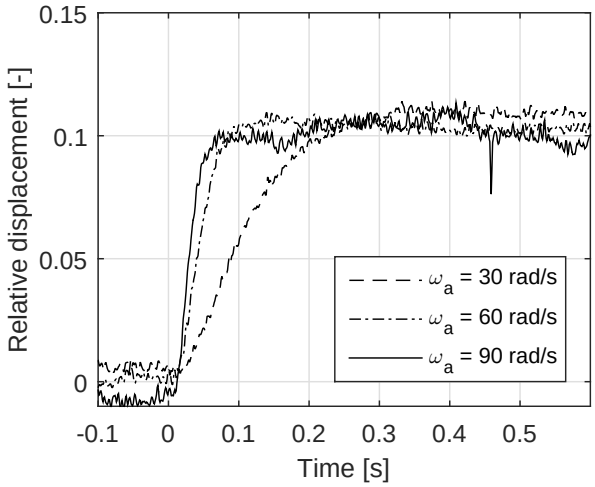

(b) P-lead-controller with $\delta_a = 0.8$.

Figure 11: Measured step responses with different values of ω_a with P-controller (a) and P-lead-controller (b).

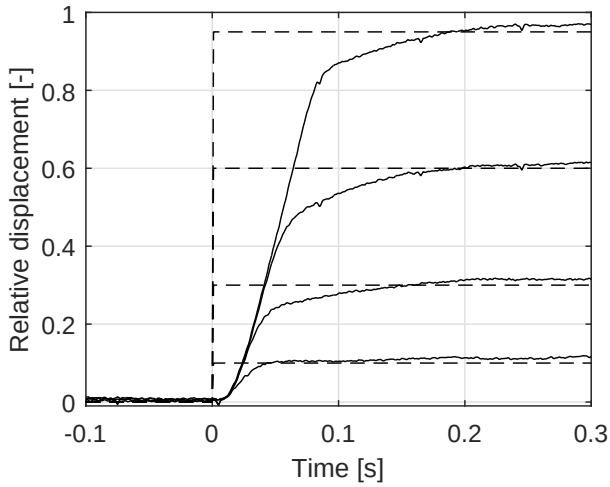

(a) Rig measurements.

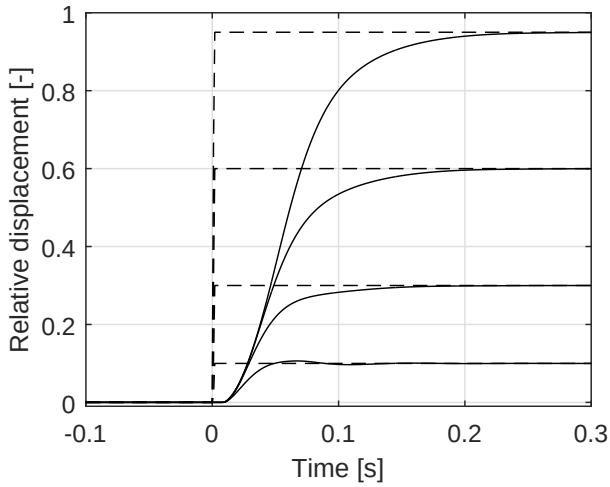

(b) Hopsan simulations.

Figure 12: Measured (a) and simulated (b) step responses at 200 bar with $\omega_a = 90$ rad/s, and $\delta_a = 0.9$ with a P-lead-controller.

6 Results

Figure 11 shows step responses with the P-controller and the P-lead-controller for different choices of ω_a. As can be seen, an increase in desired response causes a decrease in damping with the P-controller. In contrast, the response of the P-lead-controller may be increased with a constant damping. The P-lead-controller manages responses with $\omega_a = 90$rad/s with a relative damping of $\delta_a = 0.8$ while the P-controller is limited to $\omega_a = 20$rad/s for approximately the same damping.

Figure 12 shows larger step responses at 200 bar with a P-lead-controller. Figure 12a displays rig measurements while fig. 12b shows the corresponding simulated results. Due to the relatively high δ_a (0.9), the responses are still reasonably damped, even though the pressure is 200 bar (the controller was parametrised for 100 bar). Furthermore, two non-linear effects may be observed. First, the limitation in valve stroke causes constant velocity in the larger steps. Second, the voltage limitation gives extra damping at the end of the large steps. Although slightly different, the same general behaviour is present in both the model and the measurements, which should indicate that the model captures the relevant non-linearities.

Table 1 shows the measured time constants for different step sizes and system pressures. It is clear that the displacement controller becomes slower as the step size increases, which is due to the limitations in voltage and valve stroke. For step sizes below 0.3, the pressure has little effect on the response. For larger steps on the other hand, increased pressure decreases the time constant primarily because of the maximum deliverable flow of the valve that increases with the pressure.

Table 1: Measured time constants (0→63%) in milliseconds for different step sizes and different pressures. The same controller as the one used for the results in fig. 12 was used in all cases.

↓Step size, System Pressure [bar]→	100	200	300
0.1	26	25	29
0.3	39	36	38
0.6	56	49	49
0.95	81	64	60

7 Discussion

The performance of the P-lead-controller is superior to that of the P-controller in terms of fast response with high relative damping. This is because the valve response is rather slow and therefore limits the closed-loop response with the P-controller. On the other hand, the P-lead-controller can cancel out the valve dynamics and thereby increase the response significantly. For small steps, the P-lead-controller was able to produce a response with approximately 4 times higher resonance than the P-controller, with the same relative damping.

Although high, the performance of the P-lead-controller is limited for large steps. One reason for this phenomenon is the limitation in solenoid voltage. The behaviour is similar to the case when the valve is slightly faster than the controller assumes (see fig. 7a, sec. 4.2.1), and in simulations it has been found that the effect could be lowered if ω_1 is chosen as slightly higher than ω_v.

Another reason for deteriorated performance for large steps is the limited flow of the valve, a finding consistent with previous work [10]. In that particular study, however, a 4-way servo-valve with external pressure supply was used, and there was therefore no increased response at increased system pressures. With a 3-way valve configuration, in early studies the controller was found to be sensitive to system pressure fluctuations and inherently less stable [9]. This has not been a problem in the system studied in this paper, due to the inclusion of a high-capacitance accumulator in the circuit. However, if a similar concept is to be used in a system with low capacitance, dependencies of system pressure fluctuations should probably be considered.

The influence of the self-adjusting torque that acts on the swash plate has only been considered in terms of its mean value. In reality, this torque oscillates with a frequency that is proportional to the shaft speed. Therefore, in previous research it has been pointed out that this should be considered in the controller design [16]. In fact, it has been found that for the floating cup pump, oscillations of the swash plate have a negative impact on pump efficiency [17]. However, oscillations of the swash plate due to the self-adjusting torque seem to be machine-dependent, and have not yet been observed in the A11VO units studied in this paper.

As seen from the results, the pole placement approach may be used to produce a predictive response of the displacement controller. In turn, this ability relies on an accurate model as input when the controller is parametrised. The behaviour will therefore change due to model uncertainties as well as hardware limitations and operation-point-dependent parameter variations. In the studied system, however, the dominance of low-order dynamic properties in the system makes it rather robust against instability caused by changes in parameter values. Thus, the main benefit of the pole placement approach identified in this paper is its simple implementation rather than predictable behaviour. Should predictable behaviour of the displacement controller at more operating points be highly desirable, gain scheduling of the system pressure could be a beneficial extension of the control concept. It should be mentioned, however, that the pressure has not been found to have as high influence on system gain in the measurements as it has in the simulations. The valve behaviour also has a high impact on the response, which suggests that an enhanced valve model could be useful. For example, the solenoid is sensitive to temperature changes. This effect could be lowered if current control was implemented rather than voltage control. It is important to note, however, that the response for large steps is primarily limited by the maximum flow of the valve.

8 Conclusions

To conclude, the pole-placement approach used in this paper allows the displacement controller to be designed in a simple way as long as an accurate system model is available. In particular, the proportional-lead control concept is promising as it allows more than 4 times as high resonance compared to the proportional-control concept with the same relative damping. In step responses, time constants (0 →63% of final value) from 26 ms to 81 ms have been measured in hardware tests. The time constant tends to increase with system pressure and decrease with step size, due to the maximum flow of the control valve.

The realisation of heavy hydraulic hybrid construction machines relies on secondary control and thereby also on fast displacement controllers. The results reported in this paper will therefore be useful input in further research on full-vehicle control of such machines.

9 Acknowledgements

This research was partially funded by the Swedish Energy Agency (Energimyndigheten). The authors also wish to thank Bosch Rexroth for providing the prototype pumps.

References

[1] Lino Guzella and Antonio Sciaretta. *Vehicle Propulsion Systems*. Springer Verlag Berlin Heidelberg, 2013.

[2] A. Pourmovahed. Vehicle propulsion systems with hydraulic energy storage: a literature survey. *International Journal of Vehicle Design*, 12(4):378–403, 1991.

[3] Karl-Erik Rydberg. Energy Efficient Hydraulic Hybrid Drives. In *The 11:th Scandinavian International Conference on Fluid Power, SICFP'09*, Linköping, Sweden, 2009.

[4] Rolf Kordak. *Hydrostatic drives with secondary control*. Mannesmann Rexroth GmbH, 1996.

[5] Göran Palmgren. *On Secondary Controlled Hydraulic Systems*. Licentiate thesis, Linköping University, 1988.

[6] H Berg and M Ivantysynova. Design and testing of a robust linear controller for secondary controlled hydraulic drive. *Proceedings of the Institution of Mechanical Engineers, Part I: Journal of Systems and Control Engineering*, 213(5):375–386, 1999.

[7] L Viktor Larsson, Karl Pettersson, and Petter Krus. Mode Shifting in Hybrid Hydromechanical Transmissions. In *Proceedings of the ASME/BATH 2015 Symposium on Fluid Power and Motion Control (FPMC2015)*, Chicago, Illinois, USA, 2015.

[8] Jaroslav Ivantysyn and Monika Ivantysynova. *Hydrostatic Pumps and Motors*. Akademia Books International, New Delhi, India, 2001.

[9] W.L. Green and T.R. Crossley. An Analysis of the Control Mechanism used in Variable-Delivery Hydraulic Pumps. In *Proceedings of the Institution of Mechanical Engineers*, 1970.

[10] Joerg Grabbel and Monika Ivantysynova. An investigation of swash plate control concepts for displacement controlled actuators. *International Journal of Fluid Power*, 6(2):19–36, 2005.

[11] Noah D. Manring. *Fluid Power Pumps & Motors*. McGraw-Hill Education, 2013.

[12] Herbert E Merritt. *Hydraulic Control Systems*. John Wiley & Sons, Inc., 1967.

[13] L. Viktor Larsson and Petter Krus. Modelling of the Swash Plate Control Actuator in an Axial Piston Pump for a Hardware-in-the-Loop Simulation Test Rig. In *9th FPNI Ph.D. Symposium on Fluid Power*, Florianópolis, SC, Brazil, 2016.

[14] `http://www.iei.liu.se/flumes/system-simulation/hopsanng/`. Division of Fluid and Mechatronic Systems, Linköping University, Accessed: 2017-04-11.

[15] Torkel Glad and Lennart Ljung. *Reglerteknik: Grundläggande teori*. Studentlitteratur AB, 2006.

[16] Liselott Ericson. Swash Plate Oscillations due to Piston Forces in Variable In-line Pumps. In *The 9th International Fluid Power Conference, (9. IFK)*, Aachen, Germany, 2014.

[17] P. a. J. Achten, S Eggenkamp, and H. W. Potma. Swash plate oscillation in a variable displacement floating cup pump. In *The 13th Scandinavian International Conference on Fluid Power*, pages 163–176, Linköping, Sweden, 2013.

A Nomenclature

Designation	Denotation	Unit
A_1	Control piston area	m^2
α	Swash plate angle	radians
C_q	Valve flow coefficient	-
d	Valve spool diameter	m
δ_a	Desired relative damping	-
ε	Relative displacement (V/V_{max})	-
F	Controller transfer function	-
G_C	Closed loop transfer function	-
G_O	Open loop transfer function	-
k_{PWM}	Static solenoid gain	m/%Duty cycle
K	Controller gain	1/%Duty cycle
K_q	Valve flow gain	m^2/s
K_s	Static system gain	1/%Duty-cycle
L	Control piston lever	m
$\omega_{1,2}$	Controller break frequency	rads/sec
ω_a	Desired resonance frequency	rads/sec
ω_{shaft}	Shaft angular velocity	rads/sec
ω_v	Valve break frequency	rads/sec
p_1	Control piston pressure	Pa
p_b	Boost pressure	Pa
p_s	System pressure	Pa
p_T	Tank pressure	Pa
q	Volumetric flow	m^3/s
ρ	Oil density	kg/m^3
u_{PWM}	Pulse-width-modulated voltage	% Duty-cycle
V	Displacement volume	m^3/rad
x_v	Valve displacement	m

Non-Reviewed Papers

The following papers where presented at the conference but has not been peer-reviewed.

Water Hammer Induced Cavitation - A Numerical and Experimental Study

Marcus Jansson , Magnus Andersson*, Maria Pettersson , and Matts Karlsson*

Atlas Copco Rock Drills AB, SE-701 91 Örebro, Sweden
E-mail: marcus.jansson@se.atlascopco.com, magnus.andersson@liu.se, maria.pettersson@se.atlascopco.com, matts.karlsson@liu.se
*Division of Applied Thermodynamics and Fluid Mechanics, Department of Management and Engineering, Linköping University, Sweden

Abstract

Cavitation erosion is one of the main concerns in hydraulic rock drills and can reduce both performance as well as life span. Current simulation tools can detect a potential risk of cavitation, however, the equations do not include cavitation physics and therefore cannot estimate the severity nor erosion locations. In order to evaluate the cavitation damage, long term tests are performed which are both costly and time consuming. With better computational capacity and more accurate numerical flow models, the possibilities to simulate the course of cavitation have increased. So far, most numerical studies on cavitation focus on steady-state problems while studies on hydraulic transients and water hammer effects have received less attention. This paper is a step towards simulation of water hammer induced cavitation and cavitation erosion in pipe flow using Computational Fluid Dynamics (CFD). In order to validate the results, experimental measurements are performed with a test equipment that creates hydraulic transients in a pipe and records these using piezoelectric pressure sensors. The results from CFD are compared to both the experimental data and to numerical results from a software called Hopsan, a one-dimensional multi-domain system simulation tool that uses wave characteristics to calculate pressures and flows. For smaller transients where no cavitation occur, all results show good agreement. For larger transients with cavitation, the results from Hopsan do not longer agree with the measurements, while the CFD model still performs well and is able to predict both formation and collapse of cavitation.

Keywords: Cavitation, Water hammer, Hydraulic transients, Rock drills, CFD

1 Introduction

Cavitation erosion is a major failure mechanism for hydraulic rock drills and is a cause for both reduced performance and reduced life span [1,2]. With the simulation tools that are currently used it is possible to detect situations where cavitation might occur, however, these tools do not include any cavitation physics and cannot predict the severity nor the erosion sites. Therefore, long term tests, which are both costly and time consuming, are performed in order to evaluate the cavitation erosion.

Cavitation can be described as the rapid growth, and collapse, of bubbles in a liquid due to large pressure gradients. A liquid at a pressure below the saturation vapor pressure is said to be under tension. If no vapor or gas is present in the liquid it can sustain a considerable amount of tension and still remain stable. In reality however, small imperfections such as microbubbles of non-condensable gases or small suspended solid particles act as nucleation sites. At a certain tension, the liquid will rupture and form cavitation bubbles [3]. The evaporation/condensation at the bubble surface is very fast compared to the bubble dynamics and the vapor pressure inside the bubble can be considered constant. The bubbles contain mostly vapor but also small amounts of gas, e.g. air, that are dissolved in the liquid. The evaporation/condensation time scale is much shorter than that of diffusion. Thus the amount of non-condensable gases in the bubble is almost constant and the partial pressure of these gases varies with the bubble radius. When the ambient pressure is increased, the bubbles will collapse. The vapor inside the bubble will condense, however, the dissolved gases will instead be highly compressed. The pressure inside the bubble will thus increase during the collapse and eventually exceed the ambient pressure, forcing the process to revert and the bubble to rebound. The collapse of a cavitation bubble is often followed by multiple rebounds and collapses. The bubble continues to rebound and collapse until the gases have had time to diffuse to the liquid. Each collapse emits a large amplitude pressure wave [4, 5]. Bubbles collapsing close to a solid boundary tend to collapse more rapidly at the side facing away from the surface. This will form a liquid jet that punctures the bubble. This re-entrant jet can reach velocities of several hundreds of meters per second.

The bubble will eventually split into parts and the jet will instead hit the wall surface. The impact pressure from either the jet or from the pressure wave can locally exceed both the yield limit and the ultimate strength of many materials. In this case, local damage is induced. Most metals have an incubation period when the damage is isolated to small zones of plastic deformation, so called pits. During this time, no measurable mass loss occurs. When the pits become numerous they start to overlap and when the surface has been exposed to sufficiently many of these superimposed impacts the material fails. The incubation period is followed by extensive material loss. The severity of the cavitation erosion is affected by both the exposure time and the cavitation intensity [3, 6].

The use of Computational Fluid Dynamics (CFD) for solving various problems regarding fluid flow has increased as the performance of the methods and the computational resources are improved. However, CFD is not that extensively used for hydraulic systems. Often, less computationally expensive methods are used to solve for pressure and flows such as the Methods of Characteristics [7]. These methods are in most situations both quick and robust, however they lack in solving some of the physics that may be encountered. More recent studies have shown the value of CFD when determining the effects of water hammer in pipes [8]. Further, CFD have been used successfully to model cavitation and the risk of cavitation erosion in diesel injectors [9, 10] and hydraulic valves [11, 12]. However, the cavitation in these studies is a consequence of the accelerated flow and cavitation as the result of hydraulic transients has not been considered.

In addition to predict cavitation inception, the ultimate goal is to predict sites of cavitation erosion. Pressure [6], jet velocity [13] and the condensation source term in the vapor continuity equation [10] are all quantities that have shown potential for cavitation erosion prediction. This study aims to evaluate the possibility to use CFD as a tool for predicting cavitation formation and collapse caused by water hammer pulsations.

2 Experimental setup

The equipment consists of a pressurized pipe that is connecting two volumes (fig. 1), and a control valve that is located at the high pressure side of the pipe. With this valve it is possible to completely shut the flow in the pipe. At the low pressure side there are two volumes connected by an orifice. The orifice is exchangeable in order to vary the diameter and thus the flow rate. Dimensions are found in tab. 1.

Table 1: Dimensions for test equipment.

	Length [mm]	Radius [mm]
Tank 1	85	50
Pipe	755	5
Tank 2	85	50
Orifice	1	0.5-2
Tank 3	95	50

The system is in steady-state initially. The pressure in each

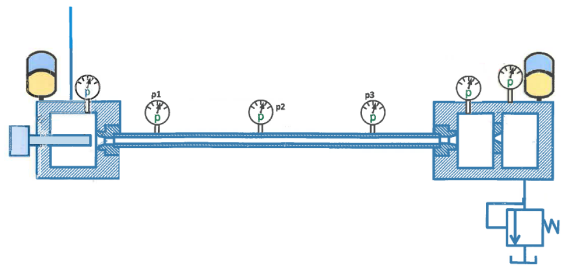

Figure 1: Simple representation of the test equipment

of the volumes are measured using silicon pressure sensors. The accuracy of these are $\pm 0.2\%$ of the full scale. In the first and second tank, i.e. the high pressure side, the measurement range is 0-25 GPa (0-250 bar). In the third tank, i.e. the low pressure side, the measurement range is 0-9 GPa (0-9 bar).

At a given time, the valve is closed rapidly. The exact movement of the valve is measured with a laser while another laser is recording any potential movement of the equipment itself.

The pressure pulsations in the pipe due to the valve closing are registered by three piezoelectric pressure sensors along the pipe which measures the pressure dynamically. These are located at a distance of P1=100 mm, P2=380 mm and P3=660 mm from the pipe opening (fig. 1). The resolution of these sensors is 0.14 kPa and the sampling rate is 1 MHz.

Tests with both 2 mm and 4 mm orifice diameters are performed. In both cases the inlet pressure is 6 GPa (60 bar) and oil viscosity 0.04 Pa·s (40 cP). With a 2 mm orifice, the flow rate is 2.68×10^{-4} m^3/s (16.1 l/min). The total stroke length of the valve is 2 mm and the closing time is 7.2 ms. The overlap between valve and pipe is 1 mm and the valve reaches the pipe opening after 1.8 ms. With a 4 mm orifice, the flow rate is 9.63×10^{-4} m^3/s (57.8 l/min). The closing time is 2.7 ms and the valve reaches the pipe opening after 0.77 ms.

3 Numerical setup

Two different numerical strategies are executed. The first is based on CFD where the Reynolds Averaged Navier-Stokes (RANS) equations are solved using the finite volume method. The second is a one-dimensional approach using the Hopsan software, which is a multi-domain system simulation tool that uses wave characteristics to calculate pressures and flows.

3.1 Computational Fluid Dynamics

The coupled pressure based solver in ANSYS Fluent 17.2 is used with the Realizable $k-\varepsilon$ turbulence model [14] and enhanced wall treatment. The medium is assumed to be a homogeneous mixture of oil and oil vapor. The oil is a compressible liquid while the vapor is treated as an incompressible gas. The mass transfer between phases is included using the Schnerr-Sauer cavitation model [15] based on the Rayleigh-Plesset equation for bubble radius [4]. The mass transfer rate for evaporation and condensation can be seen in eq. (1) and eq. (2) respectively

$$R_e = \frac{\rho_v \rho_l}{\rho} \alpha (1-\alpha) \frac{3}{R_B} \sqrt{\frac{2}{3} \frac{(P_v - P)}{\rho_l}} \tag{1}$$

$$R_c = \frac{\rho_v \rho_l}{\rho} \alpha (1-\alpha) \frac{3}{R_B} \sqrt{\frac{2}{3} \frac{(P - P_v)}{\rho_l}} \tag{2}$$

where R_e and R_c are the mass transfer rates by evaporation and condensation. ρ is the mixture density while ρ_v and ρ_l are the densities for vapor and liquid phases. α is the vapor volume fraction. P_v is the vapor pressure and P is the local far-field pressure. The bubble radius, R_B, is described by

$$R_B = \left(\frac{\alpha}{1-\alpha} \frac{3}{4\pi} \frac{1}{n} \right)^{\frac{1}{3}} \tag{3}$$

where n is the bubble number density.

The computational domain is assumed to be axi-symmetric and discretized by 413k quadrilateral cells. A fixed time step size of 1 μs is utilized, which corresponds to a Courant number below 3 (speed of sound) or 1 (fluid velocity). Sensitivity analysis on both the spatial and temporal resolution were performed and showed no major result changes with further refinement.

3.2 Hopsan

The model, seen in fig. 2, is very simplified and does not contain any of the components that are used in order to control the valve. Instead, the valve movement is controlled by a table with time and positions. These values are obtained from laser measurements of the valve motion.

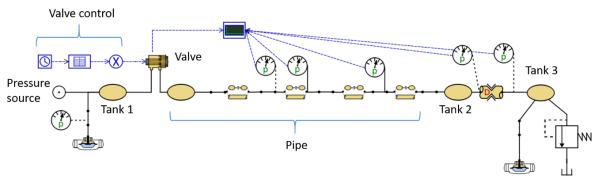

Figure 2: A simplified model of the test equipment that is used for the 1D simulations in Hopsan.

The inlet is represented by a pressure source with a specified pressure. It is possible to specify the radial clearance of the spool valve in order to take the leaking into account. Furthermore it is possible to change the diameter of the orifice.

4 Results and discussion

Results from the experimental setup are limited to the transient pressure in the pipe. These pressure curves are compared to numerical results from both Hopsan and CFD. In Hopsan, three different values for the spool radial clearance are represented. Furthermore, some brief results from methods of cavitation erosion prediction are presented.

4.1 Hydraulic transients

When using a 4 mm orifice, the cavitation is severe (fig. 3). The CFD results show that the cavitation has a higher effect than might be expected. When the pressure wave is reflected against a cavitation cloud it behaves differently compared with reflection against the valve. The result is small pressure oscillations at relatively low pressure that in some sense interfere with one and other. When the cavitation cloud eventually collapses, a large amplitude, high pressure wave appears. This wave is reflected at the tank in accordance to water hammer theory and returns to the valve as a low pressure. Cavitation occur once again and the procedure is repeated. The resulting transient pressure profile looks nothing at all like classic water hammer theory. Instead, small pressure variations are followed by a single large pressure wave and so forth.

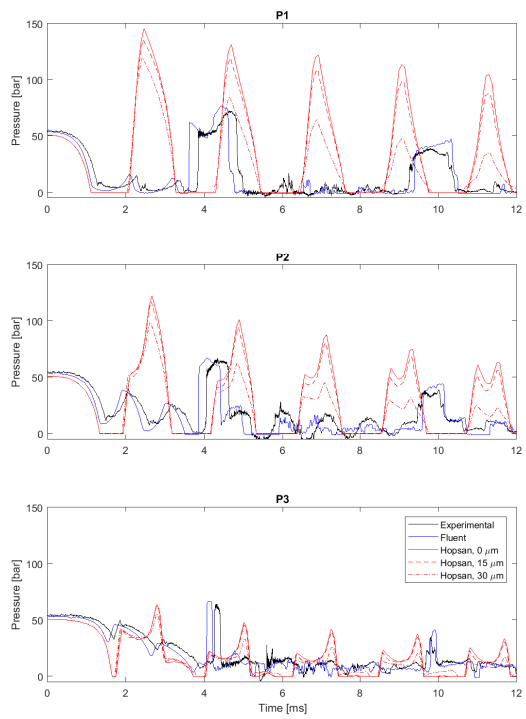

Figure 3: Experimental and numerical results for 4 mm orifice. Experimental data is presented in black and CFD (Fluent) results in blue. Hopsan results are shown in red with the different style lines representing various spool clearances.

A smaller orifice reduces the flow rate and thus the amplitude of the transients (fig. 4). The amplitude of the pressure wave is not sufficient to reduce the pressure to vapor pressure. The resulting pressure profile looks like what could be expected from water hammer. Furthermore, numerical results from Hopsan and CFD both agree fairly well with experiments. The types of damping in the different systems must

be considered. In the CFD model, it is assumed that there is no leakage at all between the valve and the pipe wall. The damping mainly consists of inertial and viscous forces. The turbulent viscosity from the turbulence model contributes to the damping. In the experimental setup, there is some leakage that greatly contributes to the damping of hydraulic transients. The difference between CFD results and experiments is most likely due to the leaking valve. In Hopsan, different values for the radial spool clearance are defined. It can be seen that the damping of transients is highly affected by this clearance, and thus the amount of leakage.

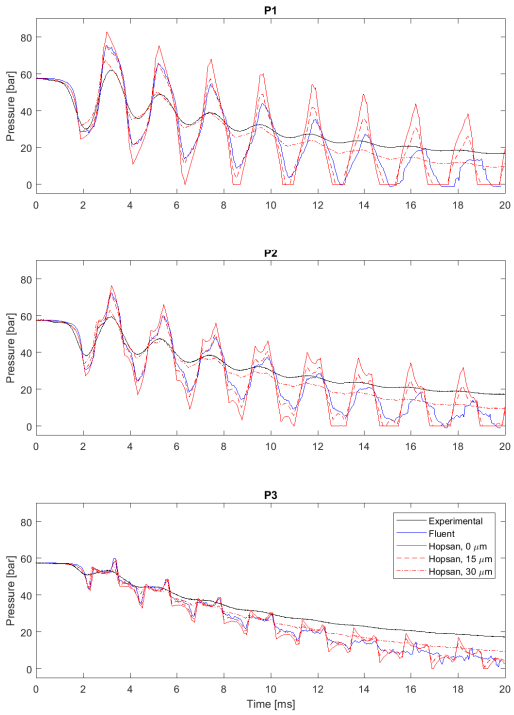

Figure 4: Experimental and numerical results for 2 mm orifice. Experimental data is presented in black and CFD (Fluent) results in blue. Hopsan results are shown in red with the different style lines representing various spool clearances.

4.2 Cavitation erosion

Prior to the moment of the first collapse (fig. 5), it is possible to detect two regions with increased wall condensation rate which might be more exposed to cavitation erosion. However, since this is just a snapshot, the transient effects of cavitation erosion cannot be determined.

The lowest wall pressure can be coupled to the regions in the pipe with vapor (fig. 6). This method cannot however distinguish between evaporation and condensation. The condensation phase should be characterized by large amplitude pressure waves from bubbles collapsing. This effect is not seen in the wall pressure.

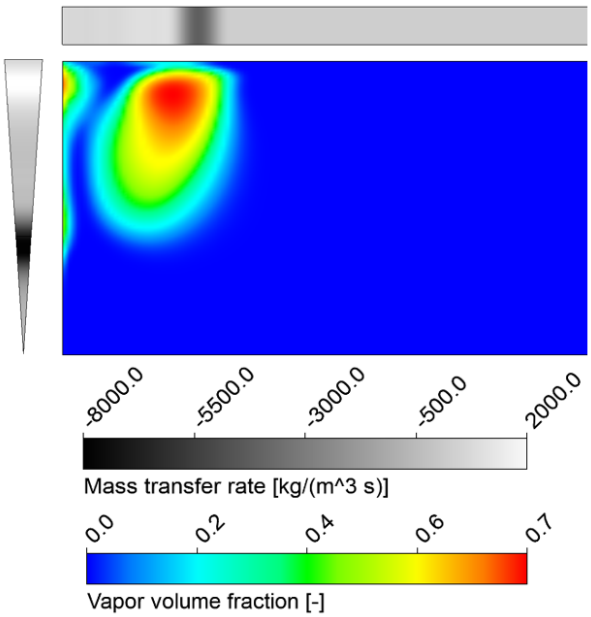

Figure 5: Vapor volume fraction inside the pipe and mass transfer rate at the pipe walls.

4.3 Limitations and future work

This study is only focused on accurately predict the pressure pulsations in a cavitating flow. The behaviour of the cavitation itself is currently not validated using any method. If the pipe in the test equipment would be of a transparent material it might be possible to detect cavitation optically and in that way validate if the cavitation bubbles are correctly modelled. If so, it could be possible to predict where the cavitation bubbles will end up and eventually collapse.

Methods for predicting the risk for cavitation erosion are not validated. However, CFD is considered a very promising tool and there are a number of different approaches that might be appropriate. The condensation source term in the vapor transport equation is a parameter that has great potential for transient flow. By using the time integral of this parameter it is possible to determine the amount of vapor that has condensated at e.g. a wall. By comparing this, or some other accumulative quantity, to experimental data of material loss it should be possible to tailor a model for prediction of cavitation erosion.

Numerical results are only compared to one set of experiments. For further studies, repeatability of the experiments should be considered and numerical results validated against averaged data.

The problem is assumed to be axi-symmetric in order to reduce the size of the CFD model. Effects from e.g. turbulence and buoyancy are clearly three-dimensional by nature. To fully evaluate these effects, three-dimensional CFD calculations should be performed together with experiments that can validate such results.

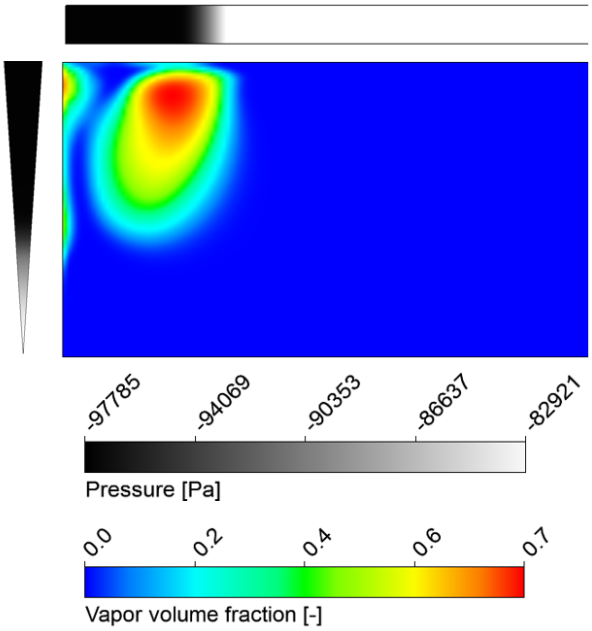

Figure 6: Vapor volume fraction inside the pipe and pressure distribution at the pipe walls.

5 Conclusions

In this study, CFD shows great potential for evaluation of hydraulic transients in pipes and exceeds the 1D methods for cavitation flow. Large amplitude hydraulic transients that result in cavitation bubble growth and collapse seem to be well predicted by the CFD model. The effects of cavitation collapse are not seen in the one-dimensional simulations.

To further validate numerical results, experiments that measure both the distribution of cavitation bubbles and the amount of cavitation erosion is necessary.

References

[1] T. Koivula. On cavitation in fluid power. In *Proceedings of 1st FPNI-PhD Symposium*, pages 371–382, Hamburg, 2000.

[2] N. Hedlund. Experimental simulation of cavitation erosion. Master's thesis, KTH Royal Institute of Technology, 2014.

[3] J.-P. Franc and J.-M. Michel, editors. *Fundamentals of Cavitation*. Springer Science & Business Media, 2010.

[4] C. E. Brennen. *Cavitation and Bubble Dynamics*. Oxford University Press, 1995.

[5] C. E. Brennen. An introduction to cavitation fundamentals. In *WIMRC FORUM 2011 – Cavitation: Turbomachinery & Medical Applications*, University of Warwick, UK, 4-6 July 2011.

[6] K. H. Kim, G. Chahine, J.-P. Franc, and A. Karimi, editors. *Advanced Experimental and Numerical Techniques for Cavitation Erosion Prediction*. Springer, 2014.

[7] M. H. Chaudhry. *Applied Hydraulic Transients*. Springer, 2013.

[8] M. R. Nikpour, A. H. Nazemi, A. Hosseinzadeh Dalir, F. Shoja, and P. Varjavand. Experimental and numerical simulation of water hammer. *Arabian Journal for Science and Engineering*, 39(4):2669–2675, 2014.

[9] F.J. Salvador, J. Martínez-López, M. Caballer, and C. De Alfonso. Study of the influence of the needle lift on the internal flow and cavitation phenomenon in diesel injector nozzles by CFD using RANS methods. *Energy Conversion and Management*, 66:246–256, feb 2013.

[10] F. Brusiani, S. Falfari, and G. M. Bianchi. Definition of a CFD multiphase simulation strategy to allow a first evaluation of the cavitation erosion risk inside high-pressure injector. *Energy Procedia*, 81:755–764, dec 2015.

[11] S. I. Bernad and R. Susan-Resiga. Numerical model for cavitational flow in hydraulic poppet valves. *Modelling and Simulation in Engineering*, 2012:1–10, 2012.

[12] R. Amirante, E. Distaso, and P. Tamburrano. Experimental and numerical analysis of cavitation in hydraulic proportional directional valves. *Energy Conversion and Management*, 87:208–219, 2014.

[13] A. Peters, H. Sagar, U. Lantermann, and O. el Moctar. Numerical modelling and prediction of cavitation erosion. *Wear*, 338-339:189–201, sep 2015.

[14] T.-H. Shih, W. W. Liou, A. Shabbir, Z. Yang, and J. Zhu. A new k-ε eddy-viscosity model for high reynolds number turbulent flows - model development and validation. *Computers Fluids*, 24(3):227–238, 1995.

[15] G. H. Shnerr and J. Sauer. Physical and numerical modeling of unsteady cavitation dynamics. In *Fourth International Conference on Multiphase Flow*, New Orleans, USA, 2001.

Nomenclature

Designation	Denotation	Unit
n	Bubble number density	-
P	Far-field pressure	Pa
P_v	Vapor pressure	Pa
R_B	Bubble radius	m
R_c	Condensation mass transfer rate	kg/(m^{3}s)
R_e	Evaporation mass transfer rate	kg/(m^{3}s)
α	Vapor volume fraction	-
ρ	Mixture density	kg/m^3
ρ_l	Liquid density	kg/m^3
ρ_v	Vapor density	kg/m^3

Early Insights on FMI-based Co-Simulation of Aircraft Vehicle Systems

Robert Hallqvist*, Robert Braun**, and Petter Krus**

E-mail: Robert.Hallqvist@saabgroup.com, Robert.Braun@liu.se, Petter.Krus@liu.se
*Systems Simulation and Concept Design, Saab Aeronautics, Linköping, Sweden
**Department of Fluid and Mechatronic Systems, Linköping University, Linköping, Sweden

Abstract

Modelling and Simulation is extensively used for aircraft vehicle system development at Saab Aeronautics in Linköping, Sweden. There is an increased desire to simulate interacting sub-systems together in order to reveal, and get an understanding of, the present cross-coupling effects early on in the development cycle of aircraft vehicle systems. The co-simulation methods implemented at Saab require a significant amount of manual effort, resulting in scarcely updated simulation models, and challenges associated with simulation model scalability, etc. The *Functional Mock-up Interface* (FMI) standard is identified as a possible enabler for efficient and standardized export and co-simulation of simulation models developed in a wide variety of tools. However, the ability to export industrially relevant models in a standardized way is merely the first step in simulating the targeted coupled sub-systems. Selecting a platform for efficient simulation of the system under investigation is the next step. Here, a strategy for adapting coupled *Modelica* models of aircraft vehicle systems to TLM-based simulation is presented. An industry-grade application example is developed, implementing this strategy, to be used for preliminary investigation and evaluation of a co-simulation framework supporting the Transmission Line element Method (TLM). This application example comprises a prototype of a small-scale aircraft vehicle systems simulator. Examples of aircraft vehicle systems are environmental control systems, fuel systems, and hydraulic systems. The tightly coupled models included in the application example are developed in Dymola, OpenModelica, and Matlab/Simulink. The application example is implemented in the commercial modelling tool Dymola to provide a reference for a TLM-based master simulation tool, supporting both FMI and TLM. The TLM-based master simulation tool *TLMSimulator* is investigated in terms of model import according to the FMI standard with respect to a specified set of industrial needs and requirements.

Keywords: FMI, TLM, Modelica, Aircraft Vehicle Systems

1 Introduction

Model Based Systems Engineering (MBSE) [1] is an outspoken strategy for aircraft vehicle systems development at Saab Aeronautics. Methods for efficient model simulator integration, as well as robust and fast simulation, are necessary if the benefits of MBSE are to be fully exploited. The *Functional Mock-up Interface* (FMI) standard is a first step towards reducing the overhead associated with connecting models of interacting sub-systems. At the time of writing, approximatly 50 commercial and open source tools support the latest version of the standard, FMI 2.0 [2]. Furthermore, as far as the authors know, none of these tools support asyncronous simulation implementing the *Transmission Line element Method* (TLM) for numerically stable partitioning of simulation models. An open source master tool, here refered to as the *TLM-Simulator*, supporting both of these key technologies is under development within the frame of the *OpenCPS* project [3]. Such a tool is predicted to be of great benefit to MBSE in aircraft vehicle systems development. Efficient model simulator integration will allow model developers, software developers, systems engineers, and flight test engineers to set up large multi-purpose simulation environments as well as small-scale simulators tailored for specific studies. An example of such a study is the investigation of how an aircraft's *Environmental Control System*'s (ECS) performance affects the pilot's thermal comfort, both physically and psychologically. Both types of simulation environments are currently being used for aircraft vehicle systems development at Saab Aeronautics. However, the authors foresee that their use could be further increased as a result of incorporating efficient and standardized methods for model simulator integration.

Here, a strategy for adapting coupled *Modelica* models of aircraft vehicle systems for simulation in an FMI-based simulation environment supporting TLM is described. The paper also describes the implementation of this strategy on an aircraft vehicle systems simulator. Reference simulations of this simulator are conducted for evaluation and development of the TLMSimulator.

This paper is structured as follows. First, a brief introduction to the concepts of FMI and TLM are given in section 1.1

and section 1.2 respectively. A subset of the needs and requirements, identified by the OpenCPS project partners, concerning an industrially applicable tool for simulation of tightly coupled aircraft vehicle system models is presented in section 2. The developed application example is described in section 3, starting with the simulator architecture and continuing with descriptions of the modelled sub-systems. The state-of-the-art open source co-simulation framework for co-simulation using both FMI and TLM is briefly described in section 4. The application example is implemented in both the commercially available Modelica tool *Dymola* and the TLMSimulator. The results obtained from application example Dymola simulations are presented in section 5.1. Finally, the concluding remarks are stated in section 6

1.1 Functional Mock-up Interface standard

The FMI standard is a standardization effort commenced in the *MODELISAR* project [4]. The standard specifies a generic format for export of model executables, referred to as *Functional Mock-up Units* (FMUs). It also includes a set of C functions for calling an FMU along with a standardized interface description xml schema. FMI is a standard for export of FMUs for both co-simulation (a suitable numerical solver is included in the exported model) and model exchange (the central solver is implemented in the integrating tool) [2]. The standard is maintained by the *Modelica association* [5] also responsible for maintaining the Modelica modelling language. The Modelica language is an object-oriented and equation-based modelling language especially suited for multi-domain modelling of physical systems. FMI is here seen as an enabler for reducing overhead costs associated with the exchange of models between tools, not only within the confines of a specific company but also with its subcontractors and suppliers.

1.2 Transmission Line element Method

The Transmission Line element Method (TLM) is a mature and well documented technique for numerically stable partitioning of simulation models. Here, a brief introduction to the most relevant aspects of TLM is given. Krus et al. [6] and Braun et al. [7] provide detailed descriptions of the presented method. Two FMUs connected to each other (FMU_1 and FMU_2) in the TLMSimulator, see section 4, communicate via TLM connections. A thermodynamic TLM connection is more or less a volume which receives information on volume flow from each interfacing FMU. The net volume flow is integrated in the TLM connection rendering a pressure which is passed back to each of the connected FMUs. The relationship between pressures and volume flows at the interface of the two FMUs is described by

$$p_1(t) = Z_c[q_1(t) + q_2(t - \Delta t_{TLM})] + p_2(t - \Delta t_{TLM}) \quad (1)$$

$$p_2(t) = Z_c[q_2(t) + q_1(t - \Delta t_{TLM})] + p_1(t - \Delta t_{TLM}) \quad (2)$$

if friction in the transmission line is disregarded. Interfacing variables of FMU_1 are p_1 and q_1 and of FMU_2 p_2 and q_2. In Equations (1) and (2), neither the pressure nor the volume flow depends on current information provided by the other FMU. Instead, the information necessary is delayed Δt_{TLM} seconds. This time delay corresponds to the time it takes for a wave to propagate through the connection. The characteristic impedance Z_c of Equations (1) and (2) can be expressed as

$$Z_c = \Delta t_{TLM}/C \quad (3)$$

where

$$C = V/\beta \quad (4)$$

for incompressible flow fluid connections. In Equation (4), V is the volume of the TLM connection and β the bulk modulus of the fluid passing through the connection. If C and Δt_{TLM} are physically accurate, then no numerical error will be introduced when connecting FMU_1 with FMU_2 via a TLM connection. Also, the delay Δt_{TLM} provides a clearly defined time window enabling numerically stable distributed simulation.

2 Requirments

A set of high-level functional and non-functional industrial requirements on a master simulation tool have been formulated by the OpenCPS project partners [3]. Saab's contribution to these requirements are derived from the currently implemented processes and methods applied for aircraft vehicle system modeling and simulation activities at Saab Aeronautics [8]. A subset of these requirements, which are relevant for this study, has been extracted and is shown in Table 1. These high-level requirements are used to guide the application example and TLMSimulator development as well as the preliminary evaluation of the TLMSimulator.

3 Application example

A combined set of interconnected aircraft vehicle systems of a generic fighter aircraft together comprise the application example. This application example is referred to as a small-scale systems simulator. Such a simulator is typically used for system development, training, software verification, fault simulation, performance prediction and evaluation, etc. The application example is specifically developed to facilitate an industry-grade platform for development and evaluation of master simulator algorithms such as the TLMSimulator, see section 4. The simulator architecture is schematically visualized in Figure 1. This prototype version includes models of the *Environmental Control System (ECS)* hardware as well as its controlling software, *ECS Control Software* in Figure 1. A model importing the relevant *Boundary Conditions* is also included. This model incorporates all flight mission data necessary for conducting simulations by reading a *<BoundaryConditions>.mat* file specified by the user. Two different subscribers of coolant air are modelled (*Consumer A* and *Consumer B*) and included along with simple *Cockpit* and *Engine* models.

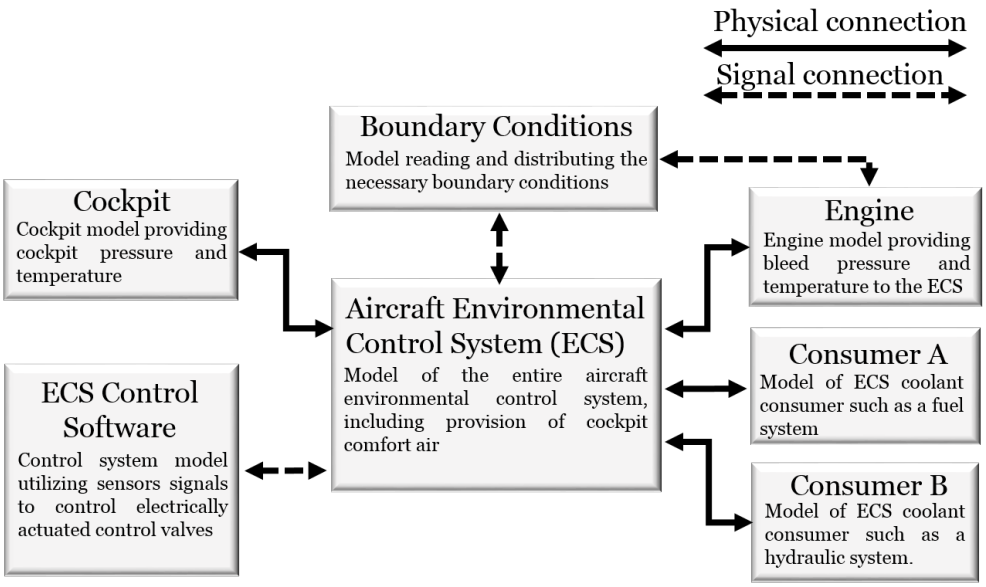

Figure 1: Schematic description of application example architecture

Table 1: Subset of requirements on an FMI compliant master simulation tool. The requirements are derived by industrial and academic partners of the OpenCPS project [3]

Number	Name	Description
1	FMU Import	Import of FMUs from tools such as Matlab/Simulink, OpenModelica, and Dymola shall be supported
2	Robustness	Given that all individual FMUs of a simulator configuration are numerically stable, numerical robustness for the simulator configuration as a whole shall be guaranteed
3	Solver configuration	Manual selection of the central solver used for FMUs for Model Exchange shall be available
4	FMU configuration	Support for setting FMU parameters. It must be possible to control start and stop times, solver step size, tolerance, etc.
5	Load simulator configuration	The end user shall be able to load a stored composition of FMUs

The dashed arrows in Figure 1 represent signal connections. The solid lines are physical connections, i.e. information about physical quantities such as volume flow and pressure is passed in its physical form. The latter type of connection is most suited to the TLM technique as it naturally contains a non-negligible time delay, see section 1.2.

3.1 Aircraft Environmental Control System

Aircraft environmental control systems are designed to provide their consumers with pressurized air at the correct mass flow and temperature. An industry-grade ECS model is included in the application example. This particular Modelica model is developed in Dymola using the Saab-developed library *Modelica Fluid Lite* (MFL) [9].

MFL is a stand-alone Modelica library with its own media functions. MFL is not a conventional Modelica library in the sense that components are connected causally strictly via two different types of power port connectors, one volume element connector and one flow element connector. Air with water content in both liquid and gaseous states is selected to be used in the application example as the presence of water greatly affects the ECS' performance limits. In MFL, pressure, mass flow, specific enthalpy and water content are passed between components for such a medium. All MFL components are classified as either volume or flow elements. As an example, one of the most fundamental flow elements in the MFL library is a frictionless pipe. The mass flow through such a pipe is computed via the pressure drop ΔP, provided by the interfacing volume elements, according to

$$\dot{m} = A\sqrt{2\rho\Delta P/Z} \tag{5}$$

where Z is the pressure drop coefficient. The pressure drop coefficient is specified as a component design parameter. The density, ρ, is computed using the pipe mean pressure along with the specific enthalpy and water content also provided by

the interfacing volume elements. The most fundamental MFL flow element is the node. The node pressure is calculated using

$$p = \rho R_{specific} T \tag{6}$$

assuming that the present medium is an ideal gas. In contrast to the volume element, the temperature, T, is computed using the specific enthalpy and water content in the node. The density in Equation (3) is computed as

$$\rho = \frac{\int_{t_0}^{t} \dot{m}_{net} dt}{V} \tag{7}$$

where V is the node volume specified as an input parameter.

The top level of the application example ECS model is shown in Figure 3. This specific model is not calibrated to represent any particular aircraft; it is a model of a generic Environmental Control System intended to be of industrially relevant complexity in terms of non-linearities and size. The heart of this system is a bootstrap configuration air-cycle machine which is supplied with conditioned air bled from the aircraft engine. The high bleed air temperature is decreased through the primary heat exchanger via a ram air intake.

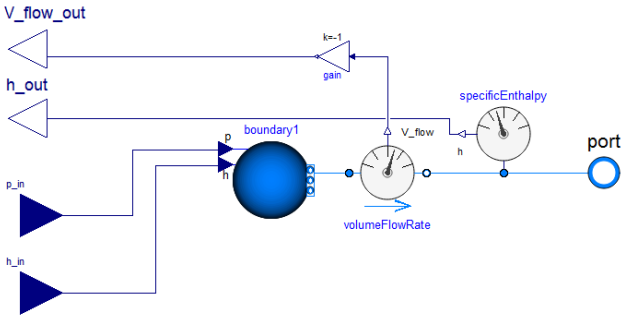

Figure 2: Example of model specifying the causality of models developed in Modelica.Fluid

This air is fed to the air-cycle machine, also referred to as a *cooling pack*, via a motorized control valve that regulates the pack outlet pressure. The cooling pack consists of a compressor, a turbine, multiple heat exchangers, and a water separator. The temperature of the conditioned air exiting the air-cycle machine is controlled to the set points specified by the consumers via two different by-pass branches. Examples of possible consumers of coolant air are the on-board avionics as well as the aircraft's fuel and hydraulic systems. The described ECS configuration is for the most part found in the majority of military fighter aircraft [10].

The ECS inputs/outputs are labelled as either *signal connections* or *physical connections* in Figure 3 just as in Figure 1. The physical connections are where applicable grouped in causal Modelica power port *connectors* [11] that pass information on volume flow, specific enthalpy, water content, and pressure in a predefined direction. Such connectors are beneficial when connecting FMUs of MFL models with one another as the causal connectors are automatically de-grouped

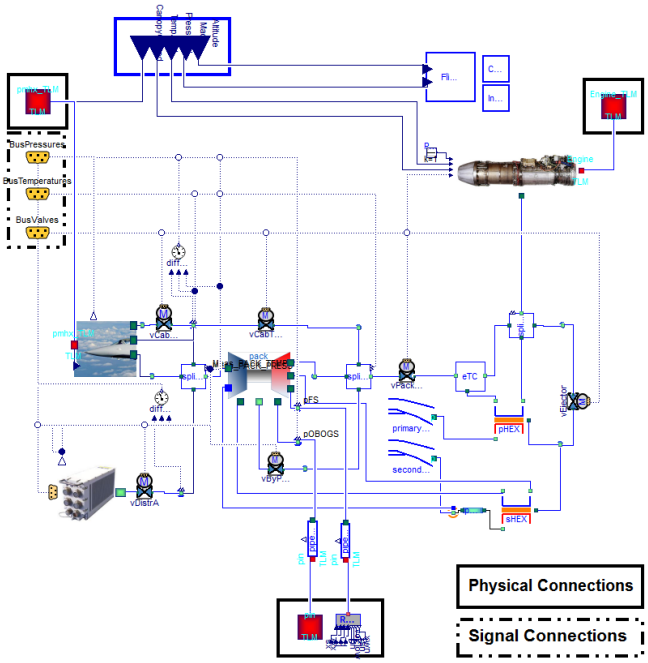

Figure 3: Modelica model of the Environmental Control System hardware

during FMU export from both Dymola and OpenModelica. Casual connectors, however, are not compatible with the acausal stream connectors generally used in Modelica libraries designed for bi-directional flow [12]. *Modelica.Fluid* is an example of such a library. The causality needs to be specified on any acausal interface if a model containing such connectors is to be connected to an MFL model or any FMU. Hirano et al. presents adaptors specifying the causality for signals in the electric and mechanics domains [13]. In Figure 2, a one dimensional thermodynamics domain adaptor for connections between Modelica.Fluid models and MFL volume type components is presented. This particular example is only suited to dry air as only information about volume flow, pressure, and specific enthalpy is passed with fixed causality. However, the adaptor can easily be modified to pass information about present water content as well.

A conventional acausal port from the Modelica.Fluid library is positioned on the right hand side of the adaptor. This port connects directly to any compatible Modelica.Fluid model such as a modelled consumer of ECS-conditioned air. The mass flow passing through the adaptor is a result of the difference in pressure between the pressure source and the connected Modelica.Fluid model. The pressure and specific enthalpy in the pressure source are specified via the two causal connectors on the left hand side of the figure.

A corresponding causal node component is shown in Figure 4. The node component utilizes input information on net volume flow to compute and return the resulting node pressure, see Equation (7). Connecting MFL flow element components with Modelica.Fluid models is easily done if the two adaptors presented in Figure 4 and Figure 2 are combined. The causal node component corresponds to the TLM connec-

tion of physical signals in the TLMSimulator. This adaptor is incorporated in the application example to simplify reference simulations in Dymola, see section 5.

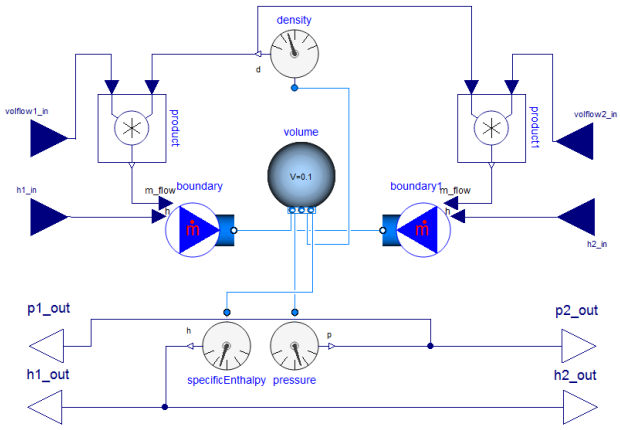

Figure 4: Example of node type model connecting Modelica models with causal interfaces. This adaptor is constructed using components from the Modelica.Fluid library

3.2 ECS Control Software

Here, the ECS Control Software refers to the Environmental Control System controlling software. Two different ECS software models of different level of detail are used in this study. A simple test-stub model is used to verify the interfaces and a slightly more detailed model used for rudimentary control. The latter model is meant to control the ECS' outputs to feasible nominal values during normal operation. Two versions of this more detailed model are developed in parallel, one in *Simulink* and one in *OpenModelica* [14]. The OpenModelica model is developed for reference simulations in any Modelica tool and the Simulink model is developed to provide the coupling between Simulink-generated FMUs and the selected integrating tool. The detailed ECS control software model consists of four proportional controllers. These controllers are empirically tuned to control four of the six motorized ECS valves. They are individually calibrated not considering the present cross-couplings. The ECS valves controlled via the proportional controllers are the valves designed for cooling pack outlet pressure control, cooling pack outlet temperature control, cockpit inlet air temperature control, and avionics cooling power control. The ejector and cockpit comfort air valves are not included. These valves are locked in nominal positions in this early prototype phase. The nominal positions are selected such that reasonable nominal flow, corresponding to normal operating conditions within the ejector flight envelope, are passed through the valves.

3.3 Consumers

Three different consumers are modelled separately and included in the application example: the Cockpit, Consumer A, and Consumer B. Models of the on-board avionics and cockpit avionics are included in the ECS hardware model. Consumers A and B are modelled as generic subscribers of coolant air. Both models consist of a series of pipes, along with a pneumatic self-regulating valve connected to a pressure sink. Such models can be seen as simple representations of an aircraft fuel or hydraulic system providing static and dynamic loads in terms of pressure and mass flow sufficient when the ECS is the system under investigation, during for example performance and fault simulations. In the application example, Consumer A is modelled using components from the Modelica.Fluid library and Consumer B is modelled using components from the MFL library. The cockpit model consists of a volume of representative size. This model provides a feasible inertia to the ECS model. It is separated from the ECS model as a first step towards including a more detailed cockpit model fulfilling the requirements associated with studies of pilot thermal comfort etc. Models of cockpit avionics, the pressure control system, and pilot *Air Ventilated Garments* (AVG) are positioned inside the ECS hardware model. The pressure control system consists of two valves controlling the cockpit pressure to a set point value depending on the aircraft's altitude. The modelled AVGs and cabin avionics are only representative in terms of pressure drop. Such a level of detail is sufficient for most studies where the ECS system is the unit under investigation. However, for in-depth studies of thermal comfort, the heat and moisture exchange between the ambient conditions, the cockpit, and the pilot also need to be considered.

4 TLMSimulator

The TLMSimulator is an open source master simulation tool originally developed by SKF, in collaboration with Linköping University, for coupling models of bearings with models from external tools [15]. The TLMSimulator is a framework for asynchronous TLM-based co-simulation. The tool's source code has been donated to the Open Source Modelica Consortium and a graphical user interface has been developed as part of the *OpenModelica Connection Editor* [16]. The master simulator is thus available both as a stand-alone tool and as a plugin to the OpenModelica environment. The OpenModelica plugin is used in this study. Models integrated in the TLM-based framework are interconnected using TLM elements, where each element has its own independent time delay Δt_{TLM}, see Equation (1) and Equation (2). Models are therefore numerically isolated from each other, which eliminates the need for complex algorithms to decipher the necessary order of model execution. Cyclic dependencies are identified by both Cremona et al. [17] and Galtier et al. [18] as a potential problem for the non-TLM-based simulation and development environments *FIDE* and *DACCOSIM*. A cyclic dependency is the occurrence of a direct dependency between an FMU input to one or more of its outputs. The TLM method avoids this issue by design as a result of the previously mentioned inherent time independence. This time independence enables each model to have its own independent step size and solver algorithm. The framework supports the FMI standard and FMUs can be imported using a wrapper executable. The framework does, however, not fully exploit the benefits of TLM in conjunction with FMI for co-simulation. As is, a brute force method of applying a number of FMU execution

Table 2: Application example sub-models exported as FMUs. FMUs for co-simulation are denoted CS *and FMUs for model exchange are denoted* ME

	Dymola	Simulink	OpenModelica
ECS H/W	ME/CS	-	ME
ECS S/W	-	ME/CS	-
Cockpit	ME/CS	-	-
Consumer A	ME/CS	-	-
Consumer B	ME/CS	-	ME
BC	-	-	ME/CS
Engine	ME/CS	-	ME

sub-steps to cope with interpolation of input variables is implemented in the framework. FMU inputs supplied at time t_1 are valid at $t_2 = t_1 + \Delta t_{TLM}$ seconds. This means that the FMU needs to determine all data necessary between $t_1 < t < t_2$ by interpolation unless an explicit fixed step solver with step length close or equal to the global time step is implemented. In the current version of the tool, the FMI function *fmiDoStep* is called a, by the user, specified number of additional times during one global time step. The FMU can then access an interpolation table located in the master to receive linearly interpolated data. This method cannot guarantee numerical stability and it results in a limited exploitation of the advantages in computational performance associated with TLM. Even so, support is provided for both FMI for co-simulation and FMI for model exchange. For the latter, the *CVODE* and *IDA* solvers from the SUNDIALS suite are provided. A constructed simulator configuration, referred to as a composite model in the TLMSimulator, is stored in an xml file format. The xml file contains information on what FMUs are included in a particular simulator configuration, I/O connections, parameter settings, and simulation settings such as simulation start and stop times.

5 Implementation

Dymola is used as reference in terms of numerical and functional verification of the application example. The reference implementation does not include any FMUs, only Modelica models developed in Dymola and OpenModelica, see Figure 5. All of the included models comply with the current version of the Modelica standard. The models included in this reference are connected via causal connections such that each individual model can be directly exported as an FMU. The TLM connections of the TLMSimulator are represented by node components, see Figure 4, placed between each sub-system Modelica model in the reference implementation. These node components are illustrated as blue and green circles in Figure 5.

The TLMSimulator currently supports FMI 2.0 for both co-simulation and model exchange. The variable step solver *CVODE* is used when applicable (FMUs for model exchange) in the application example. The architecture of the application example TLMSimulator implementation is described in the xml format supported by the tool. The OpenModelica graphical editor was used for manipulation of the simulator architecture. The different FMUs exported for TLMSimulator integration are listed in Table 2. FMUs for both model exchange and co-simulation are exported when possible. Export of FMUs for co-simulation is only possible implementing the fixed step explicit Euler solver in the used version of OpenModelica. The robustness and simulation efficiency are increased for all sub-models listed in Table 2 if a variable step solver is implemented. Only one single sub-model is therefore exported as co-simulation from OpenModelica as a proof of concept. The tool from where each FMU is exported is stated in the top row of the table. The export from Simulink is done using the Simulink toolbox *FMI Kit for Simulink* [19] provided by Dassault Systemes. The *FMU Compliance Checker* [4], a verification tool provided by the Modelica Association, is used to ensure FMU compliance with the FMI standard.

5.1 Results

This section covers simulation results from simulations of the application example Dymola implementation. A simple mission is simulated where the altitude is linearly increased from 0m to 800m in 80s. The Mach number is increased from 0.4 to 0.9 during the same time span. The engine bleed pressure and temperature are held constant at 1MPa and 177°C, respectively. Results at the interface of each included sub-system are provided. These results will serve as reference for implementing the application example in any other FMI supporting tool. The position of the six motorized ECS valves are shown in Figure 6 for an executed reference simulation of the application example in Dymola. This implementation is done using only Modelica models. The ECS Control model is specified to start controlling the ECS after 3 seconds. The four valves controlled by the software are the valves regulating the cockpit comfort air temperature, pack outlet pressure, avionics input flow of coolant air, and pack outlet temperature. As visualized in the figure, the position of the valves controlling the cockpit input mass flow and the ejector flow is kept constant throughout the simulation. The results indicate that the developed software model prototype operates as intended. The input mass flow to the two subscribers of ECS conditioned air, Consumer A and Consumer B in Figure 1, is shown in Figure 8. Consumer A receives the desired mass flow of 30g/s after approximately 30 seconds of simulation time. This simple consumer model mimics the simplified behaviour of for example an aircraft's fuel system. Consumer B extracts a periodically varying mass flow from the ECS. Such a consumer behaviour is representative of an *On-Board Oxygen Generation System* (OBOGS) which periodically switches between different beds of porous molecular sieve type material. Figure 7 shows values of simulated cockpit pressure as well as its targeted set point. The initial value of cockpit pressure deviates significantly from the set point as a result of a high pressure initial value currently necessary during application example initialization. The pressure settling time is shown as approximately 15 seconds in the figure.

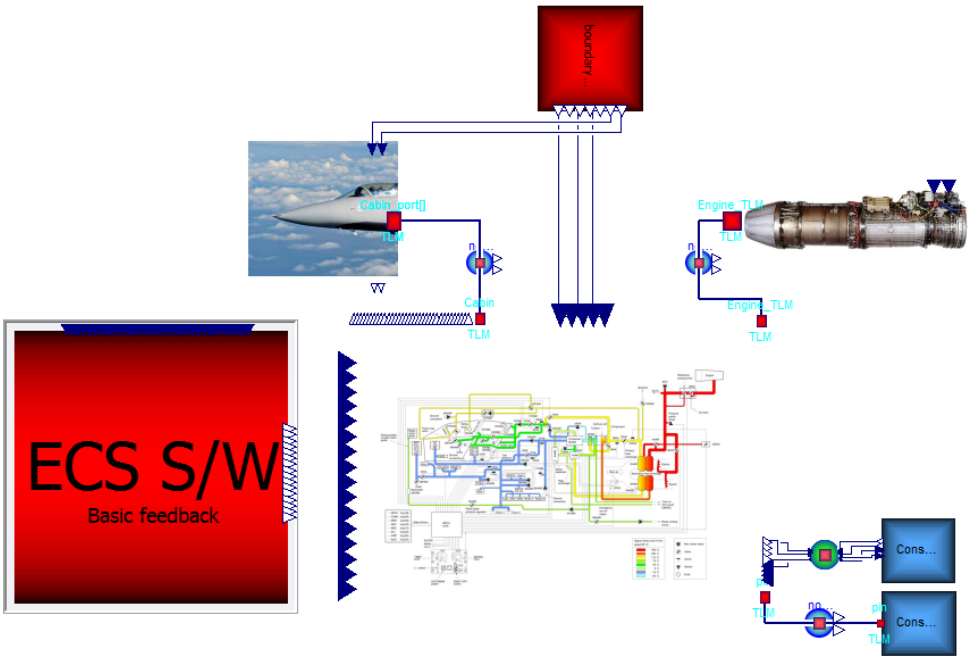

Figure 5: Graphical view of application example implementation in the commercially available modelling and simulation environment Dymola. All top level connections are causal; however, the majority of them are expressed solely in the code layer. The simulator layout is equivalent to that presented in Figure 1

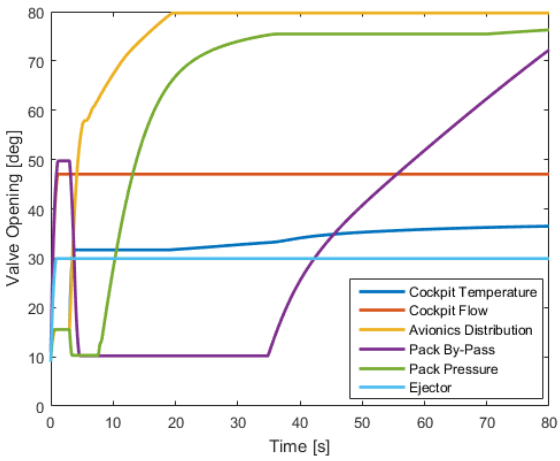

Figure 6: Position of ECS control valves during reference simulation

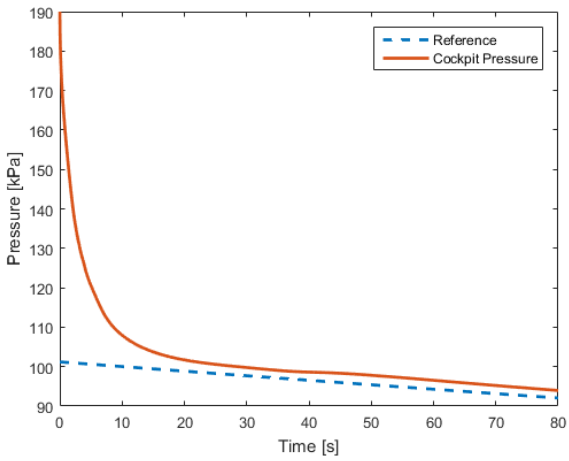

Figure 7: Simulated values of cockpit pressure along with the cockpit pressure set-point

6 Conclusions

An aircraft vehicle systems small-scale simulator is developed and implemented in Dymola. Reference simulations of this simulator are successfully conducted. The simulator can be used for evaluation, within the frame of aircraft vehicle systems simulation, of any FMI supporting master simulating tool, or any Modelica-based simulation environment. A simple and comprehensive method for separating aircraft vehicle system models, for applicability with TLM without significant additional introduced overhead, is presented along with examples from two different Modelica libraries. All separated sub-models of the application example have been exported as Functional Mock-up Units from the tool in which the sub-model was developed (Dymola, OpenModelica, and Simulink) and each individual FMU is determined as compliant with the FMI standard according to an official verification tool (the FMU Compliance Checker). The application example is implemented in the open source simulation framework supporting both FMI 2.0 and TLM; all of the application example FMUs are imported and the simulator architecture is specified using the tool's xml schema. However, no simulation results of the complete application example TLMSimulator implementation are available at the time of writing. The simulator configuration is a prototype

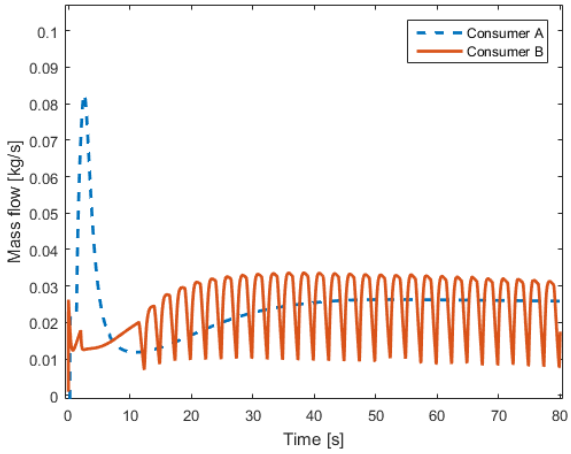

Figure 8: Simulated values of mass flow consumed by Consumer A and Consumer B

intended to be an industry-grade test case during TLMSimulator development. The application example has proven to be of great use during this development in spite of merely being a prototype and it is expected to increase in importance as it evolves.

6.1 Future work

Firstly, application example simulations in the TLMSimulator are to be conducted for verification of the application example as well as the TLMSimulator approach to simulating coupled aircraft vehicle systems. Furthermore, the developed application example is to be considered as industry-grade; however, several of the included models are severely simplified in comparison to what is being used for development etc. in the aeronautical industry. The presented small-scale simulator is an early prototype and further development is needed specifically in terms of increased detail of the sub-systems interfacing the ECS hardware. Also, industrial desktop simulators can include anything from a single sub-system to hundreds. Further inclusion of interfacing sub-systems is therefore essential. The development of the TLMSimulator is continuing within the frame of the OpenCPS project. Methods to fully exploit TLM in conjunction with FMI are currently under investigation. One approach is to utilize information on input derivatives to estimate FMU inputs in-between each global step. This development will run in parallel with the fine-tuning, and final implementation of the aircraft vehicle systems simulator application example.

7 Acknowledgements

This research has been funded via Saab Aeronautics and the ITEA 3 project Open Cyber-Physical System Model-Driven Certified Development (OpenCPS).

References

[1] International Council of Systems Engineering (INCOSE). Systems engineering vision 2020. Technical report, INCOSE, 2007.

[2] FMI development group. Functional mock-up interface for model exchange and co-simulation. Technical report, Modelica Association, 2014.

[3] Open cyber-physical system model-driven certified development. `https://www.opencps.eu/`. Accessed: 2017-03-14.

[4] Funtional mock-up interface. `http://https://www.fmi-standard.org`. Accessed: 2017-02-21.

[5] Modelica and the modelica association. `https://www.modelica.org/`. Accessed: 2017-02-21.

[6] Petter Krus. An introduction to modelling of transmission lines. Technical report, Linköping University, The Institute of Technology, 2006.

[7] Robert Braun and Petter Krus. An explicit method for decoupled distributed solvers in an equation-based modelling language. In *Proceedings of the 6th International Workshop on Equation-Based Object-Oriented Modeling Languages and Tools*, Berlin, Germany, 2014.

[8] Henric Andersson and Magnus Carlsson. Saab aeronautics handbook for development of simulation models : Public variant. Technical Report 12/00159, Linköping University, Machine Design, 2012.

[9] Magnus Eek, Hampus Gavel, and Johan Ölvander. Definition and implementation of a method for uncertainty aggregation in component-based system simulation models. *Journal of Verification, Validation, and Uncertainty Quantification*, 2, 2017.

[10] J. Shetty, C.P. Lawson, and A.Z. Shahneh. Simulation for temperature control of a military aircraft cockpit to avoid pilot's thermal stress. *CEAS Aeronautical Journal*, 6(2):319–333, 2015.

[11] Dassault Systemes AB. *Dymola User Manual*, 1 edition, September 2016.

[12] Peter Fritzson. *Principles of Object-Oriented Modeling and Simulation with Modelica 3.3*. IEEE Press, 2nd edition edition, 2015.

[13] Yutaka Hirano, Satoshi Shimada, Yoichi Teraoka, Osamu Seya, Yuji Ohsumi, Shintaroh Murakami, Tomohide Hirono, and Takayuki Sekisue. Initiatives for acausal model connection using fmi in jsae. In *Proceedings of the 11th International Modelica Conference*, 2015.

[14] Peter Fritzson and Peter Aronsson. The openmodelica modeling, simulation, and software development environment. *Simulation News Europe*, 44(45), dec 2005.

[15] Alexander Siemers, Dag Fritzson, and Iakov Nakhimovski. General meta-model based co-simulations applied to mechanical systems. *Simulation Modelling Practice and Theory*, 2009.

[16] A. Mengist, A. Asghar, A. Pop, P. Fritzon, W. Braun, A. Siemers, and D. Fritzon. An open-source composite modeling editor and simulation tool based on fmi and tlm co-simulation. In *Proceedings of the 11th International Modelica Conference*, 2015.

[17] Fabio Cremona, Marten Lohstroh, Stavros Tripakis, Christopher Brooks, and Edward A. Lee. Fide - an fmi integrated development environment. In *Symposium on Applied Computing*, April 2016.

[18] Virginie Galtier, Stephane Vialle, Cherifa Dad, Jean-Philippe Tavella, Jean-Philippe Lam-Yee-Mui, and Gilles Plessis. Fmi-based distributed multi-simulation with daccosim. In *Proceedings of the Symposium on Theory of Modeling & Simulation: DEVS Integrative M&S Symposium*, DEVS '15, San Diego, CA, USA, 2015. Society for Computer Simulation International.

[19] Dassault Systemes AB. *FMI Kit for Simulink*, October 2016.

Energy Efficiency Comparison of Electric-Hydraulic Hybrid Work Implements Systems

Björn Eriksson , Vivek Bhaskar*, and Ralf Gomm*

Global Mobile Systems (GMS), Parker Hannifin, Borås, Sweden
E-mail: bjorn.eriksson@parker.com
*Technology, Commercialization and Support team (TCS), Parker Hannifin, Charlotte, U.S.A.

Abstract

Increasing attention of electromobility creates new opportunities and even requirements to electrify traditional work implements of mobile machinery. Four possible implement system architectures are presented and compared regarding energy efficiency performance in this paper. The goal of this work is to frame the upper and lower end of system value versus complexity characteristics. Thus, an electrically powered load sensing circuit, E-LS, serves as a reference system (low added complexity, low added value) while a four quadrant electro-hydrostatic actuation, EHA, system (high added complexity, high added value) is found in the other end of the comparison. An electrically powered flow controlled system, E-IFC, and a electrically powered pump controlled system, E-PCA, are also investigated in the same framework to make the study comprehensive. A two actuator wheel loader system and a short cycle loading drive cycle serves as the platform for comparison. The results yield a 45% reduction of energy consumption with the EHA system compared to the E-LS system. This is equivalent to 82% fuel efficiency improvement.

Keywords: Hydraulics, Fluid Power, Electromobility, Efficiency, Electric Systems, Hybrid, e-LS, e-IFC, e-PCA, EHA

1 Introduction

Fuel efficiency has in the late years become a driver of technology development in the industry. Research and development in the area are extensive in both academia and industry. To minimize the dependency of fossil fuel many OEMs are investigating the use of electricity as energy carrier and storage. The electromobility era is here.

Mobile applications use internal combustion engines, ICE, as primary power source. During a work cycle, flow and pressure demands vary. The ICE efficiency is a function of the operating point, i.e. speed and torque at the engine shaft. Typically, with hydraulic implements the pump units are mechanically directly connected to the ICE. This implies that the ICE torque and speed vary with the load during operation.

A common approach when designing energy efficient mobile systems today is to decouple the load from the ICE. This can be done in various ways. The decoupling opens up the opportunity to run the ICE in or close to the efficiency sweet-spot. From a general perspective, a transmission of some kind is needed that is able to transform between the flow and effort variables. Either between torque and speed, pressure and flow or voltage and current. The criteria is that the product of the two is constant[1]. Further, if a large enough energy storage is included in this transmission both speed and torque can be chosen freely by the control system, independent of the load. Smoothing the power demand from the ICE avoiding peak demands.

This paper is limited to and focused on electric supplied hydraulic implement systems. Further, the drive-line is not studied. The systems are supplied from a common electric supply, a direct current bus, DC bus.

The systems in this paper can be split into two groups

Central pump without recovery The E-LS and the E-IFC systems use a single centralized pump approach where the functions share the supply. The pump handles only power in one direction with no recovery to the DC bus through the electric machine.

Independent pumps with recovery The E-PCA and EHA systems use one pump for each function and these pumps are also able to recover power back to the DC bus.

Hybrid mobile vehicles also often include redesigned drive-lines for the same reasons mentioned above.

The aim of this work is to compare different systems solutions electrifying the implements in a mobile application. The ap-

[1]Constant product of flow and effort variable is equivalent to constant power.

plication in this study is a wheel loader. The electric supply is not considered. System boundaries start at the DC bus and end at the function cylinders, see Figure 1.

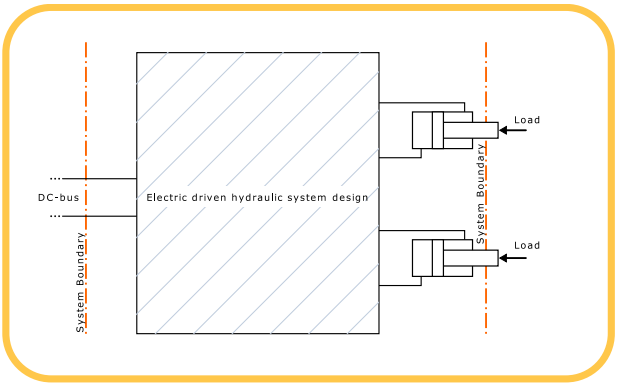

Figure 1: System boundary of studied system

The following studied systems take origin in conventional architectures presented in earlier works, but now with electrification. The exception is EHAs, which are not commonly used in traditional mobile hydraulic systems and are already electrified in all existing applications. The studied systems are

Electric load sensing, E-LS LS systems are considered as the state-of-the-art systems of today in mobile machinery, see for example [1] in [2], [3] in [4] and [5]. The most straight forward way of implementing an electric supplied system is to connect the pump in a state-of-the-art LS system to an electric motor. In this paper it is denoted by E-LS. The E-LS system serves as the reference system in this study.

Electric flow controlled system, E-IFC Flow controlled systems have gained increased popularity among researchers in the field of fluid power in the last decade, see for example [6] and [7]. Among the benefits are lower metering losses and open loop pump control, see [8] and [9].

Electric pump controlled actuators, E-PCA The approach to use displacement control instead of valves for implements has been subject for research a number of years, see [10] and [11] in [12]. This approach can be electrified similar to the E-LS system by connecting the hydraulic machine to an electric machine instead of the ICE. Here denoted E-PCA.

Electro-hydrostatic actuators, EHA One electric and one hydraulic machine are used at each function. The similarity with E-PCA is the decoupling of the functions. The use of fixed hydraulic machines removes control losses, idling losses as well as low efficiency when partly stroked. EHA was first seen in the aerospace industry, see for example [13].

Another system layout which would also fit in the comparison is the independent metering valve system, IMV. However, the IMV class of systems are excluded. The reason is that there exists a number of different approaches in the IMV area both in hardware and in controls. For some different approaches see [14], [15], [16] in [17], [18] in [19].

2 Modeling and Simulation

The evaluation is based on a combination of measurements and simulations. The loads are extracted from measurements and used as input to a simulation model. The input signals to the models are cylinder speeds and forces. The speeds are derived from filtering the position measurements. The forces are derived with chamber pressures and areas.

Static backward simulation is deployed, see Figure 2. The results, in a way, capture the dynamics of the system since measurements from a duty cycle are used. Dynamic characteristics from the cycle are therefore included through the measurements.

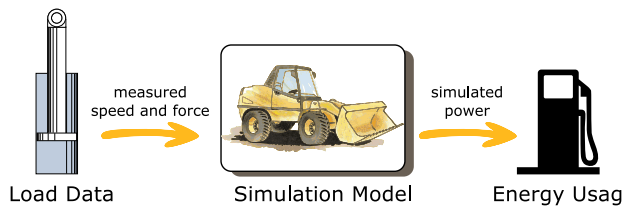

Figure 2: Explanation of backward simulation

The E-LS, E-IFC, E-PCA and EHA simulation models have been used on the same load data set to obtain a comparison in terms of power and energy consumption.

2.1 Duty Cycle

When a mobile system is to be evaluated, the load profile, work cycle or duty cycle, is as important as the fidelity of the simulation model itself. A certain system design can show completely different energy efficiency performance if the duty cycle is unrepresentative for the application.

This paper uses a wheel loader as the example application. A typical production cycle of this type of machines is the short load cycle, see Figure 3.

2.2 Modeling Description

The simulation models are simplified in a number of aspects.

Loads Inputs to the models are forces and speeds extracted from position and pressure measurements at a wheel loader running short loading cycles, see Section 2.1.

Cylinders Frictions are not part of the model since the load inputs are measured by pressure sensors. Flow losses in the cylinders are considered insignificant and are ignored.

Valves Metering out losses are estimated as function of flow. Pilot losses are ignored.

Pumps Flow and pressure dependent efficiency maps of the pumps are used. Controls losses are ignored.

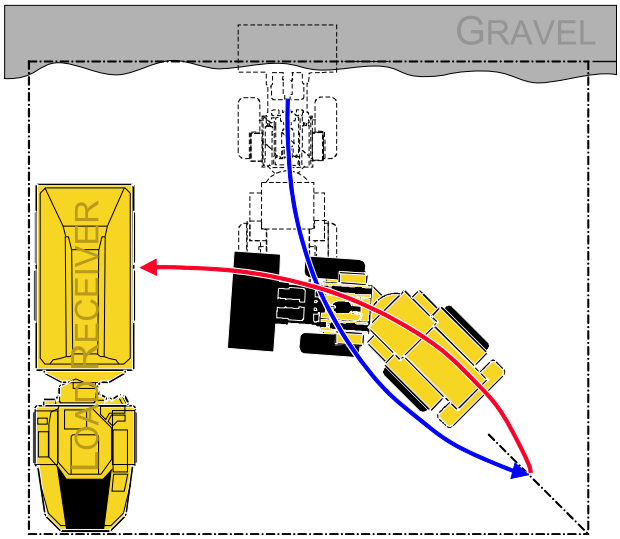

Figure 3: A short loading cycle (Reprinted from [20] with permission.)

Electric machines Permanent magnet alternating current motor, PMAC, is used for this comparison. Electric motors are modeled by accounting for current and temperature depending winding losses, rotor and stator iron losses as well as viscous damping losses.

Inverters Insulated gate bipolar transistor, IGBT, inverters serve as motor controllers to enable variable speed and torque control. A generic inverter model is used for this analysis, with losses being a function of motor current, switching frequency and supply voltage.

2.3 Electric Load Sensing Systems, E-LS

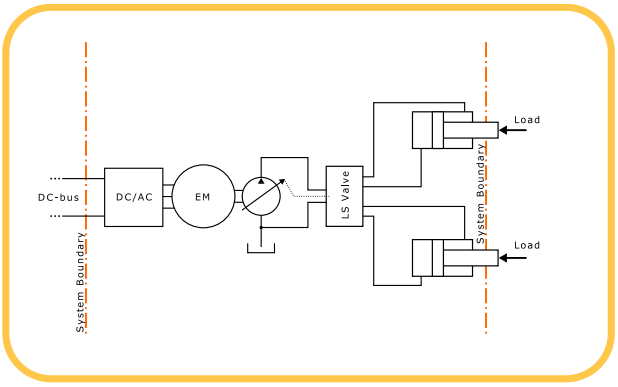

Figure 4: An E-LS system approach

The first system is an electrically driven conventional LS system, E-LS. The pump is a variable displacement pump run at constant speed. The only difference from conventional LS is that the hydraulic system is supplied from an electric motor instead of an ICE. The modeled system is shown in Figure 4. This is the reference system in this paper.[2]

[2]This is chosen as a reference system since it is the closest electrically driven hydraulic system to a conventional state-of-the-art approach.

2.4 Electric Intelligent Flow Control, E-IFC

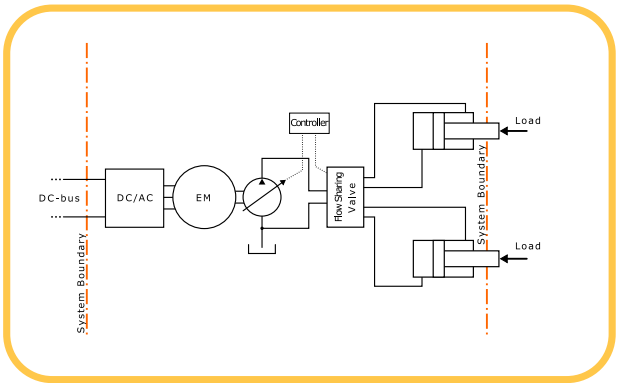

Figure 5: An E-IFC system approach

An alternative to conventional LS systems is flow controlled systems. The main difference is that the pump is controlled in an open loop flow control mode directly by the controller/joystick instead of in a closed loop with the load pressure. This is referred to as intelligent flow control, IFC. Here it is supplied with an electric pump and called E-IFC.

2.5 Electric Pump Controlled Actuation Systems, E-PCA

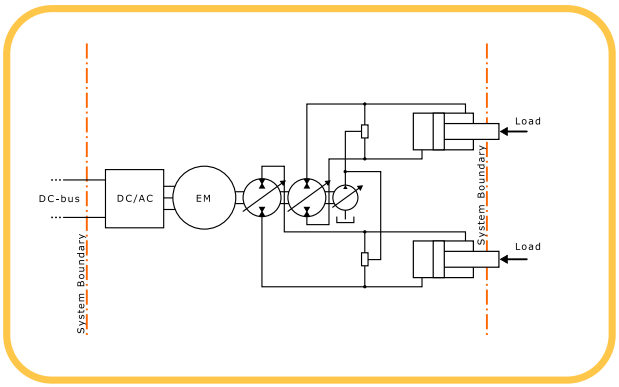

Figure 6: An E-PCA system approach

This approach uses over center hydrostatic pumps. One pump is used at each function. The loads are controlled in a decoupled manner with respect to the displacement settings. This approach is called pump controlled actuator, PCA. In this paper an electrical machine is used at the supply side instead of a ICE. It is here denoted E-PCA. See Figure 6.

2.6 Electro-Hydrostatic Actuation Systems, EHA

A system utilizing decoupled functions with fixed machines with separate electric supplies is studied as well, EHA. A benefit compared to the E-PCA is that the hydraulic machine efficiency is higher because of the use of fixed machines. The speed of the hydraulic machines is controlled independently. Compared to the E-PCA approach this allows uses of smaller machines.

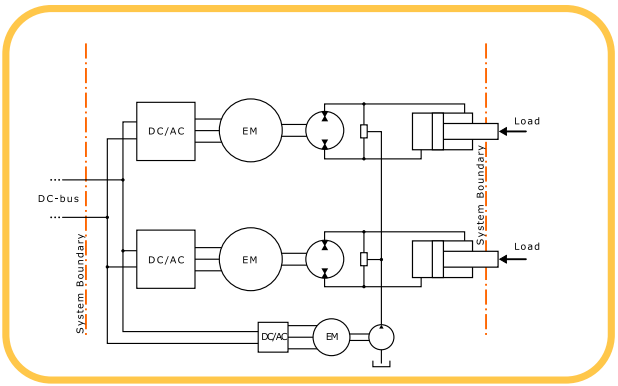

Figure 7: An EHA *system approach*

3 Simulation Results

The simulation models were run with identical input[3]. The bar diagram in Figure 8 shows the energy used with the different system layouts described in Sections 2.3-2.6. All results in the diagram are normalized to the energy input to the E-LS system. Hence, the output work is the same for all systems.

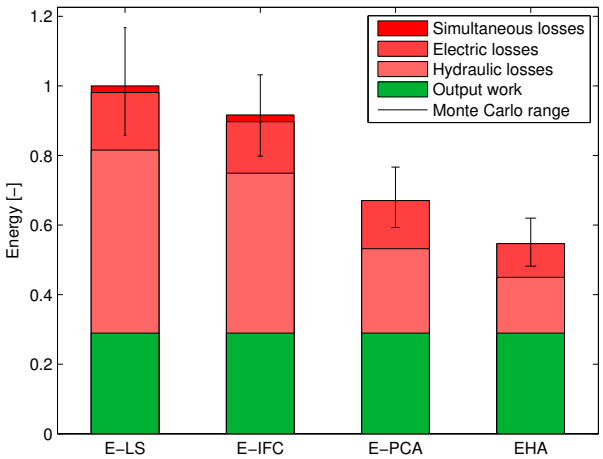

Figure 8: Relative comparison of used DC *energy in a short load cycle, see Section 2.1 (boom and bucket functions only)*

It can be seen that there are grades of potential energy savings depending on the chosen concept, the EHA system shows highest saving potential.

Systems with a centralized pump approach, such as E-LS and E-IFC, suffer from pressure losses when actuating more than one load at different load pressure levels. These types of losses are often caused by an interaction between the steering and the rest of the implements. Since steering is not a part of this study this effect is minor. This explains the low values of simultaneous losses in Figure 8.

[3]Forces and speeds as described in Section 2.

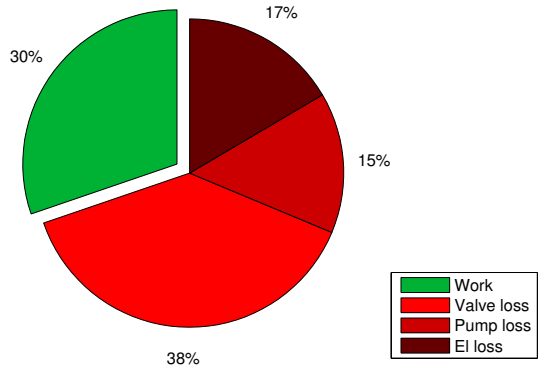

(a) E-LS system

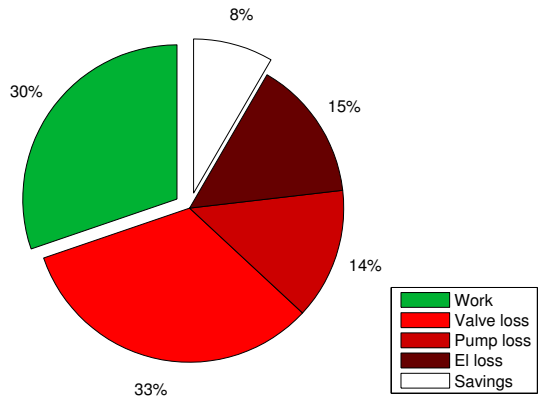

(b) E-IFC system

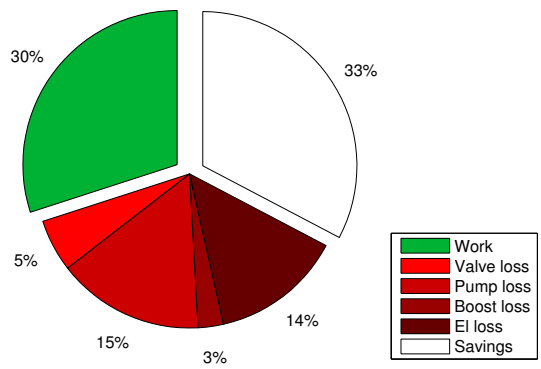

(c) E-PCA system

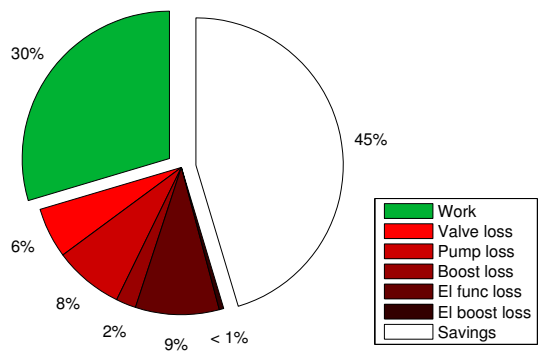

(d) EHA system

Figure 9: Energy distribution with savings compared to E-LS, *"el" losses include inverter and electric machine losses*

Figure 9 shows the distribution of the input energy for each system. The energies in Figure 8 and 9 are categorized as

Output work/Work Net work performed by the cylinders.

Electric losses/El loss All losses at all inverters and electric machines.

El func loss Inverter and electric machine losses related to the boom and bucket functions.

El boost loss Inverter and electric machine losses related to the boost system.

Hydraulic losses All flow and pressure losses in the hydraulics.

Simultaneous losses Hydraulic losses created by reducing pump pressure from a shared pump to the lighter load(s).

Valve loss All throttling losses at the valves.

Pump loss Hydraulic losses at the hydraulic machine.

Boost loss Hydraulic losses at the boost system.

Savings Energy input difference compared to the E-LS system, hence expected energy savings on a changeover from E-LS.

3.1 Sensitivity

A Monte Carlo analysis was done to show the sensitivity of parameter variations in the models. The sensitivity of some of the major parameters used in the model is shown in Figure 8. The parameter ranges are presented in Table 1.

Table 1: Parameter variations at the Monte Carlo analysis

		Applicable at			
Parameter	Uncertainty	E-LS	E-IFC	E-PCA	EHA
Pump margin pressure	±20%	x	x		
Meter-out valve Δp	±50%	x	x		
Load holding valve Δp	±50%			x	x
Pump efficiencies	±5%	x	x	x	x

4 Discussion

As mentioned in Section 2.1, the duty cycle in which a study is performed is crucial for the out coming results. The cycle used in this paper is representative for wheel loaders in the mid to large range. Generally, the larger wheel loader model it is the more time of its life is spent in production similar to the short loading cycle described in Section 2.1. This justifies the results given in this paper. However, the steering circuit is not considered in the models in this paper. In many LS systems of wheel loaders of today the steering circuit is a part of the work hydraulics. Having the work hydraulics and the steering system merged results in increased system losses, called "simultaneous losses" in Figure 8. Therefore, it is an important note to make that the steering is not included in this paper. Including steering would increase these losses in the analyses of E-LS and the E-IFC systems. The results would then separate the central pump and the independent pumps systems even more than can be seen in Figures 8 and 9. However, since some large machines at the market use separate steering systems with independent pumps this study is still valid.

The systems modeled in this paper are one representation of the different system concepts. There are variations that might impact the results. The authors have tried to cover the main characteristics of the different concepts. For example, the E-PCA system is modeled using a variable boost pump. In many publications the boost system uses a fixed pump together with an accumulator. This difference of course impacts the result. This particular difference needs to impact less then 3% since the losses of the boost system is shown to be 3% in Figure 9(c).

An opportunity when innovative energy saving systems are designed is to mix known concepts. For example, an EHA could be used at the boom and an E-LS system used at the other function or functions. However, that is out of the range of the scope of this paper.

Since IMV systems were excluded in this paper it is worth a comment. By considering the hardware layout, its capability and limitations it would be expected to find E-IMV concepts in between the E-IFC and E-PCA in Figure 8. The reasoning behind is that an E-IMV system would be capable of recovery but not continuously adopt to all load conditions without throttling. It would also need a variable machine.

Different efficiency models have been used for the fixed machine used in the EHA model compared to the variable machine used in the others. The efficiency of the fixed machine is slightly higher than the variable machine, at full displacement, in the same operating point. This is because a bent-axis technology is assumed to be used in the EHA concept. In the other models in-line machines are assumed.

In variable machines control losses come from the hydraulic controller of the machine. In LS and E-LS systems, for example, the controller is a valve and a cylinder that displace the machine depending of the pressure feedback signals, LS signal and pump pressure. This losses can be as large as 10% of the pump power in certain operating points. In fixed machines this loss is not present since there is no controller. The control losses of the machines are ignored in this paper.

The Monte Carlo analysis can be used and interpreted in different ways. Some of them are

Parameter uncertainty With varied parameters the model confidence can be increased by studying the variation in the results.

Model uncertainty In a case where most of the uncertain parameters are subject to change in a Monte Carlo analysis the model robustness is shown in the variation of the results.

Design sensitivity For a certain system, e.g. E-LS, some parameters can vary between different implementations.

By simulating with a range of parameters also a range of systems within a system design can be studied.

All three above interpretations are connected but are interesting to keep in mind when studying the results in Figure 8.

5 Conclusions

This paper shows how a number of different electric system designs for the hydraulic implements[4] of a wheel loader perform, compared to an E-LS system, in a well defined working cycle. The results are that the energy consumptions are reduced by 8% with an E-IFC system, 33% with an E-PCA system and 45% with an EHA system. It is also shown how a number of crucial parameters that usually vary at different implementations of same system layout impacts the energy consumption. For example, a conclusion from the results is that an efficient E-LS system can be more efficient than a less efficient E-IFC system. In the same way a conclusion is that an EHA system is always more efficient than both an E-LS system as well as an E-IFC system. An important remark here is that the above reasoning is valid with this particular work cycle for a wheel loader and also the parameter variations within the range presented in the paper.

References

[1] Bo R. Andersson. A survay of load-sensing systems. *The* BFPR *Journal*, 13:103–115, 1980.

[2] Bo R. Andersson. *On the Valvistor, a proportionally controlled seat valve*. PhD thesis, LiTH, 1984. ISBN 91-7372-748-2.

[3] P. Krus, T. Persson, and J-O. Palmberg. Dynamic properties of load sensing systems. In *International Conference on Fluid Power, Tampere, Finland*, 1987.

[4] Petter Krus. *On Load Sensing Fluid Power Systems - With Special Reference to Dynamic Properties and Control Aspects*. PhD thesis, LiTH, 1988.

[5] Svend Giversen. Saving energy in mobile hydraulic systems. In *The Eighth Scandinavian International Conference on Fluid Power*, 2003.

[6] Birgitta Lantto. *On Fluid Power Control with Special Reference to Load-Sensing Systems and Sliding Mode Control*. PhD thesis, LiTH, 1994.

[7] Mikael Axin, Björn Eriksson, and Petter Krus. Flow versus pressure control of pumps in mobile hydraulic systems. *Proceedings of the Institution of mechanical engineers. Part I, journal of systems and control engineering*, 228(4):245–256, 2014. ofc.

[8] Björn Eriksson and J.-O. Palmberg. How to handle auxiliary functions in energy efficient, single pump, flow sharing mobile systems. In H. Murrenhoff, editor, *The 6th International Fluid Power Conference 7.IFK*, volume 1, pages 65–78, March 2010.

[4] Boom and bucket are referred to as implements in this paper.

[9] Mikael. Axin, Björn Eriksson, J.-O. Palmberg, and Petter Krus. Dynamic analysis of single pump, flow controlled mobile systems. In *The Twelfth Scandinavian International Conference on Fluid Power*, 2011.

[10] R. Rahmfeld and M. Ivantysynova. Displacement controlled linear actuator with differential cylinder -a way to save primary energy in mobile machines. In *Fifth International Conference on Fluid Power Transmission and Control (ICFP)*, volume 1, pages 316–322, 2001.

[11] Kim Heybroek, Jonas Larsson, and Jan-Ove Palmberg. Mode switching and energy recuperation in open-circuit pump control. In J. Vilenius and K. T. Koskinen, editors, *The Tenth Scandinavian International Conference on Fluid Power*, volume 3, pages 197–210, May 2007.

[12] Kim Heybroek. *Saving Energy in Construction Machinery unsing Displacement Control Hydraulics*. Lic thesis, LiU-Tryck, Linköping, 2008.

[13] E. T. Raymond and C. C. Chenoweth. *Aircraft Flight Control Actuation System Design*. Society of Automotive Engineers, Inc., 1993. ISBN: 1–56091–376–2.

[14] Song Liu and Bin Yao. Energy-saving control of single-rod hydraulic cylinders with programmable valves and improved working mode selection. In *The 49th National Conference on Fluid Power*, pages pp. 81–91, 2002.

[15] QingHui Yuan and J.Y. Lew. Modeling and control of two stage twin spool servo-valve for energy-saving. In *Proceedings of the 2005 American Control Conference*, volume 6, pages 4363–4368, 2005.

[16] Amir Shenouda and Wayne Book. Energy saving analysis using a four-valve independent metering configuration controlling a hydraulic cylinder. In *2005 SAE Commercial Vehicle Engineering Conference, November 2005, Rosemont, IL, USA, Session: Simulation and Optimization Part 1 of 3: System Level*. SAE, November 2005.

[17] Amir Shenouda. *Quasi-Static Hydraulic Control Systems and Energy Savings Potential Using Independent Metering Four-Valve Assembly Configuration*. PhD thesis, Georgia Institute of Technology, July 2006.

[18] Björn Eriksson, Marcus Rösth, and J.-O. Palmberg. A high energy efficient mobile fluid power system - novel system layout and measurements. In *Conference proceedings of the 6.IFK*, 2008.

[19] Björn Eriksson. *Mobile Fluid Power Systems Design : with a Focus on Energy Efficiency*. PhD thesis, Linköping University, Fluid and Mechanical Engineering Systems , The Institute of Technology, 2010.

[20] Reno Filla and J.-O. Palmberg. Using dynamic simulation in the development of construction machinery. In *The 8th Scandinavian International Conference on Fluid Power*, volume 1, pages 651–667, May 2003. LiTH.

The Hydraulic Infinite Linear Actuator with Multiple Rods

Magnus Landberg, Magnus Sethson*, Petter Krus*

Saab Aeronautics, Linköping, Sweden
E-mail: magnus.landberg@saabgroup.com, magnus.sethson@liu.se, petter.krus@liu.se
* Division of Fluid and Mechatronic Systems;
Department of Management and Engineering,
Linköping University, Linköping, Sweden

Abstract

Future hydraulic actuation systems can be significantly improved by utilisation of a new type of hydraulic linear actuator technology. By enabling multiple actuating elements, integrated in a compact and lightweight single unit controlled by ordinary directional valves it is possible to achieve a high position accuracy. This is a new way to generate and distribute mechanical linear movement and force by using hydraulic actuators in a cost effective way, in less responsive closed loop systems. This is a variant on the Hydraulic Infinite Linear Actuator, HILA, invention. The technology also represents a new sort of digital hydraulics. The presented technology provides typical hydraulic actuator characteristics with high system pressure and potentially no external oil leakage. It is based on a well-known hydraulic clamping element technology used in a new way, where the piston and the piston rod can quickly be coupled and uncoupled by means of the clamping element in a failsafe way by using well defined incremental steps. HILA in its simplest usage, provides new features to hydraulic cylinders such as providing very long strokes, high rod speed, and small chamber volumes which means high stiffness and low capacitance. The aim of this study is to present a fundamentally new way of using hydraulic actuators. The invention is called the Hydraulic Infinite Linear Actuator with Multiple Rods, HILA MR. The study presents the idea, principles and feasible combinations of the technology. Also applications in the aircraft and robotic field will be presented.

Keywords: hydraulic actuator, incremental control, snake-like robot, robot arm

1 Introduction

Linear hydraulic actuators is highly competitive, unique in some aspects and have significant advantages compared with electric motor drives and electric actuators. These advantages are higher power to weight ratio, stiffer than electric drives, smoother performance at low speed, wider speed range, and greater extent of self-cooling even in stall condition [1].

In areas where high forces and precise movements are needed, hydraulic solutions are often required. Reducing the size of fluid power components and systems, by increasing power density, while maintaining power output provides a great benefit. There is a need of multiple actuator functions with high requirements for strength and stiffness to be implemented especially in confined working spaces. These are common in the aircraft and automotive production, where also compactness and agility are advantageous. These requirements are also common in robot applications, such as articulated robots and snake-like robots.

Additionally, the hydraulic cylinder needs to be designed for longer strokes for use in Cartesian/Gantry robots, tooling machines and additive manufacturing of bigger objects.

The basic invention, in this paper, is a hydraulic cylinder with a releasable piston. It is called the Hydraulic Infinite Linear Actuator (HILA) and is presented in [1]. A hydraulic membrane, the clamping mechanism, is connecting the piston and the rod when pressurised. By using simple logic valves for pressurizing, the piston and rod can be connected and disconnected with maximum secure and reliable clamping in a fast way.

The paper presents a new way of using hydraulic actuators and reports the present state of the HILA development project, that is a collaborative work between Linköping University and Saab AB. In this paper, the focus will be on finding interesting applications that can further enhance the development process of the project. Hopefully, at the same time, the study of the applications will have commercial impact. The ideas and principles of the multiple rod technology will be presented, mainly on a conceptual level. To some extent this project takes the hydraulic cylinder technology into new exciting areas, as this technology has been developed slowly in recent decades compared to electric linear actuators.

The disposition of the article is as follows. It is divided into four main parts, see fig 1. The first part is a description of the basic HILA technology with only one piston rod; the structure and its operation of a standard cylinder. It also describes how bronze bearings and boots can replace the rubber seals between the piston and the cylinder; the advantages and disadvantages, including removing of external leakage, the ability to handle lateral forces and increase the maximum rod speed.

In the second part, HILA with incremental control is presented. It adds new features to present hydraulic cylinder technology and can be a potential alternative to expensive electric and hydraulic servo systems, when high position accuracy is the primary goal within less responsive closed loop systems. The technology also represents a new sort of digital hydraulics.

An aircraft high lift flap system with trim capability has been chosen as a suitable example for aviation applications. This normally requires expensive, complex and maintenance intensive electrical or hydraulic actuation systems. The presented technology can also be used on the leading edge slat system.

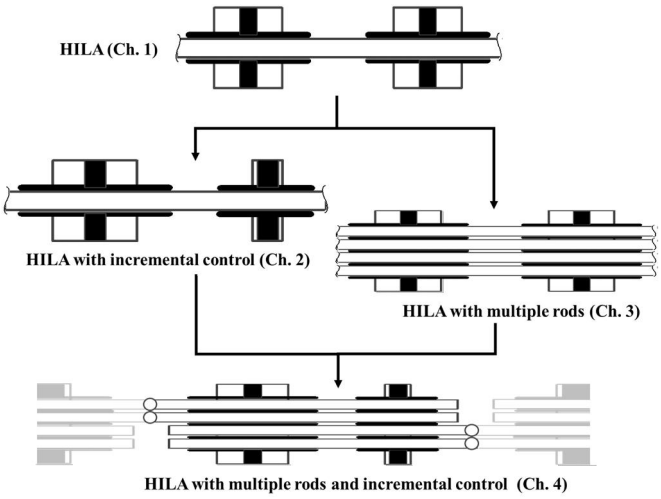

Figure 1. The disposition of the paper, chapter 1 - 4 (Grey parts are surrounding machine elements).

The third part introduces HILA with Multiple Rods (HILA MR) technology. It enables a completely new way to generate and distribute mechanical linear movement and force by using hydraulic actuators, maintaining high pressure, compactness and energy efficiency. An unmanned aircraft, which flies autonomously has been selected as another suitable example for aviation control application. It is also described how a single position sensor on the common piston can be used to determine the absolute position of the individual piston rod.

In the fourth part HILA MR technology is combined with incremental control using ordinary directional valves. It is applied to robot arm segments. By manoeuvring four piston rods simultaneously, twin rotary actuation systems for pitch and yaw in each robot arm segments end is made possible. With large and small incremental steps executed in two linked robot arm segments, it will be able to have a more accurate and time efficient method for angle positioning. The segments can be built together in series creating a snake-like robot. Such high agility robot configuration is capable of working in confined spaces and reach the farthest ends of the cavities of for example an aircraft wing tank. This is an aviation manufacturing example.

1.1 Introduction to HILA technology applied on one piston rod

The basic actuator innovation, the Hydraulic Infinite Linear Actuator (HILA) is presented in more detail in [2]. In its simplest usage it is characterised by providing very long strokes, high system pressure, power efficiency, compactness and small chamber volumes. The actuator has a higher stiffness and higher natural frequency compared to conventional hydraulic cylinders. These factors are favourable in control design [2]. The higher system pressure and symmetric piston areas allows for an even more compact system design, with lower flow levels and a smaller reservoir.

The basic invention is a hydraulic cylinder with a releasable piston. A hydraulic membrane, the clamping mechanism, is connecting the piston and the rod, when pressurised. By using simple logic valves for pressurizing, the piston and rod can be connected and disconnected with maximum secure and reliable clamping in a fast way (see fig. 1).

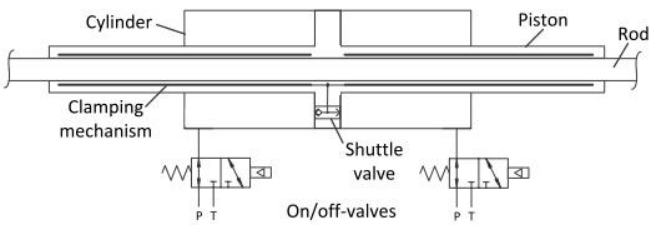

Figure 2. Hydraulic cylinder with a releasable piston.

In the concept in fig. 2 the cylinder chamber with highest pressure pressurizes the hydraulic clamping element using a shuttle valve. The clamping element's surface against the rod is large, which means that the clamping element and the working piston is partially outside the cylinder. The linear hydraulic actuator consists of two double acting cylinders with a common rod in one variant (see fig. 3). For movements one of the pistons is connected alternatively to the rod providing the drive. In this way the two pistons are moving the rod alternatingly in a kind of rope climbing motion.

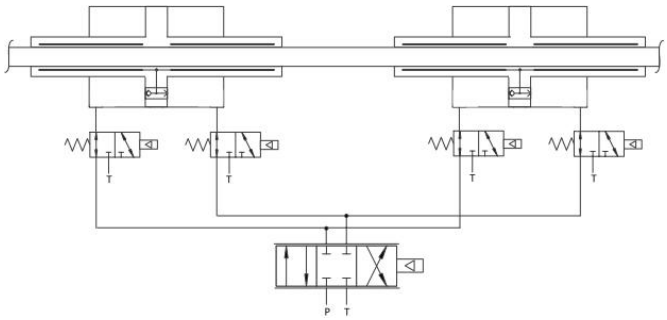

Figure 3. An example of implementation of HILA actuator.

In fig. 4 the actuation process of the cylinders is described. After step 7 the process will continue with step 2 (see also https://www.youtube.com/watch?v=tVJkqC2w5ws).

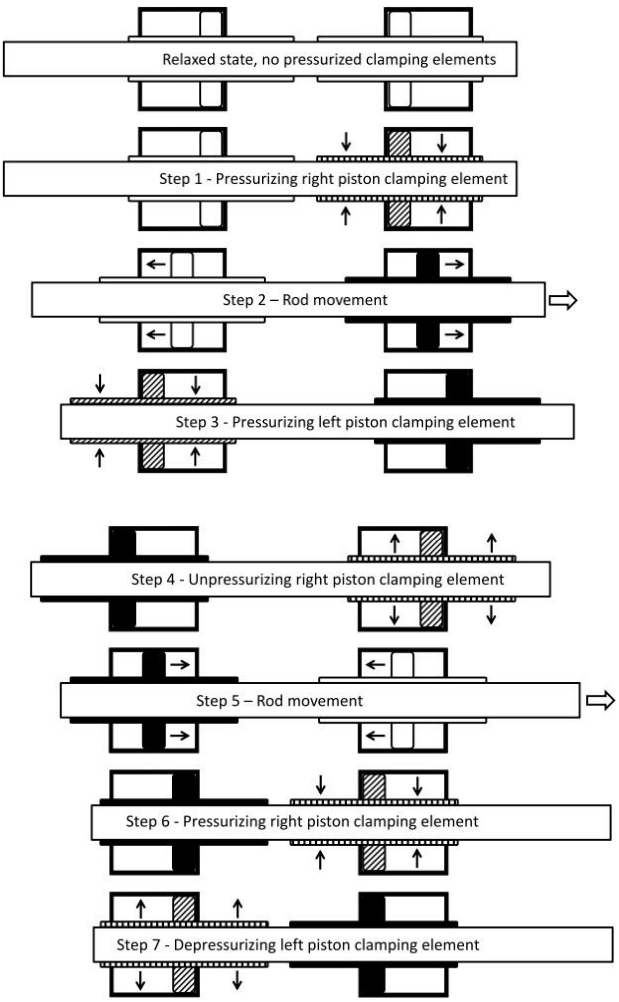

Figure 4. The actuation process of the cylinders.

A parallel to the novel hydraulic actuator is the inchworm motor. This is a device that uses piezoelectric actuators to move a shaft [3].

1.2 Separate pressurisation

An identified problem within this HILA design is unintended clamping when the piston is in retracting mode. The pressure level must be kept rather low in the cylinder chambers during retraction in order to avoid inadvertent self-clamping [4].

A solution of this problem is to separate the pressure supply to the clamping element. The pressurization of the clamping element and thus engaging can be implemented by a separate port C through the piston (see fig. 5) and using a separate 3/2 valve. The purpose is to pressurise the small membrane volume and a very small flow is needed and thus a small valve can be used.

The separate pressurisation opens up for a new degree of freedom in control. The piston and the clamping element can be independently controlled in time. The clamping element can be pressurised before or after the piston is pressurised. This solution means also that the shuttle valve in the piston can be replaced.

With this arrangement, full system pressure can be obtained and maximum performance in the clamping element between the piston and the piston rod at valve opening, regardless of the current pressure in the cylinder chambers or load case. This facilitate to minimize any micro slip between the piston rod and the piston, during the clamping and unclamping phase. Another advantage is that inadvertent self-clamping can be avoided.

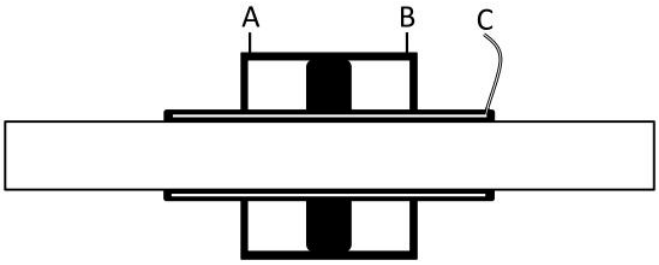

Figure 5. Separate pressurisation of the clamping element.

2 HILA with incremental control

The two predominant forms of linear motion control is hydraulic cylinders and electric linear actuators. Electric actuators are often selected as they provide a higher flexibility regarding the motion-control capabilities compared to hydraulic cylinders with directional valves, regarding position, velocity, acceleration and repeatability [5].

A conventional hydraulic cylinder, controlled by ordinary directional valves, works well for end-to-end position applications. A mid-stroke positioning application is more demanding, and requires a more complex control valve solution. Mid-stroke positioning for hydraulic with directional valves is an open-loop operation which requires manually operation.

More advanced hydraulic servo hydraulic systems, provides more accurately control position, velocity, and force, but they require a servo controller, an electrohydraulic servo valve, and a position feedback system. They also add complexity and cost to hydraulic systems and they are sensitive to contamination [5]. New digital hydraulic technology has been introduced in recent years in order to overcome this problems.

2.1 Digital Hydraulics

Digital hydraulics or digital fluid power is a broad research field and several research institutes and companies contribute the research. The technology offers several new ways to implement highly efficient hydraulic systems. New applications are emerging and several branches exists, within following areas; valves, pumps, actuators and transformers. Digital fluid power could be defined as follows: “Digital Fluid Power means hydraulic and pneumatic systems having discrete valued component(s) actively controlling system output” [6]. There are two main branches of digital fluid power; systems based on switching technologies and systems based on parallel connection. Both can be applied in several different ways.

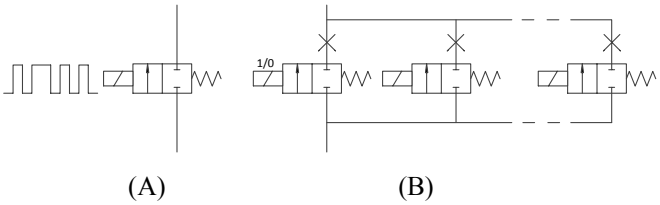

Figure 6. Systems based on switching technologies (A) and systems based on parallel connection (B).

The switching technology can be implemented as shown in fig. 6A by a switching controlled two-way valve. The valve controls the average flow area by the high frequency modulation and pulse-width modulation technology (PWM) is often used. The other way is to implement valves in parallel as shown in fig. 6B. The total flow area is the sum of the flow areas of the open valves. The main difference between the methods is that the parallel valves do not need switching to maintain a determined flow [6].

Connecting several on/off valves in parallel to form a Digital Flow Control Unit (DFCU), which is the analogue of a DA-converter, as shown in fig. 6B. This approach, needs more valves, but valves can be simpler and with a slower response. The approach gives also other benefits, good motion control with slow-response valves, improved redundancy and reduced durability requirement, when compared to PWM methods. Characteristic of digital hydraulics is that it can use standardized fast, robust and simple valves. They are insensitive for contamination and possibly zero leak. This combined with a high degree of flexibility and programmability opens up for many new design solutions. The drawbacks includes pressure pulsations and noise, durability and life time with switching technology, physical size and price with parallel connection technology and finally complicated control [6].

2.2 HILA with incremental control

One combination of HILA technology comprises a HILA cylinder which allows moving of the piston rod in combination with a static clamping unit. The piston rod movement is performed in discrete, incremental steps, like a bang-bang control strategy in a digital hydraulic system. For a feeding cylinder an end position cushioning is needed. End position cushioning ensures a controlled deceleration of the stroke velocity in both end positions. This means that the actuator will not go into hard ends. This cushions eliminates stress on the actuator elements and increase durability. The movements will be smoother.

The operating schedule is as shown in fig. 7. Ordinary directional valves are used for controlling the flow. The clamping elements in the static and moving element takes turn to keep the piston rod during the movement. This positioning technology offers a cost-effective, compact, simple and robust way to move a payload linearly from point A to point B.

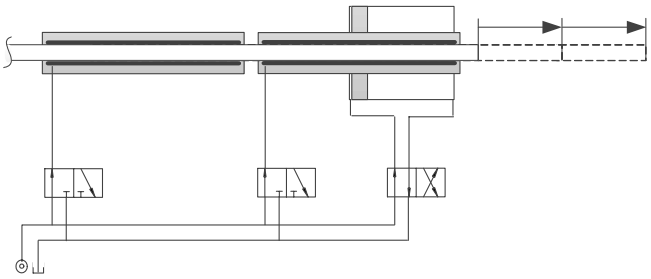

Figure 7. Incremental motion with a HILA cylinder in combination with a static clamping unit.

2.3 Adding fine tuning capability

The displacement of the load occurs in discrete steps. This means little opportunity for accurate control. Opportunities to correct and fine-tune the position is missing. But can easily be achieved by a slight modification of the design to obtain a higher positioning accuracy. The static clamping unit in the concept can be relatively easily modified. It can be replaced with a HILA cylinder with a considerably shorter stroke than the other HILA cylinder. The short stroke cylinder is very useful for enabling position fine tuning. With small corrective steps a high positioning accuracy is enabled without expensive hydraulic valve solutions, see fig. 8.

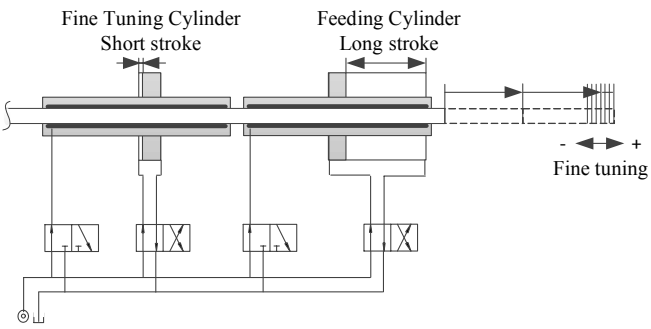

Figure 8. Incremental motion with a HILA feeding cylinder in combination with a fine tuning HILA cylinder.

The characteristic feature of this design is that the two cylinders HILA change function during the different phases. In the Discrete Feeding Mode the fine tuning cylinder acts as a static clamping unit and the feeding cylinder is moving with incremental motion. In the Fine Tuning Mode the roles are shifted, as shown in the fig. 9. The fine tuning can be done in both directions. And finally, when the required position is reached, both cylinders enters the static clamping mode, providing high stiffness.

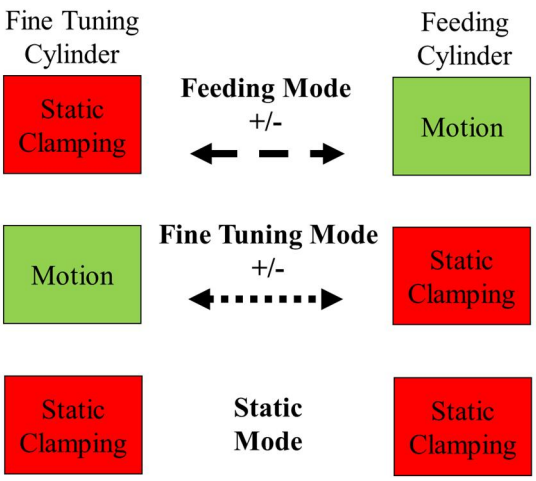

Figure 9. Discrete feeding, Fine Tuning and Static Mode.

In many actuation applications, a more advanced control system with expensive servo valves or proportional valves, is not a viable option because of the high cost associated with this type of valve technology. With the proposed concept, a system with high positional accuracy can be obtained in less responsive closed loop systems.

The proposed HILA with incremental control adds new features to present hydraulic cylinder technology and can be a potential alternative to expensive electric and hydraulic servo system, when high position accuracy is the primary goal. The technology also represents a new sort of digital hydraulics. The 3/2-valve may be implemented in the form of two on/off valves.

The needed space for a HILA system with incremental control can be smaller than for a conventional hydraulic systems as a higher system pressure and smaller reservoir is possible. A HILA system can generate 333high forces as it uses high system pressure. The present HILA technology allows pressures up to 45 MPa [7].

A HILA actuator system can advantageously be built together with a hydraulic supply including an electric motor and a high pressure hydraulic pump to a very compact system at the local site where the actuator is to be installed. And the power can be transmitted using an electrical cable instead of a long hydraulic hose or pipe. In areas where sensitive servo or proportional valves and feedback systems not are suitable, such as agricultural hydraulics, HILA with incremental control fine tuning provides a robust alternative.

2.4 Application Example – High lift systems

HILA with incremental control with fine tuning is also transferable to an aircraft context controlling surfaces. Examples of applications where positioning speed is of minor importance are secondary control surfaces, as flaps and slats on high lift systems in aircrafts.

To implement the digital hydraulic technology in an aircraft context means special adaptation must be done to deal with the pressure peaks generated in the valves which are connected to the fatigue related issues in cylinders and pipes. It is important to slow down the valve closing time in order to provide reasonable pressure peak levels for fatigue reasons.

2.4.1 Introduction to high lift systems

A high-lift device is a component or mechanism on an aircraft's wing that increases the amount of lift produced by the wing at start and landing, by increasing the wing area. Common movable high-lift devices include slats on the leading edge and flaps on trailing edge of the wing. Today's commercial airplanes are equipped with high lift devices to provide lift augmentation at low speed during take-off and landing as the wing design is optimised for the cruise speed regime. In order to keep take-off and landing speeds within reasonable limits, powerful high lift devices is required [8].

State-of-the-art high lift actuation systems often consist of a mechanical transmission shaft system (that transmits the mechanical energy from a central motor to the rotary or ball screw actuators, which are located along the transmission shaft and move the high lift surfaces [8].

This architecture assures a synchronous deployment of all flap and respectively slat panels but prohibit functional flexibility. The optimisation capabilities of today's highly optimised high lift system architectures has reached a plateau and are limited to small local improvements [8].

An advanced high lift actuation system architecture with distributed active controlled flap actuators offers the capability for implementation of additional functionalities for the trailing edge with benefits on aircraft level and simplifies manufacturing [8].

HILA actuator with incremental control with relatively simple means can be adapted for a high-lift flap system. Here it is proposed a fully independent HILA High Lift actuation system for flaps is similar to HISYS A350 XWB's high lift system concept, described in [8], but is built with HILA actuators at each drive station. The hydraulic actuators do not need dedicated power electronics. In fig. 10 two HILA actuators are installed in pairs on each inboard and outboard flap panels on left and right wing.

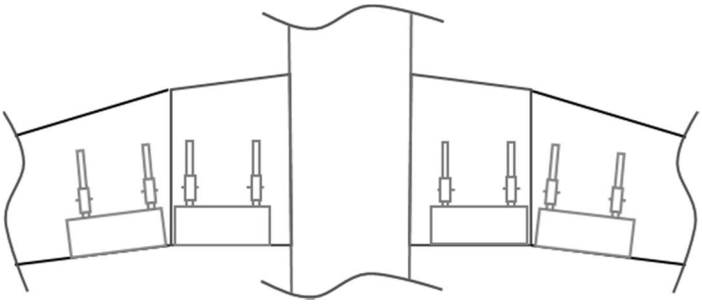

Figure 10. HILA High Lift actuation system on inner and outer flap on left and right wing.

The HISYS concept provides an advanced high lift actuation system architecture with distributed active controlled flap actuators offering the capability for implementation of additional functionalities for the trailing edge with benefits on aircraft level and improvements regarding manufacturing and assembling. Depending on the flap setting, the computer-

controlled spoiler automatically moves into the most efficient position during cruise flight. Drag can be reduced by up to two per cent at high gross weights, resulting in considerable fuel economies. Weight savings on the order of half a tonne for the wing box are feasible by using differential flap settings to alleviate loads by changing the centre of lift for loads management [8]. HILA concept also has the same functional benefits and reduced manufacturing effort as the HISYS concept.

2.5 Requirements on a high lift hydraulic actuator

The requirements that characterize a hydraulic actuator for a high-lift flap applications are as follows:

- High demands on position accuracy
- Relatively high air loads, but no mass inertia
- High stiffness
- Low operating actuator speed
- Lightweight and compact design
- High reliability, a failsafe solution and a high ability to detect errors
- Non-complex control algorithm
- No high pressure peaks during operation. Soft start and stop of cylinder manoeuvring.
- Parallel and synchronous movement of the actuators
- Low temperature

2.6 HILA High Lift System

The proposed high lift system with differential flap setting, enables optimization of the cruise aerodynamic efficiency and loads through the control of the wing centre of the lift position by differentiating the inner and outer flap. The proposed flap system can be actuated by an electric driven system with ball-screws or a HILA High Lift system, as showed in fig. 11, fig. 12A and 12B.

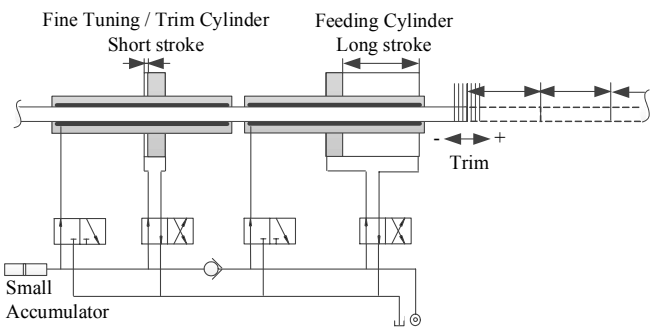

Figure 11. Incremental motion with a feeding HILA cylinder in combination with a fine tuning/trim HILA cylinder.

With HILA technology flap movement is made during take-off and landing in discrete incremental steps of 2-4 degrees, extending the wing area, as described in previously chapters, with simple, proven and robust ordinary on/off and directional valves. In cruise mode the technology enables trim capability with small incremental steps for fuel saving and load optimization using the fine tuning cylinder.

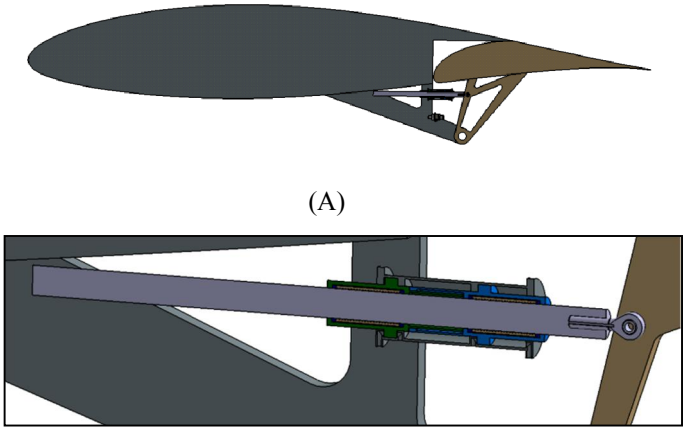

(A)

(B)

Figure 12. HILA cylinder installed between the wing and the high lift flap surface.

The feature of this solution is that the compact and leak-free cylinders combined with well-known clamping technology is used. Further a simplified wing design is provided, no rotating and bending shafts along the wing spar are required.

Furthermore, the concept is relatively simple to monitoring with detectable faults. At every start a Pre-Flight Built In Test is performed.

The system provides fail-safe position upon failure of the hydraulic and/or electric power, and at flap asymmetries. The maintenance of the hydraulic system are less demanding and less frequent in comparison with electric ball screw, which is important from a LCC perspective.

With well-known clamping technology and incremental control HILA innovation provides a new, robust and cost-effective high lift flap system that is simple in its design and provides both high-lift at start and landing also trim of flap position in cruise mode. This normally requires expensive, complex and maintenance intensive electrical or hydraulic actuation systems. HILA High Lift actuation technology can also be used on the leading edge slat system.

2.7 Redundancy with HILA technology

There are a number of fault cases that are handled in a failsafe way with sufficient redundancy in the actuator system and on a system level with HILA technology.

2.8 Loss of hydraulic and / or electric power

To handle faults the design has been supplemented with a small accumulator and a check valve, see fig. 11. In the event of loss of hydraulic and/or electrical power, hydraulic pressure on the static clamping element can be maintained by means of a small accumulator and a check valve.

2.9 Asymmetry and jamming

To ensure that the two systems HILA on respective flap panel are working in parallel and synchronously there are different

ways to detect failures together with a position sensor on each actuator.

A simple solution is provided by proximity switches at the end positions of the pistons. If the switching in the proximity switches in the right and left system do not occur simultaneously (some tenths of ms can be tolerated) a monitor detect the motion asymmetry between right and left system.

Another way to ensure the fault occurs, is to compare the hydraulic pressure in the cylinder chambers in the left and right actuator during motion. If the pressure differs too much from each other means that different speeds in the respective cylinder and a risk of jamming exists. A frozen state will be commanded and the flap panel remains in its fixed position throughout the remaining flight.

2.10 Hydraulic system failure

Normally a flight hydraulic system has two independent hydraulic systems (HS1 and HS2). The high lift system is supplied with hydraulic power from one hydraulic system, here HS1. In the event of failure of HS1, HS2 is commanded to supply the system through an emergency valve and the shuttle valve, according to fig. 13.

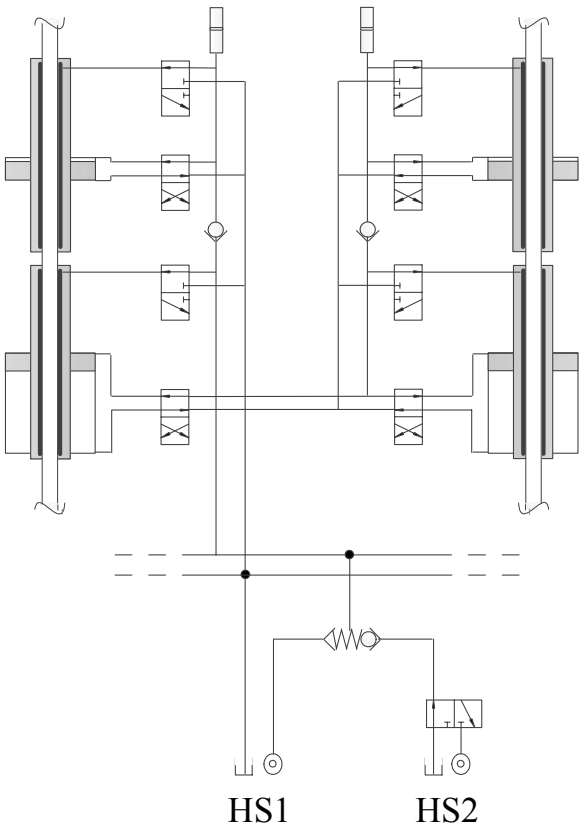

Figure 13. HILA High Lift flap system with left and right actuators, supplied normally from HS1 and in emergency case from HS2.

2.11 Pressure peaks

It is important to control the directional valves, included in HILA High Lift system, avoiding pressure peaks and cavitation during the stopping. It can be done by using a suitable opening area gradient in the directional valve. But it can also be combined with end position cushioning. End position cushioning ensures a controlled deceleration of the stroke velocity in both end positions. This means that the actuator will not “bang” into hard-stops or jolt. This cushions eliminates stress on the actuator elements. The movements can be smoother.

3 HILA technology with multiple rods

3.1 Controlling multiple rods in the same common piston

The separate pressurization of the clamping element opens up the possibility to control the movement of multiple individual linear piston rods in the same common piston.

Here it is proposed a solution in which multiple piston rods are using the same piston. A common hydraulic piston transfer simultaneous movement to a number of piston rods. Each piston rod is connected individually to the common pistons with individual clamping elements or of individual static clamping member by means of individual logic valves (see fig. 14 and 15). A common servo valve or directional valve controls the common piston.

Why gather a number of piston rods in the same piston? This way of arranging actuator movement has advantages but also present some limitations, among others regarding controllability.

In following chapter a number of ways of using this technology in different applications will be presented.

The technology is called HILA with Multiple Rods (HILA MR). HILA MR enables a completely new way to generate and distribute mechanical linear movement and force by using hydraulic actuators.

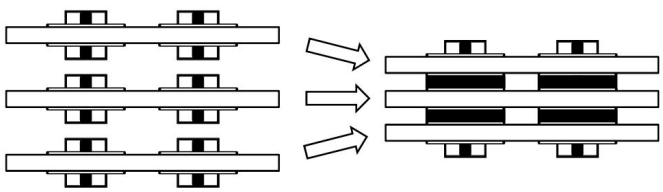

Figure 14. Six individual pistons integrated in two common pistons.

In areas where there are a great need for compact and energy-efficient drive units for multiple linear actuation are required HILA MR technology can be a suitable alternative. HILA MR enables a very compact, lightweight and cost-effective multiple actuation, especially if high hydraulic pressure can be used.

3.2 Ability to maintain static load for long time

Multiple static clamping elements integrated in common pistons together can individually perform piston rod movements in different directions. Combined with an optional static clamping element, this arrangement also has an ability to keep a high static load for a long period with almost no energy consumption. Equivalent solution for electric actuators, which do not use self-locking gears such as screwballs, requires a constant supply of current to hold the load.

In some applications, a static clamping in combination with HILA MR technology is very useful. With a static clamping, for example in a robot hand or gripper application, quick and precise positioning with low forces can be combined with high static forces for a long time. In order to control multiple rods with different requirements regarding movement and rest a static clamping unit is needed, see fig. 15 below. The static clamping element provides a parking mode for pistons rod which not are in motion.

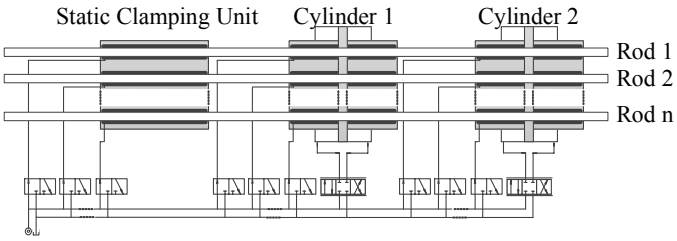

Figure 15. Hydraulic schematic of HILA MR

3.3 Separate pressurization with micro-valves

A 3/2 micro-valve controls the pressurization of the respective piston rod clamping elements. It has a switching time of a few milliseconds. Small valves with low power consumption and low flow capacity can be used because the membrane in the clamping element needs a very small volume change during pressurization and clamping.

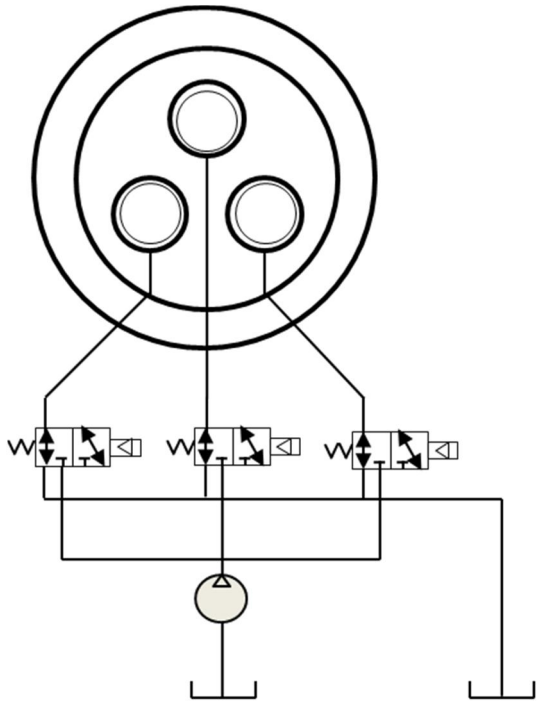

Figure 16. Individual pressurisation of each clamping element in common piston with micro-valves

With a small electric control current in the micro-valve, a large axial force in the piston can be controlled in a simple way (see fig. 16). A large mechanical force in the individual piston rod can be controlled by the micro-valve in a manner similar to how a small gate current in an electrical transistor can control a much larger current. Micro-valves may be placed as an extension of the part of the protruding piston, outside the cylinder. The supply of hydraulic power to the valves is done via a common thin hose and a thin electric multi cable. In order to decrease the clamping element area a higher control pressure may be used. The used clamping technology allows clamping pressures up to 45 MPa [7]. The 3/2 micro-valve may be implemented in the form of two on/off valves.

3.4 Thermal Handling

A well-known problem with electric actuators is that they cannot permanently be hold in a position to keep a high load, because they soon become detrimental warm and at the same time as they consume a lot of electric energy (if they do not use a self-locking gear). In a hydraulic circuit, the dissipated heat in the oil can be efficiently cooled off in an oil cooler.

HILA MR technology can handle thermal issues much better than comparable electric alternatives, due to the constantly circulating oil. Especially in applications where continuous 24/7 operation is demanded and/or in applications installed in cramped spaces where no cooling baffle fits, e.g. in a robotic limb, hand or gripper. The risk for overheating which can damage the actuator is low as the generated heat energy is taken away by the circulating oil. In an electric actuator, the heat transport to the air take place locally with bulky air baffles and/or fans.

3.5 No external leakage and lateral forces

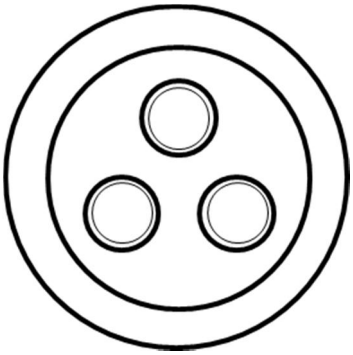

Figure 17. Piston rods not centrally located

The proposed method to locate the rods in the piston, means that all the rods are not centrally located, but distributed radially from the center, see fig. 17. That means that side lateral forces are generated in the piston if the transferred axial forces in the individual piston rod are not balanced. Lateral forces or side loading is a common cylinder problem that normally leads to premature failure. Lateral forces on a cylinder rod, particularly when the rod is extended, can damage the cylinder and shorten its useful life. Eventually, seals will suffer damage, resulting in external fluid leaks and seal failure.

Lateral forces on the common piston which occurs, can be handled in a non-destructive way by using bronze bearings in a similar way that they are used in hydraulic in-line machines, instead of using rubber sealings.

Introducing bearings, instead of using rubber sealings, provide advantages but also drawbacks, which are solvable. Among them leakage. Hydraulic equipment in general, and hydraulic cylinders especially are leaking oil externally when they are pressurized and work. This is one of the biggest drawbacks in hydraulics and a challenge to handle.

The friction is also higher in a symmetric cylinder than in a conventional asymmetrical cylinder, due to double end sealings. In order to design a power efficient system it is essential to minimize these friction losses and also to achieve better speed performance.

How can the external leakage be minimized? As the piston has a short stroke it is possible to complete the cylinder with boots (rubber or metallic) over the piston. The leaked oil is returned to the reservoir and can be reused instead of contaminating the environment (see fig. 18).

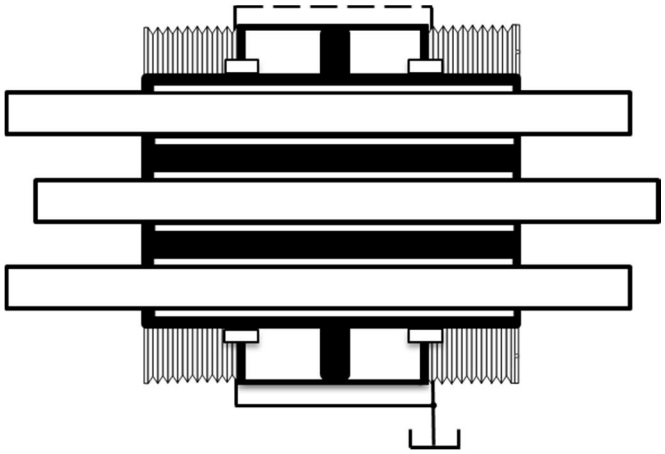

Figure 18. HILA MR with bearings which takes up lateral forces and boots preventing external leakage.

Furthermore, this means that the piston can be kept clean and it does not require a wiper, i.e., no contaminations from the environment enters through the cylinder rod and the seal into the oil chambers when the cylinder is working, which is common in many applications.

The piston can be kept clean but also the oil in the cylinder chambers. The relatively large external leakage that occurs over the seals and which constitute the lion's share of a hydraulic cylinder oil leak collected in the boot and implemented through a connecting hose back to reservoir. It is possible that the wear ring and rod seal between piston and cylinder can be replaced by bronze bearings.

The advantages of this arrangement are several. With the boot a higher leakage of cylinder seals is allowed. This reduces friction and energy losses and the power efficiency of the cylinder is increased. Furthermore, higher rod speeds are permitted when the friction is reduced. This permits in addition that cylinder may be more possible applications, for example for high-speed elevators in high-rise buildings.

Boots solution increases the potential of the cylinder innovation with the risks of oil contamination significantly reduced and higher power efficiency and rod speed can be offered. Though, if the leakage becomes too high the control accuracy can be too low.

3.6 Common position sensor

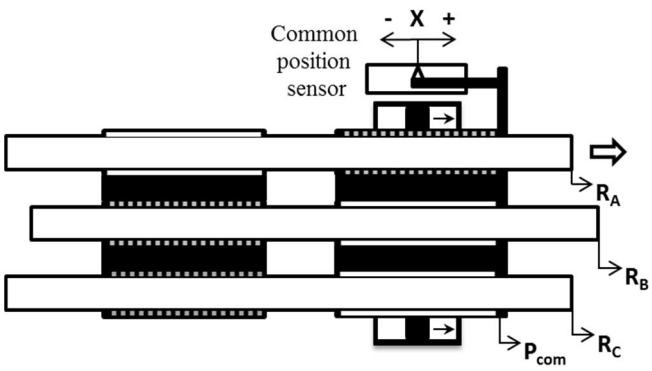

Figure 19. A HILA MR combination with a common static clamping unit and a common cylinder with clamping elements and a position sensor in the moving common piston (P_{com}) (dotted line = pressurised clamping elements).

The common piston (P_{com}) that work partially outside the cylinder housing can be equipped with a position sensor for feedback control (see fig. 19). The position sensor can be of different types, e.g. LVDT, potentiometer, etc.

In fig. 19 rod A (R_A) is clamped to the moving common piston (P_{com}). Rod B and C are static clamped. The relative motion which is done with rod A clamped to the common piston is calculated.

This relative position information, using an embedded computer, is used to estimate the absolute position for rod A and for each piston rod which is moved. This position information is essential for a control system. The common common position sensor means that a large number of individual position sensors can be eliminated. This arrangement avoids a lot of different failure modes and saves volume, weight and cost.

The position information from the common position sensor must be complemented with different types of position synchronization of the respective piston rod and built-in tests to ensure that the location information for each rod can be trusted at every time. At start up all piston rods can be positioned at a hard stop with a known position and then be synchronized. If not repeated synchronizations are performed you cannot rely on the information from the common position sensor.

It is also of great importance that no micro slip occurs between the rod and the common piston at clamping and unclamping. This risk is minimized if clamping and unclamping takes place when the piston and piston rod is stationary still or have the same speed.

3.7 Infinite stationary hydraulic stiffness

The considered concept, HILA MR, allows moving the piston without moving the disengaged rods. Thus when the desired rod positions are reached the disengaged piston can be moved to one of its end stops. After engaging the cylinder and pressurizing the one cylinder chamber to push the piston against the end stop the elasticity of the mechanical contact is dominating the cylinder stiffness, see fig. 20. Thus the hydraulic stiffness becomes infinite. In this consideration the elasticity of all mechanical components like structure and rod are neglected [4].

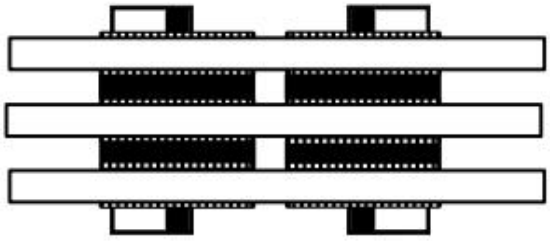

Figure 20. Two cylinders at opposed side end stops, with infinite stiffness.

3.8 Hydraulic Time Sharing

HILA MR technology enables time sharing and a load sensing.

By using a time sharing strategy for the individual piston rod movements advantages can be obtained. If a piston rod is moved at a time and the other piston rods are in static mode following advantages is obtained: The common piston area can be reduced. The force of the piston rod having largest force demand determines the common piston area. The common piston area can be reduced and the cylinder can be designed more compact and lightweight. Also the supply system can be designed with lower power requirements.

3.9 Time sharing hydraulics in an unmanned aircraft

A suitable field for the proposed time sharing hydraulic technology with HILA MR technology is in unmanned aircrafts.

An aircraft has a number of subsystems containing hydraulic actuators, among others, flight control system, landing gear system and fuel system. A Medium-Altitude Long-Endurance (MALE) unmanned aircraft, which flies autonomously has been selected as a suitable application.

The flight control system can be divided into primary and secondary control surfaces. The primary control surfaces consist of ailerons, elevators and a rudder and its task is to maintain the aircraft's stability at disturbances that occur in flight and control the aircraft in pitch, roll and yaw of a predetermined flight trajectory.

The rudder commands to maintain stability are time-critical and unpredictable due to wind gust and side winds, i.e. they must be executed without delay, and they have the highest priority. Commands for control in pitch, roll and yaw are less time-critical and follows in order of priority. Lower priority has the operation of secondary control surfaces, the flaps for high lift, and the landing gear actuation, which if necessary can be divided into phases

Besides the rudder commands required to maintain stability, the other commands can planned in advance as they are predictable and less or not time-critical. These commands need not to be performed in parallel, but they may be

commanded in series. This is possible in an UAV when a pilot is not present in the control loop.

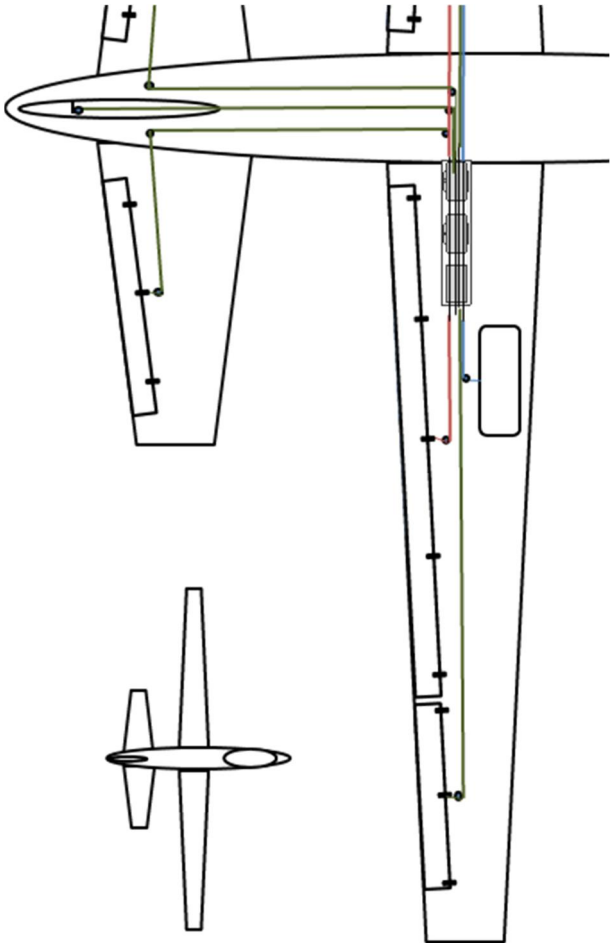

Figure 21. A MALE UAV with HILA MR technology

In most aircrafts there are active rudder activities only during a few percent of a total flight, especially during long distance flights. Under these conditions a time sharing hydraulics system is preferable. Rudder and landing gear commands can be executed in series. In case of a wind disturbance, the secondary control surfaces and/or landing gear manoeuvring can be stopped temporarily, in order to move the primary control surfaces and stabilize the aircraft.

With this conditions, a hydraulic actuator system based on HILA MR technology and a hydraulic supply system can be designed, which has low power demand, is more compact, lighter, more energy efficient, and not least cost-effective. HILA MR technology, can here be used here in combination with wire cables that transfer power and motion to the respective consumer. Wire technology has been used for many decades in aviation, controlling surfaces. See fig. 21.

In the design of hydraulic systems in mobile vehicles, and in particular, in an aircraft, a large focus is on minimizing system weight and energy consumption. In aviation, the demands on system safety is high, but for space reasons it is not described here how the system can be built fault tolerant with redundant solutions.

4 HILA MR with incremental control

HILA MR technology can be combined with the incremental control methods introduced in earlier chapters. There are interesting applications for this combination in the robotics field, which will be presented and analysed in this chapter. It will also be conceptually shown that in this field, HILA MR with incremental control enables more accurate and time efficient methods for positioning.

4.1 Robot applications

HILA MR technology is particularly suitable for applications where multiple actuator functions with high requirements of strength and stiffness have to be implemented in confined spaces. This requirements is common in robot applications, such as articulated robot and snake-like robots where also a less responsive closed loop system can be used.

4.2 Description of the base element

HILA MR technology enables a flexible, compact and rigid actuator, which is highly desirable in design of articulated robots arms or snake-like robots. This is provided by manoeuvring four piston rods simultaneously in a robot arm segment.

An articulated robot arm uses rotary joints to access its work space. Between the joints there are rigid links. The joints and links are arranged in a kinematic chain, so that one joint supports another joint via the link or spacing section in the chain. The terminus of the kinematic chain of the robot arm is called the end effector. As end effector a gripper, a device for grasping or holding a payload, or a tool, is normally used.

The rotary joint between the sections allows rotational motion. The flexibility of robot arms depends of the rotational ability between each section. Most robot arms in an articulated robot only have one axis in a single section, which is equal to one degree of freedom (DOF). In order to get better access to confined spaces access a universal joint is preferable. HILA MR technology enables a joint with two DOF, both in pitch and yaw, see fig. 22, in each center of rotation.

Figure 22. Actuation in pitch and yaw rotational direction at left and right end of the robot arm segment.

In many applications a robot arm should provide also high accuracy, repeatability, resolution and speed.

The resolution is the smallest increment of motion or distance that can be detected or controlled by the control system of the robot arm.

The best solution with respect of these requirements is to provide a hydraulic servo valve. It is not always possible to provide a servo valve for control of the respective piston rod because of cost and space reasons.

In some applications with less responsive closed loop systems, but with high resolution and high position accuracy requirements, an incremental control may be a better solution.

Here it is described such a robot arm solution where HILA MR with incremental control is used with a fine tuning cylinder and a feeding cylinder, see fig.23.

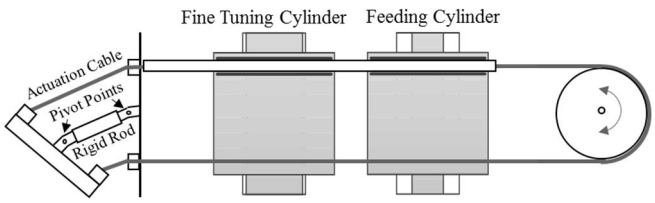

Figure 23. Rotational actuation in a segment of snake-robot arm construction with HILA MR with incremental control.

In order to employ twin rotary actuation system and two DOF in each robot arm segments end and maintain stiffness and compactness a new snake arm robot construction is used described in [10] using stiff actuation cables and wheels to close the force loop.

One cable in a pair of actuation cables pulls a distance and the other cable in this pair extracts the same distance, which causes the bending deformation of the compliant joints and holds the cables of this pair in tension in any kinematic configuration [10]. Here it is proposed that the cable is actuated by HILA technology instead of an angular actuator.

With only two ordinary directional valves and eight small 3/2 valves, four piston rods can be controlled and actuated independently and a high position accuracy can is achievable for each piston rod. These piston rods in turn control the rotation in pitch and yaw in each end of the segment by using cables, according to figure 23. The hydraulic schematic and piston rods connection to each rotational direction is described in the fig. 24. The kinematics and interaction of the actuation cables, the cable, and the wheel is presented in detail in [10].

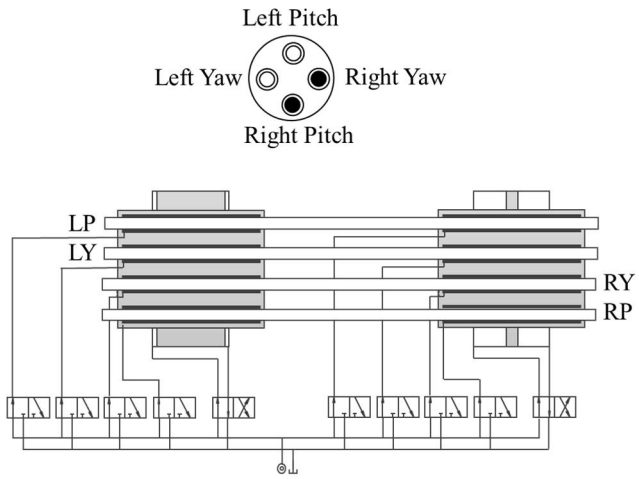

Figure 24. HILA MR hydraulic schematic and piston rods connection to each rotational direction (L=left, R=right, P=pitch, Y=yaw)

4.3 Incremental control with a piston rod pair

The same incremental control technique described for HILA applications in earlier chapters where only one rod is used, is preferably used also in this application (see fig. 25 A). Rotational actuation is obtained with two segments with HILA MR with incremental control. Angle positioning in pitch and yaw can be implemented with two piston rods, each of which is controlled by the two pistons. An even higher accuracy is achievable with this arrangement, in comparison with the previously presented technology.

The four pistons have unique stroke lengths, i.e. there are four different available strokes for incremental control of the angular position (see fig. 25 B). The piston with the shortest stroke (3) determines the resolution (r) in the control system, the next piston (2), the stroke of which is m times longer, has an incremental stroke m * r. The next piston (4) has the stroke m^2 * r and the last piston (4) has the stroke m^3 * r. The multiplication factor m can be varied depending on requirements on total stroke and time requirements, i.e. number of allowed feeding and fine tuning iterations.

The kinematics of the robot arm is described by a chain of skew transformation matrices which represents the relation between the pair of pistons to angular motion of each individual segments and are described in [10]. The largest strokes can be combined with end position cushioning in order to mitigate jerky motion.

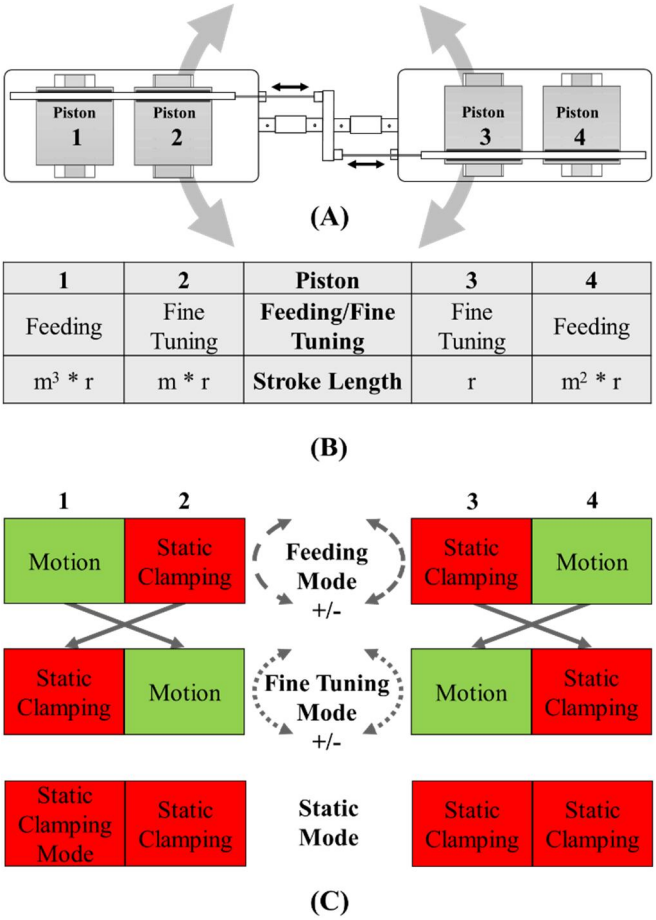

1	2	Piston	3	4
Feeding	Fine Tuning	**Feeding/Fine Tuning**	Fine Tuning	Feeding
$m^3 * r$	$m * r$	**Stroke Length**	r	$m^2 * r$

Figure 25. Incremental angular control in one DOF of two interconnected robot segments.

Fig. 25 C shows the different main modes: Feeding Mode, Fine Tuning Mode and Static Mode. In Feeding Mode is piston 2 and 3 active and clamped to the piston rod, in the subsequent Fine Tuning Mode, piston 1 and 4.

The work sequence of the incremental angular control in one DOF of two interconnected robot segments is as follows. To begin with, piston 1 and 4 work with positioning left and right piston rod and actuation cables in the Fast Feeding Mode. The longer movements of the piston rods occurs here. Then there is a changeover to the Fine Tuning Mode and piston 2 and 3 position piston rods and actuation cables are moved until the commanded angle is obtained. It is important to note that the piston rods movements can occur in both directions.

An angular position sensor, not shown in figure 25A, closes the control loop including appropriate filters. The control loop will also include corrective commands in order to reach the commanded angle position. Finally in the Static Mode all pistons are clamped to the piston rod pair, enabling high stiffness.

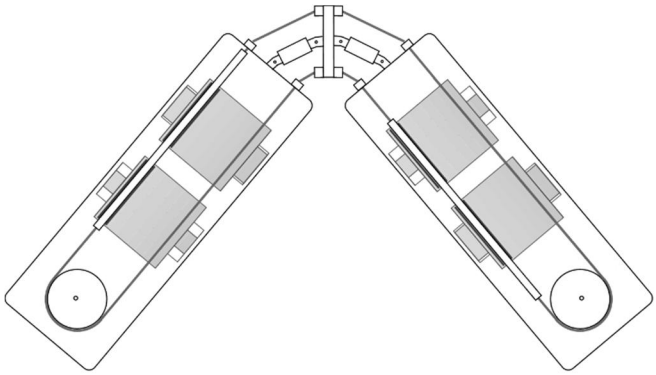

Figure 26. Example of rotational actuation enabling high agility.

Here it is showed that an incremental control strategy with a few large and small incremental steps available in four different pistons, can provide a powerful combination of high angle resolution and a large total angle stroke, enabling a high agility. The robot arm segments can be built together in series creating a snake-like robot capable of working in confined spaces and reach the farthest ends of the cavities of for example an aircraft while maintaining the rigidity and precision all the way to the end effector, see fig. 26 and 28. Also a combination with segments with HILA MR with incremental control and slave segments is a feasible solution.

4.4 Need for slim snake-like robots

Assembling modern aircrafts is, in many ways, still as much of a craft as 18th century shipbuilding, requiring loads of skill and manual labour to get the job done, because the needed industrial robots are too inflexible and reach too short [9]. There is a need for snake-like robots and lot of uses in several industrial segments today, beyond aircraft manufacturing, in automotive industry, in nuclear power plants, off-shore platforms, shipbuilding, laparoscopic surgery etc. But these robots are not on the market today, however there are some demonstrators.

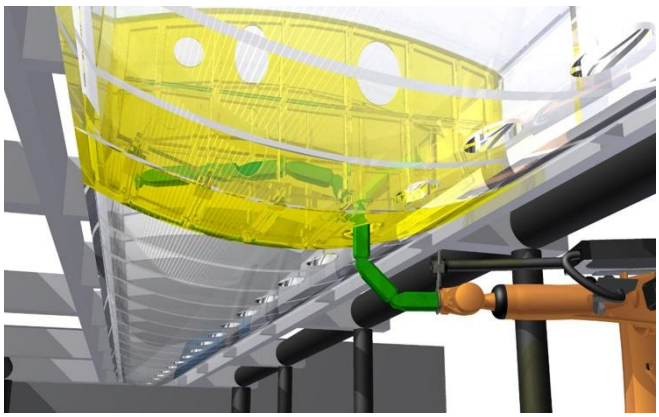

Figure 27. A snake-like robot in a wing tank (Image: FRAUNHOFER IWU).

Present articulated 6-, 7-axis electrical or hydraulic robots are too clumsy, especially in turning points, for this applications today. It requires distinct robotic arm movements performed

by slim, multi joint robotic arms in tight spaces, avoiding to collide with walls in confined spaces, see fig. 27.

A large number of snake arm robot designs have been presented, but there is no snake robot that can carry a relatively large payload, while having small diameter/length ratio, great flexibility (bending capability) and a compact actuation system [10].

Robot arm segments, based on HILA MR with incremental control, can be designed as a snake-like robot, which consists of several series-connected elements. This robot is capable of working in confined spaces and reach the furthest ends of the cavities, for example, in an aircraft wing while maintaining the rigidity and precision all the way to the end effector. The snake-like HILA robot can be divided into a part that looks more like a jig, which is not operated so frequently, and a part near the end effector which is more like an industrial robot. HILA MR with incremental control can be used especially in parts which are less frequently operated and rapid movements are not so needed.

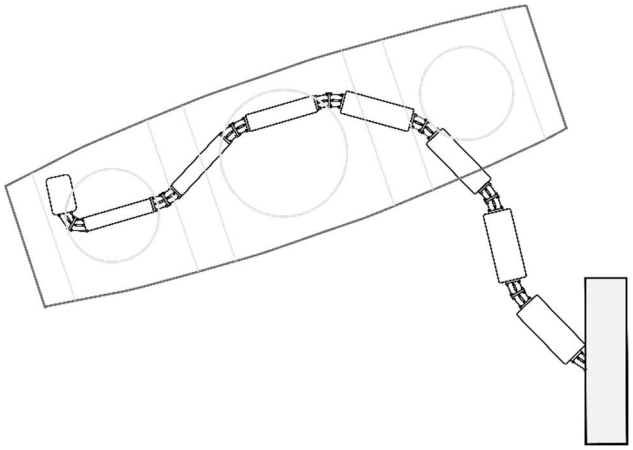

Figure 28. A snake-like HILA robot capable of working in confined spaces.

5 Discussion

HILA and its various combinations represents a quite different approach compared to conventional hydraulic cylinder technologies. The barrier is high to introduce new technology in the conservative hydraulic cylinder industry, mainly because established technology is so widely accepted. However, this industry needs new inventions to defend shrinking market segments [11].

Research has been carried out during several years in the field of digital hydraulic actuation. A number of promising concepts characterised by robustness, simplicity and reliability have been proposed. But commercial breakthrough has not yet been achieved, mainly due to the high number of needed on/off-valves and physical size and weight of the valve package.

HILA represents a new sort of digital hydraulics, especially HILA equipped with incremental control with discrete actuator stepping instead of switched valves. Various HILA technologies and concepts presented in this paper are based on few micro valves, which are working as a hydraulic transistor in each actuator. However, these high pressure and fast switching control valves require extremely low flow. HILA offers a miniaturisation of the control valve package and a neat design compared to present digital hydraulic systems.

6 Future Work

This conceptual paper presents a part of the current state of HILA development project. The basic functionality of HILA technology has successfully been proved in earlier model simulations and rig tests (see also https://m.youtube.com/watch?v=UCO-OQOdxtg). However, the work presented in this paper will be further enhanced by simulation and laboratory tests. Such future work may include that incremental control system needs to be modelled and simulated for different load and speed cases. The simulations will be done with and without mass inertia together with appropriate regulator structures, such as PID control, in order to minimise potential jerkiness and fatigue issues.

Another area of importance for further research work is finding suitable applications for proposed HILA technologies. This may include completely new applications for hydraulic cylinders in materials handling and mobile applications. All areas suitable for the variants of HILA described in this paper have not been identified for development efforts and research.

It is also important to identify industries that are in a dynamic development phase, and thus interested in new innovations in these areas. These may be found outside the traditional industries for hydraulic cylinders. To succeed in research with HILA, the technology also has to be presented to industries which today use electrical actuators to a large extent. Such an industry is the growing robot industry. HILA can offer the robot industry a more cost-effective and suitable technology for some applications, such as snake-like robots, where current electrical actuators do not fully meet the requirements for that application.

7 Conclusions

In this paper a number of concepts of HILA technology are presented. The basic invention is a hydraulic cylinder with a releasable piston. It is based on a well-known hydraulic clamping element used in a new combination, where the piston and the piston rod can quickly be coupled and uncoupled by means of the clamping element, in a failsafe way. The invention provides new features to hydraulic cylinders such as providing very long strokes, high rod speed, and small chamber volumes enabling high pressure which means high stiffness and low capacitance. The technology also represents a new sort of digital hydraulics, especially the variant with incremental control. The study presents feasible combinations of the technology.

HILA with incremental control, using ordinary directional valve and on/off valves, adds new features to present

hydraulic cylinder technology and can be a potential alternative to expensive electric and hydraulic servo systems, when high position accuracy is the primary goal within less responsive closed loop systems.

HILA with multiple rods (HILA MR) technology is presented for the first time in this paper, enables a completely new and novel way to generate and distribute mechanical linear movement and force by using hydraulic actuators, maintaining high pressure, compactness and energy efficiency. A single position sensor on the common piston can be used to determine the absolute position of the individual piston rod.

In less responsive closed loop systems, HILA with multiple rods and incremental control enables a new way to generate and distribute mechanical linear movement and force by using hydraulic actuators in a cost effective way. Multiple actuating elements together with incremental control, integrated in a compact and lightweight single unit controlled by ordinary directional valves enables a high position accuracy.

In the robotic area a high agility robot configuration that may carry a reasonable load, with a small diameter and length ratio, is needed in several areas, such as nuclear power plants, off-shore platforms, shipbuilding, laparoscopic surgery etc. The robot has to be capable of working and navigating in confined spaces and reach the furthest ends of the cavities, for example in a wing tank, a collapsed building or in military operations.

HILA with multiple rods and incremental control enables a promising solution for these issues. With large and small incremental steps executed in two linked robot arm segments, it will be able to have a more accurate and time efficient method for angle positioning in pitch and yaw. The segments can be built together in series for snake-like robot applications.

HILA technology is patent pending.

8 Acknowledgments

This work was sponsored by Saab AB and the Swedish Energy Agency.

9 References

[1] K.-E. Rydberg,"Hydraulic servo systems", https://www.iei.liu.se/flumes/tmhp51/filearchive/course material/1.105708/HydServoSystems_part1.pdf, pp. 3, 2008

[2] M Landberg, M Hochwallner, and P Krus, "Novel Linear Hydraulic Actuator". ASME/BATH 2015 Symposium on Fluid Power & Motion, Chicago, United States

[3] J Li, "Design and development of a piezoelectric linear actuator for smart structures", Department of Mechanical and Industrial Engineering, Concordia University, Montreal, Quebec, Canada, 2004

[4] M Hochwallner, M Landberg, and P Krus, "The Hydraulic Infinite Linear Actuator – properties relevant for control". In 10th International Fluid Power Conference (10. IFK), Vol. 3, pp. 411–424, 2016

[5] S Mraz, "Comparing Electric Rod Actuators and Hydraulic Cylinders", Machine Design, http://machinedesign.com/technologies/hydraulics, 2016

[6] M Linjama, "DIGITAL FLUID POWER –STATE OF THE ART", The 12th Scandinavian International Conference on Fluid Power, Tampere, Finland Linköping, 2011

[7] ETP-OCTOPUS, ETP Transmission AB, www.etptrans.se

[8] M Recksiek, "ADVANCED HIGH LIFT SYSTEM ARCHITECTURE WITH DISTRIBUTED ELECTRICAL FLAP ACTUATION", AST 2009, Hamburg, Germany

[9] "Automated assembly of aircraft wings" , https://www.fraunhofer.de/en/press/research-news/2014/may/automated-assembly-of-aircraft-wings.html

[10] X Dong, M Raffles, S Cobos Guzman, D Axinte, J Kell, "Design and analysis of a family of snake arm robots connected by compliant joints", Mechanism and Machine Theory 77 (2014) 73–91

[11] "Hydraulic Cylinders Industry Report", July 2013, InterOcean Advisors LLC, 117 North Jefferson Street, Suite 205, Chicago, IL 60661, www.ioadvisors.com

The Lattice Boltzmann Method used for fluid flow modeling in hydraulic components

Bernhard Manhartsgruber

Institute of Machine Design and Hydraulic Drives
Johannes Kepler University, Linz, Austria
E-mail: bernhard.manhartsgruber@jku.at

Abstract

The Lattice-Boltzmann Method for the approximate solution of the Navier-Stokes equations has become an interesting alternative to classical finite volume based discretization methods. Because the flow domain is not meshed in the classical sense but only voxelized and geometrically complex boundaries can be introduced in an easy form by bounce-back or off-Lattice boundary conditions, the method lends itself very well to simulations of channel flows inside hydraulic components. In this paper, a flow problem in a single acting cylinder attached to a 3/2 directional spool valve is used as a benchmark problem. The Lattice-Boltzmann simulation is used to generate a reference solution for the pressure step response of the blocked cylinder with superimposed wave propagation. From this reference data set, a non-parametric frequency domain input-output model is extracted and compared with results from classical lumped parameter modeling.

Keywords: Lattice-Boltzmann method, fluid power systems modeling

1 Introduction

The Lattice-Boltzmann method evolved out of the early ideas of Lattice gas automata [1, 2, 3] from the 1970s and early 1980s. These models were discrete in the sense that they took into account only binary information about presence or absence of a particle at a grid point in a certain time step. The very fine lattice resolution needed to produce a solution with acceptable molecular noise rendered the method inapplicable to engineering problems. However, the combination of the lattice-gas idea with a description of the fluid by the Boltzmann equation [4] resulted in a very powerful tool over the last two decades. The central idea is the description of the state of the fluid by probability densities with a simple stream and collide mechanism for updating the information from one time level to the next.

Due to the local nature of the description and the absence of the solution of large equations systems, the Lattice Boltzmann method (LBM) is very well suited for implementation on parallel computing systems. The present paper shows the use of LBM solutions of a channel flow problem including wave propagation effects for the generation of low order state space models by identification and order reduction methods. This novel approach includes minor pressure losses and wave propagation effects that are difficult to handle in classical lumped parameter modelling. Yet, the resulting mathematical models are of very low order as compared to CFD modeling.

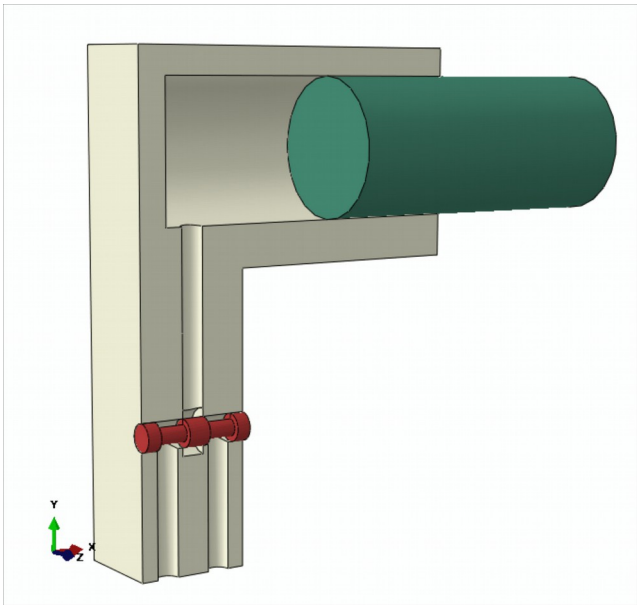

Figure 1: Geometry of the example problem.

2 The example problem

Fig. 1 shows the geometry of the example problem. A 3/2 directional spool valve controls the pressure in a cylinder chamber. The supply pressure and tank pressure attached to the valve ports at the bottom of the geometry are assumed constant. The chamber pressure controlled by the spool valve acts against an external force pushing the piston inwards.

The compuational domain shown in Fig. 2 consists of four sections:

- an 8 mm supply bore between a constant pressure boundary condition and the spool valve with a length of 45 mm
- the spool valve geometry, consisting of two annular chambers (diameters 6 mm / 10 mm and 10 mm 16 mm) with an axial valve opening of 1 mm
- an 8 mm connection bore between the spool valve and the piston chamber with a length of 62 mm
- the piston chamber with a cylindrical geometry of diameter 50 mm and height 30 mm (the height is acutally varialbe due to piston movement. Figures 1 and 2 show a longer piston chamber, the compuations results presented in this paper are for only 30 mm of height.

The goal pursued in this paper is to describe the pressure build-up in the cylinder chamber due to the valve opening in a precise way including minor losses at the connection of the bore between valve and cylinder chamber. Furthermore, the high frequency dynamics of wave propagation between the valve and the piston face should be included as far as possible in a low order model.

The approach followed to reach this goal is as follows:

- In a first step, a number of different piston motions due to valve opening have to be simulated using the Lattice-Boltzmann method. In the present paper only a first result for the blocked piston case is presented.
- From the simulation results, effective piston pressure and valve flow signals are computed.
- These signals are used to identify low order state space models describing the input-ouput behaviour of the hydraulic system.

The resulting models are in the end compared to lumped parameter modelling using just a pressure build-up equation for the cylinder chamber as described in classical fluid power text books, see e. g. [5].

3 Simulation using LBM

This paper uses a simplified approach as the motion of the valve spool and hydraulic piston is disregarded. The simulated case corresponds to the step response of the cylinder chamber pressure with blocked piston motion after an instantaneous opening of the valve. The boundary of the flow domain shown in Fig. 2 is constant in time and can be described in a very simple way as surface triangulation data in a stereo lithography (.stl) file provided by many CAD systems.

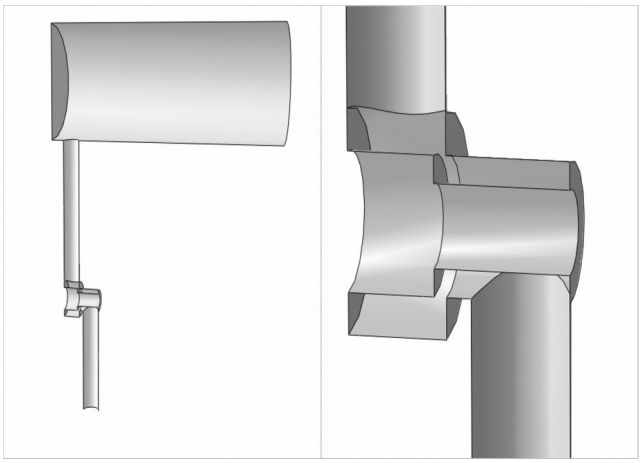

Figure 2: Geometry of the bounding walls in .stl file.

The left half of Fig. 2 shows the overall boundary geometry of the flow domain with two open faces, one at the bottom, where the bore supplying pressurized hydraulic fluid to the valve ends, and one at the top right corner, where the fluid faces the piston. The first open face is treated as a constant pressure boundary condition, while the second one is understood as a velocity boundary, where the fluid velocity normal to the boundary patch can be prescribed as a flow profile. For the case presented here – with the piston motion blocked – the flow profile will be prescribed as zero over the whole patch which is identical to using a wall boundary condition as for all the other parts of the boundary shown as shaded patches in Fig. 2. the reason for specifying the boundary with two open patches and both a pressure and a velocity boundary patch lies in the use of the Lattice-Boltzmann code PALABOS. The computation presented here uses a showcase of this software package where the flow through an aneurysm geometry is analysed [6]. This showcase readily implements the geometry import from the stereolithography (.stl) file and needs at least one inflow patch with prescribed velocity and one outlet with prescribed pressure. This setting is inverted in the present case in the sense that the inflow is blocked by setting the velocity profile to zero and the pressure at the former outflow patch may result in a velocity pointing into the flow domain reverting this boundary patch to an inflow port.

With this approach, the “aneurysm” showcase of the PALABOS software package, which can be found in the examples folder of every standard installation, is used as a starting point. By exchanging the geometry file of the

"aneurysm" showcase with the data shown in Fig. 2 and adding a few lines of code for writing the average pressure at the piston face and the average pressure and flow rate at the control edge of the valve (see the zoomed picture in the right hand side of Fig. 2) to a file at a certain sample rate during the simulation.

Lattice-Boltzmann calculations are carried out in a dimensionless framework where the time evolves in unit steps by a so called collide and stream procedure and the space is divided into cubic voxels of edge length one. The scaling between this voxelization of the flow domain and the physical length scales is represented by the spatial resolution *dx*. The dimensionless speed of sound in the lattice has a fixed value of

$$c_{LB} = \frac{1}{\sqrt{3}}.$$

In order to match this lattice speed of sound with the physical speed of sound, the grid viscosity is set to

$$\nu_{LB} = \frac{\nu}{\sqrt{3\frac{K}{\rho}} \cdot dx}$$

The physical time step follows as

$$dt = \frac{\nu_{LB}}{\nu} \cdot dx^2$$

The value of the grid viscosity influences the stability of a Lattice-Boltzmann simulation. Numerical experiments with the PALABOS code used for the present paper showed that the calculations went unstable for values below ν_{LB}=0.006. Whether this limit could be lowered by using a different implementation fo the Lattice-Boltzmann method has not been reserached in the scope of this paper. The limit for the grid viscosity poses a severe problem with respect to the necessary spatial resolution for the calculations: The speed of sound must be matched in order to resolve the wave propagation in the right way. Setting ν_{LB} to 0.006 results in

$$dx = \frac{\nu}{0.006} \cdot \sqrt{\frac{\rho}{3K}}$$

With a typical kinematic viscosity of a mineral oil based hydraulic fluid of $\nu = 40 \cdot 10^{-6}$ m²/s, a mass density of ρ = 850 kg/m³, and an effective bulk modulus of $K = 1.5 \cdot 10^9$ Pa, the lower limit for the grid viscosity around $\nu_{LB} = 0.006$ calls for a spatial resolution of $dx = 2.9 \cdot 10^{-6}$ m. Together with the physical extent of the computational domain shown in Fig. 2 of 170 by 50 by 30 mm, this results in a size of approximately 59000 by 17000 by 10000 grid cells which is way beyond the reach of available computing power.

In a first attempt to validate the tool chain of Lattice-Boltzmann simulation and frequency domain identification, the kinematic viscosity of the fluid is vastly increased to a value of $1725 \cdot 10^{-6}$ m²/s resulting in a spatial resolution of 0.125 mm which gives a computational domain of 1360 by 400 by 240 cells in the overall lattice.

Clearly, this approach will not work for the simulation of fluid power systems in a realistic parameter range. The research towards implementations of Lattice-Boltzmann methods capable of dealing with a lower value of the grid viscosity while maintaining numerical stability is hower left to future work.

In order to give the reader a first impression of the method, Fig. 3 shows five sections through the computational domain at time steps 0, 24, 48, 72, and 96 respectively. The physical time step can be evaluated as

$$dt = \frac{0.006}{1725 \cdot 10^{-6} \frac{m^2}{s}} \cdot (0.00125\,m)^2 = 5.435 \cdot 10^{-8}\,s$$

so the 96 time steps that have gone by in the rightmost part of Fig. 3 correspond to 5.2 microseconds. The colour code shows the region initially at high pressure in red and the low pressure region in blue. The initiation of a pressure wave propagating from the opened valve in both directions is clearly visible.

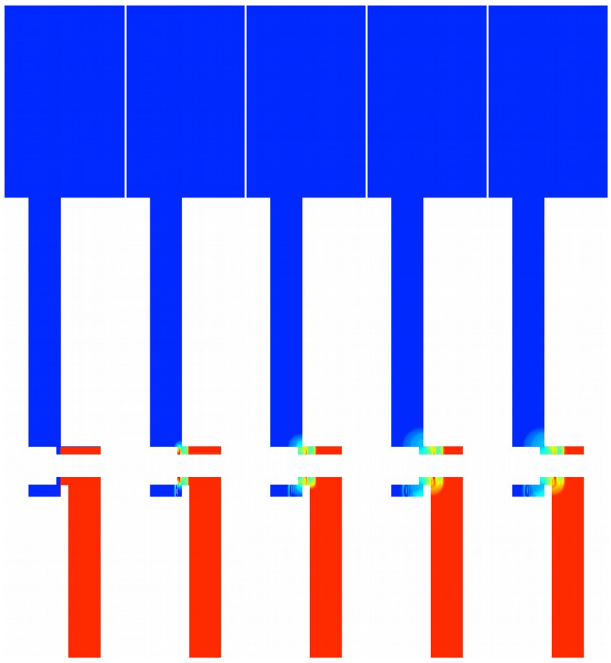

Figure 3: Pressure wave propagation shortly after initial condition (0, 24, 48, 72, 96 time steps).

Figure 4 shows the same colour coded pressure information but on a longer time scale up to 1500 time steps corresponding to roughly 82 microseconds in real time. The pressure waves travel into the two bores and are seen to be reflected at the bottom boundary condition as well as at the entry to the piston chamber which constitutes more ore less a constant pressure boundary condition on these small time scales. The velocity magnitude information is given for the same time steps in Fig. 5.

The simulation must then be run for a very large number of time steps, as the material presented so far only resembles the first moment in a flow process supplying fluid to the cylinder chamber via the control edge of the valve from the constant pressure boundary condition at the bottom.

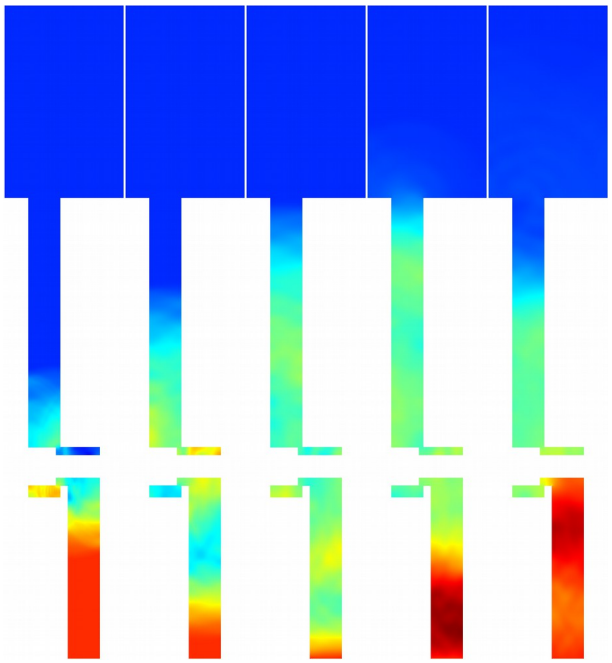

Figure 4: Pressure wave propagation at 300, 600, 900, 1200, 1500 time steps after initial condition.

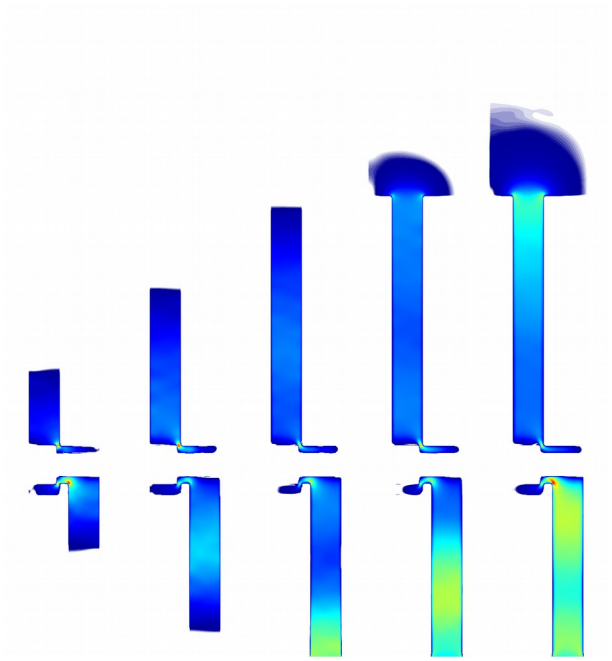

Figure 5: Magnitude of the flow velocity at 300, 600, 900, 1200, 1500 time steps after initial condition.

In order to condense the information into a low order model, the first step is the limitation of observations to input and output ports. The subsystem between the control edge of the valve and the piston face is cut out by first defining port patches and then measuring average pressure values at the patches and the net volumetric flow rates through them.

The port patch at the piston end is easily defined as the circular cross sectional area where the fluid touches the piston. In the case of the port patch defined inside the valve geometry, the geometric definition becomes clear from the initial condition of the pressure shown in the leftmost part of Fig. 3. The port patch is an annular area between the initial high and low pressure. The average pressure values and net flow rates through the two ports are given in Fig. 6 in practical engineering units of bar and l/min. The index “In” in Fig. 6 corresponds to the input at the valve orifice while “Out” corresponds to the piston face. Clearly the flow rate at the blocked piston face vanishes.

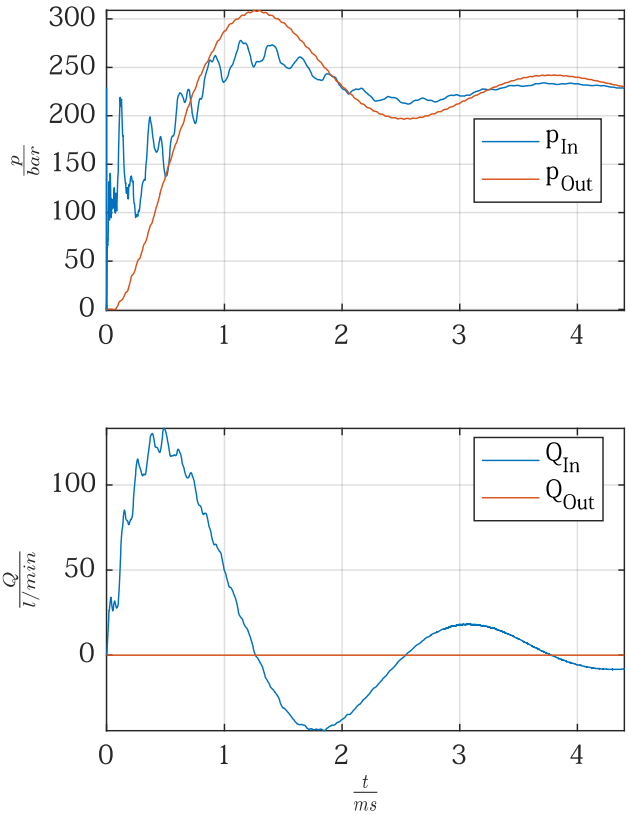

Figure 6: Simulation results: Valve Opening

A look on the flow rate chart in Fig. 6 reveals a maximum valve flow rate of approximately 120 l/min at around 0.5 milliseconds. The spatial pressure and flow rate distribution at this time is given in Fig. 7 where the sharp pressure drop at the orifice and the formation of a jet can be seen.

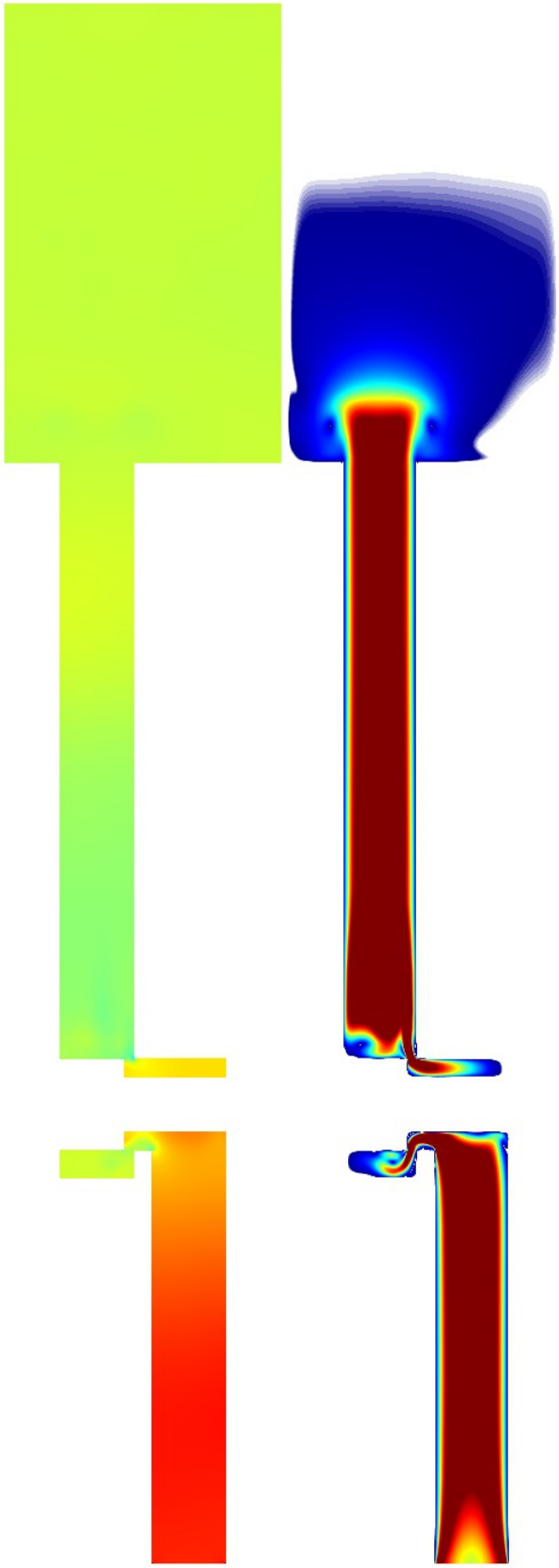

Figure 7: Pressure and velocity at the time of maximum valve flow rate around 0.5 milliseconds.

4 Extraction of a frequency domain input-output model

The information about pressures and flow rates at the subsystem input and output given in the time domain in Fig. 6 is now transferred to the frequency domain by Fast Fourier Transfrom (FFT). As the signals are neither periodic nor square integrable in time, the Fourier transform is not directly applicable. A simple trick is to differentiate both signals in time by just using the differences of successive values divided by the time step. These signals are transformed by FFT and the quotient of the frequency transformed output pressure divided by the frequency transformed input flow rate gives a transfer function describing the influence of the flow rate across the valve onto the effective piston face pressure and thus the piston force.

Figure 8 gives the resulting frequency domain information in the form of a Bode diagram commonly used in control theory. The blue line shows the frequency domain transfer function extracted from the Lattice-Boltzmann computation via Fast Fourier Transform, while the red line corresponds to a first order lumped parameter model treating the connection bore between valve and cylinder chamber and the chamber itself as one big control volume.

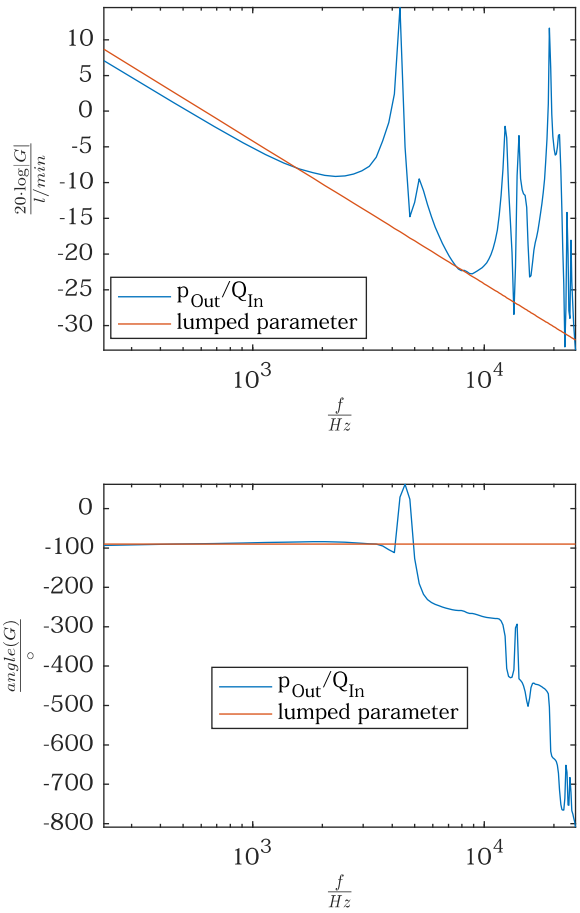

Figure 8: Simulation results: Valve Opening

Obviously, the Lattice-Boltzmann results match very well with first order low frequency behavior. Around 4500 Hz, the Lattice-Boltzmann results suggest the existence of a resonance due to wave propagation. This information could now be used to fit a low – say third order – model into the non-parametric frequency domain results presented in this paper.

In conclusion, the Lattice-Boltzmann approach can be shown to give feasible simulation times to calibrate a low order model, which can in turn be used for controller design or optimization purposes, where high dimensional computational fluid dynamics models are not usable under economical and time constraints.

5 Conclusions and outlook

In conclusion, the Lattice-Boltzmann approach can be shown to give very useful results to calibrate a low order model, which can in turn be used for controller design or optimization purposes, where high dimensional computational fluid dynamics models are not usable under economical and time constraints.

A major problem remains with respect to the stability limit preventing the application to fluid power systems in a realistic viscosity range. This issue is the topic of ongoing research and a follow-up publication with a more realistic example setting can be expected.

References

[1] J Hardy, Y Pomeau, and O de Pazzis. Time Evolution of a Two-Dimensional Classical Lattice System. *Phys. Rev. Lett.*, 31(5):276-279, 1973

[2] J Hardy, O de Pazzis, and Y Pomeau. Molecular dynamics of a classical lattice gas: Transport properties and time correlation functions, *Phys. Rev. A*, 13(5):1949-1961, 1986

[3] U Frisch, B Hasslacher, and Y Pomeau. Lattice-Gas Automata for the Navier-Stokes Equation. *Phys. Rev. Lett.*, 56(14):1505-1508, 1986

[4] G R McNamara, G Zanetti. Use of the Boltzmann equation to simulate lattice-gas automata. Phys. Rev. Lett., 61:2332-2335, 1986

[5] H E Merritt. *Hydraulic Control Systems*. John Wileys and Sons, Cincinnati, Ohio, 1967. ISBN 0-471-59617-5.

[6] B Chopard, D Lagrava, J Latt, and O Malaspinas, *A Lattice Boltzmann modeling of blood flow in cerebral aneurysms* European Congress on computational methods in applied sciences and engineering (ECCOMAS), Lisbon" 2010

[7] FlowKit Sarl, Avenue de Chailly 23, 1012 Lausanne, Switzerland, PALABOS Software, Version 1.5r1, http://www.palabos.org/images/palabos_releases/palabos-v1.5r1.tgz [accessed April 15th, 2017]

A Global Optimisation of a Switched Inertance Hydraulic System based on Genetic Algorithm

Min Pan

Centre for Power Transmission and Motion Control
Department of Mechanical Engineering, University of Bath, Bath, UK
E-mail: m.pan@bath.ac.uk

Abstract

The switched inertance hydraulic system (SIHS) is a novel high-bandwidth and energy-efficient device which can adjust or control flow and pressure by a means that does not rely on throttling the flow and dissipation of power. The three-port SIHS usually consists of a high-speed switching valve, an inertance tube and an accumulator. The device can provide an efficient step-up or step-down of pressure or flow rate by using a digital control technique. The existing analytical models of an SIHS can effectively predict the flow response, pressure loss, system characteristics and efficiency. The optimal switching frequency and ratio of an SIHS can also be accurately estimated by using the analytical models. However, there is no study related to the 'optimal inertance tube', which considers the optimal tube diameter and length corresponding to different system operating frequencies and ratios. In other words, there is inertia and resistance balance of the system. This paper investigates the global optimisation of an SIHS based on genetic algorithm. The energy cost function is proposed, and the optimal solutions are presented. Numerical simulation models are used to validate the results. It provides a general guidance of the SIHS design and its parameter optimisation.

Keywords: Switched inertance hydraulic systems; System optimisation; Cost function; Genetic algorithm

1 Introduction

The speed or force of a hydraulic system is usually controlled by using hydraulic valves to throttle the flow and therefore reduce the pressure. This approach is simple but inefficient, and it is common for more than 50% of the input power to be waste in this way.

Digital hydraulic technology was introduced to improve energy efficiency while maintaining good control flexibility and high bandwidth. The switched inertance hydraulic system (SIHS), which performs analogously to an electrical 'switched inductance' transformer, is a promising approach for raising hydraulic systems efficiency. An SIHS makes use of the natural reactive behavior of hydraulic components, and is composed of a high-speed switching valve, small diameter inertance tubes and accumulators.

Different configurations of SIHS were proposed initially by Brown [1, 2], where three-port valves and four-port valves were applied as the switching element with one and two inertance tubes, respectively. The advantages and challenges of switched hydraulic systems have been studied relative to conventional valve controlled systems. High bandwidth and great efficiency are the two main advantages [2, 3]. With a high switching frequency, the SIHS has a wider bandwidth than the conventional orifice-metered system. An ideal SIHS could perform 100% efficiency with the neglecting of power losses due to friction and leakage.

Figure 1 shows the two basic configurations of SIHSs, a flow booster and a pressure booster, which are configured by reversing the inlet and outlet connections in a three-port SIHS [3]. To achieve bi-direction control ability, the four-port SIHS is introduced, as shown in Figure 2, where two inertance tubes and accumulators were used in the system, providing real four-quadrant operation and seamless changes in direction, such as four-port modulating valves. The three-port and four-port SIHS have been investigated analytically and experimentally at the Centre for Power Transmission and Motion Control at the University of Bath [4-8].

Instead of using a three-port valve, a two-port high-speed on-off valve and a check valve were used to construct an SIHS which is also called Hydraulic Buck-Converter (HBC) [9-10]. The HBC can effectively eliminate the back flow rate as the check valve only allows the flow pass in one director. This is an advantage compared with the structures presented in Figure 1. However, the usage of the check valve introduces new characteristics to the system and a good response speed of the check valve is desired as well. The HBC has been successfully applied in robots and agricultural machines [11, 12]. The high-speed switching valves and HBC have been

studies comprehensively in the Institute of Machine Design and Hydraulic Drives at the University of Linz.

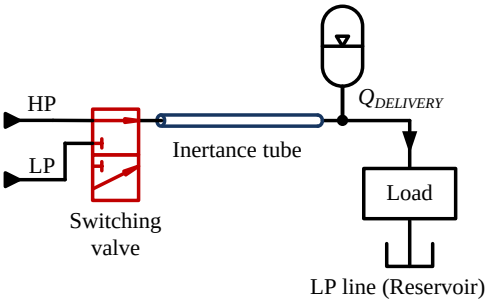

(a)

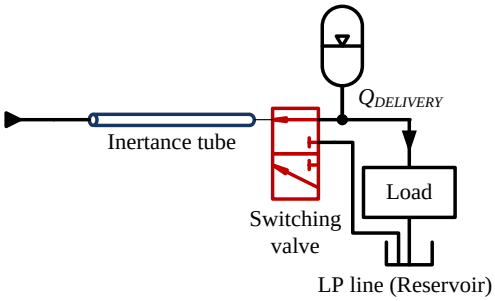

(b)

Figure 1: Schematics of switched inertance hydraulic systems (a). Flow booster configuration; (b). Pressure booster configuration

It has been concluded and agreed that the transition dynamics of the high-speed switching valve is significant to the overall efficiency [5, 13]. The 'Soft-Switching' concept is proposed to eliminate the energy losses during the switching transition [14, 15]. Also, the wave propagation effect along the pipeline has been investigated in [5, 16]. However, there is no study related to the 'optimal inertance tube', which considers the optimal tube diameter and length corresponding to different system operating frequencies and ratios. In other words, there is inertia and resistance balance of the system, which needs to be addressed.

This paper investigates the global optimisation of an SIHS based on Genetic Algorithm (GA). The energy cost function is proposed and the optimal solutions are presented. First, the enhanced analytical model of a three-port SIHS is reviewed. This is followed by system optimisation based on GA and parameter studies. Simulation investigations on numerical models of an SIHS which employs the optimal operating parameters are presented and followed by the comparisons between the 'optimal configuration' and the conventional SIHS regarding system power consumption.

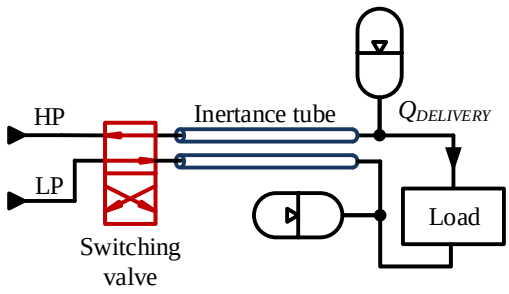

Figure 2: Schematic of a switched inertance hydraulic system in a four-port valve configuration

2 Enhanced analytical model of SIHS

An enhanced analytical model of an SIHS including switching transition dynamics, non-linearity and leakage in a three-port switching valve configuration is created and validated in author's previous work [4, 5]. The model is applied for this study. It also has been concluded in the previous work that the optimal switching frequency and ratio are highly dependent on the wave propagation in the pipeline, and that the optimal switching cycle equals to the wave propagation time divided by the switching ratio α or (1-α) with an ideal instantaneous switching.

$$T = \begin{cases} \dfrac{t_{wave}}{\alpha} & 0 \le \alpha \le 0.5 \\ \dfrac{t_{wave}}{1-\alpha} & 0.5 < \alpha \le 1 \end{cases} \tag{1}$$

where t_{wave} is the wave propagation time $t_{wave} = 2L/c$, c is the speed of sound and L is the tube length [8].

With required switching ratios (determined by load pressure), the optimal switching frequencies can be estimated and the optimal operating curve can be achieved, as shown in figure 3, where the SIHS is operating with lowest power loss. f_1, f_2 and f_3 are the optimal switching frequencies for the switching ratios α_1, 0.5 and α_2.

The power loss of an SIHS is given by [4]:

$$P_{loss} = (p_H - p_L)q_{loss} + q_m^2 R_t \tag{2}$$

where p_H and p_L are high and low supply pressures, q_{loss} is the flow loss of the system [4, 5], q_m is the average delivery flow rate and R_t is the overall system resistance.

The flow loss based on the lumped parameter model in time-domain is given by [4]:

$$q_{loss} = \frac{\tau(e^{\frac{\alpha T}{\tau}} - e^{\frac{T}{\tau}} + e^{\frac{T-\alpha T}{\tau}} - 1) + \alpha T(1-\alpha)(e^{\frac{T}{\tau}} - 1)}{(e^{\frac{T}{\tau}} - 1)TR_t}(p_H - p_L) \tag{3}$$

where α is the switching ratio, T is the switching cycle, τ is the time constant $\tau = I/R_t$;

I is the inertance of the tube:

$$I = \frac{\rho L}{A} \tag{4}$$

The flow loss based on the distributed parameter model in frequency-domain is given by [4]:

$$q_{loss} = -2\sum_{n=0}^{\infty} \mathrm{Re}\left[\frac{Q_n}{2\pi nj}(1-e^{jn2\pi\alpha})\right] \tag{5}$$

where Q_n are the Fourier coefficients of the inlet flow rate of the inertance tube,

$$Q_n = \frac{p_H(1-e^{-j2\pi n\alpha}) + p_L(e^{-jn2\pi\alpha} - e^{-jn2\pi})}{2\pi nj(jZ_0\xi\tan(\frac{\omega L\xi}{c}) + R_v)} \tag{6}$$

Z_0 is the pipe characteristic impedance,

$$Z_0 = \frac{\rho c}{A} \tag{7}$$

ξ is the viscous wave correction factor [17],

$$\xi = \left(1 - \frac{2}{z}\frac{J_1(z)}{J_0(z)}\right)^{-\frac{1}{2}} \text{ and } z = jr\sqrt{\frac{j\omega}{\nu}} \tag{8}$$

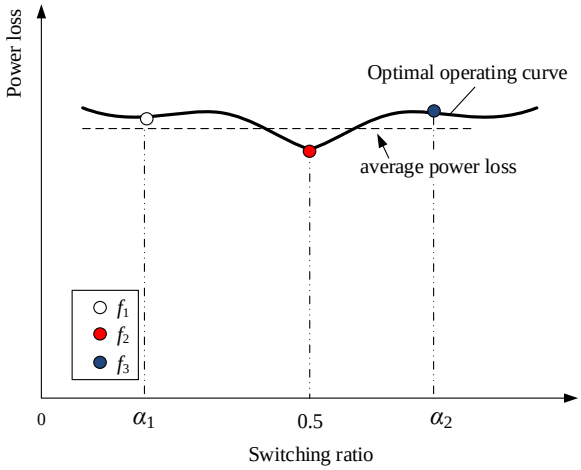

Figure 3: Optimal operating curve

3 Genetic algorithm and SIHS optimisation

An algorithm for solving optimisation problems is generally a sequence of computational steps which asymptotically converge to an optimal solution. Most classical optimisation methods generate a deterministic sequence of computation based on the gradient or higher order derivatives of the objective function. The methods are applied to a single point in the search space. The point is then improved along the deepest descending direction gradually through iterations. This point-to-point approach embraces the danger of failing in local optima. Genetic algorithm (GA) performs a multi-directional search by maintaining a set of potential solutions. The usual form of GA is described by Goldberg [18]. GAs are stochastic search algorithms based on the mechanism of natural selection and natural genetics. Figure 4 shows the flow chart of GA, and *P* (t) and *C* (t) are parents and off-spring in current generation t, respectively and the general implementation structure of GA is described as follows [18].

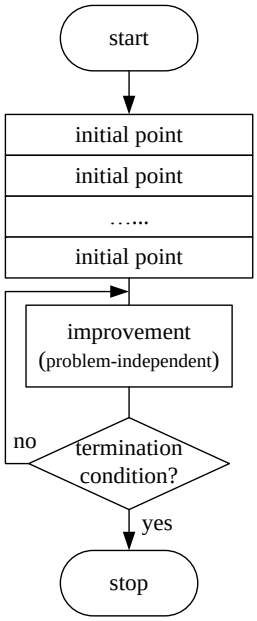

Figure 4: Flow chart of Genetic Algorithm [18]

procedure: basic GA
input: problem data, GA parameters
output: the best solution
begin
$t \leftarrow 0$;
initialize P (t) by encoding routine;
evaluate P (t) by encoding routine;
while (**not** terminating condition) **do**
create C (t) from P (t) by crossover routine;
create C (t) from P (t) by mutation routine;
evaluate C (t) by decoding routine;
select P (t+1) from P (t) and C (t) by selection routine;
$t \leftarrow t+1$;
end
output the best solution
end

The optimal operating curve of an SIHS shown in Figure 3 is symmetric with an instantaneous switching transition [4]. The optimisation process can be described as follows and the flow chart is shown in figure 5.

1. Initial α_1 and α_2 to define the considered optimisation boundary; this is determined by the load system.
2. Determine the constraints of the diameter *d* and length *l* of the inertance tube;
3. Calculate the optimal switching frequencies of the high-speed switching valve in terms of different switching ratios using equation (1).
4. Define the power loss evaluation function based on the basic or enhanced analytical model of an SIHS;
5. Apply GA to find the optimal solutions (*d* and *l*);
6. Output the best solution of the diameter and length.

The constraints of the tube length and diameter are determined in terms of valve performance beforehand. For example, the length of the inertance tube is restricted by the maximum switching frequency of the high-speed switching valve. The maximum switching frequency required would be the optimal switching frequency corresponding to the switching ratio of 0.5. An evaluation function (cost function) of system power loss is defined as:

$$F(\boldsymbol{\alpha},\mathbf{f},d,l)=\frac{1}{n}\sum_{i=1}^{n}P_i^2 \tag{9}$$

$$\mathbf{P}(\boldsymbol{\alpha},\mathbf{f},d,l)=(p_H-p_L)\mathbf{q}_{loss}+q_m^2R_t \tag{10}$$

$$n=\frac{\alpha_1-\alpha_2}{\Delta\alpha}+1 \tag{11}$$

where i is the index number, α_1 and α_2 are switching ratios, $\Delta\alpha$ is the step of the switching ratio and d is the tube diameter and l is the tube length.

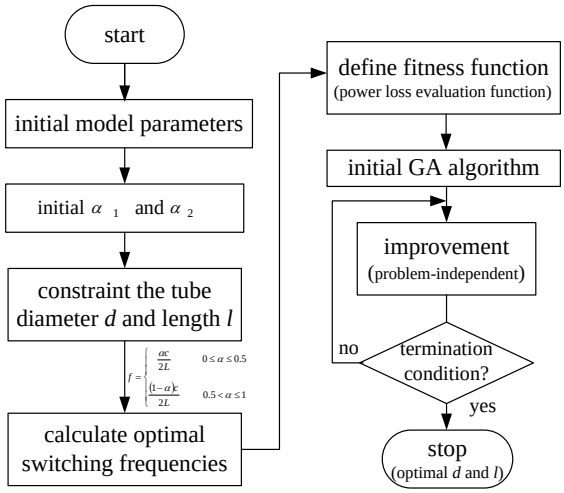

Figure 5: Flow chart of SIHS optimisation

4 Optimization studies

Different optimisation boundaries (α_1 and α_2, $0.1\le\alpha_1\le0.9$ $0.1\le\alpha_2\le0.9$) are applied for the optimisation study. The same delivery flow rate 7 L/min is assumed for different switching ratios. The constraint of the tube length is from 0.6 m to 2 m; whilst constraint of the tube diameter is from 6 mm and 20 mm. Longer tube length (> 2 m) or smaller tube diameter (< 6 mm) would cause high resistance; whilst shorter tube length (< 0.6 m) and bigger tube diameter (> 20 mm) may not be able to provide enough inertia. Three optimisation cases were investigated, and the parameters used in optimisation are listed in table 1.

Table 1 Parameters in optimisation of an SIHS

Density ρ	870 kg/m^3
Viscosity ν	32 cSt
High supply pressure p_H	100 bar
Low supply pressure p_L	50 bar
Delivery flow rate q_m	7 L/min
Switching valve orifice area A	0.337 cm^2
Switching frequency f	*Optimal*
Speed of sound c	1350 m/s
Number of spectral components	400

4.1 Case 1: $\alpha_1 < \alpha_2 < 0.5$

When the system operates with the switching ratio less than 0.5, the maximum delivery pressure is explicitly less than 75 bar (switching ratio = 0.5). Assuming the operating pressure required in this case is range from 55 bar to 70 bar, the switching ratio is corresponding from 0.1 to 0.4, as shown in Figure 6 (a) Case 1. Figure 7 (a) shows the fitness evaluation of system power loss. The best $F(x)$ 2456 W^2 was found with the tube diameter of 0.94 cm and the length of 0.6 m.

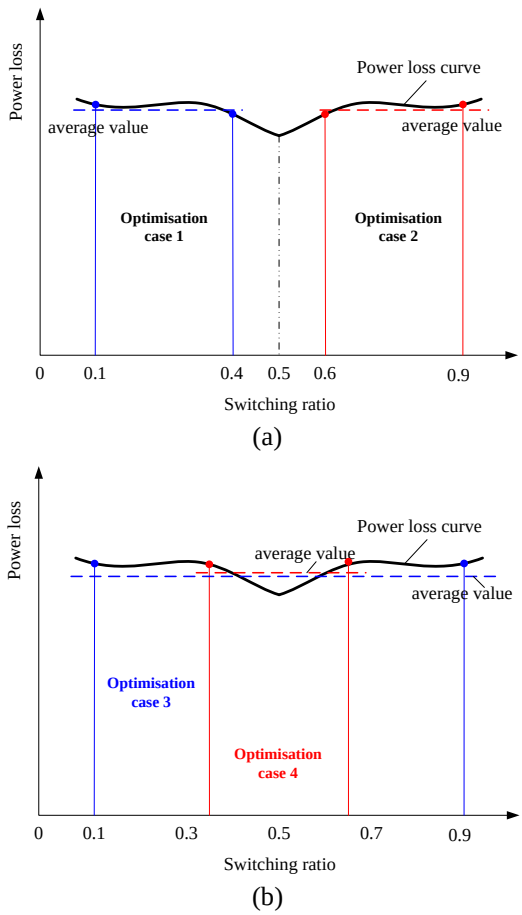

Figure 6: Different optimisation boundaries

4.2 Case 2: $0.5 < \alpha_1 < \alpha_2$

The boundary is set with the switching ratio ranging from 0.6 to 0.9, as shown in Figure 6 (a) Case 2. The SIHS can provide the delivery pressure from 80 bar to 95 bar theoretically. The best $F(x)$ 2499 W^2 was found with the tube diameter of 0.94 cm and the length of 0.61 m. The optimal solution with this boundary condition is very similar to Case 1 as the possible reason of the symmetrical optimisation area. Figure 7 (b) shows the fitness evaluation of system power loss.

4.3 Case 3: $\alpha_1 < 0.5 < \alpha_2$

Considering a wider boundary condition, the switching ratio is set from 0.1 to 0.9, as shown in Figure 6 (b) Case 3. The best $F(x)$ 2424.8 W^2 was found with the tube diameter of 0.95 cm and the length of 0.62m. Figure 7 (c) shows the fitness evaluation of system power loss. Simply narrow the boundary down of the switching ratio from 0.3 to 0.7, the best $F(x)$ 2123.6 W^2 was obtained with the tube diameter of 1.01 cm and the length of 0.63m. The fitness evaluation of system power loss was shown in Figure 7 (d).

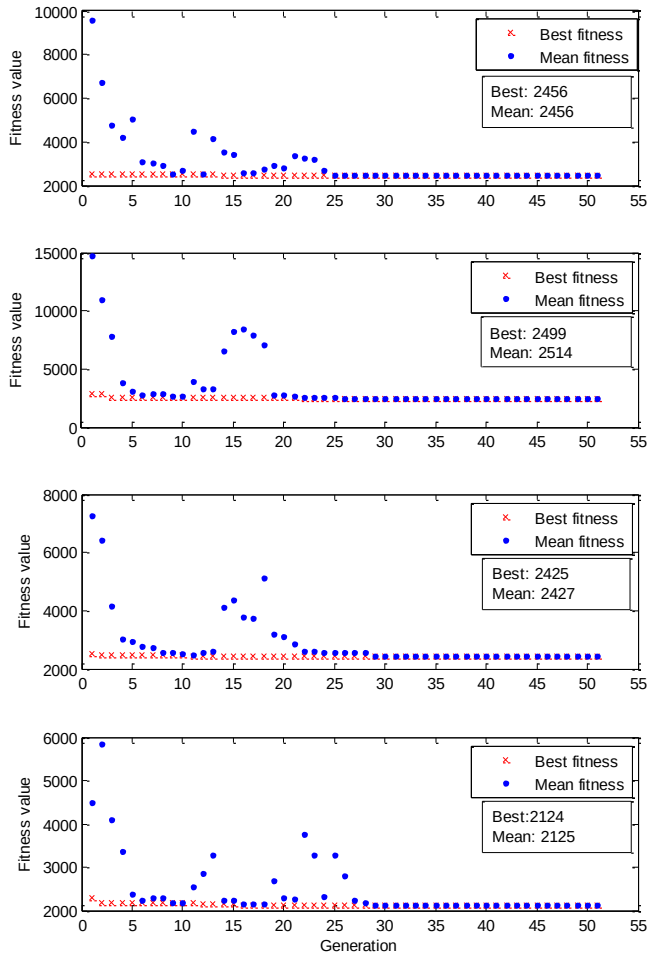

Figure 7: Fitness value against generation using GA (a). 0.1≤α≤0.4 (case 1); (b).0.6≤α≤0.9 (case 2); (c). 0.1≤α≤0.9 (case 3); (d). 0.3≤α≤0.7 (case 4)

With three cases presented above, it can be concluded that the optimal tube length is 0.62 m and the diameter is 0.95 cm for a three-port SIHS. This means the high-speed switching valve needs to be able to switch with the maximum switching frequency of 544 Hz, which seems to be achievable with the reference of previous work [2]. The compromise can be also made by constraining the tube length further. For example, with a high-speed switching valve with a maximum switching frequency of 100 Hz, the tube should at least be 3.375 m in length.

5 Simulations

A time domain numerical simulation model was created using MATLAB Simulink to verify the optimisation results. The high-speed switching valve was assumed to switch instantaneously and the switching valve flow was modelled using the standard orifice equation (12).

$$q_v(t) = C_d A \sqrt{\frac{2|\Delta p|}{\rho}} \operatorname{sgn} \Delta p \tag{12}$$

where Δp is the pressure difference through the valve, C_d is the discharge coefficient and A is the orifice area.

The Transmission Line Method (TLM) was used to model the inertance tube. The model was developed by Krus et al [19] and modified by Johnston [20] to include unsteady or frequency-dependent friction. This model accurately and efficiently represents wave propagation and laminar friction over a very wide frequency range. A small compressible volume (5 cm^3) was included between the high-speed switching valve and the TLM inertance tube model and a large volume (0.02 m^3) was included at the load to reduce the pressure pulsation. Parameters used in simulation are listed in table 1.

Figure 8 shows the power loss of an SIHS with a fixed tube diameter of 0.95 cm and different tube lengths. It illustrates the length of 0.62 m gives the lowest power loss below 25 Watt which is nearly half of using a 3 m tube and the same diameter tube.

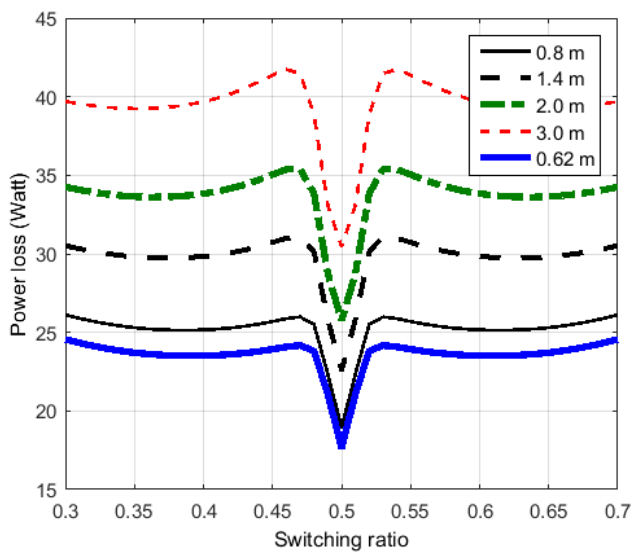

Figure 8: Power loss of an SIHS with different tube length (0.3 < switching ratio < 0.7; tube diameter = 0.95 m)

With a fixed tube length of 0.62 m, different tube diameters were used to investigate power consumption, as shown in Figure 9, where 9.5 mm diameter tube performed with the lowest power loss about 25 Watt. High energy loss occurred with the tube diameter of 20 mm, which can be caused by less inertia or high flow loss (back flow rate) to the system.

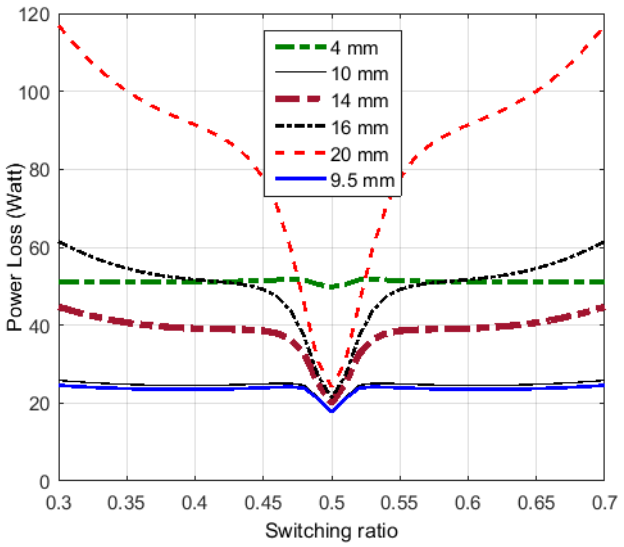

Figure 9: Power loss of an SIHS with different tube diameter (0.3 < switching ratio < 0.7; tube length = 0.62 m)

Figure 10 and 11 show the power losses with the switching ratio ranging from 0.6 to 0.9, which suits the applications requiring high operating pressures. The result confirms that the optimal tube has the length of 0.62 m and the diameter of 9.5 mm. The lowest power loss can be achieved by using this combination. Small diameter tube would cause more power loss due to its high resistance. For example, the 4 mm tube cost twice of energy than the 9.5 mm tube, as shown in Figure 11.

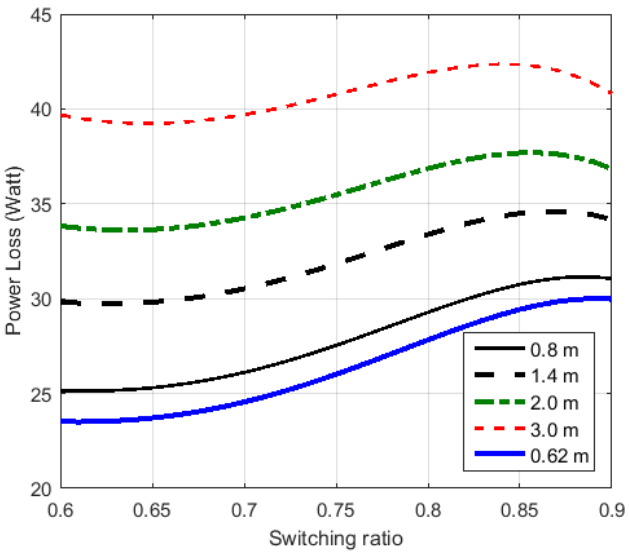

Figure 10: Power loss of an SIHS with different tube length (0.6 < switching ratio < 0.9; tube diameter = 0.95 m)

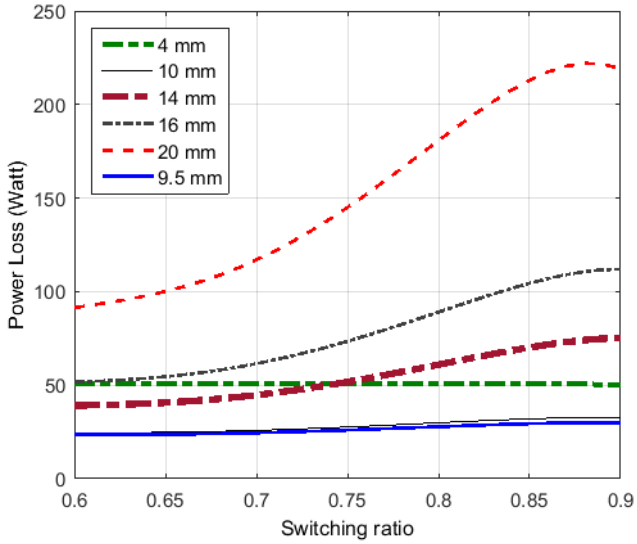

Figure 11: Power loss of an SIHS with different tube diameter (0.6 < switching ratio < 0.9; tube length = 0.62 m)

6 Discussion

The proposed optimization approach based on GA can effectively predict the optimal parameters for an SIHS, and has been validated through simulation. Some future work needs to be undertaken. The characteristics of the optimal system need to be investigated and validated through experimental work. The effect of the speed of sound needs to be investigated in depth with the optimal tube length and diameter. The author expects the varying of the speed of sound would result in an inaccuracy of the optimisation. The high-speed rotary valve developed at the Centre for Power Transmission and Motion Control at the University of Bath has been operated with the maximum switching frequency of 200 Hz. The noise becomes significant when operates the valve beyond this frequency. Although some noise attenuation research has been carried out at the Centre [21], it seems the experiments will be carried out below 200 Hz, which will constrain the tube length no shorter than 1.7 m.

7 Conclusions

The SIHS is a novel high-bandwidth and energy-efficient device which can adjust or control flow and pressure by using Pulse Width Modulation signal. The three-port SIHS in an optimal configuration has been shown to be very energy-efficient. The optimisation study concluded that the best tube length is 0.62 m and the diameter is 0.95 cm. A high-speed switching valve is required and the maximum switching frequency of the valve could constrain the boundary of considered parameters. Although duty cycle dependent, the examples given show power loss remained lowest with the optimal parameters. This study provides a general guidance for the design of an SIHS and the technique for parameter optimisation.

References

[1] Brown, F.T., Switched reactance hydraulics: a new way to control fluid power, Proceedings of the National Conference on Fluid Power, Chicago, pp.25-34, 1987.

[2] Brown,F.T., A hydraulic rotary switched inertance servo-transformer, Transactions ASME Journal of Dynamic Systems, Measurement, and Control, vol. 110, pp.144-150, 1988.

[3] Johnston, D.N., A switched inertance device for efficient control of pressure and flow, Proceedings of the Bath/ASME Fluid Power and Motion Control Symposium, Hollywood, USA, pp.1-8. 2009.

[4] Pan, M., Johnston, D.N., Plummer, A., Kudzma, S. and Hillis, A., Theoretical and experimental studies of a switched inertance hydraulic system. Proceedings of the Institution of Mechanical Engineers, Part I: Journal of Systems and Control Engineering, Vol. 228 (1), pp. 12-25, 2014.

[5] Pan, M., Johnston, D.N., Plummer, A., Kudzma, S. and Hillis, A., Theoretical and experimental studies of a switched inertance hydraulic system including switching transition dynamics, non-linearity and leakage. Proceedings of the Institution of Mechanical Engineers, Part I: Journal of Systems and Control Engineering, vol. 228 (10), pp. 802-815, 2014.

[6] Pan, M., Johnston, D.N., Robertson, J., Plummer, A., Hillis, A. and Yang, H., Experimental investigation of a switched inertance hydraulic system with a high-speed rotary valve. Transactions ASME Journal of Dynamic Systems, Measurement and Control, 137 (12), 121003. 2015.

[7] Johnston, D.N., Pan, M., Plummer, A., Hillis, A. and Yang, H., Theoretical studies of a switched inertance hydraulic system in a four-port valve configuration. In: The Seventh Workshop on Digital Fluid Power, Linz, Austria, 2015.

[8] Pan, M. Plummer, A. El Agha, A. Theoretical and Experimental Studies of a Switched Inertance Hydraulic System in a Four-Port High-Speed Switching Valve Configuration . *Preprints* 2017, 2017040177 (DOI: 10.20944/preprints201704.0177.v1). *Submitted to Energies*.

[9] Scheidl, R., B. Manhartsgruber, H. Kogler, B. Winkler, and M. Mairhofer. The hydraulic buck converter–concept and experimental results. In Proceedings of the Sixth International Conference on Fluid Power, Dresden, Germany, 2008.

[10] Kogler, H. and Scheidl, R., Two basic concepts of hydraulic switching converters. In The First Workshop on Digital Fluid Power, Tampere, Finland. Oct, 2008.

[11] Kogler, H., Scheidl, R., Ehrentraut, M., Guglielmino, E., Semini, C., and Caldwell, D. G., A compact hydraulic switching converter for robotic applications, Fluid Power and Motion Control, Bath, pp. 55–66, 2010.

[12] Scheidl, R., Garstenauer, M., and Manhartsgruber, B., Switching type control of hydraulic drives—A promising perspective for advanced actuation in agricultural machinery, SAE Technical Paper No. 2000-01-2559. 2009.

[13] Van de Ven, J. D., On fluid compressibility in switch-mode hydraulic circuits—Part I: modeling and analysis, ASME J. Dyn. Syst. Meas. Control, 135(2), p. 021013, 2013.

[14] Rannow, M.B. and Li, P.Y., Soft switching approach to reducing transition losses in an on/off hydraulic valve. Journal of dynamic systems, measurement, and control, 134(6), p.064501. 2012.

[15] Yudell, A.C. and Van de Ven, J.D., Soft Switching in Switched Inertance Hydraulic Circuits. In BATH/ASME Symposium on Fluid Power and Motion Control (pp. V001T01A040-V001T01A040). American Society of Mechanical Engineers. 2016.

[16] Kogler, H., Scheidl, R. and Schmidt, B.H., Analysis of wave propagation effects in transmission lines due to digital valve switching. In *ASME/BATH 2015 Symposium on Fluid Power and Motion Control* (pp. V001T01A057-V001T01A057). American Society of Mechanical Engineers. October 2015.

[17] Stecki, JS, Davis, D., Fluid transmission lines – distributed parameter models part 1: a review of the state of the art. Proceedings of the Institution of Mechanical Engineers, Part A: J Power and Energy; 200: 215 – 228, 1986.

[18] Goldberg, D.E., Holland, J.H., Genetic algorithms and machine learning. Machine learning, 3(2), pp.95-99. 1988.

[19] Krus, P., Weddfelt, K., Palmberg, JO., Fast pipeline models for simulation of hydraulic system. Transactions ASME Journal of Dynamic Systems, Measurement and Control, 116: 132–136. 1994.

[20] Johnston DN. The transmission line method for modelling laminar flow of liquid in pipelines. Proceedings of the Institution of Mechanical Engineers, Part I: Journal of Systems and Control Engineering; 226:586–597. 2012.

[21] Pan, M., Adaptive control of a piezoelectric valve for fluid-borne noise reduction in a hydraulic buck converter. Transactions ASME Journal of Dynamic Systems, Measurement and Control. DOI: 10.1115/1.4035613. 2017.

Non-linear Control of a Piezoelectric Two Stage Servovalve

Johan Persson, Andrew Plummer, Chris Bowen and Phil Elliott*

Department of Mechanical Engineering, University of Bath, Bath, United Kingdom
E-mail: ljp46@bath.ac.uk, A.R.Plummer@bath.ac.uk, C.R.Bowen@bath.ac.uk
* Moog Aircraft Group, Moog Controls, Ashchurch, Tewkesbury, United Kingdom

E-mail: pelliott2@moog.com

Abstract

This paper describes an algorithm to control a two stage hydraulic servovalve designed for aerospace applications. The valve has a piezoelectric ring bender actuating a first stage spool with a significant amount of overlap to reduce internal leakage. The piezoelectric ring bender is a less complex and lighter alternative to a conventional torque motor. The second stage has electrical instead of the conventional mechanical feedback. The control algorithm includes compensation for the first stage spool overlap, piezoelectric hysteresis compensation and a feed forward term. The hysteresis compensation is based on a relatively simple Bouc-Wen hysteresis model that is able to significantly reduce the amount of first stage hysteresis. The overlap compensation, increasing the gain in the overlap region, reduces the impact of amplitude change and increases performance. It can also reduce any asymmetry in the system. The controller has a superior performance compared to a PI controller, as demonstrated experimentally using step and frequency responses.

Keywords: piezoelectric actuator, two-stage servovalve, spool, hysteresis compensation.

1 Introduction and Valve Prototype

This paper describes a control algorithm used to control the position of the main stage in a two stage servovalve designed for aerospace flight control applications. It has a piezoelectric ring bender actuating the pilot stage spool and a second stage spool with electrical feedback.

A two-stage servovalve converts an electrical signal into the position of a fluid-metering spool via a hydraulic amplification stage [1]. Such a servovalve is usually used to control flow to the hydraulic actuator where high performance motion control is required.

In a typical single-aisle airliner there are approximately 40 hydraulic servovalves, which are the key control component in electrohydraulic actuation for primary flight control, landing gear deployment, on-ground braking and steering. Key drivers for new aerospace hydraulic servovalve designs are to reduce weight, reduce manufacturing cost, and improve efficiency through reduced internal leakage. For example, by reducing the internal leakage of a servovalve approximately 2200 USD per valve per year of fuel cost could be saved by the airline companies [2]. To reduce the internal leakage a small spool with significant overlap was used for the pilot stage.

In a conventional valve, the first (or pilot) stage refers to the torque motor and either nozzle-flapper, jet pipe or deflector jet amplifier, and provides the actuation to move the main spool (second stage). Torque motors can be time-consuming and expensive to set-up, requiring significant manual intervention [3]. If not adjusted precisely the first stage amplifier may not provide stable operation, and there is a continual flow loss (and power loss) through the nozzles or jet. An alternative approach is required providing a more cost effective design, which is amenable to automated manufacture.

Smart materials, and in particular piezoelectric ceramics, are a possible alternative potentially providing high forces and fast response times [4], [5]. Stack and bending actuators have been extensively researched [6]. The relatively new multilayer three wire piezoelectric ring bender is a type of bending actuator, which is a flat annular disc that deforms in a concave or convex fashion depending on the polarity of the applied voltage, see fig. 1 (c) [6], [7]. Such an actuator configuration has been chosen for first stage actuation since it exhibits a greater displacement than a stack actuator of the same mass, and an increase in stiffness in comparison to similar size rectangular bimorph type bender, resulting in a larger force output.

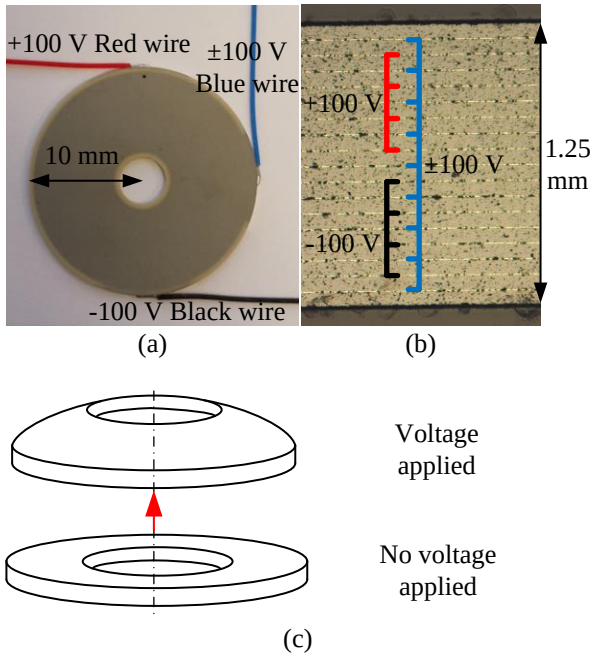

Figure 1. (a) Noliac piezoelectric ring bender (b) Microscopic section of a piezoelectric ring bender (c) Piezoelectric ring bender deformation

A Noliac CMBR08 multilayer, three wire piezoelectric ring bender is used for actuating the first stage in the prototype valve. The piezoelectric ring bender has a 40mm diameter and 1.25mm thickness, a free displacement of ±115µm and a blocking force of ±39N. Figure 1 (a) shows the ring bender with its three wire electrical connection. The bender is made up of multiple 67µm thick lead zirconium titanate (PZT) piezoelectric ceramic layers. To apply the necessary electric field across the piezoelectric ceramic and thereby actuate the device, silver palladium electrodes are located between each layer, which can be seen as light lines in fig. 1 (b). In order to deflect the ring bender in both directions the electrodes are combined into three groups, as shown in fig. 1 (b) [8].

The concept for the first stage is to use the ring bender to actuate a small spool, see fig. 2, with significant overlap to reduce the internal leakage. The piezoelectric ring bender moves the spool to control the flow to the second stage.

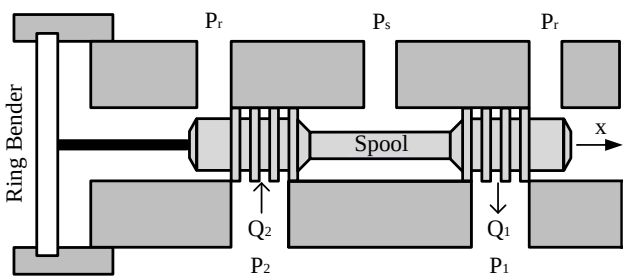

Figure 2. First stage concept.

Electrical second stage feedback allows a sophisticated digital controller to be implemented and will be more effective to counteract disturbances [9], compared to valves with mechanical feedback.

The piezoelectric actuated valve prototype was built and tested on a dedicated test bench. The second stage titanium alloy spool housing was made through Additive Manufacture (AM), which, enables a greater design freedom. Figure 3 shows the valve, where the first stage spool, piezoelectric ring bender and the LVDT's to obtain first and second stage position can be seen. A photograph of the valve tested with its AM second stage housing is shown in fig. 4. A circuit diagram of the system can be seen in fig. 5.

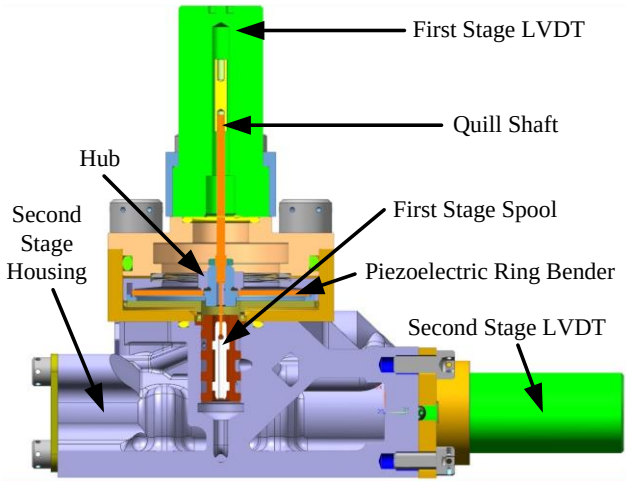

Figure 3. Cross section of the pilot stage.

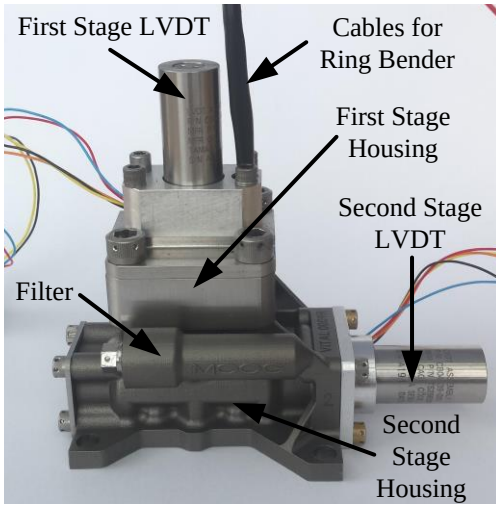

Figure 4. Photograph of the valve tested.

This paper presents a control strategy for compensating the hysteresis of the piezoelectric ring bender, without using additional sensors (such as pilot stage position feedback), which add weight, cost and complexity to the valve. The first stage LVDT in the prototype will merely be used to monitor the performance of the piezoelectric ring bender and first stage spool, and not used for control.

The influence of a reduction of first stage piezoelectric hysteresis on the second stage positioning performance was studied. The study also includes compensation for the first stage spool overlap and implementation of a feed forward term to increase the second stage spool position response.

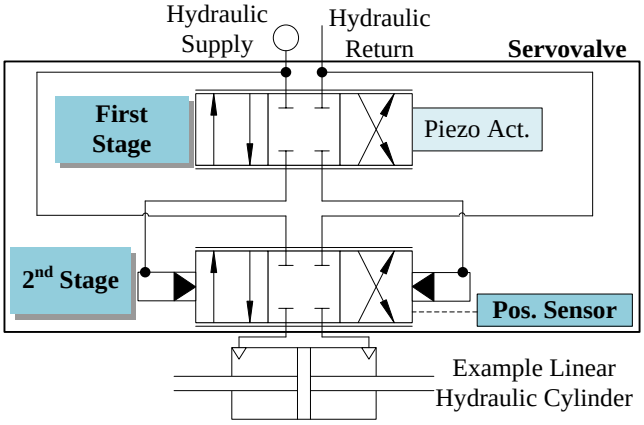

Figure 5. Internal servovalve circuit.

2 Controller Design

In traditional two stage servovalves with mechanical feedback and torque motor the steady state spool position is proportional to the electrical input current in the torque motor [10] [11]. This is achieved by the feedback spring exerting a feedback torque on the torque motor proportional to spool position. However, using an electrical second stage positioning feedback this is not the case.

The controller platform used for this investigation was an xPC system where a Simulink control model is automatically converted to real-time code to run on a PC target. A circuit diagram of the control setup can be seen in fig. 6. An amplifier was needed to drive the piezoelectric ring bender. The control computer was configured to record the first and second stage spool positions as well as the amplifier output voltage.

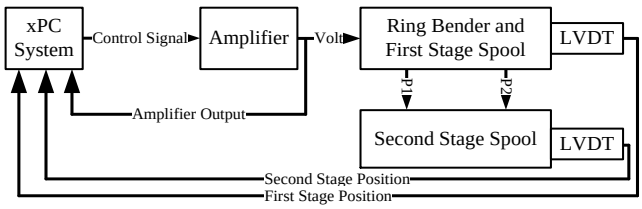

Figure 6. Circuit diagram of the control setup.

A Proportional-Integral (PI) controller is a common feedback control algorithm using Proportional, K_p, and Integral, K_i, gains as can be seen in fig. 7. Due to the piezoelectric hysteresis and a significant amount of first stage spool overlap, causing a 'dead-band', this controller not sufficient, as will be described later.

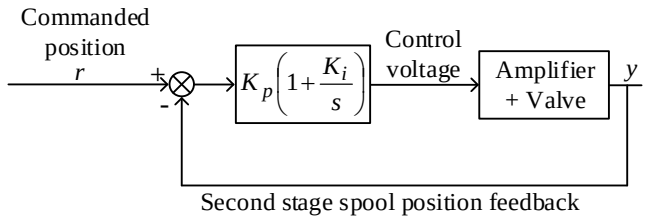

Figure 7. PI control loop.

The control algorithm proposed in this paper, see fig. 8, includes overlap compensation, hysteresis compensation and command velocity feed forward terms. The hysteresis and overlap compensation are intended to make the system more linear and the feed forward loop is to make the response faster. The controller block diagram is shown in fig. 8.

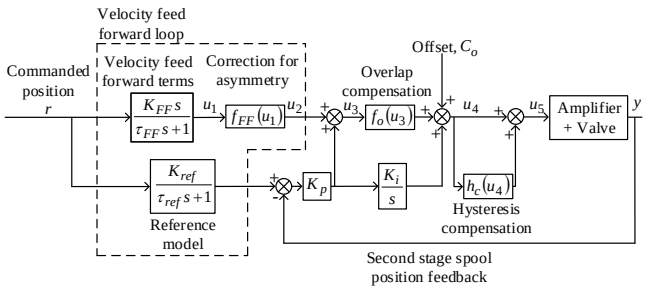

Figure 8. Proposed control algorithm.

All the parameter values used can be seen in tab. 1.

2.1 Hysteresis Compensation

Previously an inverse of the more complicated Prandtl-Ishinskii model has been used for hysteresis compensation of a piezoelectric ring bender [12]. The Bouc-Wen model has been used previously to compensate for the hysteresis of a rectangular piezoelectric bender [13]. However, in that work only static or low frequency (0.07Hz) responses were investigated.

The hysteresis compensation used for the current work is also based on a Bouc-Wen hysteresis model [14], which is a relatively simple 3-parameter model and also simple to invert to form a hysteresis compensator [13]. The Bouc-Wen model, eq. (1), has three dimensionless tuning parameters α, β and γ. The hysteresis term n is the deviation away from the linear response, and u_3 is the demanded voltage from the controller (voltage after the overlap compensation and integral gain). Figure 9 shows one experimental hysteresis loop and a simulated hysteresis loop, using the Bouc-Wen model, where n is subtracted from the linear response. It can be seen that the hysteresis model matches the experimental data. In the compensator, n times a scaling factor, is added to the control voltage, as can be seen in eq. (2) and fig. 8. The scaling factor, K_h is needed to restore the correct linear gain. The three tuning parameters values can be seen in tab. 1.

$$\dot{n} = \alpha \dot{u}_3 - \beta |\dot{u}_3| n - \gamma \dot{u}_3 |n| \qquad (1)$$

$$h_c(u_3) = K_h n \qquad (2)$$

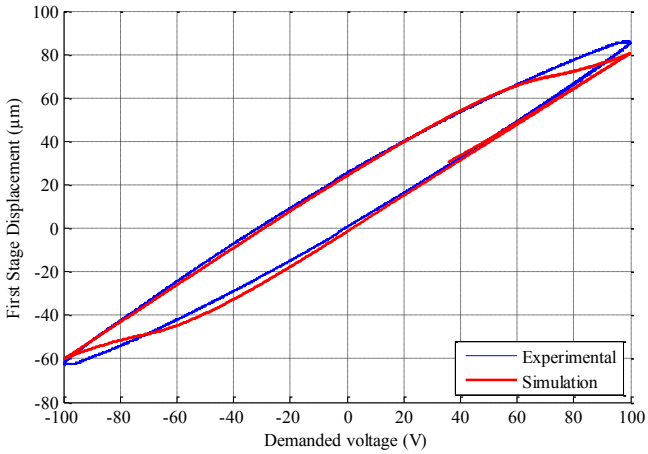

Figure 9. Experimental hysteresis loop vs simulated hysteresis loop.

Figure 10 shows two experimental hysteresis loops, one with hysteresis compensation and one without hysteresis compensation. As can be seen the hysteresis is significantly reduced.

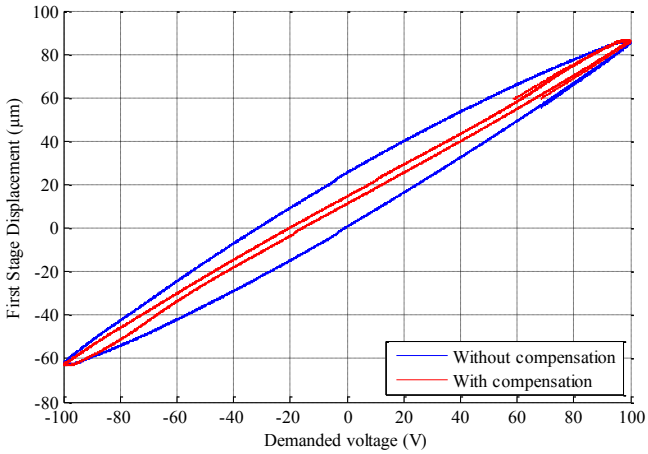

Figure 10. Experimental hysteresis compensation loop.

2.2 Overlap Compensation

The first stage spool is closed center with a significant amount of overlap, ~20µm, to reduce the internal leakage. A closed center arrangement will result in a 'dead-band' where very little flow is passing to the second stage in the overlap region [15], as can be seen in fig. 11.

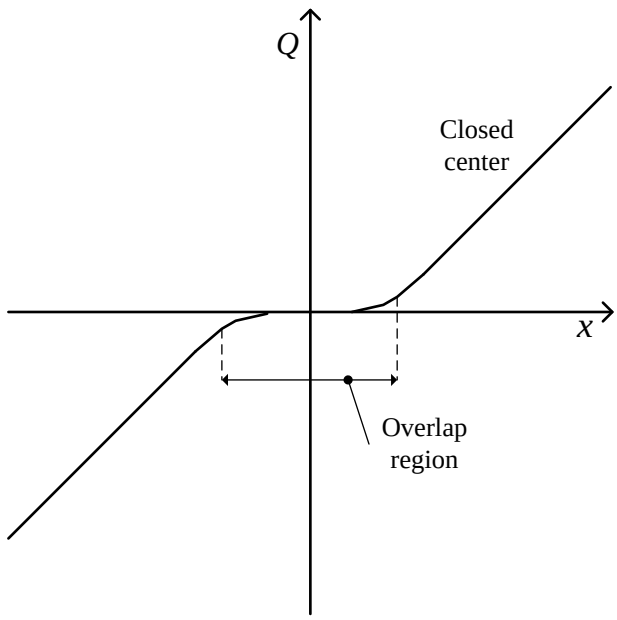

Figure 11. Flow gain for closed center spool.

To be able to linearize the system this dead-band has to be compensated for. The overlap compensation was implemented as a look-up table with a higher gain where the first stage spool was in the overlap region, see fig. 12. Figure 13 shows the measured second stage velocity versus the first stage position. The overlap compensation also compensated for some asymmetry and offset, as can be observed in fig. 13. The offset is the difference between the electrical null for the piezoelectric ring bender and the hydraulic null of the first stage spool, seen in fig. 13, and is compensated by an offset term C_o (fig. 8). In fig. 13 a small lag between the first stage position and second stage velocity can be observed.

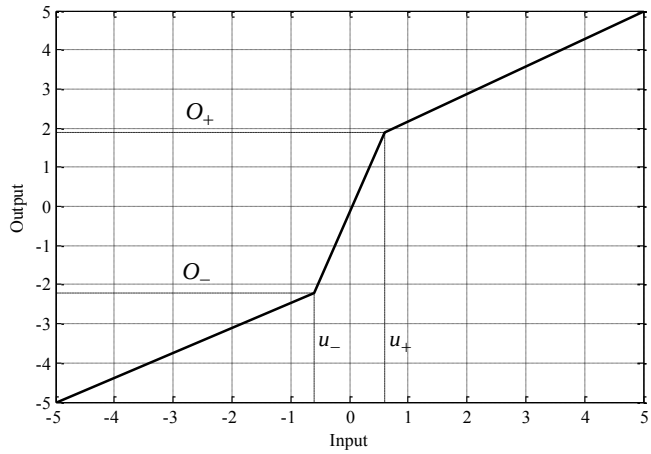

Figure 12. Overlap compensation function (f_o)

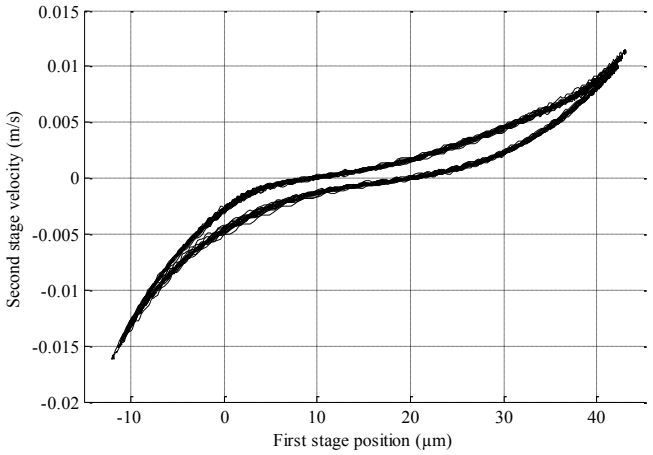

Figure 13. Velocity of the second stage spool compared to the first stage position.

2.3 Command Velocity Feedforward

The command velocity feedforward will speed up the dynamic response, which generally means increasing the bandwidth of the system [16]. The velocity feedforward consists of three parts, the feedforward terms, reference model and the model to correct for asymmetry in the second stage spool behavior. The feedforward command velocity is estimated by differentiated position filtered by a first order lag, as can be seen in fig. 8. The feedforward loop also compensates for velocity asymmetry in the system. The asymmetry is due to the null offset in the valve coupled to the non-linear stiffness of the piezoelectric ring bender mounting. The function $f_{FF}(u_1)$ term is a lookup table as shown below:

$$f_{FF}(u_1) = 1.4u_1 \text{ if } u_1 \geq 0 \qquad (3)$$

$$f_{FF}(u_1) = u_1 \text{ if } u_1 < 0 \qquad (4)$$

A reference model is included as a prediction of the response of the system to the feedforward path. The feedback control thus only acts on the error between the actual spool position and the predicted position. This error can also be thought of as a disturbance observer.

Table 1. Parameter table.

	Parameter	Value
Hysteresis compen-sation parameters	α, Hysteresis tuning parameter	0.0017 $(-)$
	β, Hysteresis tuning parameter	0.00065 $(-)$
	γ, Hysteresis tuning parameter	0.0015 $(-)$
	K_h, Hysteresis scaling factor	0.87 $(-)$
Overlap compen-sation parameters	O_+, Positive overlap compensation output	1.9 (V)
	O_-, Negative overlap compensation output	-2.2 (V)
	u_+, Positive overlap compensation input	0.6 (V)
	u_-, Negative overlap compensation input	-0.6 (V)
Feed forward loop parameters	K_{FF}, Feedforward term gain	0.00005 $(V/(\mu m/s))$
	K_{ref}, Reference model gain	1 $(-)$
	τ_{FF}, Feedforward term lag	0.0015 $(-)$
	τ_{ref}, Reference model lag	0.003 $(-)$
Controller Settings	K_p, Proportional gain for the non-linear controller	0.012 $(V/\mu m)$
	K_i, Integral gain for the non-linear controller	200 $(-)$
	K_{p1}, Proportional gain for PI1	0.05 $(-)$
	K_{p2}, Proportional gain for PI2	0.03 $(-)$
	K_{i1}, Integral gain for PI1	1 $(-)$
	K_{i2}, Integral gain for PI2	1 $(-)$
	C_o, Null offset comensation	0.25 (V)

3 Results

The valve prototype with the proposed control algorithm has been tested. The effect of the different controller parts were compared. Four different controller arrangements were tested:

- Complete controller (FF+OC+HC)
- Overlap compensation (OC) and hysteresis compensation (HC)
- Overlap compensation (OC) and feed forward (FF)
- Only overlap compensation (OC).

Two different step input sizes, 60µm and 120µm, were tested as well as a 30µm amplitude frequency response. The non-linear controller was compared to the conventional PI controller of fig. 7 at the end of this section. All tests were performed at 200 bar and at an oil temperature of 39±1.5°C.

Figure 14 shows the 60µm step response and fig. 15 shows the 120µm step response. The rise time (0-90%) and the settling time (±5%) for both amplitudes can be seen in tab. 2 and tab. 3.

By only compensating for the overlap the rise time is 8.2ms for a 60µm step and 7.3 for a 120µm step size. The settling time for 120µm step was 57.6ms, but the position did not settle within ±5% for the 60µm step. By having the overlap compensation and hysteresis compensation the response is quicker, but the device also experiences more overshoot. By having the overlap compensation and a feedforward term the response was even further improved. The complete controller had the overall fastest response.

The average difference between the commanded position and the actual position is 5.6µm for the 60µm step and 7.7µm for the 120µm step for the controller without hysteresis compensation (OC+FF). This can be compared to the complete controller that has a difference of 4µm for the 60µm step and 6.1µm for the 120µm step.

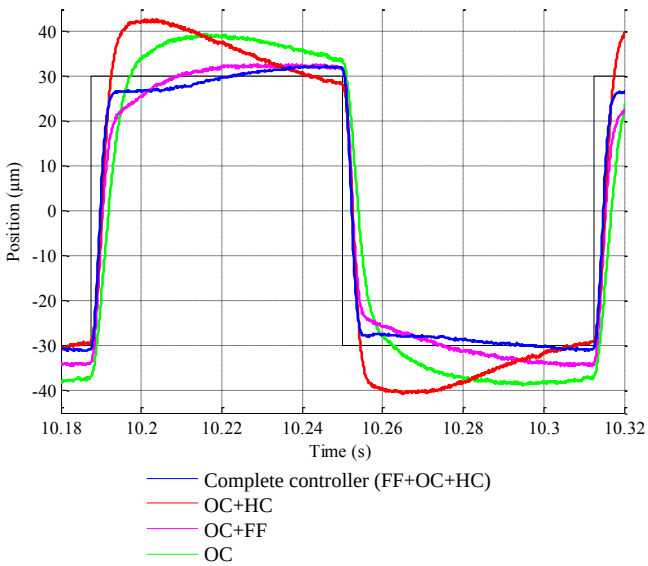

Figure 14. 60µm step response results.

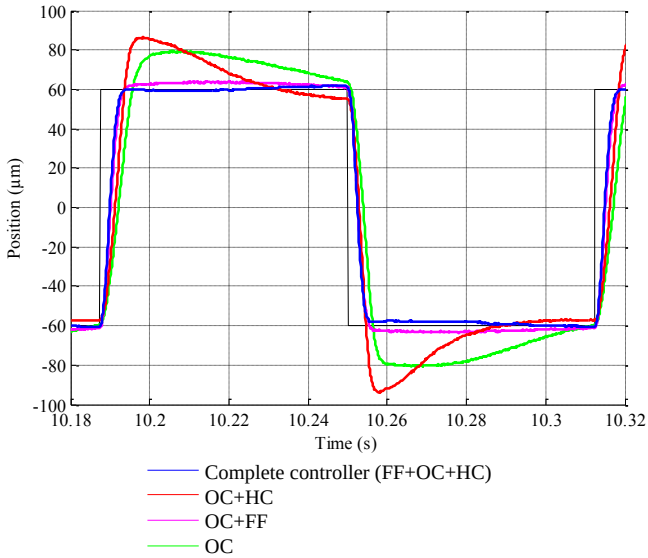

Figure 15. 120µm step response results.

Table 2. 60µm step response results with different combinations of overlap compensation (OC), feed forward (FF) and hysteresis compensation (HC).

60µm Step	**Rise time (0-90%)**	**Settling time (±5%)**
Complete controller (FF+OC+HC)	4.6ms	15.7ms
OC+HC	4.5ms	44.6ms
OC+FF	10.3ms	14.9ms
OC	8.2ms	>62.5ms

Table 3. 120µm step response results with different combinations of overlap compensation (OC), feed forward (FF) and hysteresis compensation (HC).

120µm Step	**Rise time (0-90%)**	**Settling time (±5%)**
Complete controller (FF+OC+HC)	4.3ms	4.8ms
OC+HC	5.7ms	35.8ms
OC+FF	4.9ms	5.2ms
OC	7.3ms	57.6ms

A frequency response test was completed with an amplitude of 30µm, see fig. 16. It can be seen that in the system where the feedforward loop is included both the magnitude and

phase lag first decrease then increase again. This is most likely due to inexact first stage overlap compensation.

It can also be seen in fig. 16 that the setup with overlap compensation and hysteresis compensation (without feedforward) has a better performance than the complete system until around 50 Hz for the magnitude and 30 Hz for the phase, but after those frequencies the complete setup performs better than the other control algorithms.

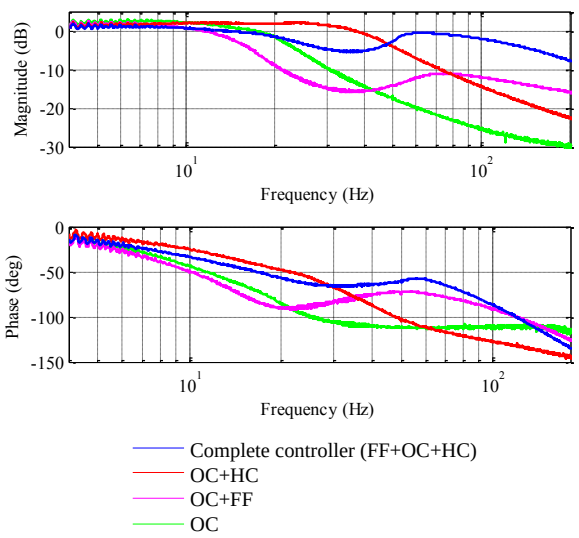

Figure 16. Frequency response results, 30µm amplitude.

The complete non-linear controller was compared to a well-adjusted conventional PI controller. Responses to steps of 60µm and 120µm were measured as well as a 30µm amplitude frequency response. Two different PI setups were tested, one was tuned to give a good response for a square wave amplitude of 30µm amplitude (60µm step, PI1) and the second for a 60µm amplitude (120µm step, PI2).

It can be seen in fig. 17, 60µm step, and fig. 18, 120µm step, that for the same PI controller for the different amplitudes significantly different results will be obtained. It can also be observed that the proposed non-linear control algorithm is the better controller when it comes to rise time and settling time, as can be seen in tab. 4 and tab. 5, as well as being less affected by the amplitude change. The PI controller setup for a 30µm amplitude (60µm step) did not settle within ±5% of the step within 62.5ms in either case.

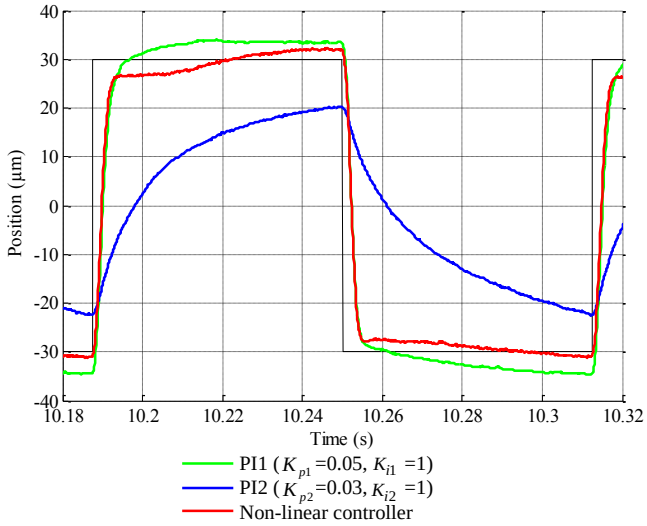

Figure 17. 60µm step, PI setup vs complete non-linear control algorithm.

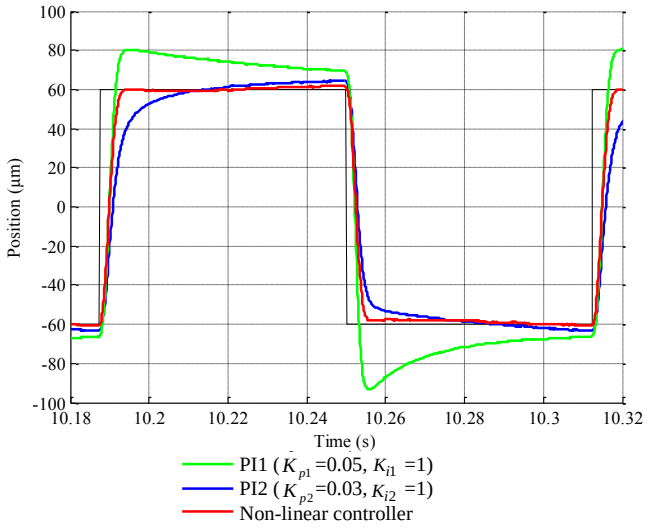

Figure 18. 120µm step, PI setup vs complete non-linear control algorithm.

Table 4. PI controller, 60µm step response.

60µm Step	**Rise time (0-90%)**	**Settling time (±5%)**
PI1 ($K_{p1} = 0.05$ **,** $K_{i1} = 1$ **)**	5.2ms	>62.5ms
PI2 ($K_{p2} = 0.03$ **,** $K_{i2} = 1$ **)**	>62.5ms	>62.5ms
Non-linear controller	4.6ms	15.7ms

Table 5. PI controller, 120µm step response.

120µm Step	**Rise time (0-90%)**	**Settling time (±5%)**
PI1 ($K_{p1} = 0.05$ **,** $K_{i1} = 1$**)**	3.7ms	>62.5
PI2 ($K_{p2} = 0.03$ **,** $K_{i2} = 1$**)**	9.4ms	14ms
Non-linear controller	4.3ms	4.8ms

A frequency response was completed for the two PI controllers and the non-linear controller, see fig. 19. It can be seen that the non-linear controller gives a better dynamic response particularly in terms of magnitude throughout the frequency range. Note that the low frequency phase lag evident in the PI controller response is due to the hysteresis.

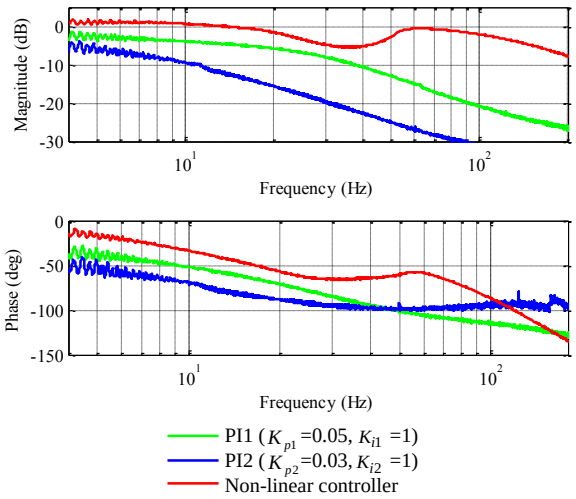

Figure 19. Frequency response of conventional PI controller vs Experimental non-linear controller.

4 Conclusions

A prototype low-leakage piezoelectric servovalve has been developed. For main spool position control, a conventional PI controller is sensitive to amplitude changes, due to the lack of compensation for the first stage overlap. A higher gain in the first stage spool overlap region is essential to remove this sensitivity. However, due to piezoelectric hysteresis, the relationship between the drive voltage and first stage position is not linear. Thus hysteresis compensation is required to enable effective overlap compensation. In addition, command velocity feedforward has been tested to improve the dynamic response. The complete control algorithm, with all three features, is shown to provide the fastest and most accurate response. It is shown that the non-linear controller significantly outperforms two PI controllers, which span the range of plausible proportional gain values.

Work currently ongoing:

i. Maximizing reliability of piezoelectric ring benders in aerospace hydraulic fluid.
ii. Optimization of mountings for piezoelectric ring benders.

Acknowledgments

The authors would like to thank Moog Aircraft Group, Renishaw and Innovate UK for supporting this research. Ownership of Intellectual Property described in this work is detailed in collaboration agreements for VITAL IUK project 17413-117299 and Moog-Bath PhD Studentship Agreement of 5/9/15.

References

[1] Moog, “Servo Valves,” 2017. [Online]. Available: http://www.servovalve.com/. [Accessed: 12-Jan-2017].

[2] Moog, “Servovalve Leakage Fuel Costs (Moog Internal Report),” 2012.

[3] D. K. Sangiah, A. R. Plummer, C. R. Bowen, and P. Guerrier, “A novel piezohydraulic aerospace servovalve. Part 1: design and modelling,” *Proc. Inst. Mech. Eng. Part I J. Syst. Control Eng.*, vol. 227, no. 4, pp. 371–389, 2013.

[4] C. Mangeot, B. Anderssen, and R. Hilditch, “New Actuators for Aerospace,” Kvistgaard, 2008.

[5] R. Le Letty, F. Claeyssen, F. Barrillot, and N. Lhermet, “Amplified Piezoelectric Actuators for Aerospace Applications,” *AMAS Work. Smart Mater. Struct.*, pp. 51–63, 2003.

[6] M. J. F. Bertin, C. R. Bowen, A. R. Plummer, and D. N. Johnston, “An Investigation of Piezoelectric Ring Benders and Their Potential for Actuating Servo Valves,” in *Proceedings of the Bath/ASME Symposium on Fluid Power and Motion Control*, 2014, p. 6.

[7] Noliac, “Ring Benders,” 2015. [Online]. Available: www.noliac.com. [Accessed: 01-Dec-2015].

[8] J. Persson, C. R. Bowen, A. R. Plummer, and P. L. Elliott, “Dynamic Modelling and Performance of a Two Stage Piezoelectric Servovalve,” in *Proceedings of the ASME 2016 9th FPNI Ph.D Symposium on Fluid Power*, 2017, pp. 1–10.

[9] J. C. Jones and T. S. Manager, “Development in Design of Electrohydraulic Control Valves From Their Initial Design Concept to Present Day Design And Applications.” Moog Australia PTY LTD., pp. 1–19, 1997.

[10] Moog, “Electrohydraulic Valves... A Technical

Look.”

[11] Moog, “Type 26 Single Inlet Flow Control Servovalves,” 2011.

[12] F. Stefanski, B. Minorowicz, J. Persson, A. Plummer, and C. Bowen, “Non-linear control of a hydraulic piezo-valve using a generalised Prandtl – Ishlinskii hysteresis model,” *Mech. Syst. Signal Process.*, vol. 82, pp. 412–431, 2017.

[13] M. Rakotondrabe, “Bouc – Wen Modeling and Inverse Multiplicative Structure Actuators to Compensate Hysteresis Nonlinearity in Piezoelectric Actuators,” vol. 8, no. 2, pp. 428–431, 2011.

[14] D. K. Sangiah, “Fluid Metering Using Active Materials,” University of Bath, 2011.

[15] K.-E. Rydberg, “Hydraulic Servo Systems.” Linköpings Universitet, Linköping, 2008.

[16] Parker Hannifin - Electromechanical Automation Div., “Fundamentals of Servo Motion Control.”

Assessment of Electric Drive for Fuel Pump using Hardware in the Loop Simulation

Batoul ATTAR, Jean-Charles MARE

Institut Clément Ader (ICA), INSA
135 avenue de Rangueil, 31077 Toulouse Cedex 4, France
E-mail: attar@insa-toulouse.fr, mare@insa-toulouse.fr

Abstract

The present communication deals with the evaluation of electric drives used in fuel system by using Hardware In the Loop (HIL) methodology. At the designing stage of electric drive, there are a lot of choices concerning electric motor technology (DC motors, AC motors, BLDC motors, PMSP motors) while there may be a lot of uncertainty in working environment, mission profile and control strategy at fuel pump level. For these reasons, HIL is suggested as solution that permits to test different motor technologies regardless the applied load. The outcome of HIL will be the most effective motor for studied application. Thermal model and power supply model are presented in this paper to be integrated in real-time model with tested electric motor model, to get virtual prototype closer to the real system. As a result, observations and restrictions of HIL methodology are presented, which point up the impact of the selection of the real motor and its drive.

Keywords: Electric drive, Fuel system, Hardware in the loop (HIL), Matlab/Simulink, Power by wire (PBW), Real-time simulation

1 Introduction

Hybrid Electric Vehicles (HEV) or totally Electric Vehicles (EV) are the new tendency in transport vehicles industry for many reasons. The first one is to protect the environment by reducing fuel consumption, e.g. CO_2 emission by 35% that is equivalent to more than a 50% increase in fuel economy[1] [1]. Furthermore, more electric vehicles will get desirable characteristics of electrical systems, such as controllability, re-configurability, and advanced diagnostics and prognostics which assure more intelligent maintenance. So, better performance and long life time for transport vehicles will be achieved.

In the field of power transmission and control, more electric vehicles involve more electrical signaling and powering of drives that still employ internally hydraulic and mechanic devices: air conditioning compressor, fuel systems (pumps, injection, air intake geometry,…) [2]. Electrically signaled (Signal-By-Wire) systems use electrical transmission of commands, sensors data, mode selection, diagnostic etc. Electrically powered (Power-By-Wire) systems supply drives with electric power, e.g. inlet guide vane actuator for engines or electro-hydrostatic actuators (EHA) for flight controls. Combining SbW, PbW and local hydraulic system can therefore take the best of all technologies for power transmission systems [3].

In this communication more electrical drives will refer to (Power-By-Wire). A closer look will be taken on engines fuel systems. Using electrical drive for the low pressure fuel pump will insure better start/priming of the engine whatever environment conditions or the topology of the system, where in some application the pump is far away from the tank, e.g. for helicopters.

In fact, during priming stage, the pump has to get off the existing air in fuel system pipes, and then deliver the fuel to the fuel metering unit. Dealing with different fluids (air and fuel) during suction phase needs different amount of driving power. Nevertheless, choosing an adequate electrical drive to the fuel pump requires knowing the exact needed power, in order to size the drive properly. This is difficult to calculate because of mixed flow at priming stage. So, drive sizing remains inaccurate at the beginning of design stage of electric derive system. Furthermore, there is a large variety of electric drive technologies that can be used in transport industry which makes the selection sometimes difficult when all aspects are to be considered (thermal balance, command and control strategy, consumed energy, natural dynamics, etc.).

The main types of electric motors used in motion control are, according to [4] [5]:

- Brushed Direct Current motors (DC)
- Brushless DC motors (BLDC)
- Permanent Magnet Synchronous Motors (PMSM)

[1] Inverse of fuel consumption

- Asynchronous Motors or Induction Motors (AC)
- Synchronous Reluctance Motors (SRM)

They are different in their operating principle as well as their weight, size, costs and even in the power drive electronics (PDE) that they require. When there is uncertainty in power which is needed to drive the fuel pump, a definitive motor cannot be chosen. Moreover, there is also a high level of uncertainty in stage of electric drive design, concerning drive technology, working environment, mission profile and control strategy.

This uncertainty requires a new methodology to deal with it in the early phases of a project. This paper presents the Hardware In the Loop (HIL) simulation as a methodology to figure out the appropriate electrical drive for the low pressure pump of an helicopter fuel system. HIL will combine a virtual drive (simulation) with the real fuel pump and fuel metering unit (hardware). In that manner, it will enable changing by simulation the type, command and control strategy while keeping realism by using the real drive load.

The main interest of using HIL comes from the support it provides for the selection of drive technology, its sizing, the assessment of command strategies, including for different operating, and even the capability to virtually inject faults in the simulated components to assess response to failure at overall system level.

2 Methodology of HIL

HIL is a vital step in design V cycle, for rapid prototyping, testing, evaluation and validation of components as well as during the design stage to get the best of new systems. It has numerous advantages, among them [6] [7]:

- Possibility/Ability of testing critical scenarios without any risk on operators or tested materials
- Possibility of simulating harsh ambient conditions, like high or low temperature, through easy modification of the virtual environment parameters
- Possibility of replacing a complicated model of any simulated component by its real hardware
- Possibility of repeating immediately the test which leads to test a component failure and its associated emergency scenarios
- Possibility of testing the hardware and software of Electric Control Unit (ECU) at an early stage of design and development

2.1 State of the art

Developing electric drives for innovative hybrid systems requires numerous tests, which are sometimes difficult, costly or even impossible to arrange [8]. HIL can facilitate and speed up the testing of new configurations of hybrid systems and gets benefit and advantages of virtual testing combined with real physical plants characteristics [7] [9].

General configuration of HIL that used in electric or hybrid vehicles is well discussed in literature [10] [7]. Two kinds of studies have been identified. The first one focusses on the testing of electric drives to assess the merits of different control strategies under various operating conditions and fault conditions, as in [11] [12]. The second one deals with the simulation of the load to be driven electrically which is often the hydraulic pump for fluid power applications.

Concerning electrically-driven pumps, HIL was used to get more information about hydraulic system performance at different working conditions (normal operation, under loading or overloading), as in [13]. It was also employed to facilitate the selection and testing of components for innovative hydraulic systems through the support of real time simulation instead of adding or removing real hydraulic and mechanical components [8]. For example, it was used to show the possibility of replacing conventional hydraulic supply and control of power (e.g. involving proportional valves) by and electro-hydrostatic module (speed-controlled electric motor and fixed displacement pump) to control rod position of this cylinder [8]. Moreover, in literature of HIL for electrically-driven pumps, a special interest is payed to define an optimum electric motor that loads the electric drive under test in order emulate the mechanical power required by the pump, as in [14] [15] regardless the electric drive to be employed in the final product. Contrary, there are not similar studies to support the definition and the assessment of the electric drive. The present communication addresses this need that can be found when there are different candidates for electric motor and drive architectures and technologies. Real-time simulation of the candidate solutions can efficiently support decision making, in particular when the mechanical characteristic of driven load is badly known and cannot be simulated. In this case, the test bench combines the real load and an electric drive that is controlled in order to behave like the candidate electric drive.

There are already some recommendations for HIL that can be found in literature as [8] [10], either for general use or for electrically-driven pumps. Unfortunately, these recommendations are vast, too much general and do not emphasize on the choice of electric drive, given the existing load to be driven. This type of HIL is addressed in this communication.

Table 1 summarizes a part of work that is presented in literature concerning HIL for electrically-driven pump in addition to what is considered in this paper.

2.2 Actual need of HIL

The physical plant of HIL, which is presented on the Figure 1, contains the electric motor with its power drive electronics (PDE), the fuel pump and the fuel metering unit (the fuel system components are kept to reuse a mature technology). On the other hand, the real electric motor is taken commercially-off-the-shelf and is chosen without any constraints of airworthiness. In the present study, the real electric motor has been chosen among 60 suppliers datasheets to display high performance (low inertia,

Ref	Real part	Virtual (simulated) Part	Objective of HIL
[8]	Electric drive + Motor emulating the hydraulic pump with PDEs	Hydraulic system (components of hydraulic mobile machine, ex. Industrial forklift)	To simplify the components choosing and testing for new hydraulic system
[14] and [15]	Electric drive + Motor emulating the hydraulic pump with PDEs	Hydraulic and mechanical components of hybrid drive of off-road mobile machinery	To choose the optimum electric motor that emulates the hydraulic pump. According to required refresh rate of electric motor's torque control loop, motor parameter limit values are suggested for required motor
[13]	Electric drive + Motor emulating the hydraulic pump with PDEs	Hydraulic Pump	To get more information about system performance at different working conditions
This paper	High performance electric drive + Real hydraulic pump	Virtual drive (supply, motor, and PDE) to be used in the final product	To test different electric motor technologies, observe limitation and give recommendations to get optimum electric drive

Table 1: Summarizing some studies concerning HIL for electrically-driven pump

torque/power capability suited to the estimated need with sufficient margin).

The main interest of the proposed HIL comes from the possibility to force the real electric motor to operate like a given motor, the virtual motor that is representative of the effective motor that would be specified, designed, manufactured and installed on the engine. The model of the virtual motor is developed in order to be consistent with real-time simulation constraints (e.g. sampling period between 1 and 5 ms). The provided torque is calculated by real-time simulation as a function of its rotor velocity and of the command signal. It is then sent to the real motor drive as a torque setpoint (torque bandwidth greater than e.g. 1000 Hz). The real motor speed is measured to feed the simulation model.

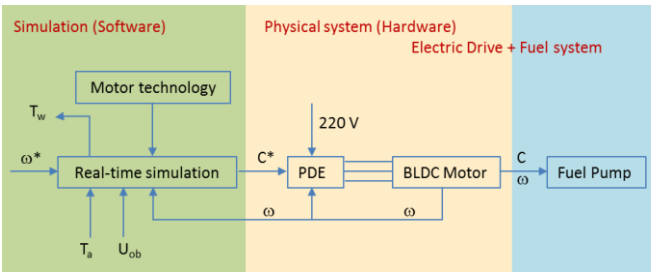

Figure 1: HIL structure

The virtual motor model is developed in order to simulate the following effects:

- Power capability (torque vs. velocity)
- Dynamics (of drive, effect of motor inertia)
- Energy consumption
- Temperature of the windings and motor frame, vs environment conditions, with impact
- Response to fault (e.g. short circuit of windings or open leg of inverter)
- Impact to the drive architecture and control (brushed/brushless motor, 6-step or field oriented control, sensorless speed control, etc.)
- Impact of the engine starting strategy (e-pump, starter, igniter, etc.).

3 Selection of electric motor

One of the most important driver to use HIL methodology here is the uncertainty that affects the selection of appropriate electric motor for the intended application.
As mentioned before, there are at least five electric motor technologies that can be used in our application. Figure 2 summarizes most used electric motor in Hybrid and Electric Vehicles and their appropriate PDE:

Motor / PDE			Synchronous			Asynchronous
			Permanent Magnets			Without PM
			Brushed DC	Brushless DC		AC Motor (IM)
				BLDC (BEMF Trapezoidal)	PMSM (BEMF Sinus)	
None			Uncontrolled speed	Impossible	Impossible	Impossible
Chopper			Ok	if: DC↑	if : DC↑	if: DC↑
Inverter	Without sensors		-	-	Sensorless	Ok
Inverter	With sensors	Hall	-	Ok	-	-
Inverter	With sensors	Resolver			Ok	-

Figure 2: PDE versus motor type

Indeed, the most important factors in choosing a motor according to [16] are weight, efficiency and cost. These factors can be combined with application requirements. For example, AC motor which the best motor for Hybrid and Electric Vehicles is no more a good choice for aeronautics application because of its mass, which can be twice that of PMSMs or BLDCs motors, without their PDE, [16].
Concerning the present application, the required motor has to supply a continuous nominal torque typically 0.5 N.m and its maximum speed is 10000 rpm. Electric power supply is imposed by aerospace standards. A wide search has been done for different types of electric motors, among 60 off-the-shelf references (25 BLDC, including 5 pancake hollow shaft, 17 DC, 12 AC), there were only 5 as potential candidates even though they did not meet all required criteria. Furthermore, some suppliers of potential motors needed a business plan to accept delivering a few samples, which was not available at this stage of the project.

For these reasons, HIL was selected as a methodology to test different motor designs and help to facilitate the development of the electrically-driven pump.

4 HIL configuration

As it is described previously, HIL contains two parts; the first one is the software part which contains a real-time model representing a tested virtual electric motor and its drive. Moreover, many submodels can be developed to predict performance at different operation conditions. As addressed later, this can help to test the effect of supply voltage and thermal equilibrium of the simulated motor.

The second one is the hardware part. The real motor is used to drive the load under test according to the simulated motor characteristic. A second real motor is used in the present case in order to load the first motor without waiting the real fuel pump and fuel metering to be available for testing. The test bench hardware includes the two motors and their PDE, additional torque/speed/temperature sensors, displays, two computers (PC for configuration and data analysis and PC to run real-time submodels) and real-time target machine which interfaces with PDEs and sensors and runs the real-time simulation.

Figure 3 shows a simple representation of HIL configuration:

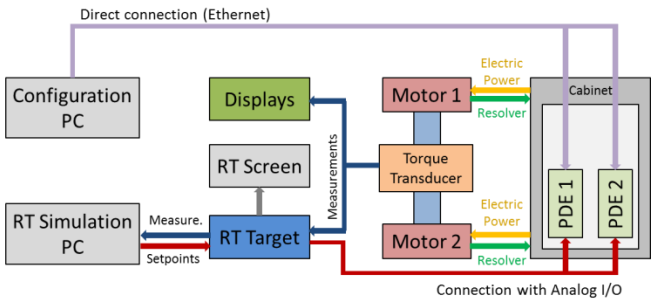

Figure 3: Simple representation of HIL configuration

5 Software (Modelling of different submodels)

The real-time model contains essentially a model of simulated electric motor. The complexity of this model can be increased step-by-step (as far as real-time constraints are met) by integrating other sub models, in order to reproduce different aspect that affects motor performance. In this paper, a thermal model is presented to take into account the effect of temperature on the motor performance, including its impact on windings resistance or heat exchange with surrounding environment. Second presented submodel is used to assess the effect of power supply variations. Figure 4 displays how these models interface through power variables: voltage and current delivered by electric supply (U_{ob}, I), heat power and motor temperature (P_{losses}, T_w).

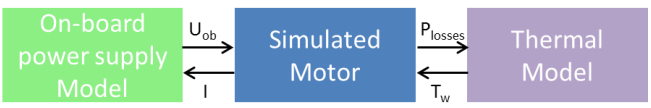

Figure 4: Different submodels developed for real-time simulation

5.1 Modelling of electric motor

As the main interest of the proposed HIL approach is to force the real electric driving motor on the test bench to operate like any given motor, named the simulated or the virtual motor. Therefore, the shaft torque of the two motors is identical, as far as friction and inertia of the coupling element are negligible with respect to the rated torque.

The approach is illustrated for two motor technologies, DC motor and AC motor as virtual motor. The shaft torque of the simulated motor will be transmitted to the driving motor of the test bench as torque setpoint, as presented in Figure 1.

Thus, shaft torque of the simulated and real motors shall be identical at any time, as illustrated in Figure 5 and eq. (1):

$$C_{ss} = C_{sr} \tag{1}$$

with C_{ss}, C_{sr} are shaft torque of simulated motor and real motor (N.m), respectively.

On a motor, the shaft torque equals to the electromagnetic torque minus the dissipative torque due to friction and the inertial torque due to the rotor inertia. Assuming the speed to not reverse in the present pump drive application and friction to be made of pure Coulomb and viscous effects brings, as presented in *(2)*:

$$\begin{aligned} C_{ss} &= C_{es} - f_s\omega - C_{fs} - J_s\dot{\omega} \\ C_{sr} &= C_{er} - f_r\omega - C_{fr} - J_r\dot{\omega} \end{aligned} \tag{2}$$

with C_e electromagnetic torque produced by the motor (N.m), f coefficient of viscous friction (N.m.s/rad), C_f Coulomb friction torque (N.m), J inertia of the motor rotor (Kg.m^2), ω rotary speed of the motor shaft (rad/s), $\dot{\omega}$ motor shaft angular acceleration (rad/s^2). Subscripts r and s are associated with the real and the simulated motors, respectively.

Thus, according to *(1)* and *(2)*, the electromagnetic torque setpoint which will be sent to the real motor drive is:

$$C^* = C_{er} = C_{es} - (C_{fs} - C_{fr}) - (f_s - f_r)\omega - (J_s - J_r)\dot{\omega} \tag{3}$$

with C* electromagnetic torque setpoint (N.m)

Figure 5 represents a simplified torque calculation for two motors:

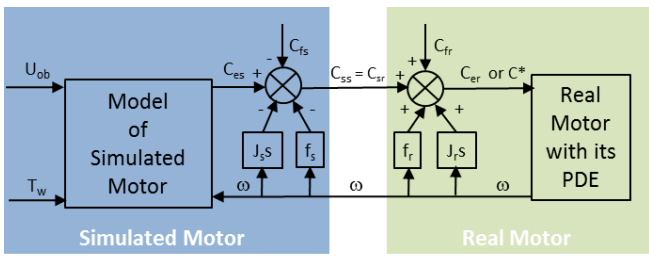

Figure 5: Simplified representation of the torque calculation for the simulated and real motors

5.1.1 Simulation of a DC Motor

The electromagnetic torque of the simulated permanent magnets DC motor is:

$$C_{es} = K_{ms} I_s \tag{4}$$

with K_{ms} torque constant of simulated motor (N.m/A), I_s current supplied to the simulated motor (A). This current can be calculated from eq. (5):

$$U_{ob} = K_{ms}\omega + R_s I_s + L_s \frac{dI_s}{dt} \tag{5}$$

with U_{ob} voltage supplied to simulated motor (V), R_s and L_s rotor windings electrical resistance (Ω) and inductance (H) of simulated motor, respectively.

From equations (3) (4) and (5), the electromagnetic torque setpoint becomes:

$$C^* = \frac{1}{H(s)}\left[K_{ms}\frac{1}{R_{ms}+L_{ms}s}(U_{ob}-K_{ms}\omega) - \right. \\ \left. -(C_{fs}-C_{fr}) - (f_s - f_r)\omega - (J_s - J_r)\dot{\omega}\right] \tag{6}$$

with H(s) dynamics of the real motor PDE torque loop.

Eq. (6) can be presented in block diagram as in Figure 6:

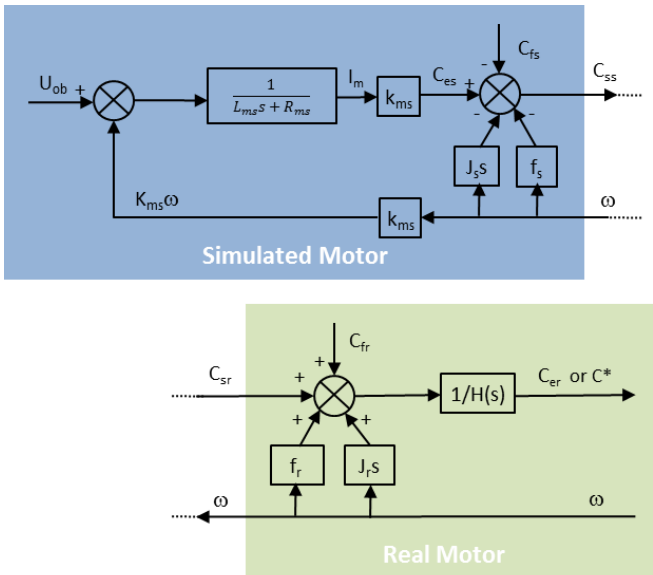

Figure 6: Calculation of the electromagnetic torque setpoint for the simulation of a DC motor

5.1.2 Simulation of an AC Motor (Induction type)

The next virtual motor to be tested as virtual motor is a three phase induction motor.

First of all, a static model is used to reproduce the motor torque-speed characteristics. Then, a dynamic model is tested to induce an electromagnetic torque as a function of motor current and parameters.

In the first model, the motor torque is extracted from characteristics curve presented in motor datasheet as a function of motor speed. These data can be implanted as a data table in the real-time model.

Concerning the second model, the motor torque is calculated as a function of current in Park's coordinates. According to [17] [18] the electromagnetic torque in squirrel cage AC motor is given by:

$$C_{es} = \frac{3}{2}\frac{P}{2}L_m(i_{qs}i_{dr} - i_{ds}i_{qr}) \tag{7}$$

with P number of poles, L_m mutual or magnetizing inductance (H), i motor current (subscript s is for stator current, r for rotor, d for direct axis and q for quadrature axis in Park's coordinates).

These currents can be calculated as a function of motor design parameters, such as rotor inductance, stator inductance, mutual inductance, flux linkage in the motor and electrical speed of the rotor, as it is presented in [17] [18].

5.2 Thermal model

5.2.1 Importance of thermal analysis

Thermal performance analysis of electric motors is a crucial step during design phase to insure long lifetime and reliable performance of the motor. Indeed, electric machines lifetime is specified by temperature at which their winding electrical insulations are exposed, which is for example (85°C, 100°C, 125°C, 155°C) [19]. So, higher temperature means shorter motor lifetime, and vice versa, where motor lifetime is reduced to half each time the temperature increases 10°C above its value at which the lifetime is calculated. For instance, if a motor has a normal lifespan of 8 years at an average temperature of 105 °C, it becomes 4 years at 115 °C, 2 years at 125 °C and one year only at 135 °C [20].

Not only motor lifetime is affected by temperature, but also its performance fluctuates with motor electromagnetic parameters variation versus temperature. For instance, the permanent magnets induction decreases by 4% for $SmCo_5$ and by 12% for sintered NdFeB when their temperature increases about 100°C. Similarly, the resistance of copper winding increases by 42% when its temperature increases by 100°C. The convective heat exchange coefficient for horizontal exchange surface at 20°C ambient increases by 38% as the exchange surface temperature rises from 50°C to 150°C, and finally the voltage drop at rated current and commutation energy for one IGBT, a widely used power transistor in PDE, rises by 25% as its temperature changes from 25°C to 125°C [21] [22].

In fact, thermal analysis is a quite complex phenomena because electromagnetic losses increase motor temperature, so motor parameters such as electric resistance R and induction B (density of flux magnetic) will change with temperature, as eq. (11) illustrates. As a result, copper losses will increase with the increasing of electric resistance and also iron losses with induction rise, which leads to more heating, and the loop continues, making a snowball effect.

At last and not least, thermal analysis is helpful to detect fault in the motor, which occurs if the temperature exceed its estimated value in normal operation, as in [23].

5.2.2 Electric motor losses

Losses are the main sources of heating in the electric machines. Generally in electric motors, the main losses are cooper losses, also known as Joule power losses, which depends on coil current and ohmic resistance, it can reach 30% of input power [19]. In second place are iron losses, which contain eddy current losses and hysteresis losses and depend on motor rotational speed. They can reach about 10-20% of the rated torque [19]. In third place, mechanical losses present as friction losses in bearings and at graphite brushes for DC motors, which is proportional to motor rotational speed, and viscous friction of rotor in the air-gap which is proportional to square of motor speed [24]. Brushes friction losses of graphite brushes are about 5% of rated torque but they are less that value for precious metal brushes [19].

Furthermore, stray losses which regroup electromagnetic losses that cannot be classified in previous losses. They occur for different raisons, for example because of a non-uniform current distribution in copper winding or because of the magnetic flux which is produced by the load current and which leads to additional iron losses. Generally, it is considered as a percentage of output power (3 to 5%) for small electric machine (less than 10kW) [25].

Brush losses disappear in permanent magnet BLDC motor where the dominant losses are electromagnetic losses, which combine copper and iron losses. For example, it is about 80% of total losses whereas bearing losses are about 12%, going up with increasing motor speed or load [26]. However, friction losses are neglected in most of studies of permanent magnet synchronous machines (PMSM), like in [27][28].

In this paper, motor total losses are divided into two parts, the first on is copper losses and the second one is stator iron losses which integrated frictional losses. Heat generated in permanent magnets from viscous friction losses are supposed small in comparison with iron losses. Next equations present PMSM losses [29] :

$$\begin{aligned} P_{Cu} &= 3\, R_{\phi} I_{\phi\, rms}^2 \\ P_{Fe} &= P_{hys} + P_{ed} \\ P_{hys} &= k_{hys} B_{max}^2 f \\ P_{ed} &= k_{ed} B_{max}^2 f^2 \\ P_{losses} &= P_{Cu} + P_{Fe} \end{aligned} \tag{8}$$

with P_{losses} total losses in electric motor (W), P_{Cu} copper losses (W), P_{Fe} iron losses (W), P_{hys} magnetic hysteresis losses (W), P_{ed} eddy current losses (W), R_{ϕ} electrical resistance of one phase (Ω), I_{ϕ} current of one phase (A), B_{max} maximum flux density (T), f frequency flux variation (Hz), k_{hys} hysteresis constant and k_{ed} eddy current constant.

k_{hys}, k_{ed} are constants determined by the manufacturer provided loss data (k_{hys} is a constant whose value depends on the ferromagnetic material and the volume of the core. k_{ed} is a constant whose value depends on the type of material and its lamination thickness [30]).

5.2.3 Thermal model with constant electrical resistance

The objective here is to show the ability to integrate the thermal model in the HIL real-time model. Considering the selected environment, the thermal model will be presented in form of block diagram which facilitates its integration with the global real-time model in Matlab/Simulink.

A simple thermal model is given by:

$$\begin{aligned} P_{losses} &= P_R + P_C \\ P_{losses} &= \frac{\Delta T}{R_{th}} + C_{th} \frac{d}{dt}(\Delta T) \end{aligned} \tag{9}$$

with P_R exchanged heat power with surrounding environment and P_C (W) stored heat power in thermal capacitance, R_{th} thermal resistance (°K/W), C_{th} thermal capacity (J/°K) and ΔT temperature difference between domain and environment (°K).

The heat power exchange is split in 2 parts; with the ambient P_a and with the hydraulic pump P_p. It is assumed at first that the first exchange occurs by natural convection and the second one is by conduction.

The simplest thermal model is to consider the whole motor as a single body. Nevertheless, the presented thermal model studies the winding separately from the motor frame. So, it has two thermal capacitances, C_{thw} for winding and C_{thf} for frame. The propagation of heat flow in the motor is from hot winding, towards the frame by conduction then to ambient through natural convection. So, the two bodies thermal model is presented in (10) and Figure 7:

$$\begin{aligned} P_{losses} - P_{wf} &= C_{thw} \frac{dT_w}{dt} \\ P_{wf} + P_p - P_a &= C_{thf} \frac{dT_f}{dt} \\ P_{wf} &= \frac{1}{R_{thwf}} (T_w - T_f) \\ P_{fa} &= \frac{1}{R_{thfa}} (T_f - T_a) \\ P_{pf} &= \frac{1}{R_{thpf}} (T_p - T_f) \end{aligned} \tag{10}$$

with R_{thwf}, R_{thfa}, R_{thpf} thermal resistances between windings and motor frame, between motor frame and ambient, between the pump and the motor frame (°K/W),

respectively. C_{thw}, C_{thf} are thermal capacitance of motor winding and motor frame (J/°K), respectively. T_f, T_w, T_a, T_p are temperatures of motor frame, motor winding, ambient and pump (°K), respectively.

Two bodies thermal model of an electric motor is presented in Figure 7:

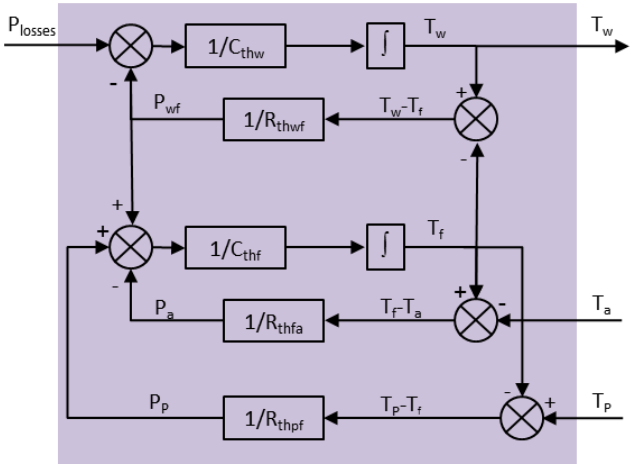

Figure 7: Block diagram of two bodies thermal model of an electric motor

The PDE losses are beyond the objective of the reported work.

5.2.4 Thermal model with varied electrical resistance

The electrical resistance and all electric motor parameters mentioned in the datasheet are measured at a constant temperature, named catalog temperature T_C which usually equals 25°C. Nevertheless, as mentioned before, electric resistance, as many other motor parameters, varies with motor operating temperature. It can be calculated as a function of its reference value $R_{(T_C)}$, at reference T_C and winding temperature T_W as in eq. (11).

$$R_{(T_w)} = R_{(T_c)}[1 + \alpha_{copper}\,(T_w - T_C)] \qquad (11)$$

with $R_{(Tw)}$ and $R_{(TC)}$ electrical resistance at actual temperature T_w and catalog temperature T_C in (Ω), respectively. α_{copper} is temperature coefficient of winding, which is equal to 0.0039 (°K^{-1}) for copper.

Figure 8 represents thermal model of electric motor with temperature sensitive windings resistance:

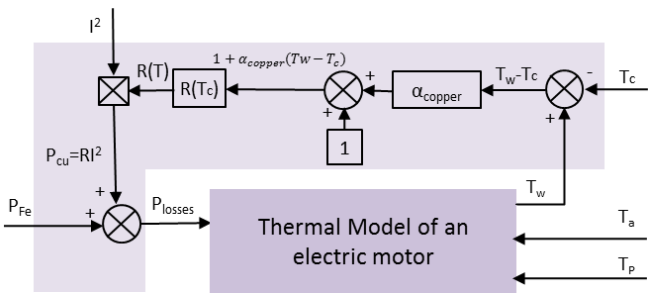

Figure 8: Block diagram of thermal model with temperature sensitive windings resistance

There is no special issue to consider the influence of temperature on magnetic induction. The process to modify the original model is Figure 7 remaining unchanged.

5.3 Model of power supply of on-board network

Another objective of the present work was to assess the impact of supply power. In the considered application, the on-board power supply is continuous DC voltage delivered by battery, according to the MIL_STD_704F and RTCA-DO160F standards [31], [32].

The supplied voltage is not constant, in particular if other consumers (e.g. starter) draw high power during the operation of the motor under study. This dynamic change of supply voltage is particularly important, especially if the electric motor is to be simulated is supplied directly without PDE.

The following intends to illustrate with a simple example how the supply conditions can be introduced in the simulated drive. Generally, the power supply of electrical on-board network depends on battery voltage, its internal resistance and the consumed current, as mentioned in (12):

$$U_{ob} = U_{bat} - R_i\, I \qquad (12)$$

with U_{ob} power supply of the on-board electrical network (VDC), R_i internal resistance of the battery (Ω) and I consumed current in the electrical circuit (A). This current represents the sum of electrical currents consumed by different electrical devices supplied.

This can be implemented extending the model of Figure 7 as given in Figure 9:

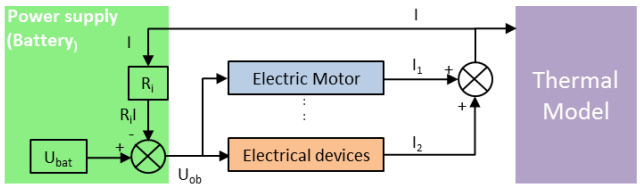

Figure 9: Simple model of on-board power supply

A major power consumer is the engine DC starter that is simple starter DC motor, which turns-on when the studied electric pump motor is running. The consumed current is:

$$I = \frac{U_{bat} - k_s \omega_{starter}}{R_i + R_L + R_s} \qquad (13)$$

with R_L, R_s electrical resistance of network cables and of starter motor (Ω), respectively, $\omega_{starter}$ and k_s the rotary speed (rad/s) and motor constant (V.s/rad) of the starter motor.

Thus, the block diagram model of the effective supply conditions of the motor under study can be added as illustrated by Figure 10:

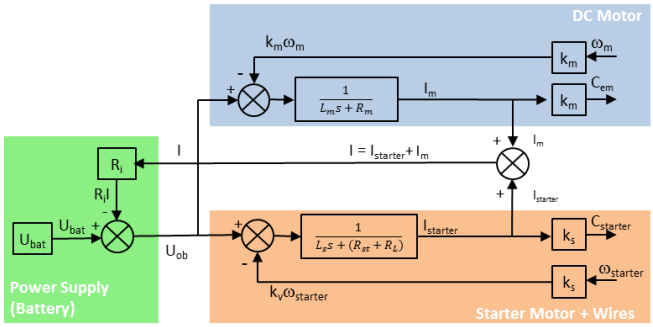

Figure 10: Model of power supply including battery, wires and starter motor (as an example)

5.4 Hardware configuration

A specific test bench has been designed to support the assessment of the proposed HIL approach. Its architecture has been introduced in Figure 11 and Figure 12. It consists of :

- A mechanical assembly with the frame that supports the driving and loading motors. The two motors are connected face to face by means of mechanical couplings and torque transducer, Figure 12.
- The rack with two motors PDEs and the electric supply unit (ESU).
- The real-time simulator, which consists of a personal computer for configuration and data analysis and a real-time board which interfaces with the PDE and the sensor and runs the real-time model.

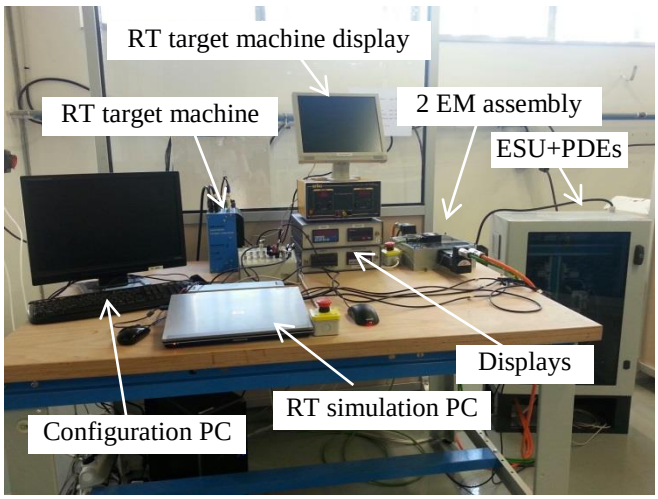

Figure 11: Test bench hardware

Used motors are off-the-shelf commercial BLDC motors from ABB. Rated torques are 0.9 N.m and 1.36 N.m for the driving and loading motors, respectively. The motors were chosen for their low rotor inertia (0.124 Kg.cm^2 and 0.18 Kg.cm^2) in order to facilitate the emulation of other motors (see equation 6).

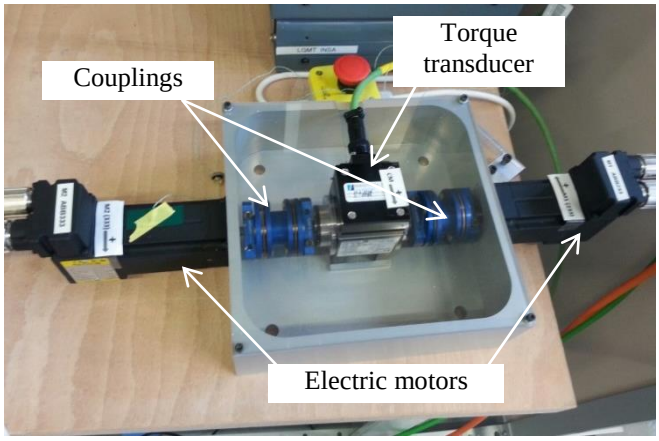

Figure 12: Two electric motors assembly

The two PDE are identical, "Microflex e150" with rated of current of 6A. Interfaces with the real-time board are either analogue or through EtherCAT bus.

The torque transducer was selected from "Magtrol" with rated torque of 5 N.m and maximum speed of 20000 rpm. Suitable couplings were picked from the same supplier "Magtrol" to protect against the effects of misalignment.

The real-time target machine is "Speedgoat" which has IntelCore2Duo 2.26 GHz processor, 2048 MB RAM and with an analog input and output I/O module 102 and EtherCAT interface. The real-time models were developed and uploaded on the target machine within the Matlab-Simulink simulation environment.

6 Test results and lessons learned

6.1 Experiments

The first simulated drive was brushed DC motor that was directly connected to the simulated DC supply without any PDE. The motor was Maxon 353295 (rated output power 250 W, nominal voltage 24V, nominal speed is 3810 rpm, nominal torque 0.501 N.m and inertia 1.29 Kg.cm^2). The simulated drive was implemented as presented on Figure 6.

An AC motor was also simulated as a Woodward AC motor (4 poles, frequency 400 Hz, synchronous speed 12000 rpm, and inertia 9.8 Kg.cm^2).

For all real-time simulations, the sampling rate was 1 ms. The average TET (total elapsed time) to run the models did not exceed 0.0213 ms with a max value lower than 0.026 ms.

6.2 Lessons learned

The reported work intended to use of-the-shelf hardware to implement a HIL platform for emulating a motor drive. The experience acquired can be summarized in terms of lessons learned and recommendations that concerns mainly the hardware:

a) Static accuracy

The torque produced by the real motor at shaft interface is far different from the electromagnetic torque produced by its PDE. This is due to motor shaft friction (bearings, seals and windage) and motor rotor inertia. PDEs generally include an estimate of these values as a feedforward action in the motor control. Moreover, the current (or torque loop) ignores the effective electromagnetic torque produced as it only uses windings current measurements. Finally, although these effects are compensated in the PDE control algorithm, the motor torque at shaft interface is not accurately related to the torque setpoint, generating errors in the HIL process. This requires an accurate identification of these effects to feed the compensators that can be either implemented in the PDE or in the real-time simulation, as given by equation (6).

b) Dynamics

The potential dynamic effects that might be intended to simulate for the virtual drive can be listed from the slowest to the fastest (typically):

- Thermal time constant (motor housing to ambient)
- Motor time constant (windings to housing)
- Cogging torque effects
- Dynamics of position control (not applicable here)
- Dynamics of speed control
- Electric time constant of the motor
- Dynamics of torque control
- Sampling
- PWM switching

In practice, what can be simulated is constrained by hardware. The real-time platform, a basic one, could run quite complex models at a sampling rate of 0.05 ms. This is consistent with the simulation of motors electric time constant and even torque (or current) loop dynamics. The main limitation came for the industrial electric drive that was used in torque control mode from external setpoint. Whatever the type of data interfacing (analog, digital bus), electric power drives sample the data exchanged (here torque setpoint input and effective velocity output) at 1 ms to 5 ms. This is the main limitation factor for simulating highest dynamics. The best option is definitely to input the torque demand directly at the PWM input to take benefit of its high frequency, typically 8 kHz to 16 kHz (62.5 µs to 125 µs).

c) Difference in motor rotor's inertia

As pointed out by equation (6), the torque setpoint involves the compensation of the difference between the simulated motor and the effective motor rotors inertia. Consequently, the measured rotor speed signal has to be time-derivated to calculate this member. Unfortunately, the speed signal is generally noisy and cannot be differentiated without noise (or phase lag if filtered efficiently). As for loading test benches, the best approach when possible is to use a real motor with the lowest inertia and to increase it through additional bodies to exactly reproduce the inertia of the simulated motor. In practice, this option is not always easy to implement as the used motor has to be interfaced with the real load, generally through adaptation joints that increase inertia (especially if a torque transducer is inserted). This is a severe limitation.

d) Causality

The proposed implement of HIL consists in generating the torque setpoint demand as a function of actual measured rotor velocity. This solution was logically selected as the torque loop is faster than the speed loop. However, the other option was tested that consisted in generating the speed demand as a function of the transmitted torque. As anticipated, performance was extremely low, due to the impact of the real motor speed loop dynamics.

7 Conclusion

The present paper has dealt with hardware in the loop (HIL) as a methodology to support the specification of electric drives in the presence of high uncertainty on the driven load power characteristic. It was intended to drive the load with off-the-shelf high performance BLDC motor and power drive electronics to emulate the candidate electric drive. The approach was applied to an electrically-driven fuel pump.

The first part of the paper introduced the proposed HIL architecture that consists in simulating in real-time the emulated electric drive and supply by generating the motor torque to be developed on the driven load as a function of the motor shaft angular velocity. Simple examples have been provided to illustrate how the supply conditions, the motor dynamics and the thermal effects can be included in the real-time simulation.

It was shown that there is no issue in reproducing the motor steady-state power characteristic as well as the thermal effects that significantly impact the electric drive sizing and effective service life. However, three main lessons have been learned and come from the limitations introduced by hardware. First, the used motor has to be identified with care. This is mandatory to get the expected torque at shaft through accurate compensation of friction, inertia and current/torque characteristic. Secondly, industrial power drive electronics sampling of setpoint and measured signals (1 to 5 ms typically) strongly limit the ability to simulate in real-time the motor dynamics. Oppositely, real-time hardware was not found to be limitative as models could be simulated with only a few tenths of microseconds step. Last, the difference between the inertia of the simulated and the used motor rotors is difficult to compensate efficiently due to noise or phase lag effect. It is therefore recommended to setup the test bench in such a way that the effective rotor inertia equals the simulated motor one.

Acknowledgement

The present work has been funded by Region Occitanie and Fonds Unique Interministériel in the frame of the 18th project call n°15061455.

Nomenclature

Designation	Denotation	Unit
C^*	Torque setpoint	N.m
α_{copper}	Temperature coefficient of copper winding	K^{o-1}
ω	Shaft rotary speed	rad/s
$\omega_{starter}$	Rotary speed of the stator motor	rad/s
$\dot{\omega}$	Derivative of shaft rotary speed	rad/s^2
ΔT	Temperature difference between studied points	K°
B_{max}	Maximum flux density	T
C_{er}	Electromagnetic torque produced by real motor	N.m
C_{es}	Electromagnetic torque produced by simulated motor	N.m
C_{fr}	Dry friction torque in real motor	N.m
C_{fs}	Dry friction torque in simulated motor	N.m
C_{sr}	Shaft torque of real motor	N.m
C_{ss}	Shaft torque of simulated motor	N.m
C_{th}	Thermal capacity	J/K°
C_{thf}	Thermal capacity of motor frame	J/K°
C_{thw}	Thermal capacity of motor winding	J/K°
f	*F*requency flux variation	rad/s
f_r	Coefficient of viscous friction in real motor	N.m.s/rad
f_s	Coefficient of viscous friction in simulated motor	N.m.s/rad
I	Consumed current in the electrical circuit	A
I_ϕ	Current of one phase	A
i_{dr}	*d*-axis rotor current	A
i_{ds}	*d*-axis stator current	A
i_{qr}	*q*-axis rotor current	A
i_{qs}	*q*-axis stator current	A
I_s	current in simulated motor	A
J_r	Inertia of real motor	Kg.m^2
J_s	Inertia of simulated motor	Kg.m^2
k_{ed}	Eddy current constant	
k_{hys}	Hysteresis constant	
K_{ms}	Constant of simulated motor	N.m/A
k_s	Motor constant of the stator motor	V.s/rad
L_m	Mutual or magnetizing inductance in AC motor	H
L_s	Inductance of simulated motor	H
P	Number of AC motor poles	pole
P_a	Heat exchange with the ambient	W
P_C	Stored heat in thermal capacitor	W
P_{Cu}	Copper losses	W
P_{ed}	Eddy current losses	W
P_{Fe}	Iron losses	W
P_{hys}	Hysteresis losses	W
P_{losses}	Total losses in electric motor	W
P_p	Heat exchange with the hydraulic pump	W
P_R	Exchanged heat with surrounding environment	W
R_ϕ	Electrical resistance of one phase	Ω
$R_{(T)}$	Electrical resistance at actual temperature T	Ω
$R_{(Tc)}$	Electrical resistance at catalog temperature T_C	Ω
R_i	Internal resistance of the battery	Ω
R_L	Electrical resistance of network cables	Ω
R_s	Electrical resistance of simulated motor	Ω
R_s	Electrical resistance of starter motor	Ω
R_{th}	Thermal resistance	°K/W
R_{thfa}	Thermal resistance between motor frame and the ambient	°K/W
R_{thpf}	Thermal resistance between the pump and the motor frame	°K/W
R_{thwf}	Thermal resistance between the winding and the frame	°K/W
T_a	Temperature of ambient	°K
T_c	Temperature considered in catalog parameters	°K
T_f	Temperature of motor frame	°K
T_p	Temperature of pump	°K
T_w	Temperature of motor winding	°K

U_{ob}	Power supply of the on-board electrical	VDC

References

[1] J. German, "Hybrid vehicles: Trends in technology development and cost reduction," *International Council on Clean Transportation, Technical Brief*, no. 1, pp. 1–18, 2015.

[2] M. H. Rashid, *Power Electronics Handbook, Devices, Circuits and Applications*, 3 rd. USA: ELSEVIER, 2011.

[3] F. Jian, "Incremental Virtual Prototyping of Electromechanical Actuators for Position Synchronization," INSA de Toulouse, 2016.

[4] M. Zeraoulia, M. E. H. Benbouzid, and D. Diallo, "Electric Motor Drive Selection Issues for HEV Propulsion Systems: A Comparative Study," *IEEE Transactions on vehicular technology*, vol. 55, no. 6, pp. 1756–1764, 2006.

[5] F. Badin, *Les Véhicules Hybrides des composants au système*. Editions TECHNIP, 2013.

[6] C. Köhler, "Enhancing Embedded Systems Simulation, A Chip-Hardware-in-the-Loop Simulation Framework," VIEWEG+ TEUBNER RESEARCH, 2010.

[7] L. I. N. Cheng and Z. Lipeng, "Hardware-in-the-loop Simulation and Its Application in Electric Vehicle Development," in *IEEE Vehicle Power and Propulsion Conference (VPPC), September 3-5*, 2008.

[8] J. E. Heikkinen, T. A. Minav, J. J. Pyrhonen, and H. M. Handroos, "Real-time HIL-simulation for testing of electric motor drives emulating hydraulic systems," *International Review of Electrical Engineering*, vol. 7, no. 6, pp. 6084–6092, 2012.

[9] H. K. Fathy, Z. S. Filipi, J. Hagena, and J. L. Stein, "Review of Hardware-in-the-Loop Simulation and Its Prospects in the Automotive Area," *Modeling and Simulation for Military Applications*, vol. 6228, no. E, 2006.

[10] O. A. Mohammed and N. Y. Abed, "Real-time simulation of electric machine drives with hardware-in-the-loop," *COMPEL: The International Journal for Computation and Mathematics in Electrical and Electronic Engineering*, vol. 27, no. 4, pp. 929– 938, 2008.

[11] J. J. Poon, M. A. Kinsy, N. A. Pallo, S. Devadas, and I. L. Celanovic, "Hardware-in-the-Loop Testing for Electric Vehicle Drive Applications," *Applied Power Electronics Conference and Exposition (APEC), Twenty-Seventh Annual IEEE*, pp. 2576–2582, 2012.

[12] C. Choi, K. Lee, and W. Lee, "Design and Temporal Analysis of Hardware-in-the-loop Simulation for Testing Motor Control Unit," *Journal of Electrical Engineering & Technology*, vol. 7, no. 3, pp. 366–375, 2012.

[13] V. Vodovozov, L. Gevorkov, and Z. Raud, "Modeling and Analysis of Pumping Motor Drives in Hardware-in-the-Loop Environment," *Journal of Power and energy Engineering*, vol. 2, pp. 19–27, 2014.

[14] J. E. Heikkinen, T. Minav, H. M. Handroos, J. A. Tapia, and J. Werner, "Modelling study of an optimum electric motor for directly driven hydraulic pump emulator in real- time HIL-simulation," in *The Fourteen Scandinavian International Conference on Fluid Power, May 20-22*, 2015.

[15] J. E. Heikkinen, T. A. Minav, H. M. Handroos, and J. A. Tapia, "Electric motor based hydraulic motor pump emulator in real time HIL-simulation : Finding the optimum emulator electric motor," in *Proceeding of the 8th FPNI Ph.D Dymposium on Fluid Power, FPNI, June 11-13*, 2014.

[16] J. G. W. West, "DC, induction, reluctance and PM motors for electric vehicles Electric," *Power Engineering Journal*, vol. 8, no. 2, pp. 77–88, 1994.

[17] A. W. Leedy, "Simulink / MATLAB Dynamic Induction Motor Model for Use as A Teaching and Research Tool," *International Journal of Soft Computing and Engineering (IJSCE)*, vol. 3, no. 4, pp. 102–107, 2013.

[18] A. W. Leedy, "Simulink / MATLAB Dynamic Induction Motor Model for use in Undergraduate Electric Machines and Power Electronics Courses," in *2013 Proceedings of IEEE Southeastcon, 4-7 April*, 2013.

[19] Maxon Motor, "Thermal Calculations of Motors." Maxon Academy, Swizerland, 2009.

[20] W. Théodore, *Electrotechnique*, 3e édition. Canada: De Boeck Université, 2000.

[21] M. Jean-Charles, *Aerospace Actuators, Vol 2, Signal-by-Wire/ Power-by-Wire*. Wiley, 2016.

[22] S. Constantinides, "Understanding and Using Reversible Temperature Coefficients," in *MAGNETICS 2010, January 28-29*, 2010.

[23] L. I. Silva, P. M. De La Barrera, C. H. De Angelo, F. Aguilera, and G. O. Garcia, "Multi-Domain Model for Electric Traction Drives Using Bond Graphs," *Journal of Power Electronics*, vol. 11, no. 4, pp. 439–448, 2011.

[24] G. LACROUX, *Les actionneurs électriques pour la robotique et les asservissements*, 2e édition. Technique et Documentation LAVOISIER, 1994.

[25] P. Andrada, M. Torrent, J. I. Perat, and B. Blanqué, "Power Losses in Outside-Spin Brushless D . C . Motors," *Renewable Energy & Power Quality Journal (RE & PQJ)*, vol. 1, no. 2, pp. 507– 511, 2004.

[26] J. Kuria and P. Hwang, "Modeling Power Losses in Electric Vehicle BLDC Motor," *Journal Of Energy Technologies and Policy*, vol. 1, no. 4, pp. 8–17, 2011.

[27] M. A. FAKHFAKH, M. HADJ KASEM, S. TOUNSI, and R. NEJI, "Thermal Analysis of Permanent Magnet Synchronous Motor for Electric Vehicles," *Journal of Asian Electric Vehicles*, vol. 6, no. 2, pp. 1145–1151, 2008.

[28] P. Mynarek and M. Kowol, "THERMAL

ANALYSIS OF A PMSM USING FEA AND LUMPED PARAMETER MODELING ANALIZA CIEPLNA SILNIKA PMSM ZA POMOCĄ METODY ELEMENTÓW SKOŃCZONYCH," *Technical Transactions, Electrical Engineering*, vol. 1, no. E, pp. 97–107, 2015.

[29] E. Andersson, "Real time thermal model for servomotor applications," 2006.

[30] P. C. SEN, *PRINCIPLES OF ELECTRIC MACHINES AND POWER ELECTRONICS*, Third edit. USA: WILEY, 2014.

[31] "RTCA DO-160F, Environmental Conditions and Test Procedures for Airborne Equipement, Section 16, Power input," 2007.

[32] "Military Standard, Aircraft Electric Power Characteristics, MIL-STD-704F," 2013.

A study on thermal behavior of pump-controlled actuator

T.A. Minav and M. Pietola

Department of Mechanical Engineering, Aalto University, P.O. Box 14400, 00076, Aalto, Finland,
E-mail: tatiana.minav@aalto.fi, matti.pietola@aalto.fi

Abstract

In this research, a time-proven concept from the aircraft industry supports development and application of an electrohydraulic actuator (EHA) in stationary application. EHA allows to achieve high power density and high performance in a compact package as well as flexibility in system architecture for stationary applications. The electrohydraulic actuator can eliminate hoses, fittings, valves and fixtures and is easy to integrate into larger systems. Due to good energy efficiency, cooling usually is not required. However, a thermo-dynamic analysis clearly indicates that the electric machine is acting as a high temperature heat source, while the hydraulics of the actuator maintain relatively lower temperature. Therefore, this paper targets the simulation of the thermal behavior of a pump-controlled actuator by means of lumped parameter model in order to predict the operational temperature. The developed model is validated against measurements utilizing thermocouples under various operative conditions. Conclusions are drawn concerning thermal behavior and energy dissipation of the proposed pump-controlled actuator.

Keywords: thermal modelling, losses, efficiency, pump-controlled actuator, stationary application

1 Introduction

In recent years, the demand for economical and energy efficient solution continuously growing due to upcoming tight exhaust limits for engine manufacturers. In stationary machines, the CO_2 emissions are not a problem since the prime mover is usually electric. However, there is a concept which can bring additional advantages to stationary applications. Zonal or decentralized hydraulics – as we will call it – is an approach first introduced in the aircraft industry [1]. This work adopts the time-proven design from the aircraft industry, simplifying its design as well as broadening its orientation to stationary application.

In a fully zonal system, the hydraulic pumps are removed from the single prime mover and replaced with multi hydraulic power-packs distributed throughout the system. In this novel architecture, multiple hydraulic power sources such as electrohydraulic actuators (EHA) may be utilized in each actuation zone in order to achieve energy savings and work as a power-on-demand approach.

Currently, electrohydraulic actuators are mostly installed and developed for aircraft applications [2, 3], where reliability requirements are very high. Most of the research studies related to electrohydraulic actuator are conducted to control the state of the servo valve [4, 5]. However, this approach results in low-energy efficiency due to throttling losses at control valves. Consequently, several techniques have been developed to overcome this drawback in order to achieve higher efficiency. In [6], the concept of a pump-controlled electrohydraulic actuator has been introduced as an alternative hydraulic system where the proposed structure of the actuator is directly operated by bidirectional variable displacement pump. By applying displacement control [7] or direct speed pump control it possible to overcome the disadvantages of a valve-controlled system radically.

Some studies were conducted to introduce electrohydraulic actuators to various applications. In [8], an electrohydraulic actuator is used for power steering of heavy vehicles. In [9] a pump-controlled system was designed for material handling machine.

Application of zonal hydraulics increases the flexibility of system design and construction because field piping and central hydraulic power units are no longer needed. In [10-12] challenges regarding thermal behavior of EHA for automation of various of linear motions was introduced and investigated. Independent research of the thermo-energetic behavior of an electrohydraulic compact drive in [13] and [14, 15] clearly indicate that the electric machine is acting as a high temperature heat source, while the hydraulics of the EHA maintain relatively lower temperature.

However, challenges for components without external cooling and electric machine running overloading conditions was not investigated. Therefore, in this research, the detailed hydraulic model of a pump-controlled actuator with a thermal resistance network will be developed at the system level for thermal analysis.

The remainder of this paper is organized as follows. The test setup is presented in Section 2, while Section 3 presents a detailed description of the thermal model. The results of experimental investigation are described in Section 4; thereafter, Section 5 and 6 contain discussion and concluding remarks.

2 Test setup

Figure 1 illustrates schematics, sensor locations, and a photograph of the experimental test setup. Speed control of the pump-controlled system is implemented by servomotor drive (via T-gear) directly without conventional hydraulic control valves. Thus, velocity of the non-symmetrical double-acting cylinder is determined by in-coming oil flow from the pump, out-going flow to the hydraulic motor and the angular speed of the electric motor.

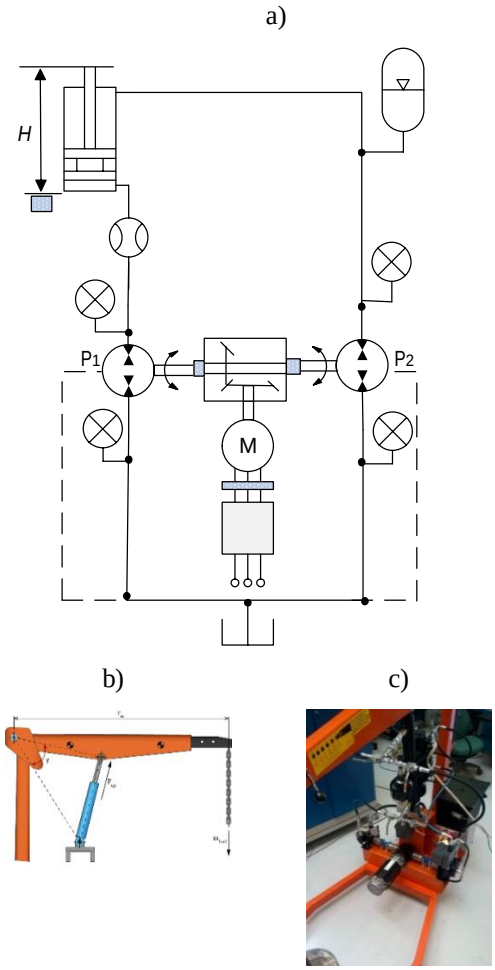

Figure 1: a) schematic of test setup, b) crane, c) photograph of test setup

Pump-controlled system test setup consists of two XV-2M internal gear pump/motor units by Vivoil with displacements of 14.4 and 22.8 cm^3/rev P_2, and P_1, respectively [16], which were chosen to match the asymmetric cylinder chambers (MIRO C-10-60/30x400) [17]. Since the B-side pump is slightly under-dimensioned, fluid from the B-chamber is not pumped out at a corresponding rate as fluid pumped into the A-chamber. This leads to a rise of pressure in the former, which is partially mitigated by the hydraulic accumulator [18]. A Bosch-Rexroth 0.7 liter hydraulic accumulator was selected (code: HAD0.7-250-1X/80G04A-1N111-BA) with a pre-charge pressure of 10 bar. In the current configuration of DDH, a permanent magnet brushless servo motor, Unimotor 115U2C manufactured by Emerson Control Techniques [19], is powered directly from power grid. The Unidrive SP1406 drive converts the AC power supply from the line and allows to set the speed of the motor [20]. Figure 1a illustrates a data acquisition system and locations of utilized sensors. Gems 3100R0400S pressure transducers [21] are used to measure the pressures of the lines, pump inlet, and outlet. The actual velocity and height of the cylinder's piston rod were measured by means of a wire-actuated encoder, the SIKO SGI (IV58M-0039) [22]. Cylinder inlet flow was measured with a Kracht VC1 gear type flow meter (code: VC1F1PS) [23]. Motor shaft speed and torque is monitored by the Unidrive SP1406 drive software [20].

3 Thermo-hydraulic modelling

Thermal modelling of the DDH is demonstrated in this section. The thermo-hydraulic model and thermal resistance network are depicted in the Figures 2 and 3. Model was built from components in Simulation X – a commercial multi domain simulation tool.

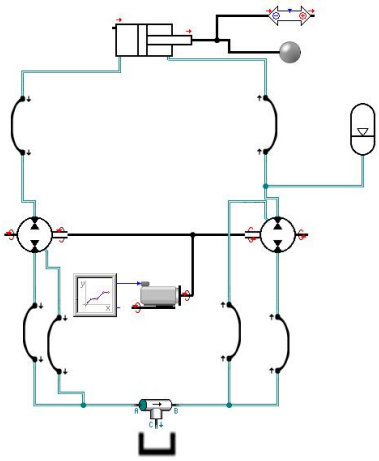

Figure 2: Thermo-hydraulic model in Simulation X

In this research, the following assumptions were:

- The test setup has an unlimited heat capacity.
- Initial component temperature is equal to ambient.
- Heat losses between hoses and oil in the tank were disregarded, as well as the cylinder's internal leakages and heat transfer between cylinder rod and piston.
- Convection between oil to air inside the tank is assumed to be neglectable.

The fluidic and solid control volumes of system's components in Simulation X are illustrated in Figure 3. There are five fluid and ten solid control volumes. The fluid control volumes (Figure 3) are trapped between the main components (in Figure 1) and include the housing of hydraulic

components and their volumes: volume **D** - Line L1, volume **E** – Line L3, volume **K** – Line L2, volume **L** – Line L4, and volume **N** - tank oil volume.
The solid volumes include solid construction elements and housings. The solid volumes are volume **A**: Cylinder chamber; volume **B**: Cylinder piston; volume **C, J, F, M**: hoses; volume **G**: unit P1; volume **I**: unit P2; and volume **O**: Tank. To each of this control volume is assigned a heat capacity. Thereafter, thermal resistances are utilized to connect control volumes to each other and to the ambient temperature.

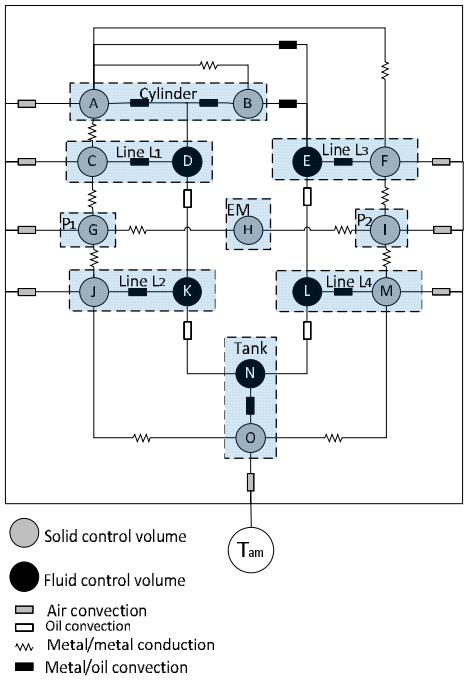

Figure 3. Thermo-hydraulic model in Simulation X

The heat transfer coefficient is estimated based on material assumptions and the thermal resistances. The following section contain simulation results for the hydraulic components.

4 Simulation results

In Figures 4 and 5, the inlet and outlet oil temperature is shown for the Pump 1 and Pump 2, respectively. The rapid variation of the flow (pumping and motoring mode) has an effect on oil temperature at the inlet and outlet of the pump units. During lifting phase (pumping) oil is heating up and cooling down during lowering phase (motoring) (valid for P1 unit, for P2 unit - inverse logic is applied, as it is working as a pump when P1 is working as a motor, and vice versa).

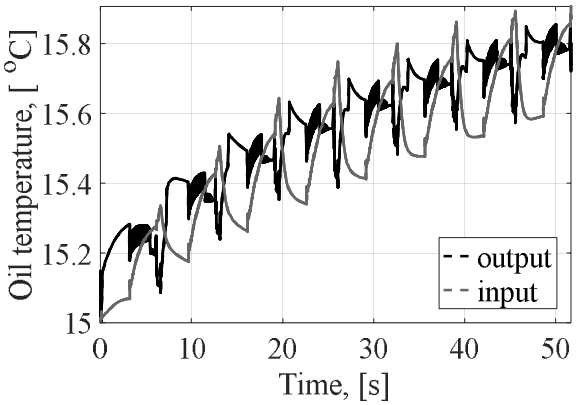

Figure 4. Simulated inlet and outlet oil temperatures of the unit P1.

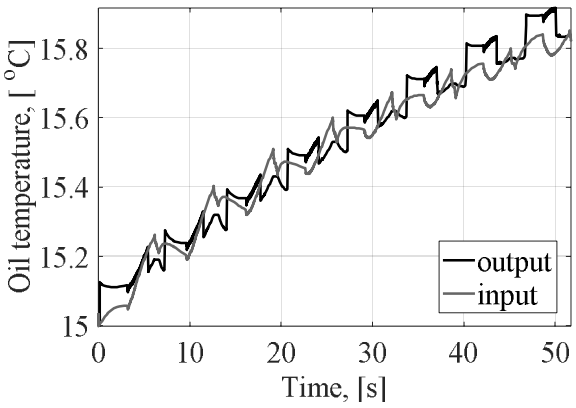

Figure 5. Simulated inlet and outlet oil temperatures of the unit P2.

Comparison of Figures 4 and 5 show difference in amplitude and slightly different pattern of rising temperature of both units. Unit P 2 characterized with more square shape.

The experimental data is presented in the following section in order to validate the proposed thermo-hydraulic model.

5 Experimental investigation

The test setup in Figure 1 was utilized for validation of the DDH thermo-hydraulic model. In this setup, the desired payload force applied to the cylinder by means of varying the amount of weight attached to the chain (illustrated in Figure 1b). The temperature at relevant locations in the system was measured with thermocouples including: oil, component surface, and the ambient temperature. Figure 6 demonstrates location of thermocouples in test setup.

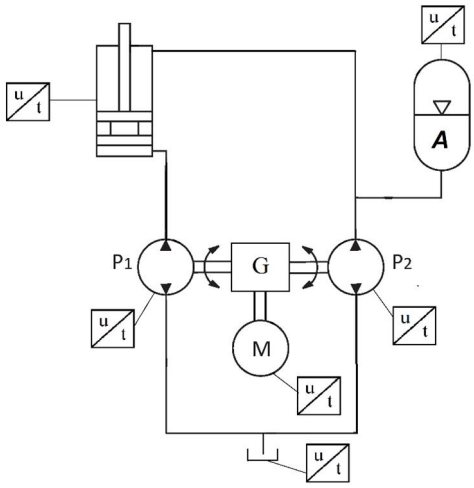

Figure 6. Location of thermocouples in test setup

These measurements were performed in an environmental chamber with various starting ambient temperatures and a fixed motor speed of 500 rpm, and a payload of 60 kg. The tests have been performed with a repeating lifting-lowering cycle with a duration of 2.5 hours. The temperature data were obtained with a single sample rate every 10 seconds with Thermocouple Data Logger TC-08 [24] and analyzed with a PicoLog Recorder program.

5.1 Electrical machine

Figure 7 illustrates the electrical machine surface temperature. The housing surface temperature starts to heat up immediately and saturates to a constant value in the end of the cycle.

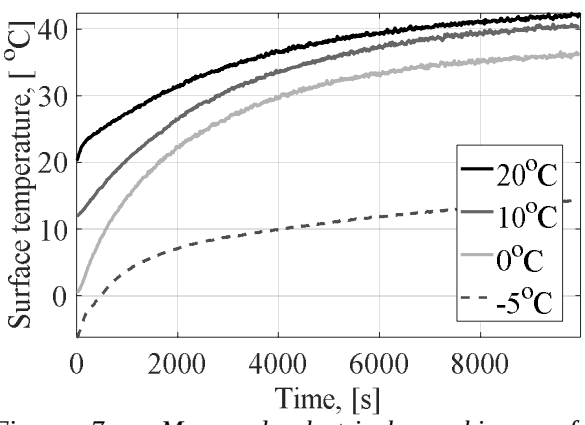

Figure 7. Measured electrical machine surface temperature

5.2 Hydraulic pump

Figure 8 illustrates the hydraulic pump surface temperature for different starting ambient temperatures.

5.3 Hydraulic cylinder

Figure 9 demonstrates a cylinder surface temperature. This figure shows a rapid rise during the first few minutes according to an exponential function trend.

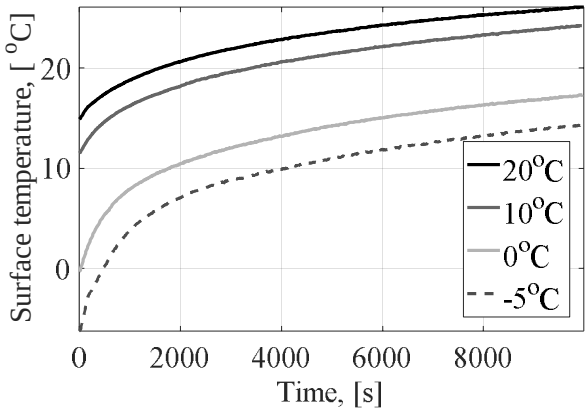

Figure 8. Hydraulic pump surface temperature with different ambient temperatures

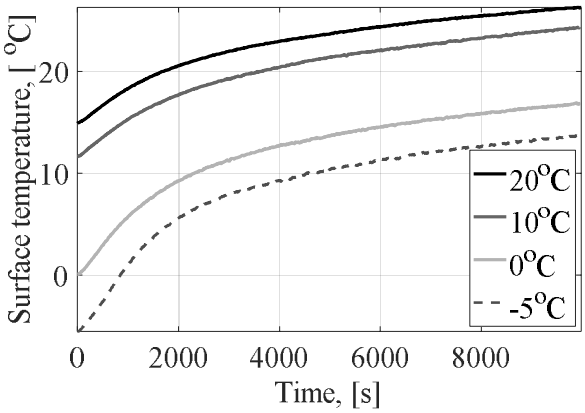

Figure 9. Hydraulic cylinder surface temperature with different ambient temperatures

5.4 Hydraulic tank

Figures 10 illustrates the oil temperature in the bottom and in the middle of the hydraulic tank with various ambient temperatures. Oil temperature in the bottom shown with solid line and in the middle of hydraulic tank is highlighted with dotted line.

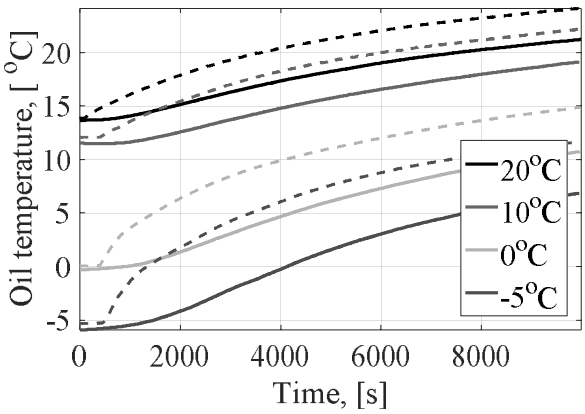

Figure 10. Oil temperature in the bottom (solid line) and in the middle (dotted line)of hydraulic tank

In Figure 10, there is a slight constant area which is longer for the low temperature region due to the high thermal inertia of

the tank, represented by the main reservoir of oil for the DDH. High thermal inertia of the tank is also noticeable from temperature "gap" between bottom (solid line) and in the middle (dotted line) temperature inside hydraulic tank.

Figure 11 illustrates the validation of the simulated oil temperature in the hydraulic tank.

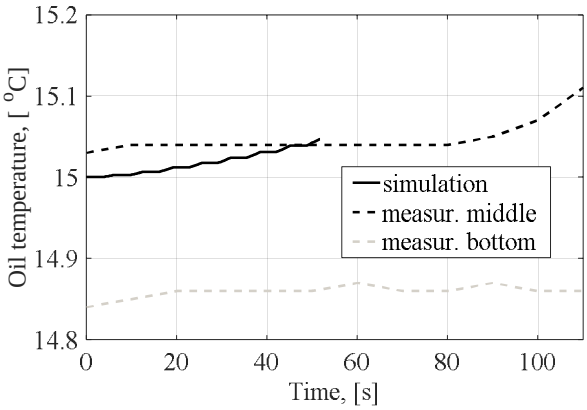

Figure 11. Oil temperature in ºC in the hydraulic tank measured (dotted lines: bottom and middle of the tank) and simulated(solid line) with initial ambient temperature +15 ºC.

Figure 11 illustrates the measured oil temperature in the middle (black dotted line) and the bottom (grey dotted line) of the hydraulic tank and the simulated oil temperature (solid line). Simulated temperature risen slowly during the first minute showing a good correlation between measured oil tank middle and simulated temperature.

6 Conclusion

In this study, direct driven hydraulics (DDH), or as commonly known a pump-controlled actuator was investigated in the practical realization of decentralized hydraulics from thermal point of view. The thermo-hydraulic model was created and was validated against measurements utilizing thermocouples. Simulation results showed good correlation to measured oil temperature in the middle of hydraulic tank.

Acknowledgments

This research was enabled by the financial support of the Academy of Finland (project ArcticWEll) and internal funding from the Department of Mechanical Engineering at Aalto University, Finland.

References

[1] Skinner J., Smith A., Frischemeoer S., Holland M., Advancements in Hydraulic systems for more electric aircraft, proceedings of MEA 2015 conference, Toulouse, France, February 2015

[2] Youzhe Ji, Song Peng, Li Geng, Zhanlin Wang, Lihua Qiu, Pressure Loop Control of Pump and Valve Combined EHA Based on FFIM, The Ninth International Conference on Electronic Measurement & Instruments, 2009 ;

[3] Qian Zhang, Bingqiang Li, Feedback Linearization PID Control for Electro-hydrostatic Actuatora, 2011

[4] Liang, B. & Li, Y. & Zhang, Z. Research on Simulation of Aircraft Electro-Hydrostatic Actuator Anti-Skid Braking System (ICMTMA), 2011;

[5] Altare G., Vacca A., Richter, C. A novel pump design for an efficient and compact Electro-Hydraulic Actuator, IEEE aerospace Conference, 2014 IEEE, 2014 , Page(s): 1 – 12

[6] Kyoung Kwan Ahn, Doan Ngoc Chi Nam, Maolin Jin, Adaptive Backstepping Control of an Electrohydraulic Actuator, IEEE/ASME Transactions on Mechatronics, Vol. 19, No. 3, June 2014.

[7] Busquets E., Ivantysynova M., The World's First Displacement Controlled Excavator Prototype with Pump Switching - A Study of the Architecture and Control 9th JFPS International Symposium on Fluid Power, 324 - 331

[8] Daher N., Ivantysynova, M., Electro-hydraulic energy-saving power steering systems of the future. Teoksessa: Proceedings of the 7th FPNI PhD Symposium on Fluid Power, 2012.

[9] Hänninen H., Minav T., Pietola M., Replacing a constant pressure valve controlled system with a pump controlled system, Proceedings of the 2016 Bath/ASME Symposium on Fluid Power and Motion Control, FPMC2016, Sept 7-9, 2016, Bath, UK

[10] Michel, S. Weber, J., Electrohydraulic compact-drives for low power applications considering energy-efficiency and high inertial loads. 2012

[11] Michel S., et.al. Energy-efficiency and thermo energetic behavior of electrohydraulic compact drives, 9th IFK conf. 2014

[12] Busquets E., An investigation of the cooling power requirements for displacement-controlled multi-actuator machines, 2013

[13] Michel, S. and Weber, J. Prediction of the thermos-energetic behavior of an electrohydraulic compact drive. Proc. of the 10th International Fluid Power Conference. Dresden, Germany, 8-10 March 2016.

[14] Minav, T., Papini L., Pietola, M. Thermal analysis of Direct Driven Hydraulics, 8-10 March 2016, Proceedings of the IFK-2016, Dresden, Germany.

[15] Karlen N., Minav T., Pietola M., Investigation of thermal effects in direct-driven hydraulic system for off-road machinery, Proceedings of the ASME 2016 9th FPNI Ph.D. Symposium on Fluid Power, FPNI2016, October 26-28, 2016, Florianópolis, SC, Brazil

[16] Vivoil motor, Data Sheet: reversible motor - series XV, [Online]. Available: http://www.vivoil.com/files/xm_en/xm201.pdf

[17] Pikapaja OY. MIRO Hydraulisylinterit hydraulcylindrar, 2009. URL http://www.pikapaja.fi/MIRO_cylinders_FIN+SWE.pdf

[18] Järf A., Minav T., Pietola M., (2016) "Nonsymmetrical flow compensation using hydraulic accumulator in direct driven differential cylinder", Proceedings of the ASME 2016 9th FPNI Ph.D. Symposium on Fluid Power, FPNI2016, October 26-28, 2016, Florianópolis, SC, Brazil

[19] Emerson Control Techniques Unimotor 115U 2C, http://www.emersonindustrial.com/en/en/documentcenter/ControlTechniques/Brochures/unimotor_fm_product_data.pdf.

[20] Emerson Control Techniques Unidrive SP1406 drive, http://www.emersonindustrial.com.

[21] Gemssensors 3100R0400S pressure transducers, http://www.gemssensors.com/Products/Pressure/Pressure-Tranducers , visited on September, 2013

[22] SIKO SGI (IV58M-0039), http://www.siko-global.com/en-de , visited on October, 2013.

[23] Kracht GmbH. Gear Type Flow Meter VC, 2012. URL http://kracht.eu/uploads/tx_ttproducts/datasheet/VC_GB_01-12_neu.pdf.

[24] Thermocouple Data Logger, [online], https://www.picotech.com/datalogger/tc-08/thermocouple-data-logger

[25] Minav T., Papini L., Järf A., Tammi K., Pietola M., Direct Driven hydraulics: What possible can go wrong? -Thermal analysis, Proceedings of the ICEM 2016, Lausanne, Switzerland September 4-7, 2016.

[26] Graessner. Power gear, 2014. URL http://www.graessner.de/en/PowerGear_GB6379.pdf.

Modeling and Verification of Accumulators using CFD

Victor Irizar , Peter Windfeld Rasmussen , Olivier Doujoux Olsen*, and Casper Schousboe Andreasen*

Fritz Schur Energy A/S, Fabriksparken 7, 2600 Glostrup, Denmark
E-mail: vie@fsenergy.dk, pwr@fsenergy.dk
*Department of Mechanical Engineering, Solid Mechanics, Technical University of Denmark, Nils Koppels Alle, B.404, 2800 Kgs. Lyngby, Denmark
*E-mail: s100196@student.dtu.dk, csan@mek.dtu.dk

Abstract

Hydraulic pitch systems provide robust and reliable control of power and speed of modern wind turbines. During emergency stops, where the pitch of the blades has to be taken to a full stop position to avoid over speed situations, hydraulic accumulators play a crucial role. Their efficiency and capability of providing enough energy to rotate the blades is affected by thermal processes due to the compression and decompression of the gas chamber. This paper presents an in depth study of the thermodynamic processes involved in a hydraulic accumulator during operation, and how they affect the energy efficiency of the component. An initial evaluation of the popular thermal time constant model is made and compared with experimental results for a 6-liter accumulator, showing that the current estimation techniques for the thermal time constant are not suited for the application studied, predicting higher heat loses in the gas and resulting in lower pressure buildup. Furthermore, it is shown that the assumption of a constant value for the thermal time constant can provide extremely accurate results, provided that the compression ratios of the process are known in advance. For varying compression ratios, dynamical effects play an important role and the accuracy of the model decreases. To study the thermal processes, a simplified axisymmetric CFD model of the accumulator is developed, using COMSOL Multiphysics for meshing and STAR-CCM+ as a solver. The model provided an interesting close up view to the gas movement and temperature distributions during operation, which describe a particularly nonlinear behavior of the heat losses and the thermal time constant. The model was successfully validated with experimental data, and provides a repeatable and accurate prediction of the gas states, regardless of the operational conditions, with maximum prediction errors of 10%. Finally, a practical approach on how to improve the thermal efficiency of the accumulators by introducing foams on the gas side is shown, effectively decreasing the heat losses in the accumulator, and improving the efficiency of the compression-expansion cycles.

Keywords: CFD, Hydraulic Accumulators, Heat Transfer, Thermal Time Constant

1 Introduction

In modern pitch controlled wind turbines, hydraulic systems play an important role regulating their power production, e.g. by controlling the pitch angle of the blades [1]. In general, these systems consist of a hydraulic pump that supplies the oil flow, which is then routed by a set of control valves to a linear actuator attached to the blade (in one or two anchor points on the blade root) and its linear displacement is converted to an angular rotation of the blade. The purpose of the hydraulic control system is to ensure an efficient power production and to protect the turbine from dangerous situations like over-speeding or blade failures. When these emergency situations arise, the hydraulic system has to be able to pitch the blades up to a position where the turbine stops, meaning turning the blades to 90 degrees compared to the wind direction, as fast and reliable as possible. Hydraulic pitch systems include accumulators that store energy during normal operation, in terms of compressed gas (see fig. 1), and when the system performs an emergency stop, the accumulators provide high pressure flow to the actuators so the blade can be turned to the desired stop position.

In an ideal situation, all the energy stored in the accumulator can be utilized and delivered to the hydraulic system without thermal losses at the gas side during compression and expansion, but in reality, the process is not adiabatic. The gas experiences pressure and temperature variations with changes in volume, thus heat is transfered to the solid parts of the accumulator, and consequently to the environment, either through

convection, conduction or radiation.

The complexity of these phenomena has been studied and modeled with empirical correlations that provide fairly accurate results for very specific situations [2–5], but little is reported about what is truly happening in the gas side of the accumulator. A better understanding of the thermo fluid dynamics of the gas in the accumulator can help improve current linear models, ultimately leading to optimization on the pitch control systems of the wind turbines, for example by reducing the size or the number of accumulators used per blade.

2 Problem Description

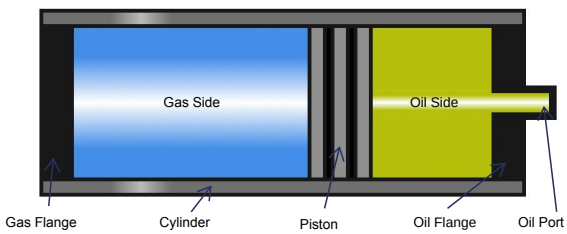

Figure 1: Basic layout of a piston type hydraulic accumulator

A general layout of a hydraulic accumulator is presented in fig. 1. The oil side has an input port through which the hydraulic oil can flow in or out. A floating piston separates the gas side from the oil. The gas is entrapped in the cylinder and is compressed by the piston when the oil starts flowing into the accumulator.

As the gas is compressed, its temperature and pressure rise. Equivalently, when the hydraulic system demands pressurized oil, the fluid leaves the accumulator and the gas expands, decreasing both its temperature and pressure. Heat transfer occurs between the gas and the solid parts of the accumulator, through convective and conductive mechanisms. The rate at which the heat transfer occurs is dependent on factors like the properties of the gas, pressure, temperature, initial conditions and the speed of the volume changes.

The challenge relies on how to model accurately and in a simplified way the state of the gas side and the heat losses to the surroundings, in order to predict the pressure and temperatures correctly, for different dimensions of accumulators and working conditions.

3 The Thermal Time Constant Model

For transient simulations, the mathematical modeling of a gas charged accumulator is often based on the thermal time constant model [2, 3, 6].

This model is based on the assumption that the gas behaves as a lumped mass, which has constant properties along its domain, and it exchanges heat with the environment directly, by means of convection. Following this model, the rate of change of temperature in the gas can follows the following relation [1]

$$\frac{dT}{dt} = \frac{T_a - T}{\tau} - \frac{T}{C_V}\left(\frac{\partial p}{\partial T}\right)_V \frac{dv}{dt} \tag{1}$$

where T is the bulk gas temperature, T_a is the temperature of the surroundings (which are assumed constant), τ is the thermal time constant, C_v is the specific heat capacity of the gas, $\frac{\partial p}{\partial T}$ is the partial derivative of the pressure w.r.t. the temperature (which is known from the equation of state) and $\frac{dv}{dt}$ is the rate of change of specific volume (volume per unit of mass). Furthermore, *tau* can be defined as

$$\tau = \frac{mC_V}{hA} \tag{2}$$

where m is the mass of the gas, h is the overall heat transfer coefficient from the gas to the surroundings and A is the area of the heat transfer.

In order to make this model work accurately, first, a proper equation of state has to be chosen to couple the pressure and temperature states of the gas. Hansen and Rasmussen [1] proved that the Soave-Redlich-Kwong (SRK) equation yields excellent results for predicting the gas states in an hydraulic accumulator.

Second, a proper value or expression for τ has to be chosen, to predict accurately the heat losses. A set authors have developed expressions for estimating the parameter [4, 5, 7], but these expressions are usually difficult to generalize when the accumulator dimensions and conditions change.

Looking deeper into the definition of τ, several things can be noted

- It is directly proportional to the mass m which means that is influenced directly by initial conditions like precharge pressure, temperature and initial volume
- It is inversely proportional to the heat transfer coefficient h, which includes the average contribution of the heat transfer processes from the gas to the wall of the accumulators, and from the accumulator outer walls to the environment. The internal heat transfer coefficient, however, is heavily influenced by the dynamics of the gas as well as it temperature and pressure, which implies that the thermal time constant is probably not "constant" during operation.

To have a in depth look of the fluid and heat transfer phenomena of the gas in the accumulator and better predictive performance, CFD modeling can provide a more accurate answer and understanding.

4 CFD Modelling

In order to study in depth the thermodynamics of the gas in the accumulator, a CFD model was developed. For the modeling

[1] The formal derivation of the model is omitted in this article for the sake of compactness, but the works of [2] and [1] provide the details

of the accumulator, the use of two softwares was implemented. For the CAD modeling and meshing, COMSOL Multiphysics was used due to its powerful and flexible mesher and STAR CCM+ was then used for solving and post-processing of the results.

4.1 Geometry

The accumulator has the advantage of being of a symmetrical cylindrical shape, so to minimize the computational effort, a three dimensional wedge of the cylindrical domain was modeled, to be able to exploit the axis-symmetrical properties of the cylindrical shape of the accumulator. This wedge has an angular length of four degrees as seen in fig. 2.

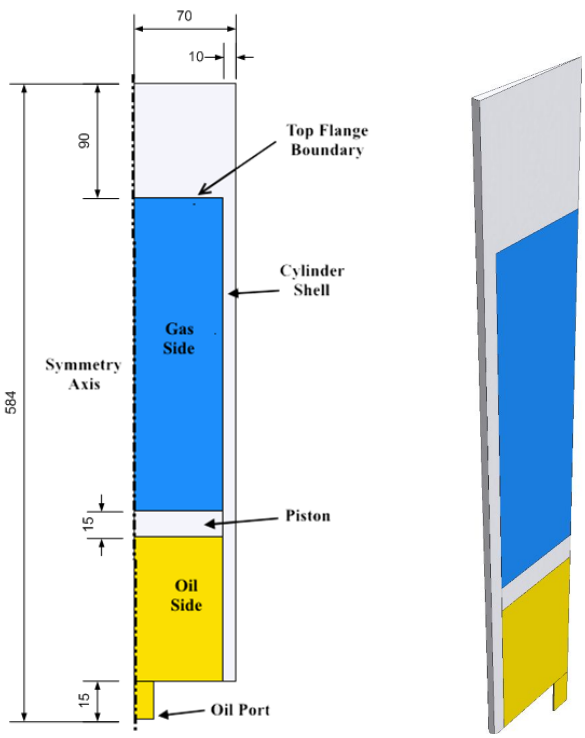

(a) Front View. Measurements in mm. (b) Isometric View

Figure 2: CAD Model of the accumulator with differentiated colored domains (yellow for oil, blue for gas and grey for steel).

The main geometry is divided in 5 sub domains which are grouped by the type of physics modeling involved in them. Grey parts are solid sections made of steel which are the piston, cylindrical shell and top flange. The yellow domains are the oil side parts, which are the inlet port and the oil cavity. Finally the blue domain represents the gas chamber. The dimensions of the model are taken from CAD models provided by the accumulator manufacturer.

4.2 Assumptions

- Simplified geometry and reduced dimensions
- Simple lumped convective heat transfer through convection from the cylinder walls to the environment, of the form $Q_{ambient} = h_{air}(T_{wall} - T_{ambient})$, where $T_{ambient}$ is a known measurable parameter from the experiments and h_{air} is the convective heat transfer coefficient of stall air, which is set to $10W/m \cdot K$ based on [8]
- No radiative heat transfer modeled, since the walls of the accumulator are usually below $40°C$, and the contribution is negligible [8].
- Oil domain modeled, considered relevant for heat transfer through the piston

4.3 Solver Setup

The transient simulation is solved by a fixed step implicit solver, with a time step of 0.001 s, and first order discretization in time. The inner solver steps are performed in a segregated manner, where the momentum, pressure, energy and turbulence equations are solved one after the other. The inner solver loops until the residuals of the main quantities fall below a predefined tolerance (below 10^{-4}). The differential equations are solved by a multi-grid method.

4.4 Regions and Domains

The model contains 3 main physical regions, corresponding to the 3 different material domains that can be found in the accumulator: Liquid for the oil domains, Gas for the accumulator's gas chamber and Solid regions for the remaining steel parts of the accumulator. Each region has an associated set of physical models selected, depending on the simulation needs.

In the gas region, the material used is diatomic Nitrogen N_2, which is built into the software's material database. Viscosity, thermal conductivity and specific heat capacity are considered functions of pressure and temperature. Force of gravity is enabled in the direction negative of the symmetry axis of the model. The turbulence model $k-\varepsilon$ is chosen based on computational efficiency and high accuracy for fully turbulent flows. A turbulence intensity of 4.5% and a turbulent viscosity ratio of 25, based on [9]. The real gas equation of state used is Soave-Redlich-Kwong.

In the liquid region, material used is Hydraulic Oil based on the specifications of Castrol AWHM 32 [10] . Viscosity, thermal conductivity and specific heat capacity are considered constant. Gravity force is neglected and the flow is considered laminar since it is a high viscosity fluid. The oil is also considered isothermal.

In the solid region, material used is Carbon Steel based on the specifications of the manufacturer of the accumulator. Constant thermal conductivity of $k = 49.8$ W/mK and specific heat capacity of $C_p = 4900$ J/kgK were chosen.

4.5 Mesh

Based on the simplicity of the geometrical model, a mapped mesh with quadrilateral elements was chosen for the fluid domains , and a free triangular mesh was chosen for the rest of the solid parts of the geometry, which adapts to parameters selected for the fluid domains. These parameters control the number of elements present in the gas and oil domains to achieve the highest quality possible during the deformation

and displacements of the domains. For accurate turbulence modeling, 10 boundary layers were added to the inner side of the boundaries of the gas domain. A close up of the mesh can be seen in fig. 3.

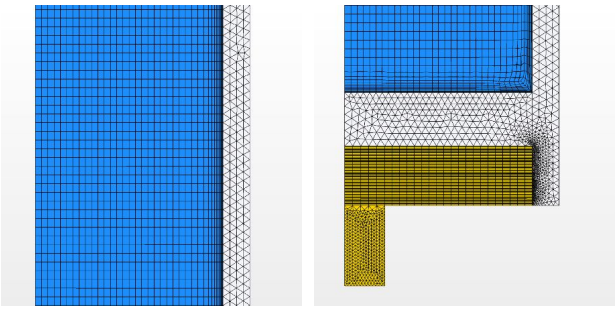

(a) Gas and Cylinder Shell (b) Oil, Piston, Gas and Cylinder Shell

Figure 3: Detail of the model's mesh. Final iteration, number of elements: 4235.

The mesh size and setup was optimized to provide the highest accuracy and smallest level of distortion in the gas side mesh. The mesh deformation compresses and stretches the elements of the gas and oil domains, but there is no re-meshing step in between the solving steps.

4.6 Calculation of Pressure and Temperature

The CFD model includes a different set of probes and sensors to calculate the relevant properties and be able to truly compare with the real measurements in the experimental setup. The gas pressure is calculated as a mass average of the pressure in every cell. The average temperature is also calculated as a mass average of the individual temperature of all the cells. In addition to that, temperature probes were set in the model following the drawing in fig. 5.

4.7 Model Validation

A validation was carried out using the experimental runs described by [1]. The data obtained from this test runs includes the piston position over time and temperature and pressure of the gas domain. The validation was carried out with data from 19 selected runs from the previous study. In general, the average maximum error in pressure between the experimental and simulated results is of 5%, and the average overall RMS error is of 2%, which demonstrates that the model generates repeatable and reliable results for the range of conditions used in the previous experimental studies. The source of the errors that can be seen between the experimental and the simulated data can be explained by different factors. First, the reduced nature of the model, which neglects geometrical features and assumes symmetric flows (no swirl). Second, the uncertainties of experimental data, which include the noise in the signals, the reliability of the sensor positioning and the filtering techniques. And third, the numerical errors introduced by the deformation of the mesh in the CFD model and the degraded cell quality in some regions.

5 Experimental Setup

In order to asses the accuracy of the CFD model, an experimental validation was carried out. The experimental procedure and test equipment used in [1] served as a base for the validation carried out in this work. The gas temperature and pressure measured on a 6 liter accumulator subjected to compression-expansion processes were compared to the predictions of the developed CFD model. A diagram of the ex-

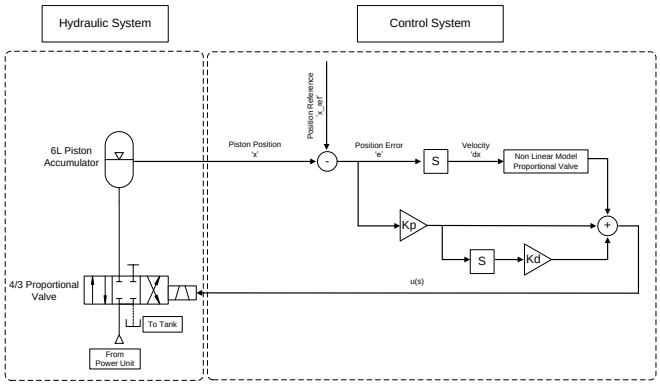

Figure 4: Hydraulic diagram of the experimental setup used for validation

perimental setup used can be seen in fig 4, with pictures of the main components presented in fig 6. The experimental setup consists of a test accumulator, mounted in a pivoting support to allow orientation changes (with the possibility to be rotated by 180 degrees from a vertical position). Oil is supplied to the test rig by an hydraulic power supply composed of two pumps and 4 accumulators. The supply is capable of delivering hydraulic oil at a maximum pressure of 250 bar.

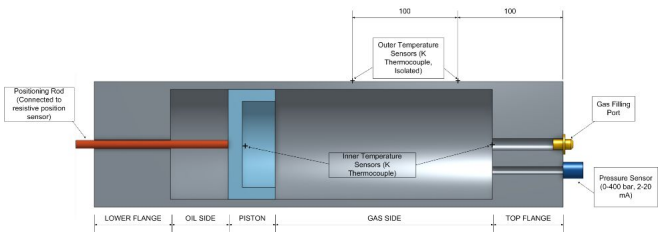

Figure 5: Basic schematic of sensor positioning in the test accumulator

The oil flow into the accumulator is controlled by a 4/3 proportional valve. The position of the piston is controlled via a P-I controller, which receives the position signal of the piston and adjusts the flow through the hydraulic valve accordingly, using also a feed-forward loop on the velocity of the piston. The test accumulator is connected to a variety of sensors to monitor pressure and temperature at different points. Figure 5 shows the sensor positioning in the accumulator. The gas chamber is connected to a 400 bar pressure transmitter. In addition to that, two temperature sensors (K type thermocouples) are positioned in the gas side, one in the center of the piston and the other on the top flange. Four more probes monitor the outer shell temperature (only two shown in the

(a) Test Accumulator (b) Hydraulic Supply

Figure 6: Main hydraulic components of the experimental rig

figure, two extra sensors are positioned in the same axial coordinates but with a radial offset of 90 degrees). The piston is attached to a rod that drives the resistive position sensor, which lies outside of the accumulator.

All the sensors are connected to a data acquisition system which is itself linked to a main computer equipped with DASYLab software for data acquisition.

p_0 [bar]	dV/dt [L/s]	V_{fin}/V_{init}
20	[0.31, 0.62, 0.93]	[1.5, 2.1, 2.7]
50	[0.31, 0.62, 0.93]	[1.5, 2.1, 2.7]
100	[0.31, 0.62, 0.93]	[1.2, 1.4, 1.5]
150	[0.31, 0.62, 0.93]	[1.1, 1.15, 1.2]

Table 1: Experimental setups for the tests made at Fritz Schur Energy. A three digit labeling system for the experimental runs is used to identify the different levels at which the above mentioned conditions can vary (ex. run 311 = Initial Pressure Level 3, Volume Change Rate Level 1, Compression Ratio Level 1).

The accumulator is subjected to compression-expansion cycles where the pre-charge pressure, compression/expansion velocity and compression ratio were varied, based on the experiments of [1]. A three digit labeling system for the experimental runs is used to identify the different levels at which the above mentioned conditions can vary, following tab. 1, for a total of 36 experimental cycles.

6 Results And Comparison

For this section, a compression-expansion case is studied which is based on the initial conditions of the run 233 described in tab. 1. The objective is to illustrate the dynamics of the system. The simulation is initialized with a temperature of 33.6°C and a pre-charge pressure of 50 bar, with an initial volume of 5.21 liters and a compression ratio of 2.7. Figure 7(a) shows the volume of the gas chamber during the process. The accumulator is oriented vertically.

For the CFD model, the reference signal of the volume changes in time were used. Unusual behavior of the heat transfer in the system was experienced when the signal inputed into the CFD model had some level of noise (when, for example, the measured piston position from the experiments was used as an input to the piston position in the CFD model). Large amounts of heat could be seen transfered from the gas to the walls of the accumulator. This sensitivity can be a consequence of the choice of the turbulence model selected. The $k-\varepsilon$ turbulence model assumes that turbulent stability is achieved, and the noise in the piston movement can excite the system enough to create a highly turbulent behavior near the walls, causing excessive heat loss and unreal results.

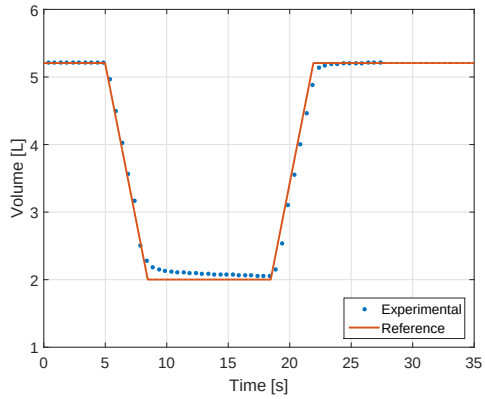

(a) Gas Volume

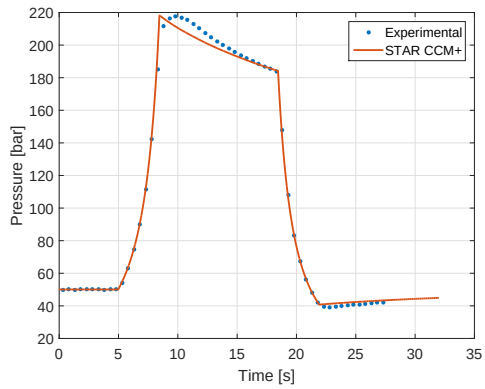

(b) Gas Pressure

Figure 7: Gas volume and pressure for the compression-expansion cycle

The pressure evolution obtained by the CFD simulation has a good level of agreement with the experimental reference, fig. 7(b), which provides a solid validation point for the model. The discrepancies may originate from the way the position of the piston is controlled in the experimental setup, which is equivalent as filtering the input signal. This smoothing is omitted in the CFD model due to the fact that it would

require the measured piston position from the experiments, which contains noise and can produce unreliable results due to the issues explained above.

6.1 Temperature Distribution

Figure 8 shows the evolution of the temperature distribution in the accumulator for the compression-expansion cycle. The compression process starts at t = 2.0 seconds, the gas increases temperature due to the reduction of the volume, however the regions close to the cylinder shell remain at lower temperatures due to the heat exchange with colder solid domain. At t = 4.0 seconds, a vortex of colder gas can be seen emerging from the piston, revolving clockwise towards the walls of the accumulator. The movement of the piston drags the colder gas in the boundary layer at the inner wall of the cylinder, and is pushed inwards into the centerline of the domain, passing above the piston. From t = 6.0 seconds to t = 14.0 seconds the compression is held. The gas reaches a maximum temperature of 184 °C, which decreases over time due to the diffusion and natural convection. It can be seen that the temperature is clearly stratified, from top to bottom of the gas domain. Temperature differences between the top of the gas domain and the bottom (where the piston lies) of up to 60°C are visible. The solid parts of the accumulator surrounding the gas domain also increase their temperature, up to 10 °C, due to heat transfer from the hotter gas. At t = 16.0 seconds, the expansion process has begun. The gas temperature near the piston decreases faster than the temperature at the top, as the gas expands faster due to the influence of the piston motion. Clear temperature gradients can be seen along the domain in the vertical direction as in the compression part. Now the heat transfer process is reversed, the solid parts of the accumulator are at a higher temperature than the gas. The shell of the accumulator remains at a higher temperature in the areas where the volume was held after the compression. The results show that temperature gradients along the gas domain exist. Experimental temperature measurements of the gas are influenced by the position of the sensor. A set of virtual probes were setup in the CFD model to compare with the experimental measurements.

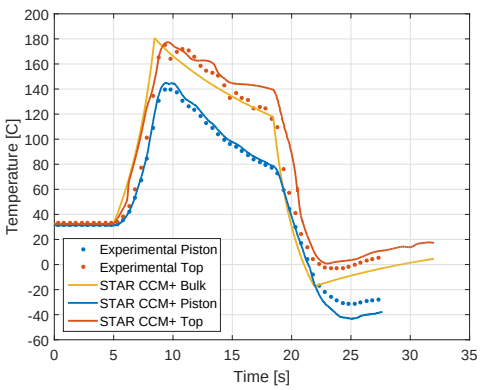

(a) Gas Domain Temperatures

Figure 9: Temperature measurements in the accumulator. Experimental vs. CFD results

Figure 9 shows the temperature measurements at different positions in the gas domain. As shown in the aforementioned results, the temperatures measured at the top of the domain are higher than the ones on the piston, due to the gradient imposed by the gravitational forces. Simulated results of the temperatures in the probes have fluctuations, a consequence of the fluid dynamics in the gas, when hotter and colder gas move near the probe. The simulated bulk (or average) temperature of the domain, calculated as the mass averaged temperature of the gas, lies in between the top and the piston temperatures, as it behaves as an average expression of the temperature in the whole domain. Experimental results show very good agreement with the simulated ones, and reflect the importance of choosing an appropriate measuring position of the temperature sensors in the experimental setup to have a good reference to compare simulation models. Measured temperatures from the top of the domain provide a good approximation to the average temperature of the gas.

6.2 Heat Transfer Across Boundaries

With the CFD model, the boundary fluxes in the walls of the gas domain can be integrated to obtain the heat transfered between bodies. The resulting rate of heat losses are presented in fig. 10(a).

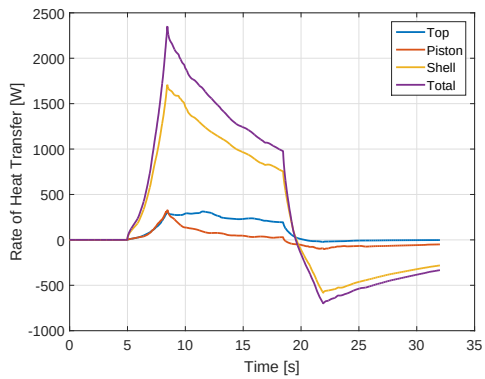

(a) Gas Domain Heat Loses

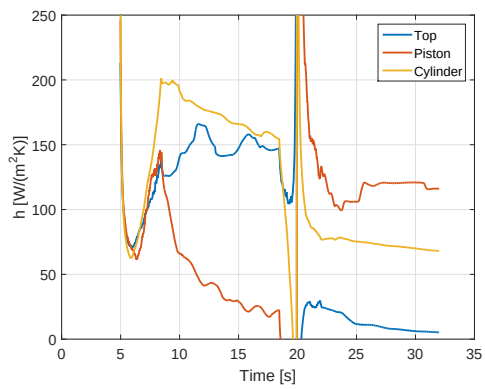

(b) Heat Transfer Coefficients

Figure 10: Boundary heat losses in the gas domain from the CFD simulation of the case studied.

It can be seen that the heat losses follow the dynamics of the compression-expansion cycle. Heat loss increases as the gas

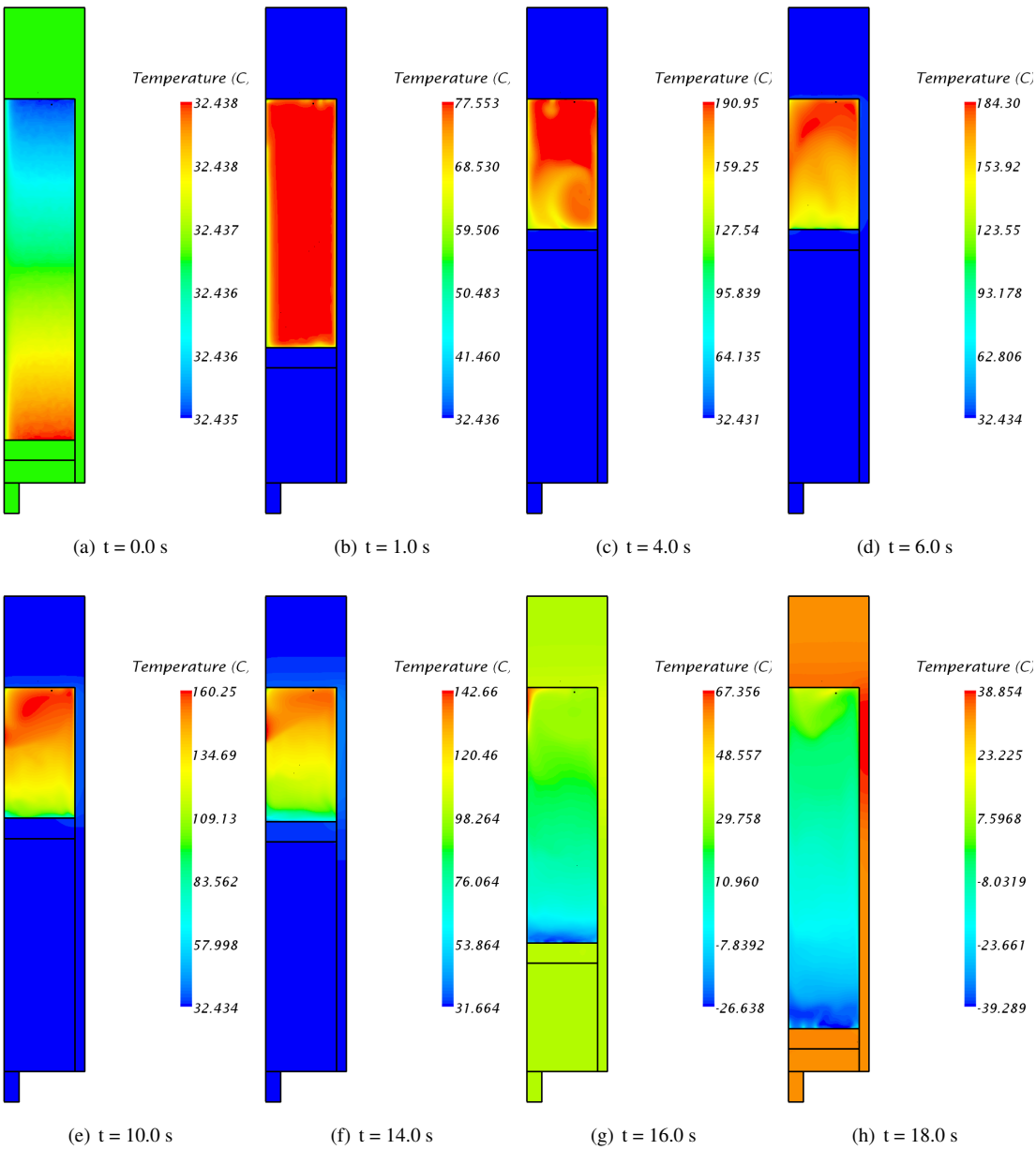

(a) t = 0.0 s (b) t = 1.0 s (c) t = 4.0 s (d) t = 6.0 s

(e) t = 10.0 s (f) t = 14.0 s (g) t = 16.0 s (h) t = 18.0 s

Figure 8: Temperature distribution in the accumulator during the compression-expansion cycle

is compressed due to the continual increase of temperature and the momentum induced in the gas due to the piston movement. After the compression, the heat transfer gradually decays due to a sustained decline of the gas temperature and the increase of temperature in the solid bodies of the accumulator. During the expansion, the heat transfer decreases gradually as the gas gets colder. At around 20 seconds into the simulation the heat transfer process reverses, now the gas receives heat from the hotter boundaries. When the expansion finalizes, the gas keeps receiving heat from the solid boundaries, and the magnitude of the heat transfer diminishes as time passes, due to the gas and the solid boundaries reaching slowly thermal equilibrium. Most of the heat is transfered through the cylinder shell boundaries. This responds to the fact that it has the biggest heat transfer area (which is between 10 and 2 times higher than the one of the piston or the top boundary) and high fluid velocities because of natural convection effects (as seen in fig. 11(a)). The heat losses through the piston and top boundary are smaller, accounting 15% of the total. It can be seen that for the top boundary the heat transfer process does not experience an inversion when the expansion begins. This is due to the small temperature difference between the gas and the boundary. In the piston, a small recovery can be seen after the compression. The lowest temperatures occur near this boundary so the temperature difference is high enough to be able to recover some of the heat.

The heat transfer and the corresponding heat transfer coefficients, associated to each boundary, (fig. 10(a) and 10(b)) show that after the compression, the highest heat transfer is experienced in the cylinder wall, while the lowest is in the

piston. The temperature difference between the piston and the cold gas at the bottom of the domain is the smallest between the boundaries, which results in lower heat transfer. On the top boundary, the higher gas temperatures are found, which increases the heat transfer coefficient. After the expansion, the piston-gas interface has the highest values of h, a consequence of the higher temperature difference between the now colder gas at the bottom of the gas domain and the piston. Still, although having a reduced heat transfer coefficient, the highest amount of heat is transfered through the cylinder walls due to the large heat transfer area.

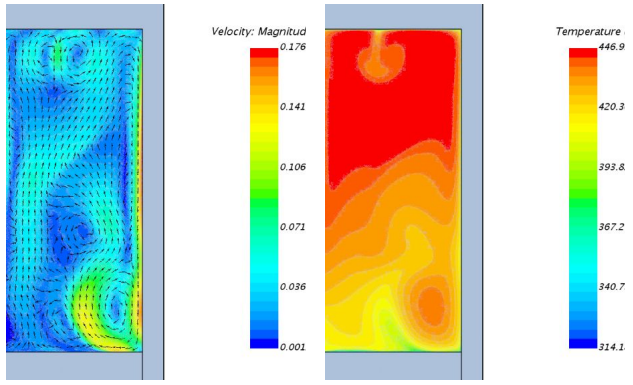

(a) Velocity Magnitude (b) Temperature

Figure 11: Velocity field and Temperature of the gas domain after compression (t = 10 seconds)

The curves represented in fig. 10(b) suggest that there is a clear non linear behavior of the heat transfer coefficient to the temperature difference between the gas and the surroundings. This implication has a direct influence in the way the heat losses are linearly modeled in eq. 1, and specifically on how τ is conceived mathematically. Non linearities arise due to the fact that the fluid flow models are naturally non linear (incompressible Navier-Stokes, turbulence modeling), and the thermodynamical behavior of the system is influenced by the momentum of the flow and the local changes of viscosity and density, which themselves are non linear functions of the temperature.

6.3 The Thermal Time Constant

The dynamic behavior of the heat transfer phenomena in the gas domain can be expected to be reflected in the thermal time constant of the gas. Figure 12 shows the variations of the thermal time constant of the gas over time. Initially, as the process is initialized, the thermal time constant has a value of zero. This is due to the way the thermal time constant is mathematically defined to be calculated in the simulation. τ can be defined as

$$\tau = \frac{mC_V(T_s - T)}{Q} \tag{3}$$

where Q is the heat loss across the boundaries of the gas domain and T_s is the temperature of the walls (which now replaces T_a since the gas in reality exchanges heat with the cylinder walls, and the temperature of these walls changes over time). When the compression starts, τ increases, and reaches a maximum value, and afterwards starts decreasing to its lowest value at the end of the compression. This behavior can be expected due to the fact that, when compression begins, the temperature increases first due to interactions of the gas molecules, and the heat transfer is low since there is no convection. After some seconds, the convective effects catch up with the increase in temperature, starting up the heat transfer to the boundaries, and lowering the thermal time constant.

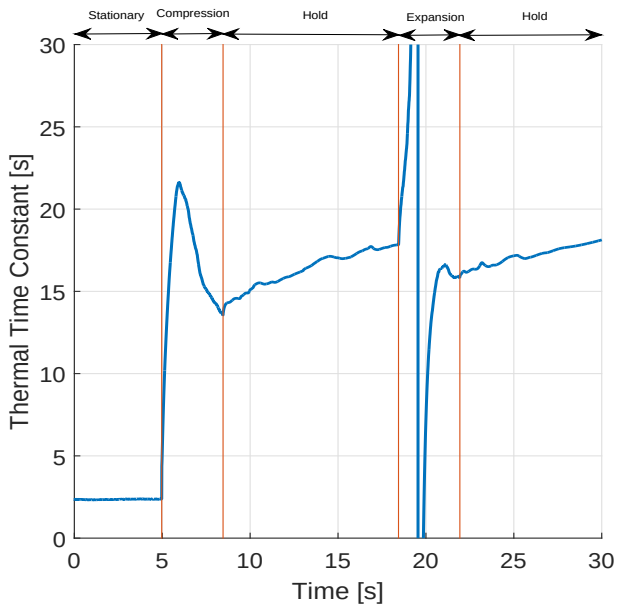

Figure 12: Thermal time constant evolution for a compression-expansion cycle

When the compressed gas is held, τ increases slowly, almost linearly. This corresponds to the steady heat transfer between the gas and the surrounding boundaries, which are slowly reaching thermal equilibrium. This behavior can also be seen after the expansion when the volume remains constant. During the expansion, the value of τ jumps from positive to negative suddenly. This is a result of how the time constant is defined mathematically. The denominator of eq. 3 is close to zero when there is no heat transfer, resulting in a visible discontinuity of the thermal time constant. This is a direct consequence of the temperature of the gas reaching lower temperatures than the boundaries due to the dilation of the chamber, and instantaneously the temperature difference is zero, thus also the heat exchange.

7 Practical Approach for Improving the Efficiency of the Accumulator

As seen from the CFD analysis, the behavior of the heat transfer in the gas is clearly non linear, and sensitive to several operational and dimensional factors. Although the CFD model provides a very good approach to a repeatable and accurate prediction of the losses in the accumulator, one may wonder if there is anything practical to be done to reduced the thermal losses in the accumulator.

Recalling the definition of τ in eq. 2, we can see that on

practice, the two parameters that can be modified in a controlled matter are the gas mass m and the heat transfer area A. The heat transfer area, though, can be tricky to modify since the size of the accumulator is usually defined based on the hydraulic system needs. Which leaves the mass as the only parameter that could be tweaked to increase performance. But how to do that?

Pourmovahed et al. [11, 12] investigated the influence of filling the gas side of the accumulator with elastomeric foams. Their research shows that, due to the porous nature of the foam, if one can effectively fill the whole gas compartment with it, the effect is the equivalent to increasing the heat capacitance of the gas, meaning that the term mC_v in the τ definition is greatly increased due to the increased mass and heat capacitance, contributed by the foam. Inspired by this results, an experimental investigation was carried out.

7.1 Experimental Setup

The same experimental setup was used as with the CFD investigation. This time however the gas side was filled with two different types of foams: PPI 80 polyester (labeled as 'Foam 1' in the results) and HR 50 polyether (labeled as 'Foam 2' in the results). For each foam, a piece was custom made to fill the dimensions of the whole gas side, and was fixed to the piston of the accumulator to prevent it to get stuck during the compression and expansion phases. Figure 13 shows the foams used in the experiment, properly shaped and attached to the piston.

p_0 [bar]	dx/dt [mm/s]	V_{fin}/V_{init}
50	[50, 100]	[1.50, 2.00, 2.50]
100	[50, 100]	[1.25, 1.50, 1.65]

Table 2: Experimental setups for foam tests made with a 6 liter accumulator.

For each foam filling, a set of experiments were carried out following the planning on tab. 2, Varying compression rations, velocities and pre-charge pressures.

7.2 Results

The use of PPI 80 polyester (foam 1) and HR 50 polyether foam (foam 2) generally showed positive results. The pressure curves of the work cycles, that are the most and the least effected by the foam filling, efficiency wise, are plotted in fig. 14. These curves give a quick overview of how the normal shaped foams affect the thermal time constant of the accumulator.

In the most effective case (fig. 14(a)) where the pre-load pressure is low, while the compression ratio is high, both foams have a remarkable effect on the pressure build up. The maximum pressure is reduced from 181 bar to 153 bar and 152 bar with foam 1 and 2 respectively. This means that less heat is lost, thus reducing the pressure drop during the holding period. The flat curves during the holding indicate a high τ

(a) Foam 1 shaped and attached to piston

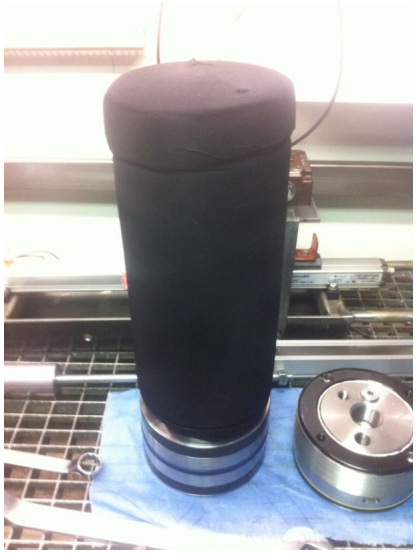

(b) Foam 2 shaped and attached to piston

Figure 13: Pictures of the filling foams used in the experiment

of the accumulator, which in this case is increased from 7 s without foam, to 46 s with foam 1 and 134 s with foam 2.

In the least affected case shown (fig. 14(b)), the pre-load pressure is high while the compression ratio is small, and the piston speed is slow. This means that the overall pressure and temperature differences are lower, resulting in a more subtle improvement of τ, which is now increased from 9 s without foam, to 34 s with foam 1 and to 74 s with foam 2.

In both cases the thermal time constant is increased, and in both cases the highest increase is obtained with foam 2. This is explained by the greater heat capacity, which is one of the main factors causing the improvements when using the foam. Since the heat capacity and density of the solid polyurethane is more or less the same for both foams, the heat capacity of foam 2 is larger, because the higher bulk density. When filling the gas chamber with foam, the effective volumetric heat ca-

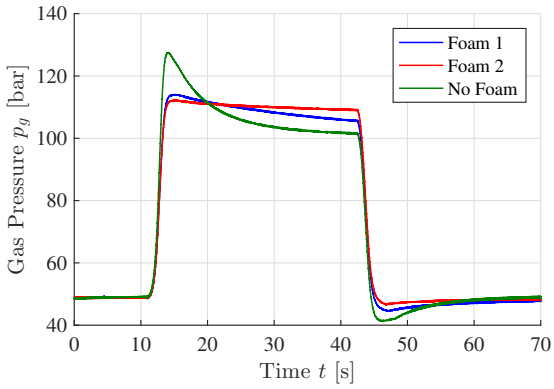

(a) p_0 = 50 bar, cr = 2.5, v_p = 100 mm/s

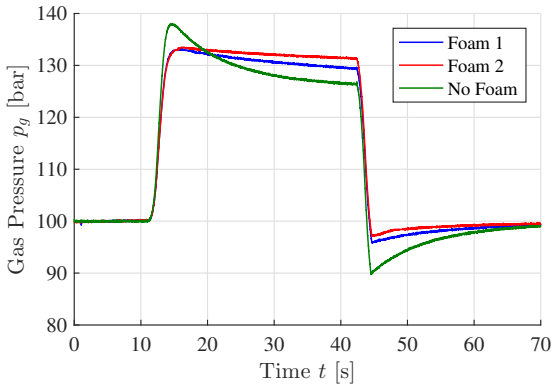

(b) p_0 = 100 bar, cr = 1.25, v_p = 50 mm/s

Figure 14: Accumulator pressures comparison for selected compression expansion cycles, with and without foam.

pacity of the gas and foam combination is higher compared to that of the gas alone. Because of the higher heat capacity, the foam works as a heat sink, which in turn reduces the temperature increase and thereby the pressure build up. Another positive effect of the foam is that gas flow is restricted due to the resistance of the porous structure. This will dampen the dynamics that are induced on the gas by the piston movement and further reduce the high temperatures that are seen in the accumulator without foam. As mentioned a lower maximum temperature means that less heat can be lost, and ultimately that the thermal efficiency is increased. In addition the restricted flow will reduce the convective heat loss to the cylinder walls.

7.3 Reduction of Thermal Losses

Since the main energy loss is the heat loss, the effect of the foam is best shown and explained with the pressure-volume (pV) diagrams, that are shown in fig. 15 for the most and least effected runs respectively. The pV diagrams demonstrates graphically how the thermal losses, with and without foam, compares to each other and to the ideal case of isothermal compression.

The high compression ratio generates higher temperatures and pressure during compression. This is seen in the pV diagram in fig. 15(a), by the exponential increase of the pressure during compression. In contradiction, when the compression ratio is small, the slope of the pV diagram during these processes, is close to being linear and closer to the isotherm, as seen in fig. 15(b) After a large compression, the high temperature lead to greater heat losses during the holding period, which increases the pressure drop and in turn decreases the potential energy of the accumulator. This is represented by the vertical lines at the end of the compression process in the pV diagram. In addition to the big pressure drop at this point, a longer expansion makes the gas reach even lower temperatures and pressure at the end of the stroke. Ultimately this means, that the expansion work is done at much lower pressure than the compression work, resulting in the lowest possible energy efficiency and therefore the biggest improvement potential.

The foam reduces the heat loss by 3 mechanisms in 3 steps:

- Compression: The foam acts as a heat sink and dampens convection - reducing
- Holding period: The foam acts as a heat regenerator - reducing temperature loss.
- Expansion: The foam acts as a heat regenerator and dampens convection reducing temperature decrease.

Since the foam works as a heat sink it is most effective when the temperature increase of the gas is high, namely for high compression ratios. A bigger step change of gas temperature, will cause a bigger temperature difference between the gas and the foam, which increases the heat transfer from gas to foam and thereby improves the effect of the foam. The regenerator effect is seen during the holding period and expansion process, where the gas temperature drops below that of the foam, and the heat transfer changes direction.

The effect of the foam is clearly seen by the reduction of the area inside the pV diagrams. And as seen with the thermal time constant the best overall effect is achieved with foam 2, namely the HR 50 polyether foam. In the most effective case shown in fig. 15(a) the heat loss of the accumulator is reduced with 23.8 percentage points from 30.8% without foam, to only 7.0% with foam 2. And in the least effective case, shown in fig. 15(b), it is reduced by 8.4 percentage points, from 10.5% without foam to 2.1% with foam 2.

8 Conclusions

The thermodynamical processes involved in an hydraulic accumulator during operation were successfully studied by the use of a CFD model. The results obtained from this model had a high level of agreement with the experimental results for a wide range of cases. The results demonstrate that the heat losses in the gas side of an accumulator are mainly associated with heat transfered to the solid parts that is later diffused into their bodies. The heat loses to the environment are relatively small for the conditions simulated, and have no meaningful effect in the system. There is also clear evidence that the there are important temperature gradients in the gas that make the heat losses not uniform throughout the boundaries.

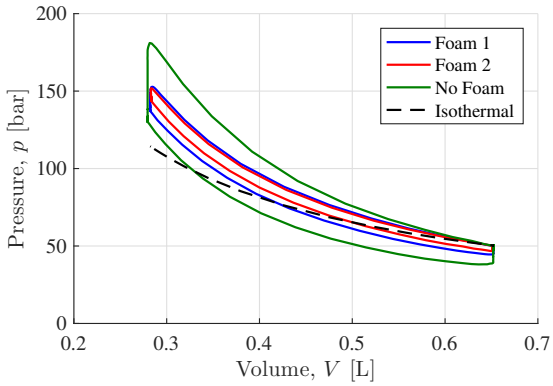

(a) p_0 = 50 bar, cr = 2.5, v_p = 100 mm/s

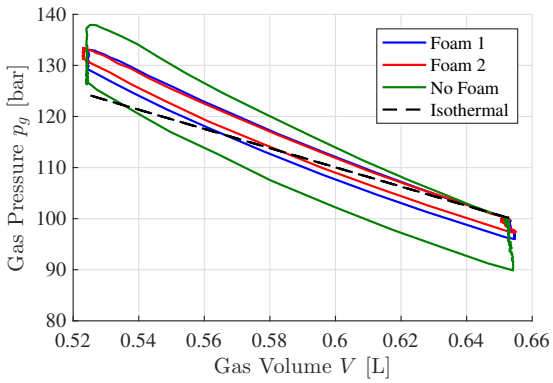

(b) p_0 = 100 bar, cr = 1.25, v_p = 50 mm/s

Figure 15: Accumulator $p-V$ diagrams comparison for selected compression expansion cycles, with and without foam, included also isothermal curves

It has been proved that the thermal time constant of the gas varies in time. It is proportionally dependent on the gas mass in the chamber, and is affected by changes in the initial conditions, orientation, compression velocity and compression ratio. The dynamics of τ are defined by the fluid flow of the gas. Convection is the main heat transfer process between the gas and the solid parts and it is affected by the piston movement, which induces momentum into the flow. The non linear behaviors of the heat transfer coefficients and thermal time constant are generated by the fluid motion and the convective processes.

A practical proof on how to improve the efficiency of the hydraulic accumulators has been presented and studied in depth, where filling the gas side with foams provides an increased heat capacitance of the gas and reduces the heat transfer to the accumulator walls, providing a better storage of the hydraulic power.

References

[1] H B Hansen and P W Rasmussen. Modelling hydraulic accumulators for use in wind turbines. *Proceedings of the 13th Scandinavian International Conference on Fluid Power*, Linköping, Sweden, 2013.

[2] D R Otis. Predicting performance of gas charged accumulators. *Proceedings of the 1st Fluid Power and Control Systems Conference*, University of Wisconsin-Madison:160–165, 1973.

[3] A Pourmovahed, N H Beachley, and F J Fronczak. Modeling of an hydraulic energy regeneration system - part i: Analytical treatment. *Transactions of the ASME*, 114:160–165, 1992.

[4] S Rotthäuser. *Verfahren zur Berechnung und Untersuchung hydropneumatischer Speicher*. Fakultät für Maschinenwesen der Rheinisch-Westfälische Technische Hochschule Aachen, 1993.

[5] K R Rupprecht. *Hydrospeicher, Experimentelle und analytische Untersuchungen zur Energiespeicherung*. Fakultät für Maschinenwesen der Rheinisch-Westfälische Technische Hochschule Aachen, 1988.

[6] D R Otis and A Pourmovahed. An algorithm for computing nonflow gas processes in gas springs and hydropneumatic accumulators. *ASME Journal of Dynamic Systems*, 107:93–96, 1985.

[7] J. Svoboda, G. Bouchard, and S. Katz. A thermal model for gas-charged accumulators based on the heat conduction distribution. *Fluid Transients and Acoustics in the Power Industry*, pages 161–167, 1978.

[8] F Incropera, D DeWitt, A Lavine, and T Bergman. *Fundamentals of Heat and Mass Transfer*. John Wiley and Sons, 2011.

[9] J E Bardina, P G Huang, and T J Coakley. Turbulence modeling validation, testing, and development. *NASA Technical Memorandum 110446.*, 1997.

[10] BP Marine Limited. Hyspin awh-m range oils. anti-wear hydraulic oils., October 19 2009. US Patent 2,331,921.

[11] A Pourmovahed, S Baum, N H Beachley, and F J Fronczak. Experimental evaluation of hydraulic accumulator efficiency with an without elastomeric foam. *Journal of Propulsion and Power*, 4:185–192, 1988.

[12] A Pourmovahed. Durability testing of an elastomeric foam for use in hydraulic accumulators. *Journal of Solar Energy Engineering*, 112:223–228, 1990.

Torque Control of a Hydrostatic Transmission Using Extended Linearisation Techniques

Robert Prabel and Harald Aschemann

Chair of Mechatronics, University of Rostock, Justus-von-Liebig-Weg 6, 18059 Rostock, Germany
E-mail: {robert.prabel, harald.aschemann}@uni-rostock.de

Abstract

This paper presents a decentralised control approach for the hydraulic motor torque provided by a hydrostatic transmission. Based on a control-oriented model of the hydrostatic transmission, a quasi-linear state-space representation with both state-dependent and input-dependent matrices is derived. Using extended linearisation techniques, a combined feedforward and feedback control is designed. Furthermore, a sliding-mode observer estimates unmeasurable states as well as disturbances. The estimates for the disturbances – an external load torque and a leakage oil volume flow – can be used for a disturbance rejection. The proposed overall control structure is investigated thoroughly in simulations and, afterwards, implemented as well as validated on a dedicated test rig.

Keywords: Hydrostatic Transmission, Torque Control, Extended Linearisation, Leakage Estimation, Disturbance Rejection

1 Introduction and Motivation

Hydrostatic transmissions (HST) are usually implemented in construction machines, e.g. wheel loaders and excavators, as well as in mining and agricultural applications. Moreover, new application fields have emerged regarding wind turbines, cf. [1, 2], and power-split systems, cf. [3], where a precise tracking of angular velocities becomes important regarding a high transmission efficiency. Suitable control concepts for a tracking of the angular velocity of the hydraulic motor are presented in [4] and [5]. Besides these velocity control approaches, it is also possible to control the hydraulic motor torque that is provided by the hydrostatic transmission to the driven vehicle. The design and the validation of such an observer-based nonlinear control structure is presented in this paper.

The set-up of a hydrostatic transmission in construction machines is typically as follows: A prime mover, e.g. an internal combustion engine, drives a hydraulic pump with a variable volumetric displacement, which is connected by hydraulic hoses in a closed circuit to the hydraulic motor. Given the overpressure between the high-pressure and the low-pressure side, the hydraulic motor, which also offers a variable volumetric displacement, generates a hydraulic torque. Fig. 1 shows a dedicated test rig for the validation of new control concepts, which is available at the Chair of Mechatronics, University of Rostock. Here, two electric motors are used to represent the prime mover as well as to generate specified disturbances, e.g. driving resistance forces. In Fig. 2, the corresponding structure of the test rig is shown.

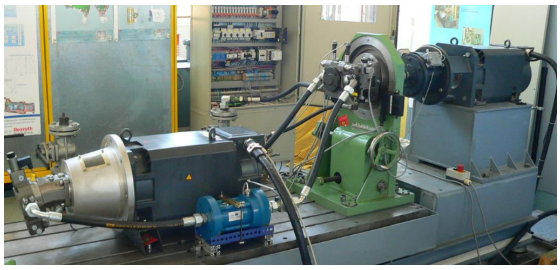

Figure 1: Drive train with a closed-circuit hydrostatic transmission.

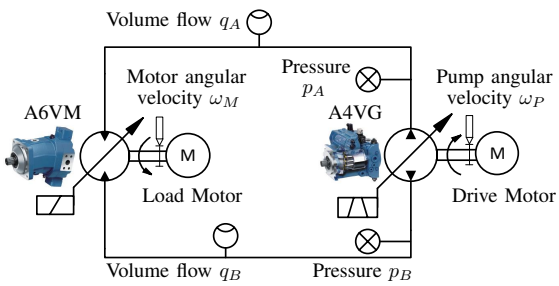

Figure 2: Structure of the dedicated test rig in a closed-circuit configuration consisting of an electric drive motor, a hydraulic pump (A4VG), a hydraulic motor (A6VM), an electric load motor, two hydraulic hoses as well as the instrumentation.

The outline of this paper is as follows: A control-oriented model is derived in Sect. 2. Next, a decentralised control-

ler based on extended linearisation techniques is derived in Sect. 3. Furthermore, the control structure is extended by a sliding mode observer, see Sect. 4, to estimate the unmeasured states – tilt angles of the hydraulic pump and motor – as well as disturbances, e.g. leakage flows and disturbance torques. Besides, the overall control structure is validated in simulations and experiments, see Sect. 5 and 6. Finally, the paper concludes with a short summary of this contribution and an outlook on further work.

2 Mechatronic Model of the Hydrostatic Transmission

A control-oriented model of the hydrostatic transmission provides the necessary information for the control design. Suitable modells for hydraulic applications can be found in [6], [7] and [8]. The mathematical description of the test rig shown in Fig. 1 can be divided in hydraulic and mechanical subsystems. Here, the hydraulic pump is driven by an electric motor that operates in a highly efficient operating point. The corresponding angular velocity of the electric drive motor is chosen as $\omega_P = const. > 0$.

2.1 Hydraulic Subsystem

The hydraulic subsystem includes the hydraulic pump and the hydraulic motor as well as the pressure dynamics in the hydraulic hoses. The corresponding models for the individual hydraulic components are described in the sequel.

Pump Flow Rate

The pump ideal flow rate q_P is determined by a nonlinear function

$$q_P = V_P(\alpha_P)\, n_P\,, \tag{1}$$

with n_P as the rotational speed of the pump shaft in rpm. The nonlinear behaviour of the volumetric displacement $V_P(\alpha_P)$ is related to the mechanical design based on a tiltable swashplate. A mathematical description according to Fig. 3 leads to

$$V_P(\alpha_P) = N_P A_P D_P \tan(\alpha_{P,\max} \cdot \tilde{\alpha}_P)\,, \tag{2}$$

with the normalised swashplate angle $\tilde{\alpha}_P = \alpha_P/\alpha_{P,\max}$. The geometrical parameters are the effective piston area A_P, the diameter D_P of the piston circle and the number N_P of pistons inside the pump. The overall pump flow can be described by

$$q_P = \underbrace{\frac{N_P A_P D_P}{2\pi}}_{\tilde{V}_P} \tan(\alpha_{P,\max} \cdot \tilde{\alpha}_P)\, \omega_P = \tilde{V}_P \tan(\alpha_{P,\max} \cdot \tilde{\alpha}_P)\, \omega_P\,, \tag{3}$$

with the pump angular velocity ω_P.

Motor Flow Rate

The used hydraulic motor is of a bent-axis design, see Fig. 4. Therefore, the ideal volume flow rate q_M into the hydraulic motor can be described by

$$q_M = V_M(\alpha_M)\, n_M\,, \tag{4}$$

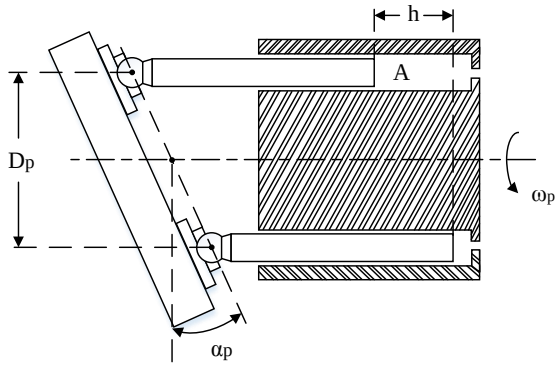

Figure 3: Geometry of the hydraulic pump with a swashplate.

similarly to the pump. In (4), $V_M(\alpha_M)$ represents the non-

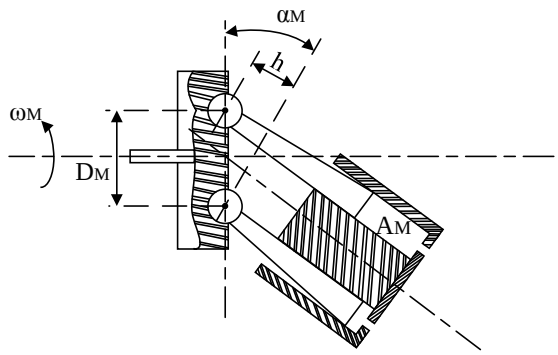

Figure 4: Geometry of the hydraulic motor in bent-axis design.

linear volumetric displacement of the motor and n_M the rotational speed of the motor shaft in rpm. With the geometrical parameters N_M, A_M and D_M of the hydraulic motor, the volume flow rate can be stated as

$$\begin{aligned} q_M &= \underbrace{\frac{N_M A_M D_M}{2\pi}}_{\tilde{V}_M} \sin(\alpha_{M,\max} \cdot \tilde{\alpha}_M)\, \omega_M \\ &= \tilde{V}_M \sin(\alpha_{M,\max} \cdot \tilde{\alpha}_M)\, \omega_M\,. \end{aligned} \tag{5}$$

Likewise to the mathematical description of the flow rate of the pump, a normalised bent-axis angle is introduced with $\tilde{\alpha}_M = \alpha_M/\alpha_{M,\max}$. The constant parameter $\tilde{V}_M$ is determined by the mechanical design of the motor.

Pressure Dynamics

The pressure dynamics of the high-pressure and the low-pressure sides of the hydrostatic transmission are given by

$$\begin{aligned} \dot{p}_A &= \frac{\beta_A}{V_A}(q_P - q_M - q_I - q_{E,A})\,, \\ \dot{p}_B &= \frac{\beta_B}{V_B}(-q_P + q_M + q_I - q_{E,B})\,, \end{aligned} \tag{6}$$

with the effective bulk moduli $\beta_k,\ k \in \{A,B\}$ and the total compression volumes $V_k,\ k \in \{A,B\}$, which take into account the hydraulic hoses and the chambers, respectively.

The volume flow balances for the compression volumes depend on the volume flows $q_i,\ i \in \{P,M\}$ of the pump and the motor, an internal leakage flow q_I as well as external leakage flows $q_{E,i},\ i \in \{P,M\}$, see Fig. 5. Next, a symmetric set-up regarding the high- and low-pressure sides is assumed. The hydraulic capacity with $C_H = V/\beta$ can be considered as nearly identical with $C_A = C_B =: C_H$. To reduce the model complexity for the control design, the difference pressure $\Delta p = p_A - p_B$ is introduced. The corresponding differential equation is given by

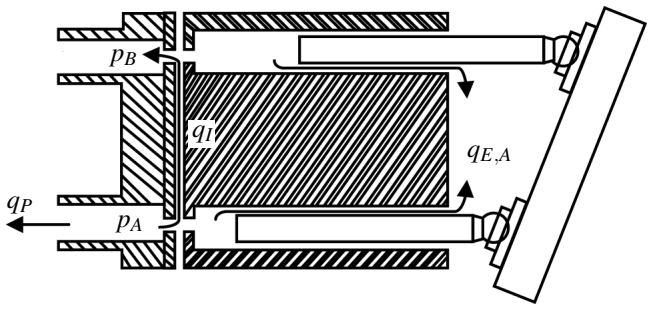

Figure 5: Example for the leakage paths for a axial piston hydraulic pump, with the internal leakage q_I and the external leakage q_E.

$$\Delta\dot{p} = \frac{2}{C_H}\left(\tilde{V}_P \tan(\alpha_{P,\max}\cdot\tilde{\alpha}_P)\,\omega_P - \tilde{V}_M \sin(\alpha_{M,\max}\cdot\tilde{\alpha}_M)\,\omega_M\right) - \frac{q_u}{C_H}\,, \tag{7}$$

where

$$q_u = 2q_I + q_{E,A} - q_{E,B} \tag{8}$$

denotes a resulting leakage oil flow that acts as a disturbance.

Actuator Dynamics

It is obvious that an instantaneous change of the displacement of the hydraulic pump as well of the hydraulic motor is impossible. To model such a lag behaviour, first-order lag models are introduced according to

$$\begin{aligned} T_{uP}\,\dot{\tilde{\alpha}}_P + \tilde{\alpha}_P &= k_P\,u_P\,, \\ T_{uM}\,\dot{\tilde{\alpha}}_M + \tilde{\alpha}_M &= k_M\,u_M\,. \end{aligned} \tag{9}$$

Here, T_{uP} and T_{uM} represents the corresponding time constants, k_P and k_M the proportional gains and u_P and u_M the analogue input voltages of the servo valves. Furthermore, the angles are bounded due to the mechanical design with $\tilde{\alpha}_P \in \{-1,1\}$ and $\tilde{\alpha}_M \in \{\varepsilon_M, 1\},\ \varepsilon_M > 0$.

2.2 Mechanical Subsystem

Typically, hydrostatic transmissions are used in construction machines. In the laboratory environment, see Fig. 1, the hydraulic motor is connected to an electric load motor, which serves for providing specified driving resistances. The set up of the remaining drive train of the test rig is depicted in Fig. 6.

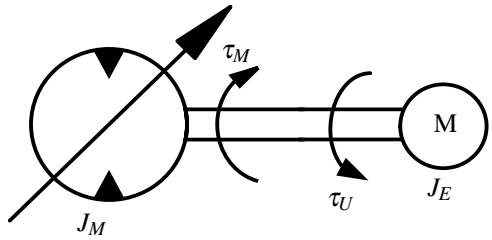

Figure 6: Kinematic structure of the drive train.

A torque balance leads to the equation of motion for the hydraulic pump shaft

$$J_V\,\dot{\omega}_M + d_v\,\omega_M = \tau_M - \tau_U\,, \tag{10}$$

with $J_V = J_M + J_E$ as the sum of the mass moments of inertia of the hydraulic motor and the electric load motor, which are rigidly connected. Unmodelled disturbances and parameter uncertainties are combined in a lumped disturbance torque τ_U. The hydraulic torque of the motor is given by

$$\tau_M = \tilde{V}_M \Delta p\,\sin(\alpha_{M,\max}\cdot\tilde{\alpha}_M)\,. \tag{11}$$

2.3 Modelling of the Complete System

The dynamics of the overall test rig consists of four first-order differential equations. By introducing the normalised tilt angles $\tilde{\alpha}_P$ and $\tilde{\alpha}_M$, the difference pressure Δp and the angular velocity of the drive shaft ω_M as state variables, the state vector becomes

$$\boldsymbol{x} = \begin{bmatrix} \tilde{\alpha}_P & \tilde{\alpha}_M & \Delta p & \omega_M \end{bmatrix}^T \tag{12}$$

and the corresponding nonlinear state-space representation results in

$$\begin{bmatrix} \dot{\tilde{\alpha}}_P \\ \dot{\tilde{\alpha}}_M \\ \Delta\dot{p} \\ \dot{\omega}_M \end{bmatrix} = \begin{bmatrix} -\frac{1}{T_{uP}}\tilde{\alpha}_P + \frac{k_P}{T_{uP}}u_P \\ -\frac{1}{T_{uM}}\tilde{\alpha}_M + \frac{k_M}{T_{uM}}u_M \\ \left[\frac{2}{C_H}\tilde{V}_P \tan(\alpha_{P,\max}\cdot\tilde{\alpha}_P)\,\omega_P \right. \\ \left. -\frac{2}{C_H}\tilde{V}_M \sin(\alpha_{M,\max}\cdot\tilde{\alpha}_M)\,\omega_M - \frac{q_u}{C_H}\right] \\ -\frac{d_V}{J_V}\,\omega_M + \frac{\tilde{V}_M}{J_V}\sin(\alpha_{M,\max}\cdot\tilde{\alpha}_M) - \frac{\tau_U}{J_V} \end{bmatrix}. \tag{13}$$

The input voltages of the proportional valves for the actuation of the hydraulic pump and motor are used as control inputs

$$\boldsymbol{u} = \begin{bmatrix} u_P & u_M \end{bmatrix}^T. \tag{14}$$

3 Nonlinear Control Design

The proposed control structure is based on a decentralised approach. In a first control loop, the normalised tilt angle of the hydraulic motor $\tilde{\alpha}_M$ is controlled by a flatness-based approach. The second control loop is responsible for the torque control of the hydraulic motor by using extended linearisation techniques.

3.1 Flatness-Based Control of the Tilt Angle of the Hydraulic Motor

The control design for $\tilde{\alpha}_M$ is performed using a flatness-based approach, see [9]. Thereby, the inverse dynamics results in

$$u_M = \frac{\tilde{\alpha}_M + \upsilon_M T_{uM}}{k_M}, \tag{15}$$

with the stabilising control law for the error dynamics

$$\upsilon_M = \dot{\tilde{\alpha}}_{Md} + k_{\alpha 0}\, e_{\tilde{\alpha}_M} + k_{\alpha I} \cdot \int_0^t e_{\tilde{\alpha}_M} d\tau \,. \tag{16}$$

Here, $e_{\tilde{\alpha}_M} = \tilde{\alpha}_{M,d} - \tilde{\alpha}_M$ represents the tracking error of the normalised tilt angle. The error dynamics $e_{\tilde{\alpha}_M}$ is parametrised with positive coefficients $k_{\alpha 0} > 0$ and $k_{\alpha I} > 0$.

3.2 State Feedback Design Using Extended Linearisation Techniques

Linear control approaches like eigenvalue placement and LQR design are well known and often used for linear state-space systems.In this paper, the eigenvalue placement method is extended to the nonlinear case, which is corresponds to extended linearisation design techniques, cf. [10]. Therefore, the system is written in the form of a quasi-linear state-space representation

$$\begin{aligned} \dot{\boldsymbol{x}}(t) &= \boldsymbol{A}(\omega_p, \tilde{\alpha}_P)\boldsymbol{x}(t) + \boldsymbol{b}\,u(t) + \boldsymbol{e}\,z(t) \\ y(t) &= \boldsymbol{c}^T(\tilde{\alpha}_M)\boldsymbol{x}(t)\,. \end{aligned} \tag{17}$$

Here, the system matrix $\boldsymbol{A} = \boldsymbol{A}(\omega_p, \tilde{\alpha}_P)$ depends on the angular velocity as well on the tilt angle of the hydraulic pump. Furthermore, the nonlinear output vector $\boldsymbol{c}^T = \boldsymbol{c}^T(\tilde{\alpha}_M)$ is affected by the tilt angle of the hydraulic motor. Note that the corresponding state equation can be neglected, and ω_M is considered as a gain-scheduling parameter. The parametrisation of the quasi-linear form results in

$$\begin{aligned} \dot{\boldsymbol{x}} = & \underbrace{\begin{bmatrix} \dfrac{-1}{T_{uP}} & 0 \\ \dfrac{2\,\tilde{V}_P\,\omega_P}{C_H}\,\dfrac{\mathrm{si}(\alpha_{P,\max}\cdot\tilde{\alpha}_P)\cdot\alpha_{P,\max}}{\cos(\alpha_{P,\max}\cdot\tilde{\alpha}_P)} & 0 \end{bmatrix}}_{\boldsymbol{A}} \underbrace{\begin{bmatrix} \tilde{\alpha}_P \\ \Delta p \end{bmatrix}}_{\boldsymbol{x}} \\ & + \underbrace{\begin{bmatrix} \dfrac{k_P}{T_{uP}} \\ 0 \end{bmatrix}}_{\boldsymbol{b}} u_P + \underbrace{\begin{bmatrix} 0 \\ \dfrac{1}{C_H} \end{bmatrix}}_{\boldsymbol{e}} \underbrace{-2\,\tilde{V}_M\,\omega_M \sin(\alpha_{M,\max}\cdot\tilde{\alpha}_M) - q_U}_{z} \,. \end{aligned} \tag{18}$$

The si-function is determined by $\mathrm{si}(\tilde{\alpha}_P) = \sin(\tilde{\alpha}_P)/\tilde{\alpha}_P$, with $\mathrm{si}(\tilde{\alpha}_P = 0) = 1$. The nonlinear output equation results in

$$y = \tau_M = \underbrace{\begin{bmatrix} 0 & \tilde{V}_M\,\sin(\alpha_{M,\max}\cdot\tilde{\alpha}_M) \end{bmatrix}}_{\boldsymbol{c}^T(\tilde{\alpha}_M)} \boldsymbol{x}\,. \tag{19}$$

A subsequent analysis regarding the controllability leads to the following condition: The angular velocity ω_P must not vanish; this holds because the drive motor operates at a constant angular velocity $\omega_P \neq 0$. The tilt angle of the motor is confined to strictly positive values $\tilde{\alpha}_M \in \{\varepsilon_M, 1\}$, $\varepsilon_M > 0$.

Based on the quasi-linear representation (18), an eigenvalue placement is performed to calculate the state-dependent feedback gains $\boldsymbol{k}^T(\boldsymbol{x})$. In a next step, a feedforward control u_{FF} is designed to achieve steady state accuracy. For a further improvement of the tracking behaviour, a dynamic disturbance rejection is introduced. The overall control input can be calculated as the sum of all three control actions

$$u_P = -\boldsymbol{k}^T(\boldsymbol{x})\,\boldsymbol{x} + u_{FF} - u_{DC}\,. \tag{20}$$

Eigenvalue Assignment Using Extended Linearisation

The quasi-linear dynamical system to be stabilised is given by (18) – characterised by a state-dependent system matrix $\boldsymbol{A} = \boldsymbol{A}(\omega_p, \tilde{\alpha}_P)$ and an input vector $\boldsymbol{b}$. The feedback control design in the form of an eigenvalue placement involves the symbolic computation of a state-dependent gain vector $\boldsymbol{k}^T = \boldsymbol{k}(\omega_p, \tilde{\alpha}_P)^T$ by a comparison of the desired characteristic polynomial of the closed-loop system

$$p_{cd}(s) = (s - s_{c1})\,(s - s_{c2})\,, \tag{21}$$

specifying two desired eigenvalues s_{ci}, $i = \{1, 2\}$, with the following characteristic equation

$$p_c(s) = \det(s\boldsymbol{I}_2 - \boldsymbol{A}_c(\boldsymbol{k}^T))\,. \tag{22}$$

In (22), $\boldsymbol{I}_2$ is the 2×2 identity matrix and $\boldsymbol{A}_c$ the closed-loop system matrix

$$\boldsymbol{A}_c := \boldsymbol{A} - \boldsymbol{b}\boldsymbol{k}^T(\omega_p, \tilde{\alpha}_P)\,. \tag{23}$$

The state feedback is calculated by $u_{FB} = -\boldsymbol{k}^T(\omega_p, \tilde{\alpha}_P)\,\boldsymbol{x}$ with the state- and parameter-dependent gain vector

$$\boldsymbol{k}(\omega_p, \tilde{\alpha}_P) = \begin{bmatrix} \dfrac{-((s_{c1} + s_{c2})\,T_{uP} + 1)}{k_P} \\ \dfrac{s_{c1}\,s_{c2}\,C_H \cos(\alpha_{P,\max}\cdot\tilde{\alpha}_P)\,T_{uP}}{2\,\tilde{V}_P\,\omega_P\,\mathrm{si}(\alpha_{P,\max}\cdot\tilde{\alpha}_P)\,\alpha_{P,\max}\,k_P} \end{bmatrix}. \tag{24}$$

Feedforward Control Design Using Extended Linearisation

For the feedforward control design, the hydraulic torque τ_M generated by the hydraulic motor according to (11) is considered as the controlled variable. Thus, the nonlinear output equation is given by (19) and depends on $\tilde{\alpha}_M$. The command transfer function can be calculated as

$$G_b(s) = \frac{Y(s)}{U_{FF}(s)} = \boldsymbol{c}^T\,(s\boldsymbol{I} - \boldsymbol{A}_c)^{-1}\,\boldsymbol{b} = \frac{b_0}{N(s)}\,. \tag{25}$$

Obviously, the numerator of the control transfer function contains no transfer zero. The main idea of the feedforward control design is the modification of the numerator of the control transfer function by introducing a polynomial ansatz for the feedforward control action in the Laplace domain according to

$$U_{FF}(s) = \left[k_{V0} + k_{V1}\cdot s + k_{V2}\cdot s^2\right] Y_d(s)\,. \tag{26}$$

For its implementation, the desired trajectory $y_d(t) = \tau_{M,d}(t)$ as well as the first two time derivatives are available from a state variable filter. The feedforward gains can be computed from a comparison of the corresponding coefficients in the numerator as well as the denominator polynomials of

$$\frac{Y(s)}{Y_d(s)} = \frac{b_0 \cdot \left[k_{V0} + k_{V1} \cdot s + k_{V2} \cdot s^2\right]}{a_0 + a_1 \cdot s + a_2 \cdot s^2} \tag{27}$$

according to

$$a_i = b_0 \cdot k_{Vi}\ , \text{ with } i = 0,1, n = 2\,. \tag{28}$$

The feedforward control is evaluated in the time domain with

$$u_{FF} = k_{V0}\,\tau_{M,d} + k_{V1}\,\dot{\tau}_{M,d} + k_{V2}\,\ddot{\tau}_{M,d}\ . \tag{29}$$

Dynamic Disturbance Compensation Using Extended Linearisation

The disturbance z in (18) depends on the unknown leakage flow q_U, which has to be estimated, and the states ω_M and $\tilde{\alpha}_M$. This disturbance has to be compensated to achieve an acceptably small tracking error. The disturbance transfer function from the disturbance input to the controlled output becomes

$$G_e(s) = \frac{Y(s)}{Z(s)} = \boldsymbol{c}^T\,(s\boldsymbol{I} - \boldsymbol{A}_c)^{-1}\,\boldsymbol{e}\,. \tag{30}$$

For an ideal disturbance compensation, the condition

$$Y(s) = G_b(s) \cdot U_c(s) + G_e(s) \cdot Z(s) \stackrel{!}{=} 0 \tag{31}$$

has to be fulfilled exactly. As an approximation, an ansatz function $G_c(s)$ for the dynamic disturbance compensation is used according to

$$U_{DC}(s) = G_d c(s) \cdot Z(s) = [k_{dc0} + k_{dc1} \cdot s] \cdot Z(s)\,. \tag{32}$$

This ansatz function requires values for the disturbance and its first time derivative. By inserting (32) in (31), the design condition becomes

$$0 \stackrel{!}{=} \underbrace{Z(s)}_{\neq 0}\underbrace{[G_b(s) \cdot G_c(s) + G_e(s)]}_{\stackrel{!}{=}0}. \tag{33}$$

For an approximate dynamic disturbance compensation, the corresponding ansatz coefficients are chosen in such a way that the first two coefficients in the nominator polynomial vanish. For the evaluation of the dynamic disturbance compensation

$$u_{DC} = k_{dc0}\,z + k_{dc1}\,\dot{z} \tag{34}$$

the required time derivative of the lumped disturbance $\dot{z}$ is calculated by real differentiation.

4 Sliding Mode State and Disturbance Observer

Regarding the state variables of the test rig, see (12), only the difference pressure and the angular velocity of the hydraulic motor are measured $\boldsymbol{y}_m = [\Delta p\ \omega_M]^T$. However, it can be seen in that the remain unmeasured states and disturbances $\boldsymbol{x}_1 = [\tilde{\alpha}_P\ \tilde{\alpha}_M\ q_U\ \tau_U]^T$ are needed for calculation of the control inputs e.g. (20, 34). The sliding mode observer design, cf. [11] for the case of a linear system, is based on the extended system model with integrators as disturbance models

$$\dot{\boldsymbol{z}}_S = \begin{bmatrix} \dot{\tau}_U \\ \dot{q}_U \end{bmatrix} = \begin{bmatrix} 0 \\ 0 \end{bmatrix}\ . \tag{35}$$

Following the idea of extended linearisation, which is already used in Sect. 3, the extended system with the corresponding state vector

$$\boldsymbol{x}_e = \left[\boldsymbol{x}_1{}^T \,\vdots\, \boldsymbol{y}_m{}^T\right]^T = \left[\tilde{\alpha}_P\ \ \tilde{\alpha}_M\ \ \tau_U\ \ q_U \,\vdots\, \Delta p\ \ \omega_M\right]^T \tag{36}$$

is rewritten in a quasi-linear form with a state-dependent system matrix $\boldsymbol{A}_e(\tilde{\alpha}_P, \tilde{\alpha}_M, \omega_M)$

$$\dot{\boldsymbol{x}}_e = \boldsymbol{A}_e(\tilde{\alpha}_P, \tilde{\alpha}_M, \omega_M)\,\boldsymbol{x}_e + \boldsymbol{B}_e\,\boldsymbol{u}\,, \tag{37}$$

$$\boldsymbol{y}_m = \boldsymbol{C}_e\,\boldsymbol{x}_e\,. \tag{38}$$

The extended input and output matrices are denoted as $\boldsymbol{B}_e$ and $\boldsymbol{C}_e$, respectively. The observability can be easily confirmed by point-wise checking the observability matrix of the quasi-linear system, which depends on both $\tilde{\alpha}_M$ and ω_M. For the observer design, the state-space representation is written as

$$\begin{bmatrix} \dot{\boldsymbol{x}}_1 \\ \dot{\boldsymbol{y}}_m \end{bmatrix} = \begin{bmatrix} \boldsymbol{A}_{11} & \boldsymbol{A}_{12} \\ \boldsymbol{A}_{21} & \boldsymbol{A}_{22} \end{bmatrix} \begin{bmatrix} \boldsymbol{x}_1 \\ \boldsymbol{y}_m \end{bmatrix} + \begin{bmatrix} \boldsymbol{B}_1 \\ \boldsymbol{B}_2 \end{bmatrix} \boldsymbol{u}\,. \tag{39}$$

The observer has the form

$$\begin{aligned} \begin{bmatrix} \dot{\hat{\boldsymbol{x}}}_1 \\ \dot{\hat{\boldsymbol{y}}}_m \end{bmatrix} &= \begin{bmatrix} \boldsymbol{A}_{11} & \boldsymbol{A}_{12} \\ \boldsymbol{A}_{21} & \boldsymbol{A}_{22} \end{bmatrix} \begin{bmatrix} \hat{\boldsymbol{x}}_1 \\ \hat{\boldsymbol{y}}_m \end{bmatrix} + \begin{bmatrix} \boldsymbol{B}_1 \\ \boldsymbol{B}_2 \end{bmatrix} \\ &\quad - \begin{bmatrix} \boldsymbol{G}_1 \\ \boldsymbol{G}_2 \end{bmatrix} (\hat{\boldsymbol{y}}_m - \boldsymbol{y}_m) + \begin{bmatrix} \boldsymbol{L} \\ -\boldsymbol{I} \end{bmatrix} \boldsymbol{v}\,, \end{aligned} \tag{40}$$

where $\hat{(\cdot)}$ represents the estimated values. $\boldsymbol{G}_1$ and $\boldsymbol{G}_2$ denotes Luenberger-type gain matrices, $\boldsymbol{L}$ gain matrix for the discontinuous switching part, which is defined by the vector $\boldsymbol{v}$ according to

$$\boldsymbol{v} = \begin{bmatrix} M_1\,\mathrm{sign}(\Delta\hat{p} - \Delta p) \\ M_2\,\mathrm{sign}(\hat{\omega}_M - \omega_M) \end{bmatrix}\,. \tag{41}$$

Here, $M_{1,2}$ represent positive, constant gains. Considering the definition $\boldsymbol{e}_1 = \hat{\boldsymbol{x}}_1 - \boldsymbol{x}_1$ and $\boldsymbol{e}_{y_m} = \hat{\boldsymbol{y}}_m - \boldsymbol{y}_m$ and introducing a new error variable $\bar{\boldsymbol{e}}_1 = \boldsymbol{e}_1 + \boldsymbol{L}\boldsymbol{e}_{y_m}$, the resulting estimation error dynamics becomes

$$\begin{bmatrix} \dot{\bar{\boldsymbol{e}}}_1 \\ \dot{\boldsymbol{e}}_{y_m} \end{bmatrix} = \begin{bmatrix} \bar{\boldsymbol{A}}_{11} & \bar{\boldsymbol{A}}_{12} \\ \boldsymbol{A}_{21} & \bar{\boldsymbol{A}}_{22} \end{bmatrix} \begin{bmatrix} \bar{\boldsymbol{e}}_1 \\ \boldsymbol{e}_{y_m} \end{bmatrix} + \begin{bmatrix} \boldsymbol{0} \\ -\boldsymbol{I} \end{bmatrix} \boldsymbol{v}\,, \tag{42}$$

where the submatrices are given by

$$\bar{\boldsymbol{A}}_{11} = \boldsymbol{A}_{11} + \boldsymbol{L}\boldsymbol{A}_{21}\ , \tag{43}$$

$$\bar{\boldsymbol{A}}_{12} = \boldsymbol{A}_{12} - \bar{\boldsymbol{A}}_{11}\,\boldsymbol{L} - \boldsymbol{G}_1 + \boldsymbol{L}\,(\boldsymbol{A}_{22} - \boldsymbol{G}_2)\ , \tag{44}$$

$$\bar{\boldsymbol{A}}_{22} = \boldsymbol{A}_{22} - \boldsymbol{G}_2 - \boldsymbol{A}_{21}\,\boldsymbol{L}\ . \tag{45}$$

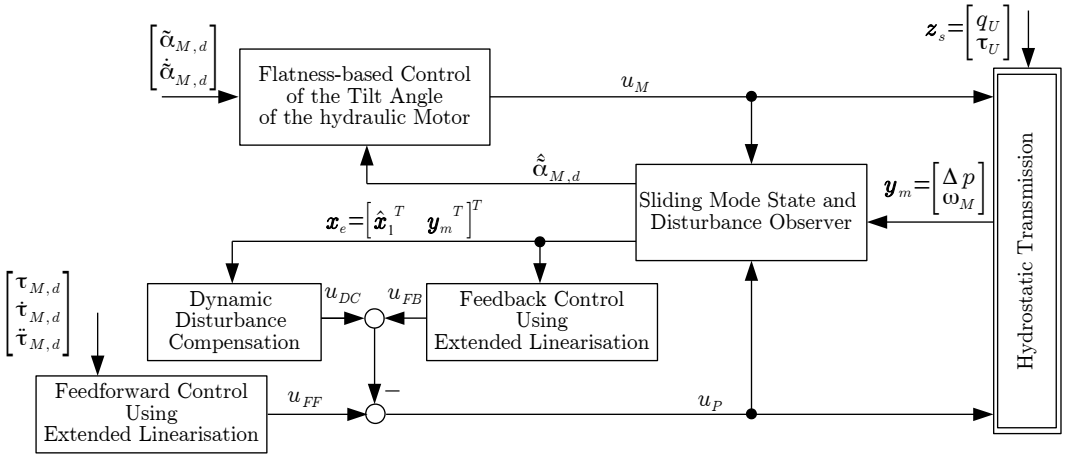

Figure 7: Block diagram of the implemented control structure.

$\bar{\boldsymbol{A}}_{12} = \boldsymbol{0}$ can be achieved by proper choice of the gain matrix $\boldsymbol{G}_1$. In the case of $\boldsymbol{\upsilon} = \boldsymbol{0}$, asymptotic stability of the error dynamics (42) is obtained by choosing the gain matrices $\boldsymbol{L}$ and $\boldsymbol{G}_2$ according to

$$\boldsymbol{A}_{11} + \boldsymbol{L}\boldsymbol{A}_{21} = \bar{\boldsymbol{A}}_{11}^{*}\,, \tag{46}$$

$$\boldsymbol{A}_{22} - \boldsymbol{G}_2 - \boldsymbol{A}_{21}\,\boldsymbol{L} = \bar{\boldsymbol{A}}_{22}^{*}\,, \tag{47}$$

where $\bar{\boldsymbol{A}}_{11}^{*}$ and $\bar{\boldsymbol{A}}_{22}^{*}$ denote asymptotically stable matrices with the following characteristic polynomials

$$\det(s\boldsymbol{I} - \bar{\boldsymbol{A}}_{11}^{*}) \stackrel{!}{=} (s - s_{B1})(s - s_{B2})(s - s_{B3})(s - s_{B4})\,,$$
$$\det(s\boldsymbol{I} - \bar{\boldsymbol{A}}_{22}^{*}) \stackrel{!}{=} (s - s_{B5})(s - s_{B6})\,. \tag{48}$$

The additional switching input $\boldsymbol{\upsilon}$ provides robustness against certain classes of model uncertainty. Considering the chattering caused by the discontinuous components, the tanh function is used in the implementation instead of the sign function.

5 Simulation Results

In this section, a simulation study of the proposed robust nonlinear control in combination with the sliding mode state and disturbance observer for the hydrostatic transmission is demonstrated. The implemented control structure is depicted in Fig. 7. To be more realistic, the parametrisation of the leakage flow is assumed to be proportional to the pressure difference according to

$$q_U = 1 \cdot 10^{-12}\,\Delta p\,, \tag{49}$$

whereas the disturbance torque is given by

$$\tau_U = 0.1\,J_V\,\dot{\omega}_M + 7\,\tanh\left(\frac{\omega_M}{0.1}\right)\,. \tag{50}$$

In addition to the disturbance models, a measurement noise is added to the difference pressure Δp and the motor angular velocity ω_M, which are the only measurable state variables at the test rig.

The obtained results from the simulation are depicted in the following figures. At first, the tracking performance of $\tilde{\alpha}_M$ and τ_{hyd} is investigated. Fig. 8 shows the desired and the simulated trajectory of the hydraulic motor torque, which match well. In addition, the tracking performance for the control

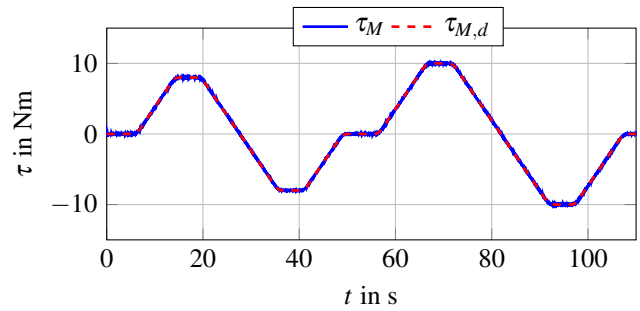

Figure 8: Tracking behaviour of the hydraulic motor torque (simulation results).

loop for the normalised tilt angle of the hydraulic motor is presented in Fig. 9, which indicates an highly accurate tracking behaviour. As a result of the balance of momentum at the

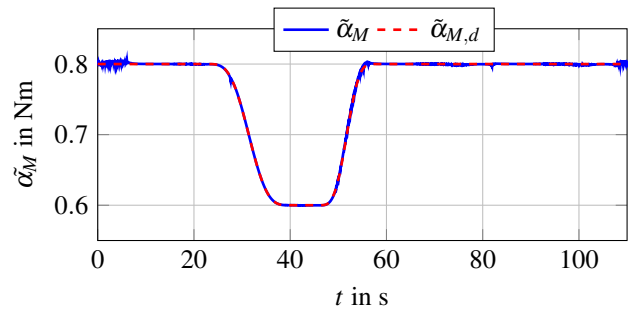

Figure 9: Comparison of desired and simulated values of the normalised tilt angle of the hydraulic motor (simulation results).

hydraulic motor, the related angular velocity ω_M is obtained as shown Fig. 10.

The next figures point out the benefits of the disturbance es-

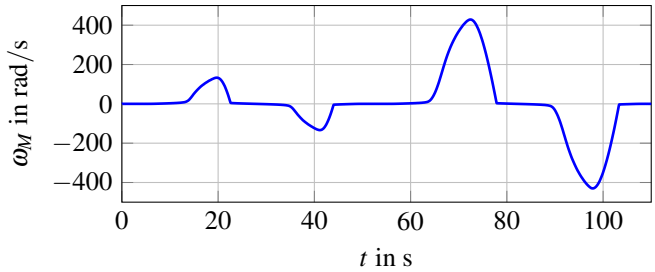

Figure 10: Angular velocity of the hydraulic motor (simulation results).

timation by the sliding mode observer. The modelled disturbance torque as well as the estimated torque are shown in Fig. 11. It becomes obvious that the observer is capable of reconstructing this unknown disturbance. The same holds for the other disturbance, the leakage flow, which is depicted in Fig. 12. Given the positive results from the simulations, the control approach is implemented and validated at the test rig, see Fig. 1.

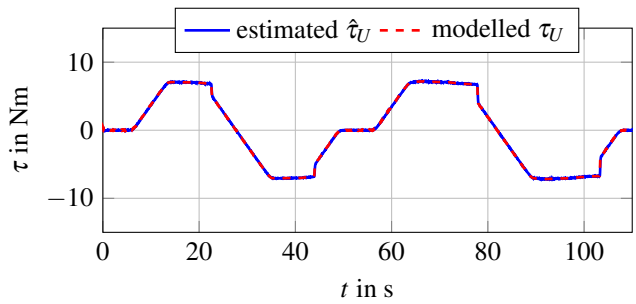

Figure 11: Comparison of the simulated and estimated disturbance torques (simulation results).

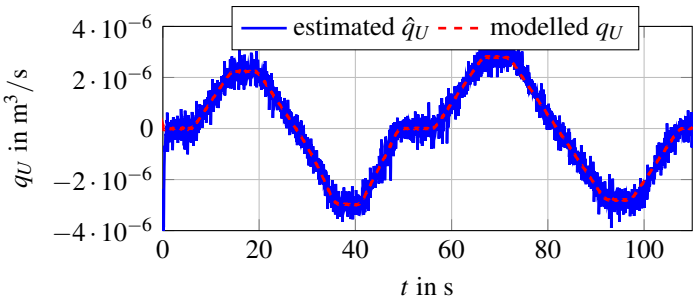

Figure 12: Comparison of the simulated and estimated leakage flow rates (simulation results).

6 Experimental Results

In the sequel, the experimental results are presented using the implementation of the control structure according to Fig. 7. A LabVIEW real-time environment is used to operate the test rig. The electric motor that drives the hydraulic pump has at a constant angular velocity of $\omega_P = 700$ rpm $=$ const. This is achieved by an underlying velocity control on a current converter. However, for the operation of the electric load motor two alternative control scenarios – either torque mode or velocity mode – are considered to validate the proposed control structure. Note that the torque of the hydraulic motor τ_M is not measured. This value is calculated by (11), where the estimated value of motor tilt angle $\hat{\tilde{\alpha}}_M$ is used.

Load Motor Operates in a Torque Mode

In the torque mode, an underlying torque control on the current converter is employed for the electric load motor. Here, the desired load torque is chosen as $\tau_U = 0$ Nm. In Fig. 13, the tracking behaviour of the normalised tilt angle of the hydraulic motor $\tilde{\alpha}_M$, which is controlled in the first loop, is depicted. As the motor tilt angle $\tilde{\alpha}_M$ is not measurable, the corresponding estimated value is plotted.

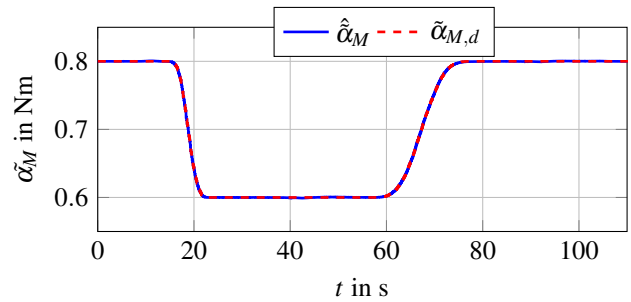

Figure 13: Comparison of actual and desired values of the normalised tilt angle of the hydraulic motor (experimental results).

Fig. 14 shows the tracking behaviour of the hydraulic torque provided by the hydraulic motor, which is controlled in the second loop. Due to the torque balance at the hydraulic motor, the angular velocity of the drive side ω_M varies, see Fig. 15.

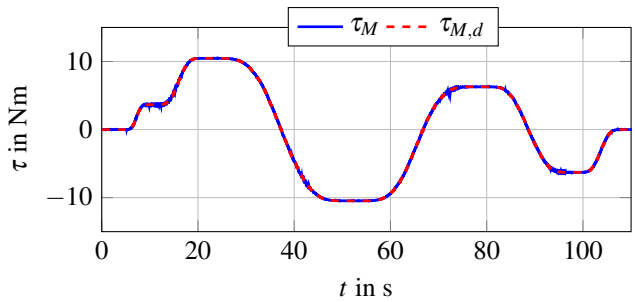

Figure 14: Comparison of actual and desired values of the torque of the hydraulic motor (experimental results, electric load motor operates in a torque mode).

Load Motor Operates in a Velocity Mode

In the second scenario the electric load motor operates at a constant velocity $\omega_M = 200$ rpm $=$ const. The necessary control for the electric load motor is provided by a corresponding current converter. The obtained tracking behaviour of the hydraulic motor torque, which is characterized by only small er-

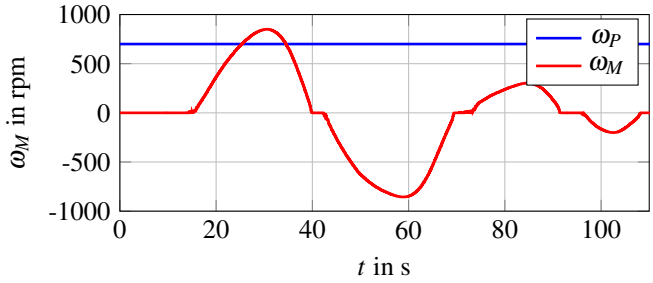

Figure 15: Angular velocities of the electric motors: constant angular velocity at the drive motor and varying angular velocity at the load motor (experimental results, electric load motor operates in a torque mode).

rors, is presented in Fig. 16. Furthermore, the corresponding pressures are depicted in Fig. 17.

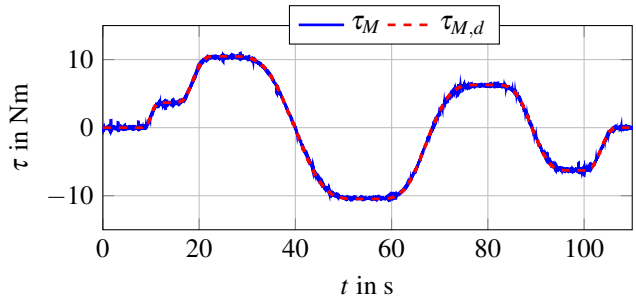

Figure 16: Comparison of actual and desired values of the hydraulic motor torque in the velocity mode (experimental results, electric load motor operates in a velocity mode).

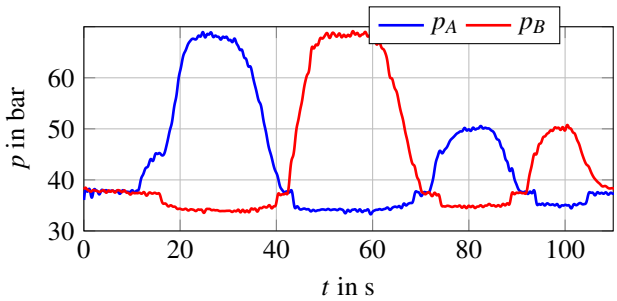

Figure 17: Pressures in both hydraulic hoses during tracking of the torque of the hydraulic motor (experimental results, electric load motor operates in a velocity mode).

7 Conclusions and Outlook on Further Work

Based on a decentralised control structure of the hydrostatic transmission, an innovative decentralised nonlinear control structure has been designed. The the hydraulic motor torque of the hydrostatic transmission is controlled using extend linearisation techniques, whereas the control of normalised tilt angle of the hydraulic motor is realized by a flatness-based approach. Moreover, a sliding mode observer – designed by using extended linearisation techniques as well – is introduced to robustly estimate unmeasurable system states and unknown disturbances. The proposed cascaded control structure has been successfully validated in simulations as well by the experimental results.

To further increase the accuracy of the identified mechatronic model of the test-rig, a torque sensor will be installed between the hydraulic motor and the electric load motor. With this future enhancement of the test rig, the tracking behaviour of the controlled hydrostatic transmission is expected to be improved.

References

[1] B. Dolan and H. Aschemann. Control of a Wind Turbine With a Hydrostatic Transmission - An Extended Linearisation Approach. In *17th Int. Conf. on Methods and Models in Automation and Robotics (MMAR)*, pages 445–450, Poland, 2012.

[2] N.F.B. Diepeveen and A.J. Laguna. Dynamics Modelling of Fluid Power Transmissions for Wind Turbine. In *EWEA Offshore*, Netherland, 2011.

[3] H. Schulte and P. Gerland. Control-Oriented Modeling of Hydrostatic Power-Split CVTs Using Takagi-Sugeno Fuzzy Models. In *7th Conf. of the European Society for Fuzzy Logic and Technology (EUSFLAT)*, pages 797–804, France, 2011.

[4] H. Sun and H. Aschemann. Quasi-Continuous Sliding Mode Control Applied to a Hydrostatic Transmission. In *European Control Conference (ECC)*, Austria, 2015.

[5] H. Sun, R. Prabel, and H. Aschemann. Cascaded Control Design for the Tracking Control of a Hydrostatic Transmission Based on a Sliding mode State and Disturbance Observer. In *21st Int. Conf. on Methods and Models in Automation and Robotics (MMAR)*, pages 432–437, Poland, Aug 2016.

[6] M. Jelali and A. Kroll. *Hydraulic Servo-Systems: Modelling, Identification and Control*. Springer-Verlag, UK, 2003.

[7] P. Rohner. *Industrial Hydraulic Control: A Textbook for Fluid Power Technicians*. John Wiley & Sons, 2004.

[8] A. Kugi, K. Schlacher, H. Aitzetmueller, and G. Hirmann. Modelling and Simulation of a Hydrostatic Transmission with Variable-Displacement Pump. In *Mathematics and Computers in Simulation*, volume 53, pages 409–414, 2000.

[9] M. Fliess, J. Levine, P. Martin and P. Rouchon. Flatness and Defect of Nonlinear Systems: Introductory Theory and Examples. In *Int. J. Control*, volume 61, pages 1327–1361, 1995.

[10] B. Friedland. *Advanced Control System Design*. Prentice Hall, 1996.

[11] C. Edwards and S.K. Spurgeon. *Sliding Mode Control: Theory and Applications*. Taylor & Francis Ltd, 1998.

Design and Optimization of a Fast Switching Hydraulic Step-Down Converter for Position and Speed Control

Marcos P. Nostrani[1], Alessio Galloni[2], Henrique Raduenz[1], Victor J. De Negri[1]

[1]Mechanical Engineering Department, Federal University of Santa Catarina, Florianópolis, SC/Brazil
E-mail: marcos.nostrani@gmail.com, alessio.galloni@hotmail.com, henrique@laship.ufsc.br, victor.de.negri@ufsc.br
[2]Università degle studi di Modena e Reggio Emilia, Modena, Italy

Abstract

This paper presents a design process of a hydraulic step-down switching converter considering the load losses in the inertance tube and switched valve. A steady state analysis for the switching converter as well as nonlinear dynamic simulation results of a digital hydraulic position and speed control system are presented. The results using the steady state and dynamic models are validated by experimental results obtained using a hydraulic test bench able to apply different loads to the system. The results show that steady-state model provides a very good approach to perform the preliminary design of hydraulic switching converters. The impact of tube parameters in the system efficiency is also discussed.

Keywords: Digital hydraulics, Hydraulic step-down converter, PWM switched valve.

1 Introduction

New hydraulic systems and components have been developed in the last decades, most of them resulting from the integration of electronic devices and improvement of manufacturing. However, hydraulic systems are known by their low efficiency, usually below 50% [1] caused by the extensive use of valves that throttle the flow to control pressure and flow rate, generating heat. Despite of that, hydraulic systems are extremely used in many fields due to the low weight power ratio and great reliability [2].

In order to improve the hydraulic systems efficiency, new technologies have been investigated. One approach is either the velocity and position control using variable displacements pumps and motors [3] or fixed and variable pumps driven by variable speed electrical motors [4] [5]. Moreover, another technology in development is the digital hydraulics [2] [6] [7] [8].

Digital hydraulics emerges as a technique to avoid the resistive pressure and flow rate control using mainly on/off valves. This new technology has two major derivations. The first denominated *Parallel Connection* connects in parallel several hydraulic components in order to provide discrete output values [9]. The second is known as *Fast Switching Hydraulics* (FSH). In these systems, the input signals usually use the pulse-width modulation technique (PWM) where the system output is set by the input duty cycle. For FSH systems, normally an inductive element is used for implementing fluid inertia. The most used element (for that purpose) is a hydraulic tube with high length and small diameter called *Inertance Tube.* The characteristic behaviour of these systems is determined by the valve-tube configuration. If the tube is placed before the valve, the system is called *pressure booster* or *step-up converter.* On the opposite case, the system is called *flow booster* or *step-down converter* [6] [10] [11].

The FSH systems were initially studied by Brown in the 1980s [12] [13] where high efficiency is expected, considering that flow and pressure control are not dissipative. However, as discussed in [1] and [14] , the valve and inertance tube introduce load losses that can reduce the efficiency considerably. Therefore, the correct choice of the parameters of the system such as diameter and length of the tube can significantly influence its performance.

In this paper, the design of a digital fast switching hydraulic step-down converter for position and speed control is presented. Experimental results obtained using a test bench are presented. Furthermore, a mathematical steady–state model and a nonlinear model of the entire system are presented-and the simulation results compared.

2 Hydraulic Step-Down Converter

The fundamental circuit of a hydraulic step-down converter is shown in fig. 1. This system is basically composed by a switching on/off valve and an inertance tube. The output pressure can be modulated from the low supply pressure to the high supply, working as a pressure regulator.

The working principle of a hydraulic step-down converter is based in the acceleration and deceleration of the fluid mass inside the inertance tube by fast switching the valve. According to Figure 1, when the valve connects ports P to A, keeping T closed, the internal pressure (p_{Ain}) increases to

the high supply pressure (p_{HS}). It causes the acceleration of the fluid inside the inertance tube. When the valve switches to the other position, linking port T to A and closing P, the fluid momentum inside the tube makes the internal pressure to fall below the low supply pressure (p_{LS}), suctioning fluid from the low pressure supply line [14]. This system arrangement needs a low supply pressure different than zero in order to avoid cavitation. The output load pressure (p_L) value can be varied by the PWM duty cycle (κ), that is the portion of time in which the valve remains opened to the high supply pressure during a certain switching period.

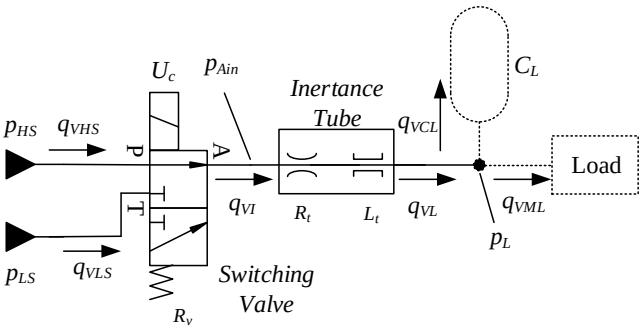

Figure 1 - Step-Down fundamental hydraulic circuit.

Figure 2 shows the PWM signal applied to the valve as well as the average load pressure.

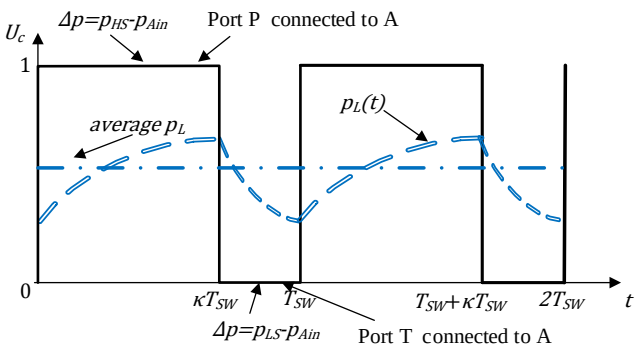

Figure 2 - System response representation.

In order to predict the real system behaviour, a mathematical steady-state was proposed in [14] and a nonlinear dynamic model presented in [15]. These models were used to design a position and speed control system aiming to achieve the higher efficiency as possible without compromising the system dynamics. The models have been developed considering the scheme shown in fig. 3.

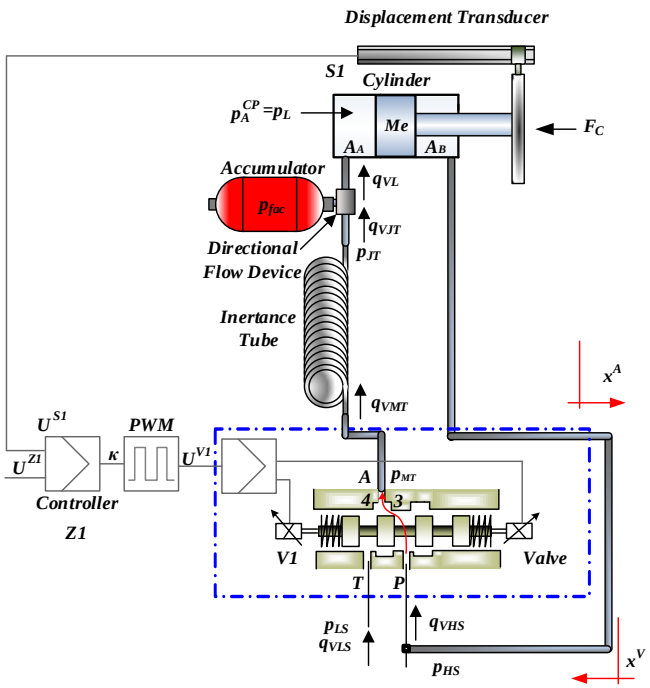

Figure 3 - Fast switching hydraulic step-down converter scheme (Adapted from [16]).

3 Dimensioning of the Step-Down Converter

3.1 Steady-State Model

A model describing the steady-state behavior of a hydraulic step-down converter was proposed in [14]. Based on that, the average output load pressure depends on the tube and valve resistances (R_{eq}), the load flow rate (q_{VL}), the supply pressures (p_{HS} and p_{LS}) and the PWM duty cycle (κ) and can be calculated by:

$$p_L = (p_{HS} - p_{LS})\kappa + p_{LS} - q_{VL}R_{eq}. \qquad (1)$$

The step down system can modulate the load pressure from the low supply pressure (p_{LS}) to the high supply pressure (p_{HS}). However, when the required flow rate is different than zero, the load pressure is reduced by the load losses inside the inertance tube and valve.

The system efficiency can be evaluated dividing the power consumed by the power supplied by [14]:

$$\eta = \frac{q_{VL}[p_{HS}\kappa + p_{LS}(1-\kappa)] - q_{VL}{}^2 R_{eq}}{\frac{(p_{HS}-p_{LS})^2\psi}{R_{eq}} + q_{VL}[p_{HS}\kappa + p_{LS}(1+\kappa)]}, \qquad (2)$$

where,

$$\psi = \kappa(1-\kappa) - \frac{\tau(1-e^{-T_{sw}(1-\kappa)/\tau})(1-e^{-T_{sw}\kappa/\tau})}{(1-e^{-T_{sw}/\tau})T_{sw}}. \qquad (3)$$

The system efficiency depends on the switching period (T_{SW}) and also the time constant (τ), besides the other

system parameters mentioned before. The time constant is a function of the tube inductance and the equivalent system resistance ($\tau = L_t/R_{eq}$), where the equivalent resistance is the sum of the valve (R_v) and tube (R_t) resistances. The tube inductance and resistance can be determined, respectively, by [17] [18]:

$$L_t = \frac{4\rho l_t}{\pi d_t^2} \tag{4}$$

and

$$R_t = \frac{128\rho l_t \nu}{\pi d_t^4} \tag{5}$$

The variation of the tube parameters (length and diameter) affects the time constant and, consequently, the system efficiency.

To have an initial estimative of tube length value, ref.[14] presents an equation for the optimum tube length for maximizing the efficiency without taking into account the valve resistance, that is:

$$l_t = \frac{-f_1\psi + \sqrt{(f_1\psi)^2 + f_2}}{f_3}\pi d_t^4, \tag{6}$$

where.

$$f_1 = 2q_{VL}^{\ 2}(p_{HS} - p_{LS})^2,$$

$$f_2 = 4q_{VL}^{\ 4}(p_{HS} - p_{LS})^2[(p_{HS}\kappa + p_{LS})^2 - p_{LS}^{\ 2}\kappa^2], \text{ and}$$

$$f_3 = 256q_{VL}^{\ 3}\rho\nu[p_{HS}\kappa + p_{LS}(1+\kappa)].$$

In the next section, the eq. (2) to (6) are used to select the tube aiming to achieve the highest efficiency.

3.2 System Design

The system analyzed is a wind turbine pitch angle (β) positioning control prototype installed in the Laboratory of Hydraulic and Pneumatic Systems – Laship at Federal University of Santa Catarina – UFSC (fig. 4). The system comprises two double acting cylinders (Bosch Rexroth CDT3MT4/80/56/500/Z/1X/B11HFDTWW), two proportional reducing valves (Bosch Rexroth DREBE6X-1X/175MG24K31A1M), a proportional directional valve (Parker D1FPE50MA9NB01) seven pressure transmitters (HBM P15RVA1, P2VA1 and Zürich PSI-420), tree flow transmitters (Webtec CT 60 and CT150) and an incremental encoder (Veerder Root). The two pressure reducing valves and one of the cylinders are used to emulate the load forces up to 30 kN.

The position control system was previously designed to operate on a classical configuration using a proportional directional valve [19]. Aiming to study the performance and efficiency of a step-down converter, the system has changed to the configuration shown in fig.4 and fig. 5.

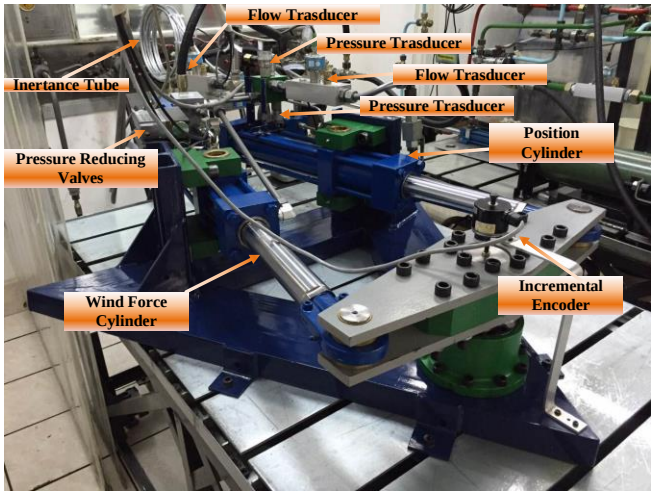

Figure 4 - Test rig: General view [15].

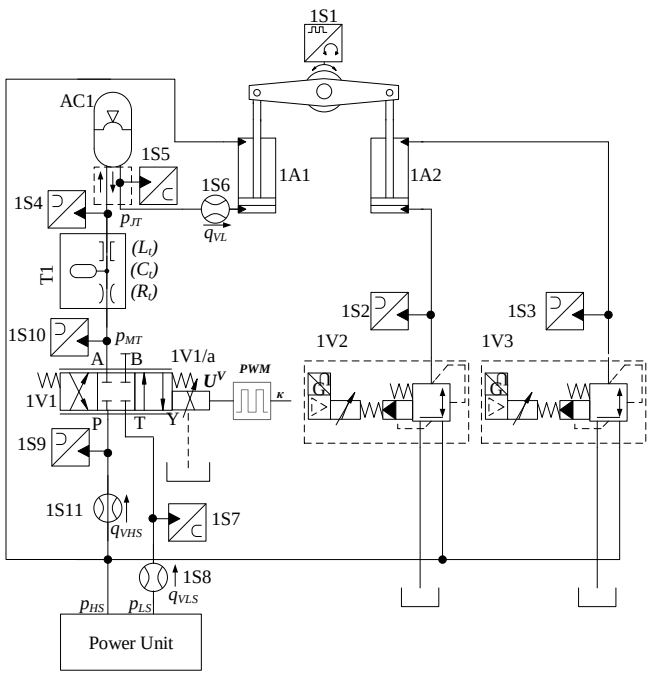

Figure 5 – Test rig: Hydraulic circuit diagram [15].

As discussed in [20] and [21], the required response of a closed loop positioning system can be described by a generic second order time step response. Therefore, assuming a critically damped behavior, the required settling time (t_s) can be related to the system natural frequency (ω_n) by:

$$\omega_n = \frac{6}{t_s} \tag{7}$$

and the maximum velocity occurring at the step response is:

$$v_{max} = 0.37x_{RP}\omega_n, \tag{8}$$

being x_{RP} the steady-state displacement.

Consequently, the corresponding maximum flow rate to the cylinder chamber A is given by:

$$q_{Vmax} = v_{max} A_A, \qquad (9)$$

where A_A is the area of chamber A.

The maximum pitch angle in a wind turbine is around 25° [22], for this reason an arbitrary angle of 8° was chosen as the step magnitude during the tests. Considering the test bench assembly (see fig. 4), this angle corresponds to a cylinder displacement of 41.6 mm. Assuming a desired settling time of 2 s, the maximum flow rate to the cylinder and, consequently, through the inertance tube, is 2×10^{-4} m^3/s for a cylinder area of 50.26×10^{-4} m^2.

As mentioned before, switching period, tube length and diameter are the main parameters that must be defined to design an efficient step-down system. The system parameters are listed in Table 1, where the switching frequency was set to 32 Hz taking into account the capability of the proportional valve to fully switch with duty cycles between 10 and 90 %. The valve time response is 3.5 ms.

Equations (1) to (6) were implemented in Matlab in order to analyze the influence of the tube length and diameter in the system efficiency. Figure 6 shows the results for a duty cycle of 50%, in which the influence of the parameters in the system performance is more significant [14].

Table 1- System parameters.

Parameter	Value
Effective Bulk modulus - β_e	1.6 x10^9 Pa
High supply pressure - p_{HS}	12 MPa
Kinematic viscosity - ν	32 x10^{-6} m^2/s
Low supply pressure - p_{LS}	1 MPa
Load average flow rate - q_{VL}	2 x10^{-4} m^3/s,
Switching period - T_{sw}	31.25 ms
Density - ρ	870 kg/m^3
Valve resistance - R_v	3.88 x10^9 Pa.s/m^3

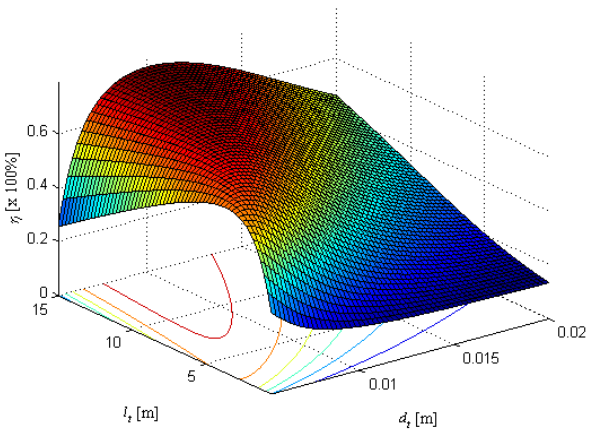

Figure 6- Efficiency for different tube length and diameters.

The results show that the system efficiency has a significant variation with different tube lengths and diameters. An initial estimative of the tube length and efficiency as function of the tube diameter can be obtained using eq. (6) and eq. (2), respectively, resulting on the curves shown in Figure 7.

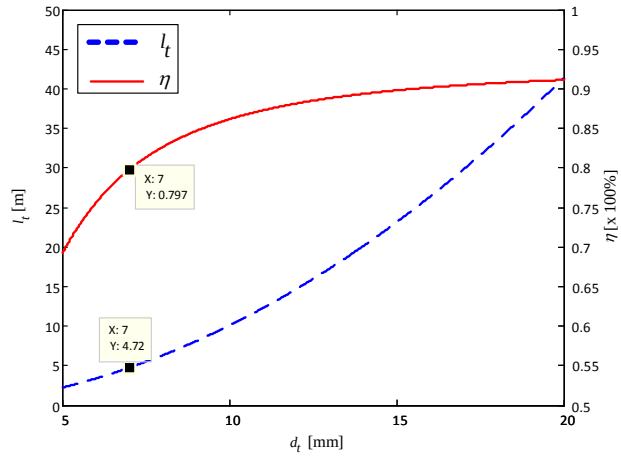

Figure 7- Tube length and efficiency versus diameter.

According to this figure, as the inner diameter of the tube increases, the length must be increased as well to result in the maximum efficiency, which also increases along with the diameter. Observing fig. 7, in this study a 7 mm tube diameter was chosen, resulting on a tube length equal to 4.72 m and a system efficiency of 79.7%.

However, as discussed in [14], the valve induces significant losses in the system and, therefore, its effect must be taken into account to calculate the final tube length. Fixing the tube diameter in 7 mm, the lengths resulting on maximum efficiencies can be calculated using eq. (2). These results are shown in fig. 8 where considering the valve resistance shown in Table 1, the resulting tube length is 7.76 m with system efficiency of 69.11%. For the experimental system, a commercial tube of 6 m length and 7 mm diameter was chosen, resulting on an efficiency of 68.22% (eq. (2)).

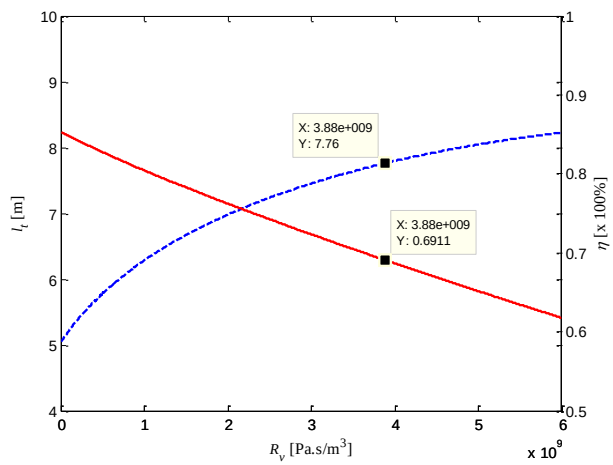

Figure 8- System efficiency with the valve resistance.

4 Dynamic Analysis

4.1 Nonlinear model

In order to predict the system dynamics using switched hydraulics, a nonlinear mathematical model was implemented in Matlab/Simulink and validated experimentally. The model has been developed considering the components shown in fig. 3 and the parameters presented in Table 2.

The flow rate q_{VMT} through the switching valve can be expressed by:

For $x^V \geq 0$ ($U^{V1} = 10\ V$):

$$q_{VMT} = \left(K_{v_A}.\frac{U^{V1}}{U_n} + K_{vin}\right).\sqrt{p_{HS} - p_{MT}} + K_{vin}.\sqrt{p_{LS} - p_{MT}}. \quad (10)$$

For $x^V < 0$ ($U^{V1} = -10\ V$):

$$q_{VMT} = \left(K_{v_A}.\frac{|U^{V1}|}{U_n} + K_{vin}\right).\sqrt{p_{LS} - p_{MT}} - K_{vin}.\sqrt{p_{HS} - p_{MT}}. \quad (11)$$

where U^{V1} is the control signal, U_n the nominal valve signal, K_{v_A} the flow coefficient, K_{vin} the leakage coefficient and p_{MT} the inlet tube pressure.

The accumulator is assembled in a flow direction device and its internal pressure, that it is equal to the tube downstream pressure, is described by:

$$\frac{dp_{fac}}{dt} = \frac{q_{VJT} - c_d A_{DC}\sqrt{\frac{2}{\rho}\left(p_{fac} - p_A^{CP}\right)}}{\frac{1}{\gamma}\frac{\left(V_0 - V_{fac}\right)^{\gamma+1}}{V_o^{\gamma}}\frac{1}{p_o} + \frac{V_{fac}}{\beta_e}}. \quad (12)$$

where q_{VJT} is the inlet flow rate to the accumulator, V_0 the initial volume, V_{fac} the fluid volume, p_o the accumulator initial pressure, p_L the load pressure, c_d the discharge coefficient, A_{DC} the flow passage area and γ the specific heat ratio of the gas.

The hydraulic actuator was modelled according the continuity equation and Newton's Second Law, resulting on:

$$q_{VL} = A_A\frac{dx^A}{dt} + \frac{V_A + x^A A_A}{\beta_e}\frac{dp_A^{CP}}{dt}, \quad (13)$$

and

$$(p_A^{CP}.A_A) - (p_{HS}.A_B) = M_e\frac{d^2x^A}{dt^2} + F_{at} + F_c, \quad (14)$$

where A_A is the chamber A area, A_B the chamber B area, p_A^{CP} the chamber A pressure, F_{at} the friction force, F_c the load force, V_{Ao} the chamber A initial volume and the V_A the chamber A volume. Friction force parameters used were based on [15], [22] and [23].

The inertance tube has been modelled according to the TLM (Transmission Line Method). More details can be found in [24], [25] and [26].

Table 2- System complementary parameters.

Parameter	Value
Effective Bulk modulus - β_e	1.6 x10^9 Pa
High supply pressure - p_{HS}	12 MPa
Kinematic viscosity - ν	32 x10^{-6} m^2/s
Low supply pressure - p_{LS}	1 MPa
Load average flow rate - q_{VL}	2 x10^{-4} m^3/s,
Switching period - T_{sw}	31.25 ms
Leakage coefficient - K_{vin}	1.4907 x10^{-9} m^3/s. Pa$^{1/2}$
Flow coefficient - K_{v_A}	3.5635 x10^{-7} m^3/s. Pa$^{1/2}$
Accumulator volume - V_0	0.350 L
Accumulator pre-load - p_o	5 MPa
Discharge coefficient - c_d	0.7
Flow passage area - A_{DC}	3.4510^{-5} m^2
Specific heat ratio - γ	1.4
Density - ρ	870 kg/m^3
Valve resistance - R_v	3.88 x10^9 Pa.s/m^3
Equivalent mass - M_e	63.4 kg

4.2 Simulation and Experimental Results

Figure 9 and Figure 10 show the pitch angle and the load pressure, respectively, for a sequence of step inputs. The system load is 5000 N against the actuator movement, and the proportional and integral gains are 0.7 and 0.1, respectively. The switched frequency used in the experiments is 32 Hz.

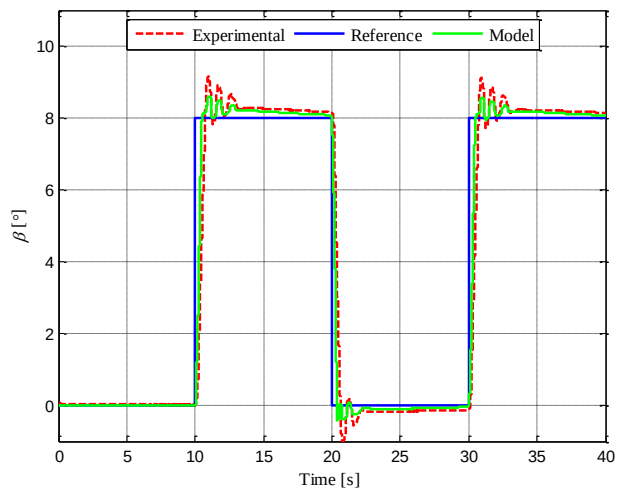

Figure 9 - Position control – Output Response.

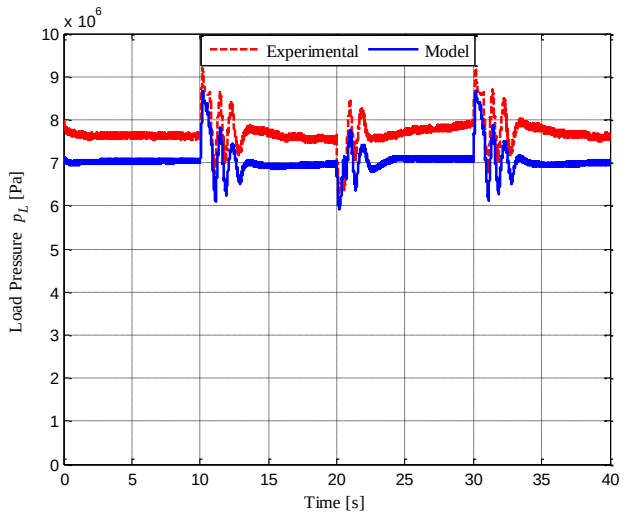

Figure 10 - Position control – Load pressure.

The results show that the model describes the real system with high accuracy, despite that the experimental load pressure is higher than the simulation results, due to the friction forces in the bearings that were not considered in the model.

The system response in open loop configuration was also analyzed by simulation. In this case, a PWM input voltage with duty cycle of 70% was applied to the valve and a constant load of 5000 N at the cylinder rod. Figure 11 shows the cylinder position in this open loop speed control configuration.

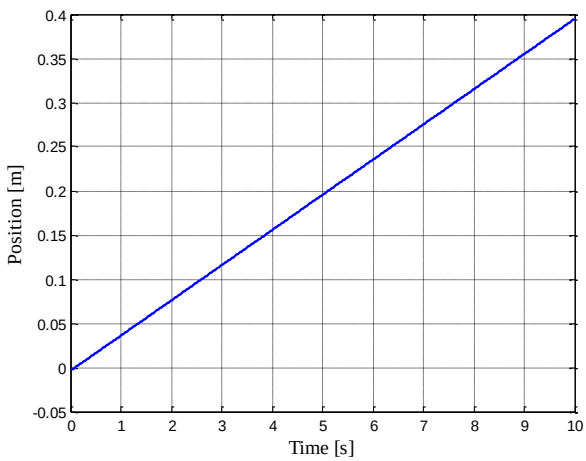

Figure 11 - Speed control – Cylinder Stroke.

Figure 12 and Figure 13 show the behavior of the load pressure and the load flow rate, respectively. The resulting velocity is 0.039 m/s and the average load pressure and average flow rate are 7.42 x10^6 Pa and 1.99 x10^{-4} m^3/s, respectively. The flow rate value is very close to those used for the system design.

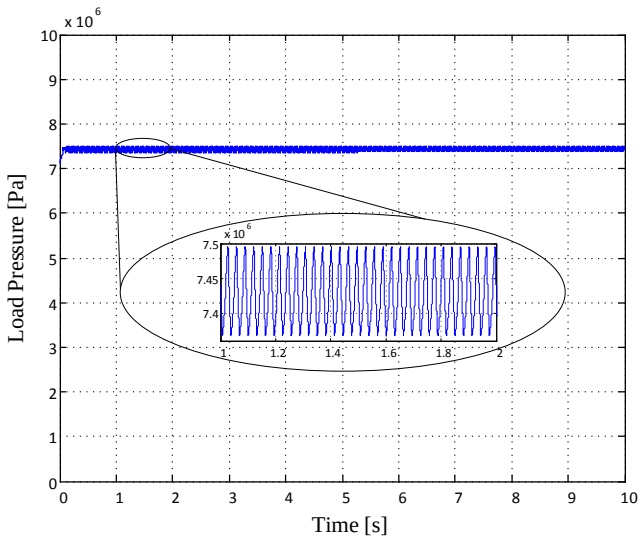

Figure 12 - Speed control – Load pressure.

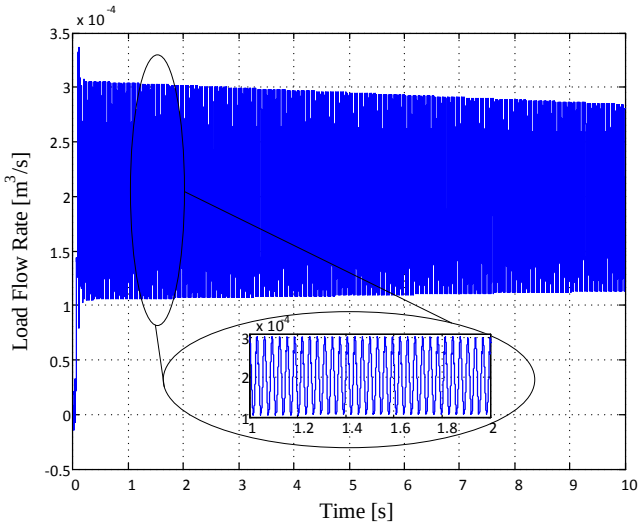

Figure 13 - Speed control - Load Flow rate.

4.3 Efficiency Analysis

In this section, the responses of the speed control system are compared with the results obtained using the steady state model presented in Section 3.1, aiming to verify the predicted performance using the chosen tube.

The energy associated to the cylinder chamber A can be evaluated according to:

$$E_A(t) = \int_0^t p_A^{CP}(t) q_{VL}(t) dt \qquad (15)$$

and the energies at the high and low supply pressure ports calculated, respectively, by:

$$E_{HP}(t) = \int_0^t p_{HS}(t) q_{VHS}(t) dt, \qquad (16)$$

and

$$E_{LP}(t) = \int_0^t p_{LS}(t) q_{VLS}(t) dt. \quad (17)$$

Therefore, based on simulation results using the nonlinear model, the system efficiency can be calculated by:

$$\eta = \frac{E_A(t)}{E_{HP}(t) + E_{LP}(t)}. \quad (18)$$

Figure 14 and Figure 15 show the load pressure and system efficiency, respectively, where the lines correspond to the results obtained using the steady-state model and the circle the operating point from the dynamic simulation. As mentioned in section 4.2, the system time response was analyzed with a duty cycle of 70 % as input.

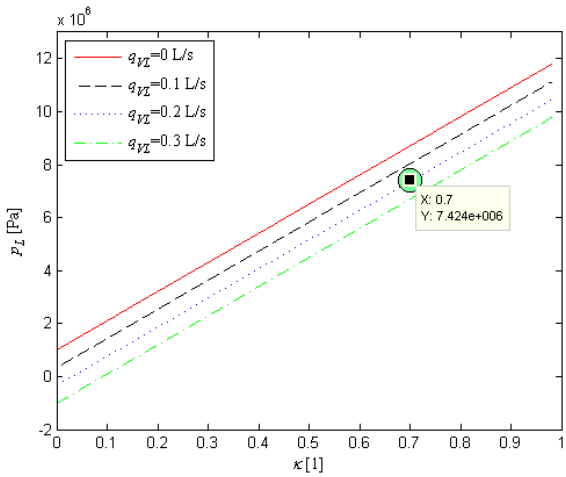

Figure 14 - Load pressure from the steady-state and dynamic models.

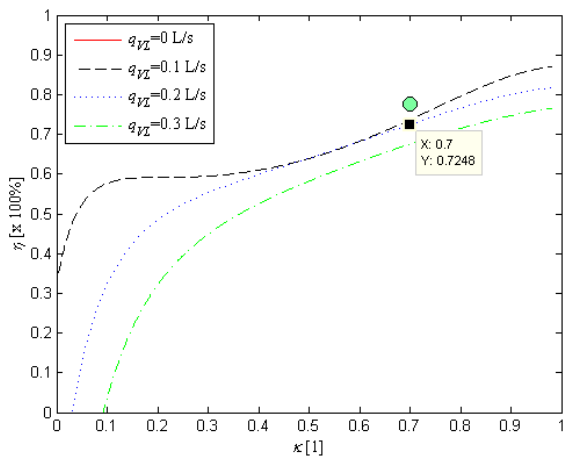

Figure 15 – Efficiency from for the steady-state and dynamic models.

As can be observed, the load pressure calculated by eq. (1) resulted on exactly the same average pressure obtained from dynamic simulation (fig. 12), that is 7.42 x10^6 Pa. The average flow rate resulting from the dynamic simulation is 1.99 x10^{-4} m^3/s, while the flow rate used for the step-down system dimensioning is 2.00 x10^{-4} m^3/s.

For the system efficiency, both models result on efficiencies higher than 70% for a duty cycle of 0.7. According to the steady state model, the efficiency is 72.48 %, higher than the estimated efficiency of 68.22 % calculated for a duty cycle of 0.5.

5 Conclusions

In this paper, the steady state equations modelling a hydraulic step-down converter were presented and used to determine the system parameters (tube length and diameter) in order to achieve the maximum efficiency.

The nonlinear dynamic equations of the position and speed control system were also introduced. Using the position control configuration (closed-loop system), the results showed that the mathematical model describes the system experimental behavior with good accuracy. As a result, the model could be used to validate the parameters obtained with the steady-state model.

Considering the system operating in open-loop configuration, the load pressure, flow rate, and efficiency predicted by the steady-state model matched very well the results obtained using dynamic simulation. Therefore, the steady-state model presented results on a very accurate design of a step-down converter. Moreover, the dynamic model can be used for system optimization and analysis of the dynamic response.

Nomenclature

Symbol	Denotation	Unit
β	Pitch angle	[°]
β_e	Bulk modulus	[Pa]
γ	Specific heat ratio	[1]
κ	Duty cycle	[1]
ν	Kinematic viscosity	[m^2/s]
η	Hydraulic efficiency	[1]
ρ	Density	[kg/m^3]
A_A	Area of Chamber A	[m^2]
A_{DC}	Flow passage area	[m^2]
c_d	Discharge coefficient	[1]
d_t	Tube diameter	[m]
E_A	Energy in cylinder line A	[J]
E_{HP}	High supply pressure energy	[J]
E_{LP}	Low supply pressure energy	[J]

F_{at}	Friction force	[N]
F_c	Load force	[N]
K_{vA}	Flow coefficient	$[\mathrm{m}^3/\mathrm{s.Pa}^{1/2}]$
K_{vin}	Leakage coefficient	$[\mathrm{m}^3/\mathrm{s.Pa}^{1/2}]$
l_t	Tube length	[m]
M_e	Equivalent mass	[kg]
p_A^{CP}	Pressure in chamber A	[Pa]
p_o	Accumulator initial gas pressure	[Pa]
p_g	Accumulator gas pressure	[Pa]
p_{fac}	Accumulator liquid pressure	[Pa]
p_{Ain}	Internal tube pressure	[Pa]
p_{JT}	Upstream tube pressure	[Pa]
p_{MT}	Downstream tube pressure	[Pa]
p_L	Load pressure	[Pa]
p_{HS}	High supply pressure	[Pa]
p_{LS}	Low supply pressure	[Pa]
q_{VJT}	Tube upstream flow rate	$[\mathrm{m}^3/\mathrm{s}]$
q_{VL}	Load flow rate	$[\mathrm{m}^3/\mathrm{s}]$
q_{VMT}	Tube downstream flow rate	$[\mathrm{m}^3/\mathrm{s}]$
U_c	Control signal	[V]
U^{V1}	Valve control signal	[V]
U_n	Nominal valve control signal	[V]
V_A	Volume of chamber A	$[\mathrm{m}^3]$
V_{Ao}	Initial volume of chamber A	$[\mathrm{m}^3]$
V_0	Accumulator initial gas volume	$[\mathrm{m}^3]$
V_{fac}	Accumulator liquid volume	$[\mathrm{m}^3]$
V_g	Accumulator gas volume	$[\mathrm{m}^3]$

References

[1] DE NEGRI, V. J., WANG, P., JOHNSTON, D. N., PLUMMER, A., 2014. Behavioural prediction of hydraulic step-up switching converters. *International Journal of Fluid Power*. Vol 15, No. 1, pp. 1-9.

[2] LINJAMA, M., VILENIUS, M., 2005. Energy-Efficient Motion Control of a Digital Hydraulic Joint Actuator. *Proceeding of the 6ht JFPS International Symposium on Fluid Power*. Tsukuba, November 7-10.

[3] EGGERS, B., RAHMFELD, R., IVANTYSYNOVA, M., 2005. An energetic comparison between valveless and valve controlled active vibration damping for off-road vehicles. *Proceedings of the 6th JFPS International Symposium on Fluid Power*. Tsukuba.

[4] WILLKOMM, J., WANLER, M. & WEBER., J., 2014. Process-adapted control to maximize dynamics of displacement-variable pumps. *Symposium on Fluid Power & Motion Control*. Bath, United Kingdom. pp. 10-12.

[5] TEIXEIRA, P. L., VIANNA, W., PENTEADO, R. D., KRUS, P. & DE NEGRI., V. J., 2015. Pressure Modeling and Analysis of a Synchronized Hydraulic Press Brake with Variable-Speed Pump. *Symposium on Fluid Power and Motion Control*. Chicago, Illinois, USA.

[6] LINJAMA, M., LAAMANEN, A., VILENIUS, M., 2003. Is it time for digital hydraulics? *The Eighth Scandinavian International Conference on Fluid Power*, May 7–9, Tampere, Finland, pp. 347–366.

[7] BELAN, H, B., LOCATELI, C. C., ENDLER, L., PIERI, E. R. D. & DE NEGRI, V.J., 2014. Aumento da eficiência energética em sistemas hidráulicos utilizando hidráulica digital. *XX Congresso Brasileiro de Automática*, Belo Horizonte, Brazil, 20 - 24 Sept.

[8] BELAN, H. B., LOCATELI, C. C., LANTTO, B., KRUS. P. & DE NEGRI, V. J., 2015. Digital Secondary Control Architecture for Aircraft Application. *The Seventh Workshop on Digital Fluid Power*, February 26-27, Linz, Austria.

[9] LINJAMA, M., VILENIUS, M., 2008. DIGITAL HYDRAULICS – Towards Perfect Valve Technology. Technology. Digitalna Hidravlika, Ventil 14. 2. pp. 138-148.

[10] SCHEIDL, R.; KOGLER, H.; WINKLER, B., 2013. Hydraulic Switching Control - objectives, concepts, challenges and potential applications. *Magazine of Hydraulics, Pneumatics, Tribology, Ecology, Sensorics, Mechatronics*, n. 1, ISSN: 1453 - 7303.

[11] SELL, N. P., JOHNSTON, D. N., A. R. PLUMMER. & KUDZMA, S., 2013. Control of a fast switching valve for digital hydraulics. *The 13th Scandinavian International Conference on Fluid Power*, SICFP2013, June 3-5, Linköping, Sweden.

[12] BROWN, F. T., 1987. Switched reactance hydraulics: a new way to control fluid power. *Proc. National Conference on Fluid Power*. Chicago, USA, pp. 25-34.

[13] BROWN, F. T. TENTARELLI, S. C., RAMACHANDRAN, S. A., 1988. A hydraulic rotary switched-inertance servo-transformer, Transactions of ASME: *Journal of Dynamic Systems, Measurement, and Control*. Vol. 110, pp.144-150.

[14] DE NEGRI, V.J., NOSTRANI, M.P., WANG P., JOHNSTON D.N., PLUMMER, A., 2015. Modelling and analysis of hydraulic step-down switching converters, *International Journal of Fluid Power*. Vol 16, No. 2, pp. 111-121.

[15] NOSTRANI, M. P., GALLONI, A., RADUENZ, H., DE NEGRI, V.J., 2016. Theoretical and experimental analysis of a hydraulic step-down switching converter for position and speed control. *The Eighth Workshop on Digital Fluid Power*. Tampere. Proceedings of DFP2016, 2016. pp. 1-19.

[16] SZPAK, R. Análise Teórico-Experimental das Pressões em Posicionadores Hidráulicos. 2008. *Dissertação (Mestrado em Engenharia Mecânica) – Programa de Pós-graduação em Engenharia Mecânica, Universidade Federal de Santa Catarina*, Florianópolis.

[17] WELLSTEAD, P. E., 2000. Introduction to Physical System Modelling. London: Ed. Academic Press Ltd., 244 p.

[18] FOX, R. W., MCDONALD, A. T., Pritchard, P. J., 2011. Introduction to Fluid Mechanics, 8th ed. Hoboken, NJ: Wily.

[19] GONZALEZ, F. E., DE NEGRI, V. J., SOARES, J. M. C., 2012. Analysis and Emulation of Actuating Forces on Wind Turbine Pitch Drives. *8th International Fluid Power Conference* - 8. IFK, Aachen-Germany.

[20] DE NEGRI, V. J., RAMOS FILHO, J. R. B., SOUZA, A. D. C. de., 2008. A Design Method for Hydraulic Positioning Systems. *51th National Conference on Fluid Power* (NCFP), Las Vegas, USA.

[21] MURARO, I., TEIXEIRA, P. L., DE NEGRI, V. J., 2013. Effect of proportional valves and cylinders on the behavior of hydraulic positioning systems. In: ASME/BATH *Symposium on Fluid Power & Motion Control*, Sarasota, FL. pp.1 – 9.

[22] GONZALEZ, F. E., 2012. Estudo das Forças Atuantes em Mecanismos de Regulação de Ângulo de Passo e Desenvolvimento de um Sistema Emulador de Cargas. *Dissertação (Mestrado em Engenharia Mecânica)-Universidade Federal de Santa Catarina*, Florianópolis,

[23] NOSTRANI, M. P., 2015. Estudo teórico-experimental de um posicionador utilizando hidráulica digital de chaveamento rápido: estudo de caso em bancada de ensaios para turbinas eólicas. *Dissertação (Programa de Pós Graduação em Engenharia Mecânica), Universidade Federal de Santa Catarina*, Florianópolis.

[24] KRUS, P., WEDDFELT, K., PALMBERG, J.-O., 1994. Fast pipeline models for simulation of hydraulic systems. *Journal of Dynamic Systems, Measurement, and Control*. Vol.116. pp. 132-136. March.

[25] JOHNSTON, D.N., 2006. Efficient Methods for Numerical Modeling of Laminar Friction in Fluid Lines. *Journal of Dynamic Systems, Measurement, and Control.* December, Vol. 128. pp. 829-834. DOI: 10.1115/ 1.2361320,

[26] JOHNSTON, D.N., 2012. The transmission line method for modelling laminar flow of liquid in pipelines. Proc. IMechE Part I: *Journal of Systems and Control Engineering*, Vol. 226. pp. 586-597. DOI: 10.1177/0959651811430035.

Analysis of Flow Angles and Flow Velocities in Spool Valves for the Calculation of Steady-State Flow Forces

Patrik Bordovsky, Hubertus Murrenhoff

Institute for Fluid Power Drives and Controls (IFAS), RWTH Aachen University, Aachen, Germany
E-mail: Patrik.Bordovsky@ifas.rwth-aachen.de, Hubertus.Murrenhoff@ifas.rwth-aachen.de

Abstract

A detailed analysis of the flow inside valves has become necessary for the optimisation of their static and dynamic performance. For this purpose, the contours of metering edges as well as the shapes of sleeves, respectively of valve blocks, can be modified, resulting in different flow patterns. In addition, the flow velocities and flow angles on defined areas inside valves are needed for the estimation of physical quantities such as flow rates, flow forces, etc.

Within this paper, measurements and CFD-simulations of a 2/2-way spool type test valve are analysed regarding flow angles and flow velocities including their distribution on the inlet and outlet areas. Different spool edge geometries are investigated in both flow directions. Furthermore, the impact of a chamfer and a fillet on a spool edge, on the flow angles and the flow velocities are analysed.

The analysis results show that the shape of a spool edge influences the flow angles and the flow velocities. Both flow variables are significantly affected by the direction of the fluid flow through the valve. Moreover, considering the same inlet area, an increasing chamfer width, respectively an increasing fillet radius, result both in lower inlet and outlet flow angles.

Keywords: Flow Angle, Flow Velocity, Steady-State Flow Force, Spool Valve

1 Introduction

The first research on jet angles was conducted by von Mises [1] in 1917. He experimentally determined the flow coefficients and jet angles of water flowing out of a circular tank with sharp-edged outlets into the surrounding air, as depicted in fig. 1.

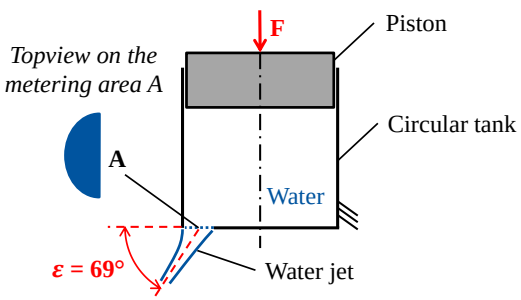

Figure 1: Experimental setup by von Mises

Based on his experiments, he found that the jet angle approaches the value 69°. As it can be seen in fig. 1, he considered the angle between the centre line of a free jet and the horizontal line. In other words, von Mises did not focus on the average jet angle evaluated on the metering area A. Consequently, before using the 69°-jet-angle value, it is necessary to review von Mises' assumptions and statements. He assumed a steady-state, inviscid, eddy-free, non-rotational and two-dimensional fluid flow. Moreover, the tank was pressurised by a piston, so the fluid motion was caused by the pressure difference and not only by the gravitational force. Nevertheless, von Mises mentioned that slight outlet edge modifications, e.g., a fillet or a chamfer, result in different jet angles. In valves, there are several unique shapes of metering edges, which are manufactured to fulfil desired valve performance. Consequently, von Mises' results should not be seen as generally valid since his assumptions are often not fulfilled in spool valves.

Backé [2] set up an approximation function for the inlet jet angle expressed by eq. (1)

$$\cos\varepsilon = 0{,}358 + \frac{0{,}577}{1 + 0{,}642\left(\frac{x_1}{\Delta r}\right)^{1{,}26}} \qquad (1)$$

where x_1 is the spool position and Δr is the height of the radial clearance between the spool and the sleeve.

Compared to the inlet jet angles, little research was conducted on the outlet jet angles. Usually, the outlet angle is considered to be 90° for the calculation of the steady-state flow-force (hereinafter referred to as flow force) [3]. However, Ye [4] claims that the outlet angle deviates from that value and Schrank [5], Tanaka [6], Lugowski [7], and

Yuan [8] suggested that the outlet angles should be considered for the calculation of flow forces since the outlet angles are greater than 90°.

Modifications of metering edges are commonly used for the compensation of flow forces. For instance, Okungbowa [9] achieved the flow force reduction by a rim-shaped geometry. Furthermore, Kipping [10] stated that the outflow from the spool chamber is highly turbulent and three-dimensional. Bordovsky [11] added that the evaluation of the outlet velocities can be inaccurate. All in all, before calculating the flow force, the flow patterns in the investigated valve should be analysed to prove the assumptions.

Several experimental studies were conducted to investigate flow patterns in valves by using dynamic similarity, e.g., by Kipping [10]. Usually, a scaled valve model was used with water instead of hydraulic oil, which results in lowering the pressure differentials, and hence the flow velocities as well. The dynamic similarity should not be seen as absolutely valid, though. Flow patterns can be also visualised by using the Particle Image Velocimetry (PIV) method. For instance, Del Vescovo [12] utilised PIV for an analysis of velocity profiles. However, he was not able to estimate the outlet angles due to issues with the camera focus.

Nowadays, flow patterns inside valves are usually investigated by CFD simulations. For instance, Ye [4] used CFD simulations to describe effects of the metering edge shape on the flow characteristics. Borghi [13] also determined jet angles of differently shaped metering edges by using CFD simulations. Besides measurements, the simulative approach was utilised in this study as well.

2 Theory

The law of the linear momentum conservation is often used to analyse the flow forces acting on a fixed control volume as shown in fig. 2.

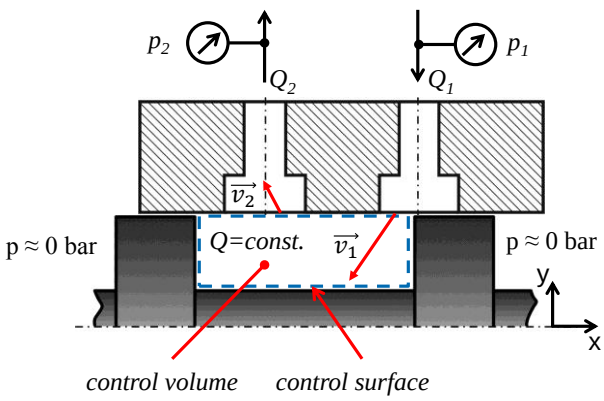

Figure 2: Sketch of a simplified valve

Among various disturbance forces, the flow forces are considered to be most relevant in spool valves. They usually act in the closing direction. The flow forces arise due to the change of momentum over time within the control volume. A detailed derivation of the flow forces can be found in the literature [3, 5, 14]. In order to approximate the flow forces, following assumptions are made: two-dimensional incompressible viscous flow, square-edged spool, no radial clearance between the spool and the sleeve, a non-deformable non-accelerating ideal annular control volume, enclosed by the control surface, only axial forces acting on the control surface. Consequently, the flow force can be calculated according to eq. (2) for the control volume defined in fig. 2, where ρ is the fluid density, Q the flow rate and $\overline{v_{1,x}}$, $\overline{v_{2,x}}$ are the average axial velocities on the inlet (A_1), respectively the outlet (A_2) area.

$$\sum F_x = \frac{d\vec{I}}{dt} = -F_{Fl} = \rho \cdot Q \cdot \left(\overline{v_{1,x}} - \overline{v_{2,x}}\right) \qquad (2)$$

As can be seen in eq. (2), the flow force equals the negative value of the net axial force acting on the control volume. For the calculation, it is necessary to evaluate the axial flow velocities on the inlet and the outlet areas as shown in fig. 3.

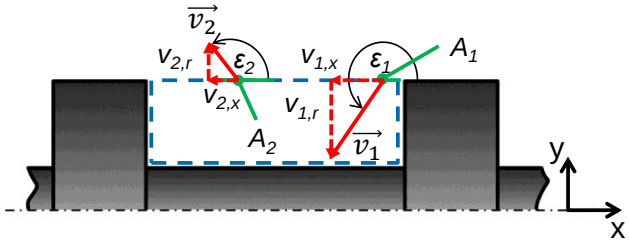

Figure 3: Flow velocities on the metering areas in case of the inlet throttling

In relation to fig. 3, the average axial flow velocities can be obtained from eq. (3)

$$\overline{v_{i,x}} = |\vec{v_i}| \cos \overline{\varepsilon_i} \qquad (3)$$

and the average radial flow velocities can be calculated according to eq. (4). The y-component of the flow velocity corresponds to the radial one.

$$\overline{v_{i,r}} = |\vec{v_i}| \sin \overline{\varepsilon_i} \qquad (4)$$

In reality, there are additional pressure losses when the fluid flows through valves. These losses are expressed by the discharge coefficient α_D. Hence, the real flow velocities are lower than the theoretical ones. The average real radial inlet velocity $\overline{v_{1,r}}$ can be approximated by eq. (5)

$$\overline{v_{1,r}} = -\alpha_D \sqrt{\frac{2\Delta p}{\rho}} \qquad (5)$$

respectively by eq. (6) for the average real radial outlet velocity $\overline{v_{2,r}}$, which can be derived from the continuity equation of the flow rate.

$$\overline{v_{2,r}} = -\frac{A_1}{A_2}\overline{v_{1,r}} = \frac{A_1}{A_2}\alpha_D \sqrt{\frac{2\Delta p}{\rho}} \qquad (6)$$

The average axial flow velocities are calculated from the radial velocities and corresponding flow angles. So the flow rate can generally be calculated from the orifice equation (eq. 7)

$$Q = \alpha_D A_1 \sqrt{\frac{2\Delta p}{\rho}} \tag{7}$$

where Δp is the pressure drop between the pressure-measurement ports 1 and 2 (see fig. 2). The area A_1 describes the real metering area, not the narrowest metering area, often referred to as vena contracta [14] since the location and the area of the vena contracta are unknown.

By combining eq. (4) with eq. (5), the absolute value of the average inlet velocity can be obtained from eq. (8).

$$|\overrightarrow{v_1}| = -\alpha_D \sqrt{\frac{2\Delta p}{\rho}} \frac{1}{\sin \bar{\varepsilon}_1} \tag{8}$$

By inserting eq. (8) into eq. (3), the approximated average inlet axial velocity is described by eq. (9).

$$\overline{v_{1,x}} = -\alpha_D \sqrt{\frac{2\Delta p}{\rho}} \frac{\cos \bar{\varepsilon}_1}{\sin \bar{\varepsilon}_1} = -\alpha_D \sqrt{\frac{2\Delta p}{\rho}} \cot \bar{\varepsilon}_1 \tag{9}$$

Similarly, the average outlet axial velocity can be approximated by eq. (10).

$$\overline{v_{2,x}} = \overline{v_{2,r}} \cot \bar{\varepsilon}_2 = \frac{A_1}{A_2} \alpha_D \sqrt{\frac{2\Delta p}{\rho}} \cot \bar{\varepsilon}_2 \tag{10}$$

As can be seen from eq. 9 and eq. 10, it is necessary to know the average inlet and outlet angles on the corresponding metering areas, which are part of the control surface. Due to the difficulty of flow-angle measurement, the flow angles are evaluated from CFD simulations.

For the reverse flow, i.e., outlet throttling, the flow quantities are denoted according to fig. 4, and distinguished by an apostrophe from the flow quantities of the inlet throttling. The area A_2' denotes the chamber inlet and the area A_1' the chamber outlet. If any of the flow angles is greater than 180°, the value of 180° can be subtracted from it for the purpose of the flow-force calculation due to the cotangent function.

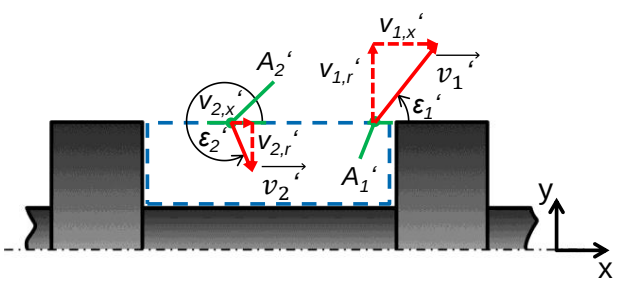

Figure 4: Flow velocities on the metering areas in case of the outlet throttling

The flow force for the outlet throttling has the same direction as for the inlet throttling and can be approximated by eq. 11.

$$\sum F_x' = -F_{Fl}' = \rho \cdot Q \cdot \left(\overline{v_{2,x}}' - \overline{v_{1,x}}'\right) \tag{11}$$

3 Experiment

The average radial flow velocities were evaluated from measurements of a 2/2-way proportional spool-type valve, which is shown in fig. 5. The valve consists of a valve block, a sleeve, two lids, and a spool, which can be replaced easily. It has two pressure ports P and T and two leakage ports L, which are drained to a pressureless external tank. All components were made of steel.

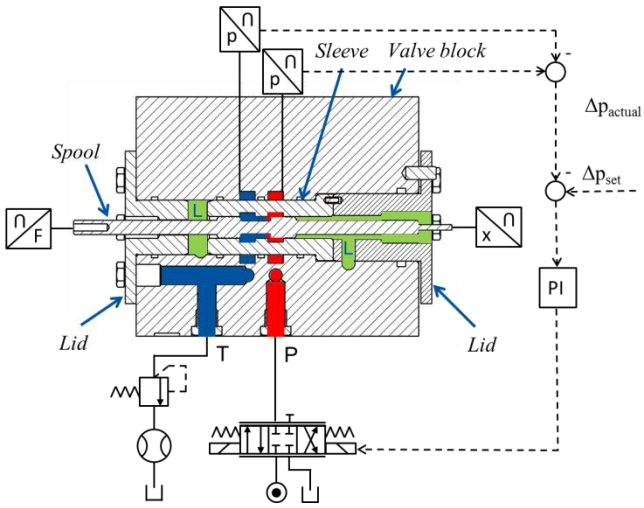

Figure 5: Test valve including a simplified hydraulic circuit diagram

A position sensor was placed on the right-hand side of the spool. A weakly preloaded spring mounted on the position sensor ensured the contact between the spool and this sensor. A load cell was placed on the left-hand side of the spool. The pressure differentials (10, 15, 20, 30, 40, 50 and 70 bar) between the ports P and T were controlled by a servovalve and a PI controller. The tank port (T) was preloaded using a pressure relief valve to the pressure of 100 bar to prevent cavitation. The flow rate was measured behind the pressure relief valve at discrete spool positions. The measurements were carried out with the oil HLP46 at an approximately constant oil temperature of 60°C.

Two square-edge spools, one with the chamber length L of 13 mm (SE13) and another one with the chamber length L of 20 mm (SE20), and a bevel-edged spool (BE) were used for flow-velocity measurements as depicted in fig. 6.

The average flow velocities of all spools were evaluated on the same inlet and outlet areas from the measured flow rate. Hence, the narrowest inlet area was not considered in case of the spool BE within this paper.

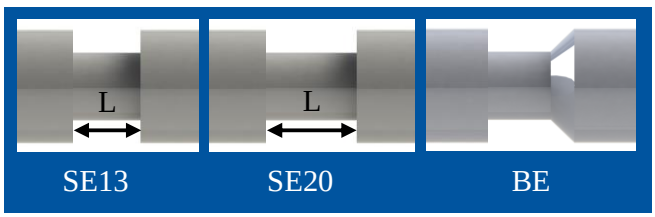

Figure 6: Spools used for measurements

The test valve is integrated into a test rig. The valve was supplied via a connection block, and the spool was moved by an electric cylinder (see fig. 7). In order to change the flow direction, an additional block was mounted between the valve and the connection block, inverting the flow direction from port T across the valve to port P.

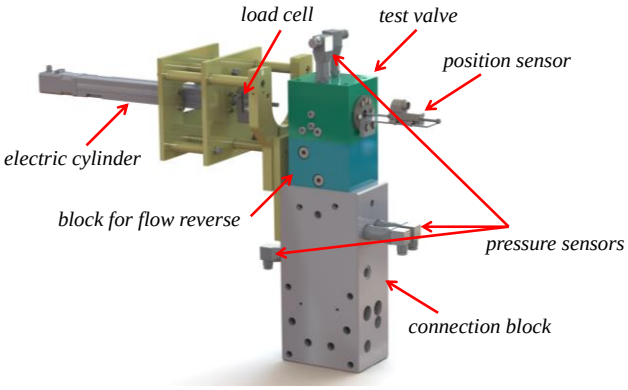

Figure 7: Test rig used for measurements

4 CFD simulation

Three-dimensional, steady, incompressible, isothermal and viscous CFD simulations were carried out in ANSYS CFX 17.0. Despite two symmetrical planes of the valve, the whole fluid domain was modelled, which resulted in better accuracy when comparing the simulation results with the measurements. The fluid domain has two inlets and two outlets. A mass flow rate on the inlets and a static pressure of 100 bar on the outlets were defined as boundary conditions. The radial clearance between the spool and the sleeve was neglected. The outlet throttling was simulated with the same boundary conditions as the inlet throttling. The mesh was generated from tetrahedrons and prism layers as it can be seen in fig. 8. The sleeve edge opposite to the spool edge was modelled with a chamfer of 0.075 mm x 45°.

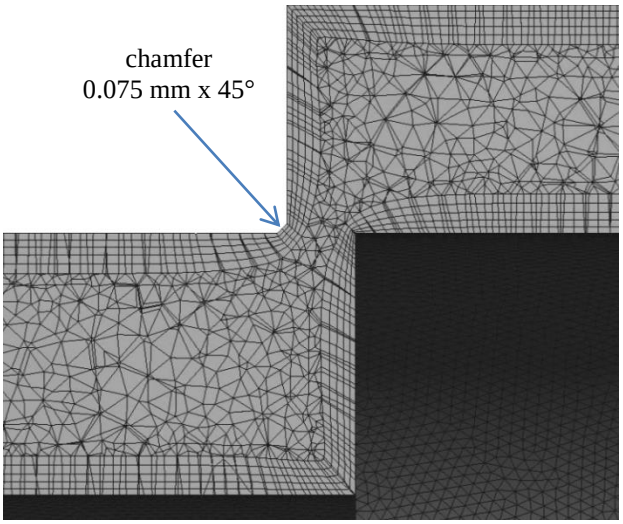

Figure 8: Detail of the mesh around the metering edge (spool SE at x = 0.6 mm)

Besides the measured spools, a fillet-edged (FE) and a chamfer-edged (CE) spool were investigated in both flow directions with different fillet radii and chamfer widths ranging from 20 to 200 µm. A constant chamfer angle of 45° was set. Additional CFD simulations were carried out with the chamfer dimensions 0.3 x 60°. Figure 9 shows spools, which were simulated in addition to the spool SE13, SE20 and BE. The flow reversal in CFD simulations was done by changing inlets to outlets and vice versa.

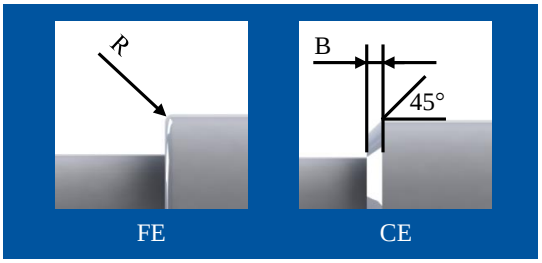

Figure 9: Geometries of additionally simulated spools

Both the average radial and the axial flow velocities were evaluated on the inlet and the outlet areas using the area-weighted average expressed by eq. 12.

$$\overline{v_{i,CFD}} = \frac{1}{A_i}\int v_i dA \tag{12}$$

The average flow angles were calculated from the axial and radial flow velocities according to eq. 13.

$$\overline{\varepsilon_i} = arccot\frac{\overline{v_{i,x,CFD}}}{\overline{v_{i,r,CFD}}} \tag{13}$$

5 Results

The average radial flow velocities were evaluated from the measurements for both flow directions. The radial flow velocities $v_{1,r}$ and $v_{1,r}'$ are shown for the spool SE at the spool positions of 0.2, 0.6 and 0.9 mm in fig. 10. The outlet radial flow velocities $v_{2,r}$ and $v_{2,r}'$ are shown in fig. 11.

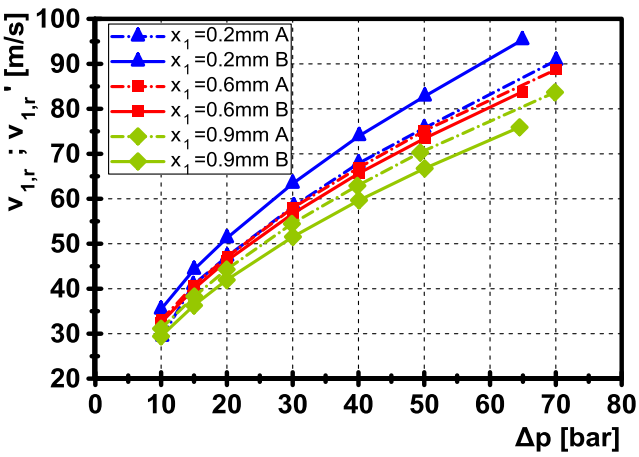

Figure 10: Measured average radial velocities $v_{1,r}$ and $v_{1,r}'$ of the spool SE20 in both flow directions (A: inlet throttling, B: outlet throttling)

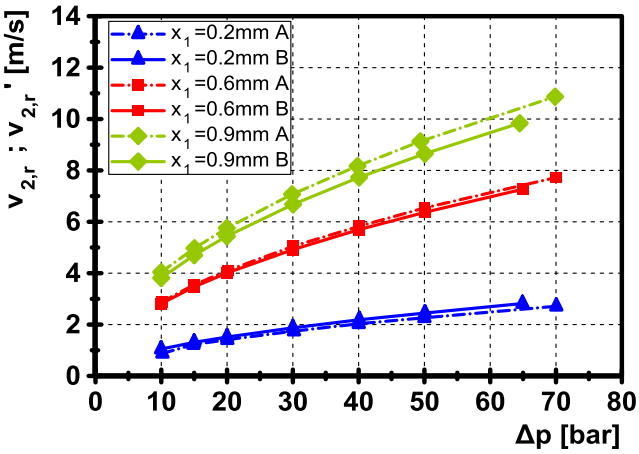

Figure 11: Measured average radial velocities $v_{2,r}$ and $v_{2,r}$' of the spool SE20 in both flow directions (A: inlet throttling, B: outlet throttling)

Figure 12 and fig. 13 show the measured radial flow velocities of different spools on the inlet, and on the outlet for the inlet throttling.

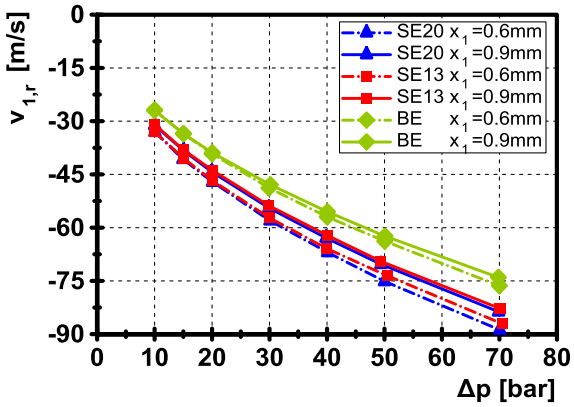

Figure 12: Comparison of the measured radial flow velocities $v_{1,r}$ for the inlet throttling of different spools

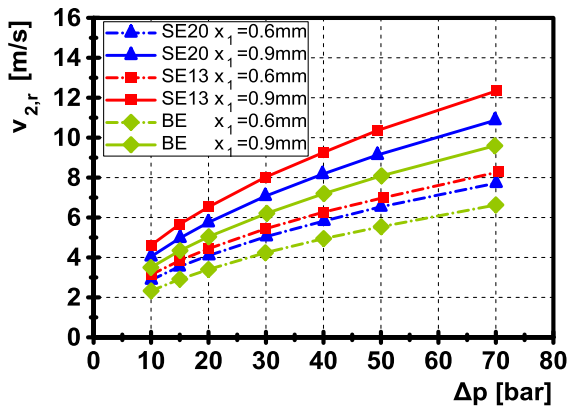

Figure 13: Comparison of the measured radial flow velocities $v_{2,r}$ for the inlet throttling of different spools

The measured and the simulated average radial flow velocities on the chamber inlet in case of the inlet throttling are compared for the spool SE in tab. 1, which also includes the relative error.

Table 1: Flow angles and flow velocities simulated for different chamfer widths in case of the inlet throttling

Δp	$v_{1,r,M}$	$v_{2,r,M}$	$v_{1,r,CFD}$	$v_{2,r,CFD}$	E_R: $v_{1,r}$	E_R: $v_{2,r}$
[bar]	[m.s^{-1}]	[m.s^{-1}]	[m.s^{-1}]	[m.s^{-1}]	[%]	[%]
10	-34,0	2,9	-32,4	2,8	-4,6	-4,4
20	-48,0	4,1	-45,9	4,0	-4,5	-3,4
30	-58,8	5,0	-56,3	4,9	-4,4	-2,5
50	-75,9	6,5	-72,6	6,4	-4,3	-1,0
70	-89,7	7,7	-85,9	7,6	-4,2	-1,0

Velocity vectors of the spool SE20 were observed for the spool position of 0.6 mm and the pressure differential of 50 bar. Figure 14 shows velocity vectors on the chamber inlet, and fig. 15 and fig. 16 show velocity vectors on two different positions on the chamber outlet: one directly under the outflow circular conduit, and the other one exactly between two outflow conduits. The vectors are plotted on lines, which are parallel to the x-axis. Those lines are invisible, and the black lines illustrate the solid-body edges.

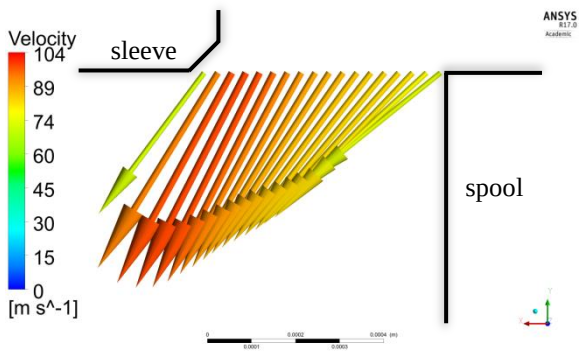

Figure 14: Spool SE20; x_1 = 0.6 mm; Δp = 50 bar Velocity vectors on the area A_1 in case of the inlet throttling

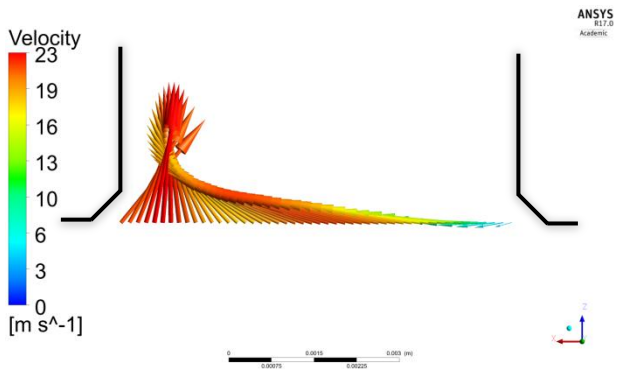

Figure 15: Spool SE20; x_1 = 0.6 mm; Δp = 50 bar Velocity vectors on the area A_2 under the circular conduit in case of the inlet throttling

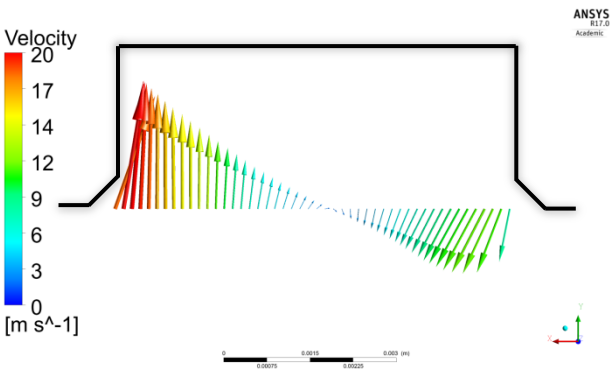

Figure 16: Spool SE20; x_1 = 0.6 mm; Δp = 50 bar Velocity vectors on the area A_2 between two circular conduits in case of the inlet throttling

Figure 17 shows profiles of radial flow velocity on the chamber inlet for the spool SE. These profiles were plotted for the spool position of 0.6 mm and the pressure differential of 10, 30, and 70 bar. Figure 18 and fig. 19 show profiles of radial flow velocity on the chamber outlet at two different positions: one directly under the outflow circular conduit, and the other one exactly between two outflow conduits. The quantity x is the x-coordinate related to the spool edge on the inlet, respectively to the groove edge closer to the origin of the coordinate frame on the outlet.

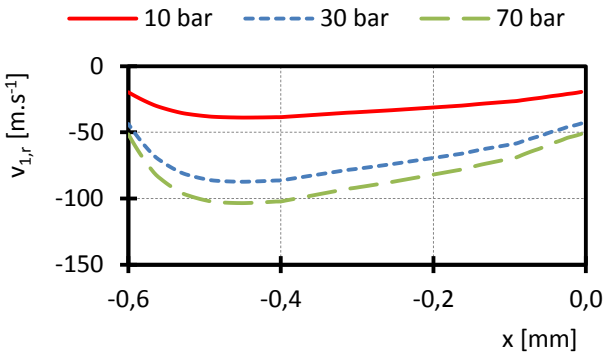

Figure 17: Spool SE20; x_1 = 0.6 mm; Profiles of radial velocities $v_{1,r}$ in case of the inlet throttling

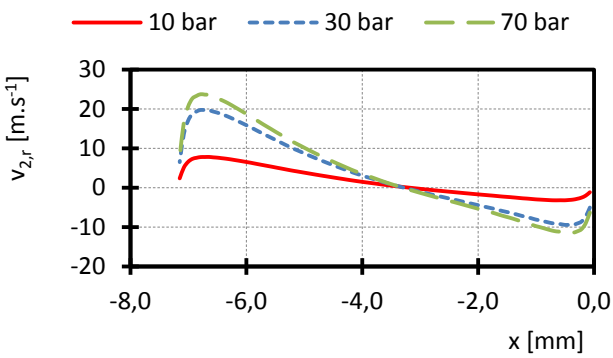

Figure 18: Spool SE20; x_1 = 0.6 mm; Profiles of radial velocities $v_{2,r}$ under the circular conduit in case of the inlet throttling

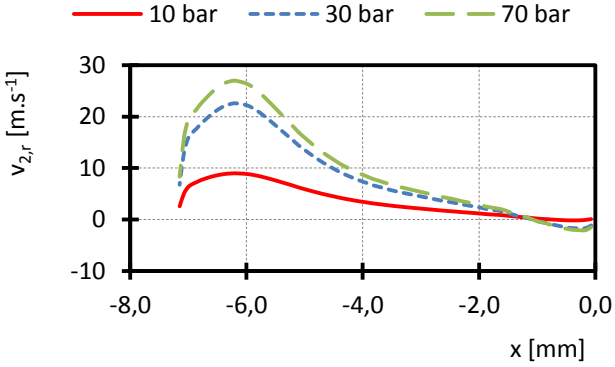

Figure 19: Spool SE20; x_1 = 0.6 mm; Profiles of radial velocities $v_{2,r}$ between two circular conduits in case of the inlet throttling

The average angles ε_1 and ε_1' of the spool SE are compared for both flow directions in fig. 20. The outlet angles ε_2 and ε_2' are depicted in fig. 21.

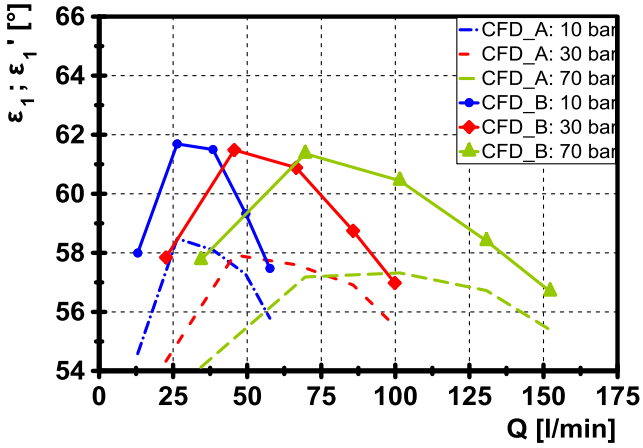

Figure 20: Comparison of the average flow angles ε_1 and ε_1' for the spool SE20 in both flow directions (A: inlet throttling, B: outlet throttling)

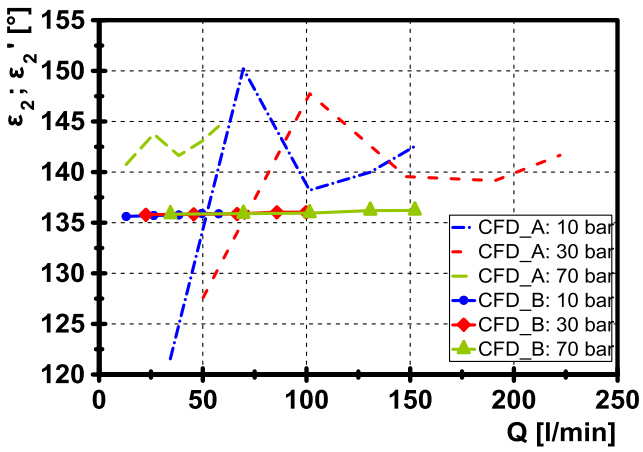

Figure 21: Comparison of the average flow angles ε_2 and ε_2' for the spool SE20 in both flow directions (A: inlet throttling, B: outlet throttling)

The flow angles ε_1' of all spools are compared for the outlet throttling in fig. 22. The flow angles ε_2' are shown in fig. 23.

In both cases, the fillet radius of the spool FE is 0.02 mm, and the chamfer dimensions of the spool CE are 0.02 mm x 45°.

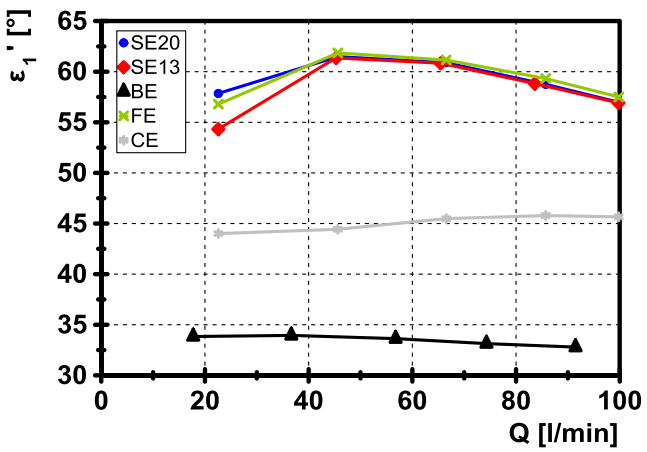

Figure 22: Comparison of the average flow angles ε_1' of all simulated spools for the outlet throttling

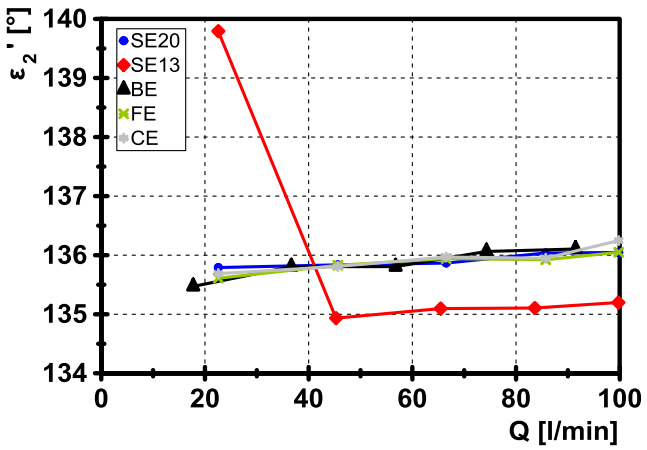

Figure 23: Comparison of the average flow angles ε_2' of all simulated spools for the outlet throttling

Table 2 and 3 list simulated flow angles and flow velocities of the spool FE with fillet radii R ranging from 20 to 200 µm for the spool position of 0.6 mm, the pressure differential of 50 bar for the inlet throttling, respectively the outlet throttling. Thus, a constant mass flow rate of 1.225 kg.s^{-1} was set in all simulations. The spool stroke was lowered by the magnitude of the radius so the inlet area remained constant in all simulations.

Table 2: Flow angles and flow velocities simulated for different fillet radii in case of the inlet throttling

R	ε_1	ε_2	$v_{1,x}$	$v_{2,x}$	$v_{1,r}$	$v_{2,r}$	F_{Fl}
[µm]	[°]	[°]	[m.s^{-1}]	[m.s^{-1}]	[m.s^{-1}]	[m.s^{-1}]	[N]
20	56,5	136,6	-50,6	-6,6	-76,3	6,3	-50,6
50	57,2	138,1	-49,2	-6,8	-76,3	6,1	-48,3
100	56,5	137,4	-50,6	-6,7	-76,4	6,2	-48,8
150	54,7	136,8	-53,9	-6,5	-76,3	6,1	-51,9
200	53,0	135,3	-57,5	-6,2	-76,2	6,2	-56,0

Table 3: Flow angles and flow velocities simulated for different fillet radii in case of the outlet throttling

R	ε_1'	ε_2'	$v_{1,x}$'	$v_{2,x}$'	$v_{1,r}$'	$v_{2,r}$'	F_{Fl}'
[µm]	[°]	[°]	[m.s^{-1}]	[m.s^{-1}]	[m.s^{-1}]	[m.s^{-1}]	[N]
20	60,7	135,9	41,2	6,6	73,4	-6,4	-40,2
50	58,1	136,0	45,9	6,6	73,8	-6,3	-47,6
100	53,8	136,1	54,0	6,6	73,8	-6,3	-60,0
150	49,1	136,0	64,2	6,6	74,2	-6,3	-74,2
200	43,3	136,1	78,7	6,6	74,1	-6,3	-91,3

Table 4 and 5 list simulated flow angles and flow velocities of the spool CE with chamfer widths ranging from 20 to 200 µm for the spool position of 0.6 mm, the pressure drop of 50 bar for the inlet throttling and the outlet throttling. Again, the spool strokes were also lowered by the magnitude of the radius so the inlet area remained constant.

Table 4: Flow angles and flow velocities simulated for different chamfer widths in case of the inlet throttling

B	ε_1	ε_2	$v_{1,x}$	$v_{2,x}$	$v_{1,r}$	$v_{2,r}$	F_{Fl}
[µm]	[°]	[°]	[m.s^{-1}]	[m.s^{-1}]	[m.s^{-1}]	[m.s^{-1}]	[N]
20	56,7	140,5	48,8	7,1	-74,3	5,8	-49,9
50	57,1	139,7	47,7	7,2	-73,9	6,1	-48,3
100	57,4	140,4	47,1	7,1	-73,5	5,9	-47,2
150	56,7	137,6	48,3	6,6	-73,5	6,1	-48,0
200	55,5	136,3	50,8	6,3	-73,9	6,0	-50,5

Table 5: Flow angles and flow velocities simulated for different chamfer widths in case of the outlet throttling

B	ε_1'	ε_2'	$v_{1,x}$'	$v_{2,x}$'	$v_{1,r}$'	$v_{2,r}$'	F_{Fl}'
[µm]	[°]	[°]	[m.s^{-1}]	[m.s^{-1}]	[m.s^{-1}]	[m.s^{-1}]	[N]
20	62,2	136,0	38,7	6,6	73,4	-6,4	-38,2
50	59,5	136,1	43,3	6,6	73,5	-6,3	-45,3
100	54,6	136,2	52,3	6,6	73,6	-6,3	-58,4
150	46,1	136,1	69,9	6,6	72,5	-6,3	-78,8
200	42,2	136,0	78,8	6,6	71,5	-6,3	-89,6

6 Discussion

Figure 10 and 11 reveal that the average radial flow velocities depend slightly on the flow direction. The flow direction influences the discharge coefficient. Since the approximated radial flow velocities are calculated according to eq. 5, respectively eq. 6 with quantities determined from the measurements, they perfectly match the measured values. The discharge coefficient depends on many factors such as metering-edge shape, flow direction, oil temperature etc. So this coefficient should be individually determined to achieve more accurate values when approximating the radial flow velocities for different metering-edge shapes. It can be seen that larger spool positions lead to lower radial flow velocities. This results from the fact that the discharge coefficient decreases when the spool position increases.

Figure 12 shows that the smallest radial velocities are obtained with the spool BE. This fits to theoretical modelling since the bevel confines the flow behind the metering area. In fact, the smallest metering area of the spool BE is cone-shaped as it is created as a perpendicular distance from the bevel to the sleeve edge. However, the smallest metering area was not considered in this study to allow the comparison of the flow angles for the same metering areas.

It can be concluded from tab. 1 that the simulated radial flow velocities match the measured ones. The approximate relative error of the inlet radial flow velocities is -4.5 percent, respectively a little less for the outlet radial flow velocities. This confirms that the evaluation method of simulated flow velocities is suitable.

The inlet-throttling velocity vectors on the chamber inlet are visualised in fig. 14 for the spool SE for a spool position of 0.6 mm and a pressure differential of 50 bar. It is evident that the maximum velocity is located closer to the sleeve edge. This can also be seen in fig. 18. It was also observed that the velocity distribution is almost independent of the angular position. On the contrary, the velocity distribution on the chamber outlet is not uniform regarding the angular position. Figure 15 shows that the flow angle strongly varies with the x-position. Moreover, fig. 16 confirms that the flow circulates in the groove between two outflow conduits. The profiles of radial flow velocities are qualitatively similar for different pressure differentials, as illustrated in fig. 17, 18 and 19.

Figure 20 reveals that the flow angles $\varepsilon_1{}'$ are greater than flow angles ε_1 when comparing both flow directions. The curves of the flow angles ε_1 and $\varepsilon_1{}'$ are qualitatively similar. On the other hand, it is apparent from fig. 21 that the flow angles $\varepsilon_2{}'$ are almost constant over the flow rate, while the flow angles ε_2 are functions of the flow rate.

Two findings are visible in fig. 22. On the one hand, the flow angles $\varepsilon_1{}'$ of the bevel-edged spool (BE) are the lowest compared to other spools. It approximately equals 33°, although the bevel angle is 45°. Thus the fluid does not flow along the bevel in case of the outlet throttling. On the other hand, a similar effect is caused by the 0.3 x 60°-chamfer-edged spool (CE) resulting in flow angle $\varepsilon_1{}'$ values of approximately 45°. Figure 23 shows that the flow angles $\varepsilon_2{}'$ of the spool SE13 deviate from the flow angles of other spools. Besides the spool SE13, the flow angles of other spools are almost equal and constant.

Table 2 shows that the average flow angles on the inlet area differ from von Mises' value of 69°, and the average outlet flow angles are much larger than the usually assumed value of 90°. Moreover, the fillet radius influences the flow angles and axial flow velocities significantly. Hence, the flow forces also vary. The radial flow velocities remain approximately constant.

It is apparent from tab. 3 that the flow direction influences the average flow angles and axial flow velocities. Compared to the values for the inlet throttling, the inlet flow angles and flow velocities for the outlet throttling vary more, which results in a larger variation of the flow force. Particularly, the maximum flow-force of the outlet throttling is -91.3 N compared to -56.0 N of the maximum inlet throttling.

It can be seen in tab. 4 and 5 that the variation of the chamfer width impacts the flow quantities. In case of the inlet throttling, this impact is much lower compared to the outlet throttling. The flow angles ε_1 are almost constant in all simulated cases, while the flow angles $\varepsilon_1{}'$ vary from 42.2° to 62.2°. Consequently, the flow forces vary much as well.

7 Conclusions

Within this paper, flow angles and flow velocities of a 2/2-way spool-type test valve were investigated from measurements and CFD-simulations. Spools with differently shaped metering edges were analysed in both flow directions.

The results show that the radial flow velocities can be accurately approximated if the discharge coefficients are known. The flow direction impacts the flow angles and hence the flow velocities. In addition, the shape of the metering edge influences the flow angles and the flow velocities. An increasing chamfer width, respectively an increasing fillet radius, both result in lower flow angles. The profiles of radial flow velocities on the chamber outlet prove that the velocity-vector distribution is not uniform regarding the angular position for the inlet throttling.

All in all, among others the flow angles and the radial flow velocities are needed to calculate the flow force. The latter can be approximated accurately when the discharge coefficient is known. The flow angles are difficult to estimate analytically since there is no analytical model describing the relations between the flow angles and different parameters. However, nowadays, the flow force can be evaluated relatively quickly using CFD simulations.

References

[1] Von Mises, R.: Berechnung von Ausfluss- und Überfallzahlen. In: *Zeitschrift des Vereins Deutscher Ingenieure*, 1917.

[2] Backé, W., Tatar, H.: *Untersuchung des Einflusses von Störkräften auf den Schaltvogang bei Wegeventilen der Hydraulik*. Forschungsberichte des Landes Nordrhein-Westfalen, Opladen: Westdeutscher Verlag, 1975.

[3] Murrenhoff, H.: *Grundlagen der Fluidtechnik. Teil 1: Hydraulik. Umdruck zur Vorlesung.* 8. Aufl. Herzogenrath: Shaker (Reihe Fluidtechnik U3), 2016.

[4] Ye, Yi et al.: Effects of groove shape of notch on the flow characteristics of spool valve. In: *Energy Conversion and Management* 86, p. 1091–1101, 2014.

[5] Schrank, K., and Murrenhoff, H.: Beschreibung der Strömungskraft in Längsschieberventilen mittels Impulserhaltung. In: *O+P Fluidtechnik* 4, 2013.

[6] Tanaka, K. et al.: Steady and Unsteady Flow Force acting on a Spool Valve. In: *Fluid Power and Motion Control*, 2012.

[7] Lugowski, J.: Steady-State Flow Force Compensation in a Hydraulic Valve. Purdue University, 2013.

[8] Yuan, Q., Li, P.Y.: Using Steady Flow Force for Unstable Valve Design: Modeling and Experiments. In: *J. Dyn. Sys., Meas., Control*, 127(3), p. 451, 2005.

[9] Okungbowa, N., et al.: Determining the Steady State Flow Forces in a Rim Spool Valve using CFD Analysis. In: *PTMC*, 2005.

[10] Kipping, M.: *Experimentelle Untersuchungen und numerische Berechnungen zur Innenströmung in Schieberventilen der Ölhydraulik*. Technische Hochschule Darmstadt, Dissertation, 1997.

[11] Bordovsky, P., Murrenhoff, H.: Investigation of Steady-State Flow Forces in Spool Valves of Different Geometries and at Different Oil Temperatures With the Help of Measurements and CFD Simulations. In: *Proceedings of BATH/ASME 2016 Symposium on Fluid Power and Motion Control*, 2016.

[12] Del Vescovo, G.; Lippolis, A.: Three-Dimensional Analysis of Flow Forces on Directional Control Valves. In: *International Journal of Fluid Power* 4 (2), 2003

[13] Borghi, M. et al.: Influence of Notch Shape and Number of Notches on the Metering Characteristics of Hydraulic Spool Valves. In: *International Journal of Fluid Power*, 6(2), pp. 5–18, 2005.

[14] Merritt, H.E.: *Hydraulic Control Systems*. New York: John Wiley & Sons Inc, 1967.

Nomenclature

Designation	Denotation	Unit
α_D	Discharge coefficient	-
ε	Jet angle at vena contracta	°
$\varepsilon_{1/2}$	Inlet/Outlet flow angle for the inlet throttling	°
$\varepsilon_{1/2}'$	Outlet/Inlet flow angle for the outlet throttling	°
ρ	Fluid density	kg/m^3
A	Area	m^2
$A_{1/2}$	Inlet/Outlet area for the inlet throttling	m^2
$A_{1/2}'$	Outlet/Inlet area for the outlet throttling	m^2
B	Chamfer width	m
F_{Fl}	Steady-state flow force for the inlet throttling	N
F_{Fl}'	Steady-state flow force for the outlet throttling	N
F_x	Net axial force	N
I	Momentum	kg.m/s
L	Length of the spool chamber	m
p	Pressure	Pa
p_1	Pressure on the valve inlet	Pa
p_2	Pressure on the valve outlet	Pa
Q	Flow rate	m^3/s
R	Fillet radius	m
$v_{1/2}$	Inlet/outlet flow velocity for the inlet throttling	m/s
$v_{1/2,r/x}$	Average inlet/outlet radial/axial flow velocity for the inlet throttling *	m/s
$v_{1/2}'$	Outlet/inlet flow velocity for the outlet throttling	m/s
$v_{1/2,r/x}'$	Average outlet/inlet radial/axial flow velocity for the outlet throttling *	m/s
x	Relative x-coordinate	m
x_1	Spool position	m
x_2	Width of the outlet circumferential groove	m
Δp	Pressure differential	Pa
Δr	Height of the radial clearance	m

* The radial flow velocities correspond to the y-components of the flow velocities.

Acknowledgments

The IGF research project 18569 N / 1 of the research association Forschungskuratorium Maschinenbau e. V. – FKM, Lyoner Straße 18, 60528 Frankfurt am Main was supported from the budget of the Federal Ministry of Economic Affairs through the AiF within the scope of a program to support industrial community research and development (IGF) based on a decision of the German Bundestag.

Barrel tipping in axial piston pumps and motors

Peter Achten, Sjoerd Eggenkamp

INNAS BV, Nikkelstr. 15, 4823AE Breda, the Netherlands
E-mail: pachten@innas.com, seggenkamp@innas.com

Abstract

In axial piston pumps and motors, the interface between the cylinder block and the port plate is one of the most complicated design details. This interface is a combination of a thrust bearing and a face sealing. The gap height, i.e. the thickness of the oil film, is only allowed to be a few micrometers. A smaller gap height results in high friction losses and possibly in metal-to-metal contact, causing wear and particle generation. On the other hand, a large gap height causes high leakage. In most cases, the barrel or cylinder block will be tipping instead of lifting, thereby causing a variable gap height and combining both high friction losses (where the gap height is small) and high volumetric losses (where the gap height is large). This paper investigates the factors that determine the barrel force and torque balance. Two axial piston pump principles are investigated and compared: a swash plate, slipper type machine and a floating cup pump/motor.

Keywords: Axial piston pump, barrel tipping

1. Introduction

Positive displacement machines (by definition) have sliding interfaces: machine components sliding on each other, with a thin oil film separating the two components. Some examples are, pistons moving up and down in cylinders, piston slippers running on swash plates and gears running in gear pumps. These interfaces often perform a combination of a bearing and a sealing function. The gap height (i.e. the height of these oil films) needs to be small, but preferably not too small, mostly in the order of a few micrometers. This poses a challenging task for the designer, especially since thermal expansion, pressure deformation and production tolerances can have a substantial effect on the size and geometry of these gaps.

An often-used design principle and solution to this problem is to allow the sliding components to find their own relative position. This solution is used in axial piston machines, for instance, in the sliding interface between the rotating barrel and the stationary port plate, in which the cylinder block is free to find its own position on the port plate (Figure 1). The barrel is connected to the shaft by means of a spline, on which, to some extend, it is allowed to move in the z-direction, and rotate around the x- and y-axis in point *A*. A spring (not shown in Figure 1) is mounted which pushes the barrel to the surface of the port plate after assembly. Furthermore, the sealing lands of the barrel ports are dimensioned as such that there is a remaining hydrostatic force pushing the barrel even harder to the port plate when the pressure level increases.

When being positioned on the port plate, it seems that the only remaining degree of freedom is the rotation around the z-axis. However, on a micro scale, the oil film still separates the barrel from the port plate, thereby allowing the barrel to move a few micrometers in the z-direction, and rotate or tip around the x- and y-axis. In the end, these small micro motions determine the volumetric and mechanical losses of the interface between the barrel and the port plate, but also wear, durability and stability of the pump or motor operation.

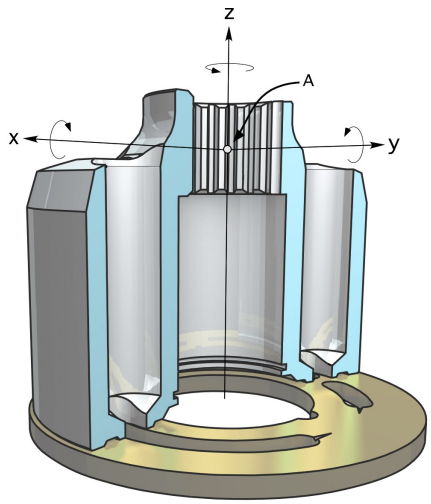

Fig. 1: Barrel and port plate of an axial piston, slipper type machine

In bent axis machines (Figure 2), the tipping around the x- and y-axis is often prevented by means of a central pin. This is possible, since bent axis machines don't have a through drive; the drive shaft stops at the drive flange. Moreover, the large tilt angle of the barrel creates a machine having a rela-

tively long piston stroke and a small barrel diameter. The small diameter of the barrel and the barrel ports is important since the pin reduces the demand for perpendicularity to the surface of the port plate.

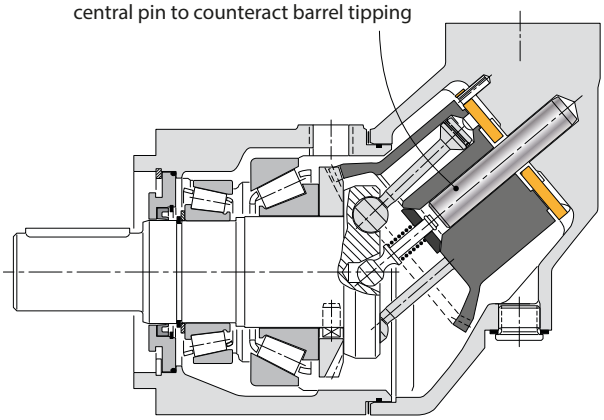

Fig. 2: Cross section of a bent axis pump or motor

Slipper type pumps and motors (Figure 2) have a shaft going through the entire length of the machine. This has the advantage that a second machine can be mounted on the back of the first, but it eliminates the opportunity to apply a central barrel pin. Furthermore, due to the limited swash angle (which is about half of the tilt angle of bent axis machines) the pistons have a shorter stroke and the barrel diameter is larger, which makes it harder to accomplish the perpendicularity between the pin and the sealing area of the barrel ports. As a consequence, the solution of a central barrel pin is not used in slipper type machines, and the barrel is free to tip around the x- and y-axis shown in Fig. 1.

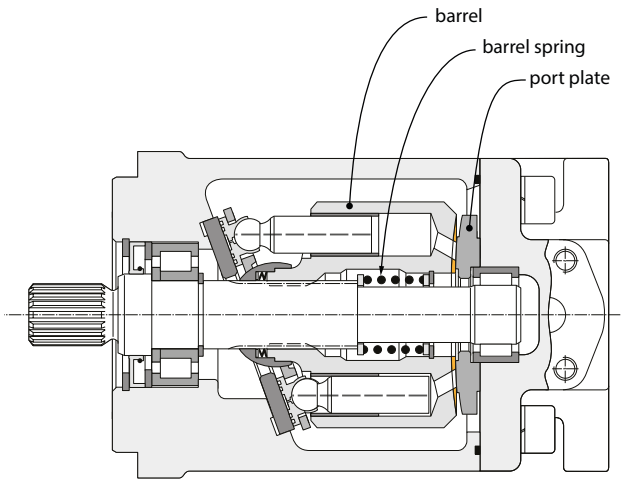

Fig. 3: Cross section of a slipper type pump or motor

Floating cup pumps and motors (Figure 4) have a different construction, in which the pistons are press-fitted into the rotor. Instead, the barrel cylinders have been isolated from the barrel. Each piston is combined with a cup-like cylinder which is floating on the barrel plate. Like in the bent axis design, the barrel has a tilted position relative to the main axis. But the tilt angle is much smaller than in bent axis machines, and even smaller than of slipper type machines. The small tilt angle results in a multi-piston design, having two rings of pistons, arranged in a back-to-back configuration.

Like in slipper type machines, the shaft is going through the entire length of the machine. Another similarity with the slipper type machine is the relatively large diameter of the barrels. The barrels are allowed to rotate around the pivot points, indicated with *A* in Figure 4.

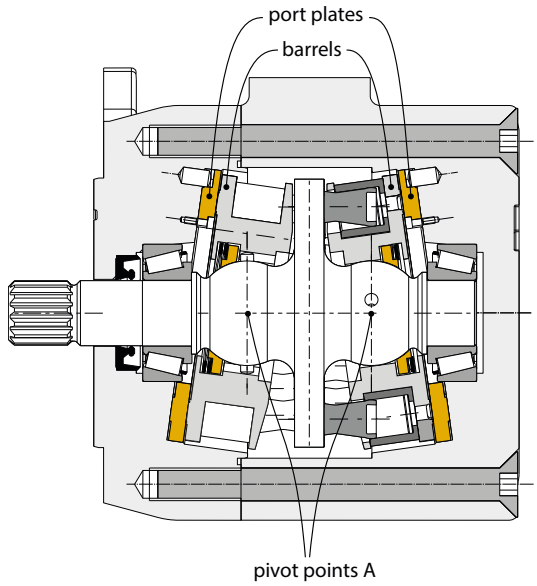

Fig. 4: Cross section of a floating cup pump or motor

The floating cup design belongs to the family of axial piston principles: the barrels are free to find its position on the port plates, thereby being positioned after assembly by a barrel spring. And, just like in other axial piston designs, the force and torque balancing is a difficult design challenge.

This paper discusses the factors that influence the tipping of the barrel in axial piston machines, in particular the amount of spring force which is needed to avoid barrel tipping at high revolutionary speeds and low operating pressures. The paper will only discuss slipper type and floating cup pumps and motors.

2. Tipping torque research

There are many different loads acting on the barrel, which result in a torque load around the x- and y-axis of the barrel:

- Hydrostatic pressure forces inside the cylinder;
- Hydrostatic pressure forces acting on the barrel ports and sealing lands;
- Centrifugal forces;
- Friction forces between the pistons and the cylinders;
- Friction between the barrel and the port plate;
- Lateral piston forces and torques;
- Force of the axial barrel spring;
- Impulse forces of the oil flow.

The hydrostatic forces from the sealing lands are dependent on the pressure profile in the gap between the barrel and the

port plate. The pressure profile is strongly influenced by elasto-hydrodynamic and thermal deformations, as well as by the variation of the viscosity of the oil, while passing the gap, due to temperature and pressure variations [1-4]. The gap profile is also influenced by the precise barrel position on the valve plate, and hence by the tipping itself.

Many of the underlying physical phenomena are, up to now, still not completely understood. The first modeling attempts started in the early 80's [5-7]. These first models were based on rigid-body models [8, 9]. By the turn of the century, the increased capacity and performance of computers allowed the addition of elasto-hydrodynamic (EHD) effects [10-12]. At first, only the deformation of the barrel and the port plate was calculated. In 2006 [13], it became clear that the deformation of the entire housing strongly affected the bearing interface between the barrel and the port plate. Most recent simulations also include the thermal expansion and deformation of the components [3, 14, 15], and the non-flatness and micro-geometry of the bearing surfaces [16, 17]. The calculation of the dynamic micro-motion of the cylinder block has become a complex, multi-domain simulation effort, combining EHD with CFD-analysis, thermal analysis and multi-body mechanical analysis. Yet, despite this enormous progress in simulation techniques, the theoretical analysis does not yet include all relevant aspects, like production tolerances, surface roughness and wear.

Aside from the analytical complexity, it is almost impossible to get a direct, experimental verification of the analytical results. Often, separate test benches are built, in which components, like the cylinder block, the pistons and the port plate, are isolated from the rest of the pump. Figure 5 shows an example of such a test bench, as was developed by Bräckelmann [18, 19]. Consequently, important effects, like the deformation of the housing, are neglected. Other factors, like the bending of the main shaft, are often enlarged, since a special shaft is often constructed for these benches.

Yamaguchi [5, 6] was one of the first to measure the gap height and tipping of a barrel-like structure running on a valve plate. Other experimental research in this area has been performed by Ivantysynova and her team [3, 4, 14-16, 20], Bergada, et al [21-23], Wegner, et al [24, 25], Shin, et al [17], Han, et al [26] and Zhang, et al [27]. Most of these studies measured a gap height between 0 and 20 µm. The experiments also showed a tilted barrel position, creating a wedge shaped fluid film with a varying gap height.

Extensive measurements were performed by Bräckelmann [18] on a relatively small 40 cc swash plate pump. The gap height was measured to be 2 to 14 µm, depending on the rotational speed and the oil pressure. Furthermore, Bräckelmann measured a tipping of the barrel of up to 0.07°. The tipping angle proved to be about linearly dependent of the rotational speed. Furthermore, a larger swash angle and a higher pressure level also increased the barrel tipping.

The influence of the rotational speed on the barrel tipping was also investigated by Noah Manring [28-30]. According to Manring, 'Tipping the cylinder block within an axial-piston swash-plate type hydrostatic machine is a phenomenon that results in a momentary and sometimes permanent failure of the machine' In his paper from 2000 [29] he presented a design criterion for the required force of the central spring of the cylinder block:

$$F_{sp} > \frac{N \cdot M \cdot r^2 \cdot \omega_{\max}^2 \cdot \tan(\alpha) \cdot \left(1 + \tan^2(\alpha)\right)}{2R} \tag{1}$$

in which F_{sp} is the spring force, N is the number of pistons, M is the mass of piston and slipper, $\omega_{\max}$ is the maximum rotational speed, r is the piston pitch radius, R is the outermost radial point of contact on the cylinder block, and α is the swash plate angle.

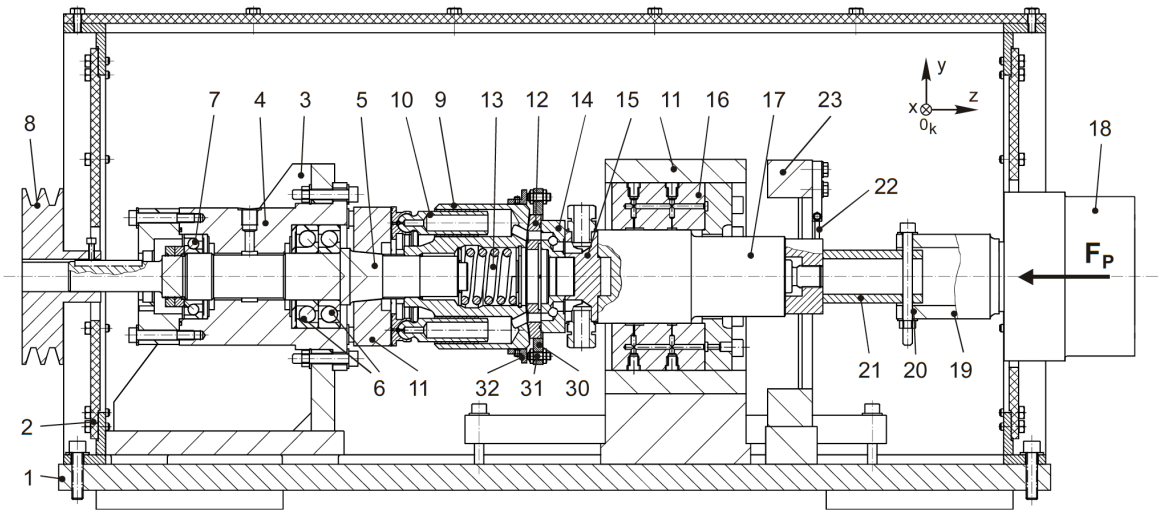

Fig. 5: Test bench for measuring the interface between the barrel and port plate of a swash plate pump [18]

In the paper from 2014 [30], Manring, et al, adapted this equation:

$$\omega^2 < \frac{2 \cdot F_{sp} \cdot R}{N\left(M_p + M_s\right) r^2 \cdot \tan(\alpha)} \tag{2}$$

M_p and M_s are the mass of the piston, respectively of the slipper. This equation can be rewritten as:

$$F_{sp} > \frac{N \cdot M \cdot r^2 \cdot \omega_{\max}^2 \cdot \tan(\alpha)}{2R} \tag{3}$$

which is essentially different from his earlier criterion (equation (1)). Manring does not offer an explanation for this difference. Manring also simplifies the reaction loads from the pistons on the cylinder block. As a result of the angled position of the slipper on the swash plate, the slipper creates a lateral load on the piston. This load results in a torque load on the cylinder block. Manring seems to ignore this torque load. He also neglects the friction between the pistons and the cylinders, which also create a tipping torque on the barrel. Finally, he does not include the friction between the barrel and the valve plate and the friction between the slippers and the swash plate. Due to the variation of the thickness of the oil film in between the barrel and the valve plate, the friction force will also vary around the circumference of the barrel sealing lands, which will cause another tipping torque. Also, the fluid film underneath the slippers varies in height.

This paper presents a new analysis of the torque loads acting on the cylinder block. The aim of the study is to determine the axial force of the cylinder block that is required to prevent the barrel from tipping. Instead of detailed deformation analysis and CFD-calculations of the bearing gaps, simple friction models will be used with constant friction coefficients. Following Manring's analysis, the analysis will be based on a simple rigid-body analysis, and will therefore not include any elasto-hydrodynamic deformations, thermal expansions, or detailed CFD-analysis. However, unlike Manring's analysis, this study also includes the torque loads of the pistons on the barrel, as well as the friction between the pistons and the cylinders.

Two machines will be considered and compared:

- A swash plate type constant displacement pump/motor from Bosch Rexroth (A4FO28 or A4FM28);
- A floating cup constant displacement pump/motor from INNAS.

Both machines have a geometric displacement of 28 cc per revolution.

3. Swash plate pump or motor

Figure 6 shows the pistons, the barrel and the barrel spring as isolated components, including some of the loads acting on these components. Only two pistons are shown, whereas in reality most swash plate machines have nine pistons. Figure 6 is also a simplification since all vectors are only shown in a two-dimensional representation, whereas, some of these forces also have a component in the third, missing dimension.

A model has been developed in which all these forces and components are combined. The model does not include the slipper friction F_{sf}. According to Bräckelmann [18], this force is negligible compared to the hydrostatic lateral piston load.

In swash plate machines, the pistons are severely loaded due to the kinematic principle. The high lateral loads in the contact between the pistons and the cylinders cause substantial friction loads on the barrel [31].

The dimensions and design parameters of the A4FM28/A4-FO28 have been determined by means of disassembling an existing machine and measurement of the dimensions, weights and other relevant parameters (Table 1). The force of the barrel spring has been measured. The data about the friction between the barrel and the valve plate are taken from the thesis of Bräckelmann [18]. The commutation in the top and bottom dead centers is assumed to be instantaneous.

Table 1: A4FM28/A4FO28 parameters

geometric displacement	28	cc/rev
Number of pistons	9	-
Swash angle	19.2	°
Piston diameter	13.5	mm
Piston and slipper mass	56.2	g
Piston length	45	mm
Piston pitch radius	31.2	mm
Port plate outer edge radius	28.45	mm
friction coefficient between the barrel and the valve plate	0.1	-
friction coefficient between the piston and the cylinder	0.1	-
Barrel spring	41	N/mm
compression of the barrel spring	9	mm
force barrel spring	369	N

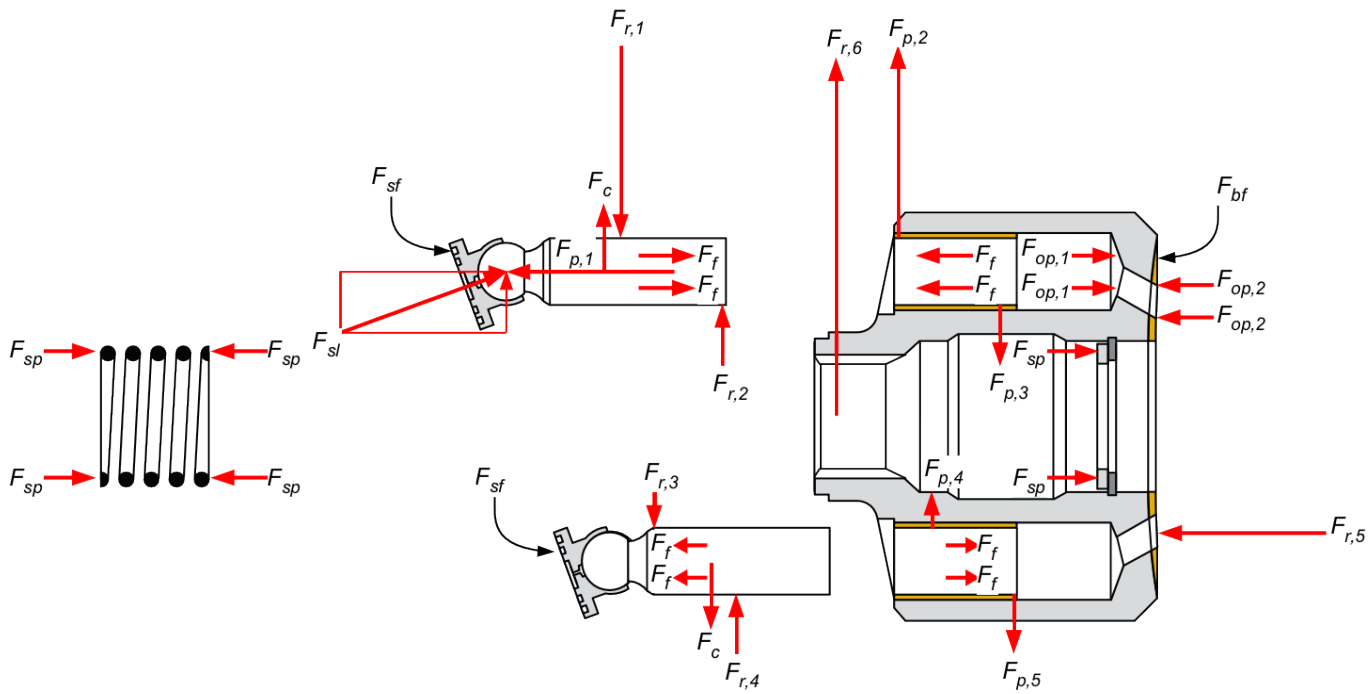

Fig. 6: Loads acting on the pistons, the cylinder block and the barrel spring of a swash plate type pump or motor, showing only 2 pistons, assuming only a pressure load on the upper piston

F_p	hydrostatic force acting on the piston
F_{sl}	Hydrostatic load of the slipper
F_c	Centrifugal force of the piston and slipper
F_f	Friction force between the piston and the cylinder
F_{sf}	Friction between the slipper and the swash plate
F_{sb}	Friction between the barrel and the valve plate
$F_{r,1}$, $F_{r,2}$, $F_{r,3}$, $F_{r,4}$	Reaction force, resulting from the contact between the piston and the cylinder, acting on the piston
$F_{p,1}$, $F_{p,2}$, $F_{p,3}$, $F_{p,4}$	Reaction force, resulting from the contact between the piston and the cylinder, acting on the cylinder
$F_{op,1}$	Hydrostatic force acting on the bottom of the hydraulic cylinder
$F_{op,2}$	Hydrostatic force acting on the barrel ports and sealing lands
F_{sp}	Force of the central barrel spring
$F_{r,5}$	Reaction force between the barrel and the port plate to counteract the tipping torque
$F_{r,6}$	Sum of all radial piston loads acting on the spline of the barrel

The parameters from Table 1 can be substituted in Equation 2 to calculate the maximum rotational speed before, according to Manring, et al [30], the cylinder block starts to tip:

$$n_{\max} = 3342 \text{ rpm} \tag{4}$$

Equation 2, however, does not contain the pump pressure as a parameter influencing the tipping torque. But, it is certain that a higher pump pressure creates a higher torque load of the pistons on the cylinders of the cylinder block, and, in addition, a higher friction torque.

In order to include the pressure load, a new simulation model has been made, which includes all the loads shown in Figure 6. The coordinate system for these calculations is defined in figure 7. The torque load acting on the barrel will make the reaction force move out of the centre. If this force moves outside the circle with radius R, the barrel will tip.

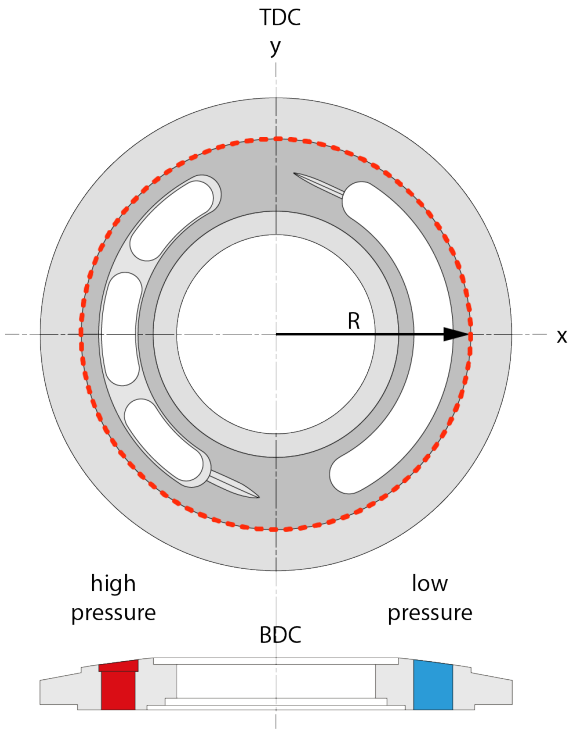

Fig. 7: Top view and cross section of the valve plate of the A4FO28-pump. The red dotted line shows the outmost radius to support the cylinder block against tipping.

In a first calculation, the hydrostatic axial force balance is assumed to be 100%: the size of the seal lands is chosen as such that the counteracting hydrostatic force is exactly equal to the hydrostatic force, which is pushing the barrel towards the valve plate. In this theoretical situation, only the barrel spring is pushing the cylinder block to the valve plate. The calculated position of the reaction force is displayed in Figure 8, for two different operating speeds and four different pump pressures.

The simulation results (Figure 8a) show the strong influence of the pump pressure on the tipping torque. Actually, the barrel will tip at almost all operating conditions. Only for low operating pressures, below 100 bar, the pump can be operated up till about 3000 rpm, without tipping of the barrel.

In a second simulation, the hydrostatic, axial balance has been changed to 93%. In other words, 7% is no longer compensated by the hydrostatic pressure field in between the barrel and the port plate. This corresponds with the actual dimensions of the components of the A4FO28.

This analysis (Figure 8b) shows that a hydrostatic force is needed to prevent the barrel from tipping. At a pressure level of 400 bar, this hydrostatic barrel force has an average value of 1850 N. The strong spring force is needed to prevent the barrel from tipping at low pump pressures in combination with a high rotational speed.

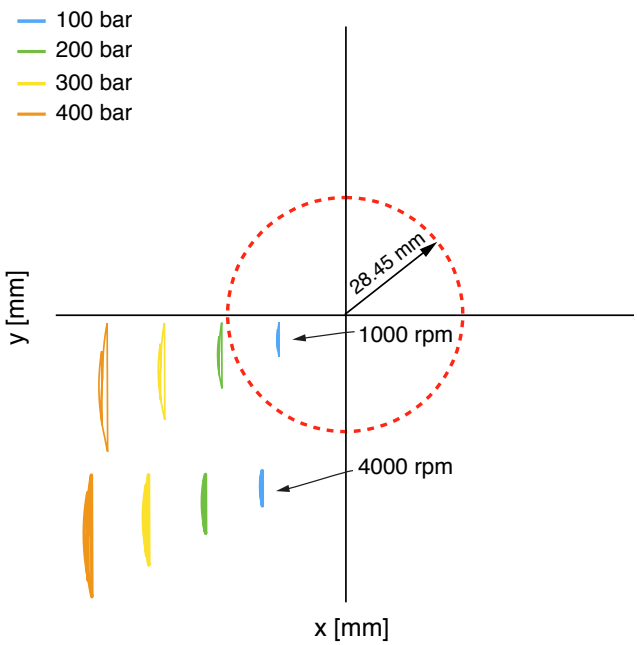

a) Calculated for a hydrostatic axial force balance of 100%

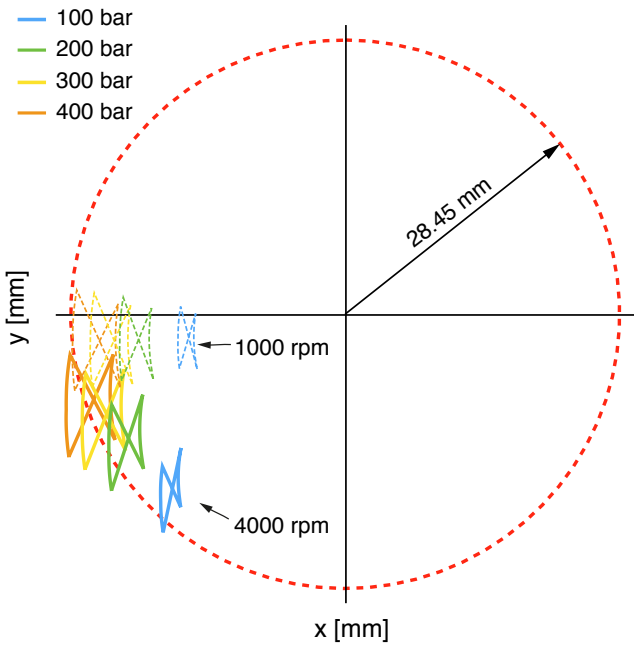

b) Calculated for a hydrostatic axial force balance of 93%

Fig. 8: Position of the axial reaction force, necessary to counteract the tipping torque, calculated for te slipper type machine for two different hydrostatic balances. The dotted red circle is the outer edge of the port plate to support the barrel. If the reaction force is outside this circle, the barrel will tip.

4. Floating cup pump or motor

A floating cup machine is essentially different from a bent axis or a slipper type pump or motor. Figure 10 shows a cross section of the main rotating parts. Figure 11 shows the main loads acting on the barrel. Table 2 gives the main parameters of the 28 cc floating cup pump or motor.

Table 2: 28 cc FC-pump or motor parameters

geometric displacement	28	cc/rev
Number of pistons	24	-
Swash angle	8	°
Piston diameter	12.5	mm
Piston and slipper mass	5.6	g
Piston pitch radius	34	mm
Port plate outer edge radius	34.28	mm
friction coefficient between the barrel and the valve plate	0.1	-
friction coefficient between the piston and the cylinder	0.1	-
force barrel spring	100	N

In floating cup machines, the pistons are press-fitted into the rotor, and can therefore not create a centrifugal load on the barrel. Instead, the cups are free to move and rotate around the piston crown. The position of the centre of gravity of the cup mostly differs from the midpoint of the piston crown, and consequently the cups will create a centrifugal torque load on the barrel. This torque load is counteracted by the forces $F_{r,1}$ and $F_{r,2}$. The number of cups per barrel (12 in this case) is larger than the number of pistons in most axial piston machines. Also the piston pitch radius is somewhat larger. Both factors increase the centrifugal load on the barrel. On the other hand, the weight of the cups is much smaller, about 10% of the piston of the axial piston pump. Also the stroke length is much smaller. In total, the centrifugal load on the barrel in the floating cup machine is 93% smaller than in the slipper type machine.

Another difference concerns the piston friction. Due to the hydrostatic balanced design of the cup, there is almost no friction between the pistons and the cups [32]. The only friction is caused by the centrifugal force of the cup and its oil contents. This (small) friction force has been included in the calculation of the barrel tipping torque.

The hydrostatic balance of the barrel is also essentially different. A new hydrostatic bearing is applied in the floating cup machine [33]. The new hydrostatic bearing creates a variable, gap height dependent pressure load in the sealing lands of each barrel port. In principle it creates a perfect axial hydrostatic balance. Only the barrel spring force remains to push the barrel towards the port plate. Compared to the slipper type pump, the barrel spring force relatively low, being about 27% of the spring force in the slipper type pump. This force is also counteracted by the new hydrostatic bearing.

The cups make a small relative movement on the barrel plate [34]. Consequently, the position of the hydrostatic cup force also moves relative to the compensating hydrostatic force of the barrel port and the corresponding seal lands. This results in an additional torque load on the barrel, which is pressure dependent.

Figure 9 shows the calculated position of the resulting barrel force, which is needed to counteract the tipping torque of the barrel. The force trajectories are calculated for two different rotational speeds and 4 different pressure levels. The calculation is performed assuming a constant pressure in the pockets of the seal lands [33]. In reality, the pressure in the pockets varies depending on the local gap height. As a result, the pockets create an additional torque load on the barrel, which counteracts the barrel tipping.

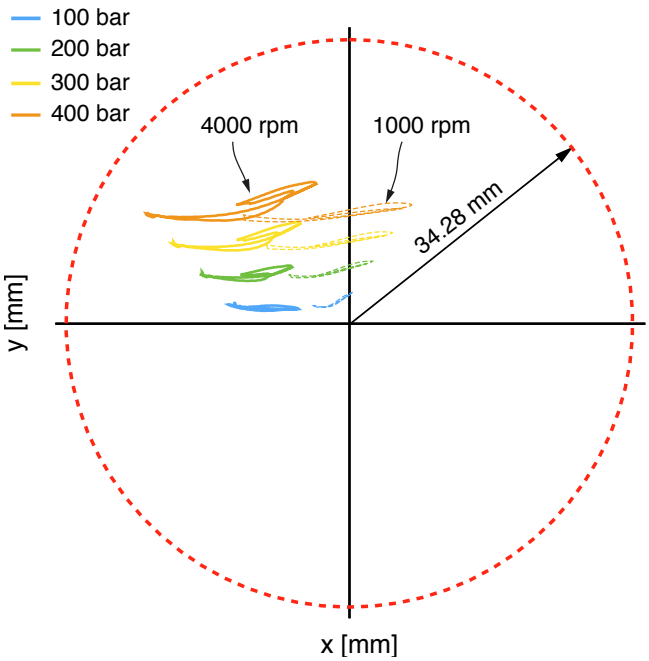

Fig. 9: Position of the axial reaction force, necessary to counteract the tipping torque, calculated for the 28 cc floating cup pump or motor. The dotted red circle is the outer edge of the barrel sealing lands to support the barrel. If the reaction force is outside this circle, the barrel will tip.

The calculation shows that the barrel in the floating cup machine does not tip at 4000 rpm, even at high operating pressures. All curves stay within the outer diameter of the largest seal land.

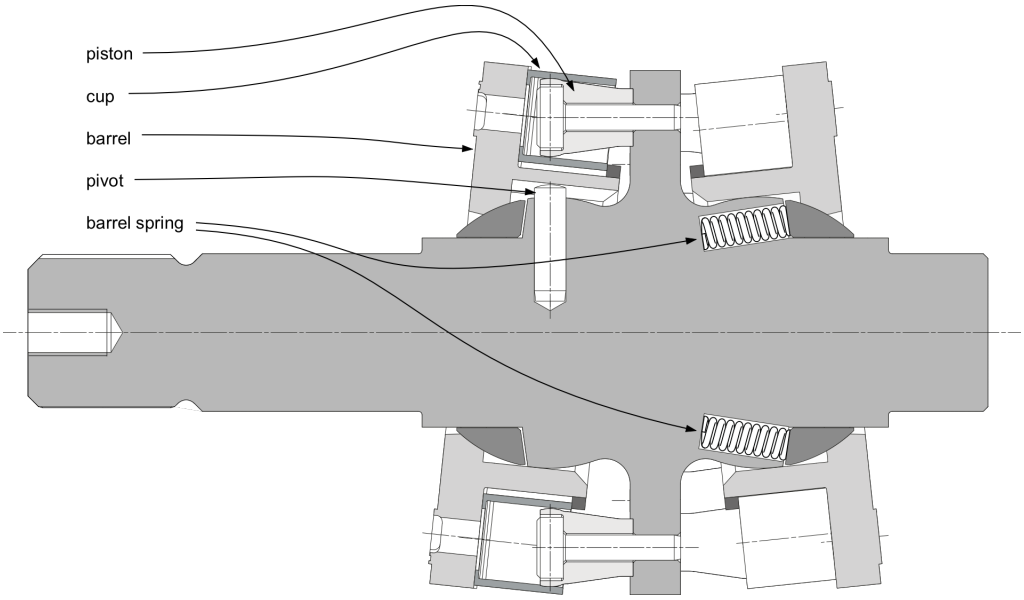

Fig. 10: Cross section of the rotating parts of a floating cup pump

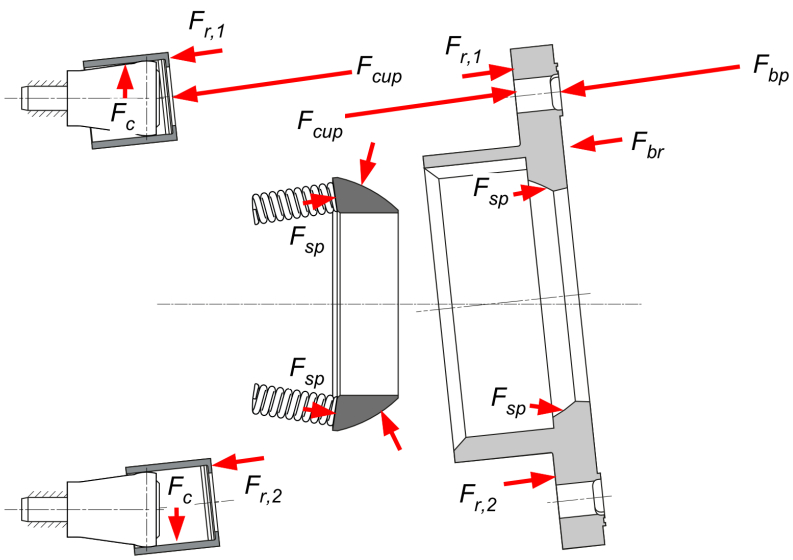

Fig. 11: Loads acting on the cups, the cylinder block and the barrel spring of a floating cup pump or motor, showing only 2 pistons, assuming only a pressure load on the upper piston

F_{cup}	axial hydrostatic force created by the cup
F_c	Centrifugal force of a cup
$F_{r,1}$, $F_{r,2}$	reaction force to counteract the centrifugal torque of the cup
F_{sp}	Force of the barrel spring
F_{bp}	hydrostatic force create by the barrel port and seal lands
F_{br}	Reaction force of the barrel to counteract the tipping torque

5. Comparison of the tipping torque

The simulations show that the tipping torque is strongly influenced by the design principle. For both design principles, the total tipping torque load on the barrel is given in Table 3, as is calculated for 16 different operating conditions. On average, the tipping torque of the floating cup design is only 3.3% of the barrel tipping torque of a slipper type design. The strong reduction is the result of a combination of improvements. Most important are, the reduction of the centrifugal forces by about 93% and the elimination of the lateral loads between the pistons and the cylinders.

Table 3: Calculated average tipping torque in Nm for a 28 cc slipper type (ST) and floating cup machine (FC)

p [bar]	1000 rpm		2000 rpm		3000 rpm		4000 rpm	
	ST	FC	ST	FC	ST	FC	ST	FC
100 bar	14.3	0.37	15.2	0.43	17.6	0.70	22.1	1.21
200 bar	28.7	0.75	29.3	0.84	31.0	1.06	34.3	1.48
300 bar	43.0	1.13	43.6	1.22	45.0	1.41	47.8	1.78
400 bar	57.4	1.50	57.9	1.59	59.2	1.77	61.6	2.11

6. Contact force between the barrel and the valve plate

The slipper type pump needs a strong axial barrel force to keep the barrel from tipping. Even a relatively strong barrel spring is not sufficient to avoid barrel tipping (see Figure 9a). Only when adding a substantial hydrostatic force, the unit can be operated to rotational speeds of about 3000 rpm.

For this last situation, the calculated contact force between the barrel and the valve plate is displayed in the diagram of Figure 12. The diagram shows the calculated contact force for four different pressure levels. Due to the simplified model of the instantaneous commutation, the calculated force is not influenced by the rotational speed.

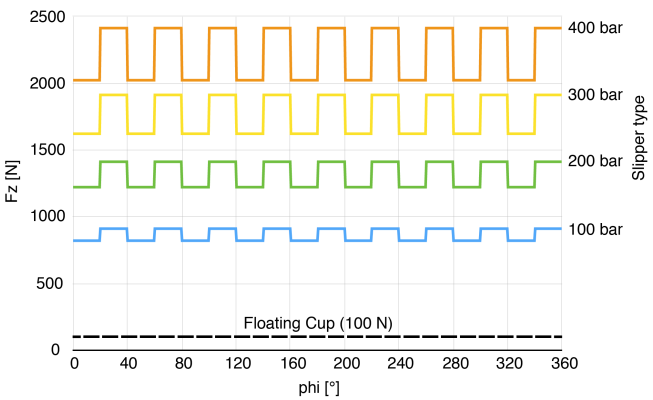

Fig. 12: Calculated contact force between the barrel and the valve plate

The calculation does not include any hydrodynamic effects, nor any elasto-hydrodynamic-deformation which could influence the gap geometry and the bearing capacity. The calculated force is therefore not necessarily a contact force but can be regarded as the force that needs to be overcome by for instance hydrodynamic effects.

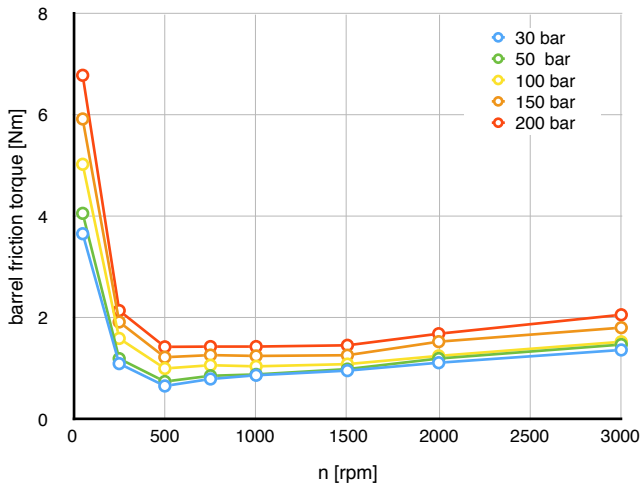

Fig. 13: Friction torque between the barrel and the port plate, measured for a 56 cc slipper type machine

The hydrodynamic lubrication is demonstrated by Bräckelmann [18] by building a separate test bench to measure the friction torque at various operating conditions (Figure 5). Figure 13 shows the measured friction torque for a 56 cc slipper type machine. The measurements are consistent with the Stribeck-effect, showing mixed lubrication conditions and high friction at low operating speeds. For operating speeds of 500 rpm and higher, the friction losses are more or less linear with the operating speed. Nevertheless, the operating pressure creates an additional friction torque, indicating coulomb friction at these conditions.

In the floating cup machine, the axial load between the barrel and the port plate is almost negligible compared to the slipper type. As a consequence, the floating cup principle does not have as much friction losses between the barrel and the valve plate, especially at startup and low operating speeds.

7. Conclusions

In axial piston machines, the operating conditions can be constrained because of tipping of the cylinder block or barrel. Manring [29, 30] has already analysed the relationship between operating speed and barrel tipping. However, in these publications, the torque balance on the cylinder block is strongly simplified, and does not include pressure dependent loads.

This paper has shown, that the operating pressure has a stronger influence on the barrel tipping than the operating speed. In order to avoid tipping in slipper type machines, the barrel and port plate geometry needs to be dimensioned as such that the barrel is not completely balanced in the axial direction. Of the total hydrostatic force exerted by the axial hydrostatic force, only 93% can be compensated by the bar-

rel ports and seal lands. The remaining 7% is needed to sufficiently press the barrel against the port plate, thereby counteracting the tipping torque created by the pistons. Nevertheless, despite the strong axial force, the maximum rotational speed is constraint by the high centrifugal forces and the strong tipping torque created by the pistons.

In this respect, the floating cup principle performs much better. The centrifugal load is decimated due to the low cup mass and the short stroke. Furthermore there are hardly any other loads created by the piston-cup-interface. The total tipping torque is reduced by about 97% compared to the slipper type machine. The force of the central barrel spring can be reduced by more than 70%. Nonetheless, floating cup pumps and motors can be operated at higher operating speeds and pressures without any barrel tipping.

This paper also shows that, in slipper type machines, barrel tipping is related to the efficiency of the pump or motor. In order to prevent barrel tipping, the barrel needs to be pushed stronger in the direction of the valve plate, which increases the friction and reduces the efficiency. In the floating cup principle, this can be avoided completely. The reduced axial force load and tipping torque results in a strong reduction of the friction losses between the cylinder block and the port plate. This results in an increased efficiency and higher startup torque.

References

1. Pelosi, M. and M. Ivantysynova, *The influence of pressure and thermal deformation on the piston/cylinder interface film thickness.* In: *Proceedings of the 52nd National Conference on Fluid Power 2011, NCFP*, 2011. I11-9.3.

2. Pelosi, M. and M. Ivantysynova, *Heat Transfer and Thermal Elastic Deformation Analysis on the Piston:Cylinder Interface of Axial Piston Machines.* Journal of Tribology, 2012. 134(041101): p. 1-15.

3. Zecchi, M., *A novel fluid structure interaction and thermal model to predict the cylinder block/valve plate interface performance in swash plate type axial piston machines.* Dissertation Purdue University, 2013.

4. Zecchi, M. and M. Ivantysynova, *Spherical valve plate design in axial piston machines - A novel thermo-elasto-hydrodynamic model to predict the lubricating interface performance.* The 8th International Conference on Fluid Power Transmission and Control (ICFP 2013), Apr. 9-11, 2013, Hangzhou, China, 2013: p. 325 - 329.

5. Yamaguchi, A. and M. Tsuchimoto, *Bearing Seal Characteristics of the Oil Film between a Valve Plate and a Cylinderblock of Axial Piston Pumps.* Hydraulics & Pneumatics, 1982. 13(1): p. 55-60.

6. Yamaguchi, A., et al., *Characteristics of Fluid Films Between a Valve Plate and a Cylinder Block of Axial Piston Pumps and Motors.* Hydraulics & Pneumatics, 1984. 15(4): p. 64-72.

7. Yamaguchi, A., et al., *Bearing/Seal Characteristics of the Film between a Valve Plate and a Cylinder Block of Axial Piston Pumps (3rd Report- Effects of Fluid Types and Theoretical Discussions).* Hydraulics & Pneumatics, 1987. 18(7): p. 543-550.

8. Wieczorek, U., *Simulation of the gap flow in sealing and bearing gaps of axial piston machines.* Proc. of 1st FPNI-PhD Symposium Hamburg, 2000.

9. Wieczorek, U. and M. Ivantysynova, *Computer aided optimization of bearing and sealing gaps in hydrostatic machines - the simulation tool CASPAR.* International Journal of Fluid Power, 2002. 3(1).

10. Ivantysynova, M., *A new approach to the design of sealing and bearing gaps of displacement machines.* Proc. 4th Int Symposium on Fluid Power, 1999.

11. Huang, C. and M. Ivantysynova, *A new approach to predict the load carrying ability of the gap between valve plate and cylinder block.* Proc. Bath Workshop on Power Transmission & Motion Control, PTMC 2003, Bath, UK, 2003.

12. Ivantysynova, M., *Prediction of pump and motor performance by computer simulation.* 1st Int. Conf. on Computational Methods in Fluid Power Technology, Melbourne, Australia, 2003, 2003.

13. Achten, P.A.J. and M.P.A. Schellekens, *Deformation effects on the load carrying capacity of the barrel bearing in axial piston pumps and motors.* Proc. IMECE2006, 2006 ASME International Mechanical Engineering Congress and Expo November 5-10, 2006, Chicago, Illinois, USA, 2006. IMECE2006-13223.

14. Schenk, A., M. Zecchi, and M. Ivantysynova, *Accurate Prediction of Axial Piston Machine's Performance Through a Thermo-Elasto-Hydrodynamic Simulation Model.* Proc. of the ASME/BATH 2013 Symposium on Fluid Power & Motion Control, FPMC2013, October 6-9, 2013, Sarasota, Florida, USA, 2013.

15. Chacon, R. and M. Ivantysynova, *An investigation of the impact of micro surface on the cylinder block/valve plate interface performance.* Proc. of the 8th FPNI Ph.D Symposium on Fluid Power June 11-13, 2014, Lappeenranta, Finland, 2014(FPNI2014-7837-0).

16. Ivantysynova, M. and J. Baker, *Power Loss in the Lubricating Gap between Cylinder Block and Valve Plate of Swash Plate Type Axial Piston Machines.* International Journal of Fluid Power, 2009. 10(2): p. 29-43.

17. Shin, J.-H. and K.-W. Kim, *Effect of surface non-flatness on the lubrication characteristics in the valve part of a swash-plate type axial piston pump.* Meccanica, 2014. 49(5): p. 1275-1295.

18. Bräckelmann, U., Reibung, *Steifigkeit und Dämpfung in Schrägscheiben-Axialkolbenpumpen und -motoren.* Thesis Ruhr-Universität Bochum, 2006.

19. Bräckelmann, U. and F. Jarchow, Reibung, *Steifigkeit und Dämpfung in Schrägscheiben-Axialkolbenpumpen und –motoren.* Wissensportal Baumaschine.de, 2006.

20. Pelosi, M., M. Zecchi, and M. Ivantysynova, *A fully coupled thermo-elastic model for the rotating kit of axial piston machines.* Proc. Bath ASME Symposium on Fluid Power and Motion Control FPMC, 2010: p. 217 - 234.

21. Bergada, J.M., J. Watton, and S. Kumar, *Pressure, Flow, Force, and Torque Between the Barrel and Port Plate in an Axial Piston Pump.* Journal of Dynamic Systems, Measurement, and Control, 2008. 130(1): p. 011011.

22. Bergada, J.M., et al., *Experimental investigation in axial piston pumps barrel dynamics.* Proc. Flucome 2009, 10th Int. Conf. on Fluid Control, Measurements, and Visualization, August 17-21, 2009, Moscow, Russia, 2009.

23. Bergada, J.M., et al., *The effect of oil pressure and temperature on barrel film thickness and barrel dynamics of an axial piston pump.* Meccanica, 2011. 47(3): p. 639-654.

24. Wegner, S., et al., *Experimental Investigation of the Cylinder Block Movement in an Axial Piston Machine.* Proc. ASME/BATH 2015 Symposium on Fluid Power and Motion Control, FPMC2015, Oct. 12-14, 2015, Chicago, Ill., USA, 2015(FPMC2015-9529).

25. Wegner, S., F. Löschner, and S. Gels, *Validation of the physical effect implementation in a simulation model for the cylinder block/valve plate contact supported by experimental investigations.* Proc. 10th IFK International Fluid Power Conference, Dresden , Germany , March 8-10, 2016. 1(269-282).

26. Han, L., S. Wang, and C. Zhang, *A partial lubrication model between valve plate and cylinder block in axial piston pumps.* Proceedings of the Institution of Mechanical Engineers, Part C: Journal of Mechanical Engineering Science, 2015. 229(17): p. 3201-3217.

27. Zhang, C., et al., *A new dynamic seven-stage model for thickness prediction of the film between valve plate and cylinder block in axial piston pumps.* Advances in Mechanical Engineering, 2016. 8(9).

28. Manring, N., *Torque on the cylinder block of an axial-piston swash-plate type hydrostatic pump.* Retrospective Theses and Dissertations. Paper 11164, 1996.

29. Manring, N.D., *Tipping the Cylinder Block of an axial-piston swash-plate type hydrostatic machine.* Transactions of the ASME, 2000. 122: p. 216-221.

30. Manring, N.D., et al., *Scaling the Speed Limitations for Axial-Piston Swash-Plate Type Hydrostatic Machines.* Journal of Dynamic Systems, Measurement, and Control, 2014. 136(3): p. 031004.

31. Jeong, H.-S. and H.-E. Kim, *On the instantaneous and average piston friction of swash plate type hydraulic axial piston machines.* KSME International Journal, 2004. 18(10): p. 1700-1711.

32. Achten, P., T.v.d. Brink, and M. Schellekens, *Design of a variable displacement floating cup pump.* Proc. SICFP'05, June 1-3, 2005, Linköping, Sweden, 2005.

33. Achten, P.A.J., T.L.v.d. Brink, and G.E.M. Vael, *A robust hydrostatic thrust bearing for hydrostatic machines.* Proc. 7.IFK, March 22-24, 2010, Aachen, Germany, 2010: p. 100-112.

34. Achten, P.A.J., T.L.v.d. Brink, and J.W. Potma, *Movement of the Cups on the Barrel Plate of a Floating Cup, Axial Piston Machine.* Int. Journal of Fluid Power, 2004. 5(2): p. 25-33.

An Open-Source Framework for Efficient Co-simulation of Fluid Power Systems

Robert Braun[1], Adeel Asghar[2], Adrian Pop[2], and Dag Fritzson[3]

[1]Division of Fluid and Mechatronic Systems, Dept. of Management and Engineering, Linköping University, Sweden
[2]PELAB - Programming Environment Lab, Dept. of Computer Science, Linköping University, Sweden
[3]SKF Group Technology, AB SKF, Göteborg, Sweden
E-mail: robert.braun@liu.se, adeel.asghar@liu.se, adrian.pop@liu.se, dag.fritzson@skf.com

Abstract

Simulation of fluid power systems typically requires models from multiple disciplines. Achieving accurate load dynamics for a system with complex geometry, for example, may require both a 1D model of the hydraulic circuit and a 3D multi-body model. However, most simulation tools are limited to a single discipline. A solution to these kinds of problems is co-simulation, where different tools are coupled and simulated together. Co-simulation can provide increased accuracy, improved modularity and facilitated collaboration between different organizations. Unfortunately, tool coupling typically requires tedious and error-prone manual work. It may also introduce numerical problems. For these reasons, co-simulation is often avoided as long as possible. These problems have been addressed by the development of an open-source framework for asynchronous co-simulation. Simulation tools can be interconnected through a stand-alone master simulation tool. An extensive range of tools is also supported via the Functional Mockup Interface standard. A graphical user interface has been implemented in the OpenModelica Connection Editor. System models can be created and edited from both a schematic view and a 3D view. Numerical robustness is enforced by the use of transmission line modelling. A minimalistic programming interface consisting of only two functions is used. An example model consisting of a hydraulic crane with two arms, two actuators and a hanging load is used to verify the framework. The composite model consists of nine multi-body models, one hydraulic system model and a controller. It is shown that models from various simulation tools can be replaced with a minimal amount of user input.

Keywords: Co-simulation, system simulation, multi-body simulation, transmission line modelling

1 Introduction

Fluid power systems often interact with other domains, such as mechanical systems, combustion engines, electric power systems or controllers. Meanwhile, most simulation tools are specialized on a specific domain or discipline. Co-simulation makes it possible to couple different tools into a composite model. In this way the best suited tool can be used for each part of the system. It can also facilitate cooperation between or within organizations by allowing each part to keep working in their favorite tool. Such an approach preserves investments in simulation tools, existing models and trained staff. Another benefit is the modularity. If two models share a common connection interface, they can easily be replaced. Increased modularity is for example useful when working with models of different fidelity.

However, setting up a co-simulation can be time consuming, error-prone and require special knowledge. There is also a risk for lock-in effects when using a commercial master simulation tool. As a consequence, tool coupling is often avoided. This paper presents an open source framework for asynchronous co-simulation. The aims of this work include extensive compatibility with other tools, a user-friendly interface and a minimalistic coupling interface. Support for the Functional Mock-up Interface (FMI) standard has been implemented for increased tool compatibility. The framework is demonstrated with example models representing a hydraulic crane and an engine connected to a pump.

2 Related work

Several master algorithms based on the FMI standard have been proposed. A simple master was developed by [1]. More advanced algorithms based on High-Level Architecture (HLA), a standard for distributed computer simulation systems, exists [2] [3] [4]. A master with adaptive communication step-size control was proposed by [5]. An approach using relaxation techniques was presented in [6]. While the two latter methods addressed the issue of numerical stability, they

both rely on rejecting simulation steps, which is not supported by all exporting tools. This paper differs in that it focuses on decoupling at the model level using TLM. In this way, numerical stability is always guaranteed. Previously, TLM-based co-simulation using FMI has been investigated for synchronous coupling of Modelica models [7] and for connection a hydraulic models in Hopsan with multi-body mechanical models in Adams [8].

3 Transmission Line Modeling

When decoupling a model into smaller parts, introducing a time delay is inevitable. Such delays may affect numerical stability unless handled properly. This is addressed by using the transmission line modeling (TLM) method [9] [10]. In reality, every physical element has a natural time delay. Mechanical wave propagation through an element is determined by equations (1) and (2).

$$F_1(t) = F_2(t-\Delta t) + Z_c\left[v_1(t) + v_2(t-\Delta t)\right] \tag{1}$$
$$F_2(t) = F_1(t-\Delta t) + Z_c\left[v_2(t) + v_1(t-\Delta t)\right] \tag{2}$$

F is the force, v the velocity, Δt the time delay and Z_c the characteristic impedance of the element. These equations are based on the assumption that friction can be neglected. A consequence of this is that resonances can occur at high frequencies. This can be addressed by filtering the delayed variables, according to equations (3) and (4) [11]. The filter variable α represents an approximated friction model.

$$F_1(t) = v_1(t) + (1-\alpha)c_1(t) + \alpha c_1(t-\Delta t) \tag{3}$$
$$F_2(t) = v_2(t) + (1-\alpha)c_2(t) + \alpha c_2(t-\Delta t) \tag{4}$$

Where:

$$c_1(t) = Z_c v_2(t-\Delta t) + F_2(t-\Delta t)$$
$$c_2(t) = Z_c v_1(t-\Delta t) + F_1(t-\Delta t)$$
$$0 \leq \alpha < 1$$

Force and velocity can be replaced by variables from other physical domains, for example pressure and flow in hydraulic systems. As can be seen, side 1 is always independent on side 2 at the same point of time and vice versa. In this way the numerical time delay introduced by the tool coupling can be replaced by a physically motivated time delay in the model equations. Hence, numerical robustness will not be affected, which makes the method suitable for co-simulation [12] [7]. Besides, TLM can also be used for parallel simulation [13] [14] [15] and detailed modeling of wave propagation [16] [17]

The use of TLM implies limiting the maximum step size of the simulation. For this reason, it is best suited for models where the step size is generally smaller than the physical time delays. It is also desirable that the model has parts with large capacitance (or compressibility) and small inductance (or inertia). Both these requirements are usually fulfilled by fluid system models.

4 Functional Mock-up Interface

The Functional Mock-up Interface (FMI) is a standardized interface for communication between simulation tools [18]. It was launched in 2009, and is currently supported by more than 90 simulation tools. There are two versions of FMI: FMI for co-simulation (FMI CS) and FMI for model exchange (FMI ME). With co-simulation, each slave solves its own equations and exchanges data on pre-defined communication points. With model exchange, the master tool handles the numerical solver, and the slave contains only the model equations. Models are exported as Functional Mock-up Units (FMU), a zip package with the file extension FMU. This package contains an XML description file and either pre-compiled binaries or source code with the actual implementation.

5 Co-simulation Framework

The co-simulation framework was originally developed by SKF in cooperation with Linköping University. It was mainly intended for simulation of bearings coupled to models in external tools [12]. The source code has been donated to the Open Source Modelica Consortium. Models from different simulation tools, called *external models*, are connected to a *composite model*. The external models communicate through network sockets, as shown in figure 1. All messages are sent through a co-simulation *manager process*, which forwards each message from the sender to the receiver. A *monitor process* is executed in parallel, and is used for logging simulation results.

External models communicate asynchronously using two functions: `getForce()` and `setMotion()`, see listing 1. Whenever a step is complete, result data is sent to the connected models. Variables are stored in interpolation tables, and can be interpolated for a requested time instance. This makes it possible for each external model to use its own local solver with an independent time step. The only requirement is that the maximum time step is limited to half the TLM time delay, in order to avoid extrapolation [19].

Listing 1: External models communicate with the master using two function.

```
void GetForce3D(int interfaceID,
                double time,
                double position[],
                double orientation[],
                double speed[],
                double ang_speed[],
                double *force);

void SetMotion3D(int interfaceID,
                 double time,
                 double position[],
                 double orientation[],
                 double speed[],
                 double ang_speed[]);
```

Perhaps the most important property of a co-simulation framework is compatibility with as many simulation tools as possible. For this reason, support for FMI been introduced. In addition, direct tool coupling is available for several tools, including SKF BEAST, Simulink, Adams, Hopsan, OpenModelica, Dymola and Wolfram SystemModeler.

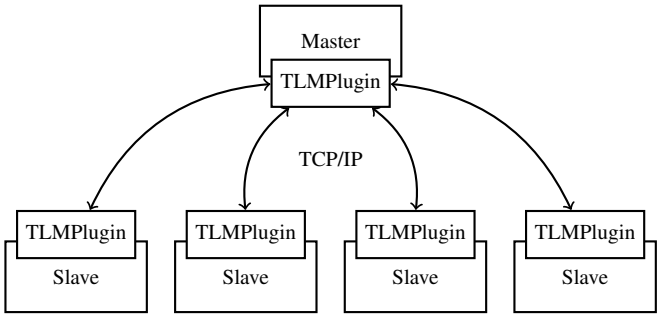

Figure 1: External models communicate with the master using network sockets.

6 Graphical User Interface

A graphical user interface [20] for the framework has been implemented as an extension to the OpenModelica Connection Editor (OMEdit) [21]. It contains an XML editor, a 2D diagram view and a 3D view. The 2D diagram view is shown in figure 2. Sub-models can be added, connected and aligned. Interface information can be fetched from each external model. A plotting tool and 3D animation can be used to analyze results after a simulation.

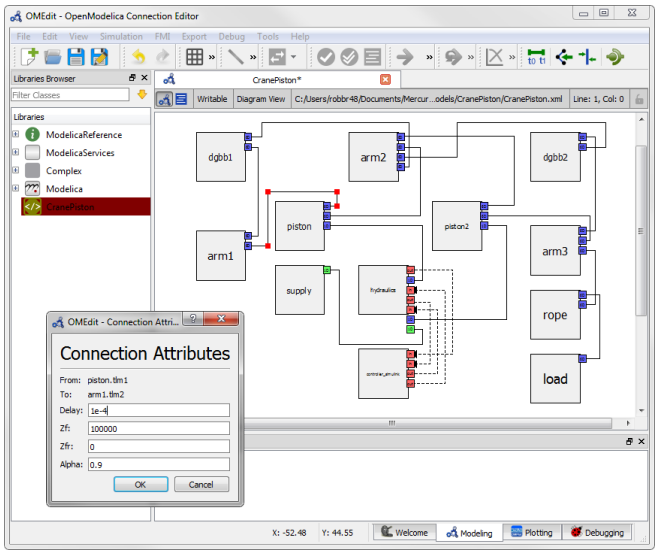

Figure 2: The graphical user interface is implemented in the OpenModelica Connection Editor.

7 Tool Description

The following tools have been used in the simulations:

OpenModelica is an open source simulation tool using the Modelica language developed at Linköping University [22].

BEAST (BEaring Simulation Tool) is a multi-body simulation tool developed by SKF [23] [24].

Hopsan is a system simulation tool mainly focused on fluid power developed at Linköping University [25] [26].

Dymola is a commercial simulation tool based on the Modelica language, developed by Dassault Systèmes [27].

Simulink is a graphical modeling and simulation tool by Mathworks, integrated with the Matlab environment [28].

Adams is a multi-body dynamics simulation tool by MSC [29].

8 Example Model 1: Hydraulic Crane

Co-simulation is often used for interfacing 1D system models with 3D multi-body mechanical models. It is also common to have the controller in a separate tool. For this reason, a model of a hydraulic crane is used to demonstrate the features of the framework, see figure 3. Two pistons are used to move two arms from a lower position (solid) to an upper position (dashed).

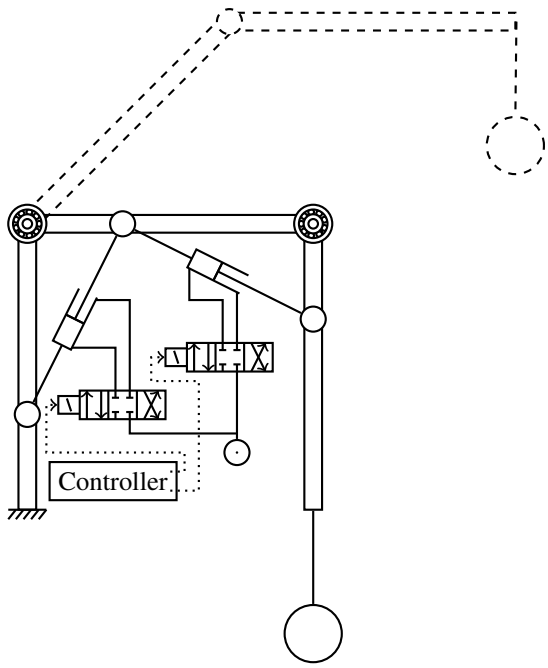

Figure 3: A composite model of a hydraulic crane controlled by two hydraulic pistons.

The crane is lifting a mass load, hanging from a stretched sling. A constant pressure hydraulic system model is driving the pistons. Two bearings are used at the joints between the arms. The motion is controlled by two position feedback controllers, one for each piston. Figure 5 shows the different parts of the composite model. Both 1D and 3D TLM connections are used, as well as directional signals. The latter are simply delayed variables, send from one external model to another.

The composite model is defined by an XML file. Two different configurations, using different external tools, are tested, see table 1. All tools mentioned above, as well as FMI CS and FMI ME, are used. This confirms the modularity of the

approach. If two tools support FMI export, models from the tools can easily be interchanged, assuming they have the same interface ports. This is performed either by modifying XML tags for model file and start script. It can also be done directly from within the graphical editor. It is not necessary to modify the TLM connection settings (time delay and characteristic impedance) when changing configurations, since these represent physical properties of the system which are independent of the surrounding sub-models. For example, the simplified controller model can be replaced with the real control code for software-in-the-loop testing. Models of individual components can also be replaced with models provided by vendors. Furthermore, different hydraulic system concepts can be analyzed and compared without changing the other parts of the complete system.

Simulation results are shown in figure 6. The two different configurations are shown as solid bright lines and dashed lines, respectively. The green lines show the positions of the center of gravity of the mass loads. As can be seen, the two configurations coincide almost perfectly with each other. This was expected, since both configurations have the same level of model fidelity. Oscillations occur due to a fast motion in combination to poor dynamic properties in the system. The model is not optimized or validated, and results are only intended to verify the feasibility of the method. Results can also be visualized in a 3D animation, as shown in figure 4.

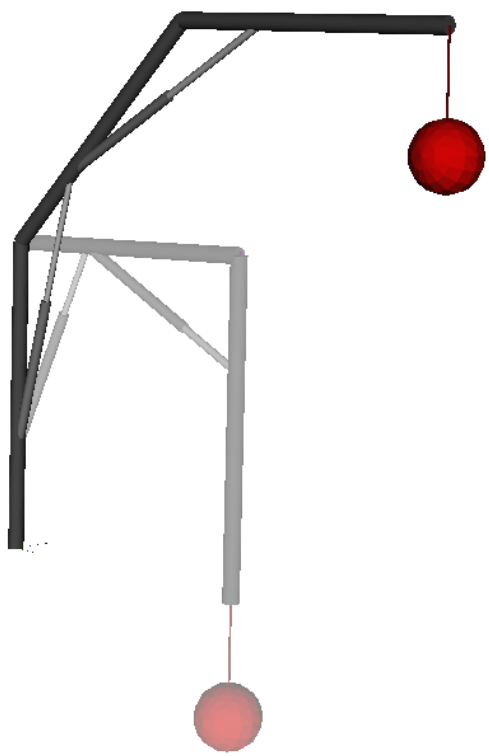

Figure 4: A 3D visualization of the upper and lower position of the crane.

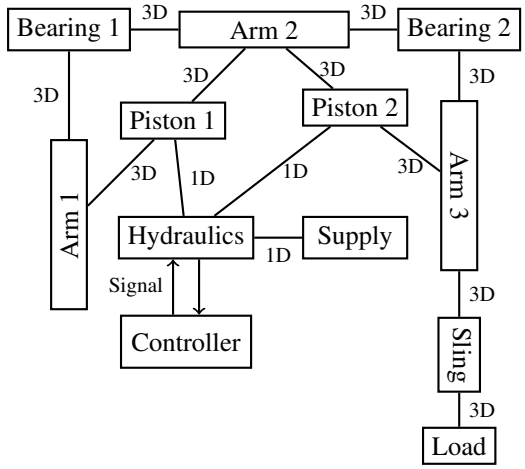

Figure 5: A schematic view of the different external models used in the hydraulic crane model.

Part	Configuration 1	Configuration 2
Arm 1	OpenModelica	Dymola
Arm 2	OpenModelica	OpenModelica
Arm 3	OpenModelica	OpenModelica
Bearing 1	BEAST	BEAST
Bearing 2	BEAST	BEAST
Piston 1	OpenModelica	OpenModelica
Piston 2	OpenModelica	OpenModelica
Sling	OpenModelica	FMI CS (OpenModelica)
Load	OpenModelica	FMI ME (OpenModelica)
Hydraulics	Hopsan	Hopsan
Controller	Simulink	FMI CS (Hopsan))

Table 1: Two different configurations, using different tools, are used for the crane model.

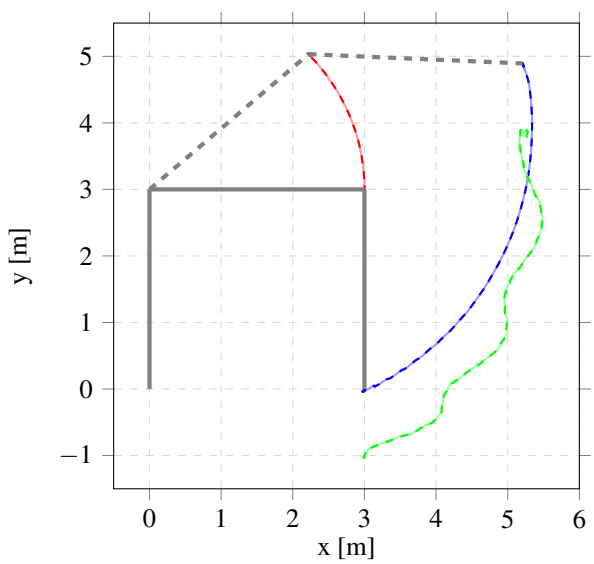

Figure 6: Simulation results for the crane model. The green line represents the position of the load.

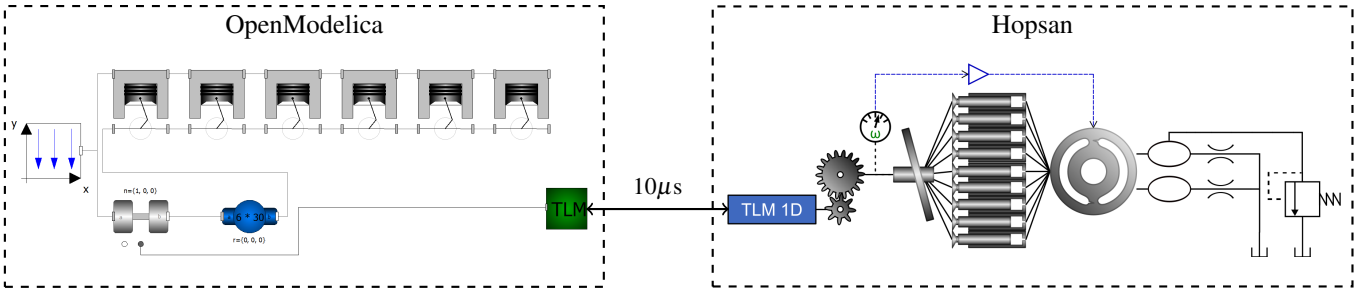

Figure 7: A combustion engine model in OpenModelica connected to a model of an in-line axial piston pump in Hopsan.

9 Example Model 2: Engine and Inline Axial-Piston Machine

As a second example, a model of a combustion engine is connected to a model of an in-line axial piston pump, see figure 7. The XML file describing the model is shown in listing 2. This makes it possible to study the interaction between the engine and the pump, without using simplified models. The engine model is an existing model from the Modelica Standard Library, and exported to FMI using OpenModelica. The pump model is a low-level system simulation model created in Hopsan. A swash plate is connected to nine pistons, which in turn are connected to a valve plate. The pressurized system is modeled using a laminar orifice and a pressure relief valve, both connected to tank. A detailed view of flow pulsations and pressure pulsations at the high-pressure side of the pump are shown in figure 8.

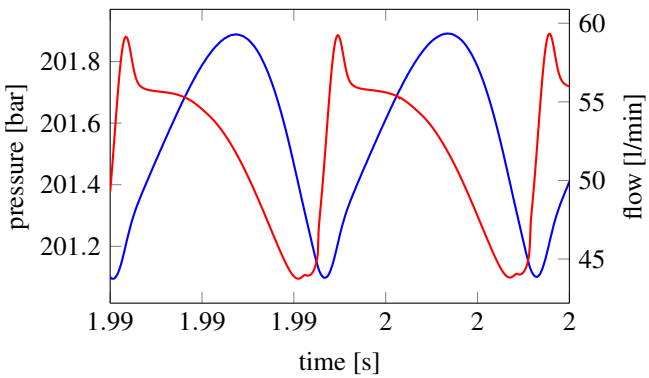

Figure 8: Pressure pulsations (blue) and flow pulsations (red) from the second example model.

Due to the modular model structure, the minimalistic interface and support for FMI, the two models can easily be replaced with more detailed ones. The pump could for example be replaced with a CFD model, and the engine with a model from a specialized engine simulation tool. Advantages of coupling 1D system models with 3D CFD models were discussed in [30]. Furthermore, the laminar orifice, representing the load, could be replaced with a more realistic model.

10 Example Model 3: Full Vehicle Model with Semi-active Suspension

In a previous experiment, a co-simulation model of semi-active hydraulic damping in a forwarder was developed in [8]. A hydraulic system in Hopsan was connected to a full-vehicle model in Adams. The main purpose was to minimize soil damage by maintaining an equal distribution of ground forces among the wheels. Tool coupling was achieved by exporting the Hopsan model as an FMU, which was imported in Adams. Adams could then read the TLM variables and convert them to forces using the TLM equations implemented as custom functions. While this experiment was successful, the method involves some drawbacks. Most importantly, the Adams model must be customized to support TLM.

By instead using the framework described in this paper, the TLM equations would be computed in the master algorithm. In this way, both the Adams and the Hopsan models could rely on general callback functions for sending velocity and receiving force. This would also make it possible for Adams to use variable step-size and implicit solvers without compromising numerical accuracy. Both tools support FMI and can be exported to the framework as FMUs. There are also direct connections available for both Hopsan and Adams, which enable more features and can reduce overhead.

11 Challenges

While the method proves to be stable and modular, there are some remaining research challenges. First, the FMI standard for co-simulation does not currently support asynchronous communication with delayed variables. Instead, input variables are assumed to be constant between communication steps (constant extrapolation). There is some support for extrapolation using time derivatives of input variables, but this is not supported by many exporting tools. Also, it does not provide guaranteed stability. An alternative solution could be adaptive step-size control with error estimation. However, this requires rollback mechanisms. Even though rollback is supported by FMI, it is optional for exporting tools to support it. Consequently, many tools are not able to do this. Hence, solving the problem completely is only possible by extending the FMI standard.

Another issue with the current framework is directional signal connections. Since there is a time delay in every connection, signals will also be delayed. Even though signals has

Listing 2: The XML file defining the second example model.

```
<Model Name="EnginePump">
  <SubModels>
    <SubModel Name="engine"
              ModelFile="engine.mo"
              StartCommand="StartTLMOpenModelica"
              Position="0,0,0"
              Angle321="0,0,0"  >
      <InterfacePoint Name="tlm"
                      Domain="Rotational"
                      Causality="Bidirectional"
                      Dimensions="1"
                      Position="0,0,0"
                      Angle321="0,0,0"  />
    </SubModel>
    <SubModel Name="pump"
              ModelFile="pump.hmf"
              StartCommand="StartTLMHopsan"
              Position="0,0,0"
              Angle321="0,0,0">
      <InterfacePoint Name="tlm"
                      Domain="Mechanical"
                      Causality="Bidirectional"
                      Dimensions="1"
                      Position="0,0,0"
                      Angle321="0,0,0" />
    </SubModel>
  </SubModels>

  <Connections>
    <Connection To="pump.tlm"
                From="engine.tlm"
                Delay="1e-5"
                Zfr="10"
                alpha="0.9"/>
  </Connections>

  <SimulationParams StopTime="2" StartTime="0"/>
</Model>
```

a natural physically motivated time delay, the magnitude is very small in for example control loops. Such small delays would impose severe limitations to simulation performance. Using larger delays, on the other hand, may affect accuracy, for example by increasing phase shift in control loops. A possible solution can be to use a wrapper with a local master algorithm for each group of signal models, which handles sorting, scheduling and stepping of these models.

Finally, the limitation on the step size can be problematic even for TLM connections. Some simulations, as for example vehicle drive cycles, requires variable step size for achieving good performance. Fixed limitations on maximum step size may then not be feasible. A possible solution could be to allow variable TLM time delays. Adaptive time-stepping in TLM models has previously been investigated [31]. Numerical stability will not be affected by a larger time delay. Instead, it will induce a modeling error in the form of a parasitic inductance. At steady-state, however, inductance will not have any effect. Hence, increasing the delays can be acceptable in certain situations.

12 Conclusions

Coupling different simulation tools is important for the fluid power domain. Hydraulic systems are typically used to transfer power from one mechanical system to another. Complex mechanics require specialized modeling and simulation tools, which are usually not suitable for simulating hydraulic circuits. Furthermore, the hydraulic system is often connected to some control software. Other simulation domains which could be of interest, although not discussed in this paper, include computational fluid dynamics and finite element analysis.

By using TLM for decoupling, numerical time delays can be avoided. Hence, there is no risk for numerical errors or instability. TLM is suitable for models which contains large time delays in comparison to the time steps required for the simulation. This includes, for example, hydraulic circuits, long electric transmission lines or mechanical models with strong dynamics. Besides, TLM can also be used for simulating wave propagation with good accuracy.

An open-source master simulation tool provides a vendor neutral co-simulation platform, without the risk for lock-in effects. Support for the FMI standard enables compatibility with a large number of simulation tools. Attaching new tools to the framework is facilitated by a minimalistic coupling interface. The example models with different configurations confirms good compatibility and modularity. Future work includes support for event handling, improved support for FMI and testing on industrial applications.

References

[1] Jens Bastian, Christoph Clauß, Susann Wolf, and Peter Schneider. Master for co-simulation using FMI. In *8th International Modelica Conference, Dresden*. Citeseer, 2011.

[2] Atiyah Elsheikh, Muhammed Usman Awais, Edmund Widl, and Peter Palensky. Modelica-enabled rapid prototyping of cyber-physical energy systems via the functional mockup interface. In *Modeling and Simulation of Cyber-Physical Energy Systems (MSCPES), 2013 Workshop on*, pages 1–6. IEEE, 2013.

[3] Muhammad Usman Awais, Peter Palensky, Wolfgang Mueller, Edmund Widl, and Atiyah Elsheikh. Distributed hybrid simulation using the HLA and the functional mock-up interface. *Industrial Electronics Society, IECON*, pages 7564–7569, 2013.

[4] Himanshu Neema, Jesse Gohl, Zsolt Lattmann, Janos Sztipanovits, Gabor Karsai, Sandeep Neema, Ted Bapty, John Batteh, Hubertus Tummescheit, and Chandraseka Sureshkumar. Model-based integration platform for fmi co-simulation and heterogeneous simulations of cyber-physical systems. In *Proceedings of the 10 th International Modelica Conference; March 10-12; 2014; Lund; Sweden*, number 096, pages 235–245. Linköping University Electronic Press, 2014.

[5] Tom Schierz, Martin Arnold, and Christoph Clauß. Co-simulation with communication step size control in an FMI compatible master algorithmnak. In *9th Int. Modelica Conf., Munich, Germany*, pages 205–214, 2012.

[6] Bernhard Schweizer, Daixing Lu, and Pu Li. Co-simulation method for solver coupling with algebraic constraints incorporating relaxation techniques. *Multibody System Dynamics*, 36(1):1–36, 2016.

[7] Robert Braun and Petter Krus. Tool-independent distributed simulations using transmission line elements and the Functional Mock-up Interface. October 2013.

[8] Robert Braun, Liselott Ericsson, and Petter Krus. Full vehicle simulation of forwarder with semi active suspension using co-simulation. In *ASME/BATH 2015 Symposium on Fluid Power and Motion Control*, October 2015.

[9] Donard De Cogan, William J O'Connor, and Susan Pulko. *Transmission line matrix (TLM) in computational mechanics*. CRC press, 2005.

[10] Petter Krus. Robust modelling using bi-lateral delay lines for real time and faster than real time system simulation. In *ASME 2009 International Design Engineering Technical Conferences and Computers and Information in Engineering Conference*, pages 131–138. American Society of Mechanical Engineers, 2009.

[11] P. Krus, A. Jansson, J-O. Palmberg, and K. Weddfelt. Distributed simulation of hydromechanical systems. In *The Third Bath International Fluid Power Workshop*, Bath, England, 1990.

[12] Alexander Siemers, Dag Fritzson, and Iakov Nakhimovski. General meta-model based co-simulations applied to mechanical systems. *Simulation Modelling Practice And Theory*, 17(4):612–624, 2009.

[13] Kaj Nyström and Peter Fritzson. Parallel simulation with transmission lines in Modelica. In *5th International Modelica Conference*, Vienna, Austria, September 2006.

[14] Martin Sjölund, Mahder Gebremedhin, and Peter Fritzson. Parallelizing equation-based models for simulation on multi-core platforms by utilizing model structure. In Alain Darte, editor, *Proceedings of the 17th Workshop on Compilers for Parallel Computing*, Lyon, France, July 2013.

[15] Robert Braun and Petter Krus. Multi-threaded distributed system simulations using the transmission line element method. *SIMULATION*, 92(10):921–930, October 2016.

[16] P. Krus, K. Weddfelt, and J-O. Palmberg. Fast pipeline models for simulation of hydraulic systems. *Journal Of Dynamic Systems Measurement And Control*, 116:132–136, 1994.

[17] Nigel Johnston. The transmission line method for modelling laminar flow of liquid in pipelines. *Proceedings of the Institution of Mechanical Engineers, Part I: Journal of Systems and Control Engineering*, 226(5):586–597, 2012.

[18] T. Blochwitz, M. Otter, M. Arnold, C. Bausch, C. Clauß, H. Elmqvist, A. Junghanns, J. Mauss, M. Monteiro, T. Neidhold, D. Neumerkel, H. Olsson, J.-V. Peetz, and S. Wolf. The Functional Mockup Interface for tool independent exchange of simulation models. In *8th International Modelica Conference 2011*, Como, Italy, September 2009.

[19] Iakov Nakhimovski. *Contributions to the Modeling and Simulation of Mechanical Systems with Detailed Contact Analyses*. PhD thesis, Linköping University, PELAB - Programming Environment Laboratory, The Institute of Technology, 2006.

[20] Alachew Mengist, Adeel Asghar, Adrian Pop, Peter Fritzson, Willi Braun, Alexander Siemers, and Dag Fritzson. An open-source graphical composite modeling editor and simulation tool based on FMi and TLM co-simulation. In Peter Fritzson and Hilding Elmqvist, editors, *Proceedings of the 11th International Modelica Conference*. Modelica Association and Linköping University Electronic Press, September 2015.

[21] Syed Adeel Asghar, Sonia Tariq, Mohsen Torabzadeh-Tari, Peter Fritzson, Adrian Pop, Martin Sjölund, Parham Vasaiely, and Wladimir Schamai. An open source Modelica graphic editor integrated with electronic notebooks and interactive simulation. In Christoph Clauß, editor, *Proceedings of the 8th International Modelica Conference*. Linköping University Electronic Press, March 2011.

[22] Peter Fritzson, Peter Aronsson, Håkan Lundvall, Kaj Nyström, Adrian Pop, Levon Saldamli, and David Broman. The openmodelica modeling, simulation, and software development environment. *Simulation News Europe*, 44:8–16, 2005.

[23] Lars Erik Stacke, Dag Fritzson, and Patrik Nordling. Beast—a rolling bearing simulation tool. *Proceedings of the Institution of Mechanical Engineers, Part K: Journal of Multi-body Dynamics*, 213(2):63–71, 1999.

[24] Dag Fritzson, Lars-Erik Stacke, and Jens Anders. Dynamic simulation–building knowledge in product development. *Evolution*, 1, 2014.

[25] Mikael Axin, Robert Braun, Alessandro Dell'Amico, Björn Eriksson, Peter Nordin, Karl Pettersson, Ingo Staack, and Petter Krus. Next generation simulation software using transmission line elements. In *Fluid Power and Motion Control*, Bath, England, September 2010.

[26] B. Eriksson, P. Nordin, and P. Krus. Hopsan NG, a C++ implementation using the TLM simulation technique.

In *The 51st Conference On Simulation And Modelling*, Oulu, Finland, 2010.

[27] Modelon. Dymola. http://www.modelon.com/products/dymola/. Accessed 2015-10-07.

[28] The Mathworks, Inc. Simulink - Simulation and Model-Based Design. https://se.mathworks.com/products/simulink/. Accessed 2016-11-22.

[29] RR Ryan. ADAMS - multibody system analysis software. In *Multibody Systems Handbook*, pages 361–402. Springer, 1990.

[30] J. Galindo, A. Tiseira, P. Fajardo, and R. Navarro. Coupling methodology of 1d finite difference and 3d finite volume {CFD} codes based on the method of characteristics. *Mathematical and Computer Modelling*, 54(7-8):1738 – 1746, 2011.

[31] S. H. Pulko, A. Mallik, R. Allen, and P. B. Johns. Automatic timestepping in TLM routines for the modelling of thermal diffusion processes. *International Journal of Numerical Modelling: Electronic Networks, Devices and Fields*, 3(2):127–136, 1990.

Towards Finding the Optimal Bucket Filling Strategy through Simulation

R. Filla[1] and B. Frank[1,2]

[1]Volvo Construction Equipment, Emerging Technologies, 631 85 Eskilstuna, Sweden
[2]Lund University, Faculty of Engineering, 221 00 Lund, Sweden

E-mail: reno.filla@volvo.com, bobbie.frank@volvo.com

Abstract

The purpose of earth-moving equipment like wheel loaders is to engage with the ground or other material. It is therefore obvious that the bucket filling phase must be included when studying optimal machine control over a complete working cycle because total productivity and efficiency of the machine are to a large extent determined by it. This paper reports and discusses the results of research into how to utilize Discrete Element Method simulations in combination with Optimal Control to find the optimal bucket filling strategy and what has been learned regarding preparing and conducting both simulations of bucket filling and physical testing for verification. This paper also discloses which bucket filling strategy appears to be optimal, based on the results so far – and why we cannot be completely certain.

Keywords: wheel loaders, bucket filling, working cycle, trajectory, optimization, simulation, optimal control, dynamic programming, tool/ground interaction, discrete-element method

1 Introduction

Construction machines can be made – and need to be – significantly more energy efficient. Industry knowledge and published research, including our own, indicate that large improvements can be achieved by approaching this task holistically. Construction machinery OEMs will have to make their journey towards significantly increased energy efficiency with these four milestones in mind:

- Understanding the machine as *one* system
- Understanding the interaction between machine, operator and working environment
- Understanding the cooperation between several machines and their operators
- Understanding the connection to regional, national and international transport and energy systems

All these milestones have been previously described in [1]. The topic of this paper relates to milestones 1 and 2 as our research is anchored in the realization that in a working machine like a wheel loader all major systems interact frequently, all phases in a working cycle are connected, and both operator and working environment play a decisive role when it comes to productivity and energy efficiency of the total system.

2 Background

Figure 1 depicts a short loading cycle with the characteristic driving pattern in the shape of a V, possible to extend to a Y-pattern, if necessary [2].

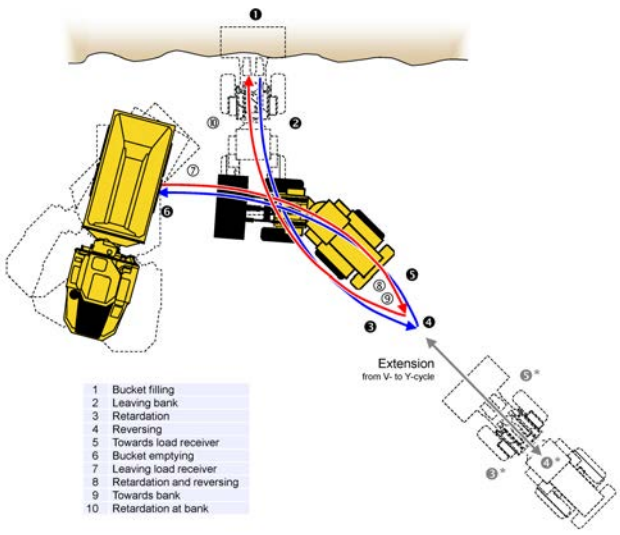

Figure 1: Short loading cycle in classic V- or Y-pattern. [2]

From phase 1 to 6, the wheel loader operator first fills the bucket in the gravel pile, then drives backwards towards the reversing point (phase 4) and steers the wheel loader to accomplish the aforementioned characteristic V-pattern. The lifting function is engaged the whole time. The operator chooses the reversing point such that having arrived at the load receiver and starting to empty the bucket (phase 6), the lifting height will be sufficient to do so without delay. In case of a bad matching between the machine's travelling speed and the lifting speed of the bucket, the operator needs to drive back the wheel loader even further than necessary

for maneuvering alone. This additional leg transforms the V-pattern into a Y.

In previous research [3][4] it has been examined whether the driving pattern necessarily has to resemble a V or Y as it appears that this pattern has emerged from the operators' desire to minimize the personal workload, rather than maximize energy efficiency, for a required productivity. The traditional cycle in Figure 1 might not necessarily be the most productive or the most energy-efficient way for new non-conventional systems like hybrids or autonomous machines where the operator's requirements are less dominant or taken out of the loop completely. However, papers [3][4] showed that the classic V- or Y-cycle is a good and robust choice and seems to be recommendable for virtually all situations where such driving pattern is not prevented by the layout of the site.

Based on this conclusion research has then been focused on how to optimally control the actuators of a wheel loader for maximum energy efficiency [5], basically covering phases 2 to 10 in Figure 1 with an assumed attachment position in the beginning. However, this exclusion of the bucket filling phase is a serious simplification because how the bucket is filled in phase 1 and at what height the bucket is retracted from the pile has a significant influence on the overall energy efficiency of a wheel loader in a short loading cycle [2][6].

We have therefore used DEM (Discrete Element Method) particle simulation to study how bucket filling can be simulated in detail [2]. In order to avoid slowing down simulation of loading cycle phases 2 to 6 a non-coupled approach was chosen for the bucket filling in phase 1, which means that the bucket was considered in isolation, moving along a (large) set of pre-defined trajectories.

As discussed at length in [7] this approach has the obvious flaw that the tight coupling of forces leading to a complex interaction of the machine's subsystems (engine, drivetrain, hydraulics etc.), the work environment and the operator is largely disregarded. Even though the loader's linkage has been represented through the way the trajectories have been generated [2] and/or how the simulation results have been analyzed [7], this limited approach falls short of the full simulation scope actually required. The overall cycle efficiency value and thus the performance of a particular bucket filling strategy are first apparent after the wheel loader has arrived at the load receiver to empty the bucket. Therefore the simulation must comprise a complete machine model operated by an adaptable operator model in a full working cycle, executed in a comprehensive model of the work place – and run in an overall optimization loop of the bucket trajectory. However, this is not feasible today and must remain a vision for the moment being.

We have thus been left with the pragmatic approach of isolating the bucket and prescribing its nominal motion independent of any resistive forces that might interfere with the actual control. Papers [1][2] have discussed the setup and results of these simulations and [1] has also shown a simplistic way of how the evaluate them in the context of a complete loading cycle.

The next step for reaching the vision of the comprehensive, integrated optimization described above has been Optimal Control of machine actuators in *all* phases of a prescribed loading cycle, using Dynamic Programming, which paper [7] reports. The machine studied is the electric series hybrid wheel loader briefly discussed in [8][9], which has been the precursor and foundation of the "LX1" concept loader [10].

In the paper at hand we will revisit the bucket filling in both simulation and practice, discuss how to prepare and conduct testing virtually and physically, and provide a self-critical assessment of the results achieved.

3 Simulation

3.1 Process

Figure 2 shows the simulation process employed: the bucket trajectories, generated in MathCad or Matlab, have been transferred as text files to the DEM particle simulation run in Pasimodo, as reported in [2]. The results have been transferred back to MathCad for postprocessing (like converting the forces acting on the bucket into cylinder forces and rim pull demand) and then either passed on to Matlab and the Optimal Control algorithm running wheel loader simulations [7] or kept within MathCad to compute the simple performance indicators published in [1].

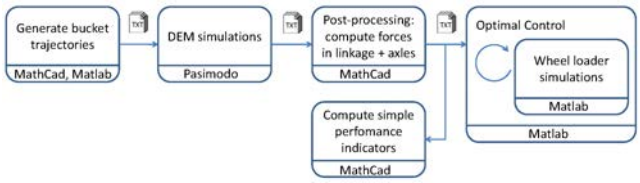

Figure 2: Simulated bucket tip trajectories in phase 1.

The MathCad parts in this process could just as well have been performed in Matlab, too (in the aftermath of this work all scripts and the toolbox developed for such calculations have in fact been ported to Matlab). The DEM simulations in Pasimodo have been set up and conducted by Martin Obermayr and Jan Kleinert from the Fraunhofer ITWM institute in Kaiserslautern, Germany [2][7].

3.2 Bucket filling: literature research

There are a great many publications, both academic papers and industrial patents (or patent applications) on the topic of bucket automation and autonomous excavation [2].

In a publication from 1994 [11] Hemami studies bucket trajectories in order to minimize energy consumption in the scooping and loading process. He concentrates on the motion pattern itself and does not consider resistive forces in this paper. One of his conclusions is that simply estimating the bucket load achieved as the area between the trajectory and the uncut contour of the material will lead to deviations that need to be corrected by an experimentally determined factor. We have used the same estimation in our study but have a different method of compensation, using results from DEM simulations [2].

3.3 Trajectory generation: overview

Ideally the DEM simulation would be part of the overall simulation that includes the Optimal Control scheme. That way both physicality and optimality (local or global, depending on the method chosen) would be ensured. However, no traditional Optimal Control algorithm can be used as the overall problem is not and cannot be made convex to find gradients for optimization. Instead we used an own algorithm based on Dynamic Programming [7]. However, running one big simulation with a complex machine model in a sufficiently detailed environment, controlled by an adaptive operator model is impossible with the calculation resources typically available, because the computational costs using Dynamic Programming would be extraordinary high (though this can change in the near future, considering cloud computing).

Instead, we disconnected the DEM bucket filling simulation from the machine simulation [1][2] by generating a total of 5781 bucket motion trajectories a priori which were then simulated in parallel on a computer cluster of 800 cores for a week. The results of these simulations have then been incorporated into the machine simulation [7].

We have developed four different principle trajectories along which the bucket is moved in DEM simulations. Each trajectory type is the result of interviews with experienced wheel loader operators and represents a different bucket filling strategy commonly employed.

In addition to the desired bucket fill factor (i.e. load mass in the bucket in relation to the nominal load) most trajectories types offer at least one parameter to vary the individual shape. The bucket trajectories are generated a priori using a kinematic model of the wheel loader's front body, complete with linkage, hydraulic cylinders, bucket, and front axle. Controlling the bucket motion indirectly through cylinder displacements and a longitudinal motion of the machine ensures that only valid bucket positions are prescribed, corresponding to a valid state of the wheel loader's linkage.

In addition to these four parametric trajectories a fifth set of bucket motions has been generated as an exploration of "all possible" ways for a bucket to move through a pile and end up with the desired fill factor. In this type of trajectory we only considered the bucket motion, initially without taking linkage constraints into account. Bucket positions that do not correspond to a valid state of the wheel loader's linkage have been filtered out afterwards.

The major simplification with both approaches is that only the nominal motion of the bucket is prescribed, independent of any resistive forces that might interfere with the actual control and without the adaptive behavior of a human operator. This lack of feedback is a significant limitation, but the study gives some meaningful answers, nonetheless. There are clearly also challenges, which will be discussed later.

3.4 Type A: "Slicing cheese"

This type is a literal implementation of the bucket filling strategy advocated by professional machine instructors who were interviewed prior to our study. Their advice was to move the bucket such as if carving a slice of constant thickness off the material pile.

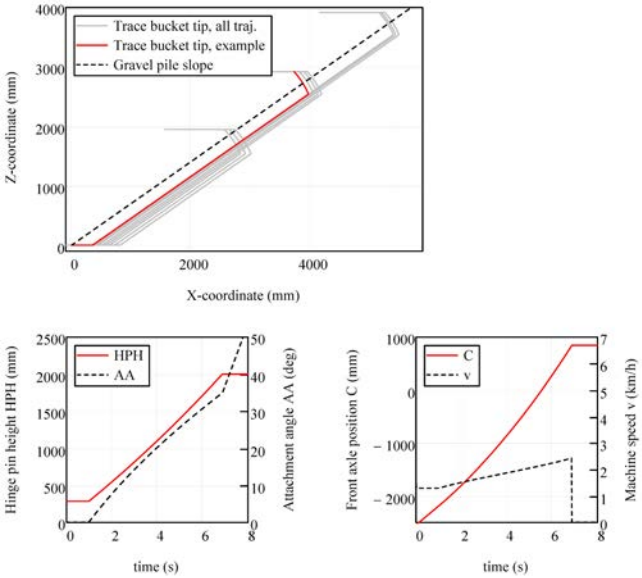

Figure 3: Example type A trajectory, optimized for exit height at 2m and fill factor 1 (grey: all 9 simulated trajectories of type A).

In the top left diagram in Figure 3 we see the trace of the bucket tip moving at a constant distance to the slope until a height of about 2.5m (corresponding to the hinge pin of the bucket being at 2m), at which point the bucket is fully tilted back. The diagrams at the bottom of Figure 3 show how this is accomplished: the bucket is constantly lifted from ground position to exit height (set a priori), while at the same time being tilted back proportionally from initial angle (zero) to maximum angle (which is the slope angle of the material pile, because once the bucket is parallel with the slope, no further advancement can be made without the bucket's bottom pushing into the material, which creates a large reaction force and is a waste of energy). After stopping at exit height the bucket is just tilted back and retracted. The forward motion of the complete machine is controlled so that the bucket tip is always at a constant distance to the pile's slope.

In this algorithm the exit height can be chosen freely, while the slice thickness is a result of the targeted fill factor and thus subject to parameter optimization (the value satisfying the fill factor requirement is calculated iteratively).

3.5 Type B: "Just in & out"

This simple algorithm mimics the bucket filling style of operators who rely mostly on momentum and rim pull (traction force) to fill the bucket: they just push the bucket into the pile, then tilt back and leave. No further advancement is made after the initial penetration.

In the top left diagram in Figure 4 we see the trace of the bucket tip accomplished purely by the motions of the hydraulic cylinders without any further longitudinal motion

after initial penetration of the pile, as exhibited in the diagram to the right. The bottom left diagram discloses that in order to fulfill the fill factor target, the bucket's hinge pin height also needed to be increased slightly (ca. 25mm) by using the lift function simultaneously with the tilt function that controls bucket angle.

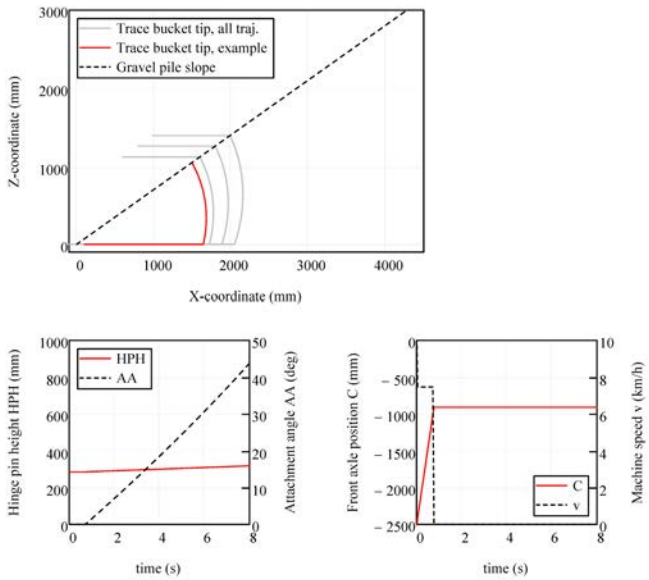

Figure 4: Example type B trajectory, optimized for fill factor 1 (grey: all 3 simulated trajectories of type B).

This trajectory type offers no additional parameter since the initial penetration is a result of the targeted fill factor and thus subject to parameter optimization.

3.6 Type C: "Parametric parabola"

This algorithm can be parameterized to generate trajectories of seemingly different shapes, mimicking the way most experienced operators fill a bucket with a wheel loader, provided the material is easily handled so that continuous actuator motions are possible. Most operators trying to fill a bucket according to type A "Slicing cheese" will probably end up with a slightly curved trajectory, i.e. type C.

In the top left diagram in Figure 5 we see the trace of the bucket tip moving on a quadratic curve in relation to the slope until a height of about 1m (corresponding to hinge pin height of 0.50m) at which point the bucket is fully tilted back. This is accomplished in a similar fashion as for trajectory type A, as can be seen in the bottom diagrams in Figure 5; however, this time the forward motion is controlled so that the bucket tip is always at that distance to the pile's slope which is prescribed by the quadratic curve.

Depending on the parameter values a type C trajectory can be made to resemble a type A "Slicing cheese" or type B "Just in & out" trajectory. The bucket exit height and the control point height where the maximum penetration depth counted from the slope is achieved can be chosen freely, while maximum penetration itself is a result of the targeted fill factor and therefore subject to parameter optimization.

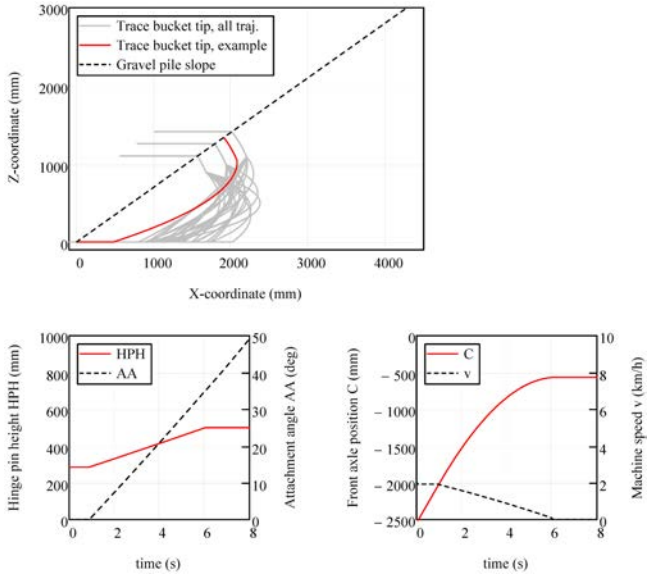

Figure 5: Example type C trajectory, optimized for exit height 0.50m, maximum chip depth at 0.4m, and fill factor 1 (grey: all 27 simulated trajectories of type C).

3.7 Type D: "Stairway"

This trajectory is composed of an adjustable, pre-defined number of steps, like a stairway. Within each step the wheel loader stands still and only the hydraulic functions lift and tilt are executed. A new step is inserted by advancing machine and bucket forward using the drive train. This mimics the way less experienced operators, or experienced ones working in tough material, *reactively* fill a bucket by repeatedly advancing into the pile using traction, lifting a little all the time and now and then, when the forward motion has ceased, breaking material by tilting backwards, which makes further advancement into the pile possible [6].

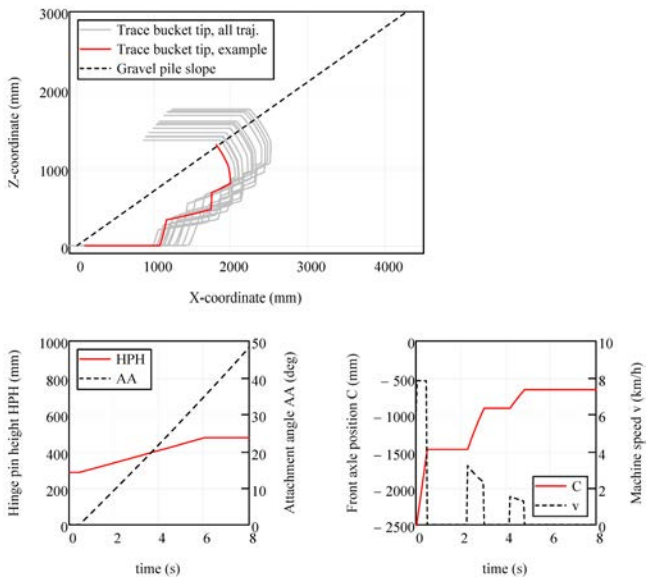

Figure 6: Example type D trajectory, optimized for two steps, depreciation factor 0.5, and fill factor 1 (grey: all 12 simulated trajectories of type D).

In the top left diagram in Figure 6 we see an example stairway consisting of two stairs after initial penetration. In between the steps the bucket is constantly lifted and tilted. During forward advancement the bucket height and angle also need to be controlled in order to avoid pressing the bucket's bottom against the cut surface of the gravel pile. At the end of the sequence the bucket is tilted back fully and then retracted.

In this algorithm the number of stairs can be chosen freely, together with a depreciation factor that controls the subsequent advancements in relation to the initial penetration (a depreciation of 0.5 means that the depth of each subsequent penetration is only half as deep as the previous one). The initial penetration depth is a result of the targeted fill factor and therefore derived through parameter optimization by means of iterations.

3.8 Type E: "Exhaustive search"

In contrast to the trajectory types A to D, each founded on real-world observations and a specific theory of how the bucket is to be moved through the gravel pile, the idea behind this trajectory type has been to move the bucket along all possible, even counter-intuitive paths as long as there are continuous motions forward and upward and as long as the resulting bucket fill factor is approximately fulfilled.

To this end the bucket's three degrees of freedom have been discretized and the bucket tip has been controlled to move from one grid point to the other with its x- and z-coordinate as two degrees of freedom and the bucket angle as the third [7]. Ideally the discretization would be extremely fine in each dimension, but in order to limit the massive amount of output trajectories the step size in x and z has been a rather coarse 375mm and 8.5° for the target bucket angle.

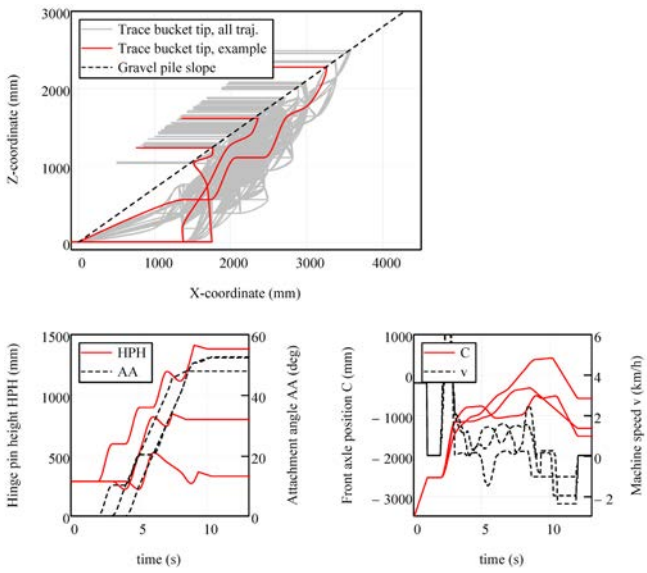

Figure 7: Three examples of type E trajectories (grey: all 4640 simulated and valid trajectories of type E).

Note that in contrast to trajectory types A to D this time only the bucket itself has been considered, not the complete loader linkage – which, among other problems, together with the coarse discretization grid results in rather step-wise control of the lift and tilt actuators as well as machine motion, which can be seen in Figure 7.

3.9 Particle simulation

The particle simulations utilize the DEM code Pasimodo. The model consists of 16000 spherical and non-rotational particles of diameters ranging from 8 to 12cm. A 5m high pile is modeled as a particle layer of 4m thickness over a solid inclined surface. More details on this setup and lessons learned can be found in [2].

All trajectories have been simulated varying each adjustable parameter in three or four steps (except for the three discretization parameters in type E), which results in the number of simulations as per table below.

Type	Name	Parameters	Simulations
A	Slicing cheese	2	9
B	Just in & out	1	3
C	Parametric parabola	3	27
D	Stairway	2	12
E	Exhaustive search	(3)	5730

The bucket fill factor achieved is determined as the ratio of the loaded mass to the rated mass of the bucket, the former obtained through the vertical force that is required to balance the bucket after complete retraction from the pile. Due to the complexity of the granular flow the amount of material loaded into the bucket always shows deviations from the target, the latter been simply estimated a priori as the area between the trajectory of the bucket tip and the uncut contour of the material pile. Our approach has therefore been to simulate each trajectory several times with various horizontal offsets and through interpolation, using the simulated fill factors, to determine which profile offset was required to reach the exact bucket fill factor that has been originally aimed for. New trajectories have then been generated with the profile offset added to the initial penetration in the beginning of the filling sequence and verified in a final simulation [2].

3.10 Particle simulation results: observations

Visualizing the simulation results of the various trajectory variants in a rendered video has been found a very suitable approach to both debug models and algorithms, and to learn about various phenomena that occur during bucket filling.

Figure 8 shows snapshots from a simulation with a type D trajectory. During the filling phase, a wedge of gravel is moved together with the bucket, as indicated by the color representing the velocity of the material particles. When the bucket is tilted back, some material gets lost. This loss of material is difficult to predict in advance without the help of

a particle simulation. Our naïve approach to estimate the bucket fill from the area that is formed between the bucket tip trajectory and the pile contour assumes the pile to remain at rest and therefore cannot account for material flow.

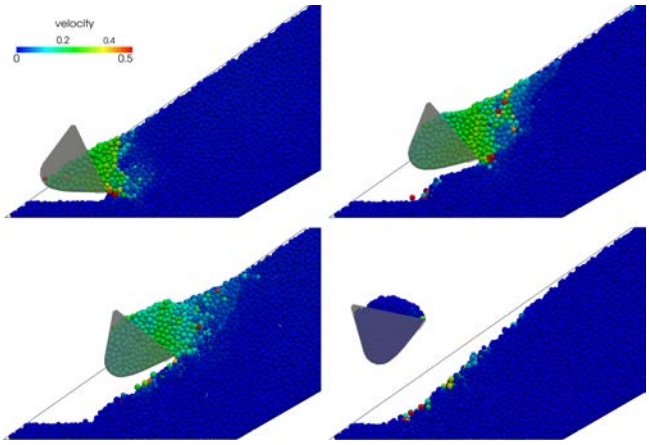

Figure 8: Snapshots from DEM particle simulation [2].

In order to demonstrate the importance of material flow for the bucket filling, Figure 9 and Figure 10 show snapshots from trajectories types A and B plotted with a vector plot of the particle velocities.

Figure 9 shows two snapshots from a simulation with trajectory type A, with a large exit height and high bucket fill factor. During the forward and lifting motion, the material moves together with the bucket. The shape of the pile is according to expectations. The theoretical approach works very well in that phase, shown on the left in Figure 9. However, when lifting the bucket out of the material and tilting back at the end of the trajectory, some material is lost (right in Figure 9) due to the fact that the granular material can only support a certain angle of repose. Excess particles flow back in an avalanche flow.

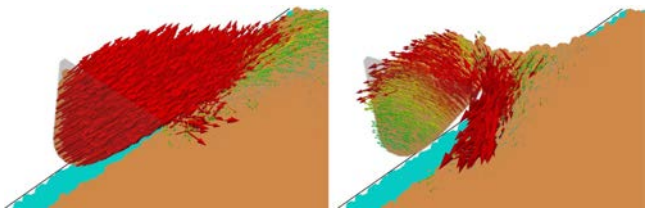

Figure 9: Bucket filling trajectory type A: particle velocities (arrows) during the lift motion (left) and at final tilt (right). Brown: current shape of the pile, light blue: initial shape.

In the case of trajectory type B this effect is even more pronounced. Figure 10 shows a snapshot from a simulation with a large bucket fill factor. Two lines drawn on top of the plot indicate the material that flows underneath the bucket and forms a new angle of repose. This observed material loss has an impact on energy efficiency of the working process, since the excess material has been pushed forward and lifted upwards by the bucket, requiring mechanical energy, but instead of keeping it in the bucket it flows back onto the pile. A way to prevent or at least minimize this loss of material would be to combine a forward motion together with tilt-in, however still adhering to the general rule of not pushing the bucket's bottom into the pile.

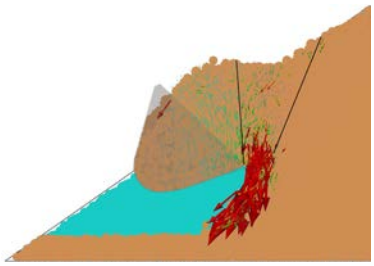

Figure 10: Bucket filling with trajectory type B: particle flow (arrows). The two lines indicate the material that flows underneath the bucket.

Figure 18 shows that there is also a loss of material during bucket retraction: when the filling of the bucket is finished, the wheel loader starts accelerating backwards to get out of the pile. In our simulations the jerk is significantly higher than what is possible in reality, which means that the simulation exaggerates the magnitude of this loss. In any case, the amount of material lost through outflow during bucket retraction is difficult to predict by conventional means.

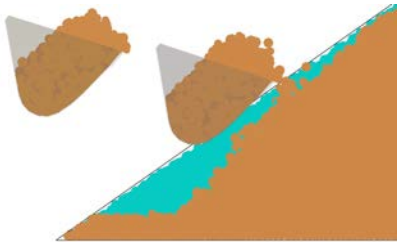

Figure 11: Material loss during bucket retraction.

Figure 18 also displays that the material does not flow fully into the bucket, but remains near the cutting edge instead. It would be desirable to fill the bucket more evenly, which human operators achieve by the "flipping movement", i.e. by briefly and distinctly activating the tilt function, possibly in combination with a longitudinal jerk [2].

3.11 Analysis with simple performance indicators

With the results from the particle simulations published and discussed in [2] and the work with Dynamic Programming at that time not yet finalized we wanted to examine how far it is possible to use the results to compare different bucket designs and different bucket filling strategies in a reasonably fair manner with simple calculations [1].

The natural choice as performance indicator of a trajectory is simply the amount of work that has been invested during its execution. A fair comparison demands acknowledging the different bucket loads achieved: as mentioned previously the obtained bucket load always deviates from the target value – by how much is specific for the trajectory type and the parameter settings.

The relationship between bucket load (in t) and invested work (in kJ) is linear only for the lifting part of a trajectory,

but non-linear for the filling sequence as a whole. This means that while one way to compare trajectories of similar fill factors is to calculate the specific work invested (in kJ/t), a fair comparison between trajectories of significantly different fill factors is more difficult to achieve. It is therefore recommended to plot performance indicators against respective bucket fill factor (i.e. the ratio of achieved bucket load and the bucket rating according to ISO 7546), also when the performance indicator is already normalized to bucket load, such as specific work invested.

We show in [1] that the pure value of the specific work invested in bucket filling is not relevant because it disregards the fact that the achieved result is not only the bucket load itself but also the potential energy achieved by lifting the bucket including its load – which in turn impacts the remainder of the working cycle shown in Figure 1. The height at which the bucket is retracted from the gravel pile thus affects the total energy efficiency of the loading cycle, because it dictates the amount of lifting work still to be performed during driving towards the load receiver, which in turn may affect the driving pattern itself (extension of V to Y). A fair performance indicator must therefore credit the lifting work performed during bucket filling.

One might assume the ratio of the potential energy achieved (affected by bucket load and bucket height) to the work invested can be a suitable performance indicator but we show in [1] that is a poor choice (at least for short loading cycles) because it implies that the sole utility of a bucket filling sequence is a load being lifted. It totally neglects the utility of the bucket actually being filled, which will always require a certain amount of work.

Besides, while the load lifting included in a bucket filling sequence should be credited, it is wrong to assume it to be essential. In a typical short loading cycle there is ample opportunity for lifting to be performed in the phases 2 to 5 (Figure 1) – and in a typical load & carry cycle (not studied here) the lifting is performed right before reaching the load receiver after a transport phase covering a certain distance. To end bucket filling at too great a height in short loading cycles is impractical because the remaining lift work might be so little that even the shortest driving phase to the load receiver will be too long. This might be a waste, also depending on the general question whether it is more efficient to drive and lift concurrently or sequentially (which in turn must be answered for each machine type, i.e. there might be differences for a conventional loader versus the electric series hybrid we have studied). Furthermore, driving and steering a wheel loader with a bucket fully loaded and raised high gives poor machine stability. Most operators therefore raise the bucket to unloading height as late as possible in the cycle, i.e. as close as possible to the load receiver. This also means that loader operators usually don't leave the pile at too great a bucket height (generally not above the position where the lifting arms are parallel to the ground). The discussed ratio of potential energy achieved and work invested however rewards higher bucket exit heights over lower values for the same bucket load, which shows that it is not a suitable performance indicator [1].

With the previously discussed measures being unsuitable performance indicators because they either ignore the utility of load lifting included in a filling sequence or over-emphasize it, we reason in [1] that a solution might be to isolate the actual bucket filling by subtracting the lifting included. Since this is a continuous and compound process it is not easily possible to calculate the actual amount of work spent for filling vs. lifting. One practical approximation is to subtract the potential energy achieved at the end of a bucket filling sequence from the work invested for executing the trajectory (Figure 12).

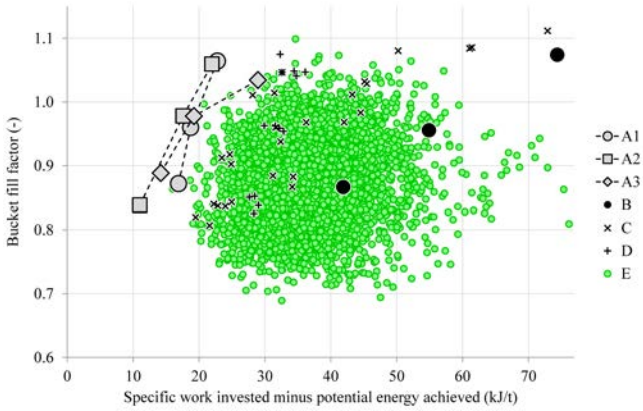

Figure 12: "SPI_1", Potential energy achieved during bucket filling subtracted from the specific work invested.

Another possibility is to do the opposite and acknowledge the lifting part, but put it into the context of a full loading cycle. As reasoned previously the bucket filling should not be considered in isolation but rather as one phase in a complete loading cycle. For unloading in phase 6 to happen the bucket needs to be lifted sufficiently in the phases prior to this. Any lifting work that has not been included in bucket filling (phase 1) needs to be performed during driving towards the load receiver (phases 2-5). In the proposed performance indicator the potential energy increase remaining after bucket filling is added to the work invested for executing the trajectory (Figure 13).

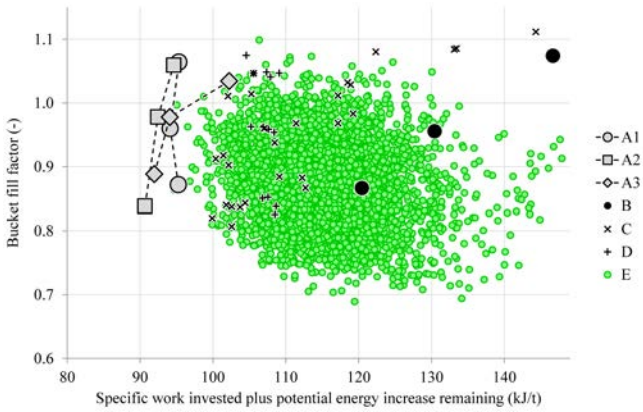

Figure 13: "SPI_2", Potential energy increase remaining after bucket filling added to the specific work invested.

It can be argued which performance indicator captures the truth better: SPI_1 that deducts included lifting from the

bucket filling sequence by subtracting the amount of potential energy achieved at the end of the trajectory or SPI_2 that acknowledges lifting by adding the increase in potential energy still remaining to be achieved in the subsequent phases of the loading cycle. In both indicators the lifting work invested to achieve an increase in potential energy is assumed without losses, which is a notable simplification.

Also, neither SPI_1 nor SPI_2 as published in [1] include the driveline work, which means that bucket filling sequences resulting in low bucket loads are not suitably punished for poor transport efficiency (basically: the longer the transport section in a working cycle the better it is to fill the bucket as much as possible).

With the results from the Optimal Control simulations at hand a new simple performance indicator SPI_3 has been formulated considering the transport work simply as rolling resistance multiplied by the distance driven, with the former assumed as 3% of the machine weight (calculated separately for loaded and unloaded). The result is shown in Figure 14.

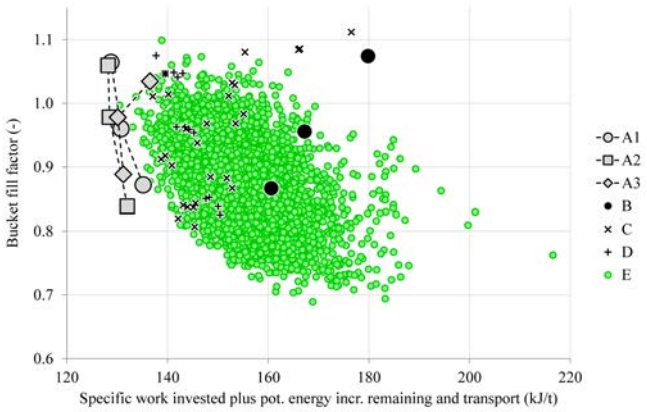

Figure 14: "SPI_3", Transport and potential energy increase remaining added to the specific work invested.

All simple performance indicators give essentially the same picture: the "Slicing cheese" trajectory type A appears superior to any other bucket filling strategy, especially compared to the B-type's "Just in & out" style, which performs strikingly poor.

The argument is sometimes made that such a type B trajectory must be surely efficient as very little work is invested into lifting the load and the work required for penetration is free because (at least initially) the momentum of the moving wheel loader is used. Of course, this work is not really "for free" in most cases, because accelerating the machine to a certain speed requires work, meaning that the energy demand is just shifted in time. However, there is at least one case where this is partly true: when the wheel loader approaches from a downhill slope and the operator instead of using the service brakes slows down by letting the bucket penetrating the gravel pile, thus using the gravel pile as an "external brake". If the machine in question is a hybrid then it needs to be analyzed in detail whether recuperative or regenerative braking would have been the better choice from an overall energy management perspective.

However, for realistic speeds the loader's momentum is not sufficient to penetrate the gravel pile as deep as needed. Furthermore a smooth penetration requires constant or even increasing rim pull, but in reality the effective forward force decreases due to the increasing resistance the deeper the bucket penetrates the gravel pile.

In [1] we show that the type B strategy is not very efficient when correctly accounting for the penetration work, even without having credited the lifting work included in all other trajectory types. In a thought experiment we investigated how the different bucket filling strategies would compete if the work required for initial bucket penetration actually was for free. Little surprising, in this thought experiment the B-type trajectories are heavily favored as per definition all penetration work is performed in one go in the beginning of this bucket filling strategy. But again, it is not realistic.

3.12 Optimal Control

In this section we describe the Optimal Control utilizing simulation of a loader in a complete working cycle. To begin with, it must be noted that the machine studied in simulation is an electric series hybrid wheel loader. All conclusions with respect to optimality of certain bucket filling strategies might need revision when a conventional wheel loader is considered. The series hybrid loader has previously been hinted on in [8] and briefly described in [9]. The machine is equipped with a downsized diesel engine, and four electric machines as can be seen in Figure 15.

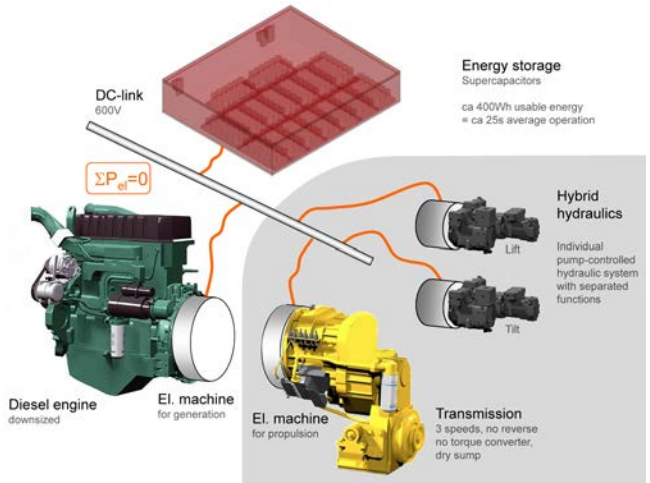

Figure 15: Electric series hybrid wheel loader [9]. *Grey background: simulated subsystems.*

In the series hybrid machine the main power systems are mechanically decoupled from each other and the main concern in terms of system control is the sum of electric power on the DC link. In contrast to this, in a conventional machine both hydraulics and driveline are mechanically coupled to each other and connected to the engine, which presents several challenges in terms of energy efficiency and operability [6]. The reason for having chosen the series hybrid for this study is that we did not want the machine system's lack of degrees of freedom stand in the way of exploring the optimal bucket filling strategy.

Dynamic Programming has been used as Optimal Control method. The specific implementation details can be found in [7], but some basic information is necessary to include here: the algorithm developed seeks the global optimum in terms of fuel efficiency, though for practicality converted to electrical actuator energy efficiency – thus excluding the generator set and energy storage, which would be a topic on its own. The simulated subsystems have been marked with a grey background in Figure 15.

For computational efficiency the Optimal Control has been split into four parts:

In part 1 bucket filling, phase 1 in Figure 1, is handled by choosing between the various bucket trajectories. Backward simulation is performed to calculate the energy required for following the trajectories without deviation.

Phases 2 to 5 are covered by the Dynamic Programming algorithm in part 2. Each bucket trajectory from part 1 gives a starting point for part 2, unique in bucket position and load. Optimal Control is performed to find the optimal, i.e. energy-minimizing way to get from the starting point to the point of unloading while maintaining cycle time and thus productivity.

Part 3 covers phase 6, bucket emptying. Ideally this should have been included in part 2 and thus treated individually for each trajectory, because of the different bucket loads. Instead, Optimal Control has been performed one time only to find the minimal energy required to empty a bucket with the load achieved on average with the simulated trajectories. The effect of this is that working cycles with comparatively low bucket load are not suitably punished for the low transport efficiency. However, it is estimated that the impact on the overall conclusions from this study is not severe.

Finally, in part 4 Optimal Control has been performed once for phases 7 to 10, as independent on the chosen bucket filling trajectory from this point on the loader starts always in the same position with the same bucket load (zero) and stops at the same position in front of the gravel pile, ready to start a new working cycle.

The details of the driving cycle in parts 2 and 4, i.e. how long to drive backward/forward, where to reverse, when to steer etc., have not been subject to optimization. Instead, we have used the values from the most energy-efficient operator in the measurements reported in [15] and refer otherwise to previous work [3][4].

The total energy requirement is the sum of required energy for all four parts. After having computed this for all 5781 bucket filling trajectories the optimal strategy has been determined as the one with the lowest specific work for the complete working cycle, i.e. the lowest ratio of total energy requirement and bucket load. Figure 16 shows the results.

Figure 17 shows the winning trajectory A_0_2 in front of the Top 10 (in terms of electrical actuator energy efficiency) trajectories in blue, with all simulated trajectories in the background in grey. The table below lists all Top 10 trajectories and provides details about their performance.

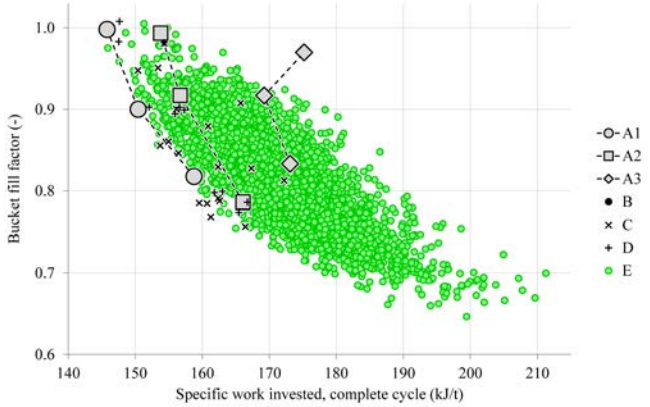

Figure 16: Simulation results for all bucket filling trajectories continued in a complete working cycle.

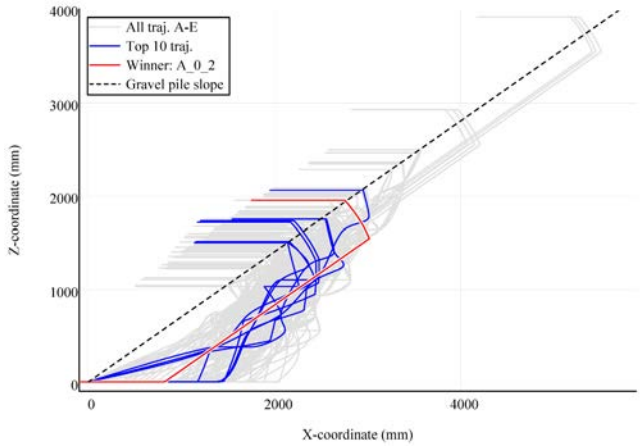

Figure 17: Winning trajectory A_0_2 in front of Top 10.

	Optimal Control, complete cycle		Simple performance indicators		
Trajectory name	Rank (#)	Delta to #1 (%)	Rank SPI_1 (#)	Rank SPI_2 (#)	Rank SPI_3 (#)
A_0_2	1		56	10	3
E_4423	2	0.09	779	146	36
D_0_2	3	1.19	1843	543	133
E_4422	4	1.25	700	148	45
D_2_2	5	1.28	1230	216	37
E_4299	6	1.91	1913	525	111
E_5780	7	2.51	1195	271	70
E_6171	8	2.72	124	20	10
E_5034	9	2.80	552	129	46
E_4426	10	2.91	798	209	78

3.13 Discussion of the simulation results and conclusions

It appears that all top trajectories are emulating the winning "Slicing cheese"-type trajectory A_0_2 to a certain degree (Figure 17).

The table above also includes the results of the simple performance indicators described previously. It show that according to the simulations the second to best trajectory E_4423 is only 0.09% less energy efficient than the winner A_0_2 (stated in relation to the absolute value of A_0_2's electrical actuator energy efficiency), however using the simple performance indicator SPI_2 the E_4423 trajectory is ranked #146 and even worse when using SPI_1 (#779). It is apparent that SPI_2, which adds the remaining increase in potential energy to the work invested in bucket filling, is a slightly better (though still not suitable) approximation than SPI_1, which subtracts the potential energy gained in bucket filling from the work invested. Both, however, suffer from not having the transport work included.

The table shows that the new SPI_3 performs best among the simple performance indicators since all the Top 10 trajectories from the simulations are also ranked high by the SPI_3 (all are within the Top 3%). However, it has become clear that these simple performance indicators have significant limitations.

From the results presented above we can conclude that with regard to bucket filling strategy the type A "Slicing cheese" trajectory is a good choice to start with – and certainly is an easy to remember mental model for the wheel loader operator – but also that moderate deviations from that ideal path don't seem to matter too much in terms of total energy efficiency.

However, it should be noted that the simulations conducted contain some significant simplifications. There are thus a number of potential improvements, which will be covered in the following two sections.

3.14 Potential improvements in trajectory generation

All trajectories that have been found valid for inclusion in further simulation are portrayed in Figure 18.

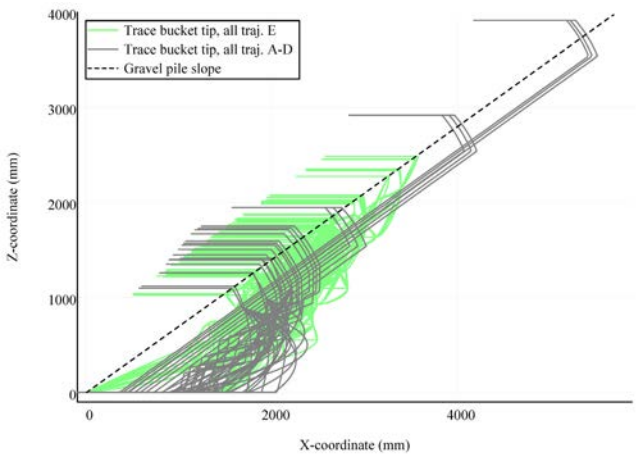

Figure 18: All simulated and valid bucket tip trajectories.

The additional attribute "valid" needs explanation: all bucket trajectories of types A to D have been generated by moving the corresponding machine actuators, lift and tilt cylinder as well generating a forward motion through simulated wheel rotation. Transmitted through the linkage these actuator movements automatically resulted in valid bucket trajectories. This has not been the case for the bucket trajectories of type E generated in the exhaustive search. Since only the bucket has been moved through the pile, with focus on the position of the bucket tip and bucket angle, several possibilities for invalid trajectories can occur (and have done so in sizeable amounts):

To begin with, a monotonically increasing (x, z)-position of the bucket tip together with a monotonically increasing bucket angle does not automatically lead to monotonically increasing actuator positions of the machine. As can be seen in Figure 7, even though the bucket tip continuously moves up and forward, the corresponding lift and tilt cylinder as well as the complete machine still can be forced to move backward on occasion, depending on the geometry of the loader linkage. These results have *not* been filtered out by us, because we reasoned that either the corresponding energy requirement will automatically punish such behavior – or, in case of actually lower energy demand, a partly or fully automated machine will be able to execute such trajectory. Also, a different kind of loader linkage might be able to produce these bucket motions with more benign actuator movements. We therefore decided to not exclude trajectories purely based on such unconventional machine actuator movements. (However, this latter consideration is inconsistent with the fact that we then ran the Optimal Control algorithm to accomplish the actuator motions that are required for today's linkage. Forcing actuators to move back and forth requires more energy than continuous forward motions, which means that these bucket trajectories might have been punished with higher energy demand purely because we employed today's wheel loader linkage to accomplish them.)

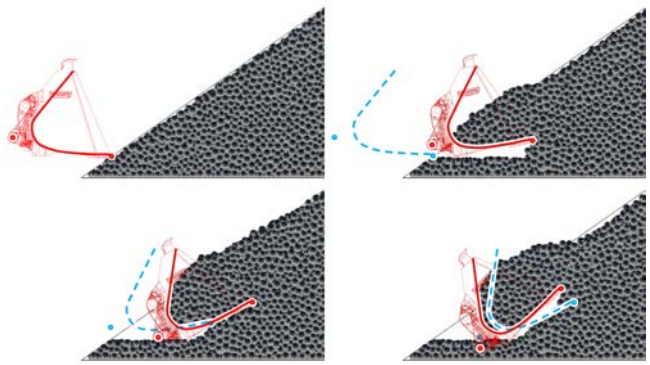

Figure 19: Example of flawed type E trajectory.

Secondly, if, as has been done in the algorithm generating the type E trajectories, "monotonic increase" is mistakenly considered sufficiently realized by adding non-negative increments to the (x, z)-position of the bucket tip and bucket angle, a null-increment in the former can still result in an actual decrease of the absolute value of a bucket tip coordinate when at the same time the bucket angle changes,

as can be seen in Figure 19. In addition, not considering a real linkage is again a disadvantage, because otherwise it would have been clear that the bucket normally cannot be lowered or raised (i.e. changed vertical position of the lower hinge pin) with also changing the horizontal position. Furthermore, Figure 19 shows an example of "bottom push" meaning that the bottom of the bucket pushes against the gravel pile, which leads to unnecessary high actuator forces and consumes energy while accomplishing nothing useful. The generating algorithm was supposed to filter these out but insufficient modeling of the outer bucket surface let several trajectories pass that should have been rejected.

Finally, trajectories can be invalid because they require too high actuator forces or too high actuator power output. The former can be filtered out before running a simulation, while the latter might only present themselves during simulation when they occur in combination with the power demands of other actuators or machine systems. None of the type A to D trajectories fell into this category, while a significant amount of type E trajectories had to be rejected. In order to not filter out too much we reasoned that too high forces or power requirements can be taken care of the machine inertia if they only occur briefly. Exceeding the performance limit of the driveline and working hydraulics is allowed for 3 time steps á 0.05s (consecutive or not), while no such concession has been made for negative rear axle load resulting in tip-over of the machine. In total 656 trajectories of type E had to be removed due to such limit violation. Unfortunately also all trajectories of type B and some type C and D trajectories had to be filtered out. The table below accounts for the reasons.

	Limit violation that triggered rejection		
Trajectory name	Hydraulics (seconds)	Driveline (seconds)	Rear axle load (-)
B_0		0.45	
B_1	0.20	0.60	
B_2	0.40	0.70	< 0
C_0_0_1	0.75	0.20	< 0
C_0_0_2	2.60	1.50	< 0
C_0_1_1	0.60		< 0
C_0_1_2	2.45	1.05	< 0
C_0_2_1	0.65		< 0
C_0_2_2	2.80	1.20	< 0
C_1_0_2	0.35	0.35	< 0
C_1_1_2	0.50		< 0
C_1_2_2	1.45	0.05	< 0
D_3_2		0.20	

All trajectories that have been simulated fulfill basic criteria such as targeted bucket fill factor range and no "bottom push". Of these 5781 trajectories only 4640 of type E are feasible with the loader linkage presently available, while all 51 trajectories of type A to D have been found valid up until this stage of the process. After having simulated these in total 4691 trajectories only 4022 of them have been found to be feasible when the machine's force and power limitations are taken into account.

In hindsight, the mix of theory-based trajectories of type A to D (51 in total) and exhaustive search-based type E (5430) should have been more balanced. We had been given a limit of how many trajectories to simulate on the computer cluster at Fraunhofer ITWM in Kaiserslautern, which we happened to generously exceed already, but perhaps 500 less of type E trajectories (−9%) and the same amount added as types A to D (+1000%) could have led to a more thorough exploration of the theory-based bucket filling strategies. The simulation results suggest that the "Slicing cheese" strategy of type A is a good choice, therefore it would have been useful to at least include additional trajectories of this type with more bucket fill factors and bucket exit heights than just the 3 tested, resulting in 9 different type A trajectories in total.

The outcome of the type E trajectories has been somewhat disappointing, mainly due to the coarse discretization grid. Our hypothesis is that a finer grid of about 10mm in (x, z)-position of the bucket tip and 1° in bucket angle would have resulted in the type E trajectories in Figure 17 following the type A winner more closely. Or perhaps there is a different optimal bucket filling strategy altogether that has not been found due to the coarse discretization grid. However, the amount of trajectories would have grown dramatically. Increasing the spatial resolution by factor 3 and the angle by factor 8 theoretically means a 72-fold increase in the amount of trajectories (not all of them necessarily valid). Our study already required a week of computation with the computer cluster solely dedicated to our task. But again, with the trend to cloud computing this might not be an issue anymore.

One solution, instead of increasing the grid resolution, could be to apply the discretization to the actuators rather than the bucket position and angle. This means controlling the type E trajectories in the same way as types A to D, i.e. through moving the linkage by means of the hydraulic cylinders (lift and tilt) and advance the complete machine by rotating the wheels. This would also solve the current issue of actuator zigzagging instead of the desired monotonical increase. On the other hand, perhaps zigzagging is the key to even more efficient bucket filling. To rule this out by definition might be a mistake. Nevertheless, including the load linkage in the generation of type E trajectories by means of an exhaustive search would lead to fewer invalid results.

3.15 Potential improvements in simulation setup

The initial, consciously made decision to decouple the DEM particle simulation and to let the bucket follow predefined trajectories of course has the consequence of a significant probability that the required actuator forces are either higher than the capability of the respective actuator or there is

unused potential for increased performance, which might result in increased bucket filling efficiency.

In real work the human operator adapts to the machine and its working environment, which should also be emulated in simulation. We have reasoned previously that the computational cost would be far too high to run an all-inclusive simulation, but perhaps a simple operator model for the decoupled particle simulation would be sufficient. For example, the bucket filling rules from [12] could be implemented to prevent the actuators from exceeding their respective performance limit: lift when rim pull is too high, tilt when lifting pressure reaches maximum, etc. Also, the aforementioned "flipping movement" at the end of bucket filling together with realistic longitudinal machine control can be taken care of in such a simple operator model.

With regard to unused potential for increased performance it is far from certain that fully utilizing the capabilities of all actuators would lead to highest efficiency of bucket filling. Also slower actuator movements are worth investigating.

Finally, it has already been mentioned that bucket emptying as currently covered in part 3 of the machine simulations should be integrated at the end of part 2, to include it in the Optimal Control considering each individual bucket load.

4 Physical testing

4.1 Setup and previously reported results

Having completed the simulation study the question arises if this is also how human operators fill a bucket in real work. The results from various physical testing of wheel loaders are available for such endeavor, for example [13] with 18 operators participating, which has been further analyzed in [14], and the subsequent study presented in [15] with 73 operators participating, further analyzed in [16]. The large number of test participants, operating in real work in three different bucket loading applications makes the latter study especially attractive. The data presented in the following are therefore taken from this measurement campaign even though the machine used was not the series hybrid or even of the same size. A detailed description can be found in [15].

All participants are either Volvo employees or operators at customers and have a different skill level (novices with less than 10 hours operating experience, average operators and experienced professionals). In all analyses the number of operators is considered to be 80 because three of the 73 participants have been asked to also operate at a different pace than what they would normally do (both slower and faster), thus emulating the behavior of a different person.

All operators used the same wheel loader in three machine applications:

- bucket loading of gravel onto a hauler in a short loading cycle (typical rehandling, performed under the roof of a large tent to keep conditions stable)
- bucket loading of gravel to a hopper in an uphill load & carry cycle (longer transport than first application, performed outside)
- bucket loading of rock onto a hauler in a short loading cycle (more difficult bucket filling than first application, performed outside)

In the paper at hand we have only used the results from the first application, bucket loading of gravel in short loading cycles. Figure 20 shows all operators' performance in terms of average cycle fuel efficiency over their respective average cycle productivity. The best performing operator has been chosen as "Shadow operator" (i.e. the one to compare with). It can be seen in Figure 20 that the operators' performance varies substantially, which would have been expected given their different skill and experience level. However, papers [15] and [16] show that also the performance of each single operator varies significantly between cycles.

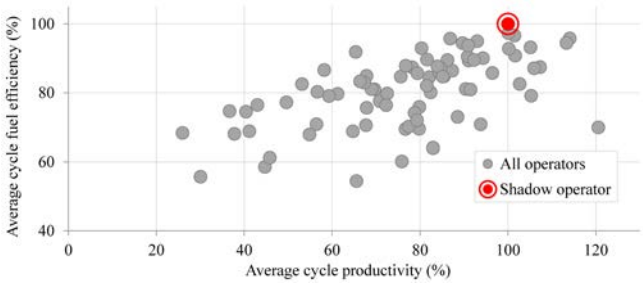

Figure 20: All operators' average cycle fuel efficiency over respective average cycle productivity. Data from [15].

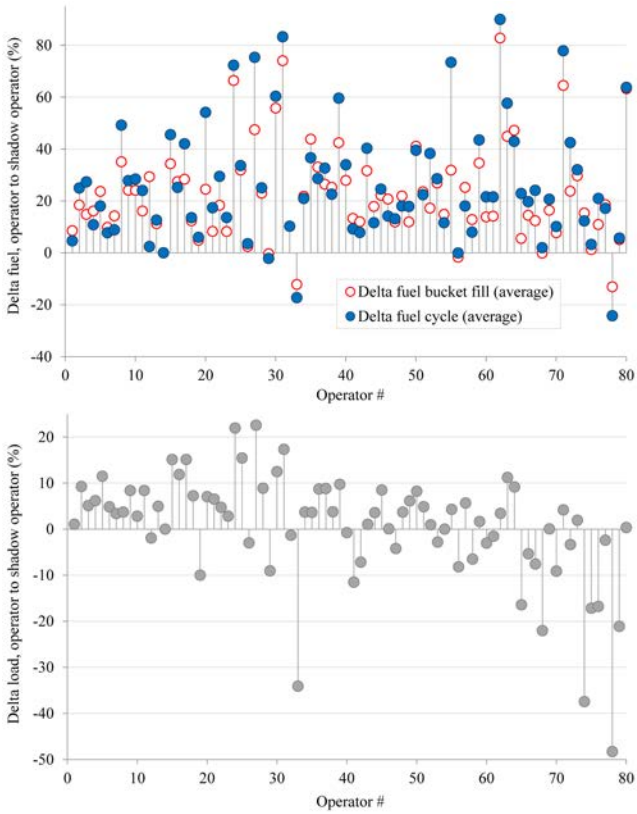

Figure 21: Top: Average fuel consumed in a complete cycle vs. only bucket filling (baseline is shadow operator). Bottom: Average bucket load relative to shadow operator. All data from [16].

The diagram in the top of Figure 21 shows with blue dots how much more fuel each operator consumes on average per cycle in comparison to the Shadow operator (normalized to 100%. The red rings in the plot show how much the bucket filling phase contributes to that additional fuel consumption per cycle. Some operators manage to consume less fuel than the most efficient Shadow operator, but the bottom diagram reveals that this is due to an even lesser bucket load (i.e. in terms of fuel efficiency they are still worse than the Shadow operator as their decrease in fuel consumption is less than their decrease in bucket load). Figure 21 confirms previous reporting [6] that bucket filling is the predominant phase in a short loading cycle when it comes to fuel efficiency.

In the context of the paper at hand it is of interest to examine whether the data from [15] can support the conclusion that following the "Slicing cheese" strategy for filling the bucket leads to an efficient (if not the most efficient) short loading cycle for a wheel loader working in gravel.

4.2 Analysis of bucket filling trajectories

The large number of data acquired in this measurement campaign necessitates an automatic analysis, one important aspect of this being the ability to automatically extract the bucket filling phase from a continuous series of time data. Ideally the location of the machine in relation to the gravel pile would be among the signals recorded (and in high resolution). However, this has not been the case. In any case the location of the gravel pile is ever changing since material is constantly removed by the wheel loader, yet more material might fall down from the pile's top like a landslide.

A solution might be to record the loading cycle on video and let automatic motion capture take care of locating both bucket and pile. In the simplest version this would be done from the side of the pile, but the constantly changing shape of the gravel pile's front might be a problem (and a loading pocket with transparent side walls seems far-fetched). Filming from a different angle with stereo cameras or time-of-flight cameras might solve this problem, but requires sophisticated image analysis. The measurement setup we used did include a forward-facing camera in the wheel loader cab, but the frame rate of 1fps and the fish-eye lens employed make the recorded video feed unsuitable for precise automatic determination of when and where bucket filling started. Also, the camera is moving with the machine and the image is therefore somewhat shaky.

Solutions for automatic detection of loading cycle phases such as bucket filling have been published [13][17][18], though it turned out that each of the underlying assumptions have been violated in our case. For example, it is not possible to let the gear shift F2→F1 (forward 2 down to 1) mark the beginning of the bucket filling or even use it to search back in time to find the beginning, because some operators such as the Shadow operator "EP15" prefer to manually activate the kick-down function. Also, each operator is unique in how deep the gravel pile is initially penetrated and how fast – both factors affect the resistance and thus the required traction force, which in turn affects when the automatic kick-down function triggers the gear shift. Basing the beginning of the bucket filling phase on this gear shift is therefore not reliable.

Another possibility seems to be to set the gear shift F1→R2 (forward 1 to reverse 2) as the end of bucket filling and normalize all filling sequences to this point in time and space. However, all operators penetrate the pile differently and to unique depths, which makes it impossible to use this to find when the bucket filling actually started.

In [13] the beginning of bucket filling is defined by the operator laying the bucket flat on the ground and not touching the hydraulic levers again until after the initial penetration of the gravel pile. In the measurements used here some operators lay the bucket down very early, farther away from the gravel pile than others – thus invalidating this possibility, too. In addition, we discovered that due to the specific setup for data acquisition the recorded signals for lift and tilt position have a varying and overall rather poor sampling rate, mostly 10Hz but sometimes as low as 1Hz.

Finally, a significantly increased torque output of the engine might indicate the beginning of bucket filling – yet again, all operators act differently and while some almost operate in a stop-motion fashion others keep all actuators moving all the time. The torque output of the engine is determined by the requirements of hydraulics and driveline, which in turn both are largely affected by the operator's use of the machine.

Having run out of options the beginning of bucket filling and the location of the gravel pile have therefore been estimated manually using the recorded test data (when is the bucket laid down, when are gears shifted, etc.) in combination with the video feed (however poor the image quality and frame rate). To cope with the amount of data this has only been done for a few selected operators, among them the Shadow operator "EP15" (Figure 22).

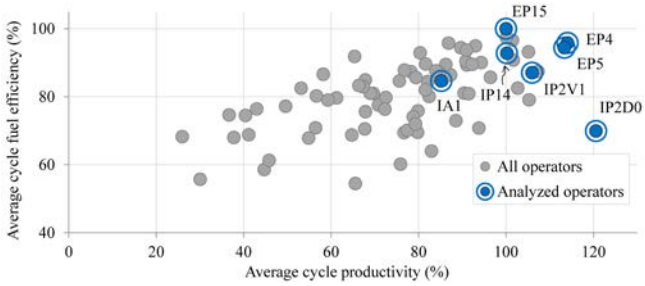

Figure 22: Manually analyzed operators from [15].

In the following only the bucket filling trajectories of three operators will be discussed (all of them professional operators at customers): "EP15", "EP4" and "EP5". The latter have both displayed approximately the same average cycle productivity and average cycle fuel efficiency, as can be seen in Figure 22. All trajectories in the following figures appear stair-shaped, however not necessarily because the operator controlled the bucket that way (like in a type D bucket filling strategy), but due to the low sampling rate of the lift and tilt position signal.

Figure 23 shows the trajectories of the Shadow operator.

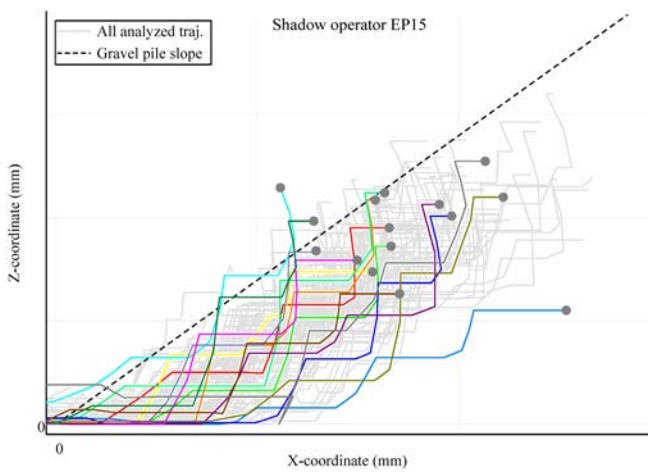

Figure 23: Bucket filling trajectories of the Shadow operator "EP15".

No clear pattern emerges in Figure 23, which may lead to the conclusion that his operator seems not to follow any specific bucket filling strategy at all – even when accounting for uncertainty in the manually estimated location of the gravel pile. Keeping in mind that this operator has been the on average most energy-efficient one of all participants, a possible explanation can be that the gravel pile's front shape changed significantly between the cycles. It is certain, that the gravel pile encountered by the various operators is different to the idealized one from the simulations. The variance between the bucket trajectories might be a sign of the Shadow operator's ability to adapt to the changing conditions better than all other participants. Lacking information about the changed shape of the pile it is difficult to perform further analysis.

Figure 24 shows the trajectories of operator "EP4" who showed higher average cycle productivity then the Shadow operator, but at the cost of slightly lower average cycle fuel efficiency (see Figure 22). These bucket trajectories do look like "Slicing cheese" and the offset to the gravel pile can be explained with material being removed.

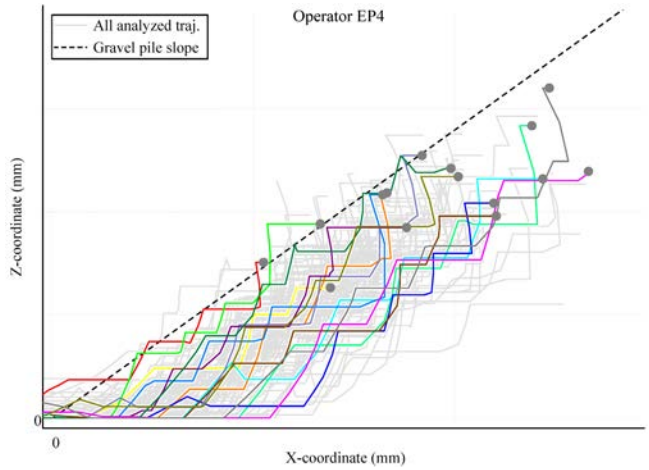

Figure 24: Bucket filling trajectories of operator "EP4".

Operator "EP5" shows a performance almost identical to "EP4" (see Figure 22) and also fills the bucket in a similar "Slicing cheese" manner, which can be seen in Figure 25.

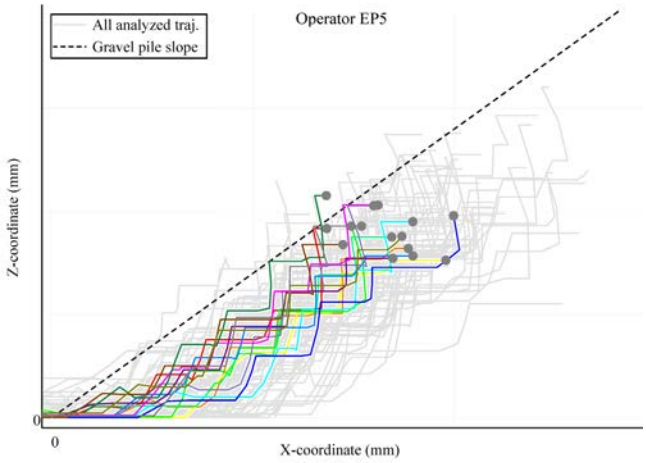

Figure 25: Bucket filling trajectories of operator "EP5".

It turned out that not only were "EP4" and "EP5" working for the same company but they are, in fact, brothers. Their uncle was also among the participants as "EP6", with a performance rivaling that of the Shadow operator (same average cycle productivity but slightly less average cycle fuel consumption).

4.3 Conclusions from physical testing

Imperfections in the measurement setup, at the time seeming negligible, prevent us from reaching solid conclusions. However, several high-performing operators produce bucket filling trajectories that are reminiscent of the type A "Slicing cheese" strategy, which we take as (tentative) support for our hypothesis that this strategy is a good, if not optimal choice.

The Shadow operator's superior performance might indicate that in addition to a general bucket filling strategy to follow, constant adaptation to the ever changing gravel pile is the key to the highest energy efficiency in short loading cycles.

5 Conclusions and outlook

In this paper we have presented the compounded results from several years of applied research into energy efficiency of wheel loaders. The focus has been on finding the optimal bucket filling strategy through simulation. We have discussed the ideal approach of an all-inclusive comprehensive simulation in an overarching loop with Optimal Control of the complete machine – and explained why (at least for now) simplifications are necessary. The results from these simulations have been compared to both simple calculations and measurement results from physical testing.

With all the evidence gathered we are confident in stating that the "Slicing cheese" bucket filling strategy (designated as "type A" throughout this paper) appears to be a good choice. Theoretical support for this statement is given by the

simulation results showing that a type A trajectory has been selected as winner by the Optimal Control algorithm and that the nine next best performing trajectories all appear to approximate the winning one. We find also practical support in the measurement results of two top-performing operators.

However, we cannot be completely certain, because the simulated bucket trajectories have not covered the complete parameter space and the physical testing requires improvements, too.

Studying both simulation and measurement results we tentatively conclude that the energy efficiency during bucket filling appears robust as long as the general trend is a bucket trajectory of type A "Slicing cheese".

This is a welcome (though still tentative) confirmation of what professional machine instructors have been advocating for many years.

The true efficiency of the type B "Just in & out" strategy depends on how much additional propulsion work needs to be invested for building up machine speed prior to ramming the pile. In most cases this bucket filling strategy should be avoided, though the general idea of utilizing the machine's momentum for initial penetration has merit, if applied correctly.

In the future the envisioned all-inclusive simulations might become possible through cloud computing. When this is the case we suggest generating type E trajectories in a revised exhaustive search with vastly improved discretization – and simulating these with an adaptive operator model in the loop.

Refined physical testing is another task to be performed in future work, with improved data acquisition and stricter control of the material, including shape of the gravel pile.

References

[1] R Filla. Evaluating the efficiency of wheel loader bucket designs and bucket filling strategies with non-coupled DEM simulations and simple performance indicators. *Schriftenreihe der Forschungsvereinigung Bau- und Baustoffmaschinen: Baumaschinentechnik 2015 – Maschinen, Prozesse, Vernetzung*, 49:273-292, 2015. http://dx.doi.org/10.13140/RG.2.1.1507.1201

[2] R Filla, M Obermayr, and B Frank. A study to compare trajectory generation algorithms for automatic bucket filling in wheel loaders. Proceedings of the *3rd Commercial Vehicle Technology Symposium 2014*, Kaiserslautern, Germany, March 12-13, 2014. http://dx.doi.org/10.13140/RG.2.1.3604.2723

[3] R Filla. Optimizing the trajectory of a wheel loader working in short loading cycles. Proceedings of *The 13th Scandinavian International Conference on Fluid Power SICFP'13*, Linköping, Sweden, June 3-5, 2013. http://dx.doi.org/10.3384/ecp1392a30

[4] V Nezhadali, B Frank, and L Eriksson. Wheel loader operation – Optimal control compared to real drive experience. *Control Engineering Practice*, 48:1-9, 2016. http://dx.doi.org/10.1016/j.conengprac.2015.12.015

[5] B Frank and A Fröberg. Establishing an Optimal Work Cycle for an Alternative Wheel Loader Concept. Proceedings of the *International Exposition for Power Transmission IFPE 2014*, Las Vegas, USA, March 4-8, 2014. ISBN 0-942220-49-8.

[6] R Filla. Quantifying Operability of Working Machines. Doctoral Thesis, Linköping University, Linköping, Sweden, 2011. http://urn.kb.se/resolve?urn=urn:nbn:se:liu:diva-70394

[7] B Frank, J Kleinert, and R Filla. On Optimal Control of Wheel Loader Actuators in Gravel Applications. Submitted to *Control Engineering Practice*, April 2017.

[8] R Filla. Alternative System Solutions for Wheel Loaders and other Construction Equipment. Proceedings of *The 1st International CTI Forum Alternative and Hybrid Drive Trains*, Berlin, Germany, December 4-5, 2008. http://dx.doi.org/10.13140/RG.2.1.3391.2801

[9] G Stein, A Fröberg, J Martinsson, B Brattberg, R Filla, J Unnebäck. Fuel efficiency in construction equipment – optimize the machine as one system. Proceedings of the *7th AVL International Commercial Powertrain Conference 2013*, Graz, Austria, May 22-23, 2013. http://dx.doi.org/10.13140/RG.2.1.2031.4089

[10] Building the world we want to live in. Volvo Spirit Magazine, 61:10-13, 2016. (URL verified May 17, 2017) https://www.volvospiritmagazine.com/wp-content/uploads/2014/02/VS61_EN.pdf

[11] A Hemami. Motion trajectory study in the scooping operation of an LHD-loader. *IEEE Transactions on Industry Applications*, 30(5):1333-1338, 1994. http://dx.doi.org/10.1109/28.315248

[12] R Filla, A Ericsson, J-O Palmberg. Dynamic Simulation of Construction Machinery: Towards an Operator Model. Proceedings of the *IFPE 2005 Technical Conference*, Las Vegas (NV), USA, pp 429-438, 2005. http://www.arxiv.org/abs/cs.CE/0503087

[13] R Filla. Study of a method for assessing operability of working machines in physical and virtual testing. *International Journal of Vehicle Systems Modelling and Testing*, 7(3):209-234, 2012. http://dx.doi.org/10.1504/IJVSMT.2012.048939

[14] R Filla, E M G Olsson, B H C von Schéele, K Ohlsson. A Case Study on Quantifying the Workload of Working Machine Operators by Means of Psychophysiological

Measurements. *The 13th Scandinavian International Conference on Fluid Power SICFP'13*, Linköping, Sweden, June 3-5, 2013. http://dx.doi.org/10.3384/ecp1392a29

[15] B Frank, L Skogh, M Alaküla. On wheel loader fuel efficiency difference due to operator behaviour distribution. Proceedings of the *2nd Commercial Vehicle Technology Symposium 2012*, Kaiserslautern, Germany, March 13-15, 2012. (URL verified May 17, 2017) http://www.iea.lth.se/publications/Papers/Frank_2012.pdf

[16] B Frank, L Skogh, R Filla, M Alaküla. On increasing fuel efficiency by operator assistant systems in a wheel loader. Proceedings of the *2012 International Conference on Advanced Vehicle Technologies and Integration*, Changchun, China, July 16-19, 2012, pp. 155-161. ISBN 978-7-111-39909-4. http://dx.doi.org/10.13140/RG.2.1.3129.1362

[17] K Ohlsson-Öhman. Identifying operator usage of wheel loaders utilizing pattern recognition techniques. Master thesis, Division of Automatic Control, Department of Electrical Engineering, Linköping University, Linköping, Sweden, 2012. http://urn.kb.se/resolve?urn=urn:nbn:se:liu:diva-78937

[18] T Nilsson, P Nyberg, C Sundström, E Frisk and M Krysander. Robust Driving Pattern Detection and Identification with a Wheel Loader Application. *International journal of vehicle systems modelling and testing*, 1(9):56-76, 2014. http://dx.doi.org/10.1504/IJVSMT.2014.059156